ETH zürich

# 17th Biennial SGA Meeting

ETH Zurich, Switzerland

August 28 – September 1

# Proceedings Volume 2

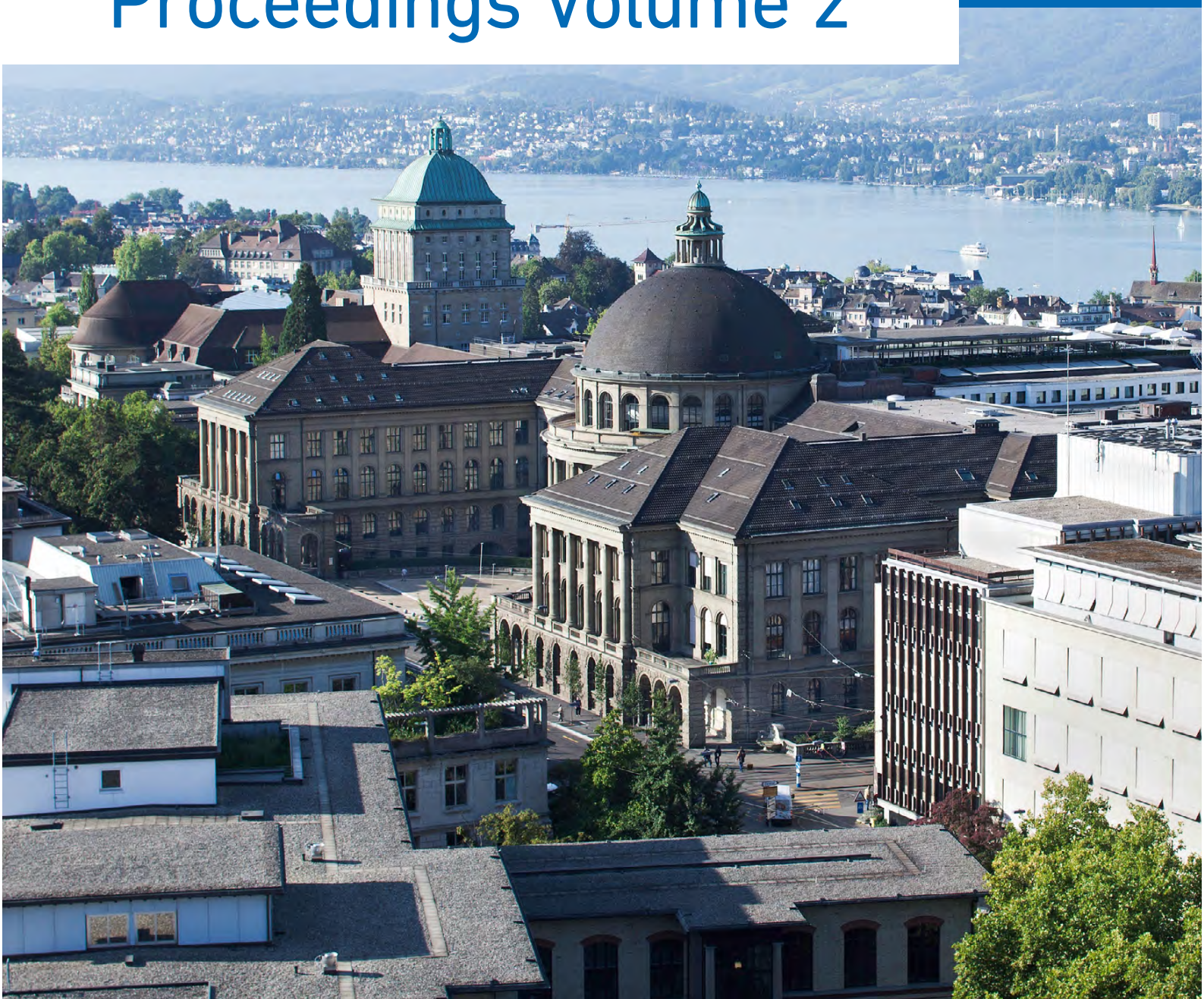

ISBN 978-2-8399-4045-0

The theme for this 17th edition is "Mineral Resources in a Changing World"

**Suggested citation for the entire proceedings:**

Proceedings of the 17th SGA Biennial Meeting, 28 August – 1 September 2023, Zurich, Switzerland, 1182 pages.

**Suggested citation for an individual paper:**

Carcamo-Valencia IC, Torró L, Proenza JA, Ramírez-Briones JS, Ayala L, Viveen W, Aiglsperger T, Baby P (2023) Cobalt-rich manganese nodules in Pliocene marine deposits of the onshore forearc Pisco Basin, Peru. In: Proceedings of the 17th SGA Biennial Meeting, 28 August – 1 September 2023, 2:280–283.

**Volume 1**

Porphyry-type and skarn deposits
Geothermal systems and epithermal ore deposits
Hydrothermal mineralization associated with highly fractionated magmas (e.g., Li, Be, Sn, W, Nb, Ta)
IOCG and magnetite-apatite deposits

**Volume 2**

VMS and seafloor mineralization
Gold: a journey from sources to precipitation sites and processes
Metallogenesis in sedimentary basins
Supergene ore forming processes

**Volume 3**

Critical minerals and geo-inspired technologies for a carbon-neutral future
Mineral deposits related to mafic-ultramafic intrusions
Ore genesis associated with alkaline-carbonatite systems
Advances in analytical techniques applied for ore deposits research and mineral exploration
New sensing instruments and processing methods in mineral exploration
Machine learning, data mining and new target generation in mineral exploration

This publication cannot be reproduced in whole or in part without the permission of The Society for Geology Applied to Mineral Deposits (SGA).

A digital version of this Proceedings is available from the SGA website www.e-sga.org

**Welcome to SGA2023,**
**Welcome to Zürich,**

Mineral Resources in a Changing World. In the context of an undeniable and threatening climate change, a suite of financial crisis, global sanitary challenges, and geopolitical tensions have stamped in a snowball effect the start of the XXI$^{st}$ century. Yet, we contend that an optimistic and united approach to lead the "Green New Deal" is possible. Thus, we have prepared a conference program comprising (1) the presentation of the latest findings in ore deposit and critical material research, (2) invited talks by plenary speakers to bring concrete insights and inspiring solutions for the challenges our economies need to face and solve in our acute awareness of climate change mitigation, and a reasoned exploitation of resources with optimal management of the environment, and (3) lively and enthusiastic scientific and social exchange between all participants from early-career researchers and students to high-ranking industry delegates and government agency representatives.

We wish you an instructive and rewarding 17$^{th}$ Biennial Meeting of the SGA.

**Your Local Organizing Committee**

| | |
|---|---|
| Conference Chairs | Cyril Chelle-Michou (ETH Zurich, Switzerland) |
| | Nicolas J. Saintilan (ETH Zurich, Switzerland) |
| Scientific Program Chairs | Massimo Chiaradia (University of Geneva, Switzerland) |
| | Zoltán Zajacz (University of Geneva, Switzerland) |
| Field trip Chairs | David Dolejš (University of Freiburg, Germany) |
| | Jochen Kolb (Karlsruhe Institute of Technology, Germany) |
| Short Course Chair | Kalin Kouzmanov (University of Geneva, Switzerland) |

ETH zürich

UNIVERSITÉ DE GENÈVE

KIT Karlsruher Institut für Technologie

UNI FREIBURG

# Preface

With its load of unexplored mineral deposits, Switzerland has no metal mining activity. Yet, it is a country at the heart of the mineral resource industry. Indeed, Switzerland focuses a third of the world metal trading and two thirds of the world gold refinement. It is also in Switzerland that the SGA was legally incorporated back in 1971. Fifty-two years later, the SGA was back in Switzerland with the first SGA Biennial meeting of the post-COVID era, hosted at ETH Zurich between August 28 and September 1 2023. The world SGA community, with over 430 international delegates from 58 countries, gathered in Zurich to share knowledge and understanding of how mineral resources formed in Earth history, and how they may be discovered and exploited in a virtuous manner towards the environment and local communities. Our delegates include students (40%), academics (37%), industry (18%), and government (5%) representative from all regions of the planet.

The conference featured a four-day program with five plenary sessions, up to four concurrent technical sessions and one poster session on display over three full days. The scientific program comprised 21 keynote presentations, 169 regular oral presentations (including 72 students) and 135 posters (including 55 students). The important student contribution was and will remain a highlight of the 17$^{th}$ SGA Biennial meeting. It shows how dynamic our community is with a clear vision into the future of the world supply of metal and study of mineral deposits in a context of unprecedented challenges, yet riddled with what should also be seen as optimistic opportunities to be grasped.

SGA Zurich 2023 would not have been possible without the dedication of the local organizing committee, the ETH event team, Symporg and the strong support from our local and international sponsors. We are deeply indebted to the presenters and their co-authors for their contributions, and the session convenors for organizing and running their session, and for reviewing their session papers.

We are delighted to present you the Proceedings of the 17$^{th}$ SGA Biennial Meeting. With this edition, the SGA council decided to come back exclusively to the 4-page-long peer-reviewed short papers, which has been the distinct signature of the SGA meetings. The Proceedings is made up of three volumes totaling almost 1200 pages and includes 309 short papers.

Cyril Chelle-Michou
Nicolas Saintilan
Conference Chairs

# Sponsors

## Patron Sponsor

BHP

## Student Patron Sponsor

GLENCORE

## Gold Sponsor

Swiss National Science Foundation

Zürich, Switzerland.

## Silver Sponsor

NEW BOLIDEN

PAN AMERICAN SILVER

Teck

## Bronze Sponsor

RoyalRoad

FIRST QUANTUM MINERALS LTD.

# We thank all convenors of SGA 2023

**Session 1a. Porphyry-type and skarn deposits**
Andreas Audétat, Bayerisches Geoinstitut, Germany
Bertrand Rottier, Université Laval, Canada

**Session 1b. Geothermal systems and epithermal ore deposits**
Isabelle Chambefort, GNS Science, New Zealand
Thomas Driesner, ETH Zurich, Switzerland

**Session 1c. Hydrothermal mineralization associated with highly fractionated magmas (e.g., Li, Be, Sn, W, Nb, Ta)**
Matthieu Harlaux, BRGM, France
Hélène Legros, University of Alberta, Canada
Mathias Burisch, Colorado School of Mines, USA
Celestine Mercer, USGS, USA

**Session 1d. IOCG and magnetite-apatite deposits**
Adam Simon, University of Michigan, USA
Tobias Schlegel, CSIRO Mineral Resources, Australia
Irene del Real, Universidad Austral de Chile, Chile

**Session 2. VMS and seafloor mineralization**
Clifford Patten, Karlsruhe Institute of Technology, Germany
Ana Patrícia Jesus, Universidade de Lisboa, Portugal
Rémi Coltat, Instituto Andaluz De Ciencias De La Tierra, Spain
Melissa Anderson, University of Toronto, Canada

**Session 3. Gold: a journey from sources to precipitation sites and processes**
Georges Beaudoin, Université Laval, Canada
Steffen Hagemann, CET - University of Western Australia, Australia
Crystal LaFlamme, Université Laval, Canada

**Session 4a. Metallogenesis in sedimentary basins**
Philippe Muchez, KU Leuven, Belgium
Garth Graham, USGS, USA
Sam Spinks, Teck Resources, Australia

**Session 4b. Supergene ore forming processes**
Nicola Mondillo, Università degli Studi di Napoli Federico II, Italy
Cristina Villanova-de-Benavent, Universitat De Barcelona, Spain

**Session 5. Critical minerals and geo-inspired technologies for a carbon-neutral future**
Alexander Gysi, New Mexico Institute of Mining and Technology, USA
Katharina Pfaff, Colorado School of Mines, USA
Daniel Harlov, Deutsches GeoForschungsZentrum GFZ, Germany

**Session 6a. Mineral deposits related to mafic-ultramafic intrusions**
Eduardo Mansur, Geological Survey of Norway, Norway
Giada Iacono-Marziano, CNRS-ISTO, France
William Smith, Carleton University, Canada

**Session 6b. Ore genesis associated with alkaline-carbonatite systems**
Sophie Decrée, Royal Belgian Institute of Natural Sciences, Belgium
Francesco Stoppa, Università Gabriele d'Annunzio, Italy
Benjamin Walter, Karlsruhe Institute of Technology, Germany

**Session 7a. Advances in analytical techniques applied for ore deposits research and mineral exploration**
Marco Fiorentini, CET - University of Western Australia, Australia
Amanda Stoltze, Ivanhoe Mines Exploration, DRC

**Session 7b. New sensing instruments and processing methods in mineral exploration**
Doug Schouten, Ideon Technologies, Inc., Canada
Glenn Chubak, Dias Geophysical, Canada
Thibaut Astic, KoBold Metals, Canada

**Session 7c. Machine learning, data mining and new target generation in mineral exploration**
Daniel Gregory, University of Toronto, Canada
Chetan Nathwani, ETH Zurich, Switzerland
Francisca Maepa, BHP, Canada

# VMS and seafloor mineralization

Ore genetic study of the Ostra polymetallic mineralization (Eastern Carpathians, Romania) ..... 1
Á. Ádámcsik, B. B. Balázs, I. Márton, S. Orbán, G. B. Kiss

The value of resampling – application of a generalised geochemical exploration model at Golden Grove VMS, Australia ..... 5
M. Arundell, L. Williams

Serpentinization of the Ronda Massif (Spain): structural control and fluid origin, a framework for metal mobility ..... 8
B. Audran, P. Boulvais, Y. Branquet, P. Gautier, M. Ulrich, G. Raymond, G. Beaudoin, D. Layton-Matthews, R. Coltat, E. Leduc, M. Bevan

Formation of large mound-shaped sulfide deposit on axial volcanic ridge – A case from the Wocan-1 hydrothermal field, Carlsberg Ridge ..... 12
Y. Cai, Y. Wang, S. Petersen, X. Han

Origin of Fe-Ca metasomatism at oceanic core complexes: implications for the formation of seafloor massive sulphide deposits (MARK area, 23°N) ..... 16
R. Coltat, M. Andreani, C. Patten, M. Godard, B. Debret, J. Escartin

A new vision of the geodynamic evolution of the Iberian Pyrite Belt: VHMS in an intra-arc basin .. 20
F. Tornos, C. Conde, C. R. de Mello, C. C.G. Tassinari

The San Miguel deposit, Iberian Pyrite Belt: reconstructing a sub-seafloor replacive VMS ..... 24
C. Conde, F. Tornos, M. Polo

VMS mineralization, recent developments, and the big remaining questions ..... 28
M. DeWolfe

Constraints on magma evolution at the epithermally mineralized Conical Seamount, Papua New Guinea ..... 29
L-M Gautreau, P. Brandl, T. Hansteen, M. Portnyagin

SEDEX deposits in the Graz Paleozoic, Eastern Alps, Austria ..... 33
A. Geringer, S. Rohrhofer, F. Melcher, C. Benold, H. Reitner, R. Schuster

Textures of Cu-Fe sulphides in hydrothermal seafloor massive sulphide deposits: indications of a new metastable mineral phase Cu2Fe3S5 ..... 37
S. Goldmann, S. Fuchs

Magmatic metal contribution to volcanic arc seafloor massive sulfides: case study of the Kolumbo volcano ..... 41
S. Hector, C. Patten, J. Kolb, S. Kilias, P. Nomikou

Distribution of Characteristic Elements in Pore Waters, Sediments and Nodules from Eastern Part of the Clarion-Clipperton Fractures Zone, NE Pacific ..... 45
A. Hikov, Z. Milakovska, I. Peytcheva, V. Stoyanova, E. Stefanova, T. Abramowski, S. Chavdarova, M. Stavrev, D. Dimitrova

Inter- and intra-caldera, stratiform Zn-Pb-Ag and iron formation at Nyberg, Bergslagen, Sweden . 49
N. Jansson, A. Fahlvik, R. Allen, J. Andersson

Lead isotope systematics of VMS deposits from Oman ..... 53

A. Jesus, T. M Belgrano, A. Cravinho, B. Pracejus, F. Kourim, K-L Wang, M. Benoit, M. Abel Gonçalves

Modelling of zinc mobilization by magmatic-hydrothermal circulation in the sub-seafloor.....55
B. Lamy-Chappuis, T. Driesner

Fluid overprinting in an oceanic detachment fault: micro-analysis of pyrite from 13°30' N on the Mid-Atlantic Ridge.....59
A. Martin, J. Jamieson, S. Petersen, M. Fayek

Formation age of Kosaka Uchinotai-West Kuroko Deposit, NE Japan, determined by Re-Os isotope analysis .....60
M. Ogasawara, J. Ohta, M. Ishida, M. Yano, K. Mimura, K. Yasukawa, Y. Kato

Geological settings, distribution, and resource potential of seafloor hydrothermal systems .....64
S. Petersen, M. D. Hannington, J. Jamieson, T. Monecke, M. Klischies

Reconstructing the formation of volcanic-associated Lahn-Dill-type iron ores from fluid venting to seafloor deposition.....68
L. Schmitt, T. Kirnbauer, T. Angerer, S. Klein, D. Garbe-Schönberg, V. Roddatis

Linking Lithofacies and Chemostratigraphy, Rävliden North VHMS deposit, Skellefte district, Sweden.....72
F. Simán, N. Jansson, F. Liwicki, T. Hermansson, E. Nordfeldt, F. Persson, P. McDonnell, S. Johnson, J. Gustafsson

The Hydrothermal History of the VOLPA Seafloor Massive Sulphide Deposit, SW Pacific.....76
J. Umbsaar, D. Gregory, M. Anderson

Iron, boron and sulfur isotope constraints on ore-forming process of the subseafloor replacement-style volcanogenic massive sulfide systems.....80
B. Xiao, H. Chen, F. Huang, Y. Feng, X. HU

The Tectonic Evolution of the North New Hebrides Backarc Troughs: A Remote-Predictive Mapping Approach.....83
D. Summer, M. Anderson, P. Brandl

## Gold: a journey from sources to precipitation sites and processes

Known and potential types of gold mineralization at the Muruntau gold district .....87
A. Antonov, V. Tsoy

Distribution of Elements in Gold Grains: Implications for Mineralization .....91
D. Banks, R. Chapman, O. Borovinskaya

Mapping Auriferous Fluid Flow along the Cadillac Larder Lake Fault Zone (Abitibi Belt, Canada) .95
G. Beaudoin, B, Quesnel, C. Scheffer, G. Raymond

In situ geochronology of hydrothermal events in the Upper Beaver Au-Cu deposit, Abitibi greenstone belt, Canada .....99
B. Lin, C. Laflamme, G. Beaudoin, C. McFarlane

Using Chlorite and White Mica Mineral Chemistry as Footprints at Alta Floresta Mineral Province – Brazil ..... 102
M. Boscato Gomes, M. J. Mesquita, I. de Camargo Moeira, R. A. Sampaio Paes, H. E. da Silva Martins, J. H. Matos, A. Ruggiero, G. Primo, D. F. Ducart, J. G. da Silva, L. Poggi, A. M. Ueno Kunifoshita, L. Zanchetta de Laurentis

Gold in the Sardis Placer Deposit: Composition and Source of King Croesus's Gold ..... 106
G. Bozkaya, D. A. Banks, Ö. Bozkaya

Multiple sulphur isotope signatures of the Fenelon gold deposit, Abitibi Greenstone Belt, Canada: Constraints on fluid origin and ore-forming processes ..... 110
E. Slater, S. Castonguay, A. Williams-Jones, J. Clark, R. Stern

Gold mineralizing fluids at the Imonga mineralization in the eastern part of the Democratic Republic of Congo ..... 114
I. Cools, P. Muchez, S. Dewaele

Timing of the Orogenic Jouhineva Au-Cu-Co and Huhta Au mineralization: Constraints from titanite U-Pb dating ..... 118
A. De Araujo Silva, C. G. C. Patten, J. Kolb, S. Hector, B. Walter, A. Beranoaguirre, E. Eiche

Role of carbonaceous material in gold precipitation for orogenic gold deposits: A case study of the Bangbu gold deposit, China ..... 122
Z. Ding, X. Sun

The role of crystal defects for the remobilisation of gold in pyrite ..... 126
D. Fougerouse, D. Sugiono, S. Sumail, N. Thebaud, S. Reddy

Precise constraints on the lifespan of gold mineralization in the giant Yixingzhai gold deposit, North China Craton ..... 130
W-S Gao, X-D Deng, J-W Li, D. Szymanowski, C. Chelle-michou

The conglomerate-hosted Jacobina gold deposits, a modified paleoplacer of the Witwatersrand-type in Brazil ..... 134
E. Garayp, H. Frimmel

Revelio Aurum! uncovering invisible gold in N. America, China, and Europe ..... 138
P. Gopon, J. Douglas, B. Jenkins, V. B. Erlandsson, S. Niederl, P. Sack, Z. Xie, P. Felfer

Reconnaissance mineral and cathodoluminescence studies of gold occurrences in the Pogo-Black Mountain area, eastern interior Alaska, USA ..... 142
G. Graham, E. Marsh, H. Lowers, R. Taylor

Precipitation of gold by wallrock sulfidation in the Val-d'Or Vein Field, Abitibi Subprovince (Québec, Canada) ..... 146
M. Herzog, C. Laflamme, G. Beaudoin, G. Barré, L. Martin, D. Savard

Utility of volcanic rock geochemistry in discriminating fertile areas for epithermal gold mineralization: A case study in Japan ..... 150
M. Ishida, K. Nakamura, H. Iwamori, T. Hosono, Y. Kato

Quantification of hydrothermal alteration associated with gold-antimony mineralization along the Antimony Line, Murchison greenstone belt, South Africa ..... 154
T. Kgarabjang, N. Hammond

Complex hydrothermal evolution during retrograde terrane exhumation, Nalunaq gold deposit, South Greenland ..... 158
J. Kolb, R-M Bell, T. Vennemann, L. Martin, M. Fiorentini, T. Waight

Constraints on the Genesis of Au Veins in Interior Alaska: Evidence from Geochronology and Vein Textures ..... 162
D. C Kreiner, W. Thompson, J. S Caine, A. Ball, C. Holm-Denoma, P. O'Sullivan, H. Stein

Fluid evolution and carbon-gold systematics at the Fairview Mine, Barberton Greenstone Belt, South Africa ..... 166
R. La Cock, B. Von Der Heyden, L. Li, Y. Du, M. Steele-MacInnes

The Control of Sulfur Fugacity on Metal Melts and Gold Mineralization: A Case Study of the Jinjingzui Au Deposit ..... 170
X. Li, G. Xie, S. Gleeson, J. Mao

Metallogenic Fingerprinting of Gold Endowment in Magmatic Hydrothermal Deposits ..... 173
C. Mafra, H. I. Kong, R. R. Loucks, M. Fiorentini

Overprinted mineralizing gold events at the Paleoproterozoic Alta Floresta Mineral Province, Brazil ..... 177
M. Mesquita, M. E. Boscato Gomes, I. Moreira, R. Paes, H. Martins, J. Matos, A. Ruggiero, G. Primo, D. Ducart, L. Poggi, L. Laurentis, A. Kunifoshita, J. Silva

Geophysical VLF prospecting for orogenic gold in the historic mining area in the Sudetes (SW Poland) ..... 181
S. Mikulski, S. Ostrowski

Multiple sulfur isotope analyses identify an Archean sulfur source for the auriferous fluids at the Meliadine gold district, Nunavut, Canada ..... 184
P. Mongeau, C. Laflamme, P. Mercier-Langevin, G. Barré, O. Côté-Mantha, P. Cartigny, L. Martin

Revisiting the Kundarkocha gold mine: A rare Paleoarchean greenstone-hosted gold deposit, eastern India ..... 188
D. Pathania, R. Chakravarti, A. Latheef

Record of the oldest vein-type gold mineralization throughout the Neoproterozoic Nubian shield: the Galat Sufar South gold deposit, NE Sudan ..... 192
J. Perret, A. Eglinger, A-S André-Mayer, J. Feneyrol, J. Ganne, M. Poujol

Mineralogical controls on the generation of gold-rich metamorphic fluids ..... 196
I. Pitcairn, T. Zack, G. Beaudoin, C. Guilmette

Metal and ligand mobility during prograde metamorphism of metasedimentary belts in the Superior Province: Implications for gold endowment ..... 200
D. Ribeiro, B. Rottier, A. Godet, G. Beaudoin, C. Guilmette, C. Patten, J. Kolb, I. Pitcairn

Petrographic and chemical characterization of superimposed Au-bearing events at the Augmitto-Bouzan deposit (Abitibi) ..... 204
R. Rodrigues, G. Beaudoin, B. Rottier, G. Raymond, B. Chapon

The trace element composition of pyrite through metamorphism at the Yukon-Tanana Terrane, Yukon ..... 208
N. Román, D. Gregory, N. Cleven, J. Ryan

Structural control of gold deposits at Eastern Alta Floresta Mineral Province Brazil, preliminary results ..... 212
R. A. Sampaio Paes, M. J. Mesquita, M. E. Gomes, I. Moreira, H. Martins, J. H. Matos, A. Ruggiero, G. Primo, D. Ducart, L. Poggi, V. Pimenta, A. Kunifoshita, L. Zanchetta, J. G. da Silva

Metallogeny of gold (from in-situ to placer) in the Loch Tay area of Central Scotland ..... 216
L. Savastano, R. J. Chapman, T. M. Torvela

Alkalic epithermal Au deposits: Insights into magma evolution and ore fertility using melt inclusions from Lihir Island, Papua New Guinea ..... 220
M. Schirra, D. Müller, Z. Zajacz

Granitoid-hosted, orogenic gold mineralization: Genetic constraints on the world-class Archean Gruyere gold deposit, Yilgarn Craton, Western Australia ..... 224
R. Schreefel, S. Hagemann, C. Davy's, J. Robinson, M. Roberts, C. Fisher, N. Thebaud, R. Creaser

The Geological Setting and Hydrothermal Alteration at the Tucano Gold Deposit, Guiana Shield, Brazil ..... 228
G. Soares, R. Figueiredo e Silva, S. Hagemann, L. Lobato, R. Lucena

World-class gold deposits and emerging exploration opportunities in the Loulo district, West Africa ..... 232
T. Stapley, P. Stenhouse, J. Lambert-Smith, A. Allibone, D. Lawrence, D. Senghor, G. Crestin

Insights into the formation of high-grade gold mineralisation at the 10 M oz. Jundee gold camp of Western Australia ..... 236
Sumail, N. Thebaud, Q. Masurel, C. Fisher

Early crustal architecture revealed by multidisciplinary data integration: implications for gold exploration targeting ..... 240
N. Thebaud, Q. Masurel, A. Aitken, H. Smithies, K. Gessner, C. Fisher, Y. Lu

Mineralogy and geochemistry of the A2 and New A2 gold deposits in the Nwe Yon–Kwinthoneze gold district, central Myanmar ..... 244
A. Myo Thu, A.Piestrzynski, G. A. Kozub-Budzyń, K. Foltyn

Spatial distribution and structural control on gold mineralisation in the Barberton Greenstone Belt (South Africa, Eswatini) ..... 248
L. Travers, J. Lehmann, A. Chauvet

Tracing gold origin: A neural network approach to trace element geochemistry ..... 252
A. Verbel, M. E. Schutesky, D. Gregory

Early Structural architecture controlling komatiite-hosted nickel sulphide and orogenic gold mineralisation at Beta-Hunt Au-Ni mine, Kambalda, WA ..... 256
L. Virnes, N. Thébaud, L. Petrella, H. McFarlane, L. Martin, D. Fourgerouse

Mineral-specific deportment of gold and other elements in mine tailings from the Witwatersrand goldfields ..... 260
B. Von Der Heyden, S. Chingwaru, M. Tadie

An integrated approach towards unravelling the gold mineralisation processes around Ardtalnaig, Scotland. ..... 264
S. Webb, T. Torvela, R. Chapman, D. Selby, R. Gooday

Superimposed orogeny as key to gold hotspot formation at the north Peruvian Gondwana Margin ..... 268
D. Wiemer, S. G. Hagemann, A. I.S. Kemp, J. Hronsky, T. Ireland, L. Martin, N. Thébaud, C. Villanes

## Metallogenesis in sedimentary basins

A lower Cambrian Moroccan Copperbelt?
(Tizert copper deposit, Morocco): preliminary results of Cu-Fe-sulfide Re-Os geochronology and stable sulfur isotope data ..... 272
F. Askkour, N. Saintilan, A. Madi, C. Chelle-michou, M. Souhassou, N. Içame, M. Ousbih, J. E Spangenberg, L. Maacha, M. Ikenne

Numerical investigation of fluid flow and Cu transport in the Katangan Basin, Central African Copperbelt ..... 276
M. Bahlali, P. Salinas, J. Woitischek, C. Jacquemyn, M. Purkiss, M. Daly, M. Jackson

Cobalt-rich manganese nodules in Pliocene marine deposits of the onshore forearc Pisco Basin, Peru ..... 280
I. Carcamo Valencia, L. Torró, J. Proenza, J. Ramírez Briones, L. Ayala, W. Viveen, T. Aiglsperger, P. Baby

Mineralogy and geochemistry of the Myeonsan Fe-Ti placer deposit, Korea: preliminary Results ..... 284
B. Chang, J. Seo, Y. Jae Lee, S. Yong Lee, G. Lee, S-G Choi

Depositional environments and metamorphic evolution of the Paleoproterozoïc Mn-rich graphitic metasediments ..... 288
A. Dekoninck, T. De Putter, G. Ruffet, F. Mees, Y. Van Brabant, Y. Zhang, O. Namur, J. Kapoma

Mineralogical variation and paragenesis of the mineralisation and alteration at the Neoproterozoic Rosh Pinah Zn-Pb-Ag deposit, Namibia ..... 292
H. Ekandjo, K. Torremans, M. Hitzman, J. Güven

Litho-structural control of Pb-Ag veins in Jbel Addana district: Case of the Igharassene deposit (Western Anti-Atlas, Morocco) ..... 296
Z. El Ouad, M. Souhassou, M. Ikenne, H. ElBilali, B. Cousens, R. Ernst

Germanium-bearing minerals in the Cu-Ag Kupferschiefer deposit in Poland ..... 299
K. Foltyn, W. Zygo, D. Węgrzynek, G. Kozub-Budzyń, P. Ducki, J. Węgrzynowicz

Mineralogy and geochemistry of the Koeris Formation –Evidence of post-depositional base metal mobility within the Aggeneys-Gamsberg ore district, South Africa ..... 303
S. Höhn, H. Frimmel, M. Schneider, N. Brodtmann, W. Price

LA-ICP-MS trace element geochemistry of chalcopyrite from Tenke Fungurume, Central African Copperbelt ..... 307
Q. Liu, M. Pascal, P. Muchez

Geology and geochemistry of the shale-hosted vanadium mineralization at the Van property, Northwest Territories ..... 312
D. McGill, D. D. Gregory, M. A. Reynolds, D. Bien C. Concepcion, S. M. Brueckner, C. Merrick

Combined Lithological and Structural Controls on Unconformity Related Uranium Deposits (Eastern Athabasca Basin, Canada) ..... 316
G. Milesi, O. Gerbeaud, T. Obin, M. Serdoun, M. Brouand, S. Bosman, C. Card, A. Doney, A. Le Beux, J. Mercadier

Solid bitumen in the Central African Copperbelt: implications for understanding the ore-forming processes ..... 320
P. Muchez, Q. Liu, P. Mambwe, R. Littke

The Iron Creek Deposit in the Idaho Cobalt Belt: On a Quest for Cobalt ..... 324
D. Schmidt, M. Lehman, K. Pfaff, T. Monecke, A. Hofstra, G. Phelps, R. Lewis, S. Kocher, Z. Jobe, V. Gillerman, W. Day, M. Caddick, E. Anderson, J. Harrison, D. Pace

The enigmatic nature of normal faults in sediment hosted Zn-Pb deposits
C. Reed, M. Wallace, M. Ryuba, N. Cawood, C. Moynihan, J. McCusker, S. Spinks

Detrital zircon mineral chemistry and U-Pb geochronology of coastal marine sands, South Africa: provenance and exploration implications ..... 331
A. Rozendaal, I. Breda, R. Heyn, C. Philander

Co-evolution of pyrite 66Zn and sphalerite-pyrite-galena modal proportions in the ca. 1,828 Ma Mississippi Valley-type Zn-Pb Black Angel deposit, Greenland: insights into the chemical potential of sedimentary carbonates for Zn mineralization ..... 335
N. Saintilan, C. Archer, K. Szilas, D. Rosa

Metallogenic models of sediment-hosted hydrothermal Zn-Pb deposits related to different tectonic settings ..... 339
M. Sosnicka

Contrasted sources of metals between small and giant sediment-hosted Pb-Zn deposits in the San Vicente district, Peru ..... 342
C. Chelle-Michou, L. Bastian, C. Filoche, J-F Wotzlaw, D. Szymanowski, L. Tavazzani, L. Fontboté

Trace elements variation in gangue carbonates reveal redox and temperature shifts in Mississippi Valley-type, Zn-Pb deposits ..... 346
L. Tavazzani, L. Fontboté, C. Chelle-Michou

Multiple mineralization and fluid flow phases in the Central African Copperbelt. Implications for the age dating of the ore-forming processes
J. Torres, P. Muchez

Mineralogical mapping of potential source, aquifer and trap rocks from the Central African Copperbelt ..... 354
V. Trevisan, J. Wilkinson, M. Purkiss, M. Daly

District scale basin development interpretations utilizing stratigraphic correlation -Structural target generation for Kipushi style Zn-Cu-Pb deposits in Southern Congolese Copperbelt ..... 358
H. Twigg, M. Hitzman

An experimental study of metal extraction from red-bed sandstones as potential source rocks for sediment-hosted copper deposits ..... 362
J. Woitischek, J. J Wilkinson, E. Humphreys-Williams, M. D Jackson

# Supergene ore forming processes

Regolith-hosted rare earth genesis under humid climates in the Coastal Cordillera of the Central Andes ..... 365
N. Bustos Müller, C. Marquardt, T. Roquer, P. Vergara

Mn-Ni-Co oxy-hydroxides from Ni-Co laterites of Moa-Bay mining district, eastern Cuba
D. Domínguez-Carretero, C. Villanova-de-Benavent, C. Domènech, J. A. Proenza

Clay-hosted REE mineralisation under the microscope ..... 373
M. Gazley, M. Knorsch, K. Lilly, M. Kartal, E. Trunfull, A. Piechocka

Zinc incorporation in carbonate minerals from the Selac area, Kosovo ..... 377
K. Kluza, J. Pršek, S. Mederski, Z. Dolníček, J. Sejkora

Germanium mineralization in subbituminous coal from the Sokolov Basin, Czech Republic: The origin and volatility of Ge ..... 381
B. Kříbek, J. Rohovec, O. Bičáková, M. Tuhý, I. Sýkorová, P. Straka, F. Pticen, A. Vymazalová, M. Poňavič

Weathering processes associated to the formation of supergene Cu-As-Pb-Zn minerals at the Cap Garonne mine (France, Provence) ..... 385
J. Poot, J. Yans, G. Rochez, P. Buelens, A. Dekoninck

A hydrous Mg silicate Ni deposit within the oxide type Moa Bay laterite mining district, eastern Cuba ..... 389
C. Villanova-de-Benavent, E. Tauler, D. Domínguez-Carretero, C. Domènech, S. Galí, J. A. Proenza

# Ore genetic study of the Ostra polymetallic mineralization (Eastern Carpathians, Romania)

**Árpád Ádámcsik[1], Boglárka B. Balázs[1], István Márton[2], Szabolcs Orbán[3], Gabriella B. Kiss[1]**
*[1]Eötvös Loránd University, Faculty of Sciences, Institute of Geography and Geosciences, Department of Mineralogy*
*[2]Dundee Precious Metals Inc*
*[3]Goldron Geoconsulting Ltd*

**Abstract.** The Ostra polymetallic mineralization is hosted in the metamorphic formations of the Tulgheș Lithogroup from the alpine Bucovinian Nappes of the Crystalline-Mesozoic Zone in the Eastern Carpathians (Romania). The polymetallic mineralization consists of pyrite, chalcopyrite, sphalerite, galena, fahlore, marcasite and barite. In terms of spatial distribution, the massive sulfides are most commonly associated with the porphyroid rocks in the examined outcrops, which were discovered through barite exploitation. During the present study, two different massive sulfide lenses from the topographically upper and lower part of the mine were studied in details. Based on whole rock geochemistry, the studied ores are unusually Pb-Zn-rich, compared to other VMS deposits, though its noble metal content normalized to primitive mantle shows similar characteristics than Cyprus-type VMS. With the help of mineral chemical analyses as well as fluid inclusion study, the formation conditions were also determined: temperature decrease from the proximal (>250°C) to distal (<200°C) parts of the massive sulfide lens. Besides, compositional differences in the ore minerals as well as in the paragenesis were recorded among the proximal and distal, as well as lower and upper massive sulfide lenses.

## 1 Introduction

The polymetallic mineralization from Ostra is located in the Eastern Carpathians, Romania. The Eastern Carpathians host a series of volcanogenic massive sulfide (VMS) deposits which were important sources of copper and barite during the mid-1900's. The massive sulfide bodies, located within the Tulgheș Lithogroup, were known since decades, but no modern ore genetic research was carried out. Ostra was actively mined during the mid-1900's, but mining started to decay by the start of early 2000's. Ostra was mainly mined for barite with no real interest in the underlying massive sulfide bodies. The geologically correlating, nearby occurrences (e.g., Leșul Ursului, Mănăila) have a proven [Cu (±Au-Pb-Zn-Ag-Ba)] content, which could give a new approach to the belt scaled exploration (Damian et al. 2023). Barite mining was the main target of the exploited area, unfortunately grade and tonnage data for the base metals is not available. Active mining of the Mănăila-Cârlibaba deposits is taking place in the northern part of this VMS belt.

The study area is located in the western part of the Eastern Carpathians, which is built up (from west to east) by the Crystalline–Mesozoic Zone, the flysch zone, and the molasses zone. The mineralization is hosted in the rocks of the low-grade metamorphic Tulgheș Lithogroup which is a part of the Crystalline-Mesozoic Zone, which structurally belongs to the Eastern Dacides (Săndulescu 1984). The Crystalline-Mesozoic Zone is made up of several Alpine tectonic units, with eastern vergence, overthrusted in the Austrian tectogenesis. This zone is overlain by a Permian-Mesozoic sedimentary cover (Balintoni et al. 2009). The main lithologies which built up the Tulgheș Lithogroup of the Crystalline-Mesozoic Zone are the following: psammite (sericite quartzites, sericite-chlorite schists); graphitic sediments (sericite-chlorite±graphite schists, graphitic metacherts±Mn deposits, carbonate rocks); volcanic rocks (felsic metavolcanics±Kuroko-type base metal deposits, sericite-chlorite schists); mix series of sericite-chlorite schists, greenschists, acid metavolcanics, metacherts, carbonate rocks (Munteanu & Tatu 2003). The main mineralizations of the polymetallic belt accumulated in the Tulgheș Lithogroup are grouped into three districts, as follows (from north to south): Borșa-Vișeu District, Fundu Moldovei-Leșul Ursului District, Bălan-Fagul Cetății District (Damian et al. 2023). The Ostra mineralization forms part of the central-positioned Fundu Moldovei-Leșul Ursului District.

## 2 Methodology

Field mapping (Fig.1.) and sample collection were completed in 2022 in order to understand the outcrop-scaled structural features and geometries of the mineralization. Based on macroscopic observations, 18 samples (out of 78) were chosen for further detailed analyses.

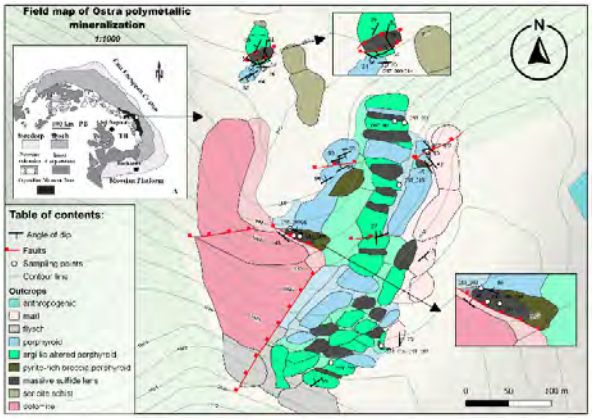


**Figure 1.** Field map of the studied area in the Ostra polymetallic mineralization, highlighting the two massive sulfide lenses studied in details, in higher resolution. A. The location of the Crystalline-Mesozoic Zone in the Carpathians (PB - Pannonian Basin, TB - Transylvanian Basin) map modified after (Munteanu et al. 2004).

The rock samples were taken from an abandoned open-pit mine, aiming to cover various lithological units, alteration assemblages and sulfide paragenesis. Besides, two chosen sections (comprising of a massive sulfide lens and its altered host rock) were sampled in details, representing two different topographic highs of the mine (Fig. 2).

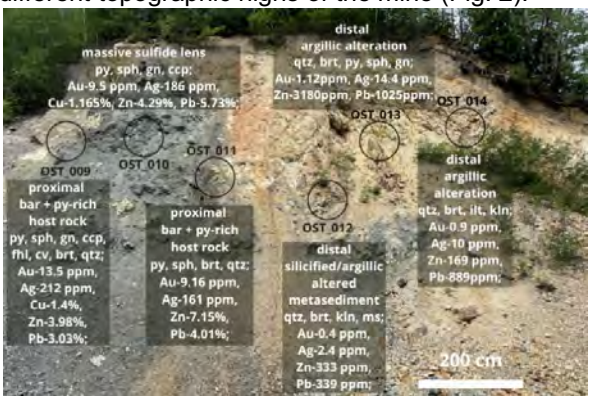


**Figure 2.** Photo of the sampling profile of the lower massive sulfide lens and its altered host rock. Sampling locations as well as the basic characteristics of the collected samples are also shown, for the massive sulfide lens and its proximal and distal alteration halo (py-pyrite, sph-sphalerite, gn-galena, ccp-chalcopyrite, fhl-fahlore, cv-covellite, brt-barite, qtz-quartz, kln-kaolinite, ms-muscovite, ilt-illite).

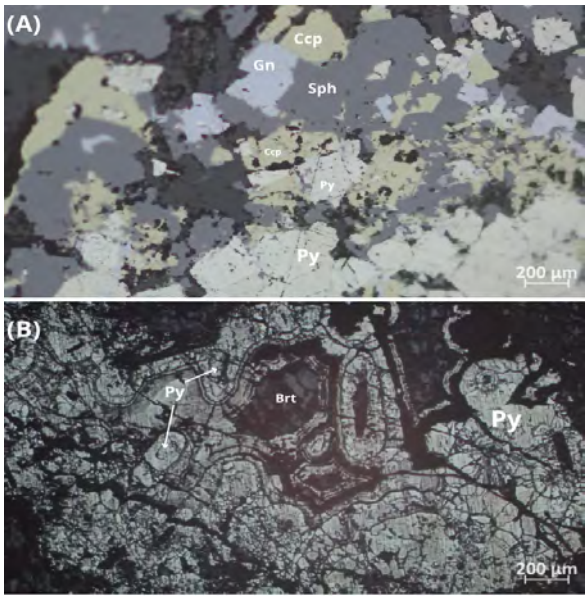


**Figure 3.** Plane-polarized reflected light photo of representative mineral assemblages from Ostra mineralization. (A) massive sulfide sample, with euhedral grains of pyrite, intergrowth with chalcopyrite, sphalerite, and galena; (B) pyrite with collomorphic texture (py-pyrite, sph-sphalerite, gn-galena, ccp-chalcopyrite, cv-covellite, brt-barite).

Detailed petrography was carried out on standard polished 30 µm thin sections (13 samples) and block sections (5 samples) using a Nikon Alphaphot polarizing microscopes at the Department of Mineralogy, Eötvös Loránd University (ELTE), Budapest, Hungary. These detailed petrographic studies were complemented with SEM-EDS observations at the Department of Petrology and Geochemistry, ELTE, on an Amray 1830I scanning electron microscope.

Argillic alteration of the host rock was examined with a Siemens D5000 X-ray diffraction equipment, to identify the clay minerals. Measurements were carried out at the Department of Mineralogy (ELTE).

The chemical compositions of sulfide minerals were determined using a JXA-8530F Field Emission Electron Probe Microanalyzer (EPMA). The analyses were carried out at the Earth Science Institute, Slovak Academy of Sciences (Banská Bystrica, Slovakia). The analyzed points were selected using the backscattered electron (BSE) images. The measurements were performed on polished carbon-coated sections using an acceleration voltage of 20 kV and a 15 nA beam current, 1-3 µm beam diameter (depending on the size of the grain). Trace element compositions were measured in pyrite, sphalerite, chalcopyrite, galena, fahlore and barite.

The whole rock geochemical analyses were conducted by ALS in Loughrea, Ireland, where rock sample compositions were determined by using fusion decomposition followed by ICP-AES measurement and four acid digestion followed by ICP-MS measurement of the 75 µm grain-sized pulverized material (for detailed documentation, see the ALS brochure). Samples that exceeded detection limits for elements of interest like Au, were reanalyzed using 30-g fire assay with gravimetric finish (ALS Geochemistry method Au-GRA21).

Fluid inclusion petrography was carried out on doubly polished 100-130 µm thick sections with an Olympus BH2 type microscope, while microthermometry was performed with a Linkam FT IR 600 stage mounted on an Olympus BX51 microscope, at the Department of Mineralogy (ELTE).

## 3 Results and their interpretations

### 3.1 Field Description, Petrography and Mineralogy

During field mapping, we have identified several massive sulfide lenses, which were always associated to the metamorphosed porphyroid rocks. Argillic alteration of the immediate host rock is common. Barite occurs in two textural and paragenetic relationships: it can be either associated with distal parts of the massive sulfide lenses, or it can form massive bodies (without sulfides) in the porphyroid rock. This porphyroid host rock consists mostly of a very complex textured grey to creamy white coloured rock, with a breccia-like appearance, including some cross-cutting barite veins. The samples are described as a porphyroid rock.

The massive sulfide lenses consist mostly of pyrite, chalcopyrite, sphalerite, galena, covellite, fahlore and marcasite, but leading to its distal parts, gangue minerals (coarse grained, euhedral barite,

rare fine-grained quartz) may also occur in them (Fig. 3). One massive sulfide sample from the higher topographic level of mine is described as a silica – pyrite-rich breccia, where the fractures have been partially filled with pyrite. The size of the massive sulfide lenses is commonly around 2-3 x 10 m.

The petrographical analyses confirm that massive sulfide samples are dominated by pyrite (often with collomorphic texture) together with sphalerite, galena, chalcopyrite and fahlore (Fig. 3). In some pyrite, galena-filled fractures were found, while the presence of covellite was observed, which partially replaced chalcopyrite or galena. The gangue minerals are barite and quartz. The distal samples are characterized by predominantly quartz and barite with disseminated sulfides.

X-ray powder diffraction analyses have shown that the alteration halo of the massive sulfide lenses is different in the lower and upper levels of the mine. In case of the lower benches of the pit, proximal alteration zone contains kaolinite group clay minerals, while the distal zone consists mostly of illite group clay minerals. As a contrary, at higher elevation, in case of the proximal zone, dickite, alunite and K-feldspar occur, while in the distal alteration zone, kaolinite group minerals were found.

### 3.2 Mineral chemistry

Pyrite, sphalerite, chalcopyrite, galena, fahlore and barite were studied with EPMA. Pyrite appears in the massive sulfide rocks as part of a compact, pyrite-rich polymetallic ore, where pyrite can be found mostly in the form of subhedral equigranular grains, associated with the rest of above-mentioned sulfides. Pyrite grains are rimmed by chalcopyrite, sphalerite and galena. Electron microprobe analysis indicates minor amounts of Sb, Zn, Ni, Co, Ag and Au in the pyrite, and a relatively high amount of As, Cu and Pb. The pyrite is rich in As (from 0.1 up to 5 wt.%), but Ag and Au are insignificant. Compositional zonation (due to variable Sb and As content) as well as tiny galena inclusions are observed in pyrite on BSE images. Based on Se content in pyrite, the ore-forming temperature (T) was estimated (Keith et al. 2018). The massive sulfide lens studied at the lower level of the mine formed at about 270±10 °C.

Sphalerite is the second most abundant mineral of the pyrite-rich polymetallic ore. It mostly appears in the form of anhedral crystals arranged in the open spaces between the pyrite grains, intergrown sometimes with chalcopyrite, galena and fahlore. Electron microprobe analysis indicates sphalerite with low Sb, Cd and Cu content, but systematically higher Fe content occurs in the proximal part of the massive sulfide lens. Sphalerite from the proximal part of the massive sulfide lens contained significantly higher amount of Fe (up to 8.1 wt.%), compared to the distal ore (0.6-1.2 wt.%). This suggests lower formation temperature for the distal ores, and higher (>200 °C) formation temperature for the proximal one, which is in good agreement with the pyrite thermometry results.

Galena is present also in our samples, intergrown with sphalerite and chalcopyrite. Fahlore is a common mineral in the lower massive sulfide lens, while it occurs only sporadically in the upper level of the mine. Galena and fahlore show compositional differences according to their location in the massive sulfide lens: distal galena contained elevated Zn (up to 1%), while distal fahlore was characterized by elevated Hg (up to 12.9%) and low Sb. The Ag content of the deposit is connected to the fahlore, no other Ag-bearing mineral was observed. Based on the composition of fahlore, tennantite, is occurring in the studied samples (most often Cu-rich tennantite) (Fig. 4).

Chalcopyrite forms anhedral grains that border mostly pyrite or sphalerite, galena, and contains fahlore inclusions. Chalcopyrite is sometimes present with covellite. Electron microprobe analyses indicates minor amounts in Pb, Zn and Au in the crystal structure of chalcopyrite.

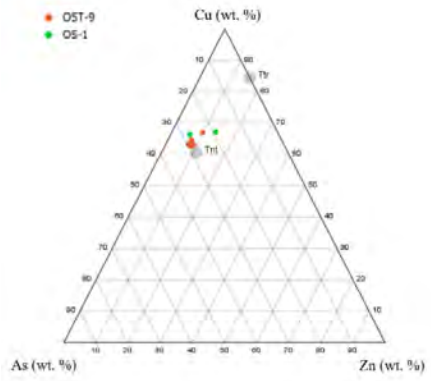


**Figure 4.** As-Cu-Zn ternary diagram for tennantite of the Ostra deposit. (orange dots - proximal massive sulfide samples; green dots - distal massive sulfide samples; tnt – tennantite, ttr - tetrahedrite)

### 3.3 Whole rock geochemistry

In terms of geochemistry, it can be said that there are significant differences between the values obtained along the two studied massive sulfide lenses. The most significant observations occur in the distribution of precious metal, such as gold or silver, and base metal content, such as copper, lead, and zinc.

Gold content of the lower massive sulfide lens can reach up to 13 ppm, while it barely reaches 1.2 ppm in the upper massive sulfide lens. The Ag content also differs significantly, with a 174.25 ppm mean value, where in the lower massive sulfide lens is up to 212 ppm and only 21.1 ppm in the higher one.

There are significant differences in the base metal content as well; such as copper (between 1.1-1.4% in the lower, and <134 ppm in the upper massive sulfide lens), lead (up to 5.73% in the lower massive sulfide lens compared to <338 ppm in the upper one) and zinc (7.15% in the lower massive sulfide lens and <294 ppm in upper one). Regardless

the structural position, studying the Cu:Zn:Pb ratio, the samples are rich in Pb and Zn (Fig. 5.). High Fe and S content of the higher massive sulfide lens prove its richness in pyrite.

As previous studies did not address the deposit type of the Ostra mineralization, we tried to examine this aspect, too. Based on studies of the nearby occurrences of the same belt (Damian et al. 2023), the VMS origin seems to be a geologically reasonable option. The observed textural features (i.e., the Ostra mineralization is associated with a porphyroid host rock, roughly with argillic alteration and with a few massive sulfide lenses) also support this assumption.

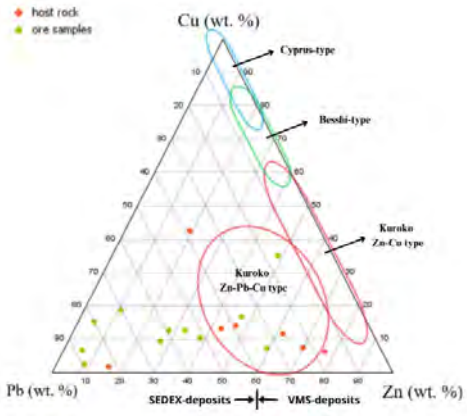


**Figure 5.** Ternary diagram of the base metal ratio of our samples. (orange dots - host rock; green dots - massive sulfide ore samples). The VMS/SEDEX ternary plot, and the reference fields for VMS types is after Ciftci (2019).

### 3.4 Fluid inclusion

Fluid inclusions of barite in the distal parts of the massive sulfide lens were studied in details. Our petrographycal observations suggest, that barite formed partly syngenetically with the sulfides, though its crystallization lasted longer. Based on our preliminary results, the primary fluid inclusions (occurring in growth zones or in the spongy cores of the baryte crystals), revealed a homogeneous parent fluid, which can be modelled in a NaCl-$H_2O$ system. Despite the small size of the primary liquid + vapour fluid inclusions (usually 3-7 μm), their chemical composition and physical properties can be determined: Th (LV-L) = 145-185°C (i.e., minimum formation temperature due to homogeneous conditions of the parent fluid) and 3.7-5.3 NaCl equiv. wt.% salinity was confirmed. This minimum formation temperature data is in good agreement with the low Fe content of the syngenetic sphalerite grains. The slightly higher salinity compared to modern seawater values can be the result of fluid-rock interaction during the hydrothermal fluid circulation in the oceanic crust.

## 4 Conclusions

In the present preliminary research, we applied the combination of field observation, whole rock geochemistry and fluid inclusion studies. The electron microprobe analyses on Ostra samples provide important information about the ore-forming conditions and geochemical variations.

In conclusion, the field mapping and petrographic analyses performed on the studied area have provided important information regarding the structural features and geometries of the mineralization. The massive sulfide lenses were found to be associated with a low-grade metamorphic porphyroid rocks, and argillic alteration occurred in the immediate host rock. Barite occurred either in association with the distal parts of the massive sulfide lenses or in the porphyroid rocks also.

The VMS origin is a geologically and texturally reasonable option for the genesis of the deposit at Ostra. Furthermore, significant differences were observed between the studied massive sulfide lenses of the mine; in the metal content, as well as mineral paragenesis, suggesting a somewhat different evolution for the different parts of the deposit.

Studying the formation conditions of a single massive sulfide lens, a temperature decrease from proximal to distal parts is clearly observed, together with compositional variations.

Overall, this information provides valuable insights into the geological and geochemical characteristics of the mineralization and helps further exploration and evaluation activities.

## Acknowledgements

This research was supported by a student research grant from the Hugh E. McKinstry Fund of the Society of the Economic Geologists. Trip to Banská Bystrica to perform EPMA analyses was supported by the Talent Support Council of ELTE Eötvös Loránd University, Budapest.

## References

Ciftci, E. (2019): Volcanogenic Massive Sulfide (VMS) Deposits of Turkey. Modern Approaches in Solid Earth Sciences, p. 427-495.

Damian, G., Apopei, A.I., Buzatu, A., Maftei, A.E., Damian, F. (2023): New Mineral Occurrences in Massive Sulfide Deposits from Mănăila, Eastern Carpathians, Romania. Minerals 13:111.

Keith, M., Smith, D.J., Jenkin, G.R.T., Holwell, D.A., Dye, M.D. (2018): A review of Te and Se systematics in hydrothermal pyrite from precious metal deposits: Insights into ore-forming processes. Ore Geology Reviews 96:269-282.

Munteanu, M., Marincea, S., Kasper, H.U., Zak, K., Alexe, V., Trandafir, V., Saptefrati, G., Mihalache, A. (2004): Black chert-hosted manganese deposits from the Bistritei Mountains, Eastern Carpathians (Romania): petrography, genesis and metamorphic evolution. Ore Geology Reviews 24:45-65.

Munteanu, M., Tatu, M. (2003): The East-Carpathian Crystalline-Mesozoic Zone (Romania): Paleozoic Amalgamation of Gondwana- and East European Craton-derived Terranes. Gondwana Research 6:185-196

Săndulescu, M. (1984): Geotectonica României. Editura Tehnică.

# The value of resampling – application of a generalised geochemical exploration model at Golden Grove VMS, Australia

**Mark Arundell[1], Lucas Williams[2]**
*[1]IMEx Consulting, Orange, NSW, Australia*
*[2]29Metals Ltd Golden Grove Operations Pty Ltd, WA, Australia*

**Abstract.** Sampling of bottom of hole historic Rotary Air Blast (RAB) drilling combined with multi-element analysis over three deposits in the Golden Grove area has led to the development of a generalised geochemical model revealing the position of the footwall/hangingwall contact and a distinct pathfinder signature proximal to mineralisation. The results from this initial pilot sampling program provided motivation for a belt wide program of reanalysis of historic bottom of hole drill samples. The geochemical model has been applied to areas under deep transported cover and led to the development of new robust prospects as well as a review of the lithostratigraphy.

## 1 Introduction

The Gossan Hill, Scuddles and Gossan Valley VMS deposits occur on the NE flank of the Warriedar Fold Belt (Figure 1), in the Golden Grove Domain, with an age of about 3.0Ga. The Golden Grove Domain has a layered stratigraphy that is laterally continuous over some 30km. Within this, the Golden Grove Formation is a layered rhyodacitic volcaniclastic succession that underlies and hosts the VMS deposits. Dacitic and rhyodacitic volcanics of the Scuddles Formation are the main rock types of the hanging wall. Bedded tuffaceous volcaniclastic rocks of the Golden Grove Formation are subdivided into six members, based on facies, grain-size variation, abundance of volcanic quartz grains and bedding characteristics (Frater, 1983; Sharpe and Gemmell, 2001, 2002).

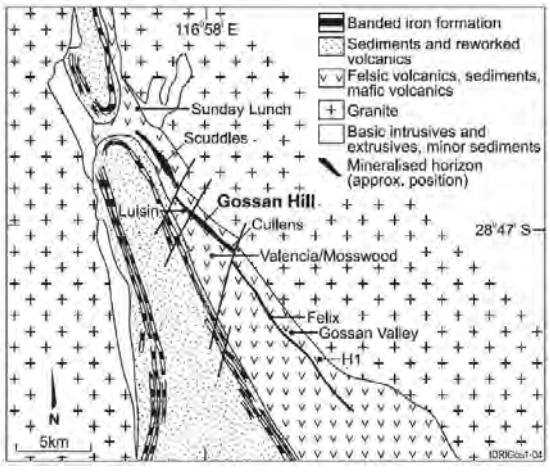


**Figure 1.** Regional geology of Golden Grove area (after Smith, 2003)

The Golden Grove Formation shows quartz, Fe-rich chlorite and lesser muscovite alteration. At Gossan Hill, alteration zones surround the deposit and are characterized by chlorite and ankerite-siderite (with FeO and MgO enrichment), grading stratigraphically upwards into intense silicification. Regional deformation has resulted in EW compression, minor faulting, cleavage, schistosity and boudinage of the rocks (Smith, 2003)

## 2 Discovery History and Mineralisation

Outcropping gossans were recognized and sampled in 1971 on what is now Gossan Hill. Five diamond drill holes tested the gossans in 1972 and four of the holes intersected significant base metal sulphides (about 1-3.5% Cu and Zn). Although, difficulties in assessing the geometry of the deposit were recognised, a resource of 15 Mt at 3.4% Cu was defined. The non-outcropping Scuddles deposit was discovered 4 km to the north of Gossan Hill in 1979. The geometry of the Scuddles deposit turned out to be relatively straightforward and much of the focus at Golden Grove then centred on delineation and development of Scuddles. The most comprehensive exploration activity has been over the Gossan Hill to Scuddles area (Figure 1) (Smith, 2003).

At the mine scale, a steep west dipping horizon of thinly bedded chert and tuff, within the Golden Grove Formation, hosts the Zn mineralisation at both Gossan Hill and Scuddles and is underlain by coarse felsic volcaniclastic rocks. The Gossan Hill deposit consists of a number of lenses of Zn and Cu mineralisation, extending over a strike of 400m and a width of 20m. The Cu ore occurs in magnetite-rich volcaniclastic rocks stratigraphically below the Zn ore. An oxidised near surface Au-Ag resource overlies the Zn sulphide lenses and an oxide Cu resource overlies the Cu sulphide lenses (Normandy, 1999).

## 3 Multi-element geochemistry

Since the discovery of Gossan Hill ~50 years ago, the Golden Grove area has been subject to intensive and systematic geological, geochemical and geophysical exploration. A number of other prospects (e.g. Gossan Valley, Felix) have been discovered associated with the “mineralised horizon” (Figure 1).

In the period between 2004 and 2014, near surface geochemical exploration had largely been neglected. Prior historic RAB (Rotary Air Blast) drilling, with associated bottom of the hole geochemical sampling, well covered the prospective stratigraphy. However, most of these samples had only been analysed for Cu, Pb, Zn and Au.

A program of systematic sampling of drillcore for low detection level multi-element geochemistry had been in place since ~2003 which enabled identification of primary rock pathfinders and alteration.

Interpretation of this multi-element drillhole data (Halley 2014a) noted that proximal footwall alteration at Gossan Valley carried a distinct Mo-Bi signature with lesser amounts of As and Sb. In the hangingwall, As values were elevated but it was interpreted not to be associated with the VMS alteration.

The advent of low-level detection ICP-MS combined with four acid digestion methods was considered to offer an opportunity to determine whether historic shallow (e.g. RAB) drill samples could offer new insights into the near surface metal pathfinder, alteration and lithogeochemistry of the Golden Grove deposits – particularly given the above signature noted at Gossan Valley.

A pilot program was conducted in 2014 where ~80 bottom of hole RAB pulp samples were reanalysed from each of the Scuddles, Gossan Hill and Gossan Valley deposits. Samples were selected on a nominal 320m north-south by 80m east-west grid centred on the deposit.

Interpretation of these new data by Halley (2014b) noted the Mo and Bi anomalies associated with the Gossan Hill deposit were spatially restricted and the values for As and Sb were considered low for a VMS system. Elevated Cd and In concentrations were also noted at Gossan Hill and high Ba and Tl at Scuddles.

In 2017, the 2014 pilot program datasets were reassessed in order to determine whether the resampling of bottom of hole RAB material should be extended away from the three known deposits. This reassessment led to the development of a Generalised Geochemical Model (Figure 2) based on all three deposits – Scuddles, Gossan Hill and Gossan Valley.

The pathfinder signature for copper mineralisation in the hangingwall dacite unit consisted of As, Bi, Mo, Sb, Sn W and Se. The zinc mineralisation pathfinder signature was As, In, Sb and Se. Also, a Pb and Tl signature was noted south and proximal to zinc mineralisation in the upper footwall position.

It was also noted that the extent of the hangingwall pathfinder anomaly was controlled by the geometry of the dacite unit. A thin hangingwall dacite produced a laterally extensive pathfinder anomaly proximal to the hangingwall contact that largely mirrored the distribution of the dacite. A thicker hangingwall dacite "dome" produced a less laterally extensive anomaly but a broader pathfinder anomaly into the hangingwall unit.

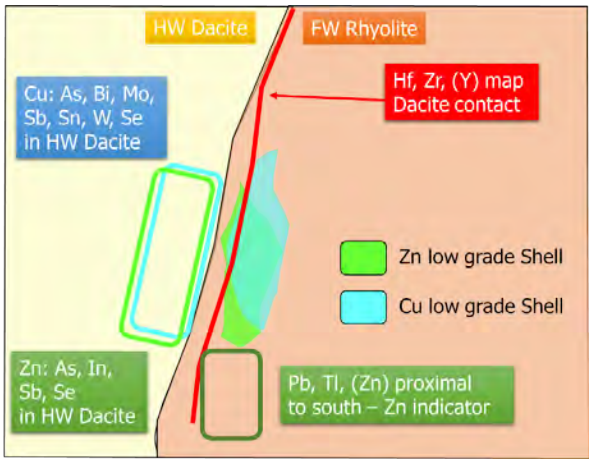


**Figure 2.** Golden Grove – schematic of Generalised Geochemical Model

The contact between the footwall units (dominantly rhyolitic) and the hanging wall units (dacitic) – the "mineralised horizon" of Figure 1 – could be mapped by the distribution of Hf, Zr and Y.

The Golden Grove mining leases contain ~35km strike extent of the "mineralised horizon" with thickening transported cover blanketing this key position to the south-east of the Gossan Valley deposit.

This area, shown as H1 on Figure 1, contained a number of historic RAB drillholes but very limited deeper Reverse Circulation (RC) percussion and/or diamond drillholes. Also, historic analysis of the RAB drilling was largely confined to Cu, Pb, Zn and Au. Fortunately, the majority of drill sample pulps from historic drilling at Golden Grove had been stored on site and thus could be retrieved for reanalysis.

Interpretation of the results of this reanalysis at H1 is presented in Figure 3.

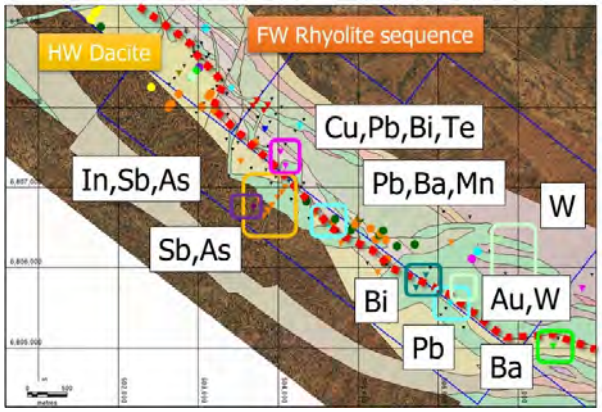


**Figure 3.** H1 area. Interpreted multi-element geochemistry on interpreted geology and aerial photograph. Green: dolerite; yellow: hangingwall Dacite & Red/pale green footwall Rhyolite units

The identification of a multi-point Sb/As/In anomaly in an interpreted hangingwall position was considered promising. However, the logged bottom

of hole lithology was dolerite (green on Figure 3) for most of the anomalous Sb/As samples which, previously, would have been interpreted to indicate that these are “false” anomalies. The dolerite is dated as Proterozoic and thus postdates and is known to crosscut mineralisation as dykes and sills. Review of data from another area identified that although dolerite may have been recorded as the end of hole lithology it is likely that the RAB drilling technique has been unable to penetrate far into this hard rock type and thus this Sb/As anomalous bottom of hole interval is more likely to be hosted in highly weathered (clay) hangingwall dacite. The presence of Cu/Pb/Bi/Te anomalous concentrations in the samples in an adjacent footwall position further indicates the high prospectivity of this area.

The presence of a Bi anomaly occurring at the interpreted position of the “mineralised horizon” with anomalous Pb proximal is also considered encouraging. Although bedrock is interpreted to be dolerite (Figure 3), the presence of these pathfinders and a Au, W anomaly in the footwall necessitates that this area be re-assessed.

Re-sampling in the H1 area was conducted by targeting the full strike extent of the “mineralised horizon” and generated multiple new targets. The integration of geological observations was critical in the interpretation of the geochemical data in order to rigorously prioritise potential targets.

## 4 Conclusions

Storage of historic drill samples may seem an unnecessary luxury but the ability to re-analyse old samples using new techniques offering not just more elements but significant lower detection limits provide the ability to generate new targets in what may be perceived to be a mature exploration terrain. Systematic sampling & multi-element analysis of bottom of hole samples over known deposits enabled a Generalised Geochemical Model to be developed and new prospects have been developed based on this model.

At Golden Grove, multi-element reanalysis has enabled “new” robust targets to be developed in the “Shallow”. This has challenged the paradigm of the area being a mature terrain and the necessity of “Deep” exploration.

## Acknowledgements

Golden Grove Operations Pty Ltd, a wholly owned subsidiary of 29Metals Limited, is thanked for permission to publish this work. This paper owes much gratitude to the excellent foundational work conducted by previous explorers, research students and consultants, in particular, geochemists Cliff Stanley and Scott Halley.

## References

Frater, K.M., 1983. Geology of the Golden Grove Prospect, Western Australia: a volcanogenic massive sulfide-magnetite deposit. Economic Geology, 78: 875-919.

Halley, 2014a. Golden Grove Geochemistry. MMG Golden Grove unpublished report.

Halley, 2014b. Golden Grove RAB Geochemistry. MMG Golden Grove unpublished report.

Normandy Golden Grove Operations, 1999. Scuddles and Gossan Hill Archaean VHMS deposits . Hand out and field excursion guide, 26 pp plus figures

Sharpe, R. and Gemmell, J. B., 2002. The Archean Cu-Zn magnetite rich Gossan Hill volcanic-hosted massive sulphide deposit, Western Australia: genesis of a multistage hydrothermal system. Economic Geology, 97:517-539.

Sharpe, R. and Gemmell, J.B., 2001. Alteration characteristics of the Archean Golden Grove Formation at the Gossan Hill deposit, Western Australia: Induration as a focusing mechanism for mineralizing hydrothermal fluids . Economic Geology, 96: 1239-1262.

Smith, R. E., 2003. Gossan Hill Cu-Zn-Au Deposit, Golden Grove, Western Australia. Regolith Expression of Australian Ore Systems, CRC LEME.

Stanley, C.R., and Radford, N., 2003. Lithogeochemical Exploration in Deep Regolith at the Golden Grove Volcanic Hosted Massive Sulphide Deposit, Western Australia. IGES 2003, Dublin, Ireland.

# Serpentinization of the Ronda Massif (Spain): structural control and fluid origin, a framework for metal mobility

**Bastien Audran[1], Philippe Boulvais[1], Yannick Branquet[1], Pierre Gautier[1], Marc Ulrich[2], Guillaume Raymond[3], George Beaudoin[3], Daniel Layton-Matthews[4], Rémi Coltat[5], Evelyne Leduc[4], Maëlys Bevan[1]**

*[1] Géosciences Rennes, UMR 6118, University of Rennes, 35042 Rennes, France*
*[2] IPGS-EOST, UMR 7516, University of Strasbourg, Strasbourg, France*
*[3] Département de géologie et de génie géologique, Centre de recherche sur la géologie et le génie des ressources minérales (E4m), Université Laval, Québec, G1V 0A6, Canada*
*[4] Queen's Facility for Isotope Research, Department of Geology and Geological Engineering, Queen's University, 36 Union Street, Kingston, Ontario, Canada K7L 3N6*
*[5] Instituto Andaluz de Ciencias de la Tierra (IACT)-CSIC, Universidad de Granada, Granada, Spain*

**Abstract.** Serpentinization is a hydrothermal transformation of ultramafic rocks which leads to metal mobility. The Ronda peridotite Massif (Andalusia, Spain) represents the largest body of subcontinental peridotites exposed at the Earth's surface. No comprehensive work on serpentinization has been conducted so far, notably because most research has focussed on the high-temperature deformation and petrology of mantle rocks. In the Massif, serpentinization rate varies from a few percent to 100%. We identified three steps of serpentinization. The first one (lizardite 1) is pervasively developed within the peridotite with common mesh-texture. The second forms corridors of lizardite 2, chrysotile and magnetite. The third is associated with cataclasis and consists of polygonal serpentine veins (plus minor chrysotile) and magnetite. Structural analysis allows identifying a regional tectonic context for the cataclasis-associated serpentinization which corresponds to a multi-directional horizontal stretching and vertical shortening direction (i.e. near pure flattening). The different stages of serpentinization show comparable isotopic compositions, with $\delta^{18}O$ values of ~ +5.0‰ and $\delta D$ of ~ -79‰, suggesting that they were developed under sub-identical conditions of fluid-rock interactions (fluid sources, temperature of formation and fluid/rock ratio). This study provides the framework in which metals can be mobilized during serpentinization.

## 1. Introduction

Serpentinization is a hydrothermal transformation of ultramafic rocks, such as the Sub-Continental Lithospheric Mantle (SCLM) which represents a reservoir of metals (e.g., Cu, Zn, Co, Ni, Cr, PGE, V, Ti, Au). During their exhumation, the mantle rocks are affected by various hydrothermal processes which can lead to economically viable metal deposits (e.g., seafloor massive sulfides; Patten et al. 2022). Despite some works (Deschamps et al. 2013; Lawley et al. 2020), the characteristics of metal mobilities during serpentinization still remain poorly constrained, notably the related spatial scales. Different approaches can be developed to address this issue: experimentation, modelling, chemical and mineralogical characterization directly on the seafloor or on terrestrial samples (such as the Ronda Massif, Spain).

The Ronda massif is the largest remnant of SCLM in the world. It is partially serpentinized and is thus perfectly suitable to characterize metal mobilities at various scales (from the centimetre to the multi-kilometres scale). To date, studies on the serpentinization of the Ronda peridotite remains scarce (Pedrera et al. 2016).

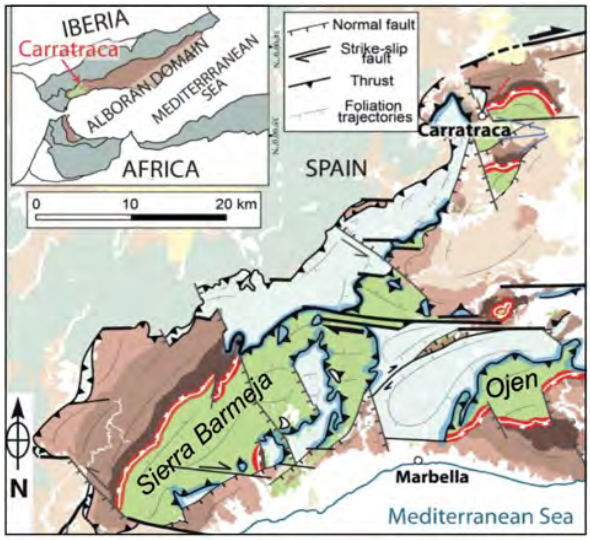


**Figure 1.** Simplified tectonic map of the Ronda peridotite Massifs (green), thrusts (blue), Crust–Mantle extensional shear zone (red) (modified after Frasca et al. 2017).

To constrain the mobility of metals during serpentinization taking the Ronda Massif as a case study, we first present the main serpentinization stages, then the structures along which serpentinization occurred. We also present stable oxygen and hydrogen isotope data, to discuss the origin of the serpentinizing fluids.

## 2. Geological context

The Ronda Massif is located in the western Betic Cordilleras (Spain) (Figure 1). The Massif is composed of peridotites with different facies: isotropic to mylonitic, containing garnet, spinel or plagioclase, with dykes of pyroxenite of various types. Structural and petrographic studies have shown the parallelism between the foliation in the SCLM and in the overlying continental crust (Figure 1). The Massif and associated crust were thrusted towards the north-west on the 'external zones' (i.e. upper continental crust; see Frasca et al. 2017) during a Cenozoic compressional event (Figure 1). However, the mechanism and the timing of thrusting have been subjects of controversy for decades, with

various proposed models (e.g., extension, compression or transpression alone; polyphased tectonic; Mesozoic or Cenozoic in age). Geochronological studies performed within the lower crust, close to the crust/mantle boundary, revealed dominant deformation during the Variscan orogen, with an Alpine overprint. Later, some felsic magmas, dated between 19 and 22 Ma intruded the SCLM Massifs (U-Pb on zircon: Esteban et al. 2011; Frasca et al. 2017). A potential source of these granitic magmas can be the underthrusted units which underwent a dynamothermal metamorphism during the thrusting of the Ronda SCLM units (Esteban et al. 2011; Tubia et al. 2012).

Pedrera et al. (2016) described two main types of serpentinization: (1) common mesh-texture and (2) veins of either antigorite or lizardite. These authors associated the latter type to the felsic intrusions during Cenozoic polyphased tectonic event.

## 3. Method

This study is mainly focused on the largest mantellic massif, the Sierra Barmeja (Figure 1). Sampling was regularly distributed to perform a large-scale characterization of mineralogy, serpentinization rate and stable isotope distribution.

The mineralogy of serpentine polytypes has been determined by Raman spectroscopy which allows discrimination of lizardite/polygonal serpentine from antigorite and chrysotile.

The structural context of serpentinization has been accessed through systematic fault kinematic analysis based on serpentine shear veins bearing slickenfibers in 17 measurements stations. We used the right dihedra method which allows calculating the stretching and shortening axes.

A total of 32 samples have been selected for a stable isotope study of oxygen and hydrogen. These samples correspond to 12 whole rocks (WR) of serpentinized peridotite (lizardite ± chrysotile), 3 serpentinized corridors (lizardite + chrysotile) and 17 veins of serpentine (polygonal serpentine ± chrysotile). For each sample, we separated magnetite from serpentine by hand magnet. In order to estimate the serpentinization temperature, the $\delta^{18}O$ values of 2 magnetite-serpentine pairs have been measured. The $\delta^{18}O$ and $\delta D$ values are reported relative to VSMOW, with an accuracy of ±0.2‰ and ±1.5‰, respectively.

## 4. Results and discussion

### 4.1 Steps of serpentinization

Three steps of serpentinization have been identified in the Sierra Barmeja Massif.

The first step presents a typical massive aspect with brown patina (Figure 2A), a result of weathering. It consists of brown lizardite (liz 1) developed as mesh-texture with remnants of olivine and pyroxene. Olivine crystals are fractured and partially replaced by a pseudomorphic lizardite 1, with rare magnetite grains. Pyroxene crystals are only fractured and mostly preserved from serpentinization. The serpentinization rate is highly variable, with a noticeable increase towards the edges of the massif which corresponds to large fault zones (Figure 1).

The second step is easily identified as white banded veins (or corridors), the white colour being due to weathering (Figure 2B). The serpentinized corridors are typically a few centimetres wide to establish fully serpentinized zones. Pyroxene within the corridors is transformed into bastite. In the centre of the corridors, pyroxene is even partially dissolved and replaced by lizardite (liz 2). This lizardite is white in thin section, always associated with magnetite veinlets/ribbons (Figure 3), and discontinuous chrysotile veins. The contacts between liz 1 and liz 2 are either sharp or gradual.

The third serpentinization step is associated with cataclasis (Figure 2C). The thickness of the cataclasites is variable, ranging from pluri-decametric to metric. Clasts are metric to sub-

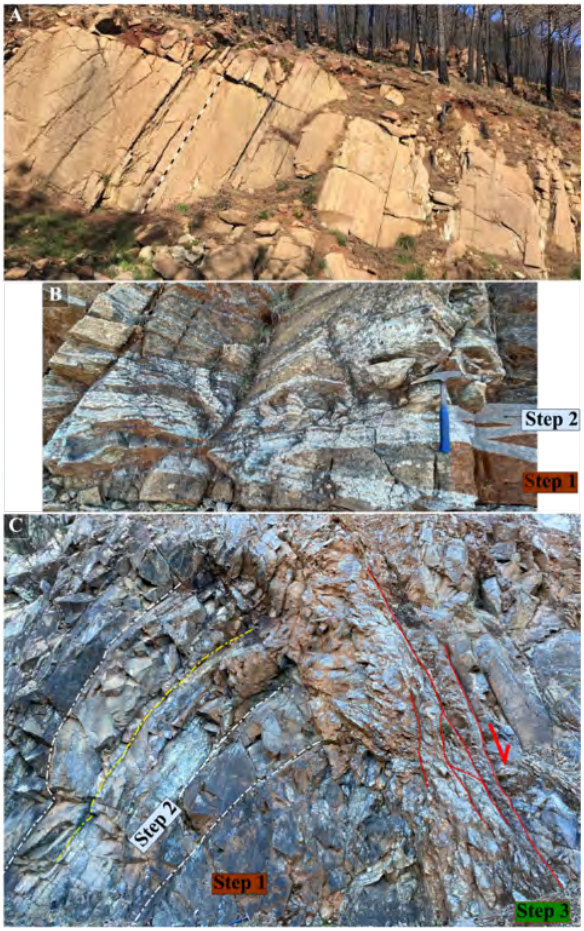


**Figure 2**. Serpentinization steps in outcrops. **(A)** First step corresponding to massive brown peridotites partially serpentinized in mesh-texture with mantellic HT foliation (dashed line); **(B)** second step characterized by multi-centimetre white band corresponding to serpentinized corridors with remnants of step 1 partially serpentinized peridotite; **(C)** the third serpentinization step results in metre-thick cataclastic zones with normal sense of shear (red lines). Step 2 corridors (white lines) and centimetric-scale felsic dyke (yellow line) are shown.

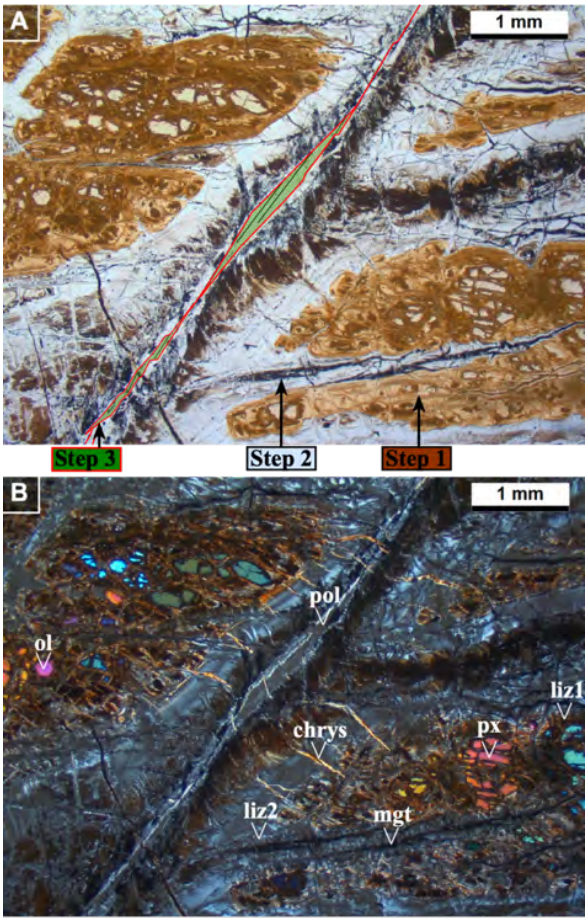


**Figure 3.** The three steps of serpentinization in thin section **(A)** in plane polarized light and **(B)** in cross-polarized. Remnants of brown, mesh-textured liz 1 with olivine (ol) and pyroxene (px) (i.e. step 1) are crosscut by lizardite 2 (i.e. step 2); liz 2 is associated with magnetite (mgt) veinlets; subsequently, a shear vein filled with polygonal serpentine (pol, in green on A) developed (i.e. step 3) and intersected liz 2; this vein is associated with magnetite crystallisation and is crosscut by chrysotile (chrys) tension gash.

centimetric in size and are often sub-rounded. Deformed bands are characterised by the development of green serpentine (mainly polygonal serpentine) filling veins. Different types of veins are encountered: shear (or hybrid shear-extensional) veins with slickenfibers and extensional veins (i.e. tension gashes with serpentine fibres normal to wallrocks). The main veins are composed of polygonal serpentine mixed with chrysotile (Figure 3). Veins are associated with a metasomatic halo in the host serpentinized peridotite. Within halos, pyroxenes are transformed into bastite, and clusters of magnetite crystals appear in the rim of vein. Locally chrysotile tension gashes cut through green serpentine veins (Figure 3).

### 4.2 Structural analysis of step 3 serpentine veins

The network of green serpentine shear veins indicates generally a normal sense of shear (e.g., Figure 2C). Nearly four hundred serpentine slickenfibers were measured and analyzed, site by site, throughout the Sierra Barmeja massif. Some dominant trends in vein orientation at the station scale (e.g., N-S, NW-SE, NE-SW, E-W) have been observed, without bulk predominant orientation at the massif scale. With the exception of station 3, where only limited data is available, all sites present a sub-vertical shortening. The horizontal stretching direction varies from site to site (Figure 4A).

When considering the whole massif as a single station, orientation and plunge of shear veins are heterogenous (Figure 4B). However, contouring of pression/tension calculated axes yields a pattern similar to that of individual stations i.e. vertical shortening and horizontal stretching during a near pure flattening deformation (Figure 4C). Therefore, step 3 serpentinization might occur at a Sierra Barmeja massif scale during an extension tectonic event.

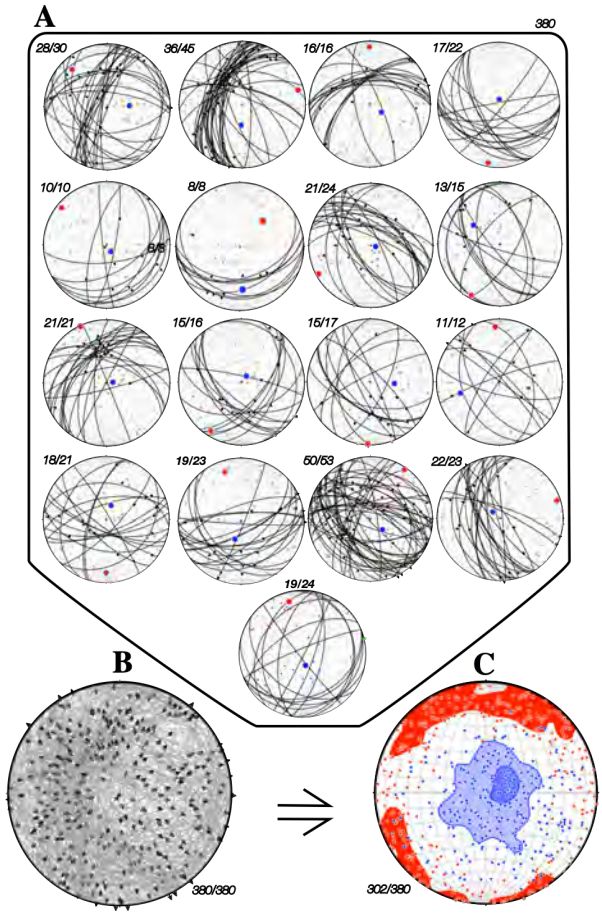


**Figure 4.** Stereoplots (Schmidt's lower hemisphere) of the step 3 serpentine veins measured throughout the Sierra Barmeja **(A)** stereograms of 17 stations, great circles are vein planes with kinematics (arrow), calculated mean shortening axis (blue circle) and stretching axis (red circle); **(B)** stereogram gathering all data (380) with their kinematics; **(C)** calculated stereogram of compatible shear veins with stretching (red) and shortening (blue) axes with contouring which yields an oblate ellipsoid (R=0.88) suggestive a pure flattening strain.

### 4.3 Oxygen and hydrogen isotope compositions

The $\delta^{18}O$ values as a whole range between +2.9‰ to +8.7‰ with most values around ~ 5.0‰ (Figure 5). The δD values are between -33‰ and -96‰ with most values around ~ -79‰.

More specifically, serpentinized peridotites of step 1 have homogeneous $\delta^{18}O_{WR}$ values around ~ +5.3‰. The measured values do not correlate with the intensity of serpentinization (from ~35 to 90% in the analysed samples). It seems that two sub-groups can be identified on the basis of their $\delta D_{WR}$ values around -75‰ and -90‰, respectively.

Serpentinized corridors (liz 2) have δD values between -71‰ and -76‰, similarly to the first sub-group of liz 1. Their $\delta^{18}O$ values range between +2.9‰ to +5.5‰.

The $\delta^{18}O$ and δD values of step 3 serpentine are scattered around the values of the serpentinized peridotites and corridors, which may result from some variation of the conditions of serpentinization (low fluid/rock ratio, variable temperatures).

Two serpentine-magnetite pairs give a $\Delta^{18}O$ value of +10.1‰ and +10.7‰, which yields a temperature of equilibrium of 180 ± 50°C, using the fractionation factor of Früh-Green et al. (1996).

From these results, consistent with the main mineralogical features of serpentinization in the Ronda Massif, it seems unlikely that seawater was involved during serpentinization. Rather, crustal fluids can be proposed for all steps of serpentinization, the fairly comparable isotopic compositions pleading for a continuum of serpentinization rather than for discrete serpentinization events.

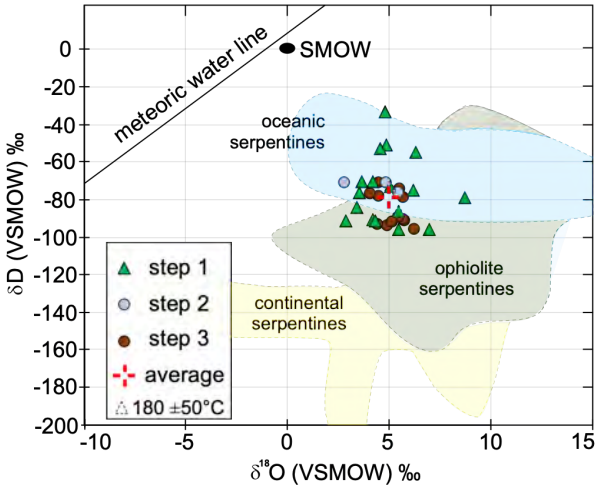


**Figure 5.** $\delta^{18}O$ vs. δD diagram of serpentinites from the Sierra Barmeja massif. The blue, green and yellow domains represent the isotopic compositions of oceanic, ophiolite and meteoric serpentines, respectively (Früh-Green et al. 2001).

## 5. Conclusion

The peridotites of the Ronda Massif (Spain) have undergone three steps of serpentinization. Pervasive lizardite 1 serpentinization occurs throughout the Massif. The second step is more localised and consists of corridors of lizardite 2, chrysotile and magnetite. The third step is marked by both polygonal serpentine and magnetite veins occurring within cataclastic zones. This syn-step 3 cataclastic deformation occurred during a regional-scale extensional tectonic event characterized by multi-directional horizontal stretching (near pure flattening strain). All serpentinization steps share similar isotopic signatures with average values of ~+5‰ and ~ -79‰ for $\delta^{18}O$ and δD, respectively. Crustal-derived fluids are favoured for serpentinization, which is thought to have occurred at temperatures around 180 ± 50°C.

## Acknowledgements

This work is part of Bastien Audran PhD thesis. Thanks are due to the CNRS-SYSTER French program for financing field work and analyses.

## References

Deschamps, F., Godard, M., Guillot, S., Hattori, K., (2013) Geochemistry of subduction zone serpentinites: A review. Lithos 178, p. 96–127. https://doi.org/10.1016/j.lithos.2013.05.019

Esteban, J.J., Cuevas, J., Tubía, J.M., Sergeev, S., Larionov, A., (2011) A revised Aquitanian age for the emplacement of the Ronda peridotites (Betic Cordilleras, southern Spain). Geol. Mag. 148, p. 183–187. https://doi.org/10.1017/S0016756810000737

Frasca, G., Gueydan, F., Poujol, M., Brun, J.-P., Parat, F., Monié, P., Pichat, A., Mazier, S., (2017) Fast switch from extensional exhumation to thrusting of the Ronda Peridotites (South Spain). Terra Nova 29, p. 117–126. https://doi.org/10.1111/ter.12255

Früh-Green, G.L., Plas, A., Lécuyer, C., (1996) Petrologic and stable isotope constraints on hydrothermal alteration and serpentinization of the epr shallow mantle at hess deep (site 895). Ocean Drilling Program, Vol. 147, p. 255–291 https://doi.org/10.2973/odp.proc.sr.147.1996

Früh-Green, G.L., Scambelluri, M., Vallis, F., (2001) O–H isotope ratios of high-pressure ultramafic rocks: implications for fluid sources and mobility in the subducted hydrous mantle. Contrib Mineral Petrol 141, p. 145–159. https://doi.org/10.1007/s004100000228

Lawley, C.J.M., Petts, D.C., Jackson, S.E., Zagorevski, A., Pearson, D.G., Kjarsgaard, B.A., Savard, D., Tschirhart, V., (2020) Precious metal mobility during serpentinization and breakdown of base metal sulphide. Lithos 354–355, 105278. https://doi.org/10.1016/j.lithos.2019.105278

Patten, C.G.C., Coltat, R., Junge, M., Peillod, A., Ulrich, M., Manatschal, G., Kolb, J., (2022) Ultramafic-hosted volcanogenic massive sulfide deposits: an overlooked sub-class of VMS deposit forming in complex tectonic environments. Earth-Science Reviews 224, 103891. https://doi.org/10.1016/j.earscirev.2021.103891

Pedrera, A., Galindo-Zaldívar, J., Acosta-Vigil, A., Azor, A., González-Menéndez, L., Rodríguez-Fernández, L.R., Ruiz-Constán, A., (2016) Serpentinization-driven extension in the Ronda mantle slab (Betic Cordillera, S. Spain). Gondwana Research 37, p. 205–215. https://doi.org/10.1016/j.gr.2016.05.008

Tubía, J.M., Cuevas, J., Esteban, J.J., (2013) Localization of deformation and kinematic shift during the hot emplacement of the Ronda peridotites (Betic Cordilleras, southern Spain). Journal of Structural Geology 50, p. 148–160. https://doi.org/10.1016/j.jsg.2012.06.010

# Formation of large mound-shaped sulfide deposit on axial volcanic ridge – A case from the Wocan-1 hydrothermal field, Carlsberg Ridge

**Yiyang Cai[1,2,3], Yejian Wang[1], Sven Petersen[2], Xiqiu Han[1,3]**
[1] *Key Laboratory of Submarine Geosciences, Second Institute of Oceanography, Ministry of Natural Resources, Hangzhou 310012, China*
[2] *GEOMAR, Helmholtz Centre for Ocean Research Kiel, Kiel 24148, Germany*
[3] *School of Oceanography, Shanghai Jiao Tong University, Shanghai, 200030, China*

**Abstract.** The hydrothermally active Wocan-1 mound is a nearly circular mound, ~260 m wide and ~50 m high, located on the northwestern slope of an axial volcanic ridge in Carlsberg Ridge. Seafloor observations and sampling indicate a large variability of venting styles as a result of local permeability control. High temperature black smokers are widely distributed over the summit area with significant metal flux indicating limited subseafloor seawater mixing. Clear vent fluids as well as diffuse fluid venting is common in the central and northern areas suggesting subseafloor metal precipitation. Copper-rich sulfides are most abundant in the summit region and along its eastern slope with chalcopyrite and atacamite being major minerals, whereas pyrite and anhydrite are the major minerals in the northern margin area. Sulfur isotope ratios reveal a larger contribution of entrained seawater in the central and the northern areas, when compared to southern area. The increase of $\delta^{34}S$ is related to recrystallization of primary sulfides in the presence of fluids with abundant sulfate-derived sulfur. The active Wocan-1 mound is larger than the well-known TAG active mound on the Mid-Atlantic Ridge indicating that axial volcanic ridges also have the potential to host large sulfide deposit.

## 1 Introduction

Large seafloor massive sulfide deposits at mid-ocean ridges are often related to off-axis tectonic massifs, ocean core complexes, or associated with detachment faults. They are only rarely observed on axial volcanic ridges. The Wocan-1 hydrothermal field on the axial volcanic ridge of the slow-spreading Carlsberg Ridge is one exception that was recently discovered.

Wocan-1 was discovered in 2013 during the Chinese DY 28th cruise. Previous studies confirmed the presence of abundant high-temperature mineralization at Wocan (Wang et al. 2017). Age dating of nearby sediment cores has revealed an intense activity over the past ~ 1070 years, with the oldest known mineralization dating back to 10,604 ± 67yr BP and the field is currently considered to be in a mature stage of hydrothermal activity (Qiu et al. 2021). In addition, the approximate area covered by hydrothermal precipitates at Wocan (~ 420 m x 320 m; Wang et al. 2017) suggests it is a comparable in scale to some of the largest off-axis vent fields known (German et al., 2016).

In 2017, during the DY 38th Cruise, further investigations were carried out by the manned submersible Jiaolong at Wocan-1. Detailed seafloor observation, high-resolution topographic mapping and accurate sampling have been undertaken, which allows further insights into the processes shaping the Wocan-1 mound. We report here on the variability of venting styles at Wocan-1, the associated mineralization types, their mineralogy, and sulfur isotope compositions and describe the causes for their spatial and temporal variations. Results from this study will contribute to a better understanding of the formation processes of large sulfide deposits on mid-ocean ridges and of the potential of axial volcanic ridges to host economically interesting sulfide deposits.

## 2 Geological background

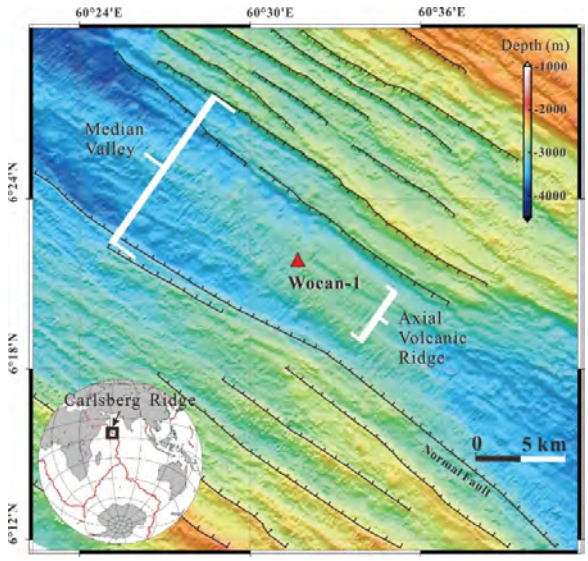


**Figure 1.** Bathymetric and structural map of the survey area over Carlsberg Ridge and location of the active Wocan-1 hydrothermal field (Wang et al. 2017).

The Carlsberg Ridge (CR), separating the Indian and Somalia tectonic plates in the northwest Indian Ocean, is a slow spreading mid-ocean ridge with a full spreading rate of 22-32 mm/yr (Kamesh Raju et al. 2008). The Wocan Ridge is a NW-SE oriented axial volcanic ridge in the median valley of a symmetrical-spreading mid-ocean ridge segment of the Carlsberg Ridge (Wang et al. 2017). The ridge

extends for ~28 km and covers a total area of about 220 km$^2$. Wocan Ridge is wide at its center and narrows at the ends, especially in the northwest, where the ridge is linearly extended. Based on TV-sled, TV-grab and manned submersible observations, two sites of hydrothermal mineralization care now recognized. The hydrothermally active Wocan-1 field is located on the Wocan Ridge at 6°22' N, 60°31' E in a water depth of 2970 ~ 3120 m. The Wocan-2 hydrothermal site is located ~1.7 km to the northwest of Wocan-1. It lacks active black smokers, but low-temperature diffuse flow is present.

## 3 Method

### 3.1 Seafloor observations and mapping

Four dives with more than 40 hours bottom time have been undertaken by the manned submersible Jiaolong in the Wocan-1 hydrothermal field and its surrounding areas. The topography was derived based on data obtained by bathymetric side-scan sonar (HRBSSS) system of the submersible which surveyed ~80 m above the seafloor at a speed of ~2 knots (Wang et al. 2021). Underwater acoustic communication devices transmitted positioning data obtained by a POSIDONIA USBL on the supporting mother ship, allowing for the determination of the initial position of the integrated navigation system. The submersibles Doppler Velocity Log provided information on the velocity over ground. Motion sensor IXSEA Octans provided data on attitude and heading. Both of them were used to supplement the HRBSSS data and to aid navigation.

### 3.2 Analytical methods

Textural interpretations and mineral identification were based on polished thin sections analyses at the Second Institute of Oceanography, Ministry of Natural Resources (SIOMNR), Hangzhou, China. The thin sections were examined under a polarizing microscope using reflected and transmitted light.
In-situ sulfur isotope analyses were taken on 135 spots in six samples. Chemical laser-ablation spot-analyses (N=95) on sulfide minerals were performed on a Neptune Plus MC-ICP-MS (Thermo Fisher Scientific, Bremen, Germany) equipped with a Geolas HD excimer ArF laser ablation system (Coherent, Göttingen, Germany) at the Wuhan SampleSolution Analytical Technology Co., Ltd, Hubei, China using the technique described by Hu et al. (2015) and Fu et al. (2016). Ion-probe analyses on 40 sulfide spots were performed by the Sensitive High-Resolution Ion MicroProbe SI (SHRIMP-SI) at Research School of Earth Sciences (RSES), Australian National University, using the technique described by Ireland et al. (2014).

## 4 Result

The hydrothermally active Wocan-1 mound is located on the northwestern slope of an axial volcanic ridge. The nearly circular mound is ~260 m wide and ~50 m high (Figure 2). The size, the abundant sulfide outcrops, and the abundance of mass wasting all over the mound surface indicate long-lasting hydrothermal activity at Wocan-1.

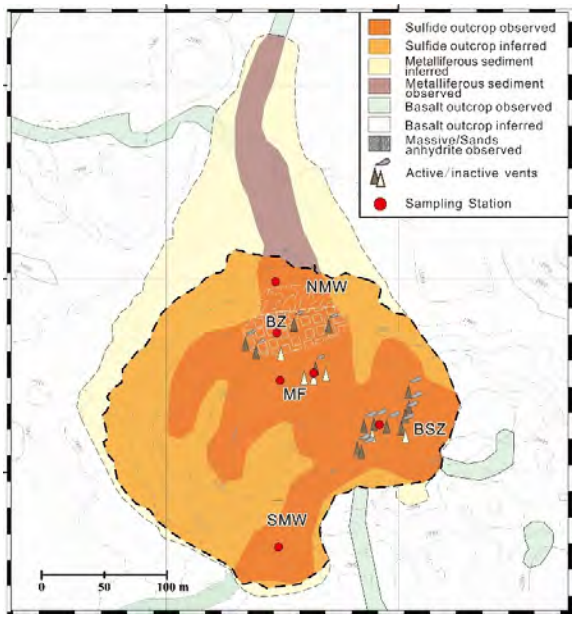


**Figure 2.** Geological map of the Wocan-1 active mound, interpreted from the high-resolution bathymetry, surface samples, and video surveys. BSZ=Black Smoker Zone, MF= Mulberry Forest, BZ= Beehive Zone, SMW= Southern Mass Wasting, NMW= Northern Mass Wasting.

### 4.1 Active vents and mass wasting

There are three distinct active vent sites on this mound, distributed over the summit area and along the northern and eastern slopes of the mound. The largest active vent site, the Black Smoker Zone (BSZ), is located near the summit and along the southeastern slope of the mound. The second area of active venting, Mulberry Forest (MF), occurs ~70 m further to the northwest, is located on a gentle slope, and consists of a dense group of chimneys resembling organ pipes. Most of the chimneys at this site are inactive with only a few active vents being present, which currently vent clear fluids. Finally, the Beehive Zone (BZ), which is furthest to the north, is constructed of beehive chimneys usually standing on top of small mounds mainly composed of massive pyrite and anhydrite.

Extensive mass wasting has been observed on the surface and along the margins of the Wocan-1 mound. The most significant mass wasting is documented at the northern margin of the mound (site NMW) with sulfide talus extending up to ~50 m away from the mound with many oxidized sulfide blocks. Anhydrite sand is also abundant in the north (Figure 3). Further down slope, fine-grained metalliferous sediments extend for a further ~200 m

in flatter areas. On the southern slope another mass wasting area is apparent (site SMW) and extends for 100 m from the summit of the mound to the bottom (Figure 2). Within the SMW area, sulfide blocks are commonly coated by atacamite and greenish sediments are also observed indicating the presence of Cu-rich material in this area.

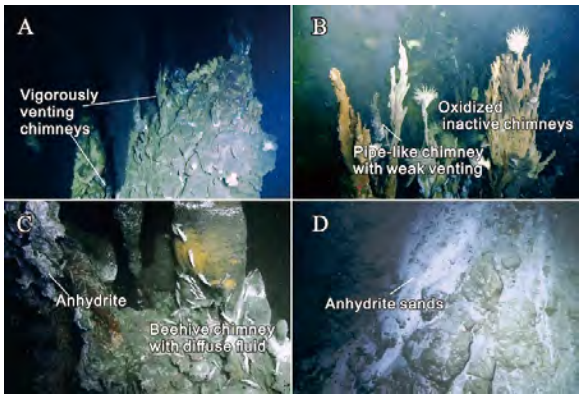


**Figure 3.** A. Vigorously venting black smoker complex, field of view ~5 m; B. Pipe-like chimneys with weak venting, field of view ~3 m; C. Beehive chimneys with diffuse fluid, field of view ~2 m; D. Anhydrite sand on the northern slope of the mound, field of view ~5 m.

### 4.2 Mineralogy of the chimneys and massive sulfides

In this study, samples from Wocan-1 mound have been classified into 1) Cu-rich chimneys, 2) Fe-rich massive sulfides and 3) massive anhydrite-pyrite. The sample types are not evenly distributed over the mound: Cu-rich chimney fragments were collected from the central and southern vent sites (BSZ, SMW and MF), while massive pyrite and massive anhydrite-pyrite samples were mainly obtained from northern areas (BZ and NMW).

Cu-rich chimney fragments collected from the central and southern vent sites are mainly composed of chalcopyrite, sphalerite, pyrite, marcasite and minor covellite, often filled with opal-CT. Based on the texture and paragenesis, pyrite can be distinguished into three types: Main stage, euhedral pyrite-I, subhedral pyrite forming the early or late stages (pyrite-II and pyrite-III), and a colloform pyrite-IV that forms at lower temperatures in the early and late stages of hydrothermal precipitation. Similarly, marcasite forms three distinct types: subhedral marcasite (both early or late stage; mrc-I, mrc-II) and colloform marcasite-III. Pyrite-I is always euhedral in texture and can be found as a core to massive chalcopyrite. High temperature chalcopyrite is commonly rimed by sphalerite and both can be replaced by later stage, subhedral pyrite and marcasite (py-III and mrc-II). Sphalerite inclusions in mrc-III and py-II are commonly observed. Colloform marcasite (mrc-III) and pyrite (py-IV) co-precipitate in the outmost layer of the sample. Covellite and opal-CT occur in the late paragenetic sequence and form in the pore space of the sulfides. Covellite may also form or as a weathering product during the warning stages of hydrothermal activity, as documented from a sample collected from the apron of SMW, where chalcopyrite was replaced by covellite in the outmost layer and atacamite is occurring on the surface of the sample.

Fe-rich massive sulfides and massive anhydrite-pyrite samples are abundant at BZ and NMW. Nodular pyrite aggregates are common in a matrix of anhydrite and massive pyrite with individual pyrite grains reaching more than 1 mm in size. Massive pyrite and nodular pyrite are generally dense and strongly recrystallized with indications of sequential overgrowth layers with rare chalcopyrite residual inclusion (Figure 4D). Chalcopyrite is rare in these samples and may overgrow early bornite or is present as fine-grained chalcopyrite set in an anhydrite matrix.

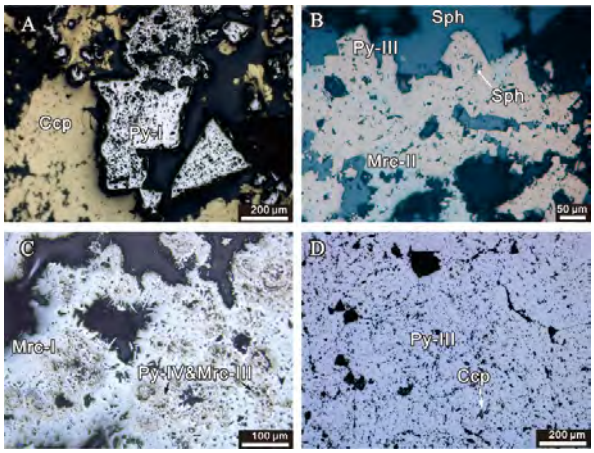


**Figure 4.** Microscopic features of selected samples of the Wocan-1 mound. A. Euhedral pyrite as a core of subhedral chalcopyrite; B. Recrystallized pyrite and marcasite with sphalerite being present as inclusions and overgrowths; C. Colloform pyrite and marcasite rimed by marcasite microlite; D. Strongly recrystallized pyrite with indications of sequential overgrowth layers with rare chalcopyrite residual inclusion.

### 4.3. Sulfur isotope

In-situ sulfur isotope analyses of six pyrite- and marcasite-bearing samples from BSZ, MF, BF and NMW. Overall, the $\delta^{34}S$ ratios of Wocan-1 pyrite and marcasite range from -1.60 ~ 5.04‰ ($\delta^{34}S_{ave}$ =2.1‰, n = 135). The $\delta^{34}S$ values vary between pyrite and marcasite in different types from various areas.

In samples from BSZ site and SMW, δ34S values of pyrite range from 0.35 ~2.98‰ ($\delta^{34}S_{ave}$ = 1.60‰, n = 24). Lighter and even negative values have been observed in marcasite ($\delta^{34}S_{ave}$ = 1.17‰, n = 22), and documented the lowest $\delta^{34}S$ value of -1.60‰. In samples from the MF site, $\delta^{34}S$ values of pyrite range from 0.22 ~ 5.00‰ ($\delta^{34}S_{ave}$ = 2.69‰, n = 26). Only pyrite was analysed in samples from the BF and NMW sites and it shows a narrow range of $\delta^{34}S$ values ranging from 2.78 ~ 4.27‰ with an average $\delta^{34}S$ value of 3.56‰ (n = 20).

## 5 Discussion and conclusion

Significant differences in fluxes of discharged fluids and transported metals have been observed between BSZ, MF and BZ. High temperature black smokers with significant loss of metal to the water column indicates limited subseafloor fluid mixing (Jamieson et al. 2014). In contrast hot, clear fluids and diffuse fluids at MF and BZ are free of metal-rich black smoke, suggesting metal precipitation prior to venting and the accumulation of minerals within the mound or beneath the seafloor by mixing with abundant seawater.

Areas such as BSZ, MF, and SMW are enriched in high-temperature Cu-rich mineral assemblages composed mainly of chalcopyrite with subordinate sphalerite and pyrite. This suggests the presence of a high-temperature upflow zone. It is, however, difficult to explain why pyrite is particularly abundant in the northern margin of the mound. Weathering processes, recrystallization, and changes in the fluid composition could all be responsible for the enrichment of pyrite in this area (Webber et al. 2015; Petersen et al. 2000; Hannington et al. 1995). Traces of growth layering are present with the samples, as are nodular pyrite aggregates in massive anhydrite-pyrite. This texture is similar to that reported for the active TAG mound, suggesting that pyrite from the BZ and NMW has experienced similar recrystallisation processes. It should be noted, that chalcopyrite and sphalerite are particularly low in such samples from Wocan-1 when compared to similar samples from TAG, implying that the fluid composition is relatively Cu- and Zn-poor. It is likely, that these nodular breccias at Wocan-1 have been stripped of most of the Cu and Zn during recrystallization.

The mean $\delta^{34}S$ values of pyrite varies between different areas: $\delta^{34}S_{BSZ\&SMW}$ = 1.60‰ < $\delta^{34}S_{MF}$ = 2.69‰ < $\delta^{34}S_{BZ\&NMW}$ = 3.56‰. Using a simple two-endmember mixing model (Ono et al. 2007), it can be calculated that the contribution of seawater-derived sulfur differs between the sites and is increased by 6% and 10% in the central and the northern areas when compared to the southern sites. Recrystallization during late-stage mixing of hydrothermal fluids with abundant entrained seawater-derived sulfur as evidenced by the abundance of anhydrite have led to this increase of $\delta^{34}S$ values.

Wocan-1 is a large deposit when compared to other sulfide occurrences at axial volcanic ridges. The mound diameter, the intense mass wasting, evidence for recrystallization of primary sulfides and seawater ingress into the mound point to long-lasting, multi-staged history of venting at this site. This and the abundance of Cu-rich material may indicate that sulfide deposits at axial volcanic ridges should be reconsidered as potential exploration targets for economically interesting mineralization.

## References


Fu J, Hu Z, Zhang W, Yang L, Liu Y, Li M, Zong K, Gao S, Hu S (2016) In situ sulfur isotopes (delta(34)S and delta(33)S) analyses in sulfides and elemental sulfur using high sensitivity cones combined with the addition of nitrogen by laser ablation MC-ICP-MS. Analytica chimica acta 911: 14–26

Hannington MD, Jonasson IR, Herzig PM, Petersen S (1995) Physical and Chemical Processes of Seafloor Mineralization at Mid-Ocean Ridges. In: Humphris SE, Zierenberg RA, Mullineaux LS, Thomson RE (ed) Geophysical Monograph Series. American Geophysical Union, Washington DC, pp 115–157

Hu Z, Zhang W, Liu Y, Gao S, Li M, Zong K, Chen H, Hu S (2015) "Wave" signal-smoothing and mercury-removing device for laser ablation quadrupole and multiple collector ICPMS analysis: application to lead isotope analysis. Analytical chemistry 87: 1152–1157

Ireland TR, Schram N, Holden P, Lanc P, Ávila J, Armstrong R (2014) Charge-mode electrometer measurements of S-isotopic compositions on SHRIMP-SI. International Journal of Mass Spectrometry 359: 26–37.

Jamieson J, Hannington M, Petersen S, Tivey M (2014) Volcanogenic Massive Sulfides. In: Harff J, Meschede M, Petersen S, Thiede J (ed) Encyclopedia of Marine Geosciences. Springer Netherlands, Dordrecht, pp 1–9

Kamesh R, Chaubey AK, Amarnath D, Mudholkar A (2008) Morphotectonics of the Carlsberg Ridge between 62°20′ and 66°20′E, northwest Indian Ocean. Marine Geology 252: 120–128.

Ono S, Shanks WC, Rouxel OJ, Rumble D (2007) S-33 constraints on the seawater sulfate contribution in modern seafloor hydrothermal vent sulfides. Geochimica et Cosmochimica Acta 71: 1170–1182

Petersen S, Herzig PM, Hannington MD (2000) Third dimension of a presently forming VMS deposit: TAG hydrothermal mound, Mid-Atlantic Ridge, 26°N. Mineral. Deposita 35: 233–259

Qiu Z, Han X, Li M, Wang Y, Chen X, Fan W, Zhou Y, Cui R, Wang L (2021) The temporal variability of hydrothermal activity of Wocan hydrothermal field, Carlsberg Ridge, northwest Indian Ocean. Ore Geology Reviews: 103999

Wang Y, Han X, Petersen S, Frische M, Qiu Z, Li H, Li H, Wu Z, Cui R (2017) Mineralogy and trace element geochemistry of sulfide minerals from the Wocan Hydrothermal Field on the slow-spreading Carlsberg Ridge, Indian Ocean. Ore Geology Reviews 84: 1–19

Wang Y, Han X, Zhou Y, Qiu Z, Yu X, Petersen S, Li H, Yang M, Chen Y, Liu J, Wu X, Luo H (2021) The Daxi Vent Field: An active mafic-hosted hydrothermal system at a non-transform offset on the slow-spreading Carlsberg Ridge, 6°48′N. Ore Geology Reviews 129: 103888

Webber AP, Roberts S, Murton BJ, Hodgkinson MR (2015) Geology, sulfide geochemistry and supercritical venting at the Beebe Hydrothermal Vent Field, Cayman Trough. Geochem Geophys Geosyst 16: 2661–2678

Zong T, Han X, Liu J, Wang Y, Qiu Z, Li H, Yu X (2019) $H_2O$ in basaltic glasses from the slow-spreading Carlsberg Ridge: Implications for mantle source and magmatic processes. Lithos 332–333: 274–286.

# Origin of Fe-Ca metasomatism at oceanic core complexes: implications for the formation of seafloor massive sulphide deposits (MARK area, 23°N)

**R. Coltat[1,2], M. Andreani[3], C. Patten[4], M. Godard[5], B. Debret[6], J. Escartin[2]**
[1]*Instituo Andaluz de Ciencias de la Tierra, IACT, CSIC-UGR, Armilla, Granada, Spain*
[2]*Laboratoire de Géologie, UMR 8538, Département de Géosciences, ENS Paris, PSL Research University, Paris, France*
[3]*Laboraoire de Géologie de Lyon, UMR 5672, ENS, Université Lyon 1, Lyon, France*
[4]*Institute of applied geochemistry, Chair for Geochemistry and Economic Geology, KIT, Karlsruhe, Germany*
[5]*Géosciences Montpellier, CNRS, Université de Montpellier, Montpellier, France*
[6]*Institut de Physique du Globe de Paris, CNRS UMR 7154, Paris, France*

**Abstract.** At (ultra)slow-spreading ridges, the circulation of hot, acidic, reduced and metal-rich fluids triggers the formation of ultramafic-hosted seafloor massive sulphides deposits (UM-SMSs). These sites display a great variability from site to site, making it difficult to build a simple genetic model. They may notably be associated with Fe-Ca metasomatism, as observed in fossil mineralized systems, thus with possible genetic implications for the formation of mineralized systems. Similar Fe-Ca metasomatism is reported in mantle rocks drilled at the Mid-Atlantic Ridge Kane (MARK) area, offering access to the vertical dimension beneath an oceanic core complex to unravel the nature and geometry of deep magmato-hydrothermal processes.
At MARK, mantle rocks record complex melt-rock and fluid-rock interactions. Magma channelling and interactions with peridotite enrich mantle silicates in Fe, Co and Zn. Subsequent hydrothermal alteration produces metamorphic mineral assemblages (e.g., amphibole, clinopyroxene, chlorite, talc, ilvaite, hydro-garnet, serpentine) and is responsible for Cu leaching. It occurs during early mantle exhumation and is followed by the serpentinization of the massif during progressive mantle denudation. Considering the lithological heterogeneity at (ultra)slow-spreading ridges, metal enrichment in mantle rocks through melt-rock interactions may be widespread, eventually accounting for metal endowment at UM-SMS

## 1 Introduction

Mid-Oceanic Ridges (MORs) are the locus of hydrothermal circulations leading to intense chemical and thermal exchanges between the oceanic lithosphere and the oceans (Alt, 1995). This results in a variability of altered rocks and hydrothermal fluids that vent at the seafloor (e.g., Schwarzenback and Steele-Mclnnis, 2020). Among them, UM-SMSs form when hot (e.g., 300-350°C), acidic, reduced and metal-rich fluids mix with ambient seawater in ultramafic dominated environments, leading to the formation of Cu-Zn-Co-(Au-Ag) mineralizations (Fouquet et al., 2010).

However, the structural, mineralogical and geochemical variability from site to site (Fouquet et al., 2010) is coupled to the difficulty to access the vertical dimension beneath UM-SMSs. This results in limited constraints on the nature and geometry of deep hydrothermal circulations, and thus on a simple genetic model. This can be partly resolved by focusing on fossil mineralized systems exposed in Alpine ophiolites and that share similarities with UM-SMSs, although they are closely associated with (Fe)-Ca silicates and are interpreted as deep portions beneath UM-SMSs (e.g., Coltat et al., 2019). This suggests that Fe-Ca metasomatism could have genetic links with the formation of UM-SMSs, and that is not documented at MORs due to the restricted access to the vertical dimension. This can be partly addressed through drill cores at exhumed mantle domes.

Here, we focus on the MARK area, an oceanic core complex (OCC) where mantle rocks showing evidence of Fe-Ca metasomatism have been drilled during ODP Leg 153 (Cannat et al., 1995). We performed a petrographic and geochemical on mantle rocks to provide i) temporal and spatial constraints on Fe-Ca metasomatism, and ii) quantify the associated chemical mobilities and their implication for UM-SMS formation.

## 2 Geological setting

The southern zone of the Kane fracture zone is referred to as the MARK area (23°N, Fig. 1). This segment is asymmetric, with development of an OCC on the western flank (Dick et al., 2010), and block-faulted basaltic pillow lavas on the eastern flank (Cannat et al, 1995). A volcanic ridge at the axial valley hosts the active Snake Pit hydrothermal field.

Mantle rocks were recovered at ODP site 920, 40 km south to the Kane transform at ~3300 meters below sea level (23°20.32'N, Fig. 1B). The holes 920B and 920D reached 126 and 200 meters below seafloor, with a cumulative recovery of 38 and 47%, respectively. Serpentinized harzburgites with minor dunite layers and gabbro veins were recovered.

Structural observations of serpentinite veins indicate hydrothermalism and alteration associated with mantle exhumation (Andreani et al., 2007). The presence of unusual Fe-Ca silicates (e.g., ilvaite, hydro-andradite and diopside) accompanied with sulphides and oxides (Gaggero et al., 1997) also suggests high temperature hydrothermal activity. After petrographic analyses, this occurs during early serpentinization (Gaggero et al., 1997)

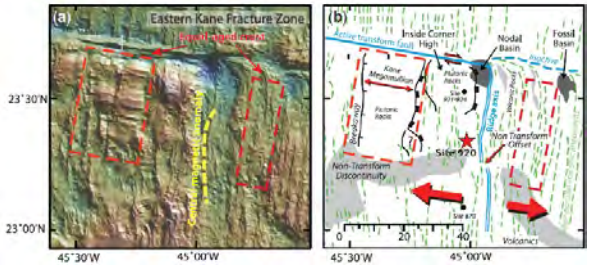


**Figure 1.** (A) Shaded relief bathymetric map of the Mid-Atlantic Ridge Kane area and (B) tectonic interpretation of the Kane megamullion (after Dick et al., 2010).

## 3 Methods

We focused on nineteen samples covering different types of petrographic facies: serpentinized peridotites, altered magmatic rocks intruding serpentinized peridotites, serpentinized peridotite-magmatic dykelets contacts, serpentine-chlorite-amphibole-talc veins, clinopyroxene-rich alteration zones and veins, and calcite-bearing veins cutting through serpentinized peridotites. This sample set is representative of the variability in hydrothermal signatures observed in mantle rocks at MARK.

Mineralogical assemblages have been determined through microscope observations and SEM analyses. EPMA and LA-ICP-MS analyses were carried out on mantle and metamorphic mineral phases from 16 samples to constrain their geochemical compositions. Finally, bulk rock geochemical compositions of sixteen mantle and magmatic rocks were measured using ICP-MS technique.

## 4 Results and interpretation

### 4.1 Petrography of the MARK mantle and magmatic rocks

The host rocks represent either serpentinized peridotites (SP) or magmatic dykelets intruding the former. Serpentinization is variable, generally less advanced near magmatic intrusions where pyroxene may be preserved. Further away, mantle silicates (olivine and pyroxenes) are almost fully replaced by serpentine, forming mesh and bastite textures. Magmatic rocks represent rodingitized and clinopyroxene-rich dykelets and oxide gabbro. They present advanced alteration with common chlorite, hydro-grossular and clinopyroxene assemblages in the rodingitized dykelet (Fig. 2A). In oxide gabbro, amphibole forms after clinopyroxene, albite after plagioclase and chlorite after Fe-Ti oxides (Fig. 2B).

At the contact with magmatic dykelets, the peridotite is altered (a few mm to few cm in size) and contains metamorphic Fe-Ca-rich assemblages including amphibole, chlorite, talc, clinopyroxene, serpentine and minor ilvaite and hydro-andradite in apparent textural equilibrium (Fig. 2C). Ilvaite forms directly at the expense of pristine Fe-rich mantle olivine (Fig. 2D) suggesting that serpentinization was not achieved during Fe-Ca metasomatism. This is supported by the presence of late serpentine veins cutting through these contacts.

Serpentinized peridotites also contain different types of veins, mm to cm thick. The veins and its serpentinized peridotite host rock are hereafter referred to as PP1, PP2 and CP. The first type (PP1) is made of amphibole (tremolitic to pargasitic composition), chlorite, talc, serpentine ± clinopyroxene assemblages with locally minor titanite.

A second type (PP2) represents clinopyroxene-rich veins, where coarse clinopyroxene grains are partially amphibolitized (Fig. 2E) and enclosed in a matrix made of tiny amphibole (tremolitic to pargasitic composition), serpentine and chlorite grains. Locally the proportion of clinopyroxene in mantle rock increases, defining a pervasive zone made of tiny imbricated clinopyroxene lathes associated with amphibole and phyllosicliates.

Finally, the third type of vein cutting through serpentinized peridotite (CP) represents calcite-bearing veins and is either made of hydro-andradite, diopside, serpentine, calcite, pyrrhotite assemblages (Fig. 2F) or serpentine, calcite, Cu-sulfides veins. While sulfides represent less than 5% in both veins, they suggest metal mobilization during the formation of calcite-bearing veins.

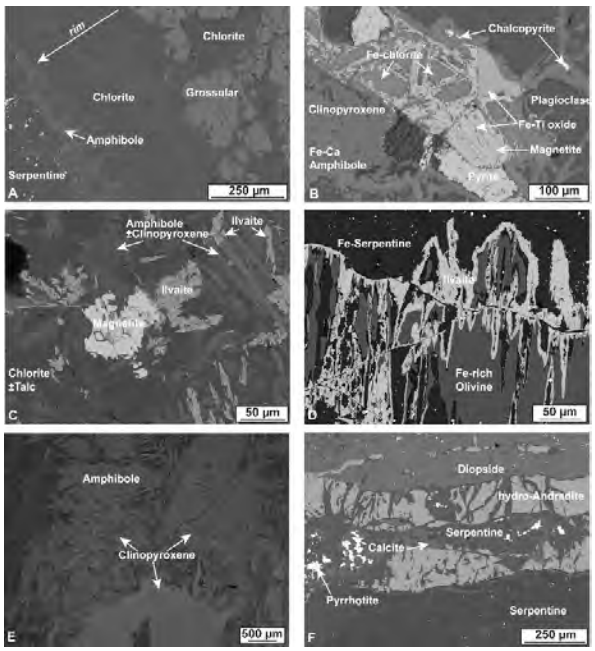


**Figure 2.** SEM pictures of magmatic and mantle rocks of ODP site 920 (A) Rodingitized magmatic dykelet-peridotite contact showing chlorite enrichment towards the rim of the dykelet. (B) Amphibolitized oxide gabbro. Amphibole and Fe-chlorite form at the expense of clinopyroxene and Fe-Ti oxides, respectively. (C) Ilvaite replacing magnetite and associated with amphibole in a fine-grained matrix of chlorite+talc. (D) Ilvaite replacing olivine and surrounded by a matrix of Fe-serpentine. (E) Clinopyroxene-amphibole-serpentine-chlorite vein cutting through the serpentinized peridotite (PP2). (F) Vein made of hydro-andradite, clinopyroxene, pyrrhotite, calcite and serpentine cutting through a serpentinized peridotite (CP).

### 4.2 Bulk rock and *in-situ* olivine geochemistry

The different samples investigated present heterogenous chemical compositions that commonly lie between the poles defined by the serpentinized peridotites and mafic rocks, locally overlapping the MARK pyroxenes (Fig. 3). The CaO content is low in SP, comparable to country serpentinized peridotites, and increases in other samples according to the presence of Ca-bearing mineral phases in these samples (Fig. 3A). PP1 and PP2 have higher FeO content compared to other samples (Fig. 3B).

SP and CP display low REE compositions comparable to country serpentinized peridotites, with a strong Eu positive anomaly and a local concave-up shape (Fig. 3C). The magmatic dykelet-peridotite contact, apart from the positive Eu anomaly, displays REE compositions that mimic those of the oxide gabbro. Finally, PP1 and PP2 are generally enriched in REE and display a positive to negative Eu anomaly compared to SP, but show REE patterns and compositions similar to those of MARK pyroxenites (Fig. 3D). This suggests that veins forming PP1 and PP2 are former pyroxenite veins intruding mantle rocks, which subsequently underwent hydrothermal alteration that produced the observed metamorphic mineral assemblages. The variable REE compositions can be ascribed to the mixing, in various proportions, between pyroxenite and peridotite components.

PP1 and PP2 are depleted in Cu compared to country serpentinized peridotites (Fig. 3E). This cannot be explained by pyroxenite-peridotite mixing as pyroxenite contains more Cu than peridotite. Hence, this suggests that Cu is removed from the rock during hydrothermal alteration. However, Zn is little sensitive to hydrothermal alteration because of the homogenous Zn content of our samples. Only one CP is enriched in Cu and Zn compared to other samples, accordingly to the presence of sulphide in this sample (Fig. 3E, F).

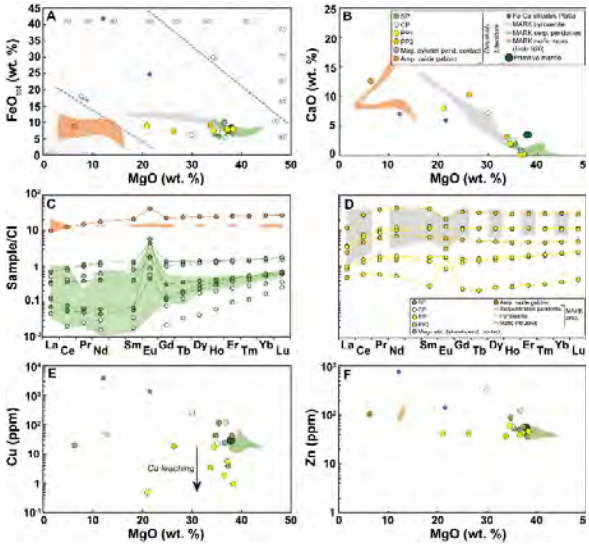


**Figure 3.** Bulk rock major, trace and rare earth element chemical compositions of mantle and mafic rocks of the ODP site 920 compared with data from the literature (Burgath et al., 1997; Cannat et al., 1997; Casey, 1997; Coltat et al., 2019). CI composition are from McDonough and Sun (1995).

Olivine in mantle rocks at MARK displays variable FeO and MgO contents, with higher FeO content in grains at the contact with magmatic dykelets compared to grains away from these contacts (Fig. 4A). This results in a strong decrease of the Mg# which is accompanied with the decrease of the NiO content and the increase of the Co and Zn contents (Fig. 4B-D).

Similar major element systematics were reported at MARK and ascribed to melt-rock interactions during magma channelling in the lithospheric mantle (Cannat et al., 1997). This suggests that melt-rock interactions may drastically modify the metal (Fe, Co, Zn) budget of mantle rocks.

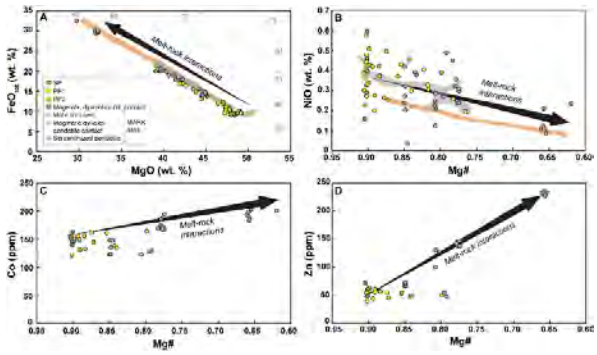


**Figure 4.** Major and trace element compositions of olivine of the ODP site 920 at MARK compared with data from the literature (Cannat et al., 1997).

### 4.3 Magmato-hydrothermal history at MARK

Several lines of petrographic and geochemical evidences plead for complex magmato-hydrothermal processes at MARK. These are synthetized in Figure 5.

First, mantle rocks are intruded by magma injections leading to melt-rock interactions with mantle silicates and enrichment of Fe, Co and Zn. As olivine at the contact with magmatic dykelets does not present evidence for recrystallization, magma channelling has to occur in a fresh, non-serpentinized mantle at depth.

In a second stage, fluid circulation along the lithological interfaces produces secondary hydrous Fe-Ca metamorphic assemblages. Ti thermometry of amphibole (Liu et al., 2021) suggests a ~420-830°C temperature formation range, agreeing with the 425 ± 75°C range estimated for the stability of ilvaite-hydro-andradite-diopside assemblages (Gustafson, 1974). Such high temperatures inhibit pervasive serpentinization (Allen and Seyfried, 2003). Fe is likely brought through former melt-rock interactions while Ca may derive from the dissolution of primary magmatic silicates (clinopyroxene,

plagioclase) or seawater-derived hydrothermal fluid. Cu is leached during this stage.

Finally, progressive mantle exhumation and cooling in a brittle regime potentially promotes thermal cracking, and allows seawater entrainment and pervasive serpentinization of the peridotite footwall as well as formation of calcite-bearing veins at temperature <400°C, locally accompanied with metal-bearing fluids.

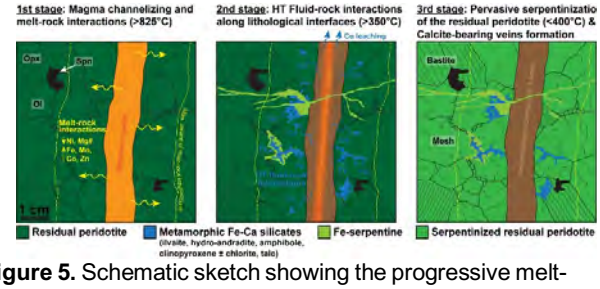


**Figure 5.** Schematic sketch showing the progressive melt-rock and late fluid-rock interactions leading to Fe-Ca metasomatism and serpentinization of mantle rocks of the ODP site 920

## 5 Conclusions

Mantle rocks at MARK record complex melt-rock and fluid-rock interactions. A petrographic and geochemical tracing carried out on mantle rocks allowed to identify i) magma channelling through mantle rocks and Fe, Co, Zn enrichment in mantle silicates through melt-rock interactions, ii) subsequent fluid circulation along lithological interfaces, prior to serpentinization, and formation of metamorphic mineral assemblages and responsible for Cu leaching iii) late serpentinization at decreasing temperatures.

This indicates that melt-rock and fluid-rock interactions may control important melt mobilities in exhumed mantle rocks, even if those are very limited at MARK. However, at slow-spreading ridges where important magma bodies may percolate through and interact with mantle rocks, those processes likely have strong implications for the metal budget of the oceanic lithosphere, while accounting for the chemical variability observed at ultramafic-hosted seafloor massive sulphide deposits.

## Acknowledgements

This work was funded through an IODP-France (OPE-2021-93) and CNRS-INSU grants to R. Coltat and J. Escartin. Analyses by LA-ICPMS at LERA are supported by the DFG fund INST121384/213-1 FUGG to C. Patten.

## References

Allen, D.E., Seyfried Jr., W.E., 2003. Compositional controls on vent fluids from ultramafic-hosted hydrothermal systems at mid-ocean ridges: An experimental study at 400°C, 500 bars. Geochimica et Cosmochimica Acta 67, 1531–1542. https://doi.org/10.1016/S0016-7037(02)01173-0

Andreani, M., Mével, C., Boullier, A.-M., Escartín, J., 2007. Dynamic control on serpentine crystallization in veins: Constraints on hydration processes in oceanic peridotites. Geochemistry, Geophysics, Geosystems 8, 24. https://doi.org/10.1029/2006GC001373

Burgath, K.-P., Marchig, V., Mussallam, K., 1997. 29. Data report: Mineralogic, structural, and chemical variability of mantle sections from Holes 920B and 920D. Proc. ODP. Sci. Results College Station, Texas 153.

Cannat, M., Chatin, F., Whitechurch, H., Ceuleneer, G., 1997. 11. Gabbroic rocks trapped in the upper mantle at the Mid-Atlantic Ridge, in: Proc. Ocean Drill. Program Sci. Results. pp. 243–264.

Cannat, M., Karson, J. a., Miller, D.J., Party, S.S., 1995. ODP Leg 153 MARK Initial Report. Proceedings ODP Initial Reports 153.

Casey, J.F., 1997. Comparison of major-and trace-element geochemistry of abyssal peridotites and mafic plutonic rocks with basalts from the MARK region of the Mid-Atlantic Ridge, in: Proceedings of the Ocean Drilling Program. Scientific Results. pp. 181–241.

Coltat, R., Branquet, Y., Gautier, P., Campos Rodriguez, H., Poujol, M., Pelleter, E., McClenaghan, S., Manatschal, G., Boulvais, P., 2019. Unravelling the root zone of ultramafic-hosted black smokers-like hydrothermalism from an Alpine analog. Terra Nova 31, 549–561. https://doi.org/10.1111/ter.12427

Dick, H.J.B., Johan Lissenberg, C., Warren, J.M., 2010. Mantle melting, melt transport, and delivery beneath a slow-spreading ridge: The paleo-MAR from 23°15′N to 23°45′N. Journal of Petrology 51, 425–467. https://doi.org/10.1093/petrology/egp088

Fouquet, Y., Cambon, P., Etoubleau, J., Charlou, J.L., Ondréas, H., Barriga, F.J.A.S., Cherkashov, G., Semkova, T., Poroshina, I., Bohn, M., Donval, J.P., Henry, K., Murphy, P., Rouxel, O., 2010. Geodiversity of Hydrothermal Processes Along the Mid-Atlantic Ridge and Ultramafic-Hosted Mineralization: A New Type of Oceanic Cu-Zn-Co-Au Volcanogenic Massive Sulfide Deposit. Geophysical Monograph Series 188, 321–367.

Gaggero, L., Cortesogno, L., Gazzotti, M., 1997. 30. Data reports: Oxides, sulfides, and asociated phases in veins and hydrothermally aletred peridotitic rocks. Proceedings of the Ocean Drilling Program, Scientific Results 153, 523–529.

Gustafson, W.I., 1974. The Stability of Andradite, Hedenbergite, and Related Minerals in the System Ca-Fe-Si-O-H. Journal of Petrology 15, 455–96.

Liao, Y., Wei, C., Rehman, H.U., 2021. Titanium in calcium amphibole: Behavior and thermometry. American Mineralogist 106, 180–191. https://doi.org/10.2138/am-2020-7409

McDonough, W.F., Sun, S. s., 1995. The composition of the Earth. Chemical Geology 120, 223–253. https://doi.org/10.1016/0009-2541(94)00140-4

Schwarzenbach, E.M., Steele-MacInnis, M., 2020. Fluids in submarine mid-ocean ridge hydrothermal settings. Elements: An International Magazine of Mineralogy, Geochemistry, and Petrology 16, 389–394.

# A new vision of the geodynamic evolution of the Iberian Pyrite Belt: VHMS in an intra-arc basin

**Fernando Tornos1, Carmen Conde[1], Caio R. de Mello[2], Colombo C. G. Tassinari[2]**
[1]*Instituto de Geociencias (IGEO, CSIC-UCM), C/Severo Ochoa, 7, 28040 Madrid, Spain*
[2]*Institute of Geosciences, University of Sao Paulo, Brazil*

**Abstract.** The Iberian Pyrite Belt (IPB) is the largest sulfur anomaly on the earth's crust, dominantly in the form of giant bodies of volcanogenic massive sulfides. VHMS deposits at the IPB are usually interpreted as formed in an intra-continental basin on the northward subducting plate and prior to continent-continent collision. Geochronology, lithogeochemistry and isotope geochemistry suggest that the Iberian Pyrite Belt formed in an intra- to back-arc setting above a southward verging subduction zone in a scenario more similar to other felsic-siliciclastic VMS belts worldwide. The original features of the arc are partially eroded during later oblique continent-continent collision.

## 1 Introduction

The Iberian Pyrite Belt (IPB) is the largest VHMS district in the world, with more than 1900 Mt of pyrite-rich massive sulfides and large underlying stockworks. It is located in SW Iberia, within the northern part of the South Portuguese Zone. The massive sulfides were deposited in a continental marine basin and interbedded with felsic volcanic rocks and shale during late Devonian to Early Carboniferous times. Here, we propose that the geodynamic scenario is identical to that of other felsic-siliciclastic VHMS systems with the mineralization formed in continental intra-arc marine basin prior to continent-continent collision.

## 2 Geological setting

The formation of the IPB reflects the evolution from a siliciclastic sequence deposited in a passive continental margin into a classical volcanic arc dominated by calc-alkaline felsic magmatism but with more accessory andesite and basalt (Volcano-Sedimentary [VS] Complex). The VS Complex was deposited in one or more E-W trending basins in which tilted blocks controlled both the depth and type of sedimentation. Along with the volcanic rocks, the sequence includes large amounts of felsic mass flows, shale and chemical sediments (Oliveira, 1990; Moreno, 1996). Systematic mapping and geochronology show that there is not a unique sequence for the whole IPB and it is made by stacked dome complexes of intermediate to felsic composition interbedded with pillowed flows and subvolcanic sills of basalt. The sequence and the style of mineralization change from south to north. In the southern part of the belt there is abundant shale interbedded with the volcanic rocks. Most VMS are exhalative to sub-exhalative within anoxic bottoms and formed in a short time span of less than 1 Ma at the Devonian-Carboniferous boundary and in relationship with catastrophic events during the onset of volcanism (Menor-Salvan et al. 2010). In the northern part of the Belt, shales are scarce and massive sulfides are found replacing porous and reactive felsic rocks such as hyaloclastite and pumice- and glass-rich mass flows (Tornos 2006). The age of these deposits is more than 10 Ma younger, early Tournaisian, than the shale hosted. Rio Tinto is the only deposit that has both deep replacive mineralization on felsic volcanic rocks and exhalative mineralization on shale (de Mello et al. 2022).

Volcanism is rooted in subvolcanic plutonic complexes that are geochemically similar and broadly coeval with the volcanism. The VS Complex is capped by the Baixo Alentejo Flysch (BAF) Group, a turbidite package, 2500 m thick, dated as late Visean to Serpukhovian age. The BAF is interpreted to be synchronous with the southward progradation of the Variscan tectonic front during continent-continent collision.

The IPB was affected by the Variscan orogeny with a thin-skinned deformation defined by the existence of large south-verging thrusts in a ramp and flat geometry (Silva, 1990). Late in this Orogeny a calc-alkaline magmatism was emplaced, which was dated between 330 ± 3 and 328 ± 3 Ma (Kramm et al. 1991; Onézime et al 2003, respectively). Regionally, the volcanic rocks were affected by very low to low grade regional metamorphism (Schermerhorn 1975; Munhá 1990; Sánchez España 2000).

## 3 Geochemistry

Volcanic rocks of the VS Complex include small amounts of dominantly tholeiitic basalt with Zr/Y ratios below 4.5. They trace primitive melts of mantle derivation that arrived to the upper crust. Their probably more voluminous underplating in the lower to intermediate crust induced partial melting and rise of large amounts of intermediate to felsic magmatic rocks with a calk-alkaline affiliation ($Zr/Y>7$; $[La/Yb]_n<5.5$) and compositions controlled by fractional crystallization in similar magmatic chambers (Silva et al. 1990; Tornos et al. 2005; Conde and Tornos 2020). However, it looks like that only the most Zr-depleted dacite and/or rhyodacite is related to the VMS deposits (<380 µg/g; Conde and Tornos 2020). The volcanic sequence also includes significant amounts of andesite, especially in the northern part of the Belt and located close to the footwall of the VS Complex. Geochemically, andesite shows negative Nb anomalies and Th-Rb-

Y values similar to those of volcanic arcs (Pearce et al. 1984). This suggests that volcanism in the Pyrite Belt is not bimodal as has been previously proposed by Soriano (1997), Mitjavila et al. (1997), Leistel et al. (1998) and others.

The shale in the southern part of the belt has $^{87}Sr/^{86}Sr_i$ values of 0.685 to 0.711 and $\varepsilon Nd_i$ values of -14.4 to -8.4, indicating that the Sr in shale did not equilibrate with ambient seawater. Both Nd and Sr seem to be inherited from a old continental crust.

Volcanic rocks have $\varepsilon Nd_i$ values indicative of a more juvenile source. Andesite to rhyolite have, as expected, somewhat lower $\varepsilon Nd_i$ values (-4.6 to +2.8) than the associated basalt (-1.8 to +5).

The isotopic composition of the massive sulfides in the southern part of the Belt ($\varepsilon Nd_i$, -11.2 to +5.4; $^{87}Sr/^{86}Sri$, 0.7067-0.7155) show that hydrothermal fluids are equilibrated with the underlying Phyllite-Quartzite (PQ) Group and/or a radiogenic basement with little or no input from volcanic rocks. The high $^{87}Sr/^{86}Sr$ initial ratios well above seawater also suggest that the ore forming fluids were either basinal brines or seawater with long residence times (Tornos, 2006).

$\varepsilon Nd_i$ values of the massive sulfides in the northern IPB (-7.2 to +2.5) are more akin to those of the volcanic rocks and reflect either inheritance from the host rocks or derivation of the hydrothermal fluids from underlying felsic igneous rocks. Nevertheless, the Sr isotope values are similar in both the volcanic and shale hosted massive sulfides indicating a old crustal provenance and extensive interchange with basinal-derived fluids.

## 4 Geochronology

U-Pb zircon ages show that the formation of the IPB took place in a rather long time span of ca. 35 Ma (see Fig 1) and probably evidencing a migration of the arc from South to North (Rosa et al., 2009). The oldest recorded volcanism is 374±2 Ma at Neves Corvo (Oliveira et al. 2013) and extends to 338.3±2 Ma in the northern part of the IPB (this work). Mineralization seems also prograde northwards, with the shale-hosted deposits being of uppermost Devonian age (ca. 360 Ma) and the volcanic-hosted deposits being on average of Early Tournaisian age. Systematic dating of the felsic volcanic rocks associated with the replacive massive sulfides suggest ages of mineralization between 355.3±3.7 Ma and 347±2 Ma (Fig 1).

Queerly, the andesite has not yielded primary zircon nor growth zones but has abundant inherited zircon of 540 to 470 Ma age, indicating the existence of an early Paleozoic magmatism beneath the cropping out IPB.

## 5 Geotectonic setting and discussion

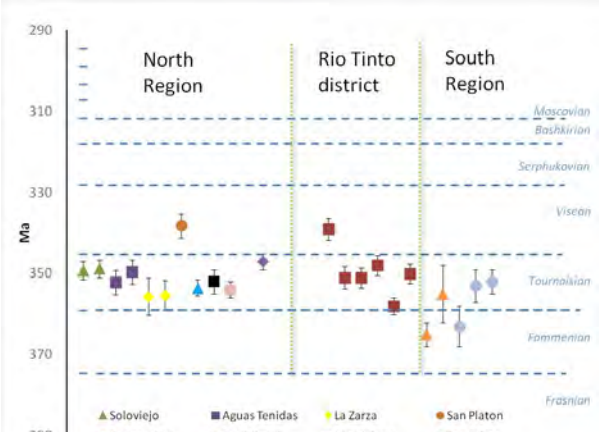


**Figure 1.** Geochronology of felsic volcanic rocks in the Pyrite Belt – most of them host the VMS deposits.

The South Portuguese Zone was an exotic terrane (Avalonia?) that during Variscan times collided with the Iberian Autochthonous Terrane that was part of Gondwana (Nance et al. 2010; Díez et al. 2016). Most studies agree that the IPB was an intracontinental pull-apart marine basin forming on the northward subducting plate prior to collision and in response to oblique subduction (Munhá et al. 1986; Quesada 1991; Onézime 2003). This scenario is at odds with the geodynamic scenario of felsic-siliciclastic massive sulfides, all formed in magmatic arcs overriding the subducting plate (Franklin et al 2005).

Geochemistry of volcanic rocks, and especially of andesite, and zonation are more consistent with that of a magmatic arc than with an intraplate setting.

Our envisaged scenario includes the formation of a back-arc basin at ca. 360 Ma in relationship with southward oblique subduction of the Gondwana plate beneath Avalonia (Fig 2). First felsic volcanism was responsible of the denudation of large amounts of vascular plants and, indirectly, instauration of anoxic brine pools. Here, mixing of deep hydrothermal fluids equilibrated with the basement with modified seawater rich in $H_2S$ due to the microbial reduction of seawater sulfate promoted the formation of the giant shale-hosted deposits (Menor-Salvan et al. 2010). Nd-Sr isotope geochemistry suggests that venting fluids are not modified seawater equilibrated with volcanic as in most VMS districts but basinal/metamorphic equilibrated with underlying (meta-)sediments.

The best physical scenario is the onset of convective hydrothermal cells during the early stages that involved the circulation of metal-rich and sulfide-poor basinal/metamorphic water. These fluids were later replaced in the cells by seawater, something that inhibited the formation of mineralization (Conde 2016).

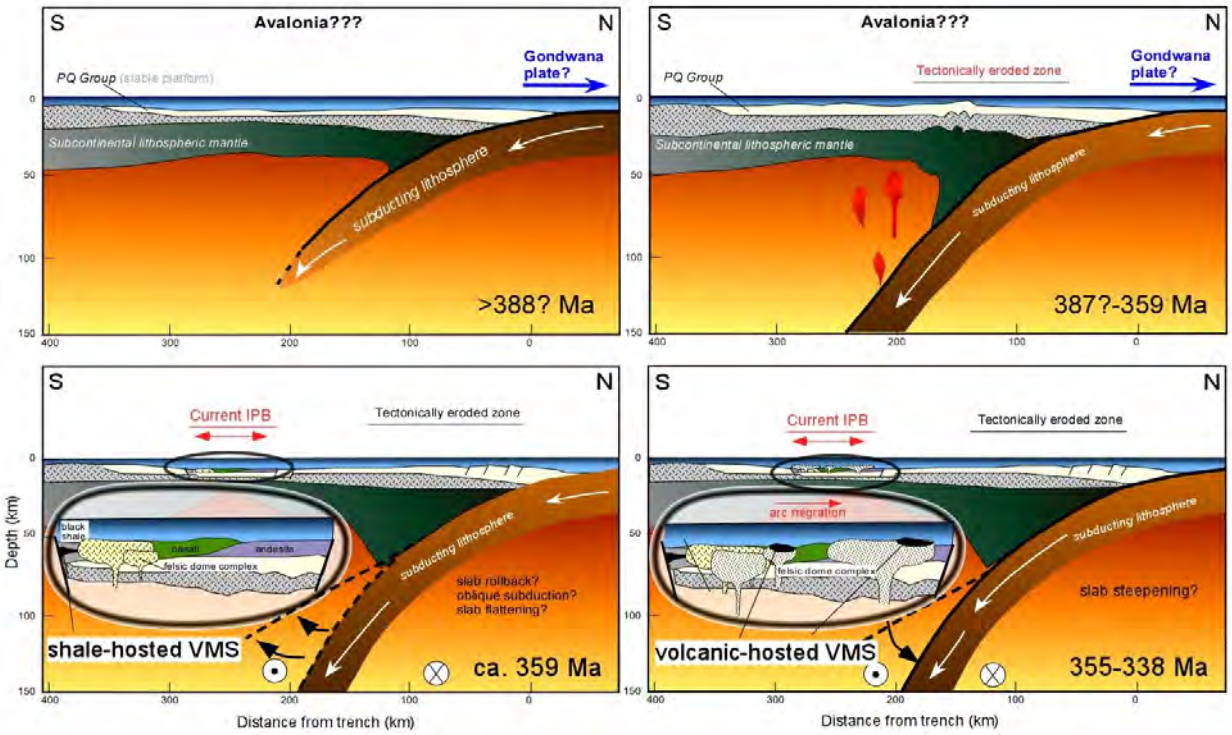


**Figure 2.** Schematic diagram of the geodynamic evolution of the Iberian Pyrite Belt.

Further northward migration of the arc due to slab flattening or rollback was accompanied by extension, increase in the volume of volcanism and extrusion of andesite followed by dominantly felsic rocks in a scenario similar to that of Taupo (Cole et al. 1990; de Ronde et al 2001). There was a second event of VMS formation that was directly related with felsic volcanism and specially with the Zr-poor dacite-rhyolite. Here, hydrothermal fluids have more negative $\varepsilon Nd_i$ values and seem to be equilibrated with the felsic volcanic rocks or their subvolcanic roots. However, we have not found evidences of the involvement of magmatic-hydrothermal fluids in the system. If so, their key contribution to the metal budget would have been masked by mixing with non-magmatic hydrothermal fluids (de Ronde et al. 2001).

The geodynamic scenario is similar to that proposed for the Bathurst Camp (van Staal et al 1992, 2003) or the Kuroko district (Yamada et al 2011). What makes different the IPB from these districts is the existence of a thick continental basement and the dominance of shale during the early stages of basin formation; these features probably control the origin of fluids and the environment of deposition of the earliest mineralization.

Further closure of the IPB during continent-continent collision at Later Visean (Onézime 2003) was followed by major strike-slip deformation along the suture and tectonic erosion of most of the magmatic arc, remnants of which are now conserved in the highly deformed and lithologically heterogeneous northern IPB (Fig 2).

## 4 Conclusions

Integration of geological and metallogenic data with geochronology, isotope geochemistry and lithogeochemistry suggest that the Iberian Pyrite Belt formed in an evolving back to intra-arc continental basin on the overriding plate of a southward verging subduction zone, a geodynamic setting similar to that of all the other VMS deposits formed in active margins.

## Acknowledgements

We are grateful for discussions with César Casquet, Juan Gomez Barreiro and José Ramon Martinez Catalán. This research is supported by the Exploration Information System (EIS) project of Horizon Europe (contract 101057357).

## References

Cole JW (1990) Structural control and origin of volcanism in the Taupo volcanic zone New-Zealand. Bull Volcanol 52: 445-459.

Conde C, Tornos F (2020) Geochemistry and architecture of the host sequence of the massive sulfides in the northern Iberian Pyrite Belt. Ore Geol Rev 127.

Conde C (2016) Geology and hydrothermal evolution of massive sulphides of the Iberian Pyrite Belt. Doctoral Thesis, Salamanca (Spain). Universidad de Salamanca: 379.

de Mello CR, Tornos F, Conde C, Tassinari CCG et al (2022) Geology, Geochemistry, and Geochronology of the Giant Rio Tinto VMS Deposit, Iberian Pyrite Belt, Spain. Econ Geol 117:1149-1177.

de Ronde CEJ, Baker ET, Massoth GJ et al (2001) Intra-oceanic subduction-related hydrothermal venting, Kermadec volcanic arc, New Zealand. Earth Planet Sci Lett 193: 359-369.

Díez RD, Arenas R, Pereira MF et al (2016) Tectonic evolution of Variscan Iberia: Gondwana–Laurussia collision revisited. Earth-Sci Rev 162: 269-292.

Franklin JM, Lydon JW, Sangster DF (1981) Volcanic-associated massive sulfide deposits. Econ Geol 75: 485-627

Kramm U, Giese U, Zhuravlev D, Walter R (1991) Isotope equilibration of magmatic and metamorphic rocks of the Aracena Metamorphic Belt, in XI Reunion sobre la Geologia del Oeste Peninsular, Univ. of Seville, Huelva, Spain.

Leistel JM, Marcoux E, Thiéblemont E et al (1998) The volcanic-hosted massive sulphide deposits of the Iberian Pyrite Belt. Miner Deposita 33: 2-30.

Menor-Salvan C, Tornos F, Fernández-Remolar D, Amils R (2010) Association between catastrophic paleovegetation changes during Devonian-Carboniferous boundary and the formation of giant massive sulphide deposits. Earth Planet Sci Lett 299: 398-408.

Mitjavila J, Martí J, Soriano C (1997) Magmatic evolution and tectonic setting of the Iberian Pyrite Belt volcanism. J Petrology 38: 727–755.

Moreno C, Sierra S, Sáez R (1996) Evidence for catastrophism at the Famenian-Dinantian boundary in the Iberian Pyrite Belt. Recent Advences. In: Strogen P., Somerville D, Jones G Ll (Eds.) Lower Carboniferous geology. Geological Society, London, Special Publication 107: 153-162.

Munhá J (1990) Metamorphic evolution of the south Portuguese/Pulo do Lobo zone. In Dallmeyer RD, Martinez Garcia E, (Eds) Pre-Mesozoic evolution of Iberia: Berlin, New York, Springer Verlag, p. 363–368.

Munhá J, Oliveira JT, Ribeiro A et al (1986) Beja-Acebuches Ophiolite: characterization and geodynamic significance. Maleo, Bol. Inf. Soc. Geol. Port. 2: 1–31.

Nance RD, Gutiérrez-Alonso G, Keppie JD et al (2010) Evolution of the Rheic Ocean. Gond Res 17: 194-222.

Oliveira JT, Relvas J, Pereira Z et al (2013) O Complexo Vulcano-Sedimentar de Toca da Moura-Cabrela (Zona de Ossa Morena): evolução tectono-estratigráfica e mineralizações associadas. In: Dias R, et al (Eds., Geologia de Portugal: 621–645.

Oliveira JT (1990) South Portuguese Sone: introduciton. Stratigraphy and synsedimentary tectonism. In: Dallmeyer RD, Martínez García E (Eds.) PreMesozoic Geology of Iberia. Springer Verlag: 333-347.

Onézime J, Charvet J, Faure M et al (2003) A new geodynamic interpretation for the South Portuguese Zone (SW Iberia) and the Iberian Pyrite Belt genesis. Tectonics 22: 1–17.

Pearce JA, Harris NBW, Tindle AG (1984) Trace element discrimination diagrams for the tectonic interpretation of granitic rocks. J Petrology 25: 956–983.

Quesada C (1991) Geological constraints on the Paleozoic tectonic evolution of the tectonostratigraphic terranes in the Iberian Massif, Tectonophysics 185: 225-245.

Rosa DRN, Finch AA, Andersen T, Inverno CMC (2009) U–Pb geochronology and Hf isotope ratios of magmatic zircons from the Iberian Pyrite Belt. Mineral. Petrol. 95: 47–69.

Sánchez España FJ (2000) Mineralogía y geoquímica de los yacimientos de sulfuros masivos en el área Nor- Oriental de la Faja Pirítica Ibérica, San Telmo-San Miguel-Peña del Hierro), Norte de Huelva, España. Unpublished Doctoral Thesis, Universidad del País Vasco: 307.

Schermerhorn LJG (1975) Spilites, regional metamorphism and subduction in the Iberian Pyrite Belt., somecomments, Geologie en Mijnbouw 54: 23-35.

Soriano C (1997) Evolución geodinámica de la Faja Pirítica Ibérica, Zona Sud Portuguesa. Ph.D. Thesis. Universitat de Barcelona: 328.

Silva JB, Oliveira JT, Ribeiro A (1990) Structural outline of the South Portuguese Zone. In: Dallmeyer RD, Martínez García E (Eds.) Pre-Mesozoic Geology of Iberia. Springer-Verlag, Verlin: 348–362.

Tornos F (2006) Environment of formation and styles of volcanogenic massive sulfides: The Iberian Pyrite Belt. Ore Geol Rev 28: 259–307.

Tomos F, Casquet C, Relvas J (2005) The metalogenesis of transpressional orogens: the Variscan of SW Iberia. Ore Geol Rev 27: 133-163

Valenzuela A, Donaire T, Pin C et al (2011) Geochemistry and U-Pb dating of felsic volcanic rocks in the Riotinto-Nerva unit, Iberian Pyrite Belt, Spain: crustal thinning, progressive crustal melting and massive sulphide genesis. J Geol Society 168: 717-731.

van Staal CR, Wilson RA, Rogers N et al (2003) Geology and tectonic history of the Bathurst Supergroup, Bathurst Mining Camp and its relationships to coeval rocks in southwestern New Brunswick and adjacent Maine - A synthesis. Econ Geol, Monograph 11: 37-60.

van Staal CR, Fyffe LR, Langton JP, McCutcheon SR (1992) The Ordovician Tetagouche Group, Bathurst camp, northern New Brunswick, Canada: History, tectonic setting, and distribution of massive- sulfide deposits. Expl Min Geology: 93–103

Yamada R, Yoshida R (2011) Relationships between Kuroko volcanogenic massive sulfide (VMS) deposits, felsic volcanism, and island arc development in the northeast Honshu arc, Japan. Miner Deposita 46: 1-18.

# The San Miguel deposit, Iberian Pyrite Belt: reconstructing a sub-seafloor replacive VMS

**Carmen Conde[1], Fernando Tornos[1] , Miguel Polo[2]**
*[1]Instituto de Geociencias (IGEO, CSIC-UCM), C/Severo Ochoa, 7, 28040 Madrid, Spain*
*[2]Emerita Resources. Av. De la Constitución 23, 41004, Sevilla, Spain*

**Abstract.** San Miguel is perhaps the most outstanding example of volcanogenic massive sulfides in the Pyrite Belt, showing excellent exposures of replacive massive sulfides and overlying gossan. Detailed geological and structural studies show that the mineralization has replaced a permeable horizon of volcanic breccias of dacitic composition and is rooted in a extensional syn-volcanic fault

## 1 Introduction

The San Miguel volcanogenic massive sulfide (VMS) is perhaps one of the best examples worldwide of massive sulfides being formed by the replacement of volcanic rocks when hydrothermal fluids channelized along an extensional fault crosscut reactive/permeable layers (Fig. 1).

San Miguel is located in the northern Iberian Pyrite Belt, in the southward overturned and thrusted limb of an E-W trending antiform. The mine was worked during the Roman Empire, with the works oriented to the exploitation of gold and silver that were enriched in the contact of the gossan and the underlying massive sulfides; this enriched layer includes clays with native gold (< 7 g/t) and several hundred ppm of silver in the form of argentojarosite (Fig. 2). The mine was reactivated in ca. 1851 when extracted Cu and pyrite, used for hydrosulfuric acid; it closed in 1960 (Pinedo-Vara, 1963). Afterwards, some of the remaining gossan has been mined for Au.

## 2 Geological setting

The Iberian Pyrite Belt (IPB) is one of the most outstanding mineral belts on Earth, being the largest crustal sulfur anomaly and hosting a significant proportion of the giant VMS. It had a total estimated pre-mining tonnage of 1900 Mt of massive sulphides and a larger tonnage of (sub-) economic stockwork (Tornos, 2006). The massive sulfides are hosted in the Volcano-Sedimentary Complex (VS Complex), a heterogeneous and up to 1,300 m thick sequence

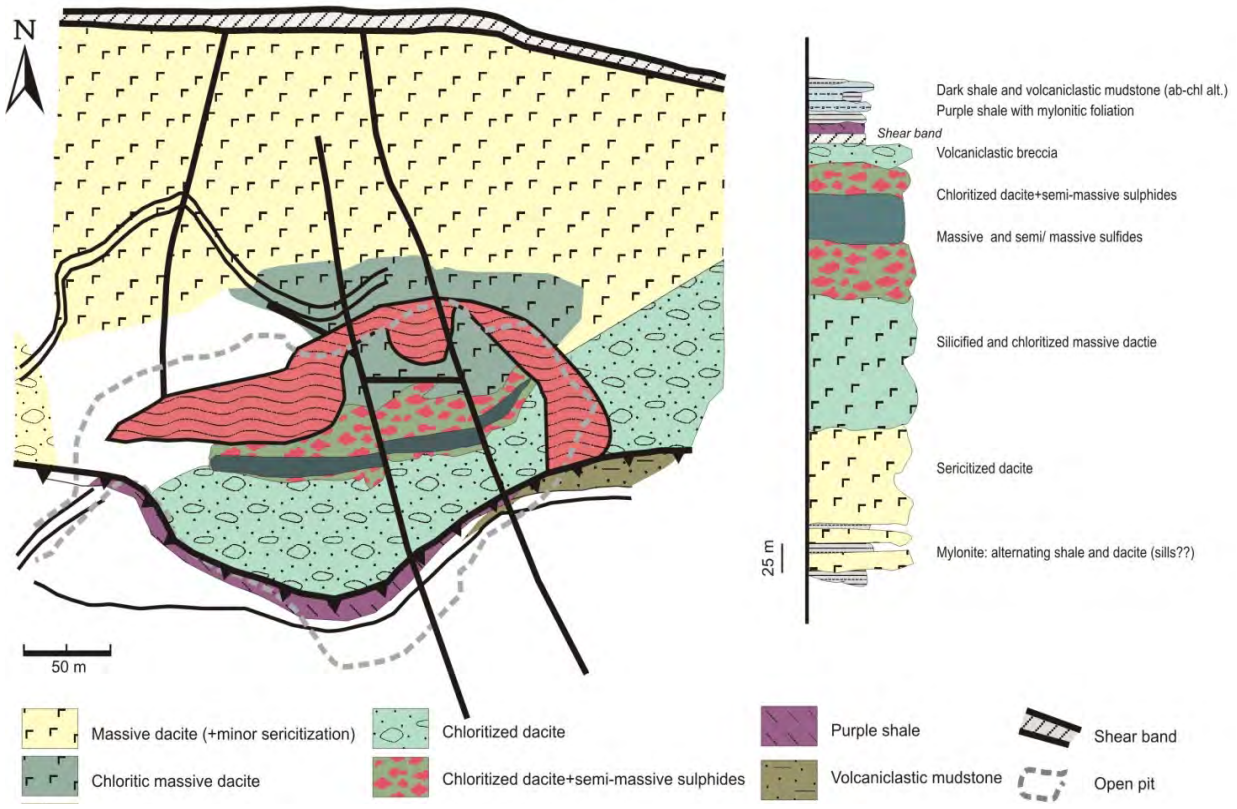


**Figure 1.** Geologic map of the open pit and simplified lithostratigraphic sequence of the San Miguel Mine showing the main volcanic rocks and hydrothermal alteration (modified of Tornos and Velasco 2007).

deposited in a continental intra- to back-arc marine basin (Tornos et al. 2023); its age is Late Devonian to Early Late Visean (Oliveira, 1990) The VS Complex is dominated by large felsic (dacite-rhyolite) dome complexes and interlayered pumice- and glass-rich mass flows and related volcaniclastic rocks. Shale is common, especially in the southern part of the Belt (Soriano et al 1999, Tornos 2006, Rosa 2007, Valenzuela et al. 2011, Conde and Tornos 2020). The sequence also includes pillowed lava flows and subvolcanic sills of basalt as well as andesite domes, which are especially abundant in the northern part of the belt. Basalt show an alkaline to continental tholeiitic affinity (Munha 1983; Mitjavila et al. 1997; Thieblemont et al. 1998) The intermediate to felsic rocks are low-Al high-Nb calc-alkaline and define an almost continuous trend.

The VS Complex is overlain by the Baixo Alentejo Flysch (BAF) Group, a synorogenic turbiditic sequence up to 2,500 m thick and dated as late Visean to Serpukhovian age and interpreted as result of the growth of a foreland basin during the onset of the Variscan orogeny.

The Variscan deformation is related with continent-continent collision and produced south-ward verging folds and thrusts. Related metamorphism is of very low- to low-grade metamorphism (Schermerhorn 1975; Munhá 1990; Sánchez España 2000). Metamorphism was followed by major I-type plutonism (Schutz et al. 1987; Thiéblemont et al. 1998).

The VMS deposits occur either as (sub-) exhalative stratiform bodies interbedded with shale above the lowermost felsic volcanic rocks (Late Famennian) or replacing felsic volcanic rocks and of early Tournaisian age (Tornos et al. 2023). In both cases, massive sulfides form large lenses with an extensive underlying stockwork. Massive sulfides are dominated by pyrite with lesser amounts of sphalerite, chalcopyrite and galena (Marcoux et al. 1996; Tornos 2006). When exposed subaerially, they are capped by well-preserved gossans and usually small cementation zones (Velasco et al. 2013).

## 3 San Miguel geology

The San Miguel Mine host several subvertical orebodies, being the largest one exposed in a small ellipsoidal open pit some 200 m in length (Fig 2a). When unaltered, the host rock is a thick felsic unit including coherent quartz-feldspar-phyric dacite interbedded with lenses of a breccia with fragments of a similar composition and a more fine grained supporting groundmass that probably correspond to in-situ and transported hyaloclastite; these layers are interbedded with more polymictic mass flows including coherent dacite, pumice-rich fragments and hyaloclastite supported by glass- and pumice-rich sandstone. The total thickness of this unit is ca. 300 m. U-Pb dating of the dacite has yielded an age of 352 ± 3Ma. Laterally, these rocks grade into a zone of distal phyllic (quartz-sericite) alteration and a pervasive proximal alteration that has replaced the volcanics by chlorite, quartz and pyrite (Fig. 2b). The VS Complex is overthrusted by a more detritic unit. The contact includes up to 1 m of mylonite with fragments of volcanic rock and shale. It grades into 4-6 m of shale and a metre thick unit of feldspar-bearing volcaniclastic mudstone and sandstone with fragments of fine-grained volcanic rocks that resemble peperite. These rocks are overlain by the Baixo Alentejo Flysch Group. Rocks in the allocthonous unit show sub-horizontal $S_o$ and $S_1$ but near the thrust plane they are almost obliterated by a younger subvertical crenulation associated with tights folds with subvertical axial plane.

The conspicuous purple colour of this hanging wall unit could be due to shallow marine oxidation, similar to that of a regional marker horizon (Routhier et al 1980, IGME 1982, Oliveira 1990) or due to syn-tectonic oxidation (Conde and Tornos 2020) related with the circulation of oxic waters during Variscan times.

### 3.1 The replacive mineralization

The massive sulfides are exposed in the northern part of the pit; they consist of a E-W trending subvertical lens, dipping ca. 70°S. In detail, they include coarse-grained pyrite intergrown with chlorite (brunsvingite-diabanite) and hydrothermal quartz (Polo 2022); the rock includes abundant inherited magmatic phenocrysts, giving a texture similar to that described by Doyle & Allen (2003) in the Maurliden deposit and unequivocally showing that sulfides replaced a porphyritic volcanic rock. The rock also includes magmatic zircon inherited from the protolith. The ratio between sulfides and silicates outlines a differential erosion that highlights the presence of ghosts of an ancient fragmental rock (Fig. 2c) that could well be an autoclastic breccia or a hyaloclastite. The fragments show a E-W subhorizontal foliation perpendicular to the orientation of the lens. In detail, there is a gradation from pyrite-poor footwall to pyrite-chlorite supporting ghosts of altered dacite and massive chlorite-bearing massive sulfides with inherited quartz phenocrysts (Fig. 2c).

The footwall of the massive sulfides includes a sub-horizontal fracture infilled with pyrite that has a sharp to replacive contacts with the dacite (Fig. 2d). If restored to the assumed original, horizontal, position, this structure should be vertical and, thus, probably corresponds to a tensional feeder zone to the San Miguel VMS system. The alignment of the fragments situated near the structure, also originally vertical, is also consistent with vertical fluid flow.

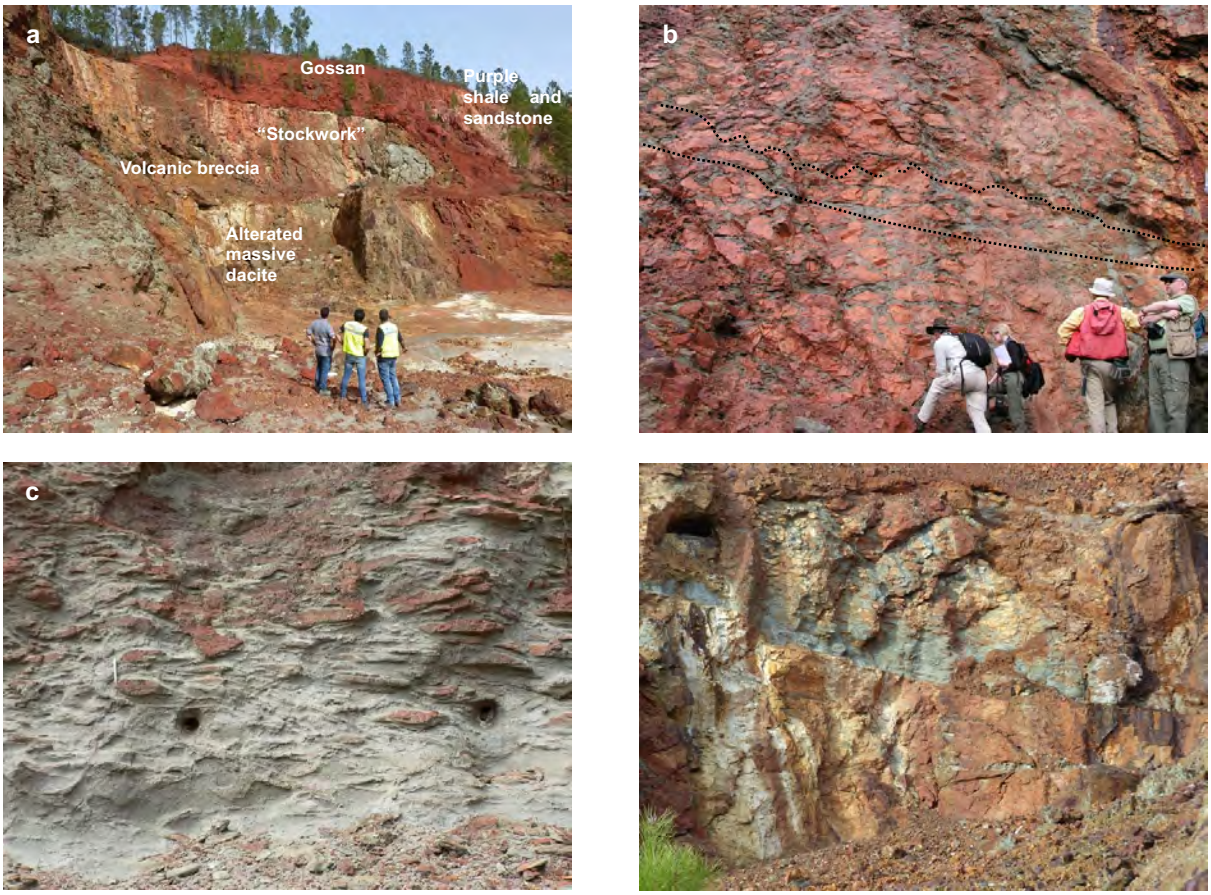


**Figure 2.** Representative photographs of the San Miguel massive sulfide. (a) Landscape of the NE wall of the open pit showing the mineralized sequence and the overthrusted siliciclastic unit. (b) Photograph of the so called "stockwork" but interpreted as semi-massive sulfides cementing a volcanic breccia. (c) Volcanic breccia partially replaced by pyrite and chlorite but showing oriented remnants of the fragments. (d) Feeder structure infilled with pyrite and located along in a normal fault that puts in contact massive and brecciated dacite.

## 4 Discussion

The San Miguel Mine has been traditionally interpreted as a stockwork zone grading into overlying exhalative massive sulfides. However, this study suggests that the mineralization is replacive on felsic volcanic rocks and the formation of the massive sulfides is probably controlled by variations in the permeability and reactivity of the host sequence. What was interpreted as a stockwork is the footwall of the mineralization and the breccia-like structure are primary structures enhanced by alteration. The San Miguel mine does not have a stockwork underlying the mineralization but a fault-controlled feeder zone (Fig. 2d). This scenario is probably more common than usually recorded in VMS systems (Doyle & Allen 2003; Tornos et al. 2015). It is unlikely that massive sulfides form and are preserved in high energy systems such as during the dynamic growth of felsic domes – any exhalative body will not have time to grow and would have been destroyed by mass flows or magmatic/hydrothermal explosions. It is much more likely that the VMS formed after the growth of the volcanic complex, something that also facilitates its preservation. Replacive VMS systems on volcaniclastic felsic rocks has been recently recorded by submarine drilling in the Okinawa Trough (Nozaki et al. 2021).

The envisaged model includes the upflow of hydrothermal fluids along a tensional fault till arrive to permeable/reactive rocks that were probably capped by impermeable rocks such as shale or coherent volcanic rocks. Reaction of the hot and metal-carrying fluids with cooler modified seawater probably rich in reduced sulfate should have promoted the precipitation of sulfides and chloritization of the host rocks. What remains intriguing is the geochemical mechanism that ultimately drives the dissolution of the Al-rich phases, leaving a rock composed by pyrite, few remnants of quartz phenocrysts and magmatic zircon.

## Acknowledgements

We are grateful for discussions with F. Velasco. This research is supported by the Exploration Information System (EIS) project of Horizon Europe (contract 101057357).

## References


Conde C, Tornos F (2020) Geochemistry and architecture of the host sequence of the massive sulfides in the northern Iberian Pyrite Belt. Ore Geol Rev 127.

Doyle MG, Allen RL, (2003) Subsea-floor replacement in volcanic-hosted massive sulfide deposits. Ore Geology Reviews 23: 183-222.

IGME (1982) Síntesis Geológica de la Faja Pirítica del SO de España IGME, Madrid: 106.

Marcoux E, Leistel JM (1996) Mineralogy and geochemistry of massive sulphide deposits. Iberian Pyrite Belt. Bol Geol Minero 107: 117-126.

Mitjavila J, Martí J, Soriano C (1997) Magmatic evolution and tectonic setting of the Iberian Pyrite Belt volcanism. J Petrology 38: 727–755.

Munhá J (1990) Metamorphic evolution of the south Portuguese/Pulo do Lobo zone. In Dallmeyer RD, Martinez Garcia E, (Eds) Pre-Mesozoic evolution of Iberia: Berlin, New York, Springer Verlag, p. 363–368.

Munhá J, (1983) Hercynian magmatism in the Iberian Pyrite Belt. Memorias Servicio Geologico Portugal 29: 39-81.

Nozaki T, Nagase T, Takaya Y, Yamasaki T et al (2021) Subseafloor sulphide deposit formed by pumice replacement mineralisation. Scientific Reports 11:8809. doi: 10.1038/s41598-021-87050-z.

Oliveira JT (1990) South Portuguese Sone: introduciton. Stratigraphy and synsedimentary tectonism. In: Dallmeyer RD, Martínez García E (Eds.) PreMesozoic Geology of Iberia. Springer Verlag: 333-347.

Polo M (2022) Cartografía y evolución mineralógica de la alteración hidrotermal en la mina San Miguel (Faja Pirítica Ibérica). Universidad de Madrid.

Pinedo-Vara I (1963) Piritas de Huelva. Su historia, minería y aprovechamiento. Summa Editorial, Madrid, 1003 pp.

Rosa CJP (2007) Facies Architecture of the Volcanic Sedimentary Complex of the Iberian Pyrite Belt, Portugal and Spain. Ph.D. thesis. University of Tasmania: 357.

Routhier P, Aye F, Boyer C, Lecolle M et al (1980) Le ceinture sud-iberique aamas sulfures dans sa partie espagnole mediane. Memoire BRGM 94, 265 pp.

Sánchez España FJ (2000) Mineralogía y geoquímica de los yacimientos de sulfuros masivos en el área Nor- Oriental de la Faja Pirítica Ibérica, San Telmo-San Miguel-Peña del Hierro), Norte de Huelva, España. Unpublished Doctoral Thesis, Universidad del País Vasco: 307.

Schermerhorn LJG (1975) Spilites, regional metamorphism and subduction in the Iberian Pyrite Belt., somecomments, Geologie en Mijnbouw 54: 23-35.

Schutz W, Ebneth J, Meyer KD (1987) Trondhjemites, tonalites and diorites in the South Portuguese Zone and their relations to the vulcanites and mineral deposits of the Iberian Pyrite Belt. Geologische Rundschau 76: 201-212.

Soriano D, Martí J (1999) Facies analysis of volcano-sedimentary successions hosting massive sulfide deposits in the Iberian Pyrite Belt, Spain. Econ. Geol. 94, 867–882.

Thieblemont D, Pascual E, Stein G (1998) Magmatism in the Iberian Pyrite Belt: petrological constraints on a metallogenic model. Miner Deposita 33: 98-110.

Tornos F (2006) Environment of formation and styles of volcanogenic massive sulfides: The Iberian Pyrite Belt. Ore Geol Rev 28: 259–307.

Tornos F, Conde C (2023) A new vision of the geodynamic evolution of the Iberia Pyrite Belt: VHMS in a intra-arc basin. 17th SGA Biennial Meeting “Mineral Resources in a Changing World. (Under submission)

Tornos F, Peter JM, Allen RL, Conde C (2015) Controls on the siting and style of volcanogenic massive sulphide deposits Ore Geol Rev 68: 142-163.

Velasco F, Herrero JM, et al (2013) Supergene features and evolution of gossans capping massive sulphide deposits in the Iberian Pyrite Belt. Ore Geol Rev 53: 181-203.

Valenzuela A, Donaire T, Pin C et al (2011) Geochemistry and U-Pb dating of felsic volcanic rocks in the Riotinto-Nerva unit, Iberian Pyrite Belt, Spain: crustal thinning, progressive crustal melting and massive sulphide genesis. J Geol Society 168: 717-731.

# VMS mineralization, recent developments, and the big remaining questions

**Y. Michelle DeWolfe**[1]
[1]*Mount Royal University*

**Abstract.** Volcanogenic massive sulfide (VMS) deposits are an important source for base and precious metals globally (Lydon, 1984; Ohmoto, 1996; Franklin et al., 2005; Hannington, 2014). Although Phanerozoic rocks contain 72% of the world's VMS tonnage, the Proterozoic accounts for ~20% of global VMS tonnage, and the Archean Eon, 8% (Mercier-Langevin, 2014). Though ore-forming processes and environments of VMS deposits are generally well understood (Allen et al., 2002, 2011; Franklin et al., 2005; Galley et al., 2007) new advances in our understanding of VMS systems continue to be made. Discovering these typically small but high-grade deposits remains a significant challenge, especially in strongly deformed and metamorphosed rocks that characterize many Precambrian volcanic belts, and understanding metal endowment variations in particular (e.g., Archean deposits tend to have higher metal endowment) remains largely elusive.

Comparative studies with modern seafloor massive sulfide (SMS) deposits, have been crucial in attempting to answer questions that remain regarding VMS deposits. This talk will explore our current understanding of VMS deposits, and how integrated research, including comparisons with SMS, field, microanalytical, geochemical and geochronological studies are facilitating, and will continue to facilitate, advances in our understanding of metal endowment, setting, genesis of, and exploration for, VMS deposits.

## Acknowledgements

I would like to acknowledge particular collaborators over the years and all-out rock stars in the field of VMS research and exploration who have had significant impact on my work and the work presented herein – H. Gibson, S. Piercey, M. Hannington, P. Mercier-Langevin A. Bailes, A. Galley, R. Allen and J. Franklin.

## References

Allen RL, Weihed P, and the global VMS research project team (2002) Global comparison of volcanic-associated massive sulphide districts: Geological Society of London, London, Special Publication 204, 13−37.

Allen RL, Tornos F, Peter JM (2011) A thematic issue on the geological setting and genesis of volcanogenic massive sulfide (VMS) deposits. Mineralium Deposita 46, 429−430.Allen et al., 2002, 2011

Franklin JM, Gibson HL, Jonasson IR, Galley AG (2005) Volcanogenic Massive Sulfide Deposits. In: Hedenquist, J.W., Thompson, J.F.H., Goldfarb, R.J., and Richards J.P. (Eds.) Econ. Geol. 100th Anniversary Volume, 523–560.

Galley AG, Hannington MD, Jonasson I (2007) Volcanogenic massive sulphide deposits: Geological Association of Canada, Mineral Deposits Division, Special Publication 5, 141−161.

Hannington MD (2014) Volcanogenic massive sulfide deposits. Treatise on Geochemistry (Second Edition). 13: 463–488.

Lydon JW (1984) Ore deposits models: Volcanogenic massive sulfide deposits. Part 1: A descriptive model: Geoscience Canada 11, 195–202.

Mercier-Langevin P, Gibson HL, Hannington MD, Gouthier J, Monecke T, Dube B, Houlé M (2014) A Special Issue on Archean Magmatism, Volcanism, and Ore Deposits: Part 2. Volcanogenic Massive Sulfide Deposits. Econ. Geol. 109, 1–9.

Ohmoto H (1996) Formation of volcanogenic massive sulfide deposits: The Kuroko perspective: Ore Geol. Reviews10, 135-177.

# Constraints on magma evolution at the epithermally mineralized Conical Seamount, Papua New Guinea

**Louis-Maxime Gautreau[1], Philipp A. Brandl[1], Thor Hansteen[1], Maxim Portnyagin[1]**
*[1]GEOMAR Helmholtz Centre for Ocean Research Kiel, Germany*

**Abstract.** The Tabar-Lihir-Tanga-Feni island chain in northeastern Papua New Guinea is host to highly alkaline magmatism and Au-rich porphyry-epithermal systems. Two examples are the Ladolam deposit on Lihir island that is the world's largest alkalic epithermal Au deposit and Conical Seamount, south of Lihir, which is the site where epithermal-style mineralization was first discovered at the modern seafloor. It has been interpreted as a juvenile analogue of the onland deposit. Previous studies focused on the mineralization process itself, but the origin and evolution of the host magmas and their contribution to the metal enrichment remain so far poorly constrained. Here we characterize the magmatic system underneath Conical Seamount and explain how the melt contributes to the gold endowment. We present new petrographic and geochemical analyses of whole rock samples, minerals and glass inclusions. The glass inclusions offer a new perspective on magma evolution at Conical Seamount. The melt within the magma chamber beneath the volcano is of tephri-phonolitic composition. Periodic replenishment includes pulses of compositionally diverse melts. The magma at Conical Seamount seems to possess a very specific ore potential, directly linked to its high alkaline content and redox evolution, which involves degassing processes influencing sulfur speciation.

## 1 Introduction

The Tabar-Lihir-Tanga-Feni island chain (TLTF) formed independent of the arc volcanism related to active subduction at the New Britain Trench. Its magma ascended through crust that occupied a forearc location at the time of active subduction along the Manus-Kilinailau Trench. More than half of the gold deposits within the Melanesian Arc are found in the TLTF island chain. Two deposits (Ladolam, Simberi) are actively exploited but at least six further prospects indicate the high Au potential of the region (Brandl et al. 2020).

One of them is located at Conical Seamount, a submarine volcano south of Lihir, which is also the first site where an epithermal-style mineralization was discovered at the seafloor (Petersen et al. 2002). It has been interpreted as a potential juvenile analogue of the world-class Ladolam deposit on Lihir island (Müller et al. 2003).

While many submarine volcanoes are present around Lihir (Figure 1), only Conical Seamount is found to host a significant gold mineralization. Our study thus aims to investigate the specific magmatic and epithermal conditions at Conical that promoted such a mineralization.

## 2 Methods

Several cruises with the German research vessel SONNE have investigated and recovered samples in the surroundings of Lihir: SO-94 in 1994, SO-133 in 1998 and SO-166 in 2002. Other expeditions like the Australian SHAARC in 2000 also recovered samples from the area.

**Figure 1.** Map of Lihir with location of the Ladolam deposit on the main island and of the surrounding seamounts.

We chose 24 representative samples for thin sections and further petrographic, mineralogical and geochemical studies. We also used polished mineral separates for the analysis of glass inclusions from eight representative rock samples.

Electron microprobe analysis was performed on the JEOL JXA-8200 at GEOMAR, Kiel, in wavelength dispersive (WDS) mode. The instrument was operated with 15 kV acceleration voltage and a focused beam (~1 µm diameter for plagioclase, pyroxene, sulfide and magnetite, 3 µm for mica and amphibole). The beam current was set to 10 nA for amphibole and mica, to 20 nA for plagioclase as well as pyroxene and to 50 nA for sulfide and magnetite. In the same thin sections, the composition of glass (formerly melt) inclusions in pyroxenes was analyzed using the same instrument. The beam current was set to 10 nA and the diameter to 5 µm.

The volatile content ($H_2O$, F, Cl, S, $CO_2$) of glass inclusions in clinopyroxene crystals embedded in indium mounts was analyzed using Secondary Ion Mass Spectrometry (SIMS) at the SwissSIMS in Lausanne. The machine was set to point analyses

mode to determine the element concentration in local spots. A primary $Cs^+$. source was used to generate secondary negative ions. Several elements could be measured at the same time in multicollection mode. The secondary ions measured were $^{12}C^-$, $^{16}O^1H^-$, $^{19}F^-$, $^{32}S^-$ and $^{35}Cl^-$ with $^{30}Si^-$ as reference.

The FeTiMM-oxybarometer (Arató and Audétat 2017) was used to calculate the oxygen fugacity. As the method involves the compositions of magnetite and melt (glass) in equilibrium, the composition of magnetite in contact with glass, all included in clinopyroxene crystals, was used.

## 3 Petrographic and geochemical overview

The rocks from Conical Seamount all possess a characteristic grey to dark grey color with a clinopyroxene-phyric texture. Clinopyroxene comprises 10-30 % of the total rock volume. Individual crystals have sizes ranging from 100 µm to several millimeters at Conical Seamount. Most of the clinopyroxene crystals at Conical Seamount contain distinct cores and show repeated growth zonation and/or sector zonation.

Other main mineral phases are plagioclase (5-15 %, 100-500 µm in size), magnetite (up to 5 %, 20-200 µm in size), and subordinate olivine (<1 %, approximately 50 µm in size) and sulfide (much less than 1 %).

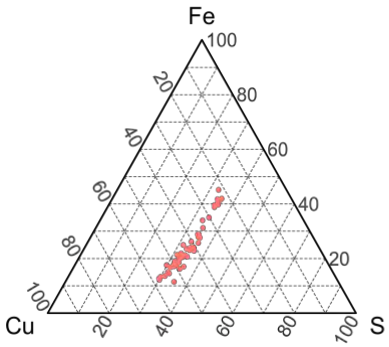


**Figure 2.** Composition of magmatic sulfides from Conical Seamount in the Fe-S-Cu ternary.

The Mg-number of clinopyroxene (Mg# = Mg / (Mg + Fe) x 100) ranges between 74 and 78 and generally decrease from the core to the rim of the minerals. However, this trend is periodically interrupted by several compositional bands of Mg# above 80.

Glass inclusions are frequently present in clinopyroxene. Most of them have an irregular shape and are typically distributed across one zone of the mineral in a grid-like pattern.

Magmatic sulfide occurs in almost every sample from Conical Seamount. Sulfide blebs are associated with magnetite, possess a subrounded shape and range in sizes between 10 and 50 µm) or occur isolated in the groundmass with a spherical, droplet shape (sizes of 10-20 µm). They correspond to intermediate solid solution-type sulfides with compositions ranging from the stochiometric composition of chalcopyrite to cubanite (Figure 2).

At Conical Seamount, glomerophyric mineral aggregates including clinopyroxene crystals are very common and present in all samples. Some consist of just two intergrown pyroxene crystals, others appear as bigger, flower-like intergrowths, where three to six pyroxene crystals, have grown in several directions from a central core that itself consists of one or several small pyroxene grains (Figure 3).

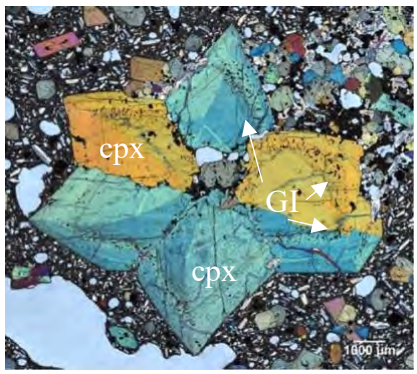


**Figure 3.** Flower-like glomerocrysts at Conical Seamount (sample 42RD10-22). Glass inclusions (GI) enriched zones occur within the clinopyroxenes (cpx).

The whole rock samples have a trachybasaltic composition. However, the glass (groundmass and inclusions) plots within the tephriphonolitic field in the TAS diagram.

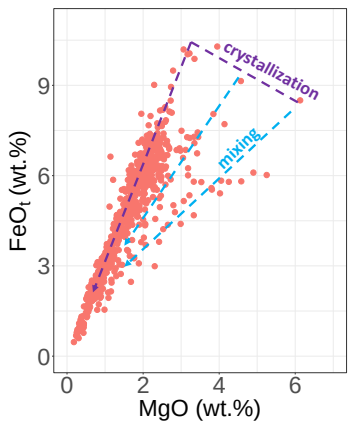


**Figure 4.** $FeO_t$ vs MgO of melt inclusions data. Inferred crystallization (purple) and magma mixing (blue) trends and clusters are highlighted.

Several compositional trends are recorded in the glass inclusion data from Conical Seamount. The MgO contents decrease linearly with increasing $SiO_2$, $Na_2O$, $K_2O$ and $Al_2O_3$ and $FeO_t$, CaO and $TiO_2$ are positively corelated with MgO. At higher MgO values (>3.8 wt. %), the glass inclusions show significant difference in $FeO_t$ contents (Figure 4). For a MgO content of 4 wt. %, one glass inclusion has an $FeO_t$ content at around 5.9 wt. %, one at 7.5 wt. % and the third one at 10.0 wt. %. The major element data systematically show a wide compositional range at any given MgO content.

Fractional crystallization alone cannot explain these observations.

The $CO_2$ contents of the glass inclusions is systematically below 400 ppm, whereas the $H_2O$ contents vary between 0.2 and 4.5 wt.%. The concentration of sulfur is up to 3600 ppm, 6800 ppm for chlorine as well as 2500 ppm for fluorine in the glass inclusions.

## 4 The magma chamber at Conical Seamount

The comparatively high abundance of clinopyroxene megacrysts, partly showing repeated zonation patterns, is consistent with extensive crystal growth in a convecting magma chamber underlying Conical Seamount. The frequent occurrence of glomerophyric mineral textures further indicates an efficient circulation/convection of magmas within the magma chamber, leading to mineral accumulation (Vance 1969).

The observed grid-like distribution of glass inclusions is interpreted to be the result of repeated growth and resorption periods for clinopyroxene (Dungan and Rhodes 1978), that reflect periodic disequilibrium between crystals and the surrounding melt. This disequilibrium may be the consequence of a rapid change in the local melt composition compared to the parental melt in which the crystal grew originally. Additionally, the peaks in Mg-number (>80) within the pyroxene profiles highlight several events in which the crystals continued to grow in a temporarily more primitive melt environment.

These observations as well as repetitive zonation patterns in pyroxene phenocrysts indicate convection in a heterogeneous magma chamber (with at least two different melts) and several magma recharging events.

While the trachybasaltic nature of the whole rocks has been reported in previous studies (Stracke and Hegner 1998; Müller et al. 2003), our new glass inclusion analyses indicate a tephriphonolitic melt composition. This is consistent with groundmass glass compositions and confirms a dominantly tephriphonolitic melt composition in the magma chamber.

The broad range in the glass inclusion chemical compositions from Conical Seamount and especially their distinct variations of FeO contents at high MgO, indicate a diversity of melts present in the magma chamber. Therefore, we assume different magmatic sources prior to pooling and mixing in a shallow magma chamber.

The flower-like intergrowths of glomerocrysts as well as normally zoned core compositions are consistent with early crystal growth prior to storage in a magma chamber, where radial growth dominates over nucleation. The negative $Al_2O_3$ and positive CaO correlation with MgO within the glass and the whole rock samples point towards clinopyroxene as the dominant fractionating phase. This is consistent with petrographic observations and confirms previous studies (e.g., Müller et al. 2003).

Involving a pressure between 1.4 and 2.1 kbar (calculated after Papale et al. 2006), the $H_2O$ and $CO_2$ contents confirm the shallow crustal level (approximately 4-6 km depth) of the magma chamber as suggested previously (Müller et al. 2003; Kamenov et al. 2005).

## 5 The melt fertility

At Conical Seamount, the absence of a volatile-bearing magmatic mineral phase such as amphibole or phlogopite, promotes the progressive enrichment of volatiles during fractional crystallization. Thus, early pyroxene fractionation increased the alkalinity of the melt, and also the volatile contents in the magma increased. Such high volatile contents allow for an optimal solubility of Au within the melt (Zajacz et al. 2012) and a high potential to exsolve a fluid phase with a high metal carrying capability (Hogg et al. 2023).

Lead (Kamenov et al. 2005) as well as sulfur (Gemmell et al. 2004) isotopic measurements indicate a significant magmatic volatile contribution in the hydrothermal ore forming process at Conical Seamount.

At Conical Seamount, the calculated values for the oxidation state of the melt (Figure 5) range between 0.6 and 3.3 log units above FMQ. These conditions correspond to the conditions of coexistence of reduced $S^{2-}$ and oxidized $S^{6+}$ sulfur species, (at $fO_2$ between 0 and 2 log units above the FMQ buffer (Jugo et al. 2010)) and existence of $S^{6+}$ only at higher $fO_2$. This also overlaps with the range of high Au solubility in the melt (at $fO_2$ between 0.5 and 1.5 log units above FMQ (Zajacz et al. 2012)).

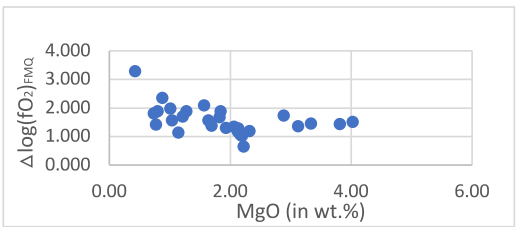


**Figure 5.** Melt oxidation state ($\Delta\log(fO_2)_{FMQ}$) calculated from magnetite-glass inclusion pairs following the method of Arató and Audétat (2017).

However, it is important to note that our constrains on melt oxidation state is limited to low MgO values (<4.5 wt.%), where magnetite is crystallizing. Magnetite crystallization consumes iron from the residual melt. This may reduce the sulfur solubility and trigger sulfide saturation (Brandl et al. 2022) and consequently the sequestration of chalcophile elements (Au, Cu, Ag) (e.g., Jenner et al. 2010). The common association of magnetite and sulfide confirms the strong link between crystallization of the two mineral phases.

Our combined observations are consistent with an efficiently convecting magma chamber being

present at shallow crustal levels underneath Conical Seamount that underwent several cycles of replenishment. We assume that the recharging magma and the chemical buffering through fractional crystallization in the chamber is maintaining the oxidation state in the range where the reduced and oxidized sulfur species coexist.

When the melt reaches the magma chamber, the subsequent fractional crystallization and the low pressure are likely to trigger fluid oversaturation. This exsolution of a magmatic volatile phase leads to the formation of a metal-bearing fluid. The remaining metals staying in the melt are sequestrated in immiscible sulfides, as the oxygen fugacity stays below FMQ+2.

The sulphide phase, associated to vapor bubbles, may be transported to the top of the magma chamber as compound drops. The metals would progressively, but almost completely, move from the sulphide melt to the vapor (Mungall et al. 2015) and thus contribute to the metal enrichment of the following exsolving fluid. The cyclic magmatic replenishment resupplies the magma chamber in metals and leads thus to the optimal and repeated formation of metal enriched fluids from the magma chamber at shallow level.

The most evolved melt, with low MgO values, seems to erupt from the magma chamber with a very high $fO_2$ (up to above FMQ+3), thus in less favorable sulfide precipitation conditions and consequently has a very highly chalcophile element carrying capability. At the same time, we assume that rising melt leaving the magma chamber entrains already precipitated sulfides on the way to the surface.

## 6 Conclusion

Here we demonstrate that the range of melts related to epithermal-style mineralization at Conical Seamount has tephriphonolitic composition. This contrasts with previous studies that solely used whole rock samples with variable contents of mafic minerals and thus assumed a trachybasaltic melt composition.

We show that clinopyroxene crystallization exerts an important control on melt composition. The alkalinity of the melt is rising, the mineral phases concentrate compatible elements and avoids the sequestration of volatiles in a crystal phase.

We provide evidence for the existence of shallow crustal magma reservoir that is undergoing continuous convection, fractional crystallization, frequent magma replenishment and continuous degassing.

Sulfide precipitation associated with fluid exsolution are optimal conditions for the metal transfer from the melt to the hydrothermal system.

## Acknowledgements

A special thank is given to Sven Petersen and Colin Devey for their valued advice and support as well as to the SwissSIMS team in Lausanne and Mario Thöner for their valuable help during SIMS and electron microprobe analyses respectively. This study is funded by the German Research Foundation (DFG) through grant BR 5297/4-1.

## References

Arató R, Audétat A (2017) FeTiMM - A new oxybarometer for mafic to felsic magmas. Geochemical Perspect Lett 5:19–23. https://doi.org/10.7185/geochemlet.1740

Brandl PA, Hannington MD, Geersen J, et al (2020) The submarine tectono-magmatic framework of Cu-Au endowment in the Tabar-to-Feni island chain, PNG. Ore Geol Rev 121:103491. https://doi.org/10.1016/j.oregeorev.2020.103491

Brandl PA, Portnyagin M, Zeppenfeld H, et al (2022) The Origin of Magmas and Metals at the Submarine Brothers Volcano, Kermadec Arc, New Zealand. Econ Geol 1–28. https://doi.org/10.5382/econgeo.4973

Dungan MA, Rhodes JM (1978) Residual glasses and melt inclusions in basalts from DSDP Legs 45 and 46: Evidence for magma mixing. Contrib to Mineral Petrol 67:417–431. https://doi.org/10.1007/BF00383301

Gemmell JB, Sharpe R, Jonasson IR, Herzig PM (2004) Sulfur Isotope Evidence for Magmatic Contributions to Submarine and Subaerial Gold Mineralization : Conical Seamount and the Ladolam Gold Deposit , Papua New Guinea. Econ Geol 99:1711–1725

Hogg OR, Edmonds M, Blundy J (2023) Water-rich magmas optimise volcanic chalcophile element outgassing fluxes. Earth Planet Sci Lett 611:118153. https://doi.org/10.1016/j.epsl.2023.118153

Jenner FE, O'Neill HSC, Arculus RJ, Mavrogenes JA (2010) The magnetite crisis in the evolution of arc-related magmas and the initial concentration of Au, Ag and Cu. J Petrol 51:2445–2464. https://doi.org/10.1093/petrology/egq063

Jugo PJ, Wilke M, Botcharnikov RE (2010) Sulfur K-edge XANES analysis of natural and synthetic basaltic glasses: Implications for S speciation and S content as function of oxygen fugacity. Geochim Cosmochim Acta 74:5926–5938. https://doi.org/10.1016/j.gca.2010.07.022

Kamenov GD, Perfit MR, Jonasson IR, Mueller PA (2005) High-precision Pb isotope measurements reveal magma recharge as a mechanism for ore deposit formation: Examples from Lihir Island and Conical seamount, Papua New Guinea. Chem Geol 219:131–148. https://doi.org/10.1016/j.chemgeo.2005.02.013

Müller D, Franz L, Petersen S, et al (2003) Comparison between magmatic activity and gold mineralization at Conical Seamount and Lihir Island, Papua New Guinea. Mineral Petrol 79:259–283. https://doi.org/10.1007/s00710-003-0007-3

Mungall JE, Brenan JM, Godel B, et al (2015) Transport of metals and sulphur in magmas by flotation of sulphide melt on vapour bubbles. Nat Geosci 8:216–219. https://doi.org/10.1038/ngeo2373

Papale P, Moretti R, Barbato D (2006) The compositional dependence of the saturation surface of H 2O + CO 2 fluids in silicate melts. Chem Geol 229:78–95. https://doi.org/10.1016/j.chemgeo.2006.01.013

Petersen S, Herzig PM, Hannington MD, Jonasson IR (2002) Submarine Gold Mineralization Near Lihir Island , New Ireland Fore-Arc , Papua New Guinea. 97:1795–1813

Stracke A, Hegner E (1998) Rifting-related volcanism in an oceanic post-collisional setting: The Tabar-Lihir-Tanga-Feni (TLTF) island chain, Papua New Guinea. Lithos 45:545–560. https://doi.org/10.1016/S0024-4937(98)00049-8

Vance JA (1969) On synneusis. Contrib to Mineral Petrol 24:7–29. https://doi.org/10.1007/BF00398750

Zajacz Z, Candela PA, Piccoli PM, et al (2012) Gold and copper in volatile saturated mafic to intermediate magmas: Solubilities, partitioning, and implications for ore deposit formation. Geochim Cosmochim Acta 91:140–159. https://doi.org/10.1016/j.gca.2012.05.033

# SEDEX deposits in the Graz Paleozoic, Eastern Alps, Austria

**Annika Geringer[1], Sandro Rohrhofer[2], Frank Melcher[2], Christian Benold[1], Heinz Reitner[1], Ralf Schuster[1]**
*[1]GeoSphere Austria, Vienna, Austria*
*[2]Montanuniversität Leoben, Leoben, Austria*

**Abstract.** The Pb-, Zn-, barite- and Ag-bearing SEDEX deposits in the Graz Paleozoic (Eastern Alps, Austria) are hosted by polyphase deformed, greenschist facies metasediments and metavolcanics of upper Silurian to Lower Devonian stratigraphic age. The stratiform mineralization is characterized by pyrite, pyrrhotite, galena and sphalerite as the predominant sulphide phases, accompanied by chalcopyrite, arsenopyrite, freibergite, marcasite, pyrargyrite, tetradymite, cobaltite, ullmannite, breithauptite and others. Whole rock major and trace element data show metal enrichment in the adjacent host rocks. A detailed local geochemical survey to identify anomalies in stream sediments, in stream waters and headwaters reveals coincidence with former surveys, but also identified additional anomalies with elevated contents of Pb, Zn and Ba and in traces of Cu, Ni, As and Cd, which can be interpreted as indications of former unknown occurrences.

## 1 Introduction

In the Graz Paleozoic (Drauzug-Gurktal nappe system, Eastern Alps) in Austria sedimentary exhalative (=SEDEX) deposits are known within an area of about 35 x 20 km. They constitute the metallogenetic district "Lead-zinc-barite district Graz Paleozoic – Schönberg Formation (Arzberg)" and form the most important ore district of non-ferrous metals in Paleozoic units of the Eastern Alps. These deposits are stratiform and occur exclusively in the Schönberg Formation (Weber 1990). They carry raw materials that have been important for basic supply for a long time (Pb, Zn and Ag), as well as raw materials (barite, Co, In, Sb) that have been put on the list of critical raw materials by the European Commission (European Commission 2020). Many of these deposits have been sites of mining for Ag, Pb and Zn for about 680 documented years. After several closures and restarts, mining was terminated in 1927. Since then, there has been repeated research work as well as an exploration phase with drilling activity in the 1970s to 1980s (Weber 1990).

## 2 Geological Overview

The Graz Paleozoic nappe stack consists of low- to medium-grade metamorphic Paleozoic (meta)sediments and metavolcanics (Flügel and Neubauer 1984). It is part of the Drauzug-Gurktal nappe system of the Austroalpine Unit and is located in the eastern part of the Eastern Alps (Figure 1). Covering an area of about 30 x 50 km, the thickness of the Graz Paleozoic is expected to be only about 1.5 km (Gasser et al. 2010). It is surrounded and underlain by epidote-amphibolite facies to eclogite facies metamorphic units of the Koralpe-Wölz nappe system, some of which are referred to by local names such as Anger crystalline or Radegund crystalline (Krenn et al. 2008). The western part of the nappe stack is locally overlain by Upper Cretaceous sediments of the Gosau Group (Kainach-Subgroup). Neogene sediments of the Styrian and Passail basins cover along the southern margin and close to Arzberg respectively (Fritz et al. 1992).

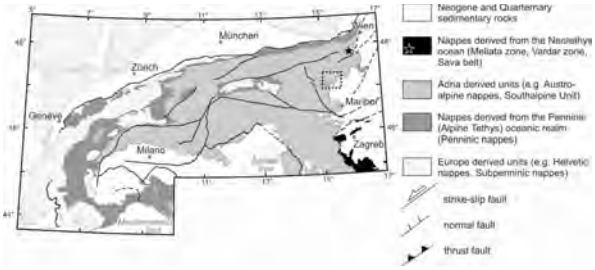


**Figure 1.** Overview map of the Alps showing the paleogeographic origin of the main tectonic units after Schmid et al. (2004). The dotted square indicates the Graz Paleozoic.

There are two concepts for the internal tectonic subdivision of the Graz Paleozoic: Fritz et al. (1992) divide the nappe stack into a lower, middle and upper nappe group, with the Rannach nappe and Hochlantsch nappe in the upper, the Laufnitzdorf nappe and Gschwendt (Kalkschiefer) nappe in the middle and the Schöckel nappe in the lower nappe group. In the concept of Gasser et al. (2010) only a lower and upper nappe system separated by the Rannach Thrust are subdivided, whereby the upper nappe system includes the Rannach nappe and Hochlantsch nappe. According to recent work the lower nappe group is formed by the Gschnaidt nappe, Schöckel nappe and Gasen nappe (Schuster et al. 2016) (Figure 2).

The lithostratigraphic subdivision of the Graz Paleozoic comprises five different sedimentological facies units termed the Laufnitzdorf, Kalkschiefer, Schöckel, Rannach and Hochlantsch facies (Gasser et al. 2010). However, these facies units are not identical with the tectonic units and therefore overlap. The successions start with lower Silurian to Lower Devonian volcanoclastics and siliciclastics, followed by Middle Devonian carbonate platform sediments. The end is defined by pelagic limestones

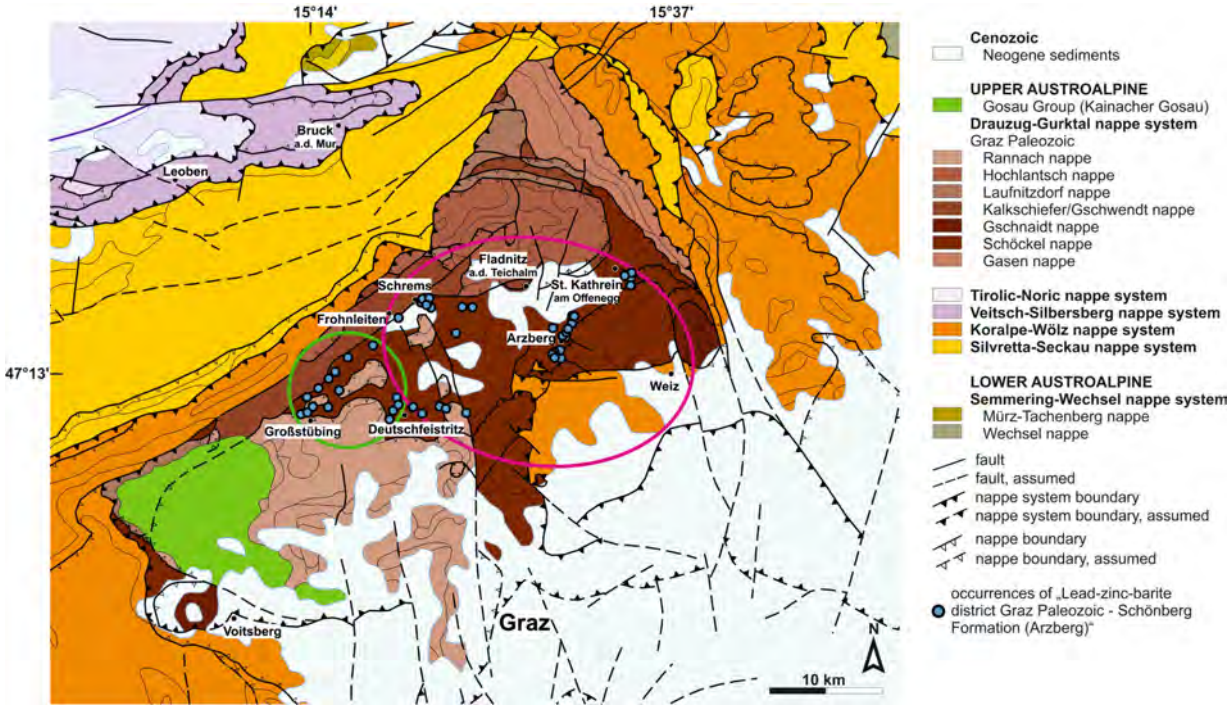


**Figure 2.** Tectonic map of the Graz Paleozoic in the Austroalpine with the occurrences of the investigated metallogenic district "Lead-zinc-barite district Graz Paleozoic – Schönberg Formation (Arzberg)". Green circle indicates the western part and pink circle indicates the eastern part of the ore district. Map according to ADB 500 of GeoSphere Austria 1.3.2023.

and slates of Upper Devonian to lower Carboniferous age (Flügel and Neubauer 1984; Fritz and Neubauer 1988; Flügel and Hubmann 2000; Gasser et al. 2010; Schantl et al. 2015). Thirty-five formations belonging to the above-mentioned sedimentological facies units are described by Flügel and Hubmann (2000).

According to the concept of Gasser et al. (2010) the nappe pile below the Rannach Thrust is characterised by a penetrative schistosity, isoclinal folds and an E-W trending stretching lineation. In the thrust zone the deformation is dominated by a stretching lineation that progressively turns from E-W to SE-NW. Krenn et al. (2008) describe open folds with NE-SW trending fold axes throughout the whole nappe pile. The Graz Paleozoic is crosscut by several brittle strike slip faults and a normal fault between the lower nappe group and the Rannach nappe, which creates a potential metamorphic break (Neubauer 1989). The borders of the nappe stack constitute a normal fault in the southwest and northeast, a transtensional strike slip fault in the northwest and a system of strike slip, normal and thrust faults in the south (Fritz et al. 1992; Neubauer et al 1995; Krenn et al. 2008).

Metamorphic conditions range from sub-greenschist to lower-most greenschist facies conditions in the middle and upper nappe group (Hasenhüttl 1994; Russegger 1996; Rantitsch et al. 2005, Krenn et al. 2008). Interestingly there is an inverted metamorphic gradient within the lower nappe group, with garnet bearing assemblages appearing in the uppermost Gschnaidt nappe. The garnet shows a polyphase growth and eoalpine temperatures for the Glöselhof Lithodeme (Gschnaidt nappe), calculated with the garnet-chlorite and garnet-amphibole thermometer, range between 510-530°C for an assumed pressure of 0.8 GPa (Schantl et al. 2015).

The age of metamorphism and deformation within the Graz Paleozoic is the basis of a long discussion. Different models ascribe the main imprint either to the Variscan or the Eoalpine (Cretaceous) tectonometamorphic events (Frank 1981; Flügel et al. 1980; Fritz 1988; Hasenhüttl 1994; Russegger 1996; Neubauer et al. 1999; Krenn et al. 2008; Gasser et al. 2010). According to the occurrence of polyphase garnet, a pre-Alpine (Variscan or Permian) metamorphic imprint is proven at least for some parts of the Graz Paleozoic (Schantl et al. 2015). However, the major metamorphic and structural overprint occurred during the Eoalpine event in the Early Cretaceous at about 125 Ma (Fritz et al. 1992; Schuster et al. 2016).

## 3 SEDEX mineralization

There are two (eastern part) to three (western part) sulphide- and/or barite-dominated ore horizons („Lager") developed (Table 1) (Weber 1990; Feichter 2005). Pyrite, pyrrhotite, galena and sphalerite are the predominant sulphide phases, accompanied by chalcopyrite, arsenopyrite, freibergite, marcasite, pyrargyrite, tetradymite, cobaltite, ullmannite, breithauptite and others. At the type locality Arzberg (Figure 3, Figure 4), Au-Ag-Hg alloys (66-84% Ag) have also been described (Feichter and Mogessie 2003). Host rocks are polyphase deformed, greenschist facies

metasediments (often black shale and carbonates) and metavolcanics (greenschist) of the Schönberg Formation (Flügel and Hubmann 2000), which are placed in the upper Silurian to Lower Devonian (Weber 1990; Gasser et al. 2010). A genetic model of sedimentary massive sulphides deposited in channel-like structures on the seafloor is widely accepted, similar to the SEDEX deposits at Rammelsberg and Meggen, Germany.

**Table 1.** Ore mineralization of the western and eastern part of the ore district (Weber 1990).

| | **Western part** | **Eastern part** |
|---|---|---|
| **Lower horizon "Liegendlager"** | Barite, (galena), pyrite | Galena, sphalerite, fahlore |
| **Middle horizon "Mittellager"** | Galena, sphalerite, some barite, pyrite | - |
| **Upper horizon "Hangendlager"** | Galena, sphalerite, pyrite | Barite, galena, little sphalerite |

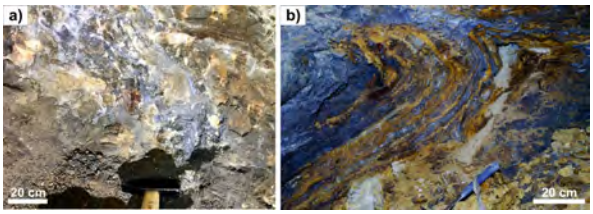


**Figure 3.** a) Ore mineralization of the lower horizon and b) folded ore mineralization of the upper horizon in the eastern part of the ore district (type locality Arzberg).

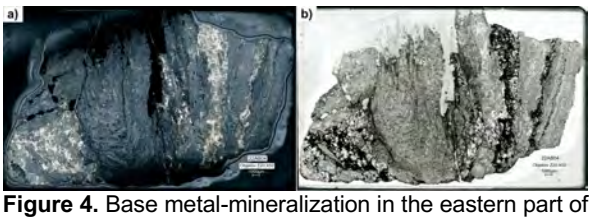


**Figure 4.** Base metal-mineralization in the eastern part of the ore district (type locality Arzberg). a) Reflected light, plane polarizers and b) transmitted light, plane polarizers. The scale bar represents 1000 µm.

In the inactive Arzberg mine, mineralization styles comprise Pb-Ag and Fe-Cu assemblages. The latter consists of major pyrrhotite, pyrite and chalcopyrite, with minor sphalerite, galena and cobaltite hosted by greenschist (Figure 4). The sulphide phases are accompanied by siderite and dolomite-ankerite as gangue minerals. Fluorapatite and monazite are connected to the ore forming processes. The sedimentary structures are partially preserved and in mica-rich areas the ore is strongly deformed.

LA-ICP-MS trace element data of Fe-Cu and Zn sulphides from the Graz Paleozoic reveal a high variability between single deposits (Onuk 2018): median Fe concentrations in sphalerite from different former mining areas range from 0.6 to 7.3 wt.%; concentrations of Mn, Co, Ga, Ag, Cd, In and Sb vary significantly, with slight In enrichment in some of the ancient mines. Sphalerites from Arzberg appear to be most enriched in Ag, those from Haufenreith carry highest In concentrations, and those from Deutschfeistritz (Elisabethbau, Friedrichbau, Ottilienstollen) are highest in Sb and Ga. Pyrite in the ores is generally enriched in Co over Ni (md Co/Ni = 1.28) and has low to moderate, but variable As contents (median 176 ppm). Chalcopyrite carries Ag, In and Sn.

First results from whole rock geochemistry by fusion ISP-OES/ICP-MS show that in the host rocks adjacent to the ore, Pb reaches up to >1 wt.%, Zn up to 2940 ppm, Ba up to 11750 ppm and Ag up to 19 ppm. The ore is characterized by Pb and Zn over 1 wt.%, Ba up to 4871 ppm and Ag exceeding 100 ppm. Sb (up to >200 ppm) and Cu contents (up to 190 ppm) in the ore are moderate and in the host rocks low to moderate (Sb up to 38 ppm, Cu up to 100 ppm). In the ore, As and Ni are below detection limit (As 5 ppm, Ni 20 ppm), but up to 140 ppm As and up to 130 ppm Ni were detected in the host rocks. Co reaches 12 ppm, In 0.8 ppm and Ga 21 ppm in the ore, whereas Co is up to 327 ppm, In below detection limit (0.2 ppm) and Ga up to 36 ppm in the host rocks.

## 4 Geochemical anomalies in stream sediments and waters

In the surroundings of deposits in the western part of the ore district a detailed local geochemical survey was carried out to identify anomalies in stream sediments and in waters of streams and headwaters. The geochemical analyses (major and trace elements) of stream sediment were obtained using the RFA and of water samples using the IC (for anions) and ICP-MS. These analyses show strong dependencies to regional geological settings, i.e. regarding hydrochemical water types. Although a number of water samples are directly related to sites of historic mining of sulphide ores, no acid mine waters were observed. Because of the prevalent carbonate content in the surrounding lithological units the waters are buffered showing near neutral or weakly basic pH-values. Regarding metal contents our first results confirm the vast majority of characteristics already shown in a previous regional geochemical survey. Nevertheless, some additional anomalies of Pb, Zn and Ba and in traces Cu, Ni, As and Cd can be interpreted as indications of former unknown occurrences which will justify further investigation.

## Acknowledgements

The authors are very grateful to Ing. Christian Auer, Univ.-Prof. Dr. Bernhard Grasemann, Ao.Univ.-Prof. Dr. Bernhard Hubmann, Priv.-Doz. Mag. Dr. Kurt Krenn, Dr. Duncan Large, Dr. Holger Paulick and Univ.-Prof. Dr. Leopold Weber for providing their great support and expertise. The Federal Ministry for Education, Science and Research of the

Republic of Austria is thanked for funding the project by the “Initiative GBA-Forschungspartnerschaften Mineralrohstoffe – MRI”.

## References

European Commission (2020) Study on the EU’s list of Critical Raw Materials – Final report. 158 pp.

Feichter MM and Mogessie A (2003) Die Sulfidmineralisation von Arzberg (Steiermark): Ergebnisse petrographischer, mineralchemischer und geochemischer Untersuchungen. Mitt. Österr. Mineral. Ges., 148, 133-135.

Feichter MM (2005) Die sedimentgebundene Pb-Zn-Ba-Lagerstätte Arzberg (Steiermark, Österreich): Mineralisation und Genese. Dissertation, Karl-Franzens-Universität Graz, 230 pp.

Flügel HW, Mauritsch H, Heinz H and Frank W (1980) Paläomagnetische und radiometrische Daten aus dem Grazer Paläozoikum. Mitteilungen der Österreichischen Geologischen Gesellschaft, 71/72, 201-211.

Flügel HW and Neubauer F (1984) Erläuterungen zur geologischen Karte der Steiermark. Verlag der Geologischen Bundesanstalt, Wien, 127 pp.

Flügel HW and Hubmann B (2000) Die lithostratigraphische Gliederung des Paläozoikums von Graz (Österreich). Österreichische Akademie der Wissenschaften/Schriftenreihe der Erdwissenschaftlichen Kommissionen, 13, 7-59.

Frank W (1981) Geochronologische Datierung frühalpiner Metamorphosevorgänge in den Ostalpen (Jahresbericht 1980 des Geochronologischen Labors). In: Die frühalpine Geschichte der Ostalpen Jahresbericht, Montanuniversität Leoben, 2, 9-43.

Fritz H (1988) Kinematics and geochronology of Early Cretaceous thrusting in the northwestern Paleozoic of Graz (Eastern Alps). Geodinamica Acta, 2, 53-62. http://dx.doi.org/10.1080/09853111.1988.11105156.

Fritz H and Neubauer F (1988) Geodynamic aspects of the Silurian and Early Devonian Sedimentation in the Paleozoic of Graz (Eastern Alps). Schweizer Mineralogische Petrographische Mitteilungen, 68, 359-367.

Fritz H, Ebner F and Neubauer F (1992) The Graz thrust complex (Paleozoic of Graz). In: ALCAPA field guide, Karl-Franzens-Universität Graz, 83-92.

Gasser D, Stüwe K and Fritz H (2010) Internal structural geometry of the Paleozoic of Graz. International Journal of Earth Sciences, 99, 1067-1081. http://dx.doi.org/10.1007/s00531-009-0446-0.

Hasenhüttl C (1994) Eine Wärmegeschichte des Grazer Berglandes. Inkohlung, Illitkristallinität, Tonmineralogie und Conodont Colour Alteration Index im nördlichen Teil des Grazer Deckenkomplex (Grazer Paläozoikum). Dissertation, Karl-Franzens-Universität Graz, 182 pp.

Krenn K, Fritz H, Mogessie A and Schaflechner J (2008) Late Cretaceous exhumation history of an extensional extruding wedge (Graz Paleozoic Nappe Complex, Austria). International Journal of Earth Sciences, 97, 1331-1352. http://dx.doi.org/10.1007/s00531-007-0221-z.

Neubauer F (1989) Lithostratigraphie und Strukturen an der Basis der Rannachdecke im zentralen Grazer Paläozoikum (Ostalpen). Jahrbuch der Geologischen Bundesanstalt, 132, 459-474.

Neubauer F, Dallmeyer RD, Dunkl I and Schirnik D (1995) Late Cretaceous exhumation of the metamorphic Gleinalm dome. Eastern Alps: kinematics, cooling history and sedimentary response in a sinistral wrench corridor. Tectonophysics, 242, 79-98. http://dx.doi.org/10.1016/0040-1951(94)00154-2.

Neubauer F, Hoinkes G, Sassi FP, Handler R, Höck V, Koller F and Frank W (1999) Pre-Alpine metamorphism in the Eastern Alps. Schweizer Mineralogische Petrographische Mitteilungen, 79, 41-62.

Onuk P (2018) High-tech metal potential of sphalerite from Eastern Alpine lead-zinc deposits and development of a matrix-matched sphalerite (ZnS) calibration material (MUL-ZnS-1) for calibration of in-situ trace element measurements by laser ablation inductively coupled plasma mass spectrometry (LA-ICP-MS). Dissertation, Montanuniversität Leoben, 196 pp.

Rantitsch G, Sachsenhofer R, Hasenhüttl C, Russegger B and Rainer T (2005) Thermal evolution of an extensional detachment as constrained by organic metamorphic data and thermal modelling: Graz Paleozoic Nappe Complex (Eastern Alps). Tectonophysics, 411, 57-72. http://dx.doi.org/10.1016/j.tecto.2005.08.022.

Russegger B (1996) Niedrigst- bis niedriggradige Metamorphose im südlichen Grazer Paläozoikum (Ostalpen). Jahrbuch der Geologischen Bundesanstalt, 139, 93-100.

Schantl P, Schuster R, Krenn K and Hoinkes G (2015) Polyphase metamorphism at the southeastern margin of the Graz Paleozoic and the underlying Austroalpine basement units. Austrian Journal of Earth Sciences, 108, 219-238.

Schmid SM, Fügenschuh B, Kissling E and Schuster R (2004) Tectonic map and overall architecture of the Alpine orogen. Eclogae Geologicae Helvetiae, 97, 93-117. http://dx.doi.org/10.1007/s00015-004-1113-x.

Schuster R, Schantl P and Nowotny A (2016) Tektonik, Metamorphose und Abkühlgeschichte des Grazer Paläozoikums auf Kartenblatt GK50 Blatt 135 Birkfeld. In: Arbeitstagung 2015 der Geologischen Bundesanstalt Geologie der Kartenblätter GK50 ÖK 103 Kindberg und ÖK 135 Birkfeld, Mitterdorf im Mürztal 21.-25. September 2015. Verlag der Geologischen Bundesanstalt, Wien, 71-87.

Weber L (1990) Die Blei-Zinkerzlagerstätten des Grazer Paläozoikums und ihr geologischer Rahmen. Archiv für Lagerstättenforschung der Geologischen Bundesanstalt, Wien, 12, 289 pp.

# Textures of Cu-Fe sulphides in hydrothermal seafloor massive sulphide deposits: indications of a new metastable mineral phase $Cu_2Fe_3S_5$

**Simon Goldmann[1], Sebastian Fuchs[1]**
*[1]Federal Institute for Geosciences and Natural Resources (BGR), Stilleweg 2, D-30655 Hannover, Germany*

**Abstract.** Seafloor massive sulphide deposits are present globally along the spreading axis of mid ocean ridges, arc volcanoes and back-arc basins. The major ore minerals are sulphides, such as pyrite, marcasite, chalcopyrite, sphalerite, and galena that occur in various proportions, assemblages and textures. In Cu-rich ore samples from the ultramafic rock-hosted Kaimana vent field from the Central Indian Ridge, the peculiar texture of the Cu-Fe sulphide mineral association of isocubanite and non-stoichiometric chalcopyrite together with a yet unnamed Cu-Fe sulphide phase of intermediate composition of $Cu_2Fe_3S_5$ occurs. The latter mineral was previously described as "Y-Phase". In this study, the texture, mineralogical assemblage, and the chemical composition of the associated sulphides were investigated in detail using polarized reflected light microscopy and electron probe microanalysis. We present new data on mineral chemistry not only of $Cu_2Fe_3S_5$, but also of associated isocubanite and chalcopyrite.

## 1 Introduction and previous work

On behalf of the German Federal Government, the Federal Institute for Geosciences and Natural Resources (BGR) holds one exploration license from the International Seabed Authority (ISA) of the United Nations for massive sulphides in the Central Indian Ocean. The exploration program comprises the outline of potential ore deposits including resource assessment, but also baseline studies for the sustainable protection of the marine environment.

In comparison to the observations during this study, similar Cu-Fe sulphide assemblages and textures were previously reported from a number of seafloor massive sulphide occurrences (e.g., Mozgova et al. 2005; Bogdanov et al. 2008; Borodaev et al. 2010; Firstova et al. 2016) as well as from the metalliferous sediments of Atlantis II Deep in the Red Sea (e.g., Missack et al. 1989).

For the first time, Rambaldi et al. (1986) identified a sulphide mineral with the formula of $Cu_2Fe_3S_5$ from one inclusion within the Qingzhen (EH3) chondritic meteorite. Beside its occurrence in meteorites, this $Cu_2Fe_3S_5$ mineral (that received the generic name "Y-Phase") was only found within the mineral assemblages of notably ultramafic rock-hosted seafloor massive sulphide deposits. Its chemical composition is close to $Cu_2Fe_3S_5$, which is intermediate between isocubanite and chalcopyrite.

## 2 Geological Setting

The hydrothermal vent field and associated massive sulphide occurrences are situated in the license area of the central Indian Ocean (Fig. 1). The samples are retrieved from the new, yet undescribed, Kaimana vent field. This vent field occurs along the Central Indian Ridge (CIR), in close vicinity to the Rodriguez Triple Junction (Fig. 1). The Kaimana vent field is located in geotectonic setting that differs from most other hydrothermal fields, which are commonly located off-axis, associated with prominent faults, and hosted by basaltic rocks. At Kaimana vent field, hydrothermal activity occurs on a tectonic massif on the slow-spreading western flank of the CIR and is associated with the exposure of mantle and lower crustal rocks. Active and inactive vent sites are scattered along the sedimented, axis-facing slope of the tectonic massif. The black smokers exhaust high-salinity fluids at a number of active vent sites in water depths ranging from 2625 to 3020 m. Highest fluid temperature measured at Kaimana vent field reached up to 349 °C. The fluid temperature measured at the investigated chimney reached 328 °C.

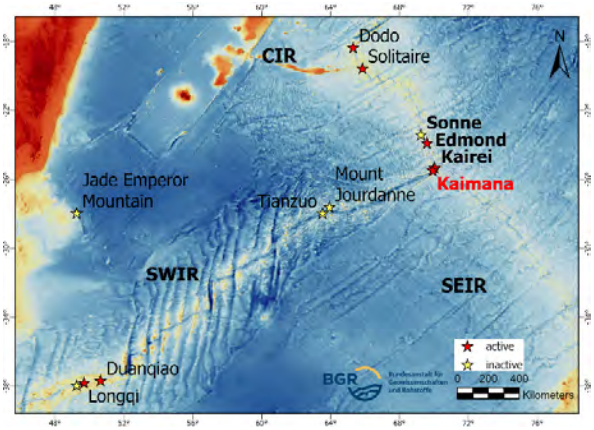


**Figure 1.** Bathymetric map of the central Indian Ocean showing the Central Indian Ridge (CIR), South-East Indian Ridge (SEIR), and South-West Indian Ridge (SWIR). Red and yellow stars indicate active and inactive vent sites, respectively. The Kaimana site (highlighted in red font colour) is close to the Rodriguez Triple Junction, where the three mid-ocean ridges converge

The samples were collected during the INDEX2018 marine expedition with the research vessel Pelagia and was conducted within the scope

of BGR's exploration work for polymetallic massive sulphide deposits. An entire suite of massive sulphide, rock and sediment samples were retrieved using the remotely operated vehicle (ROV) ROPOS. The two samples (99ROPOS-H and 99ROPOS-K) in focus of the current study were snapped from two actively venting chimneys. Both chimney fragments are composed of predominant chalcopyrite and pyrite/marcasite, minor sphalerite, isocubanite, bornite, galena, and silica plus native gold. Both samples are mineralogically zoned and form numerous conduits.

## 3 Materials and Methods

Polished sections of Cu-Fe sulphide-rich chimney samples 99ROPOS-H and 99ROPOS-K were selected for detailed analysis. Minerals and their textural relationships were investigated under reflected light using a LEICA DM4P polarization microscope.

Major element compositions of the respective Cu-Fe sulphide minerals were determined by electron probe microanalysis (EPMA) using a JEOL JXA-8350F microprobe. The instrument was set to accelerating voltage of 25 kV, beam current of 20 nA, and focussed electron beam. For spot analysis, the respective X-ray line, spectrometer crystal, measuring time in seconds, and reference material for each element were as follows (ordered by atomic number): S Kα (PET, 10 s, chalcopyrite), Fe Kα (LIFL, 10 s, cubanite), Cu Kα (LIFH, 10 s, chalcopyrite).

## 4 Results

### 4.1 Petrography

The mineral assemblage and texture were investigated by reflected light microscopy (Figs. 2 & 3). The mineral texture of this unusual mineral assemblage is characterised by isocubanite matrix with two sets of Cu-Fe sulphide lamellae, which differ in orientation and appearance.

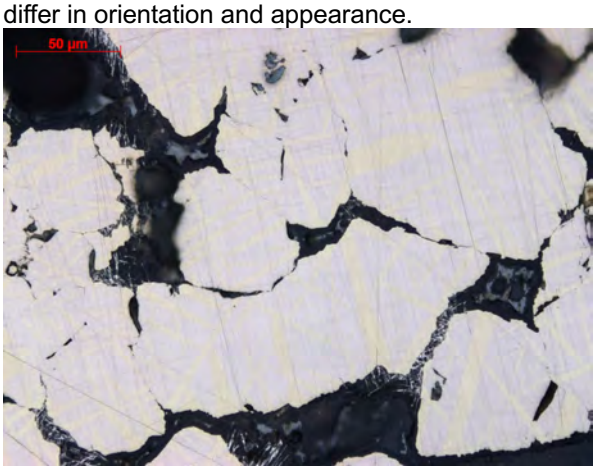


**Figure 2.** Micrograph under plane polarized reflected light showing the texture with isocubanite (cream) matrix and two sets of lamellae (yellow). Image width about 250 µm, sample 99ROPOS-K

Both sets of lamellae are oriented in parallel patterns, but of different orientation. One set forms acicular lamellae, which are oriented in two directions presumably following crystallographic structure of the isocubanite host, whereas the other set is lenticular or spindle-shaped and oriented independently from the former set of lamellae.

In reflected light, both sets of lamellae show similar optical characteristics resembling chalcopyrite with distinct yellow colour, but without any anisotropy. These lamellae are optically different from the host mineral, which is cream-coloured and isotropic as well. Chalcopyrite is also present as overgrowth along the rim of isocubanite followed by sphalerite of later stage in the paragenetic sequence (Fig. 3).

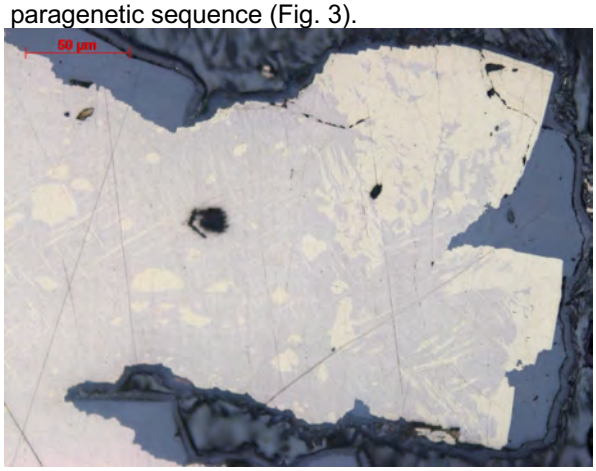


**Figure 3.** Micrograph under plane polarized reflected light showing the texture with isocubanite (cream) matrix, spindle-shaped $Cu_2Fe_3S_5$ (yellow), and chalcopyrite lamellae (yellow). This assemblage is overgrown by chalcopyrite along the rim (right) and late-stage sphalerite (grey). Image width about 250 µm, sample 99ROPOS-H

### 4.2 Mineral chemistry

The host mineral is isocubanite with an average composition (n=11) of 21.26 wt% Cu, 42.71 wt% Fe, and 35.99 wt% S, resulting in a slightly un-stoichiometric $Cu_{0.90}Fe_{2.07}S_{3.03}$ formula based on Z=6 atoms per formula unit (Fig. 4, red ellipse).

The acicular lamellae within isocubanite and the overgrowth on isocubanite are both chemically chalcopyrite with an average composition (n=14) of 30.60 wt% Cu, 34.28 wt% Fe, and 35.49 wt% S resulting in an non-stoichiometric $Cu_{0.87}Fe_{1.11}S_{2.01}$ formula based on Z=4 atoms per formula unit (Fig. 4, yellow ellipse). In comparison, the chalcopyrite from overgrowth is closer to its ideal stoichiometry than the acicular lamellae and plots between ideal $CuFeS_2$ and ideal $Cu_{0.9}Fe_{1.1}S_2$ (Fig. 4, top left within yellow ellipse).

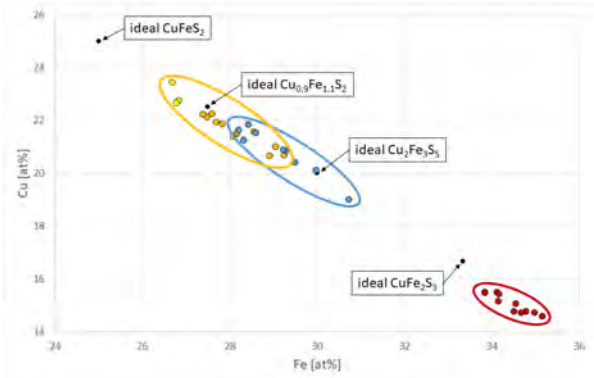


**Figure 4.** Binary diagram for Fe atomic% versus Cu atomic% showing the chemical composition of Cu-Fe sulphides (red circle: isocubanite, yellow: chalcopyrite, blue: $Cu_2Fe_3S_5$).

The chemical composition of spindle-shaped lamellae is close to $Cu_2Fe_3S_5$ (probably representing "Y-Phase"), but still mostly non-stoichiometric. Average composition (n=9) is 29.21 wt% Cu, 35.88 wt% Fe, and 35.38 wt% S resulting in a $Cu_{2.08}Fe_{2.91}S_{5.00}$ formula based on Z=10 atoms per formula unit (Fig. 4, blue ellipse). The chemical composition of $Cu_2Fe_3S_5$ was also reported by previous studies (Mozgova et al. 2005; Bogdanov et al. 2008; Borodaev et al. 2008; Firstova et al. 2016), but results were rather variable among each other at much lower Cu contents compared to our data.

Nevertheless, it has to be kept in mind that due to the very limited dimension of the lamellae, it cannot be excluded that analytical data may be affected by the chemistry of the enclosing host mineral creating the observed non-stoichiometric composition of chalcopyrite and $Cu_2Fe_3S_5$ lamellae with tendencies towards lower Cu and higher Fe contents.

## 5 Discussion

In seafloor massive sulphide deposits, isocubanite is a common mineral phase and represents the face-centred cubic polymorph of $CuFe_2S_3$, and is only stable at temperatures above 210 °C (Fleet 1971; Cabri et al. 1973; Caye et al. 1988; Pruseth et al. 1999). Authors of preceding experimental studies demonstrated the decomposition of isocubanite into stable chalcopyrite and pyrrhotite upon cooling below temperatures of 210 °C. This transformation is regarded as solid-state reaction, which does not require the presence of fluids. Because high temperatures can be easily maintained at active vent sites in modern hydrothermal systems on the seafloor, metastable mineral phases such as isocubanite can still be preserved, and are a characteristic mineral phase for recent seafloor massive sulphides (Borodaev et al. 2010). Consequently, isocubanite is only rarely reported within analogue ancient massive sulphide deposits on land (e.g., Maslennikov et al., 2017).

Chalcopyrite is generally slightly non-stoichiometric in composition. At temperatures between 300 and 350 °C, the chalcopyrite solid solution field extends from $CuFeS_2$ to $Cu_{0.9}Fe_{1.1}S_2$ (Sugaki et al. 1975), and the non-stoichimetric chalcopyrite form our study probably represents the Fe-rich and Cu-poor end-member of the solid solution field. However, as anisotropy is not observed, the present chalcopyrite may represent the isotropic variety formed at high temperatures (Missack et al. 1989). Previous studies report chalcopyrite of similar composition and coined the generic name "X-Phase" (Mozgova et al. 2005; Borodaev et al. 2010), but this may also simply represent chalcopyrite solid solution.

A first explanation for the presence of the "Y-Phase" ($Cu_2Fe_3S_5$) was provided by Bogdanov et al. (2008), who interpret this mineral phase as "a protosubstance, in which solid-phase reactions resulted in the formation of textures of the solid solution decomposition under slow cooling."

Based on our observations and analyses, we propose an updated model for the formation and preservation $Cu_2Fe_3S_5$ and its associated mineral assemblage. The occurrence of $Cu_2Fe_3S_5$ is confined to those samples that are collected from two active chimneys, where venting fluids reach high temperatures of at least 328 °C. The temperatures maintained within the chimneys have to be significantly higher than the measured ones, because hydrothermal fluids quickly cool during mixing with ambient seawater at the exhausts of the chimneys (where the temperature measurements have been conducted). This observed association with high-temperature hydrothermal fluids is in agreement with the observation from the Rainbow field, where $Cu_2Fe_3S_5$ occurs as homogenous segregations in active zonal copper-rich chimneys (Mozgova et al. 2005).

In this environment, elevated temperatures are maintained during and after mineral precipitation from the emanating fluid over long time periods, permitting the preservation of temperature-sensitive metastable mineral phases. As we also found isocubanite in absence of $Cu_2Fe_3S_5$ in other massive sulphide samples, we propose that the $Cu_2Fe_3S_5$ becomes unstable and decomposes even at higher temperatures than isocubanite.

Similar to Bogdanov et al. (2008), we suggest that $Cu_2Fe_3S_5$ represents a high-temperature proto-phase, which converts into isocubanite and chalcopyrite upon the cooling to lower temperatures according to the reaction:

$$Cu_2Fe_3S_5 = CuFe_2S_3 + CuFeS_2.$$

The observation of $Cu_2Fe_3S_5$ limited to small lentoid or spindle-shaped forms within isocubanite host mineral provides an indication that the vast majority of this mineral has already been consumed. Within this assemblage of $Cu_2Fe_3S_5$ and isocubanite, remarkably low proportions of chalcopyrite are observed in form thin acicular lamellae. The preservation of only small volumes of chalcopyrite are explained by selective dissolution

of chalcopyrite back into the vent fluid immediately after its formation. Geochemical model simulations have already shown that vent fluids in similar ultramafic rock-hosted settings are undersaturated in chalcopyrite at temperatures of 350 °C and higher (e.g., Fuchs et al. 2019). Under these conditions, chalcopyrite will dissolve into the fluid forming aqueous copper chloride and bisulphide complexes, whereas isocubanite remains stable. The vent fluids likely re-mobilize the Cu (plus Fe and S) on a limited spatial scale (within mm to cm) and re-precipitate chalcopyrite in cooler areas at temperatures below 350 °C. Such overgrowths textures of chalcopyrite have been widely observed in the studied samples and is represented by chalcopyrite of less non-stoichiometric compositions.

As temperatures cool down below 210 °C, the isocubanite host crystals become in turn unstable and transform into the final products chalcopyrite and pyrrhotite, according the solid-state reaction:

$CuFe_2S_3 = CuFeS_2 + FeS.$

Isocubanite lamella preserved within chalcopyrite host crystals and vice versa has been observed in many seafloor massive sulfide occurrences (including Kaimana) and provide evidence for the decomposition process of isocubanite. Pyrrhotite is, however, absent in the studied samples of Kaimana. This is again likely due to geochemical properties and temperatures of the vent fluid. If the redox state (oxygen fugacity) of the fluids are above the pyrrhotite-pyrite-magnetite (PPM) redox buffer and/or $H_2S$ concentrations are high, pyrrhotite would dissolve back into the fluid and likely precipitate other Fe-bearing minerals instead (e.g., pyrite).

## 6 Conclusion

The metastable mineral phase $Cu_2Fe_3S_5$ is a very rare Cu-Fe sulphide, which is until now only observed in meteorites and active high-temperature hydrothermal systems at seafloor. We propose that $Cu_2Fe_3S_5$ is the high-temperature precursor of the investigated mineral assemblage and exsolves into the two Cu-Fe sulphides isocubanite and chalcopyrite during cooling, likely at initial fluid temperatures significantly above 350 °C. The currently measured fluid temperature of 328 °C at the associated black smokers are lower, however, higher temperatures reaching 349 °C are confirmed at neighbouring chimneys, suggesting that high temperatures of ≥ 349 °C are maintained within the chimneys. Chalcopyrite dissolved back into the vent fluid leaving small non-stoichiometric residues (lamellae) behind, with a composition of close to $Cu_{0.9}Fe_{1.1}S_2$. The majority of chalcopyrite and is re-mobilized on mm- to cm-scale, and precipitated with a composition closer to its ideal stoichiometry. Isocubanite decomposed in turn into even more chalcopyrite and unstable pyrrhotite, when fluids further cool down to temperatures below 210 °C.

As an outlook, we are currently preparing a new publication addressing crystal structural properties and micro- to nano-textures of these Cu-Fe sulphides using transmission electron microscopy (TEM), especially to characterise $Cu_2Fe_3S_5$ and to verify the occurrence of isotropic chalcopyrite. Furthermore, we apply geochemical model simulations to empirically investigate the role of the vent fluids in the dissolution and re-precipitation of this mineral assemblage.

## Acknowledgements

Many thanks to the colleagues at the BGR in Hannover. Andreas Heiner ably produced polished sections and Christian Wöhrl is thanked for excellent support on electron probe microanalysis.

## References

Bogdanov YA, Lein AY, Maslennikov VV, Syaoli L, Ul'yanov AA (2008) Mineralogical-geochemical features of sulfide Ores from the Broken Spur hydrothermal vent field. Oceanology 48:679-700

Borodaev YS, Mozgova NN, Uspenskaya TY (2010) Typomorphic features of modern oceanic sulfides. Moscow University Geology Bulletin 65:66-75

Cabri LJ, Hall HT, Szymanski JT, Stewart JM (1973) On the transformation of cubanite. Canadian Mineralogist 12:33-38

Caye R, Cervelle B, Cesbron F, Oudin E, Picot P, Pillard F (1988) Isocubanite, a new definition of the cubic polymorph of cubanite $CuFe_2S_3$. Mineralogical Magazine 52:509-514

Firstova A, Stepanova T, Cherkashov G, Goncharov A, Babaeva S (2016) Composition and formation of gabbro-peridotite hosted seafloor massive sulfide deposits from the Ashadze-1 hydrothermal field, Mid-Atlantic Ridge. Minerals 6:19

Fleet ME (1971) Refinement of crystal structure of cubanite and polymorphism of $CuFe_2S_3$. Zeitschrift für Kristallographie 132:276-287

Fuchs S, Hannington MD, Petersen S (2019) Divining gold in seafloor polymetallic massive sulfide systems. Mineralium Deposita 54:789-820

Maslennikov VV, Maslennikova SP, Large RR, Danyushevsky LV, Herrington RJ, Ayupova NR, Zaykov VV, Lein AY, Tseluyko AS, Melekestseva IY, Tessalina SG (2017) Chimneys in Paleozoic massive sulfide mounds of the Urals VMS deposits: Mineral and trace element comparison with modern black, grey, white and clear smokers. Ore Geology Reviews 85:64-106

Missack E, Stoffers P, El Goresy A (1989) Mineralogy, parageneses, and phase relations of copper-iron sulphides in the Atlantis II deep, Red Sea. Mineralium Deposita 24:82-91

Mozgova NN, Borodaev YS, Gablina IF, Cherkashev GA, Stepanova TV (2005) Mineral assemblages as indicators of the maturity of oceanic hydrothermal mounds. Lithology and Mineral Resources 40:293-319

Pruseth KL, Mishra B, Bernhardt HJ (1999) An experimental study on cubanite irreversibility: Implications for natural chalcopyrite-cubanite intergrowths. European Journal of Mineralogy 11:471-476

Sugaki A, Shima H, Kitakaze A, Harada H (1975) Isothermal phase relations in the system Cu-Fe-S under hydrothermal conditions at 350°C and 300°C. Economic Geology 70:806-823

# Magmatic metal contribution to volcanic arc seafloor massive sulfides: case study of the Kolumbo volcano

**Hector S. [1], Patten C.G.C. [1], Kolb J. [1], Kilias S.P. [2], Nomikou P. [2]**
*[1]Institute of Applied Geosciences, Chair of Geochemistry and Economic Geology, KIT, Karlsruhe, Germany*
*[2]National and Kapodistrian University of Athens, Athens, Greece*

**Abstract.** Seafloor massive sulfides (SMS) form in various marine hydrothermal environments, including volcanic arcs, where magmatic fluids can contribute to the metal budget of the hydrothermal system. Here we study the Kolumbo volcano, a submarine volcano in the central Aegean Volcanic Arc, hosting an active hydrothermal system. Sulfate-sulfides chimneys forming a Zn-Pb SMS show elevated As, Ag, Au, Hg, Sb and Tl contents. These elements belong to the "epithermal suite of elements" and are usually related to magmatic input to the hydrothermal fluid. Combining volcanic whole rock chemistry, numerical modelling and in-situ magnetite analysis, we reconstruct the magmatic history and particularly, the behaviour of metals relative to sulfide saturation, magnetite crystallisation and degassing. Despite early sulfide saturation, chalcophile element concentrations in the magma do not decrease until water saturation, implying that magmatic sulfides remain in the magma and are not removed. Formation of sulfide-volatile compounds and magmatic degassing lead to metal transfer to the volatiles, depleting Cu, Au, Ag, Sn, Sb and Pb in the magma while Zn, As and Tl do not show specific behaviour.

## 1 Introduction

Arc-related hydrothermal systems differ in many aspects from those located along the mid-oceanic ridge and mature back-arc spreading centres, most notably by the shallow environment and importance of a magmatic source for fluids and metals (e.g. Hannington et al. 2005).

Magmatic volatiles in arc-related submarine hydrothermal systems indicate that ore deposits mineralization style form a continuum from volcanogenic massive sulfide to porphyry and epithermal deposits (Keith et al. 2018). In porphyry and epithermal deposits, metals are considered to be mostly carried by magmatic fluids that exsolve from hydrous magmas in the mid- to upper crust (Richards 2011). Thus, magmatic processes such as sulfide saturation, degassing and sulfide volatile compound formation are key parameters for controlling the formation of metal-rich magmatic fluids in arc-related submarine hydrothermal systems (Fontboté et al. 2017). Sulfide saturation in the melt will extract most of the chalcophile and siderophile elements (including As, Ag, Au, Hg, Sb and Tl) and concentrate them into an immiscible sulfide phase (Jenner et al. 2010). Because of its density, the sulfide phase tends to sink at the bottom of the magma chamber, physically removing the metals from the magma.

Similarly, degassing leads to formation of an aqueous fluid rich in volatiles such as S, Cl, F and $CO_2$, which can extract metals from the magma if it is still fertile (i.e. before sulfide saturation) (Fontboté et al. 2017). If the melt reached sulfide saturation before degassing, most of the chalcophile and siderophile metals will be already extracted by the sulfide melt, leaving too little metals available for the aqueous fluids and volatiles to generate metal-rich magmatic-hydrothermal fluids. However, formation of sulfide-volatile compounds and interaction between the two phases can favour metal transfer to the volatile despite early sulfide saturation (Mungall et al. 2015). Therefore, investigating the timing of sulfide saturation, water saturation in the system is crucial to understand the behaviour of metals during magmatic differentiation. To do so, detailed petrographic and whole rock analysis have been carried on volcanic rock samples from Kolumbo, coupled with magmatic differentiation and sulfur concentration at sulfide saturation (SCSS) modelling. Additionally, in-situ magnetite trace element analysis allows monitoring the metal content of the melt and refining the understanding of the metal behaviour during differentiation.

## 2 Kolumbo volcano and its SMS

The submarine Kolumbo volcano in the Anhydros basin belongs to the Christiana-Santorini-Kolumbo Volcanic Field in the centre of the Aegean Volcanic Arc, southern Aegean Sea. The last eruption of 1650CE shaped the volcanic edifice, forming a 7 kilometres wide cone with a 2.7 kilometres wide crater in its centre (Fouqué 1879; Sigurdsson et al. 2006). The seafloor of the crater is 500 meters below sea level and hosts a hydrothermal field in its northern part (Sigurdsson et al. 2006). The hydrothermal field contains active and fossil sulfate-sulfide chimneys, forming a polymetallic Zn-Pb-(As, Ag, Au, Hg, Sb, Tl)-rich SMS associated with $CO_2$-dominated fluids venting with temperature up to 220°C (Kilias et al. 2013; Sigurdsson et al. 2006). Kolumbo' s volcanic cone is formed by a superposition of 5 cone-shaped stratigraphic units labelled K1 to K5 interbedded with volcano-sedimentary units (Hübscher et al. 2015). Due to lack of drill cores at the time and limitation of remotely operated vehicle (ROV) sampling, only the outcropping units K2 and K5 units are available for study.

## 3 Methodology

Major element composition was measured on glass beads by X-ray fluorescence with a S4 Explorer at LERA. In-situ trace element analysis by laser ablation-inductively coupled plasma mass

spectrometry (LA-ICP-MS) on pressed powder pellets of representative volcanic rocks and on magnetite in thin sections was carried out at the Laboratory of Environmental and Raw Materials Analysis (LERA), KIT using a Teledyne 193 nm Excimer Laser coupled to an Element XR ThermoFisher ICP-MS. Reference materials BHVO-2, BHVO-2G, BIR-1 and NIST-612 were used for calibration and monitoring. Pellets and magnetite analysis were carried out in separate runs. Low detection limit Au analysis was carried out on the same apparatus, using the method from Patten et al. (accepted).

## 4 Results

The volcanic rock samples from Kolumbo belong to units K2 and K5. They are pumices and lavas and commonly contain mafic enclaves. Major element composition of the pumice, lava and mafic enclaves show that the K2 and K5 eruptions record similar differentiation processes, from basaltic andesite to rhyolite (own data; Cantner et al. 2014; Klaver et al. 2016). The compositional range of volcanic rocks of Kolumbo is considered to reflect continuous magmatic differentiation and magma mixing (Klaver et al. 2016). The pumices are mostly rhyolitic and exceptionally trachytic or andesitic. Magmatic enclaves in rhyolite and trachyte and mafic lavas are basaltic andesite to andesite. Detailed petrography shows that magmatic magnetite and sulfides are ubiquitous in the samples, independently of their differentiation stage.

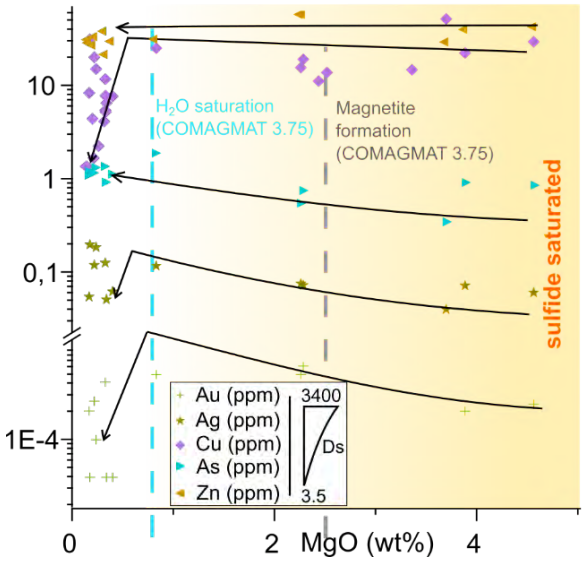


**Figure 1.** Different behaviour of metals in volcanic rocks during magmatic differentiation related to their chalcophile affinity. Ds is the partition coefficient between a sulfide liquid and the silicate melt (Patten et al. 2013 and references therein).

Trace element analysis of the volcanic rocks show that Ag, As, Au, Cu, Pb, Sb, Sn and Tl contents are slightly increasing during magmatic differentiation, while Co, Fe, Ni, Ti, V and Zn contents remain relatively constant until reaching 0.7 wt.% MgO, then Ag, Au, Cu, Pb, Sb, Sn are locally depleted (Figure 1). The $TiO_2$ and $Fe_{tot}$ contents remain relatively stable during the early magmatic differentiation, until ~2.5 wt.% MgO (~62 wt.% $SiO_2$), before decreasing strongly (Figure 2-A and B).

Trace elements content in magnetite is varying depending on the differentiation

state of the host rock. As magnetite is hosted in more felsic rocks, Al, Co, Cr, Cu, Ga, Mg, Ni, Sc and V contents are decreasing while Ge, Hf, Mn, Mo, Nb, P, Pb, Sn, Ta, Ti, W, Y, Zn and Zr contents are increasing in comparison to mafic rock-hosted magnetite.

## 5 Discussion

### 5.1 Modelling of magmatic differentiation in Kolumbo

Using an average primitive composition of the melt based on the composition of the most mafic samples (n=3), the evolution the melt composition during differentiation is modelled using COMAGMAT 3.75 (Ariskin and Barmina 2004) and compared to the major oxide composition of the volcanic rocks. The parameters modelling a melt composition evolution fitting best to the major oxide composition of the samples are $fO_2$ FMQ + 1 and 2 wt.% $H_2O$ with a pressure variation from 2.0 to 0.9 kbar. The pressure decrease is meant to reflect conditions for an ascending melt in an upper reservoir located at between 6- and 3-kilometres depth. The evolution of the SCSS during differentiation was modelled according to Smythe et al. (2017) using melt compositions calculated by COMAGMAT 3.75. Modelling predicts the following magmatic processes: (1) extensive magnetite crystallisation at ~2.5 wt.% MgO; (2) the melt is sulfide-saturated from the beginning of the differentiation; (3) water saturation starts at 0.87 wt.% MgO (Figure 1). The model is fitting well with the observations, correctly predicting early sulfide saturation and evolution of the major oxide composition during differentiation. However, it does not predict early magnetite formation, as observed in the most mafic samples. The absence of early magnetite crystallization in the model is likely caused by the higher $Fe^{2+}/FeO_{tot}$ used in the calculation to stay within range of use for COMAGMAT 3.75. Nonetheless, the model predicts correctly the magnetite crystallization observed in the samples and reflected by the drop in $TiO_2$ and $Fe_2O_3$ content in the rocks around ~2.5 wt.% MgO.

### 5.2 Metal content evolution during magmatic differentiation

Depletion in V, Ni, Co and to some extent Fe and Ti is related to crystallization and settling of magnetite in the magma chamber (Dare et al. 2014). Demixing of a sulfide melt after sulfide saturation should result in depletion of chalcophile and siderophile elements (Jenner et al. 2010; Patten et al. 2013). However,

despite early sulfide saturation, there is no significant depletion in chalcophile elements in the samples before water saturation and magmatic degassing, implying more complex metal behaviour during the evolution of the melt than sulfide exsolution and settling (Figure 1).

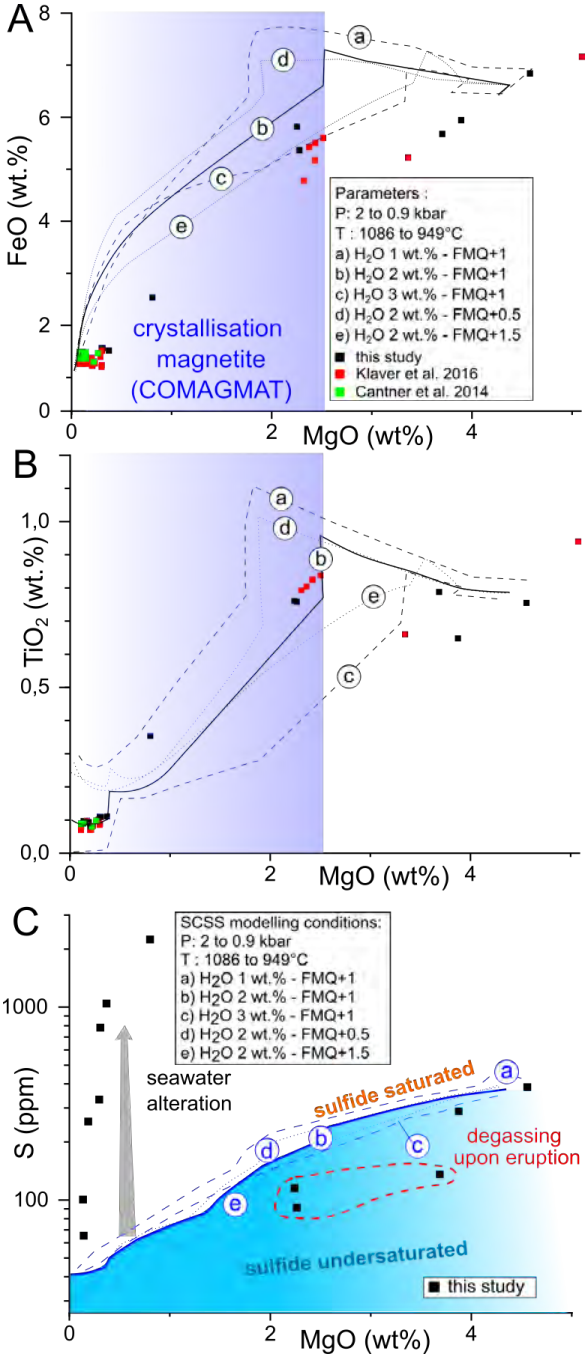


**Figure 2.** Modelling of Kolumbo' s melt evolution during magmatic differentiation. A) Modelled evolution of FeO content in the melt compared to volcanic samples for varying $H_2O$ initial content and $fO_2$ using COMAGMAT 3.75 (Ariskin and Barmina 2004); B) Modelled evolution of $TiO_2$ content in the melt compared to volcanic samples for varying $H_2O$ initial content and $fO_2$ settings using COMAGMAT 3.75; C) Modelled evolution of the SCSS (according to Smythe et al. 2017) using five different melt compositions calculated by COMAGMAT 3.75 with varying $H_2O$ initial content and $fO_2$ compared to S content in the volcanic samples.

### 5.3 Insight on metal behaviour from magnetite and sulfides

Chalcophile element content in magnetite reflects their availability in the melt at time of crystallization. Before magmatic degassing, the Cu content in magnetite decreases constantly during magmatic differentiation. Conversely, the corresponding whole rock Cu content remains relatively constant in the whole rock during magmatic differentiation (29±12 ppm on average) (Figure 3). This indicates that less and less Cu is available in the melt for magnetite during magmatic differentiation. Copper is likely trapped in magmatic sulfides, as the melt is sulfide saturated since at least formation of basaltic andesite, as observed petrographically and supported by SCSS modelling (Figure 2-C). However, the constant Cu content in the whole rock indicates that magmatic sulfides are not removed from the magma. The limited size of the sulfide phases observed in the samples and the increasing viscosity of the melt as it differentiates are greatly reducing their mobility, likely preventing them to sink and conserving the metal content of the system (Holzheid 2010).

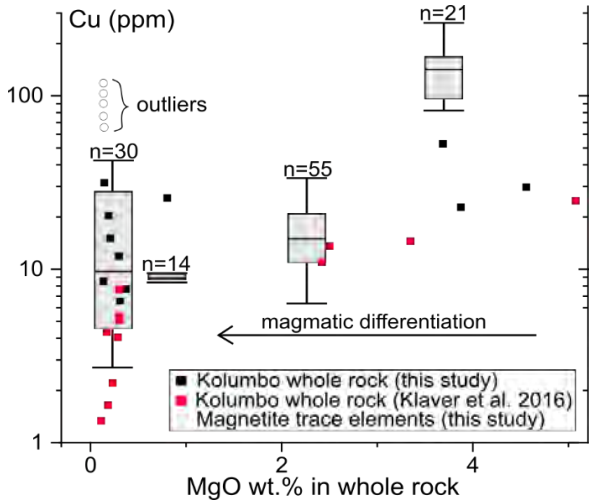


**Figure 3.** Evolution of the Cu content in volcanic rocks and their respective magnetite during magmatic differentiation.

### 5.4 Metal flux during magmatic degassing

According to the modelling, water saturation starts at 0.87 wt.% MgO, which correspond to formation of trachyte by magma mixing/differentiation. Upon degassing, the most chalcophile elements (i.e. Cu, Ag and Au and to some extend Sn, Sb and Pb) are the most depleted in the whole rock while the least chalcophile (i.e. As, Tl and Zn) are not affected (Figure 3). However, in Kolumbo' s magma, the most chalcophile elements are concentrated in the magmatic sulfide phases which remain in the magma. Thus, leaching of the sulfide phases by the

degassing volatiles is required for efficient mobilization of the chalcophile metals. Volatile phase nucleation on magmatic sulfides and formation of sulfide-volatile compounds (Mungall et al., 2015) would be a very efficient mechanism for mobilizing metals from the sulfides during degassing.

### 5.5 Magmatic input in Kolumbo' s SMS

The sulfide-sulfate chimneys at Kolumbo' s SMS are Zn-Pb-rich and show elevated As, Ag, Au, Hg, Sb and Tl content, while being relatively Cu poor (Ahmad 2018; Kilias et al. 2013). Enrichment in Au, Ag, Sb and Pb is agrees with a magmatic source, as these elements are mobilized from the magma upon degassing and can be transferred to the magmatic-hydrothermal fluids. The low Cu content in the chimneys indicates that it is most likely trapped in the deeper, hotter part of the mineralized system, as frequently observed in VMS and epithermal/porphyry systems (Hannington et al. 2005).

Conversely, As, Zn and Tl are enriched in the chimneys but do not seem to be lost during magmatic degassing, indicating another metal mobilizing mechanism is likely involved. Hydrothermal leaching can mobilize As, Ag, Au, Cu, Pb, Sb, Sn, Tl, Zn from the host rocks in VMS deposits, especially in felsic environment, and can represent an additional process occurring at Kolumbo (Shikazono 2003).

## Conclusion

Combining in-situ magnetite trace element analysis with whole rock analysis and modelling allows to track metal behaviour in the magma during magmatic differentiation. It indicates that chalcophile elements are scavenged by sulfide phases but remain in the magma. Sulfide-volatile compounds formation and magmatic degassing appear to be an important process to transfer Cu, Au, Ag, Sb, Sn and Pb from the magma to the magmatic-hydrothermal system by leaching of the sulfide phases by volatiles. However, hydrothermal leaching of the basement also provides metals to the system, especially Zn, As and Tl.

## Acknowledgements

This work is funded by the German Research Foundation (DFG - Priority Program DOME SPP 2238 and INST 121384/213-1 FUGG).

## References

Ahmad Q (2018) The source of metals in the recent polymetallic seafloor massive sulfide mineralization at the Kolumbo arc-volcano, Greece. M.Sc. thesis, Karlsruhe Institute of Technology

Ariskin AA, Barmina GS (2004) COMAGMAT: Development of a magma crystallization model and its petrological applications. Geochemistry International 42:1–157

Cantner K, Carey S, Nomikou P (2014) Integrated volcanologic and petrologic analysis of the 1650AD eruption of Kolumbo submarine volcano, Greece. Journal of Volcanology and Geothermal Research 269:28–43

Dare SAS, Barnes S-J, Beaudoin G, Méric J, Boutroy E, Potvin-Doucet C (2014) Trace elements in magnetite as petrogenetic indicators. Miner Deposita 49:785–796

Fontboté L, Kouzmanov K, Chiaradia M, Pokrovski GS (2017) Sulfide Minerals in Hydrothermal Deposits. ELEMENTS 13:97–103

Fouqué F (1879) Santorin et ses éruptions. G. Masson, Paris

Hannington M, de Ronde CEJ, Petersen S (2005) Sea-Floor Tectonics and Submarine Hydrothermal Systems. In: Hedenquist J, Thompson JFH, Goldfarb RJ, Richards JP (eds) One Hundredth Anniversary Volume. Society of Economic Geologists

Holzheid A (2010) Separation of sulfide melt droplets in sulfur saturated silicate liquids. Chemical Geology 274:127–135

Hübscher C, Ruhnau M, Nomikou P (2015) Volcano-tectonic evolution of the polygenetic Kolumbo submarine volcano/Santorini (Aegean Sea). Journal of Volcanology and Geothermal Research 291:101–111

Jenner FE, St. O'Neill HC, Arculus RJ, Mavrogenes JA (2010) The Magnetite Crisis in the Evolution of Arc-related Magmas and the Initial Concentration of Au, Ag and Cu. Journal of Petrology 51:2445–2464

Keith M, Haase KM, Klemd R, Smith DJ, Schwarz-Schampera U, Bach W (2018) Constraints on the source of Cu in a submarine magmatic-hydrothermal system, Brothers volcano, Kermadec island arc. Contrib Mineral Petrol 173

Kilias SP, Nomikou P, Papanikolaou D, Polymenakou PN, Godelitsas A, Argyraki A, Carey S, Gamaletsos P, Mertzimekis TJ, Stathopoulou E, Goettlicher J, Steininger R, Betzelou K, Livanos I, Christakis C, Bell KC, Scoullos M (2013) New insights into hydrothermal vent processes in the unique shallow-submarine arc-volcano, Kolumbo (Santorini), Greece. Sci Rep 3:2421

Klaver M, Carey S, Nomikou P, Smet I, Godelitsas A, Vroon P (2016) A distinct source and differentiation history for Kolumbo submarine volcano, Santorini volcanic field, Aegean arc. Geochem Geophys Geosyst 17:3254–3273

Mungall, J. E.; Brenan, J. M.; Godel, B.; Barnes, S. J.; Gaillard, F. (2015) Transport of metals and sulphur in magmas by flotation of sulphide melt on vapour bubbles. In : Nature Geoscience, vol. 8, n° 3, p. 216–219. DOI: 10.1038/NGEO2373.

Patten CGC, Barnes S-J, Mathez EA, Jenner FE (2013) Partition coefficients of chalcophile elements between sulfide and silicate melts and the early crystallization history of sulfide liquid: LA-ICP-MS analysis of MORB sulfide droplets. Chemical Geology 358:170–188

Patten, CGC; Beranoaguirre, A; Hector, S; Gudelius, D; Kolb, J; Eiche, E (accepted) Improved whole rock low detection limit of gold by LA-ICP-MS utilizing pressed-powder-pellets. In : International Journal of Mass Spectrometry.

Richards JP (2011) Magmatic to hydrothermal metal fluxes in convergent and collided margins. Ore Geology Reviews 40:1–26

Shikazono N (2003) Geochemical and tectonic evolution of arc-backarc hydrothermal systems: Implication for origin of Kuroko and epithermal vein-type mineralizations and the global geochemical cycle, 1st ed. Developments in geochemistry, vol 8. Elsevier, Amsterdam, Boston

Sigurdsson H, Carey S, Alexandri M, Vougioukalakis G, Croff K, Roman C, Sakellariou D, Anagnostou C (2006) Marine investigations of Greece's Santorini volcanic field. Eos, Trans. Am. Geophys. Union 87:337–342

Smythe DJ, Wood BJ, Kiseeva ES (2017) The S content of silicate melts at sulfide saturation: New experiments and a model incorporating the effects of sulfide composition. American Mineralogist 102:795–803

# Distribution of Characteristic Elements in Pore Waters, Sediments and Nodules from the Eastern Part of the Clarion-Clipperton Fractures Zone, NE Pacific

**Atanas Hikov[1], Zlatka Milakovska[1], Irena Peytcheva[1], Valcana Stoyanova[2], Elitsa Stefanova[1], Tomasz Abramowski[2], Silvia Chavdarova[1], Milen Stavrev[1], Dimitrina Dimitrova[1]**
*[1] Geological Institute, Bulgarian Academy of Sciences, Bulgaria*
*[2] Interoceanmetal Joint Organization, Poland*

**Abstract.** The geochemical characteristics of pore waters, bottom sediments and polymetallic nodules from the Interoceanmetal exploration area in the eastern part of the Clarion-Clipperton Fractures Zone (CCZ), NE Pacific were studied. Manganese has a positive correlation with Fe in pore waters but a negative correlation in the sediments and polymetallic nodules. The results suggest that Mn precipitates faster than Fe in sediments and especially in nodules that are enriched in Mn, Ni and Cu compared to the host sediments. PAAS-normalized REE patterns of pore water layers, sediments layers, bulk nodules and nodule growth layers show gradual enrichment resulting of several factors, including low sedimentation rate, high REE of the bottom seawater, oxidation conditions, certain bottom current conditions and the presence of Fe–Mn oxyhydroxides.

## 1 Introduction

The development of modern society and new emerging technologies are resulting in growing demand for rare and trace elements defined as critical raw materials (CRMs). The deep-sea metalliferous sediments and Fe-Mn polymetallic nodules formed in modern environment at the deep-sea ocean floor (>4000 m depth) were evaluated as promising new raw materials, especially for high-tech elements as Co, Ni and rare earth elements (REE) (Kato et al. 2011; Pak et al. 2019). The Clarion-Clipperton Fe-Mn Nodule Zone (CCZ) in the NE Pacific is the area of greatest economic interest for nodules and sediments (Kato et al. 2011; Hein et al. 2013).

In the present study we compare geochemical characteristics of pore waters, sediments and polymetallic nodules from the Interoceanmetal (IOM) exploration area located in the eastern part of the CCZ, NE Pacific. Our aim is to assess the main factors that control metal deposition and Fe-Mn polymetallic nodule enrichment in some CRMs.

## 2 Geological setting and sampling

The studied area covers 630 km$^2$ of the seafloor in the eastern part of the Clarion-Clipperton fractures Zone, NE Pacific between 11°06'–11°26'N latitude and 119°25'–119°42'W longitude at depth varying from 4300 to 4500 m (Figure 1). Box-core samples from six stations were collected during the 2019 Interoceanmetal cruise. The explored stations are distributed among various morphological types of the bottom relief, mostly represented by the undulating hilly plain, intersected by longitudinal ridges and sub-parallel volcanic massifs.

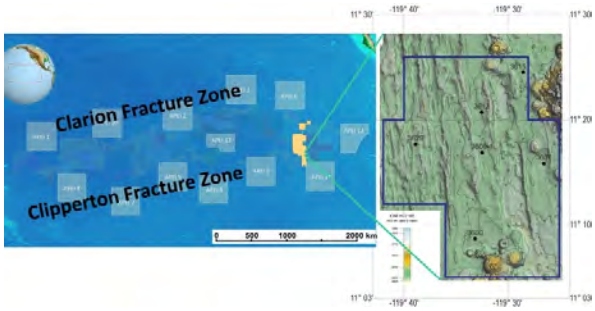


**Figure 1.** Geomorphological map of the seafloor and location of the sampling area in the IOM exploration area in the eastern part of the CCZ.

The polymetallic nodules were observed on the top of, and partly buried in the seabed sediments. The sediment composition is dominated by light brown siliceous silty clay down to 45-cm. The top semiliquid dark brown clay variety (thickness of 7–12 cm) was denoted as a geochemically active layer (GAL), i.e. it is the medium for main processes of polymetallic nodule formation. An amorphous phase (biogenic opal, authigenic Fe-Mn hydroxides and clay minerals) predominates in the mineral composition. The crystalline phases are illite, kaolinite, chlorite, quartz, andesine, halite, cristobalite and barite (Hikov et al. 2022a).

A box corer was used to yield relatively undisturbed bottom samples up to 50 cm in depth. After collecting the nodules from the surface four sediment layers at depths 0–3, 3–5, 5–10, 10–20 cm were sampled. The sediment samples for pore water extraction were collected on-board from the depth intervals 0–5, 10–15, 25–30 and 35–40 cm following the recommendations of ISBA/19/LTC/8. The water samples were stabilized by concentrated nitric acid and stored in plastic bottles.

## 3 Analytical techniques

The chemical analyses of the water samples were carried out at the Faculty of Chemistry and Pharmacy, Sofia University using ICP-MS (Perkin-Elmer SCIEX Elan DRC-e) with a cross-flow nebulizer, following the analytical techniques of Lyubomirova et al. (2020). The concentrations of 69 elements were determined. Working standard solutions were prepared from ICP-MS multi-element

calibration standard solution-2 (Ultra Scientific) and ICP-MS Multielement Standard B (High Purity Standards).

Major element composition of the sediment samples was determined by ICP-OES at AQUATERATEST LTD, Sofia. Trace element content was measured on fused pellets by LA-ICP-MS at the Geological Institute of Bulgarian Academy of Sciences (BAS), using laser ablation system New Wave UP193FX coupled to a PerkinElmer ELAN DRC-e ICP-MS. The laser beam diameter was 100 μm and laser pulse frequency - 10 Hz. The NIST 610 was used for external standard and $SiO_2$, determined by ICP-OES as internal standard.

The major element composition of the main minerals in the nodules was determined by SEM-EDS (SEM JEOL JSM-6610LV at Belgrade University, Serbia). The chemical composition of bulk nodule samples was measured on pressed pellets with LA-ICP-MS at the Geological Institute, BAS. Laser spot of 35 μm and 6 Hz pulse rate were applied. External standardization was made on NIST 610 glass and Mass1 polymetallic standards. The total major element oxides (100 wt.%) was used as standardization method for the pressed pellets after subtracting the loss of ignition (LOI). The *in situ* trace element composition was measured on polished sections, whereas Mn concentration from SEM-EDS analyses was used as internal standard.

## 4 Results

### 4.1 Pore waters

The major elements in the pore water are Na, Mg, Ca and K, and Na is clearly prevailing. The concentrations of elements of interest are as follows (in μg/L): Fe (241.4–2236.1), Mn (1.8–137.8), Co (1.73–6.09), Ni (11.6–38.8), Cu (9.0–41.7), Zn (21.1–95.1), As (39.0–82.9), Mo (5.4–34.0), Cd (0.21–44.9). Most of the stations have maximum values of Fe and Mn in the second (10–15 cm) or the first (0–5 cm) layers. Ni, Cu and Co show similar trends while As distribution is clearly opposite. The ΣREE in the pore water samples varies from 3.56 to 94.34 μg/L. Maximum REE values were observed for the first (0–5 cm) or for the second (10–15 cm) layers. A negative Ce anomaly predominates and increases with depth. The Eu anomaly is highest in the second layer in the most of the stations.

### 4.2 Sediments

The chemical composition of the sediment samples is similar with small differences depending on the station and depth interval. Iron content ranges from 4.10% to 4.99% (mean 4.60%) and increases with depth. Manganese varies from 0.16% to 0.70% (mean 0.49%), and Mn/Fe ratio - from 0.03 to 0.16. Both values are the highest in GAL and decrease with depth. Characteristic element contents in the sediments are as follows (ppm): Co (41.6–86.8), Ni (80.2–216.8), Cu (280–429.5) and Zn (105.5–132). Cobalt, Ni, Cu and Ba have the highest contents in the GAL that decrease with depth, while Zn does not show such a trend. The ΣREE in the sediments varies from 195.84 to 357.79 ppm (mean 245.79 ppm) without any significant variations between the sediment layers. PAAS-normalized REE patterns show enrichment of MREE and HREE. All samples reveal strong negative Ce anomaly, positive Eu and weak positive Y anomalies.

### 4.3 Polymetallic nodules

Bulk nodule samples show Mn content variation from 22.62 to 35.59 wt.% (mean 31.36%) and Fe one - from 3.51 to 8.26 wt.% (mean 5.38%). The Mn/Fe ratio varies from 2.74 to 10.12. The characteristic elements concentrations are as follows: Ni (0.58–1.70 wt.%), Cu (1.07–1.50 wt.%), Co (0.12–0.30 wt.%), Zn (0.09–0.26 wt.%), Mo (430–872 ppm), W (55–111 ppm), Li (77–205 ppm), Tl (53–410 ppm), Pb (247–616 ppm), Y (42–83 ppm), Ba (2197–5775 ppm). The ΣREE range is 316.33–677.49 ppm (mean 472.08 ppm). The PAAS-normalized REE patterns show enrichment of all REE, especially of middle REE (MREE) and heavy REE (HREE). The studied nodules have mainly positive or weak negative Ce anomaly, positive Eu and negative Y anomalies.

Most of the studied polymetallic nodules have high Mn/Fe ratio (>5) and are diagenetic nodules according to Kotlinski and Stoyanova (2012). Some nodules with Mn/Fe ratio 3–5 are of mixed, hydrogenetic-diagenetic type, and only one nodule (sample 3607) is hydrogenetic with Mn/Fe ratio <3. The diagenetic nodules reveal high ΣNi+Cu. The nodule 3607 has the lowest ΣNi+Cu and the highest Co content. Hikov et al. (2022b) suggested that most of the nodules are of mixed hydrogenetic-diagenetic type using different discrimination criteria.

The SEM-EDS analyses of nodule layers show Mn and Fe content variations from 10.75 to 57.63%, and from 0.10 to 24.12%, respectively. The range of the Mn/Fe ratio is 0.76–491.75.The *in situ* LA-ICP-MS analyses show high contents for Ni (0.13–3.58 wt.%), Cu (0.20–3.21 wt.%), Co (0.005–1.04 wt.%), Zn (0.03–0.85 wt.%), Ba (0.04–2.64 wt.%), Mo (195–2114 ppm), W (23–607 ppm), Li (15.5–1046 ppm), Tl (26–1101 ppm), Pb (24–2917 ppm), Y (14.8–196.6 ppm). The ΣREE varies from 119.3 to 2312.8 ppm.

The PAAS-normalized REE patterns of *in situ* nodule analyses show MREE and HREE enrichment. Approximately half of the layers reveal patterns with a negative Ce anomaly while the others are characterized with positive Ce anomaly. Most of the analyses show weak positive Eu anomaly and all have negative Y anomaly. All *in situ* analyses of nodule 3607 have positive Ce anomaly which corresponds to the low Mn/Fe ratio and low ΣNi+Cu contents in the bulk analysis.

### 4.4 Correlations

Table 1 shows the positive and negative correlations of Mn and Fe with other elements in the pore waters, bottom sediments, polymetallic nodules and nodule layers. Copper is the only element which has positive correlation with Mn in all studied components of the deep ocean floor environment. Five elements – Ni, Zn, Mo, Sb and Ba have positive correlation with Mn in sediments, bulk nodules and nodule layers. Other elements correlate either positively (Cd, W and Tl) or negatively (Si, Ti and Pb) with Mn in two components. Manganese has variable (+/-) correlations with Fe, Co and Na in different components. Iron has positive correlation with Ti, P, Zr, Nb and Pb in sediments, nodules and nodule layers and with REE, Y and Th in sediments and nodule layers.

| comp | pore waters | | sediments | | bulk nodules | | nodule layers | |
|---|---|---|---|---|---|---|---|---|
| corr | + | - | + | - | + | - | + | - |
| **Mn** | **Al**, **Fe** *Co*, *Y* Cu | | **Co** **Ni** **Cu** *Zn* *Mo*,*W* Na, Sr Sb, Ba | *Ti*, *Pb* Al, Fe K | **Sn** **Sb, Zn** *Li*, *Ni*,*Cu* *Mo* *Cd*, *Tl* V, Ag Ba | **Si**, **Al** **Fe** *Na*,*Co* *Hf*, Zr, In | **Cu**,**Cd** **Tl** *Mg*,*Na* *Ni*,*Zn* *Mo* Sb, *Ba* Li, V, Sr, W | **Si**, **Fe** **P**, **Zr** **Sn**,**Pb** *Ti*, *Sc* *As*, *Y* *Te,* Ce REE Co |
| **Fe** | **Al** **Mn** *Ba* | | **Al, Ti** **Ca**, **K** **Mg** *P*, *Y* *REE* Ga, Zr Nb, Pb Th | *Si*, *Ni* *As*,*Mo* *W* Mn | **Si**, **Al** **Na**,**Co** **Zr**, **Hf** *P*, *As* *In*, *Nb* *Pb*, *W* Ti, Ce | **Mn** **Sn**,**Sb** *Li*, *Zn* *Cd*,*Mo* Ni, Cu Ba, Tl | **P**, **Co** **As**, **Zr** **Ce**,***Pb*** *Si*, *Ti* *Y*, *Nb* *REE* *Bi, U* *Th,* Sc | **Mn** **Cu** *Ni*, *Cd* Zn, Ga Mo,Ba Sb, W Tl |

**Table 1.** Correlations of Mn and Fe in pore waters, sediments, bulk nodules and nodule layers. Abbreviations: comp – component, corr – correlation, **Al (bold)** - strong (0.7-1) correlation, *Co (Italic)* - moderate (0.5-0.69) correlation, Sr (normal) - weak (0.3-0.49) correlation, Cu - correlation in all components , Ni - correlation in 3 components .

## 5 Discussion and conclusions

The natural environment for the nodules formation (bottom sediments, pore waters, organic matter) is a result of diagenetic processes (biogeochemistry, adsorption, desorption, transformation and migration), sedimentation rate, bioturbation, oxidation conditions, and certain bottom current conditions (Kotlinski and Stoyanova 2012; Hein and Koschinsky 2014).

In the pore water, Mn and Fe have the highest concentration in the geochemically active layer (Milakovska et al. 2022).The pore waters accumulate metals from oxidation of organic matter in the deep-ocean sediments resulting in the reduction and dissolution of Mn oxides and associated elements (Ni, Cu, Li). Owing to concentration gradients in the sediment, these metals diffuse upwards and, on contact with oxygen-rich ocean water, are reoxidized and precipitate as 7Å and 10Å Mn oxides (disordered phyllomanganates) (Hein et al. 2020). Manganese has positive correlation with Fe in pore waters but the correlation becomes negative in the sediments and polymetallic nodules.

The results suggest that Mn precipitates faster than Fe in the sediments and especially in nodules. The latter are enriched in Mn, Ni and Cu compared to the host sediments. This trend can be traced on the Fe–Mn–(Co+Ni+Cu)x10 ternary diagram of Bonatti et al. (1972) (Figure 2.).

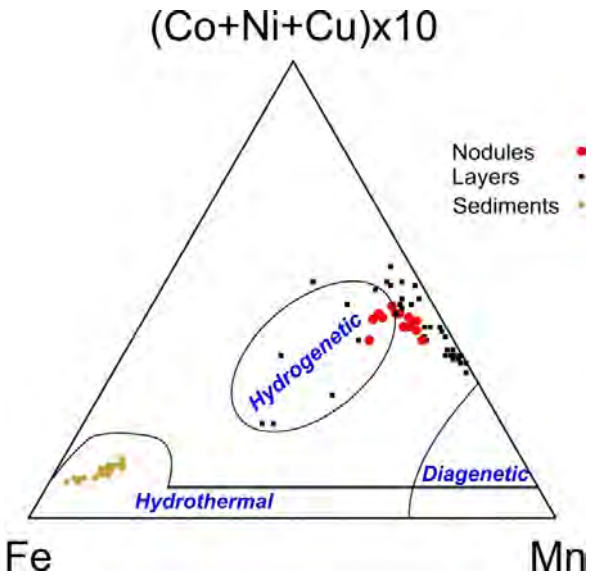


**Figure 2**. Ternary Fe–Mn–(Co+Ni+Cu)x10 diagram (Bonatti et al. 1972) for discrimination of polymetallic nodules and sediments.

The concentration of metals in the pore water depends mainly on the accumulation rate of sediments and the processes of dissolution, reduction and oxidation. In the sediments and nodules the metal deposition depends on the presence of nucleus (fragments of old nodules, sediment material, volcanoclastic rocks, bioclastic material), well oxygenated bottom waters, semi-liquid surface layer and bioturbation (Kotlinski and Stoyanova 2012). Two main types of nodule formation were distinguished – hydrogenetic and diagenetic precipitation, but often a mixed hydrogenetic-diagenetic type of precipitation was suggested (Hein et al. 2013).

The REE content in the studied pore waters is at least one order of magnitude higher than in the average bottom sea water (Li and Schoonmaker 2014) and shows MREE and HREE enrichment (Figure 3.). In contrast, the host sediments have two orders of magnitude higher REE contents than the pore waters and comparatively flat patterns. The nodules reveal 2-3 times higher REE contents than the host sediments, and in the richest nodule layers REEs are 2-3 times higher than their average content in bulk nodules.

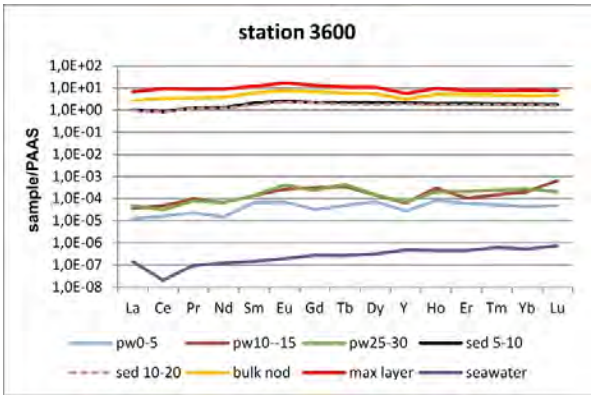


**Figure 3.** PAAS-normalized REE patterns of pore water layers (pw 0-5, pw 10-15, pw 25-30), sediments layers (sed 5-10, sed 10-20), bulk nodules (bulk nod) and the richest nodule layers (max layer) of station 3600 compared to average deep oceanic water (seawater) (Li and Schoonmaker 2014).

REE enrichment in deep-sea sediments is explained as the result of the interaction of several factors, including low sedimentation rate, presence of phosphate component near the seawater/sediment interface, high REE of the bottom seawater, oxidation conditions, and certain bottom current conditions (Ren et al. 2021). Generally, the REE accumulate mainly on Fe–Mn oxyhydroxide particulates (Dubinin 2014), and in a small degree incorporate into authigenic apatite. Our samples show positive correlation of REE with Fe and P. Negative Ce anomalies are characteristic for diagenetic Fe hydroxides, whereas a positive Ce anomaly is typical for hydrogenic nodules (Dubinin 2014; Hein and Koschinsky 2014). Our bulk analyses show no or weak positive Ce anomalies that is in line with the suggestion for a mixed hydrogenetic-diagenetic type. In the nodule layers the varying Ce anomalies suggest changing oxic/suboxic conditions. The Ce anomaly variations correlate with the Mn/Fe ratio and the genetic type (diagenetic or hydrogenetic) and could be a useful indicator for the nodule growth mechanisms (Hein and Koschinsky 2014).

The comparison of the results for the bottom sediments, pore waters and polymetallic nodules argue for a complexity of the processes that influence the formation of these deposits. The changing oxic/suboxic and anoxic conditions are well documented in the chemistry of the studied nodule layers. Probably the most important controlling factors are sedimentation rate, bioturbation, adsorption, desorption and oxidation.

## Acknowledgements

The study was supported by Bulgarian National Science Fund grant KP-06-N34/6.

## References

Bonatti E, Kraemer T, Rydell H (1972) Classification and genesis of submarine ironmanganese deposits. In: Horn D (Ed), Ferromanganese Deposits on the Ocean Floor, Natl. Sci. Found., Washington, pp 149–165

Dubinin A (2004) Geochemistry of Rare Earth Elements in the ocean. Lithology and Mineral Resources 39:289–307

Hein J, Koschinsky A (2014) Deep-Ocean Ferromanganese Crusts and Nodules. Treatise on Geochemistry 2nd Edition 7, pp. 273–291

Hein J, Mitzell K, Koschinsky A, Conrad T (2013) Deep-ocean mineral deposits as a source of critical metals for high- and green-technology applications: Comparison with land-based resources. Ore Geology Reviews 51:1–14

Hein J, Koschinsky A, Kuhn T (2020) Deep-ocean polymetallic nodules as a resource for critical materials. Nature Reviews Earth & Environment 1:158–169

Hikov A, Milakovska Z, Stoyanova V, Stefanova E, Abramowski T, Chavdarova S, Stavrev M (2022a) REE and trace elements distribution in the deep-sea sediments from the Interoceanmetal (IOM) polymetallic nodule exploration area in the Clarion-Clipperton fractures zone, NE Pacific. Compt Rend Acad Bulg Sci 75:1018–1027

Hikov, A, Stefanova E, Stoyanova V, Milakovska Z, Abramowski T, Chavdarova S, Stavrev M, Peytcheva I (2022b) Genetic types and REE composition of polymetallic nodules from the eastern part of the Clarion–Clipperton Fractures zone, NE Pacific. In: Christie, A. (ed.) Proceedings of the 16th SGA Biennial Meeting, 28-31 March 2022, 1, pp.129–132

ISBA/19/LTC/8 recommendations – (c) For chemical oceanography (i) Collect information on background water column chemistry, including water overlying the resource, in particular on metals and other elements that may be released during the mining process.

Kato Y, Fujinaga F, Nakamura K, Takaya Y, Kitamura K, Ohta J, Toda R, Nakashima T, Iwamori H (2011) Deep-sea mud in the Pacific Ocean as a potential resource for rare-earth elements. Nature Geoscience 4:535–539

Kotlinski R, Stoyanova V (2012) Nodule coverage, morphology and distribution in the Eastern CCZ. In: ISA, Technical Study No 6: Prospector's Guide for Polymetallic Nodule Deposits in the Clarion-Clipperton Fracture Zone, pp 34–42

Li Y-H, Sc hoonmaker J (2014) Chemical Composition and Mineralogy of Marine Sediments. Treatise on Geochemistry 2nd Edition 7, pp 1–35

Lyubomirova V., Mihaylova V., Djingova R. 2020. Chemical characterization of Bulgarian bottled mineral waters. Journal of Food Composition and Analysis, 93, 103595

Milakovska Z, Hikov A, Stoyanova V, Peytcheva I, Lyubomirova V, Abramowski T (2022) REY in pore waters of sediments hosting Fe-Mn nodules of the Interoceanmetal exploration area in the Clarion-Clipperton Fracture Zone, NE Pacific. Geologica Balcanica 51 (2):27–35

Pak S, Seo I, Lee K, Hyeong K (2019) Rare Earth Elements and Other Critical Metals in Deep Seabed Mineral Deposits: Composition and Implications for Resource Potential. Minerals 9 (1) 3:1–19

Ren J, Liu Y, Wang F, He G, Deng X, Wei Z, Yao H (2021) Mechanism and Influencing Factors of REY Enrichment in Deep-Sea Sediments. Minerals 11(2) 196:1–16

# Inter- and intra-caldera, stratiform Zn-Pb-Ag and iron formation at Nyberg, Bergslagen, Sweden

**Nils F Jansson[1], Anton Fahlvik[2], Rodney L Allen[3], Jenny Andersson[4]**
*[1]Division of Geosciences and Environmental Engineering, Department of Civil, Environmental and Natural Resources Engineering, Luleå University of Technology, 971 87 Luleå, Sweden*
*[2]Exploration Department, Boliden Mines, 776 98 Garpenberg, Sweden*
*[3]Volcanic Resources AB, Nås 230, 776 92 Hedemora, Sweden*
*[4]Geological Survey of Sweden, 751 28 Uppsala, Sweden*

**Abstract.** The Nyberg Zn-Pb-Ag deposit is poorly known in comparison with some other, metamorphosed, c. 1.9 Ga stratiform Zn-Pb-Ag deposits in Bergslagen, Sweden (e.g., Zinkgruvan, Lovisa). Based on facies analysis, whole-rock lithogeochemistry, U-Pb zircon geochronology and sulphur isotope analysis, we argue that the deposit formed in a redox-stratified submarine intra-caldera basin which developed after a major, felsic, pyroclastic caldera-forming event at 1900±5 Ma. The widespread (>10km) host succession of mudstone, iron formation, sulphide mineralisation and limestone accumulated during a quiescent period prior to a resurgence in volcanism at c. 1890±3 Ma, during which a younger phase of intense, caldera-forming felsic volcanism ensued. Geochemical evidence points to an association between the waning stage 1900±5 Ma volcanism and the Nyberg mineralisation, whereas the 1890±3 Ma phase volcanism is associated with coeval porphyritic intrusions and granitoids which in turn are associated with, metasomatic Zn-Pb-Ag deposits elsewhere in the area.

## 1 Introduction

Stratiform Zn-Pb-Ag mineralisation in fine-grained volcaniclastic, siliciclastic and calcareous strata (e.g., Zinkgruvan, Lovisa) is one of the main types of c. 1.9 Ga, metamorphosed base metal sulphide deposits in Bergslagen, Sweden. Several deposits exhibit an intimate relationship with magnetite iron formation; the relatively unknown Nyberg deposit in central Bergslagen being a prime example. Here, a gradational is observed along and across strata from a banded iron formation of magnetite, amphibole and chlorite, into stratiform Zn-Pb-Ag mineralisation. The iron formation is more widespread than the sulphide mineralisation and has been correlated over a distance of more than 10 km along the folded and faulted stratigraphy in the area (Fig. 1). A progressively higher content of hematite and calcite is observed away from Nyberg.

This contribution presents a geological overview of the Nyberg deposit, focusing on the genesis of the sulphide deposit and its relation to adjacent iron oxide mineralisation.

## 2 Results

### 2.1 Structure and stratigraphy

The Nyberg deposit occurs in a belt of c. 1.91–1.89 Ga, mainly felsic metavolcanic rocks. This supracrustal succession is intruded by c. 1.89 Ga granite in the south (Fig.1). The deposit is hosted by the Jugansbo formation: An approximately 100 m thick succession of pelitic siliciclastic and volcaniclastic rock with minor intervals of marble and laminated-banded magnetite and sulphide mineralisation (pyrrhotite-sphalerite>galena) in skarns with amphibole (grunerite, actinolite), garnet (almandine-dominant) and chlorite (ripidolite). The deposit is interpreted to occupy a gently–moderately plunging, isoclinal $F_1$ syncline based on younging reversals (Figs. 1 and 2A), albeit the stratigraphy differs on each limb of the $F_1$ fold. The northern part of the deposit is affected by complex faulting and shearing.

Facies analysis show that the footwall to the mineralisation on the southern limb consists of a >500 m thick unit of massive rhyolitic pumice breccia with several normal graded juvenile volcaniclastic beds at the top (Högberget formation). At Nyberg, these rocks are pervasively albitized and silicified, with a sharp alteration contact towards the more alkali-depleted rocks of the Jugansbo formation. They overlie a succession of mainly fine-grained, reworked and re-sedimented felsic volcaniclastic deposits with limestone interbeds (Armanbo formation)(Fig.1).

A unit of massive, quartz-phyric rhyolitic silt-sandstone (IBM = 'in-between member') overlies the Nyberg deposit in the core of the $F_1$ syncline. Lithological zoning in the southern and northern parts of the Nyberg deposit is perfectly mirrored on each side of the IBM, albeit the footwall on the northern limb comprises a package of chloritic mudstone with bands and dissemination of calc-silicates and sulphides, underlain by organic-rich (graphitic) mudstone with local interbeds of limestone (calcite marble)(Fig 2A).

Further north, a tectonic contact exists towards a strongly foliated lens of chlorite+sericite-altered rhyolite (intra-shale rhyolite member). This unit is geochemically similar to the Högberget formation volcanic rocks (Fig. 2D), and is likely a tectonic sliver of these. A repetition of the Jugansbo formation is found further north, which is stratigraphically overlain by coarse-grained, rhyolitic volcaniclastic rocks of the Gransjön formation (Fig. 1). These differ from the Högberget formation in a higher abundance of quartz phenocrysts and a frequent occurrence of limestone clasts and interbeds. The contact to the Gransjön formation is marked by a vertical fault (GK fault) in Fig. 2A.

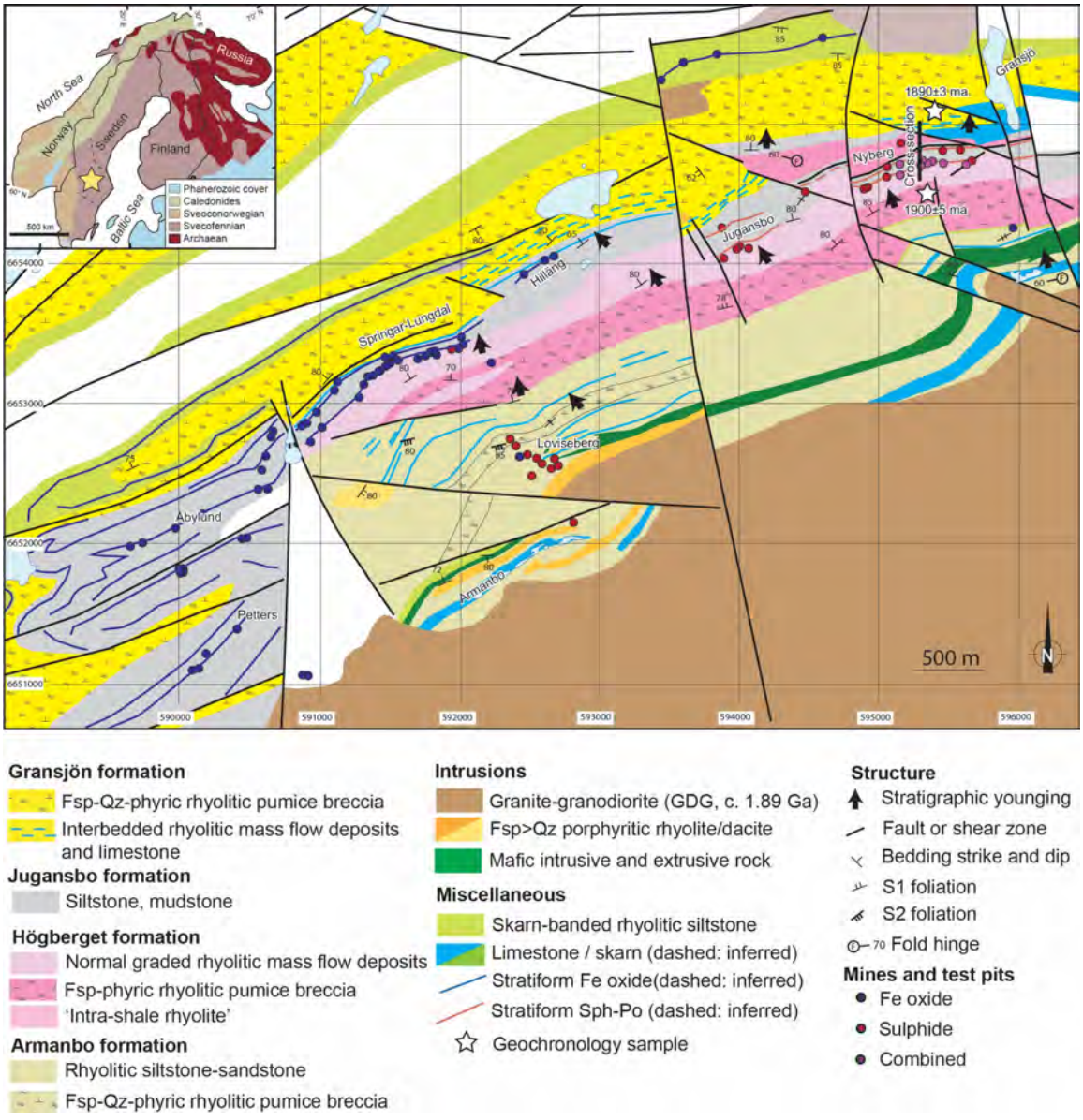


**Figure 1.** Geological map of the Jugansbo-Nyberg area, showing part of the extent of the Jugansbo formation and adjacent units. Grid is old Swedish national grid RT90. The cross-section in Figure 2 is indicated. Inset shows the location of Jugansbo in the Fennoscandian shield (Yellow star, the dashed lines show the northern and southern boundaries of Bergslagen).

## 2.2 Mineralisation

Sphalerite and pyrrhotite are the main sulphide minerals, with lesser galena and pyrite. The sulphides range from bedding-concordant laminae and dissemination to remobilized mineralisation in cross-cutting veins and breccias. The banded iron formation exhibits distinct stratification defined by interbedded magnetite, amphibole and chlorite (Fig. 2G). Hematite is entirely lacking but occurs in stratigraphically equivalent iron formation distal to Nyberg (e.g., Hilläng, Fig. 1). Iron formation at Nyberg is characterized by pronounced positive Eu anomalies ($Eu/Eu^*_{PAAS}$ = 1.13–4.43) and negative Ce anomalies (Fig. 2D), whereas iron formation distal (>1km) to known sulphide mineralisation lack Eu anomalies. The Nyberg iron formation exhibits elevated contents of Mn, Zn, Co, Cu, Pb, Tl, Cs, Sn, Cd and S.

With regards to immobile element ratios, ore zone skarns exhibit ratios of Zr, $TiO_2$ and $Al_2O_3$, intermediate between Högberget and Gransjön volcanic rocks, and end-member mudstone such as Post-Archaean Australian Shale (PAAS, McDonough and Sun, 1995)(Fig. 2E). This is interpreted to reflect that many of the ore zone rocks are hybrid volcaniclastic-siliciclastic rocks.

## 2.3 Geochronology

Two juvenile rhyolitic pumice breccias were selected for U–Pb zircon Secondary Ion Mass

Spectrometry (SIMS) analysis (Fig. 2C): one from the Högberget formation pumice breccia below the sulphide deposit, and one from the Gransjön formation pumice breccia that overlies the sulphide deposit. Eleven concordant analyses with a Concordia age of 1896±5 Ma and a weighted average $^{207}Pb/^{206}Pb$ age of 1900±5 Ma set the maximum age for deposition of the Högberget formation pumice breccia. Ten concordant analyses with a Concordia age of 1892±3 Ma and a weighted average $^{207}Pb/^{206}Pb$ age of 1890±3 Ma for zircon in the Gransjön formation pumice breccia bracket the age of the Jugansbo formation. The age and lithogeochemistry of the Gransjön formation rhyolite are identical to that of the Sala granite (1891±6 Ma, Ripa et al. 2022).

### 2.5 Sulphur isotope geochemistry

Analysis of hand-picked concentrates of pyrite, sphalerite and pyrrhotite yielded consistently negative $\delta^{34}S_{V\text{-}CDT}$ values (-10.60 to -0.25 per mil)(Fig. 2F). A mixture of sulphur derived from leaching of volcanic rocks at $\delta^{34}S_{V\text{-}CDT} \approx 0$ per mil, and isotopically lighter sulphur derived thermochemical or bacteriogenic reduction of seawater sulphate can explain the sulphur isotope pattern at Nyberg. The latter processes are consistent with the presence of graphitic mudstone in the Jugansbo formation at Nyberg, which suggest that the depositional environment at the time of sulphide deposition was at times anoxic.

## 3 Discussion

The stratigraphy of the Armanbo and Högberget formations is similar to the footwall of many other mineralized units in Bergslagen in the sense that a several 100 meter-thick unit of pumiceous pyroclastic debris overlie shallow marine limestone strata. Allen et al. (1996) invoked caldera subsidence to explain the space needed to accommodate rapid deposition of voluminous, relatively homogeneous pyroclastic material.

In detail, ore zone skarns and chlorite schist exhibit compositions intermediate between PAAS and Högberget volcanic rocks. This is consistent with formation of the Nyberg deposit during the waning stage of Högberget volcanism. The positive Eu anomalies in the Nyberg iron formation are indicative of a hydrothermal origin of the iron formations and an oxic depositional environment, whereas the sulphur isotope data and the presence of graphite are more consistent with anoxic environment. These variations can be explained by fluctuations in the redox state of the basin over time. A sharp decrease in the redox state of the basin can explain the distinct shift from early Fe-rich non-sulphide mineralisation (now magnetite) to stratiform and disseminated sphalerite-pyrrhotite mineralisation on both limbs of the syncline. Absence of sulphides and graphite in a stratigraphically equivalent hematite-bearing iron formation west of Nyberg (e.g. Springar-Lungdal, Fig. 1) suggest lateral facies variations in what was likely a stratified marine, intra-caldera basin with depth variations. We suggest that the part of the Jugansbo formation which hosts the Nyberg deposit likely formed in a fault-bounded, relatively deep part of this basin, pointing to that post-eruptive, basinal processes controlled mineralisation. Lateral facies variations may explain the different footwall stratigraphies on the northern and southern limb of the Nyberg syncline.

The caldera model is also applicable to the Gransjön formation, which similar to Högberget formation is a several 100 thick pumiceous unit overlying shallow marine limestone strata (Fig. 2). This suggests that the Jugansbo formation formed during a pause in volcanism, which was favourable for the deposition of a hybrid succession of siliciclastic, volcaniclastic, ferrugineous and calcareous sediment. Resurgent volcanism at 1890±3 Ma (Gransjön volcanism) marks the end of the syngenetic mineralizing event described above. The IBM may possibly mark the onset of this event, as indicated by similarity in immobile elements to Gransjön volcanic rocks (Fig. 2D). The Gransjön volcanic rocks are remarkably geochemically similar to the bordering granite in the south, pointing to an intimate relationship between volcanic resurgence and plutonism. Together with incremental burial due to caldera subsidence, the magmatic resurgence may have induced a transition to skarn-type, metasomatic mineralizing systems associated with emplacement of granites and porphyritic intrusions as elsewhere in the area (e.g. Jansson et al. 2021).

## Acknowledgements

This research has been carried out within the strategic innovation program Swedish Mining Innovation, a joint venture by Vinnova, Formas and the Swedish Energy Agency, with additional financial support from Boliden Mines and Björka Mineral. Martin Whitehouse and Kerstin Lindén (NordSIMS, NRM) are thanked for help during the SIMS analytical session. Jaroslaw Majka (UU) is thanked for assistance during EPMA session.

## References

Allen RL, Lundström I, Ripa M, Simeonov A, Christofferson H (1996): Facies analysis of a 1.9 Ga, continental margin, back-arc, felsic caldera province with diverse Zn-Pb-Ag-(Cu-Au) sulfide and Fe oxide deposits, Bergslagen region, Sweden. Economic Geology 91:979-1008.

Jansson NF, Allen RL, Skogsmo G, Turner T (2021): Origin of Palaeoproterozoic, sub-seafloor Zn-Pb-Ag skarn deposits, Sala area, Bergslagen, Sweden. Miner Deposita:1-26.

McDonough WF, Sun SS (1995): The composition of the Earth. Chemical geology 120, 223-253.

Ripa M, Kübler L, Persson L, Göransson M (2002): Beskrivning till berggrundskartan 11G Västerås NO. Geological Survey of Sweden Af:70.

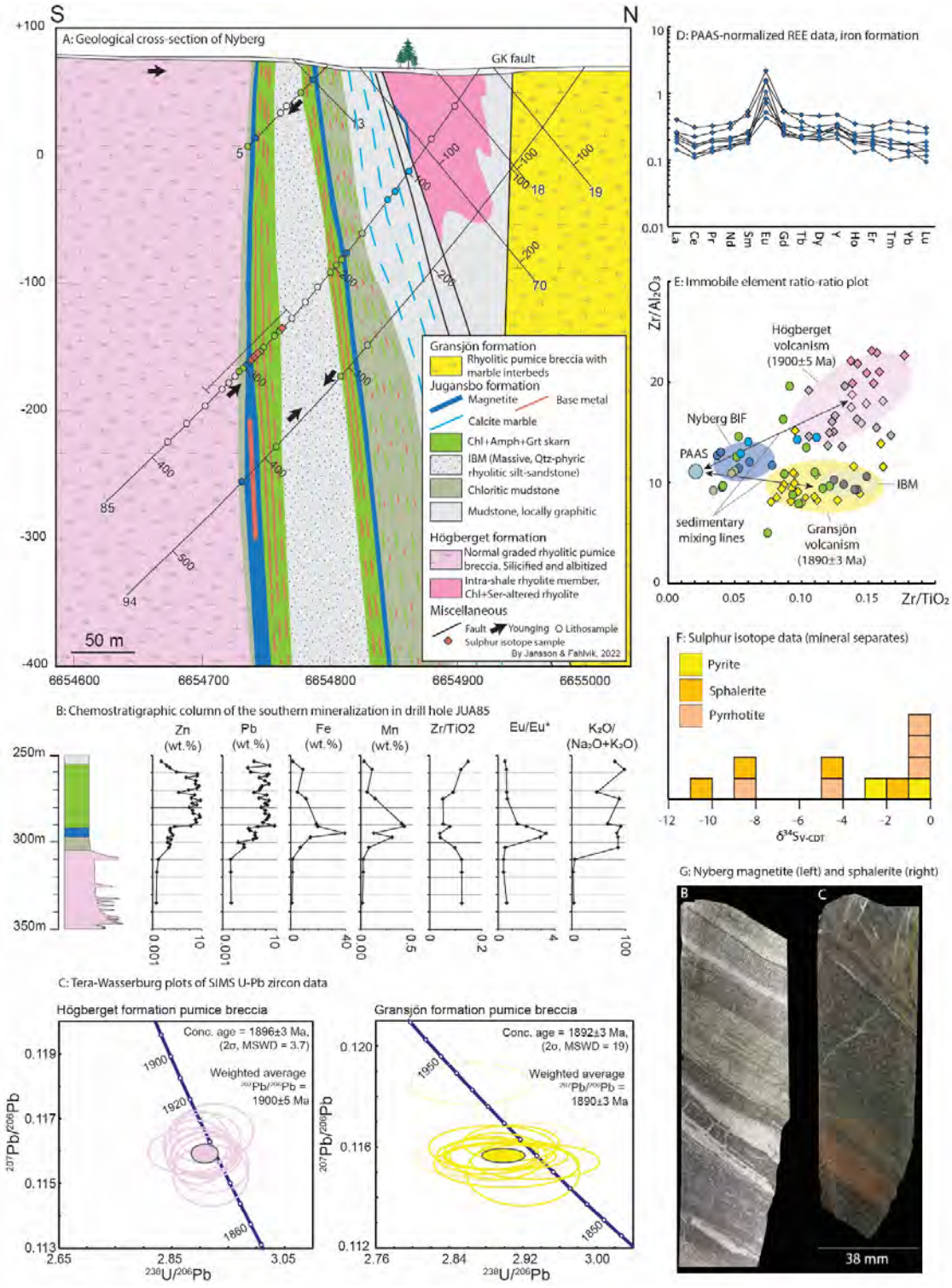


**Figure 2.** The Nyberg deposit, A: Geological cross-section, B: Whole-rock lithogeochemistry chemostratigraphy, C: Tera-Wasserburg plots of SIMS U-Pb zircon data and weighted average $^{207}Pb/^{206}Pb$ ages, D: Iron formation normalized to post-Archean Australian Shale (PAAS), using value of McDonough and Sun (1995), E: Immobile element ratio-ratio plot of key units, F: Sulphur isotope data (see Jansson et al. 2021 for method), G: Representative example of banded magnetite-tremolite-chlorite iron formation (left) and banded sphalerite mineralisation (right) from Nyberg. Dashed error ellipse in 2C indicate data omitted due to discordance or significant common Pb correction.

# Lead isotope systematics of VMS deposits from Oman

**Ana P Jesus' Thomas M Belgrano[2], André Cravinho[1], Bernhard Pracejus[3], Fatma Kourim[4], Kuo-Lang Wang[4], Mathieu Benoit[5], Mário A Gonçalves[1,6]**

[1] *Instituto Dom Luiz, University of Lisbon, Portugal*
[2] *National Oceanography Centre, University of Southampton, UK*
[3] *Sultan Qaboos University, Oman.*
[4] *Institute of Earth Sciences, Academia Sinica, Taiwan*
[5] *Geoscience-Environment Toulouse, France*
[6] *Faculty of Science, University of Lisbon, Portugal*

**Abstract.** The Samail ophiolite in Oman, represents one of the most well-preserved remnants of the Tethyan oceanic crust, and hosts numerous mafic-hosted volcanogenic massive sulfide (VMS) deposits. In this work we present Pb isotopic data from 13 VMS deposits in Oman, in different volcanostratigraphic positions, as well as pristine volcanic glasses from the ophiolite main volcanic units. Our data shows that the volcanic units and VMS deposits in Oman exhibit a wide range of Pb isotopic compositions. The volcanic glasses show an increasingly radiogenic Pb isotopic composition from the Geotimes lava unit (V1) into the uppermost Boninitic Alley unit (V2), supporting significant isotopic modification of the mantle source trough time. The VMS deposits isotopic composition generally reflects that of their host volcanic units, indicating that the footwall represents the major source of Pb for each deposit. Some deposits hosted in the uppermost Tholeiitic and Boninitic Alley units, however, show highly variable isotopic signatures, possibly due to leaching of Pb from different volcanic units at depth. These results demonstrate shallower metal sourcing than is typically considered for VMS deposits and highlights the importance of the footwall volcanic architecture in controlling the metal endowment of the VMS deposits.

## 1 Introduction

The Cretaceous (*ca.* 95 Ma) Samail ophiolite in Oman, is the largest exposed remanent of the Tethyan oceanic lithosphere and has been intensely researched to unravel processes of formation and alteration of the oceanic crust and mantle. The Samail lavas hosts 17 known VMS deposits, totalling 58 Mt of ore with a weighted average grade of 1.5 wt% Cu, of which 6 deposits totalling 22 Mt of ore remain unmined (Fig. 1). Exploration is ongoing throughout much of the ophiolite. Although most VMS deposits in Oman are classified as Au-poor, there is growing evidence that deposits hosted in the Boninitic Alley units are Au-enriched (Gilgen et al. 2014).

Recently, significant effort has been devoted to refine the mapping of the volcanic sequence (Belgrano et al. 2019) and accurately locate the deposits within the volcanostratigraphy (Gilgen et al. 2014). Pb isotope compositions of samples recently collected from drill core and ore body outcrop from 13 deposits for Pb isotopes are presented here. This work aims to assess Pb sources of Oman VMS deposits relative to their host lavas, shedding light to the evolution of the ophiolite mantle source through time and the architectural source of metals within the Samail VMS mineral system.

**Figure 1.** Schematic volcanostratigraphy of the Samail ophiolite showing the location of VMS deposits based on

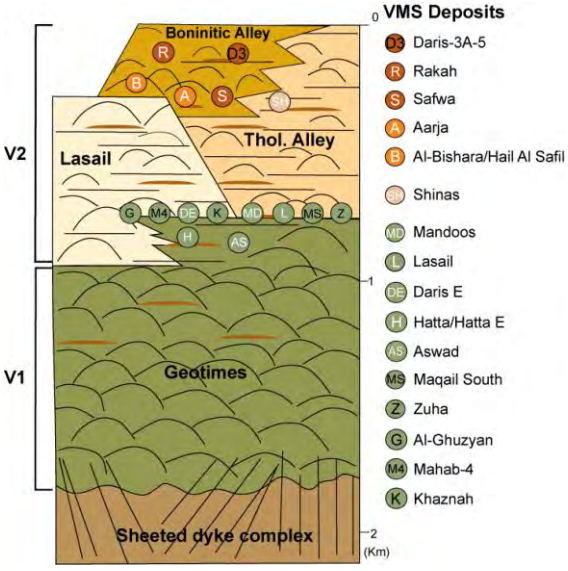


Belgrano et al. (2019), Gilgen et al. (2014) and Cravinho et al. (in press). Deposits are colour coded according to their footwall. Sampled deposits are labelled in white.

### 1.1 Samples and methods

Samples were collected from volcanic rocks and sulfide ore from throughout the Samail volcanostratigraphy (Figure 1). Samples include pristine glasses from each volcanic unit except for Geotimes, for which weakly hydrated but otherwise fresh, vitreous glass is the freshest material available. Massive ores are predominantly composed of pyrite (*Py*), chalcopyrite (*Ccp*), quartz, and minor sphalerite (*Sph*), with occasional magnetite, hematite, tennantite, and bornite.

Pb isotopes were analysed at the Institute of Earth Sciences, Academia Sinica (Taiwan) following the procedures reported in Wu and Huang (2021).

## 2 Results and discussion

Preliminary Pb isotope results are summarized in Figure 2. These results show a concomitant increase in radiogenic Pb in both the lavas and the VMS deposits they host upwards through the stratigraphy.

### 2.1 Sources of Pb in Oman VMS deposits

With few exceptions, the isotopic signatures of the VMS ores broadly reflect the signature of their assigned footwall unit. The isotopic ratios of the pristine V2 glass samples, particularly the Boninitic Alley Unit, provide the necessary components to account for the most radiogenic sulfide signatures of the VMS deposits hosted by these lavas. These constraints have two main implications. One, is that Pb in the VMS ores was predominantly leached from shallow footwall lavas, which for the upper deposits requires sourcing from within the 0.5–2km thickness of the host volcanic units (Belgrano et al. 2019). Secondly, the trend from the Geotimes (V1) towards the Boninitic Alley (V2) unit requires a highly radiogenic component that defines a mixing line through the tight isotopic array ores and lavas. Such component could be acquired through assimilation of sediments via incorporation in a subduction zone, with consequent modification of the Samail mantle source zone.

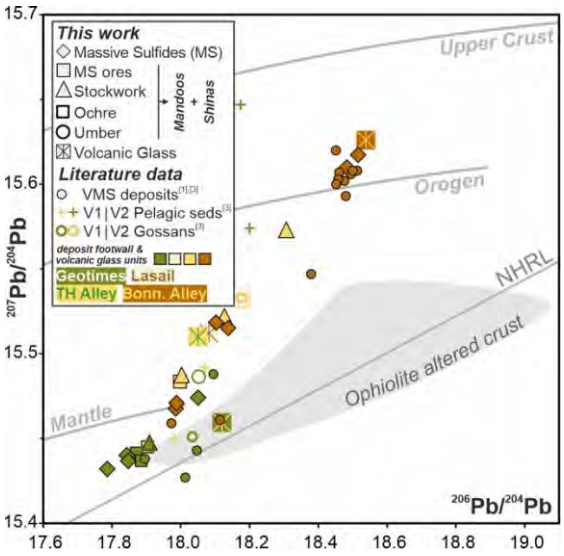


**Figure 2.** 207Pb/204Pb - 206Pb/204Pb isotopic systematics for the Samail rocks and VMS deposits. Plumbotectonic model curves for the evolution of the mantle, upper continental crust and orogen from Zartman and Doe (1981); North Hemisphere Regression Line (NHRL) from Hart (1984). Literature data (including "Ophiolite Crust"): [1] Chen and Pallister (1981); [2] Hamelin et al. (1984) and; [3] Calvez and Lescuyer (1991).

VMS deposits hosted in the V1 Geotimes lavas are less radiogenic than the Geotimes volcanic rocks. This feature may be tentatively related with the absence of pristine V1 rocks or volcanic glasses, whereas the sulfides, that do not incorporate significant radiogenic U, preserve their original Pb isotopic signatures. V1-hosted deposits may thus represent the best proxies for the original Pb isotopic composition of the Samail mantle source, prior to its modification during the V2 stage.

Deposits hosted in the Alley units show greater isotopic variation, which could be explained by hydrothermal fluids leaching a heterogenous footwall volcanic sequence. Similar reasoning can also explain the large-scale heterogeneities in the Boninitic Alley VMS deposits. Some of these present mixed compositions such as Safwa and Al-Bishara/Hail Al Safil, while others have solely compositions as unradiogenic as the Tholeiitic Alley (Daris 3) or Geotimes (Aarja) units (Figures 1 and 2). The proximity to V1 or Lasail lavas (Aarja), or the existence of deep faulting (Al-Bishara/Hail Al Safil) have been suggested as enabling leaching of lavas from more than one unit, resulting in a very large span of Pb compositions. The local crustal architecture underlying each deposit should thus be decisive to determine the pathways and metal endowment of VMS deposits in Oman.

## Acknowledgements

This project has received funding from the European Union's Horizon 2020 research and innovation programme under the Marie Sklodowska-Curie grant agreement No 894599 and Portuguese Fundação para a Ciência e a Tecnologia (FCT) I.P./MCTES through national funds (PIDDAC) - UIBD/50019/2020-IDL.

## References

Belgrano TM, Diamond LW, Vogt Y, Biedermann AR, Gilgen S, Al-Tobi K (2019) A revised map of volcanic units in the Oman ophiolite: insights into the architecture of an oceanic proto-arc volcanic sequence. Solid Earth 10:1181-1217.

Calvez JY, Lescuyer JL (1991) Lead Isotope Geochemistry of Various Sulphide Deposits from the Oman Mountains In: Peters T, Nicolas A, Coleman RG (eds) Ophiolite Genesis and Evolution of the Oceanic Lithosphere. Springer Netherlands, pp 385-397.

Chen JH, Pallister JS (1981) Lead isotopic studies of the Samail Ophiolite, Oman. Journal of Geophysical Research: Solid Earth 86:2699-2708. doi: 10.1029/JB086iB04p02699.

Cravinho A, Jesus A, Moreira B, Mateus A, Pracejus B, Figueiras J, Benoit M, Bauer W, Rocha F (in press) Contrasting Features and Volcanostratigraphy of the Mafic-Hosted Mandoos and Shinas Volcanogenic Massive Sulfide Deposits, Samail Ophiolite, Oman. Economic Geology.

Gilgen SA, Diamond LW, Mercolli I, Al-Tobi K, Maidment DW, Close R, Al-Towaya A (2014) Volcanostratigraphic Controls on the Occurrence of Massive Sulfide Deposits in the Semail Ophiolite, Oman. Economic Geology 109:1585-1610. doi: 10.2113/econgeo.109.6.1585.

Hamelin B, Dupré B, Allègre CJ (1984) The lead isotope systematics of ophiolite complexes. Earth and Planetary Science Letters 67:351-366. doi: http://dx.doi.org/10.1016/0012-821X(84)90174-2.

Hart SR (1984) A large-scale isotope anomaly in the Southern Hemisphere mantle. Nature 309:753-757. doi: 10.1038/309753a0.

Wu P-C, Huang K-F (2021) Tracing local sources and long-range transport of PM10 in central Taiwan by using chemical characteristics and Pb isotope ratios. Scientific Reports 11:7593.

Zartman RE, Doe BR (1981) Plumbotectonics—the model. Tectonophysics 75:135-162. doi: https://doi.org/10.1016/0040-1951(81)90213-4.

# Modelling of zinc mobilization by magmatic-hydrothermal circulation in the sub-seafloor

**Benoit Lamy-Chappuis[1], Thomas Driesner[1]**
*[1]Institut of Geochemistry and petrology, ETH Zürich, Switzerland*

**Abstract.** We present simulations of hydrothermal circulation triggered by the emplacement of magmatic intrusions in the sub-seafloor, we aim to understand and evaluate the processes controlling metal leaching from the host rock and transport to the seafloor. The simulations are conducted using a transport simulator allowing us to explicitly represent magmatic intrusions up to temperatures of 1000°C. We use water-NaCl as a proxy for the fluid chemical composition. To gain insights into metal mobilization, a basic zinc solubility model is added to the transport simulator, which considers the dissolution reactions of sphalerite. We present two sets of simulations, one with simplified setups and one with the real, albeit simplified topography of the seafloor resembling the TAG area of the mid-Atlantic oceanic ridge. The results show that the size and depth of the intrusion, as well as the depth of the seafloor, play a significant role in controlling the metal mobilization potential of hydrothermal fluxes. The simulations also highlighted the importance of understanding the complex interplay of structural and magmatic controls to better estimate the size and grades of seafloor resources.

## 1 Introduction

Magmatic intrusions emplaced in the sub-seafloor give rise to powerful and transient hydrothermal activity. The resulting hydrothermal fluxes can vary but the quantitative effect of possible controls such as ocean floor depth and topography, and the size and depth of intrusions have remained poorly constrained. Time-integrated fluxes may be decisive for the size of seafloor massive sulphide (SMS) deposits and more generally in determining the metal budgets of the oceans. As water is heated up in contact with the intrusion it can form a focused and hot (300-400°C) rising plume that can leach metals from the host rock. Metal solubilities strongly depend on temperature and salinity (among other parameters), which, in turn, depend on the characteristics of the hydrothermal fluxes and their complex evolution. Reactive transport modelling is a tool that can allow us to better apprehend these processes.

We conducted simulations of hydrothermal circulation driven by magmatic intrusions in generic setups and more realistic, “TAG-like” scenarios. To evaluate the metal mobilization potential of the hydrothermal fluxes we added a simplified zinc solubility model to the transport simulator. We aim to understand and evaluate the structural and magmatic controls on metal leaching of the host rock and transport to the seafloor. This might ultimately help understanding the systematics behind location, size, and grades of SMS deposits.

## 2 Concept and methods

We conduct simulations testing various scenarios of magma emplacement in the sub-seafloor to determine the controlling parameters of the metal mobilization processes. Our in-house transport simulator, developed on the CSMP++ platform allows us to explicitly represent the magmatic intrusions up to temperatures of 1000°C (Weis et al. 2014). We use water-NaCl as a proxy for the fluid properties and phase relations; this is particularly relevant for the systems under study since the fluid recharge will be of oceanic origin. Although this is probably still a crude approximation of the fluid compositions at depth, it is a fundamental improvement over simulations using pure water, in particular because we can capture salinity variations resulting from phase separation and the resulting metal fractionation as zinc will preferentially partition into the more saline liquid rather than into the low-salinity vapor phase.

We added a basic zinc solubility model to our transport simulator based on the equilibrium constants for sphalerite as $ZnCl^{+}, ZnCl_2^0, ZnCl_3^-$, and $ZnCl_4^{2-}$ as derived from the Supcrt92 database. We take advantage of the fact that the logarithms of equilibrium constants are linearly dependent on temperature when following water isochores. In practice, this allows us to use simple parametrization of the sphalerite solubility in function of temperature, density (a proxy for pressure), chloride activity, pH and sulphur activity. We make some major simplifications: chloride activity coefficients are not considered, and we do not simulate the evolution of pH and sulphur activity, instead we chose constant, plausible values that lead to solubilities in excess of the concentrations measured at active black smokers. In addition, we consider the case of 100% metal leaching efficiency.

Two sets of simulations are presented, the first one deals with simplified setups where an intrusion is emplaced at depth below a flat seafloor and where the host rock permeability does not exhibit heterogeneities. We use two intrusion sizes (4 and 16 km$^3$) and two different depths for the roof of the intrusion (3 and 5 km). The second set is derived from geophysical interpretation of the TAG area on the mid-Atlantic oceanic ridge (deMartin et al. 2007). Here we use the real, albeit simplified topography of the seafloor and include a large detachment fault that dips steeply in the crust and terminates at approximately 10 km depth near a hypothetical magmatic region. We also investigate another “TAG-like” scenario where a smaller intrusion is

emplaced at a shallower level (7 km) just below the current TAG vent field and below the detachment fault.

## 3 Simulations of zinc leaching triggered by the emplacement of a magmatic intrusion in the sub-seafloor

With these simulations using simple geometries, we aim to gain a first order understanding of the factors controlling metal fluxes to the seafloor. The models' dimensions are 10x10x10 km. The host rock permeability $k$ decreases with depth according to $\log(k) = \log(k_b) - \alpha \log(z+1)$ where $k_b$ is the baseline permeability and $z$ the depth in km. The factor $\alpha$ controls the rate of decrease of permeability with depth. The permeability can be further reduced to impermeable values ($10^{-22}$ $m^2$) once the rock reaches a temperature of 550°C. The rock porosity is constant at 5%, we assume a homogeneous initial distribution of zinc in the rock, with a mass fraction of 40 ppm. We use a heat flux bottom boundary condition of 100 $mW.m^{-2}$. The top boundary conditions are 6°C and a pressure that depends on the assumed seafloor depth (we calculate the expected hydrostatic pressure at the seafloor). Three seafloor depths are considered, 1, 2 and 3 km. At time t=0, the intrusion is instantaneously emplaced. The intrusions have a cubic shape and sizes of 4 or 16 $km^3$, the roof of the intrusions is either at 3 or 5 km depth.

Given the variations in ocean depth and intrusion size and depth, a total of 12 simulations were run. Figure 1 shows a time series of major parameters for one of the simulations. In this simulation, as in the others, we observe the formation of an intermediate density supercritical fluid directly above the intrusion, this fluid rises buoyantly towards the seafloor for as long as the intrusion is cooling. Phase separation into a low salinity vapor and high salinity brine can occur during the initial rise of the plume, particularly at lower pressures (shallower ocean) and for intrusions closer to the seafloor. The up flow remains focused directly above the intrusion for several thousands of years, its size is comparable to the size of the intrusion's roof. Figure 1 shows a constant stream of zinc-enriched fluid being established between the intrusion and the seafloor. As the hot fluids migrate towards the surface, they encounter a cold oceanic downflow, this results in a "funnel-like" zinc leaching pattern where the area of leaching gets narrower the further away from the intrusion. A direct consequence of mixing with cold oceanic water is that zinc is re-precipitated on the edge of this funnel, all the way from the intrusion to the seafloor, although this reduces the total amount of zinc reaching the seafloor it also has the effect of further focussing the zinc fluxes. This is possibly a necessary condition for obtaining high ore grades.

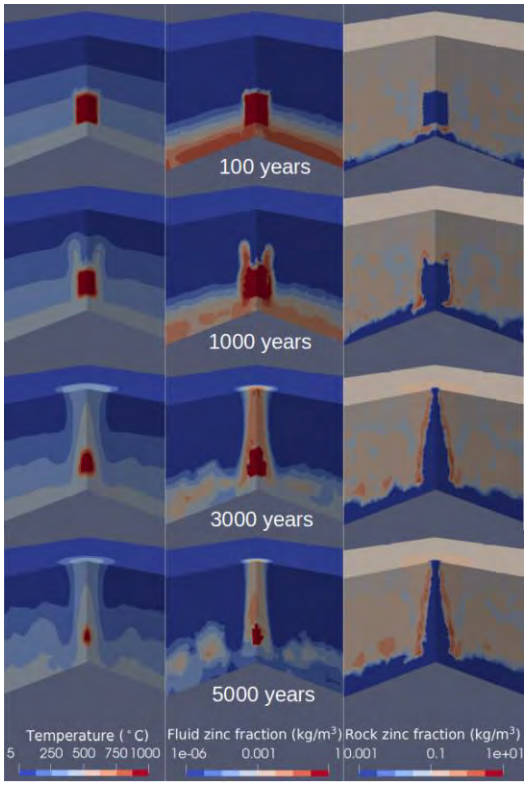


**Figure 1.** Time series of temperature, zinc mass fractions (in the rock and fluid) for the case of a 16 $km^3$ intrusion emplaced at 5 km and with a seafloor depth of 2 km.

In Figure 2 we show the total mass of zinc that exited the model on the seafloor boundary, this might be a good proxy for estimating the possible size of a deposit at the vent site. In most cases, the transport of zinc to the surface occurs over a short time frame with respect to the total magma cooling duration, it principally takes place during the initial flushing of hot fluids. This effect is most likely reinforced by our possibly unrealistic assumption of 100% leaching efficiency.

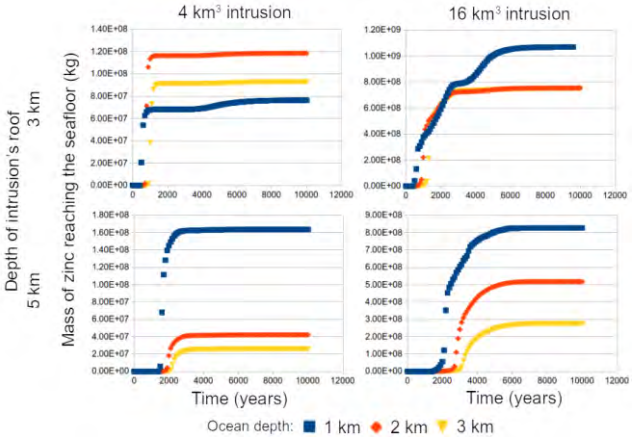


**Figure 2.** Time evolution of the total mass of zinc reaching the seafloor for 12 simulations with varying ocean depth and intrusion size and depth.

The total integrated zinc mass fluxes vary by two orders of magnitude, ranging from $2x10^7$ to $1.1x10^9$ kg. They approximately increase by one order of

magnitude for the larger intrusions (despite the fact that the volume is only multiplied by 4 and the cross-sectional area by 2). For intrusions emplaced at 5 km depth, there is a clear trend of more zinc reaching the seafloor for shallower oceans, our interpretation is that this results from the driving force for oceanic fluid downflow being decreased. This would result in an enlargement of the leaching funnel (this is mostly visible in Figure 3 for the 16 km3 intrusion case at 5 km depth). This simple interpretation is insufficient to explain the results of the shallower intrusions (3 km depth) where there are no obvious trends. Further data processing will be necessary to properly explain the results from these simulations. It is apparent that shallower intrusions will have stronger hot plumes which will possibly override the counteracting downwards oceanic flows in non-trivial ways (depending on the oceanic depth or other parameters). It is for instance interesting to observe that shallower intrusions do not result in significantly lower total zinc mass fluxes even though there would be less rock available to be leached. Another important effect of oceanic depth not yet fully analysed here is the possibly to drastically change the density of the fluids present in the subsurface (due to pressure change). For instance, much more phase separation (via condensation of a supercritical fluid) occurs for shallower intrusions and oceans, this would directly affect the zinc carrying capacity of the fluids.

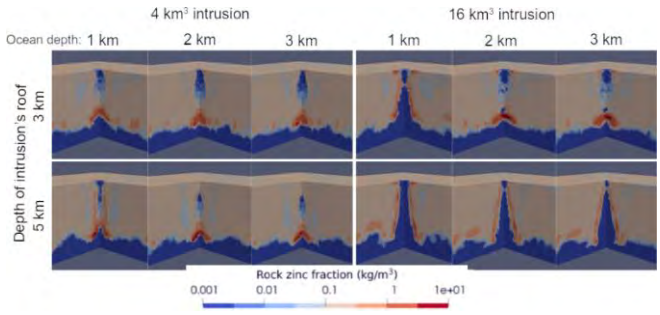


**Figure 3.** Rock zinc fractions in the centre of the models after 10000 years for all simulations.

## 4 Simulations of zinc leaching in "TAG-like" scenarios

We applied our model to a more realistic scenario. Following the interpretations of deMartin et al. (2007) and Canales et al. (2007), we designed a model aimed at resembling the TAG area on the mid-Atlantic oceanic ridge. We used bathymetric data to build a simplified geometry of the seafloor. The controls on hydrothermal fluxes towards the TAG vent field are still uncertain but one possible interpretation, put forward by deMartin et al. (2007) is that the fluids are channelled along a large detachment fault before being diverted in the hanging wall. A possible driver for the hydrothermal circulation is a large magma body at 10 km depth. It is particularly interesting to evaluate the importance of the structural and magmatic controls on the hydrothermal fluxes and consequently the metal fluxes. Is it possible to focus hydrothermal fluids with a setup such as the one shown in Figure 4? If yes, would they carry significant amounts of metals?

In our "TAG-like" setup, the permeability is behaving similarly to the previous simulations, the porosity and initial zinc rock fractions are also the same. The assumed damage area of the detachment fault is volumetrically meshed and has a permeability of 10-14 m2 and a thickness of 100m. We ran the simulations for 10000 years; the results are shown in Figure 5 and 6. We observe no strong up flow of zinc at the seafloor with this setup; however, we observe the slow development of a focused up-flow zone in the fault. This might develop further if the simulation were run for longer. Alternatively, a larger fault permeability might lead to faster and stronger up-flow and potentially zinc reaching the surface.

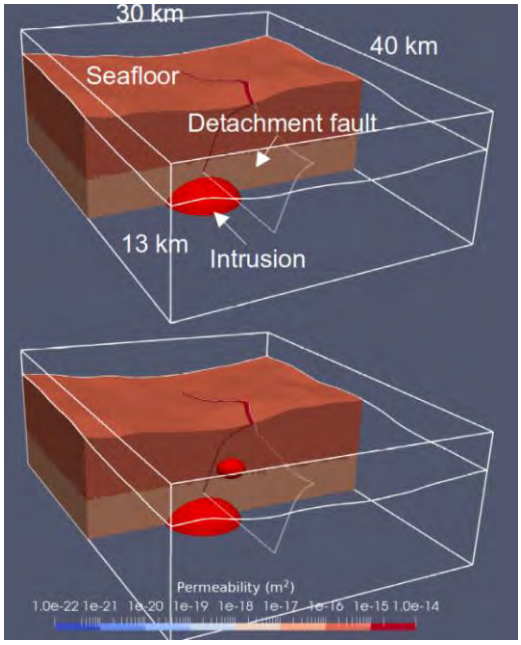


**Figure 4.** Geometry of the detachment fault, seafloor and initial intrusions for the two "TAG-like" setups.

In a second simulation, we added a hypothetical intrusion, smaller and at a shallower level, below the TAG area (see Figure 4). After 10000 years, there is now a clear zinc fingerprint at the seafloor, where the TAG main vent should be located (Figure 6). This is clearly a direct consequence of having an intrusion directly below and at a shallower level. Interestingly, the presence of the fault only had a very marginal impact on the fluid and metal fluxes which simply traversed the fault vertically.

## 5 Discussion and conclusions

Intrusions can lead to the transport of metals and energy towards a focused area on the seafloor. In our simulations, the total amount of ore depends on parameters such as ocean depth, intrusion size and

depth. It is now necessary to constrain the results of these simulations with real data to gain better insights into the subsurface processes acting in the real world.

Faults can also participate in focussing the fluids and enhancing mass fluxes due to their high permeability; however, a fault dominated hydrothermal system might not enable the significant enrichment of a seafloor deposit since one can expect that the amount of source rock would be greatly limited if fluids were to principally be transported through faults. More simulations are required to understand the effect of variations in the fault and host rock permeability.

In the case of TAG, we envision that the intermittent rise of magma batches from 10 km depth to shallower levels could explain the transient presence of anomalously high temperature flows having the capacity to carry zinc. In our scenario (second TAG-like setup), the presence of the large detachment fault has an impact on the hydrothermal fluxes but is not responsible of the zinc accumulation on the seafloor. It would be valuable to further study the relative strengths and the interplay of the structural and magmatic controls in more realistic scenarios.

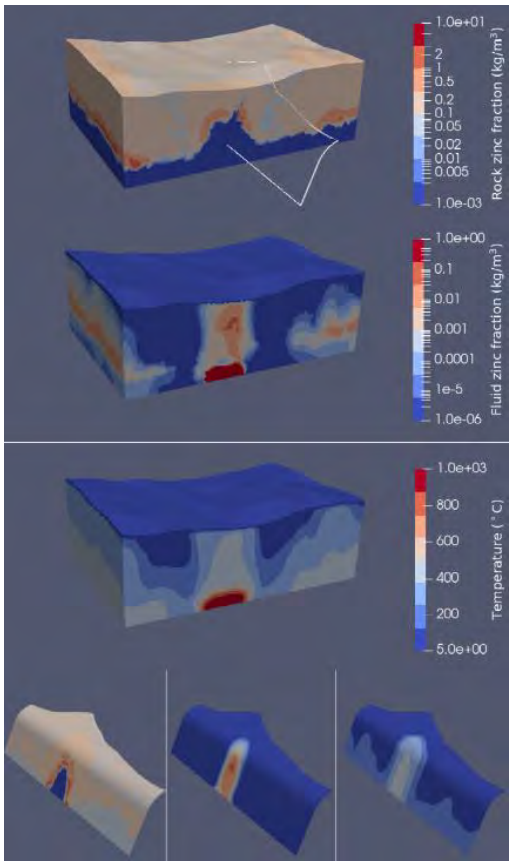


**Figure 5.** Result after 10000 years of the "TAG-like" simulation in the first setup, shown in a cross-section and on the detachment fault plane.

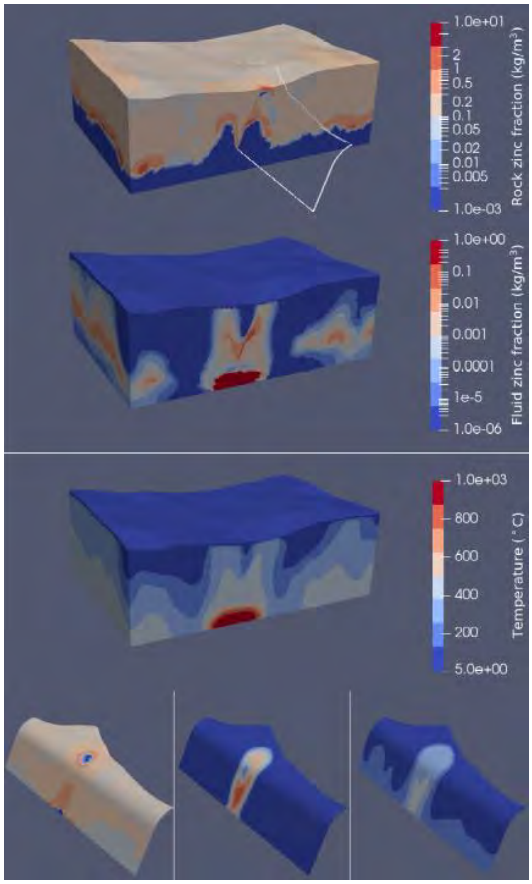


**Figure 6.** Result after 10000 years of the "TAG-like" simulation in the second setup (with a shallower intrusion added), shown in a cross-section and on the detachment fault plane.

## Acknowledgements

We would like to thank Equinor Energy AS for funding this research.

## References

Canales, J.P., Sohn, R.A., Demartin, B.J. (2007): Crustal structure of the Trans-Atlantic Geotraverse (TAG) segment (Mid-Atlantic Ridge, 26 degrees 10-Minutes-N): Implications for the nature of hydrothermal circulation and detachment faulting at slow spreading ridges. Geochemistry Geophysics Geosystems, 8: 18.

deMartin, B.J., Canales, R.A.R., Canales, J.P., Humphris, S.E. (2007): Kinematics and geometry of active detachment faulting beneath the Trans-Atlantic Geotraverse (TAG) hydrothermal field on the Mid-Atlantic Ridge. Geology, 35(8): 711-714.

Weis, P., Driesner, T., Coumou, D., Geiger, S. (2014): Hydrothermal, multiphase convection of H2O-NaCl fluids from ambient to magmatic temperatures: a new numerical scheme and benchmarks for code comparison. Geofluids, 14(3): 347-371.

# Fluid overprinting in an oceanic detachment fault: micro-analysis of pyrite from 13°30' N on the Mid-Atlantic Ridge

**Andrew J. Martin[1], John W. Jamieson[2], Sven Petersen[3], Mostafa Fayek[4]**
*[1]Geoscience, University of Nevada, Las Vegas, USA*
*[2] Department of Earth Sciences, Memorial University of Newfoundland, Canada*
*[3]GEOMAR – Helmholtz Centre for Ocean Research Kiel, Germany*
*[4]Department of Earth Sciences, University of Manitoba, Canada*

**Abstract.** Detachment faults are crustal-scale normal faults that can exhume mantle lithologies at the seafloor. Hydrothermal fluids in detachment fault hosted hydrothermal systems have been shown to be more oxidizing than those observed in a typical basalt-hosted system. Oxidizing fluids produce a hydrothermal mineral assemblage characterised by hematite, magnetite and pyrite. Microtextural and in-situ geochemical as well as isotopic ($\delta^{34}S$) analysis of pyrite from 13°30'N on the Mid-Atlantic Ridge illustrate the effect of fluctuating fluid redox on the distribution and enrichment of metals across individual mineral grains. Nickel and Co are remobilized from the grain margin toward the core during fluid overprinting, forming distinct enrichment fronts that overprint primary micron-scale oscillatory zonations that formed in response to temporal variations in the composition of primary hydrothermal fluids. Sulphur isotope ratios systematically increase (up to 9.2‰) toward the grain margin where secondary zonations are present. This increase indicates that larger amounts of sulphur are derived from thermochemical sulphate reduction of seawater, likely related to periods of fault movement and seawater ingress in the shallow subsurface. Thus, the presence of oxidizing fluids, which may be analogous to the waning stage of hydrothermal venting in many deposits, can remobilize and concentrate metals across individual sulphide grains.

# Formation age of Kosaka Uchinotai-West Kuroko Deposit, NE Japan, determined by Re-Os isotope analysis

**Mizuki Ogasawara[1], Junichiro Ohta[2,3], Mizuki Ishida[1], Moei Yano[3,1], Kazuhide Mimura[3,1], Kazutaka Yasukawa[2,1], and Yasuhiro Kato[1,3].**

*[1] Department of Systems Innovation, School of Engineering, The University of Tokyo*
*[2] Frontier Research Center for Energy and Resources, School of Engineering, The University of Tokyo*
*[3] Ocean Resources Research Center for Next Generation, Chiba Institute of Technology*

**Abstract.** The north-eastern (NE) Honshu arc of Japan is the type locality of the Kuroko-type volcanogenic massive sulphide (VMS) deposits. Major Kuroko deposits in Japan are distributed in the Hokuroku District in the NE Honshu arc, approximately 40 km × 40 km in size. This study applied rhenium (Re)-osmium (Os) radiometric dating to determine the formation age of the Kosaka Uchinotai-West deposit. The Re-Os isochron age of 13.314 ± 0.070 Ma with initial $^{187}Os/^{188}Os$ ratio of 0.7568 was obtained. The initial $^{187}Os/^{188}Os$ ratio is consistent with the Miocene seawater $^{187}Os/^{188}Os$ ratio. The isochron age implies that the Kosaka Uchinotai-West deposit was formed at the end of Nishikurosawa stage. During this period, the deep-sea environment in the Sea of Japan is considered to have been depleted in oxygen, which could have contributed to the preservation of the Kuroko deposits formed on the seafloor.

## 1 Introduction

The volcanogenic massive sulphide (VMS) deposits are defined as strata-bound massive sulphide-sulphate deposits associated with submarine volcanic activities. Because of its economic significance for producing copper and other critical metals, VMS deposits are under exploration in several countries (e.g., Tornos et al. 2015).

The north-eastern (NE) Honshu arc of Japan is the type locality of the Kuroko-type VMS deposits. Kuroko deposits in Japan are found in the Green Tuff region. Although Green Tuff is widely distributed in Japan, major Kuroko deposits are distributed in the Hokuroku District, approximately 40 km × 40 km in size (Figure 1).

Previous studies have suggested that the formation of the Kuroko deposits in Japan is associated with back-arc bimodal volcanism which formed the Sea of Japan in the early to middle Miocene (e.g., Jolivet et al. 1994; Yamada and Yoshida 2011). Direct and precise dating of the Kuroko ores will provide important constraints to understand the ore genesis in detail by correlating with the geologic events relating to the back-arc extension.

The Re-Os geochronology is an effective tool to directly determine the formation ages of sulphide deposits (e.g., Nozaki et al. 2013). Terakado (2001) analysed one to three samples from each of the four Kuroko-type deposits in the Hokuroku District (Fukazawa, Kosaka, Shakanai, and Hanaoka deposits) and reported a single isochron age of 14.32 ± 0.51 Ma with the initial $^{187}Os/^{188}Os$ ratio of 0.7563 ± 0.0047 by combining all the data for these deposits. However, individual age for each deposit has not been determined. Further analyses focusing on each deposit are necessary for discussing the Kuroko ore genesis more in detail. Here, as a first step, we implemented Re-Os isotope analysis of ore samples from the Kosaka Uchinotai-West deposit and determined its formation age.

## 2 Geological Background

Kuroko deposits in the Hokuroku District, including the Kosaka deposit, are hosted in middle Miocene Nishikurosawa Unit, which is composed of acidic tuff and rhyolite lava. Nishikurosawa Unit is conformably overlain by middle Miocene Onnagawa Unit, which consists of acidic pumice tuff and basaltic to rhyolitic lava. The inferred age of the boundary between the Nishikurosawa and Onnagawa Units is 16.7–12.4 Ma based on zircon U-Pb dating and biostratigraphy (Yoshioka et al. 2021).

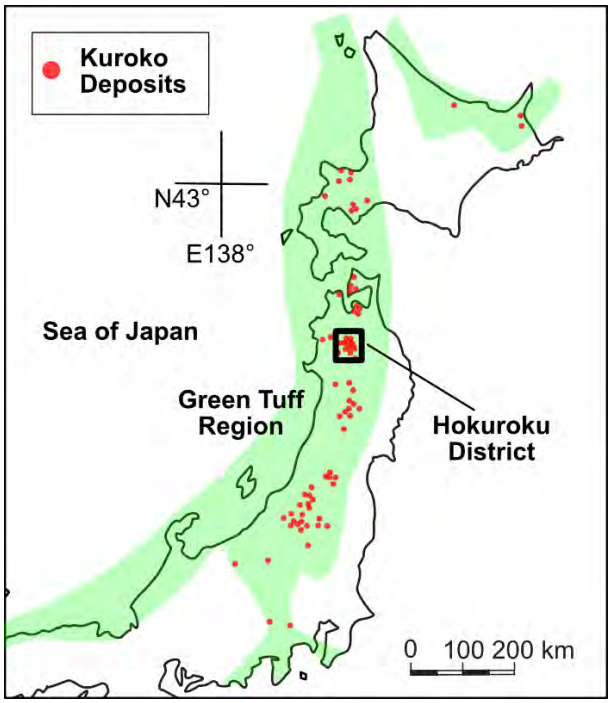

**Figure 1.** Distribution of Kuroko deposits in Japan and location of the Hokuroku District (modified after Shikazono 2003).

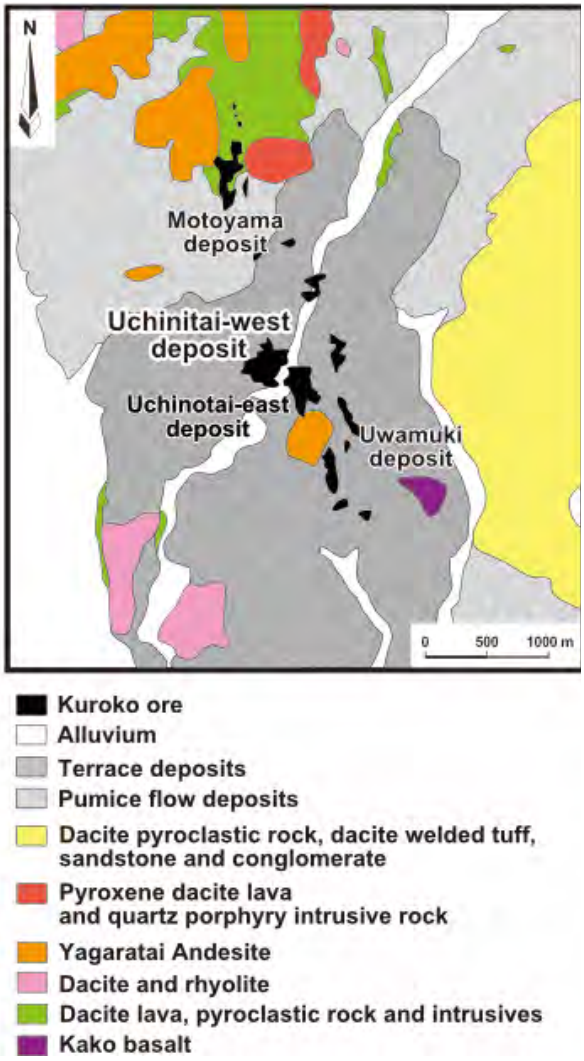


**Figure 2.** Geological map of Kosaka deposit (modified after Nakajima 1988).

The Kosaka deposit is a Kuroko-type Cu-Pb-Zn-Au-Ag deposit located at the eastern margin of the Hokuroku District. Its reserves are estimated to be about 9.2 million tons of ore (Cu 2.5 %, Pb 1.3 %, Zn 4.2%). The Kosaka deposit, covering about 2 km × 4 km in size, consists mainly of Motoyama, Uchinotai, and Uwamuki ore deposits (Figure 2). The Uchinotai deposit, discovered in 1959, is composed of two large orebodies called Uchinotai-West and Uchinotai-East and one small orebody called Otarube. The Uchinotai-West and Uchinotai-East deposits have a total reserve of about four million tons of sulphide ore (Urabe and Sato 1978).

## 3 Samples

The ores from the Kuroko deposits are classified into two types based on their mineral assemblages. Kuroko ores (black ores) consist mainly of sphalerite, galena, barite and contain minor quantities of chalcopyrite, pyrite and tetrahedrite. Oko ores (yellow ores) consist mainly of chalcopyrite and pyrite. Five black ores and three yellow ores from

**Figure 3.** Kuroko and Oko ore samples from Kosaka Uchinotai-West Deposit analysed in this study.

Kosaka Uchinotai-West deposit (Figure 3) were selected and split into 10 black ore and five yellow ore subsamples in total. This study analysed these 15 subsamples from the Kosaka Uchinotai-West deposit.

## 4 Methods

After crushing the samples, the sulphide grains were hand-picked and powdered using an agate mortar and pestle.

The Re-Os isotope analyses were performed using a multiple collector-inductively coupled plasma-mass spectrometer (MC-ICP-MS) at Ocean Resources Research Center for Next Generation (ORCeNG), Chiba Institute of Technology, Japan, following the analytical procedures by Ohta et al. (2022). Approximately 0.4 g of sulphide sample was weighed, spiked with $^{185}Re$ and $^{190}Os$, and digested with 4 mL of inverse aqua regia and 1 mL of $HClO_4$ in a sealed Carius tube heated at 220° C for 24 h. The analytical procedures applied in this study is

shown in Figure 4. Two samples, one black ore sample and one yellow sample, were analysed as duplicate to check analytical reproducibility.

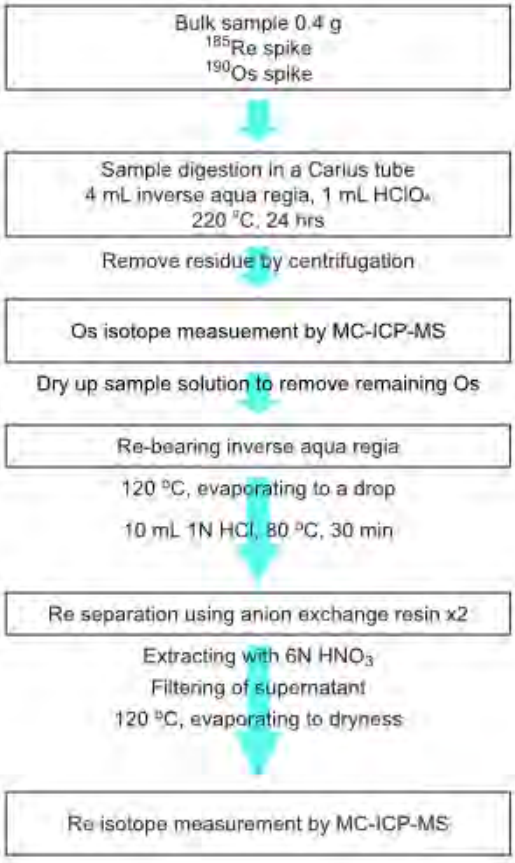


**Figure 4.** Analytical procedure for Re-Os isotope analysis in this study.

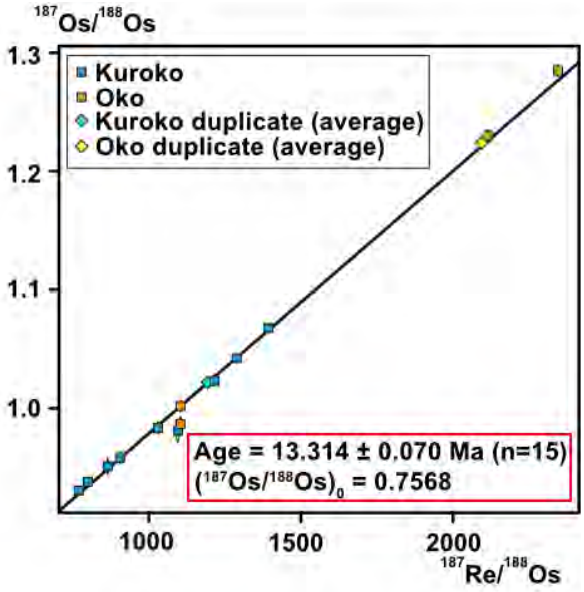


**Figure 5.** Re-Os isochron for Kosaka Uchinotai-West deposit obtained in this study. Online version for IsoplotR (Vermeesch 2018) was used.

## 5 Results

The black ore samples showed Re and Os concentrations of 10–56 ppb and 54–299 ppt, respectively. The yellow ore samples showed Re and Os concentrations of 16–50 ppb and 80–123 ppt, respectively. The duplicated analysis resulted in almost identical values, and thus we consider that the influence of analytical error on the isochron age is negligible.

$^{187}Re/^{188}Os$ and $^{187}Os/^{188}Os$ ratios of the 15 data points ranged 769.2–2345 and 0.9305–1.2849, respectively. The 15 data points yielded an isochron age of 13.314 ± 0.070 Ma with initial $^{187}Os/^{188}Os$ ratio of 0.7568 (Figure 5).

## 6 Discussion

Considering the inferred age of the boundary of Nishikurosawa/Onnagawa Units (see Geological background), the Re-Os age obtained by this study shows that the Kosaka Uchinotai-West deposit is likely to have been formed at the end of Nishikurosawa stage.

The initial $^{187}Os/^{188}Os$ ratio obtained by this study is 0.7568, which falls in the range of $^{187}Os/^{188}Os$ isotope ratio of the middle Miocene seawater, approximately 0.73–0.83 (e.g., Goto et al. 2023). It is generally accepted that VMS deposits like Kuroko deposits are produced on seafloor, with mixing of hot hydrothermal fluids and cold seawater causing precipitation of sulfides (e.g., Ohmoto 1996; Franklin et al. 2005). Therefore, the obtained initial $^{187}Os/^{188}Os$ ratio may indicate that the ores of Kosaka Uchinotai-West deposit preserve $^{187}Os/^{188}Os$ ratio of middle Miocene seawater, with relatively small influence of hydrothermal fluid, under a condition similar to the present-day submarine hydrothermal systems (Urabe and Sato 1978).

At the Nishikurosawa/Onnagawa boundary, the deep-sea environment in the Sea of Japan changed from oxic to reducing condition (e.g., Kimura et al. 2004). Since exposure to oxygenated seawater before burial into sediments would oxidize and dissolve sulphide ores, low-oxygen conditions in the water column would have played an important role in the preservation of sulphide ores of the VMS deposits (e.g., Otake et al. 2021). Therefore, the deoxygenation of seawater at the Nishikurosawa/Onnagawa boundary could have contributed to the effective preservation of the Kosaka Uchinotai-West deposit.

## 7 Conclusion

In this study, Re-Os geochemistry of the samples from Kosaka Uchinotai-West deposit were analysed using a MC-ICP-MS. The Re-Os isochron age of 13.314 ± 0.070 Ma with initial $^{187}Os/^{188}Os$ ratio of 0.7568 was obtained. The initial $^{187}Os/^{188}Os$ ratio is consistent with $^{187}Os/^{188}Os$ of the middle Miocene seawater. This may support that they originated from

seafloor hydrothermal activity in the middle Miocene. Further studies on the formation ages of each deposit would contribute to elucidating the relations between Kuroko ore formation in the Hokuroku District and the opening of the Sea of Japan more in detail.

## Acknowledgements

This research was financially supported by Japan Society for the Promotion of Science (JSPS) KAKENHI Grants No. JP20H05658 to Y.K. and No. JP20J22038 to M.I. The authors thank Mr. Kaoru Kiyota of the University Museum, the University of Tokyo, for providing us with the samples of Kosaka deposit. We also thank Ms. Kana Ashida of ORCeNG, Chiba Institute of Technology, for supporting us with the laboratory equipment.

## References

Franklin JM, Gibson HL, Jonasson IR, and Galley AG (2005) Volcanogenic Massive Sulfide Deposits. In JW Hedenquist, JFH Thompson, RJ Goldfarb and JP Richards (Eds.), One Hundredth Anniversary Volume (pp. 0). Society of Economic Geologists. 10.5382/AV100.17

Goto KT, Tejada MLG, Tajika E., and Suzuki K (2023) Enhanced magmatism played a dominant role in triggering the Miocene Climatic Optimum. Communications Earth and Environment 4(1):21-8. doi: 10.1038/s43247-023-00684-x

Jolivet L, Tamaki K, and Fournier M (1994) Japan Sea, opening history and mechanism: A synthesis. Journal of Geophysical Research - Solid Earth 99(B11):22237-22259. doi: 10.1029/93JB03463

Kimura S, Shikazono N, Kashiwagi H, and Nohara M (2004) Middle Miocene–early Pliocene paleo-oceanic environment of Japan Sea deduced from geochemical features of sedimentary rocks. Sedimentary Geology 164(1):105-129. doi: 10.1016/j.sedgeo.2003.08.003

Nakajima T (1988) Geological map for mineral resources assessment of the Hokuroku district. Geological Survey of Japan.

Nozaki T, Kato Y, and Suzuki K (2013) Late Jurassic ocean anoxic event: evidence from voluminous sulphide deposition and preservation in the Panthalassa. Scientific Reports 3(1):1889. doi: 10.1038/srep01889

Ohmoto H (1996) Formation of volcanogenic massive sulfide deposits: The Kuroko perspective. Ore Geology Reviews 10(3):135-177. doi: 10.1016/0169-1368(95)00021-6

Ohta J, Nozaki T, Sato H, Ashida K, and Kato Y (2022) A precise and accurate analytical method for determination of osmium isotope ratios at the 1-15 pg level by using a MC-ICP-MS equipped with sparging introduction and high-sensitivity discrete dynode-type ion-counting detectors. Journal of Analytical Atomic Spectrometry 37(8):16-161. doi: 10.1039/d2ja00089j

Otake T, Yamada R, Suzuki R, Nakamura S, Ito A, Shin K, and Sato T (2021) Large Fe isotope fractionations in sulfide ores and ferruginous sedimentary rocks from the Kuroko volcanogenic massive sulfide deposits in the Hokuroku district, northeast Japan. Geochimica et Cosmochimica Acta 295:49-64. doi: 10.1016/j.gca.2020.12.009

Shikazono N (2003) Geochemical and tectonic evolution of arc-backarc hydrothermal systems: implications for the origin of Kuroko and epithermal vein-type mineralizations and the global geochemical cycle. Elsevier Science.

Terakado Y (2001) Re-Os dating of the Kuroko ore deposits from the Hokuroku district, Akita Prefecture, Northeast Japan. Chishitsugaku Zasshi 107(5):354-357. doi: 10.5575/geosoc.107.354

Tornos F, Peter JM, Allen R, and Conde C (2015) Controls on the siting and style of volcanogenic massive sulphide deposits. Ore Geology Reviews 68:142-163. doi: 10.1016/j.oregeorev.2015.01.003

Urabe T, and Sato T (1978) Kuroko deposits of the Kosaka Mine, Northeast Honshu, Japan; products of submarine hot springs on Miocene sea floor. Economic Geology and the Bulletin of the Society of Economic Geologists 73(2):161-179. doi: 10.2113/gsecongeo.73.2.161

Vermeesch P (2018) IsoplotR: A free and open toolbox for geochronology. Geoscience Frontier 9(5):1479-1493. doi: 10.1016/j.gsf.2018.04.001

Yamada R, and Yoshida T (2011) Relationships between Kuroko volcanogenic massive sulphide (VMS) deposits, felsic volcanism, and island arc development in the northeast Honshu arc, Japan. Mineralium Deposita 46(5-6):431-448. doi: 10.1007/s00126-011-0362-7

Yoshioka J, Kuroda J, Takahata N, Sano Y, Matsuzaki KM, Hara H, Auer G, Chiyonobu S, and Tada R (2021) Zircon U-Pb dating of a tuff layer from the Miocene Onnagawa Formation in Northern Japan. Geochemical Journal 55(3): 185-191. doi: 10.2343/geochemj.2.0622

# Geological settings, distribution, and resource potential of seafloor hydrothermal systems

**Sven Petersen[1], Mark D. Hannington[2], John Jamieson[3], Thomas Monecke[4], Meike Klischies[1],**
*[1] GEOMAR – Helmholtz Centre for Ocean Research Kiel, 24148 Kiel, Germany*
*[2] Department of Earth and Environmental Sciences, University of Ottawa, Canada*
*[3] Department of Earth Sciences, Memorial University of Newfoundland, Canada*
*[4] Department of Geology and Geological Engineering, Colorado School of Mines, Colorado, USA*

**Abstract.** Over the past decades, the main target areas for exploration for seafloor massive sulfides (SMS) have shifted from fast spreading ridges, to back-arc basins and recently to ultra-slow and slow-spreading ridges. These changes are often linked to changes in our understanding of the importance of certain processes in the formation of large sulfide deposits on the modern ocean floor. Similarly, the growing body of information on the deposits themselves, the increasing resolution of geophysical, topographic, geological, and geochemical datasets is influencing our view on SMS formation and resource potential. This more detailed information allows us to investigate the importance of the local geological setting in deposit formation, helping us to understand the processes responsible for the formation of large and economically interesting deposits.

## 1 Introduction

Seafloor massive sulfides occurrences (SMS) have become a target of increased global exploration activity due to their presumed resource potential. Recent investigations have shown that these occurrences are more variable than previously thought (incl. native sulphur springs as well as talc-rich deposits) and that this variability is not necessarily reflected in volcanogenic massive sulfide deposits preserved in the ancient rock record.

The regional geological setting has profound impacts on water depth, source rocks, permeability, vent fluid chemistry and hence on the geochemical composition and mineralogy of the sulfides deposited at or below the seafloor. Spreading rate tends to be one of the major factors affecting the accumulation, distribution, and ultimately the resource potential of seafloor massive sulfides at spreading centers. Currently, 435 sulfide-bearing or high-temperature hydrothermal sites have been reported throughout the global ocean, indicating the widespread occurrence of this type of seafloor mineralization (Figure 1). Most of these occurrences are, however, hydrothermally active and tend to be in an early stage of development. Following the classification of Jamieson and Gartman (2020) nearly 75 % of the known sites are either actively venting high-temperature fluids (Figure 2) or they have been described as being hydrothermally active, either with low-T venting or the exit temperatures were not measured. Additionally, active vent sites commonly host chemosynthetic faunal communities that will receive strong protection by the regulation of

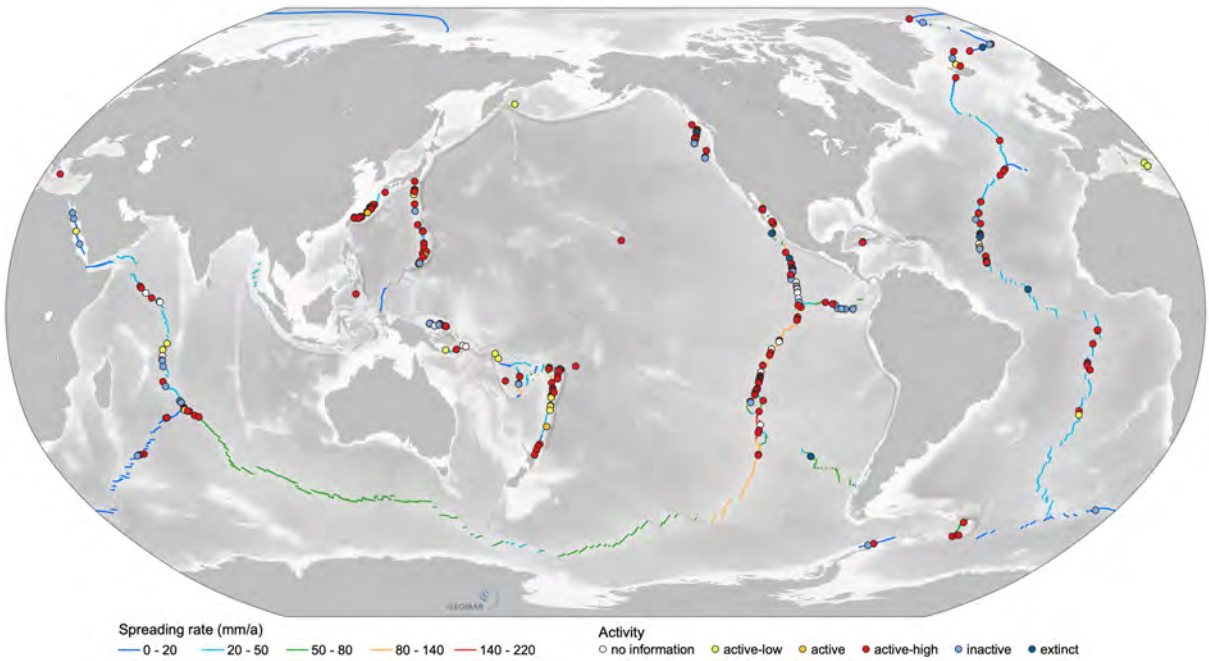


**Figure 2.** Global distribution of seafloor hydrothermal systems with respect to reported activity and spreading rate (N=435). Note that the scarcity of sites in the southern oceans is related to a lack of exploration.

mining activities in areas beyond national jurisdiction. Around 22 % of the known sites are described as being inactive. They are commonly located close to active vent sites or in an environment where a renewal of hydrothermal activity is possible or even likely. A few sites are considered to be extinct because they are located far off-axis with no evidence of any recent magmatic or hydrothermal activity in their surroundings. Inactive and extinct sites, that have gone through a full life-cycle of metal deposition, where hydrothermal activity has ceased, and where vent-specific macrofaunal communities have disappeared, are seen as a possible mining target. These systems lack the prominent water column signature and are more difficult to locate. Many extinct sites are considered to be located at even greater distance to the neovolcanic zone increasing the area that needs to be explored to several million km$^2$ (Petersen et al., 2018)

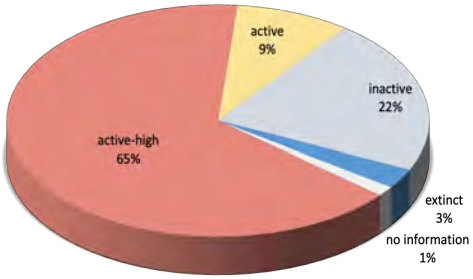


**Figure 2.** Style of activity of known SMS occurrences (N=435).

## 2 Global settings of SMS occurrences

Most of the known SMS occurrences are associated with basaltic host rocks formed at mid ocean ridges (54%; Figure 3). Additional 7 % of the currently known sites are associated with exposed mantle and/or lower crustal rocks (UM), usually at slow-spreading mid-ocean ridges. Intraoceanic back-arc basins are another important setting (15 %), followed by subduction-related arc volcanoes (12 %). Recent exploration in the Okinawa Trough, the only known intracontinental hosting seafloor massive sulfides, resulted in a large number of discoveries in this extensional setting.

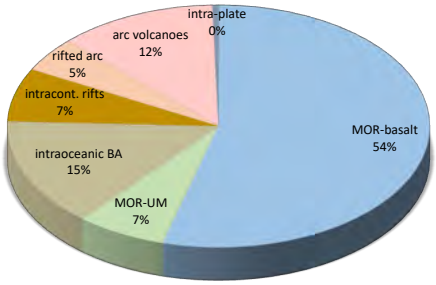


**Figure 3.** Regional geological setting of known SMS occurrences (BA = back-arc; MOR = mid-ocean ridge; UM = ultramafic).

Occurrences associated with rifted arc crust account for 5 % of the known sites. Currently, only two sulfide-bearing sites are associated with intraplate volcanism.

## 3 The importance of slow-spreading ridges

Over the past years considerable effort has focused in exploring ultra-slow- and slow-spreading mid-ocean ridges, but also slow-spreading segments within back-arc basins such as the Mariana Trough or the Lau Basin. New discoveries of large sulfide occurrence have been made, especially in the Indian Ocean (Pak et al., 2017; Wang et al., 2017; Kim et al., 2020; Tao et al., 2020; Yang et al., 2023; Schwarz-Schampera, in prep), often as a result of ongoing exploration activities of contractors to the International Seabed Authority.

These discoveries extend the variability of regional and local geological settings of SMS formation even further, providing evidence for substantial mineralization also in non-transform offsets or associated with large off-axis volcanic plateaus. Another area of intense exploration is located in the Okinawa Trough, a region with extensional volcanism and a plate separation velocity similar to those of slow-spreading ridges. Here, numerous hydrothermal sites have been discovered, with some of them of possible economic potential (Kawano and Furuya, 2022).

One of the main reasons for the intense exploration in slow-spreading environments is the favorable metal content (Cu, Au) and size of many of the documented occurrences at slow-spreading ridges (Hannington et al., 2011; German et al., 2016).

Slow-spreading ridges are, overall, tectonically very active, including the formation of deep-reaching faults in the neovolcanic zone and at some distance to it. Along some shallow-dipping faults (detachment faults) tectonic forces expose rocks of lower crustal or mantle origin in tectonic massifs and at oceanic core complexes and allow the interaction of hydrothermal fluids with these source rocks.

The presence of such large-scale faulting has been suggested to be responsible for long-lived and even periodic hydrothermal activity at some sites, possibly explaining why most of the large known SMS occurrences are located at slow-spreading ridges (Hannington et al., 2011). This includes a number of vent fields, such as the TAG and Semyenov vent fields on the Mid-Atlantic Ridge, that contain a number of individual large vent sites or mounds, each of which could be considered a possible mining target (Cherkashov et al., 2013; Graber et al., 2020).

At both these sites, some of the massive sulfide mounds occur in the hanging wall of the detachment faults and are associated with intense extensional faulting. This specific geological setting may account for the large size of these deposits. Overall, the concentration of the sulfide tonnage into smaller

areas seems to be more common at slow-spreading ridges when compared to their faster equivalents.

Available ship-based bathymetry and advances in geological interpretation indicate that a simple tectonic vs. magmatic classification (German et al., 2016) does not capture all of the important settings of SMS formation. Instead, several distinct settings for SMS formation can be classified in mid-ocean ridge environments (Klischies et al., this volume). Similar distinct classes of different deposit types can also be considered for the subduction related settings. Based on published geochemical analyses of SMS occurrences globally, an enrichment of copper, gold and other trace metals is apparent in many of the sites associated with slower spreading rates, especially those associated with the exposure of lower crustal and mantle rocks. At the same time, slow- and ultra-slow spreading ridges are a major portion of the global ridge system (36% and 24% of the global ridge length; Fig. 1) that is still under-explored, thereby representing a large permissive area.

## 4 Resource potential

The resource potential of seafloor massive sulfides is a consequence of their bulk chemical composition and their size. Geochemical data is available for over 180 sites, however, published datasets are commonly missing data for some trace elements. Still, the data shows a high variability on a regional scale reflecting plate tectonic settings and associated source rock controls. Seafloor massive sulfide deposits associated with rifted arc crust or with ultramafic host rocks at mid-ocean ridges often contain higher concentrations of copper compared to basalt-hosted deposits at mid-ocean ridges, (Fig. 4).

Gold and silver are also enriched in some settings, especially in intraoceanic back-arc basins, volcanic arcs, and at ultramafic-hosted mid-ocean ridge systems, where concentrations of these precious metals can reach several tens of ppm for gold and hundreds of ppm for silver (Fig. 4). Certain trace elements, some of which of growing importance for modern society occur in concentrations of only a few tens of ppm, but can be significantly enriched in some deposits.

Some of the uncertainty in global resource estimates for SMS lies in the enormous range in the perceived sizes (tonnage) of many modern seafloor massive sulfides. These deposits are three-dimensional but information from the subseafloor are sparse. Visual inspection of their surface morphology and from sampling indicates that some may reach a thickness of several tens of meters. However, most known sites have a diameter of less than a few tens of meters and, thus, contain only a small amount of sulfide material (a few thousand tons to 100,000 tons).

Some occurrences on the global mid-ocean ridges, however, are estimated to contain between 100,000 tons and 1 million tons of massive sulfide (Hannington et al., 2011).

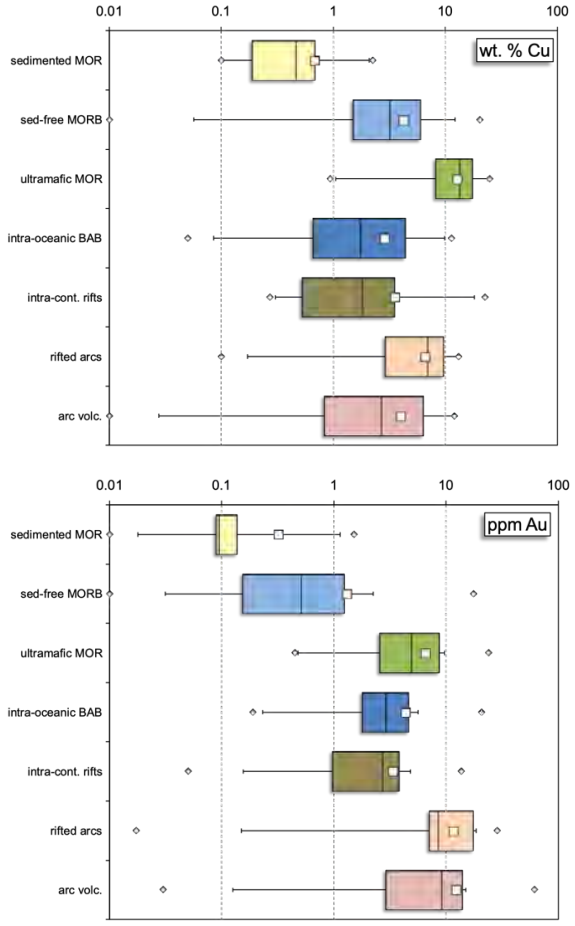


**Figure 4.** Box-and-Whisker-plot showing the range, average, and median of Cu and Au in SMS sites from various geological settings (N=185 averages of SMS occurrences; MOR = mid-ocean ridge; BAB = back-arc basin).

Very few are thought to be as large as 10 million tons. Hence, only a small number of known massive sulfide deposits are large enough to be considered as economically interesting. This contrasts with the size distribution of ancient deposits, which are generally much larger (Hannington 2014). The data for land-based deposits, however, is strongly biased towards large deposits because it includes only data for deposits that were large enough to be mined or to justify drilling. Many small sulfide occurrences are not included in resource data.

## 5 Global Exploration

At present the International Seabed Authority, responsible for administering seafloor resource in areas beyond national jurisdiction (ABNJ, “the Area”), has issued seven fifteen-year contracts for exploration of seafloor massive sulfides since 2011.

As a consequence of the presumed larger potential of SMS at slow-spreading ridges, these contract areas are all located along slow- to ultraslow-spreading ridges. All contractors are representatives of national governments (China, Russia, South Korea, France, India, Germany, and Poland). Four contract areas are located in the Indian Ocean, the remaining three in the Central Atlantic. Each original contract area covered 10.000km$^2$, however, due to mandatory relinquishments after 8 and 10 years, the area currently under contract by ISA is only 55.000km$^2$.

In addition to the work performed by the various contractors to the ISA, the last years have seen intensified exploration within the exclusive economic zones of selected countries. In Japan, a multi-year R&D project on marine mineral resources intensified seabed exploration. Within this project successful mining tests were performed at seafloor massive sulfide occurrences in the Okinawa Trough in 2012, 2015, and 2017.

In recent years, Norway has engaged in deep sea exploration within their EEZ through activities of the Norwegian Petroleum Directorate and is currently considering to open its EEZ for exploration.

## Acknowledgements

We thank the Marine Mineral Resources group at GEOMAR and the Metal Oceans team at the University of Ottawa for discussions. Numerous colleagues contributed over the years by sharing their knowledge and observations. M. Hannington was also supported through a Discovery Grant from the Natural Sciences and Engineering Research Council of Canada.

## References

Cherkashev GA, Ivanov VN, Bel'tenev V, et al (2013) Massive sulfide ores of the northern equatorial Mid-Atlantic Ridge. Oceanology 53: 607–619. https://doi.org/10.1134/S0001437013050032

German CR, Petersen S, Hannington MD (2016) Hydrothermal exploration of mid-ocean ridges: Where might the largest sulfide deposits be forming? Chemical Geology 420:114–126. https://doi.org/10.1016/j.chemgeo.2015.11.006

Graber S, Petersen S, Yeo I, et al (2020) Structural Control, Evolution, and Accumulation Rates of Massive Sulfides in the TAG Hydrothermal Field. Geochem Geophys Geosyst 21. https://doi.org/10.1029/2020GC009185

Hannington M, Jamieson J, Monecke T, et al (2011) The abundance of seafloor massive sulfide deposits. Geology 39: 1155–1158. https://doi.org/10.1130/G32468.1

Hannington MD (2014) Volcanogenic Massive Sulfide Deposits. Treatise on Geochemistry, Vol. 2 13, 463–488. http://doi.org/10.1016/B978-0-08-095975-7.01120-7

Jamieson JW, Gartman A (2020) Defining active, inactive, and extinct seafloor massive sulfide deposits. Marine Policy 117:103926. https://doi.org/10.1016/j.marpol.2020.103926

Kawano S, Furuya H (2022) Mining and processing of seafloor massive sulfides: experiences and challenges. In, Sharma R Perspective on Deep-Sea Mining. Springer Verlag. Switzerland. https://doi.org/10.1007/978-3-030-87982-2_7

Kim J, Son SK, Kim D, et al (2020) Discovery of active hydrothermal vent fields along the Central Indian Ridge, 8–12°S. Geochem Geophys Geosyst 21. https://doi.org/10.1029/2020GC009058

Klischies M, Petersen S, Schwarz-Schampera U et al (2023) Deposit models for seafloor massive sulfides from remote sensing data. This volume.

Pak S-J, Moon J-W, Kim J, et al (2017) Widespread tectonic extension at the Central Indian Ridge between 8°S and 18°S. Gondwana Research 45, 163–179. http://doi.org/10.1016/j.gr.2016.12.015

Petersen S, Lehrmann B, Murton BJ (2018) Modern Seafloor Hydrothermal Systems: New Perspectives on Ancient Ore-Forming Processes. Elements 14:307–312. https://doi.org/10.2138/gselements.14.5.307

Schwarz-Schampera U (in prep.) The INDEX exploration concept – introduction and rationale. In: U. Schwarz-Schampera (ed), Exploration of Marine Minerals – First results from the INDEX Campaign on Polymetallic Massive Sulfides.

Tao C, Seyfried WE, Lowell RP, et al (2020) Deep high-temperature hydrothermal circulation in a detachment faulting system on the ultra-slow spreading ridge. Nature Communications 1–9. http://dx.doi.org/10.1038/s41467-020-15062-w

Wang Y, Han X, Petersen S, et al (2017) Mineralogy and trace element geochemistry of sulfide minerals from the Wocan Hydrothermal Field on the slow-spreading Carlsberg Ridge, Indian Ocean. Ore Geology Reviews 84, 1–19. http://doi.org/10.1016/j.oregeorev.2016.12.020

Yang W, Liao S, Dias A, et al (2023) Geochemistry, sulfur and lead isotopic composition of hydrothermal sulfide from the Duanqiao hydrothermal field on the Southwest Indian Ridge: implications for ore genesis. International Geolology Review 65(3), https://doi.org/10.1080/00206814.2022.2081937

# Reconstructing the formation of volcanic-associated Lahn-Dill-type iron ores from fluid venting to seafloor deposition

**Leanne Schmitt[1,2], Thomas Kirnbauer[1], Thomas Angerer[3], Sabine Klein[4,2], Dieter Garbe-Schönberg[5], Vladimir Roddatis[6]**

[1]*Faculty of Georesources and Process Engineering, TH Georg Agricola, Bochum, Germany*
[2]*Institute of Geology, Mineralogy and Geophysics, Ruhr-Universität Bochum, Germany*
[3]*GeoSphere Austria, Wien, Austria*
[4]*Deutsches Bergbau-Museum Bochum, Germany*
[5]*Institute of Geosciences, Christian-Albrechts-Universität, Kiel, Germany*
[6]*Interface Geochemistry Section, Helmholtz Centre Potsdam, Germany*

**Abstract.** Volcanic-associated Fe-oxide mineralisation of the Lahn-Dill-type formed in pre-Variscan restricted, shallow marine basins. They are located in the hanging wall of thick volcaniclastic rocks marking the Middle to Upper Devonian boundary. One of the largest Lahn-Dill-type iron ore mines (Fortuna mine) has been sampled in order to elucidate the interplay of genetic processes leading to ore formation as well as the environment in which ores formed. Petrography revealed that ores most likely formed from a Fe-Si gel. Primary and diagenetic gel textures include spherules and aggregates composed of nanocrystalline hematite dispersed in quartz, or of hematite accumulations that are associated with pores in quartz. Local post-depositional Fe(III) reduction within the gel is indicated by siderite replacing hematite. In-situ mineralogical and textural microdomain (md) chemistry analysed by laser ablation ICP-MS displays four different source and formational trace element signatures related to (1) syngenetic apatite nanoinclusions, (2) scavenging by Fe-(oxyhydr)oxides, (3) (volcani)clastic contamination and (4) diagenetic mobilisation of REY in pore water. These signatures imply that ores formed related to diffused venting of a low-T fluid and subsequent rapid Fe-(oxyhydr)oxide precipitation. These processes were favoured in Silurian to Carboniferous restricted shallow marine basins that were characterised by extensive volcanic and hydrothermal activity.

## 1 Introduction

Marine volcanic-associated Fe-oxide mineralisation formed from the Precambrian until today. They are interpreted to have formed related to an interplay of volcanic-, hydrothermal-, marine- and microbial processes and therefore represent archives of basin sedimentation and marine environmental conditions, and are also important sources for iron.

Volcanic-associated Fe-oxide mineralisation of the Lahn-Dill-type formed in the restricted and shallow Rhenohercynian-, Saxothuringian- and Moravo-Silesian marine basins. They have been described mainly from the eastern Rhenish Massif, the Harz Mountains, central Saxothuringia and the Eastern Sudetes, but similar volcanic-associated marine Fe-oxide mineralisation also occur in western and southeastern Europe. Lahn-Dill-type iron ores are associated with Middle to Upper Devonian alkali basaltic volcanic and volcaniclastic rocks (Quade 1976). Ores formed either related to chemical precipitation (sedimentary-type) or to metasomatic replacement of wall rocks (replacement-type).

Lahn-Dill-type iron ores (sedimentary-type) are usually composed of hematite and quartz, with minor siderite and magnetite. Their Fe grade ranges from 30 to 40 wt.%. Due to low metamorphic overprint (< 300°C), ores display many primary and early diagenetic textures making them favourable to study mineral transformation and textural changes from sedimentation to metamorphism.

Whole rock geochemistry of marine Fe-oxide mineralisation is a conventional tool to decipher ocean chemistry and variations of the redox state. Mineral-specific minor and trace element geochemistry may however, provide a more detailed image of element fractionation during mineral formation. Trace elements in Fe-(oxyhydr)oxides are for instance interpreted to reflect the solution from which they precipitated (Bau 1999), whereas syngenetic apatites rather record ocean chemistry (Alibert 2016). Detecting these mineral-specific element fractionation mechanisms may provide insights that are masked in whole rock geochemistry.

We therefore, sampled one of the largest Lahn-Dill-type iron ores mines (Fortuna mine) and conducted a systematic petrography from the micro- to nano-scale (optical microscopy, REM, TEM) and microdomain chemistry (LA-ICP-MS) to reconstruct the unique depositional environment and venting mechanisms during Lahn-Dill-type ore formation.

## 2 Fortuna mine geology

The Fortuna mine is located within the Lahn-syncline (eastern Rhenish Massif, Germany) which is part of the Rhenohercynian Zone of the Variscan orogenic belt. Lithostratigraphy within the Fortuna mine is mainly characterised by a thick volcanic succession composed of green (distal to ore) and purple (proximal to ore) volcaniclastic rocks (Fig. 1a). Several thin (0.1 to 0.5 m) ore lenses are intercalated with purple volcaniclastic rocks near the top of the succession (position A ores; Fig. 1a, b). The main ore body is ~5 m thick and located on top of the volcaniclastic succession (position B ores; Fig. 1a, c). Sampled ore types are composed either of hematite and quartz forming sedimentary-type hematite-quartz ores, or subordinately of siderite, hematite and quartz forming sedimentary-type siderite-hematite ores. The latter occur rather at the top of the position B ore body. Hanging wall rocks

are composed of volcaniclastic and clastic sedimentary rocks with occasionally intercalated limestone. The above described stratigraphic sequence was overprinted by Variscan low-grade metamorphism, regional to local thrusting and folding and local hydrothermal carbonate-quartz-hematite-(chlorite-apatite) veins.

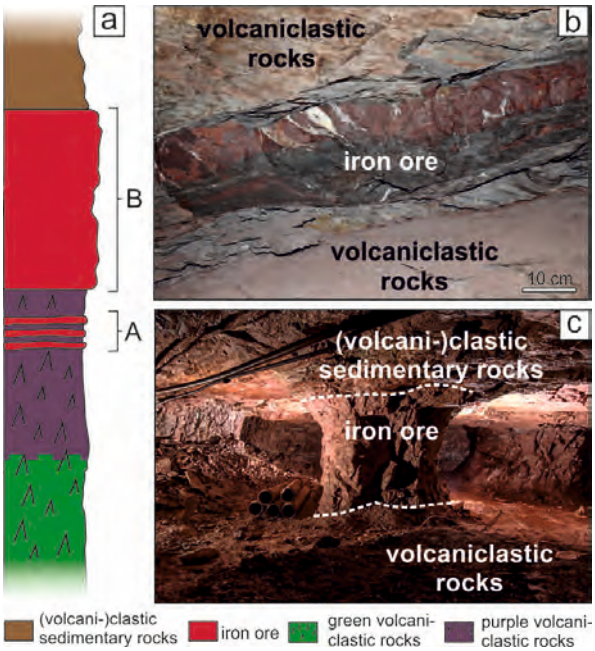


**Figure 1.** Positions of sedimentary-type iron ores in the Fortuna mine. **a** Lithostratigraphic profile depicting position A and B ores. Note that depicted thicknesses of drawn stratigraphic units do not correspond with true thicknesses due to graphic reasons. **b** Photo of position A ores and **c** of position B ores (iron ore layer ~5 m; image in **c** by courtesy of Roger Lang/Geowelt Fortuna e.V).

## 3 Methods

Fortuna mine position A and B ores were sampled and analysed using a reflected light microscope and a scanning electron microscope (SEM). High-resolution microscopy down to the nano-scale was carried out with a Thermo Fisher Scientific (former FEI) Tecnai F20 G2 and Themis Z 80-300 transmission electron microscope (TEM). For in-situ bulk microdomain geochemical analysis, a 193 nm ArF excimer laser ablation system (GeoLasPro Plus, Coherent) coupled to an Agilent 8900 inductively coupled plasma mass spectrometer (LA-ICP-MS/MS) was used. Rare earth elements and Y (REY) have been normalised to OIB, related to footwall volcaniclastic rocks displaying an OIB signature.

## 4 Petrography

### 4.1 Micro-scale petrography

Mineralogy of Fortuna mine position A and B sedimentary-type ores is simple and characterised by hematite, quartz and minor siderite. Internal textures, however, are complex and can be divided into three types of microdomains (md) - quartz-hematite-, hematite- and quartz md - in hematite-quartz ores and three types - siderite-hematite-, minor hematite- and quartz md - in siderite-hematite ores.

Quartz-hematite md are composed of microcrystalline quartz with finely dispersed tabular hematite crystals (< 200 nm; Fig. 2a). These md form specific mineral textures such as spherules often surrounded by crescent-shaped shrinking cracks, aggregates and tube- and filamentous stalk-like textures. Hematite md are characterised by accumulations of tabular hematite crystals (50 nm – 1 µm; Fig. 2a). Quartz md are completely constituted by quartz forming the fine-crystalline matrix and filling cracks around spherules. Siderite-hematite md are composed of large siderite single crystals (0.1 – 2 mm) with finely dispersed tabular hematite crystals (< 500 nm) forming aggregates and spherules. Hematite- and quartz md in siderite-hematite ores are similar to those in hematite-quartz ores.

### 4.2 Nano-scale petrography

TEM analysis of selected md in hematite-quartz- and siderite-hematite ores revealed that interfaces between quartz-hematite- and hematite md are characterised by abundant pores. Hematite from hematite md is accumulated in these pores, whereas hematite from quartz-hematite md is evenly distributed within microcrystalline quartz grains (Fig. 2a). TEM analysis also shows that at the interface between hematite- and siderite-hematite md, tabular hematite crystals are replaced by nanocrystalline siderite (Fig. 2b).

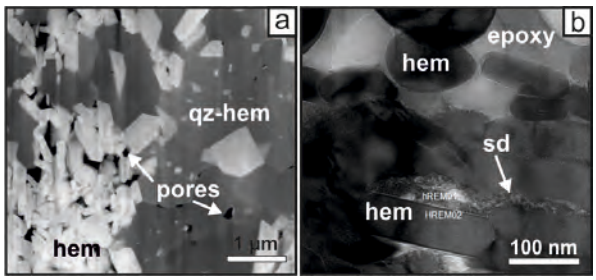


**Figure 2.** Photomicrographs of md in Fortuna mine ores. **a** Hematite md associated with pores at the interface to the quartz-hematite md (TEM HAADF). **b** Hematite replaced by nanocrystalline siderite (BFSTEM). qz = quartz; hem = hematite; sd = siderite.

## 5 Microdomain-specific geochemistry

Quartz-hematite md are dominated by total $Fe_2O_3$ and $SiO_2$ averaging 20 and 79 wt.%, respectively. Most transition metals are below 25 ppm, though V can reach 144 ppm. High field strength elements (HFSE) show individual averages < 15 ppm. ΣREE (avg. 2 ppm) correlates positively with $P_2O_5$. OIB-normalised REY patterns are characterised by negative Ce and Eu, and positive Y anomalies.

Hematite md in hematite-quartz- and siderite-hematite ores are differentiated into two types based on $Al_2O_3$, $TiO_2$, $K_2O$ and HFSE concentrations as indicator for (volcani)clastic contamination: Type 1

("pristine") is characterised by total $Fe_2O_3$ and $SiO_2$ averaging 99 wt.% and 1 wt.%, respectively (type 1). Transition metals and HFSE are enriched about tenfold compared to quartz-hematite md. ΣREE generally does not correlate with other elements in hematite md. OIB-normalised REY pattern displays negative Eu and Y anomalies, and in some samples negative La anomalies. Cerium anomalies are usually absent, but in some md weakly positive. Type 2 ("contaminated") hematite md display higher $Al_2O_3$, $TiO_2$, $K_2O$ and HFSE concentrations, and depict different REY patterns with variable Eu, Ce and Y anomalies.

Siderite-hematite md display total $Fe_2O_3$ ranging between 62 and 74 wt.%, and $SiO_2$ averaging 0.5 wt.%. CaO, MgO, MnO and $P_2O_5$ usually account together for less than 5 wt.%. Transition metal and HFSE contents are in the same range as in type 1 hematite md. Several siderite-hematite md are characterised by absence of positive ΣREE correlations, whereas some show a positive correlation of ΣLREE with $P_2O_5$. OIB-normalised REY patterns for all siderite-hematite md are however, uniform charactersied by a negative Eu and absence of other anomalies.

## 6 Discussion

### 6.1 Hematite-quartz- and siderite-hematite ore formation

In hematite-quartz ores, quartz-hematite md spherules surrounded by crescent-shaped cracks are a common feature and regarded as primary textures. They are interpreted to be a product of inorganic consolidation and dehydration of a Si-Fe gel (Grenne and Slack 2003). Aggregates formed by quartz-hematite- and hematite md are either primary textures that may have formed by fluctuating vent activity or are early diagenetic textures formed related to diagenetic gel maturation. During transient periods of high hydrothermal venting rates, Si partitions readily onto Fe-(oxyhydr)oxides (the likely precursor to hematite) forming primary quartz-hematite md. This, however, leaves temporary zones of Si depletion in the water column (Sherrell et al. 1999) through which Fe-(oxyhydr)oxides settle leading to primary hematite md formation. Hematite associated with quartz pores implies that md also formed due to diagenetic gel maturation. Uptake of silica onto Fe-(oxyhydr)oxides causes formation of a silica gel with "floating" Fe-(oxyhydr)oxides (precursor to quartz-hematite md). During diagenesis, silica transforms through coupled dissolution and reprecipitation via several steps from opal to quartz (Williams and Crerar 1985). Textures suggest that this is accompanied by dehydration, shrinking, liberation of Fe-(oxyhydr)oxides from silica polymorphs and subsequent accumulation of Fe-(oxyhydr)oxides in pores. Ferrihydrite to hematite transformation likely occurs during early diagenesis as it is triggered by Fe-(oxyhydr)oxide accumulation (Schwertmann et al. 1999). Ultimately, (incomplete) separation of Fe-(oxyhydr)oxides/hematite from silica polymorphs may led to formation of early diagenetic quartz-hematite-, hematite- and quartz md.

Siderite-hematite md in siderite-hematite ores may have either formed related to redox change in the water column or to post-depositional Fe(III) reduction. Nano-crystalline siderite replacing hematite crystals in siderite-hematite md supports the latter process. Fe(III) reduction is described from other Fe-oxide mineralisation and usually interpreted to have occurred during diagenesis (Heimann et al. 2010).

### 6.2 Microdomain-specific trace element fractionation

Most quartz-hematite- and one type 1 hematite md display REY fractionation features that are characteristic for Devonian seawater (neg. $Ce_{OIB}$, pos. $Y_{OIB}$ anomalies; Fig. 3; Nothdurft et al. 2004). Due to ΣREE correlating positively with $P_2O_5$ in these md, it is inferred that REY are associated with phosphates (likely apatite). These apatites are petrographically not visible. They likely occur as syngenetic nanoinclusions within these md, which is in good agreement with seawater sourced P and REY that are readily scavenged by Fe-(oxyhydr)oxides in modern vent systems (Feely et al. 1991).

Contrastingly, positive correlations of ΣREE with P and other elements are absent in the majority of type 1 hematite- and few quartz-hematite md. Therefore, REY are rather associated with hematite in these md. This is also evident from their REY fractionation pattern displaying typical features detected in Fe-(oxyhydr)oxides that scavenge REY in a simulated marine environment (negative $La_{OIB}$ and $Y_{OIB}$, and no to weak positive $Ce_{OIB}$ anomalies; Fig. 3; Bau 1999).

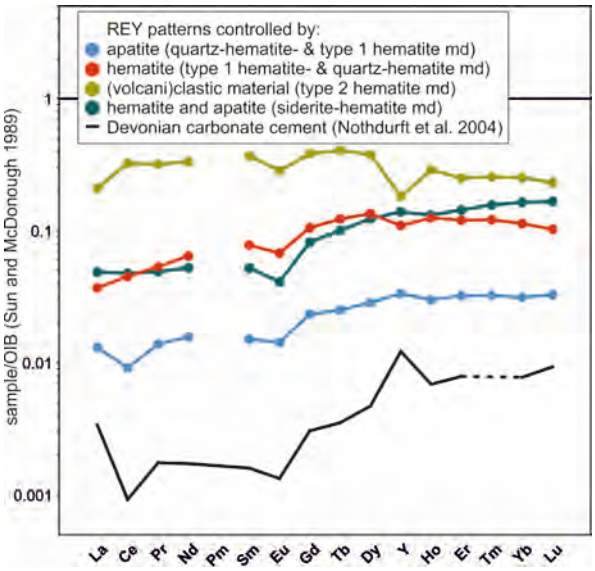


**Figure 3.** Microdomain OIB-normalised REY fractionation patterns, grouped related to mineralogical control, and in comparison with Devonian carbonate cement. Note that the patterns displayed here, only show the average of the respective md which may lead to disappearance of several

anomalies that only occur in some samples.

Type 2 hematite md that show higher $Al_2O_3$, $TiO_2$ and $K_2O$ display distinctly different REY fractionation patterns. They are controlled by finely dispersed (volcani)clastic material, which is supported by OIB-normalised REY slopes being relatively flat (Fig. 3).

Trace elements of siderite-hematite md are likely controlled by a mix of apatite (LREE) and hematite (HREE) related to several md displaying a positive correlation between ΣLREE and $P_2O_5$. They show, however, a different REY pattern compared to those controlled by hematite and apatite (Fig. 3). This may be related to mobilisation of REY during diagenetic Fe(III) reduction (see previous section). During diagenetic dissolution and reprecipitation of hematite and likely simultanous apatite, trace elements may have been released into pore water resulting in trace element excess (Chetty and Gutzmer 2012; Alibert 2016). Those processes may have led to homogenisation of $REY_{OIB}$ patterns in all siderite-hematite md.

### 6.2 Reconstruction of venting dynamics and depositional environment

Microdomain chemistry controlled by hematite and apatite show a uniform negative Eu anomaly that is consistent with low-T (<250 °C) fluids interacting with basaltic rocks (Giese and Bau 1994).

A weak positive Ce anomaly in several hematite md may be evidence for rapid Fe(II) oxidation subsequent to fluid venting. In precipitation experiments in oxidised seawater-like conditions, Ce(IV) sorption onto Fe-(oxyhydr)oxides is highest in the first few minutes and then drastically decreases (Bau 1999). Rapid Fe-(oxyhydr)oxide formation likely occurred in an environment characterised by high seawater to vent fluid ratio. This is evident from quartz-hematite- and hematite md displaying REY fractionation patterns typical for marine environments (see previous section) that rather developed during Fe-(oxyhydr)oxide- and apatite trace element scavenging from seawater and not from the vent fluid.

This may be consistent with diffused fluid venting and low fluid flux, and not with high fluid flux in focused vent systems. Diffused venting is a far more abundant venting process than focused fluid venting (Bemis et al. 2012) and may be the driving mineralisation process in all Lahn-Dill-type iron ores within the Rhenohercynian-, Saxothuringian- and Moravo-Silesian basins.

## 7 Conclusion

Lahn-Dill-type iron ores in the Fortuna mine include hematite-quartz- and minor siderite-hematite ores. The former formed related to formation of a Fe-Si gel on the seafloor. Microdomains in these ores preserve primary to early diagenetic textures that recorded vent fluid fluctuation, and gel maturation. Siderite-hematite ores formed most likely related to diagenetic Fe(III) reduction. Trace element geochemistry of md is compatible with diffused venting of a low-T fluid and subsequent rapid Fe-(oxyhydr)oxide formation. These ore forming processes appear to have been favoured during the Silurian to Carboniferous during which restricted pre-Variscan shallow marine basins have been linked to extensive volcanic and hydrothermal activity.

## Acknowledgements

We would like to thank the TH Georg Agricola for financial support. We also would like to say thank you to the “Fortuna mine” team for their support during sampling campaigns.

## References

Alibert C (2016) Rare earth elements in Hamersley BIF minerals. Geochim Cosmochim Acta 184:311–328.

Bau M (1999) Scavenging of dissolved yttrium and rare earths by precipitating iron oxyhydroxide: experimental evidence for Ce oxidation, Y-Ho fractionation, and lanthanide tetrad effect. Geochim Cosmochim Acta 63:67–77.

Bemis K, Lowell RP and Farough A (2012) Diffuse Flow: On and Around Hydrothermal Vents at Mid-Ocean Ridges. Oceanography 25:182–191.

Chetty D, Gutzmer J (2012) REE redistribution during hydrothermal alteration of ores of the Kalahari Manganese Deposit. Ore Geol Rev 47:126–135.

Feely RA, Trefry JH, Massoth GJ and Metz S (1991) A comparison of the scavenging of phosphorus and arsenic from seawater by hydrothermal iron oxyhydroxides in the Atlantic and Pacific Oceans. Deep Sea Research Part A. Oceanographic Research Papers 38:617–623.

Giese U and Bau M (1994) Trace Element Accessibility in Mid-Ocean Ridge and Ocean Island Basalt: An Experimental Approach. Mineral mag 58A:329–330.

Grenne T, Slack JF (2003) Bedded jaspers of the Ordovician Løkken ophiolite, Norway: seafloor deposition and diagenetic maturation of hydrothermal plume-derived silica-iron gels. Miner Deposita 38:625–639.

Heimann A, Johnson CM, Beard BL, Valley JW, Roden EE, Spicuzza MJ, Beukes NJ (2010) Fe, C, and O isotope compositions of banded iron formation carbonates demonstrate a major role for dissimilatory iron reduction in ~2.5 Ga marine environments. Earth Planet Sc Lett 294:8–18.

Nothdurft LD, Webb GE, Kamber BS (2004) Rare earth element geochemistry of Late Devonian reefal carbonates, Canning Basin, Western Australia: confirmation of a seawater REE proxy in ancient limestones. Geochim Cosmochim Acta 68:263–283.

Quade H (1976) Genetic problems and environmental features of volcano-sedimentary iron ore deposits of the Lahn-Dill Type. In: Wolf KH (ed) Handbook of strata-bound and stratiform ore deposits. Elsevier, Amsterdam, pp 255–294.

Schwertmann U, Friedel J, Stanjek H (1999) From Fe(III) Ions to Ferrihydrite and then to Hematite. J Colloid Interf Sci 209: 215–223.

Sherrell RM, Field MP and Ravizza G (1999) Uptake and fractionation of rare earth elements on hydrothermal plume particles at 9°45′N, East Pacific Rise. Geochim Cosmochim Acta 63:1709–1722.

Sun S-s and McDonough WF (1989) Chemical and isotopic systematics of oceanic basalts: implications for mantle composition and processes. Geological Society, London, Special Publications 42:313–345.

Williams LA, Crerar DA (1985) Silica Diagenesis, II. General Mechanisms. J Sediment Petrol 55:312–321.

# Linking Lithofacies and Chemostratigraphy, Rävliden North VHMS deposit, Skellefte district, Sweden

**Filip Simán[1], Nils Jansson[1], Foteini Liwicki[1], Tobias Hermansson[2], Erik Nordfeldt[2], Mac Fjellerad Persson[2], Paul McDonnell[2], Sean Johnson[2], Jon Gustafsson[2]**
*[1]Luleå University of Technology, Luleå, Sweden*
*[2]Boliden Mines, Boliden, Sweden*

**Abstract.** The recently discovered Rävliden North Zn-Pb-Ag-Cu deposit, located in the western Skellefte district, northern Sweden, is classified as a volcanic hosted massive sulphide (VHMS) and occurs at the contact between the Skellefte group (SG) metavolcanic rocks and the overlying predominantly metasiliciclastic rocks of the Vargfors group (VG). Alteration, metamorphism and complex internal stratigraphy makes classifying and spatially relating rocks in the area difficult, but chemostratigraphy utilising immobile elements may be a useful tool for overcoming some of these challenges. However, few comprehensive studies exist for the Rävliden North stratigraphy that link lithofacies and chemostratigraphy. This contribution advances the stratigraphic understanding of the crucial SG-VG contact at Rävliden North by linking lithofacies and immobile element signatures, resulting in the discrimination of two rhyolitic units. This study interprets a volcaniclastic facies for rhyolitic rocks located in a "transitional zone" between SG and VG rocks, whereas the footwall and immediate hanging wall rocks relate to a different rhyolitic unit, which due to high alteration intensities has more elusive facies, which are locally volcaniclastic and locally coherent. Given the complex structural relationships and discontinuous stratigraphy, this demonstrates the value in linking lithofacies to chemostratigraphy to aid core logging in altered rocks.

## 1 Introduction

The Rävliden North Zn-Pb-Ag-Cu deposit (8.4 Mt grading 4.17 % Zn, 0.64 % Pb, 81 g/t Ag, 0.98 % Cu, and 0.25 g/t Au; Boliden 2020) is located in the western part of the economically significant Skellefte district, northern Sweden (Figure 1). The deposit is classified as a volcanic hosted massive sulphide (VHMS) similar to most other deposits in the district. These deposits occur at the contact between two lithostratigraphic units: 1) the c. 1.89 – 1.88 Ga Skellefte group (SG) metavolcanic rocks, and 2) the overlying c. 1.89 – 1.87 Ga Vargfors group (VG) comprising predominantly metasiliciclastic rocks. The internal stratigraphies of the two groups and their contact relationships are highly variable throughout the district (Allen et al. 1996 and Skyttä et al. 2012), which is challenging for exploration. Furthermore, alteration and metamorphism cause difficulty in classifying rocks and, for this reason, immobile element lithogeochemistry is a useful technique for assisting classification. Previous workers have defined precursor rock-types based on immobile elements (Barrett et al. 2005 and Chmielowski et al. 2016), and some work with chemostratigraphy has been done for the footwall to the Rävliden deposit (Schlatter et al. 2003 and Årebäck et al. 2005). However, few comprehensive studies have been conducted on the full stratigraphy (Mataruga 2016), and even fewer have aimed at linking lithofacies and chemostratigraphy. This contribution aims to advance the detailed stratigraphic understanding at Rävliden North by linking lithofacies of least-altered samples to their immobile element signatures. By proxy, the possible lithofacies of more altered counterparts with similar immobile element signatures can be discussed. This approach is also useful at Rävliden North for further defining the complicated SG-VG contact where a "transitional zone" of volcanosedimentary rocks and intrusions occur.

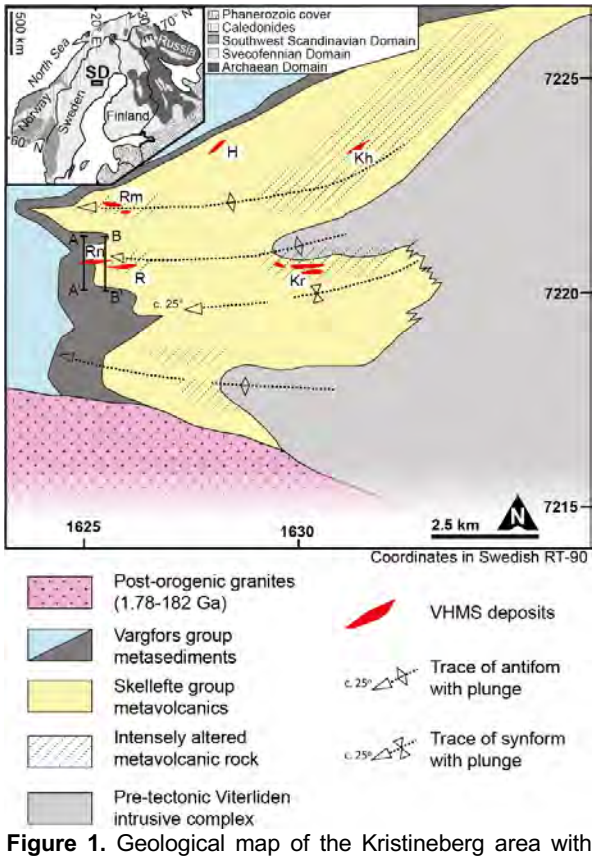


**Figure 1.** Geological map of the Kristineberg area with cross section traces A–A' and B–B' indicated, inset map of Fennoscandian Shield, H=Hornträsk, Kh=Kimheden, Rm=Rävlidmyran, Rn=Rävliden North, R=Rävliden, and Kr=Kristineberg. Modified after Skyttä et al. (2012).

### 1.1 Geological background

The Skellefte district belongs to the Bothnia-Skellefteå lithotectonic unit of the c. 2.0–1.8 Ga Svecokarelian orogen located in the Fennoscandian Shield (inset in Figure 1).

A continental intra-arc basin palaeoenvironment

is widely accepted for the district based on the dominantly felsic composition and the calc-alkaline magmatic affinity of the SG (Allen et al. 1996 and Skyttä et al. 2020). This volcanic arc formed between c. 1.90 and 1.88 Ga (Skyttä et al. 2020) and an extensional tectonic regime, which lasted from c. 1.89 – 1.88 Ga and resulted in D1 deformation, caused subsidence with associated subaqueous SG volcanism forming intermediate to felsic volcaniclastic rocks, minor lavas and minor sedimentary rocks in half-graben fault bound compartments (Allen et al. 1996; Skyttä et al. 2012; Årebäck et al. 2005). Coeval with the formation of the SG, granitoids of the Jörn suite were emplaced (Skyttä et al. 2020). The c. 1.89 – 1.87 Ga VG overlies the SG with a diachronous contact, which is a result of differential uplift and subsidence. Partly coeval with the VG are 1.88–1.86 Ga metavolcanic rocks that belong to the Arvidsjaur group, and several granitoids. At c. 1.88–1.87 Ga a transpressional tectonic regime with associated D2 deformation took over, which resulted in the closure of the intra-arc basin at c. 1.86 Ga. The corresponding peak metamorphism reached upper amphibolite facies (Weihed et al. 1992). For brevity and simplicity the prefix “meta-“ is omitted in further geological descriptions.

In terms of regional stratigraphy, the Rävliden North VHMS deposit is at the top of the SG felsic volcanic rocks. The footwall to the deposit is a weakly porphyritic rhyolite that locally exhibits texturally destructive sericite-silica±chlorite alteration. Footwall rocks proximal to mineralisation in the local stratigraphy are intensely chlorite-sericite altered with minor calc-silicate rocks that is locally tremolite rich (Barrett et al. 2005 and Årebäck et al. 2005). The ore lenses comprises semi-massive to massive sphalerite-galena-pyrite mineralisation, structurally above vein-hosted chalcopyrite-pyrrhotite-pyrite (Rincon 2022). A discontinuous graphitic phyllite, named by local workers as “Bonus shale”, locally directly overlies the mineralisation. The lower hanging wall, herein referred to as the “transitional zone”, comprises mainly rhyolitic rocks with widely unknown facies, coherent andesite with volcaniclastic margins with andesitic and dacitic composition, and a volcanosedimentary breccia-conglomerate with clasts of andesite, dacite and graphitic phyllite in a calc-silicate rich matrix. Upper hanging wall rocks comprise thick successions of graphitic phyllite, siltstone and sandstone, which are typically recognisable VG siliciclastic rocks.

## 2 Results

Legacy data from whole-rock lithogeochemical samples (n=652), taken by Boliden geologists from 44 drill cores in the Rävliden North host stratigraphy, show local intense alteration. In order to link lithofacies to chemostratigraphy the least-altered samples had to be identified, since important textures for determining lithofacies, such as phenocrysts, are better preserved in these rocks. Criteria for least altered samples are defined by the alteration box plot, where Ishikawa alteration index (AI) is plotted against the carbonate-chlorite-pyrite index (CCPI; Large et al. 2001), in tandem with criteria for LOI <4 vol.% and Na >2 vol.%, and qualitative description of alteration intensities. With these criteria, only 163 (25%) samples were classified as least altered. Two drill cores were relogged, RAVLD663 and RAVLD673. In drill core RAVLD663, there were eight least altered samples, five of which were described as volcaniclastic, two as coherent, and one as unidentifiable facies. In drill core RAVLD673, there were eleven least altered samples, four of which were described as volcaniclastic, five as coherent, and two as unidentifiable facies.

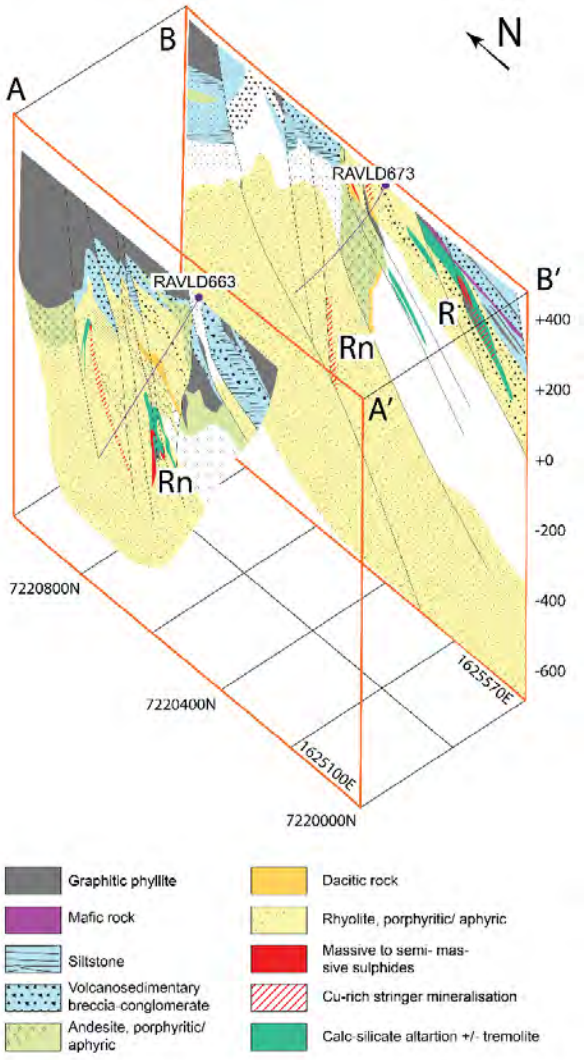


**Figure 2.** Cross sections A–A’ and B–B’ (see also Figure 1) with drill core traces RAVLD663 and RAVLD673 indicated. Rn=Rävliden North and R=Rävliden.

Immobile element plots were made for $Zr/TiO_2$ against $Al_2O_3/TiO_2$ for all data (altered and least-altered, n=652) to identify protolith compositions. Six clusters were identified by using the heat-map function in ioGAS. These were then labelled by petrographic descriptions of samples in tandem with TAS classification (Maitre et al. 2004) of the least altered counterparts (Figure 3). The "Bas 1" cluster (n=45), "And-Bas 1" cluster (n=46) and "Dac 1" cluster (n=27) likely correspond to mafic, andesitic and dacitic rocks, respectively. The "Rhy-Dac 1" (n=264) and "Rhy-Dac 2" (n=122) clusters likely both correspond to different rhyolitic-dacitic rocks. The sixth cluster, "Rhy 1" (n=12), corresponds to rhyolites in TAS classification and it did not occur in any samples from the logged drill cores.

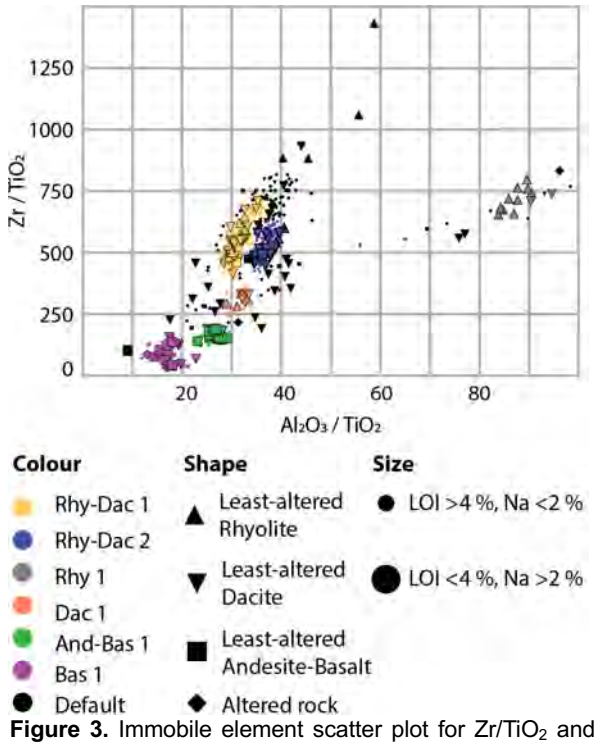


**Figure 3.** Immobile element scatter plot for $Zr/TiO_2$ and $Al_2O_3/TiO_2$ ratios for all drill cores. Colour labelling by apparent clusters, shape labelling by alteration box plot (AI vs CCPI) and size labelling by LOI and Na values.

Logged facies from RAVLD673 and RAVLD663 are linked to their respective chemostratigraphic units for both altered and least altered samples (Table 1). For "Rhy-Dac 1" no coherent facies were observed. Facies of "Rhy-Dac 2" are mostly unknow due to high alteration intensities, but both volcaniclastic and coherent facies are observed.

The "Rhy-Dac 1" chemostratigraphic unit occurring in RAVLD673 (0–100 metres, Figure 4) has weak to moderate sericite-chlorite alteration (average AI= 55 and average CCPI= 60). Only one of the samples was classified as least altered and its facies was described as volcaniclastic. Three "Rhy-Dac 1" samples found to be altered were also identified as volcaniclastic.

The "Rhy-Dac 1" chemostratigraphic unit occurring in RAVLD663 (130–280 metres) relates to

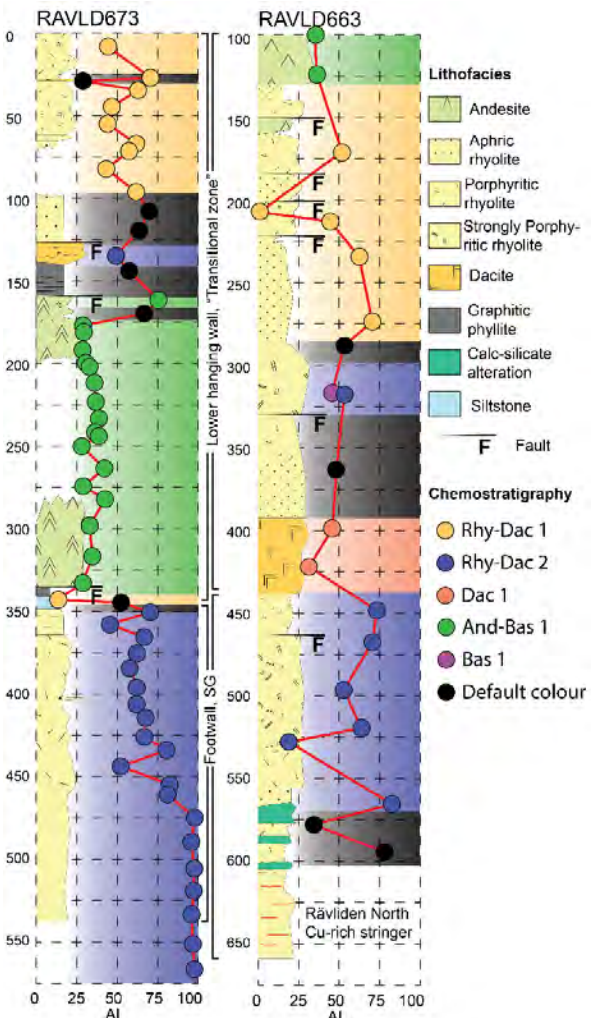


**Figure 4.** Downhole core logs of RAVLD673 and RAVLD663 linked to chemostratigraphy, AI is plotted above with red line.

strongly sericite altered rock (average AI= 57 and average CCPI= 48; excluding a carbonate altered sample with anomalous Ca values), where two samples were classified as least altered. Of these two, one was recognised as volcaniclastic facies and the other had unidentified facies. In addition, one altered sample could also be identified as volcaniclastic.

**Table 1.** Facies of the chemostratigraphic units in drill cores RAVLD673 and RAVLD663.

| | Volccl. | Coherent | Sed. | Unknown |
|---|---|---|---|---|
| Rhy-Dac 1 | 6 (55%) | 0 (0%) | 1 (9%) | 5 (42%) |
| Rhy-Dac 2 | 8 (30%) | 2 (7%) | 0 (0%) | 17 (63%) |
| Dac 1 | 1 (50%) | 1 (50%) | 0 (0%) | 0 (0%) |
| And-Bas 1 | 4 (40%) | 5 (50%) | 1 (10%) | 0 (0%) |
| Bas 1 | 0 (0%) | 1 (100%) | 0 (0%) | 0 (0%) |
| Default | 3 (33%) | 0 (0%) | 0 (0%) | 6 (66%) |

The "Rhy-Dac 2" chemostratigraphic unit, occurring in RAVLD673, has largely altered rocks with alteration intensities increasing downhole, from

AI= 62 and CCPI= 48 at 350 metres to AI= 97 and CCPI= 63 at 530 metres. Here, two samples are classified as least altered, where one could be recognised as a volcaniclastic facies and the other had unidentified facies. Taking altered samples into account, seven could be identified as volcaniclastic.

The “Rhy-Dac 2” chemostratigraphic unit occurring in RAVLD663 (460–550 metres) is phenocryst-rich (10–15 vol.%, Fsp>Qz) with locally uneven crystal distributions; however, lithofacies determination is challenged by moderate sericite-chlorite alteration and patchy strong calc-silicate alteration (average AI= 60 and average CCPI= 53). Here, one sample is classified as least altered and, despite this, its facies could not be determined. At c. 300 to 330 metres in RAVLD663, another sample classified as least altered plots as “Rhy-Dac 2”; its facies was determined to be coherent.

## 3 Discussion and conclusion

A key finding is that immobile elements reveal two different rhyolitic units at different stratigraphic positions. The “Rhy-Dac 2” unit belongs to the footwall and immediate hanging wall of the Rävliden North mineralisation and, consequently, to the SG. The “Rhy-Dac 1” unit belongs to the “transitional zone” between the SG and VG. Alteration makes determining facies difficult, but by identification of what is defined as least altered samples, it is suggested that “Rhy-Dac 1” is exclusively volcaniclastic, whereas the facies of “Rhy-Dac 2” remains elusive. Taking altered samples into account for “Rhy-Dac 2”, several volcaniclastic and no coherent facies are found in RAVLD673, whereas in RAVLD663 coherent and volcaniclastic textures were both observed.

With immobile element chemostratigraphy, a better stratigraphic understanding of the Rävliden North host rocks is achieved. Rhyolitic rocks in the “transitional zone” have been linked spatially between drill cores, as well as to a respective volcaniclastic facies. However, footwall alteration is generally strong, and finding least altered samples is difficult. Further work, with more samples, should be done with this technique to establish a stronger link between lithofacies and chemostratigraphy, and to help guide exploration efforts in these altered rocks.

## Acknowledgements

Thank you to all the geologists at the Boliden core archive and staff who have been helpful with logistics and discussions during visits for core logging.

## References

Allen RL, Weihed P, Svenson SA (1996) Setting of Zn-Cu-Au-Ag massive sulfide deposits in the evolution and facies architecture of a 1.9 Ga marine volcanic arc, Skellefte District, Sweden. Econ Geol 91-6:1022–1053. https://doi.org/10.2113/gsecongeo.91.6.1022

Barrett TJ, MacLean WH, Åreback H (2005) The Palaeoproterozoic Kristineberg VMS deposit, Skellefte district, northern Sweden; Part II, Chemostratigraphy and alteration. Miner Deposita 40-4: 368–395. https://doi.org/10.1007/s00126-005-0001-2

Boliden (2021) Boliden Summary Report, Resources and Reserves 2021, Kristineberg. 1–42. https://www.boliden.com/490e8a/globalassets/operations/exploration/mineral-resources-and-mineral-reserves-pdf/2021/bol_main-1848472-v1-resources-and-reserves-kristineberg-2021-12-31.pdf. Accessed 1 February 2023

Chmielowski RM, Jansson N, Persson MF, Fagerström P (2016) 3D modelling of hydrothermal alteration associated with VHMS deposits in the Kristineberg area, Skellefte district, northern Sweden. Miner Deposita 51-1: 113–130. https://doi.org/10.1007/s00126-014-0572-x

Large RR, Gemmell JB, Paulick H (2001) The alteration box plot; a simple approach to understanding the relationship between alteration mineralogy and lithogeochemistry associated with volcanic-hosted massive sulfide deposits. Econ Geol 96-5: 957–971. https://doi.org/10.2113/gsecongeo.96.5.957

Maitre R, Streckeisen A, Zanettin B, Le Bas M, Bonin B, Bateman P (2004) Igneous Rocks: A Classification and Glossary of Terms. Cambridge University Press, Cambridge

Mataruga Z (2016) Determining host rock protolith in an altered VMS deposit in the Rävliden area, North Sweden. Bachelor thesis, Uppsala universitet, Institutionen för geovetenskaper http://proxy.lib.ltu.se/login?url=https://search.ebscohost.com/login.aspx?direct=true&db=edsbas&AN=edsbas.4A64FBDB&lang=sv&site=eds-live&scope=site

Rincon J (2022) Textural and chemical characterization of sulphide minerals at the Rävliden North VMS deposit, Skellefte district, Sweden. Licentiate thesis, Luleå University of Technology

Schlatter DM, Barrett T (2003) Chemostratigraphy of metamorphosed and altered Paleoproterozoic volcanic rocks associated with massive sulfide deposits at Rävliden and Kristineberg West, Skellefte district, Sweden Seventh Biennial SGA Meeting, Mineral exploration and sustainable development, Athens, Greece.

Skyttä P, Bauer TE, Tavakoli S, Hermansson T, Andersson J, Weihed P (2012) Pre-1.87 Ga development of crustal domains overprinted by 1.87 Ga transpression in the Palaeoproterozoic Skellefte district, Sweden. Precambrian Res 206-207:109–136. https://doi.org/10.1016/j.precamres.2012.02.022

Skyttä P, Weihed P, Högdahl K, Bergman S, Stephens MB (2020) Paleoproterozoic (2.0–1.8 Ga) syn-orogenic sedimentation, magmatism and mineralization in the Bothnia–Skellefteå lithotectonic unit, Svecokarelian orogen. In: Stephens MB and Weihed JB (ed) Sweden - Lithotectonic framework, tectonic evolution and mineral resources. Geological Society of London, pp 83–130.

Weihed P, Bergman J, Bergström U (1992) Metallogeny and tectonic evolution of the early Proterozoic Skellefte District, northern Sweden. Precambrian Res 58-1-4:143–167. https://doi.org/10.1016/0301-9268(92)90117-7

Årebäck H, Barrett TJ, Abrahamsson S, Fagerström P (2005) The Palaeoproterozoic Kristineberg VMS deposit, Skellefte district, northern Sweden, part I: Geology. Miner Deposita 40-4:351–367. https://doi.org/10.1007/s00126-005-0476-x

# The Hydrothermal History of the VOLPA Seafloor Massive Sulphide Deposit, SW Pacific

**Jonathan Umbsaar, Melissa Anderson, Daniel Gregory**
[1]*University of Toronto, Department of Earth Sciences*

**Abstract.** The VOLPA deposit is a previously uncharacterized Seafloor Massive Sulphide (SMS) deposit on the Niua Volcanic Complex; an arc volcano located at the northernmost end of the Tofua Volcanic Arc, SW Pacific. SMS deposits form through circulating hydrothermal fluids in the oceanic crust, which are driven by anomalous geothermal gradients. Circulating fluids reach elevated temperatures, acidity, and REDOX potential, which are favourable conditions for the transport of metal cations. These deposits are enriched in a variety of critical metals, and represent a modern analogue to Volcanogenic Massive Sulphide (VMS) deposits, which are a valuable base and precious metal source. VOLPA is composed of especially barite-rich chimneys, in sulphur-encrusted trachyandesitic host rocks of variable permeability, resulting in deposit scale zonation of mineral abundances. Petrography, elemental mapping, and whole-rock geochemistry have facilitated subclassification of SMS chimneys, with implications for hydrothermal processes such as boiling, seawater mixing, magmatic volatile influx, as well as the pH, temperature, and REDOX conditions of the hydrothermal vent fluids. The conclusions of this research indicate that the distribution of critical metals across VOLPA are largely dependent on host rock permeability, depth, and the influx of magmatic volatiles, in addition to adsorption, colloidal gold transport, and structural influences.

## 1 Introduction

### 1.1 Seafloor Massive Sulphides

Seafloor massive sulphide (SMS) deposits are the modern equivalent to continental volcanogenic massive sulphide (VMS) deposits which are actively mined across the globe for Cu, Zn, Pb, Au, and Ag, with the capacity for enrichments in a host of other critical metals, including As, Bi, Co, Ga, Ge, In, Mn, Mo, Ni, Sb, Sn, and W (Robb 2005; Boschen et al. 2013). SMS deposits form on the ocean floor due to anomalous geothermal gradients generated by intruding magma bodies, and thus, tend to be localized along plate margin boundaries (Barrie 2012). The heat from these magma bodies triggers circulation of seawater (and injected magmatic volatiles), which become locally high-temperature, acidic, saline, and reducing, which are favourable conditions for the transport of metal cations, that are leached from the host rocks, and extracted from the cooling magma (Robb 2005; Barrie 2012). These metal cations precipitate out of solution when the hydrothermal fluids mix with the cold seawater, or otherwise when these fluids reach critical temperatures, resulting in boiling (Herzig and Hannington 1995). Fluid mixing destabilizes the metal complexes, causing the cations to be dropped out of solution (de Ronde et al. 2003).

To date, more than 700 hydrothermal vents have been identified, of which ~300 contain measurable quantities of metal-bearing sulphides (Beaulieu et al. 2013).

### 1.2 The VOLPA Deposit

The Volcano P Site A (VOLPA) deposit is a previously uncharacterized deposit located on the southern end of the Niua Volcanic Complex; an irregular, rectangularly-shaped arc volcano composed of multiple coalescing volcanic ridges, with accompanying, fissures, cones, and volcaniclastic mounds (Moum, unpublished thesis). This volcano is located at the northern end of the Tofua volcanic arc, along the Tonga-Kermadec trench in the SW Pacific (Figure 1).

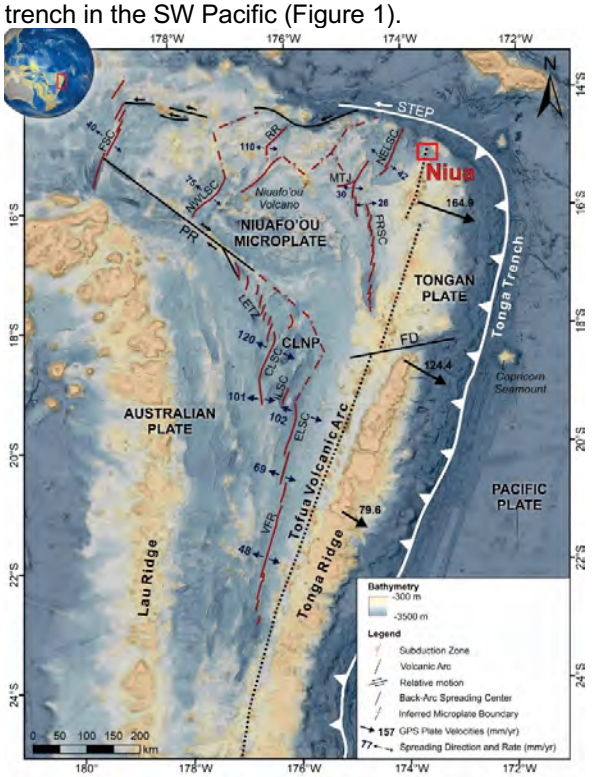


**Figure 1.** Bathymetric map of the Lau Basin. The Niua Volcanic Complex is highlighted in red.

The VOLPA deposit is situated in a volcanic crater at 1100 m depth and is roughly 1 km in diameter. It can be locally subdivided into eastern and western vent fields, with the west being composed of trachyandesitic, permeable volcaniclastics, and the east being composed of imposing trachyandesitic lava flows (Figure 2; Moum, unpublished thesis). Active venting and

seafloor boiling has been documented at the VOLPA deposit (Moum, unpublished thesis).

## 2 Methods

Samples and bathymetric data were collected by Nautilus Minerals Inc. during commercial exploration between 2011–2012, and additional bathymetric data was collected from the Niua volcanic complex in 2018 during the SO-263 cruise on board the R/V Sonne (Haase et al., 2018). 69 hand sample were selected for processing into thin sections and rock powders for bulk geochemical analysis. Thin sections were analysed using a Nikon Optiphot petrographic microscope in both reflected and transmitted light. Based on the whole rock geochemistry and petrography, samples were classified into chimney types (Sphalerite-barite, sphalerite-tennantite, chalcopyrite-pyrite, and chalcopyrite-tennantite). Twenty-five samples were then selected for electron microprobe analysis, and ten of those samples were later used to generate 1mm x 1mm laser ablation inductively coupled mass spectrometric (LA-ICP-MS) element maps.

## 3 Results and Discussion

### 3.1 Permeability of the Substrate

The VOLPA deposit is compositionally zoned in accordance with the permeability of the substrate. The west is composed of permeable volcaniclastic cover, and thus, oceanic seawater can more easily infiltrate the subsurface and interact with the hydrothermal fluids before reaching the ocean floor (Galley 1993; Andersen et al. 2015). The result is a cooler venting system that contains more sphalerite, galena, Pb-sulfosalts (gratonite, semseyite), and barite. The western vent field is compositionally enriched in Ba, Pb, Tl, and Ag. In contrast, the eastern vent field is covered by relatively impermeable lava flows, and thus, hydrothermal vents exhibit more focussed and less diffuse venting, resulting in higher temperature fluids with a greater capacity for surficial boiling. These eastern vents are enriched in Cu, Au, In, Co, and S, and generally contain more chalcopyrite and tennantite (Figure 2).

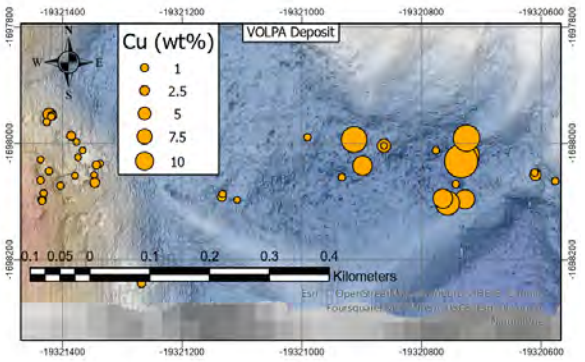


**Figure 2.** Bathymetric map of the VOLPA crater. Orange circles indicate copper wt% of SMS chimney samples

These observations complicate the classification of SMS deposits, because despite both the eastern and western vent fields being located on the same volcanic crater, they are compositionally very different.

### 3.2 Magmatic Volatile Input

There is evidence to suggest that magmatic volatiles have contributed to the formation of the VOLPA deposit.

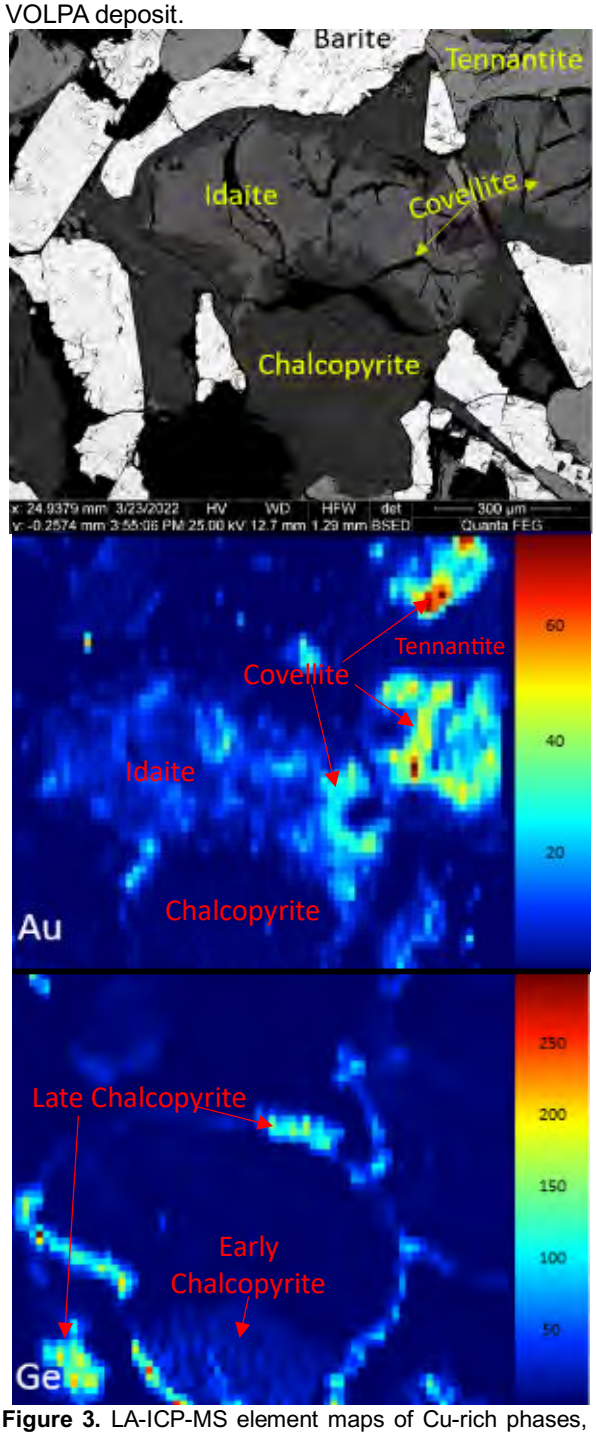


**Figure 3.** LA-ICP-MS element maps of Cu-rich phases, with chalcopyrite replaced by covellite-idaite, and late tennantite, with critical metal enrichments associated with these later phases of growth. Au and Ge element maps are shown with concentrations in ppm.

Magmatic volatiles are characterized by high-sulfidation mineral phases such as enargite, tennantite-tetrahedrite, covellite, orpiment, realgar, and native sulphur: all of which were identified at the VOLPA deposit, and consistently correlated with elevated concentrations of characteristically epithermal-associated elements (Au, Ag, As, Sb, Hg) among other critical metals (Wohlgemuth-Ueberwasser et al. 2015; Fuchs et al. 2019). Characteristics that are diagnostic of magmatic volatile flux, are ones that demonstrate changing fluid conditions to a more oxidizing, and Cu-rich system. This is evidenced in chalcopyrite-diseased sphalerite that is rimmed with tennantite.

Additionally, this phenomenon is also evident in replacement textures of chalcopyrite into idaite-covellite (representing a loss of iron, and gain in copper), with a subsequent back-reaction and exsolution of chalcopyrite from the idaite-covellite (Figure 3). Replacement, dissolution, and exsolution features are key when investigating for critical metals because these textures demonstrate rapidly changing fluid conditions. Under steady conditions, trace metal capture is low, as evidenced by depleted massive and biomineralized sulphides.

### 3.3 Comparisons to Niua South

The VOLPA deposit is adjacent to the Niua South SMS deposit, which is similarly hosted on the Niua Volcanic Complex. Relative to VOLPA, Niua South is compositionally enriched in Cu, Au, Co, In, Se, Mo, Sn, Fe, Mn, Si, Ca, and S, while VOLPA is enriched in Ba, Sr, Zn, Cd, Ge, Pb, Ag, As, and Sb. Based on these elemental enrichments and depletions, it seems that VOLPA represents a lower-temperature system, with more abundant seawater infiltration. In contrast, Niua South appears to contain more high-temperature phases like chalcopyrite, but does not contain the same high-sulfidation mineral phases that are present at VOLPA.

Although no dates have yet been calculated from the VOLPA deposit, Rb-Sr isotope age dating from Niua South indicates that the barite content of the SMS chimneys correlates with age, due to the prolonged exposure to seawater as hydrothermal activity wanes. The average Ba concentration at VOLPA is 22.98%, while only 12.69% at Niua South; therefore, it is likely that the VOLPA deposit is older than Niua South. This is further evidenced by the presence of amorphous silica at Niua South, whereas the same silica content is very rare at VOLPA. There is evidence to suggest that an amorphous silicate host housed early spheroidal pyrites (Si and O are well correlated as elemental inclusions in these pyrites), but has since been dissolved in accordance with the retrograde solubility of quartz. The abundance of silica at Niua South may indicate that the advancement of this siliceous cap is an ongoing process.

Thia age difference between VOLPA and Niua South may provide rationale for why high-sulfidation minerals associated with magmatic volatiles are much more common at VOLPA. Magmatic volatiles may have been introduced to this volcanic system relatively early, while Niua South was not yet actively venting. These observations are generally supported by the paragenetic sequences of chimney samples from VOLPA and have implications for comparisons to other SMS deposits.

### 3.4 Co-Precipitation of Phases

In addition to the aforementioned textures indicating a fluctuating hydrothermal environment, it is equally important that multiple phases are present in the system in order to accommodate the cations that are actively precipitating. The partition coefficients

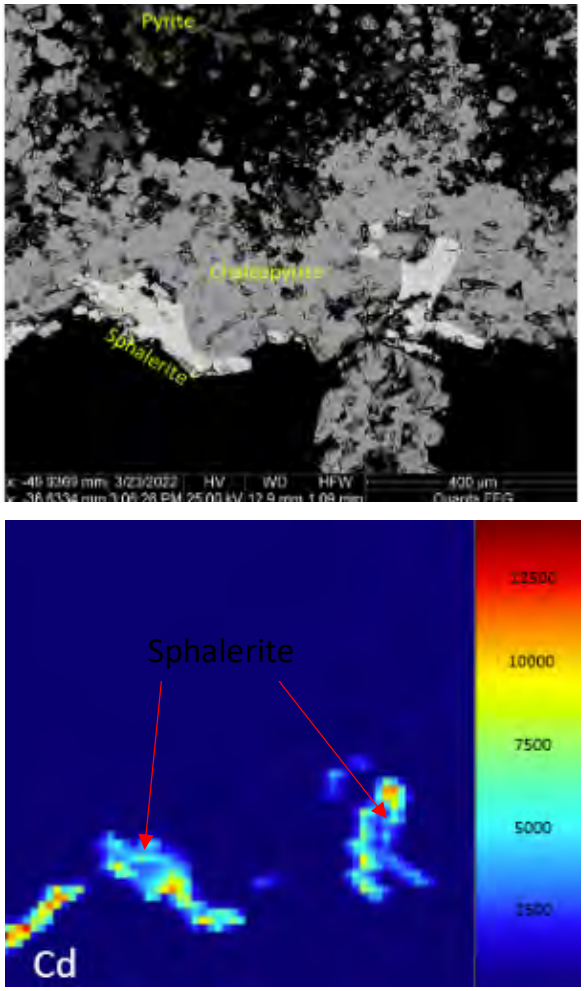


of metals from solution varies for the different sulphides present in the system. For example, at VOLPA, sphalerite is an excellent sink of Hg, Ga, Ge, and Cd (Figure 4).

**Figure 4.** LA-ICP-MS element map of Cd concentrations in a Cu-Fe-rich SMS chimney with minimal sphalerite demonstrates the importance of multi-phase systems for metal capture. Concentrations are in ppm.

Chalcopyrite is less likely to be enriched in these elements, but can generally accommodate more In, Mo, and Se. Multi-phase systems are ideal for critical metal capture, but overlapping stability fields of multiple sulphide phases can be rare. Boiling is an ideal mechanism for co-precipitating multiple phases because the system is already destabilized by the introduction of a gaseous phase.

## 4 Conclusions

The hydrothermal history of the VOLPA deposit highlights how nuanced the conditions of SMS deposit formation can be, and illustrates the difficulties in rigidly classifying and differentiating deposits based on tectonic setting and host lithology. Two distinct SMS deposits (Niua South and VOLPA) located on the same volcanic complex contain variable geochemical enrichments, petrologies, textures, and conditions of formation. There is evidence to suggest that VOLPA is an older deposit, and may have been subject to early magmatic volatile fluxes. Moreover, the VOLPA deposit can be further subdivided on the basis of the permeability of the substrate, which results in deposit-scale zonation, with low-temperature phases being enriched in regions with higher permeability.

There is reason to believe that magmatic volatiles have contributed to the critical metal endowment of the VOLPA deposit based on the high-sulfidation mineral phases and correlations of critical and precious metals with these phases.

Important textures to investigate for critical metal abundances are those that indicate fluctuating hydrothermal conditions, such as adsorption, resorption, replacement, and exsolution textures, as well as the co-precipitation of multiple sulphide phases. Finally, not all critical metals are affinitive of high-temperature systems. Some elements like Pb, Tl, and Ag, are generally more common in low-temperature venting systems, demonstrating the challenges associated with high resolution element mapping and resource estimations.

The ongoing research into these SMS deposits is indispensable for prospective private companies and government agencies attempting to navigate the burgeoning field of seafloor mining. Likewise, these insights into SMS deposits can be translated to the ancient rock record, to aid in paleoenvironmental reconstruction and investigations of the previously overlooked critical metal abundances in VMS deposits.

## Acknowledgements

Thanks to Nautilus Minerals (now SM2) for assisting with sample collection.

Thanks to NSERC-iMAGE Create and the coordinators (Dr. Mark Hannington, Dr. Alan Baxter, and Dr. Erin Bethell) for providing funding for research and learning activities.

Thanks to David Diekrup, Alexander Voinot, Matthew Laybourne and Agatha Dobosz for help with EPMA and LA-ICP-MS analyses.

Thanks to Dr. Jan Peters, Dr. Shu Xu, and Dr. Cornell Dr Ronde for guidance in this research.

Thanks to Actlabs, the University of Toronto, University of Ottawa, Queen's University, and Vancouver Petrographics for all assisting with sample preparation and analytical work.

## References

Andersen C, Rüpke L, Hasenclever J, Grevemeyer I, Petersen S. 2015. Fault geometry and permeability contrast control vent temperatures at the Logatchev 1 hydrothermal field, Mid-Atlantic Ridge. Geology. 43(1):51–54. doi:10.1130/G36113.1.

Barrie CT. 2012. Volcanogenic massive sulfide occurrence model. Economic Geology. 107(5):1073–1073. doi:10.2113/econgeo.107.5.1073.

Beaulieu SE, Baker ET, German CR, Maffei A. 2013. An authoritative global database for active submarine hydrothermal vent fields. Geochemistry, Geophysics, Geosystems. 14(11):4892–4905. doi:10.1002/2013GC004998.

Boschen RE, Rowden AA, Clark MR, Gardner JPA. 2013. Mining of deep-sea seafloor massive sulfides: A review of the deposits, their benthic communities, impacts from mining, regulatory frameworks and management strategies. Ocean and Coastal Management. 84:54–67. doi:10.1016/j.ocecoaman.2013.07.005.

Fuchs S, Hannington MD, Petersen S. 2019. Divining gold in seafloor polymetallic massive sulfide systems. Mineralium Deposita. 54(6):789–820. doi:10.1007/s00126-019-00895-3.

Galley AG. 1993. Characteristics of semi-conformable alteration zones associated with volcanogenic massive sulphide districts. Journal of Geochemical Exploration. 48(2):175–200. doi:10.1016/0375-6742(93)90004-6.

Herzig PM, Hannington MD. 1995. Polymetallic massive sulfides at the modern seafloor a review. Ore Geology Reviews. 10(2):95–115. doi:10.1016/0169-1368(95)00009-7.

Moum T. Geology and geochemistry of the newly-discovered VOLPA seafloor massive sulfide deposit, Niua volcanic arc complex , Tonga , SW Pacific. Unpublished Thesis.

Robb L. 2005. Introduction to Ore-Forming Processes. Blackwell Publishing (1-373).

Wohlgemuth-Ueberwasser CC, Viljoen F, Petersen S, Vorster C. 2015. Distribution and solubility limits of trace elements in hydrothermal black smoker sulfides: An in-situ LA-ICP-MS study. Geochimica et Cosmochimica Acta. 159:16–41. doi:10.1016/j.gca.2015.03.020.

# Iron, boron and sulfur isotope constraints on ore-forming process of the subseafloor replacement-style volcanogenic massive sulfide systems

**Bing Xiao[1], Huayong Chen[1, 2, 3], Fang Huang[4], Yuzhou Feng[1], Xia Hu[4]**
*[1]Key Laboratory of Mineralogy and Metallogeny, Guangzhou Institute of Geochemistry, Chinese Academy of Sciences, Guangzhou 510640, China*
*[2]University of Chinese Academy of Sciences, Beijing 100049, China*
*[3]Guangdong Provincial Key Laboratory of Mineral Physics and Materials, Guangzhou 510640, China*
*[4]CAS Key Laboratory of Crust-Mantle Materials and Environments, School of Earth and Space Sciences, University of Science and Technology of China, Hefei 230026, Anhui, China*

**Abstract.** A combined systematic Fe, B and S isotope investigation has been applied in the well-preserved Ashele subseafloor replacement-style VMS deposit, which comprises two stages of Cu mineralization, i.e., early massive sulfides, which were replaced by late vein-dominated chlorite-chalcopyrite assemblages. Boron isotopes of tourmaline and sulfur isotopes of sulfides indicate significant seawater participated during the formation of massive sulfides and increasing contribution of magmatic sulfur from the early to late stages. In addition, $\delta^{56}$Fe values of pyrite gradually increase outwards from the mineralization center, which is likely related to the different extent of isotopic exchange and formation temperature. The new two-stage ore-forming model shows that at the early stage, rapid mixing of hydrothermal fluid from underlying magma chamber with abundant cold seawater led to rapid deposition of pyrite and associated Cu mineralization. Long-term hydrothermal activities in relatively closed systems would promote the formation of upper massive ores, which resulted in an equilibrium system between sulfides and associated fluid with wide ranges of $\delta^{56}$Fe in sulfides. The late hydrothermal activities in relatively open system would contribute to stringer sulfides or stockworks underlying the massive ore with heavier Fe isotope compositions in sulfides.

## 1 Introduction

The subseafloor replacement-type VMS deposits are formed by the fully to partially hydrothermal replacement of subseafloor rocks and commonly have large metal reserves and economic values (Galley et al. 1995; Piercey 2015). However, their detailed sulfide precipitation processes are not well constrained by existing geochemical tracers. Furthermore, the relative proportion of fluid sources (e.g., seawater and magmatic fluid) in different alteration and mineralization stages is still unknown. In this study, we report a complete suite of B, Fe and S isotope data for whole-rocks and Fe bearing minerals, including pyrite, chalcopyrite, and chlorite from the Ashele VMS deposit. These results are used to understand sulfide precipitation processes, as well as B, Fe and S isotope compositions and behaviors in the subseafloor hydrothermal systems, and discuss the entire alteration/mineralization process of VMS deposits.

## 2 Deposit Geology

The Ashele deposit, the largest known VMS Cu-Zn deposit in the Chinese Altay, contains significant Cu (1.08 Mt. @ 2.46%), Zn (0.43 Mt. @ 0.41%) and Au (27.2 t @ 0.36 g/t; Zheng et al., 2016). Mineralization and hydrothermal alteration is generally hosted by the Ashele Formation, which mainly comprises tuff, breccia tuff, volcanic breccia, agglomerate, dacite, andesite, basalt, sedimentary tuff, and limestone (Zheng et al. 2016).

Based on previous study and our new observations, hydrothermal alteration and mineralization zonation at the Ashele deposit are well presented in the hanging wall of volcanic tuff, which can be divided into five zones (outwards from the mineralization center), i.e., the massive sulfides (I), quartz-pyrite (II), chlorite-chalcopyrite-quartz-pyrite (III), quartz-chlorite-sericite-pyrite (IV), and quartz-sericite-pyrite zones (V), and the Cu mineralization is mainly hosed in zone I and III.

## 3 Results

$\delta^{56}$Fe values for the basalt and dacite porphyry show similar and small variations (0.01‰–0.06‰ and 0.03‰–0.06‰), while the tuff has a larger range of $\delta^{56}$Fe (-0.1‰–0.24‰). Pyrite from zone I (Py1), zone II (Py2), zone III (Py3) and zone V (Py4) have $\delta^{56}$Fe of -0.46‰–-0.02‰, -0.09‰–0.07‰, 0–0.21‰ and -0.02‰–0.29‰, respectively. Chalcopyrite from zone I (Ccp1) and zone III (Ccp2) have $\delta^{56}$Fe of -1.56‰–-0.49‰ and -0.60‰–-0.04‰, respectively. Chlorite from zone III has $\delta^{56}$Fe of -0.48‰ to -0.12‰ (Fig. 1).

The $\delta^{34}$S values of Py1 ranges from -2.62‰ to 5.94‰. Compared with Py1, Py2, Py3, and Py4 have higher $\delta^{34}$S values of 1.28‰–5.00‰, 1.25‰–9.76‰, and 3.13‰–6.25‰, respectively. The $\delta^{34}$S values of Ccp1 and Ccp2 have $\delta^{34}$S values of 0.01‰–4.15‰ and 2.18‰–3.05‰, respectively (Fig. 2).

Boron isotope compositions ($\delta^{11}$B) of Mg-rich tourmaline in the zone I are of -5.57‰ to -2.73‰.

## 4 Source contribution in two stages ore-forming fluids

Boron in VMS systems could originate from seawater and magmatic fluids. Seawater usually has

heavy B isotope compositions with $\delta^{11}B$ value of about +40‰, while the average $\delta^{11}B$ value of igneous rock is around -10‰ (Trumbull et al. 2020), which therefore provides a sensitive indicator for mixing of seawater and magmatic fluid. The modal calculations indicate that the fraction of B from seawater relative to B of hydrothermal fluid would be 19% to produce an average $\delta^{11}B$ value of -1.53‰, suggesting that significant seawater participated in the processes of tourmaline and massive sulfide formation, which is also confirmed by Mg-rich characteristic of tourmaline.

Previous studies have shown that reduced sulfur ($H_2S$) for VMS systems comes from (1) bacterial sulfate reduction (BSR) of seawater sulphate, (2) thermochemical sulfate reduction (TSR) of sulfate from seawater or hydrothermal alteration products, and (3) igneous sulfur either via leaching from footwall volcanic rocks and/or direct contributions from magmatic fluids/volatiles (Seal 2006). Most of $\delta^{34}S$ values obtained from sulfides in this study are basically above 0‰, and lacking of framboidal pyrite in the Ashele deposit with relatively high temperatures (above 200 °C), indicating BSR is not a significant source of reduced sulfur in the Ashele deposit. Model calculations were undertaken to evaluate the relative contribution of igneous and TSR sulfur for sulfides, and the results show the increasing contribution of magmatic sulfur from the early (35%) to late (76%) stages.

## 5 Ore-forming process in the early massive sulfides and late vein-dominated chlorite-chalcopyrite stages

The calculated $\delta^{56}Fe$ isotope compositions of hydrothermal fluid associated with early stage Ccp1 range from -1.65‰ to -0.71‰ (avg. -1.01‰), which is lighter than the typical sub-seafloor hydrothermal fluids (-0.67‰–-0.09‰) and magmatic rocks (basalt, tuff, and dacite porphyry) in the ore district (~ 0‰). Based on Rayleigh fractionation modeling results, if Py1 and associated fluid have reached equilibrium in an open system, removal of 100% of the initial iron in the fluid as pyrite only lead to about 0.8‰ $\delta^{56}Fe$ drop of fluid, which could not explain $\delta^{56}Fe$ value of -1.65‰, however, in a closed system, the removal of 80% of the initial iron in the fluid as pyrite could shift the $\delta^{56}Fe$ of fluid from -0.30‰ towards -1.65‰. In addition, The studies of stratigraphic sequence and zircon U-Pb ages in the Ashele district have shown that basaltic magmatic activity occurred immediately after the formation of the massive ores and isolated them from oxygenated seawater. The underlying quartz-pyrite zone and the compact texture feature of massive ores would cause limited circulation between massive sulfides and the external fluid. As a result, the wide range of $\delta^{56}Fe$ in Py1 and Ccp1 of the Ashele deposit may have recorded the isotopic change controlled by pyrite-fluid equilibrium in a relatively closed system.

The calculated Fe isotope compositions of hydrothermal fluid associated with late stage Ccp2 range from -0.75‰ to -0.19‰ (avg. -0.53‰) based on the theoretical equilibrium calculation (Fujii et al. 2014), which is similar to that of seafloor hydrothermal fluids. The modal calculations indicate Fe isotope fractionations between Py2, Py3, Py4 and associated fluid have not reached equilibrium. In this study, the extent of Fe isotope exchange (F) relative to the equilibrium value for pyrite was simply calculated, and the results indicate the extent of Fe isotope exchange is gradually increasing from Py2, Py3 to Py4, represented by the increasing $^{56}Fe$ values in an open system.

The proposed model based on Fe, B and S isotope suggests long-term hydrothermal activities in the relatively closed systems promote the formation of upper massive ores at the early stage, and late hydrothermal activities in relatively open system would contribute to underlying stringer sulfides or stockworks.

## Acknowledgements

This study was funded by the National Natural Science Foundation of China (41725009, 42173065, U1603244, 41921003, 42003033), and the Strategic Priority Research Program of the Chinese Academy of Sciences (XDB42020404), the Science and Technology Planning of Guangdong Province, China (2020B1212060055), and the Guang Dong Major Project of Basic and Applied Basic Research (2019B030302013).

## References

Fujii, T., Moynier, F., Blichert-Toft, J. and Albarède, F. (2014): Density functional theory estimation of isotope fractionation of Fe, Ni, Cu, and Zn among species relevant to geochemical and biological environments; Geochimica et Cosmochimica Acta, v. 140, p. 553-576.

Galley, A.G., Watkinson, D.H., Jonasson, I.R. and Riverin, G. (1995): The subsea-floor formation of volcanic-hosted massive sulfide; evidence from the Ansil Deposit, Rouyn-Noranda, Canada: Economic Geology, v. 90, p. 2006-2017.

Piercey, S.J. (2015): A semipermeable interface model for the genesis of subseafloor replacement-type volcanogenic massive sulfide (VMS) deposits; Economic Geology, v. 110, p. 1655-1660.

Seal, R.R., II (2006): Sulfur Isotope Geochemistry of Sulfide Minerals; Reviews in Mineralogy and Geochemistry, v. 61, p. 633-677.

Trumbull, R.B., Codeço, M.S., Jiang, S.Y., Palmer, M.R. and Slack, J.F. (2020): Boron isotope variations in tourmaline from hydrothermal ore deposits: A review of controlling factors and insights for mineralizing systems; Ore Geology Reviews, v. 125, p. 103682.

Zheng, Y., Wang, Y.J., Chen, H.Y., Lin, Z.W., Hou, W.S. and Li, D.F. (2016): Micro-textural and fluid inclusion data constraints on metallic remobilization of the Ashele VMS Cu-Zn deposit, Altay, NW China; Journal of Geochemical Exploration, v. 171, p. 113-123.

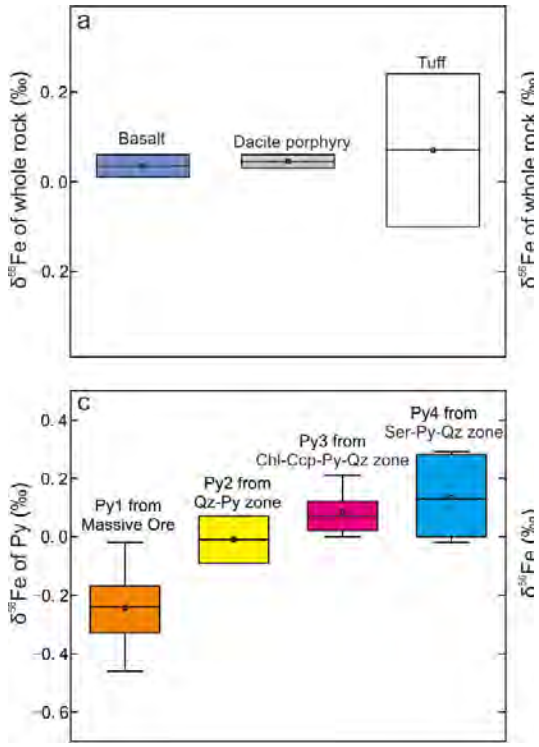


**Figure 1.** The ranges of Fe isotope for basalt, dacite porphyry and tuff (a); whole-rock from the massive ores, quartz-pyrite and chlorite-quartz-chalcopyrite-pyrite zones (b); pyrite from the massive ores, quartz-pyrite, chlorite-quartz-chalcopyrite-pyrite and sericite-pyrite-quartz zones(c); chalcopyrite and chlorite from the massive ores and chlorite-quartz-chalcopyrite-pyrite zones (d) in the Ashele Cu-Zn deposit

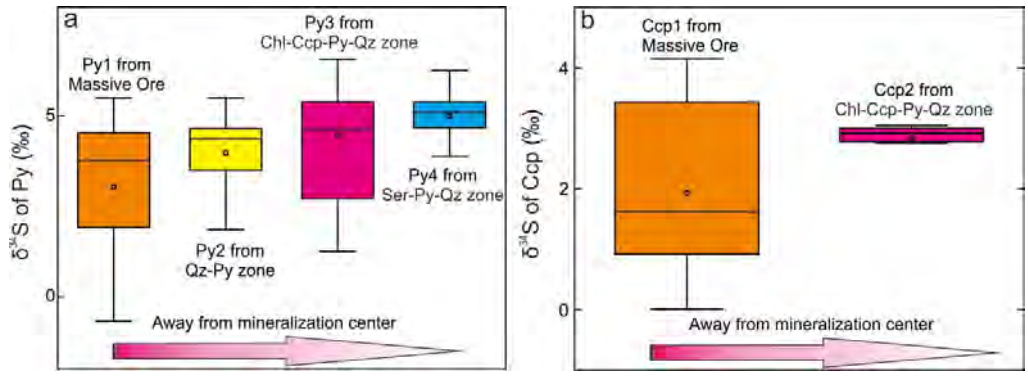


**Figure 2.** The ranges of S isotope for pyrite (a) and chalcopyrite (b) from the Ashele Cu-Zn deposi
t

# The Tectonic Evolution of the North New Hebrides Backarc Troughs: A Remote-Predictive Mapping Approach

**David J. Summer[1], Melissa O. Anderson[1], Philipp A. Brandl**
*[1]Department of Earth Sciences, University of Toronto, Canada [2]GEOMAR Helmholtz Centre for Ocean Research, Kiel, Germany*

**Abstract.** Extensional backarc basins are the modern analogue for the tectonic setting of many ancient Volcanogenic Massive Sulphide deposits and are the sites of modern Seafloor Massive Sulphide deposition. However, little is known about the tectonic processes involved in the opening of nascent backarc basins prior to the establishment of seafloor spreading. This study addresses the question: what is the tectonic evolution of the over-riding plate during the early stages of backarc basin development? To answer this, the ~3 Ma geodynamic history of the North New Hebrides Backarc (NNHB) is evaluated with respect to regional tectonic complexities. A 1:100,000 lineament map of the NNHB has been produced via integration of available bathymetry datasets. Morphotectonic and lineament classifications are accomplished via visualization in an ArcGIS workflow. Lineament mapping is used to resolve fault kinematics of centroid moment tensor data in seismically active areas. Lineament analysis, fault kinematics, seafloor morphology and crosscutting relationships of mapped features are used to assess stress regime changes in the North New Hebrides Backarc. Preliminary results reveal three stages of backarc basin opening: initial arc breakup, east-west directed rifting and ongoing transtensional rifting.

## 1 Introduction

Volcanogenic Massive Sulphide (VMS) deposits formed in a variety of submarine tectonic settings, including mid-ocean ridges, continental rifts, and backarc basins. However, most VMS deposits are interpreted to have formed in a rifted arc setting, which progress to deep backarc basins before basin closure and accretion onto continental margins (Hannington et al. 2005). In the modern seafloor setting, many Seafloor Massive Sulphide (SMS) deposits have been identified and described, including deposits located in extensional oceanic convergence zones. While the tectonic environment and local geologic controls on magmatism and hydrothermal systems are described, little is known about the early stages of arc rifting and nascent backarc basin opening in the context of magmatic-hydrothermal evolution. Specifically, it is unknown whether the magma plumbing in rifted backarc basins is inherited from the migrating arc and whether this scenario contributes to long-lived hydrothermal systems. These are fundamental gaps in our understanding about where large SMS deposits can be found.

The New Hebrides subduction zone (NHSZ) is uniquely suited to investigating the early stages of backarc basin formation. The New Hebrides Arc formed ~10 Ma, with backarc rifting commencing ~3 Ma as a result of complex tectonic events (detailed below). The recent availability of yet unexplored high- resolution bathymetry datasets provides the opportunity to visualize the backarc in detail. By developing a remote-predictive mapping approach unique to the region, interpretation of geologic features is made possible, culminating in the development of a detailed spatio-temporal model of the regional tectonic evolution.

## Tectonic Setting

The NHSZ is a ~10 Ma oceanic convergent boundary accommodating subduction of the Australia Plate beneath the North Fiji Basin (NFB) in the SW Pacific (Figure 1). Stretching from ~9.5-23°S, the subduction zone formed as a result of a

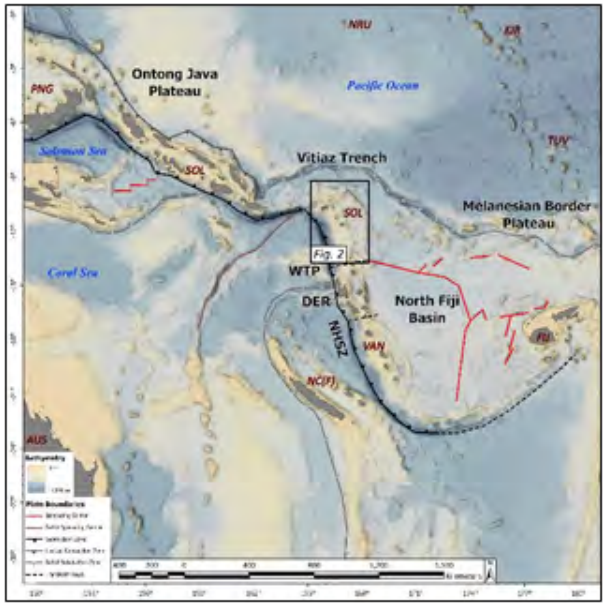


**Figure 1.** Regional map of the SW Pacific. The North New Hebrides Arc and Backarc are outlined by the Figure 2 box. Bathymetry data is from the Global Multi-Resolution Topography data syntheses.

subduction polarity reversal initiated by the arrival of the Ontong Java Plateau at the Vitiaz Trench (Petterson et al. 1999). Following subduction initiation, asymmetric rollback of the Australia Plate caused the opening of the NFB and clockwise rotation of the NHSZ (Schellart et al. 2006). Beginning ~3 Ma, arrival of the D'Entrecasteaux

Ridge (DER) at the New Hebrides Trench (NHT) between 15-16°S caused segmentation of the NHSZ with a central compression belt separating extensional zones to the north and south (Calmant et al. 2003). Extension in the North New Hebrides Subduction Zone (NNHSZ) resulted in the opening of NNHB. The NNHB widens and deepens northward from ~13.5°S, reaching depths of up to ~4000 m and terminating abruptly at a ~2 km high escarpment, the San Gerónimo Fault (SGF) at ~10°S. Collision of the DER with the New Hebrides Arc was followed by the arrival of the West Torres Plateau (WTP) at ~0.7-1.0 Ma directly north of the DER (Meffre and Crawford 2001).

## 2 Methods

### 2.1 Bathymetry Data

Seafloor visualization was achieved via the compilation of available ship-track bathymetry and the production of hillshade and slope raster datasets in an ArcGIS workflow. Raster resolutions ranges from 25- 150 m. Areas lacking ship-track bathymetry coverage are underlain by the Global Multi-Resolution Topography data synthesis.

### 2.2 Lineament mapping

Mapping of lineament feature was accomplished using a remote-predictive mapping approach, a process whereby bathymetric features are interpreted based on previously ground-truthed morphological properties. The most frequently observed lineament features observed in the NNHB are normal faults, which are characterized by an abrupt change in relief across a lineament (i.e. fault scarp), and volcanic fissures, which are characterized by symmetrical slopes on either side of the feature.

Mapped lineaments vary in length from ~100 m to several kilometers. To ensure proportional representation in lineament analysis using rose diagrams, all line segments are divided up into 100 m segments. The line segments are classified into eight different categories based on trend in order to produce a lineament orientation map (Figure 2).

### 2.2 Centroid moment tensor data

Centroid moment tensor (CMT) data for earthquake with Mw >5.0 were acquired from the global CMT project. CMTs up to a depth of 30 km were included to capture all crustal earthquakes. The dataset was imported into ArcGIS using the Arcbeachball tool. Each CMT has two possible focal planes. Where possible, the focal planes were resolved using local lineament features, assuming that fault plane of an earthquake will have a strike subparallel to the structures at surface. Where the focal plane of a CMT could not be resolved, CMTs were classified as general fault types.

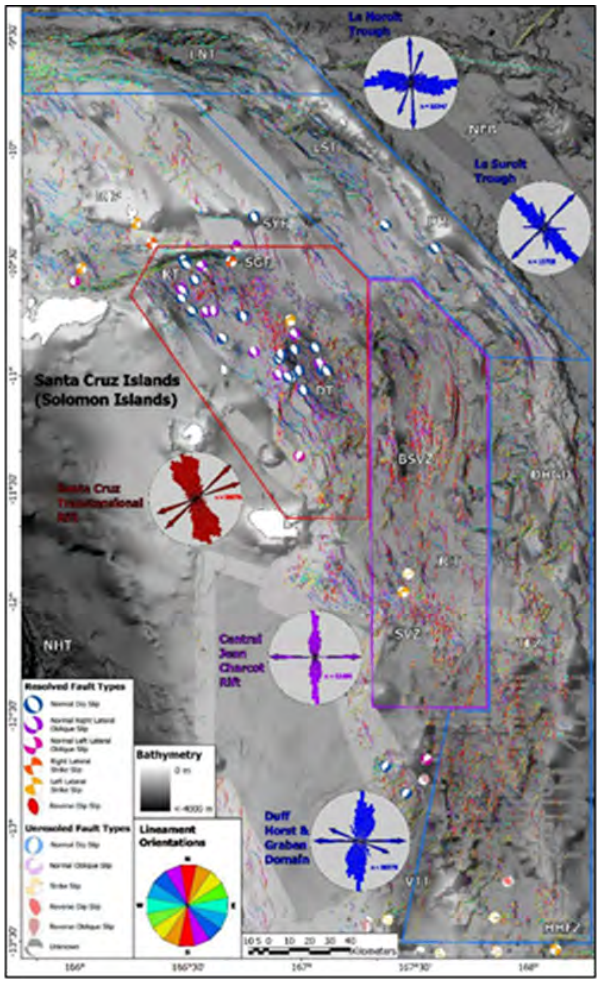


**Figure 2.** Lineament orientation map of the NNHSZ. Polygons and rose diagrams are colour-coded based on stage of backarc opening: blue = initial arc breakup, purple = central JCT rift, red = SCTR. Arrows on rose diagrams represent principal extension directions (perpendicular to lineament orientations). See in-text for acronym meanings.

## 3 Morphology and Lineament Analysis

### 3.1 North New Hebrides Arc Break-up

The Duff Ridge (DR) is arcuate ridgeline that forms the northern boundary of the NNHB, separating it from the NFB. It is a relict arc recording the position of the North New Hebrides Arc (NNHA) prior to the rift initiation (Auzende et al., 1995). Trench-ward from the DR are two sedimented, flat-bottomed rift basins elongated parallel to the ridgeline. The E-W oriented Le Noroît Trough (LNT) reaches depths of ~4300 m and is bound to the south by a series of fault scarps with a cumulative throw of ~3000 m that rise to the floor of the Reef Islands Plateau (RIP), a region of relict arc/forearc rifted from the DR. The NW-SE oriented Le Suroît Trough (LST) reaches depths of ~3600 m and is bound by a ~500 m footwall to the SW, from which the RIP shoals westward towards the Reef Islands.

At its southeast end, ~11°S, the DR curves to a N-S trend where the ridge morphology yields to the Duff Horst and Graben Domain (DHGD). The horst and graben fragmentation of the relict arc is characterized by an arrangement of tilted horst structures with prominent, anastomosing W- to WNW-dipping fault scarps which bound discontinuous sedimented half- graben basins extending south to the Tikopia Fracture Zone (TFZ). The TFZ is an E-W trending structure in the NFB that intersects the backarc at ~12.2°S. South of the TFZ, the relict arc is more heavily fragmented and consists of smaller horst structures and lower relief footwall scarps. The exception to this is a single, prominent ~100 km long escarpment which is a boundary fault separating the relict arc DHGD from a single narrow basin, the Vot Tande Trough (VTT).

Lineament analysis reveals two peak lineament orientation frequencies at 0-5° and 20-25° in the DHGD. Lineament orientations combined with left-lateral offset ridgelines indicate a transtensional stress regime with conjugate normal-oblique to oblique-strike slip faulting. From its northern extent at ~11°S, the DHGD widens from ~20 km to ~65 km at ~13.5°S where the NNHB abruptly terminates and intersects the Hazel Holme Fracture Zone (HHFZ), a slow E-W trending spreading centre in the NFB. The geometry of the DHGD together with indicators for transtensional tectonics reveals that deformation in this region accommodated clockwise rotation of the NNHA.

Lineament analysis of the troughs paralleling the DR reveal peak lineament orientation frequencies of 85-90° and 110-115° in the LNT and 140-145° in the LST. This indicates SW-directed rifting of the RIP with respect to the DR and NFB. The timing of the rifting with respect to the DHGD formation is unclear.

### 3.2 Central Jean Charcot Rift

The central NNHB is characterized by uniform N-S-trending lineament orientations, suggesting a transition from transtensional to E-W extensional tectonics. The seafloor morphology, however, is highly variable within this zone. To the north of the VTT the Starfish Volcanic Zone (SVZ) occupies an area of ~1500 km2 at the western termination of the TFZ. The SVZ has high relief relative to the surrounding basins and is characterized by high density of volcanic cones (<3 km in width) and volcanic fissures (<3 km in length) and a central large volcanic edifice, the Starfish Volcano (~10 km wide) at about 12.2°S.

To the north of the SVZ, is the sedimented Jean Charcot Trough (JCT), which lacks volcanism and has a sparsity of lineaments. The JCT reaches a maximum depth of ~3200 m and is bound to the west by rifted arc volcanic crust and to the west by an oceanic core complex (OCC). The OCC rises to a depth of 1900m and lies just to the west of the DHGD. Striations on the exhumed OCC record an extension direction consistent with the principal WNW-ESE extension indicated by lineament analysis in the DHGD.

In the north end of the JCT is the Brittle Star Volcanic Zone (BSVZ) with an area approximately the same as the SVZ. This area features prominent N-S striking normal faults with scarp lengths of up to ~80 km. At the centre of the volcanic zone is a ~10 km wide rift valley reaching up to ~3500 m in depth with ridge crests up to 1500 m high. The axial valley has a hummocky floor indicating recent volcanic activity. To the east, a parallel, long and narrow rift valley has a sedimented floor, suggesting that rifting has migrated from east to west. North of the BSVZ, the main rift valley deepens to a maximum depth of ~4000 m. North of ~10.8°S, N-S trending lineaments become sparse in hummocky terrain that shoals northward to depths of 2200-1700m.

### 3.3 Santa Cruz Transtensional Rift

To the east of BSVS lies the Santa Cruz Transtensional Rift (SCTR). The southwestern end of this zone features the Dolphin Trough (DT), a ~65 km long, ~20 km wide sigmoidal shaped basin. The morphology of this basin is characteristic of transtensional basins (cf. Wu et al. 2009). The basin footwall scarps reach maximum throws of ~1700 m and ~2600 m on the eastern and western flanks, respectively. The two bounding horsts have been offset oblique to the cross-basin axis of the basin. South from the western basin footwall, the escarpment fans out into a series of en echelon normal faults. To the southwest of the basin, a sequence of parallel NNW-SSE trending faults produces a terraced morphology, stepping up towards an arc-front volcano. To the northwest of the basin is the Kaiyo Trough (KT), which deepens northward, has a hummocky and heavily faulted morphology and is populated with numerous volcanic fissures and rifted volcanic edifices. The KT terminates at the E-W trending SGF. The SCTR is the most seismically active location in the NNHB. The resolved focal planes of the CMT data reveal prevalent NW-SE striking normal dip slip to left lateral oblique slip fault kinematics. Lineament analysis of the region reveals two peak lineament orientation at 145-150° and 160-165°. The morphology of the basin, lineament analysis, and the fault kinematics in both the KT and DT indicate transtensional tectonics accommodating counter-clockwise rotation of the northernmost region of the arc (i.e., the Santa Cruz Islands). As indicated by CMTs, the SGF and a parallel fault to the north, the Santa Ysabel Fault (SYF) are crustal-scale faults that accommodate dextral displacement of the active NNHA from the dismembered, relict arc RIP segment.

## 4 Discussion and Conclusion

The opening of the NNHB troughs began ~3 Ma (Monjaret et al., 1991), coeval the DER collision. The resultant compression in the central NHSZ and continued retreat of the subducting plate to the north created the conditions for arc segmentation and rifting in the NNHB. The timing of the opening of the LNT and LST relative to the formation of the DHGD is unclear but occurred earlier than rifting in the JCT as indicated by the sedimented basin floor in the former as compared to the hummocky morphology indicating relatively recent volcanism in the latter. Rifting of the RIP from the DR can be attributed to continued retreat of the subducting slab. The RIP had been the northern most extent of the NNHA but had translated away from the subducting slab during the earlier ~10-3 Ma clockwise arc rotation and no longer experienced the force of slab suction. Slab retreat induced the crustal- scale rupturing that formed the SYF and SGF, suspended extension in the LNT and LST, and dislocated the RIP from the rest of the arc.

Formation of the SGF boundary likely permitted the JCT rift stage of backarc opening by accommodating dextral motion in the north. Rifting was accompanied by profuse volcanism in the SVZ and the BSVS, with the latter developing a deep axial valley reminiscent of slow ocean spreading centers. Dating of dredged seafloor samples with backarc basin basalt signatures from the SVZ indicate opening of the JCT at ~2.3 Ma (Monjaret et al. 1991; Maillet et al. 1995). It is unknown how volcanically active the JCT rift is currently, however seismic quiescence in the region suggests reduced volcanism in the region.

Transtension in the seismically active SCTR was likely induced by the arrival of the WTP at the NHT at ~0.7-1.0 Ma. Incipient compressional tectonics inboard of the trench is evidenced by forearc uplift (West Torres Islands; Calmant et al. 2003) and may explain discontinuation of rifting in the JCT. Arrival of the WTP likely caused emplacement of a rotation hinge point in the NNHA. This agrees with a pole of rotation just south of the SVZ as determined Bergeot et al. (2009). Current convergence rates at the north end of the NNHSZ are ~150-170 mm/yr, with ongoing slab retreat being accommodated by ~80 mm/yr of backarc extension (Calmant et al. 2003). The asymmetry in convergence caused by compression induced by the arc-plateau collision in the south and slab retreat in the north can explain the current transtensional tectonics in the SCTR.

## Acknowledgements

The authors gratefully acknowledge IFREMER, Neptune Minerals Inc., and Nautilus Minerals Inc. for contributing bathymetry data to this study. Funding for this project was provided by OGS and NSERC-CREATE grants awarded to D.J.S.

## References

Auzende JM, Pelletier B, Eissen JP (1995) The North Fiji Basin geology, structure, and geodynamic evolution. In: Taylor B (ed) Backarc basins: Tectonics and magmatism: 139-75.

Bergeot N, Bouin MN, Diament M, Pelletier B, Régnier M, Calmant S, Ballu V (2009) Horizontal and vertical interseismic velocity fields in the Vanuatu subduction zone from GPS measurements: Evidence for a central Vanuatu locked zone. J Geophys Res: Solid Earth 114: B6.

Calmant S, Pelletier B, Lebellegard P, Bevis M, Taylor FW, Phillips DA (2003) New insights on the tectonics along the New Hebrides subduction zone based on GPS results. J Geophys Res: Solid Earth 108: B6.

Hannington MD, de Ronde CEJ, Petersen S (2005) Sea-Floor Tectonics and Submarine Hydrothermal Systems. In: Hedenquist JW, et al. (eds) 100th Anniv Vol Econ Geol, SEG, Littleton, CO: 111–141.

Maillet P, Ruellan E, Gérard M, Person A, Bellon H, Cotten J, Joron JL, Nakada S, Price RC (1995) Tectonics, magmatism, and evolution of the New Hebrides backarc troughs (Southwest Pacific). In Taylor B (ed) Backarc basins: Tectonics and magmatism: 177-235.

Meffre S, Crawford AJ (2001) Collision tectonics in the New Hebrides arc (Vanuatu). Island Arc 10: 33-50.

Monjaret MC, Bellon H, Maillet P (1991) Magmatism of the troughs behind the New Hebrides island arc (RV Jean Charcot SEAPSO 2 cruise): K-Ar geochronology and petrology. J of Volcanol and Geotherm Res 46: 265-80.

Petterson MG, Babbs T, Neal CR, Mahoney JJ, Saunders AD, Duncan RA, Tolia D, Magu R, Qopoto C, Mahoa H, Natogga D (1999) Geological–tectonic framework of Solomon Islands, SW Pacific: crustal accretion and growth within an intra-oceanic setting. Tectonophys 301: 35-60.

Schellart WP, Lister GS, Toy VG (2006) A Late Cretaceous and Cenozoic reconstruction of the Southwest Pacific region: tectonics controlled by subduction and slab rollback processes. Earth-Sci Rev 76:191-233.

Taylor FW, Bevis MG, Schutz BE, Kuang D, Recy J, Calmant S, Charley D, Regnier M, Perin B, Jackson M, Reichenfeld C (1995) Geodetic measurements of convergence at the New Hebrides island arc indicate arc fragmentation caused by an impinging aseismic ridge. Geology 23: 1011-4.

# Known and potential types of gold mineralization in the Muruntau gold district

**Alexander Antonov[1], Vladimir Tsoy[2]**
*[1]Canada Eurasia Chamber of Commerce, Uzbekistan Chapter, Tashkent, Uzbekistan*
*[2]Institute of Mineral Resources, Tashkent, Uzbekistan*

**Abstract.** The conducted assessment of structural features of Muruntau district's gold deposits together with clarification of their mineral composition has revealed that besides the well-known and mined mineralization in sandstone/shale strata, mineralization of Carlin type, represented by "invisible" micron and nano-sized gold particles in carbonate sedimentary rocks, may be revealed in the mineralized zones. It is shown that gold-bearing zones of silicification concordant to hosting rocks at the super-large Muruntau deposit are metasomatically altered carbonate sedimentary rocks. One of the criteria for the original carbonate nature of the concordant silicification zones is the predominance of carbon dioxide in the gas-liquid inclusions of the ore matrix. The highest probability for discovering Carlin-type mineralization is f the Kokpatas-Okzhetpes trend in the northern part of the Muruntau district. Further studies of ore zones and the presence of invisible nano-sized gold can stimulate the improvement of ore processing flowsheets and increase the gold recovery at the processing mills of the district.

## 1 Introduction

Muruntau (Central Kyzylkum) district is one of the largest gold districts in the world (Shayakubov 1998). The discovered reserves and resources are of similar amounts to the gold systems in northeastern Nevada (Carlin trend, etc.).

Large sediment-hosted gold deposits (Daugyztau, Amantaytau, Kokpatas, etc.), including the super large Muruntau deposit (initial reserves about 180 Moz), were formed in the area at the end of the Hercynian epoch (Permian-Triassic) after the Turkestan Paleo-ocean closure.

In contrast to the north-eastern Nevada deposits, where terrigenous and carbonate layers are interbedded, the Muruntau district's deposits are hosted by terrigenous sandstone-shale units. The opinion that gold-bearing fluids do not penetrate limestones and are blocked by the Devonian carbonate rocks dominated the local literature in the past. The nature of primary carbonate within the silicified layers in the predominantly terrigenous Besapan ore-bearing suite was not recognized.

The authors disagree that the ore-bearing strata of interbedded sandstones, siltstones, shales and flints has no interlayers of carbonate rocks. Tsoy (2001) proposed the theory of "apo-carbonate" origin of interlayers and lenses of quartzite and flint. They are considered as the original carbonate rocks - limestone and dolomite, altered during the metasomatism until complete replacement by silica.

This extended abstract considers the results of the analyses of silicified, interbedded rocks at the Kokpatas deposits in the Muruntau district. At the north-eastern flank of Muruntau, 2200-meter-deep boreholes intersect flat ore bodies of apo-carbonate origin, concordant to the bedding of the sedimentary rock.

The Kokpatas deposit is considered by the authors as the most realistic target, within the Muruntau district, for detecting Carlin type mineralization including invisible gold. This extended abstract draws attention to the insufficient study of micron- and nano-sized gold inclusions in sulfide minerals. It is indicated by Sanakulov et al. (2019) that the concentration of invisible gold can reach 2-5 g/t for the entire gold-bearing ore mass. The study of "invisible" gold and exploration of Carlin type mineralization in the Muruntau district can have great economical impact.

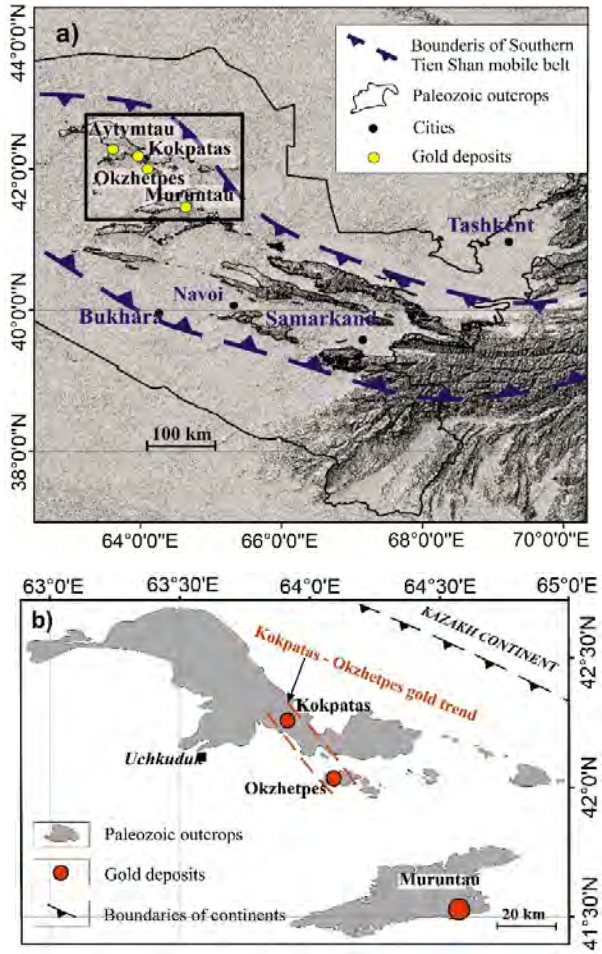


**Figure 1. a** Location of the Muruntau gold district in the Southern Tien-Shan mobile belt (box; see part b); **b** Schematic map of gold deposits in the Muruntau district from which samples were taken.

## 2 Methodology

The mineralized zones exposed by boreholes and trenches were studied during the research. Various samples were taken for further mineralogical-petrographic and geochemical studies.
The chemical composition of ores and ore-bearing rocks was studied by total silicate analysis. Contents of main and associated components were determined by spectral semi-quantitative, ICP mass-spectrometric, atomic absorption methods.
Mineral composition of ores, their structural-textural features, and hydrothermal alteration characteristics are determined by research of thin sections, polished thin sections (Nikon Eclipse LV100 Pol), and mineralogical analysis of heavy fractions. The composition of the main and associated components was identified by X-ray spectral local analysis on a microprobe (JEOL "Superprobe" JXA -8800R).
Fluid inclusion study of different quartz taken from the deep drill holes shows that one of the main components of vacuole fluids is carbon dioxide. The presence of carbonic acid in the gas-liquid inclusions indicates the original carbonate composition of layered or metamorphogenic quartz veins.

## 3 Apocarbonate mineralization: metasomatic processes cause limestone and dolomite layers to be altered into silicified, concordant gold-bearing zones.

The presence of carbonate rocks at the Muruntau and Daugyztau deposits, where the main gold value is associated with concordant silicification zones, is confirmed by silicate analysis (Table 1). The gold content of the carbonate rocks depends on the degree of silicification. Intensely silicified dolomites and limestones usually contain higher gold mineralization. Less silicified carbonate rocks, when their original composition is distinguishable, contain gold up to tenths of g/t. In addition to gold, scheelite, pyrite, arsenopyrite, stibnite?, and other minerals are found in these rocks.
Silicified carbonate interlayers, lenses altered into quartzites and jasperoids with gold and antimonite mineralization were identified at the Daugyztau deposit. XRD phase analysis revealed quartz, dolomite and sericite in apocarbonate formations.
Table 1 lists the results of silicate analyses of two metallurgical samples suggesting that ore-bearing rocks contain carbonates (dolomite and ankerite) in the amount of CaO – 1,06-3,23 wt% and MgO – 1,25-1,08 wt%. The converted mineral composition is presented by quartz, feldspars, carbonates (dolomite and ankerite), hydromicas, kaolinite, carbonaceous matter, jarosite, goethite, hydrogetite, pyrite, arsenopyrite, skorodite, galenite, sphalerite, valentinite, chalcopyrite, cerargyrite, embolite, Ag sulphosalts, native gold and silver, confirming the former findings of Zairi (1992).
These results show that the ore-bearing rocks contain carbonate interlayers, which were silicified, with the formation of quartzites, flints, and jasperoids. In the latter, antimonite mineralization was identified.
According to Graupner et al. (1999) layered and intersecting Muruntau quartzes have differences in gas-liquid inclusions. Thus, in layered quartz phase separation does not occur, whereas in intersecting quartz there is evidence for phase separation. Layered quartz is less gold-bearing, opposite to the intersecting ones. The composition of the gas phase is dominated by carbon dioxide. These facts confirm the validity of our point of view with regards to the apocarbonate nature of layered quartz.

**Table 1.** Results of silicate analyses of metallurgical samples at Daugyztau deposit (Irgiredmet data).

| Component | Content, % | | Component | Content, % | |
|---|---|---|---|---|---|
| | sample № 48 | sample № 65 | | sample № 48 | sample № 65 |
| SiO2 | 61,46 | 64,32 | S total | 2,34 | 1,76 |
| Al2O3 | 14,72 | 12,08 | S sulf. | 0,44 | 1,75 |
| Fe2O3 | 6,53 | 3,73 | As | 0,04 | 0,09 |
| TiO2 | 0,36 | 0,35 | Sb | 0,04 | 0,028 |
| CaO | 1,06 | 3,23 | C total | 1,07 | |
| MgO | 1,25 | 1,08 | C organic | 0,11 | |
| K2O | 2,92 | 2,18 | Au g/t | 1,8 | 1 |
| Na2O | 1,24 | 1,24 | Ag g/t | 4 | 53,2 |

## 4 Prospects for discovery of Carlin type gold deposits in the structures of the Kokpatas - Okzhetpes trend

The northwest striking Kokpatas - Okzhetpes trend is one of 10 trends in the Kyzylkum ore district, at the marginal sutural zone of the closed Turkestan Ocean (Antonov and Nurtayev 2022).
The Kokpatas and Okzhetpes deposits are most similar to the Carlin-type mineralization. In contrast to other Kyzylkum trends, ore bodies are mostly localized in limestone layers (Bulutkan, Barkhanniy, zones 2, 9, Sardor of Okzhetpes ore cluster). We define silicified carbonate interlayers and lenses in terrigenous formations at the Kokpatas-Okzhetpes trend. They are similar to those identified in the Muruntau deposit, which were previously mapped as metamorphosed quartz veins. The findings of our research confirm the data of Graupner et al. (1999) on the compositional differences of gas-fluid inclusions in: 1) layered, and 2) intersecting quartz-vein systems. The layered quartz veins lack evidence for phase separation, whereas the intersecting quartz veins record phase separation. Importantly, layered quartz is less gold-bearing than intersecting quartz. Carbon dioxide predominates in the gas phase. These facts indicate the apo-

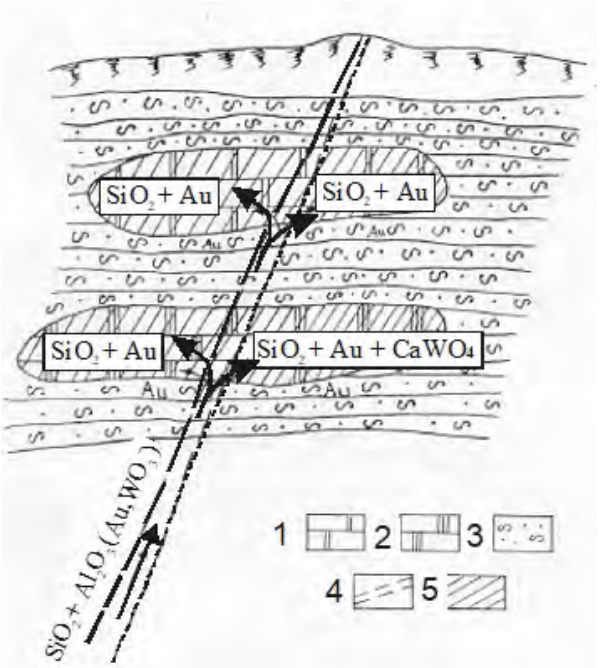


**Figure 2.** Scheme of the formation of apocarbonate gold mineralization at the Muruntau district. 1-dolomites, 2-quartzites, 3-terrigeenous rocks, 4- ore-bearing fault, 5- ore bodies.

carbonate nature of layered quartz. The following pattern of gold mineralization formation is assumed for the reviewed deposits, including the Kokpatas-Okzhetpes trend.

Carbonate and terrigenous rocks with lenses, interlayers of carbonate rocks (at the Kosmanachi strata, Taskazgan, Besapan, Kokpatas and other suites) are affected by hydrothermal siliceous fluids with gold and WO3 anions, resulting in the formation of quartzites, jasperoids, gold-hosting flints, scheelite, locally stibnite and others. Gold is deposited in the process of the neutralization of acidic hydrothermal fluids in interaction with carbonate rocks. The association of gold mineralization with carbonate relics in quartz is commonly observed under the microscope and on the raster images of microprobe studies (Figure 3 a and b).

The Kokpatas-Okzhetpes trend's deposits have one more feature similar to the Carlin-type mineralization - the presence of micron- and nano-sized gold inclusions. Sanakulov (2019), Koneev et al. (2019), and Tsoy et al. (2011) provide evidence that colloidal and ionic forms of disseminated gold prevail in the "black-shale" ore deposits of gold-sulfide type, whereas the native form is predominantly represented by fine-dispersed nano-sized particles.

Its practical significance is that the main losses in the commercial gold extraction are associated with micron- and nano-sized gold fines. According to the above analytical studies, the amount of nano-sized gold contained in sulfide, arsenide and other ore minerals reaches 2-5 g/t for the whole mass of the gold-bearing ore.

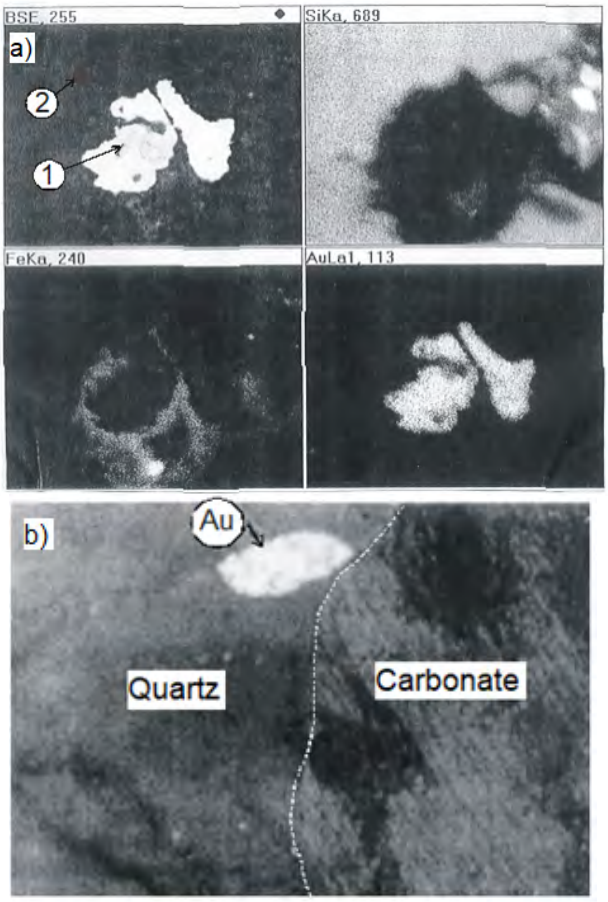


**Figure 3.** **a** Native gold (1) in quartz (2). Raster pictures show the presence of Si, Fe, Au. Photo from the Barkhanniy deposit, magnification 2000x zoom. **b** Native gold (1) in quartz (2). Raster pictures show the distribution of Si, Fe, Au. Photo from the Barkhanniy deposit, 2000x zoom

## 5 Conclusions

The study of mineralogical features in deposits from the Muruntau district shows that, in addition to long-term developed and mined gold deposits in sandstones-shales sequences, gold mineralization in limestones and dolomites of Carlin style can be revealed. We have concluded that the nature of layered silicified gold-bearing zones in the Muruntau ore field is primary carbonate, which is supported by the predominance of carbon dioxide in the gas phase of vacuoles. "Invisible" micron- and nano-sized gold dissemination, which can reach 20-30% of the total amount, is widespread in the deposits of the Kokpatas-Okzhetpes gold trend. Additional study of "invisible" gold will help increasing gold recovery in processing plants of the Muruntau gold district (Sanakulov et al. 2021).

## References


Antonov AE, Nurtayev BS (2022) Typical features of Carlin type gold deposits (CTGD)how consistent are they? KTGD (Kyzylkum type gold deposits), Uzbekistan, Southern Tien-Shan, vs CTGD. Proceedings of the 16th SGA Biennial Meeting, 28-31 March 2022, 2:5-8

Graupner T, Kempe U, Spooner ETC, Bray CJ, Kremenetsky AA (1999) Characterization of fluids from the giant Muruntau Au-ore field, Uzbekistan, utilizing fluid inclusion microthermometry, volatile and dissolved anion/cation data. Mineral Deposits: Processing, Stanley et al. (eds), Balkema, Rotterdam.

Koneev RI, Khalmatov RA, Krivosheeva AN (2019) Forms of occurrence and micro-nano ensambles of gold as indicators of formation conditions, spatial distribution, and type of orogenic deposits in Uzbekistan (South Tien Shan), Zapiski RMO (Proceedings of the Russian Mineralogical Society). Vol. 148, N. 4, pp 30-46

Sanakulov K, Adizov LA, Tkachenko ES (2021) Improvement of technological processes for processing gold-containing ore at Hydrometallurgical plant № 2. Gorniy Vestnik of Uzbekistan #4 (87), pp 51-55 (in Russian)

Sanakulov KS, Khvan AB (2019) Nanogold and the possibility of its extraction (review). Gorniy Vestnik of Uzbekistan#1 (76), pp 96-102

Shayakubov TSh (ed.) (1998) Gold deposit Muruntau. FAN, Tashkent, 539 pp (in Russian)

Tsoy VD (2001) Quartz-carbonate-gold (apocarbonate) formation and its role in the expansion of the mineral resource base of Uzbekistan. Proc. of Conf. Actual Problems of Development of Mineral Deposits. Tashkent, pp 136-137 (in Russian)

Tsoy VD, Koroleva IV, Munduzova MA et al. (2011) Unconventional apocarbonate type of gold mineralization in Uzbekistan. Tashkent: GP NIIMR. 174 pp (in Russian)

Zairi NM (1992) Isotopic-geochemical models of formation of deposits of gold-carbon formation: Abstract. Dissertation. 46 pp (in Russian)

# Distribution of Elements in Gold Grains: Implications for Mineralization

**David Banks[1,2], Robert Chapman[1], Olga Borovinskaya[3]**
*[1] School of Earth and Environment, University of Leeds, Leeds, LS2 9JT, U.K.*
*[2] Department of Geological Engineering, Istanbul University-Cerrahphasa, Istanbul, Turkiye.*
*[3] TOFWERK, Thun, Switzerland.*

**Abstract.** Multi-element analyses by LA-ICPMS is a well-established technique for many minerals. The superior detection limits compared with EPMA offers the possibility that many elements can be used to understand the mineralizing process and act as discriminants between deposits. In studies of placer gold grains, different elements have been used to infer the style of mineralization and the possible source. However, the mode of occurrence of elements within the gold grains is largely unknown and therefore has implications when data is interpreted. LA-ICPMS(ToF) element mapping of gold grains, at a resolution of 5µm, revealed different modes of occurrence. Ag is always an alloy element and where their concentration is high enough as are Cu, Hg, Sb and Pd. A variety of mineral inclusions are also present with pyrite containing a large number of elements that are not present in the gold. Other elements, such as the PGE's, are present but predominantly as nanoparticles. Interpretation of analyses must consider how elements are present and associated with each other.

## 1 Introduction

Natural gold grains are an alloy of different elements, the most common and in the highest concentration being silver. Other frequent alloy elements are copper, mercury, antimony and palladium which can have concentrations at the percent level but are usually much lower. Many additional elements can be present at ppm or ppb concentrations (Banks et. al. 2018). Analysis by EPMA depends on the concentration and frequently for the latter elements is below the detection limits. Grains are often not homogeneous and may contain inclusions of different minerals which can observed and identified by SEM-BSE (Chapman et. al. 2021a). However, inclusions come in a range of sizes and the smallest are often not identified or may be below the surface. Thus, when analysed by Laser Ablation the data may erroneously be attributed to the composition of the gold especially when prior SEM investigation of the polished grains is not carried out (Chapman et. al. 2021b). This is evident in some previous research.

LA-ICPMS is an established technique for determining the spatial distribution of elements in various minerals. In ore deposit studies pyrite is commonly analysed and the element concentrations and distributions has led to a greater understanding of mineralizing processes. Mass spectrometry analysis utilises a sequential measurement of the individual elements. Recent advances in instrumentation have greatly reduced the time for a sweep through the masses chosen, improving the ability to determine elemental associations. However, the elements to be determined must be chosen prior to analysis. This study uses Laser Ablation with Time of Flight Mass Spectrometry (LA-ToFMS) of the different elements. This essentially determines the presence of all elemental isotopes, that are above the detection limit, instantaneously. This avoids missing elements that are present, but were not chosen to be analysed, and a better understanding of element associations.

## 2 Analytical Method

Placer gold grains were mounted in resin blocks with the flattest surface at 90° to the horizontal plane. These were then polished to expose the maximum area of the centre and the minimum of the external surface. The selected grains were ablated, and the material analysed by ToF-MS at TOFWERK, Thun, Switzerland using an ArF excimer laser at 20 Hz frequency, continuously scanning over lines at 100 µm/s, providing no interpixel overlap. An area of 550 µm x 500 µm could be mapped at 5-µm resolution in 12 min, with all isotopes measured simultaneously for each 5-µm pixel. The element maps in Figures 1-3 are based on the signal intensity and not concentration.

## 3 Element Distributions

As gold is a metal, the nature of the bonding with elements that form an alloy is different to other minerals. Alloys are defined by their metallic bonding and can be classified as substitutional where a gold atom is replaced by another element, most commonly silver. Where substitution does not occur as the replacement element is too small to fit in the structure the alloy is deemed to be interstitial in nature. Where different elements are present, the alloy may be both substitutional and interstitial. Alloys can be manufactured using different elements to produce desirable characteristics. In nature silver is the most common alloy element and may also include copper and mercury in many instances with antimony and palladium in a lesser number of cases. Whether individual gold grains are a homogeneous alloy is a matter of chance. In Figure 1, the first grain shows a homogeneous alloy of gold silver and, to a degree, mercury. There is increased gold and decreased silver around the edges which is normal for grains from a placer environment.

In Figure 2 an area of with a high number if inclusions (part of Figure 1) is shown in greater

**Figure 1.** Element maps of two gold grains at a resolution of 5µm. The top 3 images show a homogeneous distribution of Au and Ag and to a slightly lesser degree Hg. Au concentrations are highest at the edge and Ag lowest. Hg shows a diffusion from the center to the edge where the concentration is highest. The second grain (middle and bottom 6 images) shows variability in the Au and Ag concentrations and is not homogeneous. Hg has areas of very high concentrations and again a diffusion to grain boundaries. This grain has several different mineral inclusions of variable size and different element content.

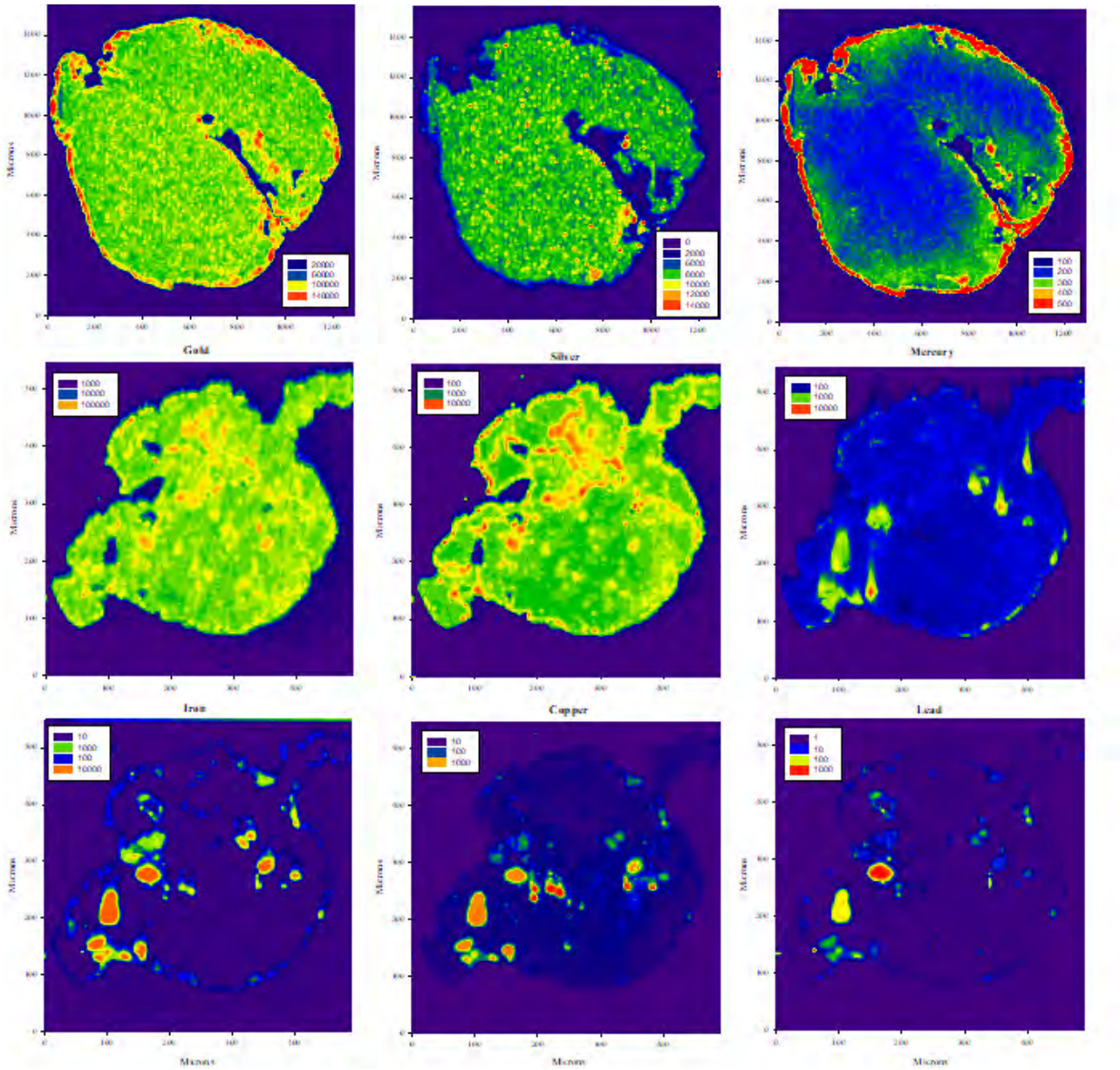


detail. Iron (pyrite) is greater than copper in some inclusions but there are also copper only inclusions with very low concentrations of iron. Other elements shown are also contained in the pyrite. The 4 copper inclusions have no other associated elements. Bismuth and lead are associated with pyrite and together with uranium, tellurium and antimony also occur as much smaller inclusions. All REE were determined, but these are not distributed evenly within the pyrite or relative to each other, cerium being an example. Clearly there is information from the analyses of the different inclusions that can be combined with the alloy data to improve interpretation of the mineralization process.

**Figure 2.** Element maps of some of the larger mineral inclusions. Pyrite is the host for the majority of elements, including those not shown here. Mn, Hg, Ce, for example, are not homogeneously distributed in the pyrite and may be different minerals or exsolution features.

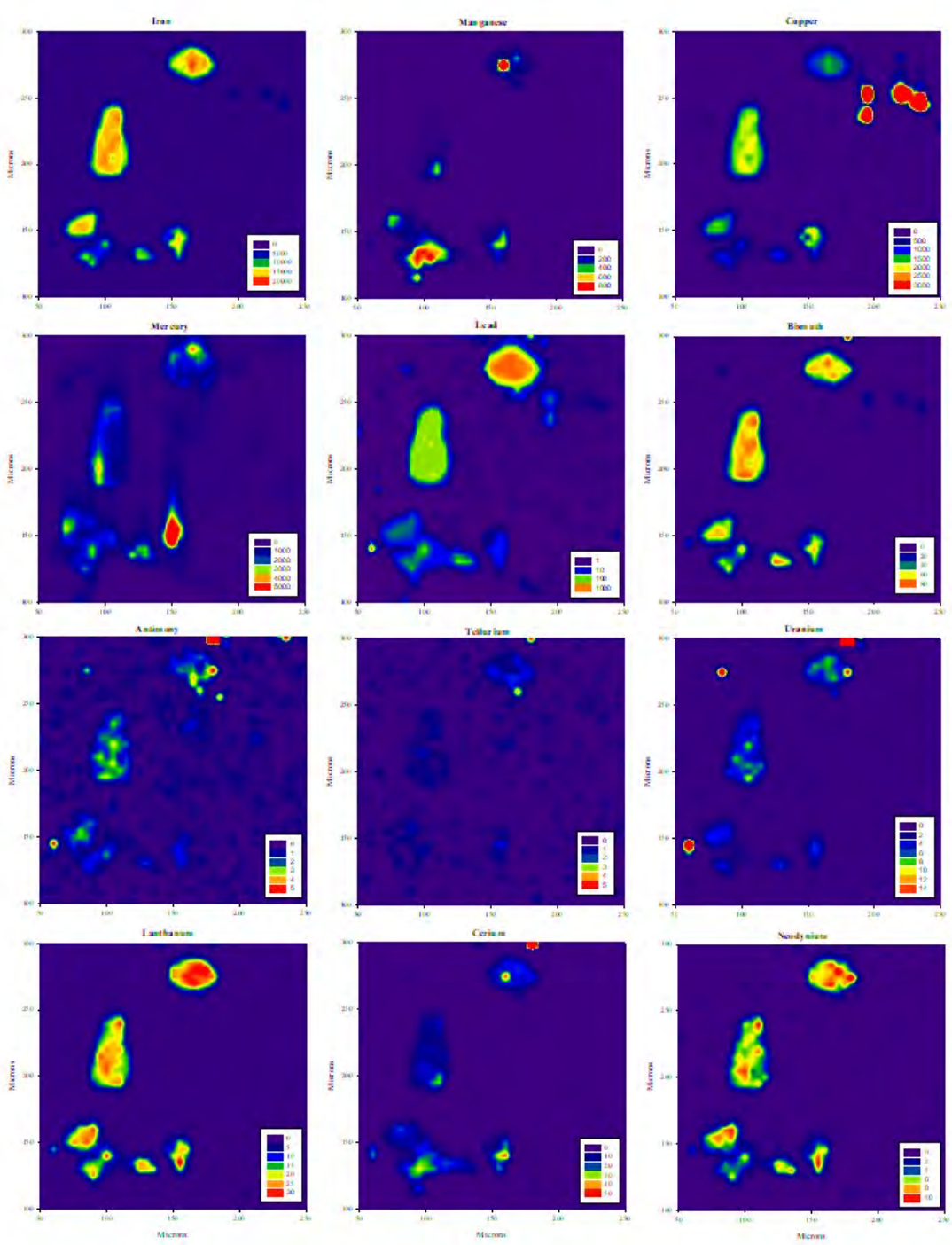


In Figure 3 there are examples of elements that are present as inclusions at ppb or lower concentrations contained in one 5µm ablation spot They are best described as nanoparticles, possibly transported by the mineralizing fluid and trapped as the gold was precipitated or co-precipitated with the gold particles. Other PGE and transition metals can occur in the same manner. Rhenium-osmium and platinum-iridium always show a strong association.

Analysis of gold grains by LA-ICPMS(ToF) clearly shows that any elemental analyses needs to be carefully considered with respect to how it may be present in the sample. The location for ablation must exclude any visible inclusions, but these may be present beneath the surface and hence unavoidable when ablated. SEM observation should be made to identify any visible inclusions which can then be used to interpret their element analyses after laser ablation.

## 4 Conclusions

**Figure 3.** PGE element maps with nanoparticles in individual ablation spots. These are likely to have been transported in this form and trapped as the gold precipitated.

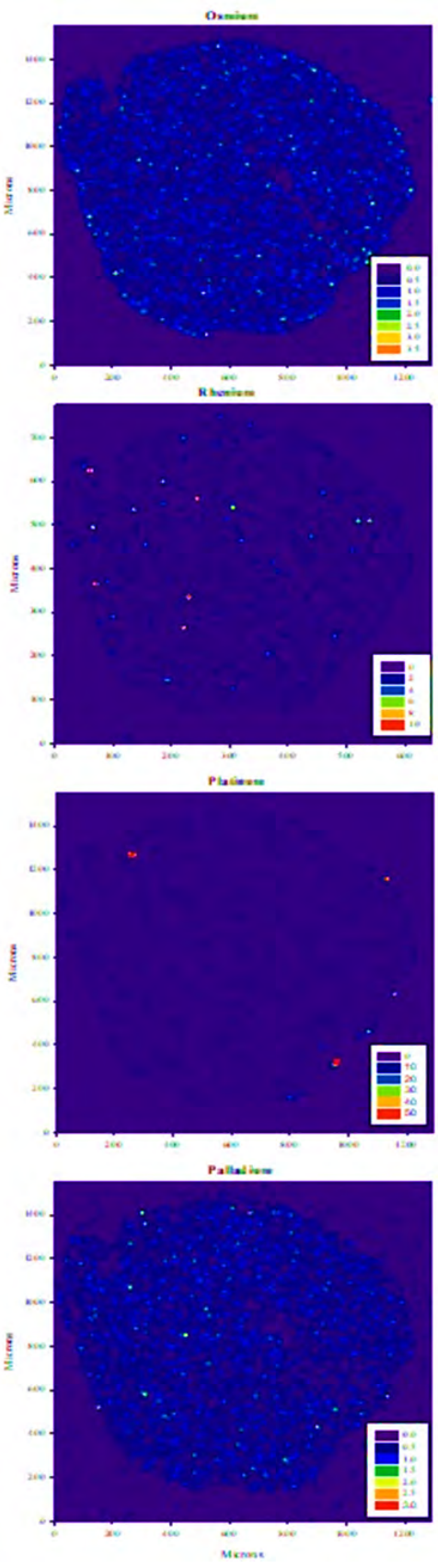

Analyses from a single ablation per grain can lead to a false analytical impression of the homogeneity of the alloy composition. Therefore, many grains per location and for some grains many ablations are required to ensure a representative analysis is obtained. There is a wealth of data possible from ToFMS and the analyses represents the best overall composition of the gold grains.

The analyses of elements trapped in mineral inclusions can be used to interpret the style of mineralization and be used as a means of discriminating different sources. We have observed that most elements are present in pyrite, and other minerals contain far fewer elements and at much lower concentrations. Discrete nanoparticles of different elements/minerals also appear to be a ubiquitous feature. It is likely that mineral inclusions, the elements they contain, and the presence of nanoparticles may be more diagnostic of the source deposit type. Apart from diffusion of mercury within the gold grains it appears that there is no diffusion of elements from inclusions into the gold or vice versa. The presence of some elements as nanoparticles poses a problem for analysis by quadrupole mass spectrometry. They are so small that they do not persist long enough to ensure they would be detected and if they are they are likely to represent a single small signal. Such signals are considered as spikes and have been ignored in the past when they are real analyses. The presence of PGE's may be indicative of mafic-ultramafic involvement. Other nanoparticles we have observed, such as Ga, Cd, Se, Sn, U, Th, may be specific to a particular style or source of gold mineralization.

## References


Banks, DA., Chapman, RJ., Spence-Jones, C. 2018. Detrital gold as a deposit-specific indicator mineral by LA-ICP-MS analysis. Geoscience BC Report 2018-21.

Chapman, RJ., Banks, DA., Styles, MT., Walshaw, RD., Piazolo, S., Morgan, DJ., Grimshaw, MR., Spence-Jones, C., Matthews, TJ., Borovinskaya, o. 2021a. Chemical and physical heterogeneity within native gold: Implications for the design of gold particle studies. Mineralium Deposita, 56, 1563-1588.

Chapman, RJ., Craw, D., Moles, NR., Banks, DA., Grimshaw, MR. 2021b. Evaluation of the contributions of gold derived from hypogene, supergene and surficial processes in the formation of placer gold deposits. Geological Society of London, Special Publication 516.

# Mapping Auriferous Fluid Flow along the Cadillac Larder Lake Fault Zone (Abitibi Belt, Canada)

**Georges Beaudoin[1,2], Benoit Quesnel[1,2], Christophe Scheffer[1,2], Guillaume Raymond[1,2]**
*[1]Département de géologie et de génie géologique, Université Laval, Québec QC Canada*
*[2] Centre de recherche sur la géologie et l'ingénierie des ressources minérales (E4m)*

**Abstract.** The O-H isotope composition of orogenic gold-bearing veins along the Cadillac Larder Lake Fault Zone (CLLFZ) between Val-d'Or and Kirkland Lake is documented in detail to unravel the fluid sources of orogenic gold deposits. Coexisting vein minerals show common oxygen isotope equilibrium, which yields temperatures between ~250 and ~550°C. Temperature covariation with fluid O and H isotope compositions demonstrates mixing between a higher temperature (> 500°C), deep-seated metamorphic fluids with high $\delta^{18}O_{H2O}$ (>9‰), low $\delta D_{H2O}$ (<-40‰), with lower temperature (<250°C) upper crustal fluids with lower $\delta^{18}O_{H2O}$ (<4 ‰), and higher $\delta D_{H2O}$ that ranges from 0 to 30‰. Along the Augmitto-Bouzan segment (Rouyn-Noranda), decreasing temperatures from 420ºC at 700 m depth, to 230ºC at 100 m depth, show the vertical ascent of the deep-seated metamorphic fluids along the CLLFZ. In the eastern part of the CLLFZ (Val-d'Or to Malartic) the metamorphic fluid has an end-member O isotope composition of 9-10‰, whereas to the west from Malartic to Kirkland Lake, it has a $\delta^{18}O_{H2O}$ between 11-13‰. The switch in metamorphic fluid reservoirs occurs where the CLLFZ has an inflection in strike. The upper crustal fluids, that cannot be distinguished despite differences in the composition of the country rocks hosting the orogenic gold deposits.

## 1 Introduction

The typical mineralizing fluid in orogenic gold deposits is aqueous-carbonic with a moderate temperature (250-500ºC), low salinity (3-12 wt.% NaCl eq.) near neutral pH, $CO_2$-rich composition (<10 mol%), but the source of the fluids and the processes leading to metal deposition remains debated (Goldfarb et al., 2005). The fluids have high $\delta^{18}O_{H2O}$ (~2 to10‰) and variable $\delta D_{H2O}$ (-60 to 30‰) values (Quesnel et al. in press). The two most proposed sources of fluids are magmatic and metamorphic, despite evidence for a magmatic source being questioned (Goldfarb and Pitcairn 2023, Quesnel et al. in press). Beaudoin and Chiaradia (2016) showed that the auriferous fluids in the Val-d'Or vein field were the product of mixing between a deep-seated, high-temperature (>550ºC), high $\delta^{18}O_{H2O}$ (>9‰) and low $\delta D_{H2O}$ (<-60‰), and upper crustal fluids with a lower temperature (<250ºC), lower $\delta^{18}O_{H2O}$ (<2‰) and higher $\delta D_{H2O}$ (>0‰). A similar mixing trend is characteristic of the orogenic deposit class (Quesnel et al. in press).

Documenting the mixing of deep-seated and upper crustal fluids in orogenic gold deposits requires detailed district-scale studies such as that of the Val-d'Or vein field by Beaudoin and Pitre (2005). Here we extend this study along the 250 km length of the Cadillac Larder Laker Fault Zone (CLLFZ), between Val-d'Or and Kirkland Lake, to document the sources of auriferous fluids in this classical orogenic gold vein field.

## 2 Geological Setting

The Cadillac-Larder Lake Fault Zone (CLLFZ) is one of the most endowed orogenic gold-rich shear zone worldwide (Robert, 1994). The CLLFZ is a 250 km long east-west structure that separates the southern volcanic zone of the Abitibi Subprovince, to the

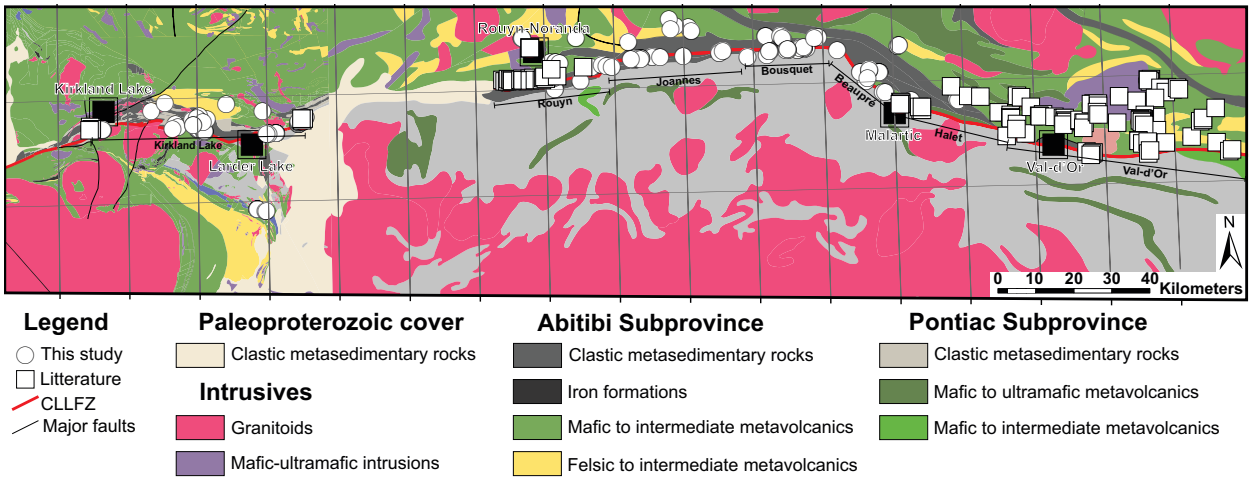


**Figure 1.** Geology along the Cadillac Larder Lake Fault Zone, with location of samples.

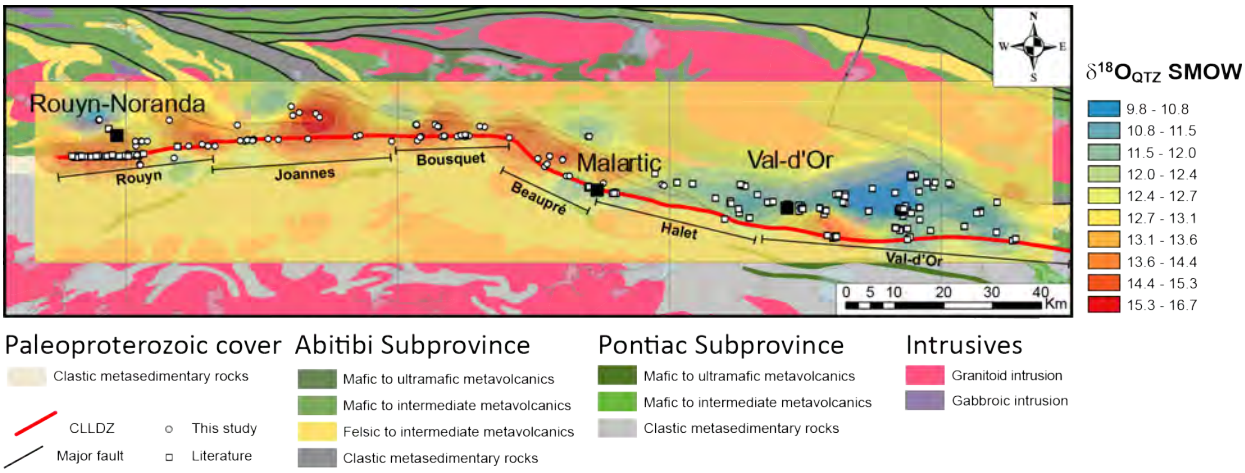


**Figure 2.** Distribution of quartz d18O values along the CLLFZ, between Val-d'Or and Rouyn-Noranda.

north, from the Pontiac metasedimentary Subprovince, to the south (Fig. 1). The CLLFZ has been divided into six segments, between Val-d'Or and Rouyn-Noranda, to better understand the distribution of gold mineralization along the CLLFZ (Bedeaux et al. 2017). Here we add one additional segment for the Kirkland-Larder Lake area (Fig. 1).

## 3 Sampling and Methods

The samples (n=168) have been collected in orogenic gold deposits and veins, mostly composed of quartz-tourmaline-carbonate (QTC), hosted in higher order shear zones, along the CLLFZ between Kirkland Lake and Val-d'Or. These samples yield 214 $\delta^{18}O$ values from quartz (n=168) and tourmaline (n=46), and 44 $\delta D$ values from tourmaline.

Samples of quartz and tourmaline were reacted with $BrF_5$ at the Stable Isotope Laboratory of Université Laval. The evolved $CO_2$ was analyzed by a Micromass Isoprime 100 isotope ratio mass spectrometer coupled to a Micromass MicroGas system in continuous flow mode at GEOTOP. Samples of tourmaline were crushed and loaded into a zero-blank auto sampler. The hydrogen isotopic composition was measured using a Thermo-Finnigan thermo-combustion elemental analyzer coupled to a Thermo-Finnigan MAT253 Continuous-Flow Isotope-Ratio Mass Spectrometer) at Queen's Facility for Isotope Research. Isotope ratios are reported in the $\delta$-notation relative to Vienna Standard Mean Ocean Water (VSMOW) with a precision better than 0.2‰ for O and 3‰ for H.

## 4 Results

The QTC vein quartz $\delta^{18}O$ values along the CLLFZ from this study and literature range from 9.2 to 18.5‰. The spatial distribution of quartz $\delta^{18}O$ values along the CLLFZ are contoured in Figure 2 between the Val-d'Or and Rouyn segments, where sufficient data exist for spatial analysis. Figure 2 shows that higher quartz $\delta^{18}O$ values, above 13‰, are mostly found west of Malartic, in contrast to the eastern segments of the CLLFZ where $\delta^{18}O$ values are as low as 9.8‰. There is a zone of overlap in the Beaupré segment, where there is an inflection in the strike of the CLLFZ near Malartic (Fig. 2). There is, however, no systematic change in quartz $\delta^{18}O$ values along the strike of the CLLFZ west or east of Malartic. Quartz $\delta^{18}O$ values tend to decrease north of the trace of the CLLFZ, as shown in the Val-d'Or vein field by Beaudoin and Pitre (2005). Figure 2

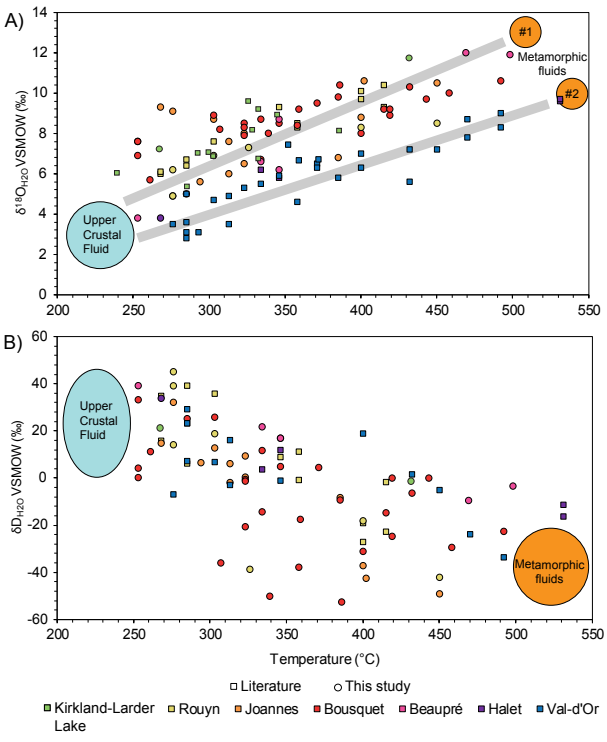


**Figure 3.** A) Covariation of $\delta^{18}O_{H2O}$ with the quartz-tourmaline temperature of equilibrium along the CLLFZ. Composition of the 2 metamorphic fluids (#1 and #2) and of the Upper Crustal fluid end-members are shown. B) Covariation of $\delta D_{H2O}$ with quartz-tourmaline temperature of equilibrium along the CLLFZ. End-member Upper Crustal and Metamorphic fluids compositions are shown.

shows that the E-W distribution of $\delta^{18}O$ values is not correlated with the types of country rocks.

Tourmaline $\delta^{18}O$ values from this study and literature range from 6.1 and 13.6‰, with a spatial distribution similar to that of quartz. Tourmaline δD values range from -132 to -17‰, but no systematic east-west variation in composition is documented.

Tourmaline and quartz display oxygen isotope equilibrium at temperatures between 240 and 530ºC. There is no systematic variation of temperature along the CLLFZ. The water in equilibrium with quartz and tourmaline, using the quartz-$H_2O$ oxygen fractionation of Sharp et al. (2016) and the tourmaline-$H_2O$ hydrogen fractionation of Kotzer et al. (1993), yields a correlation between temperature and O-H isotope compositions (Fig. 3). Water compositions of the CLLFZ segments west of Malartic have higher $\delta^{18}O_{H2O}$ values than those from segments east of Malartic, defining two sub-parallel arrays (Fig. 3). Both arrays converge towards a common lower temperature (<250ºC), low $\delta^{18}O_{H2O}$ (<4‰), and high $\delta D_{H2O}$ (>0‰) end-member fluid composition. The two sub-parallel arrays define two slightly different high temperature (>550ºC), high $\delta^{18}O_{H2O}$ (11-13‰, west of Malartic; 9-10‰ east of Malartic), and low $\delta D_{H2O}$ (<-60‰) end-members.

The spatial variation of $\delta^{18}O_{H2O}$ values along the CLLFZ is similar to that of quartz $\delta^{18}O$ values (Fig. 3) but the number of locations where a quartz-tourmaline pair enables calculation of the temperature of equilibrium and fluid composition does not allow for spatial analysis as in Figure 3. The distribution of $\delta D_{H2O}$ values along the CLLFZ does not show a systematic trend, consistent with the single array of temperature-$\delta D_{H2O}$ in Figure 3B.

## 5 Discussion

As shown by Beaudoin and Pitre (2005) for the Val-d'Or vein field and by Quesnel et al. (in press) mixing between deep-seated metamorphic and upper crustal fluids is common for the class of orogenic gold deposits. We show here that mixing of these fluid reservoirs occurs along the 250 km length of the CLLFZ. In the Rouyn segment, Raymond (2022) has documented a vertical temperature gradient of 30ºC/km, from 420ºC at 700 m depth to 230ºC at 100 m depth, showing the vertical ascent of the deep-seated metamorphic, and mixing with the upper crustal, fluids along a sub-vertical panel of the CLLFZ at the Augmitto-Bouzan deposit.

Along the CLLFZ, the temperature-water O-H isotope composition indicates a common low temperature (<250ºC), low $\delta^{18}O_{H2O}$ (<4‰) and high $\delta D_{H2O}$ (>0‰) Upper Crustal fluid reservoir (Fig. 3). These characteristics are most compatible with surface water that has resided for some time in the porosity of the regional country rocks, where it has become heated, and its isotope composition has been modified by water-rock reactions. In the Archean setting of the orogenic gold deposits along

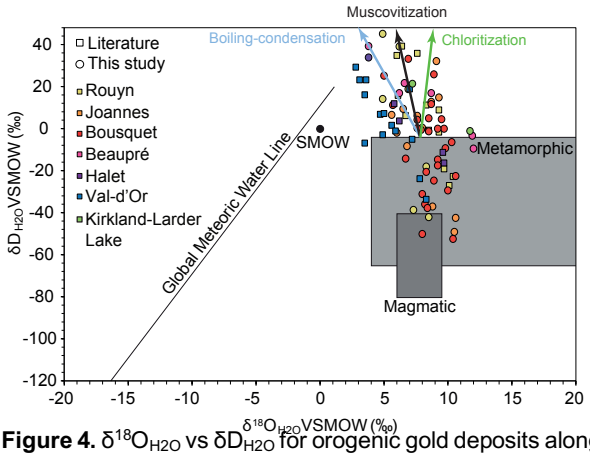


**Figure 4.** $\delta^{18}O_{H2O}$ vs $\delta D_{H2O}$ for orogenic gold deposits along the CLLFZ. O-H isotope trends during boiling-condensation, and of muscovite and chlorite alteration of host rocks are from Quesnel et al. (in press). Fields for metamorphic, magmatic and meteoric waters, and seawater (SMOW) are from Sheppard (1986).

the CLLFZ, the ultimate fluid source was likely seawater.

There is a spread of $\delta D_{H2O}$ values (0 to 40‰, Fig. 4) that is common to orogenic gold deposits worldwide (Quesnel et al. in press). Two processes most likely explain the high $\delta D_{H2O}$ values: 1) boiling-condensation cycles and 2) formation of hydrothermal mica in vein and wallrock alteration. Boiling-condensation cycles are likely due to the dynamic pressure fluctuation environment of orogenic gold deposits (Robert et al. 1995). Quesnel et al. (in press) showed that the high $\delta D_{H2O}$ values can result from successive events of flash boiling during pressure drop, enabling migration of light hydrogen vapor along the vein network, leaving heavier hydrogen water in the veins. Furthermore, muscovite and chlorite are common in veins and wall rock alteration of orogenic gold deposits. Precipitation of mica in veins and alteration halos will also yield heavier hydrogen residual water because of the negative H fractionation between water and mica. Thus, it is likely that the wide spread of $\delta D_{H2O}$ values at any given temperature in Figure 3 is the results of these two processes during vein formation. The deep-seated metamorphic fluids (Fig. 4) most likely are the product of prograde metamorphism of the regional country rocks at depth, consistent with the high temperature (>550ºC), high $\delta^{18}O_{H2O}$ (>9‰) and low $\delta D_{H2O}$ (<-60‰). Although some water compositions in Figure 4 could be compatible with magmatic water, the probability of such an occurrence is unlikely due to the lack of a systematic spatial and temporal association with magmatic rocks, as discussed for orogenic gold deposits by Goldfarb and Pitcairn (2023).

The two arrays in the temperature-$\delta^{18}O_{H2O}$ diagram (Fig. 3) show that slightly different metamorphic fluid reservoirs were tapped on each side of the strike inflection along the CLLFZ, near Malartic. The two reservoirs have similar fluid temperatures and $\delta D_{H2O}$ values but are different in the oxygen isotope composition. Metamorphic fluid

#1, west of Malartic, has a higher $\delta^{18}O_{H2O}$ values (11-13‰) than that of Metamorphic fluid #2 (9-10‰), east of Malartic. The difference in composition suggests that Metamorphic fluid #1 is sourced from country rocks with a higher proportion of sedimentary, or low temperature altered, country rocks that would yield prograde metamorphic fluids with a heavier oxygen isotope composition.

The fact that both metamorphic fluid end-members display no variation along the CLLFZ strike indicates a homogenized metamorphic fluid source at depth on each side of the inflexion in strike near Malartic. In contrast, there is no evidence of compositional differences of the Upper Crustal fluid end-member on both sides of the inflexion point along the CLLFZ, indicating a largely similar fluid composition in the country rocks resident pore fluids. In addition, this suggests that fluid-rock isotope exchange at the site of mineralization did not significantly modify the composition of the auriferous fluids.

It is intriguing that there is an overlap of both fluid reservoirs at the regional inflexion in strike of the CLLFZ. According to Bedeaux et al. (2018), a NE-SW segment could have linked, on each side, two E-W segments of the CLLFZ during the main N-S deformation event in the southern part of the Abitibi Subprovince. The main N-S shortening was followed by late dextral strike-slip deformation. This would be consistent with our fluid reservoir mapping that shows that metamorphic reservoirs #1 and #2 are yielding slightly different fluid compositions on each side of the linking NE-SW segment.

## 6 Conclusion

We show that the orogenic gold deposits along the CLLFZ formed by mixing two slightly different, deep-seated metamorphic fluids, with common upper crustal fluids. The two metamorphic reservoirs provided fluids along E-W segments of the CLLFZ that are separated by an inflexion of the trace of the fault zone, which likely segmented fluid sources from the two reservoirs.

## Acknowledgements

We thank Canada First Research Excellence Fund Metal Earth program for funding this study.

## References

Beaudoin G, Pitre D (2005) Stable isotope geochemistry of the Archean Val-d'Or (Canada) orogenic gold vein field. Mineralium Deposita 40:59-75.

Beaudoin G, Chiaradia M (2016) Fluid mixing in orogenic gold deposits: Evidence from the H-O-Sr isotope composition of the Val-d'Or vein field (Abitibi, Canada). Chemical Geology 437:7-18.

Bedeaux P, Pilote P, Daigneault R, Rafini S (2017) Synthesis of the structural evolution and associated gold mineralization of the Cadillac Fault, Abitibi, Canada. Ore Geology Reviews 82:49-69.

Bedeaux P, Rafini S, Pilote P, Daigneault R (2018) Modelling Seismically Induced Mesothermal Goldfields along the Deep-Rooted Cadillac-Larder Lake Fault, Abitibi, Canada. Geofluids 2018:21.

De Souza S, Dubé B, McNicoll V, Dupuis C, Mercier-Langevin P, Creaser R, Kjarsgaard IM (2017) Geology and Hydrothermal Alteration of the World-Class Canadian Malartic Gold Deposit: Genesis of an Archean Stockwork-Disseminated Gold Deposit in the Abitibi Greenstone Belt In: Monecke T, Mercier-Langevin P, Dubé B (eds) Archean Base and Precious Metal Deposits, Southern Abitibi Greenstone Belt, Canada. Society of Economic Geologists, pp 263-291.

Goldfarb RJ, Baker T, Dubé B, Groves DI, Hart CJR, Gosselin P (2005) Distribution, character, and genesis of gold deposits in metamorphic terranes In: Hedenquist JW, Thompson JFH, Goldfarb RJ, Richards JP (eds) Economic Geology 100th Anniversary Volume. Society of Economic Geologists, pp 407-450.

Goldfarb RJ, Pitcairn I (2023) Orogenic gold: is a genetic association with magmatism realistic? Mineralium Deposita 58:5-35.

Quesnel B, Scheffer C, Beaudoin G, in press. The light stable isotope (hydrogen, boron, carbon, nitrogen, oxygen, silicon, sulfur) composition of orogenic gold deposits. In Huston D and Gutzmer J (eds) Isotopes in Economic Geology. SpringerNature. ISBN 978-3-031-27896-9.

Raymond G, 2022. Variation spatiale des conditions de circulation des fluides à l'origine de la minéralisation en or orogénique dans le segment Augmitto-Bouzan (Sous-Province de l'Abitibi, Québec, Canada). MSc thesis, Université Laval 107p.

Robert F (1994) Vein fields in gold districts: The example of Val-d'Or, southeastern Abitibi province. Current Research Part C. Geological Survey of Canada, pp 295-302.

Robert F, Boullier A-M, Firdaous K (1995) Gold-quartz veins in metamorphic terranes and their bearing on the role of fluids in faulting. Journal of Geophysical Research 100:12861-12879.

Sheppard SMF (1986) Characterization and isotopic variations in natural waters. Reviews in Mineralogy and Geochemistry 16:165-183.

# In situ geochronology of hydrothermal events in the Upper Beaver Au-Cu deposit, Abitibi greenstone belt, Canada

**Bin Lin [1, 2], Crystal Laflamme [1], Georges Beaudoin [1], Chris McFarlane [3]**
[1] *Department of Geology and Geological Engineering, Université Laval, QC G1V 0A6, Canada*
[2] *Institute of Mineral Resources, Chinese Academy of Geological Sciences, BJ 100037, China*
[3] *Department of Earth Sciences, University of New Brunswick, NB, E3B 5A3, Canada*

**Abstract.** Three hydrothermal events were identified in the Archean Upper Beaver Au-Cu deposit, Abitibi greenstone belt (Canada). Extensive epidote, K-felspar, carbonate, sericite, chlorite, minor andradite, and hematite, magnetite alteration, as concordant stratabound replacement, with chalcopyrite, pyrite, pyrrhotite, Au, and Bi and Te-bearing minerals represent the early Dog's Breakfast event. The main hydrothermal event consists of discordant veins of quartz-carbonate ± chlorite ± anhydrite, minor tourmaline, with chalcopyrite, magnetite, pyrite, molybdenite, scheelite, cobaltite, pyrrhotite, Au, Bi and Te-bearing minerals. The late hydrothermal event is characterized by quartz-carbonate-chlorite ± epidote ± tourmaline ± anhydrite veins with minor chalcopyrite, pyrite, specularite, scheelite and Au. In situ U-Pb dating of hydrothermal zircon and xenotime constrain the timing of the main and late hydrothermal events at about ca. 2679 Ma and 2575 Ma, respectively, indicating multi-hydrothermal events in the formation of Upper Beaver, and refining the time-framework for Au metallogeny in the southern Abitibi greenstone belt.

## 1 Introduction

The Abitibi greenstone belt, one of the word-class Archean gold mineralization regions, is in the southern Superior Province (Fig.1A). Despite a relative structural framework, efforts to constrain the timing of formation of numerous gold deposits in Abitibi greenstone belt yield a timespan of > 100 million years (Dubé and Mercier-Langevin 2020). Geochronological data from molybdenite, rutile, and titanite indicate that several orogenic gold deposits in the southern Abitibi greenstone belt (Val-d'Or region) formed between 2660 and 2640 Ma. New structural-geochronological evidence from the Val-d'Or district indicates that orogenic gold formed during three discrete hydrothermal events at 2686 ± 15 Ma, 2643 ± 3 Ma and 2607 ± 5 Ma, respectively (Herzog et al. 2023). Whereas the relationships and relative timing between the gold deposits and regional volcanism, magmatism, and lithospheric-scale faults are well documented, the absolute age for hydrothermal event remains unclear in other Archean gold districts in the southern Abitibi greenstone belt (e.g., Kirkland Lake, Larder Lake). More geological and geochronological data show that not all Au events are solely orogenic, some of them can be closely related to magmatism with Cu mineralization (e.g., Upper Beaver).

The Upper Beaver Au-Cu deposit is associated with an intrusive complex in the southern Abitibi greenstone belt. In situ LA-ICP-MS (laser ablation-inductively coupled plasma-mass spectrometry) U-Pb geochronology from accessory minerals (zircon, xenotime) is used to refine the multi-phased hydrothermal events based on detailed core logging and petrography. It provides an improved timeframe for the Upper Beaver deposit and regional Au metallogeny of the Abitibi greenstone belt.

## 2 Regional geology and deposit geology

The Abitibi greenstone belt consists of volcano - sedimentary rocks of low to moderate-grade metamorphism between ca. 2750 and 2695 Ma (Fig.1A). The volcanic units are unconformably overlain by sedimentary basins of the Porcupine and Timiskaming groups (Fig.1B). Several intrusions are distinguished according to the emplacement ages and petrology, including syn-volcanic, pre-Timiskaming (post-volcanic), early- to syn-Timiskaming, and post-Timiskaming categories (Dubé and Mercier-Langevin 2020). Two major first-order structures are related to major precious and base metal deposits in the southern Abitibi greenstone belt: the Destor-Porcupine fault zone (DPfz) and the Larder Lake-Cadillac fault zone (LLCfz) (Fig.1B).

The Upper Beaver deposit lies roughly 8 km north of the LLCfz and 30 km east of Kirkland Lake (Fig.1B). It is hosted in a succession of volcanic and volcaniclastic rocks of the Blake River and Tisdale assemblages. Simplified surface map, and a composite cross section show the geology and distribution of mineralization in Figure 2. The Upper Beaver deposit is an atypical Au-Cu deposit that contrasts with orogenic gold deposits as it preserves widespread and pervasive magnetite, K-feldspar, epidote, carbonate, and sericite alteration, surrounding the polyphase of Upper Beaver Intrusive Complex (UBIC). The UBIC consists of several magmatic pulses as diorite or monzodiorite with different compositions and textures, but were named mafic syenite porphyry, mafic syenite altered breccias, mafic syenite, crowded porphyry, and spotted porphyry in the mine, respectively. All these intrusions are cut by a Proterozoic diabase dike (Fig.2).

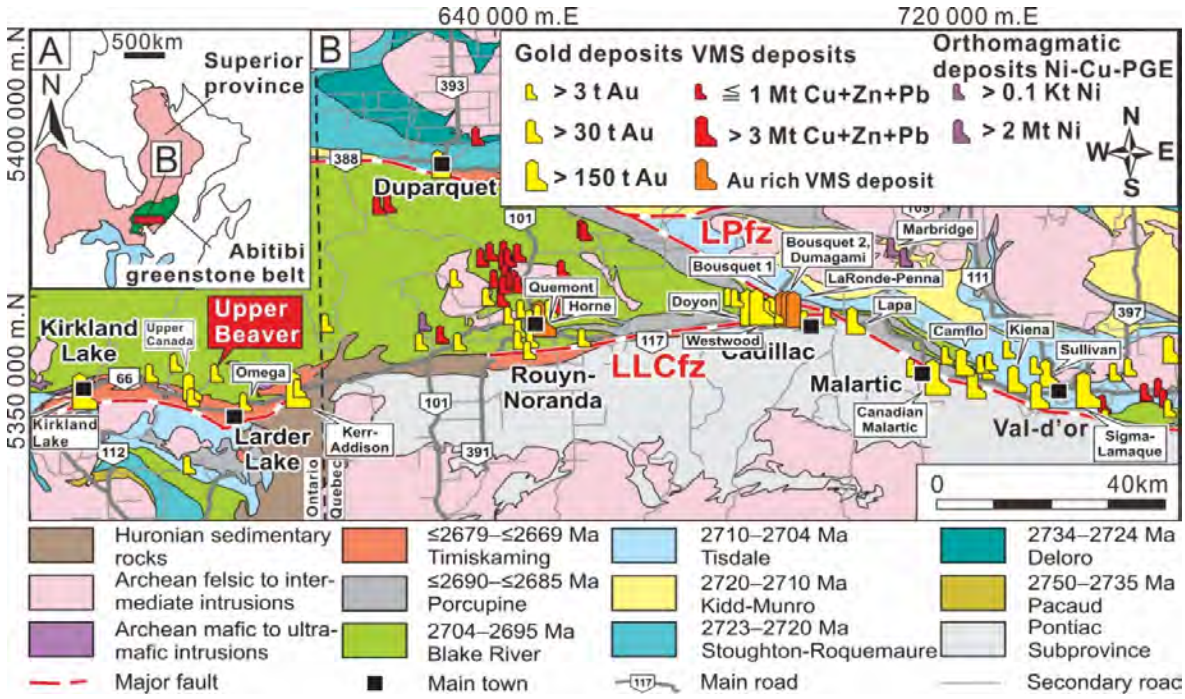


**Figure 1.** Location (A) and geological map (B) of the southern Abitibi greenstone belt (modified from Monecke et al. 2017)

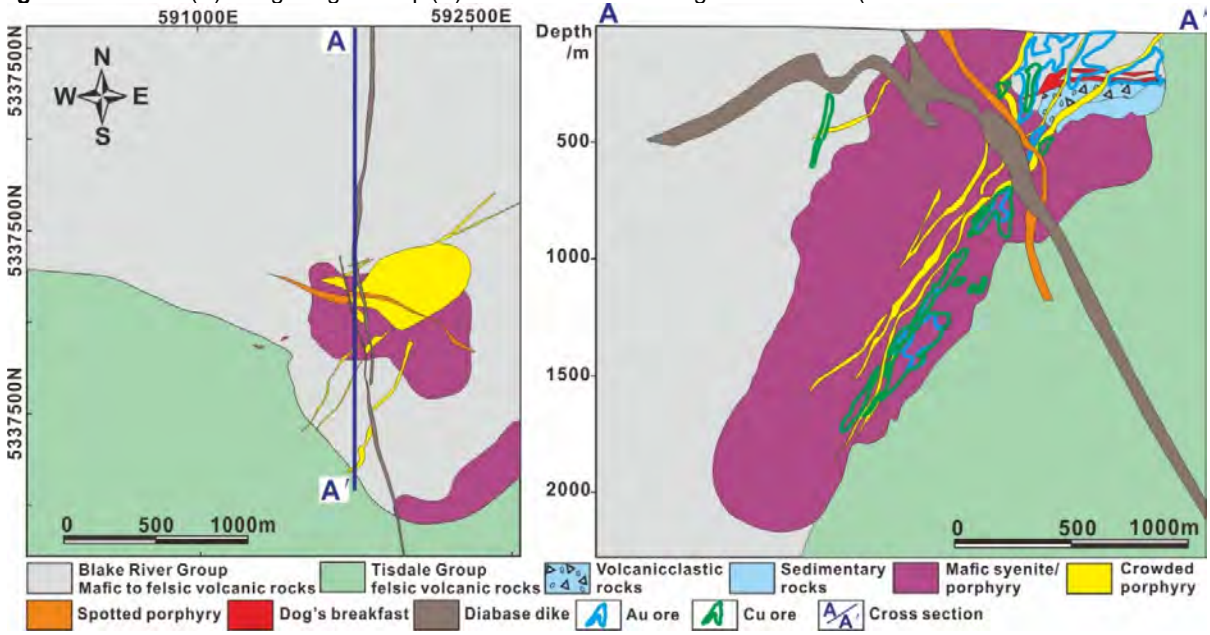


**Figure 2.** Geological map and the cross section (A-A') at the Upper Beaver Au-Cu deposit (from Agnico Eagle, unpub)

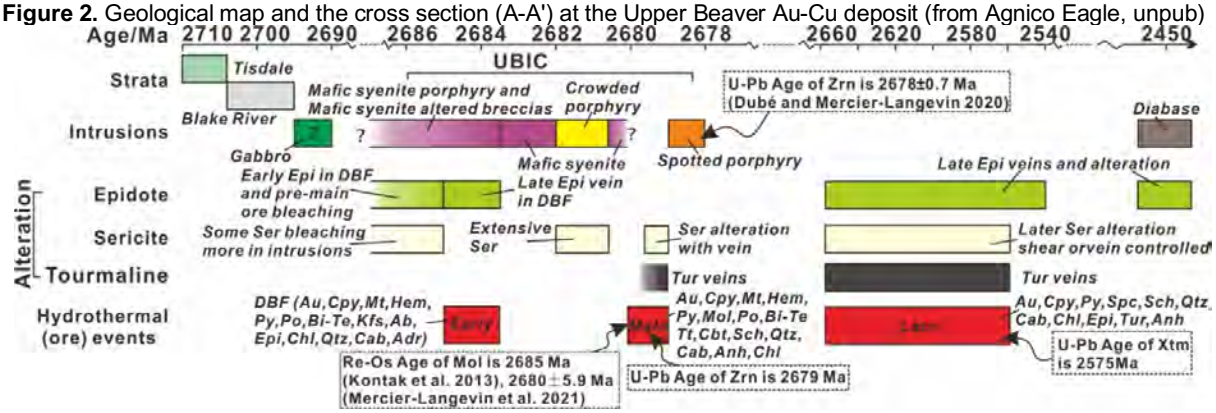


**Figure 3.** Timeline of geology and hydrothermal events in the Upper Beaver Au-Cu deposit (modified from Agnico Eagle, unpub). Abbreviation: Adr-andradite, Anh-anhydrite, Cab-carbonate, Chl-chlorite, Cpy-chalcopyrite, Cbt- cobaltite, DBF-Dog's Breakfast, Epi-epidote, Kfs-K feldspar, Mol-molybdenite, Mt-magnetite, Po-pyrrhotite, Py-pyrite, Sch-scheelite, Ser-sericite, Spc- specularite hematite, Tur-tourmaline, Zrn-zircon.

## 3 Methods

To constrain the timing of hydrothermal events in the Upper Beaver deposit, in situ U-Pb geochronological data was acquired on hydrothermal zircon and xenotime in veins associated with the main and late hydrothermal events. Petrography, micro-X-ray fluorescence (μXRF) mapping, energy dispersive spectrum (EDS) and electron microprobe (EPMA) analysis were conducted to reveal the presence, location, and major and trace element composition of these accessory minerals in thin sections. Zircon, and xenotime in different hydrothermal events were analyzed for in situ U-Pb geochronology using LA-ICP-MS at the University of New Brunswick, Canada.

## 4 Results

From the main hydrothermal event, zircons from the quartz - carbonate ± chlorite ± anhydrite± tourmaline veins are colorless and forms 8 ~ 50 um prismatic grains The zircon grains occur primarily in equilibrium with vein-hosted sulfide minerals (molybdenite, pyrite). Petrography and the REE composition of zircon indicate that they are hydrothermal in origin (Hoskin 2005). A total of 19 zircon grains yields a concordia age of ca. 2674 Ma (n=23 analyses spots) and a weighted mean $^{207}Pb/^{206}Pb$ age of ca. 2679 Ma (n=23) (Fig.3).

The quartz ± carbonate ± chlorite ± epidote ± tourmaline ± anhydrite veins represent the late hydrothermal event. Xenotime grains from these veins are up to 20 μm in diameter and occur either in equilibrium with sulfide minerals (chalcopyrite, pyrite) and Au, or in equilibrium with gangue minerals (quartz, carbonate). The xenotime grains are moderately to strongly enriched in MREE and HREE, with a subtle or no negative Eu anomaly, and a wide range in Lu contents, which suggests a hydrothermal origin (Herzog et al. 2023). Xenotime analyses yield a concordia age of 2582 Ma (n=41 analyses in 40 grains) and a weighted mean $^{207}Pb/^{206}Pb$ age of ca. 2575 Ma (n = 34).

## 5 Discussion

The main Cu-Au mineralization crosscuts the 'crowded porphyry' and is cut by the 'spotted porphyry'. A zircon ID-TIMS U-Pb age from the spotted porphyry is ca. 2678 ± 0.7 Ma (Fig.3) (Dubé and Mercier-Langevin 2020) constraining the timing of the main gold mineralization to earlier than ca. 2678 Ma. Two N-TIMS molybdenite Re-Os date from this hydrothermal event constrains it at ca. 2685 (Kontak et al. 2013) or. 2680 ± 5.9 Ma (Mercier-Langevin et al. 2021). The new in-situ U-Pb age of hydrothermal zircon at ca. 2679 Ma represents the absolute age for the hydrothermal event and confirms the timing of main Au-Cu event at Upper Beaver. It coincides with Re-Os age (2675 ± 6 Ma) from quartz-molybdenite-Au vein in Kirkland Lake (Ispolatov et al., 2008) and in situ U-Pb age of xenotime (2686 ± 15 Ma) from quartz-carbonate veins at the S-50 Kiena deposit (Herzog et al., 2023).

The late quartz ± carbonate ± chlorite ± epidote ± tourmaline ± anhydrite veins which cut the spotted porphyry (ca. 2678 Ma) indicate that a later hydrothermal event affected the Upper Beaver deposit. In situ U-Pb age of hydrothermal xenotime is ca. 2575 Ma (Fig.3), younger than the time of main Au-Cu event and much younger than the spotted porphyry. Only minor sulfides (chalcopyrite, pyrite) and Au occur in late hydrothermal event veins.

## 6 Conclusions

Upper Beaver is an Archean Au-Cu deposit with close spatial and temporal relationships with the UBIC in southern Abitibi greenstone belt. In-situ U-Pb dating of hydrothermal zircon and xenotime confirms that the timing of main hydrothermal event is at about 2679 Ma, consistent with zircon U-Pb age of younger spotted porphyry. The age of xenotime from later veins suggests a late hydrothermal evet at about 2575 Ma. The geochronology of hydrothermal events in Upper Beaver help to reveal its genesis and refine the Au metallogeny in southern Abitibi greenstone belt.

## Acknowledgement

The authors greatly appreciate the financial support for this study by NSERC and Agnico-Eagle Mines Limited.

## References

Dubé B, Mercier-Langevin P (2020) Gold deposits of the Archean Abitibi Greenstone Belt, Canada. Econ Geol Spec Pub 23:669–708. https://doi. org/10.5382/SP.23

Herzog M, LaFlamme C, Beaudoin G, Marsh J, and Guilmette C (2023) U–Pb vein xenotime geochronology constraints on timing and longevity of orogenic gold mineralization in the Malartic-Val-d'Or Camp, Abitibi Subprovince, Canada: Miner Deposita 58:105–133. https://doi.org/10.1007/ s00126 - 022-01131-1.

Hoskin P W O (2005) Trace - element composition of hydrothermal zircon and the alteration of Hadean zircon from the Jack Hills, Australia. Geochim Cosmochim Acta 69, 637–648.

Ispolatov V, Lafrance B, Dubé B, Creaser R, and Hamilton M (2008) Geologic and structural setting of gold mineralization in the Kirkland Lake-Larder Lake gold belt, Ontario: Econ Geol 103:1309–1340. https://doi.org/ 10.2113/gsecongeo.103.6.1309.

Kontak D J, Dubé B, McNicoll V, Creaser R, and Kyser T K (2013). The Upper Beaver Au-Cu deposit, Kirkland Lake, Ontario, Canada: An Archean IOCG analogue or just an intrusion-related iron oxide copper gold deposit(?) Geological Association of Canada-Mineralogical Asso- ciation of Canada (GAC-MAC) Annual Joint Meeting,122.

Mercier-Langevin P, Creaser R A, Dubé B, Dubé J, Kontak D J, Sutton J, and Côté-Mantha O (2021) Molybdenite Re-Os ages of a gold-rich vein, Porphyry zone, Upper Beaver deposit, Abitibi greenstone belt, Ontario; Geological Survey of Canada, Open File 8789, 13. https://doi.org/ 10.4095/328239

Monecke T, Mercier-Langevin P, Dubé B, Friedman M (2017) Geology of the Abitibi Greenstone Belt: Rev. Econ Geol 19:7–50. https:// doi.org/10.5382/ Rev.19. 01.

# Using Chlorite and White Mica Mineral Chemistry as Footprints at Alta Floresta Mineral Province – Brazil.

**Márcia Elisa Boscato Gomes[2]; Maria José Mesquita[1]; Igor de Camargo Moreira[1]; Renata Augusta Sampaio Paes[1]; Hevelyn Eduarda da Silva Martins[1]; José Henrique Matos[1]; Alberto Ruggiero[1]; Guilherme Primo[1]; Diego Fernando Ducart[1]; João Gabriel da Silva[1]; Luciano Poggi[1]; André Massanobu Ueno Kunifoshita[1], Leonardo Zanchetta de Laurentis[1].**

[1]*Universidade Estadual de Campinas -Unicamp*

[2]*Universidade Federal do Rio Grande do Sul – UFRGS*

**Abstract.** The mineral chemistry of chlorite and white mica from Type 1, Type 2 and Type 3 ore deposits from Alta Floresta Mineral Province, Brasil were investigated to develop footprints of their alteration processes. Mg-rich chlorite and Mg- and Si-rich phengite are footprints for the older orogenic-gold event with high crystallisation temperature (420-300ºC) and variable pressure (3-7 kbar). Fe-rich and Al-Fe-rich chlorite and white mica are the footprints for younger magmatic-hydrothermal event with porphyry and epithermal undeformed alterations respectively. The temperatures (380-120ºC) and low pressures (4.6-0.6 kbar) are coherent to the cooling of a shallow hydrothermal-magmatic system. These data contribute to the understanding of the two ore events overprint.

## 1 Introduction

White mica and chlorite mineral chemistry is a sensitive indicator of hydrothermal and metamorphic processes (Sillitoe 2010; Gaillard *et al.* 2018). These minerals frequently show a wide compositional range in different ore deposits in response to the activities of water, Si and Al, pH and redox, P and T (Guidotti and Sassi 1998; Halley *et al.* 2015) and can provide valuable footprints of hydrothermal fluid pathways in and around the deposits. In this abstract we evaluate chemical patterns of chlorite and white micas from the Paleoroterozoic Alta Floresta Mineral Province (AFMP). The results from Paraiba, Peteca, and Serrinha do Guarantã deposits, and Luiz Bastos target of the Type-1, União do Norte District of Type-2, and Juruena District of Type-3 (Mesquita et al, 2022) are discussed to develop footprints of Type-1, -2, and -3 deposits and their alteration processes.

## 2 Geology

The AFMP is one of the promising Brazilian provinces for gold and copper. It comprises an inlier nucleus of 2.05 to 1.97 Ga arc-related rocks surrounded and cut by younger 1.82 to 1.52 Ga magmatic-arc rocks.

The current mineralization models defined three deposit types: Type-1 Au ± Cu shear zone-hosted veins, entirely hosted in the older granitic, granitic-gneiss and metamafic rocks of the inlier, and Type-2 Au-Cu porphyry deposits and Type-3 Au ± Ag ± base metals epithermal deposits, in the younger rocks. (Detailed geology and location of the studied deposits are in Mesquita et al. 2022.)

## 3 Results

We constructed a database of 680 quantitative electron microprobe analyses (EPMA), including revised previous data and new chlorite and white mica chemical compositions.

In the Type-1 deposit, chlorite and white mica substitute for biotite in the chlorite–carbonate alteration (Fig. 1a). In Type-2 and -3 deposits, the analysed chlorite and muscovite are from the phyllic/sericitic, chlorite–sericitic and chloritic alteration zones (Fig.1b, c).

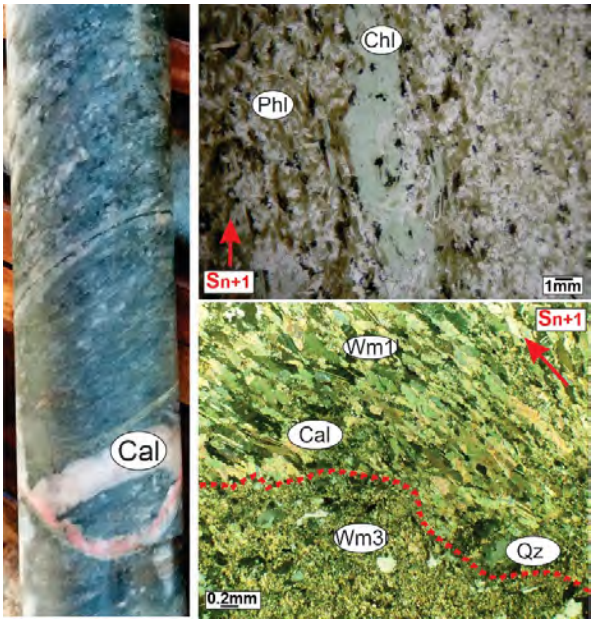


**Figure 1**. a) chlorite phyllonite cut by calcite (Cal) vein; (b) Phlogopite (Phl) and sulfide (black) alteration replaced by chlorite (Chl) and sulfide; (c) White mica (Wm-3), quartz (Qz) and pyrite overprinting the Sn+1 foliation defined by white mica (Wm-1) and calcite in a muscovite phyllonite.

### 3.1 Chlorite

Most chlorite classifies as brunsvigite; however, the Fe# allows a general characterization of Type-1deposits chlorite as more magnesian (Fe#, 0.43), and Types-2 and -3 as the Fe-richest (Fe#. 0.5).

In Type-1 deposits, the chlorite composition is strongly controlled by $Mg^{2+}$ for $Fe^{2+}$ substitution. chlorite from distal propylitic (Mg 3.5–4.1 apfu) and proximal sericitic (Mg 3–3.3 apfu) alterations of the Portera–Buriti deposit and the biotite–phlogopite

(Mg 3.1–3.3 apfu) and chlorite–carbonate (Mg 3.1–3.5 apfu) alterations and ore quartz vein (Mg 2.5–2.7 apfu) of the Paraíba deposit are individualized in small clusters with less extensive replacements. Peteca and Luiz Bastos chlorite of chloritic–carbonate alteration clusters in two populations in the high-Fe extreme.

In the Type-2 and -3 deposits, Serrinha de Matupá's chlorite has a broad range of Mg↔Fe exchange reactions, with those from incipient alterations showing an intermediate to high Mg (1.6–3.0 apfu), those of sericitic alteration high Mg (2.4–4.0 apfu), and the Fe-richest ones (0.8–1.4 apfu) in the Mn chloritic ore. In the high-Mg (Serrinha do Matupá and Buriti-Porteira sericitic alterations) and particularly in the high-Fe extremes (Luiz Bastos and Serrinha de Matupá Mn chlorite alteration), other variables than Fe–Mg substitution modify the chlorite's composition.

The Tschermak substitution ($Si^{IV}$ + (Mg +$Fe^{2+}$) $^{VI}$ = ($^{IV}$ Al + $^{VI}$ Al) best describes the chlorite's chemical behaviour in most deposits. In Type-1 deposits, the highest chlorite (Si + Fe +Mg) values are found in Serrinha de Guarantã deposit and chlorite–carbonate alteration (Ch-2) of the Paraíba deposit. The opposite occurs in Ch-1 of Type-1 Luiz Bastos deposit, which plots in the higher Al extreme. Although the Tschermak is also the essential substitution in chlorite formation from Type-2 and -3 deposits, especially those of the Paraíba and Peteca deposits and Serrinha de Matupá,the data are much more spread out than in Type-1 deposits.

The classification diagram Si v. $R^{2+}$ by Wiewióra and Weiss (1990) combines composition and temperature estimations. Most Type 1 deposits' chlorite plots over the zero vacancies line, clustering around intermediate $R^{2+}$ and $R^{3+}$, indicating the octahedral site's total occupation and high crystallization temperature (Fig. 2a). The Type-2 and -3 deposits' chlorite shows (Fig. 2b) increasing Si, $R^{2+}$ and vacancies and lower crystallization temperatures. The Type-3 Luiz Bastos chlorite composition remarkably extends to decreasing $R^{2+}$ and increasing Si (Fig. 2c). These data suggest that the di-trioctahedral substitution also plays an important role, increasing vacancies in the mineral structure and decreasing temperature (up to 100°C). Applying the quantitative geothermometer of Inoue et al. (2009), the temperatures obtained for chlorite of Type-1 deposits were between 250 and 498°C. The Type-2 chlorite exhibits scattered temperatures between 152 and 402°C. The Type-3 chlorite shows the lowest and variable temperatures (68–378°C).

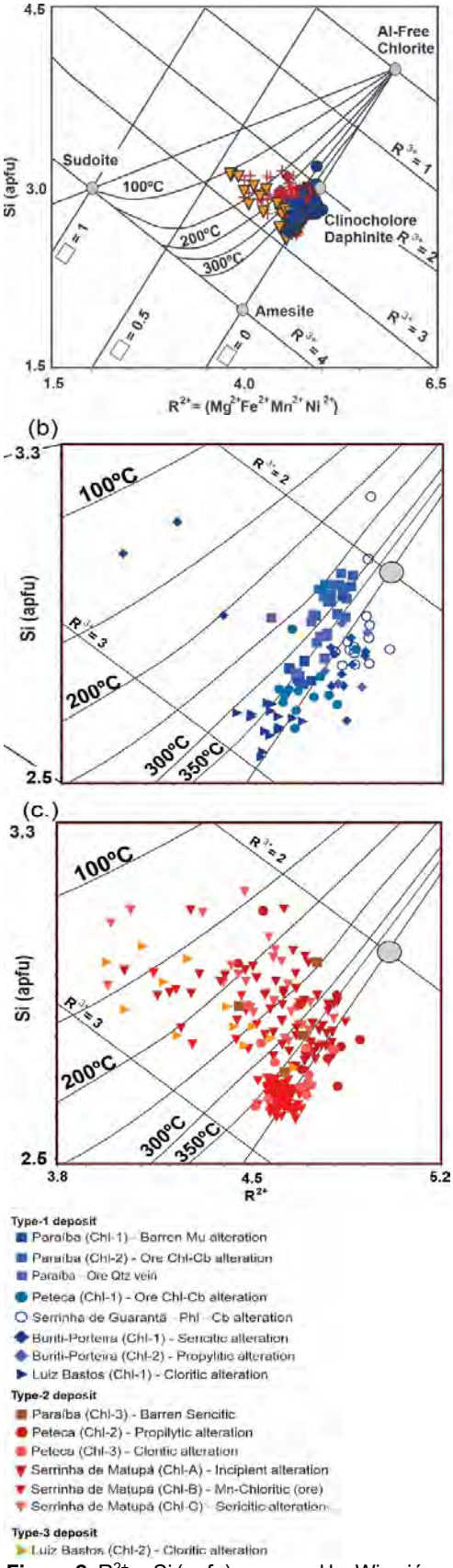


**Figure 2.** $R^{2+}$ v. Si (apfu) proposed by Wiewióra and Weiss (1990), in which R2 = $Fe^{Tot}$ + Mg + Mn+ Ni, allows identification of the chlorite composition and the correlation to the presence of vacancies, R3 ($Al^{Tot}$ +Cr + Ti) and temperature (Bourdelle and Cathelineau 2015).

### 3.2 White Mica

The major white mica has an interlayer population 0.8 apfu and a Si excess over 3 apfu, characteristically phengitic in composition.

The general broad compositional field depicted in Figure 3 indicates that the control of chemical variations in white micas is the ferriphengite–ferrimuscovite–phengite(FPh–FMu–Ph) compositional substitutions (Guidotti 1987). The main substitution from the ideal muscovite follows the tie-line muscovite–ferriphengite (Mu–FPh) end members. This chemical approach highlights the muscovite–Fe–phengitic compositions of the white micas from the Type-1 deposits. The Type-2 and -3 white micas show a compositional field's enlargement towards the ferrimuscovite trend. The Type-3 Luiz Bastos and Trairão deposits white micas fall essentially on the Mu–FPh join. Even with no $Fe^{2+}$–$Fe^{3+}$ distinction by EPMA analysis, the Mu deviation to ferrimuscovite suggests that $Fe^{3+}\leftrightarrow Al^{3+}$ substitution could also have occurred (Guidotti 1987). The Type-2 and -3 samples show significant variations from Mu to FMu, suggesting the $Fe^{3+}$ replacing $Al^{VI}$.

Considering all samples, the Tschermak exchange reaction is the most significant controller of compositional variations since most points cluster around the negative linear correlation of (Fe + Mg + Si) v. total Al. The Type-1 white mica plots in the field of higher phengitic substitution (Ph), those of muscovite–phyllonite being more aluminous and those of chlorite–carbonate phyllonite showing a broader substitution interval. Tschermak substitution within the white mica of the Type-2 Serrinha de Matupá and Peteca deposits is the most extensive, from muscovite to phengite end members, and their compositional trends overlap. The substitutions along this general negative trend are associated with samples from different hydrothermal alteration zones of Type-2 and -3.

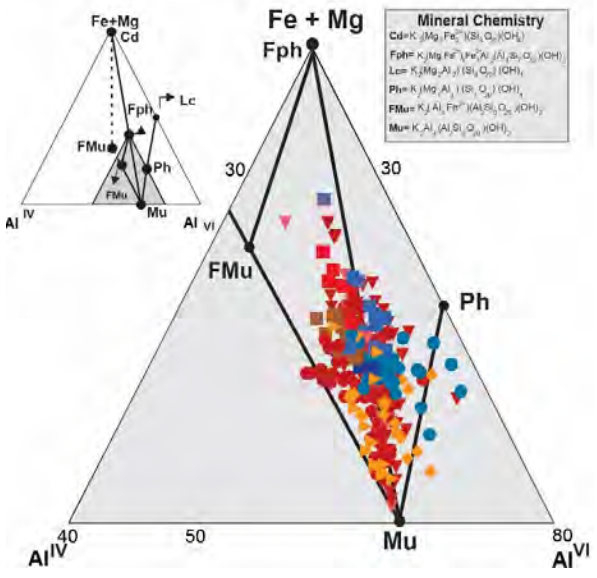


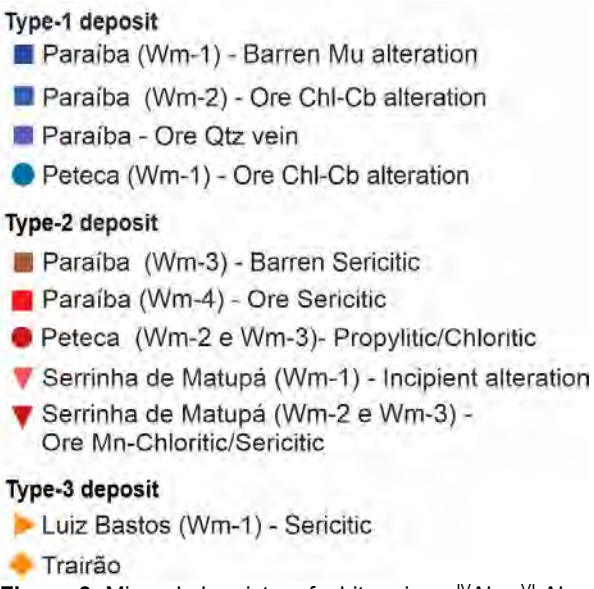


**Figure 3.** Mineral chemistry of white mica. $^{IV}Al - {}^{VI}Al - (Mg + Fe^{Tot})$ diagram classification of white mica with all AFMP data (Guidotti 1987). White mica end members: Mu, muscovite; Ph, phengite; FMu, ferrimuscovite; FMu*, ferrimuscovite; Fph, ferriphengite; Lc, leucophyllite; Cd, celadonite.

The pressures obtained using the phengite barometer in the Paraíba deposit distal muscovite alteration zone (Wm-1) is between 2.7 and 3.7 kbar. However, the Paraíba proximal Chl–Cb phyllonite ore veins and Peteca white mica are predominantly over 4.0 kbar. The pressures calculated using the phengite barometer define a broad field from 1 to 5 kbar. However, the pressures of the ore zones in all deposits are more limited and higher, from 3 to 4.5 kbar.

## 4 Conclusions

Chlorite and white micas in phyllonite and mineralization of the orogenic gold deposits (Paraíba, Peteca, and Serrinha de Guarantã deposits) have characteristic Mg- and Si-rich footprints. The chlorite broadly shows a high-Mg brunsvigitic to clinochlore composition, mainly controlled by the Fe↔Mg and Tschermak exchanges. The consistent high temperatures (above 350°C) and the Si ‹ 3 ‹ 4 ‹ $R^{2+}$ ‹ 5, and 2 ‹ $R^{3+}$ ‹ 3 ranges (apfu) correspond to metamorphic chlorite and support the correlation to the metamorphic and metamorphic–hydrothermal environments with pressures over 4 kbar, as indicated by the Peteca and Paraíba phyllonites. These temperatures and the Mg-high tendency are consistent with the typical mesozonal orogenic gold deposits elsewhere.

The white mica shows Mg- and Si-rich composition (Mg = 0.63, Si = 3.4) with restricted compositions controlled by the end members phengite, $K\,(Mg\,Fe^{2+})_{0.5}\,Al_{1.5}\,Si_{3.5}\,Al_{0.5}\,O^{10}\,(OH)^2$ and ferriphengite, $K(Mg\,Fe^{2+})_{0.5}\,Fe^{3+}{}_{0.5}\,Al\,Si_{3.5}\,Al_{0.5}\,O_{10}(OH)^2$ . High fluid pressures favour the production of phengitic mica (Ernst 1963), compatible with a

3.0–6.5 kbar field defined for the orogenic gold deposits assemblages. According to this author, the higher P and T favour the more significant extension of the solid solution between phengite and ferriphengite, which is also a characteristic feature of the phyllonites Wm-1 and Wm-2. The P–T, depth and fluid conditions are comparable with those proposed for orogenic gold mineralizations globally (5–15 km, e.g., Goldfarb and Groves 2015).

The magmatic–hydrothermal event formed the porphyry–epithermal deposits (Type-2 and -3 deposits). In the Paraíba deposit, the phengite of pervasive porphyry phyllic alteration (Wm-3) overprinted the Wm-1, obliterating the Sn+1 of the older muscovite phyllonite related to the orogenic gold phase. The Peteca deposit porphyry propylitic/chloritic alteration formed over a wide range of P–T (1–4 kbar and 290–380°C), yet at lower pressures than the earlier Peteca chlorite–carbonate phyllonite related to the orogenic gold phase. Both porphyry–epithermal deposits have the Fe-rich chlorite and ferrimuscovite trend as the common characteristic footprint, but the porphyry (Type-2) and epithermal (Type-3) deposits display in detail distinct characteristics. Porphyry chlorite (Serrinha de Matupá, and parts of the Paraíba, Peteca deposits) is mainly high-Fe brunsvigite to ripidolite. The temperatures range from intermediate to high (270–370°C) and have 1–5 kbar pressures.

White mica compositions are controlled mainly by the end members' muscovite, $KAl_2\ Si_3\ Al\ O^{10}(OH)^2$ and ferrimuscovite, $KFe^{3+}{}_{0.5}\ Al_{1.5}\ Si_3\ Al\ O^{10}(OH)^2$. The mean Si ranges from 3.45 to 3.12 apfu, the total Al ranges from 2.34 to 2.25 afpu, and the Fe + Mg + Mn ranges from 0.32 to 0.65 apfu, indicating that muscovite is not an end member but contains important ferriphengite compositions. The observed chemical variations are controlled mainly by theTschermak substitution. Porphyry white mica, especially Wm-3 and Wm-4 from Paraíba and Wm-2 and Wm-3 from the Peteca deposit, scatter the Tschermak substitution line towards lower Al values, which suggest variable amounts of $Fe^{2+}$ and $Fe^{3+}$ in the structure.

The epithermal-type chlorite and white micas (Luiz Bastos and Trairão deposits), on the other hand, have Al- and Fe-rich main footprints. Chlorite varies from diabanite to ripidolite, with high-Fe and Al ($Al^{VI}$ 1.97, $Fe^{tot}$ 0.61), controlled by Tschermak substitution. The vacancy variations (0–0.5) are governed by di-trioctahedral substitution. Temperatures range between 120°C and 260°C, and pressure ranges from 0.6 to 3 kbar. The white mica is dominantly in the muscovite–ferrimuscovite trend, richer in the muscovite end member and displaying the same scattering from the Tschermak substitution line, suggesting $Fe^{3+}$ substitution. These high-Al and lower-$Fe^{tot}$ characteristics of epithermal white mica are, however, also seen in part of Serrinha de Matupá and Peteca porphyry white mica. This fact and the extensive chlorite deviation from the amesite–clinochlore line towards higher vacancies and the Si of these hydrothermal populations could represent an evolution of the porphyry alterations with decreasing temperature. Interestingly, the Serrinha de Matupá incipient and phyllic alteration P–T field superimposes the Luiz Bastos chlorite–sericite alteration field, suggesting that the Serrinha de Matupá porphyry may have evolved towards an epithermal system.

Finally, the phyllonites' chlorite and white mica chemical composition have characteristic Mg-rich chlorite and Mg- and Si-rich muscovite–phengite footprints. The consistent high crystallization temperature (above 350°C) and almost zero vacancies suggest metamorphic chlorite. In contrast, Fe-rich and Al–Fe-rich alterations are the main footprints for the porphyry and epithermal deposits, respectively.

## Acknowledgements

The authors are grateful to the Institute of Geosciences of the University of Campinas, and the Microprobe Laboratory of Institute of Geosciences – UFRGS for supporting the analytical data.

## References

Bourdelle, F. and Cathelineau, M. 2015. Low-temperature chlorite geothermometry: a graphical representation based on a T–R2+–Si diagram. *European Journal of Mineralogy*, **27(5)**, 617-626. https://doi.org/10.1127/ejm/2015/0027-2467

Ernst, W. G. 1963. Significance of phengitic micas from low-grade schists. *American Mineralogist: Journal of Earth and Planetary Materials*, ***48*(11-12)**, 1357-1373.

Gaillard, N., Williams-Jones, A.E. et al. 2018. Mica composition as a vector to gold mineralization: deciphering hydrothermal and metamorphic effects in the Malartic district, Quebec. Ore Geology Reviews, 95, 789–820, https://doi.org/10.1016/j.oregeorev.2018.02.009

Goldfarb, R.J. and Groves, D.I. 2015. Orogenic gold: Common or evolving fluid and metal sources through time. Lithos, 233, 2–26, https://doi.org/10.1016/j.lithos.2015.07.011

Guidotti, C.V. and Sassi, F.P. 1998. Petrogenetic significance of Na–K white mica mineralogy: recent advances for metamorphic rocks. European Journal of Mineralogy, 10, 815–854, https://doi.org/10.1127/ejm/10/5/0815

Halley, S., Dilles, J.H. and Tosdal, R.M. 2015. Footprints: hydrothermal alteration and geochemical dispersion around porphyry copper deposits SEG Newsletter, 100, 1–17, https://doi.org/10.5382/SEGnews.2015-100.fea

Mesquita et al. 2022. Paleoproterozoic gold deposits at AFMP, Brazil: two overprinted mineralizing events? From: Torvela, T., Lambert-Smith, J. S. and Chapman, R. J. (eds). Recent Advances in Understanding Gold Deposits: from Orogeny to Alluvium. Geological Society, London, Special Publications, 516. https://doi.org/10.1144/SP516-2021-64

Sillitoe, R.H. 2010. Porphyry copper systems. Economic Geology, 105, 3–41, https://doi.org/10.2113/gsecongeo.105.1.3

Wiewióra, A. and Weiss, Z. 1990. Crystallochemical classifications of phyllosilicates based on the unified system of projection of chemical composition: II. The chlorite group. Clays and Clay Minerals, 25, 83–92, https://doi.org/10.1180/claymin.1990.025.1.09

# Gold in the Sardis Placer Deposit: Composition and Source of King Croesus's Gold

**Gülcan Bozkaya[1], David A. Banks[2,3], Ömer Bozkaya[1]**
*[1] Department of Geological Engineering, Pamukkale University, Denizli, Türkiye*
*[2] School of Earth and Environment, University of Leeds, Leeds, LS2 9JT UK*
*[3] Department of Geological Engineering, Istanbul University-Cerrahpaşa, Türkiye*

**Abstract.** In history, Sardis was important for its wealth derived from placer gold in the Pactolus River which erodes an alluvial fan containing the gold, thought to be derived from erosion of the Menderes Massif. We have shown that the exterior of gold grains was modified in the placer by biological and chemical processes. LA-ICPMS analyses indicate the presence of significant numbers of PGE particles and mineral inclusions that cast doubt on the source of the material in the alluvial fan. We propose that the gold in this alluvial fan was derived from laterization of the ophiolites that now form the Çaldağ laterite deposit prior to tectonic movement of the ophiolite unit to the NW. This is a Ni deposit and contains gold in some of the laterite units. The mineralogy in the alluvial fan at Sardis is also similar to some laterite units at Çaldağ.

## 1 Introduction

The legend of King Midas, and all that he touched turning to gold, is an etiological myth used to explain the rich alluvial gold deposits of the Pactolus River. In the legend, King Midas asked for the power to turn everything he touched into gold because he believed it would bring him great wealth and prosperity. According to the myth, King Midas was granted his wish by the god Dionysus, but he soon realized that his newfound power was more of a curse than a blessing as all he touched, including his daughter, turned to gold. Midas prayed to Dionysus to remove his power, who replied that this could only be done by washing in the river Pactolus. Thus, the power was transferred to the river and all the alluvium was turned to gold. The Legend of King Midas probably relates to King Croesus who ruled the Lydian empire from 560 to 546 BC. So rich was the gold resources in the river that the Lydians based their economy on its resources. An estimate of the richness can be made by the offering Croesus made to the Oracle at Delphi prior to his battle with Cyrus. The offering included 117 ingots of pure gold each weighing 150 lbs, a pure gold lion weighing 600lbs and a golden vat weighing some 522lbs. In total approximately 10,000 troy ounces with a current value of approximately $15 million. Lydia acquired great wealth and influence from the gold extracted from the Pactolus River and by the development of a process that separated gold and silver from electrum. This process ensured that for the first-time coins of a reliable and consistent value were used for commerce.

## 2 Location

The Pactolus River, now called Sart Çayı, from where the gold was extracted, originates from Mount Tmolus and runs north through ancient Sardis into the Gediz river which in ancient times was called the river Hormus. This cuts the same alluvial fans that are currently exploited commercially for several mineral resources including gold. However, despite there being a succession of alluvial fans in the Sardis area and along the margins of the Menderes Massif and the Gediz basin it is only in the oldest Neogene alluvial fan at Sardis is there any appreciable gold in specific conglomerate layers (Topkaya 1975). Today it does not have a steep gradient and its flow is quite inconsequential and would not have been able to account for the amount of placer gold recovered. Possibly tectonic movement has reduced the flow rate and the ability for gold to be eroded.

The study area is part of the larger extensional domain of the Alpine-Himalayan belt. The basement rocks of the study area are the Precambrian-early Mesozoic metamorphic rocks (Menderes Massif) and Upper Cretaceous-Paleocene ophiolitic rocks (Çaldağ unit) (Figure 1). Metamorphic rocks of the Menderes Massif were derived from a micro-continental block (the Anatolide–Tauride Block) and collision with the Sakarya continent,belonging to Eurasia during? the Mesozoic (Şengör and Yılmaz 1981). This metamorphic core-complex forms the western nuclei of the Anatolides and comprises a pre-Alpine "gneissic core" and an Alpine "schist and marble envelope". The core of the Menderes Massif consists, in ascending order of migmatites, para- and orthogneisses (leptites), amphibolites, granulites and eclogites (Candan et al. 2001).

## 3 External Features

The gold grains are flat, sub-rounded and essentially two dimensional, approximately 2-3 mm in size with the surface having a porous texture.

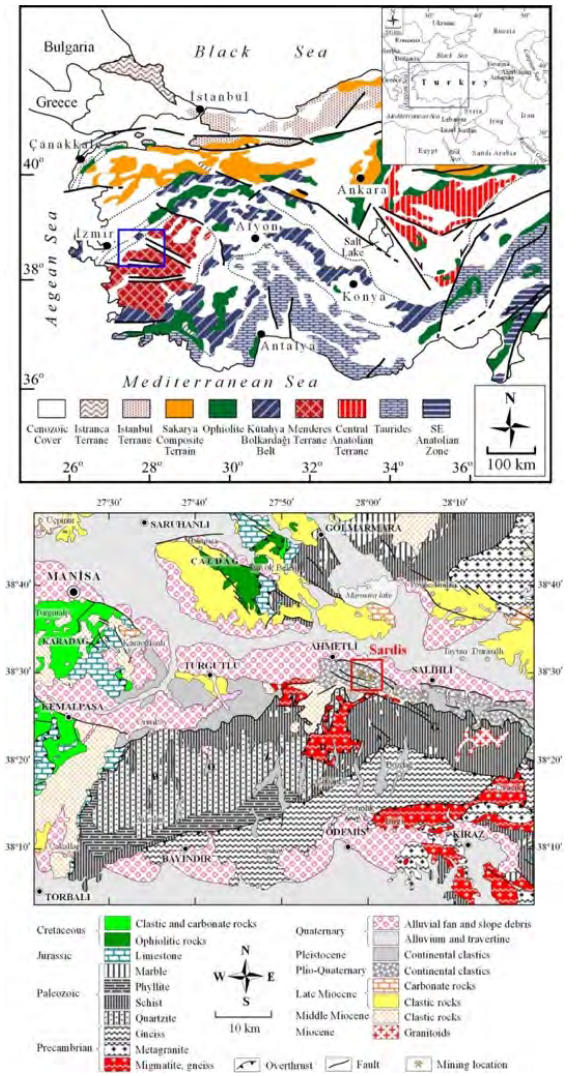


**Figure 1.** The distribution of the main Alpine terranes in Turkey and regional geology of Sardis and surrounding area (top). Modified from MTA (2002) and Göncüoğlu et al. (1997)**.** Location of Sardis is at the western end of the Gediz basin close to Izmir in Western Turkey**.** The alluvial fan located on the fault adjacent to the Menderes Metamorphic Complex to the south. The Çaldağ deposit and ophiolite are now located to the NW (bottom).

SEM images (Figure 2) shows this to be the result of the growth of new gold on top of the original gold grains. Layers of new gold are commonly seen to form a columnar structure (Figure 2a, c) with layers of gold stacked on top of each other. It is within these spaces that calcite, baryte and clays have been precipitated on top of the gold. These are the latest phase of mineral precipitation and always on top of the gold.

The outermost areas of the gold grains (Figure 3) have features that are consistent with a biological origin. All the features are of gold and are generally elongate with a smooth appearance. They are likely of bacterial origin, possibly as a result of conditions at the bacteria-water interface that was conducive to gold deposition. Similar features are found in gold grains from placer deposits in New Zealand (Reith et al. 2006). Certain bacteria can generate sub-micron gold particles or at the bacterial-water interface.? the conditions may induce the precipitation of gold nanoparticles. On all the smooth bacterial surfaces there are aggregates of gold particles (Figure 3. d,e g, h, i). that can be seen to be made from clusters of much smaller gold particles and may eventually reach the size of the ball-like accumulation in Figure 3e. The size of the individual particles is approximately 20nm or less. These particle aggregates are also found on the plate-like growths of the new gold described in the previous section (Figure 2c).

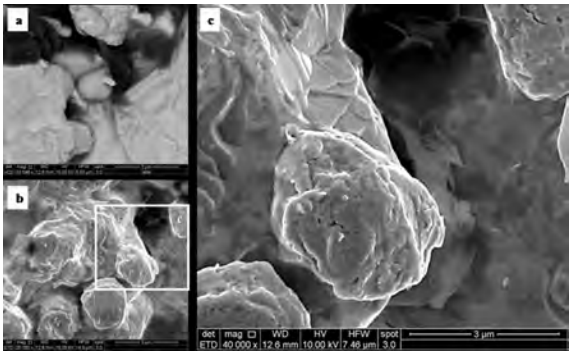


**Figure 2.** Exterior surface showing the presence of new euhedral gold crystals and columnar structures made from plates of new gold. These structures create the impression of porosity on the grain surfaces.

SEM-BSE images of polished grains (Figure 4) shows these have a dark core. Au and Ag element maps indicate Ag is depleted around the edges leaving an almost pure gold surface (Figure 4. a,b,c) Numerous mineral inclusions are also present in the centre of the grains involving elements such as Ni, Sb, Fe, Sn, Cu, As and Pt (Figure 4d. e,f). The example in Figure 4 shows a euhedral crystal and several smaller crystals of a Sb-Ni phase.

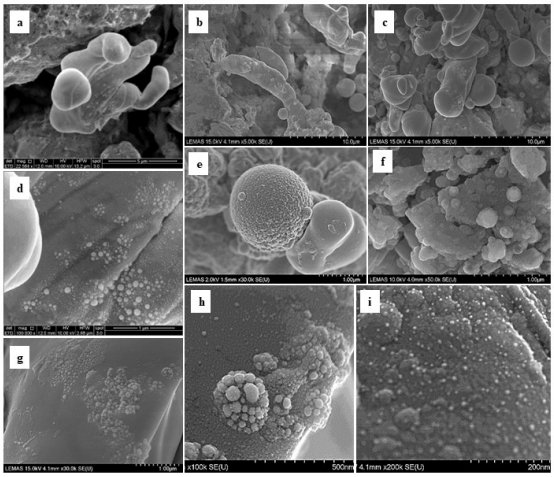


**Figure 3.** Bacterial-like features coated in Au on the surface of the grains. At high magnification these can be seen to be coated with nano-particles (20nm) of Au that aggregate to form larger spherical structures that can reach c. 1µm.

## 4 LA-ICPMS Analyses

The LA-ICPMS system uses an Agilent 7500c quadrupole mass spectrometer, with a Geolas ablation system to determine the composition of individual grains. The Geolas ablation system uses a Compex 103 ArF excimer laser at a wavelength of 193nm, delivering an energy density of 6 Jcm$^{-2}$ on the sample surface at a pulse frequency of 5Hz with spot sizes of 50 and 100µm. Calibration of the different elements was made using the standards AuRM2, MASS-1, NIST481 and 610.

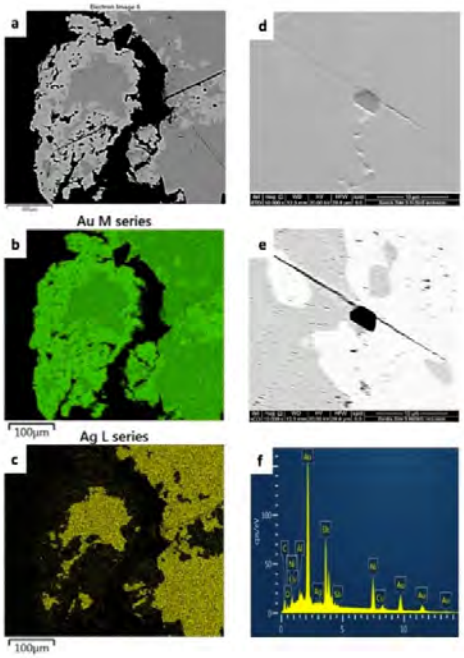


**Figure 4.** SEM-BSE images of the polished gold grains showing an Au-rich-edge and an Au-Ag alloy in the centre. Inclusion of a mineral trapped as the gold was precipitated. It is located at the margin of the Au-Ag alloy and the au-rich rim.

The analyses of the new formed gold on the outside of the original grains shows it is almost pure with Au content that averages 99.4% with low Ag averaging 0.4%. Many transition elements are present in the grains at low ppm or ppb levels except for Fe which is between a few 100's to 1000's ppm and Hg which is between a few 10's to a few 100's. The presence of a large number of elements likely arises from contamination whilst in the placer. The original placer grains have modified edges from the removal of Ag, in the placer environment, and show the same range and concentrations of transition elements as the newly formed gold. The main difference between new gold and the rims of the original placer grains are that Ag can be between 1 and 9% and Hg is between 100 and 3000 ppm which is much greater than in the newly formed gold.

The analyses from the central parts of the gold grains represent the original composition, essentially an alloy of Au, Ag, Hg and perhaps Cu and Sb which are homogeneously distributed at low concentrations. The concentrations of Au are between 90 and 80%, the Ag concentration is between 9 and 20% and Hg which has a reasonably consistent concentration between 3000 and 5000 ppm. All samples have effectively the same Cu concentration of 1 to 4ppm and unlike the other analyses low levels of Sb. Fe is present in less than half the analyses, occurring as small mineral inclusions, and averages 140 ppm. A few analyses contain Pb and Bi but these are due to mineral inclusions being ablated. Other elements present are from small inclusions within the grains. Examples of the elements that are part of the alloy and those that are present as particles are shown in Figure 5. The analysis of PGE's required a larger laser spot, longer dwell times on the elements and only Au and PGE being analysed. Rh, Pd, Re, Ir and Pt are recorded as individual spikes (Figure 6) averaging concentrations of a few 10's ppb. These nanoparticles are however relatively numerous. For 24 individual ablations the number of spikes recorded were Ru 17, Rh 41, Pd 29, Re 21, Os 13, Ir 52 and Pt 18.

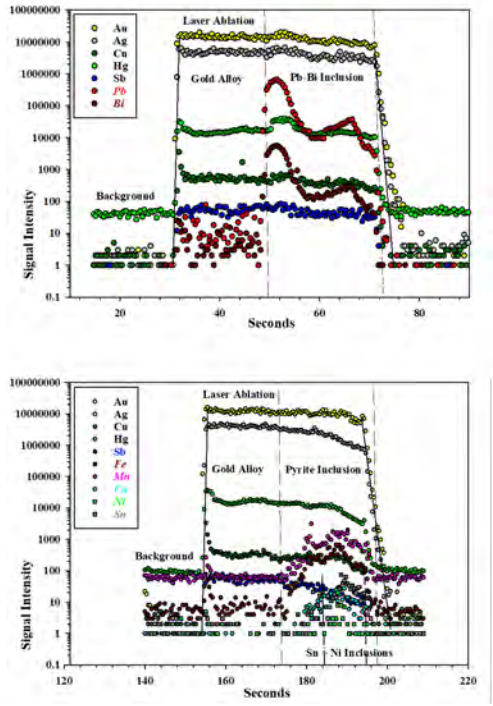


**Figure 5.** LA-ICPMS ablation profile of two gold grains. The alloy composition is Au, Ag, Cu Hg and Sb as indicated by their parallel profile. Beneath the surface there has been ablation of a Pb-Bi inclusion (top) and pyrite which contains some additional elements. There has also been ablation of Sn and Ni inclusions (bottom).

## 5 Discussion

Previous SEM analysis of the grains indicated they were almost pure gold (Rammage and Craddock 2000). This questioned the need for the process of separating gold and silver from electrum. If the grains were pure gold, then perhaps, they were actually separating the gold and silver from older

coins made from the electrum. It was also suggested that the porous surface of the grains was the result of grains being directly processed rather than beating gold grains to make thin sheets which were then processed to extract the silver. Our analyses show the grains are electrum but have a surface of pure gold consistent with previous SEM analyses that was used to assume the entire grains were pure gold.

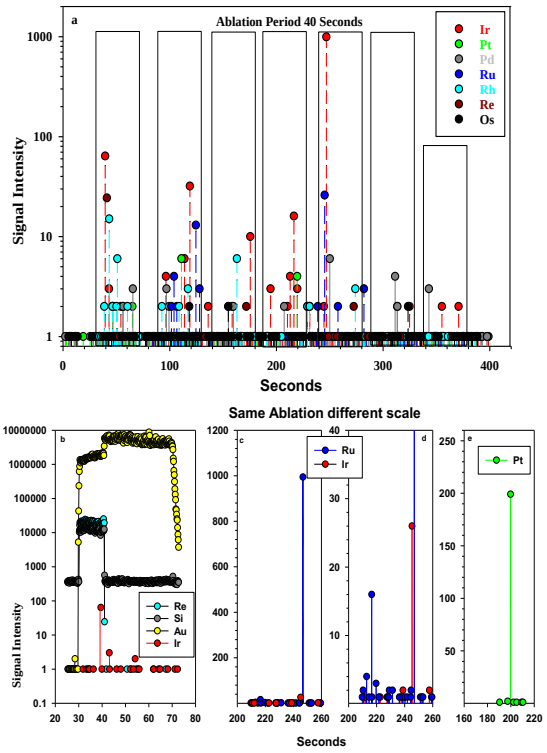


**Figure 6.** Several ablation profiles specifically for PGE's that are present as single large spikes indicating their presence as very small (nanoparticles?) inclusions in the grains.

A supposed distinctive feature of the artifacts recovered from Sardis is the presence of 50-150µm silver-coloured inclusions which when analysed are predominantly platinum, iridium alloys with some variable concentrations of osmium. These are observed in Achaemenian jewellery and Lydian coins (Young 1972) and are inferred to have been included in the gold. Similar gold artefacts were recovered from a royal tomb in Ur, Mesopotamia with the same size and composition of platinum, iridium osmium gold alloy. Such inclusions are uncommon in gold and only occur in specific geological environments such as ophiolites and related chromite deposits. Inclusions of PGE elements which were supposedly absent in Sardis grains led to interpretations that gold containing PGE's or only PGE's were brought to Sardis from different locations with various trade routes being proposed. However, we have shown that the gold does include numerous PGE inclusions that are consistent with the elements present in the artifacts.

The physical source of the placer gold is from the oldest alluvial fan on the northern margin of the Menderes Massif and it is thought that erosion of rocks of the massif was the source. However, the analyses of the gold with the presence of PGE elements and mineral inclusions with Pt, Ni, Sb, Sn, etc is more consistent with a ultramafic or ophiolitic source. The low concentrations of Cu and the appreciable concentrations of Hg together with the general absence of inclusions of pyrite, and galena are not consistent with an orogenic or magmatic style of mineralization. There is no indication that comparable units were present in the Menderes Massif. The Pactolus River is not very long or large and for the amount of recovered gold it must have been flowing through a very rich source in which the gold had been pre-concentrated.

We propose that the source of the gold was the Çaldag Ni-laterite deposit, now to the NW, but was previously located at Sardis prior to relocation by lateral movement on the main faults. The deposit lies on the Çaldağ horst of the Gediz Graben and covers approximately 10 km$^2$. This developed from the ultramafic rocks of the Late Cretaceous - Early Paleocene ophiolitic mélange of the flysch zone, located on the northern edge of the Menderes Massif, within the Gediz Graben (Figure 1). The laterite also contains electrum that has an Au and Ag composition consistent with the grains we have analysed.

## Acknowledgements

POMZA Export Company is thanked for supplying gold grains from their current mining operation.

## References

Candan, O, Dora, OÖ, Oberhansli, R, Çetinkaplan, M, Partzsch, JH, Warkus, FC, Dürr, S (2001) Pan-African high-pressure metamorphism in the Precambrian basement of the Menderes Massif, western Anatolia, Turkey. Int. J. Earth Sci 89: 793-811.

Göncüoğlu, MC, Kozlu, H, Dirik, K (1997) Pre-Alpine and Alpine terranes in Turkey: explanatory notes to the terrane map of Turkey. Ann. Geol. Pays Helleniques, 37: 515-536.

Helvacı, C, Gundogan, I, Oyman, T, Sözbilir, H, Parlak, O (2013) Geology, Mineralogy and Geochemical Properties of the Caldag Ni-Co Laterite Deposits. Bulletin of the Earth Sciences Applications and Research Centre of Hacettepe University, 34: 101-132.

MTA (2002) 1: 500,000 scaled geological map series of Turkey. Izmir section. Miner. Res. Explor. Ankara.

Ramage, A, Craddock, P (2000) King Croesus' Gold: Excavations at Sardis and the History of Gold Refining. Harvard University Art Museums and the British Museum Press. 272p.

Reith, F, Rogers, SL, McPhail, DC., Webb, D. (2006) Biomineralization of Gold: Biofilms on Bacterioform Gold. Science, 313: 233-236.

Şengör, AMC, Yılmaz, Y (1981) Tethyan evolution of Turkey: a plate tectonic approach. Tectonophysics 75: 181-241

Topkaya, YA (1975) Recent Evaluation of the Sart Placer Gold Deposit. MTA Report.

Young, WJ (1972) The Fabulous Gold of the Pactolus Valley. Boston Museum Bulletin 70: 4-13.

# Multiple sulphur isotope signatures of the Fenelon gold deposit, Abitibi Greenstone Belt, Canada: Constraints on fluid origin and ore-forming processes

**Evan Slater[1], Sébastien Castonguay[2], Anthony Williams-Jones[1], James Clark[1], Richard Stern[3]**
[1]*McGill University, Montreal, Canada*
[2]*Geological Survey of Canada, Québec, Canada*
[3]*Canadian Centre for Isotopic Analysis, University of Alberta, Edmonton, Canada*

**Abstract.** This study presents in situ multiple S isotope data ($^{32}S$, $^{33}S$, $^{34}S$) for sulphide phases from the Fenelon gold deposit (>4 Moz), in the Neoarchean Abitibi Greenstone Belt, to evaluate the nature of ore fluids and processes responsible for the formation of the deposit. Gold mineralization at Fenelon consists of two main stages: 1) auriferous quartz veins with molybdenite, and 2) gold- and sulphide-rich mineralization comprising early arsenopyrite, zoned and colloform pyrite, and lastly pyrrhotite-chalcopyrite-sphalerite-arsenopyrite-Bi-tellurides. All stages are interpreted to have formed during orogenic shortening. Multiple S isotope data for arsenopyrite and pyrite show near zero $\Delta^{33}S$ and positive $\delta^{34}S$ values. For zoned pyrite, $\delta^{34}S$ increases from grain cores (1.7‰ avg.) to rims (3.6‰ avg.), which is compatible with progressive reduction of the ore fluid. Chalcopyrite and pyrrhotite are characterized by near zero $\Delta^{33}S$ and similarly positive $\delta^{34}S$ values; however, there is a mixing trend with another S source with near zero $\delta^{34}S$ and positive $\Delta^{33}S$ (~0.5‰). The data are compatible with Fenelon having formed from magmatic fluids which incorporated S either from local country rock or by mixing with metamorphic-derived fluids near the site of deposition.

## 1 Introduction

The study of gold deposits in greenstone belts is challenging since regional metamorphism and deformation often overprint mineralization, masking geochemical signatures, ore textures and alteration parageneses. Therefore, an important question remains highly debated: whether Archean orogenic gold mineralization—i.e., synchronous with the main phase of shortening—form from dominantly metamorphic or magmatic fluids. The Fenelon gold deposit, a recent >4 Moz discovery in the Neoarchean Abitibi Greenstone Belt ('Abitibi'), Quebec, Canada, appears to have formed during shortening in a ductile-brittle environment, yet the mineralization has characteristics which differ from typical orogenic deposits. We have evaluated the mineralization at Fenelon by analysing multiple S isotopes to gain insight into the fluid origin and ore-forming processes.

The Abitibi is a prolific gold mining region with >200 Moz of past production and diverse mineralization styles (Dubé and Mercier-Langevin 2020 and references therein). Some deposits have been shown to pre-date the main phases of shortening such as the syngenetic Horne deposit and intrusion-related Coté gold deposit. However, most of the gold endowment of the Abitibi occurs within deposits that formed during the main phase of shortening when both metamorphism and magmatism were potentially active; e.g., the Young Davidson and Dome deposits. Such deposits are nevertheless considered to be orogenic, and there is ongoing debate on the origin of their ore fluids (e.g., Goldfarb and Pitcairn 2022).

### 1.1 S Isotopes in Ore Deposit Research

In most circumstances, the stable isotopes of S ($^{32}S$, $^{33}S$, $^{34}S$, and $^{36}S$) fractionate during physicochemical processes proportional to their respective masses. Fractionation occurs dominantly because of the speciation of S, and the heavier isotope preferentially fractionates into the oxidized species (e.g., Hutchison et al. 2020). This mass dependent fractionation of sulphur (MDF-S), typically traced using $^{34}S$, can be challenging to interpret as it is a function of both changes in the S reservoir and/or physicochemical processes including variations in pH, redox and temperature.

In Archean rocks, variations in $^{34}S$ inherited form reservoir can be distinguished from physicochemical processes by tracking the mass independent fractionation of sulphur (MIF-S), traced by $^{33}S$ ($\Delta^{33}S = [(\delta^{33}S/1000 +1) – (\delta^{34}S/1000 + 1)^{0.515}] \bullet 1000‰$; Farquhar et al. 2010); once set, $^{33}S$ remains unaffected by physicochemical processes. In the Archean oxygen-poor atmosphere, through which ultraviolet rays could pass freely, volcanic $SO_2$ dissociated to oxidized and reduced species imparting MIF-S signatures (Farquhar and Wing 2003). The oxidized species have been shown to have both positive and negative $^{33}S$ values, but reduced species have just positive values (Paris et al. 2014). These MIF-S signatures are preserved in rocks which interacted with the Archean atmosphere, mainly sediments, but also in magmatic rocks that incorporated sedimentary rocks or components of recycled oceanic lithosphere (LaFlamme et al. 2018a). Therefore, analysing $^{34}S$ in combination with $^{33}S$ can be a useful tool to evaluate fluid origin and evolution in Archean ore deposits (e.g., LaFlamme et al. 2018b).

## 2 Geology

### 2.1 Regional Geology

The Abitibi straddles the border between Ontario and Quebec in eastern Canada, and consists of east-west trending successions of folded

Neoarchean volcanic and sedimentary rocks settled between or faulted against intrusive domes and stocks (e.g., Monecke et al. 2017). Most gold deposits occur proximal to major E-W trending transcrustal fault zones such as the Destor-Porcupine and Larder Lake-Cadillac faults in the southern Abitibi (Dubé and Mercier-Langevin 2020, and references therein).

The Fenelon deposit is located within the Harricana-Turgeon Belt (Lacroix 1990), the most north-western belt in the Abitibi, which is bisected by the Sunday Lake Deformation Zone (SLDZ); the latter is a major E-W fault zone analogous to those in the southern Abitibi (Figure 2). Despite hosting the Detour Lake gold mine, the single largest such deposit in Canada (~40 Moz past production + reserves + resources; Leite et al. 2020), the belt and its ore deposits have seen limited research, most of which has focused on Detour Lake (Castonguay et al. 2020, and references therein). This belt shares many characteristics with the southern Abitibi including similar large-scale E-W trending deformation zones, syn-volcanic and syn-tectonic magmatism, sedimentary basins, and mineralization and alteration styles.

## 2.2 Local Geology

There are few outcrops in the deposit area, and thus the geology is interpreted mostly from diamond drill hole and aeromagnetic data (Fig. 1). Based on the latter, the stratigraphic units appear to be arranged in NW-SE trending packages. The immediate deposit area is dominated by ~2707 Ma argillite, which grades into <2705 Ma conglomeratic quartz-wacke (Carter 2022) to the southwest. Proximal to the SLDZ is a wedge of polymictic conglomerate which resembles 'Timiskaming-type' conglomerates associated with major deformation zones in the southern Abitibi (e.g., Bleeker 2015).

The sedimentary rocks are intruded by and interlayered with several calc-alkaline intrusions. To the northwest of the deposit lies the Jeremie Pluton, a polyphase granodiorite to diorite (Faure 2015). The ~2697 Ma Jeremie Diorite, possibly linked genetically to the Jeremie Pluton, is an important host rock for Au mineralization (Carter 2022). Mafic dykes of pyroxenite, gabbro and leucogabbro cut the sedimentary rocks and Jeremie diorite and are locally spatially associated with gold mineralization.

A penetrative foliation occurs throughout the deposit area affecting all rock types. To the northeast of the deposit and within it, a NW-SE-trending subvertical foliation is dominant whereas to the southwest the steep foliation is NE-SW trending.

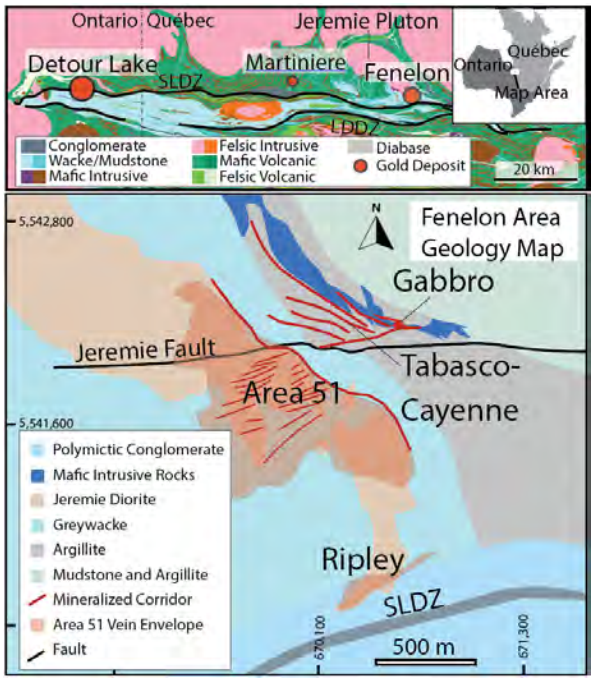


**Figure 2**. (Top) Geological map of the Harricana-Turgeon belt showing the locations of gold deposits (modified from Faure 2015). (Bottom) Fenelon deposit area geological map. The units are simplified, based on the geological model for the deposit interpreted from drill hole data. SLDZ – Sunday Lake Deformation zone, LDDZ – Lower Detour Deformation Zone. (Coordinates: UTM NAD83; zone 17).

## 2.3 Gold Mineralization

Gold mineralization at Fenelon is divided into several zones differentiated mainly by their host rocks and orientations (Figure 2). The Gabbro Zone consists of high-grade mineralization which follows steep SE-striking internal contacts and enclaves within a polyphase mafic sill. The Tabasco and Cayenne zones consist of steep SE-striking mineralized panels hosted in strained argillite that coalesce into the Contact Zone, which follows the near vertical contact of the Jeremie Diorite. There is an apparent spatial association between gold mineralization, graphitic argillite, and gabbroic intrusions in the Tabasco and Cayenne zones. Area 51 consists of multiple, parallel, ENE-striking, steeply dipping zones that are well mineralized in the Jeremie Diorite but also extend into the surrounding sedimentary rocks. To the south near the SLDZ is the Ripley zone which similarly consists of ENE-striking zones hosted mostly in a quartz diorite.

There are two main stages of mineralization at Fenelon. Stage 1 (M1) consists of sulphide-poor auriferous quartz veins with rare molybdenite. Stage 2 (M2) consists of sulphide-rich veins and lenses with three substages (Fig. 2): M2A is characterized by coarse-grained arsenopyrite; M2B comprises zoned and colloform pyrite; and M2C consists of intergrown pyrrhotite, chalcopyrite, sphalerite, arsenopyrite, Bi-tellurides, and native gold.

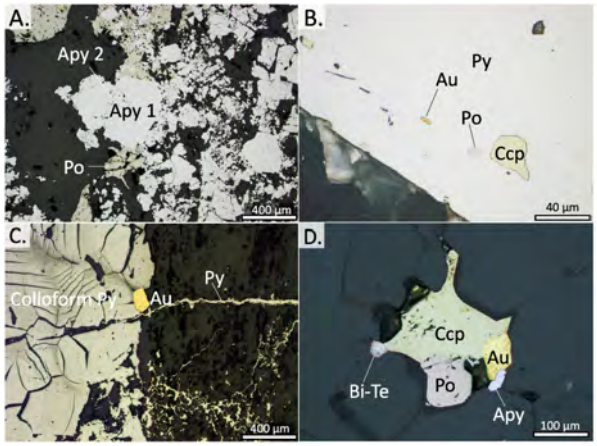


**Figure 3.** Reflected light images of sulphide mineralization from Fenelon. A) Coarse-grained M2A arsenopyrite (Apy 1) with fine-grained M2C arsenopyrite overgrowths (Apy 2) from Area 51. B) Zoned M2B pyrite with inclusions of gold (Au), pyrite (Py), pyrrhotite (Po), and chalcopyrite (Ccp) from Area 51. C) Colloform M2B pyrite associated with gold, and cut by pyrite veinlets in the Gabbro Zone. D) M2C gold intergrown with chalcopyrite, pyrrhotite, arsenopyrite and Bi-telluride (Bi-Te) from the Contact Zone.

## 3 Multiple S Isotopes

### 3.1 Methodology

Following a wholistic study of the mineralization at several scales, 17 representative polished sections that include the major ore zones were selected for isotopic analyses. From these, 19 regions of interest (2-4 mm diameter) were cored and arranged along with Canadian Centre for Isotopic Microanalysis (CCIM) reference materials into 25 mm diameter epoxy mounts. Backscattered electron (BSE) characterization of the samples was conducted by scanning electron microscopy (SEM) utilizing a Zeiss EVO M15 instrument.

Sulphur isotope ratios ($^{34}S/^{33}S/^{32}S$) were determined using the IMS-1280 multi-collector ion microprobe at the CCIM at the University of Alberta, Canada. Primary beam conditions utilized 20 keV $^{133}Cs^+$ ions focused to form a probe with a diameter of ~10 µm and beam current of ~ 1.2 nA. All secondary ions ($^{32}S$-, $^{33}S$-, and $^{34}S$-) were analysed simultaneously in Faraday cups (L2 using 1010Ω amplifier, L1 with 1012 Ω, and H1 with 1011 Ω, respectively) at a mass resolution of ~4000, sufficient to resolve potential isobaric interferences. The analytical protocol involved interspersing analyses of unknowns with CCIM primary reference material for pyrite (CCIM S0302A, $\delta^{34}S_{VCDT}$ = 0.0 ±0.2‰), pyrrhotite (S0322, $\delta^{34}S_{VCDT}$ = +1.2 ±0.1‰), chalcopyrite (CCIM S0321, $\delta^{34}S_{VCDT}$ = +0.2 ±0.2‰), and arsenopyrite (S0551, $\delta^{34}S_{VCDT}$ = +1.8 ±0.2‰). All primary reference materials have no known significant mass independent isotopic anomalies, i.e., $\Delta^{33}S = 0$.

The standard deviations of $^{33}S/^{32}S$-, $^{34}S/^{32}S$-, and $\Delta^{33}S$ for the pyrite, pyrrhotite, chalcopyrite, and arsenopyrite reference materials ranged from 0.05‰ to 0.1‰. Propagated uncertainties in $\delta^{33}S_{VCDT}$ and $\delta^{34}S_{VCDT}$ are reported at 95% confidence level (2σ) and have typical values of ±0.15 – 0.3‰, and for $\Delta^{33}S$ are assigned a conservative ± 0.15‰.

### 3.2 Results

Multiple S isotope data are presented in Figure 4 and Figure **5**. Data for arsenopyrite (n = 26) show a narrow range of $\delta^{34}S$ (-1.0 to +3.6‰, avg. = +2.4‰) with all $\Delta^{33}S$ values near zero (-0.12 to +0.15‰, -0.02‰ avg.). In sample GRAB-5080-001 (Figure 3A) from Area 51, two stages of arsenopyrite were analysed (M2A and M2C). The $\delta^{34}S$ values for M2C Apy (+2.6-+3.6‰, +3.6‰ avg., n=6) are higher than those for M2A Apy (+1.5-+2.9‰, +2.4‰ avg., n=4).

Data for M2B pyrite show a consistent trend wherein $\delta^{34}S$ increases from core (+0.8 to +2.9‰, +1.7‰ avg.) to rim (+2.7 to +5.0‰, +3.6‰ avg.). Data for sample D00116475D indicate that the growth zone with Au, pyrrhotite and chalcopyrite inclusions has elevated $\delta^{34}S$ (+2.4-+3.3‰, +3.0‰ avg.) relative to earlier growth stages. Despite the variations in $\delta^{34}S$, $\Delta^{33}S$ is consistently near zero showing no evidence of MIF-S (-0.15 to +0.12‰, 0.00 avg.).

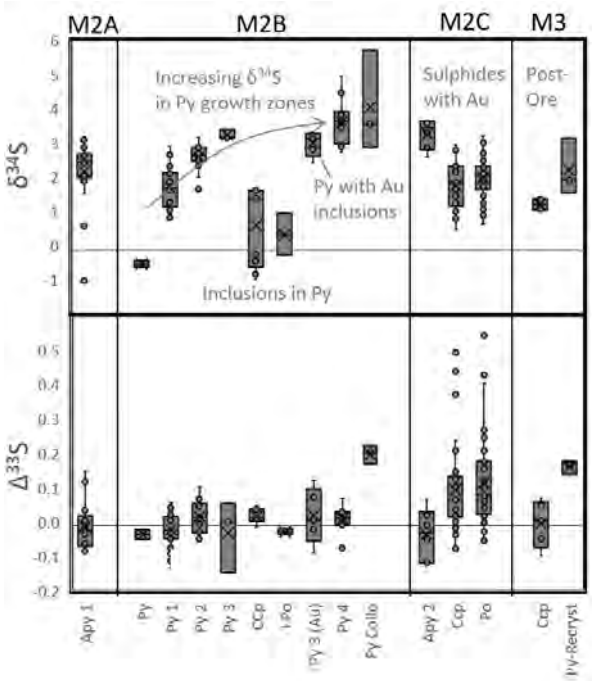


**Figure 4**. Whisker plots of multiple S isotope data grouped by paragenetic stage (M2A, M2B, M2C, M3) and sulphide phase. For M2B pyrite, $\delta^{34}S$ increases from core (py 1) to rim (py 2), yet $\Delta^{33}S$ stays near zero. The $\Delta^{33}S$ values for M2C chalcopyrite and pyrrhotite are elevated. Py – pyrite, Apy – arsenopyrite, Ccp – chalcopyrite, Po – pyrrhotite, Py – collo – Colloform pyrite.

Colloform pyrite from the Gabbro Zone yields positive $\delta^{34}S$ values (+2.9 to +5.7‰, +4.0‰ avg.)

and includes the highest $\delta^{34}S$ measured in this study. Data for post-ore pyrite that recrystallized from colloform pyrite indicates positive but slightly lower $\delta^{34}S$ values (+1.5-+3.2‰, +2.2‰ avg.). Both the colloform and recrystallized pyrite have $\Delta^{33}S$ values which are slightly positive (+0.14-+0.22‰, +0.18‰ avg.).

Chalcopyrite and pyrrhotite data cluster around $\delta^{34}S$ of ~+2.5‰ and $\Delta^{33}S$ of ~ 0‰, but some of the date appear to define a linear trend with a negative slope (Figure 5). Data for samples from the Tabasco and Contact zones have the most positive $\Delta^{33}S$ values (+0.37 to +0.54‰, +0.44 avg., and +0.13 to +0.28‰, +0.23‰ avg., respectively), indicating significant MIF-S. Inclusions of pyrrhotite and chalcopyrite in the zoned M2B pyrite from Area 51 have lower $\delta^{34}S$ values (-1.0 to +1.6‰, +1.1‰ average) than the rest of the data, and near zero $\Delta^{33}S$ (-0.10 to +0.07‰, 0.00‰ avg.). The inclusion analyses, therefore, diverge from the negative $\delta^{34}S$ vs. $\Delta^{33}S$ trend and do not show evidence of MIF-S.

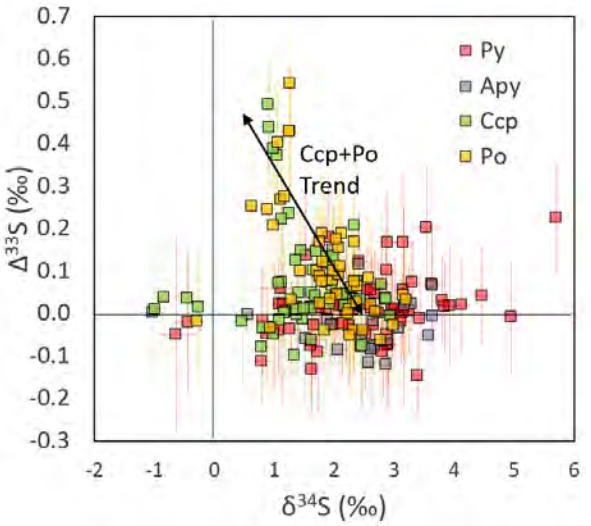


**Figure 5.** $\delta^{34}S$ vs. $\Delta^{33}S$ for all analyses coloured by mineral. Py – pyrite, Apy – arsenopyrite, Ccp – chalcopyrite, Po – pyrrhotite.

## 4 Conclusions

Multiple S isotope data indicate that gold mineralisation at Fenelon formed from a fluid dominated by mantle sulphur. This reservoir mixed with a small component of sedimentary S in the later stages of mineralisation, in association with elevated base metal concentrations. This is compatible with the main ore fluid being magmatic or metamorphic but derived from magmatic rocks (e.g., basalts). This fluid mixed with sedimentary S from either the country rock or metamorphic fluids with a sedimentary S component. A genetic model with predominantly magmatic fluids is favoured over metamorphic fluids to explain the elevated base metals in the deposit. Therefore, Fenelon is interpreted as a syn-orogenic intrusion-related deposit. It may be an example of a less common magmatic fluid-dominated endmember on a spectrum of orogenic deposits that form from predominantly metamorphic fluids, but with variable proportions of magmatic fluids.

## Acknowledgements

This study was funded by Wallbridge Mining Company, the Targeted Geoscience Initiative (Geological Survey of Canada), and a NSERC Alliance Grant. We thank Wallbridge's exploration geology team for providing their expertise and support during the research.

## References

Bleeker W (2015) Synorogenic gold mineralization in granite-greenstone terranes: the deep connection between extension, major faults, synorogenic clastic basins, magmatism, thrust inversion, and long-term preservation. Geological Survey of Canada, Open File 7852, pp 24–47

Carter J (2022) The geology of the Fenelon Deposit, Québec, Canada. M.Sc. Thesis, University of Toronto

Castonguay S, Dubé B, Wodicka N, Mercier-Langevin P (2020) Geological setting and gold mineralization associated with the Sunday Lake and Lower Detour deformation zones, northwestern Abitibi greenstone belt, Ontario and Quebec. Geological Survey of Canada, Open File 8712, pp 127–142

Dubé B, Mercier-Langevin P (2020) Gold Deposits of the Archean Abitibi Greenstone Belt, Canada. SEG Special Publications 23, pp 669–708.

Farquhar J, Wing BA (2003) Multiple sulfur isotopes and the evolution of the atmosphere. Earth Planet Sci Lett 213:1–13. https://doi.org/10.1016/S0012-821X(03)00296-6

Farquhar J, Wu N, Canfield DE, Oduro H (2010) Connections between sulfur cycle evolution, sulfur isotopes, sediments, and base metal sulfide deposits. Economic Geology 105:509–533.

Faure S (2015) Prolongement de la faille Sunday Lake (Mine Detour Gold, Ont) au Québec et son potentiel pour les minéralisations aurifères et en métaux de base. CONSOREM, rapport 2013-02

Goldfarb RJ, Pitcairn I (2022) Orogenic gold: is a genetic association with magmatism realistic? Miner Depos. https://doi.org/10.1007/s00126-022-01146-8

Hutchison W, Finch AA, Boyce AJ (2020) The sulfur isotope evolution of magmatic-hydrothermal fluids: insights into ore-forming processes. Geochim Cosmochim Acta 288:176–198. https://doi.org/10.1016/j.gca.2020.07.042

Lacroix S (1990) Géologie de la région des rivières Turgeon et Théo. Ministère des ressources naturelles du Québec, MB 90-28

LaFlamme C, Fiorentini ML, Lindsay MD, Bui TH (2018a) Atmospheric sulfur is recycled to the crystalline continental crust during supercontinent formation. Nat Commun 9. https://doi.org/10.1038/s41467-018-06691-3

LaFlamme C, Sugiono D, Thébaud N, et al (2018) Multiple sulfur isotopes monitor fluid evolution of an Archean orogenic gold deposit. Geochim Cosmochim Acta 222:436–446. https://doi.org/10.1016/j.gca.2017.11.003

Leite A, Dupont J-F, Raizman V, Fournier PA (2020) Detour lake operation Ontario, Canada NI 43-101 technical report

Monecke T, Mercier-Langevin P, Dubé B, Frieman BM (2017) Geology of the Abitibi Greenstone Belt. Reviews in Economic Geology 19:7–49

Paris G, Adkins JF, Sessions AL, et al (2014) Neoarchean carbonate-associated sulfate records positive δ33S anomalies. Science (1979) 346:739–741. https://doi.org/10.1126/science.1258211

# Gold mineralizing fluids at the Imonga mineralization in the eastern part of the Democratic Republic of Congo

**Inge Cools[1], Philippe Muchez[1], Stijn Dewaele[2]**
*[1]KU Leuven, Department of Earth & Environmental Sciences, Belgium*
*[2]Ghent University, Department of Geology, Belgium*

**Abstract.** In order to understand the origin of the gold mineralizing fluid in Central Africa, the formation history of the quartz veins hosted gold mineralization at Imonga (eastern Democratic Republic of Congo) has been studied. Imonga is part of a metallogenic province known to host various types of mineralization, including Sn-W-Nb-Ta-Li-Au. The characterization of the mineralizing fluid comprises a detailed study of the paragenesis of the mineralization, microthermometry, Raman spectroscopy and modelling. The analysis of fluid inclusions in the mineralized quartz veins indicates an $H_2O$-NaCl-KCl-$CO_2$ fluid composition and a $CO_2$-$N_2$-$CH_4$(-$H_2S$) gaseous system, which is compatible with a metamorphic origin of the fluid. The presence of $H_2S$ is characteristic for fluids carrying Au as reduced sulfur complexes. Calculated fluid salinity values range between 3.1 and 5.2 eq. wt% NaCl. The P-T formation window is proposed to range from 350°C to 400°C, with at 350°C an upper lithostatic pressure limit of 240 MPa, a burial depth of 9.2 km, and a lower hydrostatic pressure limit of 90 MPa. The corresponding density ranges between 0.78 g/cc and 0.91 g/cc. All observations allow the classification of the gold mineralization at Imonga as an orogenic gold deposit.

## 1 Introduction and geological setting

The Maniema province in the Democratic Republic of Congo (DRC) is part of the Central Africa Great Lakes area, well known for the occurrence of various types of mineralization, of which many are rich in elements critical for a high-tech and green industry. This metallogenic province also features substantial gold mineralization, of which the geological history is largely unknown. Previous studies of Walemba et al. (2004) and Fernandez-Alonso et al. (2012) linked the formation of the gold mineralization to the assembly of Gondwana, however, more recent studies propose an early Neoproterozoic timing linked to the assembly of Rodinia (Wouters et al. 2020).

In order to understand orogenic gold deposits in metamorphic belts, a thorough knowledge concerning the deformation, metamorphism and mineralization phases, age of the mineralization, characteristics and source of the mineralizing fluid, the architecture of the hydrothermal system and deposition mechanisms are required (Groves et al. 2003).

To enhance the knowledge on orogenic gold mineralizing fluids in Central Africa, more specifically in the Western Domain (WD) of the Karagwe-Ankole Belt (KAB), deposits and prospects within this area are being studied, among which the Imonga prospect. Besides a preliminary study of exploration drill cores and previous knowledge regarding gold mineralization at Imonga formulated by Van Eykeren (1950) and Kazmitcheff (1954, 1961), no in-depth studies concerning the gold mineralization at Imonga were carried out. The aim of this study is to characterize the mineralizing fluids and to deduce the precipitation conditions of the gold.

### 1.1 Geological setting

From a geological point of view, the southern part of Maniema is a complex area where the Mesoproterozoic Karagwe-Ankole Belt (KAB), Kibara Belt (KIB) and the Paleoproterozoic Rusizi-Ubende Shear Belt (RUB) meet (Figure 1) (Fernandez-Alonso et al. 2012). Within the KAB, two distinct structural domains are identified: (1) the Western Domain (WD), occurring in Rwanda, Burundi, Uganda and the DRC provinces of Kivu and Maniema, and (2) the Eastern Domain (ED) in Burundi and NW Tanzania (Tack et al. 2010).

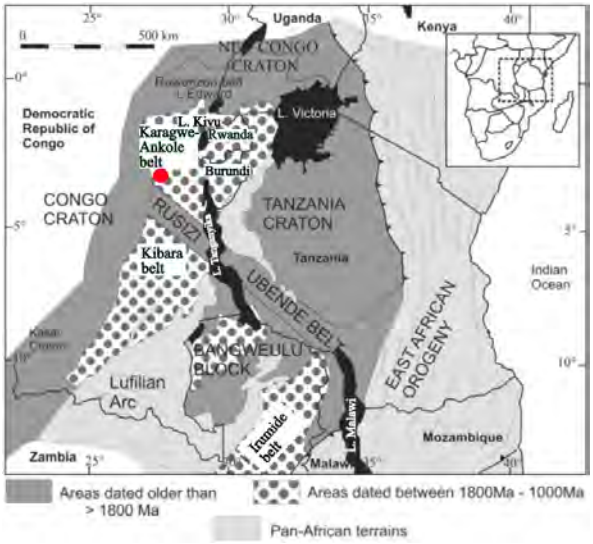


**Figure 1.** Tectonic setting of the KIB and the KAB in Central Africa (modified after Dewaele et al. 2015). The red dot indicates the study area.

### 1.2 The Imonga mine and prospect

The Imonga mine and prospect are located in the Maniema province, close to the border with South Kivu. This region hosts numerous gold mineralization of which some have been actively mined. The formation conditions of gold deposit, e.g., precipitation mechanism and P-T conditions, and the source of gold mineralization have, however, not been previously studied.

The Imonga prospect is part of the Imonga mine site (3°35'40.9"S 27°03'16.2"E) where alluvial and eluvial gold deposits were actively mined from 1931 until 1958 (Kazmitcheff 1961). Drilling was conducted near the mine site in order to perform a preliminary exploration (Kazmitcheff 1961). Representative rock samples from two cores have been preserved at the Royal Museum of Central Africa (RMCA) in Belgium.

## 2 Petrography and paragenesis

The current study started with a detailed petrographic and paragenetic study, of which results are discussed in Cools et al. (2022).

The host rocks of Imonga have been strongly altered, deformed and underwent foliation to the greenschist metamorphic grade. Post-foliation porphyroblasts of different minerals have been observed, with the characteristic occurrence of andalusite porphyroblasts. Four different generations of veins have been identified. The second vein generation (V2) consists of post-foliation quartz-ferroan dolomite-chlorite veins, that are strongly associated with sulfide (pyrite, chalcopyrite and arsenopyrite) and gold mineralization. This generation displays quartz deformation structures such as crystalplastic deformation (undulose extinction, bulging and subgrain recrystallization), as well as variation in vein growth morphology and inclusion bands which indicate crack-seal mechanisms. The third vein generation (V3) are post-foliation quartz-ferroan calcite-chlorite veins, strongly associated with sulfide (pyrite and chalcopyrite) mineralization.

Andalusite porphyroblasts in greenschist facies are thought to have formed post-foliation, both prior and after the second vein generation, thus closely related with the gold mineralization and can therefore be used to constrain the P-T window.

## 3 Methodology

The nature of the mineralizing fluid related to the gold mineralization has been studied by analyzing fluid inclusions (FI) in quartz crystals in three samples of V2 (IM78, IM79 and IM80) and one sample of V3 (IM77).

The analysis of the mineralizing fluid involved (1) a petrographic study of primary FI's, followed by (2) a microthermometric study using a Linkam THMSG 600 heating-freezing stage, mounted on an Olympus BX51 microscope, and (3) the analysis of the composition of the gaseous phases by Raman spectroscopy using a Horiba Labram HR Evolution, linked to an Olympus BX41 microscope. All the obtained data were used to (4) model the fluid characteristics and to (5) determine the P-T formation conditions using isochores.

## 4 Results and discussion

### 4.1 Fluid inclusion petrography

Two main types of primary FI's were distinguished in the veins studied: (1) FI's that consist of two phases, a liquid and a gaseous phase; (2) FI's that consist of three phases at room temperature, namely two liquid phases and a vapor phase. Both fluid inclusion types occur in the second vein generation, while in the third vein generation almost exclusively two-phase inclusions have been observed.

### 4.2 Microthermometry

Results of the microthermometric analysis have been incorporated in Table 1. The observed temperatures of phase transitions provide information regarding the composition of the fluid: (1) for both V2 and V3, $Tm_{CO2}$ ranges from - 59.9 to - 56.6°C. Observations of $Tm_{CO2}$ at lower temperatures than for a pure carbonic phase (- 56.6°C) indicate the presence of other gaseous components besides $CO_2$ (Shepherd et al. 1985). These additional gases have been identified by Raman spectroscopy of the gaseous phase (section 4.3); (2) Tfm ranges for both vein generations from - 24.5 to - 20.1°C. The comparison of the observed Tfm with eutectic temperatures of known systems (Goldstein and Reynolds 1994), indicates the presence of an $H_2O$-NaCl-KCl fluid. Eutectic temperatures lower than - 23.5°C indicate the presence of divalent salt cations; (3) final ice melting differs for both vein generations. $Tm_{ice}$ of V2 ranges from - 8.7°C to - 5.4°C, while data for V3 vary between - 7.6°C and - 2.1°C; (4) $Tm_{clath}$ ranges from + 6.4°C to + 10°C; (5) $Th_{CO2}$ has only been observed for three-phase FI's of V2, ranging from + 27.5°C to + 31.2°C; (6) for V3, the low number of observations of $Tm_{CO2}$ and $Tm_{clath}$, as well as the lack of $Th_{CO2}$ observations, could indicate a limited occurrence of gaseous $CO_2$; (7) for both vein generations, the minimum formation temperature is initially estimated to lie between + 210°C and + 250°C, based on the $Th_{tot}$.

### 4.3 Raman spectroscopy

Molar fractions of $CO_2$, $N_2$ and $CH_4$ have been calculated based on peak area calculations of Raman spectroscopic analysis (Burke 2001; Frezzotti et al. 2012). Raman spectroscopic analyses show a range in the gaseous composition of V2 inclusions between 69 and 99 mol% $CO_2$, 0 and 31 mol% $N_2$ and between 0 and 5 mol% $CH_4$ with minor $H_2S/HS^-$. This composition is compatible with a metamorphic origin of the fluid (Dewaele et al. 2004; Kenis et al. 2005). Increasing $N_2$-content, linked to a decreasing $CO_2$-content, is interpreted to result from reactions during metamorphism and fluid-rock interaction during circulation of the fluids (Kenis et al. 2005).

The composition of the V3 inclusions ranges between 60 and 100 mol% $N_2$, 0 and 35 mol% $CO_2$ and between 0 and 10 mol% $CH_4$. None of the spectra indicates the presence of $H_2S/HS^-$. The high

$N_2$ content could indicate an increased influence of water-rock interaction (Kenis et al. 2005).

**Table 1.** Overview of the microthermometric data[1].

| | V2 | V3 |
|---|---|---|
| $Tm_{CO2}$ | - 59.3 to - 56.6°C<br>$\bar{X}$ = - 56.9°C<br>n = 73 | - 57.7 to - 56.7°C<br>$\bar{X}$ = - 57.0°C<br>n = 3 |
| Tfm | - 24.5 to - 20.1°C<br>$\bar{X}$ = - 22.7°C<br>n = 227 | - 24.4 to - 20.1°C<br>$\bar{X}$ = - 22.9°C<br>n = 78 |
| $Tm_{ice}$ | - 8.7 to - 5.4°C<br>$\bar{X}$ = - 6.8°C<br>n = 189 | - 7.6 to - 2.1°C<br>$\bar{X}$ = - 5.5°C<br>n = 84 |
| $Tm_{clath}$ | + 6.4 to + 8.9°C<br>$\bar{X}$ = + 7.4°C<br>n = 73 | + 6.9 to + 10 °C<br>$\bar{X}$ = + 8.9°C<br>n = 4 |
| $Th_{CO2}$ | + 27.5 to + 31.2°C<br>$\bar{X}$ = + 29.9°C<br>n = 17 | No observations |
| $Th_{tot}$ | + 207 to + 250°C<br>n = 43 | + 210 to + 250°C<br>n = 9 |
| Salinity (eq. wt% NaCl) | 3.1 to 5.2<br>$\bar{X}$ = 4.4<br>n = 65 | 3.5 to 4.4<br>$\bar{X}$ = 4.0<br>n = 4 |
| Density (g/cc) | 0.74 to 0.95 g/cc<br>$\bar{X}$ = 0.83 g/cc<br>n = 70 | 0.85 to 0.90 g/cc<br>$\bar{X}$ = 0.87 g/cc<br>n = 4 |

[1] n = number of FI's; $Tm_{CO2}$ = final melting of the carbonic phase; Tfm = first melting of the solid aqueous phase; $Tm_{ice}$ = final ice melting; $Tm_{clath}$ = melting of the clathrate; $Th_{CO2}$ = homogenization of carbonic phases into the liquid phase; $Th_{tot}$ = total homogenization.

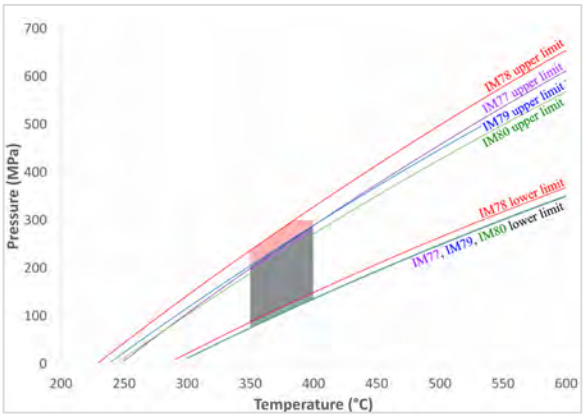


**Figure 2.** The upper and lower limit isochores, obtained by the 'Isoc' program (Bakker 1997, 2003) for each sample. The areas indicate the P-T formation conditions.

### 4.4 Fluid characterization and formation conditions

All obtained results have been used to characterize and model the fluid properties. The combination of the microthermometric and Raman spectroscopic results are indicative of the presence of a fluid with an $H_2O$-NaCl-KCl-$CO_2$-$N_2$-$CH_4$-$H_2S$ composition.

Calculated salinity and density values, by the program 'Ice' (Bakker 1997, 2003), for both vein generations fall within the same range (Table 1). Salinity values range from 3.1 to 5.2 eq. wt% NaCl. The density values range from 0.74 to 0.95 g/cc.

Based on the isochores, constructed by the program 'Isoc' (Bakker 1997, 2003), the P-T conditions for the formation conditions of the two vein generations studied, have been determined. Constraints on the P-T window include: (1) the minimum formation temperature based on $Th_{tot}$ which ranges between +200°C and +250°C; (2) the metamorphic grade of greenschist metamorphism characterized by andalusite porphyroblasts indicating a P-T range between 350°C and 450°C and 50 MPa and 300 MPa, respectively (Bushmin and Glebovitsky 2008); (3) quartz deformation structures that have been observed which are typically formed at temperatures from 300°C to 400°C (Passchier and Trouw 2005). The combination of all these constraints results in an applied temperature window ranging from 350°C to 400°C.

The P-T formation conditions deduced for both V2 and V3 fall within the same range (Figure 2) . For example, the isochores obtained for sample IM78 of V2 are discussed (Figure 2). At the proposed temperature of 350°C, an upper, lithostatic pressure limit of 240 MPa is deduced from the top isochore, corresponding to a depth of 9.2 km. The lower, hydrostatic, pressure limit corresponding to this depth is 90 MPa. The density of the fluids within this P-T formation window ranges from 0.78 up to 0.91 g/cc, with salinity between 3.1 to 5.2 eq. wt% NaCl. Combination of all the samples yields a highest upper limit of 240 MPa (9.2 km) and a lowest lower limit of 72 MPa (Figure 2).

## 5 Discussion and conclusion

Gold mineralization at Imonga has been observed in post-foliation V2 quartz-ferroan dolomite-chlorite veins, that formed closely related to andalusite porphyroblasts. It is associated with sulfide mineralization, including pyrite and chalcopyrite. The mineralizing fluid has an $H_2O$-NaCl-KCl-$CO_2$-$N_2$-$CH_4$-$H_2S$ composition and a temperature between 350 and 400°C, compatible with a metamorphic origin (Kenis et al. 2005). The salinity of this fluid ranges from 3.1 to 5.2 eq. wt% NaCl, with a density between 0.87 and 0.94 g/cc. The presence of $H_2S$ is characteristic for fluids carrying Au as an $Au(HS)^-_2$ or $Au(HS)_0$ complex (Robb 2005). The variation in the fluid pressure between 90 and 240 MPa can be explained as (cyclic) fluctuations between the lithostatic and hydrostatic pressure during vein development, as described by the fault-valve model for mesothermal and orogenic gold systems (Sibson et al. 1988).

An orogenic origin is proposed for the gold mineralization at Imonga, based on the correspondence with the fluid characteristics of orogenic gold in metamorphic belts, such as salinity and P-T formation conditions (Groves et al. 2003).

Gold at Imonga was most likely transported by gold-sulfur complexes. The close association between the gold and Fe-sulfides indicates that these complexes could have been destabilized through interaction of the mineralizing fluid with the iron-bearing host rock. Such interaction not only explains the precipitation of gold, but also of the Fe-sulfides. However, the variation in fluid pressure observed and which likely resulted from fault-valve activity, could also have contributed to the precipitation of gold (Mikucki 1998).

## Acknowledgements

We would like to thank Herman Nijs (KU Leuven) for carefully preparing the thin, polished, and double polished sections. We are grateful to Florias Mees and the RMCA for providing access to the Imonga samples. The Raman equipment was acquired via the medium-scale research infrastructure FWO grant Raman-SIM2 (number I000718N).

## References

Bakker, R.J. (1997) Clathrates: Computer programs to calculate fluid inclusion V- X properties using clathrate melting temperatures. Computers & Geosciences 23(1): 1–18. https://doi.org/10.1016/S0098-3004(96)00073-8

Bakker, R.J. (2003) Package FLUIDS 1. Computer programs for analysis of fluid inclusion data and for modelling bulk fluid properties. Chemical Geology 194(1):3–23. https://doi.org/10.1016/S0009-2541(02)00268-1

Burke, E.A.J. (2001) Raman microspectrometry of fluid inclusions. Lithos 55(1):139–158. https://doi.org/10.1016/S0024-4937(00)00043-8

Bushmin, S., Glebovitsky, V. (2008) Scheme of Mineral Facies of Metamorphic Rocks. Geology of Ore Deposits 50:659-669. https://doi.org/10.1134/S1075701508080011

Cools, I., Muchez, Ph., Dewaele, S. (2022) Mineralogical and geochemical study of the Au mineralization at Imonga, Maniema (DRC). Geologica Belgica vol. 25, nr. 3-4:185-190. https://popups.uliege.be/1374-8505/index.php?id=7030.

Dewaele, S., Muchez, P., Banks, D. A. (2004) Fluid evolution along multistage composite fault systems at the southern margin of the lower Palaeozoic Anglo-Brabant fold belt, Belgium. Geofluids 4(4):341–356. https://doi.org/10.1111/j.1468-8123.2004.00096.x

Dewaele, S., Hulsbosch, N., Cryns, Y., Boyce, A., Burgess, R., Muchez, P. (2015) Geological setting and timing of the world-class Sn, Nb-Ta and Li mineralization of Manono-Kitotolo (Katanga, Democratic Republic of Congo). Ore Geology Reviews 72:373-390. https://doi.org/10.1016/j.oregeorev.2015.07.004

Fernandez-Alonso, M., Cutten, H., De Waele, B., Tack, L., Tahon, A., Baudet, D., Barrit, S.D. (2012) The Mesoproterozoic Karagwe-Ankole Belt (formerly the NE Kibara Belt): the result of prolonged extensional intracratonic basin development punctuated by two short-lived far-field compressional events. Precambrian Research 216:63-86. https://doi.org/10.1016/j.precamres.2012.06.007

Frezzotti, M.L., Tecce, F., Casagli, A. (2012) Raman spectroscopy for fluid inclusion analysis. Journal of Geochemical Exploration 112:1–20. https://doi.org/10.1016/j.gexplo.2011.09.009

Goldstein, R.H., Reynolds, T.J. (1994) Systematics of fluid inclusions in diagenetic minerals. Society for Sedimentary Geology, SEPM Short Course Notes 31. https://doi.org/10.2110/scn.94.31

Groves, D.I., Goldfarb, R.J., Robert, F., Hart, C.J.R. (2003) Gold deposits in metamorphic belts; overview of current understanding, outstanding problems, future research, and exploration significance. Economic Geology and the Bulletin of the Society of Economic Geologists 98(1):1-29. http://dx.doi.org/10.2113/gsecongeo.98.1.1

Kazmitcheff, A. (1954) Etude des sondages d'Imonga & Résultats d'analyse et problème de l'or d'Imonga. Service des prospections Kampene, à COBELMIN. N° S.P. 20/54.

Kazmitcheff, A. (1961) Les roches albitiques et carbonatés des sondages d'Imonga (Maniema). Mémoires de l'Institut Géologique de l'université de Louvain. Tome XXII:69-96.

Kenis, I., Muchez, P., Verhaert, G., Boyce, A., & Sintubin, M. (2005) Fluid evolution during burial and Variscan deformation in the Lower Devonian rocks of the High Ardenne slate belt (Belgium); sources and causes of high-salinity and C-O-H-N fluids. Contributions to Mineralogy and Petrology 150(1): 102-118. https://doi.org/10.1007/s00410-005-0008-9

Mikucki, E.J. (1998) Hydrothermal transport and depositional processes in Archaean lode-gold systems: A review. Ore Geology Reviews 13:307–321. https://doi.org/10.1016/S0169-1368(97)00025-5

Passchier, C., Trouw, R. (2005) Microtectonics (2nd, Revised and Enlarged ed.). Springer, Berlin / Heidelberg. https://doi.org/10.1007/3-540-29359-0

Robb, L. (2005) Introduction to ore-forming processes. Blackwell, London.

Shepherd, T.J., Rankin, A.H. and Alderton, D.H. (1985) A Practical Guide to Fluid Inclusion Studies. Blackie and Sons, Glasgow.

Sibson, R., Robert, F., Poulsen, K. (1988) High-angle reverse faults, fluid-pressure cycling, and mesothermal gold-quartz deposits. Geology (Boulder) 16(6):551-555. https://doi.org/10.1130/0091-7613(1988)016<0551:HARFFP>2.3.CO;2

Tack, L., Wingate, M.T.D., De Waele, B., Meert, J., Belousova, E., Griffin, B., Tahon, A., Fernandez-Alonso, M. (2010) The 1375 Ma "Kibaran event" in Central Africa: Prominent emplacement of bimodal magmatism under extensional regime. Precambrian Research 180:63–84. https://doi.org/10.1016/j.precamres.2010.02.022

Van Eykeren, H. (1950) Les Gisements Aurifères de Mukukutshi, Itabatshi, Imonga et Katulu. Cobelmin – A.G.A., Rapport 6/50, RMCA Archives.

Walemba, K.M.A., Viljoen, M.J., Viljoen, R.P. (2004) Geological setting, genesis and evolution of the Twangiza gold deposit, Kivu, eastern D.R.Congo. in: Geoscience Africa 2004 Conference, Abstracts Volume 2,University of the Witwatersrand, Johannesburg, 12–16 July 2004, 682–683.

Wouters, S., Hulsbosch, N., Kaskes, P., Claeys, Ph., Dewaele, S., Melcher, F., Onuk, P., Muchez, Ph. (2020) Late orogenic gold mineralization in the western domain of the Karagwe-Ankole Belt (Central Africa): Auriferous quartz veins from the Byumba deposit (Rwanda). Ore Geology Reviews 125:103666. https://doi.org/10.1016/j.oregeorev.2020.103666

# Timing of the Orogenic Jouhineva Au-Cu-Co and Huhta Au mineralization: Constraints from titanite U-Pb dating

**Andressa A. Silva[1], Clifford G.C Patten[1], Jochen Kolb[1], Simon Hector[1], Benjamin Walter[1], Aratz Beranoaguirre[1], Elisabeth Eiche[1,2]**

*[1]Chair of Geochemistry and Economic Geology (EGG), Institute of Applied Geosciences (AGW), Karlsruhe Institute of Technology (KIT), Karlsruhe, Germany*

*[2]Laboratory for Environmental and Raw Materials Analysis (LERA), EGG-AGW, KIT Karlsruhe, Germany*

**Abstract.** The Pojahnmaa Belt (PoB) hosts orogenic gold deposits with unusual metal contents. These deposits are hosted by metavolcanic and metasedimentary rocks and by similar structures as orogenic Au-only deposits. The reason for the different metal associations in the deposits is not well understood. This study investigates the Jouhineva Au-Cu-Co deposit and the Huhta Au occurrence from the PoB by combining in-situ titanite dating with detailed petrography. Six titanite types associated with the As-Au-Co and Cu-Au mineralization events were described and U-Pb dating from these titanite types was carried out. Jouhineva contains titanite associated with arsenopyrite veins ($Ttn_{1.1J}$), in the alteration halo ($Ttn_{1.2J}$), and with sericite-chlorite alteration ($Ttn_{2J}$). Huhta contains titanite in quartz-actinolite-pyrite-arsenopyrite veins ($Ttn_{1.1H}$) associated with arsenopyrite in the alteration halos ($Ttn_{1.2H}$). A titanite generation is associated with chalcopyrite, and sericite alteration ($Ttn_{2H}$). The dated titanite associated with the As-Au-(Co) mineralization was formed at 1854 ± 15 Ma ($Ttn_{1.1H}$) and 1816 ± 12 ($Ttn_{1.1J,}$ and $Ttn_{1.2J}$). The titanite associated with chalcopyrite and sericite-chlorite alteration was formed at 1760 ± 14 and 1744 ± 30 Ma ($Ttn_{2H}$ and $Ttn_{2J}$, respectively). These ages indicate that the mineralization in the PoB was multi-stage and formed over, at least, three different periods.

## 1 Introduction

Orogenic Au deposits are generally considered Au-only deposits, where Au is the only commodity that can be mined economically (Goldfarb et al. 2005). Recently, several orogenic Au deposits have been discovered, particularly in Finland, which contain Cu, Co, Ni, Sb, U, and REE that are mined or of potential economic interest (Eilu 2015). Two hypotheses can account for this atypical endowment (1) an overprinted porphyry Cu mineralization by an orogenic Au one; or (2) a multi-stage orogenic Au mineralization (Eilu 2015, Patten et al. 2022, Hector et al. 2023).

The Paleoproterozoic Pohjanmaa Belt (PoB) is located in southwestern Finland and hosts the Jouhineva Au-Cu-Co deposit and the Huhta Au-only occurrence (Figure 1A-B; Hector et al. 2023). Jouhineva and Huhta are at a large scale controlled by the same structure, share the same host rocks, and are located close to felsic plutonic rocks (Figure 1C). We chose Jouhineva and Huhta because they form in the same conditions but have a different metal endowment. By comparing them we can characterize the key mechanisms. For this purpose, we combine careful petrography with in situ mineral dating.

## 2. Regional Geology

### 2.1 Pohjanmaa Belt

Finland sits within the Fennoscandia Shield which comprises the Archean Karelian provinces in the north, and Svecofennian domain in the south (Lahtinen et al. 2005). The PoB is located in the western Svecofennian domain (Lahtinen et al. 2005, 2014). This domain was formed during the Lapland-Savo, Fennian, Svecobaltic, and Nordic orogenies (Lahtinen et al. 2005). The Lapland-Savo orogeny (1930-1890 Ma) occurred due to the collision between Archean and Paleoproterozoic cratons, and the accretion of island arcs (Lahtinen et al. 2005). The Fennian orogeny (1900-1850 Ma) is related to the collision between the Keitele microcontinent and Karelian craton, and the accretion of volcano-sedimentary belts, such as the the PoB (Lahtinen et al. 2005, 2014). Between 1870 and 1850 Ma, associated with the Fennian Orogeny (Lahtinen et al. 2014), NNW-SSE shortening caused buckling of the orogen into the Bothnian orocline (Figure 1B; Lahtinen et al. 2005, 2014, 2018). The Svecobaltic orogen (1840-1780 Ma) was formed during the collision of the Sarmantia microcontinent with the southeastern margin of the Fennoscandian crustal segment. The Nordic orogen (1820-1770 Ma) was related to the collision of the Amazonia continent with the northwestern margin of Fennoscandia (Lahtinen et al. 2005). Orogenic collapse and voluminous intrusions between 1790 and 1770 Ma are followed by cooling until 1750 Ma ( Lahtinen et al. 2018).

The Pohjanmaa Belt is characterized by volcano-sedimentary units that are stratigraphically divided into the Ylivieska and Eviärji fields (Kähkönen 2005). The Ylivieska field comprises volcanic, volcanoclastic, and related sedimentary rocks. The Evjärji field consists of graywackes, mudstone, shales, and volcanic rocks with mid-ocean-ridge basalt to within-plate basalt affinities (Kähkönen 2005). The metamorphic peak in the Ylieviaska field reached medium amphibolite facies conditions and in the Evijävi field lower-granulite facies conditions (Mäkitie 1999, 2000). Syn-orogenic granodiorite, granite, and tonalite of the Central Finland Granitoid Complex (CFGC) intruded the PoB at 1890-1870 Ga (Figure 1B-C; Nironen 2005). The Rautio batholith belongs to the Central Finland Granitoid Complex (Huhma 1986) and it has been suggested that

Rautio is related to a porphyry copper mineralization in the PoB (Geological Survey of Finland 2022a).

The Jouhineva deposit and Huhta occurrence are hosted in the Ylivieska field, located ~ 2.8 km from each other (Figure 1B, Geological Survey of Finland 2022a, 2022b). They are along with the same NW-SE trending structure and are located less than 1 km northeast of the Rautio Batholith. Both of them are hosted in metavolcanic rocks, plagioclase porphyrite, amphibolite, and biotite schist metamorphosed at lower amphibolite conditions (545 ± 30 °C) (Figure 1C; Hölttä et al. 2019; Hölttä and Heilimo 2017).

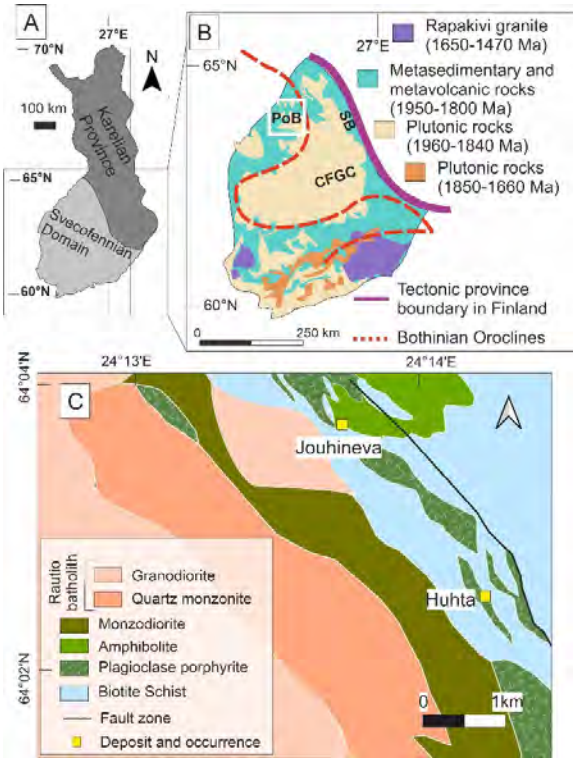


**Figure 1**. A) Map of Finland showing the location of the Archean Karelian province and Proterozoic Svecofennian Domain (Lahtinen et al. 2005). B) Geological map of the Svecofennian domain showing the Savo Belt (SB) localization. Central Finland Granitoid Complex (CFGC) and Pohjanmaa Belt (PoB) (Modified from Lahtinen et al. 2022). C) Geological map of the Jouhineva deposit, Huhta occurrence, and Rautio batholith. Map modified from Bedrock of Finland – DigiKP.

### 2.2 Jouhineva Au-Cu-Co deposit

The Jouhineva deposit contains total resources of 8.2 Mt Co, 3.6 Mt Cu, 3.5 t Ag and 0.39 t Au (Geological Survey of Finland, 2022a). Two ore mineral assemblages are described for Jouhineva: 1. Co- and Ni-bearing arsenopyrite with gold inclusions hosted in quartz veins; and 2. Chalcopyrite in actinolite-chlorite veins and free gold. This second vein type is associated with hydrothermal chlorite-sericite alteration in centimeter- to meter-scale wide halos around the auriferous veins (Hector et al. 2023).

### 2.3 Huhta Au occurrence

Huhta is characterized by mineralized quartz and actinolite veins (Geological Survey of Finland 2022b, Hector et al. 2023). It contains auriferous löllingite included in arsenopyrite hosted in quartz veins, and chalcopyrite-pyrite-pyrrhotite-sphalerite in actinolite-chlorite veinlets (Hector et al. 2023).

## 3. Sampling and Methodology

Four representative samples containing titanite associated with the different ore mineral assemblages were selected. Detailed transmitted and reflected optical microscopy was carried out to characterize the mineral assemblages and the titanite generations.

In-situ U-Pb dating of titanite by laser ablation-inductively coupled mass spectrometry (LA-ICP-MS) was done at the Laboratory for Environmental and Raw Materials (LERA) at the Karlsruhe Institute of Technology (KIT) using a Teledyne 193 nm Excimer Laser coupled with a ThermoFischer Scientific Element XR sector field mass spectrometer.

## 3 Results

### 3.1 Petrography and geochronology

#### 3.1.1 Jouhineva Au-Cu-Co deposit

Two samples were studied from Jouhineva. The first sample has Co-bearing arsenopyrite, biotite, quartz, plagioclase, minor titanite-ilmenite, and sericite. Titanite ($Ttn_{1.1J}$) is subhedral to anhedral, 200-300 µm in diameter, and is on ilmenite rims. Titanite is often included in arsenopyrite. The alteration halo contains plagioclase, sericite, chalcopyrite, biotite, traces of arsenopyrite, titanite ($Ttn_{1.2J}$), ilmenite, actinolite, and pyrite. $Ttn_{1.2J}$ is intergrown with chalcopyrite. The second sample from Jouhineva is characterized by arsenopyrite and actinolite veins. The alteration halo contains plagioclase, quartz, actinolite, biotite, arsenopyrite, and traces of ilmenite. Biotite is strongly chloritized, plagioclase is strongly sericitized and ilmenite is replaced by titanite ($Ttn_{2J}$). The titanite associated with this alteration is anhedral, 300-500 µm in diameter, and is intergrown with pyrite.

$Ttn_{1.1J}$ and $Ttn_{1.2J}$ were analyzed (35 spots) and the concordia age for these spots is 1816 ± 12 (MSWD = 1.43, Figure 2A). The concordia age for $Ttn_{2J}$ (9 spots) is 1744 ± 30 Ma (MSWD = 0.83, Figure 2B).

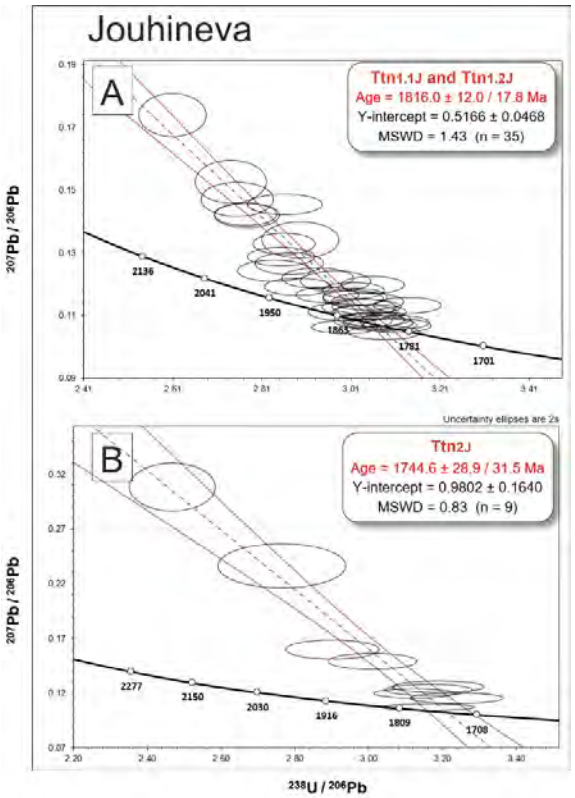


**Figure 2.** Titanite U-Pb concordia diagrams of A) $Ttn_{1.1J}$ and $Ttn_{1.2J}$ and B) $Ttn_{2J}$.

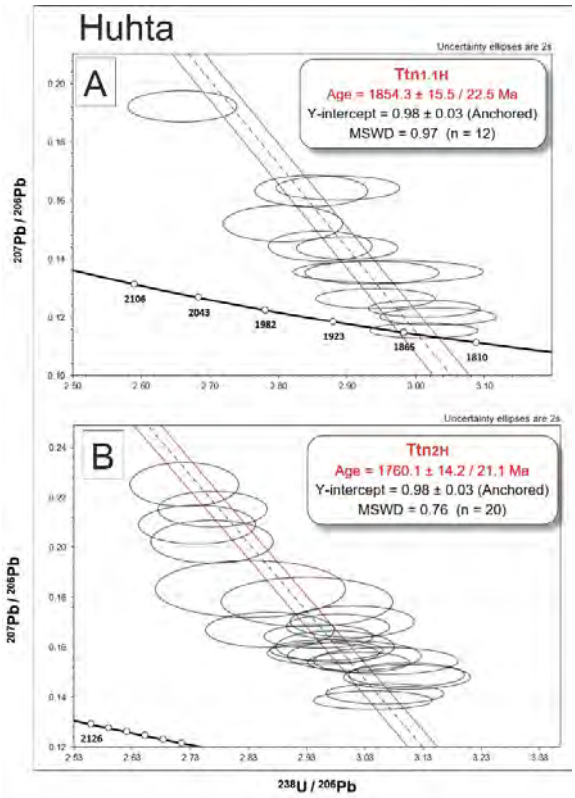


**Figure 3.** Titanite U-Pb concordia diagrams of A) $Ttn_{1.1H}$ and B) $Ttn_{2H}$.

### 3.1.2 Huhta Au occurrence

Two samples were studied from Huhta. The first sample contains vein-hosted arsenopyrite, quartz, pyrite, and prismatic actinolite$_1$ with traces of biotite and ilmenite replaced by titanite. Titanite ($Ttn_{1.1H}$) is subhedral, 100-300 µm in diameter, and is intergrown with pyrite and arsenopyrite.

The alteration halo of this vein consists of quartz, plagioclase, biotite, sericite, ilmenite rimmed by titanite, arsenopyrite, and traces of pyrite and chalcopyrite$_1$. Biotite forms clusters with titanite and arsenopyrite. Titanite ($Ttn_{1.2H}$) is 100-300 µm in diameter and anhedral.

The second sample from Huhta contains veins with actinolite$_2$, pyrrhotite, minor quartz, chalcopyrite$_2$, and ilmenite replaced by titanite. Actinolite$_2$ forms acicular grains obliquely oriented to prismatic actinolite$_1$. Titanite ($Ttn_{2H}$) is euhedral to subhedral, 100-300 µm in diameter, and is intergrown with chalcopyrite$_2$ and pyrrhotite. The alteration halo of this vein is characterized by sericite, chalcopyrite, pyrrhotite, and chlorite. Sericite replaces plagioclase and is associated with chalcopyrite$_2$.

The concordia age for the spots in $Ttn_{1.1H}$ is 1854 ± 15 Ma (MSWD = 0.97, Figure 3A). The concordia age from $Ttn_{2H}$ (20 spots) is 1760 ±14 Ma (MSWD = 0.76, Figure 3B).

## 4. Discussion and conclusions

Our data indicate that the mineralization in Jouhineva and Huhta took place at least in three different periods: 1854 ± 15 Ma, 1816 ± 12 Ma, and a combined age between 1760 ±14 and 1744 ± 30 Ma.

Mineralization of quartz, arsenopyrite, pyrite, actinolite$_1$, and titanite ($Ttn_{1.1H}$) is dated at 1854 ± 15 Ma. The arsenopyrite mineralization is part of the As-Au mineralization event in Huhta (Hector et al. 2023). Based on isotopic Pb studies in galena from the PoB and Skellefte district, Sundblad et al. (1993) suggested that the gold mineralization in the PoB took place at approximately 1880-1850 Ma. It indicates that the gold mineralization in the studied area occurred during the Fennian orogeny when the PoB was accreted to the Keitele microcontinent (Lahtinen et al. 2005, 2014). Furthermore, the mineralisation age of the first event in Huhta (1854 Ma) is coeval with the buckling of the Fennian orogen, between 1870 and 1850 Ma (Lahtinen et al. 2014).

The mineralization of arsenopyrite, biotite, quartz, plagioclase, titanite ($Ttn_{1.1J}$ and $Ttn_{1.2J}$), and sericite in Jouhineva at 1816 ± 12 Ma postdates the first mineralization event in Huhta. Hector et al (2023) observed that gold is included in Co-bearing arsenopyrite in Jouhineva and concluded that arsenopyrite was formed during the As-Au-Co-Ni mineralization event. The different age for the Au-only mineralization in Huhta and As-Au-Co-Ni in Jouhineva indicates that mineralizing fluid metal

content might have evolved over time or was locally different. The younger age coincides with the Svecobaltic (1840 to 1780 Ma) and Nordic (1820 to 1770 Ma) orogenies. These orogenies are characterized by continent-continent collisions (Lahtinen et al. 2005).

The second generations of titanite in Jouhineva and Huhta ($Ttn_{2J}$ and $Ttn_{2H}$) associated with chalcopyrite and chlorite-sericite alteration were dated at 1760 ±14 and 1744 ± 30 Ma, respectively. This period is coeval to orogenic collapse (Lahtinen et al. 2005, Kohrja et al. 2006) and close to the final cooling of the Fennoscandia orogen (Lahtinen et al. 2018).

Jouhineva was considered a porphyry copper overprinted by an orogenic gold deposit formed during the intrusion of the Rautio batholith (Eilu 2015, Geological Survey of Finland 2022a). However, Rautio was formed at 1890-1880 Ma (Höltä et al. 2019) and, thus, approximately 65 Ma before the first mineralization period in Jouhineva (1816 Ma). Moreover, the overprinted porphyry copper model for Johineva is unlikely due to the lack of porphyry copper alteration zones (Hector et al. 2023).

In conclusion, the results confirm that the mineralization of Au, Co, and Cu is multi-stage hydrothermal formed during the complex orogenic evolution of the PoB between 1850 and 1740 Ma.

## Acknowledgments

The authors gratefully acknowledge the Ferenc Molnár and Geological Survey of Finland (GTK) for providing access to the national drill core archive in Loppi. This work is funding by the Deutsche Forschungsgemeinschaft (DFG, N° INST 121384/213-1 FUGG).

## References

Eilu, P. (2015). Overview on Gold Deposits in Finland. In: Mineral Deposits of Finland. Elsevier 377–410.

Geological Survey of Finland (2022a) Jouhineva. Mineral Deposit Report n◦ 309.

Geological Survey of Finland (2022b) Huhta. Mineral Deposit Report n◦ 309.

Goldfarb RJ, Baker T, Dubé B, Groves DI, Hart CJR, Gosselin P (2005) Distribution, Character, and Genesis of Gold Deposits in Metamorphic Terranes. In: Hedenquist JW (ed) Economic geology: One hundredth anniversary volume : 1905-2005. Society of Economic Geologists, Inc, Littleton, CO, pp 407–450

Hector S, Clifford P, Kolb J, Silva AA, Walter B, Molnar F (2023) Orogenic Au deposits with atypical metal association (Cu, Co, Ni): insights from the Pohjanmaa Belt, western Finland. Ore Geology Reviews. https://doi.org/10.1016/j.oregeorev.2023.105326

Hölttä P, Heilimo E (2017) Metamorphic map of Finland. In: Nironen M (ed) Bedrock of Finland at the scale 1:1 000 000: Major stratigraphic units, metamorphism and tectonic evolution. Geological Survey of Finland, Espoo, pp 77–128

Hölttä P, Huhma H, Lahaye Y, Mänttäri I, Lukkari S, O'Brien H (2019) Paleoproterozoic metamorphism in the northern Fennoscandian Shield: age constraints revealed by monazite. International Geology Review 30:1–28. https://doi.org/10.1080/00206814.2019.1611488

Huhma, H. (1986). Sm-Nd, U-Pb and Pb-Pb isotopic evidence for the origin of the Early Proterozoic Svecokarelian crust in Finland. Bulletin.

Kähkönen Y (2005) Svecofennian supracrustal rocks. In: Lehtinen M, Nurmi PA, Rämö OT (eds) Precambrian geology of Finland: Key to the evolution of the Fennoscandian shield, 1. ed. Elsevier, Amsterdam, pp 343–406

Lahtinen R, Korja A, Nironen, M (2005) Palaeoproterozoic tectonic evolution of the Fennoscandian Shield. In: Lehtinen, M., Nurmi, P., R¨am¨o, T. (Eds.), The Precambrian Bedrock of Finland - Key to the evolution of the Fennoscandian Shield. Elsevier Science B.V, pp. 418–532.

Lahtinen R, Johnston ST, Nironen M (2014) The Bothnian coupled oroclines of the Svecofennian Orogen: a Palaeoproterozoic terrane wreck. Terra Nova 26:330–335. https://doi.org/10.1111/ter.12107

Lahtinen R, Huhma H, Sayab M, Lauri LS, Hölttä, P (2018) Age and structural constraints on the tectonic evolution of the Paleoproterozoic Central Lapland Granitoid Complex in the Fennoscandian Shield. Tectonophysics 745: 305–325.

Lahtinen R, Salminen PE, Sayab M, Huhma H, Kurhila M, Johnston ST (2022) Age and structural constraints on the tectonic evolution of Paleoproterozoic Saimaa orocline in Fennoscandia. Precambrian Research 369: 106477.

Mäkelä M (1984) Raahen Laivakankaan kvartsi-arseenikiisu-kultaesiintymä. (in Finnish): The quartz-arsenopyrite-gold mineralization of Laivakangas, Raahe, Finland. Unpublished M.Sc thesis, University of TurkuMäkitie H (1999) Structural analysis and metamorphism of Palaeoproterozoic metapelites in the Seinajoki-Ilmajoki area, western Finland. BULLETIN-GEOLOGICAL SOCIETY OF FINLAND 71:305–328

Mäkitie, H. (1999). Structural analysis and metamorphism of Palaeoproterozoic metapelites in the Seinajoki-Ilmajoki area, western Finland. BULLETIN-GEOLOGICAL SOCIETY OF FINLAND 71, 305–328.

Mäkitie, H. (2000). Granitoids (1.89-1.87 Ga), diatexites (1.89-1.88 Ga) and granitic pegmatites (1.80-1.79 Ga), and structural-metamorphic evolution in the Sein¨ajoki region, western Finland. Ph. D. Thesis.

Nironen, M. (2005). Proterozoic orogenic granitoid rocks. In: Lehtinen, M., Nurmi, P.A., R¨am¨o, O.T. (Eds.), Precambrian Geology of Finland: Key to the Evolution of the Fennoscandian Shield, 1. ed. Elsevier, Amsterdam, pp. 443–480.

Patten, C.G.C., Molnár, F., Pitcairn, I.K., Kolb, J., Mertanen, S., Hector, S. (2022). Multi-source and multi-stage metal mobilisation during the tectonic evolution of the Central Lapland Greenstone Belt, Finland: implications for the formation of orogenic Au deposits. Mineral Deposita.

Sundblad, K., Weihed, P., Billström, K., Markkula, H., Makelä, M. (1993). Source of metals and age constraints for epigenetic gold deposits in the Skellefte and Pohjanmaa districts, central part of the Fennoscandian Shield. Mineralium Deposita 28, 181–190.

# Role of carbonaceous material in gold precipitation for orogenic gold deposits: a case study of the Bangbu gold deposit, China

**Zhengpeng Ding[1], Xiaoming Sun[1]**
*[1]School of Earth Sciences and Engineering, Sun Yat-sen University, China*

**Abstract.** Carbonaceous material (CM) is widely distributed at the Bangbu deposit. Despite being closely ore-related, the CM nature and genesis, as well as its possible role in gold metallogeny, remain unclear. Hence, we investigated the role of five ore-related CM types using Raman spectroscopy and thermodynamic modeling. CM1 only occurs in disseminated ores. Raman spectroscopy analysis shows that CM1 has undergone high-temperature metamorphism. Geochemical modeling shows that Au precipitation can be attributed to the fluid-rock interactions of CM1 and the ore fluids. CM2 occurs in quartz veins. Raman spectroscopy of CM2 experienced a temperature of ~455 °C. Methane is commonly found in fluid inclusions closely associated with CM2. Geochemical modeling shows that methane can be a more efficient Au-bisulfide reductant than CM2. CM3 intergrows in black veins, and its formation temperature is calculated at ~290 °C. During the sulfidation process, $H_2S$ and $CO_2$ from the ore fluids may have reacted with Fe-bearing minerals, precipitating CM3 and Py3. CM4 occurs in the wall rocks and have similar structural features to semi-graphite but has no association with ores. Our study proposes the most likely roles of CM in gold precipitation, which bear important implications for a better understanding of the formation of ores.

## 1 Introduction

Carbonaceous material (CM) is carbon-rich material containing C-O and C-H bonds, including organic matter, graphite, bitumen, and hydrocarbons (Gaboury 2021), and is considered a crucial component of sedimentary rocks (Hu et al. 2017). Previous studies on gold deposits have indicated a significant correlation between various types of CM and different types of gold deposits (Large et al. 2011). Firstly, CM can serve as an effective carrier of gold and other trace elements in carbonaceous sedimentary rocks. Alternatively, metals may have been mobilized from the deeper parts of carbonaceous rocks into the carbonic fluids and migrated to the shallow crust (Gaboury 2013). Moreover, graphite and methane can act as efficient metal reductants that are responsible for gold precipitation (Fuchs et al. 2021), while hydrocarbons and petroleum may also play a role in gold migration in hydrothermal fluids (Crede et al. 2019).

The Bangbu gold deposit is situated in the southwestern part of Jiacha city, China. The disseminated ores are confined inside a fragmented zone of carbonaceous phyllite and have straight contact with stringer quartz veins. The vein-type ores are confined into large ore-controlling structures, which are mainly quartz veins. At Bangbu, different types of CM are widely reported in the ore bodies and wall rocks, yet its relations with the gold ores remain ambiguous (Ding et al. 2023). This study aims to integrate petrography, Raman spectroscopy, and thermodynamic modeling to reveal the origin of CM and its gold metallogenic role.

## 2 Analytical methods

The mineral assemblages and different types of CM in the ores were identified using a ZEISS AXIO microscope and SEM. Raman spectra of CM were measured using a Renishaw inVia Reflex Raman spectrometer. The analysis conditions included 9 mW output laser power, and a 100 to 3500 $cm^{-1}$ spectroscopic range, which covers all CM peaks. Temperature is a key parameter for the origin and evolution of CM. Temperature is a crucial factor in the origin and evolution of CM. Based on prior research, CM areas can be identified and used to determine the temperature experienced by the CM (Rahl et al. 2005).

A quantitative evaluation of the role of different CM types in gold precipitation at Bangbu was carried out using the Geochemist's Workbench software. For a more intuitive representation of reaction-path modeling, carbonaceous sericite phyllite was defined as graphite and mixed as unmineralized rock. The LA-ICP-MS trace element data of individual fluid inclusion from Bangbu were used to define the initial ore fluid compositions (Zhao et al. 2020).

## 3 Results

### 3.1 Petrographic characteristics

Detailed petrographic observations reveal the spatial association of the five CM types (CM1-4 and methane), native gold, and three auriferous pyrite generations from the disseminated and vein-type ores. CM1 is exclusively present in the disseminated ores. CM1 occurs as an elongate or filamentous morphology in clusters in the disseminated ores and forms black conglomerate (Fig. 1a). Methane, commonly found as fluid inclusions in coarse vein-type ores, is spatially associated with CM2 (Fig. 1b).

CM3 occurs as black irregular particles or elongate bodies with an average diameter of 0.002 mm and are combined into randomly oriented black veinlets in coarse vein-type ores (Fig. 1c). In addition to Py2, CM3-Py3 veinlets coexist with quartz veins in the vein-type ores. CM4 appears as slivery white irregular semi-graphite in wall rocks and has a

stronger reflectance under the microscope than other types of CM (Fig. 1d). No petrographic relationships between CM4 and sulfides or native gold was observed.

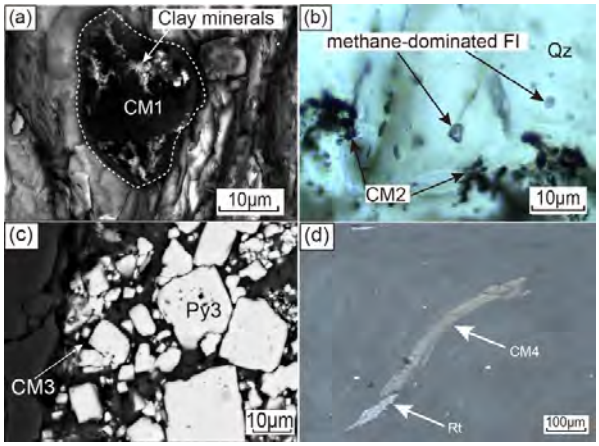


**Figure 1.** Photographs of CM1, CM2, methane, CM3, and CM4. Abbreviations: Py = pyrite; Qz = quartz; Rt = rutile.

### 3.2 Raman thermometer of solid CM

All four types of CM show well-developed D (1350 $cm^{-1}$) and G (1580 $cm^{-1}$) bands, as well as D2 (1600 $cm^{-1}$) and S1 (2690 $cm^{-1}$) bands, commonly accompanied by S2 (2940 $cm^{-1}$) and S3 (3200 $cm^{-1}$) bands (Fig. 2). CM1 has a strong G band, relatively weak D and D2 bands, an additional high S1 band, and a low S2 band, resembling typical flaky graphite with high crystallinity (Fig. 2a). Although CM2 has mostly similar spectra as CM1, the peak intensity was weaker (Fig. 2b). On the contrary, CM3 has a higher D band than the G band, and a lower D2 band than that of CM1 and CM2, indicating a disordered structure (Fig. 2c). CM4 is characterized by similar D and G bands, and clear D2, S1, S2, and S3 bands, suggesting that the experienced temperature of CM4 is lower than CM1 and CM2, but higher than CM3 (Fig. 2d). For the CM temperature calculation, it depends on the D, G, and D2 band area values. Using the thermometer of Rahl et al. (2005), the R1 and R2 of CM1-4 were calculated to be the averages of 510 °C, 455 °C, 290 °C, and 388 °C, respectively.

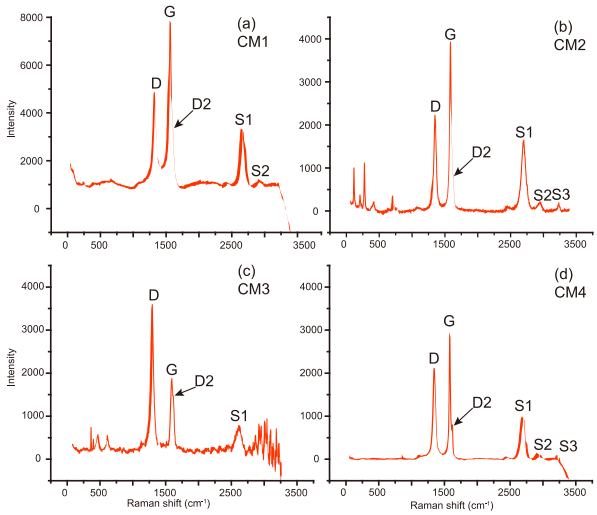


**Figure 2.** Raman spectra of the four CM types from Bangbu.

### 3.3 Thermodynamic modeling

We established several gold precipitation thermodynamic models for the different types of CM, based on petrographic observations, geochemical analyses, and mineral assemblages. In this study, the pH and temperature data of the ore fluids were provided by the ore-stage methane-dominated fluid inclusions (Zhao et al. 2020). Combined with the LA–ICP–MS data from individual fluid inclusions, the ore fluids were determined to be low temperature (avg. 250 °C), high sulfur activities (0.01mol as $SO_4^{2-}$), low-medium salinity (avg. 1mol/L NaCl), and weakly acidic to neutral (pH =5.2). The oxygen fugacity of the ore fluids to be -34 to -37 log units and are generally fixed below the QFM redox buffers.

## 4 Discussion

### 4.1 Role of CMs in gold precipitation

We defined the unmineralized wall rocks as a series of individual minerals, each containing 100g, including annite (representing biotite), graphite (representing CM), quartz, albite, K-feldspar, and chlorite, which reacted with the fluid under rock-buffer conditions, to establish the role of CM1 in gold precipitation with React module. Our reaction modeling indicates that 1g of CM1 would precipitate 43% of Au from the fluid (Fig. 3a). Meanwhile, further CM increases would not lead to major changes in the fluid in our model. We therefore suggest that this reaction can cause physico-chemical variations in the ore fluids and thereby promote redox and acid-base equilibria. Stability of Au complexes were thus destroyed and caused Au precipitation in Py1. Model results are consistent with patterns of observed mineral paragenesis in disseminated ores, further supporting this view.

In the phase separation process, the fugacity of methane was increased and accompanied by the decrease of Au concentrations in the ore fluids under acidic conditions. We consider that when the fluids

enter brittle-ductile shear zones in wall rocks, the pressure may have decreased and gradual transformation of liquid to vapor phase of methane may take place, causing the boiling of $methane_{(aq)}$ to $methane_{(g)}$ in the residual ore fluids and accompanied by a decrease of temperature. The significantly increased contact surface area between methane and the ore fluids, further exacerbating gold precipitation and may cause further driving the precipitation of Au.

We test the hypothesis of phase separation of methane in the ore fluids by the model 2, with adding methane to the initial fluids. As shown in Figures 3b, the reaction of only 1 g methane with 1 kg fluid would reduce the gold solubility from 100 to 22 ppb, resulting in the precipitation of $Au^+$ (78%). This model suggests that the methane phase separation is more effective for gold precipitation than fluid-rock reactions.

Sulfidation is commonly associated with orogenic-type gold ores (Groves et al. 2020). Au was incorporated into pyrite during the sulfidation process and usually caused the deposition of minerals. We propose that the deeper carbonic ore fluids ascended into the ore-hosting structures and that $CO_2$ and $H_2S$ may have degassed from the fluids. During this reaction, the deposition of these sulfide phases might have depleted $H_2S$ from the ore fluids, which destabilized Au-bisulfide complexes and drove Au deposition. To test our model in a simple way, we defined the sulfidation as a continuous addition of FeO, $H_2S$, and $CO_2$ to the initial fluid (model 3). The results are presented in Figures 3c, which show a drop in fluid $Au^+$ content (~20%) due to the deposition of Py3 and CM3. It is noteworthy that gold precipitation efficiency during the sulfidation is poor in this model and is unlikely to be the primary gold precipitation mechanism at Bangbu.

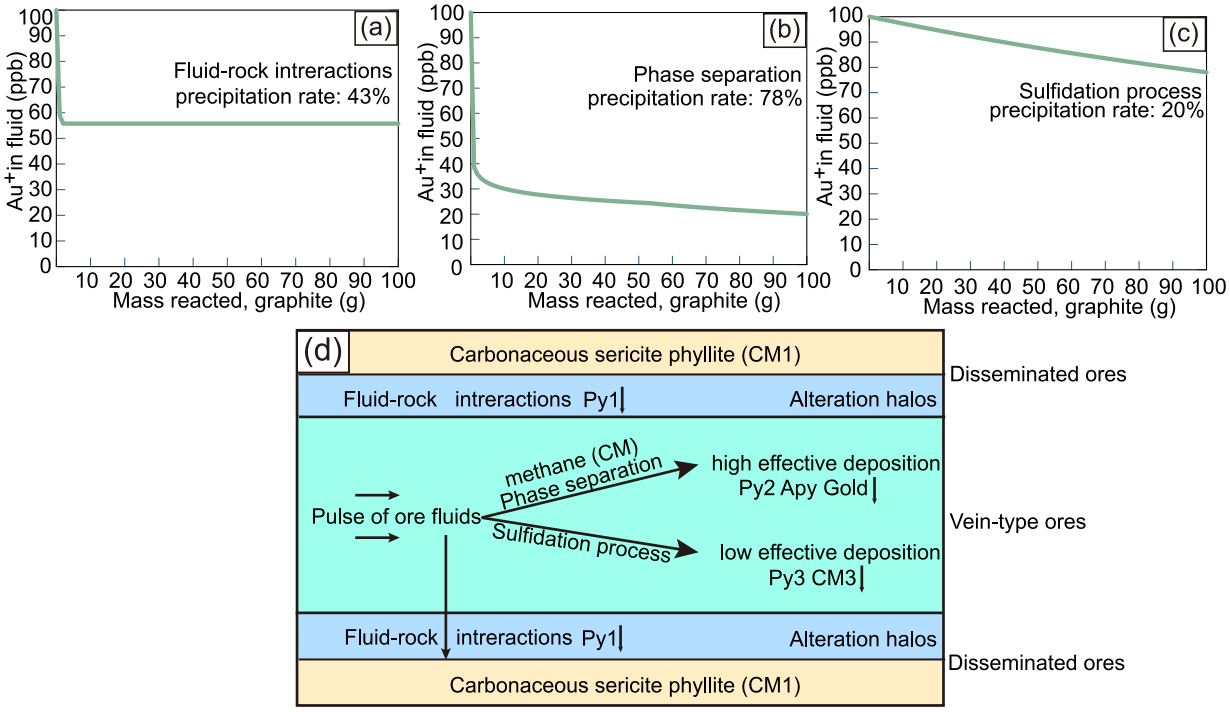


**Figure 3.** Thermodynamic modeling simulations of CMs added into the ore fluids: **a** Concentrations of $Au^+$ from model 1; **b** Concentrations of $Au^+$ from model 2; **c** Concentrations of $Au^+$ from model 3. The green line denotes the reacting concentration of $Au^+$ in the model; **d** The role of CM in the gold precipitation process illustrated in a pattern diagram.

Although our study indicates that many CMs could play an important role in gold precipitation, it may not be the case for all types of CM. Here, our data have shown that CM2 and CM4 have no role in gold precipitation, even though there is a spatial association between CM2, Py2, native gold, and methane-dominated fluid inclusions in the ores. Firstly, the experienced temperature of CM2 is much higher than the ore fluid temperature, which could indicate that CM2 could not have originated from the ore fluids, unlike CM3. CM2 was most likely sourced from indigenous CM and produced by the deep-lying carbonaceous rocks through pyrolysis or directly from CM1 particles via structural super-imposition and reformation. We suggested that CM2 would play a similar role in gold precipitation to that of CM1, but methane can precipitate more Au than CM2 in the ore fluids. Our study does not support that CM2 was a major reductant for gold precipitation but may have played a minor role. Secondly, CM4 is a completely different type with a unique flake structure compared to other types of CM and is similar to structural-bound semi-graphite. In addition, CM4 also occurs with hydrothermal sericite in wall rocks, but no auriferous minerals were identified. Meanwhile, Raman geothermometric results indicate that CM4

was formed during the post mineralization stage and had no relation to gold mineralization at Bangbu.

## 5 Implications

Different types of CM may have played a distinct role in the gold precipitation at Bangbu (Fig. 3d). Indigenous CM1 and hydrothermal CM3, representing fluid-rock interaction and sulfidation, respectively, could explain the formation of gold-poor pyrite. In contrast, methane may have played a key role in the formation of native gold grains. Considering CM has been widely distributed in other orogenic gold deposits, we propose that the different types of CM could be important associated mineral in sediment-hosted orogenic gold deposits worldwide. In practice, however, our study also suggests that there is no unique association between some hydrothermal CM (e.g., CM4) and gold mineralization in gold deposits. Each hydrothermal event may trigger the production of hydrothermal CM.

## Acknowledgements

This research was financially supported by the National Natural Science Foundation of China (91855213, 41972070, 41672071, and U1302233).

## References

Crede L, Liu W, Evans KA, Rempel KU, Testemale D, Brugger J (2019) Crude oils as ore fluids: An experimental in-situ XAS study of gold partitioning between brine and organic fluid from 25 to 250 °C. Geochimica Et Cosmochimica Acta 244: 352-365.

Ding ZP, Sun XM, Hu SY, Chen HJ, Li DF, Fu Y, Xu L, Wu ZY, Huang F (2023) Role of carbonaceous material in gold precipitation for orogenic gold deposits: A case study of the Bangbu gold deposit in southern Tibet, China. Ore Geology Reviews 152: 105231.

Fuchs S, Schumann D, Martin RF, Couillard M (2021) The extensive hydrocarbon-mediated fixation of hydrothermal gold in the Witwatersrand Basin, South Africa. Ore Geology Reviews 138: 104313.

Gaboury D (2013) Does gold in orogenic deposits come from pyrite in deeply buried carbon-rich sediments?: Insight from volatiles in fluid inclusions. Geology 41: 1207-1210.

Gaboury D (2021) The neglected involvement of organic matter in forming large and rich hydrothermal orogenic gold deposits. Geosciences 11: 344.

Groves DI, Santosh M, Deng J, Wang Q, Yang L, Zhang L (2020) A holistic model for the origin of orogenic gold deposits and its implications for exploration. Mineralium Deposita 55: 275-292.

Hu S, Evans K, Craw D, Rempel K, Grice K (2017) Resolving the role of carbonaceous material in gold precipitation in metasediment-hosted orogenic gold deposits. Geology 45: 167-170.

Large RR, Bull SW, Maslennikov VV (2011) A carbonaceous sedimentary source-rock model for Carlin-type and orogenic gold deposits. Economic Geology 106: 331-358.

Rahl JM, Anderson KM, Brandon MT, Fassoulas C (2005) Raman spectroscopic carbonaceous material thermometry of low-grade metamorphic rocks: Calibration and application to tectonic exhumation in Crete, Greece. Earth and Planetary Science Letters 240: 339-354.

Zhao X, Yang Z, Zhang X, Pei Y, Liu Y, Han D (2020) Geochemical compositions of ore-related pyrite, quartz and fluid inclusions of Bangbu gold deposit in the Indus–Yurlung Zangbo suture zone, Tibet. Ore Geology Reviews 120: 103441.

# The role of crystal defects for the remobilisation of gold in pyrite

**Denis Fougerouse[1,2], Dennis Sugiono[3], Sumail[3], Nicolas Thebaud[3], Steven M. Reddy[1,2]**
*[1]School of Earth and Planetary Sciences, Curtin University, Perth, Australia*
*[2]Geoscience Atom Probe Facility, John de Laeter Centre, Curtin University, Australia*
*[3]Centre for Exploration Targeting, The University of Western Australia, Crawley, Australia*

**Abstract.** Gold hosted in sulfides represents a large proportion of the Au resource globally. Sulfide-hosted Au is refractory, meaning that its recovery necessitates a full oxidation of the minerals. Despite this characteristic, numerous evidence has been documented that Au can be remobilised naturally, through geological processes, improving the economic value of an ore deposit. However, the mechanistic process operating at the nanoscale for the remobilisation of Au in pyrite still remains poorly understood. In this study, we apply a correlative suite of techniques from the grain-scale to the nanoscale in order to determine the mechanism for Au mobility in pyrite. We selected samples from three orogenic Au deposits, including the Cambrian Huangjindong deposit (Jiangnan Orogen, China), the Archean Kanowna Belle and Jundee deposits (Yilgarn craton, Western Australia). Our data suggests a strong role of crystal defects, and in particular dislocations, for the remobilisation of Au from pyrite.

## 1 Introduction

Refractory Au ores are defined by trace amounts of Au hosted in sulfide minerals, mainly pyrite and arsenopyrite (Cook and Chryssoulis, 1990). Refractory Au ores represent a large proportion of global Au resources and it has been defined that Au can be hosted in the sulfide crystal lattice (Cabri et al., 1989), occur as discrete metallic nano- and microparticles (Palenik et al., 2004), and can be hosted in crystal defects such as dislocations (Fougerouse et al., 2021).

Secondary geological processes have been shown to affect the distribution of Au in sulfide and cause the liberation of gold from refractory ores, increasing the economic value of gold deposits. Remobilisation can improve the recovery of Au by simple cyanidation, but also be responsible for the formation of high-grade ore shoots (Fougerouse et al., 2016). The mineralogical processes responsible for Au remobilisation operate at the nanoscale, however the documentation of the distribution of trace elements at the nanoscale is notoriously difficult. In this study, we used a combination of advanced analytical instrumentation including electron backscattered diffraction (EBSD), nanoscale and time-of-flight secondary ion mass spectrometry (NanoSIMS and ToF-SIMS), transmission electron microscopy (TEM) and atom probe tomography (APT), in order to determine the mechanisms responsible for gold mobility in pyrite.

## 2 Samples and geological settings

Three samples from orogenic gold deposits were selected, including one mineralised sample from the Cambrian Huangjindong deposit (Jiangnan Orogen, China), and one from the Archean Jundee and Kanowna Belle deposit (Yilgarn craton, Western Australia).

The Huangjindong deposit is located in the Jiangnan Orogen (Southern China). Mineralisation at Huangjindong is dominated by gold-bearing pyrite and arsenopyrite (Zhang et al., 2018).

The Jundee deposit is hosted in the Yandal greenstone belt in the Eastern Goldfields province of the Archean Yilgarn craton. Mineralisation at Jundee is hosted in brecciated dolomite veins and is dominated by visible gold with a minor component of gold associated with arsenian pryrite (Yeats et al., 2001).

The Kanowna Belle deposit is located on the eastern edge of the Kalgoorlie terrane of the Yilgarn craton within the volcano-sedimentary units of the Black Flag Group (Sugiono et al., 2021). Gold at Kanowna Belle is hosted dominantly in laminated quartz-pyrite-gold veins.

## 3 Methods

The NanoSIMS and TEM measurements were performed at the Centre for Microscopy, Characterisation and Analysis, The University of Western Australia (CMCA, UWA), whereas the EBSD, ToF-SIMS and APT investigation were conducted at the John de Laeter Centre (JdLC), Curtin University.

We used a Tescan Clara field emission gun scanning electron microscope (FEG-SEM) equipped with an Oxford Symmetry EBSD detector at Curtin University, for quantifying crystal misorientation and define regions of interest for further work. A Cameca NanoSIMS 50L with a $Cs^+$ primary source (CMCA, UWA) and an IONTOF M6 ToF-SIMS instrument with a $Bi^+$ primary source (JdLC) were used to map the distribution of $^{75}As$ and $^{197}Au$. The experiment conditions for both instruments resulted in a pixel size of approximately 100 nm.

TEM and APT specimens were prepared using a FEI Helios NanoLab G3 and a Tescan Lyra3 $Ga^+$ focused ion beam (FIB) instruments, respectively. TEM analyses were conducted on a FEI Titan G2 TEM (CMCA), whereas APT analyses were performed using a Cameca LEAP4000X HR (JdLC).

## 4 Results

### 4.1 Microscale results

EBSD results from all three samples investigated indicate that the internal pyrite misorientation is relatively weak. At Huangjindong, a maximum distortion of ~10° is accommodated by a low density of low-angle boundaries cutting across the grain. At Jundee, the pyrite studied is composed of an aggregate of grains. Each individual grain is weakly deformed but low-angle boundaries can be observed where grains impinge each other. At Kanowna Belle, evidence for crystal-plastic deformation can be observed in areas of the grain aggregate, but low-angle boundaries are associated with the growth zoning, mimicking the shape of the As-Au-rich domains (Fig. 1).

In all three samples investigated, the primary As and Au distribution is in the form of oscillatory bands following the pyrite crystal growth faces. Commonly, the cores of the pyrites are As and Au poor, whereas the rims of the grains are enriched in As and Au.
In the case of Jundee and Kanowna Belle, the primary oscillatory zoning is overprinted by pyrite with a dark backscattered (BSE) signal (Fig.1 E&I). The BSE-dark regions have sharp, curviplanar boundaries with the oscillatory zoned primary pyrite. NanoSIMS and ToF-SIMS analyses reveal that the BSE dark domains are As and Au poor compared to the oscillatory zoning (Fig 1. G, H, K&L). At Jundee, the BSE-dark zones are penetrating inward the pyrite from the grain edges and from low-angle boundaries. At Kanowna Belle, Within the As-Au-rich rim, convoluted As-depleted domains occur either parallel to the As-Au oscillatory zoning or as channels of As-depleted zones cutting across the oscillatory zone textures. Importantly, the location of the As-depleted zones at Kanowna Belle is associated with the presence of low-angle boundaries .

### 4.2 Nanoscale results

The APT analysis of a low-angle boundary at Huangjindong reveals that the boundary is composed by a succession of dislocations aligned within the boundary plane (Fig. 2). Dislocations are enriched in trace elements such as As, Ni, Cu, Sb, Pb and Au. Chemical profiles normal to the dislocations reveal a local depleted zone in proximity of the dislocation.

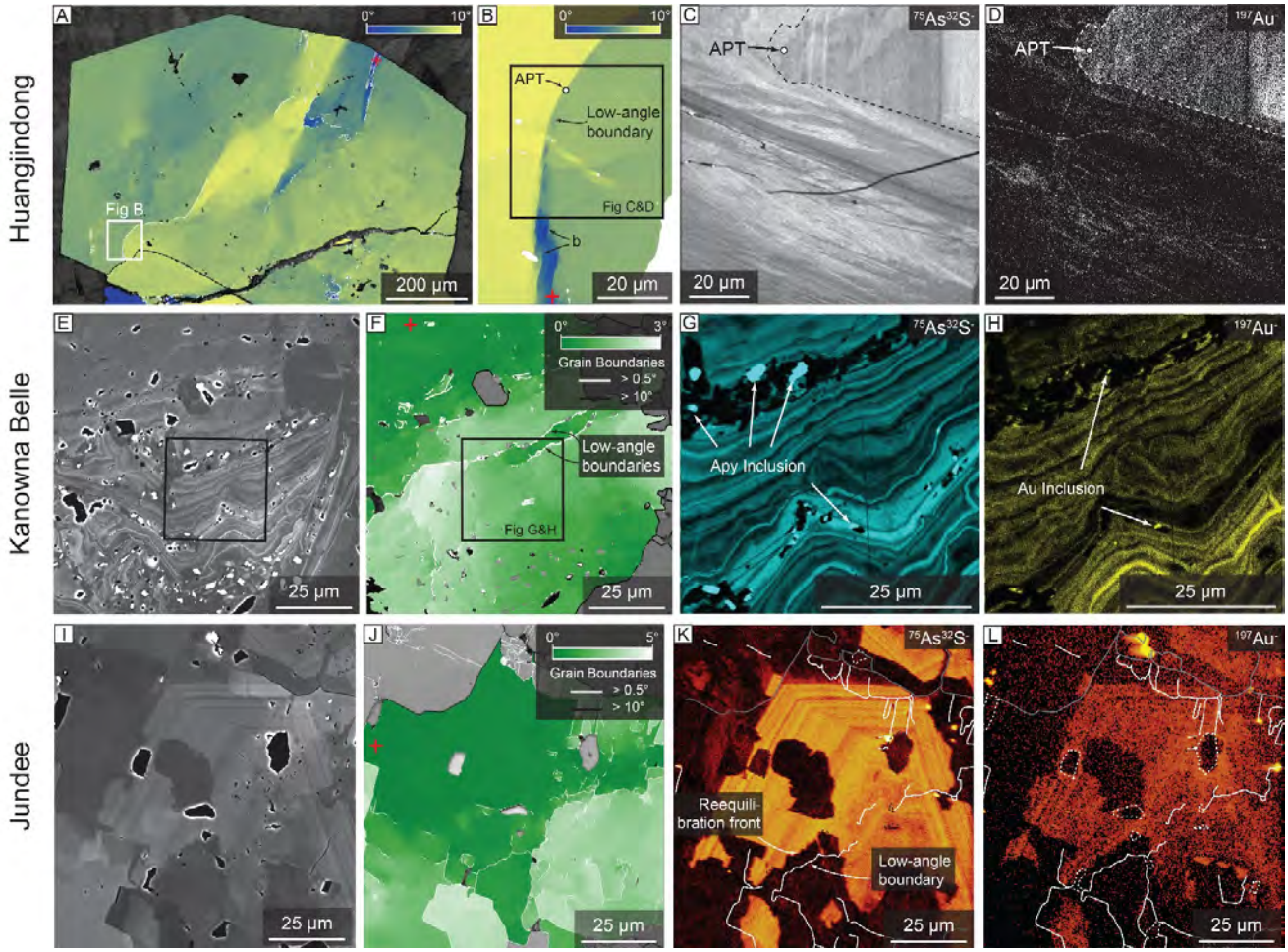


**Figure 1. Microscale results for pyrites of the Huangjindong, Kanowna Belle and Jundee deposits.** A, B, F and G) EBSD texture component maps showing crystal Distortion. Low-angle boundaries (>0.5°) are plotted in white and high-angle boundaries (>10°) in black; C, D, G and H) NanoSIMS maps for As and Au; E and I) BSE images; K and L: ToF-SIMS maps showing the distribution of As And Au.

TEM investigation of the Kanowna Belle textures reveal that the boundary of the domain depleted in Au and As is sharp at the nanoscale. The TEM analyses also revealed that in the As-Au-depleted zones, small arsenopyrite crystals and sub-micrometre gold particles are present. At Jundee, the APT investigation of the sharp boundary between the As-Au-rich and As-Au-poor domains reveal complex heterogeneities in the As distribution and the identification of crystal defects is ongoing.

## 5 Discussion

### 5.1 The role of crystal defect for gold mobility

The As-Au oscillatory zoning observed in all samples can be explained by the diffusion-limited self-organisation of ions at the crystal-fluid interface and is a reflection of growth kinetics rather than variations in fluid chemistry (Wu et al., 2019).
Secondary textures can be observed in all samples. At Huangjindong, a clear link between crystal-plastic deformation and the mobility of Au was established. Local concentration profiles suggest that Au was sourced from the pyrite, locally and migrated at the same time of the dislocation through the dislocation-impurity pair model (Fougerouse et al., 2021).
At Kanowna Belle, low-angle boundaries mimic the shape of the As-Au rim, indicating that they are not related to crystal-plastic deformation. The incorporation of large As atoms in pyrite leads to the staining and distortion of the crystal lattice (Simon et al., 1999). The close association of the low-angle boundaries and the high-As rim suggests that the low-angle boundary formed in response to lattice distortion caused by As incorporation.

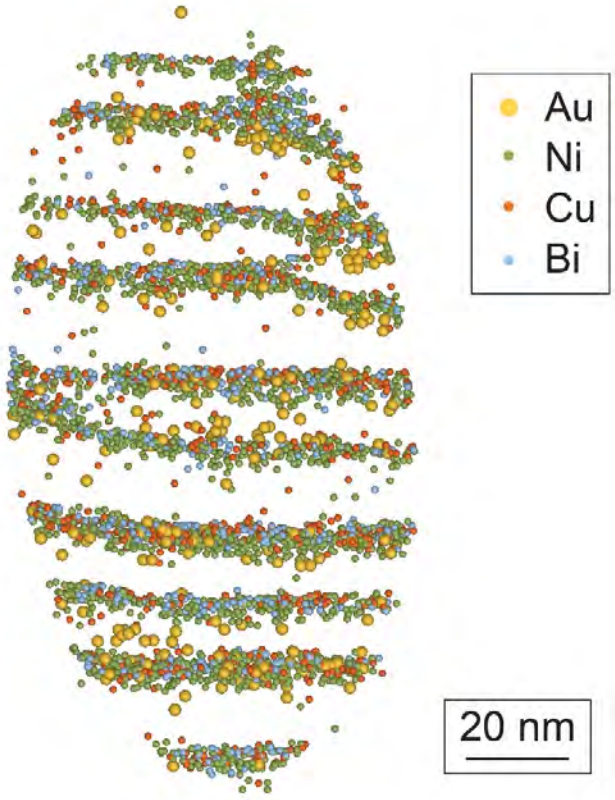


**Figure 2.** Nanoscale APT imaging of the low angle boundary indicated in Figure 1A-D. Each sphere represents an atom. The low angle boundary plane is composed of sub-horizontal Au, Ni, Cu and Bi enriched dislocations.

In turn, within the As-Au-rich oscillatory zoned rim at Kanowna Belle, there is a relationship between the location of the low-angle boundaries and convoluted As-Au-poor domains. Similar observations are made at Jundee, with As-Au-poor domains cross-cutting As-Au-rich oscillatory zones. In both case studies, the As-Au-poor domains have sharp, curviplanar boundaries and penetrate inward the pyrite along grain boundaries and low-angle boundaries. These features are interpreted to form through a re-equilibration process. The driving force of the re-equilibration is the minimisation of free energy from a distorted pyrite lattice due to the incorporation of As and Au to a pyrite closer to stoichiometric composition. The fluid-mediated interface-coupled dissolution-reprecipitation model for re-equilibration is likely to be responsible for these textures (Fougerouse et al., 2016; Morey et al., 2008; Putnis, 2009).
In all three examples, we have documented a clear link between low-angle boundaries, crystal defects and the mobility of Au. Dislocations along low-angle boundaries can lead to several mechanisms for Au mobility. At Huangjindong, the dislocation-impurity pair model suggests that no fluids are necessary for the local redistribution of Au in pyrite. On the other hand, at Kanowna Belle and Jundee, re-equilibration textures forming through a fluid mediated process are well developed around low-angle boundaries. This relationship indicates that fluids, or H, preferentially utilise the microstructure network and dislocations to infiltrate pyrite and cause Au remobilisation.

### 5.2 Implications

Refractory Au ores require oxidation to liberate Au locked in sulfides. The oxidation of sulfides requires significant amount of energy contributing to greenhouse gas emissions, produces acids and wastes rich in heavy metals.
Our study indicates that natural gold remobilisation processes exist and are efficient at the micrometre scale. Gold was observed in crystal defects along low-angle boundaries formed during deformation and fluids have been showed to use the low-angle boundary networks to initiate re-equilibration of pyrite. Such mechanism should be investigated for alternative method of selective or in situ leaching (Heath et al., 2008). Indeed, it has been demonstrated that crystal defects are more prone to dissolution than bulk crystal, thus reducing energy consumption necessary for extraction.

Acknowledgements
The study is supported by the Science and Industry Endowment Fund (SIEF RI13-01). DF acknowledges Australian Research Council

(DE190101307 and LP200200897) and Mineral Research Institute of Western Australia funding. We thank Northern Star Resources for providing samples and site access. The authors acknowledge the facilities, and the scientific and technical assistance of Microscopy Australia at the Centre for Microscopy, Characterisation & Analysis, The University of Western Australia, a facility funded by the University, State and Commonwealth Governments. Paul Guagliardo, William Rickard and David Saxey and thanked for their help with NanoSIMS, ToF-SIMS and APT, respectively.

## References

Cabri L. J., Chryssoulis S. L., de Villiers J. P., Laflamme J. G. and Buseck P. R. (1989) The nature of" invisible" gold in arsenopyrite. *The Canadian Mineralogist* **27**, 353-362.

Cook N. J. and Chryssoulis S. L. (1990) Concentrations of invisible gold in the common sulfides. *The Canadian Mineralogist* **28**, 1-16.

Fougerouse D., Reddy S. M., Aylmore M., Yang L., Guagliardo P., Saxey D. W., Rickard W. D. and Timms N. (2021) A new kind of invisible gold in pyrite hosted in deformation-related dislocations. *Geology* **49**, 1225-1229.

Fougerouse D., Micklethwaite S., Tomkins A. G., Mei Y., Kilburn M., Guagliardo P., Fisher L. A., Halfpenny A., Gee M. and Paterson D. (2016) Gold remobilisation and formation of high grade ore shoots driven by dissolution-reprecipitation replacement and Ni substitution into auriferous arsenopyrite. *Geochimica et Cosmochimica Acta* **178**, 143-159.

Heath J., Jeffrey M., Zhang H. and Rumball J. (2008) Anaerobic thiosulfate leaching: Development of in situ gold leaching systems. *Minerals Engineering* **21**, 424-433.

Morey A. A., Tomkins A. G., Bierlein F. P., Weinberg R. F. and Davidson G. J. (2008) Bimodal distribution of gold in pyrite and arsenopyrite: examples from the Archean Boorara and Bardoc shear systems, Yilgarn Craton, Western Australia. *Economic Geology* **103**, 599-614.

Palenik C. S., Utsunomiya S., Reich M., Kesler S. E., Wang L. and Ewing R. C. (2004) “Invisible „gold revealed: Direct imaging of gold nanoparticles in a Carlin-type deposit. *American Mineralogist* **89**, 1359-1366.

Putnis A. (2009) Mineral Replacement Reactions. *Reviews in Mineralogy and Geochemistry* **70**, 87-124.

Simon G., Huang H., Penner-Hahn J. E., Kesler S. E. and Kao L.-S. (1999) Oxidation state of gold and arsenic in gold-bearing arsenian pyrite. *American Mineralogist* **84**, 1071-1079.

Sugiono D., Thébaud N., LaFlamme C., Fiorentini M., Martin L., Rogers J., Lorusso G. and McFarlane C. (2021) Integration of multiple sulfur isotopes with structural analysis unveils the evolution of ore fluids and source of sulfur at the Kanowna Belle Archean orogenic gold deposit, Yilgarn Craton, Western Australia. *Mineral. Deposita* **56**, 1471-1490.

Wu Y.-F., Fougerouse D., Evans K., Reddy S. M., Saxey D. W., Guagliardo P. and Li J.-W. (2019) Gold, arsenic, and copper zoning in pyrite: A record of fluid chemistry and growth kinetics. *Geology* **47**, 641-644.

Yeats C. J., Kohler E. A., McNaughton N. J. and Tkatchyk L. J. (2001) Geological setting and SHRIMP U–Pb geochronological evidence for ca. 2680–2660 Ma lode-gold mineralization at Jundee–Nimary in the Yilgarn Craton, Western Australia. *Mineral. Deposita* **36**, 125-136.

Zhang L., Yang L.-Q., Groves D. I., Liu Y., Sun S.-C., Qi P., Wu S.-G. and Peng J.-S. (2018) Geological and isotopic constraints on ore genesis, Huangjindong gold deposit, Jiangnan Orogen, southern China. *Ore Geology Reviews* **99**, 264-281.

# Precise constraints on the lifespan of gold mineralization in the giant Yixingzhai gold deposit, North China Craton

**Wen-Sheng Gao[1, 2, 3], Xiao-Dong Deng[1], Jian-Wei Li[1, 2], Dawid Szymanowski[3], Cyril Chelle-Michou[3]**
*[1]State Key Laboratory of Geological Processes and Mineral Resources, China University of Geosciences, China.*
*[2]School of Earth Resources, China University of Geosciences, China.*
*[3]Department of Earth Sciences, Eidgenössische Technische Hochschule (ETH) Zurich, Switzerland.*

**Abstract.** The North China Craton hosts ~7000 t Au that was deposited in the Early Cretaceous. These deposits have been proposed to be of magmatic-hydrothermal origin with a low gold abundance of the source rock, indicating that the longevity of magmatic-hydrothermal processes might be key to achieving the giant size of some of the deposits. Here, we present results of zircon petrochronology with chemical abrasion isotope dilution thermal ionization mass spectrometry (CA-ID-TIMS) U-Pb dating to precisely constrain the timing and duration of gold mineralization in the Yixingzhai deposit (~100 t Au). The youngest zircons in two pre-ore and post-ore intrusions overlap within a short time interval of 0.04 ± 0.22 Ma in the Yixingzhai deposit. The results confirm a genetic link between gold mineralization and underlying magmatism. In addition, the findings suggest that it is possible to form a giant gold mineralization within a short time interval.

## 1 Introduction

The North China Craton (NCC) hosts several dozen gold deposits, which combined have proven reserves of ~7000 t Au (Wang et al. 2020a). These gold deposits are dated mainly at 140–120 Ma, coinciding with the peak of NCC decratonization during the late Mesozoic. Most of the gold deposits show a close temporal-spatial relationship to mafic/intermediate dykes/stocks (Yang et al. 2003). Recent studies on stable isotopes of ore and gangue minerals, noble gas geochemistry of fluid inclusions in Au-bearing pyrite, LA-ICP-MS melt inclusion analysis of the ore-related mafic/intermediate dikes, and gold and platinum group element contents of mantle xenoliths and basalts suggest that mafic/intermediate magmas from metasomatized lithosphere mantle have played a key role in the formation of the giant gold deposits in the NCC (Tan et al. 2012; Wang et al. 2020a; Wang et al. 2020b; Chang et al. 2021). Wang et al. (2020b) advocate that the extensive mantle metasomatism and hydration cannot form a gold-enriched mantle source because the basalts that are contemporary with lode gold have only negligibly high gold contents. Thus, gold pre-enrichment of the magma might not have played an essential role in the giant gold mineralization in the NCC. Instead, the volume and lifespan of the underlying magma and its physical and hydrothermal evolution processes at shallower levels may have been a key control.

Syn-mineralization porphyry intrusions provide snapshots of the evolution of the underlying magma reservoir. Trace elements in zircon, one of the most refractory minerals in porphyries, retain a key record of petrological evolution of the magma even in strongly hydrothermally altered samples. With the improvement of the high-precision zircon U-Pb dating procedures, the analytical precisions could be better than 0.03 % for a single zircon grain (Condon et al. 2015). Therefore, zircon petrochronology combined with high-precision zircon U-Pb dating provides a robust tool for establishing a temporal sequence of magmatic processes that contribute to forming magmatic-hydrothermal deposits (Chelle-Michou et al. 2014).

The Yixingzhai deposit (~100 t Au) in the Central Taihangshan District (CTD) of NCC is characterized by a suite of late Mesozoic intrusions and several different gold mineralization episodes during a short period (Zhang et al. 2020), making it an excellent place to constrain the duration of gold mineralization. In the present study, CA-ID-TIMS U-Pb zircon dates and in-situ zircon trace elements were obtained from the pre-, syn-, and post-ore intrusions at Yixingzhai to determine the timescale of gold mineralization in the deposit.

## 2 Geological background

The NCC is an ancient craton that consists of two blocks, the Western and Eastern block, which are separated by the Trans North China Orogen (Zhao et al. 2005; Figure 1A). The NCC experienced a long period of stability from the late Paleoproterozoic to the end of the Palaeozoic. However, the eastern part of the NNC was reactivated during the Mesozoic, as largely manifested by voluminous magmatism (granitoid intrusion, intermediate to mafic dikes, bimodal volcanic rocks) and widespread extensional tectonics (Figure 1A; Zhu et al. 2015). Within this period, many lode and disseminated gold deposits were formed in the eastern part of NCC (Figure 1 A; Chang et al. 2021).

The Yixingzhai gold deposit hosts several episodes of gold mineralization, such as breccia-hosted Fe-Au mineralization, lode gold mineralization, and porphyry-hosted disseminated gold mineralization (Figure 1B). Besides, various intermediate to felsic dikes/porphyries are identified at the pre-/syn-/post-ore stage of each gold mineralization (Figure 2; Gao et al. 2022). porphyry-hosted disseminated gold mineralization (~60 t Au) is the most economically important gold mineralization episode at Yixingzhai and is characterized by strong sericite alteration and

native gold-bearing sulfides (Zhang et al. 2018). It overprinted early felsite and early granite porphyry and was cut by a late granite porphyry (Figure 2). Zircon U-Pb dates of intrusions (ca. 140–135 Ma; Zhang et al. 2017), garnet U-Pb dates of breccia-hosted gold mineralization (ca. 140 Ma; Zhang et al. 2020), and sericite $^{40}Ar/^{39}Ar$ dates of porphyry-hosted disseminated gold and lode gold mineralization (ca. 139 Ma, Gao et al. 2022) all indicate a close temporal and possibly genetic relationship between the magmatism and mineralization at Yixingzhai (Figures 1 and 2).

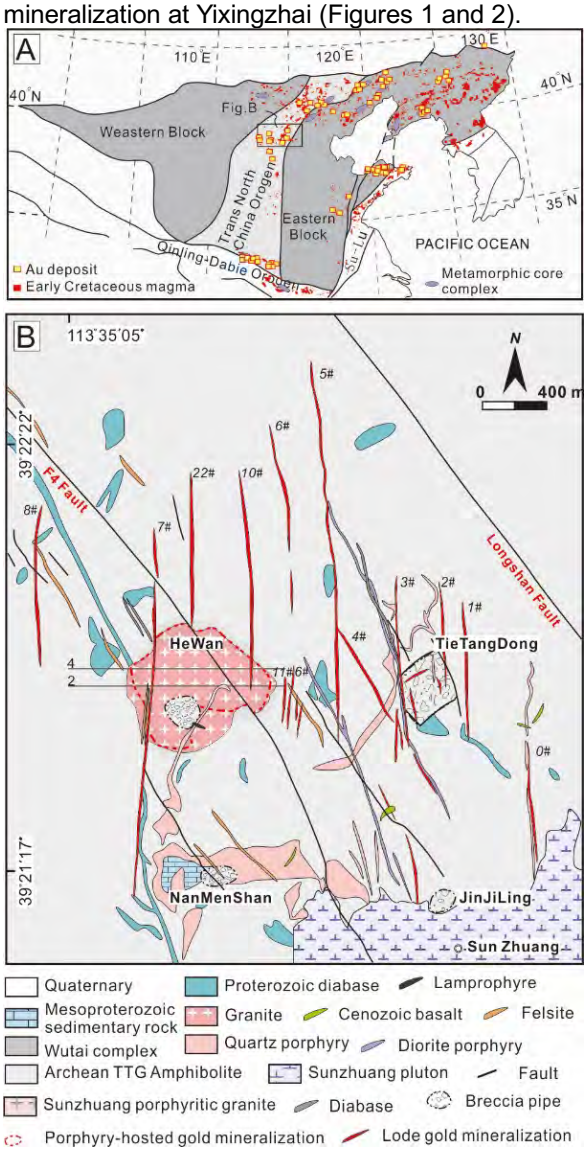


**Figure 1. A** Simplified map showing the tectonic division of the NCC and the location of the Yixingzhai deposit. The distribution of Early Cretaceous magmatism, gold deposits, and metamorphic core complexes are shown (Zhao et al. 2005). **B** Geological map of the various intrusions and mineralization in the Yixingzhai deposit (Zhang et al. 2017).

## 3 Samples and Methodology

Zircons were extracted from samples of the pre-ore early felsite (HW-1), pre/syn-ore early granite porphyry (HW-2), and post-ore late granite porphyry (HW-4), using conventional mineral separation techniques including jawbreaker, sieving, panning and heavy liquid mineral separation. Hand-picked zircons were annealed for 48 h at 900°C. Zircons were mounted in epoxy resin, polished, and imaged with cathodoluminescence (CL) on a JEOL JSM-6390LA Scanning Electron Microscope at the Department of Earth Sciences, ETH Zurich.

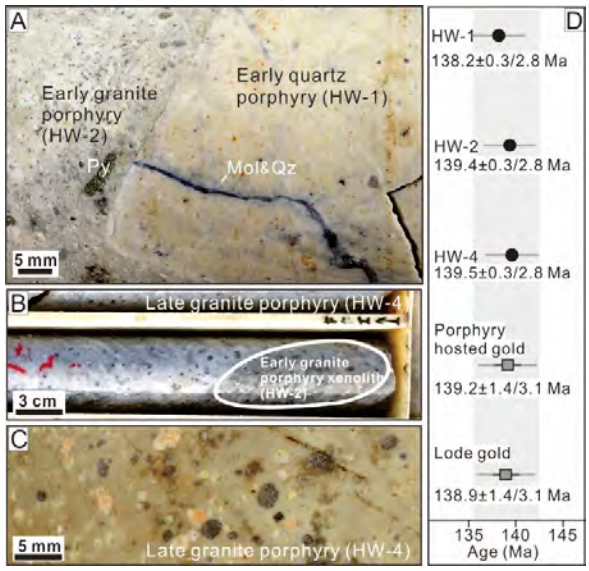


**Figure 2.** Photomicrographs showing the petrographic and textural features of the intrusions. **A** Early felsite clast enclosed by the early granite porphyry, both overprinted by the strong sericite alteration. **BC** Late granite porphyry with minor sericite alteration and a mineralized early granite porphyry xenolith. **D** Summary of the zircon U-Pb (black circle, this study) and sericite 40Ar/39Ar (grey box, Gao et al. 2022) data. Note the dark grey error bar is measurement uncertainty (2σ), while the grey error bar is full external uncertainty (2σ) plus decay constant. Py - Pyrite, Mol - Molybdenite, Qz - Quartz.

LA-ICP-MS geochemistry and geochronology analyses of cores and rims of individual crystals were conducted at ETH Zurich. NIST 610 glass was used as reference material for trace element analyses, with stochiometric concentrations of Si (zircon) as internal standards. The accuracy of the measurements was monitored by repeated analyses of secondary zircon standards (GJ-1, 91500, Plešovice, and synthetic zircon). Most trace elements have uncertainties better than ± 5% (2 RSD) based on secondary standard and glass standard reproducibility.

Fifteen zircons from the three samples showing no evidence of inheritance or contamination by inclusions were selected for CA-ID-TIMS analyses. The selected crystals were removed from the epoxy mount and chemically abraded for 12 h at 190°C using techniques modified from Mattinson (2005). Zircons were spiked with the EARTHTIME $^{202}Pb$-$^{205}Pb$-$^{233}U$-$^{235}U$ tracer solution (ET2535; Condon et al. 2015; McLean et al. 2015) and dissolved in high-pressure Parr bombs at 210°C for 60 h. Dissolved samples were dried and redissolved in 6N HCl at 190°C for 12 h. U and Pb were separated using a single-column HCl-based ion exchange

chromatography and loaded on outgassed Re filaments with a silica gel emitter. All measurements were performed at ETH Zurich employing a Thermo Scientific Triton Plus thermal ionization mass spectrometer. Pb and U were both measured in static mode.

## 4 High-precision zircon U-Pb dates and trace element compositions

Zircon LA-ICP-MS U-Pb dating results are graphically illustrated in Figure 2C. The weighted mean $^{206}Pb/^{238}U$ ages of the Hewan early felsite (HW-1), early granite porphyry (HW-2), and late granite porphyry (HW-4) are 138.2 ± 0.3/2.8 Ma, 139.4 ± 0.3/2.8 Ma, and 139.5 ± 0.3/2.8 Ma (2σ, analytical uncertainty/full external uncertainty including decay and calibration factors), respectively. They overlap with each other. These dates also overlap with the $^{40}Ar/^{39}Ar$ dating of the hydrothermal sericite, confirming a close temporal and genetic link between magmatism and mineralization.

Zircon ID-TIMS U-Pb dating results are graphically illustrated in Figure 3. Three of fifteen zircons were not considered due to high analytical uncertainties. The emplacement age interpretation for each sample is based on the youngest zircon. Thus, the ID-TIMS U-Pb data of the Hewan early felsite, early granite porphyry, and late granite porphyry are 138.25 ± 0.18 Ma, 137.93 ± 0.46 Ma, and 138.21 ± 0.12 Ma, respectively. All three ages overlap with each other within 2σ uncertainty. Zircon dates from the early felsite and late granite porphyries bracketing hydrothermal ore formation at Yixingzhai point to a maximum duration of mineralization of 0.04 ± 0.22 Ma, indicating a short period of ore-formation of porphyry-hosted disseminated gold at Yixingzhai. In addition, zircons from the pre-ore early felsite (HW-1) and the syn/post-ore granite porphyry (HW-2/HW-4) are accompanied by a pronounced difference in zircon geochemistry which may reflect the variety of magma origin and evolution (Figure 4). In contrast, zircons from the syn/post-ore granite porphyry (HW-2 and HW-4) exhibit overlapping trace element geochemistry, likely reflecting similar chemistry of the two porphyries (Figure 4).

## 5 Conclusion

Based on clear field relations and the state-of-art zircon petrochronology, the characteristic timescale of the porphyry-hosted disseminated gold mineralization at Yixingzhai is established to be no more than 0.04 ± 0.22 Ma, showing a short duration of ore-forming processes. In addition, the difference in zircon trace element compositions between the pre-ore felsite and post-ore granite might indicate they are derived from two different magma reservoirs. The results confirm a genetic link between gold mineralization and underlying magmatism. Furthermore, they suggest that it is possible to form a giant gold mineralization within a short time interval.

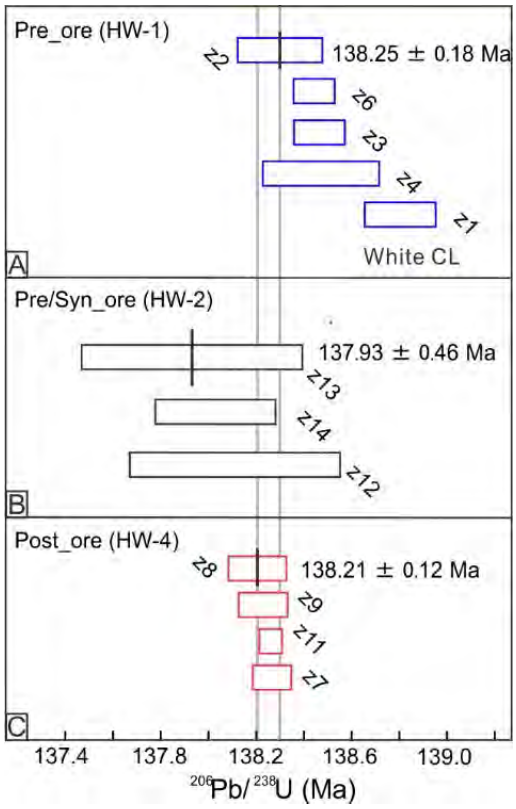


**Figure 3.** Summary of the zircon U-Pb ID-TIMS data (Th corrected, $Th/U_{(magma)}$ = 3.5) from the magmatic rocks in the Yixingzhai deposit.


## Acknowledgments

This work is supported by the Ministry of Science and Technology of China (2016YFC0600104) and the MOST Special Fund from the GPMR, China University of Geosciences (Wuhan). Wensheng Gao acknowledges funding through the China Scholarship Council. We thank Yu-Xiang Li, Hong-Qiang Wang, Zhe Chi, Adrianna Luiza Virmond, Sava Markovic, Lorenzo Tavazzani, and Julien Allaz for their assistance with the fieldwork, sample preparation, SEM-CL, and LA-ICPMS analysis. We thank Chetan Nathwani for comments on an early version of the manuscript.

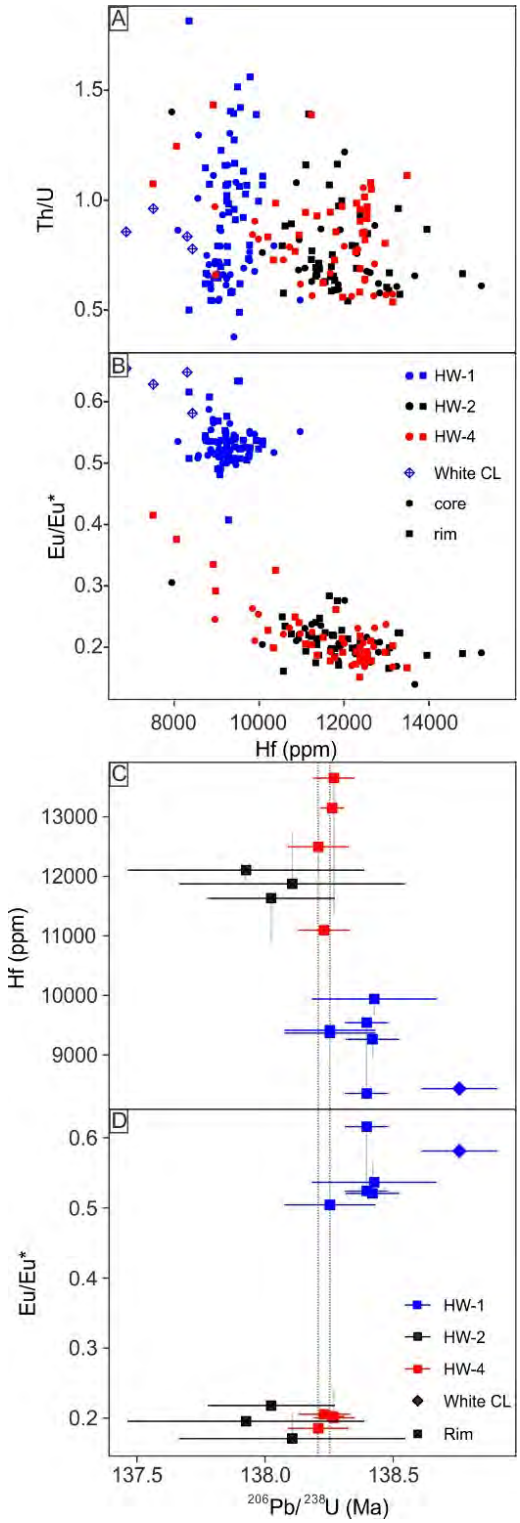


**Figure 4. AB** Trace element correlation diagrams for zircons from the Yixingzhai deposit. **CD** Trace element composition of ID-TIMS-dated zircons plotted against individual zircon crystallization ages. Note that the rim analyses are plotted as color-coded boxes with grey vertical lines extending to the compositions of the respective cores. Vertically dotted grey lines indicate the emplacement ages of the pre- and post-ore porphyry intrusions based on the youngest respective zircon.

## References


Chang, J., Audétat, A., and Li, J.W. (2021): Tectono-magmatic controls on decratonic gold deposits, Contributions to mineralogy and petrology, v. 176, p. 1-18.

Chelle-Michou, C., Chiaradia, M., Ovtcharova, M., Ulianov, A., and Wotzlaw, J.F. (2014): Zircon petrochronology reveals the temporal link between porphyry systems and the magmatic evolution of their hidden plutonic roots (the Eocene Coroccohuayco deposit, Peru), Lithos, v. 198, p. 129–140.

Condon, D. J., Schoene, B., McLean, N.M., Bowring, S.A., and Parrish, R.R. (2015): Metrology and traceability of U-Pb isotope dilution geochronology (EARTHTIME Tracer Calibration Part I), Geochimica et Cosmochimica Acta, v. 164, p. 464–480.

Gao, W.S., Deng, X.D., Chelle-Michou, C., Zhang, L.Z., Li, J.W. (2022): 40Ar/39Ar ages constraints on lode gold and porphyry-hosted gold mineralization of the Yixingzhai gold deposit in Taihangshan District, North China Craton. SMRS 2022. Sustainable Mineral Resources Supply: Challenges for Future Generations. Geneva. p. 21.

Mattinson, J.M. (2005): Zircon U-Pb chemical abrasion ("CA-TIMS") method: combined annealing and multi-step partial dissolution analysis for improved precision and accuracy of zircon ages, Chemical Geology, v. 220, p. 47-66.

McLean, N. M., Condon, D.J., Schoene, B., and Bowring, S.A. (2015): Evaluating uncertainties in the calibration of isotopic reference materials and multi-element isotopic tracers (EARTHTIME Tracer Calibration Part II), Geochimica et Cosmochimica Acta, v. 164, p. 481–501.

Tan, J., Wei, J., Audétat, A., and Pettke, T. (2012): Source of metals in the Guocheng gold deposit, Jiaodong Peninsula, North China Craton: link to early Cretaceous mafic magmatism originating from Paleoproterozoic metasomatized lithospheric mantle, Ore Geology Reviews, v. 48, p. 70–87.

Wang, H.Q., Gao, W.S., Deng, X.D., and Li, J.W. (2020a): Zircon U-Pb dating reveals Late Jurassic gold mineralization in the Jidong district of the northern North China Craton, Ore Geology Reviews, 103798.

Wang, Z., Cheng, H., Zong, K., Geng, X., Liu, Y., Yang, J., and Wang, C.Y. (2020b): Metasomatized lithospheric mantle for Mesozoic giant gold deposits in the North China craton, Geology, v. 48, p. 169–173.

Yang, J.H., Wu, F.Y., and Wilde, S.A. (2003): A review of the geodynamic setting of large-scale Late Mesozoic gold mineralization in the North China Craton: an association with lithospheric thinning, Ore Geology Reviews, v. 23, p. 125–152.

Zhang, J.Q., Li, S.R., Santosh, M., Niu, S.D., Li, Q., and Lu, J. (2017): The magmatic-hydrothermal mineralization systems of the Yixingzhai and Xinzhuang gold deposits in the central North China Craton, Ore Geology Reviews, v. 88, p. 416–435.

Zhang, L.Z. (2018): Element geochemistry and age of the altered-porphyry gold mineralization in Yixingzhai gold deposit, Fanshi city, Shanxi Province, Geology and Mineral Resources of South China, v. 34, p. 134–141. (In Chinese with English abstract)

Zhang, L.Z., Chen, L., Wang, G.P., Deng, X.D., and Li, J.W. (2020): Garnet U–Pb dating constraints on the timing of breccia pipes formation and genesis of gold mineralization in Yixingzhai gold deposit, Shanxi Province, Earth Science, v. 45, p. 108–117. (In Chinese with English abstract)

Zhao, G.C., Sun, M., Wilde, S.A., and Li, S.Z. (2005): Late Archean to Paleoproterozoic evolution of the North China Craton: Key issues revisited, Precambrian Research, v. 136, p. 177–202.

Zhu, R., Fan, H., Li, J., Meng, Q., Li, S., and Zeng, Q. (2015): Decratonic gold deposits, Science China Earth Sciences, v. 58(9), p. 1523–1537.

# The conglomerate-hosted Jacobina gold deposits, a modified paleoplacer of the Witwatersrand-type in Brazil

**Enzio Garayp[1], Hartwig E. Frimmel [1,2]**
*[1]Bavarian Georesources Centre, Department of Geodynamics and Geomaterials Research, Institute of Geography and Geology, University of Würzburg, Am Hubland, D-97074 Würzburg, Germany*
*[2]Department of Geological Sciences, University of Cape Town, Rondebosch 7701, South Africa*

**Abstract.** The genesis of the Neoarchean conglomerate-hosted Jacobina gold deposits in Brazil has been highly controversial, with both syngenetic and epigenetic models having been proposed. Here we show that they represent, analogous to Witwatersrand-type deposits (WTD), paleoplacers that became partly remobilized during later metamorphic overprint. Evidence of this includes strong lithological and sedimentological control on the Au grade, presence of detrital gold particles and other detrital clasts with gold inclusions. Detrital, syn-sedimentary and post-depositional pyrite generations can be distinguished. Syn-sedimentary pyrite has the highest Au content, from which elevated Au concentrations in Archean meteoric waters are inferred. The nature and extent of post-depositional alteration, mainly during the Paleoproterozoic Transamazonian Orogeny, distinguishes the Jacobina deposits from other WTD. Zr-in-rutile thermometry indicates peak metamorphic temperatures of >650°C, and chlorite thermometry retrograde local fluid infiltration at ca. 280°C-340°C. Local remobilized gold associated with Fe-oxides near intrusive rocks is attributed to late-Transamazonian mafic/ultramafic magmatism Remobilization during regional metamorphism was insufficient to form substantial secondary orebodies but led to purification of the gold particles that contain relatively little Ag and Cu and lack Hg.

## 1 Introduction

The Neoarchean metaconglomerate-hosted Jacobina gold deposits in the São Francisco Craton in eastern Brazil (Fig. 1) have been mined episodically on a small scale for more than 200 years. Presently operated by Yamana Gold Inc., they produce >6 t of Au per year. Current resource estimates indicate proven and probable resources of 100 t of Au at an average Au grade of 2.18 g/t with potential resources open at depth. The genesis of these deposits has been a matter of debate: some workers argued for a paleoplacer origin (Minter 1975; Hendrickson 1984; Molinari 1988) whereas others favored an entirely epigenetic formation (Teixeira et al. 2001; Milesi et al. 2002). This study aims at resolving this conflict on the basis of assessing the geological control on Au grade, textural observations, and mineral chemical analyses.

The gold-hosting Jacobina sequence is composed predominantly of quartzite with interlayered metaconglomerate beds and represents the fill of the Jacobina Basin, which is enclosed by the oldest terranes in South America, including a >3.4 Ga tonalite-trondhjemite-granodiorite (TTG) suite and 3.3 Ga granite-greenstone belts. Detrital zircon ages constrain the source of the Jacobina sediments to between 3251 ± 52 and 3614 ± 67 Ma (Teles et al. 2015). The Jacobina basin fill became squeezed into a major suture zone, the Contendas-Jacobina Lineament, in the course of collision of three Archean blocks during the ca. 2.0 Ga Transamazonian Orogeny (Fig. 1). This resulted in in westward thrusts and sinistral transcurrent faults due to east-west transpressive shortening. Cross-cutting abundant mafic/ultramafic sills and dikes, though not precisely dated, are probably related to the Transamazonian Orogeny.

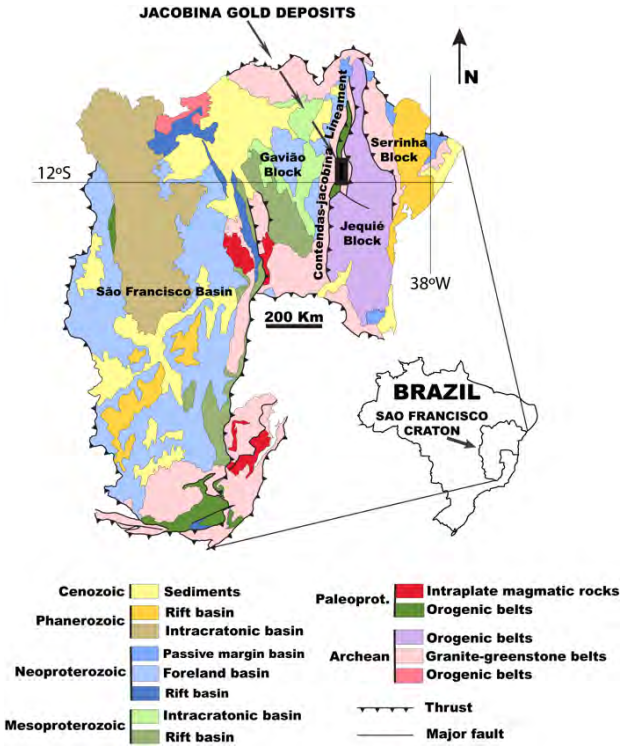


**Figure 6** Location of the Jacobina gold deposits in the São Francisco Province, Brazil (modified from Delgado et al. 2003).

## 2 Results

Gold grade is strongly controlled by lithology: The bulk of the gold is hosted by metaconglomerates and subordinately pebbly quartzite. The orebodies (reefs) extend for several kilometers along strike and on dip at different stratigraphic levels (at least 13 reefs; Pearson et al. 2005). The Au grade is strongly related to sedimentary structures, such as specific small-pebble beds, the most densely packed conglomerates, or the bottom of large-pebble

conglomerate beds deposited at the base of channels or on unconformities.

A total of 74 polished thin sections from 12 different (reefs) were analyzed petrographically. Whereas well-rounded quartz pebbles and sand particles are undoubtedly detrital, pyrite occurs in a wide variety of textures: Round compact pyrite, which is the predominant type in most Archean conglomerates worldwide (e.g. England et al. 2002), is common also in Jacobina (Fig. 2 A). By analogy with round compact pyrite elsewhere, this type is regarded as detrital, a notion that has been consolidated throughout the years by petrography, trace element data, and isotope geochemistry (Frimmel 2014 and references therein; Guy et al. 2014). Variably rounded, inclusion-rich ("porous") pyrite is considered syn-sedimentary (Fig. 2B). Post-depositional pyrite occurs predominantly as overgrowth (Fig. 2C) and subordinately remobilized into veins with quartz (Fig. 3A).

Although a considerable proportion (ca. 25 %) of the gold occurs in texturally late positions, such as microfractures, and is thus clearly epigenetic, the majority occurs as interstitial grains within the conglomerate matrix, many of which display circular to elliptical outlines with smooth rounded boundaries in thin section (Fig. 3B). The latter are considered detrital. Of particular significance is the observation of gold inclusions within both detrital pyrite (Fig. 2A) and detrital quartz. Most of the post-depositional gold is associated with secondary pyrite but locally, near magmatic intrusive bodies, secondary gold is associated with hematite and goethite (Fig. 3C). In the latter case, hematite crystals overprint the metamorphic fabric, and oxidation affected both primary and secondary pyrite. The oxidized samples come from >600 m below surface, which precludes recent weathering.

The gold composition, as determined by electron microprobe, is, on average, 98.3 wt% Au, 1.54 wt% Ag, and 0.07 wt% Cu. Mercury was not detected. Systematic differences were noted between detrital and post-depositional gold: As an example, very pure gold veinlets contrast side by side with Ag-bearing gold inclusions in a quartz pebble, indicating that the late gold generation was depleted in Ag. This is also evident in Ag-depleted rims in detrital gold grains.

Trace element analyses of the various pyrite generations by LA-ICPMS (Table 1) revealed that the synsedimentary pyrite has the highest Au content (mean 1.86 ppm), followed by the detrital pyrite (mean 0.22 ppm) and the almost Au-free post-depositional pyrite (0.04 ppm). Relatively lower Au/Ag ratio in the post-depositional pyrite compared with the previous generations (Table 1) suggests that Au was decoupled from Ag during pyrite remobilization.

Abundant secondary pyrite and other metamorphic/hydrothermal minerals like chlorite, fuchsite, rutile, tourmaline and Fe-oxides are the most evident indicators of post-depositional alteration in the Jacobina ore assemblage. Zr-in-rutile thermometry (Meinhold 2010; Zack and Kooijman 2017) indicates peak metamorphic temperatures in excess of 650°C ($ZrO_2$ between 170 and 610 ppm, lower limit of detection = 160 ppm). Retrograde conditions were estimated by chlorite thermometry (Cathelineau 1988; De Caritat et al. 1993) as 280°C – 340°C. Based on its texture, most of the tourmaline is regarded as metamorphic, and its composition corresponds largely to that of tourmaline known from siliciclastic metasedimentary rocks (Fig. 4).

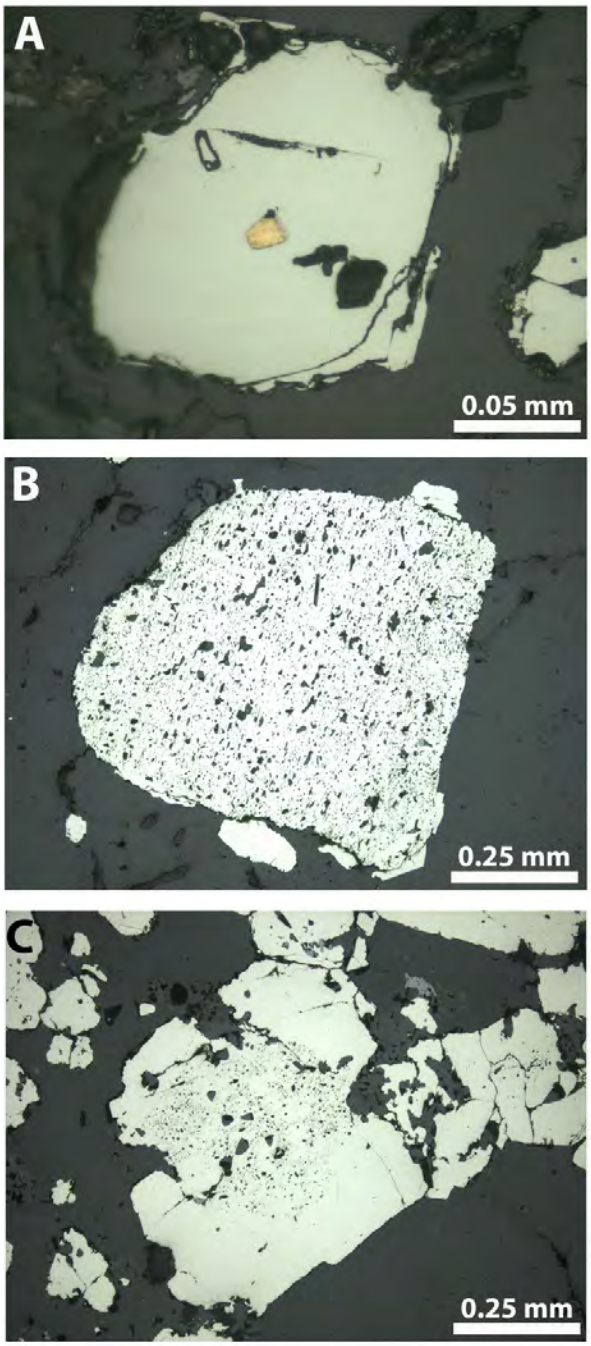


**Figure 7.** (A) Microphotograph of a compact detrital pyrite grain with gold-pyrrhotite inclusion in the center, (B) Microphotograph of a synsedimentary porous pyrite grain, (C) Microphotograph of euhedral pyrite overgrowth around synsedimentary pyrite (inclusion-rich core).

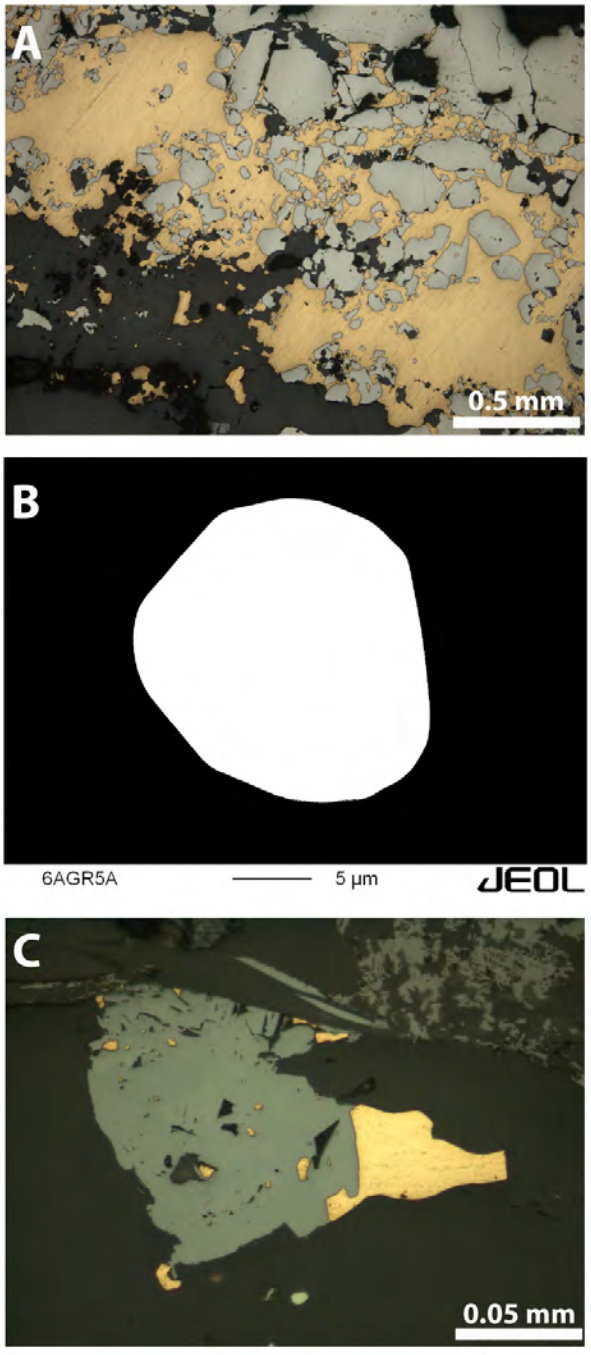


**Figure 3.** (A) Gold filling quartz-pyrite vein, (B) Back scattered image of a detrital gold grain (C) Remobilized gold with hematite.

**Table 1** Trace element concentrations in different types of pyrite

| Element | Round compact pyrite | | Round porous pyrite | | Secondary compact | |
|---|---|---|---|---|---|---|
| | Mean | Range (ppm) | Mean | Range (ppm) | Mean | Range (ppm) |
| As | 202 | 30.7 – 703 | 833 | 32.5 – 9,180 | 320 | 0.61 – 1,121 |
| Co | 363 | 25.1 – 1,38 | 446 | 74.7 – 1,654 | 519 | 1.84 – 1,240 |
| Ni | 404 | 46.9 – 1,35 | 277 | 40.7 – 787 | 298 | 8.53 – 1,352 |
| Pb | 7.17 | 1.80 – 15.50 | 41.0 | 1.86 – 158 | 2.30 | <0.01 – 53.3 |
| Cu | 1.70 | <0.20 – 4.73 | 3.21 | <0.20 – 11.4 | 0.68 | <0.15 – 9.00 |
| Au | 0.22 | 0.11 – 0.39 | 1.34 | 0.07 – 10.9 | 0.04 | <0.01 – 0.08 |
| Ag | 0.11 | <0.02 – 0.22 | 0.33 | 0.03 – 1.82 | 0.04 | <0.01 – 0.26 |
| Tl | 1.09 | <0.01 – 3.86 | 0.09 | <0.01 – 0.68 | 0.11 | <0.01 – 2.90 |
| Cd | 0.21 | <0.07 – 0.37 | 0.14 | <0.07 – 0.23 | 0.20 | <0.01 – 0.50 |
| Au/Ag | 2 | | 4 | | 1 | |

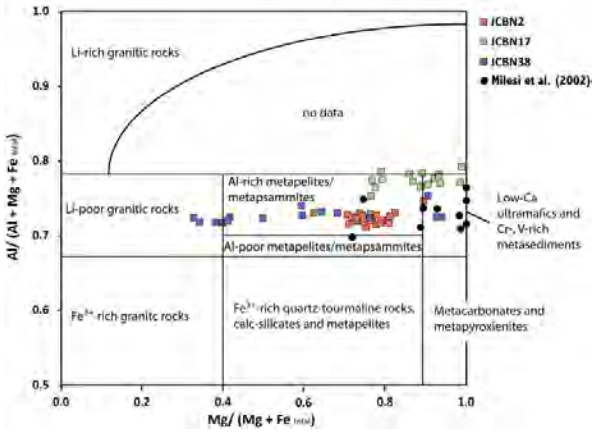


**Figure 4.** Tourmaline composition in the Al-Mg-Fe Diagram (Henry and Dutrow, 2018), classifying different genetic types.

## 3 Conclusions

There is substantial evidence of primarily placer gold concentration at Jacobina, that is, strong lithological and sedimentological control on Au grade at different scales, presence of detrital minerals with gold inclusions within heavy mineral layers, and the presence of detrital gold particles.

Three genetic types of pyrite were recognized: detrital, synsedimentary and post-depositional pyrites, analogous to Witwatersrand-type deposits elsewhere in the world. Each pyrite type had a particular role in the gold mineralization: whereas the detrital and the synsedimentary types accompanied gold accumulation, the post-depositional pyrite can be associated with Au dispersion by fluid-induced Au-depletion in detrital and synsedimentary pyrite.

The presence of synsedimentary pyrite with significantly higher Au concentrations in relation to the other pyrite types supports elevated Au contents, probably dissolved as Au-sulfide complex, in meteoric waters at the time as suggested for the Witwatersrand deposits (Frimmel 2014).

What distinguishes the Jacobina deposits from other Witwatersrand-type deposits are the nature and extent of the post-depositional alteration, mainly in the course of the Transamazonian Orogeny. Metamorphism and to a limited extent magmatism caused the partial dissolution and reprecipitation of various minerals including pyrite and gold. This remobilization changed their trace-element contents thus resulting in gold of greater fineness. It was, however, insufficient to form any substantial orebodies.

There is indication of local magmatic influence on the gold mineralization history. Mafic/ultramafic intrusives caused a thermal overprint, whereas late to post-tectonic granite emplacement triggered hydrothermal fluid circulation and further partial remobilization of ore components. The latter took place under very different redox conditions, evident from the presence of Fe-oxides/hydroxides associated with remobilized gold. This suggests

some gold remobilization after the Great Oxidation Event, probably by circulation of meteoric waters during uplift in the final stages of the Transamazonian Orogeny, which agrees with the age of the late to post-tectonic magmatism (1970 to 1800 Ma). In summary, based on the evidence of placer gold concentration and the intense post-depositional alteration, the modified paleoplacer model best fits the Jacobina gold deposits.

## Acknowledgements

S. Höhn, U Schüßler and N. Koglin assisted with microprobe analyses, and H. Brätz is thanked for the LA-ICPMS analyses. We also thank Yamana Gold Inc. for providing access and logistic support to their operations in Jacobina. The analytical costs were covered by the Department of Geodynamics and Geomaterials Research at the University of Wuerzburg.

## References

Cathelineau M (1988) Cation site occupancy in chlorites and Illites as a function of temperature. Clays and Clay minerals

De Caritat P, Hutcheon I, Walshe J L (1993) Chlorite geothermometry: A Review. Clays Clay Minerals 41: 219-239

Delgado IM et al. (2003) Geotectônica dos escudos das Guianas e Brasil-Central In: Bizzi LA, Schobbenhaus C, Vidotti RM, Gonçalves JH (eds) Geologia, Tectônica e Recursos Minerais do Brasil. Serviço Geológico do Brasil CPRM, Brasília, Brasil

England GL, Rasmussen B, Krapez B, Groves D (2002) Paleoenvironmental significance of rounded pyrite in siliciclastic of the Late Archean Witwatersrand Basin: oxygen-deficient atmosphere or hydrothermal alteration? Sedimentology 49:1133–1156

Frimmel HE (2014) A giant Mesoarchean crustal gold-enrichment episode: Possible causes and consequences for exploration. Society of Economic Geologists Inc. Special Publication 18:209–234

Guy BM, Ono S, Gutzmer J, Beukes NJ (2014) Sulfur sources of sedimentary “buckshot” pyrite in the auriferous conglomerates of the Mesoarchean Witwatersrand and Ventersdorp supergroups, Kaapvaal Craton, South Africa. Miner. Deposita 49:751–775

Henry DJ, Dutrow BL (2018) Tourmaline studies through time: contributions to scientific advancements. Journal of Geosciences 63:77-98

Hendrickson BR (1984) Stratigraphic position, mineralogy, depositional environment, and gold distribution of the Main Reef at Morro do Cuscuz and Morro do Vento near Jacobina, Bahia, Brazil. Unpublished MSc. Thesis, South Dakota School of Mines and Technology, Rapid City, USA

Meinhold G (2010) Rutile and its applications in earth sciences. Earth Sciences Reviews 102:1-28

Milesi JP et al. (2002) The Jacobina Paleoproterozoic gold-bearing conglomerates, Bahia, Brazil: a "hydrothermal shear-reservoir" model. Ore Geology Reviews 19:95–136

Minter WEL (1975) Sedimentological Aspects of the Serra do Córrego Formation with particular reference to the Main Reef Unit at Cuzcuz and Morro do Vento near Jacobina, Bahia, Brazil. Internal Report Unigeo Unpublished Report

Molinari L, Scarpelli L (1988) Depositos de Ouro de Jacobina in Principais Depositos Minerais do Brasil DNPM Brazil 3:463–478

Pearson W et al. (2005) Geology and gold mineralization of the Jacobina Mine and Bahia Gold Belt, Bahia, Brazil, and a comparison to Tarkwa and Witwatersrand. Window to the World: 2005 Symposium Proceedings Geological Society of Nevada Reno/Sparks 757–785

Teixeira JBG et al. (2001) Gold Mineralization in the Serra de Jacobina region, Bahia Brazil: tectonic framework and metallogenesis. Mineralium Deposita 36:332–344

Teles G, Chemale Jr. F, Oliveira CG (2015) Paleoarchean record of the detrital pyrite-bearing, Jacobina Au-U deposits, Bahia, Brazil Precambrian Research 256:289–313

Zack T Kooijman E (2017) Petrology and geochronology of rutile. Reviews in Mineralogy and Geochemistry 83(1):463-467

# Revelio Aurum! uncovering invisible gold in N. America, China, and Europe

**Philip Gopon[1,2], James O. Douglas[2,3], Benjamin Jenkins[2,4], Viktor Bertrandsson Erlandsson[1], Sandra Niederl[1], Patrick Sack[5], Zhuojun Xie[6], Peter Felfer[7]**

*[1] Dept. of Applied Geosciences and Geophysics, University of Leoben, 8770, Leoben, Austria*
*[2] Dept. of Materials, University of Oxford, OX1 3PH, Oxford, UK*
*[3] Dept. of Materials, Imperial College London, SW7 2AZ, London, UK*
*[4]Groupe de Physique de Matériaux, University of Rouen, 76800, Saint Etienne du Rouvray, FR*
*[5] Dept. of Energy, Mines, and Resources, Yukon Geological Survey, Y1A 2BF, Whitehorse, CA*
*[6] State Key Laboratory of Ore Deposit Geochemistry, Institute of Geochemistry, Chinese Academy of Sciences, 550081, Guiyang, P.R. China*
*[7] Dept. of Materials Science and Engineering, Friedrich-Alexander Universität Erlangen-Nürnberg, 91058, Erlangen, Germany*

**Abstract.** Despite extensive study, Carlin-type gold (CTG) mineralization is still poorly understood. These deposits predominantly along major regional faults and are characterized by invisible gold thought to be hosted in sulfide minerals (Cline et al., 2005). CTG was until recently only thought to occur in central-Nevada, but discoveries in the Yukon Territory, China, and Kyrgyzstan have made us re-evaluate this. Additionally, a significant invisible gold component in other deposit types (epithermal, orogenic, porphyry, etc.) is drastically increasing the importance of these deposits. We investigated four invisible gold occurrences (Yukon, Nevada, Guizhou, and Austria) and reveal that gold is hosted in these deposits (in part) as lattice bound gold.

Our study combines high-resolution electron probe microanalysis and nano-secondary ion mass spectrometry with atom probe tomography to better understand the commonalities / differences in how gold is hosted in these geographically distant deposits and why sulfide minerals make such great hosts for gold and other critical metals. Furthermore, our atomic scale characterization suggests that the presence of arsenic is integral to the mechanisms by which gold is accommodated into the pyrite lattice, and is a commonality shared by all deposits we investigated.

## 1 Introduction

The Carlin-type gold (CTG) mineralization has been known in north-central Nevada since the early 1960s, but until the early 2000s was assumed to be a Nevadan phenomenon. In Nevada CTG deposits occur along 5 so called 'trends' which align with major regional faults, are hosted in silty-carbonate rocks, and are characterized by their large volume and generally low ore grade (Cline et al., 2005). Gold (the mineral) or electrum are rarely if ever reported, with the gold (element) being almost exclusively hosted in sulfide minerals.

The discovery of similar deposits in China, Kyrgyzstan, and Canada has forced us to re-think that Nevada is alone in hosting these massive and massively important gold deposits (Xie et al., 2018; Pinet et al., 2022). Furthermore, the presence of gold associated high-tech metals (ex. Te) in some of these deposits makes this deposit type potentially even more important for the Green Energy Transition and mineral resource security.

There are enough similarities between the host lithologies, tectonic setting, and gold occurrence (i.e. within sulfide minerals) but also enough dissimilarities in the same, where coming to a complete understanding of the ore-forming processes is still elusive. Notably, the most basic information, exactly how the gold is hosted in these sulfide minerals, is still something that is an open question for all of these deposits, and has large implications for the mineralization model as well as ore processing.

Our study has focused on the similarities and differences between the CTG deposits in N. America, China, and deposits with CTG like properties in Europe. The CTG deposits we investigate are all hosted in silty-carbonate host rocks, and al deposits investigated are associated or aligned with large regional fault structures. Some differences exist in the tectonic setting, but a common theme is a low energy and partially reducing depositional setting for the host rocks, be it a continental edge or an interior basin (Cline et al., 2005; Liang et al., 2021; Pinet et al., 2022). Gold is always hosted in arsenic containing pyrite which grows on top of a sedimentary or diagenetic pyrite core. The pyrite core, as well as the overgrowths, have variable trace elemental signatures as well as different textural forms. Despite this, all gold occurs as bound within the crystal lattice of arsenian-pyrite (Gopon et al., 2019), with an intimate link between arsenic and gold noted at the regional, meter, micrometer (Figure 1), nanometer (Figure 2), and atomic scale (Figure 2).

Our study combines high-resolution electron probe microanalysis (EPMA) and nano-secondary ion mass spectrometry (nanoSIMS) with atom probe tomography (APT). Using a select number of examples from North America, Europe, and China we present data that help to constrain how gold is hosted in these deposits, why sulfide minerals make such great hosts for gold and other critical metals, and share insights from atomic scale trace element and isotopic analysis into the formation mechanisms of these deposits.

## 2 Methods

### 2.1 High resolution mapping

High resolution maps where conducted using low voltage EPMA as well as a nanoSIMS to determine the micrometer scale distribution of trace elements in arsenic and gold containing pyrite. nanoSIMS analyses were conducted using a CAMECA 50L at Tianjin University and EPMA maps were acquired on a field emission gun sourced CAMECA SX5 at the University of Oxford.

### 2.2 Atomic probe tomography

Focused ion-beam scanning electron microscope (FIB-SEM) liftouts where taken from gold containing sub-domains identified in the high resolution maps. The liftouts on the three Carlin deposits (Yukon, Guizhou, and Nevada) were done using a Zeiss Crossbeam at the University of Oxford, and the liftouts from the Austria deposit (Flatschach district, Styria) where conducted on a FEI Helios at the University of Erlangen. APT experiments on the three Carlin deposits where conducted on a CAMECA LEAP 5000HR at the University of Oxford, and the Austrian gold containing pyrite was analyzed with a CAMECA LEAP 4000HR at the University of Erlangen.

## 3 Results

### 3.1 Mapping results

High resolution mapping of the gold containing pyrite from the three Carlin type deposits show similar features in terms of a barren sedimentary or detrital core overgrown by a gold and arsenic rich hydrothermal pyrite (Figure 1). The gold and arsenic tends to occur in complicated oscillatory zoned, micrometer scaled, overgrowths in the pyrite from Nevada and Guizhou. The Yukon gold containing overgrowths do not appear zoned at the micrometer scale and in general tend to be much smaller in size compared to those from Nevada and Guizhou (1-2 micrometers vs 5-20 micrometers). The Austrian gold containing pyrite showed a much more complicated zoning pattern within the pyrite compared to the CTG deposits, with no clear barren core- gold rich rim pattern discernible. The zoning appeared ‘washed out’ in places, in especially along fractures.

In all samples analyzed a correlation between high gold and high arsenic containing regions was noted, but not in all cases where high arsenic regions noted to be elevated in gold.

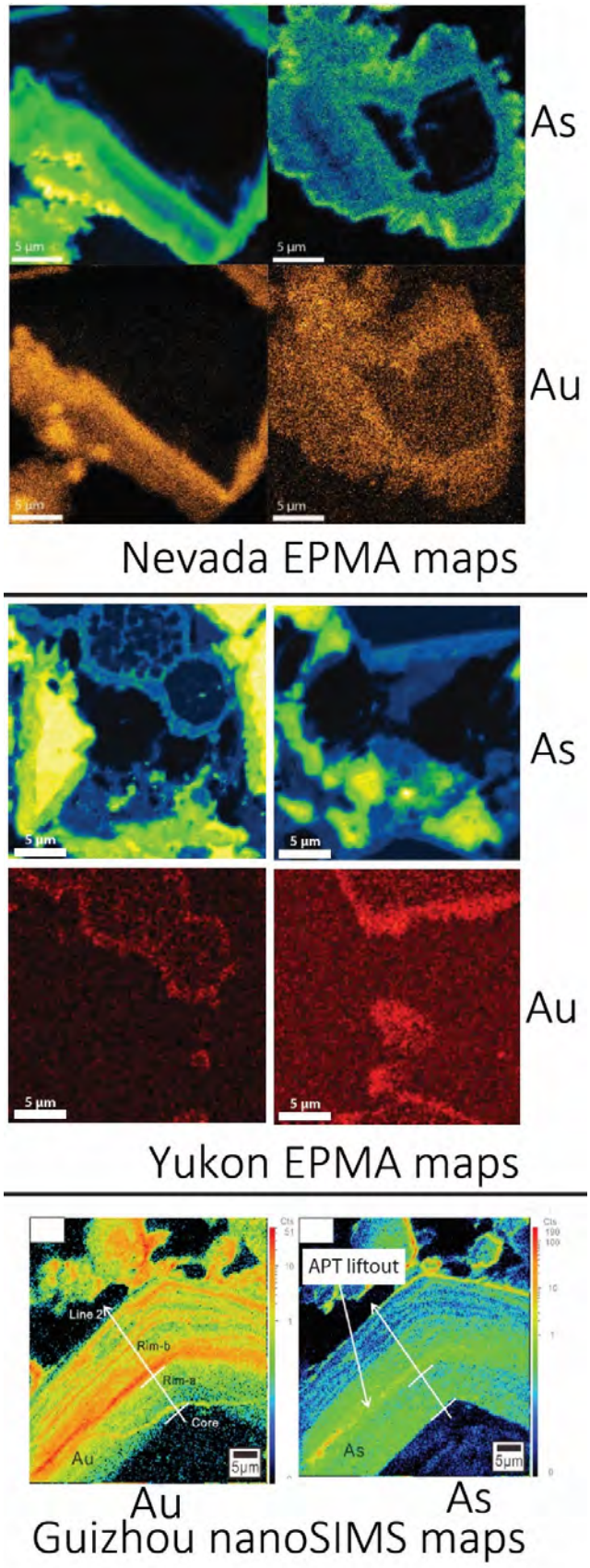


**Figure 8.** EPMA and nanoSIMS maps showing the distribution of arsenic and gold in pyrites from Nevada (top), Yukon (middle), and Guizhou (bottom).

### 3.2 APT results

Pyrite from the Yukon and Guizhou deposits showed nanoscale zoning, which were not noted in
APT datasets from the Nevadan pyrites. Within these zones, atomic scale characterization of the gold containing pyrite reveals homogenously distributed gold and arsenic (Figure 2). A correlation between high gold and arsenic was similarly noted within these nanoscale zones, as noted at the µm scale.
Atomic scale spatial analysis using the 3-depict software package revealed that there is higher arsenic concentration, compared to the matrix, surrounding individual gold atoms.

## 4 Discussion

High resolution mapping revealed similar textures (barren core, gold and arsenic containing rim) at the micrometer scale in all studied Carlin type deposits. The similarities of the host rock (interbedded shales and carbonates) of these deposits suggest that this lithology is important in the mineralization model for this deposit type (Muntean et al., 2011). Similarly, the oscillatory zoning that was present in all the Carlin deposits suggest similar processes where at work. This oscillatory zoning could have been caused by either growth from multiple fluid pulses, a constantly evolving single fluid pulse, or diffusion driven self-reorganization (Gopon, et al., 2019; Fougerouse et al., 2016).

The host rock (amphibolite) in the Austrian deposit is much different than the Carlin deposits. The deposit was originally mined as a Cu-Au resource in the Middle Ages-Renaissance, and visible gold and copper-sulfides where the primary minerals won. However, we note that the pyrite in the old mine waste piles, is similarly gold and arsenic rich as the pyrite from the Carlin deposits. It is notable that there is no barren (sedimentary or detrital) core to the pyrites, but simply a complicated oscillatory zoning that is often locally distributed, especially surrounding fractures in the pyrite. This suggests that the arsenic, and gold, were remobilized during later metamorphic overprinting.

## 5 Conclusion

Gold containing pyrite from three Carlin type deposits, show very similar textural features at the micrometer, nanometer, and atomic scale. Gold is contained within arsenic rich overgrowths, on a barren core. The non-Carlin deposit investigated showed very different core-rim patterns, but where found to be similarly oscillatory zoned as the overgrowth in the Carlin pyrites. Within the gold/arsenic rich zones, gold and arsenic is noted to be homogenously distributed (i.e. lattice bound). Moreover, our atomic scale spatial analysis shows that there is an enrichment of arsenic surrounding individual gold atoms, suggesting that arsenic is key to the incorporation mechanism of gold into the pyrite lattice (Gopon et al., 2019).

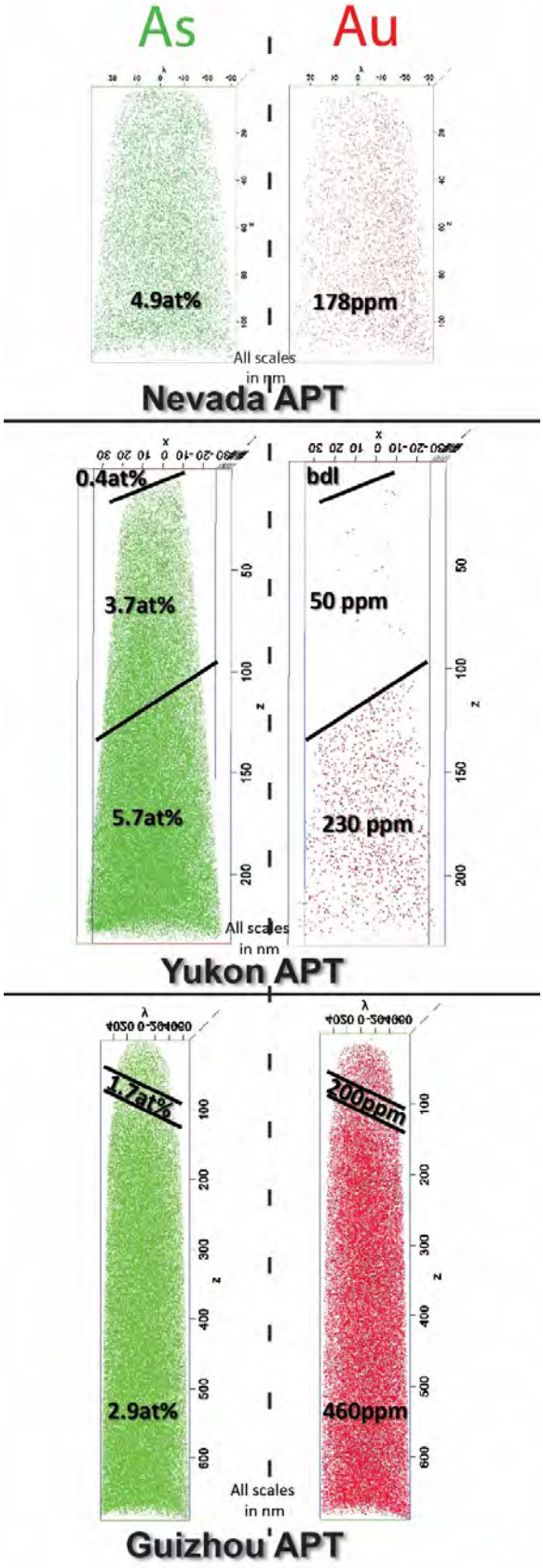


**Figure 9**. 3-D atom probe reconstructions showing the distribution of arsenic (left) and gold (right), in pyrite from Nevada (top), Yukon (middle), and Guizhou (bottom).

## References


Cline, J.S., Hofstra, A.H., Muntean, J.L., Tosdal, R.M., and Hickey, K. a., 2005, Carlin-Type Gold Deposits in Nevada: Critical Geologic Characteristics and Viable Models: Economic Geology, v. 100th Anni, p. 451–484

Fougerouse, D., Reddy, S.M., Saxey, D.W., Rickard, W.D.A., Van Riessen, A., and Micklethwaite, S., 2016, Nanoscale gold clusters in arsenopyrite controlled by growth rate not concentration: Evidence from atom probe microscopy: American Mineralogist, v. 101, p. 1916–1919

Gopon, P., Douglas, J.O., Auger, M.A., Hansen, L., Wade, J., Cline, J.S., Robb, L.J., and Moody, M.P., 2019, A Nanoscale Investigation of Carlin-Type Gold Deposits: An Atom-Scale Elemental and Isotopic Perspective: Economic Geology, v. 114, p. 1123–1133

Liang, Q.L., Xie, Z., Song, X.Y., Wirth, R., Xia, Y., and Cline, J., 2021, Evolution of invisible au in arsenian pyrite in carlin-type Au deposits: Economic Geology, v. 116, p. 515–526

Muntean, J.L., Cline, J.S., Simon, A.C., and Longo, A. a., 2011, Magmatic–hydrothermal origin of Nevada's Carlin-type gold deposits: Nature Geoscience, v. 4, p. 122–127

Pinet, N. et al., 2022, Yukon's Carlin-Type Gold Deposits (Rackla Belt, Canada): Main Characteristics and New Insights on Alteration Styles and Geochemistry: Economic Geology, v. 117, p. 875–904

Xie, Z., Xia, Y., Cline, J.S., Koenig, A., Wei, D., Tan, Q., and Wang, Z., 2018, Are There Carlin-Type Gold Deposits in China ? A Comparison of the Guizhou , China , Deposits with Nevada , USA , Deposits: Reviews in Economic Geology, v. 20, p. 187–233

# Reconnaissance mineral and cathodoluminescence studies of gold occurrences in the Pogo-Black Mountain area, eastern interior Alaska, USA

**Garth E. Graham[1], Erin E. Marsh[1], Heather A. Lowers[1], Ryan D. Taylor[1]**
*[1]U.S. Geological Survey, Geology, Geophysics and Geochemistry Science Center, Denver, CO*

**Abstract.** The Pogo Au deposit is the largest of a number of gold occurrences in eastern interior Alaska, that occur along a broad trend from west of Pogo to Black Mountain. Some of these occurrences are hosted in amphibolite facies gneisses and others in middle Cretaceous igneous rocks that intruded the older metamorphic rocks. All occurrences contain arsenopyrite and pyrite. Whole rock geochemical trends distinguish most metamorphic rock-hosted vein prospects (strong Bi-Te-Au correlations) and intrusion-hosted occurrences (weak As-Au correlations). Brecciated quartz veins in metamorphic rocks have paragentically late Bi-Te (±S) + Au that post-dates Fe-As sulphide deposition. High grade vein samples from the Tibbs Creek intrusion-hosted deposits contain pyrite and arsenopyrite, generally lack Bi-Te minerals, but can contain paragentically younger euhedral quartz, stibnite and carbonate. Cathodoluminescence (CL) studies of gold-rich samples indicate that quartz dissolution occurred during the syn- to post-tectonic Bi-Te-Au deposition, and the later stibnite event. In the case of metamorphic rock-hosted deposits (e.g., Pogo, Gray Lead), Bi-Te and gold deposition commonly occurs in microfractures within quartz veins; the limited quartz in these fractures have distinctive CL response. We propose that gold deposition is related to changes in pressure-temperature (P-T) conditions rather than fluid-rock chemical reactions. Similar quartz dissolution textures affect the void-filling euhedral quartz before or during stibnite and carbonate mineralization in high-grade Au samples from Blue Lead.

## 1 Introduction

Pogo is a significant quartz-vein-hosted Au mine (e.g., Rombach et al., 2002) operating in the Big Delta quadrangle, eastern interior Alaska. Historic and ongoing regional exploration programs have identified many additional gold prospects over the past several decades (Fig. 1). These include occurrences 40 km east in the vicinity of Black Mountain (Fig. 1; U.S. Geological Survey (USGS), 2018). Some prospects are hosted within gneiss and schist of the Lake George sequence and others are hosted in middle Cretaceous igneous rocks that intrude the metamorphic sequence (Foster et al., 1994; Teck Resources Inc., 1998; Dusel-Bacon et al., 2017). The two prevailing models for the genesis of Pogo and other deposits based on the presence of proximal Cretaceous intrusions: 1) magmatic-hydrothermal (e.g., Thompson and Newberry, 2000; Thompson, 2020), and 2) metamorphic fluid (orogenic) deposit (Goldfarb et al., 2007).

We present a reconnaissance-scale summary of geochemical signatures of mineralized rock from these deposits and quartz- and ore-mineral textural data on select high grade Au samples from certain occurrences. The observations provide relative timing of mineralization stages among the mineral occurrences. Kreiner et al. (this volume) provides complimentary details on the geochronology of igneous units and ore and gangue minerals.

## 2 Deposit and prospect characterisations

General descriptions of mineral occurrences discussed in the study area (Fig. 1) are provided in U.S. Geological Survey (2018) and Rimfire Minerals (2008). Examples of metamorphic rock-hosted occurrences examined in this study are from Pogo, Hill 4021 (Pogo property deposit), Gray Lead, and Boundary. Intrusion-hosted deposits include West Pogo, and Blue Lead/Michigan and other prospects north of Gray Lead on Black Mountain. Most of the sampling conducted in our study was in surface dumps and trenches, and samples from the Pogo mine were collected from faces and drill core was examined Black Mountain area deposits (Fig. 1).

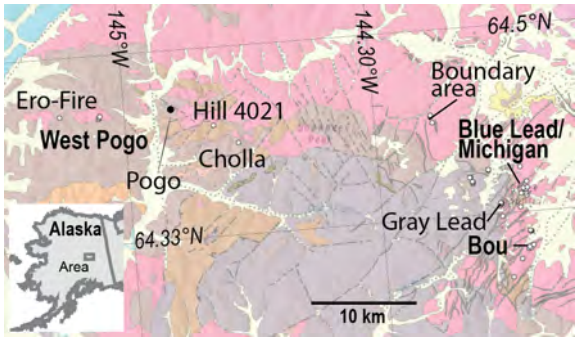


**Figure 1.** Location map of selected Au occurrences. Intrusion-hosted sites are bolded. Blue Lead, Gray Lead, and Bou occur along Black Mt. Pink=igneous rocks, yellows=cover, grays and browns=metamorphic rocks (Wilson et al., 2015).

Metamorphic rock-hosted quartz veins cut across foliation of amphibolite facies Lake George orthogneiss and paragneiss. At Pogo, where veins are up to 20 meters thick, alteration assemblages include early biotite and later sericite-dolomite. A surface exposure of an auriferous quartz vein at Gray Lead is approximately ~ 0.7-m true thickness with minor bleaching of wall rock. Veins in intrusive rocks can be meter-scale but are often narrower, typically sheeted to cross-cutting cm-scale-thickness vein sets in typically bleached/ sericitized granitoids (e.g., Blue Lead/Michigan.)

### 2.1 Whole Rock Geochemistry

Geochemical datasets (Graham et al., 2021; Rimfire Minerals, 2008) permit broad comparison of elemental ratios among different mineral occurrences. The Au:Bi ratios are highly correlative in Pogo, Gray Lead, and Boundary sites, where Bi and Au can exceed 1000 ppm and 100 ppm, respectively (Fig. 2a). Other metamorphic rock-hosted quartz vein occurrences proximal to Boundary contain high Bi (100s to ~3500 ppm), but relatively low <~1ppm Au. In contrast, Au:Bi does not correlate in most intrusion-hosted vein samples north of Gray Lead (Graham et al., 2021; tiny dots, Fig. 2a). These occurrences are generally Bi-poor despite gold concentrations locally exceeding ~20 ppm. Notable exceptions are the Blue Lead intrusion-hosted prospect and a four sample subset from West Pogo (Fig. 2a,b). The Te:Bi ratios have $r^2$ values of >0.86 for the Pogo, Grey Lead, and Boundary sites. Occurrences proximal to Boundary lack detectable Te (Fig. 2b). The intrusion hosted Blue Lead occurrence has a comparable Te:Bi correlation but with lower average Te and Bi concentrations then the suite of metamorphic hosted occurrences. A four sample subset collected at West Pogo also shows a distinct Te:Bi correlation.

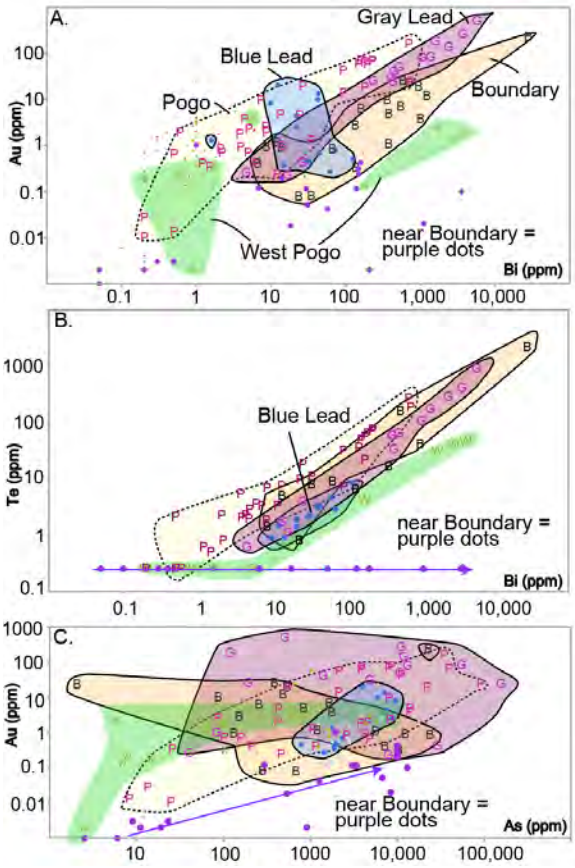


**Figure 2.** Grab sample whole rock geochemistry. (A) Bi vs Au, (B) Bi vs Te, and (C) As vs Au. Occurrences discussed in text are labelled. Data include Graham et al., 2021 and Rimfire Resources (2008).

Despite ubiquitous arsenopyrite(±loellingite) in all occurrences (see section 3.2), the Au:As correlation is relatively poor among occurrences. There is a qualitatively weak trend in our Pogo data as well as the near Boundary samples (Fig. 2c). Neither Gray Lead nor Boundary display a significant correlation. The Blue Lead intrusion-hosted system displays a somewhat tighter correlation, but with relatively more limited Au and As grades. There are some weak potential trends between Au:Sb, particularly for West Pogo, Blue Lead, and prospects near Boundary (Graham et al., 2021; not shown).

## 3 Vein textures

Mineralized vein samples from several different occurrences were examined initially using optical microscopy. Reconnaissance studies were then focused to samples that contain visible gold in thin sections. Samples from Pogo and Hill 4021 (Pogo project area), Gray Lead and Blue Lead/Michigan, and Boundary occurrences were included (Fig. 1).

Mineralized quartz veins from these occurrences typically demonstrate multi-stage development. There are one or more quartz generations and common evidence of brecciation, recrystallization, and dissolution. Sulphide and ore minerals are dominantly interpreted to be paragenetically late relative to one or more stages of quartz deposition.

### 3.1 Quartz and gangue mineral textures

Most of the quartz appears to be the earliest paragenetic stage. It is relatively coarse grained, with numerous secondary fluid inclusion trails/microfractures (Fig. 3a), and areas recrystallized to finer-grained mosaic quartz (not shown). Irregular boundaries are invariably present between quartz grains. White mica, chlorite, and Ti-oxides are present within the veins and are likely remnants of now-altered wall rock inclusions. Carbonate occurs as mm-scale through-going veins or spotty patches along some fractures in the Pogo samples. Samples from the Blue Lead and Michigan areas (Fig. 1) contain distinct late inward-terminating coarse quartz crystals overgrowing brecciated and recrystallized quartz. This texture suggests reopening of pre-existing veins. Carbonates can fill the remaining open space.

### 3.2 Sulphide/Bi±Te-Au mineralogy and textures

Petrographic and qualitative scanning electron microscopy (SEM) observations of the selected samples indicate similar, if incomplete parageneses among the different occurrences. Most deposits contain trace amounts of jamesonite, boulangerite, and/or other sulfosalts. Sulphide/ore mineral paragenesis in our sample suite broadly includes one or multiple stages of pyrite and arsenopyrite ± minor Au à Bi-Te-Au in most metamorphic-rock hosted occurrences. In a few of the intrusion hosted samples, minor As-Bi-Te-Au mineralization is

associated with brecciated quartz, whereas stibnite fills voids associated with the paragentically younger euhedral quartz.

Pyrite and arsenopyrite can occur as 10's of microns-scale euhedral crystals and aggregates as well as have highly milled textures, sometimes as mm's-scale masses and bands with broken edges and extensive fracturing, particularly in Pogo property (Pogo proper and Hill 4021) and Gray Lead samples. Gold has been observed within pyrite (but not our reconnaissance samples), and minor visible-Au is seen within arsenopyrite; Both sulphides can also locally be overgrown by Au or contain Au in cross-cutting fractures.

The vast majority of visible Au (electrum) in metamorphic rock-hosted occurrences is associated with influx of Bi/Bi-Te (±S) minerals. These minerals occur as complex 1-50+ µm intergrowths in late microfractures. When present with pyrite and arsenopyrite the Bi-Te-Au assemblages typically drape the sulphides. The late fractures can contain carbonate minerals.

In our selected high Au-grade samples from intrusion-hosted occurrences, arsenopyrite-pyrite bearing quartz vein generations are paragenetically early and associated with the older quartz described above. Bi-Te minerals are very rare. Late-stage massive stibnite and carbonate that fill the remaining space in these veins have irregular boundaries that cross-cut growth zones observed in CL in euhedral quartz, suggesting quartz dissolution in the vuggy space prior to or during stibnite deposition (not shown). Only one micron-scale gold grain was observed in massive stibnite. Euhedral quartz or massive stibnite were not observed in our metamorphic rock-hosted samples.

### 3.3 Vein Cathodoluminescence (CL) and Preliminary Raman Fluid Inclusion Analysis

CL imaging using a JEOL 8530F Plus at the USGS microbeam laboratory in Denver, Colorado, is a powerful tool for imaging quartz textures associated with sulphide and visible gold that were not obvious using standard optical microscopy (Fig. 3).

The CL spectral results demonstrate key aspects of the paragenesis among vein samples. First, at the ~2.8 eV position (broadly equivalent to the position of Ti in quartz), ghosts of original quartz, sometimes with preserved distinct growth/sector zoning are visible in what is now a series of mosaic quartz grains (Fig. 3a,c,d). Second, a later, spectrally distinct, lower intensity at the 2.8 eV position signature defines "microveinlets" – these correspond to zones of obvious and cryptic fractures in optical microscope images.

The imaging reveals important empirical relationships in the paragenesis of the occurrences. The images highlight: 1) the deformation and recrystallization of the original quartz; 2) sulphides (e.g., arsenopyrite in Fig. 3) cut across apparent growth zoning the now deformed quartz; 3) Bi-Te and Au minerals and lesser pyrite-arsenopyrite are almost ubiquitously in direct contact with the lower intensity quartz microveinlets. In the examples from the intrusion-hosted occurrences, the youngest euhedral quartz is partially dissolved, and space replaced by massive stibnite (not shown).

Preliminary Raman examination of the vapor phases in 2-phase liquid-gas fluid inclusion assemblages associated with low spectral-response quartz zones and sulphides (Fig. 3c,d) contain unquantified but distinct methane and $CO_2$ peaks.

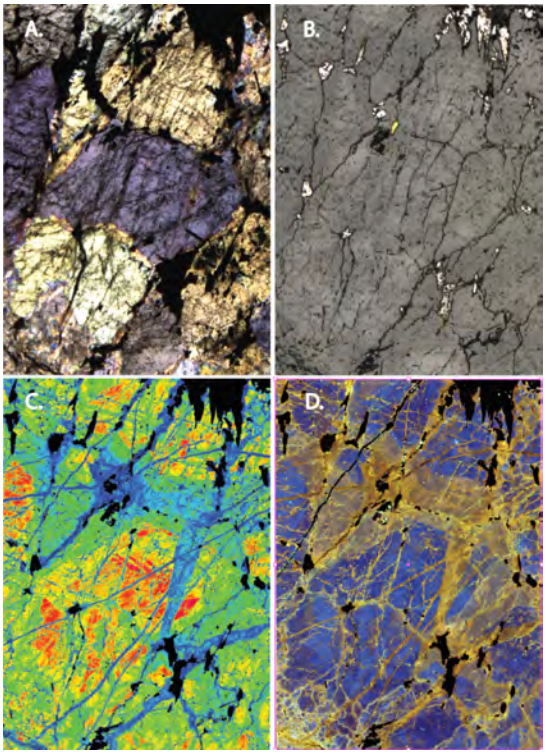


**Figure 3.** Arsenopyrite (upper right in images) and Bi-Te minerals and gold in quartz vein from Gray Lead. A. cross polarized image, B. reflected light, C. ~2.8 eV peak intensity, and D. false color RGB overlay. Image width = 2 mm.

## 4 Discussion

Gold mineralization involved at least two overlapping geochemical signatures. Low-grade gold was introduced, both as minor Au inclusions and possibly as enrichments within arsenopyrite, pyrite, and sulfosalts. The Bi-Te-Au assemblages, which produce significant free gold affected nearly wholly metamorphic rock-hosted quartz veins. This in part enhances the apparent grades of these occurrences. Interestingly, despite high Bi values in vein samples from prospects near Boundary (purple dots; Fig. 2) they lack high Au or Te grades, highlighting the relationship between Au and Te.

The cause of the chemical differences between prospects, and localized overprint of stibnite in some intrusion hosted occurrences is uncertain. Host rock composition (meta-sediment vs Cretaceous

intrusion), differential depths of emplacement/zoning and/or different fluid events (e.g. stibnite-rich zones observed in igneous-hosted Black Mountain occurrence) are some viable options.

The CL imaging provides important insights as to quartz-sulphide relationships that are not fully apparent using optical microscopy. Fe-As sulphide deposition (observed across prospects) appears to be syn- to post-deformation of original quartz veins. The CL imaging (Fig. 3) further shows that sulphide grains cross-cut growth zones in quartz and that Bi-Te-Au±sulphide minerals occur in "microveinlets" that do not always appear as distinct visible manifestations in the quartz they cut when examined by optical microscopy. These textures demonstrate that quartz was either soluble (case 1) or at least not being deposited in volume (case 2) during these mineralizing events. The "microveinlets" may represent alteration of quartz chemistry along the edges of micro-scale fractures.

The absence of quartz deposition during the main mineralizing events (and localized carbonate precipitation) may be related to $CO_2$-rich nature of the ore-forming fluids observed in preliminary Raman analyses. These fluids are likely equivalent to similarly described low salinity methane-$CO_2$-rich fluids, inferred to be syn-Au ore (Baker et al., 2006; Rombach et al. 2002). Modelling by Li et al. (2020) demonstrates that $CO_2$-rich fluids can cause retrograde quartz solubility we observe under reasonable conditions due to isobaric cooling or isothermal decompression; these types of fluids have been observed in fault-valve related orogenic gold deposits. The predominance of sulphides, and particularly Au-bearing assemblages in quartz veins, some in apparent isolation from wall-rock slivers (and suggestions of decreased Ti contents in fractures/ late quartz implied in CL) supports changes in pressure-temperature (P-T) conditions as a controlling factor. Similar chemistry across a broad area (Pogo property prospects to Gray Lead) suggests a reduced (metamorphic(?)) ore fluid, at least for the Au and Au-Bi-Te stages of mineralization in the metamorphic rock-hosted systems. Further study could help to enhance our understanding of the relationships between the metamorphic hosted occurrences and the intrusion-hosted deposits overprinted by the Sb-dominant event.

## 5 Conclusions

The Pogo-Black Mountain study area contains both metamorphic rock- and intrusion-hosted gold-rich deposits/occurrences. There may have been a relatively widespread Fe-As (Sb-Pb) mineralizing event. Bi-Te-Au deposition impacted predominantly metamorphic-rock-hosted prospects, whereas a late Sb± minor gold event affected the intrusion-hosted deposits on Black Mountain. The high-grade Bi-Te-Au event(s) (and Sb at Blue Lead/Michigan) identified in our limited sample set appear decoupled from quartz deposition. Relationships through space and time between metamorphic rock and igneous-hosted deposits could be refined with further research.

## Acknowledgements

This work was funded as part of the U.S. Geological Survey Mineral Resource Program initiatives. Doug Kreiner and George Case provided thoughtful reviews. Any use of trade, firm, or product names is for descriptive purposes only and does not imply endorsement by the U.S. government.

## References

Baker T, Ebert S, Rombach C, Ryan CG (2006) Chemical compositions of fluid inclusions in intrusion-related gold systems, Alaska and Yukon, using PIXE microanalysis. *Econ Geol 101*(2), 311-327.

Dusel-Bacon C, Holm-Denoma C, Jones III J, Aleinikoff J, Mortensen J. (2017) Detrital zircon geochronology and provenances of quartzose metasedimentary rock sfrom paraytochthonous north America, East-Central Alaska. Lithosphere, v.9 p.927-952.

Foster HL, Keith TE, and Menzie WD (1994) Geology of the Yukon-Tanana terrane of east-central Alaska. in The Geology of Alaska. edited Plafker G and Berg HC. Geol. Soc. Amer. Boulder CO, The Geology of North America, G-1:205-240

Goldfarb RJ, Marsh EE., Hart, CJR., Mair JL, Miller ML, and Johnson C. (2007) Geology and origin of epigenetic lode gold deposits, Tintina Gold Province, Alaska and Yukon: Chapter A in Recent U.S. Geological Survey studies in the Tintina Gold Province, Alaska, United States, and Yukon, Canada—results of a 5 year project. U.S Geological Survey Scientific Investigations Report 2007-5289, pA1-A18.

Graham GE, Peterson ML, Marsh EE, and Taylor RD (2021) Whole rock geochemical data from the eastern part of the Yukon-Tanana Upland region, Alaska, USA: U.S. Geological Survey data release, https://doi.org/10.5066/P95OKTU7.

Li XH, Klyukin YI, Steele-MacInnis, M, Fan, HR, Yang KF, Zoheir B, (2020) Phase equilibria, thermodynamic properties, and solubility of quartz in saline-aqueous-carbonic fluids: Application to orogenic and intrusion-related gold deposits: Geochim et Comochim. Acta, v. 283, p. 201-221.

Rimfire Minerals (2008) 2008 Technical Report on the Goodpaster district properties, Rimfire internal report. Last accessed on sedar: Feb 26, 2022.

Rombach, C.S., Newberry, R.J., Goldfarb, R.J., and Smith, M, (2002) Geochronology and mineralization of the Liese zones, Pogo deposit, Alaska [abs.]: Geol Soc of America Abstracts with Programs, v. 34, no. 6, p. 114.

Teck Resources Inc. (1998) Pogo project advanced exploration program, Stage II application and plan of operations: Teck Resources Inc. report, 75 p.

Thompson W (2020) Geochemical, spatial, and temporal relationships of the intrusives and meta-intrusives of the Pogo deposit, eastern interior Alaska. MS Thesis, University of Alaska, Fairbanks. 146p.

Thompson JFH, Newberry RJ (2000) Gold deposits related to reduced granitic intrusions. In: Hagemann SG, Brown PE (eds) Gold in 2000: Rev Econ Geol 13:377–400.

U.S. Geological Survey (2018) Alaska Resource Data File (ARDF): U.S. Geological Survey, http://ardf.wr.usgs.gov.

Wilson, FH, Hults CP, Mull CG, and Karl SM (2015) Geologic map of Alaska: U.S. Geological Survey Scientific Investigations Map 3340. compilers 2 sheets, scale. 10.3133/sim3340, 1:1,584,000, 196 p. pamphlet

# Precipitation of gold by wallrock sulfidation in the Val-d'Or Vein Field, Abitibi Subprovince (Québec, Canada)

**Michael Herzog[1], Crystal LaFlamme[1,2], Georges Beaudoin[1], Guillaume Barré[1], Laure Martin[2], Dany Savard[3]**
*[1]Département de géologie et de génie géologique, Université Laval, Québec, Canada*
*[2]Centre for Microscopy, Characterisation & Analysis, University of Western Australia, Western Australia, Australia*
*[3]Laboratoire des Matériaux Terrestres, Université du Québec à Chicoutimi, Québec, Canada*

**Abstract.** Orogenic gold deposits hosted in meta-sedimentary basins are known to precipitate gold through coupled Au-As redox reactions, resulting in As-rich pyrite (As>>1 wt%) containing native Au inclusions and lattice-bound Au. Gold precipitation mechanisms in gold districts not hosted in meta-sedimentary wallrocks remain poorly understood. Five quartz-tourmaline-carbonate vein orebodies (Goldex, Triangle, Plug #4, Pascalis Gold Trend, Beaufor) of the Val-d'Or Vein Field, hosted in a greenstone belt sequence, contain gold in vein- and wallrock-hosted pyrite-rich (>95 vol%) sulfide aggregates, displaying a porous core (Py1; 0<Au<<30 ppm) and homogeneous rim (Py2; Au<1250 ppm). Py2 hosts bulk of the native Au or polymetallic (Au-Ag-Te-Bi) inclusions, primarily calaverite. An ubiquitous isotopic shift in $\delta^{34}S$ values (+3.0‰) from Py1 to Py2 in the orebodies suggests that fluid desulfidation-wallrock sulfidation controls gold precipitation. This mechanism leads to a decrease in fluid $fS_2$ by removal of $Au(HS)^-$ under reducing $fO_2$ conditions, supported by a corresponding decrease and consistently low contents in Co and Ni from Py1 (4500 ppm and 635 ppm) to Py2 (<550 ppm and <2200 ppm). Here, we show that a coupled decrease in fluid $fS_2$, $fO_2$, and $fTe_2$, induced by wallrock sulfidation, can lead to efficient gold deposition as inclusions in As-poor (<0.1 wt%) pyrite.

## 1 Introduction

Changes in fluid chemistry that result in the formation of orogenic gold deposits (OGD) depend on several physico-chemical parameters including temperature, pressure, as well as the fluid sulfur ($fS2$) and oxygen ($fO2$) fugacities. Both can have significant destabilizing impacts on reduced $HS^-$ complexes, the most important Au-transporting ligands in OGD. Particularly, a decrease in fluid $fS2$ (i.e., removal of H2S) and/or increase in fluid $fO2$ (i.e., removal of H2), represent leading causes for gold precipitation (Palin and Xu 2000; Sugiono et al. 2022). Auriferous fluid chemistry may be traced using the $\delta^{34}S$ signature, as well as Au, Ag, As, Te, Co and Ni composition of precipitating sulfides, as these parameters are sensitive to $fS2$ and $fO2$. For instance, in As-rich sedimentary wallrocks, the As-content in pyrite can limit the incorporation of lattice-bound Au or coupled Au-As redox reactions can effectively form lattice-bound gold in OGD (Reich et al. 2005; Pokrovski et al. 2021). Moreover, Bi-rich fluids may scavenge gold through Bi-Te adsorption mechanisms on sulfide growth surfaces (Tooth et al. 2011).

However, in many As-poor, greenstone belt-hosted orogenic gold districts these fluid processes remain poorly understood at the sulfide mineral grain scale. Recent advances in in-situ microanalytical techniques, combined with detailed textural observations and a sulfide paragenesis, have the potential to elucidate these physico-chemical processes and, thereby, identify a gold precipitation mechanism. Here, we explore whether common physical fluid mechanisms (i.e., fluid immiscibility, fluid mixing, fluid-rock reactions) can control gold solubility in several orebodies (Goldex, Triangle, Plug #4, Pascalis Gold Trend, Beaufor) of an important gold district located in the Neoarchean, southern Abitibi subprovince, the Val-d'Or Vein Field (VVF).

## 2 Geological setting

The Neoarchean Abitibi and Pontiac subprovinces form the southeastern margin of the Superior Craton (Figure 1A) are juxtaposed by the sub-vertical, E-W trending Larder-Lake-Cadillac fault zone (LLCfz). Both subprovinces were affected by a major N-S shortening period (D2) during the Abitibi-Wawa orogenic cycle, between ca. 2669-2643 Ma, forming the transcrustal LLCfz and a penetrative E-W trending S2 foliation (Bedeaux et al. 2017).

The VVF, located in the southern Abitibi subprovince, contains ca. 54.7 Moz of orogenic gold mineralization (Figure 1B). It formed between ca. 2710-2685 Ma, comprising ultramafic, mafic and felsic submarine volcano-sedimentary rocks. These were intruded by contemporaneous tonalitic, granodioritic, dioritic and monzonitic sills that contain Fe-oxides, typically ilmenite, titanomagnetite and magnetite (Pilote et al. 2000) and all rocks were metamorphosed to sub- and upper greenschist-facies (Powell et al. 1995).

### 2.1 Orogenic gold mineralization

Metamorphosed intrusive and volcanic rocks contain the bulk of the VVF orogenic gold mineralization in brittle-ductile, fault-fill, shear and associated extensional veins, formed during D2 shortening at ca. 2643 Ma, sub-parallel to S2 with a dominant dip to the south (Robert and Brown 1986; Herzog et al. 2022). These veins consist of quartz-tourmaline-carbonate (QTC) and can display m-wide, strongly chloritized quartz-tourmaline-albite-muscovite-pyrite alteration halos. Pyrite-rich, vein- and wallrock- hosted sulfide assemblages contain gold either as native Au or polymetallic (Au-Ag-Te-Bi) inclusions in pyrite, together with minor base metal inclusions (Robert and Brown 1986).

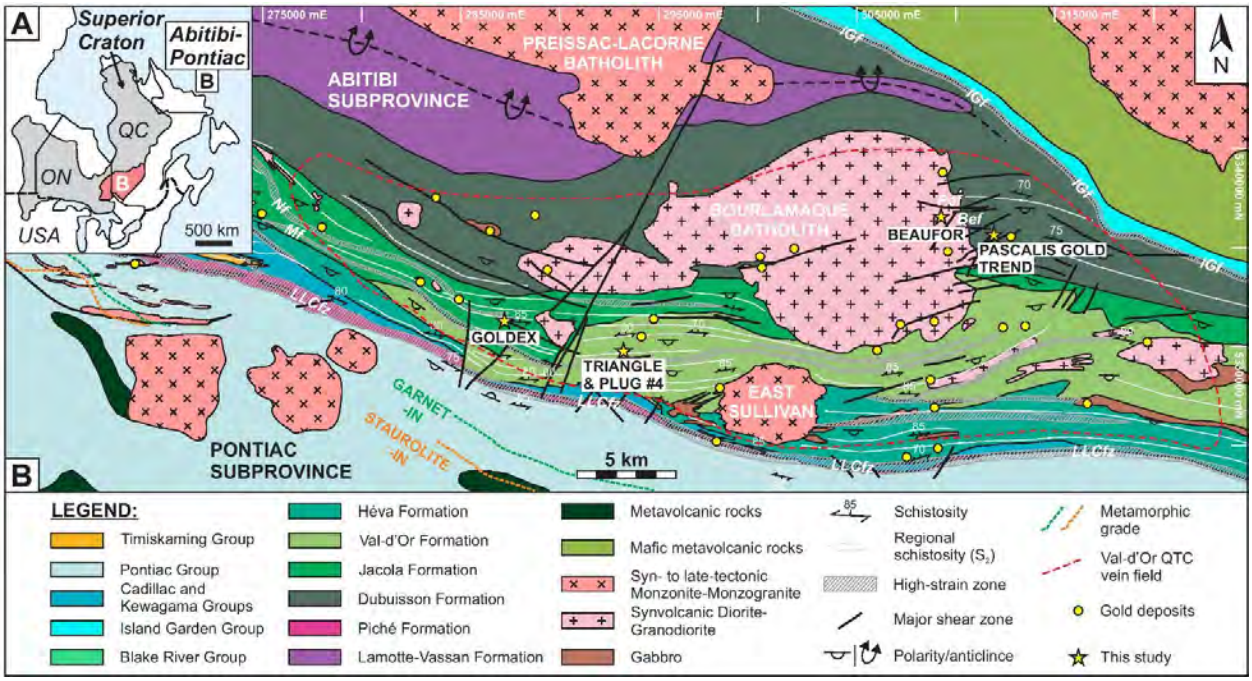


**Figure 1A.** Schematic map of the Superior Craton showing the Abitibi and Pontiac subprovinces. **1B**. Geological map of the VVF outlining the location of the studied orebodies (modified from Pilote et al. 2000).

## 3 Methodology

Drill cores from five QTC vein orebodies (Goldex, Triangle, Plug #4, Beaufor, Pascalis Gold Trend), described in detail in Herzog et al. (2022), were investigated. For this study, key cross-cutting relationships between sulfide minerals, texture and paragenesis were determined in thin sections for each orebody.

Based on the paragenesis, 26 representative samples were prepared in five epoxy mounts, containing three to four 6 mm cylindrical rock cores that were drilled out of samples. The mounted samples were characterised for their texture in detail by reflected light microscopy, as well as for their major element composition, internal heterogeneity and zonation by energy dispersive spectroscopy and backscattered electron imaging using a FEI 50 scanning electron microscope. Fe was analysed on a CAMECA SX-100 electron probe micro-analyser.

### 3.1 Multiple sulfur isotopes

In-situ multiple sulfur isotopes ($\delta^{34}S$, $\Delta^{33}S$) were determined (CAMECA IMS1280 SIMS at UWA) in pyrite (n=91), which contained standard blocks of matrix-matched Sierra pyrite reference material (LaFlamme et al. 2016). Spot analyses used a focused, 10 µm, Gaussian $Cs^+$ beam at 20 kV and 2.3 nA and measurements of $^{32}S$, $^{33}S$ and $^{34}S$ followed the protocol outlined in LaFlamme et al. (2016), including absolute propagated $\delta^{34}S$ and $\Delta^{33}S$ error calculations. Matrix-matched reference material was interspersed with unknown sample material measurements and the Sierra pyrite was used to monitor standard repeatability, analytical drift and to correct for instrumental mass fractionation. Secondary pyrite standards 248474 (Isua) and Balmat, located in a separate mount, were used to monitor the accuracy of sulfur isotope data measurements. Calibrated against Sierra, they returned $\delta^{34}S$ and $\Delta^{33}S$ values +2.4±0.6‰, +2.9±0.4‰ (n=10, 2SD), respectively, and +16.1±0.2‰, +0.03±0.05‰ (n=10, 2SD) for $\delta^{33}S$.

### 3.2 Sulfide trace element compositions

Thirty-four analytes were measured in pyrite in five, uncoated, epoxy mounts comprising 69 spot and line analyses, using a RESOlution 193 nm ArF Excimer laser system coupled to an Agilent 7900 ICPMS, as well as five quantitative maps on the same laser system coupled to a Tofwerk time of flight-ICPMS at UQAC. Spots, lines and maps were analysed at various conditions (beam sizes 7-55 µm, pulse rates 15-120 Hz, scan speeds 10-210 µm/s and fluences of 3-6 J/cm$^2$), including the following external reference materials: Laflamme, MASS1 and GSE, which were used, with Fe EPMA data as an internal standard, for raw data normalization in Iolite v.4. Averaged values (ppm) for each sulfide domain are reported. UQAC-FeS1, FeS5, MSS5 and GSE reference materials were used to monitor individual laser sessions.

## 4 Results

### 4.1 Major sulfide textures and paragenesis

Laminated, m-wide QTC veins of the Goldex, Triangle, Plug #4, Pascalis Gold Trend and Beaufor orebodies are contained within reverse shear zone in chloritized wallrocks, particularly in gabbroic to dioritic intrusions (Figure 2A). These veins host

the bulk of the gold in pyrite-rich (>95 vol%) sulfideassemblages that frequently form cm- to dm-sized vein- and wallrock-hosted sulfide aggregates (Figure 2B). These sub- to euhedral pyrite aggregates display a porous core (Py1) consisting of abundant carbonate and tourmaline inclusions up to several 10s of µm, as well as minor sulfide inclusions including chalcopyrite, sphalerite and galena (Figure2C). Homogeneous pyrite rims (Py2) surround the porous Py1 core and host nm- to µm sized native Au and polymetallic Au-Ag-Te-Bi inclusions, which are primarily calaverite. Minor petztite and metallic BiTeare frequently associated with calaverite and chalcopyrite inclusions (Figure 2D). Texturally late Py2 rims have also been recognized to be associated with the deposition of pyrrhotite (Robert and Brown 1986).

**Figure 2A and 2B.** Field photographs of QTC orogenic gold mineralization hosted in pyrite-rich aggregates acrossthe VVF. **2C and 2D.** Porous Py1 core domain in

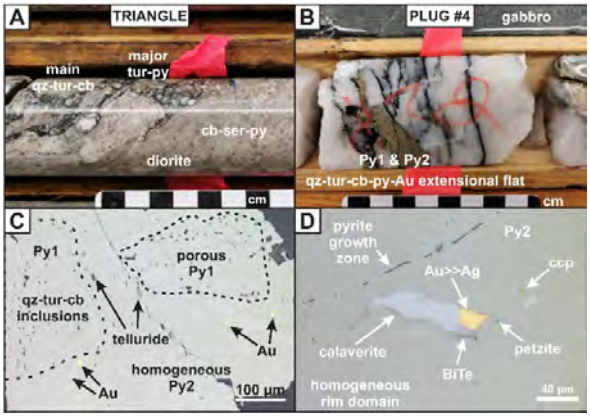


pyrite with a homogeneous Py2 rim overgrowth, which contains bulk of the native Au and polymetallic (Au-Ag-Te-Bi) inclusions. Cb=carbonate, py=pyrite, qz=quartz, ser=sericite, tur=tourmaline.

### 4.2 Multiple sulfur isotopes

In-situ sulfur isotope analyses of pyrite hosted in the five QTC vein sets define a wide range in $\delta^{34}S$ (from -0.4‰ to +6.3‰), with the lowest and highest values recorded in Py1 and Py2 of the Goldex and Beaufor orebodies, respectively. In all five orebodies, the two pyrite domains display a consistent isotopic shift in $\delta^{34}S$ of up to +3.0‰ (Figure 3), from a slightly lower Py1 domain (n=32) towards a $^{34}S$ enriched homogeneous Py2 rim (n=59). All orebodies show a small negative $\Delta^{33}S$ from the mass-dependent fractionation field for sulfur for Py1 and Py2 (from - 0.20‰ to +0.01‰).

### 4.3 Pyrite trace elements

Elemental analyses of Py1 core domains and gold-rich Py2 rims reveal that besides Ag-Te-Bi, commonly associated with gold, only five (Co, Ni, As, Se, Sb) of the 34 elements measured occur at measurable concentrations, while all other analyzed elements are below detection limit. The Py1 cores are enriched in localized Co (4500 ppm) and Ni (635ppm) in the Pascalis Gold Trend and Goldex orebodies, respectively, and yield comparably low As(<67 ppm) and Au (0<<30 ppm) concentrations. The homogeneous Py2 rims of all five orebodies yield low, minor and trace concentrations and displayelevated Au (<1250 ppm) contained in weakly oscillatory-zoned Py2 with Co (<2200 ppm), Ni (<550 ppm) and As (<550 ppm). Native Au and polymetallic inclusions in Py2 are unrelated to the oscillatory-zoned pyrite areas in the five orebodies.

**Figure 3.** Multiple S isotope data from Py1 and Py2 hostedin

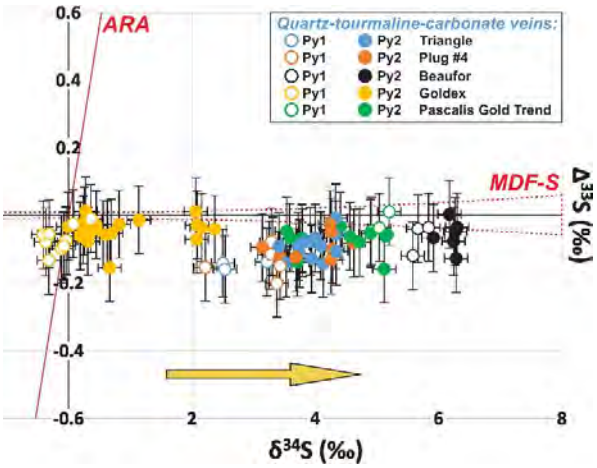


the five QTC vein sets. The golden arrow indicates the observed sulfur isotope evolution of up to +3.0‰ from Py1to Py2. ARA=Archean Reference Array of $\Delta^{33}S \approx 0.89*\delta^{34}S$ from Ono et al. (2009), MDF-S = mass-dependent fractionation field for sulfur from LaFlamme et al. (2018).

## 5 Conclusions

The recognition of texturally late pyrrhotiteassociated with QTC vein formation in the VVF implies that the pyrite-rich assemblages deposited native gold in homogeneous Py2 rims under more reducing *f*O2 conditions within the pyrite stabilityfield. A decrease in *f*O2 is also supported by lower Ni and Co concentrations in Py2, both known to have alower solubility at lower *f*O2, compared to the locally enriched Py1 core (Jansson and Liu 2020). The lack of hematite-bearing assemblages in alteration halos also supports a more reducing environment. The consistent isotopic shift in $\delta^{34}S$ values (+3.0‰) observed from Py1 core to Py2 rims in the five orebodies suggests fluid desulfidation (Figure 4A), through the removal of $Au(HS)^-$ complexes, thereby causing a decrease in fluid *f*S2, is the main driver of gold deposition in these orebodies. The consistent, negative $\Delta^{33}S$ values excludes sulfur mixing as a precipitation mechanism. Particularly, the replacement of ilmenite, titanomagnetite and magnetite by pyrite in intrusive wallrocks contributes to efficient gold mineralization. At 300°C, typical for OGD formation (Goldfarb and Groves 2015), these decreases in fluid *f*O2 and *f*S2, induced by pervasive fluid desulfidation-wallrock sulfidation, are also associated with a decrease in fluid *f*Te2 (Figure 4B), resulting in the formation of calaverite related with

Ag-Te-Bi assemblages hosted as inclusions in Py2. Our findings show that in As-poor (<0.1 wt%) pyrite in meta-volcanic orogenic gold districts a coupled decrease in fluid *f*O2, *f*S2 and *f*Te2, as a result of wallrock sulfidation presents a key mechanism leading to efficient OGD formation.

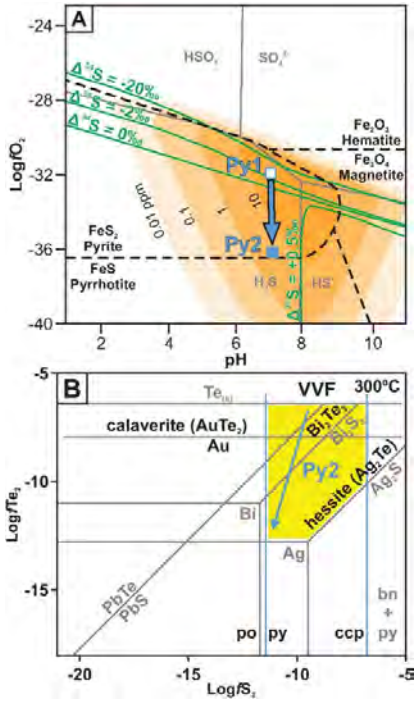


**Figure 4A.** A pH vs. log$fO_2$ diagram showing changes in $\delta^{34}S$ values related to gold solubility. Modified from Ohmoto (1972) and Hodkiewicz et al. (2009). **4B.** Log$fTe_2$-Log$fS_2$ diagram showing relationship between a decreasein fluid $fTe_2$ and $fS_2$ activities and telluride formation during Py2 growth in the VVF. Modified from Afifi et al. (1988).


## Acknowledgements

The authors appreciate financial support by the Canada First Research Excellence Fund Metal Earth project. M.H. thanks for support at Agnico Eagle Mines Ltd. by R. Morel, J.A. Marcotte, D. Yergeau, at Eldorado Gold Corp. by J. Thelland, É. Gagnon, M. Le Bacq, B. Gagnon and at Probe Metals Inc. by M. Gagnon, B. Beh.


## References


Afifi AM, Kelly WC, Essene EJ (1988) Phase relations among tellurides, sulfides, and oxides: I. Applications to telluride-bearing ore deposits. Econ Geol 83:395-404. https://doi.org/10.2113/gsecongeo.83.2.395

Bedeaux P, Pilote P, Daigneault R, Rafini S (2017) Synthesisof the structural evolution and associated gold mineralization of the Cadillac fault, Abitibi, Canada. Ore Geol Rev 82:49-69. https://doi.org/10.1016/j.oregeorev.2016.11.029

Goldfarb RJ, Groves DI (2015) Orogenic gold: Common or evolving fluid and metal sources through time. Lithos 233:2-26. https://doi.org/10.1016/j.lithos.2015.07.011

Herzog M, LaFlamme C, Beaudoin G, Marsh J, Guilmette C (2022) U-Pb vein xenotime geochronology constraints ontiming and longevity of orogenic gold mineralization in theMalartic-Val-d'Or Camp, Abitibi Subprovince, Canada. Miner Deposita 7:1-29. https://doi.org/10.1007/s00126- 022-01131-1

Hodkiewicz PF, Groves DI, Davidson GJ, Weinberg RF, Hagemann SG (2009) Influence of structural setting on sulphur isotopes in Archean orogenic gold deposits, eastern Goldfields Province, Yilgarn, Western Australia. Miner Deposita 44:129-150. https://doi.org/10.1007/s00126-008-0211-5

Jansson NF, Liu W (2020) Controls on cobalt and nickel distribution in hydrothermal sulphide deposits in Bergslagen, Sweden – constraints from solubility modelling. GFF 142.2:87-95. https://doi.org/10.1080/11035897.2020.1751270

LaFlamme C, Martin L, Jeon H, Reddy SM, Selvaraja V, Caruso S, Bui TH, Roberts MP, Voute F, Hagemann S, Wacey D, Littman S, Wing B, Fiorentint M, Kilburn MR (2016) In situ multiple sulfur isotope analysis by SIMS of pyrite, chalcopyrite, pyrrhotite, and pentlandite to refine magmatic ore genetic models. Chem Geol 444.9:1-15. https://doi.org/10.1016/j.chemgeo.2016.09.032

LaFlamme C, Jamieson JW, Fiorentini ML, Thébaud N, Caruso S, Selvaraja V (2018) Investigating sulfur pathways through the lithosphere by tracing mass independent fractionation of sulfur to the Lady Bountiful orogenic gold deposit, Yilgarn Craton. Gond Res 58:27- 38. https://doi.org/10.1016/j.gr.2018.02.005

Ohmoto H (1972) Systematics of sulfur and carbon isotopes in hydrothermal ore deposits. Econ Geol 67:551-578. https://doi.org/10.2113/gsecongeo.67.5.551

Ono S, Kaufman AJ, Farquhar J, Sumner DY, Beukes NJ (2009) Lithofacies control on multiple-sulfur isotope records and Neoarchean sulfur cycles. Precam Res 169:58-67. https://doi.org/10.1016/j.precamres.2008.10.013

Palin JM, Xu Y (2000) Gilt by Association? Origins of pyritic gold ores in the Victory mesothermal gold deposit, Western Australia. Econ Geol 95.8:1627-1634. https://doi.org/10.2113/gsecongeo.95.8.1627

Pilote P, Moorhead J, Mueller W (2000) Partie A.Développement d'un arc volcanique, La region de Vald'Or, ceinture de l'Abitibi: Volcanologie physique etévolution métallogénique.Québec Ministère des Ressources Naturelles, MB 2000-09, pp 20. https://gq.mines.gouv.qc.ca/documents/examine/MB200 009/MB200009.pdf

Pokrovski GS, Escoda C, Blanchard M, Tesyemale D, Hazemann J-L, Gouy S, Kokh MA, Boiron M-C, de Parseval F, Aigouy T, Menjot L, de Parseval P, Proux O, Rovezzi M, Béziat D, Salvi S, Kouzmanov K, Bartsch T, Pttgen R, Doert T (2021) An arsenic-driven pump for invisible gold in hydrothermal systems. Geochem Persp Let 17:39-44. https://doi.org/10.7185/geochemlet.2112

Powell WG, Carmichael DM, Hodgson CJ (1995) Conditions and timing of metamorphism in the southern Abitibi greenstone belt, Quebec. Can J Earth Sci 32:787-805. https://doi.org/10.1139/e95-067

Reich M, Kesler SE, Utsunomyia S, Palenik CS, Chryssoulis SL, Ewing RC (2005) Solubility of gold in arsenian pyrite.Geochim Cosmochim Acta 69.11:2781-2796. https://doi.org/10.1016/j.gca.2005.01.011

Robert F, Brown AC (1986) Archean Gold-Bearing Quartz Veins at the Sigma mine, Abitibi greenstone belt, Quebec: Part II. Vein Paragenesis and Hydrothermal Alteration. Econ Geol 81:593-616. http://dx.doi.org/10.2113/gsecongeo.81.3.593

Sugiono D, LaFlamme C, Thébeaud N, Martin L, Savard D, Fiorentini M (2022) Fault-induced gold saturation of a single auriferous fluid is a key process for orogenic gold deposit formation. Econ Geol 117.6:1405-1414. https://doi.org/10.5382/econgeo.4923

Tooth B, Ciobanu CL, Green L, O'Neill B, Brugger J (2011) Bi-melt formation and gold scavenging from hydrothermal fluids: An experimental study. Geochim Cosmochim Acta75:5243-5443. https://doi.org/10.1016/j.gca.2011.07.020

# Utility of volcanic rock geochemistry in discriminating fertile areas for epithermal gold mineralization: A case study in Japan

**Mizuki Ishida[1], Kentaro Nakamura[1], Hikaru Iwamori[2], Takahiro Hosono[3], Yasuhiro Kato[1,4]**
*[1]Department of Systems Innovation, School of Engineering, The University of Tokyo, Tokyo, Japan*
*[2]Earthquake Research Institute, The University of Tokyo, Tokyo, Japan*
*[3]Faculty of Advanced Science and Technology, Kumamoto University, Kumamoto, Japan*
*[4]Ocean Resources Research Center for Next Generation, Chiba Institute of Technology, Chiba, Japan*

**Abstract.** Epithermal gold deposits are formed in shallow crustal environments by precipitation of ore minerals from hydrothermal fluids, associated with magmatic activities. Previous epithermal gold exploration has heavily relied on the presence of hydrothermal alteration zones and geological structures as exploration guides, and the natureof magmas is rarely considered. Here we show from the whole-rock geochemistry of volcanic rocks that ore- forming magmas of large (>200 t Au) Hishikari epithermal gold deposit in Japan is likely to have formed by combination of three geological processes which could have maintained a relatively high sulfur solubility in magmas: (i) oxidized source mantle of primary magmas,
(ii) differentiation in deep crust without significant assimilation of accretionary sediments and (iii) late magnetite saturation relative to the timing of fluid release in shallow crust. In contrast, representative, previously explored areas in Japan (Toyoha, Nansatsu, Iriki) failed to meet more than one of the above criteria, which likely explain the smaller or lack of gold mineralization in these areas. We suggest that elemental source conditions represented by the geochemistry of regional volcanic rocks can be utilized in early stages of epithermal gold exploration in addition to the conventional indicators of elemental transport/precipitation.

## 1 Introduction

The expanding global population and the transition to a low-carbon society will require a wide range of minerals in increasing quantities for the foreseeable future. The discovery and extraction of new primary resources will continue to play a central role in sustaining mineral supplies (Ali et al. 2017).However, recent years have seen a marked decline in the number of new mineral deposits discovered, despite considerable increases in exploration expenditures (Schodde 2019); exploration efficiencymust therefore be improved to ensure mineral resources remain available to industry. Since near half of the world exploration expenditure is spent for gold, effective methods for gold exploration will be of particular interest.

Many gold deposits are primarily formed in association with magmatic activity. Among them, epithermal deposits, producing more than 10% of world's gold production, are important sources of gold and associated critical metals (Frimmel 2008). Epithermal gold deposits are distributed in subduction zones and formed in shallow (less than 1 km) crustal environments by the precipitation of ore minerals from magmatic-hydrothermal fluids.

Previous epithermal gold exploration, especially in Japan, have heavily relied on the presence of hydrothermal alteration zones (evidence of elemental transport) and geological structures (facilitates elemental precipitation) as exploration guides. Although hydrothermal fluids and ore- forming elements are largely sourced from magmas (Richards 2011), the nature of those magmas is rarely considered in epithermal gold exploration due to a lack of understanding and effective methodologies. This study therefore aims to determine the geochemical features of magmas that are capable of forming large epithermal gold deposits by using case studies in Japan, utilizing syn-mineralization volcanic rocks near deposits as the surface expression of ore-forming magmas. Then we try to establish new exploration guidelines for epithermal gold deposits that incorporate the magmatic processes, using whole-rock geochemistry of volcanic rocks.

## 2 Case study areas

The study takes place in the Hokusatsu and the Nansatsu regions of south Kyushu and the Toyoha region of southwest Hokkaido, Japan (Figure 1). These regions have been the subject of epithermal gold exploration by the Ministry of International

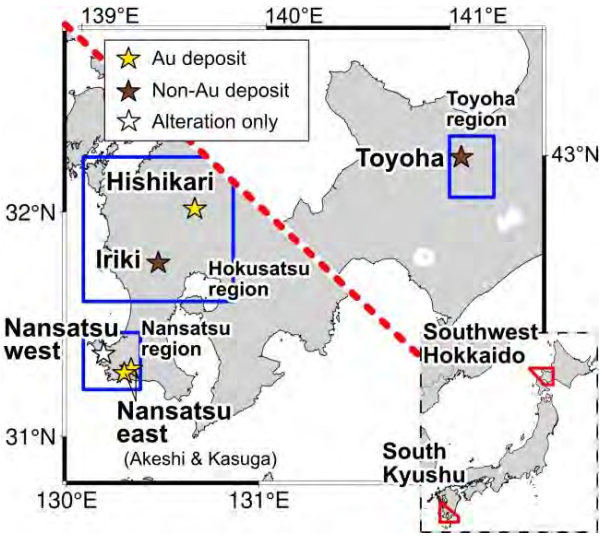


**Figure 1.** Study areas of this study.

Trade and Industry (MITI, what is now METI) of Japan in 1963–2003 (METI 2004).

### 2.1 Hokusatsu region

The Hishikari area in Hokusatsu region hosts a large (more than 200 t) gold deposit (Hishikari deposit), which is a low-sulfidation deposit formed in 1.3 – 0.6 Ma (Watanabe 2005). In contrast, the Iriki area hosts a clay deposit (Iriki high- to low-sulfidation deposit) formed at 0.5 Ma, with much smaller (less than 10 t) gold mineralization.

### 2.2 Nansatsu region

The eastern part of the Nansatsu region (Nansatsu east) hosts high- to low- sulfidation gold deposits formed around 4 Ma. The Akeshi and Kasuga high-sulfidation deposits are medium-sized (more than 10 t) gold deposits (Ishida et al. 2021). In contrast, no gold mineralization is known in the western part of Nansatsu region (Nansatsu west).

### 2.3 Toyoha region

The Toyoha region is home to an intermediate-sulfidation Pb-Zn deposit (Toyoha deposit) formed in 3 – 0.5 Ma. The Toyoha deposit have produced more than 1.2 Mt Zn and 0.4 Mt Pb, but only endowed with minor (less than 1 t) gold mineralization (Watanabe 2002).

## 3 Methods

Composition of volcanic rocks in Nansatsu and Toyoha regions were analysed in this study. The major element contents were determined using a Rigaku ZSX Primus II X-ray fluorescence (XRF) spectrometer, and the trace element contents were analysed using an inductively coupled plasma mass spectrometer (ICP-MS; Thermo Fisher Scientific iCAP Q) at the Department of Systems Innovation, the University of Tokyo (Yasukawa et al. 2014). Strontium and Nd isotope analyses were acquired by thermal ionization mass spectrometry (TIMS) with Thermo Finnigan TRITON XT, and the Pb isotopic compositions were measured using a Thermo Finnigan NEPTUNE multiple collector ICP-MS at the Ocean Resources Research Center for Next Generation, Chiba Institute of Technology (Machida et al. 2009; Tanimizu and Ishikawa 2006).

## 4 Potential geochemical indicators of gold in magmas

Gold-rich fluids that are favorable for gold mineralization require gold-rich magmas (Zajacz et al. 2012). The solubility of gold in magma is controlled by S2-, while the solubility and speciation of sulfur is in turn governed by the magma oxygen fugacity (Jugo et al. 2010). However, gold, sulfur, and oxygen fugacity in magmas are relatively hard to analyze from volcanic rocks, especially in the context of exploration where large number of samples must be processed. We therefore sought alternative geochemical indicators related to magma oxygen fugacity that might allow us to estimate the behavior of gold in magmas and to discriminate between gold-mineralizing and barren areas. We divided the magma evolution process into three stages (mantle, deep crust, and shallow crust) and found indicators corresponding to each stage.

### 4.1 Mantle

The generation of gold-rich primary magma in the mantle requires relatively high oxygen fugacity in which both S2- and S6+ are stable (Li and Audétat 2013). The V/Yb ratio of high-MgO rocks (more than 6 wt.%) is known as an indicator of oxygen fugacity during mantle melting (Laubier et al. 2014). We found a higher V/Yb ratio (160–220) in the South Kyushu volcanic rocks except for Iriki rocks (Figure 2; denoted as Hishikari and Nansatsu east) than the global average (158; Cottrell et al. 2021), indicating the presence of gold-rich primary magmas in these gold-mineralized areas. In contrast, V/Yb ratio of volcanic rocks in southwest Hokkaido (corresponding to the Toyoha region) are close to the global average, and those in the Iriki area were close to mid-ocean ridge basalt (MORB).

### 4.2 Deep crust

The assimilation of accretionary sediments in the deep part of the crust is the most prominent process in reducing subduction zone magmas, which can be recognized from the Sr-Nd-Pb isotope ratios of volcanic rocks. When the oxidizing magma is reduced and the sulfur speciation changes, the solubility of sulfur decreases rapidly, precipitating large amounts of sulfide minerals in the magma

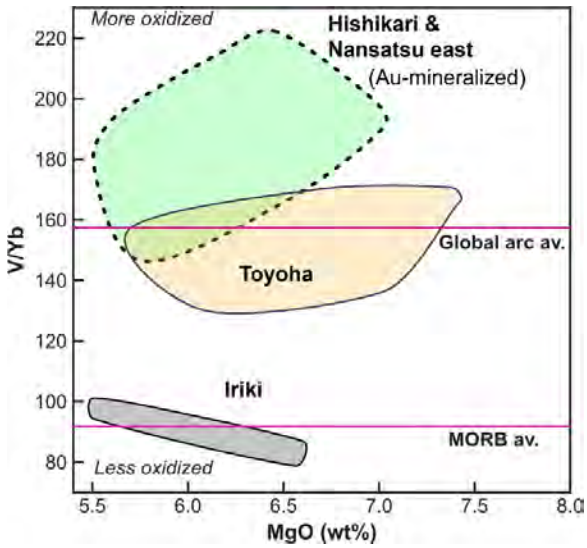


**Figure 2.** V/Yb ratio of high-MgO volcanic rocks corresponding to the studied area. Data from GEOROC.

(Tomkins et al. 2012). Since sulfide phases precipitate with gold in magma, this process could hinder the formation of gold deposits. In this study, volcanic rocks in the Nansatsu west area (Oldest stage Nansatsu volcanic rocks) had enriched isotope signatures that were close to those of the Shimanto supergroup (accretionary sediments), indicating that the magma reduction resulting from assimilation had inhibited the formation of gold deposits in this area (Figure 3). In other areas, the magmas were likely to have ascended without such reduction processes.

### 4.3 Shallow crust

In the shallow part of the crust, the timing of magnetite saturation relative to fluid release from the magma can have a profound effect on the gold content of the fluid because magnetite saturation can also reduce magmas (Jenner et al. 2010). The timing of magnetite saturation can be estimated from the MgO content of the volcanic rocks in which total Fe sharply decreases, and this can be compared with the timing of fluid release estimated generally to be <2.5 wt.% MgO (Hao et al. 2022). We found that volcanic rocks in the Hishikari area (except for the oldest unit K-IA) experienced magnetite saturation at around 2 wt.% MgO (Figure 4). We argue that this was likely late enough to enrich the released fluid with gold. Timing of magnetite saturation was close to the global average (MgO 4–5 wt.%; Park et al. 2021) or earlier in other areas, which could have hindered the formation of large gold deposits.

## 5 Implications for exploration

The above results demonstrated that the following geochemical indicators can be used to identify the presence of magma suitable for gold mineralization:

- V/Yb > 160 for volcanic rocks with MgO > 6 wt.%
- Sr-Nd-Pb isotopic ratios that do not extend toward the isotopic ratio of accretionary sediments
- Total Fe of volcanic rocks sharply declining only when MgO < 2.5 wt.%

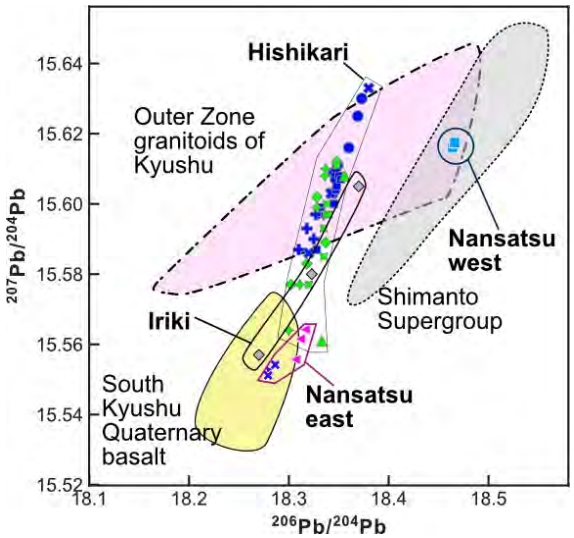


**Figure 3.** Pb isotopic composition of the volcanic rocks in south Kyushu. Data of Hishikari area from Hosono et al. (2003) and Iriki area from Hosono et al. (2008).

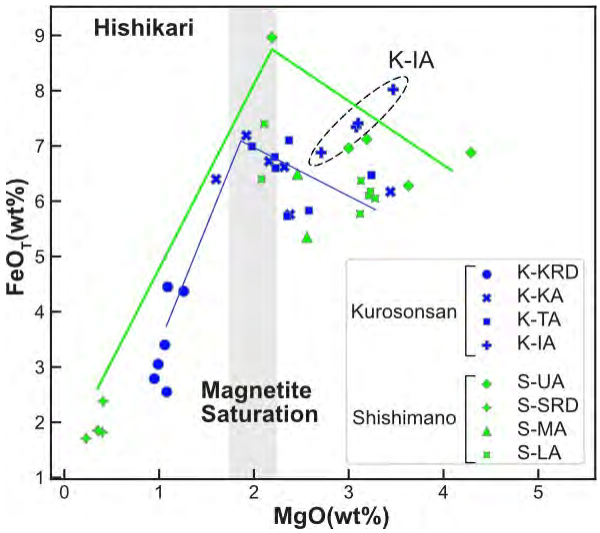


**Figure 4.** Timing of magnetite saturation for the Hishikari volcanic rocks. Data from Hosono and Nakano (2003).

Transport of Au in magma from mantle to shallow crust

| Area | Primary magma $fO_2$ | Assimilation of reducing crustal materials | Timing of magnetite saturation | Result |
|---|---|---|---|---|
| **Hishikari** (Except for K-IA) | High | Minor | Late | **Large Au deposit** |
| Nansatsu east | High | Minor | Average | Middle Au deposit |
| Iriki | Low | Minor | Average | Minor Au mineralization |
| Toyoha | Low | Minor | Average | Minor Au mineralization |
| Nansatsu west | unknown | Significant | unknown | Hydrothermal alteration only |

**Figure 5.** Factors which influenced the epithermal gold mineralization of the studied area. Green: Facilitated gold mineralization; Pink: Hindered gold mineralization

The fact that only the volcanic rocks from the Hishikari area fulfilled all three criteria indicates that all the conditions along magma ascent must be met in order to generate a large gold deposit (Figure 5). The smaller or lack of gold mineralization in the other studied areas can thus be explained by unfavorable magma conditions. We suggest that conventional indicators of elemental transport/precipitation combined with the elemental source conditions (i.e., magma) described here should allow the identification of promising areas for exploration. The collection of additional geochemical data should also allow further refinement of these exploration guidelines.


## Acknowledgements

We thank Dr. S. Machida, Ms. K. Ashida, Ms. Y. Itabashi, Ms. R. Tajiri, Prof. M. Nakagawa, Mr. S. Murakami and Mr. Y. Hieda for help in sample preparation and chemical analyses. Discussion with Assoc. Prof. K. Yasukawa, Dr. J. Ohta, Dr. K. Fujinaga, Prof. S. Koshizuka and Prof. A. Nakao improved the quality of the abstract. This research was funded by Japan Society for the Promotion of Science KAKENHI Grant No. JP20J22038 given to the first author.


## References


Ali SH, Giurco D, Arndt N, Nickless E, Brown G, DemetriadesA, Durrheim R, Enriquez MA, Kinnaird J, Littleboy A, Meinert LD, Oberhänsli R, Salem J, Schodde R,Schneider G, Vidal O, Yakovleva N (2017) Mineral supply for sustainable development requires resource governance. Nature 543:367-372. doi:10.1038/nature21359.

Cottrell E, Birner SK, Brounce M, Davis FA, Waters LE, KelleyKA (2021) Oxygen Fugacity Across Tectonic Settings. Magma Redox Geochemistry 33-61. doi: 10.1002/9781119473206.ch3

Frimmel HE (2008) Earth's continental crustal gold endowment. Earth and Planetary Science Letters 267:45- 55. doi: 10.1016/j.epsl.2007.11.022.

Hao H, Park J-W, Campbell IH (2022) Role of magma differentiation depth in controlling the Au grade of giant porphyry deposits. Earth and Planetary Science Letters 593:117640.doi: https://doi.org/10.1016/j.epsl.2022.117640.

Hosono T, Nakano T (2003) Petrochemistry of Volcanic Rocksin the Hishikari Mining Area of Southern Japan, with Implications for the Relative Contribution of Lower Crust and Mantle-derived Basalt. Resource Geology 53:239- 259. doi: https://doi.org/10.1111/j.1751-3928.2003.tb00174.x.

Hosono T, Nakano T, Murakami H (2003) Sr–Nd–Pb isotopic compositions of volcanic rocks around the Hishikari gold deposit, southwest Japan: implications for the contributionof a felsic lower crust. Chemical Geology 201:19-36. doi: 10.1016/s0009-2541(03)00205-5.

Hosono T, Nakano T, Shin K, Murakami H (2008) Assimilationof lower to middle crust by high alumina basalt magma asan explanation for the origin of medium-K volcanic rocks in southern Kyushu, Japan. Lithos 105:51-62. doi: 10.1016/j.lithos.2008.02.007.

Ishida M, Romero R, Leisen M, Yasukawa K, Nakamura K, Barra F, Reich M, Kato Y (2021) Auriferous pyrite formed by episodic fluid inputs in the Akeshi and Kasuga high-sulfidation deposits, Southern Kyushu, Japan. Mineralium Deposita. doi: 10.1007/s00126-021-01053-4.

Jenner FE, O'Neill HSTC, Arculus RJ, Mavrogenes JA (2010) The Magnetite Crisis in the Evolution of Arc-related Magmas and the Initial Concentration of Au, Ag and Cu. Journal of Petrology 51:2445-2464. doi: 10.1093/petrology/egq063.

Jugo PJ, Wilke M, Botcharnikov RE (2010) Sulfur K-edge XANES analysis of natural and synthetic basaltic glasses: Implications for S speciation and S content as function of oxygen fugacity. Geochimica et Cosmochimica Acta 74:5926-5938. doi: 10.1016/j.gca.2010.07.022.

Laubier M, Grove TL, Langmuir CH (2014) Trace element mineral/melt partitioning for basaltic and basaltic andesitic melts: An experimental and laser ICP-MS study with application to the oxidation state of mantle source regions. Earth and Planetary Science Letters 392:265-278. doi: 10.1016/j.epsl.2014.01.053.

Li Y, Audétat A (2013) Gold solubility and partitioning between sulfide liquid, monosulfide solid solution and hydrous mantle melts: Implications for the formation of Au-rich magmas and crust–mantle differentiation. Geochimica et Cosmochimica Acta 118:247-262. doi:10.1016/j.gca.2013.05.014.

Machida S, Hirano N, Kimura J-I (2009) Evidence for recycled plate material in Pacific upper mantle unrelated to plumes. Geochimica et Cosmochimica Acta 73:3028-3037. doi: 10.1016/j.gca.2009.01.026.

METI (2003) Report on the regional geological structure survey in the fiscal year Heisei 15: Domestic Survey Overall Evaluation.

Park J-W, Campbell IH, Chiaradia M, Hao H, Lee C-T (2021) Crustal magmatic controls on the formation of porphyry copper deposits. Nature Reviews Earth & Environment 2:542-557. doi: 10.1038/s43017-021-00182-8.

Richards JP (2011) Magmatic to hydrothermal metal fluxes in convergent and collided margins. Ore Geology Reviews 40:1-26. doi: 10.1016/j.oregeorev.2011.05.006.

Schodde R (2019) Trends in Exploration. International Mining and Resources Conference. Melbourne, Australia.

Tanimizu M, Ishikawa T (2006) Development of rapid and precise Pb isotope analytical techniques using MC-ICP-MS and new results for GSJ rock reference samples. Geochemical Journal 40:121-133. doi:10.2343/geochemj.40.121.

Tomkins AG, Rebryna KC, Weinberg RF, Schaefer BF (2012) Magmatic sulfide formation by reduction of oxidized arc basalt. Journal of Petrology 53:1537-1567. doi: 10.1093/petrology/egs025.

Watanabe Y (2002) Late cenozoic metallogeny of southwest Hokkaldo, Japan. Resource Geology 52:191-210. doi: 10.1111/j.1751-3928.2002.tb00130.x.

Watanabe Y (2005) Late Cenozoic evolution of epithermal gold metallogenic provinces in Kyushu, Japan. Mineralium Deposita 40:307-323. doi: 10.1007/s00126-005-0025-7.

Yasukawa K, Liu H, Fujinaga K, Machida S, Haraguchi S, Ishii T, Nakamura K, Kato Y (2014) Geochemistry and mineralogy of REY-rich mud in the eastern Indian Ocean. Journal of Asian Earth Sciences 93:25-36. doi: https://doi.org/10.1016/j.jseaes.2014.07.005.

Zajacz Z, Candela PA, Piccoli PM, Wälle M, Sanchez-Valle C (2012) Gold and copper in volatile saturated mafic to intermediate magmas: Solubilities, partitioning, and implications for ore deposit formation. Geochimica et Cosmochimica Acta 91:140-159. doi:10.1016/j.gca.2012.05.033.

# Quantification of hydrothermal alteration associated with gold-antimony mineralization along the Antimony Line, Murchison greenstone belt, South Africa.

**Thabo S. Kgarabjang[1], Napoleon Q. Hammond[1]**
*[1]Department of Geology and Mining, University of Limpopo, South Africa.*

**Abstract.** The Antimony Line in the Archaean Murchison greenstone belt hosts several gold-antimony mineralizations within massive, fractured talcose and quartz-carbonate host rocks. Samples from three orebodies, Athens, Beta and Monarch along the Antimony Line were studied to quantify hydrothermal alteration and characterize the geochemical distribution of the gold-antimony mineralization. Mass-balance studies of the hydrothermally altered assemblage indicated variable degree of enrichment of the trace and pathfinder elements (Au, As, Sb and Ag) in the deposits. In particular, antimony recorded the highest enrichment at Beta while gold enrichment is highest at Monarch. Antimony generally shows an increasing trend of enrichment from 3083% at Monarch to 7167% at Beta, while gold enrichment increases from 67% at Beta to 9761% at Monarch. The arsenic and gold distribution in the orebodies show similar pattern, suggesting a close association with gold mineralization, which can be used as a vector to identify extensions of the mineralization within the belt.

## 1 Introduction

The Murchison greenstone belt dated 3.0 Ga forms part of the several Archaean volcano-sedimentary belts within the Kaapvaal Craton. It is located in the northeastern portion of the craton approximately 200 km north of the Barberton greenstone belt. The Antimony Line is a 250 m wide shear zone located centrally within this greenstone belt and extends for about 50 km. The sheer zone is characterized by intense semi-brittle deformation and hosts several gold and antimony orebodies within massive fractured talcose and quartz-carbonate host rocks of the Weigel Formation (Fig. 2).

Studies on the chemistry, mineralogical and textural characteristics of the host rocks in three orebodies, Athens, Beta and Monarch deposits along the Antimony Line show extensive hydrothermal alteration. As characterized in most hydrothermal ore deposits, the intensity of the alteration increases towards the mineralized zones from the unaltered sections of the host rocks. In this study, quantitative evaluation of the chemical compositional changes (major and trace elements) of the host rocks linked to the hydrothermal alteration processes was undertaken using the isocon method of Grant (1986). This method is a widely used technique to quantify the changes in mass/volume/concentration of elements associated with alteration processes.

**Figure 10.** Locality map of the Murchison greenstone belt. Map adapted from Madisha (1996).

### 1.1 Gold and Antimony Mineralization

*Gold Mineralization*

The Antimony Line hosts major gold mineralization within massive, fractured talcose and carbonate schist host rocks, with epigenetic gold-antimony occurring along the ENE-trending shear from the Gravelotte, Athens, Beta, and Monarch orebodies along a distance of about 12 km (Fig. 2). Previous studies on gold-antimony mineralization along the Antimony Line in the Murchison greenstone belt (e.g. Davis et al. 1986; Vearncombe et al. 1992; Madisha 1996) have documented that the Au mineralization occurs in close association with the sulphides, and is present either as free gold or occluded in sulphides (Vearncombe et al. 1992; Ward and Wilson 1998). Additionally, gold is associated with the arsenopyrite horizons, which form discrete lenses at or near the antimony mineralization.

*Antimony Mineralization*

Antimony mineralization occurs as disseminations within the quartz-carbonate schists throughout the Antimony Line. Most of the antimony, often accompanied by gold, occurs as veins of quartz-carbonate-stibnite which occupy tension fractures along the Antimony Line (Davis et al. 1986). Antimony mineralization in the stibnite ($Sb_2S_3$) form is documented to be the richest in the core of the orebody while the mineralization in berthierite

($FeSb_2S_4$) form is more concentrated towards the margin of the orebody (Davis et al. 1986).

were identified to be Ga and $Al_2O_3$. Given that, an immobile element has little or no change in

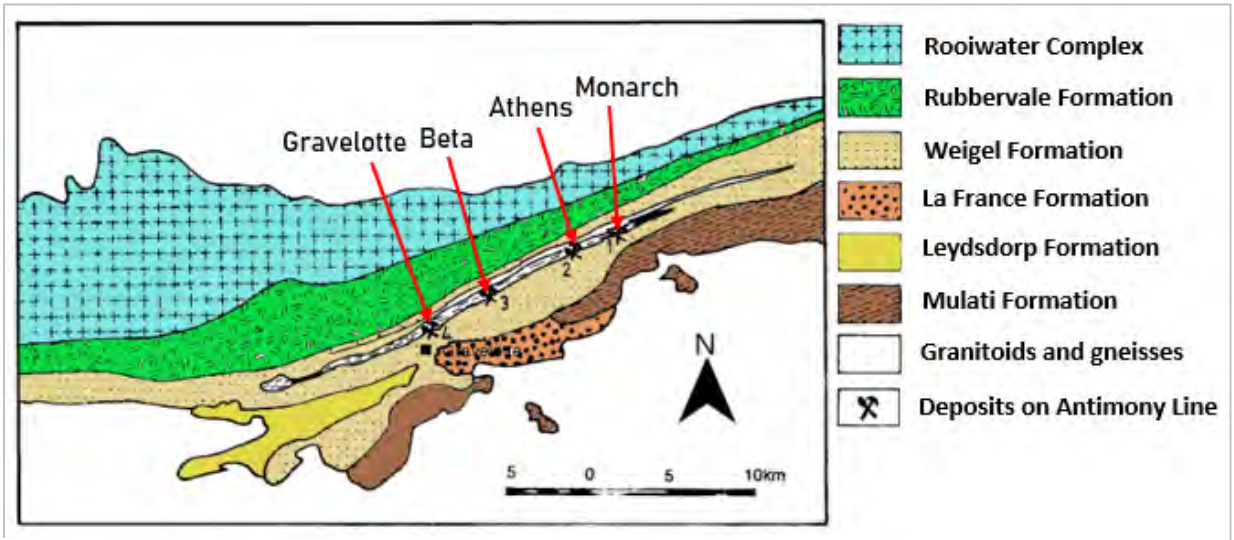


**Figure 11.** Generalized geology of the Murchison greenstone belt showing the locations of orebodies along the Antimony Line. Map adapted from Maiden and Boocock (1984).

## 2 Methodology

Two hundred and sixty-six (266) borehole samples were taken from Athens, Beta and Monarch orebodies collectively. Out of this, fifteen (15) samples from Athens, twenty-one (21) samples from Monarch and fifteen (15) samples from Beta orebody were selected and prepared for geochemical analysis. The geochemical analysis was undertaken using X-ray fluorescence (XRF) and inductively coupled plasma mass spectrometry (ICP-MS) to determine major and trace element concentrations including Sb, As, Au and Ag in host rocks respectively. The Grant (1986) mass-balance method was used to plot isocon diagrams to investigate alteration along the Antimony Line. Ore elements and the pathfinders were plotted on ternary diagram to understand their association and distribution across the three deposits, Athens, Beta, and Monarch.

## 3 Mass-balance calculations

The basic equation used by Grant (1986) for mass balance calculation to quantify changes in mass/volume/concentration of elements associated with alteration processes relates the concentration of element "$i$" in the altered rock ($Ci^A$) to its concentration before alteration ($Ci^0$) is given as follows:

$$Ci^A = M^0/M^A\,[Ci^0 + \Delta Ci] \quad \text{..... (1)}$$

Where $M^0$ is the mass of the host rock before alteration, $M^A$ is the mass of the host rock after alteration and $\Delta C_i$ is the concentration change of element "$i$" after alteration. Using the method of Maclean and Kranidiotis (1987), the most immobile element in the Athens, Beta and Monarch deposits concentration, that is its concentration before and after alteration is the same, equation (1) can be expressed as follows:

$$Ci^A = M^0/M^A\,[Ci^0] \quad \text{..... (2)}$$

Equation (2) can further be expressed as:

$$y = mx \quad \text{..... (3)}$$

Where: $y = Ci^A$, $m = M^0/M^A$, and $x = Ci^0$

The $M^0/M^A$ for Ga in Athens, Beta, and Monarch were calculated and values are expressed in Table 1.

**Table 1.** Ga constants for Athens, Beta and Monarch orebodies.

| Athens | Beta | Monarch |
|---|---|---|
| $M^0/M^A$ = 1.08 | $M^0/M^A$ = 0.54 | $M^0/M^A$ = 0.53 |

Ga constants for the Athens, Beta and Monarch deposits are substituted into equation (3) to create best-fit isocons:

Athens: y = 1.08x..... (4)
Beta: y = 0.54x..... (5)
Monarch: y = 0.53x..... (6)

These equations (4), (5) and (6) were used to create isocon diagrams to determine the relative enrichments or depletions of elements in the Athens, Beta and Monarch host rocks during alteration. Elements that were added to the host rocks plot above the reference line (best fit isocon) and elements that were removed from the host rocks during alteration plot below the best fit isocon. The isovolumetric isocon is a line of:

$$y = mx \quad \text{..... (7)}$$

Where: $m = M^0/M^A = 1$

Host rocks that have been reduced in volume/mass as a result of alteration are characterized by best-fit isocon plotting below the isovolumetric isocon, while host rocks that have increased in volume/mass are characterized by the best fit isocon plotting above the isovolumetric isocon. The isocon diagrams for Athens, Beta, and Monarch deposits are shown in Figures 3, 4 and 5 respectively.

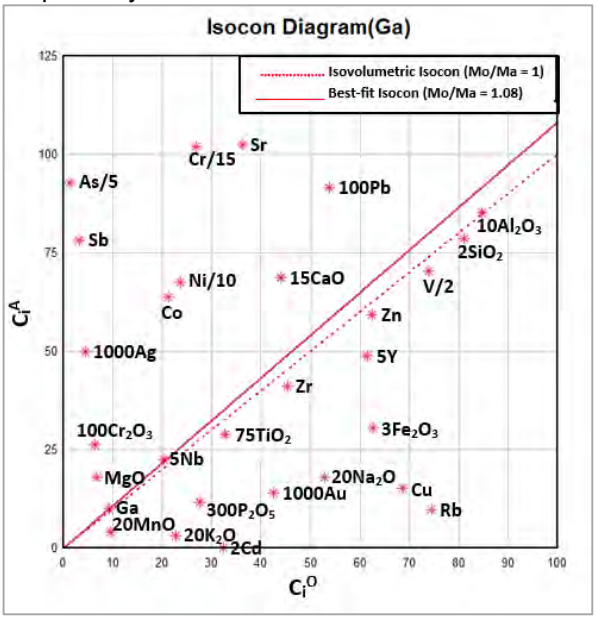


**Figure 12.** Isocon diagram for major oxides and trace elements to determine mass changes using Ga constant at the Athens Orebody. Isocon diagram adapted from Grant (1986).

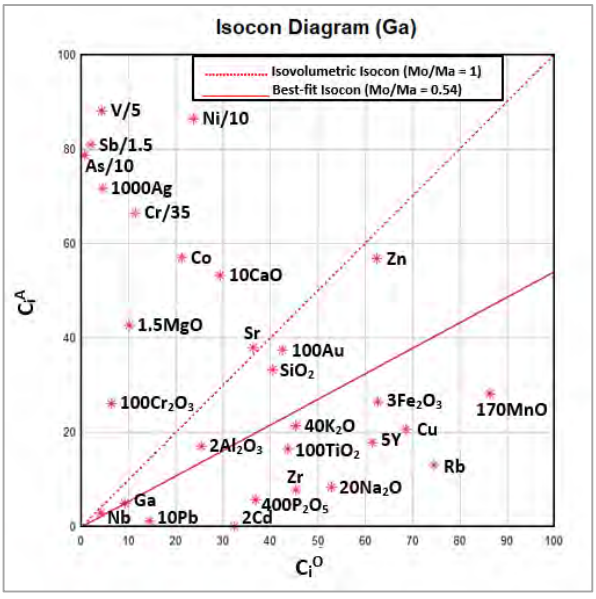


**Figure 13.** Isocon diagram for major oxides and trace elements to determine mass changes using Ga constant at the Beta Orebody. Isocon diagram adapted from Grant (1986).

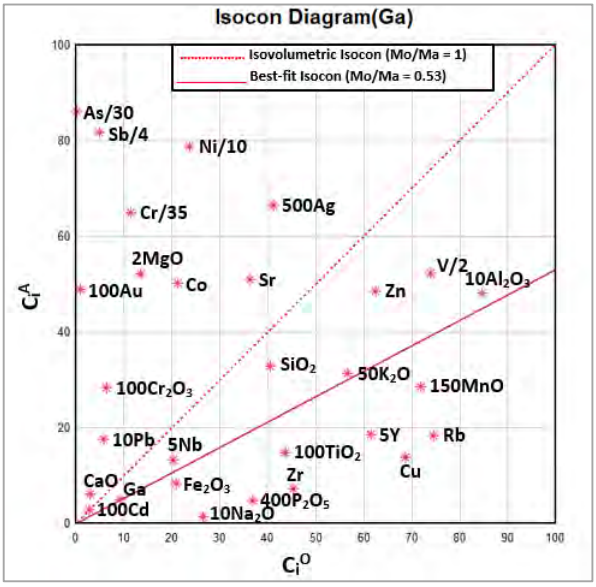


**Figure 14.** Isocon diagram for major oxides and trace elements to determine mass changes using Ga constant at the Monarch Orebody. Isocon diagram adapted from Grant (1986).

## 4 Gold, Arsenic and Antimony distribution along the Antimony Line

The distribution of Au, As and Sb in the Athens, Beta, and Monarch deposits varies significantly and shows variable enrichments from one deposit to another (Fig. 6). These variations may be attributed to physicochemical inconsistencies in hydrothermal alteration along the Antimony Line. Gold shows higher concentrations in Monarch than in the Beta and Athens deposits, where Au concentration is relatively low. Antimony shows a scattered distribution across Beta and Monarch. Gold and arsenic show similar distribution patterns in the orebodies, with high As concentrations and high Au concentrations in the Monarch deposit.

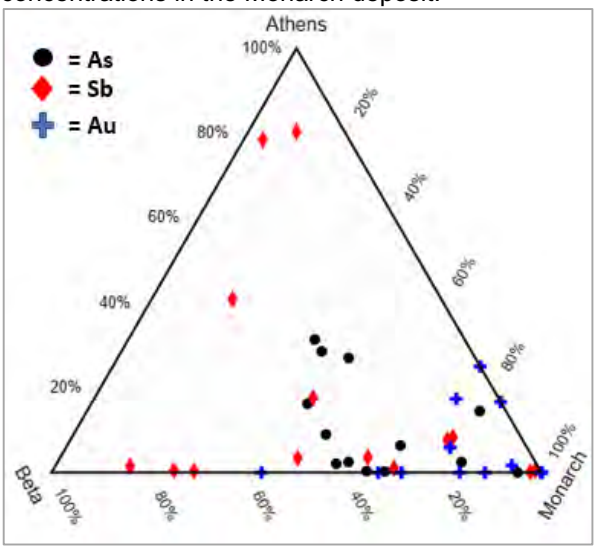


**Figure 6**. Ternary plot showing the distribution of gold, antimony, and arsenic in the three ore bodies, Athens, Beta and Monarch along the Antimony Line.

## 5 Conclusions

The mass-balance changes associated with alteration indicate enrichments of $SiO_2$, MgO, CaO $Cr_2O_3$, Sb, Au, As, Ag, Cr, Ni, and Co in the host rocks while elements including MnO, $P_2O_5$, and Rb were removed (Fig. 3-5). There is however variable degree of enrichment of the trace and pathfinder elements (Au, As, Sb and Ag) in each of the orebodies, Athens, Beta and Monarch. In particular, Au enrichment is highest at Monarch, while antimony recorded the highest enrichment at Beta. Thus, antimony shows an increasing trend from Monarch (3083%) to Beta (7167%), while gold enrichment increases from Beta (67%) to Monarch (9761%). In general, The Au enrichment is highest in the Monarch compared to Beta and Athens deposits. There was no significant change in the mass/volume of host rocks at the Athens deposit during hydrothermal alteration (Fig. 3). However, the volume/mass of host rocks in the Beta and Monarch deposits show significant reduction (>50%) as a result of removal of elements (such as MnO, $Na_2O$, Cu, Rb) (Fig. 4-5). The Au and As distribution pattern in the orebodies shows co-variation (Fig. 6), with highest enrichments of the two elements at the Monarch deposit, suggesting a close association with Au mineralization. The close association between Au and As is consistent with the reported Au and As relationships in many greenstone belts (Boyle and Jonasson 1973) and as such, both Au and As can be useful pathfinder tool for gold exploration in the Murchison greenstone belt.

## Acknowledgements

The support of the Department of Science and Innovation through its funding agency, the National Research Foundation, and the Centre of Excellence for Integrated Mineral and Energy Resource Analysis (DSI-NRF CIMERA) towards this research is hereby acknowledged. We are thankful to the geological staff at the Mopani Stibium Mine for their assistance during visits to the site.

## References

Boyle, R.W. and Jonasson, I.R. (1973): The geochemistry of arsenic and its use as an indicator element in geochemical prospecting. Journal of Geochemical Exploration, v. 2 (3), p. 251-269.

Davis, D.R., Paterson, D.B., Griffiths, D.H.C. (1986): Antimony in South Africa. Journal of the Southern African Institute of Mining and Metallurgy, v. 86 (6), p.173-193.

Grant, J.A. (1986a): The isocon diagram; a simple solution to Gresens' equation for metasomatic alteration. Economic geology, v. 81 (8), p.1976-1982.

MacLean, W.H. and Kranidiotis, P. (1987): Immobile elements as monitors of mass transfer in hydrothermal alteration; Phelps Dodge massive sulfide deposit, Matagami, Quebec. Economic Geology, v. 82 (4), p. 951-962.

Madisha, M.E. (1996): Carbonate alteration of serpentinite in the Murchison greenstone belt, Kaapvaal Craton: implication for gold mineralization. Unpublished MSc thesis, Rand Afrikaans University, p. 178.

Maiden, K.J. and Boocock, C.N. (1984): Deformational and metamorphic features of antimony ores of the murchison antimony line, north-eastern Transvaal. Transactions of the Geological Society of South Africa, v. 87, p. 327-333.

Vearncombe, J.R., Barton, J.M., Cheshire, P.E., de Beer, J.H., Stettler, E.H., and Brandl, G. (1992): Geology, geophysics and mineralization of the Murchison Schist Belt, Rooiwater Complex and surrounding granitoids. Geological Survey of South Africa, p. 139.

Ward, J.H.W. and Wilson, M.G.C. (1998): Gold outside the Witwatersrand Basin. In: Wilson, M.G.C. and Anhaeusser, C.R. (Eds.). The Mineral Resources of South Africa. Handb. Counc. Geosci., v. 16, p. 350-386.

# Complex hydrothermal evolution during retrograde terrane exhumation, Nalunaq gold deposit, South Greenland

**Jochen Kolb[1], Robin-Marie Bell[2], Torsten Vennemann[3], Laure Martin[4], Marco L. Fiorentini[4], Tod Waight[5]**
[1]*Karlsruhe Institute of Technology*
[2]*Copenhagen*
[3]*University of Lausanne*
[4]*University of Western Australia*
[5]*University of Copenhagen*

**Abstract.** The Paleoproterozoic orogenic gold deposit of Nalunaq in South Greenland is located in a NW-vergent thrust in an amphibolite facies terrane. Gold mineralization is hosted in a quartz vein system with biotite-arsenopyrite alteration zone. We present the stable isotope characteristics of four hydrothermal alteration assemblages at Nalunaq. The isotopes indicate that a metamorphic fluid of similar composition is responsible for hydrothermal alteration lasting from the ca. 1785 Ma, pre-gold, peak metamorphic stage at ~650°C to the ca. 1765 Ma, post-gold stage at ~500°C. Ca. 1745 Ma, post-gold hydrothermal alteration is contemporaneous with late-orogenic granite. The fluid is most likely derived from Paleoproterozoic rocks. Stable isotopes indicate a meteoric fluid source in equilibrium with the late-stage hydrothermal alteration assemblage at ca. 250°C. The retrograde evolution of the terrane hosting Nalunaq is initially characterized by hydrothermal overprint by a metamorphic fluid. Economic gold mineralization is likely related to focused fluid flow in a thrust. The hydrothermal system drastically changed to meteoric fluids upon further terrane exhumation and development of hydrothermal fluid cells by widespread granite intrusion overprinted the gold mineralization.

## 1 Introduction

Orogenic gold deposits are structurally controlled hydrothermal deposits that are hosted by metamorphic rocks and are formed by orogenic processes. They are often one of many stages in a complex evolution, involving locally several hydrothermal stages, which may not all be auriferous. This geological setting allows detailed investigation of hydrothermal fluids present during orogeny. Stable isotopes of hydrothermal alteration minerals allow interpretations of T, precipitation mechanisms and fluid source, although stable O, D, C, S isotopes are often equilibrated with the metamorphic host rocks of the gold deposits (Hoefs 2015). Thus, the stable isotope composition of the fluids often is not a direct link to the fluid source, and fluid-rock interaction along the fluid pathway has to be taken into account (Ridley and Diamond 2000). However, detailed investigations of orogenic gold quartz veins in the Val-d'Or vein field (Canada) show that the stable isotope compositions are the result of fluid-rock reaction and mixing between an upper crustal fluid and a metamorphic fluid (Beaudoin and Pitre 2005).

We present stable isotope data from four hydrothermal stages and wall rocks of the Paleoproterozoic orogenic gold mineralization in Nalunaq, South Greenland. The data indicate a complex hydrothermal evolution during the retrograde exhumation of the auriferous terrane in the Paleoproterozoic Ketilidian Orogen.

## 2 Regional Geology

The Nalunaq gold deposit is an orogenic gold deposit that is situated in the Paleoproterozoic Ketilidian Orogen in South Greenland (Bell et al. 2017a, b; Kaltoft et al. 2000; Steenfelt et al. 2016). The Ketilidian Orogen developed at the southern margin of the Archean North Atlantic Craton (Garde et al. 2002). It is divided into three domains; the Northern, the Central and the Southern domains (Steenfelt et al. 2016). The Northern Domain represents the hinterland, where Archean rocks are unconformably overlain and intruded by Paleoproterozoic rocks, and ca. 1845-1800 Ma, north-vergent nappes are thrust over Archean rocks (Garde et al. 2002; Steenfelt et al. 2016). The wedge-shaped Central Domain consists of variably deformed, ca. 1854-1795 Ma, calc-alkaline monzogranite and granodiorite, with subordinate tonalite, hornblende diorite and gabbro (Julianehåb Igneous Complex; Garde et al. 2002; Steenfelt et al. 2016). Major, NE-trending, near-vertical, ca. 1815-1800 Ma, sinistral shear zones form the contact between the Central and Northern domains and transect the Central Domain (Garde et al. 2002).

The northern part of the Southern Domain consists of < ca. 1800 Ma meta-sedimentary rocks with detritus derived from igneous rocks of the Central Domain (Mueller et al. 2002). The dominantly siliciclastic rocks overly the rocks of the Central Domain tectonically or unconformably. They are interlayered with ca. 1808 Ma meta-volcanic and meta-volcanoclastic rocks (Mueller et al. 2002). Peak metamorphism was estimated at 580 °C and ~3 kbar (Garde et al. 2002).

The southern part of the Southern Domain consists of paragneiss, amphibolite and migmatite, with the PT conditions increasing to the south to > 800°C and ~5 kbar (Garde et al. 2002). Anatectic granite with ages of ca. 1790-1780 Ma constrains the age of peak granulite facies metamorphism (Garde et al. 2002).

Deformation in the Southern Domain is complex

with up to five stages and lasted from > 1800 Ma to ca. 1730 Ma (Garde et al. 2002). Early folds are SE-vergent and overprinted by shear zones that indicate NE-directed transport at ca. 1792 Ma. Up to three stages of later folding with initial NW-directed deformation overprinted the shear zones and the associated regional foliation. Late-orogenic granite of the Ilua Plutonic Suite intruded at ca. 1755–1732 Ma (Garde et al. 2002).

## 3 Geology of the Nalunaq gold deposit

The Nalunaq gold deposit (ca. 11t Au) is located in the NW-vergent Nanortalik Nappe of the Southern Domain close to the contact with the Central Domain (Bell et al. 2017a, b; Kaltoft et al. 2000; Steenfelt et al. 2016). The Nanortalik Nappe consists of meta-pelitic schist, calcareous meta-sedimentary rock, quartz-graphite-sulfide rock, amphibolite and meta-volcanoclastic rocks (Kaltoft et al. 2000). The nappe was intruded by granite of the Ilua Plutonic Suite at ca. 1745 Ma (Bell et al. 2017b).

Gold mineralization is hosted in amphibolite composed of plagioclase, hornblende and clinopyroxene, with minor quartz, biotite and traces of pyrite, chalcopyrite, pyrrhotite and ilmenite (Bell et al. 2017b). Four hydrothermal alteration stages are defined (Bell et al. 2017b):

5. The clinopyroxene-plagioclase-garnet alteration zone is ubiquitous and surrounds quartz-plagioclase veins and rods. Minor constituents are chalcopyrite, pyrite, sphalerite and titanite. The titanite was dated at 1783 ± 9 Ma, which is the age of peak metamorphism in the Southern Domain.
6. The biotite-arsenopyrite alteration is developed around the contemporaneous auriferous quartz veins. The alteration assemblage comprises biotite, quartz, chlorite, sericite, actinolite, arsenopyrite, pyrrhotite, tourmaline, titanite, maldonite, löllingite, pyrite, chalcopyrite, Bi-sulfosalts and gold.
7. The calcite-titanite alteration forms centimetre-scale calcite pockets with minor clinopyroxene, plagioclase and quartz, and a halo of plagioclase, titanite, quartz, pyrrhotite, spinel, chalcopyrite and ilmenite. Titanite was dated at 1766 ± 9 Ma, which is indistinguishable from a zircon age of 1762 ± 9 Ma for an aplite dyke that crosscuts auriferous quartz veins.
8. The epidote-calcite-zoisite alteration consists of calcite, zoisite, epidote, chlorite, titanite, muscovite, prehnite, hematite, microcline, apatite and clay minerals. Titanite was dated at 1745 ± 5 Ma, which is the age of the local granite intrusion.

The auriferous quartz veins have a lateral extent of ~2 km (Bell et al. 2017a). One single vein system, the Main Vein, was mined. It is continuous throughout the deposit, 0.5–2.0 m wide, and surrounded by discontinuous extension veins (Bell et al. 2017a). It is hosted in a reverse, NW-vergent shear zone, with pinch and swell structure, dipping between 25° and 80° to the SE (Bell et al. 2017a). Locally, ~20 cm wide reverse shear zones cross the Main Vein. The Main Vein is further cut by an array of post-mineralization faults, pegmatites and the 1762 Ma aplite.

## 4 Methods

Stable sulfur isotopes were measured using in situ multi collector SIMS analysis with the CAMECA IMS 1280 ion probe at the Centre for Microscopy and Microanalysis of the University of Western Australia, using methods described in detail by Farquhar et al. (2013). Pyrite and pyrrhotite grains were drilled from polished thin sections and mounted with the standards Sierra (pyrite) and Alexo (pyrrhotite) (LaFlamme et al. 2016). The average standard deviation on standard Alexo is 0.09‰ for $^{33}S$, 0.14‰ for $^{34}S$ and 0.37‰ for $^{36}S$. The large uncertainty for $^{36}S$ makes this data not useful for interpretation. The S-isotope data are expressed in the typical -notation versus the Vienna Canon Diablo meteorite (VCDT) standard in permil (‰) (Ding et al. 2001). The $\Delta^{33}S$ and $\Delta^{36}S$ values were calculated using calibrated $^{33}S$ and $^{34}S$ values and the theoretical equation of mass-dependent fractionation for sulfur isotopes.

Stable oxygen, carbon and hydrogen isotope ratios were measured in 24 silicate and carbonate separates from 17 samples of hydrothermal alteration zones and one whole rock sample from an unaltered fine-grained amphibolite using facilities at the University of Lausanne, Switzerland. The O-isotope composition was determined using methods described by Sharp (1990) and Vennemann et al. (2001). The O-isotope ratio is measured by a Finnigan MAT 253 isotope ratio mass spectrometer. Oxygen isotope compositions are given in the standard -notation, expressed relative to VSMOW in permil (‰). Replicate O-isotope analyses of the standard (NBS-28 quartz; n=5) has an average precision of ±0.1‰ for $^{18}O$. The accuracy is better than 0.2‰ compared to accepted $^{18}O$ values for NBS-28 of +9.64‰.

The C- and O-isotope composition of carbonates was measured with a GasBench II connected to a Finnigan MAT DeltaPlus XL mass spectrometer, using a He-carrier gas system according to methods adapted after Spötl and Vennemann (2003). Samples are normalized using an in-house standard calibrated against $^{13}C$ and $^{18}O$ values of NBS-19 (+1.95 and –2.20‰, relative to VPDB). External reproducibility for the analyses estimated from replicate analyses of the standard was ±0.04‰ for $^{13}C$ and ±0.07‰ for $^{18}O$.

Measurements of the H-isotope composition of minerals were made using the high-temperature (1450°C) reduction method with He-carrier gas and a TC-EA linked to a Delta Plus XL mass spectrometer from Thermo-Finnigan according to a method adapted after Sharp et al. (2001) and Bauer

and Vennemann (2014). The results are given in the standard -notation, expressed relative to V-SMOW in permil (‰). The precision of the in-house kaolinite and G1 biotite standards for hydrogen isotope analyses was better than ±2‰ for the method used.

## 5 Results

Stable isotopes were measured on mineral separates of all hydrothermal alteration stages, the crosscutting aplite dyke and the least altered host rock amphibolite.

### 5.1 Pre-gold mineralization stable isotope characteristics

The host rock amphibolite yields a $\delta^{18}O$ of 9.3‰, which is high compared to typical amphibolite or tholeiitic basalt (Hoefs 2015). Garnet (n=2) of the clinopyroxene-plagioclase-garnet alteration zone has a $\delta^{18}O$ of 8.0‰ and clinopyroxene (n=2) has a value of 8.7‰. Isotopic equilibrium between garnet and clinopyroxene indicates temperatures of ca. 650°C (Zheng 1993) for this hydrothermal alteration stage. Pyrite (n=21) shows a wide variation in $\delta^{34}S$ between 0.73 and 5.55‰. The $\Delta^{33}S$ values cluster tightly between -0.01 and -0.08‰, which means that all data are within the range of mass-dependent fractionation of ± 0.2‰ (Ohmoto et al. 2006).

### 5.2 Syn-gold mineralization stable isotope characteristics

The $\delta^{18}O$ values of quartz from the auriferous veins (n=6) and the hydrothermal biotite-arsenopyrite alteration zone (n=6) vary in a narrow range between 12.2 and 13.7‰. Biotite (n=5) yields $\delta^{18}O$ values between 8.3 and 8.7‰ with one value at 6.9‰, and $\delta D$ values between -68 and -74‰. The compositional range is relatively wide, which is reflected in a wide range of equilibrium temperatures between 460 and 650°C (Bottinga and Javoy 1975). Pyrrhotite (n=16) shows a variation in $\delta^{34}S$ between 2.16 and 4.50‰. The $\Delta^{33}S$ values cluster tightly between 0.01 and 0.09‰ (one at 0.21‰), which means that all data are within the range of mass-dependent fractionation of ± 0.2‰ (Ohmoto et al. 2006).

### 5.3 Post-gold mineralization stable isotope characteristics

Calcite (n=2) from the calcite-titanite alteration zone has $\delta^{18}O$ of 12.4‰ and $\delta^{13}C$ of 2.6‰. Plagioclase of the contemporaneous aplite yields $\delta^{18}O$ of 8.9‰. Epidote and calcite (n=3) from the epidote-calcite-zoisite alteration zone yield variable isotopic compositions, indicating local disequilibrium. The $\delta^{18}O$ of epidote ranges between -1.2 and 2.8‰. Calcite has $\delta^{18}O$ of 5.2-7.7‰ and $\delta^{13}C$ between -7.0 and -9.4‰. Meaningful equilibrium temperatures are at ~250°C for this hydrothermal overprint.

## 6 Discussion and interpretation

The stable isotope data of the auriferous stage of the Nalunaq gold deposit are typical of orogenic gold deposits (McCuaig and Kerrich 1998; Ridley and Diamond 2000). Assuming temperatures of ~500°C for the auriferous stage (this paper; Bell et al. 2017b), both, quartz and biotite (Bottinga and Javoy 1975; Zheng 1993) indicate $\delta^{18}O$ of the water component of the hydrothermal fluid of ~10‰. This is in the general range of orogenic gold deposits ($\delta^{18}O$=4-15‰) and consistent with the observation that $\delta^{18}O$ increases with increasing temperature of hydrothermal mineralization in orogenic gold deposits (Ho et al. 1992). The $\delta D$ of the water component of the hydrothermal fluid estimated from biotite compositions (Suzuoki and Epstein 1976) is -33‰ and within the typical range for orogenic gold ($\delta D$=-80 to -5‰). Also $\delta^{34}S$ of pyrrhotite overlaps with the typical range for orogenic gold deposits of -3 to +9‰ (McCuaig and Kerrich 1998). Sulfur isotopes lack evidence for mass-independent fractionation, indicating a Paleoproterozoic source. The stable isotope systematics of the auriferous stage indicate a metamorphic fluid that formed during metamorphism of the Paleoproterozoic terrane. In particular, oxygen isotopes are heavier than typical primary magmatic fluids. The $\delta D$ values may be influenced by fractionation during phase separation in the fluid during the mineralization stage (Hoefs 2015).

Estimating the isotopy of water in equilibrium with the pre-gold alteration assemblage (Zheng 1993) yields $\delta^{18}O$ of ~10‰. A fluid of such an isotopic composition is also in equilibrium with the host rock amphibolite, which is isotopically heavier than similar rocks (Hoefs 2015). This indicates pervasive hydrothermal alteration of the rocks at Nalunaq during the peak metamorphic stage. Hydrothermal gold mineralization has a similar oxygen isotope composition, which is either, explained by continuous evolution from the early hydrothermal stage or by total equilibration of the auriferous hydrothermal fluid. Calcite of the post-gold mineralization calcite-titanite alteration zone is also in equilibrium with $\delta^{18}O$ of ~10‰, indicating hydrothermal alteration at Nalunaq with metamorphic fluid(s) at ca. 1785-1765 Ma. In contrast, plagioclase from the ca. 1765 Ma aplite dyke is in equilibrium with typical values for primary magmatic waters (Hoefs 2015) that are too low to be in equilibrium with the hydrothermal assemblages, indicating only minor or no magmatic influence on the regional hydrothermal evolution.

Stable isotope systematics of the ca. 1745 Ma alteration stage yield $\delta^{18}O$ of the water component of ~0‰ and $\delta^{13}C$ of -6.7‰ (Chacko et al. 2001). Although this alteration stage is contemporaneous with the Ilua Plutonic Suite, these values are outside the typical field of primary magmatic water. They are consistent with the composition of meteoric water and atmospheric $CO_2$ (Hoefs 2015), indicating the

development of hydrothermal cells of meteoric fluids triggered by the granite intrusions. The Ilua Plutonic Suite is late orogenic, which is consistent with the lower-greenschist facies conditions of the contemporaneous hydrothermal alteration system and the meteoric nature of the fluids. This indicates exhumation of the auriferous terrane to shallow crustal levels by ca. 1745 Ma and a complete change of the hydrothermal system from metamorphic to meteoric fluids.

We can show by careful petrography and fieldwork that the hydrothermal evolution at Nalunaq was complex involving both, metamorphic and meteoric fluids. Starting with peak metamorphism, overprint by metamorphic fluids derived from Paleoproterozoic rocks was accompanied by cooling from ~650 to ~500°C. It is likely that economic gold mineralization was controlled by focusing of fluids into progressively developed discrete shear zones during the retrograde tectonic exhumation. A drastic change of the hydrothermal system to meteoric waters occurs ≥20 m.y. after gold mineralization, when the terrane was at shallow crustal levels and late-orogenic granites intruded the terrane.

## References


Bauer K, Vennemann T (2014) Analytical methods for the measurement of hydrogen isotope composition and water content in clay minerals by TC/EA. Chemical Geology 363:229-240.

Beaudoin G, Pitre D (2005) Stable isotope geochemistry of the Archean Val-d'Or (Canada) orogenic gold vein field. Mineralium Deposita 40:59-75.

Bell R-B, Kolb J, Waight TE (2017a) Assessment of lithological, geochemical and structural controls on gold distribution in the Nalunaq gold deposit, South Greenland using three-dimensional implicit modelling In: Gessner K, Blenkinsop TG, Sorjonen-Ward P (eds) Characterization of Ore-Forming Systems from Geological, Geochemical and Geophysical Studies. Geological Society Special Publications, London, pp 385-405.

Bell R-B, Kolb J, Waight TE, Bagas L, Thomsen TB (2017b) A Palaeoproterozoic multi-stage hydrothermal alteration system at Nalunaq gold deposit, South Greenland. Mineralium Deposita 52:383-404. doi: doi:10.1007/s00126-016-0667-7.

Bottinga Y, Javoy M (1975) Oxygen isotope partitioning among minerals and triplets in igneous and metamorphic rocks. Reviews of geophysics and Space Physics 13:401-418.

Chacko T, Cole DR, Horita J (2001) Equilibrium oxygen, hydrogen and carbon isotope fractionation factors applicable to geologic systems In: Valley JW, Cole DR (eds) Stable Isotope Geochemistry. Reviews in Mineralogy and Geochemistry, Mineralogical Society of America, pp 1-82.

Ding T, Valkiers S, Kipphardt H, de Bievre P, Taylor PDB, Gonfiantini R, Krouse HR (2001) Calibrated sulfur isotope abundance ratios of three IAEA sulfur isotope reference materials and V-CDT with a reassessment of the atomic weight of sulfur. Geochimica Cosmochimica Acta 65:2433-2437.

Farquhar J, Cliff J, Zerkle AL, Kamyshny A, Poulton SW, Claire M, Adams D, Harms B (2013) Pathways for Neoarchean pyrite formation constrained by mass-independent sulfur isotopes. Proceedings of the National Academy of Sciences 110:17638-17643. doi: 10.1073/pnas.1218851110.

Garde AA, Hamilton MA, Chadwick B, Grocott J, McCaffrey KJW (2002) The Ketilidian orogen of South Greenland: geochronology, tectonics, magmatism, and fore-arc accretion during Palaeoproterozoic oblique convergence. Canadian Journal of Earth Sciences 39:765-793.

Ho SE, Groves DI, McNaughton NJ, Mikucki EJ (1992) The source of ore fluids and solutes in Archean lode gold deposits of Western Australia. Journal of Volcanology and Geothermal Research 50:173-196.

Hoefs J (2015) Stable Isotope Geochemistry. Springer, Heidelberg.

Kaltoft K, Schlatter DM, Kludt L (2000) Geology and genesis of Nalunaq Palaeoproterozoic shear zone-hosted gold deposit, South Grenland. Transactions of the Institution of Mining and Metallurgy (Section B: Applied Earth Sciences) 109:B23-B33.

LaFlamme C, Martin L, Jeon H, Reddy SM, Selvaraja V, Caruso S, Bui TH, Roberts MP, Voute F, Hagemann S, Wacey D, Littman S, Wing B, Fiorentini M, Kilburn MR (2016) In situ multiple sulfur isotope analysis by SIMS of pyrite, chalcopyrite, pyrrhotite, and pentlandite to refine magmatic ore genetic models. Chemical Geology 444:1-15. doi: https://doi.org/10.1016/j.chemgeo.2016.09.032.

McCuaig TC, Kerrich R (1998) P-T-t deformation fluid characteristics of lode-gold deposits: evidence from alteration systematics. Ore Geology Reviews 12:381-453.

Mueller WU, Dostal J, Stendal H (2002) Inferred Palaeoproterozoic arc rifting along a consuming plate margin: insights from the stratigraphy, volcanology and geochemistry of the Kangerluluk sequence, southeast Greenland. International Journal of Earth Sciences vol.91:209-230.

Ohmoto H, Watanabe Y, Ikemi, Poulsen SR, Taylor BE (2006) Sulphur isotope evidence for an oxic Archaean atmosphere. Nature Letters 442:908-911.

Ridley JR, Diamond LW (2000) Fluid chemistry of orogenic lode gold deposits and implications for genetic models In: Hagemann S, Brown PE (eds) Gold in 2000. Reviews in Economic Geology, pp 141-162.

Sharp ZD (1990) A laser-based microanalytical method for the in-situ determination of oxygen isotope ratios of silicates and oxides. Geochimica et Cosmochimica Acta 54:1353-1357.

Sharp ZD, Atudorei V, Durakiewicz T (2001) A rapid method for determining the hydrogen and oxygen isotope ratios from water and solid hydrous substances. Chemical Geology 178:197-210.

Spötl C, Vennemann TW (2003) Continuous-flow IRMS analysis of carbonate minerals. Rapid Communications in Mass Spectrometry 17:1004-1006.

Steenfelt A, Kolb J, Thrane K (2016) Metallogeny of South Greenland: a review of geological evolution, mineral occurrences and geochemical exploration data. Ore Geology Reviews 77:194-245.

Suzuoki T, Epstein S (1976) Hydrogen isotope fractionation between OH-bearing minerals and water. Geochimica et Cosmochimica Acta 40:1229-1240.

Vennemann TW, Morlok A, von Engelhardt WE, Kyser TK (2001) Stable isotope composition of impact glasses from the Nördlinger Ries impact crater, Germany. Geochimica et Cosmochimica Acta 65:1325-1336.

Zheng Y-F (1993) Calculation of oxygen isotope fractionation in anhydrous silicate minerals. Geochimica et Cosmochimica Acta 57:1079-1091.

# Constraints on the Genesis of Au Veins in Interior Alaska: Evidence from Geochronology and Vein Textures

**Douglas C Kreiner[1], William Thompson[2], Jonathan S Caine[3], Ashleigh Ball[4], Christopher Holm-Denoma[3], Paul O'Sullivan[5], Holly Stein[6,7]**

*[1]U.S. Geological Survey, Anchorage, United States, [2]Northern Star Resources, Pogo, United States, [3]U.S. Geological Survey, Denver, United States, [4]Northern Star Resources, Perth, Australia, [5]GeoSep Services, Moscow, United States, [6]AIRIE Program, Fort Collins, United States, [7]University of Oslo, Oslo, Norway*

**Abstract.** Genesis of Au-bearing, low sulfide quartz veins in the Pogo and Tibbs Creek regions of interior Alaska remain enigmatic. New geochronology of igneous and mineralization phases indicates that gold veins post-date regional metamorphism. Re-Os geochronology on arsenopyrite coeval with gold constrains mineralization to ca. 105 Ma, during a magmatic lull. LA-ICP-MS U/Pb zircon constrains a pre-mineral peraluminous granitic event at ca. 114-110 Ma and a post-mineral dioritic event at ca. 99-93 Ma. Petrographic observations of veins show multiple stages of Au-Bi-Te(-As) mineralization in quartz dominant veins. Veins textures are diverse with early, generally barren, plasticly deformed quartz, later granular quartz, and multiple styles of brecciation. The latest event is characterized by bladed carbonate-euhedral quartz veins, indicating boiling and shallow crustal levels of formation. These observations are inconsistent with traditional orogenic and intrusion-related models and require a new genetic model for interior Alaska veins.

## 1 Introduction

Gold-quartz vein deposits in the Pogo-Tibbs region include the 8 Moz Pogo gold district, including the newly discovered 1 Moz Goodpaster deposit (Northern Star Resources, 2022). Active exploration along a 50 km trend is focused on defining additional resources. Veins are hosted in regionally metamorphosed gneiss and schist intruded by pulses of Cretaceous granitoids.

Previous estimates on the age of mineralization at Pogo are based on a single ~104 Ma molybdenite Re-Os date (Selby et al. 2002). Broadly coeval magmatism documented between 107-105 Ma (Day et al. 2003; Dilworth et al. 2007) in the region has led to the hypothesis that the veins are magmatic hydrothermal in origin. However, molybdenite is not coeval with gold in the veins – and igneous zircon crystallization ages are not well documented. Others have inferred the veins are orogenic, forming at 7-10 km depth (Dilworth, 2003). This study applies new U-Pb zircon crystallization ages of igneous phases with Re-Os geochronology on arsenopyrite coeval with gold in multiple paragenetic events to constrain the age of ore formation. Detailed petrographic observations of vein textures and mineralogy and geochemistry constrain the structural styles and depth of vein formation. New data suggest no temporal relation to magmatism, and shallow depths of ore formation evidenced by boiling textures require a new genetic model that changes the paradigm for new discovery in the region.

## 2 Geologic Setting of Vein Deposits

Host rocks to the veins include biotite-quartz-feldspar Devonian orthogneiss and Mississippian paragneiss of the Lake George assemblage of Foster et al. (1994) of parautochthonous North American basement (Dusel-Bacon et al. 2006; Fig. 1). Devonian and Mississippian gneisses underwent regional amphibolite facies metamorphism in the Cretaceous (Foster et al., 1994).

Deformation across the region is poorly constrained, with some evidence for mid Paleozoic, Jurassic, and Early Cretaceous pulses of contraction and extension (Dusel-Bacon et al. 2006). Plastic regime contractional deformation ceased by ca. 115 Ma (Day et al., 2003). During the formation of veins, the region is interpreted to have been undergoing extension (Rhys et al. 2003).

Felsic and intermediate plutonic rocks intruded episodically from the Permian, through early Tertiary. In the Pogo and Tibbs Creek region. Mid Cretaceous (114-90 Ma) felsic plutonism is predominant, with sparse early Tertiary felsic intrusions in the district.

## 3 Igneous Geochronology and chemistry

### 3.1 U-Pb zircon geochronology

Twelve new LA-ICPMS zircon U-Pb dates combined with existing geochronology highlight three major pulses of mid Cretaceous magmatism. Early unfoliated to weakly foliated and recrystallized two-mica and garnet-bearing granite and granodiorite yield U-Pb zircon crystallization ages of ca. 113-108 Ma. An intermediate age suite, characterized by tonalite to granodiorite, yields U-Pb monazite, zircon, and SHRIMP-RG zircon crystallization ages of ca. 107-105 Ma (Day et al., 2003; Dilworth et al., 2007). The youngest suite is characterized by granodiorite to quartz diorite with LA-ICPMS U-Pb zircon crystallization ages of ca. 98-93 Ma.

### 3.2 Igneous geochemistry

Secular trends in the geochemistry are pronounced. Early granite is strongly peraluminous and straddles the syn-collisional to volcanic arc fields on a Y+Nb and Yb+Ta versus Rb Pearce plot. Intermediate tonalite is characterized by weakly peraluminous to

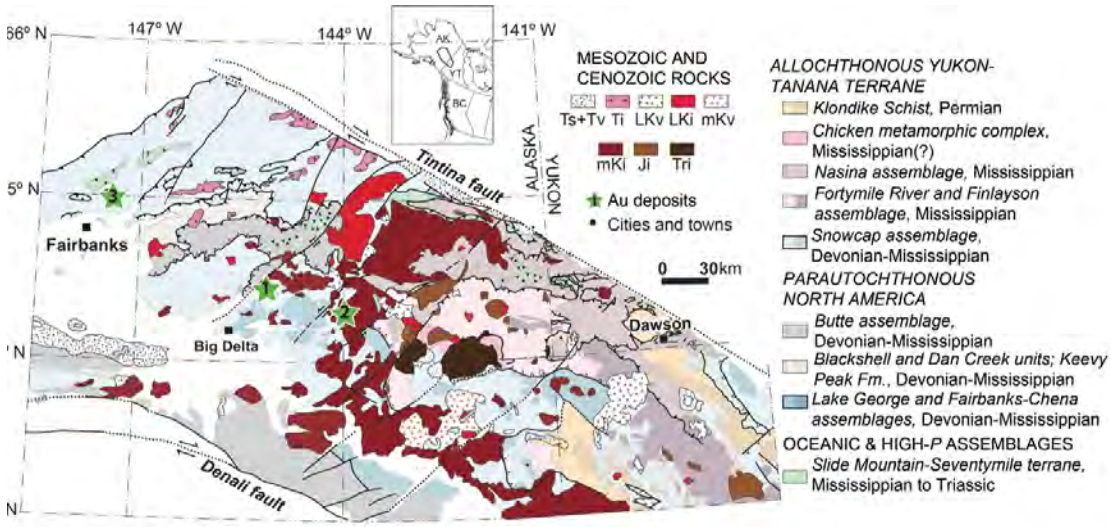


**Figure 1.** Geologic map of eastern interior Alaska. Gold deposits as green stars: 1: Pogo; 2: Tibbs Creek; 3: Fort Knox. Map modified and nomenclature of all units from Dusel-Bacon et al. (2006).

metaluminous phases. Late diorite to granodiorite plot in the volcanic arc field on the Pearce plot.

Zircon trace elements analyzed on the SHRIMP-RG in all igneous suites exhibit steep light and flat middle to heavy REE patterns. These patterns are consistent with shallow non-garnet residual sources. Ti-in-zircon calculations indicate metaluminous diorite crystallized at higher temperatures than peraluminous granites. All suites exhibit strong negative Eu anomalies with weak to absent Ce anomalies and are strongly depleted in Eu and Ce compared to typical intermediate arcs.

## 4 Vein Textures

Veins in the Pogo district are quartz dominant; sulfide minerals are sparse, commonly less than 1% of veins. Within individual veins, massive arsenopyrite or pyrrhotite-pyrite occur. Veins exhibit diverse textures ranging from massive quartz with thicknesses ranging from 10s of cms to >10m to pervasive breccias. Quartz is described as milky white and massive, sugary light to dark grey, and granular milky white to grey or brecciated.

### 4.1 Quartz and carbonate vein textures

Early quartz is recrystallized and is preserved as clasts within brecciated quartz veins, or as massive interlocking quartz veins. Quartz veins are commonly brecciated, cemented by younger generations of granular quartz(±sulfides or sericite and carbonates), sulfides with minor quartz, or extremely fine-grained dark grey cataclastic material. Megascopic breccia textures are often obscured but readily apparent in thin sections.

Wide zones of vein quartz are cut by thin arsenopyrite, pyrite, or pyrrhotite dominant veinlets ranging from mm scale to cm scale. Other crosscutting veinlets include mm-scale sulfide-poor quartz (±sericite) and carbonate assemblages. Sulfide ubiquitously post-dates early quartz.

Brecciation is common across both the Pogo and Tibbs Creek occurrences. Hydrothermal breccias are characterized by angular to sub-angular clasts cemented by varying amounts of quartz, sulfide, carbonate, and sericite (Fig. 2a). Clasts are predominantly broken quartz fragments or polygranular quartz vein. Clasts locally exhibit superimposed secondary strain textures. Sulfide clasts observed are more commonly associated with cataclasite breccias. Cataclasite consists of milled subrounded to rounded clasts commonly composed of arsenopyrite and pyrite cemented by dark, very fine-grained cataclasite that often contains minor arsenopyrite and pyrite (Fig. 2b).

Bladed carbonate veins with terminated euhedral quartz crystals (Fig. 2c) and local open space in the vein are ubiquitous throughout the mineralized occurrences. Carbonates are dolomite throughout the Pogo veins, but pure calcite in the Tibbs Creek occurrences. Terminated quartz crystals show strong growth zoning around the crystal faces demarcated by abundant fluid inclusions (Fig. 2c) with coexisting liquid-vapor and vapor rich assemblages. Associated with the bladed carbonates are open space veins, and strongly silicified sinter-like replacement textures.

### 4.2 Sulfide mineral textures and paragenesis

Sulfide assemblages in the veins are characterized by abundant pyrite, pyrrhotite, and arsenopyrite with less abundant Au, bismuthinite, native bismuth, loellingite and Bi-telluride. Sulfides can be massive – particularly pyrite-pyrrhotite and arsenopyrite – or disseminated. Where massive, grain size can range from mm- to cm-scale. Bismuthinite, native bismuth, and tellurides are most common as inclusions within arsenopyrite but also occur as principal phases in quartz veins.

Gold is strongly correlated with bismuth and tellurium and shows little correlation with arsenic or antimony. Gold occurs as inclusions within As, Bi,

and Te sulfides and sulfosalts, is intergrown with sulfides, or as free gold interstitial to quartz grains.

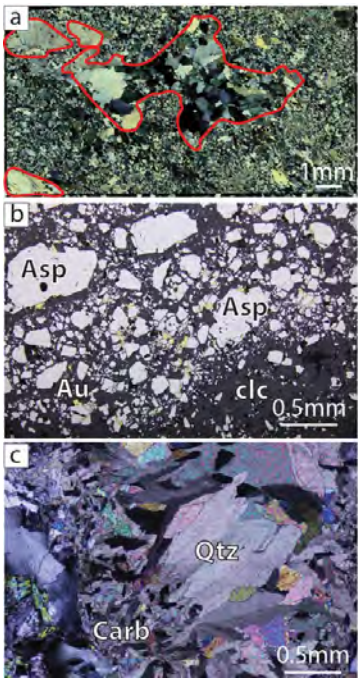


**Figure 2.** Vein textures. A) hydrothermal breccia with early quartz vein clasts (red) cemented by later granular quartz. B) milled arsenopyrite (Asp) clasts cemented by cataclasite (clc) matrix with gold (Au) growing on clast margins. C) terminated quartz (Qtz) crystals with inclusion rich growth zones and bladed carbonate (Carb).

Gold is present in multiple paragenetic stages in the veins. Early Au-bearing quartz clasts (Fig. 3) represent the earliest stages of gold. Subsequent generations of gold are recorded in quartz-gold, or arsenopyrite-gold matrix or veinlets. Gold is also found in syn- mineral cataclastic breccias (Fig. 3) and locally post-dates the milling event, where it occurs as rims or patchy cement between arsenopyrite grains (Fig. 2b). Sulfide events ubiquitously cut earlier quartz, and are commonly characterized by Au-Bi, or Au-Te assemblages. Gold-bearing carbonate and bladed carbonate-quartz veins that cut the breccias record the latest gold-bearing events.

## 5 Geochronology of Mineralization

A Re-Os NTIMS age of ca. 104 Ma was determined for molybdenite at the Liese deposit (Selby et al. 2002). New Re-Os NTIMS dating of arsenopyrite coeval with multiple gold-bearing assemblages in the paragenesis at Pogo yields ages ranging from ca. 106-103 Ma for Au mineralization. At Tibbs Creek, direct dating of mineralization via Re-Os is in progress, though veins at Blue Lead and Wolverine, are hosted within the 108-104 Ma granite indicating a similar age of veins across the region.

Preliminary Lu-Hf dating via LA-ICPMS of bladed carbonate vein assemblages that occur within the mineralized zones, and co-precipitate with quartz yield Mesozoic isochron ages of 138 and 110.4 Ma.

**Figure 3.** Gold generations at Pogo. 1: early quartz-gold clast cemented by 2: gold-arsenopyrite cataclasite. Events 1 and 2 are cut by 3: second generation of gold-bearing cataclasite that truncates a carbonate vein (blue outline). The latest generation is 3/4: quartz-gold vein.

However, the 2-sigma uncertainties are large, ca. 45 and 53 Ma, respectively. Despite the significant uncertainties, interpreted ages are Mesozoic, and based on relative timing constraints, places the bladed-carbonate event coeval with gold mineralization.

Orthogneiss adjacent to a diorite pluton ~20km east of Pogo hosts a ca. 95 Ma (Re-Os) molybdenite bearing quartz vein that distinctly lacks Au, As, Bi, Te (Dave Selby, pers. communication; Fig. 4).

## 6 Discussion

Regional synthesis of the igneous geochronology and mineralization ages indicates there is little temporal overlap between Au mineralization and mid Cretaceous magmatism (Fig. 4). Dilworth et al. (2007) documents the ca. 107-106 Ma tonalite suite in a series of small stocks or dikes adjacent to the deposit. This event ceased prior to mineralization (Fig. 4). Tonalite of this age is unmineralized and rarely altered. At Tibbs Creek, gold-bearing quartz veins are locally hosted within the largely unaltered ~108-104 Ma Black Mountain granite of Day et al. (2003). Mapping and field observations indicate sparse alteration of igneous phases younger than 110 Ma, no zoning of hydrothermal assemblages around igneous bodies, and a distinct lack of magmatic hydrothermal alteration. Despite the close temporal relations between emplacement and vein formation, a direct link has not been identified.

Previous studies of Al-in-hornblende barometry from granitoids and fluid inclusions have placed inferred depths of vein formation and gold mineralization at ~5-9km (Dilworth 2003). New observations of vein textures during our study suggest at least four generations of Au mineralization in highly brecciated, cyclical depositional events. Recognition of Au-bearing calcite and associated bladed carbonate-quartz veins with coeval liquid-vapor and vapor rich fluid inclusions across the Pogo and Tibbs Creek occurrences suggest boiling occurred in the veins. Geochronology of bladed carbonate indicates boiling events occurred in the mid Cretaceous. Given the Re-Os arsenopyrite ages in multiple gold-

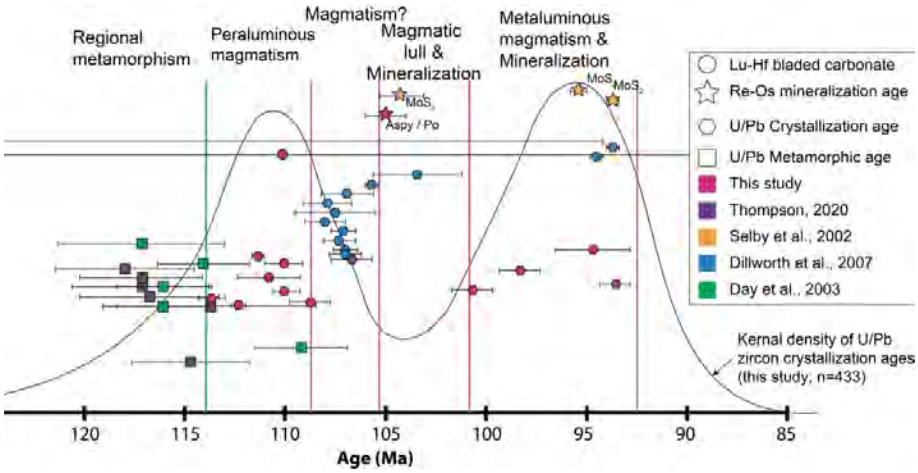


**Figure 4.** Geochronology summary for the Pogo deposit. Kernel density plot is inclusive of geochronology from this study.

bearing paragenetic stages plot within a span of ~2 My, boiling likely occurred at the same time. These constraints, combined with the observations of cyclic brittle deformation textures in breccias, place the depth of formation for Au-As-Bi veins at <2 km.

Models for typical orogenic gold veins suggest the depth of formation for Au-As mineralization occurs at depths of >6 km, and Hg-Sb assemblages are predominant at shallow depths (Groves et al., 1998), the latter is distinctly lacking in interior Alaska. Therefore, we propose a hybrid model for the formation of Au-As-Bi quartz veins in eastern interior Alaska. Our model invokes the circulation of shallow meteoric waters that mix with $CO_2$ derived from prograde metamorphic reactions percolating upwards. Metals were stripped from host rocks by the bicarbonate fluid along flow paths and concentrated in upwelling zones where boiling plays a role in deposition of Au, As, and Bi.

## Conclusions

New igneous and mineralization geochronology indicate that Au-bearing quartz veins formed at ca. 105 Ma. during a magmatic lull between peraluminous magmatism from ca. 114-110, and metaluminous dioritic magmatism at ca 107-106, and 99-93 Ma. Textural evidence of boiling suggests shallow levels of ore formation. These new observations in the region are incompatible with traditional models invoked for the formation of Au-veins and require a new genetic model. Shallowly circulating fluids stripped metals from wall rocks along the flow path, were concentrated in permeable structural zones where boiling played an important role for deposition of Au, As, Bi, and Te in the veins.

## Acknowledgements

The authors would like to thank Northern Star Resources Pogo team for continued support of our research. Any use of trade, firm, or product names is for descriptive purposes only and does not imply endorsement by the U.S. Government.

## References

Day WC, Aleinikoff, JN, Roberts P, Smith M, Gamble, BM, Henning, MW, Gough, LP, and Morath, LC (2003) Geologic map of the Big Delta B–2 quadrangle, eastcentral Alaska: U.S. Geological Survey Geologic Investigations Series I–2788.

Dilworth, KM, 2003, Geological setting, nature, and evolution of reduced intrusions and gold bearing quartz veins of the 4021 prospect, Goodpaster District, East-Central Alaska: University of British Columbia, unpublished MS thesis, 192 p.

Dilworth K, Mortensen JK, Ebert S, Tosdal RM, Smith MT and Roberts P (2007) Cretaceous reduced granitoids in the Goodpaster mining district, east-central Alaska. Can J Ear Sci 44:1347–1373.

Dusel-Bacon C, Hopkins MJ, Mortensen JK, Dashevsky SS, Bressler JR and Day WD (2006) Paleozoic tectonic and metallogenic evolution of the pericratonic rocks of east-central Alaska and adjacent Yukon: in Colpron M and Nelson JL (eds), Paleozoic Evolution and Metallogeny of Pericratonic Terranes at the Ancient Pacific Margin of North America, Canadian and Alaskan Cordillera: Geological Society of Canada Special Paper 45: 25-74.

Groves DI, Goldfarb RJ, Gebre-Mariam M, Hagemann SG, Robert F (1998) Orogenic gold deposits: A proposed classification in the context of their crustal distribution and relationship to other gold deposit types. Ore Geol Rev 13:7–27

Foster HL, Keith TE, and Menzie WD (1994) Geology of the Yukon-Tanana terrane of east-central Alaska. in The Geology of Alaska. edited Plafker G and Berg HC. Geol. Soc. Amer. Boulder CO, The Geology of North America, G-1:205-240.

Northern Star Resources (2022) https://www.nsrltd.com/investor-and-media/asx-announcements/2022/may/resources,-reserves-and-exploration-update. Accessed February 8, 2023.

Rhys D, DiMarchi J, Smith M, Friesen R, Rombach C (2003) Structural setting, style, and timing of vein-hosted gold mineralization at the Pogo deposit, east central Alaska. Miner Deposita 38:863–875

Selby D, Creaser RA, Hart CJ, Rombach CS, Thompson JFH, Smith MT, et al. (2002) Timing of sulphide and gold mineralization at Fort Knox and Pogo gold deposits, Tintina Gold Belt: evidence from Re-Os molybdenite dates for distinct gold mineralization episodes. Geology 30:791-794.

Thompson W. (2020) Geochemical, spatial, and temporal relationships of the intrusives and meta-intrusives of the Pogo deposit, Eastern interior AK. University of Alaska, Fairbanks unpub. MS Thesis, 146p

# Fluid evolution and carbon-gold systematics at the Fairview Mine, Barberton Greenstone Belt, South Africa

**Rutger La Cock[1], Bjorn von der Heyden[1], Long Li[2], Yifan Du[2], Matthew Steele-MacInnes[2]**
*[1]Department of Earth Sciences, Stellenbosch University, South Africa*
*[2]Department of Earth & Atmospheric Sciences, University of Alberta, Canada*

**Abstract.** The Fairview mine is one of the most profitable gold mines within the Barberton Greenstone Belt (BGB). Recent work has centred around the structural aspects controlling mineralisation, but little work has been done regarding the chemical controls on mineralisation. With the help of scanning electron microscopy (SEM) and laser ablation inductively coupled plasma mass spectrometry (LA-ICP-MS), this research shows how the variation in carbonate species and sulphide trace element composition can be utilized to track different fluid flow events. Field evidence suggests that graphite has an important role to play in gold deposition as it is frequently found within high-grade shear zones. This graphite is shown to be nanocrystalline in size and have a high degree of structural disorder. Geothermometry calculations based off Raman spectra of graphite show that shear zones were subjected to maximum temperatures of around 400 ºC. Carbon isotope signatures provide insights into the potential source of ore-fluids which led to mineralisation at Fairview. These findings have significant implications for ore-forming models pertaining to Archaean greenstone belts.

## 1 Introduction

The Barberton Greenstone Belt (Figure 1) represents one of the oldest and best-preserved fragments of continental crust on Earth (Brandl et al. 2006). Like many other greenstone belts, the BGB hosts a number of economically significant gold deposits, with over 350 tons of gold extracted from the belt since 1882 (Agangi et al. 2019). Recent studies have focussed on characterising the structural controls on gold mineralisation within the well-endowed, Sheba-Fairview Complex (Gloyn-Jones & Kisters 2018, 2019; Pintos Cerda et al. 2020; Jones & Kisters 2022). However, the chemical controls on mineralisation are still poorly understood.

To understand the chemical controls on mineralisation it is important to know how the auriferous fluid may have evolved over time. As there is evidence for multiple phases of fluid flow at Fairview (Altigani et al. 2016), SEM and LA-ICP-MS were used to differentiate between temporally separate fluids based on sulphide chemistry. These methods also provided insights into ore textures and mineral composition, allowing for a detailed characterisation of the Fairview gold ore.

A connection between carbon and mineral deposits has long been recognised (Agricola 1556). Specific links between carbon and gold have been a subject of much debate with some authors suggesting that they play a crucial role in the formation of high-grade, orogenic gold deposits (e.g., Gaboury 2021). Gloyn-Jones & Kisters (2019) highlight the importance of carbon in the form of graphite at Fairview and its role in strain localisation.

However, the role of carbon in deposit formation has not been fully assessed. As there is a strong association between Au-bearing sulphides and graphite, the present research focussed strongly on this association. Raman spectroscopy was used to classify the nature of the graphite found in and around high-grade shear zones at Fairview. Carbon isotopes were measured for both carbonates and graphite and serves to provide information on the source of auriferous fluids, the temperatures reached in shear zones and degree of fluid-rock interaction. Knowing how carbon contributes to gold deposition at Fairview will help geologists discern whether or not graphite is a useful parameter to consider during exploration, for example, by utilising graphite's electrically conductive geophysical response as an exploration guide.

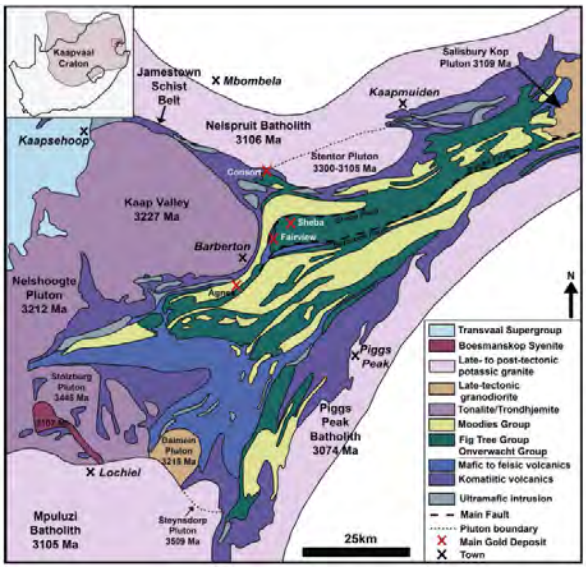


**Figure 15**: Barberton Greenstone Belt along with the position of economically significant gold mines. The Sheba-Fairview Complex is located within an arcuate corridor in the NW portion of the belt (map taken from Jones 2021, initially adapted from Anhaeusser, 2016). The ages of plutons surrounding the belt are after Robb (2006).

## 2 Methodology

### 2.1 Ore classification

Ore classification comprised of reflected/transmitted light microscopy, SEM and LA-ICP-MS, all of which were done at Stellenbosch University at the Central Analytical Facility (CAF). Over 20 thin-sections were available from previous studies for transmitted light

microscopy. Ten thick-sections were prepared for reflected light microscopy with five of these being used for subsequent SEM and LA-ICP-MS.

SEM data were collected using a MERLIN Zeiss with an Energy Dispersive X-ray Spectrometer (EDX) being used to determine major oxide weight percentages and element percentages on each mineral. The beam energy for EDS was set to 20 kV, with a current between 19 and 21 µA, and a set working distance of 8 mm. Standards were set according to the elements expected to be seen in the different sulphide and carbonate phases.

LA-ICP-MS spot analyses were used to decipher whether there were any significant chemical differences between the two pyrite generations. R software was used to generate box plots comparing the trace element distribution between the two different pyrite generations. Line scan data were then collected to augment the spot analyses as line scan data is more effective in detecting uneven trace element distributions within solid phases (Sanborn & Kelmer 2003). The following elements were tested for during LA-ICP-MS analysis: $^{34}$S, $^{47}$Ti, $^{51}$V, $^{53}$Cr, $^{55}$Mn, $^{57}$Fe, $^{59}$Co, $^{60}$Ni, $^{63}$Cu, $^{66}$Zn, $^{75}$As, $^{77}$Se, $^{95}$Mo, $^{107}$Ag, $^{111}$Cd, $^{115}$In, $^{118}$Sn, $^{121}$Sb, $^{125}$Te, $^{182}$W, $^{197}$Au, $^{202}$Hg, $^{205}$Tl, $^{208}$Pb and $^{209}$Bi. A spot size of 20 µm was used with laser energy and frequency at 3 J/cm$^2$ and 6 Hz respectively.

### 2.2 Raman spectroscopy

Raman spectroscopy data were collected from graphite samples using a HORIBA Scientific LabRAM HR Evolution confocal Raman Spectrometer at the University of Alberta, Canada. This spectrometer is equipped with a 532 nm wide laser and an Olympus MPLN 10 x objective. Laser power was set to 100 % (i.e., no neutral density filter) with the confocal hole size being 200 µm. Acquisition time was set to 40 seconds with three accumulations run per sample. The spectral range over which data was collected was 1000-1800 cm$^{-1}$. Raman spectra were fitted using the open-source software by Fityk (Wojdyr 2010).

### 2.3 Carbon isotopes

Carbon isotope analyses were conducted at the University of Alberta, Canada, on three mineral separates: graphite, carbonates and black quartz (which contains very fine-grained graphite). Slightly different protocols were used depending on the mineral separate. The generated $CO_2$ gas is cryogenically purified and collected into a glass sampler and sent to a Thermo Scientific Delta V Plus isotope-ratio mass spectrometer for isotope measurements at a dual-inlet mode. Isotopic compositions were reported as δ notation relative to the Vienna PeeDee Belemnite standard for $\delta^{13}C$ and the Vienna Standard Mean Ocean Water for $\delta^{18}O$. The analytical uncertainty of 2σ (less than 0.2 ‰) is based on repeated analyses of international reference materials and laboratory internal standards.

## 3 Fairview gold ore and fluid evolution

The samples analysed during this study originate from the Main Reef Complex at the Fairview mine. Economically significant shear zones show a quartz-carbonate sulphide mineralogy (Gloyn-Jones & Kisters 2019). The major sulphides are pyrite and arsenopyrite, with pyrite having the strongest association with native gold. Two generations of pyrite were identified. The first generation of pyrite ($Py_1$) occurs as small (< 1 mm), independent, anhedral to subhedral grains or as cores to pyrite generation two ($Py_2$). $Py_2$ grains are large (up to 5 mm), euhedral, and occur as independent grains or as rims to $Py_1$. The LA-ICP-MS analyses served to differentiate between the two generations of pyrite, and thereby document how the ore fluid evolved over time. From the results of the spot analyses (Figure 2), the two generations of pyrite appear fairly similar in terms of their trace element composition. However, grain mapping of large, zoned, pyrite allows for easy discernment between the two pyrite generations (Figure 3). The trace element maps suggest that $Py_1$ formed from a single fluid flow event, whereas $Py_2$ formed during a later event which involved multiple pulses of fluids with slight variations in chemistry. The $Py_2$, which is most closely associated with free gold, shows significant elevations in nickel and arsenic.

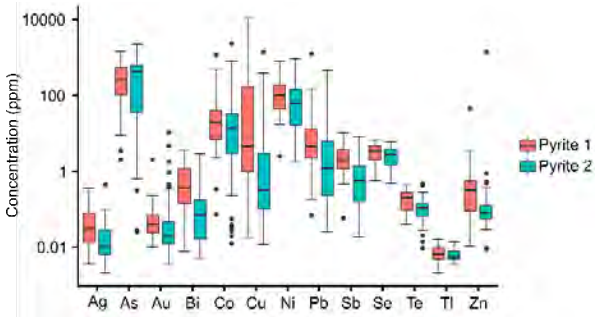


**Figure 16**: Box and whisker plot comparing the trace element composition of the two different pyrite generations (n = 76).

Changes in carbonate chemistry within shear zones at the Fairview mine document the changes in Ca/Fe/Mg concentrations of different fluids. Changes in carbonate speciation in shear zones is significant as it can influence desulphidation reactions (Goldfarb et al. 2005), which is a primary mechanism by which gold is deposited. When wall rocks contain initial molar ratios of Fe / (Fe + Mg) ≤ 0.5, nearly all Fe is incorporated into the magnesite-siderite series of carbonates. This prevents pyritization of Fe-bearing phases and thereby hinders gold deposition which takes place via desulphidation reactions.

At Fairview, carbonate species were used to track changes in fluid composition in terms of its major and minor elements whereas changes in trace element

compositions of ore fluids were traced using grain maps of zoned pyrite.

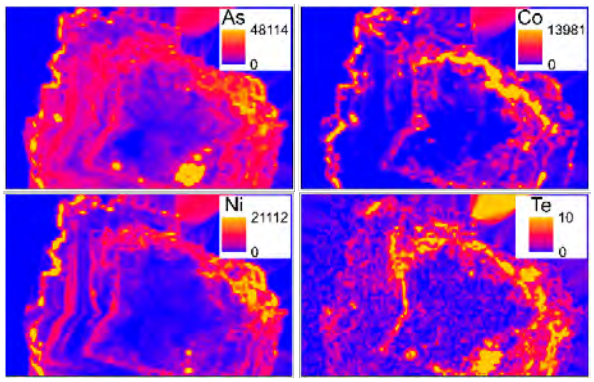


**Figure 17**: Trace element maps of a zoned pyrite grain illustrating the variability in trace element chemistry between $Py_1$ in the core and $Py_2$ towards the rim (concentrations are in parts per thousand).

## 4 Characterisation of graphite and C isotopes

Seven graphite samples from various levels of the Fairview mine were analysed using Raman spectroscopy. All samples exhibited a strong graphite peak (G band) and disorder peak (D band). The graphite peak wavelength ranged between 1560-1585 $cm^{-1}$ whilst the disorder peak wavelength ranged between 1335-1350 $cm^{-1}$. Based on the ratio of the peak intensities of the D and G bands, the graphite is interpreted to have a high degree of structural disorder. Tuinstra & Koenig (1970) pointed out the relationship between the ratio of peak intensities (D and G bands) and graphite crystal size. Graphite from Fairview is calculated to have an average crystal size of 16.34 nm. Geothermometry calculations based off the Raman spectra show that graphite experienced an average maximum temperature of 403 ºC (n = 21), which is slightly higher than the average temperature of 320 ºC experienced at the greenstone belt scale (Cloete 1999).

Carbon isotopes were measured primarily to gain insights into the source of the fluids, which formed Fairview's gold deposits. The average value for graphite found in shear zones is -21,7 ‰ and is similar to that of Fig Tree shales which have an average of -23,7 ‰ (Figure 4). This implies that the graphitic carbon found in shear zones may have a genetic relationship with the carbon in the Fig Tree shales, although an externally derived fluid with similar carbon isotopes signatures cannot be discounted. The C isotope signatures of the different carbonate minerals mostly fall within the expected range for carbonate carbon. Although most of the values lean to the boundary between sedimentary carbonate and the mantle range, they can be explained by metamorphic effect rather than involvement of mantle-derived fluids. These carbonates likely derived their carbon from decarbonation/dissolution reactions of pre-existing carbonate-bearing country rocks such as those studied by Toulkeridis et al. (1998). At this stage, the C isotope data on quartz appears to show a mixed signature and is, therefore, not considered a robust interpretation regarding fluid source, and more work is being done to understand the reason for this signature. Carbon isotope compositions of both graphite and carbonates seemingly argue in favour of the ore fluids being sourced from within the greenstone belt. Black shales of the Fig Tree group appear as a likely candidate for the source of auriferous fluids based on the similar isotope values of carbonaceous material in Fig Tree shales and graphite from shear zones. However, black shales from outside the greenstone belt may have similar C isotope signatures (Jaguin et al. 2014) and one can, therefore, not rule out the possibility that fluids were derived from an external subducting slab, outside the BGB.

As this research represents the first instance of carbon isotopes being run on individual carbonate minerals in Barberton, it is useful to look more closely at their C isotope signatures and assess whether they can serve as a tracer for fluid flow events. Slight variations can be seen in the different carbonate species (Fig.4); however, all fall within a fairly narrow range of 2.8 ‰. The minor variations in $\delta^{13}C$ values of different carbonates can be due to: 1) changes in oxygen fugacity and pH of the fluid, 2) variability of country rock, and 3) degree of fluid-rock interaction (Ohmoto, 1972; Sharp, 2007). Changes in $fO_2$ and pH can alter the $\delta^{13}C$ values of carbon species within the fluids which will impact the $\delta^{13}C$ composition of the carbonates formed from these fluids. Given that the individual carbonates examined in this study are frequently co-occurring, and that no major differences in isotope composition are seen between what are interpreted as temporally separate carbonates, it does not appear viable to utilize C isotopes as a tracer for different fluid pulses. More detailed investigations into carbonate growth textures may reopen the possibility of using C isotopes to trace fluid flow events.

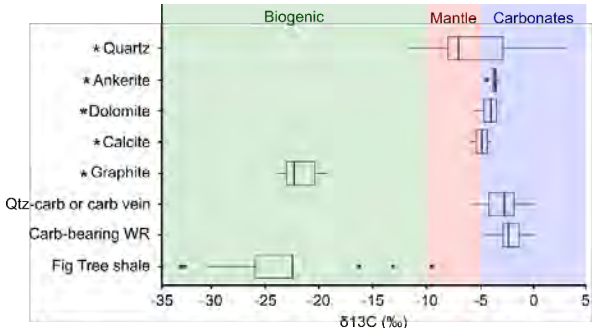


**Figure 18**: Compilation of carbon isotope work done in the BGB, those box plots marked with an asterisk indicates data which emulated from this study (existing data from Hayes et al. 1983; de Ronde et al. 1992; Strauss & Moore, 1992; de Ronde & Ebbesen 1996; Grassineau et al. 2006). The green, pink and blue background colours correspond to the different carbon sources of biogenic, mantle and carbonates respectively (ranges after Luque et al. 2012).

## 5 Conclusions

Through use of SEM and LA-ICP-MS it is possible to detect the changes in major, minor and trace compositions of the ore fluid and, thereby, understand how the fluid evolved over time. Nanocrystalline graphite within shear zones that is closely associated with Au-bearing sulphides has a high degree of structural disorder, with Raman geothermometry suggesting that it may have experienced temperatures of up to 400 ºC. Carbon isotope analyses suggest that the ore-forming fluids may have been derived from Fig Tree Group sedimentary rocks from within the greenstone belt. This research shows that carbon has an important role to play in forming high-grade gold deposits in greenstone belts. It is recommended that further investigations be made into the degree of interaction between nanocrystalline graphite and gold/sulphides.

## Acknowledgements

The authors' gratitude is extended towards the helpful staff at both Stellenbosch University and the University of Alberta who aided in various analyses. Thank you to the DSI-NRF CIMERA for their generous funding of this research project.

## References

Agangi A, Hofmann A, Eickmann B, Marine-Carbonne J (2019) Mesoarchaean Gold Mineralisation in the Barberton Greenstone Belt: A Review. (eds) The Archaean Geology of the Kaapvaal Craton, Southern Africa; Regional Geology Reviews. pp 171-184

Agricola G (1556) De re metallica (Hoover HC, Hoover LH trans., 1950), Dover Publications, New York.

Altigani MAH, Merkle RKW, Dixon RD (2016) Geochemical evidence of episodes of gold mineralisation in the Barberton Greenstone Belt, South Africa. Ore Geology Reviews. 75:186-205

Anhaeusser CR (2016) The Barberton-Makhonjwa mountainland - an ancient landscape yielding clues to the origin of the Earth and life. In: Anhaeusser CR, Viljoen MJ, Viljoen RP (ed) Africa's Top Geological Sites; Struik Nature, Cape Town. pp. 61-66

Brandl G, Cloete M, Anhaeusser CR (2006) Archaean Greenstone Belts. In: Johnson MR, Anhaeusser CR, Thomas RJ (ed) The Geology of South Africa; Geological Society of South Africa., Council for Geoscience, Pretoria. pp 9-56

Cloete M (1999) Aspects of volcanism and metamorphism of the Onverwacht Group lavas in the south-western portion of the Barberton greenstone belt. Geological Survey of South Africa Memoir. 84. 232.

de Ronde CEJ, Ebbesen TW (1996) 3.2 b.y. of organic compound formation near sea-floor hot springs. Geology. 24.9:791-794

de Ronde CEJ, Spooner ETC, de Wit MJ, Bray CJ (1992) Shear Zone-Related, Au Quartz Vein Deposits in the Barberton Greenstone Belt, South Africa: Field and Petrographic Characteristics, Fluid Properties, and Light Stable Isotope Geochemistry. Economic Geology. 87:366-402

Gaboury D (2021) The neglected Involvement of Organic Matter in Forming Large and Rich Hydrothermal Orogenic Gold Deposits. Geosciences. 11.344:1-13

Gloyn-Jones J, Kisters A (2018) Regional folding, low-angle thrusting and permeability networks: Structural controls of gold mineralization in the Hope reef at Fairview Mine, Barberton greenstone belt, South Africa. Ore Geology Reviews. pp 1-56

Gloyn-Jones J, Kisters A (2019) Ore-shoot formation in the Main Reef Complex of the Fairview Mine – multiphase gold mineralization during regional folding, Barberton Greenstone Belt, South Africa. Miner Deposita. 54.8:1157-1178

Goldfarb RJ, Baker T, Dubé B, Groves DI, Hart CJR, Gosselin P (2005) Distribution, Character, and Genesis of Gold Deposits in Metamorphic Terranes. In: Hedenquist JW, Thompson JFH, Goldfarb RJ, Richards JP (ed) Economic Geology 100th Anniversary Volume (1905-2005). pp 407-450

Grassineau NV, Abell P, Appel PWU, Lowry D, Nisbet EG (2006) Early life signatures in sulfur and carbon isotopes from Isua, Barberton, Wabigoon (Steep Rock), and Belingwe Greenstone Belts (3.8 to 2.7 Ga). Geological Society of America Memoirs. 198:33-52

Hayes JM, Kaplan IR, Wedeking KW (1983) Precambrian organic geochemistry: Preservation of the record. In: Schopf JW (ed) Earth's Earliest Biosphere: Its Origin and Evolution; Princeton University Press, New Jersey. pp 93-134

Jaguin J, Boulvais P, Boiron M-C, Poujol M, Gapais D, Ruffet G, Briant N (2014) Stable isotopes (O, C) and fluid inclusion study of quartz-carbonate veins from the antimony line, Murchison Greenstone Belt. American Journal of Science. 314:1140-1170

Jones C & Kisters A (2022) Regional and local controls of hydrothermal fluid flow and gold mineralization in the Sheba and Fairview mines, Barberton Greenstone Belt, South Africa. Ore Geology Reviews. 104805:1-20

Luque FJ, Crespo-Feo E, Barrenechea JF, Ortega L (2012) Carbon isotopes of graphite: Implications on fluid history. Geoscience Frontiers. 3.2:197-207

Ohmoto H (1972) Systematics of Sulfur and Carbon Isotopes in Hydrothermal Ore Deposits. Economic Geology. 67.5:551-578

Pintos Cerda LP, Jones C & Kisters A (2020) Multi-stage alteration, rheological switches and high-grade gold mineralization at Sheba Mine, Barberton Greenstone Belt, South Africa. Ore Geology Reviews. pp 1-73

Robb LJ, Brandl G, Anhaeusser CR, Poujol M (2006) Archaean granitoid intrusions. In: Johnson MR, Anhaeusser CR, Thomas RJ (ed) The Geology of South Africa; Geological Society of South Africa. Council for Geoscience, Pretoria. pp 57-94

Sanborn M, Telmer K (2003) The spatial resolution of LA-ICP-MS line scans across heterogeneous materials such as fish otoliths and zoned minerals. Journal of Analytical Atomic Spectrometry. 10:1231-1237

Sharp S (2007) Principles of Stable Isotope Geochemistry (2nd edition). Chapter 12: Metamorphic Petrology. Pearson, Michigan.

Strauss H, Moore TB (1992) Abundances and Isotopic Compositions of Carbon and Sulfur Species in Whole Rock and Kerogen Samples. In: Schopf JW, Klein C (ed) The Proterozoic Biosphere: A Multidisciplinary Study; Cambridge University Press. pp 709-797

Toulkeridis T, Goldstein SL, Clauer N, Kroner A, Todt W, Schdlowski M (1998) Sm–Nd, Rb–Sr and Pb–Pb dating of silicic carbonates from the early Archaean Barberton Greenstone Belt, South Africa Evidence for post-depositional isotopic resetting at low temperature. Precambrian Research. 92:129-144

Tuinstra F, Koenig JL (1970) Raman Spectrum of Graphite. Journal of Chemical Physics. 53:1126-1130

Wojdyr M (2010) Fityk: a general-purpose peak fitting program. Journal of Applied Crystallography. 43:1126-1128

# The Control of Sulfur Fugacity on Metal Melts and Gold Mineralization: A Case Study of the Jinjingzui Au Deposit

**Xinhao Li[1,2,3], Guiqing Xie[1,2], Sarah A. Gleeson[3,4], Jingwen Mao[1,2]**
*[1]School of Earth Sciences and Resources, China University of Geosciences, Beijing, China*
*[2]MNR Key Laboratory for Exploration Theory & Technology of Critical Mineral Resources, China University of Geosciences, Beijing, China*
*[3]GFZ German Research Centre for Geosciences, Potsdam, Germany*
*[4]Institute of Geological Sciences, Freie Universität Berlin, Berlin, Germany*

**Abstract.** Bismuth and Te melts are thought to collect Au from hydrothermal fluids based on previous experimental and modelling studies. This study documents an early phase of Bi-Te-Au formed at low sulfidation states (pyrrhotite stability) and a Te-Au association under higher sulfidation states (pyrite stability) in the Jinjingzui Au deposit. Here, we present EPMA data on bismuth tellurides and LA-ICP-MS data of sulfide minerals. We propose that low sulfidation states can keep Bi in the melt phase by preventing the formation of bismuth sulfide (solid), whereas the stability of the Te-melts may not be affected by sulfidation.

## 1 Introduction

Metal melts have long been inferred to contribute to mineralization because of the mosaic and droplet derived textures of certain minerals, some of which intimately coexist with gold. Bismuth-Te(-Se) minerals widely occur in Au-rich systems of different origins (Ciobanu and Cook 2005; Li et al 2023). The capability of Bi to form a melt phase and efficiently collect Au in hydrothermal conditions without Au saturation has been proven by experimental and modelling studies (Douglas et al. 2000; Tooth et al. 2008). This model has been applied to Au mineralization in different systems; most of the studies emphasize the low oxidation state as a major factor in Bi melt generation. Recent petrographic and microthermometric studies in vein-type deposit indicate that metal melts collecting gold mechanism can also be applied to Te-rich systems (Jian et al. 2021).

The Jinjingzui Au deposit has early Bi-Te-Au associations and late Te-Au associations. The early Bi-Te-Au association occurs in quartz with pyrrhotite mineral inclusions indicating low sulfidation states. The Te-Au association occurs with late pyrite indicating higher sulfidation states. With in-situ major and minor element contents of bismuth tellurides, and trace element concentrations of sulfide minerals from the deposit, this study explores the role of sulfidation state upon the Bi-Te melts stability and their Au collecting mechanism.

## 2 Deposit geology and Au occurrence

Located in Edong ore cluster, Middle–Lower Yangtze River metallogenic belt, China, the Jinjingzui Au deposit contains 7.6 metric tons of Au at an estimated 7.4 g/t average grade with no economic Cu (Li et al. 2007). Despite the skarn alteration in the contact zones between the diorite intrusion and the limestone host rock, Au mineralization occurs in veins inside the intrusion. Field studies indicate a sequence of early thin quartz ± K-spar ± pyrite I veins, intermediate thick quartz + pyrite ± chalcopyrite ± bornite II veins and late calcite ± pyrite III veins (Figure 1). The III veins are barren. Some I and II veins can be divided into a quartz dominated domain and a sulfide dominated domain (Figure 2a). Sulfide minerals are interstitial between quartz crystals, indicating they formed later than the quartz (Figure 2b c d).

**Figure 1.** Field pictures showing vein sequence of the Jinjingzui deposit

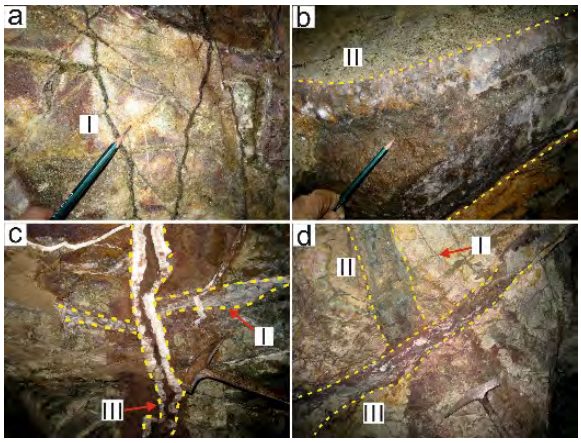


Microscopic observations indicate that abundant Bi-Te-Au associations (bismuth tellurides coexisting with native Au) occur in the quartz dominated domains of the I and II veins (Figure 3a b); the quartz crystals contain small pyrrhotite inclusions (Figure 3c). The sulfide dominated domains contain minor Te-Au association (native Au + calaverite; Figure 3d).

## 3 Methodology

The compositions of native Au, Bi- and Te- bearing minerals were determined using a JOEL JXA–8230 electron microprobe at the Key Laboratory of Metallogeny and Mineral Assessment, Institute of Mineral Resources, Chinese Academy of

Geological Sciences (CAGS), Beijing. The operating conditions are: accelerating voltage of 20 kV, beam current of 20 nA, and beam diameter of 1 μm. The counting time was 10 s on the peak, and 5 s each on left–hand and right–hand background position for each element. ZAF corrections were made with proprietary JEOL software.

**Figure 2. a** The quartz dominated domain and sulfide dominated domain of II vein; **b, c, d** hand-specimen and photomicrographs showing sulfides infilling the interstitial spaces of quartz crystals. Cal-calcite; Py-pyrite; Qz-quartz.

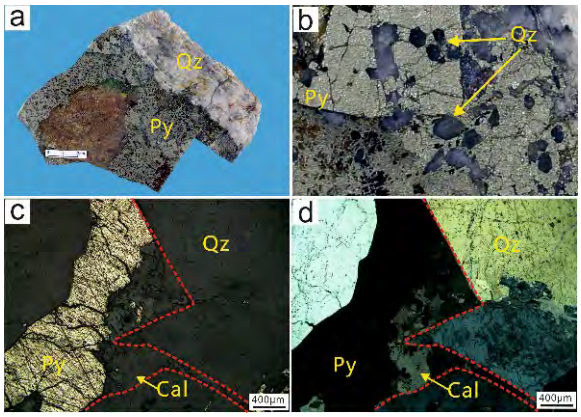


Trace element analysis of pyrite, chalcopyrite, bornite and pyrrhotite was carried out using LA-ICP-MS at the Beijing Createch Testing Technology Co., Ltd., Beijing, China, adopting a RESOlution 193 nm laser ablation system that consists of a COMPex Pro 102 ArF excimer laser and a Micro Las optical system. The chemical composition of the sulfides was corrected using the USGS MASS-1 sulfide standard value. The offline concentration calculation was carried out using the ICPMS Data Cal program.

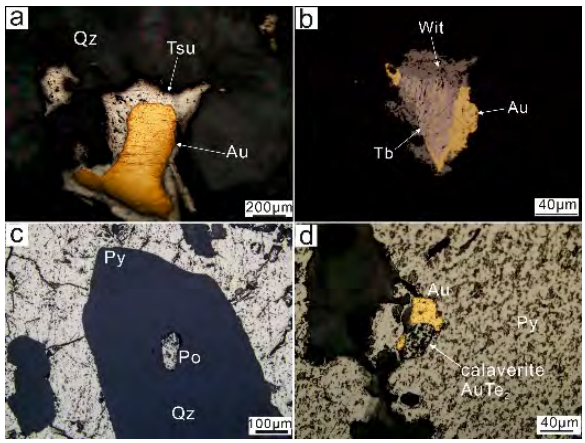


**Figure 3. a** Photomicrographs showing bismuth tellurides coexisting with native Au in quartz dominate domains; **b** Bi-Te-Au association is typically coated by later bismuth sulfides (wittichenite in this picture); **c** pyrrhotite inclusions occur in the early quartz crystals; **d** calaverite coexisting with native gold and pyrite occur in sulfide dominate domains. Au-native Au; Po-pyrrhotite; Py-pyrite; Qz-quartz; Tb-tellurobismuthite; Tsu-tsumoite; Wit-wittichenite ($Cu_3BiS_3$).

## 4 Results and interpretation

A ternary plot of bismuth telluride contents from I veins and II veins shows that the bismuth tellurides from II veins generally have higher Te and S contents (Figure 4). The Au concentrations are low in all sulfide minerals (Figure 5), including the As-rich pyrites in III veins, which means that native Au is the major form of Au mineralization in the deposit.

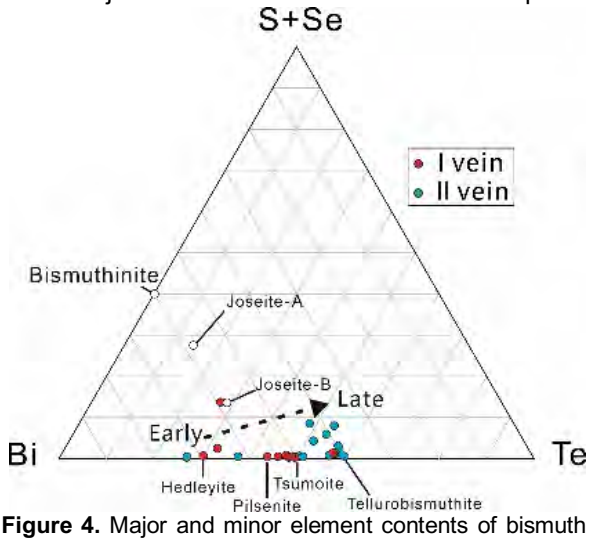


**Figure 4.** Major and minor element contents of bismuth tellurides showing that bismuth tellurides from the II veins are S- and Te- rich.

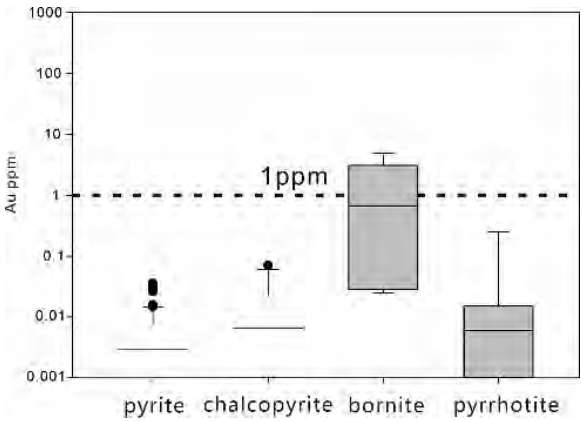


**Figure 5.** Trace element concentrations showing sulfide minerals generally do not contain Au in the Jinjingzui deposit.

The intimate coexistence of bismuth telluride and native Au in early stages can be explained by Bi-Te melts scavenging Au. The higher S contents of bismuth tellurides from the later II vein imply an increase in sulfidation state probably due to the declining temperature (Einaudi et al. 2003, Fig 4; Ciobanu et al. 2010). This higher sulfidation state stabilizes Bi sulfide and prevents the formation of Bi melts (Tooth et al. 2008, Fig 2b). Tellurium, however, does not react with sulfur (Snelling, 1912; Aravamudan et al. 1973), thus, it remains in the melt phase. This is supported by the late Te-Au association observed in the sulfide dominated stage. The early Au mineralization (in I and II veins) caused by Bi-Te melt collection may have depleted the Au in the hydrothermal fluid, therefore, no Au is

incorporated into the late As-rich pyrites from the late III veins.

## 5 Conclusions

The early Au mineralization at Jinjingzui is caused by the Bi-Te melts collecting Au under low sulfidation states. Later high sulfidation states result in Bi sulfide formation at the expense of the Bi-melts, yet Te-melts may still exist. Sulfidation state is an important parameter controlling the geochemical behaviour of Bi and Te in hydrothermal fluids, which can affect the mechanism of efficient Au mineralization.

## Acknowledgements

We thank Xiaodan Chen and Zhenyu Chen for their assistance in the electron microprobe analysis. This study is financially supported by the National Science Foundation of China (41925011 and 92162217).

## References

Aravamudan G, Sethuraman PR, Udupa MR (1973) Complexation of tellurium(II) with thioglycolic acid and reactivity patterns of the system. J inorg nucl Chem 35:3291–3298

Ciobanu CL, Birch WD, Cook NJ, Pring A, Grundler PV (2010) Petrogenetic significance of Au-Bi-Te-S associations: The example of Maldon, Central Victorian gold province, Australia. Lithos 116:1–17

Ciobanu CL, Cook NJ, Pring A (2005) Bismuth tellurides as gold scavengers. In: Mao JW, Bierlein FP (eds) Mineral deposit research: meeting the global challenge. Springer, Berlin, pp 1383–1386

Douglas N, Mavrogenes J, Hack A, England R (2000) The liquid bismuth collector model: An alternative gold deposition mechanism. 15th Austral Geol Conv Abstr 59:135

Einaudi MT, Hedenquist JW, Inan EE (2003) Sulfidation state of fluids in active and extinct hydrothermal systems: transitions from porphyry to epithermal environments. In: Simmons SF, Graham I (eds), Volcanic, Geothermal, and Ore-Forming Fluids: Rulers and Witnesses of Processes within the Earth. Soc Econ Geol Spec Publ 10:285–313

Jian W, Mao JW, Lehmann B, Cook NJ, Xie GQ, Liu P, Duan C, Alles J, Niu ZJ (2021) Au-Ag-Te-rich melt inclusions in hydrothermal gold-quartz veins, Xiaoqinling lode gold district, central China. Econ Geol 116:1239–1248

Li J, Jiang ZG, Chen MS, Yuan HW (2007) Detailed Investigation Report of Gold Mine in Jinjingzui Mining Area, Daye City, Hubei Province. 1–120 (In Chinese)

Li XH, Xie GQ, Gleeson SA, Mao JW, Ye ZC, Jin YL (2023) Palladium, platinum, selenium and tellurium enrichment in the Jiguanzui-Taohuazui Cu-Au deposit, Edong ore district: Distribution and comparison with Cu-Mo deposits. Ore Geol Rev 154:105335

Snelling WO (1912) Sulfide of tellurium. J Am Chem Soc 34:802–811

Tooth B, Brugger J, Ciobanu CL, Liu WH (2008) Modeling of gold scavenging by bismuth melts coexisting with hydrothermal fluids. Geol 36:815–818

# Metallogenic Fingerprinting of Gold Endowment in Magmatic Hydrothermal Deposits

**Carolina N. Mafra[1], Hoi Ian Kong[1], Robert R. Loucks[1], Marco Fiorentini[1]**
*[1]The University of Western Australia, Perth, Australia*

**Abstract.** The variable gold endowment in magmatic-hydrothermal deposits has been ascribed to the nature of the underlying lithospheric mantle, geodynamic settings, $K_2O/SiO_2$ in parental melts, and depth of hydrothermal fluid exsolution. However, the ultimate parameters affecting gold magmatic fertility are still largely unconstrained. The distinction in chemical composition of primitive melts temporally and spatially associated with gold-fertile arc segments and unmineralised arc segments constrain differences in sources of gold-rich and gold-poor mantle-derived melts. Furthermore, it suggests that gold fertility is a primary feature acquired at the mantle source. Gold-rich mantle-derived melts are consistently enriched in Nb, Ta, and Zr— evidence for lithospheric mantle metasomatism by low-degree partial melts from deeper asthenospheric mantle. In this framework, magmatic-tectonic triggers capable of selectively melting metasomatic enriched zones of the lithospheric mantle would play a first-order genetic control on gold fertility. Calc-alkalic and shoshonitic magmas that exsolved the hydrothermal fluid that formed gold-rich magmatic-hydrothermal deposits display distinct lithophile trace element compositions, that is a proxy of the degree to which the lithospheric mantle source was previously refertilised. We have defined a series of trace element ratios reflecting the participation of an enriched source in the generation of fertile magmas that are effective in discriminating them from ordinary, barren systems.

## 1 Introduction

Magmatic processes control the metallogenic potential of magmatic-hydrothermal Cu and Au districts. Magmatic fertility represents the potential of a melt to exsolve hydrothermal fluids capable of forming ore deposits. It is controlled by source and magmatic differentiation processes. The former corresponds to primary features favouring the generation of metallogenic camps, whereas the latter modifies the physiochemical properties of the intruding magmas, affecting their potential to form distinct ore deposits.

It is well recognised that copper fertility is an emerging property of the melt, developed under compressive stress by the intermittent replenishment of magma chambers at Moho depths (Loucks 2014; 2021). In such conditions, amphibole is an early phase to crystallise, whereas plagioclase crystallisation is delayed. Consequently, ore-forming intrusions have higher Sr/Y ratios compared to Cu-infertile intrusions.

Conversely, the origin of gold fertility is poorly understood, and formulating trustworthy petrochemical indicators for gold-rich deposits is still needed. Comparing the lithophile element chemical composition of gold-ore-forming magmas with barren reference suites is expected to lead to the recognition of trace element ratios that may be interpreted to represent petrogenetic processes responsible for the observed variable gold endowment in magmatic-hydrothermal deposits. Additionally, it should shed light on tectono-magmatic settings favourable for gold mineralisation. This research shows that moderate-to-high-potassium calc-alkalic magmas that exsolved hydrothermal fluid that formed gold-rich magmatic-hydrothermal deposits have distinct incompatible lithophile element compositions. Trace element ratios representing incipient melting of an enriched source can sort gold-fertile from gold-infertile intrusions on a province scale.

### 1.1 First-order controls on gold fertility in magmatic-related gold deposits

Magmatic-related gold-rich mineral systems form a wide range of deposit types globally (Sillitoe 2020). It has been proposed that a key ingredient common to all these mineral systems is that gold fertility is controlled by the nature of the underlying metasomatised lithospheric mantle (Hronsky et al. 2012; Loucks 2012; Tassara et al. 2017, 2018; Saunders et al. 2018; Holwell et al. 2019; Rielli et al. 2022; Wang et al. 2022). Contrarily, gold-rich magmatic-hydrothermal systems have also been attributed to magmatic fractionation processes (Murakami et al. 2010; Chiaradia 2020, 2021, 2022; Park et al. 2021; Hao et al. 2022), post-subduction and extensional settings and alkaline magmatism. However, although magmatic differentiation may favour gold enrichment in magmatic-hydrothermal systems, these aspects seem to exert a second-order influence on gold metallogenic fertility (Rielli et al. 2022).

Primitive melts in gold-bearing arc segments have distinctive incompatible element compositions compared to unmineralised arc segments (Figure 1) (Loucks and Ballard 2003; Loucks 2012; Hronsky et al. 2012). Interestingly, primitive melts spatially and temporally associated with gold deposits are consistently enriched in high-field-strength elements (HFSEs: Nb, Ta, Zr, etc.) compared to primitive basalts unrelated to mineralisation (Arima and Kerrich 1988; Loucks 2012; Saunders et al. 2018). The association between Au enrichment simultaneously with Nb indicates participation of an enriched source. Niobium is the most incompatible of the HFSEs in mantle minerals and metamorphic fluids, and its concentration in the mantle source is very sensitive to melt addition and extraction. Nevertheless, the fact that Nb, Ta, and Zr have negligible solubilities in slab-derived hydrothermal fluids (Ayres 1998; Keppler 2017; Rustioni et al.

2019) precludes aqueous fluids as the agents of relevant refertilisation, favouring low degree partial melts of underlying mantle as the fertilising agent.

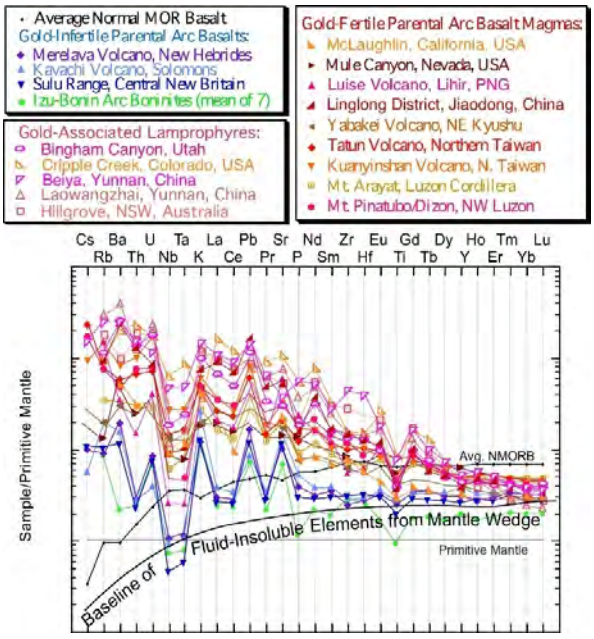


**Figure 1.** Incompatible lithophile trace element series, ordered by melt/restite partition coefficients, comparing primitive basalts from unmineralised arc segments with basalts and lamprophyres (6 to 12 wt.% MgO, Mg# > 60) that are spatially and temporally associated with major gold districts of late Neogene-Quaternary age. The elements are normalised to abundances in primordial mantle (McDonough and Sun 1995). Modified from (Loucks 2012; Hronsky et al. 2012).

Therefore, gold fertility seems to be a multi-stage petrogenetic process. In this framework, in a first stage, a geodynamic setting conducive to fertilisation of the lithospheric mantle is necessary. Accordingly, magmatic-tectonic triggers capable of selectively melting these metasomatic enriched domains are required in order to form any gold mineralised camp in the mid-to-upper crust.

## 2 Methodology

In order to have a meaningful perspective on petrochemical processes that control gold endowment in magmatic-hydrothermal deposits, it is required to acquire and investigate a representative sample set with a diverse compositional range as well as broad coverage of geodynamic settings. The most efficient approach to accomplish the extensive amount of data required to fully understand the origin of gold metallogenic fertility is compilation of existing analytical data from literature.

This work relies primarily on geochemical data from the north and south American Cordillera, the western Tethyan Orogenic belt, and the western Pacific Rim compiled into an extensive database. The compiled data was combined with new data from the Western USA. Figure 2 summarises sample localities covered by this project.

Magmatic rocks associated with magmatic-hydrothermal deposits are inevitably affected by post-magmatic processes. Consequently, petrographic and chemical filters were applied to consider only magmatic features in the whole rock.

Only samples described to best represent the magma composition that exsolved the mineralising hydrothermal fluids were considered. The compilation did not include passively mineralised rocks, extrusive rocks, nor crystal cumulates to a noticeable degree (whole-rock analyses having $Al_2O_3$ > 20 wt. % or Eu/Eu* > 1.3). All the analyses from altered or weathered samples, yielding a total volatile content (LOI) greater than 3.5 wt. %, analytical totals outside the 97.5 – 101.5 wt.% range (volatile-free basis), $Na_2O$ and CaO content plotting outside the magmatic range for continental arc magmas, or samples containing altered plagioclase and amphibole grains were eliminated.

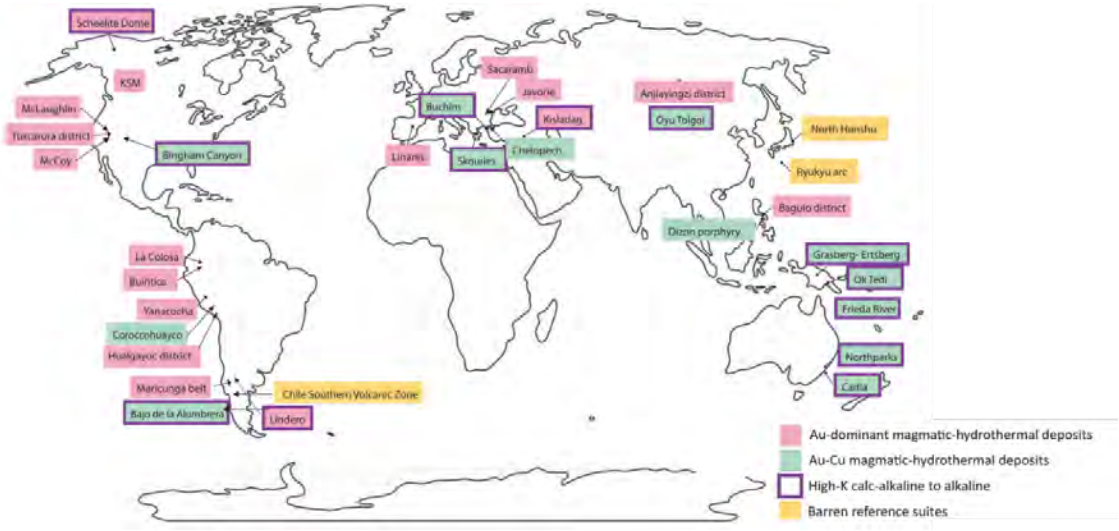


**Figure 19.** Locations of the samples considered in this study. Least-altered samples of ore-forming intrusions parental to major Au and Cu-Au deposits of Phanerozoic age worldwide are compared with barren reference suites from unmineralised arc segments and time intervals.

## 4 Results

The degree to which the lithospheric mantle has been refertilised can be represented by element ratios having highly incompatible elements in the numerator and mildly incompatible elements in the denominator. In Figure 3, an element from the left-hand side of the spidergram (Figure 1) is divided by an element on the right side to represent its general slope. These trace element ratios efficiently sort gold-fertile from gold-infertile intrusions. Ratios containing Nb in the numerator are particularly efficient in sorting gold-fertile from gold-infertile intrusions.

## 5 Discussion

Au-rich magmatic-hydrothermal deposits have distinct chemical characteristics compared to magmas from unmineralised arc segments and time intervals. These distinctions can be recognised in primitive mafic rocks contemporaneous to ore-forming intrusions (Figure 1) and in the ore-forming intrusions themselves (Figure 3). The fact that gold-fertile magmas are compositionally distinct from gold-infertile magmas across the whole magmatic differentiation series (low- to high $SiO_2$) is strong evidence that Au fertility is a primary property acquired at the magma source and not an emergent property developed during atypical chemical evolution within the crust.

The plots in Figure 3 show that the chemical distinction characteristic of gold fertility is shared by ore-forming magmas that generated Au-dominant and Cu-Au deposits, meaning that they may share a similar enriched source, whereas magmas from barren arc segments plot in the bottom left part of the diagrams. The lower trace element ratios from ordinary arc magmas are consistent with their source being the depleted upper asthenospheric mantle.

These trace element ratios suggest that gold-ore-forming intrusions have consistently higher HFSEs, and other highly incompatible lithophile elements concentrations than barren arc magmas. Interestingly, Nb is the most incompatible of the wedge-controlled HFSEs and is a proxy for source enrichment by low degree partial melts. Thus, the results show that gold-fertile magmas are formed by incipient melting of a source that was previously enriched in these elements.

## 6 Conclusions

Plots of U/Hf vs. Nb/Lu, Nb/Yb vs. U/Y, and Nb/Y vs. Nb/Zr are efficient in sorting gold-ore-forming from gold-infertile intrusions at convergent margins and post-subduction settings throughout the Phanerozoic. These plots aid in screening terrains and geodynamic settings favourable for hosting gold-rich magmatic-hydrothermal deposits. Using Nb as a proxy for gold fertility in whole rock is advantageous because Nb is relatively resistant to post-magmatic alteration. The systematic enrichment of gold-fertile magmas in Nb also provides reliable indications about the origin of gold fertility.

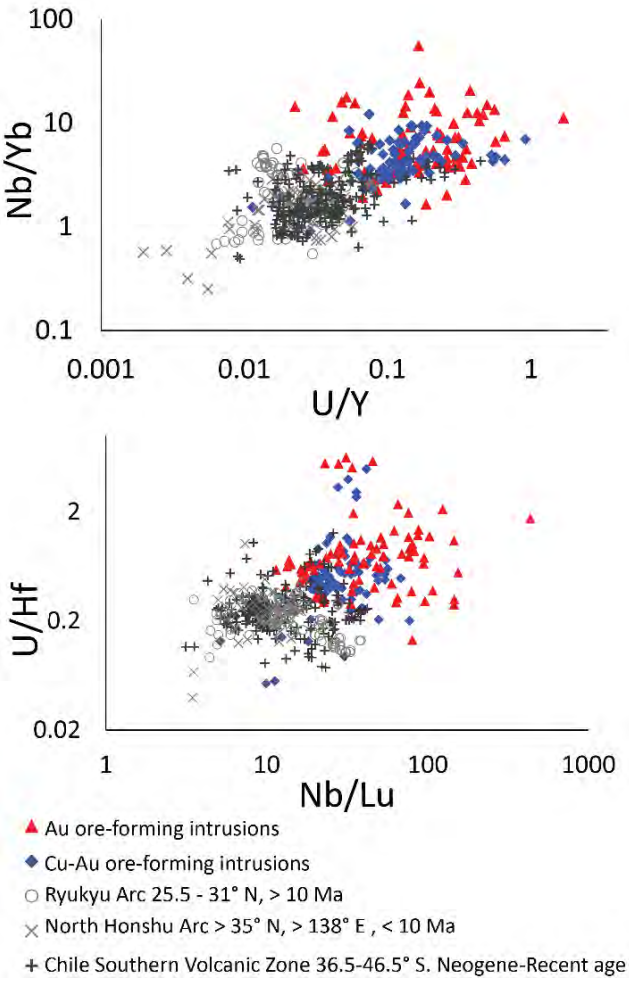


**Figure 3.** Trace element ratios having a highly incompatible element in the numerator and a mildly incompatible element in the denominator are efficient in sorting gold-fertile ore-forming intrusions from barren reference suites.


## Acknowledgements

This study is part of the Australian Research Council-Industry Linkage Project 190100785 to develop exploration guides to magmatic-hydrothermal gold-rich ore deposits. The authors are grateful to the sponsoring companies and support institutions of the project who provided samples and data.


## References


Ayers J (1998) Trace element modeling of aqueous fluid–peridotite interaction in the mantle wedge of subduction zones. Contrib Mineral and Petrol 132: 390-404.

Arima M, Kerrien R (1988) Jurassic kimberlites from Picton and Varty Lake, Ontario: Geochemical and stable isotopic characteristics. Contrib Mineral and Petrol 99: 385-391.

Chiaradia M (2020) Gold endowments of porphyry deposits controlled by precipitation efficiency. Nat Commun 11:1-10.
Chiaradia M (2022) Distinct magma evolution processes control the formation of porphyry Cu–Au deposits in thin and thick arcs. Earth Planet Sci Lett 599: 117864.
Hao H, Park J W, Campbell I H (2022) Role of magma differentiation depth in controlling the Au grade of giant porphyry deposits. Earth Planet Sci Lett 593: 117640.
Holwell D A, Fiorentini M, McDonald I et al (2019) A metasomatized lithospheric mantle control on the metallogenic signature of post-subduction magmatism. Nat Commun 10: 3511.
Hronsky J, Groves D I, Loucks R R, Begg G C (2012) A unified model for gold mineralisation in accretionary orogens and implications for regional-scale exploration targeting methods. Mineral Deposita 47: 339-358.
Keppler H (2017) Fluids and trace element transport in subduction zones. Am Mineral 102: 5-20.
Loucks R R, Ballard J R (2003) Report 2C: Petrochemical characteristics, petrogenesis and tectonic habits of gold-ore-forming arc magmas. Unpublished report for industry-sponsored research project: Predictive Guides to Copper and Gold Mineralization at Circum-Pacific Convergent Plate Margins. 69p
Loucks R R (2012) Chemical characteristics, geodynamic settings, and petrogenesis of gold ore-forming arc magmas. CET Quarterly News, issue 20.
Loucks R R (2014) Distinctive composition of copper-ore-forming arcmagmas. Aust J Earth Sci 61: 5-16.
Loucks R R (2021) Deep entrapment of buoyant magmas by orogenic tectonic stress: Its role in producing continental crust, adakites, and porphyry copper deposits. Earth-Sci Rev 220: 103744.
Murakami H, Seo J H, Heinrich C A (2010) The relation between Cu/Au ratio and formation depth of porphyry-style Cu–Au±Mo deposits. Mineral Deposita 45: 11-21.
Park J W, Campbell I H, Chiaradia M, Hao H, Lee C T (2021) Crustal magmatic controls on the formation of porphyry copper deposits. Nat Rev Earth Environ 2: 542-557.
Rielli A, Tomkins A G, Nebel O et al (2022) Incipient metal and sulfur extraction during melting of metasomatised mantle. Earth Planet Sci Lett 599: 117850.
Rustioni G, Audétat A, Keppler H (2019) Experimental evidence for fluid-induced melting in subduction zones. Geochem Perspect Lett 11: 49-54.
Saunders J E, Pearson N J, O'Reilly S Y, Griffin W L (2018) Gold in the mantle: A global assessment of abundance and redistribution processes. Lithos 322: 376-391.
Sillitoe R H (2020) Gold deposit types: An overview. Society of Econ Geol Spec Pub 23: 1–28.
Tassara S, González-Jiménez J M, Reich M et al (2017) Plume-subduction interaction forms large auriferous provinces. Nat Commun 8: 1-7.
Tassara S, González-Jiménez J M, Reich M et al (2018) Highly siderophile elements mobility in the subcontinental lithospheric mantle beneath southern Patagonia. Lithos 314: 579-596.
Wang X, Wang Z, Cheng H et al (2022). Gold endowment of the metasomatized lithospheric mantle for giant gold deposits: Insights from lamprophyre dykes. Geochi et Cosmochim Acta 316: 21-40.

# Overprinted mineralizing gold events at the Paleoproterozoic Alta Floresta Mineral Province, Brazil

**Maria José Mesquita[1]; Márcia Elisa Boscato Gomes[2]; Igor de Camargo Moreira[1]; Renata Augusta Sampaio Paes[1]; Hevelyn Eduarda da Silva Martins[1]; José Henrique Matos[1]; Alberto Ruggiero[1]; Guilherme Primo[1]; Diego Fernando Ducart[1]; João Gabriel da Silva[1]; Luciano Poggi[1]; André Massanobu Ueno Kunifoshita[1], Leonardo Zanchetta de Laurentis[1].**

[1]*Universidade Estadual de Campinas -Unicamp*

[2]*Universidade Federal do Rio Grande do Sul - UFRGS*

**Abstract.** The Large gold provinces commonly show complicated mineralization histories, and the Paleoproterozoic Alta Floresta Mineral Province is a good example. The current models defined three deposit types, all connected to a single (1.88–1.75 Ga) magmatic-hydrothermal event. However, diverse geodynamic environments and older ages of Type-1 mineralization weaken the single metallogenic event. By scale-integrated analyses, we revise tectonic-geological context, structural-hydrothermal alterations, and chlorite-white mica geothermobarometer and propose the type-1 as granitoid-hosted orogenic gold deposits and the overprinting of the two events. The older orogenic-gold event developed orogenic gold deposits on WNW-trending shear zones in Peixoto de Azevedo inlier granitic-gneiss rocks. Phengite, biotite, chlorite-carbonate phyllonite (3.3-6.1kbar, 300º-420ºC) host fault-fill quartz veins (pyrite-chalcopyrite-magnetite-pyrrhotite-gold-Bi-Ag tellurides). Mg-rich chlorite-phengite is a footprint. A younger magmatic-hydrothermal event in Juruena magmatic-arc rocks produced Fe-rich chlorite-white mica alteration zones (0.6-4.6kbar, 120º-380ºC), and stockwork-breccia ore (pyrite-chalcopyrite-gold-Ti minerals-molybdenite-allanite) in porphyry-epithermal deposits. Phyllic alteration destroyed the phengite phyllonite foliation. The ages of two pyrite populations (1.98 and 1.84 Ga) in fault-fill veins and molybdenite in late fractures (1.81-1.78 Ga) or disseminated in ca. 1.79 Ga syenogranite porphyry distinguish two episodes. The AFMP multi-scale approach enlightens the two ore events overprint, allowing a new explorational potential.

## 1 Introduction

The world's largest hydrothermal deposits and metallogenic provinces have shown complex events superposition. Multistage mineralization events are mandatory to enrich most giant deposits (Meffre et al. 2012; Augustin and Gaboury 2018). Especially in Archean and Paleoproterozoic provinces, the literature describes many deposits with two or more stages of mineralization, magmatic activity, and multiple deformation histories (Fougerouse et al. 2017; Le Mignot et al. 2017; Augustin and Gaboury 2018).

However, in many mineral provinces, the possibility and implications of multiple mineralizing episodes are yet to be appropriately recognized, and the Alta Floresta Mineral Province (AFMP) is an example of this. AFMP is one of the promising Brazilian provinces for gold and copper.

The AFMP has an inlier nucleus, called Peixoto de Azevedo domain (PdA inlier), of the older Tapajos-Parima Geochronological Province (ca. 2.05 to 1.97 Ga volcanic arc-related rocks) surrounded and cut by younger rocks of the Rio Negro-Juruena Geochronological Province (arc-related or rifting-related environment of ca.1.82 to 1.52 Ma; Santos et al. 2001). Type-1 (Au ± Cu shear zone-hosted veins) are entirely hosted in the older granitic, granitic-gneiss, and metamafic rocks of the PdA inlier, while Type-2 (Au-Cu porphyry deposits) and Type-3 (Au ± Ag ± base metals epithermal deposits) are in the younger rocks of the Rio Negro-Juruena Province.

The current AFMP metallogenic models connect the three deposit types as part of a single magmatic-hydrothermal system restricted to a ca. 1.88–1.75 Ga event but at different crustal levels (Acevedo 2014; Assis et al. 2017; Rocha et al. 2020). They constrained it to the last stages of the Statherian magmatic arc evolution in the Rio Negro-Juruena Province. However, the mineralization ages are restricted to porphyry and epithermal deposits (Type-2 and Type-3), while two ages for Type-1 Paraiba deposit's pyrite yielded ca. 1.98 and 1.84 Ga (Paes de Barros 2007; Santos 2011 respectively), open for older mineralization events. Motivated by the tectonic position in older metamorphic rocks, the ore structural control in all scales, the older ages of Type-1 deposits' mineralization, and gaps between the reported productions, the present text presents some of the published AFMP data and new data to propose the type-1 deposits as granitoid-hosted orogenic gold and search for an alternative to a single-episode mineralization scenario.

## 2 Results

The results are based on mostly new data on structural control, hydrothermal alteration, and mineralization of the Paraiba, Peteca, and Serrinha do Guarantã deposits, and Luiz Bastos target of the Type-1, União do Norte District of Type-2, and Juruena District of Type-3. In addition, the overprinted characteristics of Type-2 and -3 of Peteca and Paraiba deposits and Luiz Bastos targets and reviewed chlorite and muscovite mineral chemistry from the literature are also presented. For complete results, consult Mesquita et al. (2022).

### 2.1 Type-1 deposits

The Type-1 deposits are entirely developed in the 2.04-1.98 Ga PdA inlier of the Tapajos-Parima Province, hosted within ductile shear zones.

Granitoids, quartz-feldspathic gneiss, mafic and ultramafic amphibolites are the primary host rocks, which show two foliations ($S_n$ and $S_{n+1}$). $S_n$ is a well-developed spaced foliation trends 00-050º and dips 70-90 º WNW (Fig. 1).

**Figure 1.** Type-1 deposit host rock: $S_n$ (040/80SE) banding transposed by $S_{n+1}$ (340/88SW) discrete shear band in 1.98 Ga (Miguel Jr. 2011) metagranodiorite.

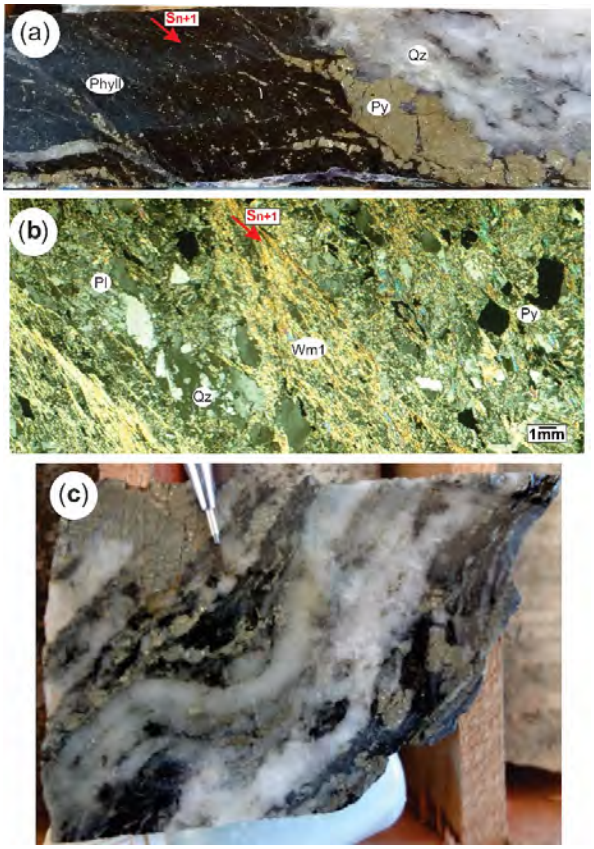


**Figure 2.** (a) phlogopite-carbonate phyllonite (Phyill) host the quartz vein (Qz) (Paraiba deposit); (b) phyllonite fabric with strong muscovite alteration defining $S_{n+1}$ foliation. Plagioclase replaced by mica; (c) Anastomosed ore quartz vein with laminated texture (quartz bands alternate phlogopite-carbonate phyllonite bands (black) and sulphide films).

A WNW-trending first-order shear zone system develops a mylonitic $S_{n+1}$, which deflects $S_n$ (Fig. 1). The high-strain zones are composed of phyllonite hosting the quartz veins (Fig. 2a). In the phyllonite, $S_{n+1}$ is a continuous schistosity defined by muscovite, biotite, and chlorite bands alternated with quartz bands (Fig. 2b).

The Type-1 gold-quartz veins concentrate in shear zones subsidiary to the transcurrent first-order shear zones: either N-trending (Paraíba, Luiz Bastos, and Buriti-Porteira deposits) or E-trending (Peteca, João Fidelis, and Queiroz deposits). The Serrinha do Guarantã vein deposit is the only one in a first-order shear zone.

Hydrothermal alteration and phyllonite formation are concomitant and restricted to the shear zones. The alteration sequence varies from distal (from the ore vein) muscovite alteration (muscovite Wm-1, quartz, pyrite, and chlorite) to proximal biotite-carbonate (biotite-phlogopite, quartz, calcite, chlorite Chl-1, pyrite and traces of gold), and chlorite-carbonate alteration (Chlorite Chl-2, calcite, muscovite Wm-2, pyrite, chalcopyrite and traces of gold). Quartz-calcite veinlets with pyrite, chalcopyrite, and traces of gold cut the phyllonite rocks. The veinlets are sub-horizontal to low angle (<30º), and the internal mineral growth indicates dilational veinlets.

The fault-fill veins are steeply dipping and oblique to parallel to the shear zone $S_{n+1}$ foliation. Internal vein textures vary from massive-milky in the center and towards the vein walls, a characteristic laminated texture, as in the Peteca deposit. The Paraíba and Serrinha de Guarantã veins are laminated (Fig. 2c). The veins show a strong oblique quartz lineation along the shear margins, characteristic of an L-tectonite, with gold filling the space between the quartz rods. Under the microscope, the vein quartz is heterogeneously deformed, showing different microstructural domains (Fig. 3). Early relict quartz (Qz1) occurs with large pyrite (Py-1) grains surrounded by sizeable recrystallized quartz (Qz2) grains. Discrete anastomosed shear bands and fractures, subparallel to the vein walls, cut the previous quartz domains, developing bands of small recrystallized quartz grains (Qz3), chlorite, and pyrite (Py2) (Fig.3).

The ore mineralization is restricted to the quartz veins and rare in phyllonites. The gold orebodies in the Paraiba and Peteca deposits are massive in irregular long stripes and lenses or as free-gold.

Gold also occurs as inclusions and infilling fractures in pyrite Py1 (Fig.3). The fractures are filled by chalcopyrite altered to covellite, galena and sphalerite, and Bi-Ag tellurides. At the Paraiba deposit, fractures with molybdenite cut the phyllonite. In the Serrinha de Guarantã orebodies, gold occurs with bornite-chalcopyrite aggregates.

### 2.2 Type-2 and -3 deposits

All Type-2 and -3 deposits and occurrences lie in a corridor up to 400 km from União do Norte District (Type-2 Jaca deposit) to beyond Apiacás town (Type-3 Juruena deposit), forming in various tectonic environments.

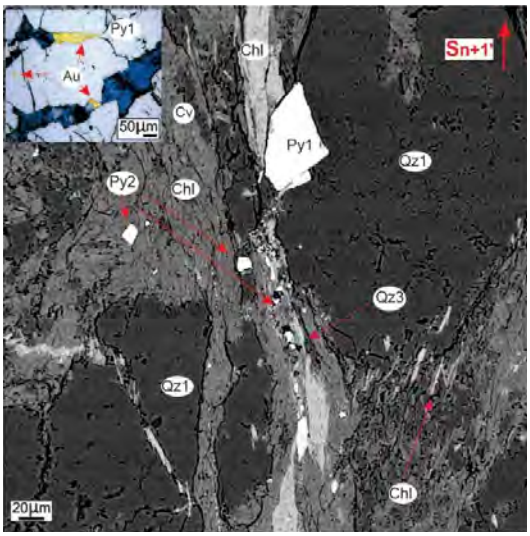


**Figure 3.** Gold-quartz vein textures: quartz (Qz1) and pyrite (Py1) cut and deformed by discrete, anastomosed shear bands ($S_{n+1'}$) defined by chlorite (Chl), Qz2, and a new generation of fine pyrite grains (Py-2) (EMP back-scattered electron image). In cart image: pyrite (Py1) with gold inclusions and in fractures with chalcopyrite altered to covellite (red arrows) (Peteca ore).

These deposits occur within the 1.80 to 1.75 Ga Juruena Magmatic arc and the 1.90–1.85 Ga post-orogenic rocks of the Cuiu-Cuiu magmatic arc. NE-trending faults and fractures crosscut and dislocate the WNW first-order shear zones and the $S_{n+1}$ foliation (hosting the Type-1 deposits) and control most of the Type-2 and -3 deposits (Paes et al. in this volume).

The União do Norte District consists of an epiclastic volcaniclastic sequence intruded by several mostly alkaline quartz-feldspar porphyries and rare plagioclase porphyries (Fig. 4a, b). Additionally, several mafic dykes of unknown ages cut all the rocks and hosted many gold occurrences. The mineralization is intimately related to a sericite alteration, mainly associated with stockworks composed of Type-D pyrite veinlets with well-developed sericite or sericite-quartz halo (Fig. 4b). A-type or EM-type veinlets are absent at the moment of research.

In the Juruena District, the main host rocks are 1.82-1.77 Ga high K calc-alkaline to alkaline volcanic rocks and 1.84-1.78 Ga granitoids and lamprophyre dikes (Fig. 2). A pervasive K-feldspar-hematite alteration is overprinted by quartz-sericite alteration, cut by several hydrothermal breccias and veinlets. There are sericite polymictic breccia, chlorite cement-supported carbonate breccia, and sulphide-silica breccia, mostly chalcopyrite cement. There are three populations of silica veinlets, named vl 1, 2, and 3. Vl 1 is a banded quartz-sericite veinlet. The sulphide-quartz vl 2 has a wavy morphology, composed of milky quartz, chalcopyrite, pyrite, minor galena, and sphalerite (Fig. 4c, d). The silica-calcite-fluorite vl 3 has straight, well-defined walls and cut the sulphite-quartz vl 2. Coarse grain idiomorphic calcite has a massive or zonal growth texture (Fig. 4d).

In other respects, the Paraiba and Peteca deposits also show Type-2 and -3 characteristics. Distal from the pair phyllonite/fault-fill ore veins, non-foliated potassic (K-feldspar-hematite, quartz, biotite, and molybdenite), sericitic (Wm-3 muscovite, quartz, calcite, pyrite, rutile, ilmenite, and titanite), propylitic, and epidote-carbonate (epidote, allanite, calcite, Mn-calcite, chalcopyrite, molybdenite, pyrite, rutile, ilmenite, titanite, gold) alterations are observed, pervasive or in veinlets. Sericitic alteration veinlets are mineralized and composed of quartz, pyrite, molybdenite, and chalcopyrite with sericite halos (Paraiba deposit). A pervasive sericitic alteration cuts and obliterates the muscovite phyllonite $S_{n+1}$. The propylitic alteration evolved into an epidote-carbonate-stockwork. In the Paraíba deposit, epidote-carbonate breccia is high-grade copper and gold and one of the orebodies (Poggi et al. 2022).

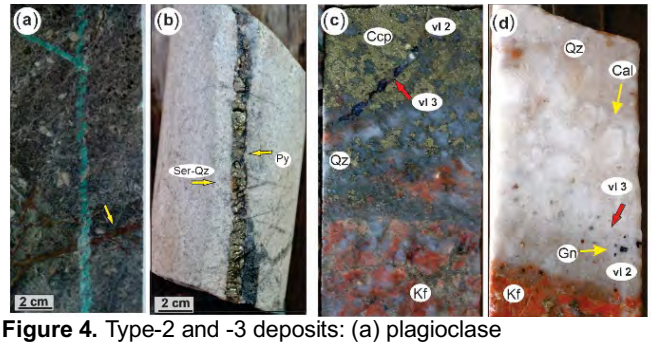


**Figure 4.** Type-2 and -3 deposits: (a) plagioclase porphyric intrusions strongly sericitized and affected by pyrite veinlets (arrow). Phenocrysts of polymorphic plagioclase and biotite; (b) typical Type-D pyrite veinlet (in the sense of Gustafson and Hunt 1975) with sericite-quartz or sericite halo host in arkose of the epiclastic-volcaniclastic sequence; (c) 6 cm thick quartz-sulphide (in the walls) to massive sulphide (in the centre) vl 2 cut by millimetric quartz-fluorite vl 3 in a K-feldspar-hematite altered granite. Note the absence of alteration halo in the vl 2 wall; (d) ) quartz-sulphide vl 2 with disseminated galena evolved to calcite vl 3. Calcite shows a zonal growth texture (yellow arrow). Sílica halo in the K-feldspar-hematite altered rock.

### 2.3 Chlorite and white mica

The available chlorite and white mica chemical composition of Type-1, -2, and -3 deposits are presented in Gomes et al. (in this volume). The main results suggest the Type-1 deposits show Mg-rich chlorite and Mg- and Si-rich muscovite-phengite footprints. The consistently high crystallization temperature (above 350ºC) and almost zero vacancies suggest metamorphic chlorite. Chlorite-white mica thermobarometers show a limited temperature variation (420-300ºC) and significant high-pressure variation (3-7 kbar) attributed to supralithostatic fluid pressure regimes.

In contrast, Fe-rich and Al-Fe-rich alterations are the main footprints for the porphyry (Type-2) and epithermal (Type-3) deposits, respectively. The P-T evolution has more substantial temperature

variation (380-120ºC) and lower pressure (4.6-0.6 kbar), coherent with the cooling of a shallow hydrothermal-magmatic system.

## 3 Discussion and conclusions

Many authors have already interpreted the Type-2 and Type-3 deposits as Au-Cu-Mo porphyry and intermediated Au-Pb-Zn-Cu epithermal, respectively, developed due to the same evolved magmatic-hydrothermal event, together with the Type-1 Au-Cu veins in shear zones (Paes de Barros 2007; Moura et al. 2006; Assis 2011, 2015; Miguel Jr. 2011; Rodrigues 2012; Acevedo 2014; Trevisan 2015; Assis et al. 2017; Galé 2018; Rocha 2016). However, our findings based on new and reinterpreted data suggest that a distinct hydrothermal event during active shearing created the Type-1 deposits.

The main Type-1 deposits' characteristics such as (a) hosted in deformed and metamorphosed metagranitoids of the Paleoproterozoic PdA inlier; (b) compressional to transpressional regimes of post-orogenic environments related to the NW-trending shear zone system; (c) hydrothermal alteration associated with ore mineralization is restricted to the shear zones; (d) and fault-fill quartz veins in phyllonites of the subsidiary structures suggest the Type-1 deposits are consistent with the orogenic gold model, as stated by many authors, as the seminal Groves et al. (1998).

At the Type-2 deposit, the large and undeformed hydrothermal alteration zones and the widespread sericitic zone hosting the D-type pyrite veinlets in stockworks, suggest porphyry deposits (Sillitoe 2010). At the Type-3 deposits in the Juruena District, several generations of hydrothermal breccias (sericitic, chloritic, carbonatic, and quartz-sulphide) and veinlets (vl-1, vl-2, and vl-3) suggest epithermal deposits (Hedenquist et al. 2020; Wang et al. 2019). The Type-3 relationship with the porphyry deposits (Type-2), both hosted in oxidized calc-alkaline granitic and volcanic rocks of the Juruena magmatic arc, are common features of intermediate-sulphidation (IS) epithermal deposits (Wang et al. 2019).

The mineral assemblages point to hydrated minerals of the orogenic event in phyllonite, defining $S_{n+1}$ foliation (Fig. 2). Contrastingly, the magmatic-hydrothermal event that created the Type-2 and Type-3 deposits formed minerals in a lower rock-fluid ratio (r/w) and variable accessory minerals. The sericite (Wm-3) in the sericitic zone, the Wm-4 in the sericitic ore veinlets and their halos, and the chlorite (Chl-3) in the propylitic alterations are characteristic non-foliated.

The main ore assemblage also shows differences between the two events. The orogenic gold deposit fault-fill quartz veins are composed of pyrite, chalcopyrite, pyrrhotite, magnetite, gold, and Bi-Ag tellurides. In contrast, the quartz veinlets and halos of phyllic/sericitic alteration consist of pyrite, molybdenite, chalcopyrite, rutile, ilmenite, and titanite, and the epidote-carbonate stockworks consist of epidote, allanite, calcite, Mn-calcite, chalcopyrite, molybdenite, pyrite, rutile, and gold.

Recognizing the granitoid-hosted orogenic gold deposits as a distinct ore-hydrothermal event, separate from the magmatic-hydrothermal one, and recognizing their overprint relationships will assist exploration within the Alta Floresta Mineral Province.

## References


Alves, C. L., et al. 2020. The Orosirian Cuiú-Cuiú magmatic arc in Peixoto de Azevedo domain, Southern of Amazonian craton. Journal of South American Earth Sciences, 102, 102648. https://doi.org/10.1016/j.jsames.2020.102648

Assis R.R., et al. 2017. Linking the Timing of Disseminated Granite-Hosted Gold-Rich Deposits to Paleoproterozoic Felsic Magmatism at Alta Floresta Gold Province, Amazon Craton, Brazil: Insights from Pyrite and Molybdenite Re-Os Geochronology. Economic Geology, 112: 1937–1957. https://doi.org/10.5382/econgeo.2017.4535

Augustin, J. and Gaboury, D. 2018. Multistage and multi-sourced fluid and gold in the formation of orogenic gold deposits in the world-class Mana district of Burkina Faso – Revealed by LA-ICP-MS analysis of pyrites and arsenopyrites. Ore Geology Reviews, 104, 495–521. https://doi.org/10.1016/j.oregeorev.2018.11.011

Fougerouse, D. et al. 2017. Evidence for two stages of mineralization in West Africa's largest gold deposit: Obuasi, Ghana. Economic Geology, 112, 3–22. https://doi.org/10.2113/econgeo.112.1.3

Le Mignot, E. et al. 2017. The Paleoproterozoic copper-gold deposits of the Gaoua district, Burkina Faso: Superposition of orogenic gold on a porphyry copper occurrence?. Economic Geology, 112(1), 99-122. https://doi.org/10.2113/econgeo.112.1.99

Meffre, S. et al. 2016. Multistage enrichment processes for large gold-bearing ore deposits. Ore Geology Reviews, 76, 268-279. https://doi.org/10.1016/j.oregeorev.2015.09.002

Mesquita et al. 2022. Paleoproterozoic gold deposits at AFMP, Brazil: two overprinted mineralizing events? From: Torvela, T., Lambert-Smith, J. S. and Chapman, R. J. (eds). Recent Advances in Understanding Gold Deposits: from Orogeny to Alluvium. Geological Society, London, Special Publications, 516. https://doi.org/10.1144/SP516-2021-64

Moura, M.A. et al. 2006. Granite-related Paleoproterozoic, Serrinha gold deposit, Southern Amazonia, Brazil: hydrothermal alteration, fluid inclusion and stable isotope constraints on genesis and evolution. Economic Geology, 101, 585-605. https://doi.org/10.2113/gsecongeo.101.3.585

Pogi et al. 2022. New Insights into the Evolution and Footprints of the Paraíba Au-Cu-Mo Deposit, Alta Floresta Mineral Province (Brazil), through Integration of Spectral and Conventional Methods. Minerals 2022, 12, 1327. https://doi.org/10.3390/min12101327

Santos, J.O.S. et al. 2001. Gold deposits of the Tapajós and Alta Floresta domains, Tapajós-Parima orogenic belt, Amazon Craton, Brazil. Mineralium Deposita, 36, 278-299. https://doi.org/10.1007/s001260100172

Groves, D.I. et al. 1998. Orogenic gold deposits: A proposed classification in the context of their crustal distribution and relationship to other gold deposit types. Ore Geology Reviews, 13, 7–27. https://doi.org/10.1016/S0169-1368(97)00012-7

Sillitoe, R.H. 2010. Porphyry copper systems. Economic Geology, 105, 3–41. https://doi.org/10.2113/gsecongeo.105.1.3

Wang, L. et al. 2019. A review of intermediate sulfidation epithermal deposits and subclassification. Ore Geology Reviews, 107, 434-456. https://doi.org/10.1016/j.oregeorev.2019.02.023

# Geophysical VLF prospecting for orogenic gold in the historic mining area in the Sudetes (SW Poland)

**Stanisław Z. Mikulski[1], Szymon Ostrowski[1]**
*[1]Polish Geological Institute-National Research Institute*

**Abstract.** The abandoned historic gold mining areas in the Sudetes are prospective for vein-type gold deposits. The applied VLF geophysical survey showed a number of linear anomalies indicating the possibility of occurrence of the new ore veins between the areas of former mining exploitation. In the light of the obtained VLF results as well as previous bulk-rock geochemistry and mineralogical study, which showed high gold content in the ores from mining wastes, this area is very promising for successful gold prospecting.

## 1 Introduction

The application of geophysical methods such as VLF (very low frequency electromagnetic technique) in the fast mapping of the structural features (Gnaneshwar et al. 2011; Ramesh Babu et al. 2007), and search for vein-type deposits (Ostrowski 2014) in former metal ore mining areas has been used for a long time and in many places it has enabled the recognition of the continuation of the course of already known ore veins or indicated their completely new occurrences.

VLF is the geophysical technique known and widely used for decades, although its applications are diminishing nowadays due to mostly to the fact that obtained results are usually qualitative. The full description of the technique basics can be found in (Paterson and Ronka 1971; Phillips and Richards 1975; Sharma et al. 2014), and attempts of more quantitative approach to the VLF results has been made recently (Singh and Sharma 2016). The VLF surveying technique is one of the techniques based on the electromagnetic induction phenomena. The electromagnetic fields effecting from the phenomena and generated by some geological features might be measured from surface and translated to the geological model.

Polish Geological Institute conducted a geophysical survey with VLF technique in a former gold mining area in the Klecza-Radomice Ore District (KROD), (Mikulski et al. 2021). In KROD during the years 1922-33, small-scale mining of arsenic and gold ores was carried out there, from quartz veins intersecting Lower Paleozoic shales.

## 2 Geological background and gold mineralization

The Klecza-Radomice Ore District KROD is hosted by rocks of to the Kaczawa Metamorphic Complex (KMC) that belongs to the basement of the Western Sudetes unit considered as a continuation of the Saxothuringian Zone of the European Variscides in the north-eastern part of the Bohemian Massif. KMC is representing there by flysch-like sediments of Ordovician-Devonian age that were deformed and metamorphosed to lower green schist facies (Kryza and Muszyński 1992). In the KROD the gold bearing quartz-sulfide mineralization consist of 8 main and more than 9 smaller veins (Mikulski 2007). Veins have major NE-SW and minor NW-SE strike directions, and are steep dipping (65-85°) to W. They were explored on a length of about 90-150m and down dip to 100m below surface, showing different thickness from 0.25 to 1.5m. Most frequently veins cut host rocks but locally may appear as saddle reefs. Bigger veins are preferentially located in fractured zones discordant to the bedding and run close to, or along the axial planes of $F_1$ anticlines. Several veins run oblique in direct surroundings of the Pławna fault zone of inverse character (Figure 1).

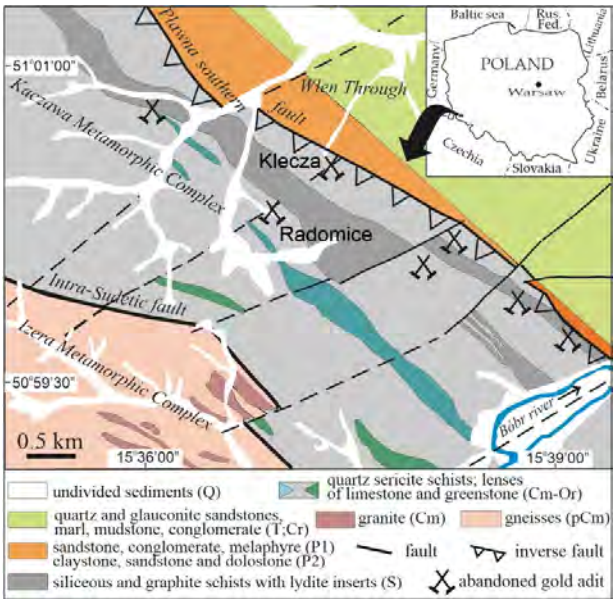


**Figure 1.** Location of the Klecza-Radomice Ore District (KROD; after Mikulski 2007) on the schematic geological map (modified from Milewicz 1962; Milewicz and Frączkiewicz 1983; Milewicz and Kozdrój 1994)

The richest in gold ore mineralization is of a massive type and dominated by arsenopyrite and in places by pyrite. The content of gold and arsenic in ore veins was in the range of 3-40ppm Au and 2-12% As. Sericite and graphitic schists are favourable host of sulfides mineralization. These rocks are strongly altered due to silicification, sericitization,

carbonatization, chloritization, feldspathization and sulfidization. The ore massive mineralization is fractured and overprinted by rare base metal sulfide (chalcopyrite galena and sphalerite) associated with common carbonates (mainly ankerite and dolomite). Gold occurs as refractory and microscopic gold. Separated pyrite and arsenopyrite contained up to 68.5ppm and 15ppm of gold, respectively (Mikulski 2007). Fineness of the microscopic gold is variable from very low (630) to very high (940) (Paulo and Salomon 1973; Olszyński and Mikulski 1997; Mikulski 2007). The mineralization in KROD has been classified as an orogenic gold deposit due to geological setting between metamorphic terranes, strong structural control of ores, low Au/Ag ratios, not significant base-metal contents, and low salinity of mineralizing fluids (<7 wt% NaCl equivalent), (Mikulski 2003). The Re-Os isotopic age obtained for Co-arsenopyrite from the northern ore field in Klecza revealed an age value of 316.6±0.4 Ma (Mikulski et al. 2005).

## 3 Geophysical prospecting with application of the VLF methods

Geophysical survey was carried in 2017-2018 in two sites, in radius of approximately 1 km from two historic mines. The survey was done with VLF technique. Measurements were acquired along 30 acquisition lines of 0,3 to nearly 1,5 km long and of total length of more than 30 km, covering the area of ca. 3 km$^2$ - virtually entire area of interest. The field measurements were performed along parallel traverses spaced ca. 100 m in between. Primary field intensity, in-phase (IP) and quadrature (QUAD) components of phase shift were measured for three different frequencies generated by three far-field transmitters. The Fraser filtration (Fraser 1969) was applied to all obtained datasets of phase shift components, and the results (both unfiltered and filtered) were compiled to the series of point-maps (Figure 2). Hand interpretation of the resulting maps by connecting VLF anomalies on subsequent traverses yielded linear anomalies that can be regarded as probable course of ore veins (Figure 3).

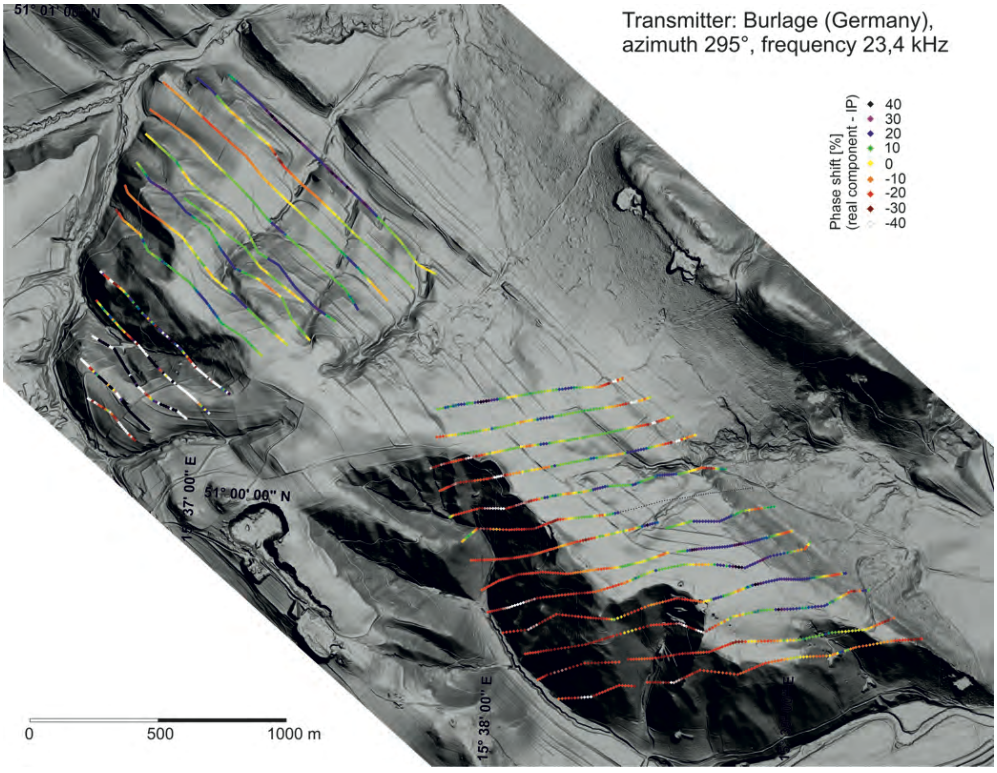


**Figure 2.** Point-map of in-phase component of induced VLF field. Illustration of the survey setting and one of the unfiltered phase shift components.

## 4 Final remarks

On the basis of prepared maps of Fraser-filtered VLF datasets the course of linear anomalies were identified. Four lineament populations (or modes) are present (Figure 3). The lineaments can be attributed to different structural elements and different stages of deformations. In our opinion the most promising places for further ore investigations (including drilling locations) are nexuses where lineaments of mode (7) and mode (10) and (9) are intersecting and ore enrichment might take place.

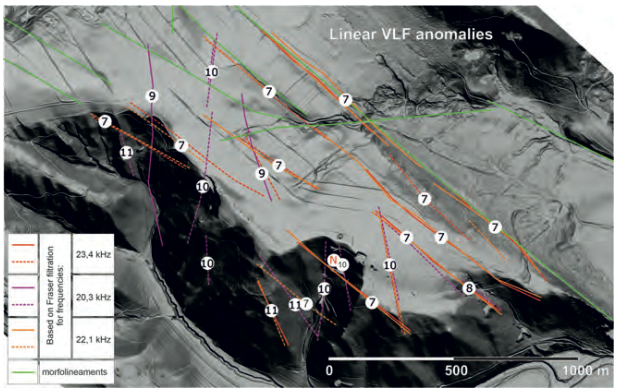


**Figure 3.** A fragment of the map of interpreted linear VLF anomalies. The anomalies are results of linear structural features with conductivity contrasting to the surrounding medium.

## Acknowledgements

The presented results were obtained in PGI-NRI during performing the project financed by the National Fund for Environmental Protection and Water Management, in accordance with the grant agreement No. 289/2018.

## References

Fraser DC (1969) Contouring of VLF-EM data. Geophysics 34:958–967

Gnaneshwar P, Shivaji A, Srinivas Y, Jettaiah P, Sundararajan N (2011) Very-low-frequency electromagnetic (VLF-EM) measurements in the Schirmacheroasen area, East Antarctica. Polar Science 5:11–19

Groves DI, Goldfarb RJ, Gebre-Mariam M, Hagemann SG, Robert F (1998) Orogenic gold deposits: A proposed classification in the context of their crustal distribution on relationship to other gold deposit types. Ore Geol Rev 13:7–27

Kryza R, Muszyński A (1992) Pre-Variscan volcanic-sedimentary succession of the central southern Góry Kaczawskie, SW Poland: outline geology. Annales Societatis Geologorum Poloniae 62:117–140

Mikulski SZ (2003) Orogenic quartz-sulfide-gold veins from the Klecza-Radomice ore district in the Kaczawa Mountains (W Sudetes). In: Eliopoulos et al. (eds) Mineral Exploration and Sustainable Development. Millpress, Rotterdam: 787–790

Mikulski SZ (2007) The late-Variscan gold mineralization in the Kaczawa Mountains, Western Sudetes. Polish Geological Institute Special Papers 22: 1–162. PGI Warszawa

Mikulski SZ, Markey RJ, Stein HJ (2005) Re-Os ages for auriferous sulfides from the gold deposits in the Kaczawa Mountains (SW Poland). In: Mao J and Bierlein FP (eds) Mineral Deposit Research: Meeting the Global Challenge, Springer-Verlag Berlin, Germany: 793–796

Mikulski SZ, Ostrowski S, Cymerman Z, Małek R, Sadłowska K, Handke B, et al. (2021, unpublished) Evaluation of the possibility of obtaining rare raw materials (especially some metals) from areas and deposits not yet explored in this respect. Task 4.1. NGA no 1955/2021. Warszawa (In Polish)

Milewicz J (1962) Detailed geological map of the Sudety Mountains in the scale of 1:25,000. Lubomierz sheet. Wydawnictwa Geologiczne Warszawa

Milewicz J, Frąckiewicz W (1983) Detailed geological map of the Sudety Mountains in the scale of 1:25,000. Wleń sheet. Wydawnictwa Geologiczne Warszawa

Milewicz J, Kozdrój W (1994) Detailed geological map of the Sudety Mountains in the scale of 1:25,000. Proboszczów sheet. Państwowy Instytut Geologiczny Warszawa

Olszyński W, Mikulski SZ (1997) Native gold in crystalline schists from Radomice near Wleń: Noble metals in NE part of Bohemian Massif and its surroundings, genesis, occurrence, perspectives. Jarnoltowek 19-21.06.1997. Wrocław: 86–90 (In Polish)

Ostrowski S (2014) Mapping with VLF tool - gold investigation case study that yielded unexpected structural minutiae. Geologia Sudetica 42:68

Paterson NR, Ronka V (1971) Five years of surveying with the very low frequency electromagnetic method. Geoexploration 9:7–26

Paulo A, Salamon W (1973) Native gold in ore veins of the Western part of Góry Kaczawskie Mts. (West Sudetes). Mineralogia Polonica 4(2):85-91

Phillips WJ, Richards WE (1975) A study of the effectiveness of the VLF method for the location of narrow mineralized zones. Geoexploration 13:215–226

Ramesh Babu V, Ram S, Sundararajan N (2007) Modeling of magnetic and VLF-EM with an application to basement fractures - a case study from Raigad, India. Geophysics 71:133–140

Sharma S, Biswas A, Baranwal V (2014) Very Low-Frequency Electromagnetic Method: A Shallow Subsurface Investigation Technique for Geophysical Applications. In: Sengupta D (ed) Recent Trends in Modelling of Environmental Contaminants. Springer, New Delhi, pp 119–141

Singh A, Sharma SP (2016) Interpretation of very low frequency electromagnetic measurements in terms of normalized current density over variable topography. Journal of Applied Geophysics 133 (2016):82–91

# Multiple sulfur isotope analyses identify an Archean sulfur source for the auriferous fluids at the Meliadine gold district, Nunavut, Canada

**Philippe Mongeau[1], Crystal LaFlamme[1], Patrick Mercier-Langevin[2], Guillaume Barré[1], Olivier Côté-Mantha[3], Pierre de Cartigny[4], Laure Martin[5]**
[1]*Département de Géologie et de Génie Géologique, Université Laval, Québec, Québec*
[2]*Geological Survey of Canada, Québec, Québec*
[3]*Agnico Eagle Mines Limited, Exploration Division, Val-d'Or, Québec*
[4]*Institut de Physique du Globe de Paris, Université Paris Cité, Paris, France*
[5]*Centre for Microscopy, Characterisation & Analysis, University of Western Australia, Western Australia, Australia*

**Abstract.** In Canada, orogenic gold deposits are the main source of gold, but the origin of hydrothermal fluids remains equivocal. The Meliadine gold district (3.7 Moz Au), located in the Churchill Province in Nunavut, contains a series of deposits emplaced during the Paleoproterozoic Trans-Hudson orogenesis, hosted in Archean metavolcanic and metasedimentary rocks of the Rankin Inlet greenstone belt. This project aims to document the multiple sulfur isotope signature ($\delta^{34}S$, $\Delta^{33}S$, $\Delta^{36}S$) of gold-associated sulfides in quartz-carbonate veins through the paragenetic sequence, and to track the source and evolution of auriferous fluids. Samples containing arsenopyrite+pyrrhotite±(pyrite, galena, chalcopyrite) were collected across unmineralized host-rock, intermediate alteration zones and gold-rich vein-related mineralization. In-situ (SIMS) and bulk (IRMS) isotope analyses show that $\delta^{34}S$ does not vary much across the paragenetic sequence and at the sample, drillhole and deposit scale with an average $\delta^{34}S$=3.1±2.8 ‰ (2SD; n=238). Sulfur mass-independent fractionation (S-MIF) is present in all samples, yielding average values of $\Delta^{33}S$=0.32±0.24 ‰ (2SD; n=129) and $\Delta^{36}S$=-0.70±0.56 ‰ (2SD; n=58). This new dataset shows that the devolatilization of deep-seated metasedimentary and metavolcanic units during prograde metamorphism may play an important role in sourcing sulfur, a key ligand for gold.

## 1 Introduction

The importance of multiple fluid generations and/or long-lived fluid flow for orogenic gold deposits is well established (e.g. Robert et al. 2005; Dubé and Mercier-Langevin, 2020). However, the source of the mineralizing auriferous hydrothermal fluids remains equivocal (Goldfarb and Pitcairn, 2023). Recent studies demonstrate that sulfur isotopes represent an additional tool for gold exploration (e.g., LaFlamme et al. 2018a). It is possible to gain insight into the source and the evolution of the mineralizing fluid chemistry through space and time by multiple sulfur isotope analysis on gold-hosting sulfide grains. Changes in the oxygen fugacity ($fO_2$) of the fluid largely control the behavior of gold in the fluid, i.e., its transport or precipitation (Williams-Jones et al. 2009). Because $\delta^{34}S$ is highly sensitive to $fO_2$ variation (Ohmoto and Rye, 1979), $\delta^{34}S$ can serve as a marker of the change (redox conditions) responsible for destabilizing gold-sulfides complexes (LaFlamme et al. 2018a). Therefore, isotopic signatures representing prospective areas for exploration can be identified by characterizing the $\delta^{34}S$ of gold-associated sulfides and by comparing gold-rich and gold-poor zones.

Moreover, Archean sulfur mass-independent fractionation (S-MIF), as $\Delta^{33}S$ and $\Delta^{36}S$ values, can help distinguish between magmatic and sedimentary sources or reservoirs of sulfur from auriferous hydrothermal fluids further helping assess ore-forming processes and area fertility.

The Paleoproterozoic Meliadine gold district (MGD) is hosted in the Archean Rankin Inlet greenstone belt of Nunavut. It is host to orogenic gold deposits within typical structurally controlled quartz-carbonate (calcite ± ankerite) veins. These veins contain multiple arsenopyrite generations that host gold, and thus represents an excellent opportunity to explore the chemical controls on sulfide-related orogenic gold in an Archean greenstone belt. Here, we aim to define the source of sulfur for the mineralizing fluids and test the hypothesis that the multiple sulfur isotope signatures and their variations in space and time (through the paragenetic sequence of sulfides) can help define vectors between poor and rich zones at the deposit and district scale.

## 2 Geological setting

The MGD, located in the western Churchill Province in northern Canada (Figure 1), hosts 3.7 million ounces of gold in proven and probable reserves (Agnico Eagle Mines Ltd., 2022). This gold district is thought to have been emplaced during the Paleoproterozoic Trans-Hudson orogenesis (THO: Carpenter et al. 2005; Lawley et al. 2015). The MGD comprises multiple deposits that are hosted in the Archean meta-volcanic (e.g., Wesmeg, Normeg and Pump) and meta-sedimentary (e.g., Tiriganiaq and Discovery) rocks of the Rankin Inlet greenstone belt and are associated with the Pyke and Lower faults (Figure 1).

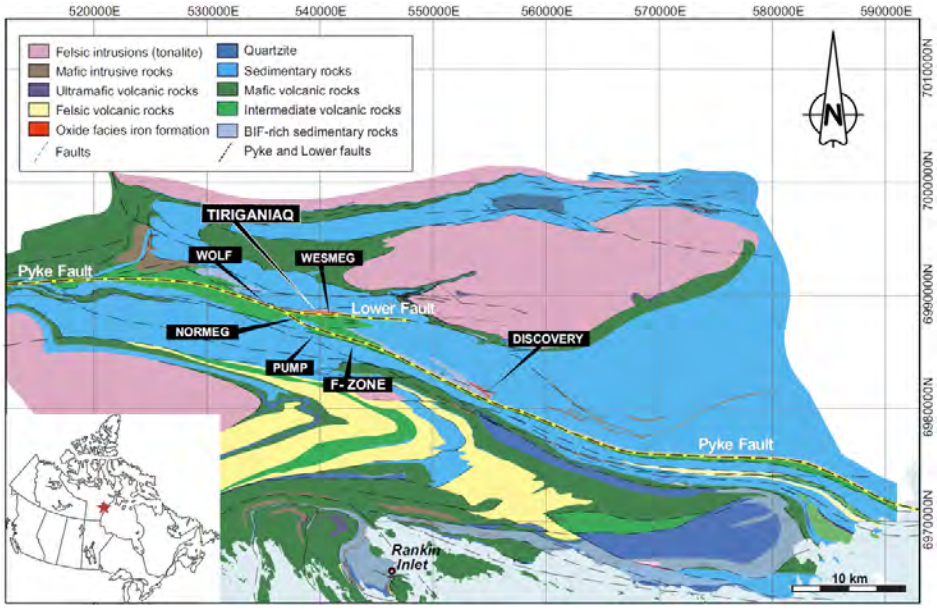


**Figure 1.** Geology map of the Meliadine Gold District highlighting the geological context and location of the various deposits, modified after St. Pierre et al. (2020).

### 2.1 Tiriganiaq deposit

The Tiriganiaq deposit is located in the hanging wall of the Lower Fault within an overturned turbiditic succession, located in the central part of the district. The deposit is hosted within several formations that include: 1) the mineralized Tiriganiaq Formation, which is composed of laminated siltstones and graphitic argillite; 2) the Upper Oxide Formation, a package of iron rich turbidites and silicate-oxide-facies iron formations that hosts the majority of the ore, and 3) the Sam Formation, composed of sub-economic greywackes and laminated siltstones, (St. Pierre et al. 2020). These formations have undergone several deformation episodes between 2.56 and 1.8 Ga (MacQuoid, Arrowsmith, Taltson-Thelon, and Trans-Hudson orogenies: Lawley et al. 2015). Gold lodes form as stacked, semicontinuous, gold-rich intervals of quartz-carbonate veins, where replacement style mineralization occurs in sulfidized iron-rich lithologies subparallel to the Lower Fault. Gold is often found in microtextural sites of low deformation (e.g. pressure shadows) and as inclusions in recrystallized and idioblastic arsenopyrite crystals but is also found in the absence of arsenopyrite. Re-Os dating also shows that while the most gold-rich arsenopyrite crystals are associated with the THO (~1.9 Ga), older generations of gold-associated, lower grade, arsenopyrite (~2.27 Ga) are also recognized (Lawley et al. 2015).

### 2.2 Wesmeg, Normeg and Pump deposits

The Wesmeg, Normeg, and Pump deposits, are all found in the Wesmeg Formation, forming the footwall of the Lower Fault. The Wesmeg Formation consists of mafic volcanic rocks that are interbedded with narrow oxide-facies iron formations cut by gabbro and lamprophyre dykes (St. Pierre et al. 2020). Similar to the Tiriganiaq deposit, gold-rich intervals occur as stacked lodes of quartz-carbonate veins and replacement-style mineralization that are subparallel to the Lower Fault, but are mainly spatially constrained to iron formations (Lawley et al. 2015). Gold is often found microtextural sites of low deformation and as inclusions in idioblastic arsenopyrite crystals, along with a sulfide assemblage consisting of arsenopyrite + pyrrhotite ± (pyrite - chalcopyrite - galena - sphalerite), and oxides (magnetite and ilmenite; Lawley et al. 2015).

## 3 Methodology

### 3.1 Sampling strategy

Samples were collected from underground stopes and drill-core from the unmineralized zones towards the high-grade zones, considering the location of the zones, grades, depths, alteration, etc. Samples considered altered are near the main ore zones, whereas unaltered samples are collected as far as possible from the alteration associated with the mineralized zones. Samples from the intermediate alteration zones were collected between the mineralized and unmineralized zones.

### 3.2 Textural and chemical composition of sulfides

Micro-analytical characterisation was completed on selected sulfides in thin-section at Université Laval. Major and minor elemental analyses were carried out by wavelength dispersive spectrometry using a CAMECA SX-100 EPMA with a beam size of 5 µm at 15 kV and 20 nA. To gain insight into the microtextural characteristics of the various sulfide assemblages and their relationship to gold, back-scatter electron imaging was completed on a FEI Inspect F50 Scanning Electron Microscope using a

beam at 50 kV and 600 µA with a step-size of 20 µm and a 10 ms acquisition time.

### 3.3 Bulk sulfur isotope analyses

High precision multiple sulfur isotopes measurements ($\delta^{34}S$, $\Delta^{33}S$, $\Delta^{36}S$) were completed on a total of 58 samples of pyrrhotite, arsenopyrite, pyrite and galena (including duplicates). For this purpose, sulfide powders were collected from targeted sulfides within selected samples using a Dremel rotary tool. The extraction of sulfur from the sulfide phases was completed at Université Laval by wet chemistry. Powdered sulfides were dissolved in HCl for pyrrhotite and galena, and with chromium reduced sulfides (CRS) solution following the protocol established by Canfield et al. (1986) for pyrite. In both cases, the produced $H_2S$ was then converted to $Ag_2S$ by reacting with a $AgNO_3$ solution. The measurements of $^{32}S$, $^{33}S$, $^{34}S$ and $^{36}S$ on $Ag_2S$ and arsenopyrite samples were then carried out at the *Institut de Physique du Globe de Paris* using a fluorination line ($SF_6^+$) coupled to a ThermoFinnigan MAT253 dual inlet gas-source mass spectrometer. The recovered $Ag_2S$ were fluorinated overnight to produce $SF_6$ in nickel reaction bombs by reaction with $F_2$ in excess at 250 ºC. As arsenopyrite does not react with acid solutions, the powders were introduced directly into the nickel reaction bombs to react with $F_2$. The produced $SF_6^+$ was sequentially purified using cryogenic traps and gas chromatography, then introduced into the mass spectrometer. Measurement accuracy and reliability was monitored by introducing samples of International Atomic Energy Agency (IAEA-S1) $Ag_2S$ standard over the course of the analyses.

### 3.4 In-situ sulfur isotope analyses

In situ multiple sulfur isotopes ($\delta^{34}S$, $\Delta^{33}S$) of pyrrhotite (n=53), pyrite (n=8) and chalcopyrite (n=7) were completed by a CAMECA IMS 1280 secondary ion mass spectrometry (SIMS) analyses that were carried out at the University of Western Australia, allowing to get spatial resolution of individual sulfide analyses. Small pucks (n=10) of a few millimetres in diameter containing sulfides were extracted from the samples selected for analysis, placed in an epoxy mount and polished and paired with standard blocks of matrix-matched Alexo pyrrhotite, Sierra pyrite and Nifty-b chalcopyrite (LaFlamme et al. 2016). To ensure standard repeatability and to account for analytical drift and instrumental mass fractionation, unknown samples were interspersed with matrix-matched reference materials and analyses monitored using respective standards. Measurements of $^{32}S$, $^{33}S$, $^{34}S$ and by spot analyses were carried out following the protocol as defined by LaFlamme et al. (2016) with slight modifications, with the ion microprobe operating in multicollection mode using a focussed, 10 µm $Cs^+$ beam with impact energy of 20 kV and intensity 2.3 nA.

## 4 Results

### 4.1 Sulfide paragenesis

The paragenesis of sulfides was established for the Tiriganiaq deposit, where multiple generations of sulfides have been categorized as generations 1, 2a and 2b (Figure 2). Generation 1 pre-dates gold and is characterized by pyrrhotite ± pyrite that is deformed and oriented within the host-rock foliation (Figure 2A) of laminated siltstones, argillites, iron-rich turbidites, silicate-oxide-facies iron formations and greywackes, but is less abundant in areas rich in veining and gold. Generation 2a is formed of arsenopyrite and 2b is formed of arsenopyrite+pyrrhotite±pyrite and both are discernible from Generation 1 based on texture and major/minor chemical composition, showing As enrichments in generations 2a and b. Pyrrhotite 2b displays elevated arsenic contents correlating sample with gold grade. The differences between 2a and 2b arsenopyrite are based on the different textures, relationship to gold, alteration and recrystallisation haloes observed with the SEM. Generation 2b arsenopyrite and pyrrhotite are commonly related to gold (Figure 2B/C). Pyrrhotite and arsenic-rich recrystallisation haloes of arsenopyrite are associated with free gold. Figure 2D shows an example of the complex sulfide paragenesis, where textural relationships between different phases can be equivocal.

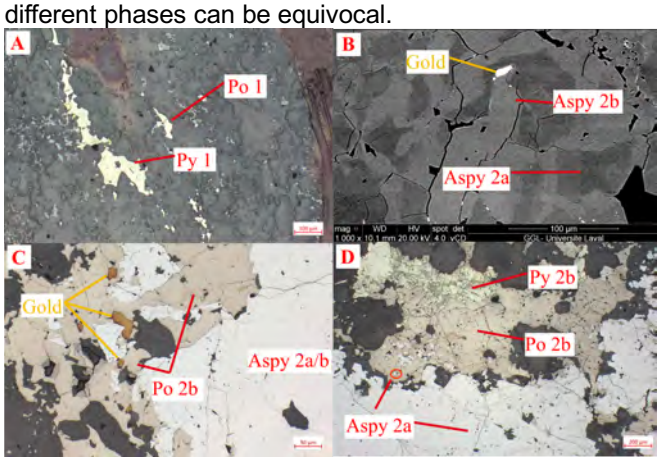


**Figures 2A, 2C, 2D:** Reflected light photomicrographs of various sulfide generations, textural relationships, and association with gold. **Figure 2B:** Backscatter electron image of gold-rich arsenopyrite, highlighting the arsenic-rich recrystallisation haloes and their relationship to gold.

### 4.2 Multiple sulfur isotope analyses

Multiple sulfur isotope analyses completed both in situ (SIMS) and in bulk (IRMS) show that $\delta^{34}S$ sees little variation at the sample, drillhole and deposit scale with an average $\delta^{34}S$ = 3.00 ± 2.85 ‰ (2SD; n = 129) and does not correlate with gold grade. Mass-independent fractionation of sulfur (MIF-S) is present in all the in situ and bulk samples yielding average values of $\Delta^{33}S$ = 0.32 ± 0.24 ‰ (2SD; n=129) and $\Delta^{36}S$ = -0.70 ‰ ± 0.56 (2SD; n=58). Plotted $\delta^{34}S$ versus $\Delta^{33}S$ in Figure 3 shows that the $\Delta^{33}S$ values

remain stable across all samples but plot outside of the mass-dependent fractionation array (MDF-S). Sulfide generations from older to most recent also show a shift towards enriched $\delta^{34}S$ values, consistent between all phases and analytical methods (in bulk and in situ) while the $\Delta^{33}S$ remains stable.

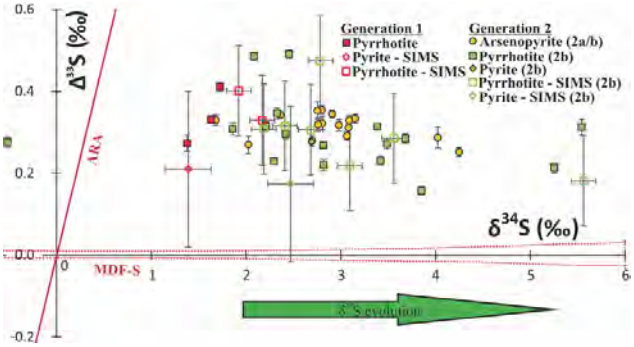


**Figure 3.** Multiple sulfur isotopes values ($\delta^{34}S$ and $\Delta^{33}S$) of various sulfide phases and generations obtained from SIMS and bulk analyses. Archean Reference Array (ARA, $\Delta^{33}S=0.89*\delta^{34}S$) after Ono et al. (2009). Mass-dependent fractionation of sulfur (MDF-S) after LaFlamme et al. (2018b). The green arrow represents the evolution between relict sulfides (1) and gold-associated sulfide generations (2a/2b). Note the homogeneous $\Delta^{33}S$ during this evolution, a sign of a single source of sulfur.

## 5 Conclusions

Monitoring fluid-rock reactions is essential to understand gold precipitation mechanisms. While the timing of generation 1 of sulfides remains uncertain, the homogeneous $\Delta^{33}S$ signature with generations 2a and 2b supports the idea of a common local source of fluid (i.e. metavolcanics and metasediments of the host-rock) that has been recycled by subsequent sulfur-poor hydrothermal fluids through fluid-rock reactions. It implies that gold could have been introduced much earlier than previously postulated and have undergone multiple stages of remobilization along with the recycling of sulfur at the district scale (e.g. Lawley et al. 2015). The evolution of the $\Delta^{33}S$ and $\delta^{34}S$ through the paragenetic sequence (Figure 3) shows that the samples remain outside of the MDF-S array, but don't follow the Archean trend either. This suggests a mixing source of sulfur from meta-sedimentary with positive S-MIF $\Delta^{33}S$ values and meta-volcanic rocks with likely near-zero $\Delta^{33}S$ values (i.e., magmatic origin, Siedenberg et al. 2016) that would buffer the overall $\Delta^{33}S$ signature of the mineralization, and/or the remobilization of sulfur and gold at the deposit scale through mass-dependant processes. This new dataset shows that the source of these auriferous fluids clearly recorded an influence of Archean metasedimentary rock, and that the devolatilization of deep-seated metasedimentary and metavolcanic units during prograde metamorphism plays an important role in sourcing sulfur, key to the transportation of gold at the crustal scale.


## Acknowledgements

This study is financially supported by Mitacs, Agnico Eagle Mines Ltd., and the TGI 6. Thanks to Marc Choquette, Suzie Côté, Karine Lavallée and Edmond Rousseau at Université Laval, to Matvei Aleshin at the University of Western Australia and to Agnico Eagle Mines Ltd. Staff for technical and scientific support.


## References


Canfield D, Raiswell R, Westrich J, Reaves C, Berner R (1986) The use of chromium reduction in the analysis of reduced inorganic sulfur in sediments and shales. Chem. Geol. 54:149-155. https://doi.org/10.1016/0009-2541(86)90078-1,

Dubé B, Mercier-Langevin P (2020) Gold deposits of the Archean Abitibi Greenstone Belt, Canada. Geology of the World's Major Gold Deposits and Provinces. Soc. Econ. Geol. Special Publication 23. https://doi.org/10.5382/SP.23.32,

Goldfarb R.J, Pitcairn I (2023) Orogenic gold: is a genetic association with magmatism realistic? Miner. Depos. 58:5–35. https://doi.org/10.1007/s00126-022-01146-8,

LaFlamme C, Martin L, Jeon H, Reddy S.M, Selvaraja V, Caruso S et al. (2016) In situ multiple sulfur isotope analysis by SIMS of pyrite, chalcopyrite, pyrrhotite, and pentlandite to refine magmatic ore genetic models. Chem. Geol. 444:1-15. https://doi.org/10.1016/j.chemgeo.2016.09.032,

LaFlamme C, Sugiono D, Thébaud N, Caruso S, Fiorentini M, Selvaraja V, et al. (2018a) Multiple sulfur isotopes monitor fluid evolution of an Archean orogenic gold deposit. Geochim. Cosmochim. Acta 222:436-446. https://doi.org/10.1016/j.gca.2017.11.003,

LaFlamme C, Jamieson JW, Fiorentini ML, Thébaud N, Caruso S, Selvaraja V (2018b) Investigating sulfur pathways through the lithosphere by tracing mass independent fractionation of sulfur to the Lady Bountiful orogenic gold deposit, Yilgarn Craton. Gondwana Res. 58:27-38. https://doi.org/10.1016/j.gr.2018.02.005,

Lawley C.J.M, Creaser R.A, Jackson S, Yang Z, Davis B, Pehrsson S, Dubé B, Mercier-Langevin P, Vaillancourt D. (2015) Unraveling the Western Churchill Province Paleoproterozoic gold metallotect: constraints from Re-Os arsenopyrite and U-Pb xenotime geochronology and LA-ICP-MS arsenopyrite trace element chemistry at the BIF-hosted Meliadine gold district, Nunavut, Canada. Econ. Geol. 110:1425-1454. https://doi.org/10.2113/econgeo.110.6.1425,

Ohmoto H and Rye R.O (1979) Isotopes of sulfur and carbon, in Barnes, H.L., ed., Geochemistry of hydrothermal ore deposits, second edition. New York, John Wiley and Sons, Inc., pp. 509-567,

Robert RK, Poulsen KH, Cassidy KF, Hodgson CJ (2005) Gold metallogeny of the Superior and Yilgarn Cratons. Econ. Geol. 100th anniversary volume. https://doi.org/10.5382/AV100.30,

Siedenberg K, Strauss H, Hoffman E.J (2016) Multiple sulfur isotope signature of early Archean oceanic crust, Isua (SW-Greenland). Precambrian Res. 283:1-12 https://doi.org/10.1016/j.precamres.2016.07.002

St. Pierre B, Mercier-Langevin P, Blais J-C, Servelle G, Simard M, Côté-Mantha O, Malo M (2020) Structural controls and relative timing of gold mineralization of the banded iron formation associated Tiriganiaq deposit, Meliadine district, Rankin Inlet greenstone belt, Nunavut. Geol. Surv. Can. 8712:237-250. https://doi.org/10.4095/326041,

William-Jones A.E, Bowell R, Migdisov A (2009) Gold in Solution. Elements 5(5):281-287. http://dx.doi.org/10.2113/gselements.5.5.281.

# Revisiting the Kundarkocha gold mine: A rare Paleoarchean greenstone-hosted gold deposit, eastern India

**Dhruv Pathania[1], Rajarshi Chakravarti[1], Abdul Latheef T P[1]**
*[1]Department of Earth Sciences, Indian Institute of Technology, Roorkee, India*

**Abstract.** The Kundarkocha mine is a rare example of a Paleoarchean greenstone-hosted gold deposit. The deposit is situated in the ~ 3.25 Ga (Ghosh et al. 2019) Gorumahisani-Badampahar greenstone belt in Singhbhum Craton of eastern India. Mining operations at Kundarkocha were put to a halt in 2018, owing to inefficient exploration strategies and subsequent low productivity. Gold mineralization at Kundarkocha is hosted predominantly within carbonaceous phyllites and graphitic schists. Native gold grains are recorded in the smoky quartz veins emplaced along the $S_2$ axial planar foliations and in close spatial association with syn-deformational hydrothermal pyrite, referred to as Pyrite-3 here. Occasionally, native gold occurrences are also noted along brittle-ductile deformed metamorphic pyrite (Pyrite-2). However, this second mode of occurrence is volumetrically less significant and was possibly sourced from pre-existing diagenetic pyrite (Pyrite-1) during metamorphism. Our new textural and mineralogical data reveals that the main gold mineralizing event was coeval with $D_2$ deformation (shearing) and is hosted in second or third-order brittle structures, possibly associated with a crustal-scale shear zone. Combining our new results with known tectono-thermal events in the area provides useful insights into the nature, controls, and possible timing of gold mineralization at the Kundarkocha.

## 1 Introduction

Neoarchean greenstone belts dated at ca. 2.8 – 2.5 Ga stand out as the most fertile environments for the formation of orogenic gold deposits. Thus, logically, it may be speculated that significant proportions of gold had already accumulated in the Earth's crust before 2.8 Ga, which was redistributed and concentrated to economic levels with the advent of plate tectonics in the Neoarchean (Frimmel 2018). However, before ~ 3 Ga, there is an apparent dearth of economic orogenic gold deposits, the reasons for which remain unclear. The study related to the gold mobility and possible Paleoarchean gold sink was published by Hoffmann et al. (2017) where the author put forward pervasive seafloor silicification, the rarity of black shales, and low gold content in the ultramafic rocks to be the potential causes behind the low mineralization potential of Paleoarchean greenstone belts for orogenic gold formation. To this end, here we investigate a rare Paleoarchean greenstone-hosted gold deposit, i.e., Kundarkocha, situated in the Singhbhum Craton in eastern India.

The Kundarkocha deposit is situated within the ~ 3.25 Ga Gorumahisani-Badampahar greenstone belt in the Singhbhum Craton. The mine was operated for a short span of 12 years, having an annual gold production of ~ 15 kg at an average grade of 3 g/ton (India Minerals Yearbook 2018), before being de-commissioned in 2018. Previous studies in the Kundarkocha deposit recognize a close spatial association of gold with pyrite, along second or third-order brittle-ductile structures (Hazarika et al. 2013; Sahoo and Venkatesh 2015). Those studies, however, provide contrasting views on the origin of gold at Kundarkocha, i.e., a sedimentary pyrite-hosted origin vs an arsenopyrite proto-ore possibly derived from the alteration of ultramafic rocks. Moreover, the paragenetic position of gold remains unclear. To this end, here we revisit the Kundarkocha mine and present detailed textural observations and mineralogical data, which enhance our understanding of the nature and control of gold mineralization at the Kundarkocha.

## 2 Geological setting

The current study area, i.e., the Kundarkocha deposit lies in the Gorumahisani-Badampahar greenstone belt (GBG) in the Singhbhum Craton. The arcuate GBG belt in eastern Singhbhum has two arms with curvilinear outcrops of volcano-sedimentary successions moulded against plutons of the Singhbhum granite batholith (Saha et al. 2021). The GBG is divided into lower and upper sequences, with the lower sequence comprising komatiite with the pillow to massive basalts with subordinate chemical sediments and the upper sequence consisting of mafic volcanic rocks overlain by clastic sediments (Saha et al. 2021). The region has undergone polyphase deformation with at least three phases that have been well documented (Ghosh et al. 2019). The first phase ($D_1$) led to the development of the regional isoclinal fold ($F_1$) plunging NNE. The second phase ($D_2$) caused extensive shearing and tight folding ($F_2$) plunging NE-SW with the development of $S_2$ foliation. The third phase ($D_3$) caused open folds ($F_3$) plunging NW.

### 2.1 Deposit Geology

Kundarkocha deposits belong to the lower sequence of the GBG and consist of basal altered ultramafic rocks and deformed ocelli pillow basalts overlain by green chert, massive black chert, carbonaceous phyllites, graphitic schists, Cr-bearing mica schists and talc-chlorite-serpentinite schists with abundant fuchsite (Jodder et al. 2021).

The major lithologies with which gold is associated are carbonaceous phyllites and graphitic schists. Gold bearing smoky quartz veins are present along the interface between the carbonaceous phyllites and chlorite-fuchsite-serpentine schist and are emplaced parallel to the axial planar foliations (Sahoo and Venkatesh 2015).

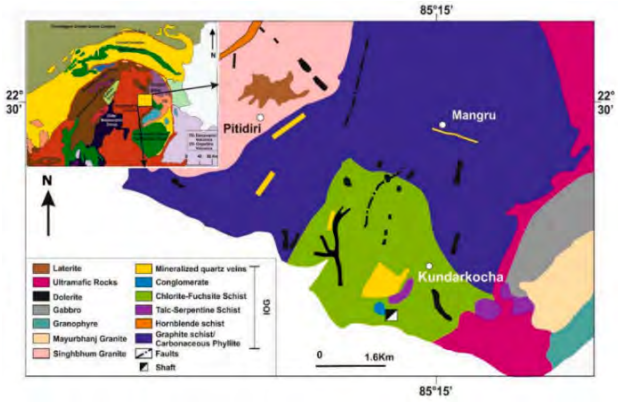


**Figure 1.** Geological map of Kundarkocha area (Modified after Banerjee and Thiagarajan 1965).

## 3 Pyrite morphology and paragenesis

Pyrite is the most ubiquitous sulfide in the studied samples and shows a close spatial association with gold. The following genetic varieties of pyrite have been identified based on textural analysis.

Diagenetic pyrite, containing numerous inclusions of aluminosilicates and carbonaceous material, is designated as Pyrite-I. These grains are rarely preserved and have been overprinted by metamorphic and hydrothermal pyrite. This pyrite variety often forms the core of late-stage pyrite.

Metamorphic pyrite containing inclusions of aluminosilicates and silicates, designated as Pyrite-2. It is coarse-grained showing rotation of inclusions and brittle-ductile deformation with secondary foliations cutting across (Figure 4. b), suggestive of its formation during early regional metamorphism.

Pyrite-3 is interpreted to be hydrothermal in nature and is represented by two morphological types, Pyrite-3a and Pyrite-3b. Pyrite-3a occurs as euhedral overgrowths around metamorphic Pyrite-2. Pyrite-3b occurs as fracture free subhedral to euhedral grains in the veins interacting with carbonaceous matter. Both Pyrite-3a and Pyrite-3b have formed during the emplacement of syn-deformational hydrothermal veins and contain inclusions of sphalerite, chalcopyrite, galena, and monazite.

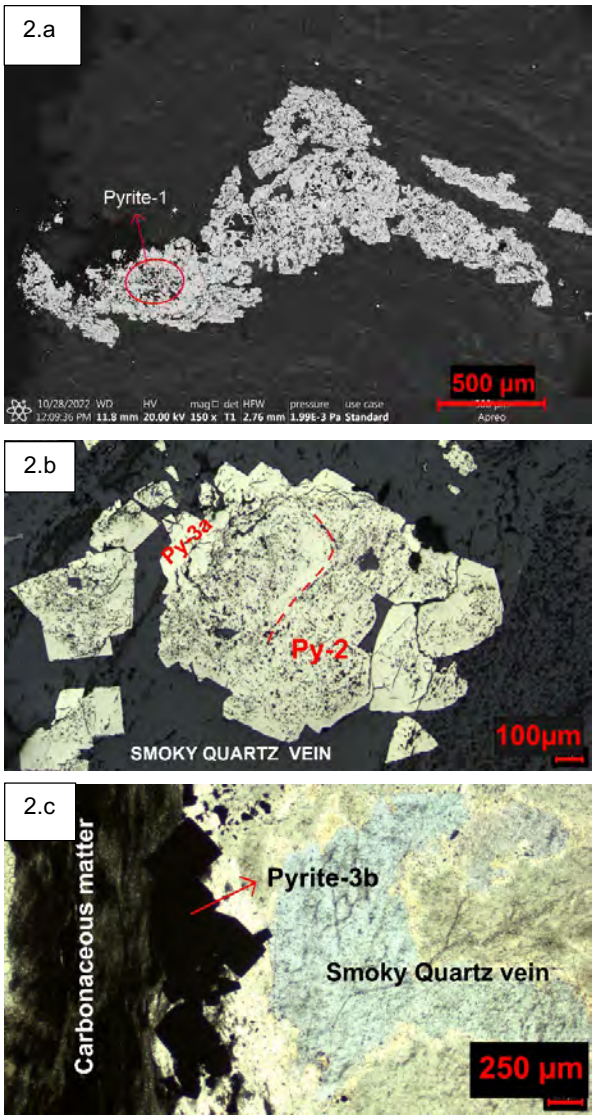


**Figure 2. a** SEM backscattered electron (BSE) image of folded and fractured metamorphic Pyrite-2 with the inclusion rich core of diagenetic Pyrite-1 (marked by the red circle). **b** Reflected light petrographic image of Pyrite-2 which is of metamorphic nature (rotated inclusions marked by a curved red line) indicating syn-metamorphic nature with overgrowth of hydrothermal Pyrite-3a. **c** Transmitted light petrographic image of Pyrite-3b forming along interaction between the carbonaceous matter and smoky quartz veins.

## 4 Nature of gold mineralization

Gold mineralization at Kundarkocha exhibits structural as well as lithological control. Our study reveals two modes of occurrence of gold. Native gold on euhedral overgrowths around metamorphic Pyrite-2 and gold mineralization in dilatational smoky quartz veins in spatial association with carbonaceous matter. The latter mode of occurrence, however, is more abundant throughout the deposit. These Au-bearing smoky quartz veins have been sheared and emplaced parallel to the foliation planes ($S_2$) along the axial planar folds and

show bulging recrystallization texture indicating the depth of emplacement to be 10-15 km which is the characteristic depth of brittle-ductile transition zone.

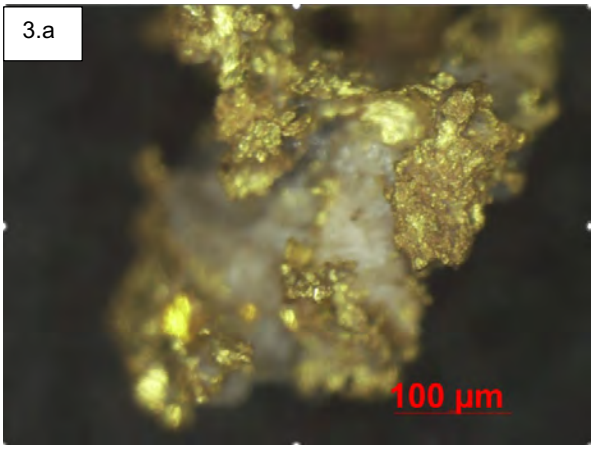

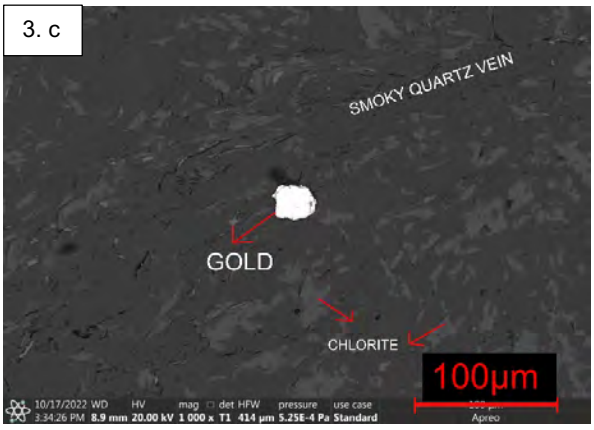


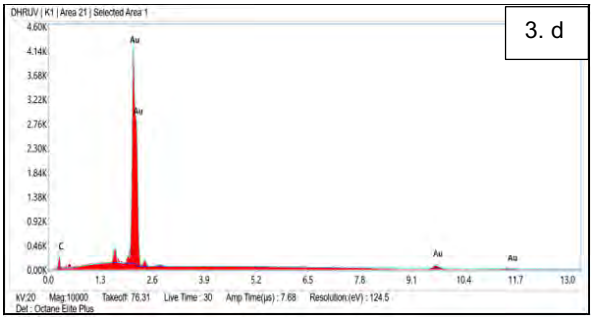


**Figure 3. a** Stereomicroscopic image of gold in association with the smoky quartz vein. **b** SEM (BSE) image of gold on the euhedral edges of metamorphic Pyrite-2 (inclusion rich). **c** SEM (BSE) image of native gold grain encountered in the carbonaceous phyllites intruded by smoky quartz vein. **d** Representative peak of gold grain obtained from SEM-EDS analysis.

## 5 Discussion and conclusion

Microstructures encountered in the petrographic study indicate atleast two phases of deformation in the Kundarkocha area (Figure 4. a). The auriferous smoky quartz veins are shear-controlled and emplaced parallel to the $S_2$ axial foliation planes. The $S_2$ foliations cut across the folded and fractured metamorphic Pyrite-2 (Figure 4. b). Native gold grains are encountered at the hinge of axial planar microfolds formed during $D_2$ deformation in close association with these Pyrite-2 grains (Figure 4. c). Hence, it can be deduced that the $D_2$ deformation event not only led to the emplacement of auriferous smoky quartz veins along $S_2$ axial foliations but also aided in the mobilization of gold from earlier generation pyrite. The gold grains encountered at the euhedral edges of Pyrite-2 are the remnant grains left over during the process.

The gold mineralization as already discussed, is associated with the smoky quartz veins paralleling the axial planar foliations ($S_2$). The close association of gold with carbonaceous rocks indicates the possible destabilization of the gold-ligand complex by carbon-induced Eh change. The occurrence of native gold grains showing close spatial association to pyrite and within the fractures in euhedral edges overgrowing metamorphic Pyrite-2 indicate possible mobilization of the lattice-bound gold from diagenetic Pyrite-1during subsequent progressive deformation and hydrothermal events (Figure 3. b).

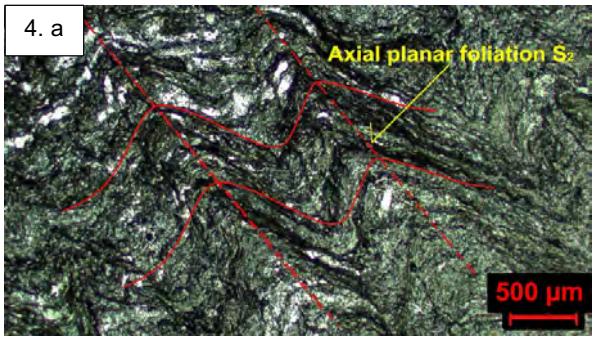


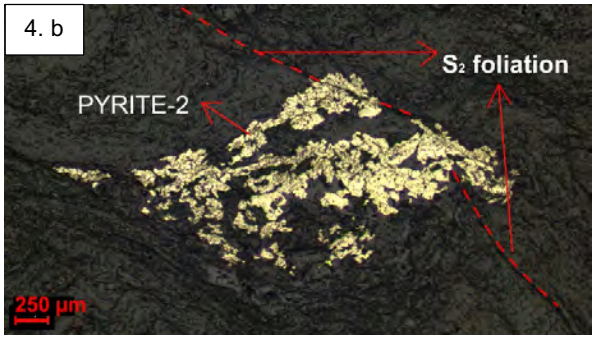

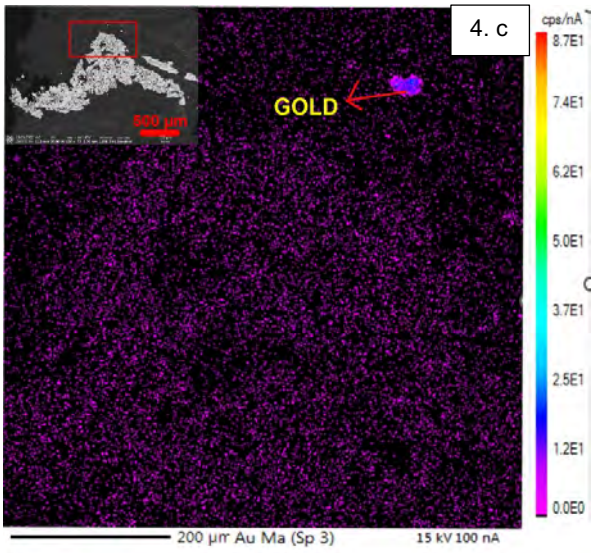


**Figure 4. a** Transmitted light petrographic image of carbonaceous phyllite indicating atleast two stages of deformation ($S_2$ foliation marked by the dotted straight red line). **b** Reflected light petrographic image of metamorphic Pyrite-2 cut by $S_2$ foliation (marked by the dotted curved red line). **c** X-ray elemental map of pyrite-2 for Au, showing gold grain at the hinge of the fold (top left is the SEM (BSE) image of Pyrite-2 with a red box indicating the area of analysis)

The mineralization event and the occurrence of gold either in association with pyrite or with smoky quartz veins can be summarised by the following steps:

1. Regional progressive deformation $D_1$, at ~ 3.3 Ga to 3.25 Ga (Saha et al. 2021) led to the folding and metamorphism of the host rock. Diagenetic Pyrite-1 present got metamorphosed and underwent ductile deformation producing metamorphic Pyrite-2.
2. $D_2$ deformation event, at ~ 3.1 Ga to 3.0 Ga (Saha et al. 2021) is related to the shearing event that led to the emplacement of gold-bearing smoky quartz veins along the secondary foliations. This deformation event led to the fracturing of the metamorphic Pyrite-2 (Figure 2. a, Figure 4. b). During this event, late-stage hydrothermal fluids overprinted the metamorphic pyrite and also precipitated individual grains of Pyrite-3b (Figure 2. b, Figure 2. c). This event led to the mobilization and concentration of gold in the form of native gold grains in close vicinity to Pyrite-2 along structurally favourable sites (Figure 4. c).

The source of gold at Kundarkocha, however, remains debatable. Gold could have been sourced from diagenetic pyrite hosted in the protolith of the carbonaceous phyllites, i.e., black shales. However, given the Paleoarchean age, organic-rich black shales were possibly volumetrically insignificant as a gold source, which could explain the small deposit size of Kundarkocha. Alternatively, sub-seafloor hydrothermal alteration of the mafic-ultramafic rocks of the lower GBG belt could have also led to the mobilization and precipitation of Au in structurally and chemically favourable sites. To this effect, this study also highlights the importance of industry-academia collaboration in India for better understanding and effective exploration of mineral deposits.

## Acknowledgements

Authors are thankful to director, IIT Roorkee for necessary permissions to carry out the work. IIC, IIT Roorkee is thanked for SEM-EDS analysis. Manmohan minerals private limited is thanked for providing the samples for this work. Prof. Sajeev Krishnan, IISC Bangalore is thanked for help with EPMA analysis. Dr. Rohit Pandey, BHU Varanasi is thanked for help with the X-ray elemental mapping of the sulphides. RC acknowledges a Faculty Initiation Grant (FIG 100930), for funding the research work.

## References

Frimmel HE (2018) Episodic concentration of gold to ore grade through Earth's history. Earth-Science Reviews 180:148-158

Ghosh R, Vermeesch P, Gain D, Mondal R, (2019). Genetic relationship among komatiites and associated basalts in the Badampahar greenstone belt (3.25–3.10 Ga), Singhbhum Craton, Eastern India. Precambrian Research 327:196–211

Hazarika P, Mishra M, Chinnasamy SS, Bernhardt (2013) Multi-stage growth and invisible gold distribution in pyrite from the Kundarkocha sediment-hosted gold deposit, eastern India. Ore Geology Reviews 55:134-145

Hofmann A, Pitcairn I, Wilson A (2017) Gold mobility during Paleoarchean submarine alteration. Earth and Planetary Science Letters 462:47-54

Indian Minerals Yearbook 2018 (2019). In: Part-I General Reviews Indian Bureau of Mines 57:1-8

Jodder J, Hofmann A, Ueckermann H (2021) 3.51 Ga old felsic volcanic rocks and carbonaceous cherts from the Gorumahisani Greenstone Belt – Insights into the Palaeoarchaean record of the Singhbhum Craton, India. Precambrian Research 357:106109

Sahoo PR, Venkatesh AS (2014) 'Indicator' carbonaceous phyllite/graphitic schist in the Archean Kundarkocha gold deposit, Singhbhum orogenic belt, eastern India: Implications for gold mineralization vis-à-vis organic matter. Journal of Earth System Science 123 (7):1693-1703

Sahoo PR, Venkatesh AS (2015) Constrains of mineralogical characterisation of gold ore: Implications for genesis, controls and evolution of gold from Kundarkocha gold deposit, eastern India. Journal of Asian Earth Sciences 97:136-149

Saha D, Bachhar P, Deb GK, Deb SP, Banerjee A (2021) Tectonic evolution of the Paleoarchean to Mesoarchean Badampahar-Gorumahisani belt, Singhbhum Craton, India- Implications for coexisting arc and plume signatures in a granite-greenstone terrain. Precambrian Research 357:106094

Singh S, Chakravarti R, Barla A, Behera RC, Neogi S (2021) A holistic approach on the gold metallogeny of the Singhbhum crustal province: Implications from tectono-metamorphic events during the Archean-Proterozoic regime. Precambrian Research 365:106376

# Record of the oldest vein-type gold mineralization throughout the Neoproterozoic Nubian shield: the Galat Sufar South gold deposit, NE Sudan

**Julien Perret[1,2,3], Aurélien Eglinger[2], Anne-Sylvie André-Mayer[2], Julien Feneyrol[3], Jérôme Ganne[4], Marc Poujol[5]**
*[1]present address: Centre for Exploration Targeting, School of Earth Sciences, University of Western Australia, 35 Stirling Highway, Crawley, WA 6009, Australia*
*[2]GeoRessources, Université de Lorraine, CNRS, 54000 Nancy, France*
*[3]Arethuse Geology SARL, 29 Allée St Jean, ZAC La Barque, 13170 Fuveau, France*
*[4]IRD, UR234, GET, Université Toulouse III, 14 Avenue Edouard Belin, 31400 Toulouse, France*
*[5]Géosciences Rennes, UMR CNRS 6118, OSUR, Université Rennes 1, 35042 Rennes Cedex, France*

**Abstract.** Despite the booming interest in Nubian shield for gold exploration, much more remains to be done to constrain geodynamical settings favorable for gold mineralization in a mineral system approach. Constraining pressure-temperature-timing-deformation (*P-T-t-d*) conditions relative to the formation of the structurally controlled Galat Sufar South (GSS) deposit is a case in point and represents a step forward in the understanding of the Pan-African gold mineral system along the westernmost Atmur-Delgo suture. The formation of the GSS gold deposit, hosted in an arc-related volcanosedimentary sequence metamorphosed and deformed by sheath folding, occurred at 738±16 Ma (*in situ* laser ablation inductively coupled plasma mass spectrometry (LA-ICP-MS) U-Pb dating of hydrothermal apatite coeval to gold mineralization). Additional chlorite-phengite-quartz-water multi-equilibria calculations in ore-hosting meta-volcanosediments suggest that the gold event occurred under lower amphibolite facies conditions (~7.2 kbar - 420 °C), probably during the tectonic accretion of the sedimentary wedge formed during Atmur-Delgo intra-oceanic subduction. To date, the GSS deposit is the oldest lode gold occurrence documented throughout the Nubian shield and the only one formed at regional peak metamorphism conditions in such a setting.

## 1 Geological setting

The Galat Sufar South (GSS) gold deposit (indicated resources of 75.6 Mt @ 1.27 g/t Au for a total of 3.08 Moz Au with a 0.6 g/t Au cut-off; Duckworth 2020) lies in NE Sudan, within the western portion of the Neoproterozoic Arabian–Nubian shield (ANS). The ANS belongs to the East-African-Antarctica orogen and results from the tectonic accretion and collision between terranes that accreted onto the Saharan meta-craton during a ~850–550 Ma 'Supercontinent Cycle', (*e.g.,* Johnson et al. 2011; Fritz et al. 2013).

GSS is encompassed within a complexly deformed zone at the junction between the Atmur–Delgo and Keraf sutures, both structures hosting gold occurrences (Johnson et al. 2017; Perret et al. 2020; Gaboury et al. 2020; Perret et al. 2021a). The mineralization is hosted by a strongly deformed meta-volcanosedimentary unit enclosed within interleaved lava flows, pyroclastic horizons and primary volcanic breccia (Perret et al. 2020). This assemblage is surrounded by meta-pelites interlayered with marbles.

The deposit-scale structural framework is dominated by a high-strain ductile $D_{2GSS}$ deformation stage, expressed by the main penetrative $L_2$ stretching lineation and $S_2$ penetrative fabric throughout the GSS area (Perret et al. 2020). These structures are contemporaneous to gold mineralization and control the ore-shoot geometry from the hundreds of kilometers up to the micrometer scales (Perret et al. 2021b). They likely relate to Atmur-Delgo suturing, *i.e.*, intra-oceanic subduction and arc-continent collision (Perret et al. 2020).

## 2 Sampling and analytical techniques

### 2.1 Sampling

The studied samples are part of the ore-bearing meta-volcanosedimentary sequence dominating the local lithological framework. The two samples analysed in this study (GS-55-02 and -04) have been collected along a diamond drill core crosscutting the GSS ore zone.

### 2.2 U-Pb dating of apatite

Prior to dating, apatite grains were imaged by cathodoluminescence at the GeoRessources laboratory (Université de Lorraine-CNRS, Nancy, France). *In situ* LA-ICP-MS U-Pb dating on apatite was conducted at Géosciences Rennes (Université de Rennes-CNRS, France).

### 2.3 Chlorite-phengite-quartz-water multi-equilibria calculations

The $D_{2GSS}$-related GSS mineral assemblage displays textural association between chlorite - a geothermometer -, phengite - a geobarometer - and quartz. Inferring geochemical equilibria between these mineral phases enables to carry out multi-equilibria calculations (*e.g.,* Vidal and Parra 2000), following the procedure detailed in Ganne et al. (2012). Calculations are completed from electron microprobe analyses (EMPA) of coexisting chlorite and phengite coeval to gold mineralization, carried out at the GeoRessources laboratory (Université de Lorraine-CNRS, Nancy, France).

## 3 Results

### 3.1 Petrography

Chlorite, phengite and quartz form most of the mineralizing $D_{2GSS}$ deformation stage-related silicate mineral assemblage in the ore-bearing tuffaceous horizon (Fig. 1; Perret et al. 2020).

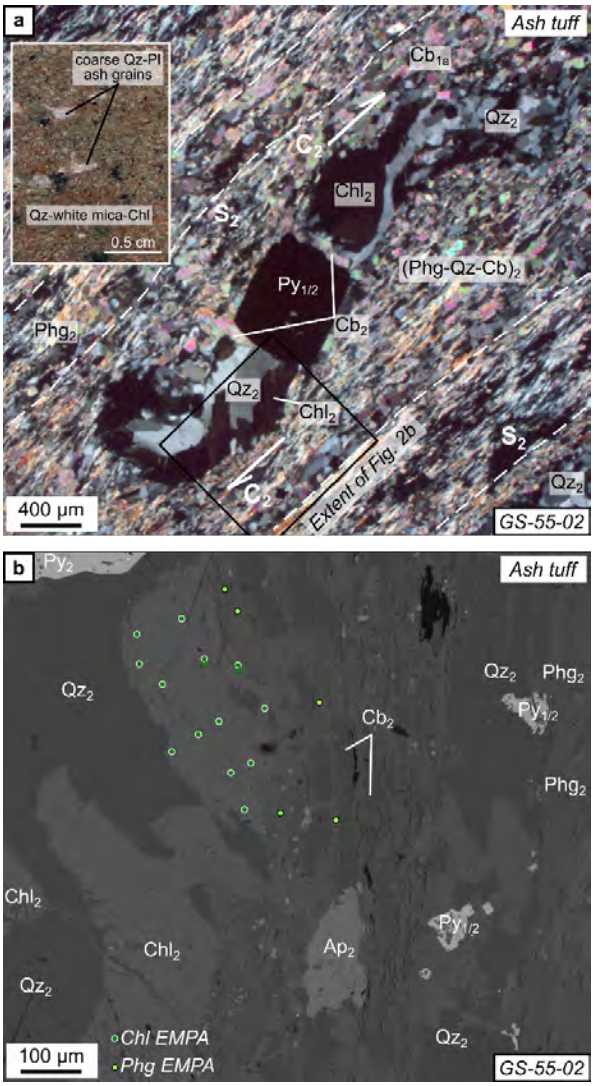


**Figure 1.** Syn-gold mineralization, $D_{2GSS}$-related, quartz-chlorite-phengite-apatite-pyrite mineral assemblage in ash tuffs**. a** $D_{2GSS}$-related quartz-chlorite asymmetrical strain fringes formed around $Py_{1/2}$ grains in the phengite-dominated schistose mineral gangue (cross-polarized, transmitted light). **b** Chlorite-phengite-apatite textural association and position of EMPA dataspots (BSE-SEM)

These mineral phases are in textural equilibrium (i) in the mineral gangue and (ii) between quartz-chlorite strain fringes around ore-related pyrite grains and the surrounding phengite-dominated matrix (Fig. 1a). Besides, apatite forms up to 500 µm-long, subhedral grains intergrown and elongated in the phengite-chlorite mineral gangue affected by the $S_2$ fabric in these pyroclastics (Fig. 1b). Scarcer apatite also consists of mineral inclusions in altered pyrite cores where overgrown by a mineral inclusion-free pyrite rim.

### 3.2 U-Pb dating of apatite

Dated apatite typically shows a rounded bright core and a large subhedral darker rim overgrown by a late, thin and brighter apatite external rim. Apatite rims are almost not radiogenic (<1.1 ppm U except for two datapoints with 2.5 and 2.7 ppm U) whereas cores are slightly U-enriched (~1.5-6.5 ppm U) but U/Th ratio is almost systematically <1.

Despite their low radiogenic content, plotting U-Pb isotopic compositions of apatite in a Tera-Wasserburg diagram enables to draw a *Discordia* line with a lower intercept at 738±16 Ma (*n*=76 on thirty grains, MSWD=1.2, Fig. 2). The 738±16 Ma date is considered as a reliable hydrothermal crystallization age as the initial $^{207}Pb/^{206}Pb$ value obtained is ~0.88, which is close to the expected common Pb ratio at this age following the Pb evolution model of Stacey and Kramers (1975).

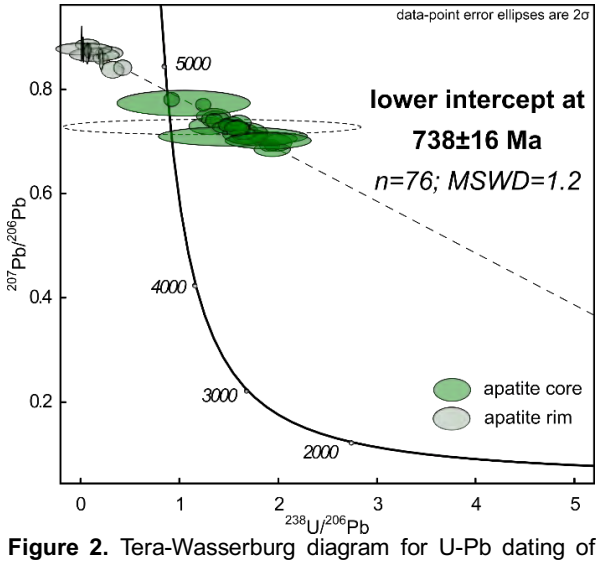


**Figure 2.** Tera-Wasserburg diagram for U-Pb dating of apatite coeval to Galat Sufar South gold mineralization produced using the Isoplot program

### 3.3 Chlorite-phengite-quartz-water multi-equilibria calculations

Approximately half of chlorite compositions measured involve elemental exchanges between the (Fe, Mg)-amesite-sudoite-(clinochore-daphnite) end-members. Phengite compositions are mostly muscovite- and celadonite-enriched although some datapoints are up to 20% pyrophyllite-rich where celadonite proportion is below 10%. Both chlorite and phengite compositions highlight the predominance of the Tschermak substitution ($Al^{VI}Al^{IV} \leftrightarrow (Fe^{2+},Mg)^{VI}Si^{IV}$) with little contribution of the pyrophyllitic substitution ($K^{XII}Al^{IV} \leftrightarrow \square^{XII}Si^{IV}$ where $\square^{XII}$ represents a vacancy in the A1 site of a white mica) for phengite.

Prior to multi-equilibria calculations, data were filtered on the basis of the compositional criteria

detailed in Vidal and Parra (2000). Eighteen out of forty-one chlorite analyses and one out of forty-five phengite analyses were removed from the original dataset. Multi-equilibria calculations then lead to consider multiple *P-T* couples associated to a $\sqrt{\Sigma\Delta G^2}$ free Gibbs energy. If several *P-T* equilibria are calculated from a given phengite composition and distinct chlorite compositions, they are classified as redundant, except for the one associated to the lower $\sqrt{\Sigma\Delta G^2}$ value, *i.e.*, the non-redundant equilibrium.

The statistical processing of calculated equilibria demonstrates the existence of two stability gaps, *i.e., P-T* windows where equilibria with relatively low $\sqrt{\Sigma\Delta G^2}$ are clustered: ~2.6 kbar - 330°C and ~7.2 kbar - 420 °C (Fig. 3).

## 4 Discussion

### 4.1. Timing of the Galat Sufar South gold mineralization

The GSS petrographic-structural model suggests that (i) the pervasive chlorite-phengite mineral gangue, (ii) the main penetrative fabric, (iii) dissolution-reprecipitation of pyrite and (iv) core-hosted mineral inclusions all relate to the deformation stage when the economic gold mineralization occurred (Perret et al. 2020, 2021b). As apatite either occurs as intergrown with chlorite and phengite or as mineral inclusion in pyrite cores, it leads to infer that it likely records the main gold event forming the GSS deposit. The obtained 738±16 Ma date is therefore interpreted as the age of $D_{2GSS}$ deformation and concomitant GSS gold mineralization. The obtained age is consistent with the timing of intra-oceanic subduction initiating Atmur-Delgo suturing (~750-650 Ma; Harms et al. 1994), in agreement with the mineralization timing inferred from tectonic-mineralization relationships (Perret et al. 2020, 2021b).

Despite the apparent spatial relationship between the GSS deposit and the Keraf shear zone, dating of the GSS gold deposit confirms that it is not genetically associated to late orogenic Keraf strike-slip shearing (~650-550 Ma; Abdelsalam et al. 1998; Bailo et al. 2003; Perret 2021). GSS should therefore not be interpreted as orogenic gold *sensu stricto* anymore (*e.g.,* Johnson et al. 2017) as it rather relates to early Atmur-Delgo suturing, as previously inferred (Perret et al. 2020).

### 4.2. Geodynamical setting associated to the Galat Sufar South gold mineralization

On one hand, the syn-$D_{2GSS}$ chlorite-phengite-quartz assemblage records ~7.2 kbar - 420 °C stability conditions corresponding to lower amphibolite facies conditions. Such conditions, corresponding to regional peak metamorphism (Johnson et al. 2011; Fritz et al. 2013) are interpreted as the mineral assemblage crystallization conditions, *i.e.,* related to the $D_{2GSS}$ deformation stage and concomitant GSS gold mineralization, for several reasons.

First, they are consistent with the trace element evolution pattern in pyrite observed at the GSS deposit, indicative of syn-gold mineralization pyrite recrystallization under amphibolite facies metamorphism (Perret et al. 2021b). Second, the obtained *P-T* constraints are in line with the structural patterns observed throughout the studied area, *e.g.*, sheath folding and non-coaxial ductile flow of pyroclastics and marbles (Perret et al. 2020). We thus suggest that the ore-related mineral gangue recorded lower amphibolite facies conditions coeval to gold mineralization and consistent with regional-scale deformation regime. Last but not least, mineralization likely occurred within the sedimentary wedge formed during Atmur-Delgo intra-oceanic subduction, supported by the record of comparable *P-T* conditions in wedges at accretionary-type subduction settings (Guillot et al. 2009).

On the other hand, the *P-T* field of stability at ~2.6 kbar - 330°C corresponds to the most stable calculated thermodynamic equilibria with $\sqrt{\sum\Delta G^2}$<500 J. It more likely relates to resetting of the chlorite-phengite-quartz compositions and greenschist-facies retrograde metamorphism during exhumation of rocks within the sedimentary wedge.

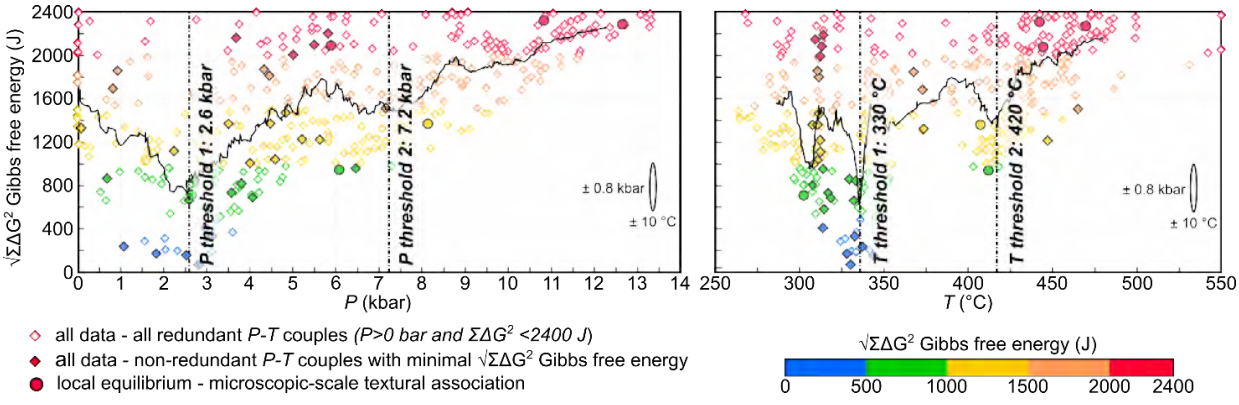


**Figure 3.** Statistical processing of *P-T* conditions estimated from chlorite-phengite-quartz-water multi-equilibria calculations for the syn-gold mineralization $D_{2GSS}$ deformation stage at the Galat Sufar South deposit. *P* (left) and *T* (right) are sorted by increasing values and plotted against $\sqrt{\Sigma\Delta G^2}$ Gibbs free energy. The black line gives the Gibbs free energy running mean over 21 points

### 4.3. Insights into the Pan-African gold mineral system in the Nubian shield

The synchronism between Atmur-Delgo intra-oceanic subduction and GSS gold mineralization suggests that mineralizing fluids may be derived from prograde to peak metamorphism devolatilization during early Atmur-Delgo suturing. The timing of the mineralizing event (738±16 Ma) thus strongly differs from the typical ~650-600 Ma age of late tectonic, crustal shear zone-hosted, orogenic and intrusion-related gold deposits described throughout the Arabian-Nubian shield, formed under retrograde greenschist facies metamorphic conditions (*e.g.,* Zoheir et al. 2019).

To date, the new *P-T-t-d* constraints on GSS gold mineralization make it (i) the oldest lode gold occurrence documented throughout the Nubian shield and (ii) the only one to occur at regional peak metamorphism conditions at a intra-oceanic subduction site. In terms of timing, the tectonic accretion-related GSS therefore formed in a similar geodynamical setting as porphyry copper deposits described in the Nubian shield (*e.g.,* Bierlein et al. 2020). It is thus strongly disconnected from late collisional orogenic gold *sensu stricto*. The GSS gold deposit therefore brings critical insights into the understanding of the Pan-African gold mineral system of the Nubian shield as it exemplifies the existence of syn-tectonic accretion lode gold mineralization in the region.

## 5 Conclusions

The Galat Sufar South gold deposit formed at 738±16 Ma (*in situ* LA-ICP-MS U-Pb dating of hydrothermal apatite coeval to mineralization) under ~7.2 kbar - 420 °C lower amphibolite facies conditions (syn-mineralization chlorite-phengite-quartz-water multi-equilibria calculations). In agreement with the nature of host rocks and deformation style already documented, these data support that the Galat Sufar South mineralization occurred within the sedimentary wedge formed during Atmur-Delgo intra-oceanic subduction, rather than during late tectonic Keraf strike-slip shearing as previously thought. The GSS deposit is (i) the oldest lode gold occurrence documented throughout the Nubian shield to date and (ii) the first evidence of lode gold mineralization related to tectonic accretion and formed under regional peak metamorphism conditions in the province.

## Acknowledgements

The authors are grateful to Orca Gold Inc., which used to operate the GSS deposit back in 2019-2020 when we conducted field work, for its welcome on site and its substantial logistical support. This work is part of Julien Perret's PhD project which benefited of a CIFRE funding, reference CIFRE N°2017/1737, attributed by the French National Research and Technology Agency (ANRT).

## References

Abdelsalam MG, Stern RJ, Copeland P, et al (1998) The Neoproterozoic Keraf Suture in Ne Sudan: Sinistral Transpression Along the Eastern Margin of West Gondwana. J Geol 106:133–148.

Bailo T, Schandelmeier H, Franz G, et al (2003) Plutonic and metamorphic rocks from the Keraf Suture (NE Sudan): a glimpse of Neoproterozoic tectonic evolution on the NE margin of W. Gondwana. Precambrian Res 123:67–80

Bierlein FP, Potma W, Cernuschi F, et al (2020) New Insights into the Evolution and Age of the Neoproterozoic Jebel Ohier Porphyry Copper Deposit, Red Sea Hills, Northeastern Sudan. Econ Geol 115:1–31.

Duckworth G (2020) Feasibility study - NI 43-101 TECHNICAL REPORT - Block 14 gold project. Lycopodium Minerals Pty Ltd

Fritz H, Abdelsalam M, Ali KA, et al (2013) Orogen styles in the East African Orogen: A review of the Neoproterozoic to Cambrian tectonic evolution. J Afr Earth Sci 86:65–106.

Gaboury D, Nabil H, Ennaciri A, Maacha L (2020) Structural setting and fluid composition of gold mineralization along the central segment of the Keraf suture, Neoproterozoic Nubian Shield, Sudan: implications for the source of gold. Int Geol Rev 1–27.

Ganne J, De Andrade V, Weinberg RF, et al (2012) Modern-style plate subduction preserved in the Palaeoproterozoic West African craton. Nat Geosci 5:60–65.

Guillot S, Hattori K, Agard P, et al (2009) Exhumation Processes in Oceanic and Continental Subduction Contexts: A Review. In: Lallemand S, Funiciello F (eds) Subduction Zone Geodynamics. Springer Berlin Heidelberg, Berlin, Heidelberg, pp 175–205

Harms U, Darbyshire DPF, Denkler T, et al (1994) Evolution of the Neoproterozoic Delgo suture zone and crustal growth in northern Sudan: geochemical and radiogenic isotope constraints. Geol Rundsch 83:591–603

Johnson PR, Andresen A, Collins AS, et al (2011) Late Cryogenian–Ediacaran history of the Arabian–Nubian Shield: A review of depositional, plutonic, structural, and tectonic events in the closing stages of the northern East African Orogen. J Afr Earth Sci 61:167–232.

Johnson PR, Zoheir BA, Ghebreab W, et al (2017) Gold-bearing volcanogenic massive sulfides and orogenic-gold deposits in the Nubian Shield. South Afr J Geol 120:63–76

Perret J (2021) Répartition spatio-temporelle du système métallogénique de l'or panafricain au sein du bouclier arabo-nubien: étude multiscalaire le long de la suture de Keraf (Soudan). PhD Thesis, Université de Lorraine

Perret J, André-Mayer A-S, Eglinger A, et al (2021a) Structural and geochemical ore-forming processes in deformed gold deposits: towards a multi-scale and -method approach. Geol Soc Lond Spec Publ SP516-2021–37.

Perret J, Eglinger A, André-Mayer A-S, et al (2020) Subvertical, linear and progressive deformation related to gold mineralization at the Galat Sufar South deposit, Nubian Shield, NE Sudan. J Struct Geol 135:.

Perret J, Feneyrol J, Eglinger A, et al (2021b) Tectonic record and gold mineralization in the central part of the Neoproterozoic Keraf suture, Gabgaba district, NE Sudan. J Afr Earth Sci 181:104248.

Stacey J t, Kramers 1JD (1975) Approximation of terrestrial lead isotope evolution by a two-stage model. Earth Planet Sci Lett 26:207–221

Vidal O, Parra T (2000) Exhumation paths of high-pressure metapelites obtained from local equilibria for chlorite-phengite assemblages. Geol J 35:139–161.

Zoheir B, Emam A, Soliman N, Holzheid A (2019) Gold Metallogeny of the Egyptian South Eastern Desert. In: Doronzo D, Schingaro E, Armstrong-Altrin Z, Zoheir B (eds) Petrogenesis and Exploration of the Earth's Interior. Springer Berlin Heidelberg, Berlin, Heidelberg, pp 261–263

# Mineralogical controls on the generation of gold-rich metamorphic fluids

**Iain Pitcairn[1], Thomas Zack[2], Georges Beaudoin[3], Carl Guilmette[3]**
*[1]Department of Geological Sciences, Stockholm University, Stockholm Sweden*
*[2]Department of Earth Sciences, University of Gothenburg, Gothenburg, Sweden*
*[3] Département de géologie et de génie géologique, Université Laval, Québec, Canada*

**Abstract.** Gold becomes enriched in metamorphic fluids produced by chlorite breakdown through liberation during transition of pyrite (Py) to pyrrhotite (Po). However, in some terranes the metamorphic window where the Py to Po transition occurs doesn't match the window of metamorphic fluid production. We describe the sulfide mineral evolution in metasedimentary rocks from the Pontiac subprovince, Abitibi Greenstone Belt, Canada. Samples from the biotite and garnet zones are particularly interesting as they have undergone the transition from Py to Po but still have high whole rock Au and H2O content. We have identified 3 potential occurrences of Au in these samples; within cobaltite and rarely other sulfides, as micro or nano scale particles along sulfide and silicate grain boundaries and within the background silicate minerals. The micro or nano scale Au particles were identified through LA-ICP-MS line scans across samples where Au peaks do not coincide with sulfide minerals. Gold particles along grain boundaries would very easily become dissolved in metamorphic fluids and this set of mineral changes may be an important control on the production of strongly Au enriched metamorphic fluids.

## 1 Introduction

A critical step in the development of world-class orogenic gold terranes is the generation of gold-rich metamorphic fluids. The model for the enrichment of gold in metamorphic fluids is through the release of gold during the transition of pyrite (Py) to pyrrhotite (Po) during prograde metamorphism in the presence of metamorphic fluid produced dominantly by the breakdown of chlorite (Pitcairn et al. 2006; Large et al. 2007; Tomkins 2010). Maximising the gold enrichment in the metamorphic fluid requires 1) that the metamorphic window of fluid production matches that of the Py-Po transition, 2) that the gold released by the Py-Po transition is easily available for dissolution within the fluid and 3) that the fluid has the appropriate composition to take the gold into solution. Tomkins (2010) suggests that chlorite breakdown drives the Py-Po transition as increased $H_2S$ is required to maintain equilibrium fluid conditions as $H_2O$ is released from chlorite.

In a number of metamorphic belts however, it is clear that the window of metamorphic fluid release does not always perfectly match the timing of gold mobility from the rock or the window of the Py-Po transition. In the Otago and Alpine Schists in New Zealand for example, whole-rock gold concentrations decrease between 300°C and 550°C whereas the main temperature of fluid release is 500°C to 550°C (Pitcairn et al. 2006). Another example is the Pontiac metasedimentary rocks from the Abitibi Greenstone Belt, Canada. Here the gold mobility occurs between biotite and staurolite zones equivalent to between 450°C and 550°C, which matches the window of metamorphic fluid release (Pitcairn et al. 2021). However, the Py-Po transition is more diffuse with both Py and Po occurring in some samples from chlorite to the sillimanite zones. Of particular interest are samples from the biotite and garnet zones that contain high whole-rock gold contents and abundant chlorite yet the dominant sulfide is Po. If the Py-Po transition is driven by fluid released from breakdown of chlorite then these Po bearing rocks should have no chlorite and depleted gold concentrations. It is clear on a local-scale at least, that there are more factors involved in the release of gold from pyrite during metamorphism.

In this study we present in-situ analyses of sulfide minerals from the Pontiac metasedimentary rocks, Abitibi Greenstone Belt, Canada. We focus specifically on samples from the biotite and garnet zones that have yet to lose their gold during metamorphic dewatering as these samples provide a window into the mineral processes involved in removal of the gold from pyrite.

## 2 Geological Setting

The Abitibi belt is the world's most well mineralised Archean greenstone belts with a total gold endowment of over 9000t (Dubé and Mercier-Langevin, 2020). The belt comprises E-W trending successions of metamorphosed volcano-sedimentary rocks deposited 2795 to 2669 Ma (Ayer et al., 2002; Daigneault et al., 2002; Thurston et al., 2008) with intervening bodies of intrusive rock. Linear belts of sedimentary rocks including graywacke- and mudstone-dominated turbidites are spatially associated with major fault zones such as the Porcupine-Destor fault zone and the Larder Lake–Cadillac fault zone. Metamorphism in the southern Abitibi occurred between 2669 ± 1 Ma and 2643 ± 4 Ma (Dubé and Mercier Langevin, 2020).

The orogenic gold deposits of the Abitibi belt occur as arrays of quartz-carbonate veins containing native gold and enrichments in As and Sb ± W, Se, Te, Bi, and Mo (Robert et al., 2005; Dubé and Mercier-Langevin, 2020). Orogenic gold deposits of the southern Abitibi belt and northern Pontiac subprovince formed between ca. 2670 and 2640 ± 10 Ma, with the bulk of deposits formed during the D3 deformational event between 2660 and 2640 Ma (Dubé and Mercier Langevin, 2020).

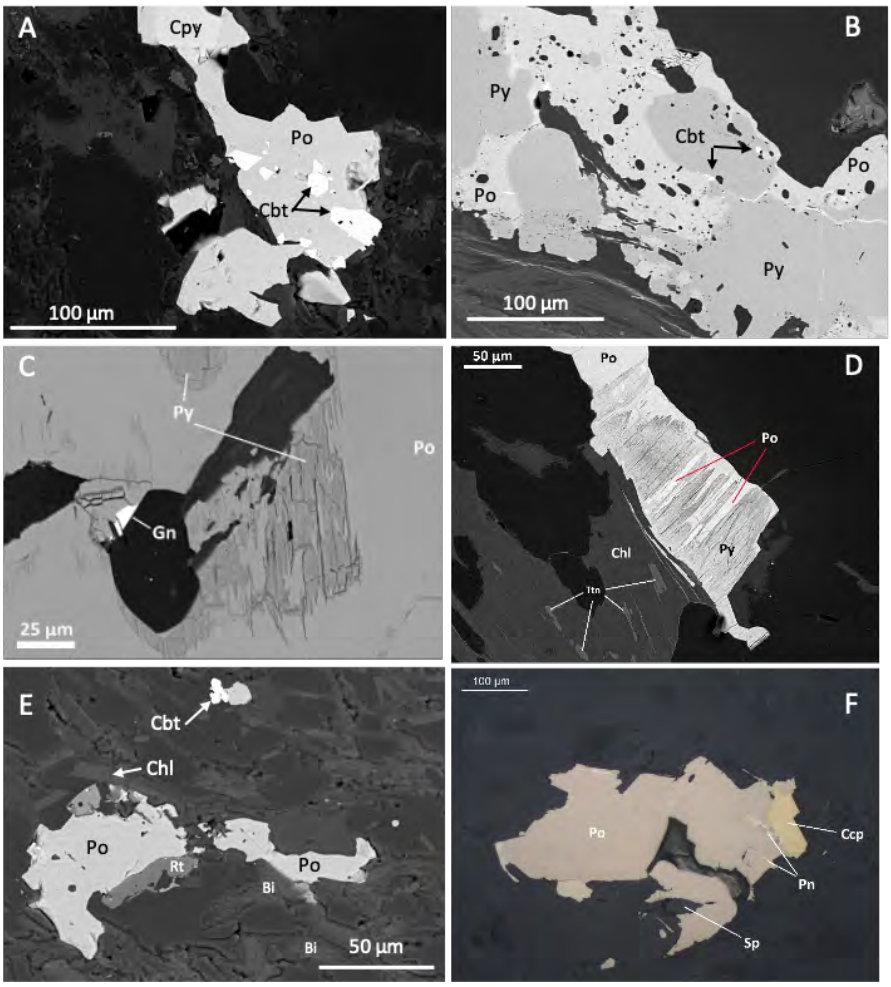


**Figure 20**. Electron backscatter and reflected light images of sulfide minerals from the Pontiac subprovince and Abitibi belt metasedimentary rocks, Canada. A: Porcupine group chlorite zone sample AB115 (1.5ppb Au) showing Cbt inclusions within Po. B – Pontiac biotite zone sample AB97 (22.7ppb Au) showing a large Py undergoing transition to Po with Cbt inclusions on grain boundaries. C - Pontiac biotite zone sample AB65 (2.8ppb Au) showing relicts of Py within Po. D – Pontiac garnet zone sample AB28 (1.1ppb Au) showing transition of Py to Po along preferential crystallographic orientations. E – Pontiac garnet zone sample AB34 (5.9ppb Au) with irregular Po and associated Cbt. F – Pontiac Kyanite zone sample AB43 (0.45ppb Au) showing Po with Pn inclusions and Ccp. Abbreviations: Bi – biotite Cbt – cobaltite, Ccp – chalcopyrite, Chl – chlorite, Gn – galena, Ilm – ilmenite, Pn – pentlandite, Po – Pyrrhotite, Py – Pyrite, Rt – rutile.

## 3 Sampling and analytical methods

Metasedimentary rock samples were collected in 2016 from the Abitibi belt and Pontiac subprovince which exposes a metamorphic transition from biotite-zone in the north to sillimanite-zone in the south (Benn et al., 1994). Whole-rock gold concentrations and their variations with metamorphic grade are reported in Pitcairn et al. (2021). The sulfide mineralogy was characterised using the polarising microscope and the scanning electron microscope at the Natural History Museum, Stockholm, Sweden.

In-situ mineral analyses were carried out at the Department of Earth Sciences, University of Gothenburg, Sweden in two separate batches, one in 2017 , one in 2023 using an Agilent 8800QQQ triple Quadrupole ICP-MS coupled to a New Wave NWR 213 laser ablation system. Spot analyses used spot-sizes of 30µm and 15µm, and energy output and the repetition rate were 4.3 J/cm2 and 10Hz respectively. Line scans were performed using a 50 µm spot size, and energy output and the repetition rate were 5.5 J/cm2 and 10Hz respectively. The following isotopes were measured for spot analyses: $^{27}$Al, $^{29}$Si, $^{34}$S, $^{57}$Fe, $^{59}$Co, $^{60}$Ni, $^{63}$Cu, $^{66}$Zn, $^{75}$As, $^{77}$Se, $^{95}$Mo, $^{107}$Ag, $^{121}$Sb, $^{125}$Te, $^{197}$Au, $^{202}$Hg, $^{208}$Pb and $^{209}$Bi. Line scans included also the following; 31P, 39K, 44Ca, 49Ti, 181Ta and 205Tl. Instrument calibration was performed using glass reference materials NIST-SRM-610 and GSD-1G. Accuracy, precision and fractionation effects due to matrix differences

between the glass standard and the sulphide minerals were controlled using sulphide reference materials MASS-1 and Po-725. Data processing and reduction were carried out using Glitter with $^{57}$Fe used as internal standard to convert counts per seconds (CPS) to concentrations for each element in the case of the spot analyses.

## 4 Results and discussion

As reported in Pitcairn et al. (2021) the dominant Fe sulfide in the Pontiac and Abitibi sedimentary

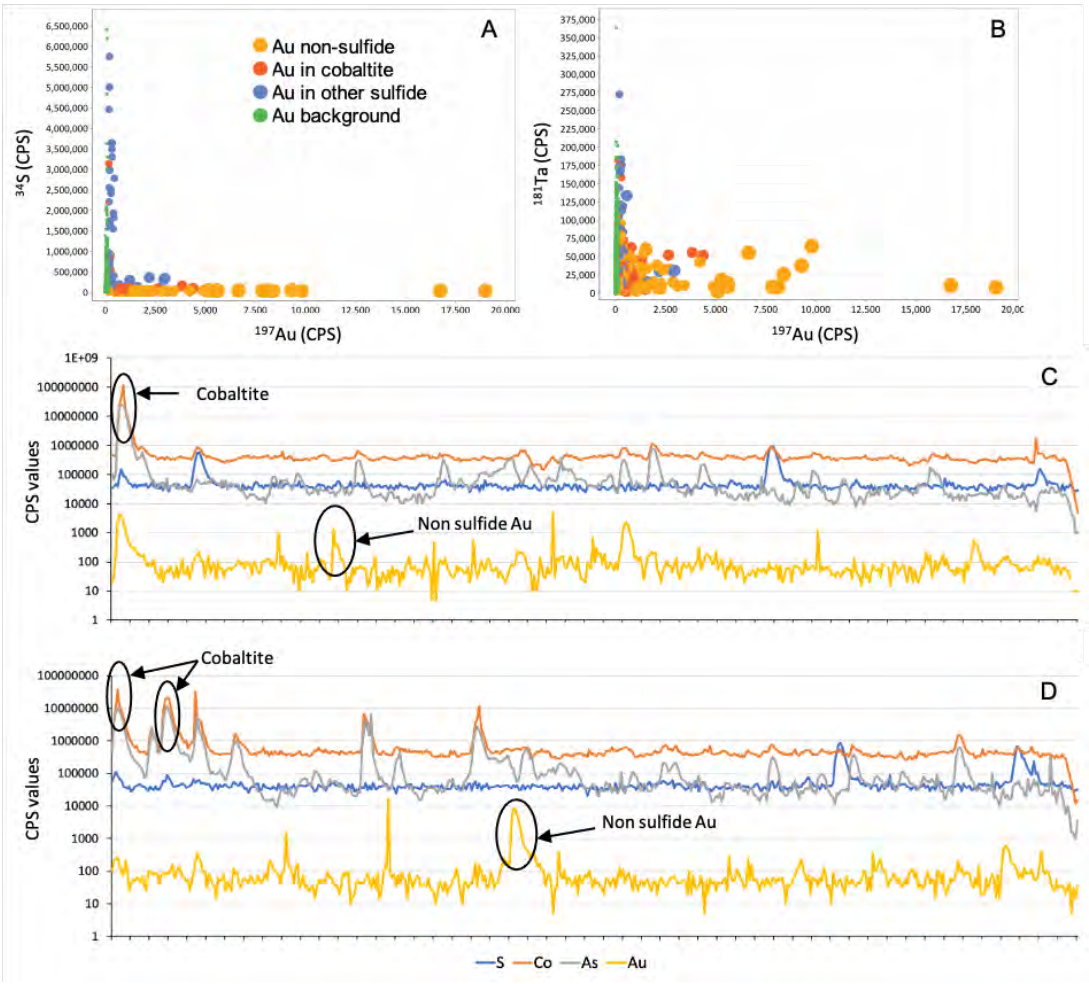


**Figure 21** LA-ICP-MS line scan data from Pontiac garnet zone sample AB34 (5.9ppb Au). A: CPS values of $^{34}$S vs $^{197}$Au showing the different Au occurrences in the sample. B: CPS values of $^{181}$Ta vs $^{197}$Au showing the lack of correlation between Ta and Au. In images A and B sample point size increases with increasing Au content. C and D: CPS values for S, Co, As and Au showing the different occurrences of Au such as within cobaltite and as non-sulfide Au.

rocks changes from Py at lower metamorphic grades to Po at higher grades (Fig. 1). Pyrrhotite occurs locally in chlorite zone samples and Py is also observed in some kyanite and sillimanite zone samples indicating that the transition is not driven solely by PT conditions but by the composition and availability of metamorphic fluid (e.g., Ferry 1981). Pitcairn et al (2021) estimates that the Py:Po ratio changes from 0.7 to 0.25 between chlorite and sillimanite zones. Abundances of the minor sulfides such as cobaltite are currently being determined. Cobaltite is most abundant in samples from the biotite-garnet zones (Fig. 1), and is not observed in any sample from staurolite, kyanite and sillimanite zones. An interesting textural observation is the occurrence of porus Po in the chlorite-biotite zone samples. This is an intermediary stage of the Py-Po transition as this texture is not observed at the higher metamorphic grades such as the kyanite and sillimanite zones where Po textures are more compact, subhedral and blocky (Fig. 1F)

Gold concentrations in the sulfide phases are shown in Table 1. Samples are grouped into 3 metamorphic facies groups; chlorite-biotite (which includes samples from the Porcupine and Pontiac groups), garnet-staurolite and kyanite sillimanite. The most consistently gold enriched mineral is cobaltite with mean concentrations of 0.43 +/- 0.35 ppm Au. Only 2 in 109 individual spot analyses of Po contain gold above detection limit (Table 1). Porus Po which occurs on the margins and relict grain boundaries of Po aggregates (Fig. 1B)

**Table 2**: Gold concentrations in ppm in different sulfide minerals from the Pontiac and Abitibi. The data combine analyses carried out in 2017 and 2023 which had different detection limits (d.l.) - 0.01 in the 2017 analyses and 0.003 in 2022. Abbreviations as Figure 1.

| | Py | Po | Porus Po | Cbt | Cpy |
|---|---|---|---|---|---|
| **Chlorite-biotite zones** | | | | | |
| **Mean** | 0.14 | 0.04 | 0.23 | 0.43 | 0.07 |
| **SD** | 0.73 | 0.12 | 0.61 | 0.35 | 0.04 |
| **MAX** | 5.84 | 0.76 | 2.46 | 1.05 | 0.11 |
| **MIN** | d.l. | d.l. | d.l. | d.l. | d.l. |
| ***n*** | *63* | *38* | *16* | *9* | *5* |
| **Garnet-staurolite zones** | | | | | |
| **Mean** | 0.03 | d.l. | | | 0.04 |
| **SD** | 0.01 | | | | 0.02 |
| **MAX** | 0.06 | d.l. | | | 0.08 |
| **MIN** | d.l. | d.l. | | | d.l. |
| *n* | *9* | *45* | | | *8* |
| **Kyanite sillimanite zones** | | | | | |
| **Mean** | d.l. | d.l. | | | 0.04 |
| **SD** | | | | | 0.04 |
| **MAX** | d.l. | d.l. | | | 0.11 |
| **MIN** | d.l. | d.l. | | | d.l. |
| *n* | *10* | *26* | | | *6* |

contains much higher Au contents of up to 2.4 ppm (Table 1). Pyrite contains average Au concentrations of 0.14 ppm with individual analyses as high as 5.8 ppm (Table 1). The high variability indicates the Au is heterogeneously distributed in the Py.

In samples from the biotite and garnet zones the whole rock gold concentration is high despite the majority of sulfide being essentially gold-free Po. In these samples we carried out line scan analyses in order to identify the host of the gold. The data clearly show an association of gold within cobaltite but not all cobaltite is gold-enriched (Fig. 2), and enrichments are patchy with gold peaks occurring on the margins of As-Co peaks. The line scans also show a large number of gold peaks not associated with cobaltite or any other sulfide. These peaks are often narrower than those associated with cobaltite but are more abundant. We interpret these peaks to represent micro particles of gold within the rock most likely occurring on silicate grain boundaries.

In sample AB34 (garnet zone with gold concentration of 5.9ppb), 17 separate line scans were carried out with a total of 7145 individual spot analyses. 88% of the spots represent "background gold" (CPS values between 60 and 150), 7% are non-sulfide gold with CPS values up to 19000, 3.5% are cobaltite gold and 1.5% gold in other sulfide (Fig. 2A). The lack of correlation between gold and tantalum (Fig. 2B) indicates that interference by $^{181}Ta^{16}O$ is not occurring.

The line scan results indicate that gold micro particles may be an important form of gold in biotite and garnet zone samples. We interpret these microparticles to be the product of the Py-Po transition where gold is liberated from Py, not incorporated into Po but not yet removed from the rock until the major flush of metamorphic fluid. The occurrence of non-sulfide gold at other metamorphic grades is currently being investigated but it is assumed that they are less abundant in rocks that have produced their major pulse of metamorphic fluid. These results may have considerable importance for the production of gold-rich metamorphic fluids as the gold micro particles will most likely be easily dissolved in $H_2S$-bearing metamorphic fluids.

## Acknowledgements

We thank Natural Resources Canada (NRCAN) for a TGI5 research grant and Stockholm University for research funding. We also acknowledge Nikolaos Leventis for data produced during his MSc thesis at Stockholm University.

## References

Ayer J, Amelin Y, Corfu F, Kamo S, Ketchum JF, Kwok K, Trowell NF (2002) Evolution of the Abitibi greenstone belt based on U-Pb geochronology: Autochthonous volcanic construction followed by plutonism, regional deformation and sedimentation. Precamb Res 115:63–95

Benn K, Miles W, Ghassemi MR, Gillett J (1994) Crustal structure and kinematic framework of the northwestern Pontiac subprovince, Quebec: An integrated structural and geophysical study. Can J Earth Sci 31:271–281

Daigneault R, Mueller W, Chown EH (2002) Oblique Archean subduction: Accretion and exhumation of an oceanic arc during dextral transpression, Southern volcanic zone, Abitibi subprovince, Canada. Precamb Res 15:261–290

Dubé B, Mercier-Langevin P (2020) Gold deposits of the Archean Abitibi greenstone belt, Canada. In Sillitoe, RH et al. eds, Geology of the World's Major Gold Deposits and Provinces:
Soc Econ Geol Spec Pub 23:669–708

Ferry J (1981) Petrology of graphitic sulfide-rich schists from south-central Maine: an example of desulfidation during prograde regional metamorphism. Am Min 66:908-930 Large RR, Maslennikov V, Robert F, Danyushevsky LV,

Chang, Z (2007) Multistage sedimentary and metamorphic origin of pyrite and gold in the giant Sukhoi Log deposit, Lena gold province, Russia. Econ Geol 102:1232−1267 Pitcairn IK, Teagle DAH, Craw D, Olivo GR, Kerrich R,

Brewer TS (2006) Sources of metals in orogenic gold deposits: insights from the Otago and Alpine Schists, New Zealand. Econ Geol 101:1525-1546

Pitcairn IK, Leventis N, Beaudoin G, Faure S, Guilmette C. Dubé B. (2021) A metasedimentary source of gold in Archean orogenic gold deposits? Geology 49:862-866

Robert F, Poulsen KH, Cassidy KF, Hodgson CJ (2005) Gold metallogeny of the Yilgarn and Superior cratons. Econ Geol 100th Ann Vol:1001–1033

Tomkins AG (2010) Windows of metamorphic sulphur liberation in the crust: Implications for gold deposit genesis. Geochim Cosmochim Acta 74:3246-3259

Thurston PC, Ayer JA, Goutier J, Hamilton MA (2008) Depositional gaps in Abitibi greenstone belt stratigraphy: A key to exploration for syngenetic mineralization. Econ Geol Bull Soc Econ Geol 103:1097–1134

# Metal and ligand mobility during prograde metamorphism of metasedimentary belts in the Superior Province: Implications for gold endowment

**Diogo Ribeiro[1,2], Bertrand Rottier[1,2], Antoine Godet[1,2], Georges Beaudoin[1,2], Carl Guilmette[1,2], Clifford Patten[3], Jochen Kolb[3], Iain Pitcairn[4]**

[1] *Département de Géologie et Génie Géologique, Faculté des Sciences et de Génie, Université Laval, Canada*

[2] *Centre de Recherche sur la Géologie et l'Ingénierie de Ressources Minérales (E4m), Université Laval, Canada*

[2] *Institut für Angewandte Geowissenschaften, Karlsruher Institut für Technologie, Germany*

[3] *Institutionen för Geologiska Vetenskaper, Stockholms Universitet, Sweden*

**Abstract.** The metasedimentary subprovinces of the Superior craton are exposed in the vicinity of, and are overthrust by, Au-endowed greenstone belts, suggesting that they could have sourced significant volumes of metals (e.g. Au, As, Sb) and ligands (Cl and S) to the overlying orogenic gold deposits. We track metal and ligand concentrations in the metasedimentary rocks, and the textural and chemical evolution of sulfides during prograde metamorphism. Representative samples were collected across different metamorphic zones along three transects featuring contrasting Au endowment: well-endowed (Rouyn-Noranda, Pontiac), moderately-endowed (Geraldton, Quetico), and poorly-endowed (Thunder Bay, Quetico) areas. In the three areas, Au, As and Sb concentrations are identical in low-grade metamorphic rocks, and As and Sb contents decrease with increasing metamorphic grade. However, decrease of Au concentration with increasing metamorphic grade is only observed in the well- and moderately-endowed areas, suggesting that gold was mobilized during prograde metamorphism. At Geraldton, sulfide textural and in-situ analysis suggest two main prograde continuous reactions: (1) pyrite I, the main host for Au, As, and Sb, to pyrrhotite; and (2) pyrrhotite to pyrite II. Our results show that Au, As, and Sb were mobilized during prograde metamorphism and may have migrated to the overlying mineralized systems.

## 1 Introduction

It is generally accepted that the majority of the fluids involved in orogenic gold deposits result from metamorphic devolatilization (Goldfarb and Pitcairn 2022). The breakdown reactions of chlorite and pyrite at the greenschists to amphibolite facies transition are seen as major contributors of fluid, metals, and sulfur (Phillips and Powell 2010; Tomkins 2010). Previous studies have shown that metasedimentary rocks release orogenic Au-related elements (e.g., S, Au, As, and Sb) during prograde metamorphism, indicating that they may represent a viable source of metals and ligands for orogenic gold deposits (Pitcairn et al. 2006; Tomkins, 2010; Zhong et al. 2015). Although metasedimentary rocks are generally recognized as a source of metals in Phanerozoic deposits, they have been often overlooked in Archean greenstone belts, given their low abundance. However, in the Superior Province, high-grade metasedimentary belts (up to granulite facies) occur adjacent to and are commonly overthrust by low- to medium-grade greenstone belts (up to lower amphibolite facies). This tectonometamorphic setting suggests that the devolatilization of the metasedimentary belts may have sourced significant volumes of metals and ligands to the overlaying greenstone belts. This is the case in the Pontiac and Quetico subprovinces exposed in the vicinity of the world-class Abitibi gold camp and the Beardmore-Geraldton belt, respectively. They consist of a sequence of metamorphosed turbiditic graywacke and mudstone interlayered with minor basaltic and komatiitic volcanic units, intruded by abundant felsic plutonic series of various geochemical affinities. These sequences expose apparently continuous metamorphic gradients and field isograds from the biotite to the sillimanite zone toward the south in the Pontiac subprovince, and from the chlorite zone to the partial melting zone inward in the Quetico subprovince.

While a systematic decrease of Au, As, and Sb concentrations with increasing metamorphic grade was recently documented in the Pontiac subprovince (Pitcairn et al. 2021), which is consistent with their mobilization during prograde metamorphism, their mobility at the mineral scale and the metal mobility in the Quetico subprovince at the basin scale are still unknown.

We report whole-rock geochemistry data for trace elements, and whole-rock ultra-low detection limit data for Au acquired by pressed powder pellet (PPP)-LA-ICP-MS from a suite of representative metasedimentary and subordinate interlayered mafic volcanic rocks across three transects featuring contrasting gold endowment, as well as textural and in-situ geochemical analysis of sulfides in metasedimentary rocks from a transect located in the Quetico subprovince.

## 2 Sampling and analytical methods

Sampling was carried out in three different areas across the Pontiac and Quetico subprovinces, representing well-endowed (Rouyn-Noranda, Pontiac), moderately endowed (Geraldton, Quetico), and poorly endowed (Thunder Bay, Quetico) sectors. The classification of each area regarding its endowment is based on the abundance of nearby orogenic gold deposits in the adjacent greenstone

belts. Representative samples of metasedimentary and subordinate interlayered mafic volcanic rocks were collected from all the metamorphic zones and 143 samples were selected for whole-rock trace element and ultra-low detection limit Au analysis.

Whole-rock analysis was performed at ALS laboratories (Sudbury, Canada). The samples were crushed and pulverized, followed by 4-acid digestion. Major elements were analysed by ICP-AES; Ba, Ce, Cr, Cs, Dy, Er, Eu, Ga, Gd, Ge, Hf, Ho, La, Lu, Nb, Nd, Pr, Rb, Sm, Sn, Sr, Ta, Tb, Th, Tm, U, V, W, Y, Yb, Zr were acquired by ICP-MS after lithium borate fusion; Ag, Cd, Co, Cu, Li, Mo, Ni, Pb, Sc, Zn were analysed by ICP-MS; S and C were acquired by IR spectroscopy; and Cl and F were analysed by IC after KOH fusion.

The ultra-low detection limit analysis for Au were acquired by Pressed Pellet Powder (PPP)-LA-ICP-MS in the Laboratory for Environmental and Raw Materials Analysis (LERA, Institute of Applied Geosciences, KIT). The production of nano-powders and pellets followed a procedure adapted from Peters and Pettke (2016) and Belgrano et al. (2022). The ultra-low detection limit analysis for Au was acquired using a Teledyne 193 nm Excimer Laser coupled to a ThermoFisher Scientific Element XR Sectorfield ICP-MS. The instrumental set up, oxide interference corrections, and data reduction followed the method developed by Patten et al. (2023).

Electron probe microanalysis of sulfides was done using a CAMECA SX-100 five-spectrometer electron probe micro-analyzer at Laval University. Analytical conditions for spot analyses were 15 kV, 20 nA with 20 s counting time on peaks and 10 s on background.

Sulfide LA-ICP-MS analyses were acquired using a RESOlution-SE 193nm Excimer laser coupled to an Agilent 8900 ICP-MS at Laval University. Laser pulse frequency and laser energy density were set to 10 Hz and 2.5 J $cm^{-2}$, respectively. The list of isotopes monitored for quantitative analyses included $^{23}Na$, $^{27}Al$, $^{28}Si$, $^{32}S$, $^{34}S$, $^{43}Ca$, $^{44}Ca$, $^{47}Ti$, $^{55}Mn$, $^{59}Co$, $^{60}Ni$, $^{63}Cu$, $^{66}Zn$, $^{75}As$, $^{78}Se$, $^{95}Mo$, $^{107}Ag$, $^{111}Cd$, $^{115}In$, $^{118}Sn$, $^{121}Sb$, $^{125}Te$, $^{178}Hf$, $^{181}Ta$, $^{182}W$, $^{197}Au$, $^{205}Tl$, $^{208}Pb$, $^{209}Bi$. The beam diameters varied among 24, 30, and 38 µm according to the size of the targeted grains. The analyses were performed for 30 s followed by 45 s blanks.

## 3 Results

### 3.1 Whole-rock geochemistry

Across the three areas, the low-grade metasedimentary rocks display similar mean concentration values for Au (~1 ppb), As (12.8 – 22.4 ppm), and Sb (0.16 – 1.02 ppm). A systematic decrease of the mean concentrations of As and Sb towards higher metamorphic grade rocks is observed for all the transects: (1) 12.82 to 0.25 ppm As and 0.16 to 0.08 ppm Sb from the biotite to the sillimanite zone in Rouyn Noranda, (2) 22.44 to 0.44 ppm As and 1.02 to 0.06 ppm Sb from the chlorite to the melt zone in Geraldton, and (3) 13.73 to 0.33 ppm As and 0.23 to 0.03 ppm Sb from the chlorite to the melt zone in Thunder Bay. In contrast, the decrease of gold concentrations with increasing metamorphic grade is only detected in the well- and moderately-endowed areas (from 1.03 to 0.16 ppb from the biotite to the sillimanite zone in Rouyn Noranda and from 1.04 to 0.25 ppb from the chlorite to the melt zone in Geraldton), whilst no consistent Au depletion is observed in Thunder Bay (Figure 1).

Carbon and $H_2O$ mean contents also decrease consistently with increasing metamorphic grade in the three areas: (1) 0.12 to 0.02 wt% C and 2.45 to 1.57 wt% $H_2O$ from the biotite to the sillimanite zone in Rouyn Noranda, (2) 0.46 to 0.02 wt% C and 2.73 to 1.32 wt% $H_2O$ from the chlorite to the melt zone in Geraldton, and (3) 0.17 to 0.03 wt% C and 2.37 to 1.00 wt% $H_2O$ from the chlorite to the melt zone in Thunder Bay. However, the mean concentration of S and Cl, as well as Se, Bi, Te, and Hg, show no systematic variation (Figure 1).

The suite of mafic volcanic rocks yields similar trends to the metasedimentary rocks regarding the variation of their Au, As, and Sb contents (Figure 1), which is consistent with Patten et al. (2020), however, the limited dataset is not robust enough to accurately access the mobility of these elements in these protoliths across the full spectrum of metamorphic conditions.

### 3.2 Textural and chemical evolution of sulfides

In the Geraldton area, on average the sulfides represent around 0.5 vol.% of the metasedimentary rocks. The textural and chemical evolution of the sulfides across different metamorphic grades was accessed to evaluate their role on Au, As, and Sb mobilities. The sulfide evolution features two main continuous reactions: (1) the pyrite I to pyrrhotite transition occurred from the biotite to the cordierite zones and produced transitional sulfide phases with an intermediate composition between pyrite and pyrrhotite; (2) the pyrrhotite to pyrite II transition took place in the sillimanite and melt zones and is expressed by the growth of euhedral pyrite inside pyrrhotite.

Pyrite I is present from the chlorite to the staurolite zones. It often displays subhedral and inclusion-poor cores surrounded by anhedral and inclusion-rich rims. The relative abundance of inclusions gradually decreases toward higher metamorphic grades, resulting in increasingly homogeneous pyrite grains. The Au, As, and Sb median concentrations of pyrite I decrease progressively with increasing metamorphic grade: 33.6 ppb Au, 410.3 ppm As, 17.4 ppm Sb in the chlorite zone (n = 34); 22.3 ppb Au, 127.2 ppm As, 12.7 ppm Sb in the biotite zone (n = 26); and 18.2 ppb Au, 93.5 ppm As, 2.2 ppm Sb in the garnet zone (n = 29).

The transitional sulfide phases produced during the breakdown of pyrite I show linear replacement textures of pyrite gradually transitioning into

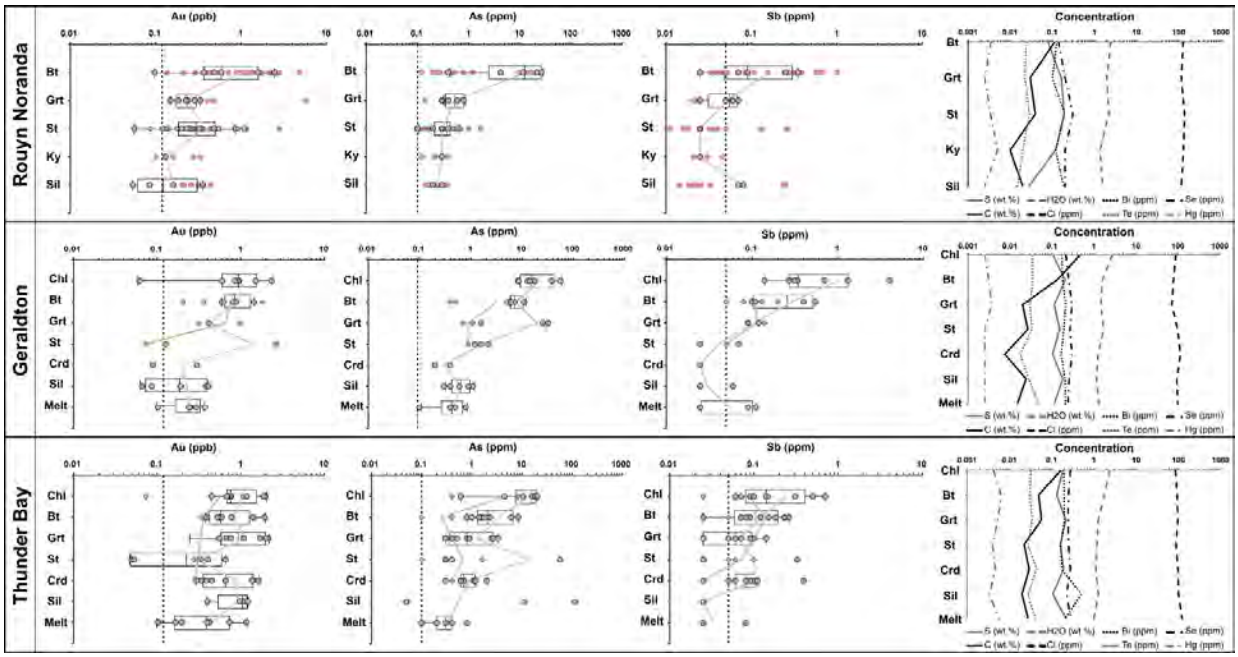


**Figure 1.** Concentrations of Au, As, and Sb for metasedimentary rocks (gray circles) and mafic volcanic rocks (green diamonds) from Rouyn Noranda, Geraldton and Thunder Bay. Gray and green lines connect the mean concentrations of metasedimentary and volcanic rocks, respectively, in each metamorphic zone. Vertical dashed black lines are the limits of detection. Red circles represent data for metasedimentary rocks from Pitcairn et al. (2021). Diagrams on the right show lines connecting mean concentrations for S, C, $H_2O$, Cl, Bi, Te, Se, Hg of metasedimentary rocks.

pyrrhotite. These also record a general decrease of mean Au, As, and Sb concentrations with increasing metamorphic grade: 17 ppb Au, 27.3 ppm As, 42.35 ppm Sb in the biotite zone (n = 4); 4 ppb Au, 1.9 ppm As, 0.59 ppm Sb in the garnet zone (n = 2); and 3 ppb Au, 104.3 ppm As, 0.24 ppm Sb in the staurolite zone (n = 8); these concentrations are within the range of values measured for pyrite I and pyrrhotite coexisting in the same metamorphic zone (Figure 2).

Pyrrhotite is present from the biotite to the melt zone, becoming significantly more abundant from the staurolite zone. It commonly displays flames of pentlandite and the grains become more rounded towards higher grades. The median Au, As, and Sb concentrations in pyrrhotite (Figure 2) decrease continuously from 16 ppb Au, 3.64 ppm As, 2.62 ppm Sb in the biotite zone (n = 6); 6 ppb Au, 1.10 ppm As, 0.18 ppm Sb in the garnet zone (n = 8); 5 ppb Au, 11 ppm As, 0.03 ppm Sb in the staurolite zone (n = 10), to 3 ppb Au, 0.07 ppm As, 0.02 ppm Sb in the cordierite zone (n = 25).

Pyrite II grows as euhedral crystals inside pyrrhotite. Their size and distribution are controlled by the pre-existent pyrrhotite grains. Eventually, pyrite II completely consumes pyrrhotite forming clusters of intergrown euhedral pyrite grains, whose shape mimics the boundaries of the precursor pyrrhotite grains. A slight increase of the median Au, As, and Sb contents is observed from pyrrhotite to pyrite II, from 3 ppb Au, 0.11 As, 0.02 Sb in pyrrhotite (n = 40) to 2 ppb Au, 1.49 ppm As, 0.22 ppm Sb in pyrite II (n = 23) in the sillimanite zone; and from 3 ppb Au, 0.24 As, 0.02 Sb in pyrrhotite (n = 28) to 13 ppb Au, 1.80 ppm As, 0.01 ppm Sb in pyrite II (n = 29) in the melt zone. In the melt zone, eventually all sulfides become unstable, remaining preserved only inside porphyroblasts.

## 4 Discussion and conclusions

Identical Au, As, and Sb contents at low-grade conditions and a systematic decrease of As and Sb concentrations with increasing metamorphic grade are observed in the metasedimentary sequences across the three areas. However, Au depletion toward higher metamorphic grades was not detected in the Thunder Bay area. This indicates that, even though As and Sb were mobilized during prograde metamorphism in all areas, Au release was more efficient in metasedimentary rocks from the endowed areas (Rouyn Noranda and Geraldton) compared to the poorly endowed area (Thunder Bay). The parameters influencing the contrasting gold mobility across the different transects are currently under evaluation.

The Au, As, and Sb concentrations of sulfides in the Geraldton yield similar decreasing trends. The gradual removal of inclusions and trace element depletion in pyrite I with increasing metamorphic grade is interpreted as a continuous structural reorganization, which seems to be an important mechanism for metal mobilization. The pyrite I to pyrrhotite transition is accompanied by a substantial decrease of Au, As, and Sb concentrations, and is likely the main reaction responsible for the release of significant amounts of these elements from the metasedimentary rocks. Similar to pyrite I, the trace element depletion and rounding of pyrrhotite grains toward higher metamorphic grade should be related to its gradual structural reorganization, however, the

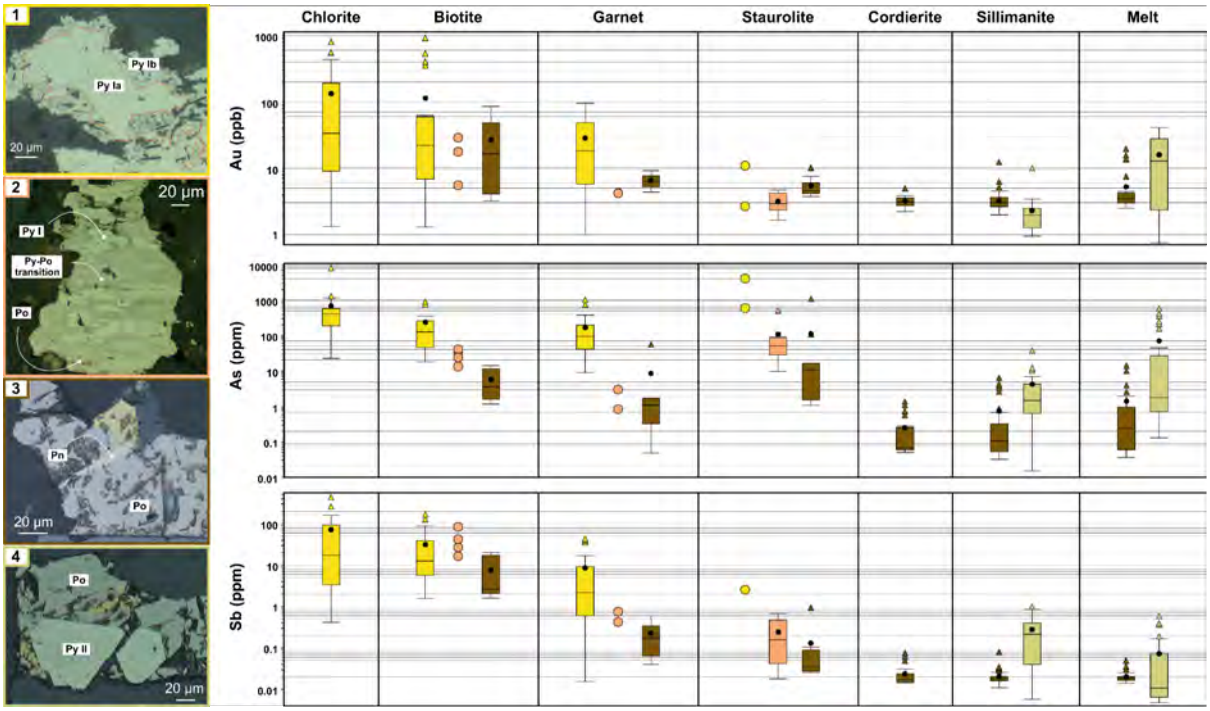


**Figure 2.** Textures (left) and Au, As, and Sb concentrations (right) of sulfides from metasedimentary rocks in the Geraldton transect. 1 – Pyrite I featuring subhedral and inclusion-poor cores and anhedral and inclusion-rich overgrowths; 2 – Transitional sulfide phases displaying linear replacement textures; 3 – Pyrrhotite with pentlandite flame; 4 – Euhedral pyrite II crystals growing in pyrrhotite. Box-plots (n > 5; black circles are mean values) and circles (n ≤ 5) represent data for pyrite I (yellow), transitional sulfide phases (orange), pyrrhotite (brown), and pyrite II (green) in each metamorphic zone.

volume of metals released should be significantly lower, given its lower metal content.

Although pyrrhotite is present up to the melt zone, the transition to pyrite II indicates that, from the sillimanite zone, pyrrhotite is no longer the main stable sulfide species. The slightly higher Au, As, and Sb of pyrite II compared to coexisting pyrrhotite suggest that these elements were reconcentrated during the transition from pyrrhotite to pyrite II. Nonetheless this reaction should have had limited impact on the mobilization of these elements, given their low concentrations and the low volume percentage of sulfides, which is consistent with the whole-rock data.

Even though the transition from pyrite I to pyrrhotite should release sulfur, no significant sulfur loss during prograde metamorphism is recorded by the whole-rock data, which suggests that sulfur was not significantly mobilized. The sulfur liberated from pyrite may have reacted with Fe released upon the breakdown silicate minerals, such as chlorite, to form pyrrhotite (Zhong et al. 2015).

Both the whole-rock and the sulfide in-situ data record a systematic decrease of Au, As, and Sb concentrations with increasing metamorphic grade. Moreover, there seems to be a correlation between Au mobility in the metasedimentary belts and the Au endowment in the overlying greenstone belts. This suggests that devolatilization of the metasedimentary belts may have sourced significant volumes of these metals to the orogenic gold deposits in the greenstone belts and may be a key factor controlling Au endowment.

## Acknowledgements

The authors would like to thank Adrian Rhem, Isaac Malta, and Doug Tinkman for discussion, Marc Choquette and Guillaume Barré for the analytical work, and Metal Earth for founding this project.

## References

Goldfarb RJ, Pitcairn IK (2023) Orogenic gold: is a genetic association with magmatism realistic? Mineralium Deposita, 58(1), 5-35.

Patten CGC, Beranoaguirre A, Hector S, Gudelius D, Kolb J, Eiche E (2023) Improved whole rock low detection limit gold analysis by LA-ICP-MS utilizing pressed-powder-pellets. International Journal of Mass Spectrometry, 488, 117039.

Patten CGC, Pitcairn IK, Molnár, Kolb J, Beaudoin G, Guilmette C, Peilod A (2020) Gold mobilization during metamorphic devolatilization of Archean and Paleoproterozoic metavolcanics rocks. Geology, 48(11), 1110-1114.

Phillips GN, Powell R (2010) Formation of gold deposits: a metamorphic devolatilization model. Journal of Metamorphic Geology, 28(6), 689-718.

Pitcairn IK, Leventis N, Beaudoin G, Faure S, Guilmette C, Dubé B (2021) A metasedimentary source of gold in Archean orogenic gold deposits. Geology, 49(7), 862-866.

Pitcairn IK, Teagle DAH, Craw D, Olivo GR, Kerrich R, Brewer TS (2006) Sources of Metals and Fluids in Orogenic Gold Deposits: Insights from the Otago and Alpine Schists, New Zealand. Economic Geology, 101(8), 1525-1546.

Tomkins AG (2010) Windows of metamorphic sulfur liberation in the crust: Implications for gold deposit genesis. Geochimica et Cosmochimica Acta, 74(11), 3246-3259.

Zhong R, Brugger J, Tomkins AG, Chen Y, Li W (2015) Fate of gold and base metals during metamorphic devolatilization of a pelite. Geochimica et Cosmochimica Acta, 171, 338-352.

# Petrographic and chemical characterization of superimposed Au-bearing events at the Augmitto-Bouzan deposit (Abitibi)

**Rita Rodrigues[1], Georges Beaudoin[1], Bertrand Rottier[1], Guillaume Raymond[1], Baptiste Chapon[2]**
*[1]Departement de génie et génie géologique, Université Laval, Québec, Canada*
*[2]CEGEP de l'Abitibi-Témiscamingue, Rouyn-Noranda, Québec, Canada*

**Abstract.** At the Augmitto-Bouzan deposit, gold endowment is the result of syn- and post-shear mineralization events. Syn-shear quartz-carbonate-tourmaline (QCT) veins and associated alteration halos represent orogenic gold-type mineralization and constitute the most important hydrothermal event, yet account for minor gold contents. Nevertheless, these structures still constitute primary exploration targets as they host two superimposed mineralization events responsible for most gold endowment at the deposit. The first occurs as reopening of QCT veins and consists of carbonate precipitation accompanied by free gold. The second is characterized by carbonate-chlorite-pyrite/pyrrhotite (CCP) veinlets and accounts for major gold contributions, particularly when spatially associated with arsenopyrite. To understand the spatial and temporal controls on the mineralization at the Augmitto-Bouzan deposit, in situ chemical analyses were performed on gold-related sulfides. Arsenopyrite from QCT vein selvages and alteration halos and pyrite from CCP veinlets show variable Ni+Co contents yielding a trend towards the Astoria orebody. This pattern is consistent with observed changes in mineral associations from CCP veinlets. Given that the Astoria segment hosts late Proterozoic gabbro dykes, this spatial relationship raises questions regarding the influence of the dykes on the formation of CCP veinlets and, thus, their role in gold remobilization and/or as a late gold source.

## 1 Introduction

Orogenic Gold Deposits (OGD) usually consist of gold-rich veins spatially constrained to major crustal compressional to transpressional discontinuities and their subsidiary structures (Groves et al. 2003). At the deposit scale, these systems are often characterized by irregular distribution of gold grades. This feature is commonly the product of multiple vein generations with contrasting gold contents, illustrating a sequence of superimposing hydrothermal events that have taken place in areas marked by long-lived deformation. Recognizing such processes is fundamental to understand gold distribution and therefore to: (**i**) interpret gold grade patterns; (**ii**) accurately assess the prospectivity of exploration targets; and (**iii**) identify ore shoots. Straddling the Cadillac-Larder Lake Tectonic zone (CLLTz), the Augmitto-Bouzan deposit is a prime example of the irregular gold distribution patterns amongst OGD. At the property, gold grades vary significantly along strike of the fault and economic grades are mostly restricted to the western sector, in several steeply east-plunging orebodies (Fig.1). In the eastern sector of the deposit, equivalent veins are largely barren.

Here we provide textural, mineralogical, and chemical data on the mineralization events responsible for gold endowment at the Augmitto-Bouzan deposit in order to better understand gold grade patterns.

## 2 Geological context

The Cadillac-Larder Lake Tectonic zone is an east-west trending first-order structure at the southeastern limit of the Abitibi greenstone belt, at the contact with the Pontiac Subprovince to the south (Card and Ciesielski 1986). This crustal-scale shear zone is known as an important metallotect for gold mineralization in the region (Poulsen 2017).

The Augmitto-Bouzan deposit covers 12 km along strike of the CLLTz and comprises 8 contiguous segments where mineralization is associated with the main deformation zone (Fig.1). From west to east, these are: Augmitto, Cinderella, Lake Gamble, Astoria, East-Bay, and Bouzan (Fig.1). Gold mineralization is preferentially hosted in the altered mafic and ultramafic metavolcanic rocks of the Piché Group, with higher grades being confined to its contact with the metasedimentary rocks of the Timiskaming Group. Across the property, albitic dykes intrude the Piché Group and may locally host mineralization. In the Astoria segment, two late Proterozoic gabbro dykes (metric to hectometric) intrude both the metavolcanic and metasedimentary units (Fig.1). These two bodies are part of the regional scale Abitibi Dyke swarm event and result in a contact metamorphic aureole of approximately 50m in width (Powell et al. 1995).

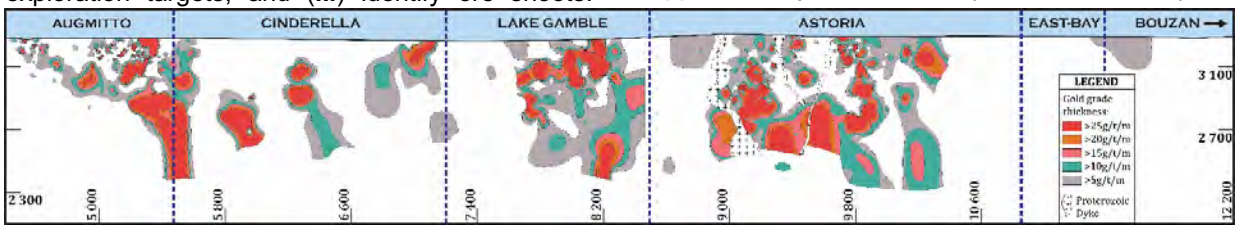


**Figure 1.** Spatial distribution of gold grade grades in the Piché Group across the different segments of the deposit. The Bouzan segment extends for more 3km to east and is barren. Coordinates are in UTM Zone 17 NAD83.

## 3 Methods

Core logging was performed on 93 drillholes spatially distributed across the 12 km of the deposit. Transmitted- and reflected-light microscopy was carried out on 99 polished thick sections aiming spatial coverage of the deposit.

Quantitative micro-XRF data were obtain from polished thick sections using an M4 Tornado Micro X-Ray Fluorescence instrument at Université Laval (Québec, Canada). Analytical conditions were 20 µm step size, 50 kV acceleration voltage, 600 µA field intensity, and 5 ms dwell time. Geochemical maps were produced using the AMICS software.

Major and minor elements analyses were performed on (**i**) arsenopyrite from QCT alteration halos and selvages, (**ii**) pyrite from CCP veinlets, and (**iii**) gold from different mineralization stages. Analyses were obtained using a CAMECA SX-100 Electron Probe Micro-analyser equipped with 5 WDS spectrometers at Université Laval (Québec, Canada). For sulfides, S, Cd, Sb, Zn, Cu, Mn, Fe, Co, Ni, and As were analysed using a 5 µm beam size, 15 kV acceleration voltage, and 20 nA beam current. For gold analyses, Au, Ag, and Te concentrations were obtain under the same conditions. Data processing included the imputation of censored values (values below detection limit) using the lrEM (log-ratio Expectation-Maximization) algorithm (Palarea-Albaladejo and Martín-Fernández 2015). Elements with more than 40% of censored values were not considered in the interpretation of the dataset.

## 4 Results

### 4.1 Paragenesis of hydrothermal episodes

Six hydrothermal episodes, associated with both barren and gold-bearing events, have been identified at the Augmitto-Bouzan deposit (Fig.2).

The first hydrothermal episode is recorded by barren, deformed, early carbonate ± quartz (ECQ) veins located along the main deformation fabric. The development of microcrystalline quartz-chlorite (MQC) veins (2nd hydrothermal episode, Fig.2) is synchronous to the main shear and marks the earliest gold event identified, where mineralization occurs as free gold in the quartz-chlorite matrix.

The second gold event consists of micrometric gold inclusions in arsenopyrite from vein selvages and mica-rutile-tourmaline-sulfide alteration halos associated with the emplacement of syn-shear quartz-carbonate-tourmaline (QCT) veins (3rd hydrothermal episode, Fig.2). In mafic and ultramafic units, the presence of arsenopyrite is mostly restricted to QCT vein selvages whereas the alteration halos are dominated by gersdorffite. In sedimentary units, arsenopyrite occurs both in QCT vein selvages and in proximal alteration halos (Fig.3c). Both MQC and QCT hydrothermal episodes appear to account for a small percentage of the overall gold budget of the deposit. The third gold event is spatially constrained to QCT veins from endowed areas between Augmitto and Astoria. Petrography combined with micro-XRF multi-element maps revealed that free gold within these structures is associated with late carbonate infillings (CI) overprinting the QCT veins (Fig.3a,b).

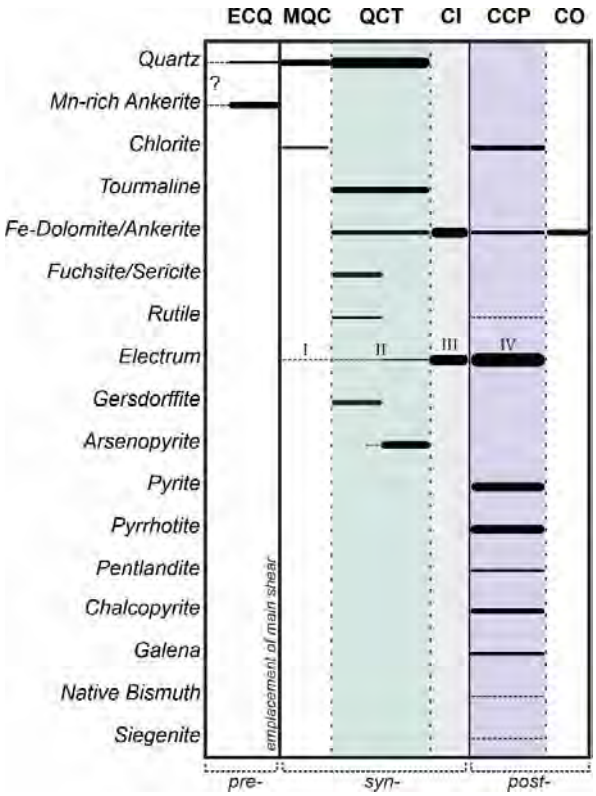


**Figure 2.** Paragenetic sequence of hydrothermal episodes at the Augmitto-Bouzan deposit.

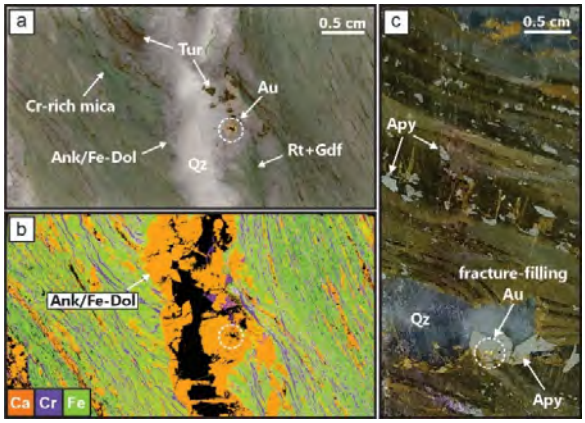


**Figure 3. a**, fuchsite-tourmaline-rutile-gersdorffite halo in ultramafic unit and associated QCT vein; **b**, micro-XRF Ca-Cr-Fe geochemical map of **a** illustrating the superimposition of a late gold-bearing carbonate infilling (CI); **c**, sericite-tourmaline-rutile-arsenopyrite alteration halo in sedimentary rock and associated QCT vein.

The last gold event is associated with the fifth hydrothermal episode (Fig.2) and is characterized by carbonate-chlorite-pyrite/pyrrhotite (CCP) millimetric to centimetric veinlets, commonly associated with minor chalcopyrite, galena, and native bismuth (Fig.4), that crosscut all previous vein generations. The prevalence of pyrite over pyrrhotite in CCP veinlets seems to be closely related with increased

distance from the Astoria orebody. In Astoria, pyrrhotite is predominant, and minor phases such as chalcopyrite and galena are more abundant, with locally siegenite. Additionally, pentlandite is common as exsolution "flames" in pyrrhotite (Fig.4e). Gold mineralization linked with this episode is particularly important when spatially associated with arsenopyrite from QCT vein selvages and alteration halos, where micrometric free gold is observed filling fractures in arsenopyrite (Fig.4b-f).

When arsenopyrite is absent from QCT halos and selvages, CCP veinlets tend to be barren of gold. Less commonly, mineralization associated with this event can also occur as micrometric free gold inclusions in pyrite or inside the veinlets (Fig.4a). Together, CI and CCP account for most of the gold endowment of the deposit.

The latest hydrothermal episode recorded is marked by barren carbonate-only veins that crosscut all previous assemblages (Fig.2).

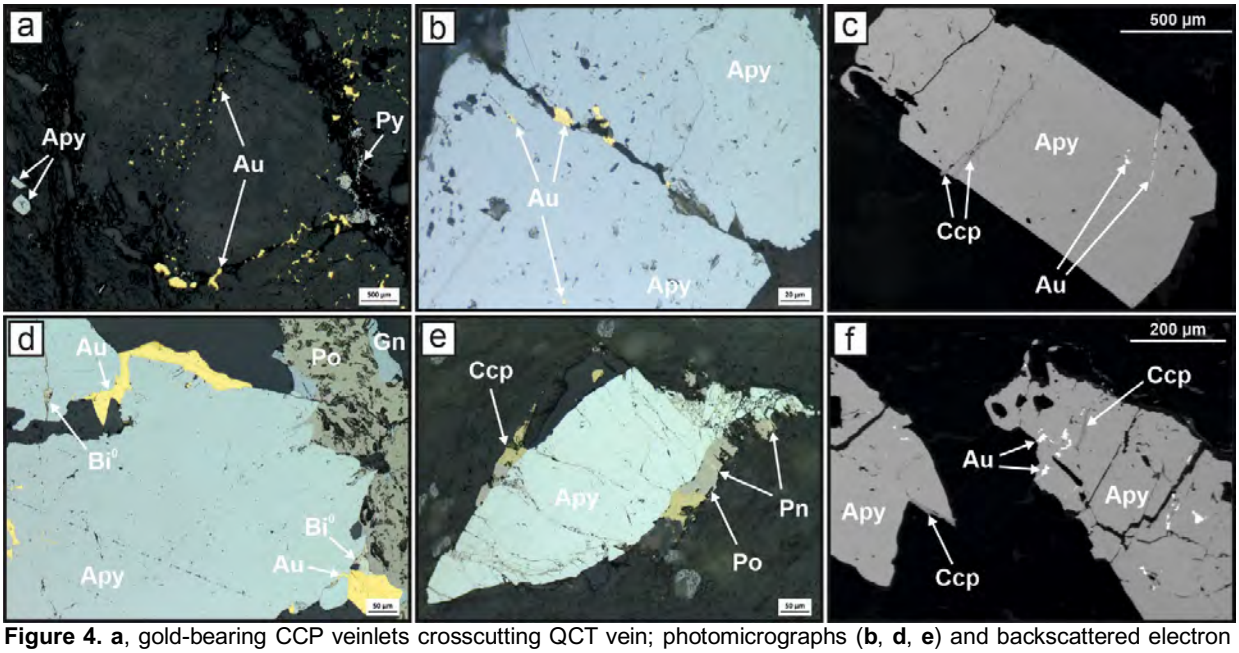


**Figure 4.** **a**, gold-bearing CCP veinlets crosscutting QCT vein; photomicrographs (**b**, **d**, **e**) and backscattered electron images (**c**, **f**) of CCP assemblages filling fractures in arsenopyrite from QCT selvages and alteration halos.

### 4.2 Mineral chemistry of Au and Au-associated sulfides

Gold mineralization associated with CI and CCP mineralization events occurs as electrum with variable Au and Ag contents. Electrum associated with CCP veinlets presents lower average Au contents (±91 wt%) when compared to the CI event (±93 wt%). No clear relationship was observed between electrum composition and the different segments of the deposit, or its textural context (pyrite inclusions, veinlets, or arsenopyrite fracture-filling).

There is a significant compositional variation of Ni+Co in arsenopyrite (Fig.5a).

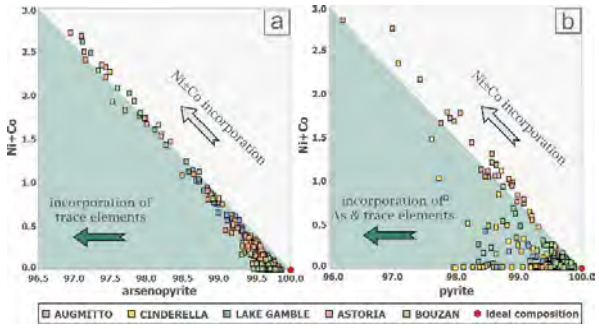


**Figure 5.** Arsenopyrite (**a**) and pyrite (**b**) deviation from ideal compositions by incorporation of Ni+Co (wt%) from the different segments of the deposit. Vectors for As and trace-elements incorporation are shown.

This variation yields a trend marked by increasing Ni+Co values from the western end of the property towards the Astoria orebody (Fig.6a). In the eastern sector of the property (Bouzan), Ni+Co contents in arsenopyrite decrease considerably, except for one sample, where significant Co±Ni enrichment (up to 2.11 wt% Co and 0.35 wt% Ni) is documented in arsenopyrite rims (Fig.4e). An identical trend is shown by pyrite, in which Ni+Co concentrations progressively increase towards the Astoria orebody (Fig.6b), where considerably higher Ni+Co values are documented (up to 2.85 wt%).

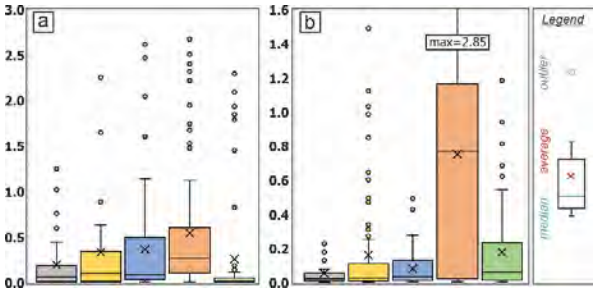


**Figure 6.** Arsenopyrite (**a**) and pyrite (**b**) Ni+Co contents (in wt%) from the different segments of the deposit, from left to right: Augmitto, Cinderella, Lake Gamble, Astoria, and Bouzan.

East of this segment, Ni+Co contents in pyrite drop significantly (Fig.6b). Pyrite analyses also

register considerable compositional deviation marked by As incorporation (Fig.5b). Arsenic content in pyrite displays an opposite trend to that of Ni+Co, in which As values tend to progressively decrease towards the Astoria orebody; from approximately 388 to 266 ppm from Augmitto to Lake Gamble, reaching below detection limit in Astoria.

## 5 Discussion and conclusions

A detailed study of samples regularly distributed across the Augmitto-Bouzan deposit allowed the identification of six hydrothermal episodes, four of which contain gold mineralization.

Of all gold-bearing episodes, MQC veins appear to be responsible for the smallest percentage of the overall gold budget of the deposit, and QCT veins for slightly higher gold contributions. Given the timing of emplacement, mineralogy, and regional context, QCT veins have been interpreted as classical OGD-type veins. During the initial stages, the development of mica-tourmaline-rutile-sulfide alteration halos is probably related to fluid infiltration along the main deformation fabric. In the mafic and ultramafic units of the Piché Group, gersdorffite is the main sulfide phase in the alteration halos and occurs as abundant, small (<25µm), euhedral crystals. The fracturing stage of this episode is marked by the precipitation of large euhedral arsenopyrite in vein selvages. In contrast, in the sedimentary units of the Timiskaming Group, where Ni+Co contents of the host rocks are significantly lower, arsenopyrite is the main sulfide phase in both the alteration halos and selvages of QCT veins. Although observation shows that the most significant gold contributions are late relative to QCT veins, these still constitute primary exploration targets. QCT veins and associated selvages and alteration halos host later mineralization events which account for most of the overall gold budget of the deposit, such as the CI and CCP hydrothermal episodes. The presence of CI was only observed in the western sector of the deposit, between the Augmitto and Astoria segments (Fig.1). This gold-bearing episode occurs exclusively as reopening of QCT veins along host rock contacts. This observation, together with the recurrent development of associated extensional veins, both filled by undeformed euhedral carbonate, suggests that the emplacement of these structures occurred during the seismic failure periods of the shear.

The latest gold event corresponds to CCP veinlets, which can be found across the entire property crosscutting all previous assemblages. In the gold-poor eastern sector of the deposit (Bouzan segment), these veinlets represent the only evidence of gold mineralization. Petrography shows that gold contents linked with this episode are particularly relevant when spatially associated with arsenopyrite from QCT selvages and alteration halos. This observation suggests that arsenopyrite constitutes an important geochemical trap enabling gold deposition and therefore its presence played a major role during the CCP mineralization stage. These findings are consistent with gold grades at the deposit, where higher values are associated with the ultramafic and mafic units of the Piché Group at its contact with sedimentary units of the Timiskaming Group where arsenopyrite is more abundant. A particularity of CCP veinlets is that they show variable mineralogical associations with the relative distance towards the Astoria segment. For example, the predominance of pyrrhotite over pyrite as the main Fe-sulfide gradually increases with decreased distance from the Astoria orebody. This pattern is also accompanied by higher abundance of minor phases, including pentlandite as exsolutions in pyrrhotite, and the occurrence of siegenite in Astoria. This data is consistent with the Ni+Co trend documented in pyrite from CCP veinlets. An identical pattern is registered in arsenopyrite from QCT vein selvages and alteration halos.

Thus, a clear change in CCP mineral associations and chemical signature of gold-related sulfides occurs towards the Astoria segment. Given that this segment is also host of late Proterozoic gabbro dykes, this spatial relationship brings into question the plausible influence of the emplacement of the dykes on the formation of the CCP veinlets; either solely acting as a thermal source responsible for remobilization and reconcentration of previously established gold contents, or as a direct source of a late gold input. In order to better comprehend these chemical and mineralogical modifications and overcome censored data, major and minor elements data will be completed with LA-ICP-MS analyses on arsenopyrite and pyrite.

This study shows that mineralization at the Augmitto-Bouzan deposit results from superimposed syn- and post-shear gold events. These findings provide new exploration targets for the segment and, thus, revaluation of barren areas could prove significant.

## Acknowledgements

This research is supported by the FRQNT (grant #FT130375). The authors would like to thank Yorbeau Inc. and IamGold for allowing access to the property and support during logging and sampling.

## References

Card KD, Ciesielski A (1986) DNAG#1. Subdivisions of the Superior Province of the Canadian Shield. Geoscience Canada 13(1), 5-13

Groves DI, Goldfarb EJ, Robert F, Hart CJR (2003) Gold deposits in metamorphic belts: overview of current understanding, outstanding problems, future research, and exploration significance. Econ. Geology 98(1), 1-29

Palarea-Albaladejo J, Martín-Fernández JA (2015) zCompositions – R package for multivariate imputation of left-censored data under a compositional approach. Chemometr Intell Lab Syst 143:85-96

Poulsen KH (2017) The Larder Lake-Cadillac Break and its gold districts. Reviews in Econ. Geology 19(1), 133-167

Powell W, Carmichael D, Hodgson C (1995) Conditions and timing of metamorphism in the southern Abitibi greenstone belt, Quebec. Canadian Journal. of Earth Sciences 32(6), 787-805

# The trace element composition of pyrite through metamorphism at the Yukon-Tanana Terrane, Yukon

**Nelson Román[1], Daniel D. Gregory[1], Nathan R. Cleven[2], James J. Ryan[2]**
*[1] Department of Earth Sciences, University of Toronto, Ontario, Canada*
*[2] Geological Survey of Canada, British Columbia, Canada*

**Abstract.** This study aims to constrain how the composition of pyrite changes through metamorphism prior to its transition to pyrrhotite. For this, we used metasedimentary rock samples with different metamorphic grades from the Yukon-Tanana terrane, Yukon. Sulfide composition was analyzed by LA-ICP-MS, and metamorphic grades were constrained by Raman spectroscopy analyses of carbonaceous matter. Peak metamorphic temperatures in the sample suite range from 347 ± 9°C to 598 ± 34°C, consistent with a variation from greenschist to amphibolite metamorphic facies. Compositional changes in pyrite were observed as a function of increasing metamorphic grades. Manganese, Cu, Mo, Ag, As, Sb and Tl show consistent decreasing trends, while Co and Ni concentrations increase with prograde metamorphism. The magnitude of these changes is smaller than the element release associated with the transformation of pyrite into pyrrhotite.

## 1 Introduction

The trace element chemistry of sedimentary-diagenetic pyrite has been used to understand its parental fluids, and its application ranges from determination of past ocean chemistry (e.g.: Large et al. 2014, 2017; Gregory et al. 2017) to mineral deposit formation (e.g.: Large et al. 2011; Gregory et al. 2015). Moreover, pyrite chemistry has been used to evaluate the metallogenic fertility of sedimentary rock units in orogenic Au deposit districts, considering its potential role as a source of Au in metamorphic devolatilization genetic models (Pitcairn et al. 2006; Large et al. 2011). However, it is not well understood how pyrite trace element content is retained prior to the pyrite–pyrrhotite transition. For evaluating this, we studied samples with variable metamorphic grade from the Yukon-Tanana terrane, Yukon. This study provides some of the first empirical data testing how well pyrite trace element content is retained through metamorphism, expanding on the studies of Pitcairn et al. (2010) and Finch and Tomkins (2017).

## 2 Geological Background

The Yukon-Tanana terrane (YTT) is one of the pericratonic terranes that constitute the North American Cordillera accretionary orogen in Yukon, Canada (Fig. 1). The YTT formed as an independent crustal fragment in the Late Devonian when it rifted from the western Laurentian continental margin, and it evolved as a pericratonic continental- to island-arc terrane during the Paleozoic (Colpron et al. 2006; Nelson et al. 2013). Its evolution during this period is recorded by four main tectonic assemblages: (1) the Snowcap assemblage, a basal assemblage of siliciclastic rocks with continental margin affinity; and the (2) Finlayson, (3) Klinkit and (4) Klondike assemblages, all younger volcano-sedimentary assemblages with arc and back-arc affinity (Colpron et al. 2006; Nelson et al. 2013).

Widespread regional metamorphism occurred in YTT, mostly driven by its accretion to the western margin of Laurentia and starting as early as the Early Mississippian and continuing, intermittently, to the mid-Cretaceous (Staples et al. 2016). Metamorphism in the YTT reached amphibolite facies metamorphic grade (Staples et al. 2016), but lower metamorphic grades have been reported in southeastern Yukon (Read et al. 1991).

The YTT hosts orogenic Au mineralization in the Klondike, White Gold and Dawson Range mineral districts (Fig. 1; Allan et al. 2013). It has been suggested that coeval metamorphism and associated rock dehydration of an underplated portion of the YTT could have provided mineralizing metamorphic fluids for orogenic Au mineralization in some of these districts (Staples et al. 2016).

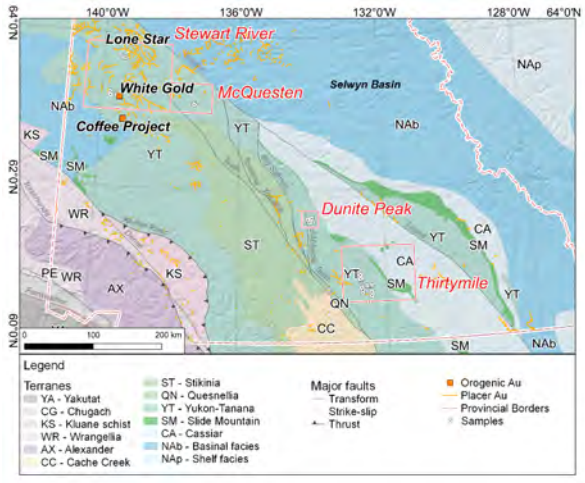


**Figure 1**. Terrane map of Yukon, showing the location of the YTT (YT in the map; Nelson et al. 2013). The regions considered for sampling are indicated with red rectangles.

## 3 Samples and Methods

Seventeen metasedimentary samples from the Finlayson and Snowcap assemblages were used for this study. The sample suite includes micaceous quartzite and metapelite with variable content of carbonaceous matter. To represent different metamorphic grades, rock samples from the Thirtymile and Dunite Peak regions, in southeast Yukon, and from the Stewart River and McQuesten regions in west-central Yukon were utilized (Fig. 1).

The trace element composition of pyrite and pyrrhotite was analyzed using laser ablation inductively coupled plasma mass spectrometry (LA-ICP-MS), at the Department of Earth Sciences, University of Toronto (UofT), and at the Geological Survey of Canada (GSC) in Ottawa, Ontario. The following isotopes were measured: $^{23}$Na, $^{25}$Mg, $^{27}$Al, $^{29}$Si, $^{34}$S, $^{39}$K, $^{42}$Ca, $^{47}$Ti, $^{51}$V, $^{55}$Mn, $^{57}$Fe, $^{59}$Co, $^{60}$Ni, $^{65}$Cu, $^{66}$Zn, $^{75}$As, $^{77}$Se, $^{95}$Mo, $^{109}$Ag, $^{121}$Sb, $^{125}$Te, $^{181}$Ta, $^{182}$W, $^{197}$Au, $^{205}$Tl, $^{206}$Pb, $^{207}$Pb, $^{208}$Pb and $^{209}$Bi. Calibration was done using matrix-matched reference materials. After data reduction, data were normalized to account for the matrix material ablated together with the target sulfide grain during analysis. Spots with more than 30% matrix were discarded. Additionally, only spots with a S measured/S expected ratio between 0.75-1.25 were considered. Using this scheme, 78 pyrite and 28 pyrrhotite spot analyses of a total of 203 spots comply with these quality control criteria.

The degree of graphitization of carbonaceous matter in the samples was used as a proxy for the peak metamorphic temperature, and this, in turn, as an indication of the metamorphic grade of the samples (Beyssac et al. 2002, Aoya et al. 2010). This was studied through Raman spectroscopy on carbonaceous materials (RSCM), at the Royal Ontario Museum, Toronto, Canada, following the analytical conditions recommended by Aoya et al. (2010). Each sample was characterized by the acquisition of at least 20 spot analyses. The RSCM temperatures reported here were calculated following the Aoya et al. (2010) procedures, with one standard deviation as the associated error.

## 4 Results

### 4.1 Sulfide occurrence

The main sulfides occurring in the samples are pyrite and pyrrhotite (Fig. 2). Chalcopyrite, galena and sphalerite were also found in some samples.

Pyrite occurs in most samples, but with low abundance (<0.5% modal). It occurs primarily as small (<20 µm) euhedral to subhedral grains, between recrystallized quartz grains or included in them (Fig. 2A, B). Pyrrhotite is present in the four YTT regions and it is less common than pyrite. Its main occurrence mode is as inclusions in quartz as small grains (<20 µm) associated with pyrite (Fig. 2C), or also it can be present as larger grains (>500 µm) associated with chalcopyrite (Fig. 2D).

### 4.2 Pyrite and pyrrhotite LA-ICP-MS analyses

The trace element composition of pyrite and pyrrhotite in the YTT samples is presented in Figure 3. The most abundant element in the analyzed pyrite grains is Ni, with a median concentration of 656 ppm. Other elements with median concentrations above 100 ppm are Co, As, Se and Pb. Gold was above the detection limit only in 22 of the 78 pyrite spot analyses, with a median concentration of 0.18 ppm after matrix correction. The most abundant elements in pyrrhotite are Ni and Co, with medians of 1359 and 653 ppm, respectively. Other elements detected and quantified in most spots were Mn, Se, Ag, Pb and Bi. Conversely, As and Au concentrations were mostly below the detection limit.

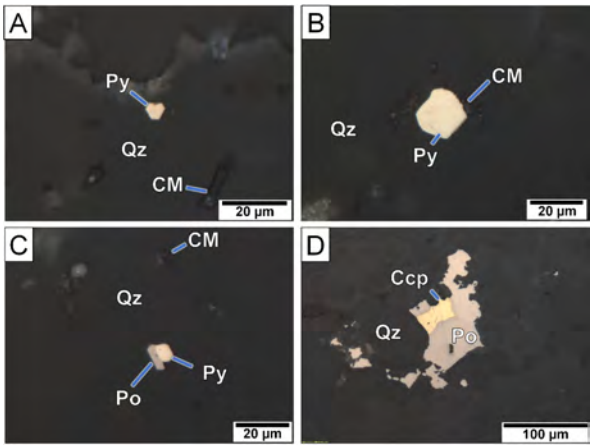


**Figure 2**. Reflected light microphotographs of the sulfides in YTT samples. A: euhedral pyrite grain between quartz grains; B: euhedral pyrite grain included in quartz and associated with carbonaceous matter. C: pyrite and pyrrhotite grains included in quartz. D: Composite pyrrhotite-chalcopyrite grain between quartz crystals. Abbreviations: CM: carbonaceous matter, Ccp: chalcopyrite, Po: pyrrhotite, Py: pyrite, Qz: quartz.

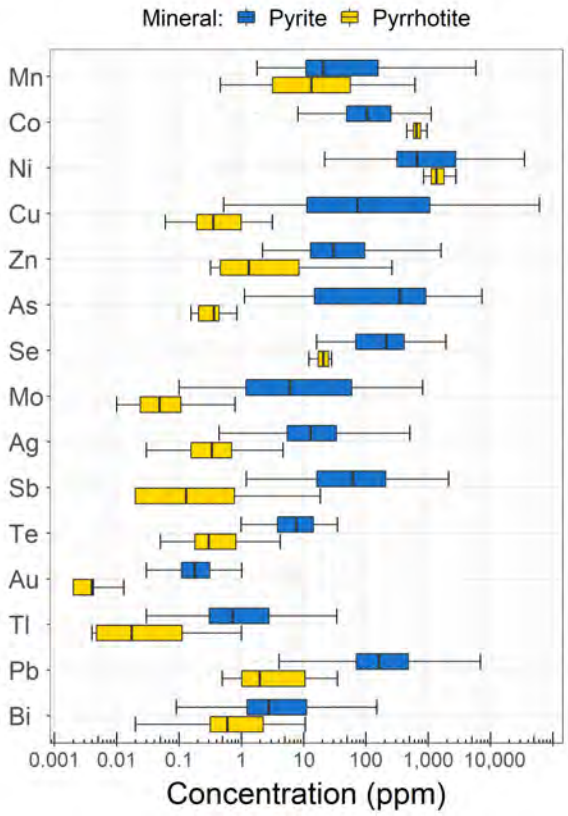


**Figure 3**. LA-ICP-MS trace element concentrations in pyrite and pyrrhotite in the YTT samples.

Most trace elements are depleted in pyrrhotite compared to pyrite, except Co and Ni (Fig. 3). The most notable differences between both minerals are their Cu, As, Mo and Sb concentrations, where pyrrhotite has concentrations of at least two orders of magnitude less than pyrite.

### 4.3 RSCM Temperatures

RSCM temperatures range from 347 ± 9°C to 598 ± 34°C in the analyzed samples (Table 1). The temperatures vary across regions and the lowest temperatures are found in the Thirtymile region. Two distinct RSCM temperature groups occur in the Thirtymile region: one ~340-360°C and another group with higher temperatures (~400-500°C). Similar temperatures were obtained for samples in proximity to each other, denoting spatial consistency in the RSCM results.

**Table 1**: RSCM temperatures of the YTT samples.

| Region | Sample | RSCM (°C) | |
|---|---|---|---|
| | | Temp. | St.Dev. |
| Stewart River | 03RAY052B1 | 598 | 35 |
| | 00RAY271A | 578 | 30 |
| | 03GGA028A01 | 576 | 33 |
| McQuesten | 09RAYEK010A01 | 583 | 27 |
| | 09RAYEK002A01 | 526 | 28 |
| Dunite Peak | 16RAYAP072A | 510 | 32 |
| | 16RAYAP192A | 492 | 17 |
| Thirtymile | 18RAYNC128A | 509 | 30 |
| | 18RAYNC030B | 476 | 17 |
| | 18RAYNC091A | 472 | 23 |
| | 18RAYNC024A | 460 | 17 |
| | 18RAYNC057A | 355 | 10 |
| | 18RAYNC070A | 351 | 3 |
| | 18RAYNC062A | 347 | 9 |

## 5 Discussion

### 5.1 The origin of pyrite in the YTT

The Co/Ni ratios of pyrite in YTT is <2 for most analyzed spots (Fig. 4), suggestive of a sedimentary or diagenetic origin (e.g.: Gregory et al. 2015). In addition, Co and Ni concentrations of pyrite in YTT are similar to the pyrite in the Road River and Earn groups of the Selwyn basin (Fig. 4), interpreted as sedimentary to diagenetic (Sack et al. 2018). Further, the pyrite textures in the YYT samples (Fig. 2) resemble the small euhedral pyrite textures reported by Gregory et al. (2015) in black shales, also interpreted as early diagenetic. Considering this, pyrite in YTT could have a sedimentary-diagenetic origin, justifying the use of it to study how sedimentary pyrite composition evolves through metamorphism.

### 5.2 Peak temperatures of metamorphism

Based on their peak metamorphic temperatures, the samples used for pyrite compositional analyses can be subdivided in three groups, with generalized temperature in the following ranges: 340-360°C (Group 1), 450-500°C (Group 2) and 500-600°C (Group 3). These groups broadly represent greenschist, upper greenschist to lower amphibolite and amphibolite facies, respectively.

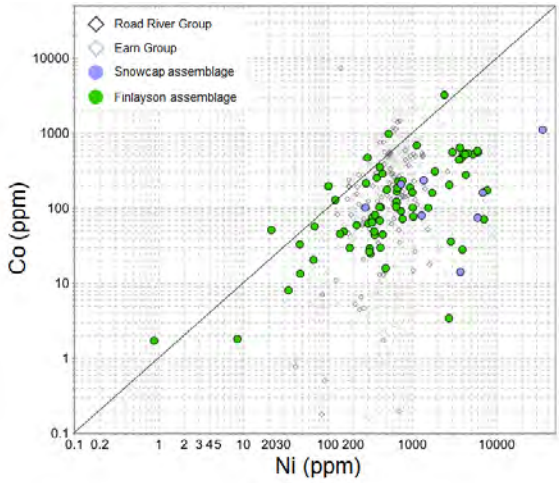


**Figure 4**. Co vs. Ni concentrations in pyrite of YTT, compared with pyrite of the Road River and Earn Groups of the Selwyn Basin (from Sack et al. 2018).

### 5.3 Trace element composition in pyrite and metamorphic grade

Clear decreasing concentration trends with higher metamorphic grades are observed for Mn, Cu, Mo, Ag, As, Sb and Tl in YTT pyrite (Fig. 5). Conversely, the concentrations of Co and Ni increase with higher metamorphic grades. Other elements, such as Zn, Se, Te, Au, Pb and Bi, do not show obvious trends.

The enrichment of Co and Ni could be caused by a relative enrichment caused by the loss of other elements (S). The loss of Cu could be linked to the formation of chalcopyrite. Similarly, the loss of Ag and Sb could be due to remobilization to galena, a process suggested by Pitcairn et al. (2010) during prograde metamorphism. The same process could be acting on Tl, an element commonly enriched in galena (George et al. 2018). More data is required to accurately evaluate the loss of Au and Te, especially considering that most analyses were below the detection limit for these elements.

The remobilization trends shown in Figure 5 do not reflect how elements are lost during breakdown of pyrite into pyrrhotite, one of the main mechanisms proposed for explaining release of metals to form orogenic Au deposits (Tomkins 2010). The data compiled by this study suggests that the magnitude of the compositional variation of pyrite through metamorphism (Fig. 5) is smaller than the change provoked by the breakdown of pyrite into pyrrhotite (Fig. 3), supporting the fundamental role of this process for metal release.

Since some elements show the same trends with metamorphism, concentration ratios between them might constitute robust source trackers that could be preserved through metamorphism. This seems to be the case for Co/Ni ratios. Conversely, the results

here suggest that caution must be exerted for the use of single element thresholds as paleo-chemical proxies or gold fertility indicators.

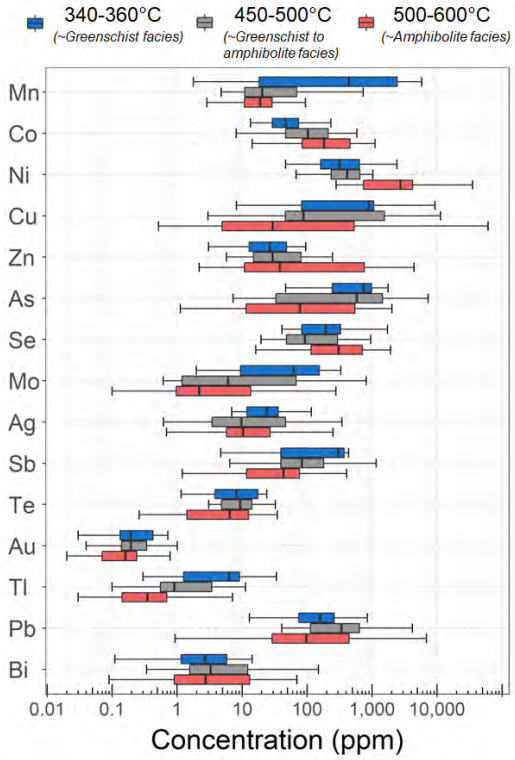


**Figure 5**. LA-ICP-MS trace element concentrations in pyrite, subdivided by metamorphic grade.

## 6 Concluding remarks

This study suggests that the trace element composition of pyrite changes through metamorphism, however, the magnitude of this change is less than the change associated with pyrite-pyrrhotite transformation. Ratios between elements with similar behavior during metamorphism could constitute robust trackers of the original trace element composition of pyrite.

## Acknowledgements

This study was funded by the Geological Survey of Canada, through the Research Affiliate Program. Additional funding was provided through a NSERC Discovery Grant to D. Gregory. N. Román thanks financial support provided by the Hugh Snyder International Scholarship in Earth Sciences (Ph.D. scholarship). We thank Xu Chu, Veronica Di Cecco and Ivano Gennaro for their help with RSCM analyses, and Hehe Jiang and Colin Bray for their help with LA-ICP-MS analyses.

## References

Allan MM, Mortensen JK, Hart CJR, et al (2013) Magmatic and Metallogenic Framework of West-Central Yukon and Eastern Alaska. In: Colpron M, Bissig T, Rusk BG, Thompson JFH (eds) Tectonics, Metallogeny, and Discovery: The North American Cordillera and Similar Accretionary Settings. Society of Economic Geologists, pp 111–168

Aoya M, Kouketsu Y, Endo S, et al (2010) Extending the applicability of the Raman carbonaceous-material geothermometer using data from contact metamorphic rocks. Journal of Metamorphic Geology 28:895–914

Beyssac O, Goffé B, Chopin C, Rouzaud JN (2002) Raman spectra of carbonaceous material in metasediments: a new geothermometer. Journal of Metamorphic Geology 20:859–871

Colpron M, Nelson JL, Murphy DC (2006) A tectonostratigraphic framework for the pericratonic terranes of the northern Canadian Cordillera. In: Colpron, M. and Nelson, J.L., eds., Paleozoic Evolution and Metallogeny of Pericratonic Terranes at the Ancient Pacific Margin of North America, Canadian and Alaskan Cordillera: Geological Association of Canada, Special Paper 45. pp 1–23

Finch EG, Tomkins AG (2017) Pyrite-Pyrrhotite Stability in a Metamorphic Aureole: Implications for Orogenic Gold Genesis. Economic Geology 112:661–674

George LL, Biagioni C, D'Orazio M, Cook NJ (2018) Textural and trace element evolution of pyrite during greenschist facies metamorphic recrystallization in the southern Apuan Alps (Tuscany, Italy): Influence on the formation of Tl-rich sulfosalt melt. Ore Geology Reviews 102:59–105

Gregory DD, Large RR, Halpin JA, et al (2015) Trace Element Content of Sedimentary Pyrite in Black Shales. Economic Geology 110:1389–1410

Gregory DD, Lyons TW, Large RR, et al (2017) Whole rock and discrete pyrite geochemistry as complementary tracers of ancient ocean chemistry: An example from the Neoproterozoic Doushantuo Formation, China. Geochimica et Cosmochimica Acta 216:201–220

Large RR, Bull SW, Maslennikov VV (2011) A Carbonaceous Sedimentary Source-Rock Model for Carlin-Type and Orogenic Gold Deposits. Economic Geology 106:331–358

Large RR, Halpin JA, Danyushevsky LV, et al (2014) Trace element content of sedimentary pyrite as a new proxy for deep-time ocean–atmosphere evolution. Earth and Planetary Science Letters 389:209–220

Large RR, Mukherjee I, Gregory DD, et al (2017) Ocean and Atmosphere Geochemical Proxies Derived from Trace Elements in Marine Pyrite: Implications for Ore Genesis in Sedimentary Basins. Economic Geology 112:423–450

Nelson JL, Colpron M, Israel S (2013) The Cordillera of British Columbia, Yukon, and Alaska: Tectonics and Metallogeny. In: Colpron M, Bissig T, Rusk BG, Thompson JFH (eds) Tectonics, Metallogeny, and Discovery: The North American Cordillera and Similar Accretionary Settings. Society of Economic Geologists, pp 53–109

Pitcairn IK, Teagle DAH, Craw D, et al (2006) Sources of metals and fluids in orogenic gold deposits: Insights from the Otago and Alpine schists, New Zealand. Economic Geology 101:1525–1546

Pitcairn IK, Olivo GR, Teagle DAH, Craw D (2010) Sulfide evolution during prograde metamorphism of the Otago and Alpine schists, New Zealand. Canadian Mineralogist 48:1267–1295

Read PB, Woodsworth GJ, Greenwood HJ, et al (1991) Metamorphic map of the Canadian Cordillera: map 1714A. Geological Survey of Canada

Sack PJ, Large RR, Gregory DD (2018) Geochemistry of shale and sedimentary pyrite as a proxy for gold fertility in the Selwyn basin area, Yukon. Mineralium Deposita 53:997–1018

Staples RD, Gibson HD, Colpron M, Ryan JJ (2016) An orogenic wedge model for diachronous deformation, metamorphism, and exhumation in the hinterland of the northern Canadian Cordillera. Lithosphere 8:165–184

Tomkins AG (2010) Windows of metamorphic sulfur liberation in the crust: Implications for gold deposit genesis. Geochimica et Cosmochimica Acta 74:3246–3259

# Structural control of gold deposits at Eastern Alta Floresta Mineral Province Brazil, preliminary results

**Renata Augusta Sampaio Paes' Maria José Mesquita', Márcia Elisa Boscato Gomes[2], Igor de Camargo Moreira', Hevelyn Eduarda da Silva Martins', José Henrique Matos', Alberto Ruggiero', Guilherme Primo', Diego Fernando Ducart', Luciano Poggi', André Massanobu Ueno Kunifoshita' Leonardo Zanchetta de Laurentis' and João Gabriel da Silva'**

*[1]Campinas University, Campinas, São Paulo, Brazil*

*[2]The Rio Grande do Sul Federal University, Porto Alegre, RS, Brazil*

**Abstract.** The linear features acquired through satellite and aerogeophysics data, in association with structural measures of foliation and mineralised veins orientation in field mapping, provide a previous analysis from the area's structural framework, a routine suitable for the Alta Floresta Mineral Province, a high areal extension, important and weakly understood Brazilian mineral province. This work points out the existing correlation between the primary gold deposits hosted in rocks of calcium-alkaline to the alkaline composition of the province to the presence of NW first-order shear zones, NS and EW secondary shear zones, as well as relatively more recent NS and NE faults and fractures.

## 1 Introduction

The Alta Floresta Mineral Province (AFMP) has an extensive and productive history of artisanal and small-scale mining and is currently one of the most promising regions for gold and copper exploration in Brazil. Consequently, research projects and investments have increased exponentially, particularly following the discovery of significant copper and gold occurrences in 2018 (Bloomberg 2018.).

Located at northern Mato Grosso State, the AFMP presents an approximately 500 km² areal extension, with dozens of primary gold mineralisations that can be grouped into three major types according to the ore typology (Mesquita et al. 2022): (i) Au ± Cu in shear zone veins, following the example of the Edu, Paraíba, Basilio, Peteca, Porteira-Buriti, Viúva, Serrinha de Guarantã (and Luiz Bastos; (ii) Cu + Au ± Mo deposits disseminated in breccias or in stockworks, for example the Pé Quente, X1, Luizão, Serrinha and Jaca and (iii) Au + base metal deposits in veins developed on faults as for example the Francisco Bigode, and Luiz Bastos deposits. The detailed set of work carried out on these deposits is available at Mesquita et al (2022).

There are several metallogenetic models described for the mineralisation, such as porphyry (Moura et al. 2006; Assis 2015) and intermediate sulfidation epithermal (Assis et al. 2017), orogenic type (Paes de Barros 1994; Siqueira 1997; Silva Abram 2008; Moreton and Martins 2005) and Intrusion related gold system - IRGS (Santos et al. 2001). However, the spatial relationships between mineralisation and the structural framework remain poorly understood, and a lack of integration, data is necessary to construct of robust exploratory models that make exploration in the area feasible and more dynamic.

## 2 Geological context

The PMAF is in the southwestern Amazon Craton in northern Mato Grosso state (Projeto Radambrasil - Brazil, 1980), between Tapajós-Parima (2.03-1.88 Ga) and Rondônia-Juruena (1.82-1.54 Ga) provinces (Santos et al. 2000).

The PMAF is elongated in a WNW-ESE direction, bordered to the north by the Cachimbo Graben and to the south by the Caiabis Graben. In simplified form, it is composed of an older core, called the Peixoto de Azevedo domain (Figure 2), of the former Tapajós-Parima Province (c. 2,05-1,97 Ga, rocks related to the Cuiú-Cuiú volcanic arc) surrounded and cut by younger rocks of the Rondônia-Juruena Province (c.1,82-1,52 Ma, rocks related to the Rondônia-Juruena volcanic arc) (Santos et al. 2000, 2015; Duarte et al. 2012, 2019) (Figure 1).

Some authors point to the origin of the deposits as a single hydrothermal magmatic event developed at different crustal levels in the Estatherian period (Trevisan 2015; Assis 2015; Assis et al. 2017). While for others, the deposits are differentiated into two mineralizing hydrothermal events, one hydrothermal-shear, generating orogenic gold deposits, and another magmatic-hydrothermal generating porphyry-epithermal deposits (Pimenta 2018; Poggi 2019; Mesquita et al. 2022; Poggi et al. 2022).

## 3 Mineralisation's structural analysis, an overview

The mineralisation's host rocks are 2.04-1.98 Ga granitoids, quartz-feldspathic gneiss, and ultramafic amphibolites, they present at least two deformations episodes. The first one, Dn presents foliation Sn trending to 00-50° and dips 70-90 WNW (Fig 2), that progress from millimeter-scale alternating feldspar-quartz-rich and phyllosilicate-rich domain in orthogneiss to a well-developed spaced foliation in metagranitoids and metamafic rocks (Fig. 3a)

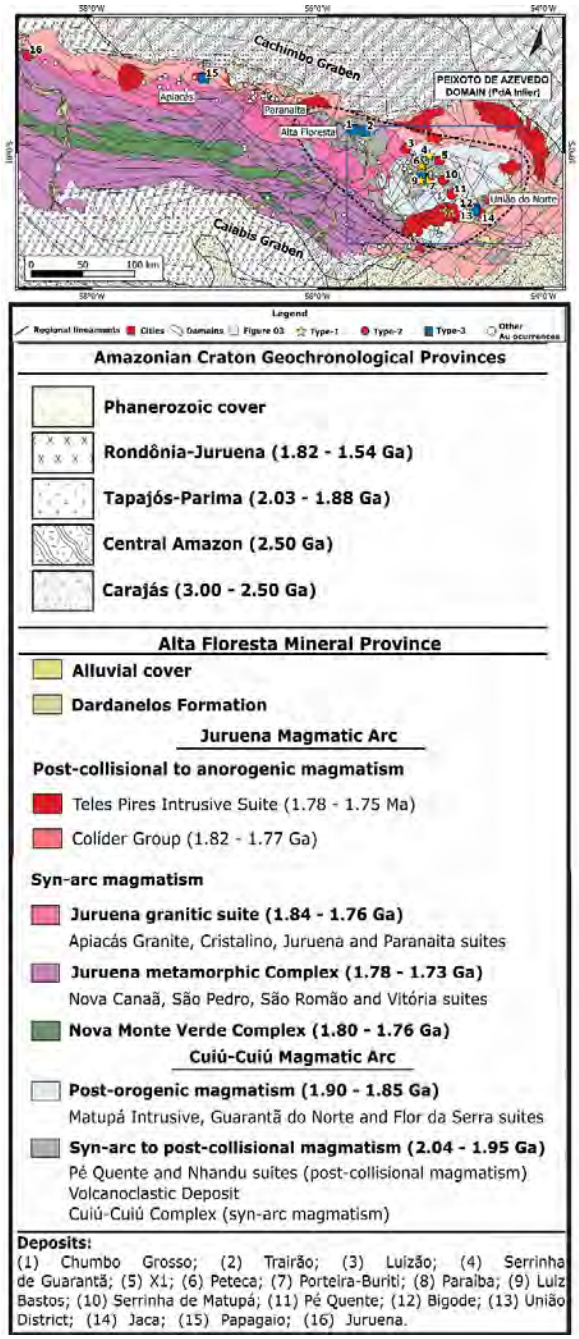


**Figure 1.** Simplified geological map of the Alta Floresta Mineral Province, highlighting the Peixoto de Azevedo Domain (contour dotted in black.). modified from Lacerda Filho et al. 2004.

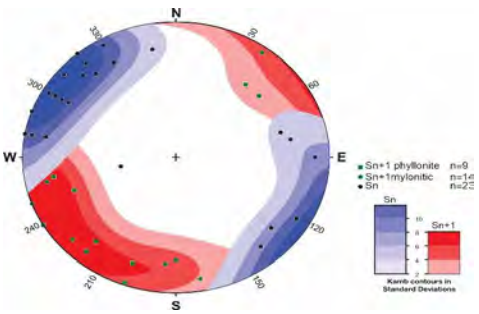


**Figure 2.** Stereogram (equal area, lower hemisphere) of Sn foliation poles in the host rocks and Sn+1 foliation mylonite and phyllonite.

A second deformation episode (Dn+1) developed several WNW-trending first-order shear zones (Fig. 2). They are transpressional to strike-slip, mostly with dextral movements. Dn+1 develops tens of meters of mylonites (Fig. 3b) transposed to the previous granitoids' Sn. Feldspars porphyroclasts wrapped by an anastomosed mafic matrix (biotite-magnetite/ilmenite-pyrite) define the mylonitic foliation Sn+1 (Fig. 3c). Sn+1 displays an average N20-40W dipping 50-70°SW (Fig. 2). There is a metric to centimetric gradation between mylonites and phyllonites. In the phyllonite, Sn+1 is a continuous schistosity defined by muscovite, biotite and chlorite bands alternating with quartz bands. The feldspars are partially or entirely substituted by micas (Fig. 3d).

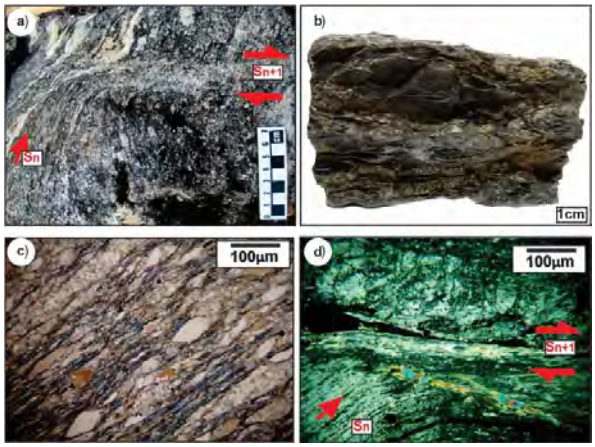


**Figure 3.** (a) Sn banding transposed by Sn+1 (discrete shear band in 1.98 Ga (Miguel 2011) metagranodiorite (Mesquita et al. 2022); (b) Banded ultramafic amphibolites, with pyrite veinlets associated to the Sn+1 banding; (c) mylonitic foliation defined by tremolite-actinolite associated with white mica chlorite, and quartz ribbon microlithon; (d) Sn banding intercepted by Sn+1.

## 4 Interpretation

Through the integration of aero-geophysics data, available from the Brazil Geological Service (Alves et al. 2019), and shuttle radar topography (SRTM), used free of charge from the SRTM image catalog on the United States Geological Survey website, in association with field mapping, linear features were interpreted.

Flat topography with a few rocks outcrops characterizes the eastern part of Alta Floresta Mineral Province. We identify different linear features orientations in which the WNW family direction is highlighted, associated with NE continuous structures and NS and NE discontinuous structures (Fig. 4) There are some NW structures already described in the literature as first-order shear zones (Paes de Barros 2007; Miguel Jr. 2011 and Quispe 2016), associated with mineralised veins.

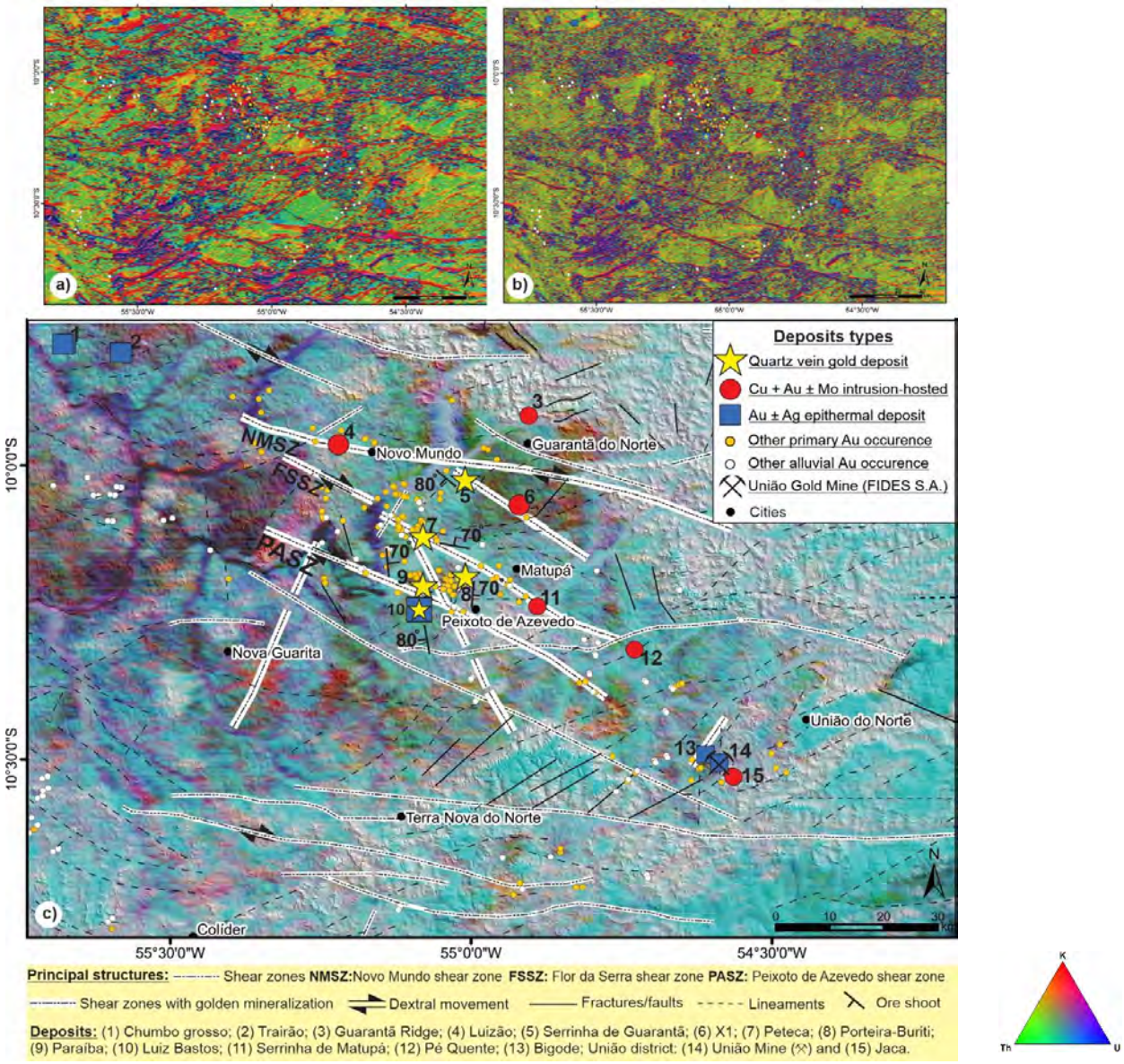


**Figure 4.** The eastern part of the Alta Floresta Mineral Province aero-geophysics and SRTM images: (a) First vertical derivative from the total magnetic field; (b) Second vertical derivative; (c) Eastmost Alta Floresta Mineral Province geological map, with the main mineral deposits and structures from structural interpretation, with SRTM and ternary aero-gamma spectrometric. Modified from Alves et al. (2019)

Parallel to the first-order shear-zones is found high-grade and low tonnage deposits, restricted to the principal structure, as the Serrinha de Guarantã deposit (Fig 5), the thickest gold quartz vein at the area (1-5m) (Fig. 6c). The mineral assemblage is phlogopite, calcite, quartz, bornite, chalcocite, and chalcopyrite (Fig. 6d) (Rios 2019).

Most gold-quartz veins concentrate in subsidiaries to the first-order shear zones (Fig. 5). These subsidiary shear zones are north-trending, controlling the Paraíba mine (Fig. 6a), Luiz Bastos and Buriti–Porteira deposits, or east-trending, controlling the Peteca mine (Fig. 6e), João Fidelis and Queiroz deposits. The ore is ccp+py, and gold occurs as inclusions, infilling fractures in pyrite and as free gold (Fig. 6b and 6f).

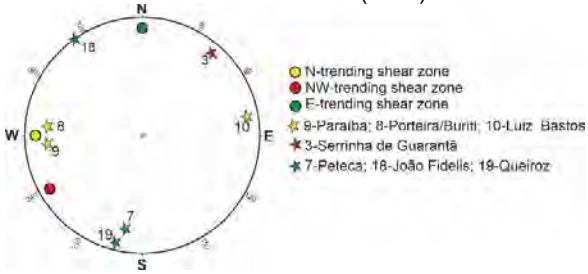


**Figure 5.** Stereogram (equal area, lower hemisphere) of poles of phyllonite foliation Sn+1 and respectively quartz vein orientations in the shear zone system.

NE-trending faults and fractures crosscut and dislocate the first-order shear zones.

These NE-trending faults appear as discontinuous and discrete lineaments, shallow

structures which draw the landscape. These structures controlled mafic dykes (Rios 2019) and most of the magmatic-hydrothermal deposits, notably the epithermal ones as Trairão, Luiz Bastos, and Francisco-Bigode and União Gold Mine (União do Norte District).

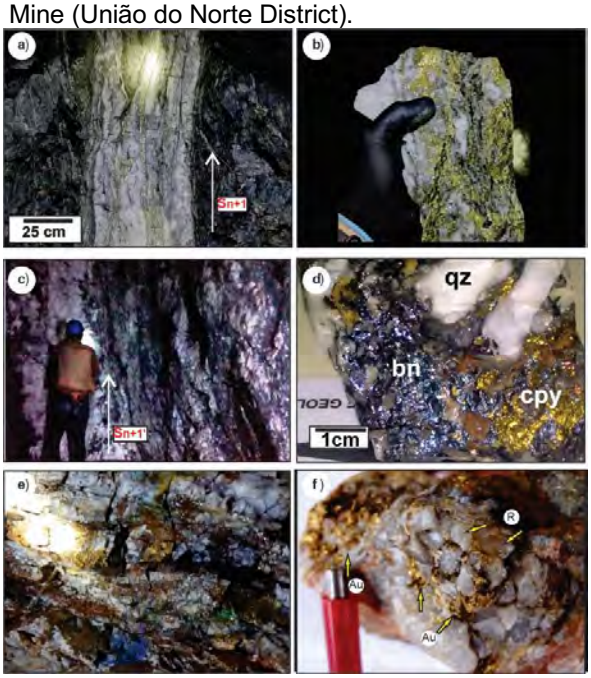


**Figure 6.** Characteristics of structural controlled ore bodies. Paraiba Mine: a) Mineralised laminated quartz vein at (b) Anastomosed ore vein (Caption from the company public website); Serrinha de Guarantã deposit: (c) Four meters thick mineralised quartz vein and (d) Ore sample; Peteca mine: (e) intensively fractured quartz vein (Caption from the company public website), (f) Free-gold sample (Mesquita et al. 2022).

There is a close relationship between the presence of structurally controlled deposits and the presence of shear zones, fractures, and faults. But the relationship between these requires geochronological studies to establish their temporal evolution. Research that is in progress.

## 5 Conclusions

The Type-1 gold-quartz veins concentrate along the anastomosing NW lineaments defined by the first-order shear zones. Most of them concentrate in the subsidiary shear zones as N-trending (Paraíba, Luiz Bastos, and Buriti-Porteira deposits) and E-trending (Peteca, João Fidelis, and Queiroz deposits).

NE-trending faults and fractures control most of the Type-2 and -3 deposits. The NE faults crosscut and dislocate the WNW first-order shear zones and the Sn+1 foliation (hosting the Type-1 deposits). The NE-trending faults appear as discontinuous and discrete lineaments. Many Type-3 veinlets are within these NE faults and fractures and their subsidiaries, or in the intersection between the older WNW-trending shear zones and the NE-trending faults.


## Acknowledgements

The authors are thanked to the Institute of Geosciences of the University of Campinas, PA Gold Mineração e Metalurgica LTDA, FIDES Mining and METAMAT - Companhia Matogrossense de Mineração. This research has been financially supported by the CAPES - Coordination of Superior Level Staff Improvement through student grant number 88887.481707/2020-00 and SEG -The Society of Economic Geologists, with the Student Research Grant program 20-110 provided by the Hugh E. Mckinstry Fund.


## References


Alves CL, et al (2020) The Orosirian Cuiú-Cuiú magmatic arc in Peixoto de Azevedo domain, Southern of Amazonian craton. Journal of South American Earth Sciences, 102, 102648. https://doi.org/10.1016/j.jsames.2020.102648

Assis RR et al (2017) Linking the Timing of Disseminated Granite-Hosted Gold-Rich Deposits to Paleoproterozoic Felsic Magmatism at Alta Floresta Gold Province, Amazon Craton, Brazil: Insights from Pyrite and Molybdenite Re-Os Geochronology. Economic Geology, 112: 1937–1957. https://doi.org/10.5382/econgeo.2017.4535

Bloomberg (2018) Has Anglo American found something big in Brazil?. http://www.bloomberg.com/news/articles/2018-07-26/has-anglo-american-found-something-big-in-brazil

Lacerda Filho JV et al (2004) Geologia e Recursos Minerais do Estado de Mato Grosso: texto explicativo dos mapas geológicos e de recursos minerais do Estado de Mato Grosso. MME/CPRM/ SICME-MT. Programa Integração, Atualização e Difusão de Dados da Geologia do Brasil e Subprograma Mapas Geológicos estaduais, escala (1:1.000.000). Cuiabá: MME/CPRM/SICME-MT. v. 1. 235 [in Portuguese].

Mesquita MJ et al (2022) Paleoproterozoic gold deposits at AFMP, Brazil: two overprinted mineralizing events? From: Torvela, T., Lambert-Smith, J. S. and Chapman, R. J. (eds). Recent Advances in Understanding Gold Deposits: from Orogeny to Alluvium. Geological Society, London, Special Publications, 516. https://doi.org/10.1144/SP516-2021-64

Moura MA et al (2006) Granite-related Paleoproterozoic, Serrinha gold deposit, Southern Amazonia, Brazil: hydrothermal alteration, fluid inclusion and stable isotope constraints on genesis and evolution. Economic Geology, 101, 585-605. https://doi.org/10.2113/gsecongeo.101.3.585

Pogi L et al (2022) New Insights into the Evolution and Footprints of the Paraíba Au-Cu-Mo Deposit, Alta Floresta Mineral Province (Brazil), through Integration of Spectral and Conventional Methods. Minerals 2022, 12, 1327. https://doi.org/10.3390/min12101327

Santos JOS et al (2001) Gold deposits of the Tapajós and Alta Floresta domains, Tapajós-Parima orogenic belt, Amazon Craton, Brazil. Mineralium Deposita, 36, 278-299. https://doi.org/10.1007/s001260100172

Santos JOS, et al (2000) A new understanding of the provinces of the Amazon Craton based on integration of field mapping and U–Pb and Sm–Nd geochronology. Gondwana Research, 3,453–488, https://doi.org/10.1016/S1342-937X(05)70755-3

Trevisan VG (2015) Estudo comparativo entre mineralizações filonares de Au+Cu e Au + metais de base do setor leste da Província de Alta Floresta (MT), Cráton Amazônico. Master's thesis, Institute of Geosciences, University of Campinas, Brazil.

# Metallogeny of gold (from in-situ to placer) in the Loch Tay area of Central Scotland

**Lucia Savastano[1], Robert J. Chapman[1], Taija M. Torvela[1]**
*[1]School of Earth and Environment, University of Leeds, United Kingdom*

**Abstract.** The Loch Tay area of Central Scotland hosts gold mineralisation in the form of both vein-sited and widespread placer occurrences. This work seeks to elucidate the unresolved genetic relationships between these two gold occurrence types and to provide insights into the local mineralisation styles. Assessing the compositional features of in-situ gold against those of their proximal eluvial and placer expressions provides: i) a template to investigate the origins of placer gold for which the hypogene source is unknown; ii) insights into the compositional variations of gold between paragenetic stages where the hypogene source is known. The microchemical signature (alloy composition and inclusion mineralogy) of gold has quantitatively been determined on a particle basis and detailed paragenetic sequences have been established for nearby, gold-bearing hydrothermal veins. Gold precipitates at least twice in the Calliachar Burn, River Almond and Lead Trial hydrothermal systems, which have ultimately resulted in distinguished genetic features. Although wider, the range of signatures exhibited by placer gold populations is compatible with that of local eluvial and in situ gold samples, suggesting subtle mineralogical variations within geographically proximal and genetically related vein systems.

## 1 Introduction and geological background

Particulate gold is highly stable in most surface settings, retaining compositional features that can be representative of the environment of gold precipitation. The intrinsic gold/silver ratios of the particles are controlled by the chemical and physical conditions at the point of precipitation from a hydrothermal fluid (Gammons and Williams Jones, 1995). Natural gold alloy may also contain minor amounts of Cu, Pd or Hg, which may form useful complementary discriminants (e.g., Leake et al., 1997; Chapman et al., 2000a). Alluvial gold populations are generally the product of relatively large volumes of mineralised material, therefore exhibit wider ranges in silver content than vein-hosted gold due to greater variations in the conditions of gold precipitation (Chapman et al., 2000a). Consequently, a detailed evaluation of the particle gold/silver ratios yields the potential to inform on the (evolving) mineralising conditions within the related ore body.

Consideration of the gold alloy composition has contributed to the definition of detailed paragenetic sequences in various hydrothermal systems (e.g., Parnell et al., 2000; Arif and Baker., 2004; Spence-Jones et al., 2018). Because an increased Ag content derives from lower temperatures and/or the lower Au/Ag ratio of the modifying fluids, with respect to the initial mineralizing fluids (Gammons and William Jones, 1995), it can be deduced that silver-rich gold alloys generally form later in the paragenesis. Mineral inclusions in placer gold can inform on the nature and proximity of the in-situ mineralisation, if similar species and assemblages are found in the hypogene environment (e.g., Leake et al., 1997; Chapman et al., 2010b).

Our methodology allows the correlation of compositional features of gold from specific paragenetic stages with that of nearby eluvial and gossan-derived gold, to inform on the potential source of proximal placer gold.

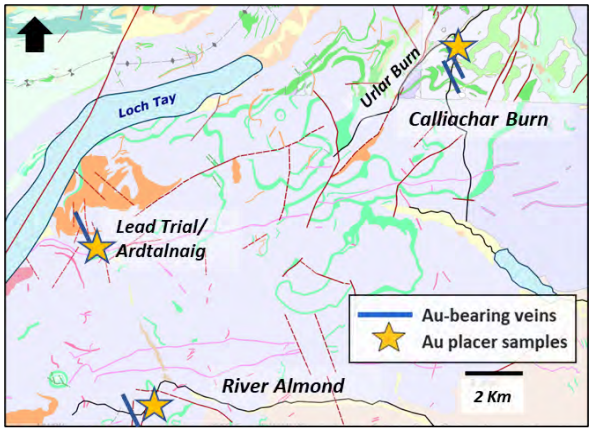


**Figure 1.** Map with locations of the sites of interest (after the geological map from https://digimap.edina.ac.uk/).

Near Loch Tay (Perthshire, Central Scotland), NNW-SSE-striking vein arrays outcrop across the Southern Highland Group of the Grampian Highlands. At Calliachar-Urlar Burn, River Almond and the 'Lead Trial' (Green Glen Minerals, 2023), some of these veins have been identified as high-grade, gold-bearing ones (Figure 1; e.g., Mason 1990, Ixer et al. 1997). Their mineralogy mainly consists of quartz plus sulphide assemblages which partially vary upon location (commonly pyrite, galena and chalcopyrite). The whole area is generally overgrown by vegetation, and gold can more frequently be recovered as placer particles in stream sediments, particularly at Calliachar Burn and River Almond (e.g., Chapman et al. 2023).

## 2 Methodology

### 2.1 Hydrothermal vein sampling and analysis

Sulphide/gold-bearing veins were sampled at the main localities indicated in Figure 1. Samples of six different veins from the Calliachar-Urlar system and of five veins from Lead Trial/Ardtalnaig were

analysed to reconstruct overarching vein parageneses for both localities; a vein paragenetic history at River Almond was established by extensive analysis of a single gold-bearing vein. The analytical protocol consists of the application of SEM-CL (cathodoluminescence) on quartz and SEM-EDS detection of mineral phases in the BSE (Back-Scatter) mode.

### 2.2 Gold particle sampling and analysis

The gold sample suite analysed for this study is indicated in Table 1. The in-situ gold samples (Calliachar_6V and Almond_6V) are located in the same veins from which the gossan-related (Calliachar_6G) and the crushed-ore (Almond_6H) gold samples were respectively retrieved. Placer gold populations were recovered downstream in Calliachar Burn, upstream in River Almond and in the Ardtalnaig Burn, in proximity to the ore-bearing veins. Gold compositional signatures (e.g., Chapman et al., 2000a) were determined on a particle basis by the application of i) EPMA on gold alloy; ii) SEM-EDS on mineral inclusions.

**Table 1.** Gold samples used for this study, with details on sample types/sizes and respective localities.

| Sample ID | Locality/sample type | No of particles |
|---|---|---|
| Calliachar_1 | *Calliachar Burn_placer* | 333 |
| Calliachar_6G | *Calliachar Burn_gossan* | 77 |
| Calliachar_6V | *Calliachar Burn_in situ* | 16 |
| Almond_5 | *River Almond_placer* | 605 |
| Almond_6H | *River Almond_crushed ore* | 104 |
| Almond_6V | *River Almond_in situ* | 18 |
| Lead Trial | *Lead Trial_crushed ore* | 204 |
| Ardaltnaig | *Ardtalnaig Burn_placer* | 58 |

## 3 Parageneses of the Au-bearing veins

The paragenetic histories of the Calliachar-Urlar Veins (overarching) and of the Almond Vein (individual) are reported in Table 2. Vein paragenetic analysis at the Lead Trial has revealed a higher degree of textural complexity and it is here illustrated by a slightly expanded text description.

### 3.1 Calliachar Burn and River Almond

Two main paragenetic stages are associated with gold mineralisation at Calliachar Burn (S1 and S3, Table 2a). S1 comprises euhedral/mottled quartz (Q1) enveloping euhedral pyrite (Py1, Figure 2a) which, in turn, hosts a relatively low amount of visible gold (Au1) as ~10µm size inclusions. The S3 is initiated by fractures in which quartz precipitates to form open-space textures (Q3) and is characterised by the greatest variety in sulphide mineralogy (especially cataclastic pyrite and galena). The dominant, coarser and more silver-rich gold input in the vein paragenetic history occurs within fractures (Au3) in shattered pyrite grains.

At River Almond, the assemblage of pyrite-galena-chalcopyrite-sphalerite is located alongside the second quartz event (Q2_av; CL-dark bands). Gold mineralisation entirely takes place over this paragenetic stage (S2; Table 2b), in the form of both inclusions (earlier) and fracture-fills (later) in sulphides. It is found as inclusions (Au2_a) in pyrite and chalcopyrite; and as fracture-fills (Au2_b) in pyrite, chalcopyrite and sphalerite (Figure 2e). The sample Au2_b shows a higher Ag content and is overall coarser (up to ~80µm size) than Au2_a. (e.g., Webb et al. 2023, under revision).

**Table 2.** Paragenetic tables for a) Calliachar-Urlar Veins; b) River Almond Vein.

| | S1 | S2 | S3 | S4 | S5 |
|---|---|---|---|---|---|
| *a)* | *Q1 (mottled)* | *Q2 (overprint)* | *Q3 (fractures)* | *Q4 (fractures)* | *Dol/Calcite* |
| Pyrite | | | cataclastic | | cataclastic |
| Arsenopyrite | | | cataclastic | | |
| Chalcopyrite | | | | | inclusions |
| Galena | | | | | inclusions |
| Sphalerite | | | | | |
| Gold | inclusions | | in-cracks | | |

| *b)* | *Q1 (mottled)* | *Q2 (overprint)* | *Dolomite* | *Q3 (fractures)* |
|---|---|---|---|---|
| Pyrite | | | | |
| Chalcopyrite | | | | |
| Galena | | | | |
| Sphalerite | | | | |
| Gold | | in-cracks | | |

### 3.2 Lead Trial

Detailed SEM-CL analyses of hydrothermal quartz from the Lead Trial revealed a variety of internal textural features. The second paragenetic stage (S2) has been classified as the ore-bearing one. This corresponds to an evolution of precursors comb crystal into well-defined euhedral crystals (Q1_LTb) as a result of gradual cooling. Sphalerite and galena systematically overgrow the euhedral quartz (Q1_LTb), thence co-precipitate at this point; in hand specimen, gold mineralisation is consistently found in association with this (dominant) sulphide assemblage and, when rarely observed in thin section, on the surface of CL-bright euhedral crystals (Figure 2c). Therefore, it is assumed to have been introduced in the system at or immediately after this stage. From thin section analysis, sub-spheric and plumose crystals in a moss texture (Q1_LTc, Figure 2b) appear embedded in the Q1_LTb texture. The galena-sphalerite agglomerates that overgrow Q1_LTb become more densely distributed towards the Q1_LTc patterns, where gold is no longer observed. Quartz dissolution and recrystallisation, represented by CL-darker, microcrystalline bands (Q2_LT) that brecciate the CL-bright euhedral cores, constitute a later paragenetic stage.

The internal compositional heterogeneity observed in several gold particles (Figure 2d, 'Lead Trial' sample), can be attributed to evolving/cooling (>Ag) conditions of the same hydrothermal fluid. Furthermore, based on hand-specimen observations, the frequency of gold mineralisation appears to decrease from the margins (coarser quartz, vein breccia) towards the inner parts of the veins. Both pieces of evidence support a hypothesis

of i) gold precipitation during earlier/intermediate stages of the paragenesis; ii) two gold mineralising pulses, with a later one taking place at shallower (lower-T) crustal levels of the system. The paragenetic (textural and mineralogical) associations at this locality suggest a low-sulphidation epithermal mineralisation style.

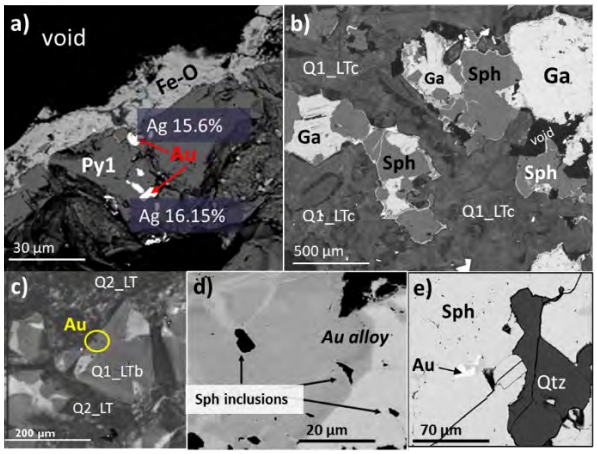


**Figure 2.** Mineral assemblages and textures from vein paragenetic analyses: a) Calliachar Burn; b) Lead Trial; c) Lead Trial; d) Lead Trial; e) River Almond.

## 4 Gold alloy analysis

Results are presented in Figure 3, where each data point on the plots corresponds to the silver content of a single gold particle from the respective population. The 'Calliachar_6V' (in-situ) gold is hosted in pyrite, in the form of both inclusions and fracture-fills; the lowest silver contents (~16 to ~18 wt.%) have been observed for the few gold inclusions, which broadly correspond to the smallest (~10µm) particles of the sample, as opposed to the more abundant (and richer in silver) fracture-fills. Similarly, most of the gold forming the 'Almond_6V' (in-situ) sample has been found as coarser particles filling fractures in sulphides (i.e., py, cpy and sph), which record the highest silver contents (~34 to ~42 wt.%) in the alloy. As per both the Calliachar_6V and Almond_6V samples, the generally coarser, silver-rich gold can be attributed to a later or separate mineralising event than the gold observed as inclusions in sulphides.

Callichar_6G and Almond_6H (Ag plots in Figure 3) are gold populations derived from gossan-related and crushed-ore material, respectively. As these were both mechanically recovered through panning procedures, the smallest, generally low-silver particles (≤50 µm) could hardly be retained. Evidence of this can be found in the 'Calliachar_6G' silver profile, which does not appear to be coincident with the 'Calliachar_6V' one, despite having been obtained from the same vein material. On the other hand, the dominant silver-rich trend displayed by the Almond_6V plot (Figure 3) is hardly reflected in the Almond_6H plot (Figure 3), hinting at notable variations in the silver content distribution across gold from the same hypogene environment. In addition, the sub-horizontal Ag distribution in the 'Calliachar_6G' (gossan-derived gold) plot suggests mainly stationary physicochemical conditions of the hydrothermal fluid responsible for the local gold precipitation, in contrast to the 'Calliachar_1' profile (representative of placer gold).

The 'Lead Trial' silver profile (Figure 3) displays a clear partitioning of the population into two main classes, which respectively show steady (median of ~27 wt.%) and increasing (from ~29 to ~57 wt.%) silver values in the gold particle alloys. These trends were confirmed by SEM-BSE imaging of the same set of particles, indicating the co-existence of two different alloy phases (in the form of Ag-rich patches or tracks) internally to many of the grains. Modified conditions of the fluid(s) responsible for gold precipitation are invoked to explain this evidence (e.g., Chapman et al. 2021b).

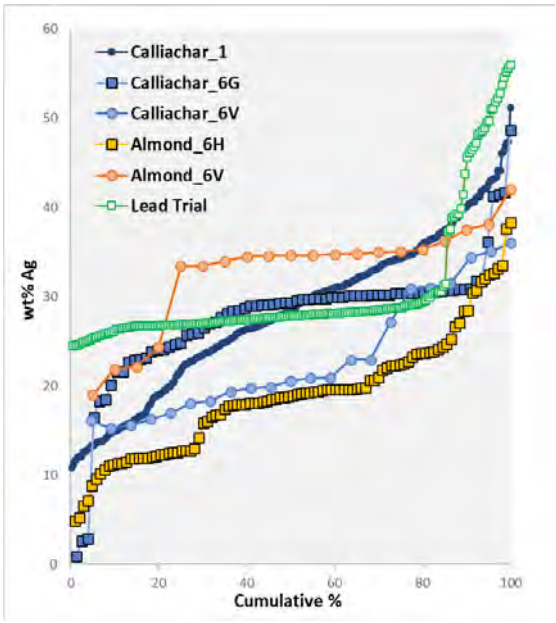


**Figure 3.** Cumulative percentile of the number of particles vs increasing wt.% Ag plots, for the studied gold samples.

## 5 Paragenetic constraints inferred frommineral inclusions in gold

Mineral inclusions were found in eluvial and placer gold samples from sites adjacent/proximal to the veins. The inclusion assemblages in the eluvial samples were evaluated in parallel with the silver contents of their hosting gold particles, to complement the gold-bearing vein parageneses.

At Calliachar Burn, the mineral inclusions in gossan-related gold can be used to underpin the sulphide mineralogy coeval with the auriferous stage of mineralisation, as it would be reflected in the associated hydrothermal vein(s). Figure 4 illustrates the distribution of the identified inclusion species across the two 'Calliachar_6G' alloy classes (by wt.% Ag). A distinct compositional signature (i.e., Ag content in the alloy and associated sulphide

assemblage in vein) has been deduced for Au3 in Calliachar_6V, which is perfectly consistent with the signature (Ag content and mineral inclusions) of Calliachar_6G. The placer gold (Calliachar_1) signature (Py-dominated) has also appeared to be broadly compatible with the 'Au3' signature.

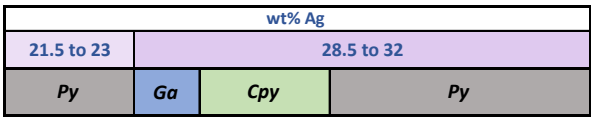


**Figure 4.** Relative abundance of inclusion species by gold particle (wt.% Ag) classes (Calliachar_6G).

The inclusion mineralogy of the placer sample from Upper River Almond (Almond_5), used for comparison with the respective vein-sited assemblage (Au-Py-Ga-Sph-Cpy), is indicated in Figure 5a. The in-situ mineral associations are more effectively reflected in the first alloy class (up to ~27 wt.% Ag), where Py, Ga and Sph were observed.

Galena, sphalerite and molybdenite inclusions are located in both the gold alloy classes (Figure 5b; wt.% Ag <29.5 and >29.5) distinguished from the analysis of the Lead Trial gold (from crushed-ore). Therefore, they are deemed coeval with the earlier (in-situ) gold paragenetic stage. The inclusion species recorded in the proximal Ardtalnaig (placer) sample revealed higher Mo and Cu and lower Zn and Pb relative abundancies (e.g., Webb et al., SGA 2023), suggesting a linkage with a different phase of mineralisation and subsequent variability in the silver content of the gold alloy.

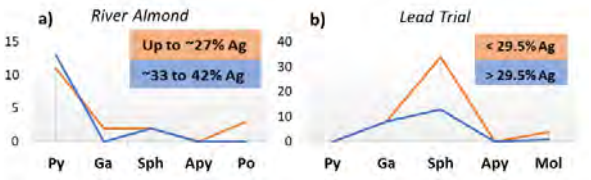


**Figure 5.** Mineral inclusions in a) Almond_5 (placer gold sample) and b) Lead Trial (crushed-ore gold sample)

## 5 Conclusions

Our results demonstrate that paragenetic histories of gold-bearing veins from a given locality can be firmed up by assessing the in-situ mineralogical assemblages against the microchemical signatures of adjacent eluvial gold. At least two separate gold mineralising episodes have been identified at Calliachar Burn, River Almond and Lead Trial/Ardtalnaig; the gold signatures combined with the vein parageneses indicate i) the overlap of multiple fluid sources at the first two localities and ii) an evolving hydrothermal fluid responsible for gold precipitation at the Lead Trial. Placer gold can be used to underpin the associated mineralisation styles on a broader scale; a genetic mineralogical linkage can be drawn between the Calliachar Burn and River Almond hydrothermal systems, whereas the Lead Trial system is suggestive of a dominant low-sulphidation epithermal style with variations in the mineralogical assemblage towards Ardtalnaig.

## Acknowledgements

L.S. PhD work has been supported by a NERC-DTP scholarship (no 2114866) and an IOM3 grant (2020). Thanks to Green Glen Minerals for having provided access to the field area and rock samples, and to Dr R. Walshaw for assistance with EPMA.

## References

Arif J, Baker T (2004) Gold paragenesis and chemistry at Batu Hijau, Indoneisa: implications for gold-rich porphyry copper deposits. Mineral Deposita 39:523–535

Chapman RJ, Leake R, Moles NR, Earls G, Cooper C, Harrington K, Berzins R (2000a) The application of microchemical analysis of alluvial gold grains to the understanding of complex local and regional gold mineralization: a case study in the Irish and Scottish Caledonides. Econ Geol 95:1753–1773

Chapman RJ, Mortensen JK, Crawford EC, Lebarge WP (2010b) Microchemical studies of placer and lode gold in the Klondike District, Yukon, Canada: 2. Constraints on the nature and location of regional lode sources. Econ Geol 105:1393–1410. https://doi.org/10.2113/econgeo.105.8.1393

Chapman RJ, Banks DA, Styles MT, Walshaw RD, Piazolo S., Morgan DJ, Grimshaw MR, Spence-Jones CP, Matthews TJ, Borovinskaya O. (2021b) Chemical and physical heterogeneity within native gold: implications for the design of gold particle studies. *Miner Deposita* 56, 1563–1588 https://doi.org/10.1007/s00126-020-01036-x

Chapman RJ, Torvela TM, Savastano L. (2023) Insights into Regional Metallogeny from Detailed Compositional Studies of Alluvial Gold: An Example from the Loch Tay Area, Central Scotland. Minerals 2023, 13, 140. https://doi.org/10.3390/min13020140

Gammons CH, Williams-Jones AE (1995) Hydrothermal geochemistry of electrum; thermodynamic constraints. Econ Geol 90:420–432. https://doi.org/10.2113/gsecongeo.90.2.420

Hancock EA, Thorne AM (2011) Mineralogy of lode and alluvial gold from the western Capricorn Orogen, Western Australia. Aus J Earth Sci 58:793–801

Ixer, R., Pattrick, R. and Stanley, C. (1997) Geology, mineralogy and genesis of gold mineralization at Calliachar-Urlar Burn, Scotland; Transactions of the Institution of Mining and Metallurgy Section B-Applied Earth Science, 106, p.99-108.

Leake RC, Chapman RJ, Bland DJ, Condliffe E, Styles MT (1997) Microchemical characterization of gold from Scotland. T I Min Metall B 102:65–82.

Parnell J, Earls G, Wilkinson JJ, Hutton DHW, Boyce AJ, Fallick AE, Ellam RM, Gleeson SA, Moles NR, Carey PF, Legg I (2000) Regional fluid flow and gold mineralization in the Dalradian of the Sperrin Mountains, Northern Ireland. Econ Geol 95:1389–1416

Spence-Jones CP, Jenkin GRT, Boyce AJ, Hill NJ, Sangster CJS (2018) Tellurium, magmatic fluids and orogenic gold: an early magmatic fluid pulse at Cononish gold deposit, Scotland. Ore Geol Rev 102: 894–905

Webb S, Torvela TM, Chapman RJ, Jamieson R, Selby D (2023) An integrated approach towards unravelling the gold mineralisation processes around Ardtalnaig, Scotland; 17th SGA Biennial Meeting.

Webb S, Torvela TM, Chapman RJ, Savastano L (2023) Textural mapping and building a paragenetic interpretation of hydrothermal veins, with a case study from an Au-Cu-Zn-Pb vein in Glen Almond, Loch Tay, Scotland.

# Alkalic epithermal Au deposits: Insights into magma evolution and ore fertility using silicate melt inclusions from Lihir Island, Papua New Guinea

**Michael Schirra[1], Daniel Müller[2], Zoltan Zajacz[1]**
[1]*University of Geneva, Switzerland*
[2]*Consulting Geologist, Las Condes, Santiago, Chile*

**Abstract.** The fundamental controls on the ore fertility of alkaline high-K melts for the formation of epithermal Au deposits are not well understood. Silicate melt inclusion (SMI) LA-ICP-MS analyses from mafic rocks genetically linked to the formation of the giant Ladolam Au deposit on Lihir Island provide unique insights into magma evolution and its consequences for ore formation. Based on compositional variations in SMIs, textural and geochemical information from mafic phenocrysts and thermobarometric considerations, melting within a variably metasomatized mantle wedge and subsequent deep and shallow crustal magma storage were essential steps in the evolution of Lihir Island and its Au mineralization. Melts that have been extracted from a long-lived, deep (4-7 kbar) magma reservoir can be anomalously Au-rich, whereas melts without evidence for deep storage do not show such an enrichment. Therefore, open-system magma chamber processes in the lower crust appear to be decisive for the ore-forming potential of alkaline melts. Mass balance predict that melt volumes on the order of few tens of km$^3$ were sufficient to provide the required amount of Au.

## 1 Introduction

Potassic alkaline magmas formed in extensional tectonic settings (e.g., post-collisional arcs or intra-plate rift systems) have the potential to give birth to world-class porphyry and epithermal Au(-Cu-Ag-Te) deposits (Jensen and Barton 2000). Prominent examples are Cripple Creek (Colorado, USA), Vatukoula (Viti Levu, Fiji), and Ladolam (Lihir Island, Papua New Guinea). Although the association of alkaline magmas with these deposits is well established, the fundamental igneous processes that lead to ore formation remain enigmatic.

Different models have been proposed to explain the geochemical character of high-K alkaline melts and their potential for mineralization (e.g., Richards 2009; Fiorentini et al. 2018). All models have in common that alkaline melts are produced by low-degree partial melting resulting in small volumes of magma. Consequently, the alkaline melts are supposed to be anomalously Au-rich to account for high-grade and high-tonnage mineralization (e.g., > 1500 tons of Au at Ladolam). Although experimental studies indicate that volatile-rich, alkaline, ultramafic to intermediate melts can be Au-rich (Botcharnikov et al., 2011; Zajacz et al., 2012), Au contents of natural melts associated with economic mineralization have never been determined.

Primitive melt compositions are difficult to obtain due to late-stage AFC processes, fluid exsolution, and hydrothermal alteration. A promising approach to investigate primary magmatic processes and their implications for subsequent ore formation are silicate melt inclusions (SMIs) hosted in mafic phenocrysts. They represent melt droplets entrapped during crystal growth and hence provide insights into magmatic processes at depth. LA-ICP-MS analysis allows for the adequate determination of melt compositions from SMIs, including the concentrations of ore-relevant elements such as S, Cl, Cu and Au (Chang and Audétat 2021 and references therein).

This study focuses on the alkaline magmatism that created Lihir Island, Papua Guinea, which hosts the world-class Ladolam epithermal Au deposit in the partially collapsed Luise volcano (Figure 1). Based on SMI and mineral compositions, we reconstruct the magmatic evolution of the system and identify the key parameters and processes that may influence ore fertility. In addition to the subaerial volcanoes on the island itself we also include samples from the Conical Seamount (Figure 1), a small submarine volcano associated with Au mineralization close to Lihir (Petersen et al. 2002).

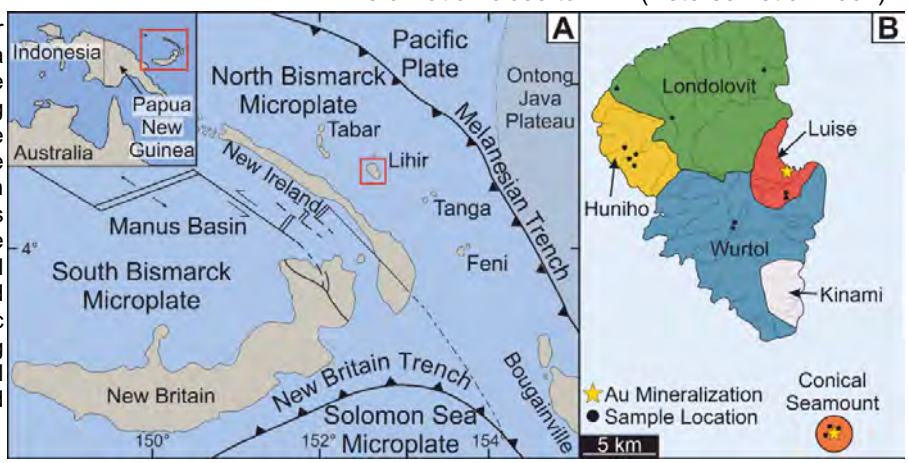


**Figure 22**: Location of Lihir Island in Papua New Guinea (inset). A) Overview of the Bismarck archipelago showing non-active and active subduction zones along the Melanesian and New Britain Trech, respectively, as well as back-arc spreading within the Manus Basin. B) Geological overview of Lihir Island showing the main volcanic edifices on the Island, including the submarine Conical Seamount volcano (modified from Müller et al. 2001).

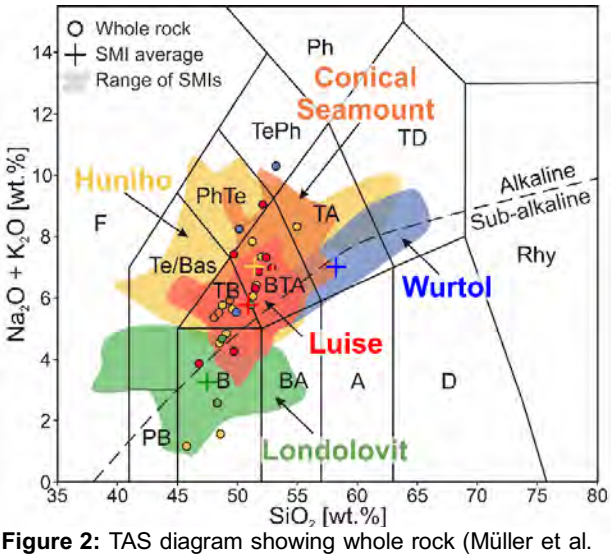


**Figure 2:** TAS diagram showing whole rock (Müller et al. 2001) and SMI compositions.

## 2 Geologic setting

Lihir Island is located within the fore-arc region of New Ireland and part of the Tabar-Lihir-Tanga-Feni (TLTF) island chain (Figure 1A). It consists of five Pliocene to Pleistocene volcanic centres, namely Huniho, Wurtol, Luise, Londolovit and Kinami (Figure 1B; Müller et al. 2001). The volcanoes erupted porphyritic, clinopyroxene (cpx)-rich alkali basalts, trachybasalts and basaltic trachyandesites (Figure 2; Müller et al. 2001). Despite the location within the fore-arc of the Kilinailau subduction zone, alkaline magmatism is not related to subduction but to post-collisional extension after cessation of SW-ward subduction due to the collision of the Ontong Java Plateau with the Melanesian trench (Figure 1A; McInnes and Cameron 1994; McInnes et al. 2001). Magmatism in the TLTF island chain is explained by adiabatic decompressional melting of metasomatised mantle along deep, extensional structures which facilitated rapid magma ascent (McInnes and Cameron 1994; Lindley 2016).

Conical Seamount is a small and pristine submarine volcano towards the SE of Lihir (Figure 1B), which erupted high-K cpx-rich trachybasalt similar to rocks from Lihir (Petersen et al. 2002).

Geochronologic data from Lihir is scarce. Biotite K-Ar dating indicate that volcanism may have lasted from 0.9 to 0.3 Ma whereas Conical Seamount is slightly younger with an Ar-Ar biotite age of 0.29 Ma (Brandl et al. 2020 and references therein).

Economic Au mineralization has been discovered within the Luise crater (Ladolam deposit, Müller et al. 2001) and the on top of Conical Seamount (Petersen et al. 2002). Mineralization style differs between the two locations: at Ladolam ore occurs as hydrothermal breccias overprinted by fine-grained auriferous pyrite whereas at Conical Seamount polymetallic quartz-feldspar-sericite veins host most of the Au (Petersen et al. 2002; Müller et al. 2003).

## 3 Petrography and Mineral Geochemistry

Petrographically, the samples from Lihir Island and Conical Seamount are cpx-dominated, porphyritic rocks with aphanitic to fine-grained, plagioclase-dominated matrix. Olivine and plagioclase phenocrysts can be present but are less abundant than cpx. In addition, magnetite and apatite occur as micro-phenocrysts in some samples. Rare and intensively altered amphibole phenocrysts are present in evolved samples from the Luise volcano.

Texturally, cpx grains can be colourless and largely unzoned (Londolovit), contain colourless cores with intensive green overgrowths (Huniho and Luise, Figure 3) or exhibit oscillatory (Conical Seamount) or sector zoning (Wurtol). Colourless cores often display wavy and diffusive contacts with coloured overgrowth zones, indicating partial dissolution during open-system magma chamber processes. Normal zonation (Mg-rich cores (Mg# 80-93), Fe-rich rims (Mg# 65-80); Figure 3b) indicate replenishment of more evolved by primitive magmas. Chondrite-normalized REE patterns (Sun and McDonough, 1989) show a general REE enrichment from the most primitive (Londolovit) to more evolved cpx compositions (Wurtol). Slightly negative Eu anomalies are only visible in cpx from Wurtol, indicating co-crystallization with plagioclase.

Olivine phenocrysts are usually altered along the rims, but pristine, clear and colourless cores have

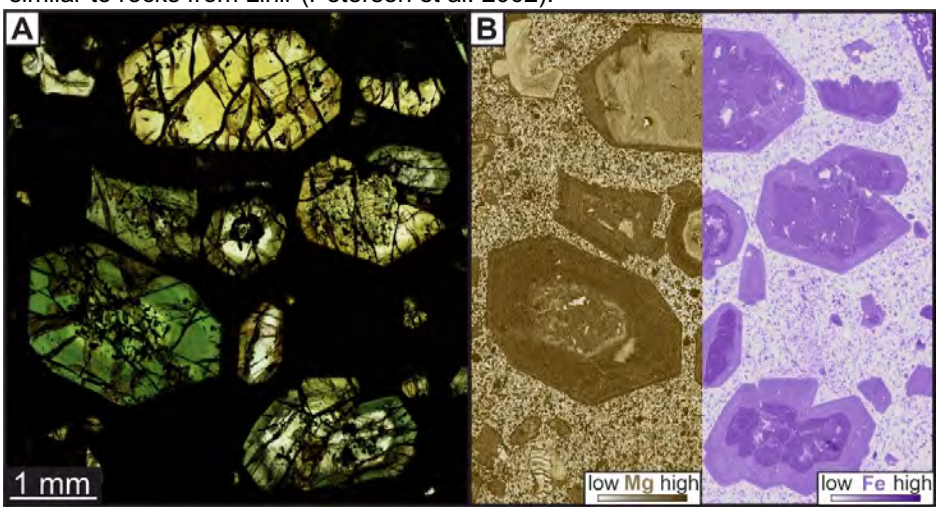


**Figure 3:** A) Transmitted light image of thick section for SMI petrography showing zoned cpx phenocrysts from the Luise volcano with inherited, colourless cores and concentrically zoned green rims. B) Qualitative QEMSCAN images of the same section shown in A), highlighting the remarkable difference between cores and rims regarding Mg and Fe content of cpx. Note the wavy and irregular boundary between core and rim, indicating dissolution.

been preserved. Most olivine grains have high Mg# (85-90) with relatively high CaO (0.35-0.55 wt.%) and low NiO (< 0.15 wt.%) contents. Olivine from Wurtol contains low CaO (0.15-0.20 wt.%) and high NiO (0.20-0.25 wt.%) at similar Mg# and hosts abundant Cr-rich spinel inclusions, which are absent in olivine from other volcanoes. No olivine has been found in the samples from Conical Seamount.

Plagioclase phenocrysts are anorthite-rich (Bytownite), normally zoned with more evolved rims (Labradorite) and typically exhibit sieve textures.

## 4 Melt Compositions

Fully enclosed SMIs in olivine and cpx were entirely ablated and the host-mineral contribution was subtracted from mixed signals to derive original melt compositions. Figure 4 shows a typical SMI and the corresponding time-integrated LA-ICP-MS signal.

Analysed SMI compositions overlap with whole rock data (Figure 2 and 5). Slightly wider and overlapping ranges of major oxide compositions (Figure 2) indicate that interaction of different melts produced whole rocks. Primitive mantle-normalized trace element arrays (Sun and McDonough, 1989) display enrichment in fluid-mobile and depletion in fluid-immobile elements, typical for subduction-related melts (Figure 5). High Ba/Th and Pb/Ce ratios indicate the involvement of subduction-derived fluids, while MORB-like Cs/Rb ratios suggest negligible contribution from sediment melts. Trace element systematics are inherited from previous subduction that caused metasomatism of the mantle wedge (McInnes and Cameron 1994; McInnes et al. 2001). Differences between the melts might stem from melting of variously metasomatized regions in the mantle (Londolovit and Conical Seamount SMIs display the lowest and highest

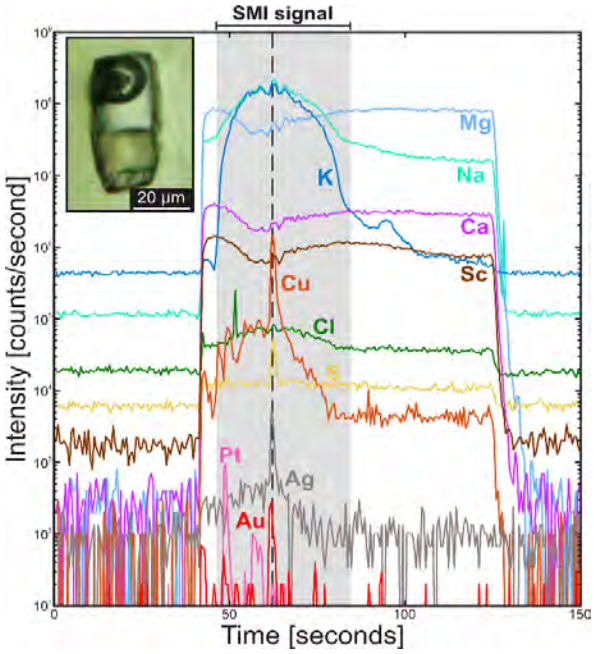


**Figure 4:** Time-integrated LA-ICP-MS signal of SMI (upper left corner) with a well visible Au peak, overlapping with increased Cu, S and Ag intensities (marked by dashed

Ba/Th ratios, respectively). Strong depletions in Nb and Ta are indicative for flux melting of the mantle source and constant Nb/Zr suggests similar degrees of melting for the different volcanoes. Wurtol is an exception with higher Nb, Ta contents and Nb/Zr ratios pointing towards lower degrees of partial melting, which might also explain the difference of SMI and whole rock compositions (Figure 2 and 5).

Concentrations of S and Cl in the SMIs vary between 500 to 3000 and 1000 to 4000 µg/g, respectively, and show no correlation with proxies for fractional crystallization. With mean Au contents between 3 (Londolovit) and 10 ng/g (Conical Seamount), SMIs are slightly more enriched than melts reported from porphyry Cu deposits (≤ 4 ng/g, Grondahl and Zajacz, 2017) and back-arc basins (≤ 7 ng/g, Jenner et al. 2010). However, few SMIs from Huniho, Wurtol and Conical Seamount contain significantly more Au, up to 100 ng/g. In time-integrated LA-ICP-MS signals elevated Au coincides with S, Cu, and Ag peaks (Figure 4).

## 5 Thermobarometry and Oxygen Fugacity

Temperature and pressure were estimated from SMI-cpx pairs by applying the thermometer of Scarlato et al. (2021) and the barometer of Masotta et al. (2013). Temperatures range from 1300°C for the most primitive melt (Londolovit) down to 1050°C for the more evolved compositions (Wurtol). Pressure estimates scatter between 1 and 10 kbar, with two distinctive clusters at 1-2 and 4-7 kbar. Oxygen fugacity has been calculated from V partitioning between SMIs and olivine using the method of Shishkina et al. (2018), yielding highly oxidized values of +3 (±1) relative to the FMQ buffer.

## 6 Magma Evolution and Implications for Ore Formation

High-K alkaline magmatism on Lihir Island and Conical Seamount produced epithermal Au mineralization. Trace element signatures of SMIs indicate that magma generation occurred within a heterogeneously metasomatized mantle wedge by variable degrees of melting. Major element data show that whole rock compositions represent an amalgamation of compositionally variable melt batches which are preserved as SMIs (Figure 2). The metasomatized and refertilized lithospheric mantle is probably the source of Au. Anomalously Au-rich SMIs (≥ 10 ng/g) originate from the deeper crust (4-7 kbar) and are absent in samples from Londolovit, which ascended to and fractionated in the shallower crust (1-2 kbar). This suggests a lower crustal control on the ore fertility of the alkaline melts. Furthermore, the clustering of melts from the Huniho, Luise and Conical Seamount volcanoes within the same high-pressure interval indicates the presence of a long-lived (≥ 0.5 Myrs), frequently replenished magma reservoir in the lower crust.

Conical Seamount is presumably the youngest volcano (0.29 Ma, Brandl et al. 2020) and is the

closest in age to the flank collapse of the Luise

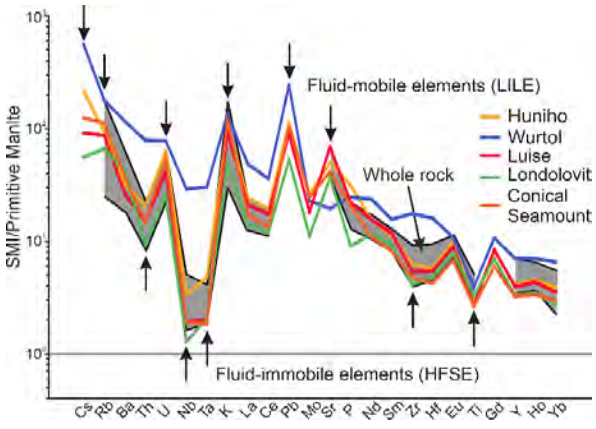


**Figure 5:** Primitive mantle-normalized (Sun and McDonough, 1989) trace element signature of SMIs and whole rock data from Müller et al. (2001).

volcano (0.19 Ma, Blackwell, 2010), which triggered Au deposition at Ladolam (Müller et al. 2001). Accordingly, the latest melts extracted from the lower crustal magma reservoir appear to be linked to the known Au deposits. The concentric zonation pattern and the scarcity of more mafic (inherited) cores in cop from Conical Seamount suggest longer storage times in the lower crust, which resulted in enhanced ore fertility. Alternatively, high Au contents of SMIs from Huniho and Wurtol could also indicate the presence of not yet discovered Au deposits.

Assuming 10 ng/g Au in the initial melt, simple mass balance predicts that approximately 50 $km^3$ of melt is required to account for the 1500 t of Au at Ladolam. If the few exceptionally Au-rich SMIs are representative for the ore-related melt, only 5 $km^3$ would be sufficient. Such small amounts of melt could be extracted from the deeper magma reservoir during periods of extension that facilitate magma ascent from depth to the surface without accumulation at shallower crustal levels. Melts that raise directly to shallower depths (≤ 2 kbar) without significant fractionation are not enriched in Au. Consequently, deep open-system magma chamber processes enhance ore fertility of small melt batches for the generation of alkalic-type epithermal Au deposits. Which processes are decisive for ore fertility is still in the focus of ongoing research.

## References


Blackwell, J.L. (2010): Characteristics and origins of breccias in a volcanic-hosted alkalic epithermal gold deposit, Ladolam, Lihir Island, Papua New Guinea; PhD thesis, University of Tasmania.

Botcharnikov, R.E., Linnen, R.L., Wilke, M., Holtz, F., Jugo, P.J., and Berndt, J. (2011): High gold concentrations in sulphide-bearing magma under oxidizing conditions; Nature Geoscience, v. 4, p. 112-115.

Brandl, P.A., Hannington, M.D., Geersen, J., Petersen, S., and Gennerich, H.H. (2020): The submarine tectono-magmatic framework of Cu-Au endowment in the Tabar-to-Feni island chain, PNG; Ore Geology Reviews, v. 121, 103491.

Chang, J., and Audétat, A. (2021): LA-ICP-MS analysis of crystallized melt inclusions in olivine, plagioclase, apatite and pyroxene: quantification strategies and effects on post-entrapment modifications; Journal of Petrology, v. 62, egaa085.

Fiorentini, M.L., LaFlamme, C., Denyszyn, S., Mole, D., Maas, R., Locmelis, M., Caruso, S., and Bui, T.H. (2018): Post-collisional alkaline magmatism as gateway for metal and sulfur enrichment of the continental lower crust; Geochimica et Cosmochimica Acta, v. 223, p. 175-197.

Grondahl, C., and Zajacz, Z. (2017): Magmatic controls on the genesis of porphyry Cu-Mo-Au deposits: The Bingham Canyon example; Earth and Planetary Science Letters, v. 480, p. 53-65.

Jenner, F.E., O´Neill, H.St.C., Arculus, R.J., and Mavrogenes, J.A. (2010): The magnetite crisis in the evolution of arc-related magmas and the initial concentrations of Au, Ag, and Cu; Journal of Petrology, v. 51, p. 2445-2464.

Jensen, E.P., and Barton, M.D. (2000): Gold deposits related to alkaline magmatism; Reviews in Economic Geology, v. 13, p. 279-314.

Lindley, I.D. (2016): Plate flexure and volcanism: Late Cenozoic tectonics of the Tabar-Lihir-Tanga-Feni alkalic province, New Ireland Basin, Papua New Guinea; Tectonophysics, v. 677, p. 312-323.

Masotta, M., Mollo, S., Freda, C., Gaeta, M., and Moore, G. (2013): Clinopyroxene-liquid thermometers and barometers specific to alkaline differentiated magmas; Contributions to Mineralogy and Petrology, v. 166, p. 1545-1561.

McInnes, B.I.A., and Cameron, E.M. (1994): Carbonated, alkaline hybridizing melts from a sub-arc environment: Mantle wedge samples from the Tabar-Lihir-Tanga-Feni arc, Papua New Guinea; Earth and Planetary Science Letters, v. 122, p. 125-141.

McInnes, B.I.A., Gregoire, M., Binns, R.A., Herzig, P.M., and Hannington, M.D. (2001): Hydrous metasomatism of oceanic sub-arc mantle, Lihir, Papua New Guinea: petrology and geochemistry of fluid-metasomatized mantle wedge xenoliths; Earth and Planetary Science Letters, v. 188, p. 169-183.

Müller, D., Franz, L., Herzig, P.M., and Hunt, S. (2001): Potassic igneous rocks from the vicinity of epithermal gold mineralization, Lihir Island, Papua New Guinea; Lithos, v. 57, p. 163-186.

Müller, D., Franz, L., Petersen, S., Herzig, P.M., and Hannington, M.D. (2003): Comparison between magmatic activity and gold mineralization at Conical Seamount and Lihir Island, Papua New Guinea; Mineralogy and Petrology, v. 79; p. 259-283.

Petersen, S., Herzig, P.M., Hannington, M.D., Jonasson, I.R., and Arribas, A. (2002): Submarine gold mineralization near Lihir Island, New Ireland fore-arc, Papua New Guinea; Economic Geology, v. 97, p. 1795-1813.

Scarlato P., Mollo, S., Petrone, C.M., Ubide, T., and Di Stefano, F. (2021): Interpreting magma dynamics through a statistically refined thermometer: Implications for clinopyroxene Fe-Mg diffusion modelling and sector zoning at Stromboli; In - Crustal Magmatic System Evolution: Anatomy, Architecture, and Physico-Chemical Processes, Geophysical Monograph 264, First Edition.

Shishkina, T.A., Portnyagin, M.V., Botcharnikov, R.E., Almeev, R.R., Simonyan, A.V., Garbe-Schönberg, D., Schuth, S., Oeser, M., and Holtz, F. (2018): Experimental calibration and implications of olivine-melt vanadium oxybarometery for hydrous arc magmas; American Mineralogist, v. 103, p. 369-383.

Sun, S.S., and McDonough, W.F. (1989): Chemical and isotopic systematics of oceanic basalts: implications for mantle composition and processes; Geological Society, Lodon, Special Publications, v. 42, p. 313-345.

Zajacz, Z., Candela, P.A., Piccoli, P.M., Wälle, M., and Sanchez-Valle, C. (2012): Gold and copper in volatile saturated mafic to intermediate magmas: Solubilities, partitioning, and implications for ore deposit formation; Geochimica et Cosmochimica Acta, v. 91, p. 140-159.

# Granitoid-hosted, orogenic gold mineralization: Genetic constraints on the world-class Archean Gruyere gold deposit, Yilgarn Craton, Western Australia

**Ravi Schreefel[1], Steffen G. Hagemann[1], Clayton Davy's[2], Jamie A. Robinson[3], Malcolm P. Roberts[4], Christopher M. Fisher[1], Nicolas Thébaud[1], Robert A. Creaser[5]**

[1]*Centre for Exploration Targeting, School of Earth Sciences, The University of Western Australia, Perth, Australia*
[2]*Hamelin Gold Ltd, Perth, Australia*
[3] *Gold Road Resources Ltd, Perth, Australia*
[4] *Centre for Microscopy, Characterisation and Analysis, The University of Western Australia, Perth, Australia*
[5] *Department of Earth and Atmospheric Sciences, University of Alberta, Edmonton, Canada*

**Abstract.** In 2013, the 6.8 Moz Gruyere gold deposit was discovered at the eastern margin of the Yilgarn Craton in Western Australia. Gold mineralization at Gruyere is hosted by the 2830 ± 4 Ma Gruyere monzogranite. Mineralizationis related to contemporaneous chlorite-rich veinlets and sheeted quartz veins crosscutting the foliation, with pervasive wall rock alteration characterized by quartz- sericite-albite-calcite-chlorite ± pyrite-pyrrhotite-arsenopyrite
-gold-telluride assemblages. Chlorite and arsenopyrite geothermometry indicate temperatures between 304-365°Cand 360-425°C, respectively. Arsenopyrite Re-Os geochronology yield a single-analysis model age of 2675 ± 66 Ma. On the basis of these results, gold mineralization at Gruyere is interpreted to reflect a late-Archean, granitoid- hosted, orogenic gold mineral system, with the granitic intrusion behaving as a brittle, rigid body within more ductile, soft supracrustal rocks during mineralization. This implies that the 2675-2630 Ma orogenic gold mineralization event in the Yilgarn Craton was widespread and extends into the easternmost exposed part of the craton.

## 1 Granitoid-hosted gold deposits

The close spatial relationship between granitic rocks and gold ores have been long recognized (Niggli 1929). Although this invokes a link between intrusions and gold mineralization, their genetic association is highly debated (Duuring et al. 2007; Goldfarb and Pitcairn 2023). Difficulties arise especially in classifying granitoid-hosted, gold-only deposits. Granitic intrusions are suggested to be the source of fluids and metals, implying a similar timing of the intrusion and mineralization (e.g., Robert 2001). The host granitic intrusions may, however, also act as favourable rigid structural sites for fluid flow and/or as geochemical traps for gold mineralization (e.g., Cassidy et al. 1998). Multiple overprinting styles of gold mineralization within a granitic intrusion have also been demonstrated (e.g., Bucci et al. 2002). This has led to debates of the genetic role of the granitic intrusions in the gold mineralization process, with granitoid-hosted gold deposits in different Archean regions classified as 'orogenic', 'intrusion-related', 'skarn', or 'porphyry' (Sillitoe and Thompson 1998; Duuring et al. 2007).

In the well-endowed Archean Yilgarn Craton in Western Australia (Fig. 1), the majority of gold deposits are classified as 'orogenic' (Groves 1993), with most of these deposits hosted by greenschist- facies, meta-volcanic rocks. Although granitic rocks are the dominant lithology in the Yilgarn Craton, only minor orogenic gold deposits are hosted by granitoids. These granitoid-hosted orogenic deposits generally have smaller mineral resources compared to the meta-volcanic hosted deposits, and historically represent a minor fraction of the total gold resource in the Yilgarn Craton (Cassidy et al. 1998). A few Archean intrusion-related and porphyry gold systems are documented in the Yilgarn Craton and, with the possible exception of the Boddington deposit, are generally small (<0.5 Moz Au). The 6.8 Moz Gruyere gold deposit was discovered in 2013 with gold mineralization solely confined within an Archean granitic intrusion, making it one of the largest Archean granitoid-hosted, gold-only systems globally.

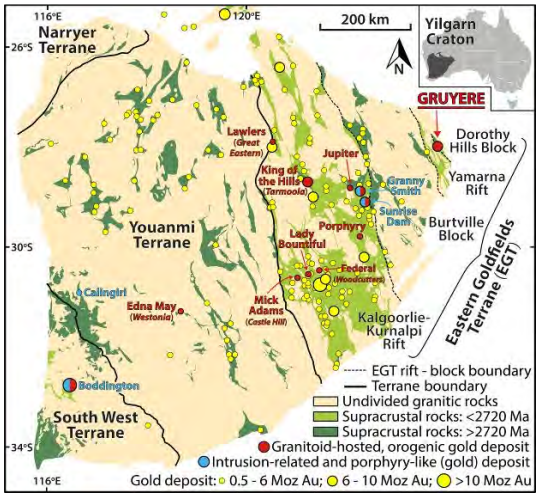


**Figure 1**. Simplified geological map of the Yilgarn Craton showing gold resource estimates by project (data from DMRIS 2022). In addition, (partially) granitoid-hosted lode gold deposits as well as intrusion-related and porphyry-like systems are shown. The current subdivision of the Yilgarn Craton and the age of supracrustal rocks is also illustrated (modified after Cassidy et al. 2006; Masurel et al. 2022; Schreefel et al. 2023).

This study focuses on the world-class, granitoid-hosted Gruyere gold deposit located at the north-eastern margin of the Yilgarn Craton in West Australia (Fig. 1). As gold mineralization is solely restricted to the Gruyere monzogranite, it provides anexcellent opportunity to examine the genetic link, if any, between a granitoid host and gold mineralization. In this contribution, we present preliminary results from an ongoing study of the lithostratigraphical, structural, and hydrothermal architecture related to gold mineralization at Gruyere.

## 2 Geological setting

### 2.1 Lithostratigraphy

The Gruyere intrusion (GYI) is a small monzogranitic body (2,500x200 m; Fig. 2) of predominantly medium-to coarse-grained albitised feldspar and quartz with medium-grained biotite. The GYI is geochemically consistent with the 'high-HFSE' granitic group in the Yilgarn Craton (Champion and Sheraton 1997; Schreefel et al. 2023), which is a rare component (<5%) of all the granitic rocks in the Yilgarn Craton. Furthermore, the GYI yields a magmatic crystallization age of 2830 ± 4 Ma (Schreefel et al. 2023), which is relatively old compared to other lithologies in the Eastern Goldfields Terrane.

Low-Th basalts (Kansas basalt) are present in the south-eastern hanging wall of the GYI, and fine-grained, folded, intermediate to mafic volcanoclastic sedimentary rocks (Wizard Formation - 2840 ± 13 Ma; Tunjic 2019) in the north-eastern hanging wall and western footwall. Several variably deformed felsic to mafic dykes (<1m wide) crosscut the lithostratigraphic sequence, with a massive basaltic dyke (up to 5m wide) present along strike within the GYI proximal to the hanging wall.

### 2.2 Structural setting

The GYI is located at a major change in the geometryof the Dorothy Hills Shear Zone, where the strikechanges from the regional NW-SE trend to ~N-S,based on aeromagnetic imagery. The cryptic NW-striking, arcuate Alpenhorn and Northern faults (Fig. 2) have been interpreted from aeromagnetics, but appear to not offset the GYI (Osborne et al. 2017).

The GYI displays sharp lithological contacts with the supracrustal lithologies and is steeply (65 - 80°) NE to ENE-dipping, which is similar to the strike of the shear zone. Non-coaxial deformation is variably developed in the GYI and country rocks, with the shear intensity higher at the lithological contacts. Crosscutting dykes trend generally subparallel to the orientation of the GYI. Furthermore, the dominant fabric throughout the entire lithostratigraphy is a pervasive steeply ENE-dipping foliation, with the orientation of biotite S-C fabrics indicating a predominantly sinistral reverse movement, although the orientation of a minor amount of kinematic indicators also indicate dextral movement. Auriferous veins generally dip steeply to the ESE to SE and crosscut the foliation.

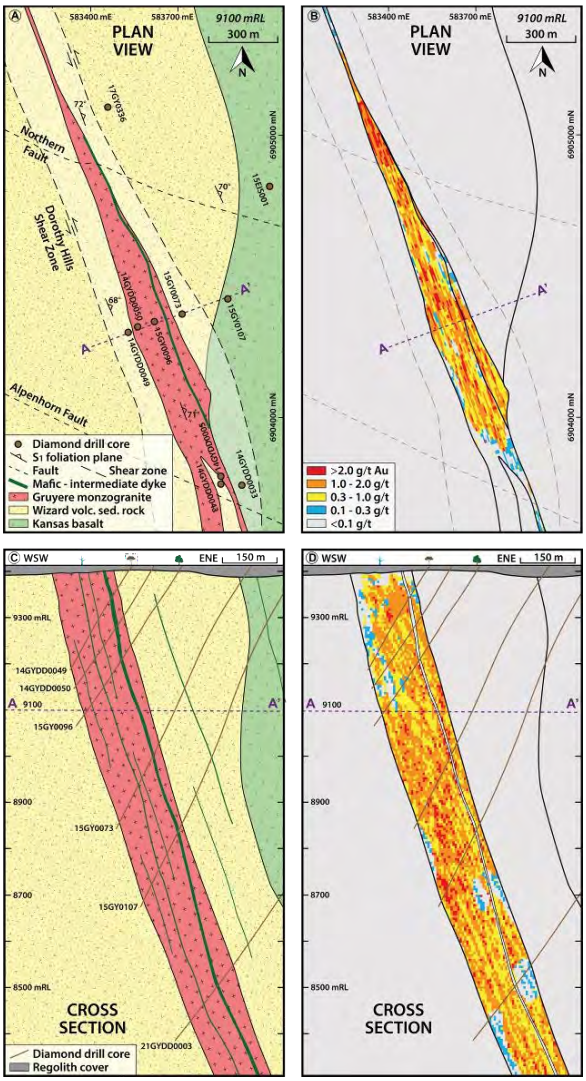


**Figure 2**. Simplified geological map and cross section of the Gruyere gold deposit; modified after Bath and Walshe (2015) and Gold Road Resources (Written Comm.). A) Map showing the main (metamorphosed) lithostratigraphic units and structures including logged diamond drill holes mostly displayed at 9200 mRL. B) Plan view block model of the gold assay data at 9100 mRL after Gold Road Resources (Written Comm.). C) Cross section including drill traces. D) Block model in cross section. mRL: metres relative level.

## 3 Hydrothermal alteration and mineralization

### 3.1 Vein types

Four main groups of veins can be distinguished within the GYI at Gruyere: (1) early, unmineralized $V_1$ quartz ± feldspar veins, (2) $V_2$ quartz-chlorite-magnetite veins, (3) gold mineralized $V_{3A}$ to $V_{3D}$ quartz-chlorite-

carbonate veins (Fig. 3), and (4) late, unmineralized $V_4$ carbonate veins. Gold mineralization at Gruyere is associated with the $V_3$ veins within the GYI, therefore, this study is mostly focused on these auriferous veinsand related hydrothermal alteration assemblages.

Thin chlorite-pyrite ± pyrrhotite stringer veins (2 - 4 mm; $V_{3A}$) are abundant and occur in a discontinuous, subparallel sheeted to stockwork-like pattern. Massive, sheeted quartz-rich veins (1 - 20 cm; $V_{3B}$) are common throughout the GYI, and often have a chlorite-rich vein margin (1 mm - 1 cm). These planar,tabular quartz veins comprise variable amounts offine- to coarse-grained calcite, albite, chlorite, and sub- to euhedral pyrite-pyrrhotite ± arsenopyrite. Locally, quartz veins have a more laminated texture ($V_{3B-1}$) or massive biotite-chlorite margins ($V_{3B-2}$) with minor coarse-grained magnetite altered to pyrite ±chlorite. Massive quartz veins (2 - 30 cm; $V_{3C}$) with narrow slivers of the granitic wall rock are characteristic for the higher gold grade zones (>2.0 g/t). These irregular to sheeted quartz veins havegenerally the same mineral assemblages as the $V_{3B}$ quartz veins, although they locally contain very coarse-grained arsenopyrite, pyrite, and/or pyrrhotite. Coarse-grained arsenopyrite-rich trails ($V_{3D}$) with minor quartz, pyrite, and chlorite are observed locally.

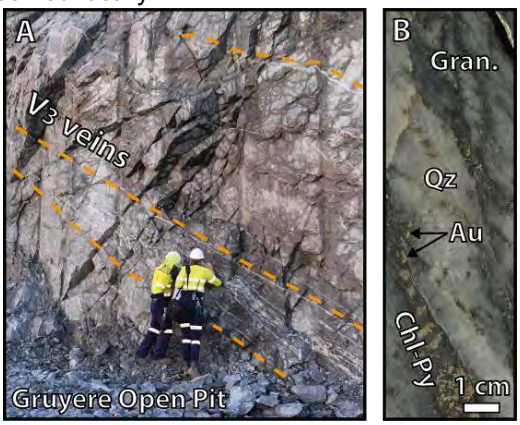


**Figure 3**. A) Gruyere open pit exposure (looking ENE)illustrating the high frequency of SE-ESE dipping V3B and V3C quartz vein sets within GYI (photo by Kyle Prentice). B) Granitic rock crosscut by a V3C vein consisting of quartz (Qz) with a chlorite-pyrite-gold (Chl-Py-Au) vein margin.

### 3.2 Proximal wall rock alteration related to $V_3$

The auriferous $V_3$ quartz veins in the GYI are typically characterized by semi-concentric zones of hydrothermal alteration assemblages. As multiple $V_3$ veins are located throughout the GYI, it is interpreted that extensive metasomatic fluid rock interactions (i.e., high fluid-rock ratios) resulted in pervasive hydrothermal alteration of the entire GYI, with a progressive decrease in alteration intensity away from the $V_3$ veins. The proximal alteration zones (>2.0 g/t Au; 0.5 cm to 10 m wide) are characterized by a 'bleached', beige appearance of the granitic wall rock with pervasive destruction of igneous and metamorphic minerals and textures. The wall rock alteration is characterized by quartz-sericite-albite-calcite ± chlorite ± Fe-Ti oxides ± arsenopyrite-pyrite-pyrrhotite-gold assemblages.

Quantitative micro-analyses (EPMA) were conducted to characterize and classify hydrothermal alteration minerals associated with the $V_3$ veins. Analyses on gold and telluride show that most grains represent native gold (i.e., >80 wt. % Au) with minor petzite, altaite, and rucklidgeite. Analyzed carbonate grains indicate that calcite is the main carbonate species. The arsenopyrite geothermometer from Kretschmar and Scott (1976) was applied to the arsenopyrite-bearing assemblages, which are all in textural equilibrium with pyrite. The mineralization temperature of arsenopyrite from $V_{3C}$ and $V_{3D}$ veins (n = 295 from 11 samples) ranges from 360°C to 425°C with an average of 395 ± 41°C (31.5 ± 0.7 at. % As; 1SD; Fig. 4A). The sulfur fugacity ranges from -6.4 to -8.4 log $f_{S2}$, with an average log $f_{S2}$ of -7.3 ± 1.2 (1SD). Chlorite from $V_3$ veins and associated proximal alteration zones (n = 161 from 11 samples) are Fe-rich and can be classified as chamosite (Bailey 1980). The chlorite geothermometer from Kranidiotis and MacLean (1987) yields temperatures ranging from 304 ± 34°C to 365 ± 28°C (Fig. 4B; 1SD). The average temperature of all chlorites associated with auriferous $V_3$ veins is 328 ± 51°C (n = 226; 1SD).

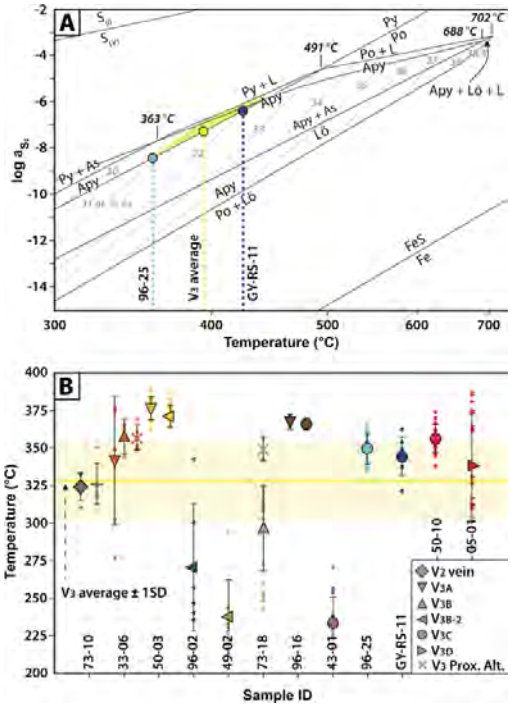


**Figure 4**. A) Log fS2 – T projection of the stability of arsenopyrite contoured in at. % of As, including the lowest (96-25) and highest (GY-RS-11) sample (Kretschmar and Scott 1976). B) Chlorite temperature estimates for V2 andV3 vein samples (Kranidiotis and MacLean 1987).

### 3.4 Absolute timing of gold mineralization

Four samples with visible arsenopyrite associated with gold (i.e., in equilibrium or in micro-fractures) were selected for rhenium-osmium (Re-Os) geochronology. Initial testing showed, however, that all samples yield very low Re contents (ca. 0.1 - 0.3 ppb Re), therefore, a complete Re-Os analysis by N- TIMS was only performed on sample GY-RS-11. Thisis a massive arsenopyrite-bearing sample with a higher Re content (0.3 ppb Re). The Re-Os analysis yielded a single-analysis mantle model age of 2675 ±
66 Ma. Despite the large error, interpreted to be mainly caused by the low Re and Os contents, this date provides currently the best geochronological constraint for the age of mineralization at Gruyere.

## 4 Discussion and implications

The auriferous $V_3$ veins exhibit similar orientations, have mutual cross-cutting relationships and similar hydrothermal alteration halos. This implies that these veins formed progressively during the same deformation and mineralization event (Bath and Walshe 2015; Osborne et al. 2017). Based on field observations, $V_3$ veins are interpreted to overprint regional metamorphic foliation assemblages (ca. 2663-2649 Ma; Fielding et al. Written Comm.). In addition, constraints from U-Pb and Re-Os geochronology show that gold mineralization must have occurred ca. 150 Myr after the emplacement of the GYI. Furthermore, alteration assemblages related to $V_3$ veins at Gruyere are common for granitoid- hosted, orogenic gold deposits formed under P-T conditions of 250-400°C and <1-2 kbars at a paleo- depth of <5-8 km (Cassidy et al. 1998).
The GYI is interpreted to have behaved as a brittle, dilatant granitic body within more ductile supracrustal rocks during high fluid pressure and shear zone reactivation with associated hydrothermal alteration and gold mineralization. Fluids were focused within a broad shear zone well after the crystallisation of the GYI; i.e., the intrusion had no genetic relationship with the gold mineralization. For these reasons, gold mineralization at Gruyere is, interpreted to reflect a late-Archean, granitoid-hosted, orogenic gold mineral system. Despite the broad Re-Os age constraint, Gruyere is suggested to be part of the 2675-2630 Ma orogenic gold mineralization event in the Yilgarn Craton (e.g., Groves 1993). This implies that the 2675-2630 Ma event, known to be widespread in the Yilgarn Craton (e.g., Vielreicher et al. 2015), extends into the easternmost exposed greenstone belt, and nearly 385 km from the giant Golden Mile deposit.
Further work (e.g., sulfur isotopes and trace elements on pyrite) is conducted to more precisely constrain the nature of gold mineralization in order to form a robust genetic model that can be used for exploration targeting, particularly in the search of concealed gold ore bodies in the Yilgarn Craton.

## Acknowledgements

This work is part of the Yilgarn 2020 research project,which is funded by multiple industry sponsors,MRIWA (M530), GSWA and UWA. SIRF funding fromUWA and assistance from CMCA is acknowledged. We are very thankful for the logistical support and geological input from Gold Road Resources Ltd. G. Beaudoin is thanked for the review of this abstract.

## References

Bailey SW (1980) Summary of recommendations of AIPEA nomenclature committee on clay minerals. Am Mineral 65:1–7
Bath AB, Walshe JL (2015) Mineral systems study of the world-class Gruyere gold deposit. CSIRO, pp 1–27
Bucci LA, Hagemann SG, Groves DI, Standing JG (2002) The Archean Chalice gold deposit: A record of complex, multistage, high-temperature hydrothermal activity and gold mineralisation associated with granitic rocks in the Yilgarn Craton, Western Australia. Ore Geol Rev 19:23–67
Cassidy KF, Champion DC, Krapež B, Barley ME, Brown SJA, Blewett RS, Groenewald PB, Tyler IM (2006) A revised geological framework for the Yilgarn Craton, Western Australia. Geol Surv West Aust Rec 2006/8 1–8
Cassidy KF, Groves DI, McNaughton NJ (1998) Late-Archean granitoid-hosted lode-gold deposits, Yilgarn Craton, Western Australia: deposit characteristics, crustal architecture and implications for ore genesis. Ore Geol Rev 13:65–102
Champion DC, Sheraton JW (1997) Geochemistry and Nd isotope systematics of Archaean granites of the Eastern Goldfields, Yilgarn Craton, Australia: Implications for crustal growth processes. Precambrian Res 83:109–132
DMRIS (2022) MINEDEX resource estimates by project - gold. Dep Mines, Ind Regul Safety, Gov West Aust
Duuring P, Cassidy KF, Hagemann SG (2007) Granitoid-associated orogenic, intrusion-related, and porphyry style metal deposits in the Archean Yilgarn craton, WA. Ore Geol Rev 32:157–186
Goldfarb RJ, Pitcairn I (2023) Orogenic gold: Is a genetic association with magmatism realistic? Miner Depos 58:5–35
Groves DI (1993) The crustal continuum model for late-Archaean lode-gold deposits of the Yilgarn Block, Western Australia. Miner Depos 28:366–374
Kranidiotis P, MacLean WH (1987) Systematics of chlorite alteration at the Phelps Dodge massive sulfide deposit, Matagami, Quebec. Econ Geol 82:1898–1911
Kretschmar UH, Scott SD (1976) Phase relations involving Apy in the system Fe-As-S and their application. Can Mineral 14:364–386
Masurel Q, Thébaud N, Sapkota J, De Paoli MC, Drummond M, Smithies RH (2022) Stratigraphy of the Agnew-Wiluna Greenstone Belt: Review, synopsis and implications for the late Mesoarchean to Neoarchean geological evolution of the Yilgarn Craton. Aust J Earth Sci 1–28
Niggli P (1929) Ore Deposits of Magmatic Origin: Their Genesis and Natural Classification. Thomas Murby & Co, London
Osborne JP, Levett J, Donaldson J, Berg R, Davy's C, Prentice K, Tullberg D, Lubieniecki LZ, Tunjic JA, Bath AB, Libby JW (2017) Gruyere gold deposit, Yamarna. In: Philips GN (ed) Australian Ore Deposits, 6th edn. The Australasian Institute of Mining and Metallurgy: Melbourne, pp 267–272
Robert F (2001) Syenite-associated disseminated gold deposits in the Abitibi greenstone belt, Canada. Miner Depos 36:503–516
Schreefel R, Fisher CM, Kemp AIS, Hagemann SG, Masurel Q, Thebaud N, Davy's C, Martin LAJ, Lowrey JR, Lu Y, Cassidy KF (2023) Crustal growth in the Archaean: Insights from zircon petrochronology of the far east Yilgarn Craton, WesternAustralia. Precambrian Res - In Review Sillitoe RH,
Thompson JFH (1998) Intrusion-related vein gold deposits: Types, tectono-magmatic settings and difficulties of distinction from orogenic gold deposits. Resour Geol 48:237–250
Tunjic JA (2019) Laying the foundations of geology for further discoveries. In: AEGC Conference Presentation. Perth, Australia Vielreicher N, Groves DI, McNaughton
NJ, Fletcher IR (2015) Thetiming of gold mineralization across the eastern Yilgarn Craton using U–Pb geochronology of hydrothermal phosphate minerals.Miner Depos 50:391–428

# The Geological Setting and Hydrothermal Alteration at the Tucano Gold Deposit, Guiana Shield, Brazil

**Gabriel A. R. Soares[1], Rosaline C. Figueiredo e Silva[1], Steffen G. Hagemann[2], Lydia M. Lobato[1,3], Rogério A. Lucena[4]**
*[1]Geology Graduate Program, Institute of Geosciences, Federal University of Minas Gerais, Belo Horizonte, MG, Brazil*
*[2]Centre for Exploration Targeting, University of Western Australia, Crawley, WA, Australia*
*[3]Hydro Fluids & Minerals, Rio de Janeiro, RJ, Brazil*
*[4]Great Panther Mining Limited, Pedra Branca do Amapari, AP, Brazil*

**Abstract.** The Tucano gold deposit, located in northern Brazil, is an open-pit gold mine that produced 1.4 Moz Au as of 2021. The Tucano deposit is located and controlled by the N-S-striking and steeply W-dipping Urucum Shear Zone. This shear zone is characterized by intense hydrothermal alteration and gold mineralization, and located in chemical metasedimentary rocks – marble and banded iron formation (BIF). Alteration assemblage comprises first stage quartz-clinopyroxene-garnet ± biotite and second stage amphiboles-phlogopite-biotite-magnetite-sulfides. Locally, Na-bearing amphiboles and phlogopite vector proximal alteration zones. Visible gold shows textural relationship with sulfides (pyrrhotite, arsenopyrite), loellingite, silicates (mainly amphibole) and magnetite. Arsenopyrite geothermometry yields temperature estimates of 500 ± 17 °C (1σ, n = 6). Current data support that Tucano is an orogenic, hypozonal hydrothermal deposit developed post-metamorphic peak at amphibolite facies conditions.

## 1 Introduction

Gold-only deposits in metamorphic belts are structurally controlled and typically found in greenschist metamorphic facies terranes formed at mesozonal crustal levels (Groves et al. 1998). This setting largely complies with the metamorphic model for orogenic fluid source as the bulk of such fluids is produced by chlorite breakdown at the greenschist-amphibolite facies transition (Tomkins 2010). High-temperature hypozonal orogenic gold deposits pose a challenge as metamorphic fluids formed at temperatures of mid-amphibolite facies or higher are thought to be of limited volume and devoid of much S and Au (Tomkins 2010). Thus, the reporting of orogenic gold deposits generated at high grade metamorphic conditions brings forth the need for review of the classic crustal continuum model (Groves et al. 1998). This would require either a different fluid source (magmatic- or mantle-derived) or more complex tectonic settings where high-grade metamorphic terranes are juxtaposed on top of still fertile low-grade rocks (Kolb et al. 2015).

## 2 Deposit geology

The Tucano gold deposit is located in the north-eastern segment of the Amazon Craton, within a Paleoproterozoic belt stretching from northern Brazil to eastern Venezuela (Rosa-Costa et al., 2006). This tectonic province comprises granulite-migmatite-gneiss complexes, greenstone belts and granitoid plutons assembled in a NE-SW structural architecture and recording several episodes of juvenile crustal accretion followed by crustal reworking (Rosa-Costa et al. 2006).

The Tucano deposit is hosted in the NE-SW trending Serra do Navio greenstone belt, which lies unconformably on a reworked Archean continental landmass (Rosa-Costa et al., 2006). The greenstone belt stratigraphy consists of a lower mafic-dominated volcanic unit, an intermediate chemical-exhalative interval, and an upper siliciclastic package, with metamorphic conditions ranging from greenschist to upper amphibolite facies (Scarpelli and Horikava 2017).

The deposit area features mainly chemical-exhalative and siliciclastic rocks, with restricted metavolcanic rocks (Figure 1). The regional structural architecture is locally affected by a N-S deflection associated with the development of the north-south striking, steeply dipping Urucum Shear Zone. Granitic stocks and dikes crosscut the supracrustal rocks and the variable strain record across intrusions indicate more than one magmatic episode. In this contribution, we present preliminary results from an ongoing study of the lithostratigraphic, structural and hydrothermal control related to gold mineralization at the Tucano gold deposit. This study provides an excellent opportunity to examine the hydrothermal alteration and gold mineralization in amphibolite facies metasedimentary host rocks and test the hypothesis of high temperature orogenic gold mineralization. This is relevant once a significant number of orogenic gold deposits hosted in high metamorphic grade terranes are indeed overprinted mesothermal deposits rather than systems originally formed at high-temperature settings (Kolb et al., 2015).

## 3 Methodology

Open pit mapping and drill core logging of selected diamond drill cores were carried out and enabled a comprehensive sampling strategy. Analytical work comprised petrographic investigations, SEM-BSE imaging and electron microprobe (EPMA) analyses (at the Federal University of Minas Gerais) of silicate, carbonate, oxide and sulfide minerals.

## 4 Results

### 4.1 Regional metamorphic P-T conditions

Gold mineralization at the Tucano deposit is located in a sequence of chemical metasedimentary rocks that consists of a lower BIF package, overlain by marble, which is in turn succeeded by metapelites and quartzites. The BIF is an oxide-type magnetite-quartz banded rock, with ubiquitously disseminated, fine-grained amphiboles (grunerite > actinolite). The marble is a fine- to medium-grained isotropic grey rock consisting of abundant olivine, locally featuring phlogopite and more rarely tremolite. Temperature estimates of 592 ± 25 °C (1σ, n = 5) and 612 ± 28 °C (1σ, n = 5) were obtained via garnet-biotite (Holdaway 2000) and Ti-in-biotite (Henry et al. 2005) geothermometry for peak metamorphic conditions in nearby metapelitic rocks. In addition, pressure estimates at 4.1 ± 0.6 kbars (1σ, n = 5) were obtained via application of the garnet geobarometer calibrated by Wu (2019).

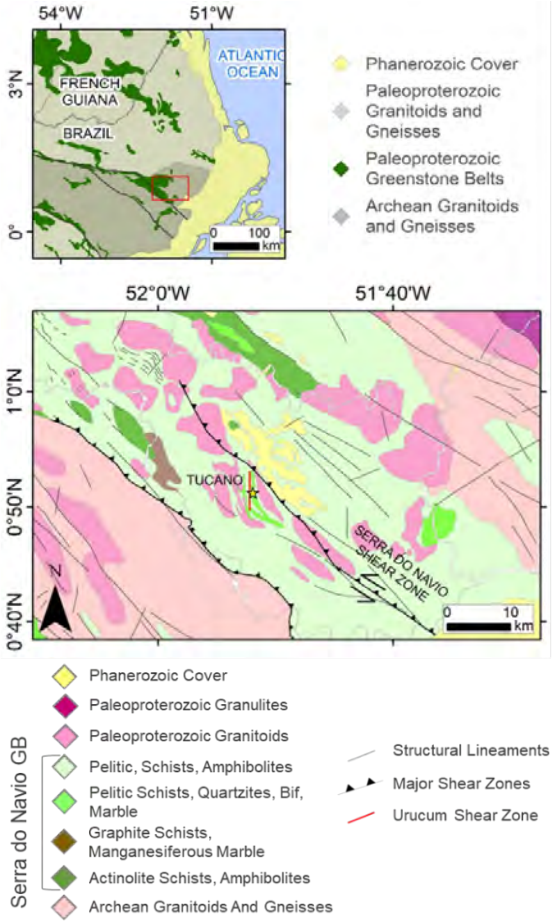


**Figure 1.** Simplified geologic map of the study area (after Barbosa et al. 2015).

### 4.2 Hydrothermal alteration assemblages and P-T conditions at the time of gold mineralization

The hydrothermal alteration event can be subdivided in two major stages. The early stage is represented by deformed quartz-clinopyroxene and clinopyroxene ± garnet nodules and lenses. Locally, hydrothermal biotite was formed in equilibrium with garnet, allowing for temperature estimates using the garnet-biotite geothermometer (578 ± 26 °C - 1σ, n = 4) (Holdaway 2000). Similar values were obtained using the Ti-in-biotite approach (568 ± 23 °C - 1σ, n = 4) (Henry et al. 2005). The second and main stage of hydrothermal alteration is marked by distinct distal and proximal hydrothermal alteration zones in marble and BIF. Distal alteration in marble is characterized by hydrothermal amphibole (tremolite-actinolite) replacement after metamorphic olivine, hydrothermal phlogopite and locally biotite, with traces of sulfides and magnetite. Proximal zone features abundant amphibole (tremolite-actinolite and/or hornblende ± cummingtonite) ± phlogopite/biotite commonly with altered early-stage hydrothermal diopside ± garnet. Magnetite and pyrrhotite are common. Locally, proximal zones are centred about early quartz-clinopyroxene veins superimposed by stringers of amphibole ± sulfides, with no magnetite. Distal alteration zone in BIF is typically characterized by grunerite ± ferroactinolite, and locally, commonly corroded, hedenbergite, concordantly replacing metamorphic quartz-magnetite, but preserving the precursor fabric. The proximal zone is characterized by ferroactinolite-grunerite-pyrrhotite-magnetite but lack metamorphic quartz. The original fabric is partially to totally destroyed. Ti-in-biotite geothermometry (Henry et al. 2005) for stage 2 biotite yielded temperature estimates of only two grains, 550° and 577 °C.

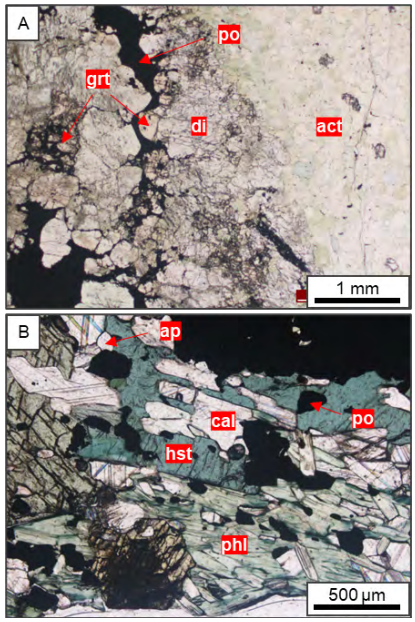


**Figure 2.** A) Strongly altered marble in the proximal zone showing a characteristic calc-silicate mineral assemblage (grt - garnet, di – diopside) with interstitial pyrrhotite (po). B) Strongly altered marble in a proximal zone displaying Na-bearing amphibole (hst - hastingsite) and phlogopite (phl – phlogopite-aspidolite). Except for the highlighted pyrrhotite, all other opaque grains are magnetite. All photomicrographs are taken under plane polarized transmitted light.

Pyrrhotite is the main sulfide species and can be largely ascribed to the main stage of hydrothermal alteration. It can be found as: (i) lenses and stringers subparallel to the shear zone foliation; (ii) tension gash infill in altered marble; (iii) shear zones that contain networks of anastomosing veinlets, and; (iv) disseminated grains locally showing preferred growth directions parallel to shear zone foliation. The textural relationship between pyrrhotite and magnetite indicates a period of synchronous crystallization, followed by pyrrhotite-only precipitation. Other sulfides such as chalcopyrite, arsenopyrite, pyrite and the arsenide loellingite are rare.

Integration of petrographic observations, gold grade distribution and mineral chemistry data show a direct correlation between Na content in amphibole and Na/K ratio in phlogopite with gold distribution (Figure 3). Thus, calcic-sodic amphiboles (pargasite and hastingsite) and micas from the phlogopite-aspidolite series (Figure 2B) are observed almost exclusively in the proximal alteration zone. In contrast, sodium-poor amphiboles and biotite/phlogopite are featured in both unmineralized and proximal alteration zones.

Visible gold (Figure 4) is locally in equilibrium with pyrrhotite and loellingite, Moreover, gold is also documented in equilibrium with silicates, including amphibole, and magnetite.

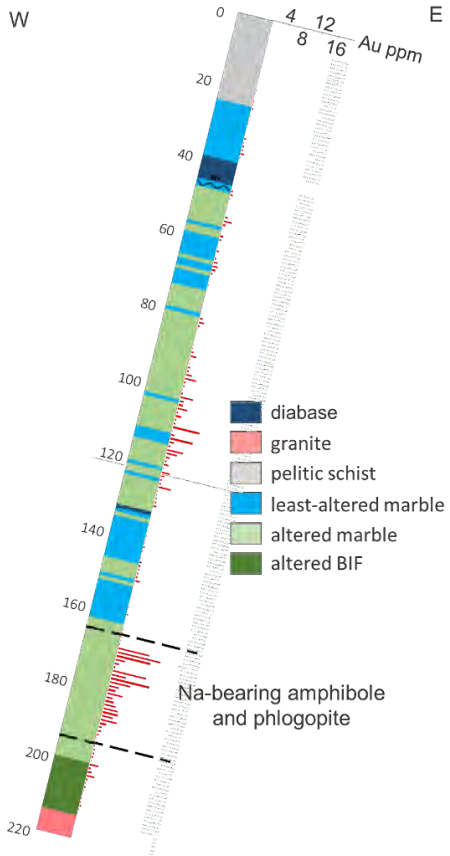


**Figure 3.** Graphic log of drillhole DDH A29 displaying major lithologies, altered equivalents and gold grades in ppm. Note the interval where Na-bearing amphibole and phlogopite are reported.

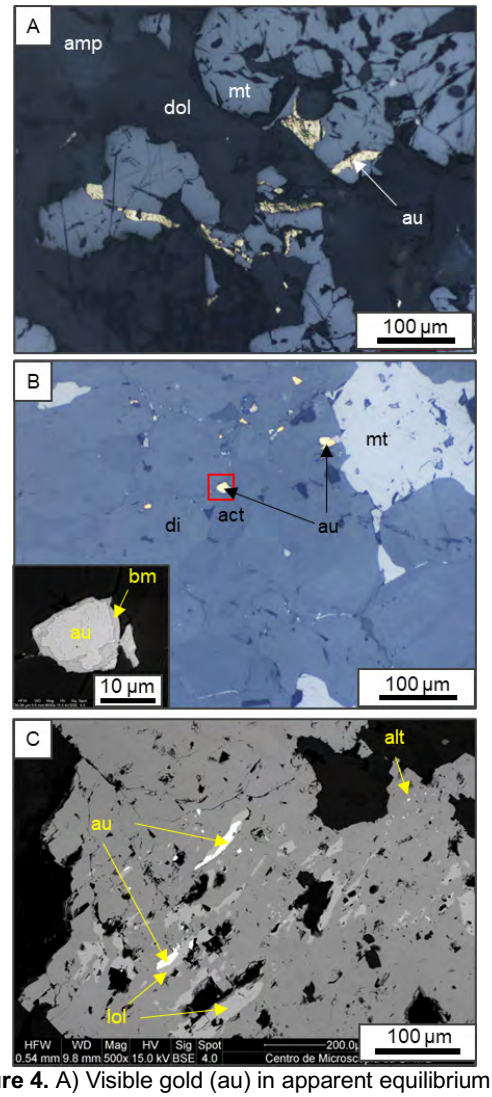


**Figure 4.** A) Visible gold (au) in apparent equilibrium with pyrrhotite (po) and arsenopyrite (asp), in an altered marble (dol – dolomite). B) Visible gold in amphibole (amp) that replaces subequant diopside (di) grains along grain boundaries. The inset in the lower left corner highlights one of the gold grains being surrounded by bismuthinite (bm). C) Equilibrium gold and loellingite (lol) lamellae hosted in a coarse-grained arsenopyrite. Very fine-grained altaite (alt) inclusions are also documented. A) and B) are photomicrographs taken under plane polarized reflected light, and C) is a backscattered electron image.

Equilibrium assemblage pyrrhotite-loellingite-arsenopyrite enables the use of the arsenopyrite geothermometer (Kretschmar and Scott 1976). Textural evidence suggests simultaneous crystallization of pyrrhotite and loellingite and subsequent retrograde solid-solid reaction to produce arsenopyrite. Thus, a temperature estimate using this geothermometer would track the cooling path as the system crosses the arsenopyrite – pyrrhotite + loellingite buffer curve in the $\log a_{S2}$-T space (Figure 5, Kretschmar and Scott 1976, modified by Sharp et al. 1985). In fact, temperature estimates at 500 ± 17 °C (1σ, n = 6), are significantly lower than those obtained using silicate minerals, yet complying with the high-temperature character of this alteration event.

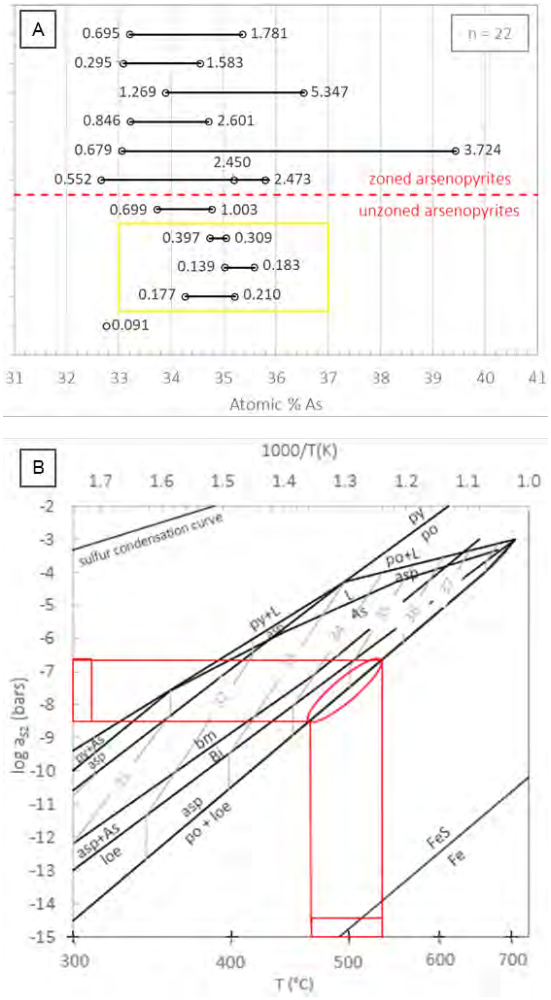


**Figure 5.** A) Atomic % As measured in core-margin pairs of arsenopyrite grains in zoned and unzoned crystals. Figures beside data points indicate the weight percent sum of trace elements (Co+Ni+Sb). The yellow box outlines the data points used for temperature estimates, i.e., grains having <1 atomic As % difference between core and margin and low trace elements. B) Arsenopyrite geothermometer (Sharp et al. 1985, after Kretschmar and Scott 1976) showing with red lines the crystallization conditions of arsenopyrite in log$a_{S_2}$ – temperature space.

## 5 Conclusions

The Tucano gold deposit is a shear-zone hosted hydrothermal system with distinct high temperature alteration assemblages in marble (tremolite-actinolite - hornblende - phlogopite - diopside - garnet - magnetite - pyrrhotite) and BIF (ferroactinolite - grunerite - hedenbergite - magnetite - pyrrhotite). Gold is found in equilibrium with sulfides (pyrrhotite, arsenopyrite), loellingite, silicates and magnetite.

Arsenopyrite geothermometry suggests minimum temperatures of 500 ± 17 °C (1σ) during the main stage of hydrothermal alteration. These temperatures are compatible with the amphibolite metamorphic facies conditions, as indicated by the garnet-biotite and Ti-in-biotite geothermometers. The equilibrium assemblage gold-loellingite, the location of gold in silicates and the high temperature alteration assemblages suggest that gold mineralization at the Tucano gold deposit is part of an orogenic, hypozonal gold system (Kolb et al. 2015). Tucano distinguishes itself from most described orogenic hypozonal gold deposits by the significant amount of hydrothermal magnetite and Na-bearing silicates in the proximal alteration zone.

## Acknowledgements

This work has been supported through the South American Exploration Initiative. We thank AMIRA Global and industry sponsors, as well as Great Panther Mining for their support of the project, especially their exploration team that kindly assisted us during field activities and provided us with crucial data indispensable for the success of this project. We also thank Coordenação de Aperfeiçoamento de Pessoal de Nível Superior (CAPES) for the granted scholarship.

## References

Barbosa JPO, Costa Neto MC, Rosa-Costa LT, Anjos GC, Chaves CL (2015) Geologia e recursos minerais da Folha Macapá NA.22-Y-D, estado do Amapá, escala 1:250.000: Belém, Brazil. Brazilian Geological Survey – CPRM, 118 p. (in Portuguese).

Groves DI, Goldfarb RJ, Gebre-Mariam M, Hagemann SG, Robert F (1998) Orogenic gold deposits: a proposed classification in the context of their crustal distribution and relationship to other gold deposit types. Ore Geol Rev 13(1-5):7-27.https://doi.org/10.1016/S0169-1368(97)00012-7

Henry DJ, Guidotti CV, Thomson JA (2005) The Ti-saturation surface for low- to medium-pressure metapelitic biotites: implications for geothermometry and Ti-substitution mechanisms. Am Min 90(2-3):316-328. https://doi.org/10.2138/am.2005.1498

Holdaway MJ (2000) Application of new experimental and garnet Margules data to the garnet-biotite geothermometer. Am Min 85(7):881-892. https://doi.org/10.2138/am-2000-0701

Kolb J, Dziggel A, Bagas L (2015) Hypozonal lode gold deposits: A genetic concept based on a review of the New Consort, Renco, Hutti, Hira Buddini, Navachab, Nevoria and the Granites deposits. Precambrian Res 262:20-44. https://doi.org/10.1016/j.precamres.2015.02.022

Kretschmar U, Scott SD (1976) Phase relations involving arsenopyrite in the system Fe-As-S and their application. Can Mineral 14:364-386.

Rosa-Costa LT (2006) Geocronologia 207Pb/206Pb, Sm-Nd, U-Th-Pb e 40Ar-39Ar do segmento sudeste do Escudo das Guianas: evolução crustal e termocronologia do evento transamazônico. PhD thesis, Federal University of Pará.

Scarpelli W, Horikava EH (2017) Gold, iron and manganese in central Amapá, Brazil. Braz J Geol 47(4):703-721. https://doi.org/10.1590/2317-488920172017011 4

Sharp ZD, Essene EJ, Kelly WC (1985) A re-examination of the arsenopyrite geothermometer: pressure considerations and applications to natural assemblages. Can Mineral 23(4):517-534.

Tomkins AG (2010) Windows of metamorphic sulfur liberation in the crust: Implications for gold deposit genesis: Geochim Cosmochim Acta 74:3246-3259. https://doi.org/10.1016/j.gca.2010.03.003

Wu CM (2019) Original calibration of a garnet geobarometer in metapelite. Minerals 9(9):540. https://doi.org/10.3390/min9090540

# World-class gold deposits and emerging exploration opportunities in the Loulo district, West Africa

**Thomas Stapley[1], Paul Stenhouse[1], James Lambert-Smith[2], Andrew Allibone[1], David Lawrence[1], Dioumacor Senghor[1], Germain Crestin[1]**
*[1]Barrick Gold Corporation, Toronto, ON, Canada*
*[2]School of Earth and Environmental Sciences, Cardiff University, Main Building, Cardiff CF10 3AT, United Kingdom*

**Abstract.** The Paleoproterozoic Loulo district in Western Mali contains +20Moz of gold, representing a key gold producing district on the African continent and host to the world-class Yalea, Gara and Gounkoto deposits. The Loulo district is comprised of two contrasting geological domains: the metasediment-dominated Kofi domain to the east, and the intrusion-dominated Falémé domain to the west which hosts the voluminous Falémé batholith and associated intrusions. At the district scale, the syn-deformation and syn-mineralisation, high-K, calc-alkaline Falémé intrusives are interpreted to be an important source of heat for the mineralising system. Stable isotope and fluid inclusion studies also support direct involvement of magmatic fluids in several of the deposits, particularly within and proximal to the Falémé domain. At the target-scale, mineralisation within the Kofi domain is commonly associated with local reactivation of N-striking, D1 structures, withing jogs/relays/bends, intersections, and minor folds commonly localising ore shoots. In contrast, exploration within the Falémé domain has begun to highlight possible oxidised intrusion-related styles of mineralisation, associated with lower syn-mineralisation strain hosted in magmatic-hydrothermal breccias and adjacent porphyries and metasedimentary rock.

## 1 Introduction

The Paleoproterozoic (Birimian) gold deposits of the Loulo district in Western Mali, including the world-class Gara, Yalea and Gounkoto deposits, contain a combined +20Moz endowment (Figure 1). The district is one of three major gold systems (wider Loulo, Sadiola, Sabodala-Massawa), within a window of the Paleoproterozoic Birimian (ca. 2300-2100 Ma), known as the Kedougou-Kenieba Inlier (KKI). The KKI is the second most highly endowed region in West Africa and a key global gold producer.

This article summarises and expands upon key studies from the Loulo district over the past decade (Allibone et al. 2020, Lambert-Smith et al. 2020, Lawrence et al. 2013b), incorporating recent findings from the underexplored Falémé domain.

## 2 Geological setting of the Loulo district

The Loulo district hosts two contrasting geological domains, the western, intrusive-dominated Falémé domain, and the eastern, metasediment-dominated Kofi domain (Figure 2). Previously, the district-scale boundary between these two domains was interpreted as a crustal-scale shear zone known as the Senegal-Mali Shear Zone (SMSZ), but the existence of the SMSZ at surface has been largely disproven. The nature of the domain boundary is still debated, with some outcrops suggesting a direct intrusive relationship with the Kofi domain.

The sedimentary succession in the Kofi domain comprises siliciclastic, marble and evaporitic rocks deposited around 2120-2105 Ma. In contrast, the Falémé domain is dominated by voluminous high-K, calc-alkaline granitoids (2100-2065 Ma), associated Fe-skarns, and subordinate magmatic-hydrothermal breccia systems intruding a siliciclastic- and carbonate-dominated sedimentary package that is similar to the Kofi domain metasediments (Figure 2).

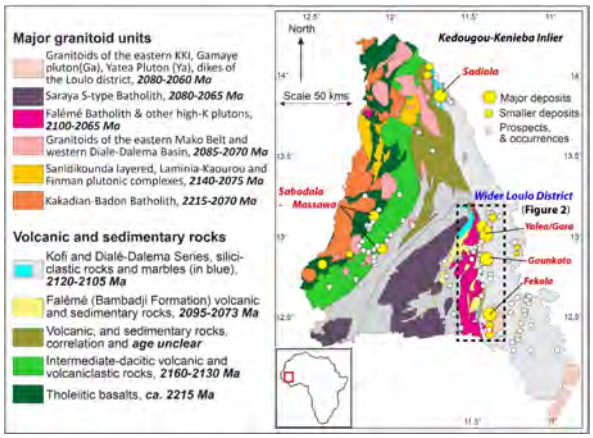


**Figure 1.** Geological map of the KKI, showing three key gold districts including Sabodala-Massawa, Sadiola and the wider Loulo district (modified after Allibone et al. 2020).

Two deformation phases have been recognised in the Loulo district between 2100 and 2070 Ma. D1 is associated with an early contractional period in which the Kofi sediments were folded and thrusted into their current sub-vertical geometries. D2 comprises one or more minor phases of deformation that involved localised folding and reactivation of N-striking D1 structures (Allibone et al. 2020). The kinematics of D2 are complex, with evidence for both normal and sinistral slip directions. Mineralisation in the district occurred between 2090 and 2070 Ma, which is broadly synchronous with emplacement of the high-K, calc-alkaline Falémé batholith and Fe±Au skarn formation.

## 3 Major gold deposits of the Loulo district

More than 30Moz of gold endowment in the wider Loulo district occurs along a narrow corridor, only 4-5km wide and +100km in strike (Figure 2), where most of the gold is hosted in four key deposits: Gara, Yalea, Gounkoto, and Fekola to the south.

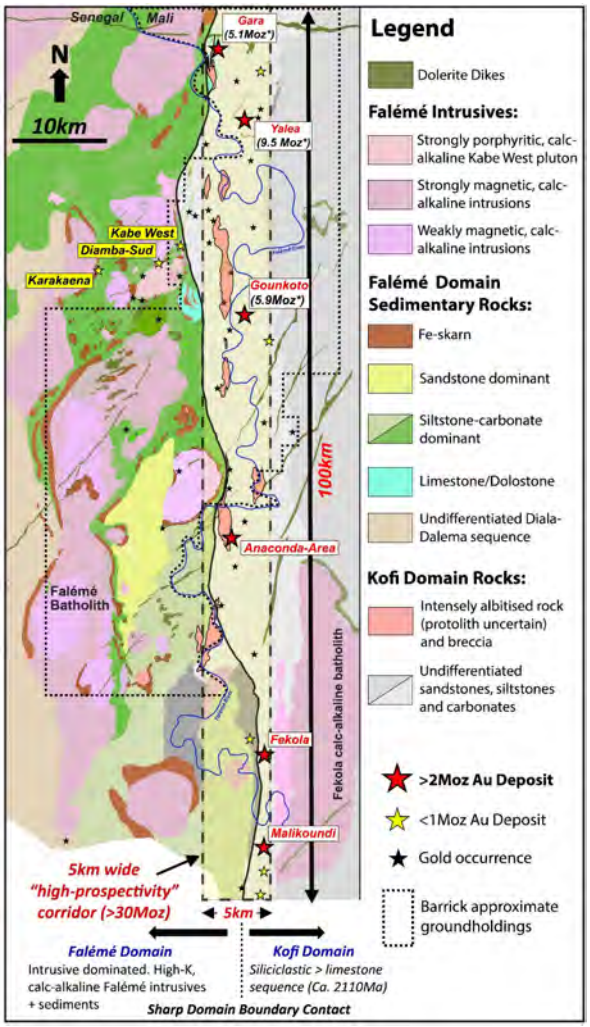


**Figure 2.** Simplified geological map of the wider Loulo district, showing locations of key deposits and prospects.

### 3.1 The Gara Deposit (5.1Moz @ 3.9g/t)

The Gara orebody comprises a stockwork of quartz-carbonate-pyrite-tourmaline veinlets and subordinate disseminated pyrite within an F2-folded layer of a quartz-rich sandstone, typically <30m thick (Figure 3A). An early phase of carbonate alteration is overprinted by strong tourmaline-quartz alteration. The tourmaline alteration increased competency, causing the host unit to fracture during deformation, increasing permeability, whilst adjacent rocks deformed in a dominantly ductile manner.

Mineralised veins at Gara are typically <5 cm thick but comprise between 10-50% of the volume of the sandstone host, with vein density greatest where early tourmaline-quartz alteration is strongest (Figure 3C). The dominant sulfide at Gara is pyrite, approximately 15% of which is a Ni-Co-rich variety. Accessory sulfide minerals include chalcopyrite, gersdorffite, pentlandite, pyrrhotite, and monazite, with only trace amounts of arsenopyrite having been observed (Lawrence et al. 2013b).

Mineralised vein orientations in the fold limbs are comparable to those in the fold hinges, implying veining occurred late- or post-F2. However, the overall shallow-SSW plunge of the orebody is sub-parallel to the $F2_A$ fold axes, while high-grade shoots within are more sub-parallel to the steeper $F2_B$ fold axes, suggesting some relationship between folding and vein formation (Figure 3B).

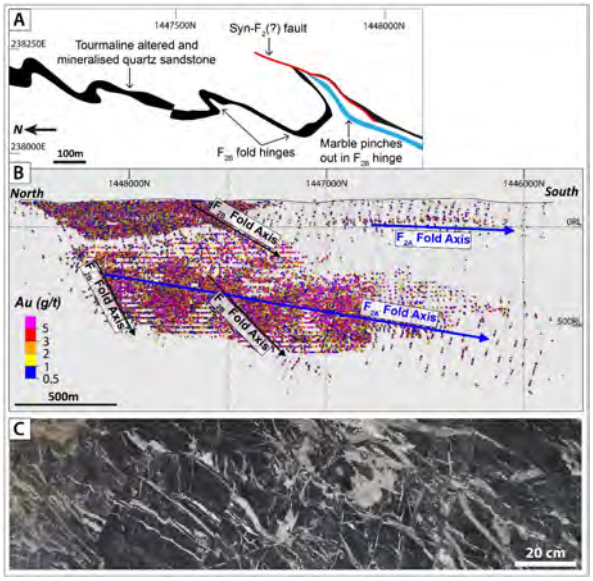


**Figure 3. A** Plan map showing the folded tourmalinised sandstone host. **B** Gara gram-tonne long section (looking east), showing the dominant $F2_A$ and sub-ordinate $F2_B$ fold controls on grade distribution. **C** Quartz-carbonate stockwork veining in tourmalinised sandstone at Gara.

### 3.2 The Yalea Deposit (9.5Moz @ 5.06g/t)

In contrast to Gara, Yalea is hosted along a 2.5km, N-striking, dominantly E-dipping shear zone comprised of variably altered, foliated and brecciated siliciclastic rocks and subordinate strongly sheared marble layers. Within the core of Yalea, these altered and deformed units range from 250m to <30m wide (Allibone et al. 2020).

The alteration and deformation at Yalea is attributed to two main N-striking, E-dipping structures, the Yalea Shear Zone and the Yalea Structure, which are broadly coincident through most of the deposit. The Yalea Shear Zone is discontinuous, mineralised and interpreted to have a syn-D2 timing, while the Yalea Structure is considered to be an early D1 structure that is continuous beyond the limits of the deposit and locally juxtaposes domains with different dips.

Ore shoots within the Yalea orebody are mostly shallowly S-plunging and related to both changes in the geometry of the Yalea Shear Zone, particularly increases in dip or rotations to a westerly dip direction, and structural intersections (Figure 4).

Mineralisation is intimately associated with zones of early, pervasive albite alteration which increased the competency of the host rocks and was subsequently overprinted by mineralised, carbonate-pyrite ± arsenopyrite ± sericite ± chlorite shear zones, fault breccias and vein/fracture

stockworks, with >10g/t zones commonly associated with massive pyrite-arsenopyrite.

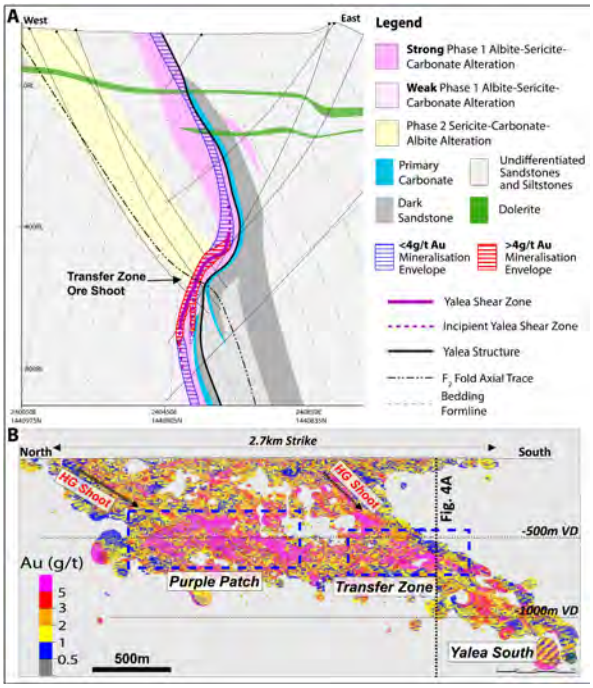


**Figure 4. A** Yalea Transfer Zone cross-section showing key structural control on high-grade (+4g/t) within a prominent rotation of the structure into a westerly dip. **B** Yalea gram-tonne long section looking east, sub-horizontal, high-grade Purple-Patch and Transfer Zone, and plunging Yalea South.

### 3.3 The Gounkoto Deposit (5.9Moz @ 4.09g/t)

The N-striking, E-dipping Gounkoto deposit occurs approximately 20km south of Yalea and Gara (Figure
5) and shares many similarities with Yalea, including its geometry, shear-hosted style of mineralisation, alteration assemblage (including albite, carbonate, and chlorite), and the reactivation of an early D1 structure which coincides with discontinuous sheared marbles and a change in dip of the dominant fabric (Figure 5). Intensely altered rocks in the vicinity of mineralised lodes grade outward, into haloes of partially to pervasively albitised rock up to 50m wide, comparable to that of Yalea.

High-grade mineralisation is characterised by auriferous pyrite-chlorite-carbonate ± magnetite ± hematite ± arsenopyrite shear zones, locally grading in and out of hydrothermal fault breccias and albitite.

Controls on high-grade mineralisation at Gounkoto include left-hand bends and relays along the main N-striking shear zone, and intersections with hangingwall and footwall structures (Figure 5). In contrast to Yalea and Gara, the geometry of high-grade (>8g/t Au) shoots is variable, ranging from steep- to shallow-plunging orientations.

## 4 An emerging gold district in the Falémé domain showing magmatic affinities

Recent exploration in the intrusive-dominated Falémé domain has highlighted substantial differences in the mineralisation style and structural setting compared with deposits in the Kofi domain. These differences are typified by the Kabe West deposit, where gold mineralisation is dominantly associated with disseminated pyrite ± tellurides ± chalcopyrite in the cement/matrix of clast-supported to matrix-supported hydrothermal breccia pipes and dykes (Figure 6A). These breccia systems comprise numerous cross-cutting breccia generations, with some phases containing possible juvenile mafic clasts (Figure 6B). Subordinate disseminated and vein-hosted mineralisation also occurs within adjacent primary carbonates and porphyry dykes and sills. Deposit-scale structures at Kabe West are incipient and syn-mineralisation strain is much lower than in most Kofi domain deposits.

Known deposits within the Falémé domain are all spatially associated with voluminous, hypabyssal intrusives with common porphyritic textures (Figure 6C) but variable compositions. Most of these Falémé intrusives fall within the magnetite-series, highlighting the possibility that these deposits might be oxidised intrusion-related systems, comparable to more typical porphyry-epithermal mineralisation. The combined total resources for the three main Falémé domain projects, Kabe West, Diamba-Sud and Karakaena now exceeds 1Moz, demonstrating that the domain has potential to become a significant mining district with further exploration (Figure 2).

## 5 Isotopic and fluid-inclusion analyses

The $\delta^{34}S$ signatures from vein and host rock material across the Kofi domain show a distinct metasedimentary source ($\delta 34S_{CDT}$: 5.8 – 15.5‰), contrasting that of prospects occurring closer to the Falémé batholith which show $\delta^{34}S$ signatures more indicative of sulfur having likely been sourced from a

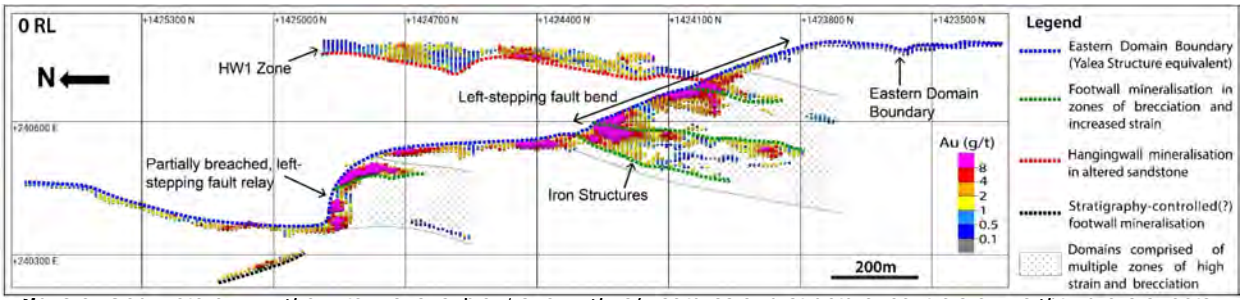

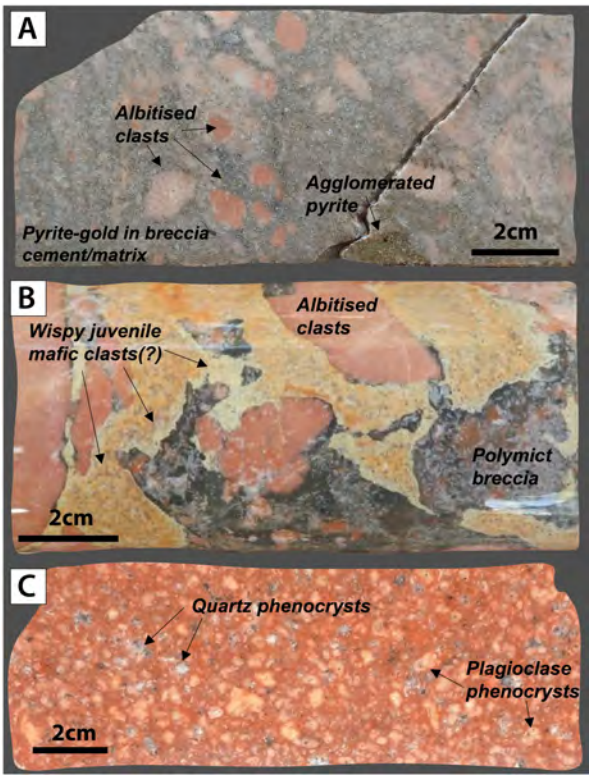


**Figure 6. A** Mineralised Kabe West breccia with disseminated semi-massive pyrite in cement/matrix. **B** Possible juvenile mafic clasts/fragments occurring within the mineralised polymict breccias. **C** Feldspar-quartz porphyry, typical of the hypabyssal intrusions commonly spatially associated with breccia formations and mineralisation occurrences.

magmatic fluid, particularly at Kabe West ($\delta^{34}S_{CDT}$: –4.6 to 3.9‰) (Lambert-Smith et al. 2020). Carbonate vein $\delta^{18}O$ and $\delta^{13}C$ compositions from Gara, Yalea and Gounkoto are consistent with water-rock reactions between a metamorphic fluid and the Kofi Series carbonates. However, carbonate vein compositions from Kabe West and other prospects closer to the Falémé domain have $\delta^{13}C_{PDB}$ values between -5.9 and -8.6‰ and $\delta^{18}O_{SMOW}$ values between 13.3 and 14.8‰, which is consistent with the direct involvement of cooling magmatic fluids (Lambert-Smith et al. 2020). Furthermore, fluid inclusion studies have indicated mixing with magmatic fluids elsewhere in the Loulo district, particularly at Gara where atypical $H_2O$-$CO_2$-NaCl-$FeCl_2$ inclusions occur (Lawrence et al. 2013b).

## 6 Discussion and Conclusions

The Loulo district can be subdivided into two domains based on differences in geology and mineralisation styles. The eastern Kofi domain is dominated by metasedimentary rocks and mineralisation is more typically orogenic, with gold focussed along reactivated D1 structures and pre-mineralisation alteration playing an important role by creating competency contrasts. In contrast, the western Falémé domain contains large amounts of broadly syn-mineralisation, high-K, calc-alkaline intrusive rocks (i.e., the Falémé batholith) and mineralisation is similar to oxidised intrusive-related systems with distinctly lower syn-mineralisation strain and mineralisation spatially associated with large hydrothermal ± magmatic breccia complexes, hypabyssal intrusives and primary carbonates.

While mapping indicates the SMSZ does not appear to exist at surface, it is considered probable that the intrusion of the Falémé batholith was accommodated along a trans-lithospheric structure. Heat from the emplacement of the Falémé batholith was probably an important driver of the synchronous, district-scale hydrothermal system in both the Falémé and Kofi domains. There is also isotopic and fluid inclusion evidence for the direct involvement of magmatic-derived fluids in mineralisation, particularly within and adjacent to the Falémé domain. Evidence for magmatic fluids generally becomes more equivocal to the east (Lambert-Smith et al. 2020).

This reinterpretation of the structural break implied by the previously interpreted SMSZ and the increasing evidence for magmatic influence in both the Falémé and Kofi domains has emphasised the link between the Falémé batholith and mineralisation in the Loulo district. It has also highlighted the exploration potential of the Falémé domain, which is underexplored compared to the Kofi domain.

In addition to ongoing exploration focussed on assessing the endowment of the Falémé domain, further work will also involve increasing confidence in the classification of the Falémé domain mineralisation and assessing any differences in the depth of mineralisation, as implied by the transition from orogenic-like mineralisation to the east, to oxidised intrusive-related mineralisation to the west.

## Acknowledgements

Special thanks go to the authors responsible for the supporting studies discussed in this article, and to Barrick Gold Corporation for funding/access.

## References

Allibone A, Lawrence DM, Scott J, Fanning M, Lambert-Smith J, Stenhouse P, Harbidge R, Vargas C, Turnbull R, Holliday J (2020). Paleoproterozoic gold deposits of the Loulo district, Western Mali. Society of Economic Geologists 23: 141-162. doi: 10.5382/SP.23.07

Lambert-Smith JS, Allibone A, Treloar PJ, Lawrence DM, Boyce AJ, Fanning M (2020). Stable C, O, and S isotope record of magmatic-hydrothermal interactions between the Falémé Fe skarn and the Loulo Au systems in western Mali. Economic Geology, 115: 1537-1558. doi: 10.5382/econgeo.4759

Lawrence DM, Treloar PJ, Rankin AH, Boyce A, Harbidge P, (2013b). A fluid inclusion and stable isotope study at the Loulo mining district, Mali, West Africa: Implications for multifluid sources in the generation of orogenic gold deposits. Economic Geology 108: 229–257. doi: 10.2113/econgeo.108.2.229

# Insights into the formation of high-grade gold mineralisation at the 10 Moz. Jundee gold camp of Western Australia

**Sumail[1], Nicolas Thébaud[1], Quentin Masurel[1], Chris Fisher[1]**
*[1]Centre for Exploration Targeting, School of Earth Science, The University of Western Australia, Perth, Australia*

**Abstract.** Although orogenic gold deposits form one unified class, individual deposits vary significantly in terms of their mineral paragenesis, deformation styles and associated gold grades. Understanding the processes that control the variation in gold grade has significant implications for predicting how and more importantly where high-grade mineralisation is formed. In this study, we focus on the 10 M oz. Jundee gold camp, located in the Yandal greenstone belt in the Yilgarn Craton of Western Australia. The mining camp comprises the high-grade Jundee gold mine (9 Moz. at 5 g/t Au) and the low-grade Bogada deposit (1 Moz.) hosted in Archean mafic sequences. Detailed structural evolution of the gold camp reveals that gold mineralisation developed over at least three distinctive events. Early low-grade mineralisation hosted in shallow-crustal veins is overprinted by dominantly brittle structures comprising free gold mineralisation. Late thrusting in the gold camp is further associated with the gold remobilisation. At the Bogada deposit, limited evidence exists for punctuated gold episodes and gold mineralisation resulted from a single low-grade event. Based on the detailed structural and paragenetic framework established in this study, we conclude that the high-grade gold mineralisation at Jundee resulted from gold enrichment over three polyphased deformation events.

## 1 Introduction

Ore quality in orogenic gold deposits can be classified into two categories; free milling and refractory, based on the recovery efficiency of the metallurgical processes (Lunt and Weeks 2005; Petrella et al. 2021). Refractory-style gold mineralisation hosted in sulfide ore usually corresponds to lower gold grade and requires more sophisticated processes for extraction of gold. Contrarily, high-grade free-gold mineralisation is relatively easily recovered with significantly lower energy consumptions. Understanding the physical and chemical processes leading to enrichment of high-grade free-Au mineralisation is critical and important for a more efficient targeting of such ores.

High-grade gold mineralisation has been previously suggested to form as a result of subsequent enrichment of gold over several episodes of mineralisation. However, deciphering individual events in such systems can be extremely challenging and requires understanding the detailed paragenetic evolution of such deposits.

Our study focusses on the 10 Moz. Jundee gold camp comprising of the high-grade Jundee gold mine (9 Moz. at 5 g/t Au) and the low-grade Bogada deposit (1 Moz.) hosted in mafic-ultramafic sequences. The occurrence of high-grade and low-grade mineralisation in a single gold camp provides a unique opportunity to understand the process leading to the formation of high-grade gold mineralisation. By combining structural geology and mineralogy, this study examines in detail the structural and alteration paragenesis at the two deposits and places relative timing constraints on events leading to the formation of gold mineralisation.

## 2 Regional Geology

### 2.1 Yandal greenstone belt

The Neoarchean Jundee gold camp is located 600 km north of Kalgoorlie in the Yandal greenstone belt (Figure 1) of the Eastern Goldfields Superterrane (EGST) that hosts several other major deposits including Bronzewing and Darlot in the south. The Yandal greenstone belt represents a 300-km-long and 40-km-wide, poorly exposed N-NW-trending litho-tectonic complex (Figure 2) of metamorphosed and poly-deformed Archean volcanic and sedimentary rocks which are flanked by Late Archean granitoids on either side (Yeats et al. 2001; Baggott et al. 2005). In addition to the Jundee deposit, the Yandal greenstone belts host several other major deposits (> 1 M oz. Au; figure 2) including Bronzewing (Phillips et al. 1998), Mount McClure and Mt Joel in the centre of the belt, and Darlot in its southern end. Rocks in the Yandal belt have been metamorphosed to lower greenschist facies with amphibolite facies metamorphism restricted to granitoid margins (Vearncombe et al. 2000). The stratigraphic succession of the belt reciprocates that of EGST and comprises of mafic-ultramafic volcanism, differentiated mafic sills, felsic volcanics and clastic sedimentary rocks (Kohler and Phillips 2003).

The Yandal belt has been affected by polyphase deformation and thus not all but most of the primary contacts coincide with shear zones (Vearncombe 1998). To the west, the belt is bounded by the Moongarnoo and Moilers shear zones and to the east by Celia shear zone, which at the outcrop-scale, are characterised by protomylonites and foliated schists. The protomylonitic fabric exhibits a steeply dipping geometry, parallel to the greenstone bedding and is dominated by a flattening strain with locally developed asymmetric S-C fabrics (Vearncombe et al. 2000). The structural evolution of the Yandal belt was first described by Vearncombe (1998) through

his works on shear zones, which he later summarised into three progressive deformation events (Vearncombe et al., 2000), consistent with the regional D2 – D4 deformation event scheme proposed for the EGST by (Swager 1997).

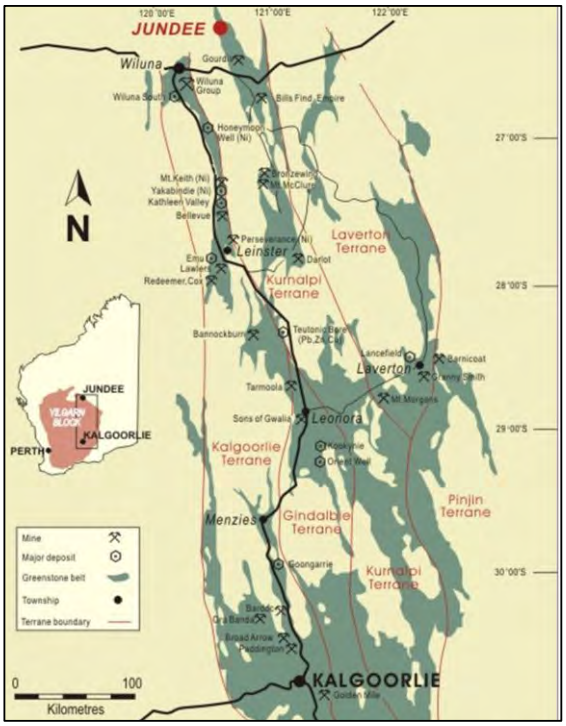


**Figure1**. Map showing location of Jundee gold deposit in the Yandal greenstone belt of the Eastern Goldfields Superterrane of Yilgarn Craton. Modified after Newmont (2008).

The Yandal greenstone belt is characterised by crosscutting brittle-ductile shear zones which trend from 000-150° and correlate with the D4 event (Kohler and Phillips 2003) in the D1 – D4 regional deformation scheme outlined for the EGST by (Swager 1989). The D3 event in the Yandal is represented by the Moilers, Moongarnoo and Celia shear zones resulting from an E-W progressive shortening deformation. An episode of NNW-trending upright folding has been recognised in the southern Yandal belt and results from an ENE-WSW shortening D2 deformation (Phillips et al. 1998; Vearncombe et al. 2000). Like elsewhere in EGST, evidence for D1 N-S shortening deformation is cryptic in the Yandal belt (Kohler and Phillips 2003).

## 2.2 Jundee goldfields

The 9 Moz. Jundee gold deposit is located in the northern end of the Yandal greenstone belt with host sequence striking NNW and dipping moderately (40-55°) towards the SW (Yeats et al. 2001). The mine sequence at Jundee (Figure 2) has an approximate thickness of ~2.5 km and is dominated

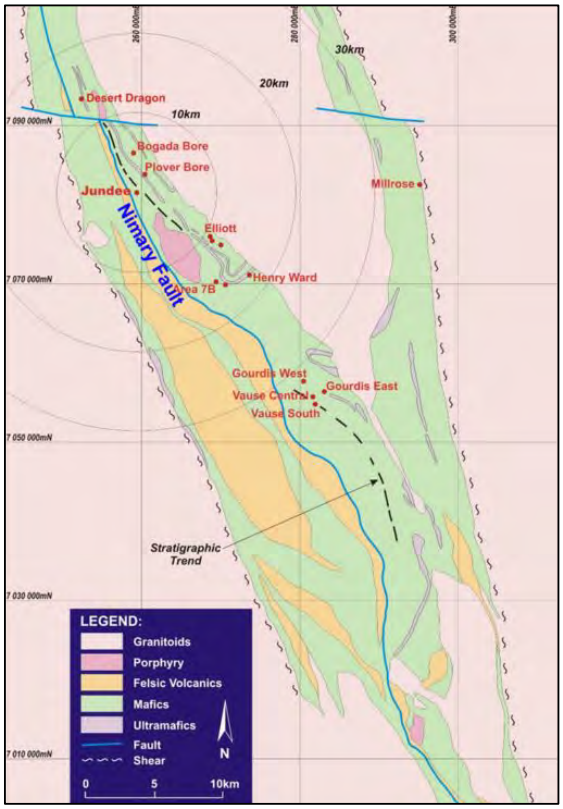


**Figure 2**: Detailed map displaying the geology of the Yandal greenstone belt. Modified after Newmont (2008).

by tholeiitic basaltic rocks, the Fisher and Lyons basalts which were originally separated by an horizon of 100 m thick sedimentary rocks (carbonaceous shales, cherts and siltstone). The present-day geometry is such that this sedimentary horizon has been separated into four individual units as it has been intruded by three strike-continuous differentiated gabbroic sills (Barton, Hughes and Lyons Dolerites). The differentiated sills represent individual separate intrusions based on geochemical analysis and absence of tectonic repetition (Hergt et al. 2000). A deformed succession of dacitic –to -rhyodacitic volcanoclastic rocks with minor shale, chert and basalt lies to the west of the mine sequence and is interpreted to be related to the Lake Violet Sequence (Phillips et al. 1998; Vearncombe et al. 2000). The mine sequence at Jundee is intruded by suites of dacitic porphyries, porphyritic granodiorites and lamprophyres which range from pre- to post-mineralisation in age. The dacitic porphyries are common, have variable trends, host economic gold mineralisation and can be up to 300 m thick (Yeats et al., 2001). These pre-mineralisation dacitic intrusions are dated at 2678 ± 5 Ma, thus providing a minimum age for the main mineralisation event (Yeats et al. 2001). The granodiorite porphyry dykes lack economic mineralisation (> 0.7 g/t Au) and are mostly barren and usually truncate the gold-bearing structures. These dykes can be up to 50 m wide and have a consistent NE to NNE-orientation (Kohler and Phillips 2003).

Gold mineralisation is hosted by a network of brittle-ductile cross-cutting shear zones trending 000-160° with variable dips. Vearncombe et al. (2000) argued that these faults represented a conjugate set where the NE-striking (040-060°) shear zones displayed dextral kinematics and the SE-striking (090-120°) shear zones were sinistral. Most veins consist of massive- to variably laminated, amorphous and finely crystalline quartz, with carbonate and minor chlorite, muscovite, pyrite and arsenopyrite. Visible gold is common, and grades can range up to several thousands of grams per tonne Au. Vein margins are usually sharp and planar, but locally exhibit evidence of wall rock replacement. Some veins show millimetre- to centimetre-wide, symmetrical, wall rock alteration zones. Some basalt-hosted shear zones, contain syn-deformational crustiform- and colloform-textured veins containing multiple, subparallel, quartz-carbonate bands 0.5 - 10 mm thick. The grade of the veins is rarely more than 2-3 g/t Au.

## 3 Structural Setting of the Jundee Gold Camp

### 3.1 $V_{J1}$ veins

Thin (<5cm) fault-fill veins dominated by a chlorite calcite composition are ubiquitously present throughout the Jundee system and provide the evidence for first hydrothermal activity in the deposit. These veins are dominantly found along the lithological contacts between basalts, gabbros and dacitic porphyries. The $V_{j1}$ veins display a consistent NW-trending orientation parallel to the stratigraphy along with an N-S trending conjugate pair. These early veins are barren in terms of gold and lack any significant associated alteration.

### 3.2 $V_{J2A}$ Colloform veins

Relatively thick (up to 2 m wide) $V_{J2A}$ veins show occurrences of colloform-crustiform textures along with cockade textured breccias. These open-space growth textures are commonly interpreted to form in shallow crustal environments. The $V_{J2A}$ colloform veins represent the first introduction of gold in the Jundee system. These veins have a consistent NW-trending and SW-dipping structural orientation and are associated with normal kinematics. The colloform veins are also frequently associated with conjugate pairs and vertical tension veins which together suggest their formation in an extensional setting. These dominantly brittle, mineralised structures lack any significant displacement along them with limited evidence for associated kinematics such as slickenlines or stepfibres. However, where present, mineral lineation associated with the colloform veins plunges shallowly (15° - 20°) towards the SE. Gold mineralisation associated with the colloform veins is low-grade (<2 g/t), where gold is dominantly hosted in sulfides alteration associated with such veins.

### 3.3 $V_{J2B}$ hydrothermal breccia and laminated veins

The $V_{J2B}$ structures account for the high-grade gold event at Jundee and represent bulk of the gold mineralisation at the Jundee deposit. These highly endowed structures form a network of dominantly brittle fractures with multiple orientation o gold-bearing shear zones that parallel and cross-cut the stratigraphy. The $V_{J2B}$ structures are characterised by tabular zones of dominantly brecciated and veined rocks that hosts the high-grade gold mineralisation. These structures consistently reactivates earlier preferentially oriented structures. The $V_{J2B}$ structures dominantly occurs as hydrothermal breccia in basalts and as laminated veins in doleritic host rocks. Gold grades associated with these structures can be as high as 10 wt % of the rock volume. The mineralised structures are often narrow (up to 2 m wide) with strikes continuous over a few tens to several hundreds of metres. Although considerably variable in orientation, the mineralised $V_{J2B}$ structures can be categorised into broad discrete trends based on associated kinematics. Shear zones striking NW to WNW appear to host most of the gold mineralisation in the deposit and are dominantly associated with normal kinematics with minor sinistral strike-slip component. These bedding parallel structures are occasionally associated with ENE-trending vertical tension veins further suggestion their formation in an extensional setting. Secondary trends includes the ENE-trending faults dipping moderately towards the SE. These faults often form a conjugate pair the WNW-trending mineralised faults which display evidence for normal displacements. Mineralisation related lineation associated with the ENE-trending faults plunges down-dip the structures with step-fibres suggesting a dominantly normal-dextral kinematics associated with the gold mineralisation. The dominant free-Au occurring mineralisation found in the Jundee deposit occurs mostly in the hydrothermal matrix. Matrix composition comprises of fine crystalline grey groundmass dominated with a quartz-calcite composition along with chlorite, muscovite and sulfide. The sulfide composition is dominated by pyrite along with arsenopyrite, tennantite and chalcopyrite. Pyrite occurs ubiquitously either in disseminated form or as millimetre-wide stingers. Euhedral to subhedral pyrite grains form larger irregular composites. SEM imaging of the pyrite grains reveals evidence for complex internal zoning with inclusion-rich spongy cores surrounded by arsenic-rich pyrite mantles. Gold preferentially occupies internal boundaries between zoned pyrite and there is significant evidence present for remobilisation of gold from internal pyrite zones to external parts of pyrite and outside pyrite grains.

### 3.4 $V_{J3}$ gold rich veins

The high-grade $V_{J2A}$ hydrothermal breccias are locally overprinted and crosscut by dark green chlorite-calcite $V_{J3}$ veins. The $V_{J3}$ veins are thin (<2 cm) and continuous over few 10's of metres. The $V_{J3}$ veins hosts abundant visible gold mineralisation that can be >10 % of the vein material. Vein composition is dominated by a calcite-quartz with minor amounts of chlorite. However, interestingly the $V_{J3}$ veins themselves host a low grade (<2 g/t) mineralisation when distant from the $V_{J2B}$ hydrothermal breccias. These $V_{J3}$ veins are dominantly associated with reverse kinematics resulting in thrusting of earlier structures. The occurrence of $V_{J3}$ faults in the Jundee system is extremely limited and often observed when overprinting the earlier structures.

## 4 Summary

Through a detailed evaluation of the structural framework for the Jundee-Bogada gold camp, we have been able to establish that (i) the poorly preserved $V_{J1}$ calcite-chlorite veins are the first evident hydrothermal event at the Jundee deposit; (ii) the widespread colloform-crustiform veins ($V_{J2A}$) represent the first introduction of gold in the Jundee deposit; (iii) the most prominent structural event '$V_{J2B}$' and associated high-grade gold mineralisation accounts for the majority of gold mined at the Jundee deposit; (iv) locally occurring ultra-high grade $V_{J3}$ veins represent the third and last evidence for gold mineralisation in the Jundee deposit. In the high-grade Jundee deposit, initial low-grade gold mineralisation hosted in the colloform structures ($V_{J2A}$) is overprinted by a high-grade gold mineralising event ($V_{J2B}$). Moreover, there is further evidence for a third event associated with the $V_{J3}$ chlorite-calcite veins. The local enrichment of gold in these veins is restricted to localities where they intersect the earlier high-grade $V_{J2B}$ structures. Therefore, we propose that some (if not all) of the gold may be locally remobilised from the high-grade $V_{J2B}$ structures into the $V_{J3}$ veins.

## 5 Conclusions

At the 10 M oz. Jundee gold camp of EGST, two distinctive orogenic gold deposits exist within 2 km of each other: the 9 M oz. Jundee gold deposit and the 1 M oz. Bogada gold deposit. The two deposits are characterised by significantly contrasting gold grades with high-grade (>10 g/t) gold mineralisation hosted at the Jundee deposit and low-grade mineralisation (< 2g/t) at the Bogada deposit. The structural paragenesis established at the two deposits provides evidence for a protracted and polyphased deformation associated with multiple episodes of gold mineralisation. The first episode of gold mineralisation hosted in colloform veins includes refractory-style gold associated with sulphide assemblage dominated by pyrite, sphalerite and tennantite. The second mineralisation event resulted in dominantly free-Au mineralisation associated with complexly pyrite, arsenopyrite, tennantite and chalcopyrite. Evidence for the last gold mineralisation episode is recorded by thrust faults associated with contractional deformation. This late gold mineralisation resulted in dominantly refractory ore except where remobilising from previous stages ($V_{J3}$). Our results demonstrate that a key characteristic of the high-grade Jundee gold deposit is the overprinting of successive mineralisation events compared to the single gold event at the low-grade Bogada deposit.

## Acknowledgements

This study would like to acknowledge its parent project 'Yilgarn 2020' (MRIWA M530) for providing the financial and technical support required for this study. The authors would also like to acknowledge the in-kind and financial support provided by Northern Star Resources and Creasy Group, specifically Jamie Rogers, Peter Le Roux, Chris Scott and Kris Wright for their invaluable input.

## References

Baggott MS, Vielreicher NM, Groves DI, McNaughton NJ, Gebre-Mariam M (2005) Zircons, Dikes, and Gold Mineralization at Jundee-Nimary: Post ca. 2.66 Ga Archean Lode Gold in the Yandal Belt, Western Australia. Economic Geology 100:1389-1405.

Hergt JM, Preston P, Bright RMJ, Phillips GN (2000) Differentiated mafic sills in the Yandal greenstone belt. AIG Bulletin 32:55-67.

Kohler EA, Phillips GN (2003) Jundee goldfield, Yandal gold province, Yilgarn Craton, Western Australia. National Library of Australia CSIRO Exploration & Mining, Box 312, Clayton South, Victoria.

Lunt D, Weeks T (2005) Process flowsheet selection. Developments in Mineral Processing 15:73-96.

Newmont (2008) Jundee Geology Overview. Newmont Pty Ltd, Australia.

Petrella L, Thébaud N, Evans K, LaFlamme C, Occhipinti S (2021) The role of competitive fluid-rock interaction processes in the formation of high-grade gold deposits. Geochimica et Cosmochimica Acta 313:38-54.

Phillips GN, Vearncombe JR, Eshuys E (1998) Yandal greenstone belt, Western Australia: 12 million ounces of gold in the 1990s. Mineralium Deposita 33:310-316.

Swager C (1989) Structure of Kalgoorlie Greenstones: Regional Deformation History and Implications for the Structural Setting of the Golden Mile Gold Deposits. Report25:59-84.

Swager C (1997) Tectono-stratigraphy of late Archaean greenstone terranes in the southern Eastern Goldfields, Western Australia. Precambrian Research 83:11-42.

Vearncombe JR (1998) Shear zones, fault networks, and Archean gold. Geology 26:855-858.

Vearncombe JR, Kohler E, Meyers J, Phillips GN, Rothery E, Ryan D (2000) Regional, structural and exploration geology in a terrain with minimal outcrop—the Yandal belt. Yandal greenstone belt: Perth, Australian Institute of Geoscientists, Bulletin 32:17-39.

Yeats CJ, Kohler EA, McNaughton NJ, Tkatchyk LJ (2001) Geological setting and SHRIMP U–Pb geochronological evidence for ca. 2680–2660 Ma lode-gold mineralization at Jundee–Nimary in the Yilgarn Craton, Western Australia. Mineralium Deposita 36:125-136.

# Early crustal architecture revealed by multidisciplinary data integration: implications for gold exploration targeting

**Nicolas Thébaud[1], Quentin Masurel[1,2], Alan Aitken[1], Hugh Smithies[3], Klaus Gessner[3], Chris Fisher[1], Yongjun Lu[3]**
*[1]Centre for Exploration Targeting, School of Earth Sciences, The University of Western Australia, 35 Stirling Hwy, Crawley 6009, Western Australia*
*[2] Minerals Targeting International Pty Ltd, West Perth, Wester Australia*
*[3]Geological Survey of Western Australia, Department of Mines, 100 Plain Street, East Perth 6004, Western Australia*

**Abstract.** Metallogenic systems are intimately linked with zones of mechanical weakness that occur in the lower-middle crust and continental lithospheric mantle. Where preserved, these zones of lithospheric heterogeneity ("lithospheric discontinuities") reflect the finite cumulative lithospheric damage associated with paleo-tectonic events such as rifting and collision. Understanding this fundamental architecture is crucial for explorers to enhance their predictive capacity, as it exerts a primary control on the location of tier one ore deposits. To identify and map this architecture in the deep crust and continental lithospheric mantle, we conducted a multidisciplinary study of the Yilgarn Craton. Our analysis revealed regional scale lineaments, some of which oblique to the main structural grain established during the craton's assembly. We propose that these lineaments were active during intra-cratonic rifting and the emplacement of the Kalgoorlie-Kurnalpi supracrustal cover between c. 2720 and 2690 Ma. They were subsequently reactivated during the Kalgoorlie Orogen, c. 2680-2635 Ma, and played a critical role in controlling the location of tier one gold deposits in the region.

## 1 Introduction

Transcrustal to translithospheric discontinuities have been suggested to exert control over a diverse array of mineral systems. Such discontinuities are thought to provide the fundamental pathways connecting enriched continental lithospheric mantle domains to the upper crust (e.g. Hronsky et al. 2012). As noted by Holdsworth et al. (2001), hydrous fluids and magmas tend to migrate preferentially along long-lived, inherited structures in continental margins. This phenomenon has been observed in many mineral-rich areas worldwide, particularly at the intersection of fundamental basement structures with orogen-parallel crustal-scale structures. For example, orogenic gold deposits have been found to occur in such settings (Love et al. 2004), as have epithermal gold deposits (Bahiru et al. 2019) and porphyry Cu-Au deposits (Gow and Walshe 2005).

Identifying the crustal and lithospheric architecture within a continental mass is challenging due to its cryptic nature. In the field, such features are frequently overlooked or misinterpreted. As an alternative the early craton architecture may be indirectly mapped via a set of techniques including large-wavelength geophysical methods (e.g. gravity, magnetics), and radiogenic isotopes (e.g. Lu-Hf and U-Pb on zircon). Such an approach has been instrumental in revealing the architecture of the Yilgarn Craton of Western Australia and evaluating the role of this architecture in the generation of gold and nickel mineral systems (Fig 1., Mole et al. 2014).

## 2 Regional geology

The Yilgarn Craton, located in Western Australia, is divided into several terranes, including the Narryer Terrane, Youanmi Terrane, South West Terrane, and Eastern Goldfields Superterrane. The latter encompasses the Kalgoorlie, Kurnalpi, Burtville, and Yamarna terranes. The Narryer Terrane and northern Southern Cross Domain are ancient crustal blocks within the Yilgarn Craton and have a shared geological history extending back to c. 4000 Ma (Mole et al. 2019). A major felsic magmatic event affected the proto-craton between c. 3050 and 2900 Ma (e.g. Mole et al. 2019). An embryonic stage of subduction occurred between c. 2830 and 2740 Ma and resulted in the docking of the Narryer Terrane against the Youanmi Terrane at c. 2740 Ma. At c. 2720-2690 Ma, the Kalgoorlie-Kurnalpi Large Igneous Province (Hayman et al. 2015) occurred in a failed intra-cratonic rift related to a mantle upwelling zone focused along a zone of pre-existing lithospheric heterogeneity referred to as the Ida Fault (Masurel et al. 2022).

The tectonic inversion of the Kalgoorlie-Kurnalpi intracontinental rift occurred during the Kalgoorlie Orogen between c. 2680 and 2630 Ma. At that time the NNW-striking structural grain of the Eastern Goldfields Superterrane was acquired under ENE-WSW-directed bulk crustal shortening (Swager 1997).

## 3 Methodology

Our approach relies on the interpretation of multidisciplinary dataset combining aeromagnetic, gravity and seismic data together with radiogenic isotopic data (Sm-Nd) and the regional geological record. In this study, we: (i) identify the orientations of basement discontinuities in the lower-middle crust and continental lithospheric mantle of the Yilgarn Craton through the integrated geological interpretation of isotopic and deep-penetrating geophysical data; and (ii) assessing their geological robustness through comparison between independent dataset.

Our approach involves the interpretation of a multidisciplinary dataset that combines aeromagnetic, gravity, and seismic data, as well as radiogenic isotopic data (Sm-Nd), with the regional geological record. Here, we aim to (i) identify the orientations of basement discontinuities in the lower-middle crust and continental lithospheric mantle of the Yilgarn Craton by integrating isotopic and deep-penetrating geophysical data and (ii) evaluate their geological robustness by comparing them with independent datasets. Our approach enables us to validate the lineaments delineated in the range of datasets analyzed and to assess their relative timing of emplacement. We suggest that this combination is crucial for confidently verifying the presence of an inferred lithospheric architecture and refining its geological origin.

## 4 Results

The documented basement discontinuities can be grouped into three main categories. The first category consists of orogen-parallel trends that were likely acquired during the protracted assembly of the Yilgarn Craton. The second category mimics that of the craton's margins, and likely indicates post-cratonization modifications of the Yilgarn Craton. The third category comprises orogen-oblique trends, the origin of which remains cryptic.

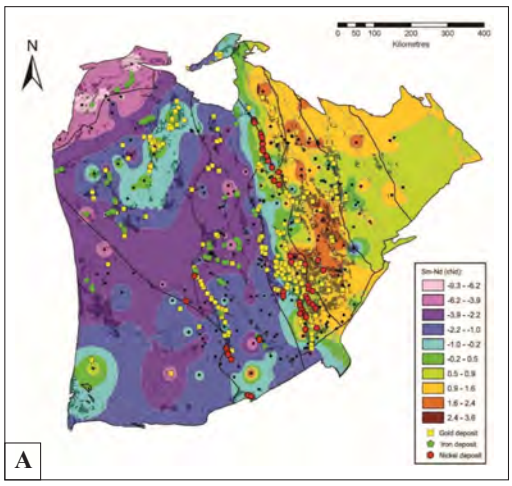


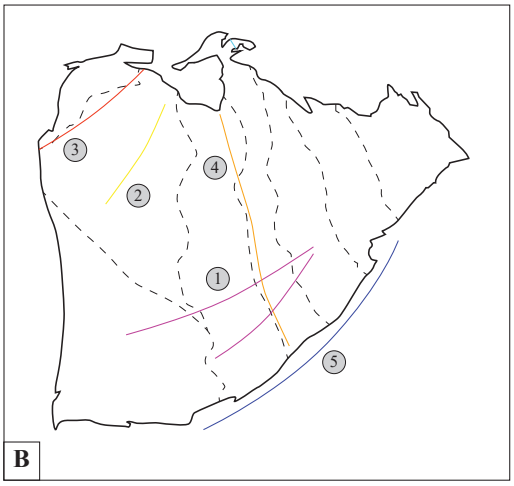


**Figure 1.** A) Sm-Nd isotopic contour map showing the spatial variation of εNd values (modified after Mole et al. 2013). B) Cartoon showing major structural architecture of the Yilgarn Craton: (1) Intracratonic rift zone across the Yilgarn proto-craton between c. 3050 and 2900 Ma resulting in the eruption of the Forrestania and Lake Johnston ultramafic units. (2) Intra-continental rift zone the Murchison Domain of the Youanmi Terrane between c. 2825 and 2740 Ma. (3) Collision front between the Narryer and Youanmi Terranes at c. 2740 Ma. (4) Kalgoorlie-Kurnalpi failed intracratonic rift axis (5) Albany-Fraser intracratonic rift at c. 1805 Ma. Dash line represents Terranes.

## 5 Discussion

### 5.1 Interpreting oblique-orogen structural architecture

Our analysis of potential field, topographic, isotopic, and seismic data indicates that both the orogen-parallel trends and trends parallel to the margins of the Yilgarn Craton exhibit similar expressions. Through comparison with existing geological knowledge of the Yilgarn Craton's evolution, we have validated each identified trend as representing a preserved expression of multiple tectonic events that affected the crust from the Neoarchean to the Proterozoic.

The geological validity of orogen-oblique trends identified in potential field, topographic, seismic, and isotopic data is harder to evaluate within the geological record of the Yilgarn Craton. Yet, the coincidence of the orogen-oblique lineaments in multiple datasets provides a higher degree of confidence with regards to their existence. The problem remains as to explain what these orogen-oblique trends may represent.

In the Yilgarn Craton, the development of the Kalgoorlie-Kurnalpi terranes developed within an extensional environment (e.g. Masurel et al. 2022). Stratigraphic, isotopic, and geochemical data, collectively, indicate that emplacement of the c. 2720-2690 Ma occurred in a failed intra-continental rift and was related to a mantle upwelling zone focused along the NNW-striking Ida Fault (e.g.

Hayman et al. 2015). Within such extensional context, one may suggest that oblique-orogen structures may represent ancient transfer faults that helped accommodating rifting of the proto-Yilgarn continental mass.

Such interpretation echoes with that made in more recent geological terrains of the Andes whereby orogen-oblique structures have been recognised across scales. For instance, in the Cu-Zn Antamina mine in Peru, the deposit architecture and structural setting is controlled by orogen-oblique structures that have been interpreted as transform segments accommodating early rifting of the continental margin (Love et al. 2004). Wiemer et al. (2022) did generalise this conclusion suggesting that cross structural lineaments along the NW-striking Peruvian crustal architecture were related to transfer structures that had accommodated the rifting of the continental margin associated with the Rodinia break up.

### 5.2 Implication for Gold mineralisation

In recent studies, a strong connection has been proposed between the formation of ore deposits and the inversion of early tectonic architecture. In the Cu-Zn Antamina mine, the oblique-orogen structure is interpreted to have controlled the intrusion and related mineralised skarn development during the rift inversion that took place during the Eocene and Miocene (Love et al. 2004). Following a similar interpretation, Wiemer et al. (2022) investigated the northern Peruvian Andean Cordillera and suggested that successive inversion of the Andean margin played a primary role in the clustering of gold deposits. There, the intersection between the so-called oblique-orogen Pataz lineament appear to mark the locus of a cluster of major Carboniferous and Cenozoic gold deposits in northern Peru. Such spatial coincidence is suggested to highlight the critical role of early rifting architecture in providing the plumbing system required to efficiently transfer ore-fertile magmas and fluids in the crust (Wiemer et al. 2022).

We propose that the spatial association between oblique-orogen structures in the Yilgarn Craton and gold deposit clusters in the Kalgoorlie and Kurnalpie Terrane supports the hypothesis that these structures play a crucial role in ore deposit localization. This conclusion is consistent with previous studies conducted at the camp scale, such as St Ives (Miller et al., 2010) and Yakabindie (Perring, 2016), as well as with interpretations presented in Doutre (2017). These studies suggest that oblique-orogen basement structures were either incipiently reactivated and upward-propagated through overlying c. 2720-2690 Ma greenstones; or remained inactive but controlled the segmentation and geometry of transfer zones along orogen-parallel upper to mid-crustal shear zones during the structural inversion that occurred between c. 2690 and 2650 Ma.

## 6 Conclusion

The identification and mapping of the fundamental early architecture of the deep crust is crucial for explorers to enhance their predictive capability. In the Yilgarn Craton, we identify strike-extensive lineaments, some of which appear oblique to the main structural grain established during tectonic assembly. We propose that this architecture developed between c. 2720 and 2690 Ma during lithospheric thinning, forming the critical early architecture that controlled the emplacement of tier-1 gold deposits in the region during c. 2690-2650 Ma basin inversion. Although the geological and structural expression of such architecture may be cryptic, the multidisciplinary workflow developed in this study provides a toolbox that can help validate its occurrence at the craton scale.

## Acknowledgements

The authors acknowledge support from the Minerals Research Institute of Western Australian, Northern Star Resources Ltd, Gold Road Resources Ltd, BHP - Nickel West Pty Ltd, Evolution Mining Ltd, Gold Fields Australia Ltd, and Bogada Gold Ltd under the MRIWA collaborative research project M0530 Yilgarn 2020.

## References

Bahiru, E.A., Rowland, J.V., Eccles, J., kellett, R.L., 2019. Regional crustal-scale structural control on epithermal deposits within the Hauraki Goldfield, Coromandel Volcanic Zone, New Zealand: insight from integrated geological and aeromagnetic structural patterns. New Zealand Journal of Geology and Geophysics 62

Holdsworth, R.E., Stewart, M., Imber, J., Strachan, R.A., 2001. The structure and rheological evolution of reactivated continental fault zones: a review and case study. Geological Society of London Special Publication 184:115–137.

Doutre R (2018) Multi-scale organisation and geological controls on large orogenic gold deposits. Doctoral Thesis, 10.26182/5bb2bacd25b5c

Hayman PC, Thébaud N, Pawley MJ, Barnes SJ, Cas RAF, Amelin Y, Sapkota J, Squire RJ, Campbell IH, Pegg I (2015) Evolution of a ~2.7 Ga large igneous province: a volcanological, geochemical and geochronological study of the Agnew Greenstone Belt, and new regional correlations for the Kalgoorlie Terrane (Yilgarn Craton, Western Australia). Precambr. Res. 270:334–368.

Hronsky JMA, Groves DI, Loucks RR, Begg GC (2012) A unified model for gold mineralisation in accretionary orogens and implications for regional-scale exploration targeting methods. Mineralium Deposita 47:339–358.

Love DA, Clark AH, and Glover JK (2004), The lithologic, stratigraphic, and structural setting of the giant Antamina copper-zinc skarn deposit, Ancash, Peru: Economic Geology, 99:887–916.

Miller J, Blewett R, Tunjic J, Connors K (2010) The role of early formed structures on the development of the world class StIves Goldfield, Yilgarn, WA. Precambrian Res.183,292–315.

Mole DR, Fiorentini ML, Cassidy KF, Kirkland CL, Thébaud N, McCuaig TC, Doublier MP, Duuring P, Romano SS, Maas R, Belousova EA, Barnes SJ and Miller J (2013) Crustal evolution, intra-cratonic architecture and the metallogeny

of an Archaean craton, Geological Society, London, Special Publications, 393
Mole DR, Kirkland CL, Fiorentini ML, Barnes SJ, Cassidy KF, Isaac C, Belousova EA, Hartnady M, Thébaud N (2019) Time-space evolution of an archean craton: a Hf-isotope window into continent formation. Earth-Science Rev. 196, 102831.
Perring CS, (2016) Yakabindie revisited – volcanological and structural controls on the komatiite-hosted Six Mile Well and Goliath North deposits and implications for the architecture of the 2.7 Ga rift event in the Agnew-Wiluna belt, Yilgarn Craton, Western Australia. Econ. Geol. 111:1159-1185.
Wiemer D, Hagemann, SG, Hronsky J, Kemp AIS, Thébaud, N, Ireland T, Villanes C 2022 Ancient structural inheritance explains gold deposit clustering in northern Perú. Geology 50/10:1197-1201

# Mineralogy and geochemistry of the A2 and New A2 gold deposits in the Nwe Yon–Kwinthoneze gold district, central Myanmar

**Aung Myo Thu[1,2], Adam Piestrzyński[1], Gabriela A. Kozub-Budzyń[1], Krzysztof Foltyn[1]**
*[1]Faculty of Geology, Geophysics and Environmental Protection, AGH University of Science and Technology in Krakow, Poland*
*[2]Department of Geology, Mandalay University, Myanmar*

**Abstract.** The A2 and New A2 gold deposits are located in the New Yon-Kwinthoneze gold district in central Myanmar. The ore bodies are primarily hosted in marble and gneiss, and the contact between these two host rocks. The principal ore minerals are pyrite, chalcopyrite, sphalerite, pyrrhotite, marcasite, native gold, and telluride assemblages. Native gold occurs as fissure filling, inclusions in sulphide minerals, and Au-Ag-Te associations. Gangue minerals are mostly quartz, calcite, siderite, ankerite, W-bearing rutile, and minor chlorite. The wall-rock hydrothermal alterations include silicification and carbonatization. C-O isotopic compositions suggest that the ore-forming fluids were most likely derived from magma with limited contributions from the host rocks and later mixed with the meteoric water. The $\delta^{34}S$ values of sulphides from the A2 and New A2 deposits are consistent with a homogeneous magmatic source. The analyses of S, C, and O isotopic data suggested that the ore-forming fluids were mainly derived from the magmatic fluids and later mixed with meteoric water in the ore-forming process.

## 1 Introduction

In the last two decades, intrusion-related gold systems have been considered separately from orogenic gold systems (Thompson and Newberry 2000; Baker 2002; Hart and Goldfarb 2005). However, the distinction between these two gold systems remains a subject of debate because of many similarities (e.g., Sillitoe and Thompson 1998; Hart and Goldfarb 2005). Myanmar has more than 300 gold occurrences, including intrusion-related gold deposits (IRGDs), orogenic gold deposits (OGDs), and skarn type Au-(Cu) deposits (Swe et al. 2017).

The Mogok Metamorphic Belt (MMB) is one of the most important metallogenic belts in Myanmar (e.g., Zaw 2017), and gold is by far the most important mineral product after gemstones (Mitchell 2017). The Nwe Yon-Kwinthoneze gold district is located in the middle segment of the MMB and contains two significant economic orebodies (i.e., A2 and New A2 deposits). Artisanal mining started in at least the 1980s, and more recently, commercial-scale underground mining developed in this gold district (Mitchell 2017). However, the total gold reserves and the resources are not available. There are two viewpoints on the genesis of the Nwe Yon-Kwinthoneze gold district: (1) epithermal and skarn affinity (Myint et al. 2014) and (2) epizonal orogenic gold deposit (Myint et al. 2022).

In this paper, we present a detailed investigation of geological, mineralogical, and stable (C, O, S) isotopic studies conducted to determine the possible sources of the ore-forming fluid and the genesis of the A2 and New A2 deposits in the Nwe Yon – Kwinthoneze gold district.

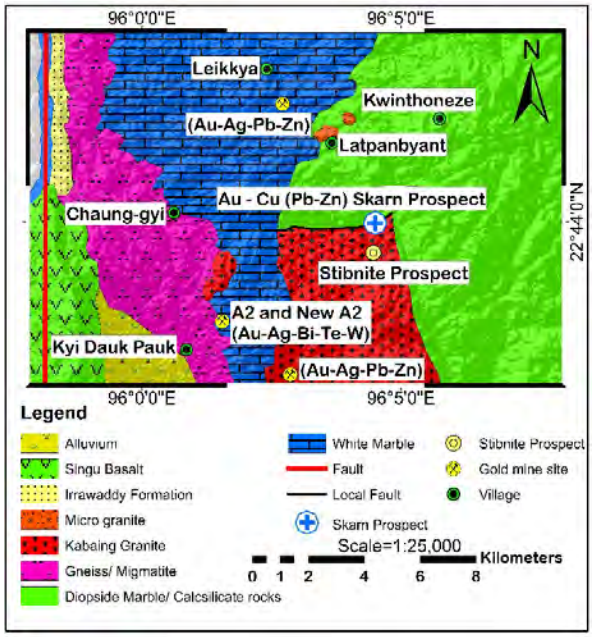


**Figure 1.** Geological map of the Nwe Yon-Kwinthoneze gold district (modified after Lamont et al. 2021).

## 2 Geological setting

Myanmar can be divided geologically into two parts: eastern and western provinces, which were separated by the 1200 km long north-south trending, dextral strike-slip Sagaing fault. The eastern province is a part of the Sibumasu Block and the western province is the West Burma Block. The MMB is located between Sibumasu Block and West Burma Block. It contains Jurassic to Early Cretaceous subduction-related magmatism and was exhumed by compressional deformation during the Tertiary metamorphic event (Searle et al. 2007).

The ore-hosting rocks in the Nwe Yon-Kwinthoneze gold district are dominated by the Mogok Metamorphic groups of migmatitic biotite gneiss, biotite-gneiss, garnet-biotite migmatite, white marble, diopside marble, phlogopite marble, and calc-silicates, which were intruded by Kabaing granite and minor micro-granite to the east of the Sagaing Fault (Figure 1). The Kabaing granite is the

largest intrusive body in this gold district. The age of the granite is constrained by zircon U-Pb ages of 16.8±0.5 Ma near the Mogok Valley to the north of the study area (Gardiner et al. 2016). Minor occurrences and thin (less than 15 cm wide) pegmatite dykes crosscut the Kabaing granite and biotite-rich hornfels near the Zee Phyu Kone skarn formation (Thu et al. 2022). The high-grade Mogok metamorphic groups are unconformably overlain by the Late Miocene-Pliocene Irrawaddy Formation and Singu Quaternary trachybasalt in the southern part of the study area (Figure 1). The metamorphism in this segment has been dated by using the monazite U-Pb method on migmatites from the Kyi-Tauk-Pauk gold mining area. It shows an early high-grade granulite event at 43–32 Ma and a later, upper amphibolite facies, sillimanite-grade event peaking at 23–20 Ma (Lamont et al. 2021).

The A2 and New A2 gold deposits are situated in the Nwe Yon – Kwinthoneze gold district. The host rock geology of these deposits is similar, primarily comprising marble and gneiss, and the contact between these two host rocks. The currently known A2 and New A2 Au-ore segments contain more than 16 auriferous quartz veins of NNE striking, parallel gold lodes, with a spacing of 40–50 m. Individual gold lodes strike between 10° and 35°, dipping 40° to 60° northeast, and parallel to the metamorphic foliations of the host rocks. Each lode is typically 50–150 m long and 0.5–1 m wide, locally wedged out along fracture zones, and shows typical pinch-and-swell features. The structure of the A2 and New A2 deposits are dominated by NE–SW trending compressional–shear faults. The primary contact between marble and gneiss, the A2 and New A2 shear zones, formed due to the rheological differences. The gold orebodies are characterized by sulphide-quartz-carbonate veins, disseminated, and massive sulphides. The principal ore minerals in the A2 and New A2 deposits are pyrite, chalcopyrite, sphalerite, pyrrhotite, marcasite, native gold, and telluride assemblages. Gangue minerals are mostly quartz, calcite, siderite, ankerite, W-bearing rutile, and minor chlorite.

The A2 and New A2 ore bodies have the same wall-rock hydrothermal alteration, mainly silicification and carbonatization. Silicification is the most widespread and significant alteration along the quartz veins in the host rocks (gneiss and marble). It is closely related to gold mineralization. Carbonatization is also common, with euhedral–subhedral carbonate minerals such as calcite and siderite occurring in veins and veinlets.

## 3 Analytical techniques

Detailed textural observation and preliminary mineral identification were performed using optical microscopy and EPMA (JEOL 8230) at the laboratory of Critical Elements AGH-KGHM at AGH-UST. Sulphur, Carbon, and Oxygen isotopes were analysed at the Laboratory of Petroleum Geochemistry at AGH University of Science and Technology, Krakow.

## 4 Results

### 4.1. Selected ore mineralogy

Pyrite, the most abundant sulphide phase, is the major host for gold and telluride minerals in the A2 and New A2 deposits. It forms at every stage of mineralization and usually occurs as euhedral to anhedral grains. The largest crystals, ranging from coarse to medium-grained (sizes ranging from 100 µm to 3 mm), have a porous, spongy texture and are commonly filled with sulphide minerals and native gold (Figure 2A).

Chalcopyrite and sphalerite are primarily subhedral to anhedral minerals that replace the gold-hosting pyrite and/or fracture fill within micro-fissures in pyrite (Figure 2A, B). Minor pyrrhotite inclusions are observed in chalcopyrite (Figure 2C).

Two types of gold occurrences were observed in the A2 and New A2 deposits. Native gold independently occurs as fissure filling, inclusions in sulphide minerals, and Au-Ag-Te associations (Figure 2A, B). The telluride minerals are petzite, hessite, tellurobismuthite, altaite, melonite, coloradoite, and mettagamite. Gold is widespread and exists as irregular grains, typically along the grain boundaries or as a filling of microfractures in quartz, pyrite, chalcopyrite, and telluride minerals.

Petzite is closely associated with gold and hessite (Figure 2B). Individual grains range in size from 5 to 100 µm. The EPMA analysis of some petzite grains shows a lower Au content (19.91-28.81 wt.%;) compared to ideal petzite (25.39 wt.%;), and its formula based on average composition is calculated as $Ag_{2.87-3.45}Au_{0.78-1.12}Te_{1.56-2.03}$.

Hessite frequently coexists with petzite, altaite, and native gold in the form of medium- to fine-grained, irregular grains and is also observed as cluster inclusions in pyrite. Hessite contains 60.03-60.40 wt.% Ag and 35.56-39.38 wt.% Te, with its calculated chemical formula as $Ag_{1.89-2.0}Te_{0.95-1.05}$.

Tellurobismuthite is less abundant than petzite and hessite, and it was observed as lath-shaped crystals that overprinted the hessite (Figure 2C). It has 50.55-50.36 wt.% Bi and 46.41-46.79 wt.% Te. Its chemical formula can be expressed as $Bi_{1.94-2.01}Te_{2.92-2.95}$.

Altaite is grey-white and less abundant than Au-Ag tellurides. It occurs commonly along the edge of or as inclusions in pyrite and chalcopyrite and is also closely associated with pyrrhotite and hessite (Figure 2D). Altaite contains 58.25 to 59.94 wt.% Pb, 36.56 to 37.26 wt.% Te (n = 5). The calculated general formula of altaite is $Pb_{0.91-1.19}Te_{0.75-0.95}$.

Melonite is the only Ni-telluride mineral detected in the A2 gold deposit. It is observed as inclusion and associated with hessite in chalcopyrite (Figure 2D). It contains 17.93 to 18.41 wt.% Ni, 81.40 to 82.37 wt.% Te, and a trace amount of Ag (0.19 wt.%), Bi (0.15 wt.%), and Sb (0.50 wt.%) on average (n = 3).

The general formula of melonite is $Ni_{0.93-0.97}Te_{1.95-1.99}$.

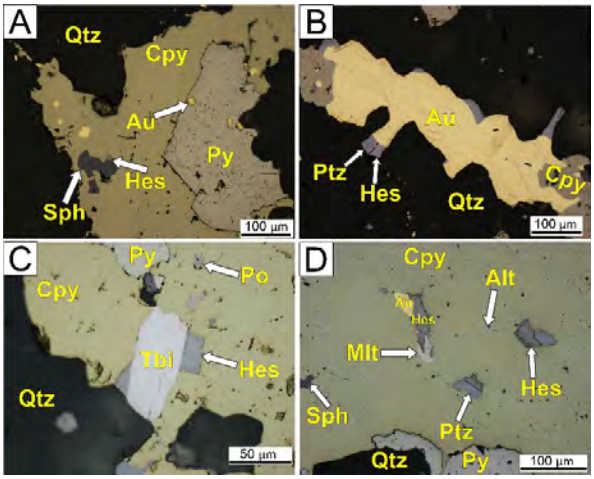


**Figure 2.** Representative gold-telluride mineralization of the A2 and New A2 gold deposits. Py-pyrite, Cpy-Chalcopyrite, Po- Pyrrhotite, Sph- Sphalerite, Au- Native gold, Hes- Hessite, Ptz- Petzite, Mlt- Melonite, Alt- Altaite, Tbi- Tellurobismuthite, Qtz- Quartz.

### 4.2 Carbon, oxygen, and sulphur isotopic compositions

The carbon and oxygen isotopic compositions of five calcite samples from the quartz-carbonate veins of the A2 and New A2 deposits, together with the Zee Phyu Kone Au-Cu-(Pb-Zn) skarn prospect (Thu et al. 2022), and local gold prospects around these deposits (unpublished data), are illustrated in Figure 3. The $\delta^{13}C_{PDB}$ values of calcite grains from the quartz-carbonate veins of the A2 and New A2 deposits range from -4.5 to 2.6‰, with $\delta^{18}O_{PDB}$ values of -17.2‰ to -12.3‰, and calculated $\delta^{18}O_{SMOW}$ values are in the range of 13.1‰ to 18.2‰.

The sulphur isotope compositions of six pyrite, six chalcopyrite, and three sphalerite samples from the A2 and New A2 deposits are illustrated in Figure 4. The auriferous $\delta^{34}S$ values of pyrite range from 2.1 to 3.4‰, chalcopyrite from 2.1 to 2.7‰, and those of sphalerite from 1.6 to 2.6‰, respectively.

## 5 Discussion

Hydrothermal calcite precipitation is generally controlled by fluid mixing, $CO_2$ degassing, and fluid-rock interactions (Zheng and Hoefs 1993). In the $\delta^{13}C_{PDB}$ vs. $\delta^{18}O_{SMOW}$ diagram, one wall rock sample from this gold district falls into the meta-carbonate field, and all of the hydrothermal calcite shows a depletion trend, which is evidence of the fluid-rock interaction (e.g., Bowman et al. 1985). All hydrothermal calcite samples from the Nwe Yon-Kwinthoneze area have $^{13}C$ values lower than seawater (0‰; Ohmoto and Goldhaber 1979), much higher than reduced carbon in sedimentary or metamorphic rocks (-25‰; Hoefs 2015), and close to magmatic fluids and/or mantle $CO_2$ (-7 to -2‰; Deines and Gold 1973). All of the samples fall into the field between within or close to the metasedimentary carbonate field to the meteoric water field in the late ore-forming stage (Figure 3), which is distinct from marine carbonate and organic matter, indicating that the carbon in the calcite perhaps was related to deep-seated magma or a mixed crustal source with limited contribution from the host rocks. The ore-forming fluids most probably experienced the involvement of meteoric water in the late stage. So, the primary source of carbon for the Nwe Yon-Kwinthoneze gold district was magmatic-hydrothermal.

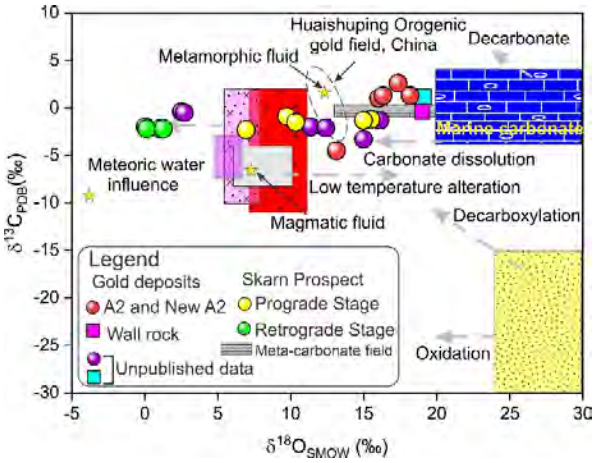


**Figure 3.** Carbon and oxygen isotopic compositions of calcite from the Nwe Yon-Kwinthoneze gold district comparison with the most known rock types (mineralising fluid and Huaishuping orogenic gold field are adapted from Wang et al. 2021).

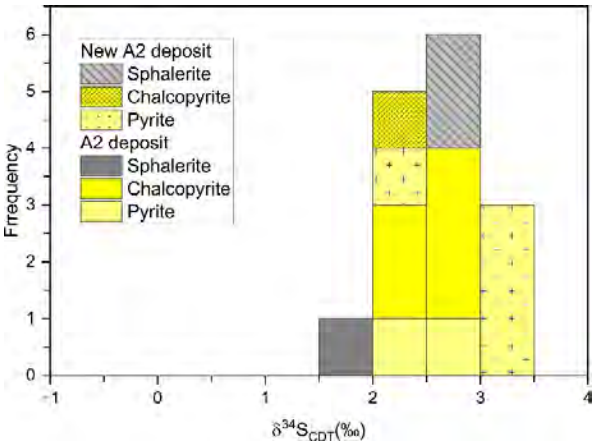


**Figure 4.** Sulphur isotope of the sulphides from the A2 and New A2 gold deposits.

The $\delta^{34}S$ values of sulphides from the A2 and New A2 deposits range from 1.6‰ to 3.4‰ (mean = 2.5; n= 15), which is consistent with many magmatic deposits with $\delta^{34}S$ values of -3‰ to +3‰ (Hoefs 2015). Furthermore, the uniformity of $\delta^{34}S$ values of sulphides indicates that the sulphur sources may be the same and are of the homogeneous magmatic sulphur source (Ohmoto and Goldhaber 1979).

Many telluride-rich gold deposits are associated with alkaline igneous rocks (e.g., Ciobanu et al. 2010) and tellurium is transported preferentially in the gaseous phase in magmatic fluids (Cooke &

McPhail 2001). Based on previous geochronological data of ore-hosting metamorphic rocks (23–20 Ma, Lamont et al. 2021) and the timing of magmatic intrusion (16.8±0.5 Ma, Gardiner et al. 2016), the gold-telluride mineralization of the A2 and New A2 deposits is thought to have resulted from the Kabaing granite intrusion. The analyses of S, C, and O isotopic data also showed that the ore-forming fluids mainly derived from the magmatic fluids and later mixed with meteoric water during the ore-forming process. Therefore, based on mineral assemblages, and C-O-S isotopic data, the A2 and New A2 deposits of the Nwe Yon-Kwinthoneze gold district can be classified as intrusion-related gold deposits. Moreover, metal zonation and a temporal and/or spatial relationship with I-type granite (Kabaing granite) with evidence of hydrothermal fluid generation (Zee Phyu Kone Au-Cu-(Pb-Zn) skarn alteration), which is typical of the intrusion-related gold deposits (Sillitoe and Thompson 1998; Lang et al. 2000), could be found (Figure 1).

## 6 Conclusions

(1) Orebodies of the A2 and New A2 deposits are primarily hosted in marble, gneiss, and contact between these two rocks. The principal ore minerals are pyrite, chalcopyrite, sphalerite, pyrrhotite, native gold, and telluride assemblages: petzite, hessite, tellurobismuthite, altaite, melonite, coloradoite, and mettagamite.
(2) C-O isotopic compositions suggest that the ore-forming fluids were most likely derived from magma with limited contributions from the host rocks and later mixed with the meteoric water into the ore-forming process. The sulphur isotopic compositions of the A2 and New A2 are homogeneous and indicative of a magmatic source of sulphur.
(3) Based on the mineral assemblages, and C-O-S isotopic data, the A2 and New A2 deposits of the Nwe Yon-Kwinthoneze gold district can be classified as intrusion-related gold deposits.

## Acknowledgments

This study was financially supported by UNESCO-AGH and the Newmont Mining Corporation Fund of the Society of Economics Geologists.

## References

Baker T (2002) Emplacement depth and carbon dioxide-rich fluid inclusions in intrusion-related gold deposits. Econ Geol 97:1111-1117.

Bowman JR, O'Neil JR, & Essene EJ (1985) Contact skarn formation at Elkhorn, Montana; II, Origin and evolution of COH skarn fluids. American Journal of Science, 285:621-660.

Ciobanu CL, Birch WD, Cook NJ, Pring A & Grundler PV (2010) Petrogenetic significance of Au–Bi–Te–S associations: the example of Maldon, Central Victorian gold province, Australia. Lithos, 116:1-17.

Cooke DR & McPhail DC (2001) Epithermal Au-Ag-Te mineralization, Acupan, Baguio district, Philippines: numerical simulations of mineral deposition. Econ Geol, 96:109-131.

Deines P & Gold DP (1973) The isotopic composition of carbonatite and kimberlite carbonates and their bearing on the isotopic composition of deep-seated carbon. Geochimica et Cosmochimica Acta, 37:1709-1733.

Gardiner NJ, Robb LJ, Morley CK, Searle MP, Cawood PA, Whitehouse MJ, Kirkland CL, Roberts NM., Myint TA (2016) The tectonic and metallogenic framework of Myanmar: a tethyan mineral system. Ore Geol Rev 79, 26–45.

Hart CJR & Goldfarb RJ (2005) Distinguishing intrusion-related from orogenic gold systems. In New Zealand Minerals Conference Proceedings (Vol. 2005, pp. 125-133).

Hoefs J (2015) Stable Isotope Geochemistry, (Vol. 2015, pp. 1–389). Switzerland.

Lamont TN, Searle MP, Hacker BR, Htun K, Htun KM, Morley CK, White RW (2021) Late Eocene-Oligocene granulite facies garnet-sillimanite migmatites from the Mogok Metamorphic belt, Myanmar, and implications for timing of slip along the Sagaing Fault. Lithos, 386, 106027.

Lang JR, Baker T, HART CJ & Mortensen JK (2000) An exploration model for intrusion-related gold systems. SEG Discovery, 40:1-15.

Mitchell AHG (2017) Geological Belts, Plate Boundaries and Mineral Deposits in Myanmar. Elsevier.

Myint TA, Than TN, Min A (2014) Precious and Base Metal Mineralization in Kwinthonze-Nweyon area, Singu, and Thabeikkyin Townships, Mandalay Region, Myanmar. Proc. Sundal. Resources. Indonesia.

Myint, AZ, Wagner T & Zaw K (2022) Telluride-bearing Au-Ag mineralization in the Singu-Tabeikkyin gold District, Mogok metamorphic Belt, Myanmar: New constraints on an intermediate-sulfidation epizonal orogenic ore system. Journal of Asian Earth Sciences, 227, 105120.

Ohmoto H, Rye RO (1979) Isotopes of sulphur and carbon. In: Barnes HL (ed) Geochemistry of hydrothermal ore deposits. Wiley, New York, pp 509–567.

Searle MP, Noble SR, Cottle JM, Mitchell AHG, Hlaing T, Horstwood MSA (2007) Tectonic evolution of the Mogok metamorphic belt, Burma (Myanmar) constrained by U-Th-Pb dating of metamorphic and magmatic rocks. Tectonics 26, TC3014.

Sillitoe RH, & Thompson JF (1998) Intrusion–Related Vein Gold Deposits: Types, Tectono-Magmatic Settings and Difficulties of Distinction from Orogenic Gold Deposits. Resource Geology, 48:237-250.

Swe YM, Aye CC & Zaw K (2017) Chapter 25 Gold Deposits of Myanmar. Geological Society, London, Memoirs, 48: 557-572.

Thompson JF & Newberry RJ (2000) Gold deposits related to reduced granitic intrusions. Econ Geol, v. 13, p. 377–400.

Thu AM, Piestrzyński A, Foltyn K, Kozub-Budzyń G (2022) Formation of the Zee Phyu Kone Au-Cu (Pb-Zn) skarn mineralization in the Mogok Metamorphic Belt, Central Myanmar: Insights from mineral chemistry and C-O-S isotopes. In: Christie AB (ed.) Proceedings of the 16th SGA Biennial Meeting, 28-31 March 2022, 1:384-387.

Wang C, Deng J, Bagas L, He X, Zhang J (2021). Origin and classification of the Late Triassic Huaishuping gold deposit in the eastern part of the Qinling-Dabie Orogen, China: implications for gold metallogeny. Miner Depos, 56, 725-742.

Zaw K (2017) Overview of mineralization styles and tectonic metallogenic setting in Myanmar. In Barber AJ, Zaw K and Crow MJ (eds.) Myanmar: Geology, resources, and tectonics, Geological Society Memoirs 48, London.

Zheng YF & Hoefs J (1993) Carbon and oxygen isotopic covariations in hydrothermal calcites: Theoretical modelling on mixing processes and application to Pb-Zn deposits in the Harz Mountains, Germany. Miner Depos, 28, 79-89.

# Spatial distribution and structural control on gold mineralisation in the Barberton Greenstone Belt (South Africa, Eswatini)

**Laurine Travers[1,2], Jérémie Lehmann[2], Alain Chauvet[1]**
*[1] Géosciences Montpellier, University of Montpellier, CNRS, France*
*[2] Department of Geology, University of Johannesburg, South Africa*

**Abstract.** The Barberton Greenstone Belt (BGB) contains over 350 gold occurrences and an estimated production of 342 tons, mainly from Fairview, New Consort, Sheba and Agnes mines. Many studies target these active mines to understand gold mineralisation. This study focuses on the distribution and structural control of hydrothermal veins, including in old mining areas and low-grade gold occurrences. The gold-bearing event is studied using spatial statistical analysis combined with structural field geology and mineralogical analysis. The hydrothermal/gold occurrences are distributed in several clusters. Two main tectonic events are involved in the formation of hydrothermal veins. A main deformation event related to large-scale folding and thrusting controls emplacement of gold-bearing veins during a single or pulsed NW-SE shortening in the northern BGB, and during an E-W shortening in the southern BGB. A late deformation event, produced by NE-SW shortening in the southern BGB is also related to late hydrothermal quartz veins. Quartz-carbonate veins are found in the northern mineralised system, whereas quartz-tourmaline-feldspars-carbonate +/- sulfides veins are present mainly in the southern BGB. The mineralised event in the BGB is structurally controlled by the main NW-SE to E-W shortening whereas additional quartz systems, not mineralised, seem to be controlled by an enigmatic NE-SW shortening.

## 1 Introduction

The Barberton Greenstone Belt in South Africa and Eswatini is a typical Archean belt with over 350 gold occurrences and has an estimated production of 342 tons of gold (Anhaeusser 2019), mainly extracted from the Fairview, Sheba, New Consort and Agnes mines. These mines are located in the northern BGB, mainly in a complex fold and thrust zone. Nevertheless, hundreds of lower grade, poorly studied, gold occurrences occur elsewhere within the belt. These occurrences may represent significant information for the formation mode of the gold-bearing event and its spatial distribution at the belt scale.

**Figure 1.** Location of the Barberton Greenstone Belt and geological map (modified from the metallogenic map Council for Geoscience 2000) with gold occurrences and extracted Kernel Density map (blue is high density, white is low density).

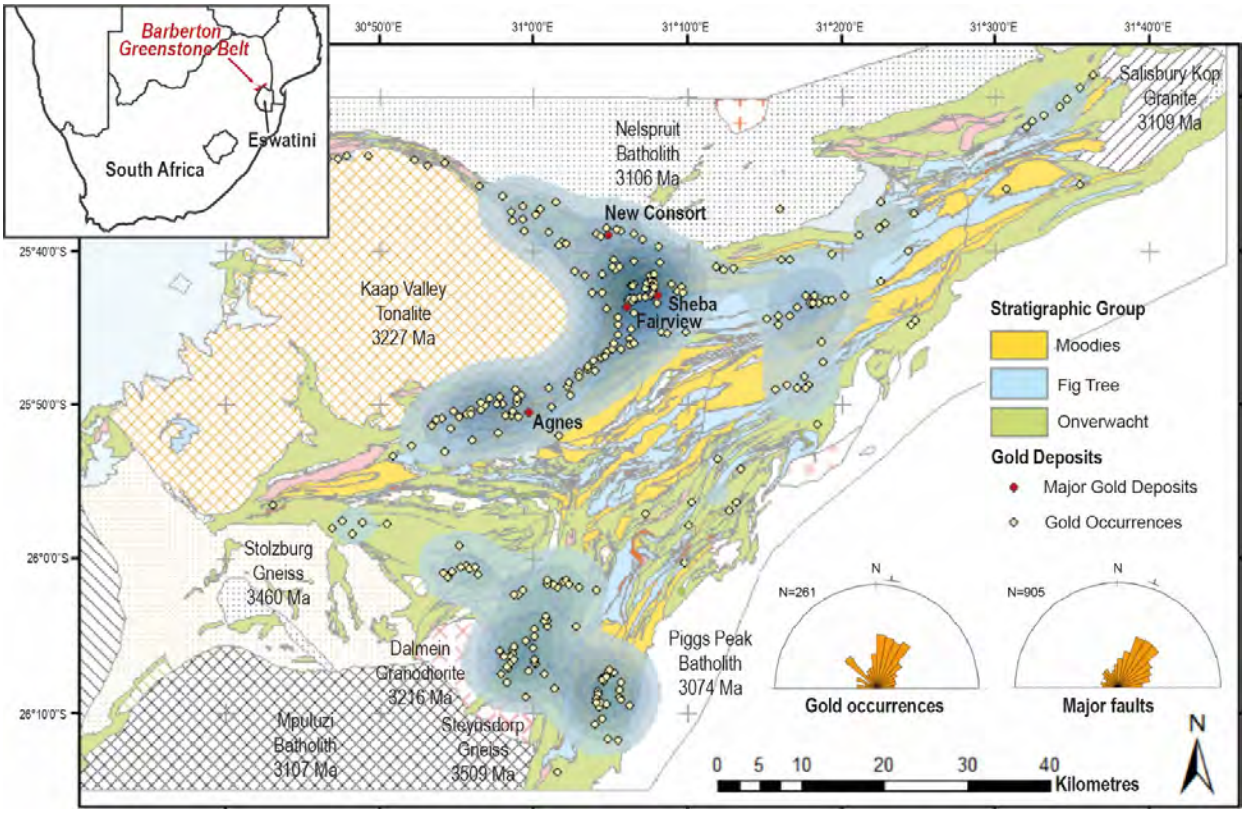

This study aims to establish the structural framework of the multiple gold occurrences within the Barberton Greenstone Belt. The objective is to understand the gold forming event and its potential link with regional deformation and magmatism. A detailed structural, microstructural and mineralogical analysis leads to propose a model for the tectonic-hydrothermal evolution of the study area. This model suggests that gold-bearing quartz veins formed during the shortening of the entire belt and perhaps involves the role of some neighbouring granites. The structural characterisation of the Archean gold event in the Barberton Greenstone Belt allows for a better understanding of the formation of Archean gold deposits and of Archean geodynamics.

## 2 Geological setting

The Barberton Greenstone Belt (BGB), in South Africa and Eswatini, is located in the eastern part of the Kaapvaal Craton. It is composed of volcano-sedimentary units surrounded by variably gneissic TTG rocks (Tonalite-Trondhjemite-Granodiorite), in turn intruded by granite batholiths. The stratigraphic succession of the BGB shows three main units named, from bottom to top: Onverwacht, Fig Tree and Moodies groups (Lowe and Byerly 2007, Figure 1). The Onverwacht Group (3.55 to 3.29 Ga) is mainly a mafic to ultramafic meta-volcano-sedimentary series. The Fig Tree Group (3.26 to 3.22 Ga) is formed by calc-alkaline lavas and detrital rocks. Lastly, the Moodies Group (3.22 to 3.21 Ga) represents the upper detrital series. The architecture of the BGB seems to be the result of several contraction events mainly oriented NW-SE (De Ronde and de Wit 1994).

Over the 350 gold occurrences in the BGB (Barberton 1:100,000 metallogenic map, Council for Geoscience, 2000), the most studied and best-known ones are the active Fairview, Sheba and New Consort mines, which are all located in the northern BGB (Figure 1). The numerous other gold occurrences are mainly former mines and mining exploration areas which few have been the subject of in-depth studies, which will be the focus of this study.

Overall, there are two opposing theories on the interpretation of the Barberton gold mineralisation, it may have formed during: i) a late phase of regional extension (Otto et al. 2007; Dziggel et al. 2010), which postdates the tectonic and thermal stabilisation of the belt (Dirks et al. 2013), or ii) a late NW-SE shortening episode (Gloyn-Jones and Kisters 2019; Jones and Kisters 2022; Cerdas et al. 2022).

Several ages for the mineralisation have been published. At New Consort, the mineralisation has been dated at ca. 3027 ± 7 Ma (Dziggel et al. 2010), which is consistent with the age between 3009 ± 16 Ma and 3017 ± 18 Ma obtained at Golden Quarry (Dirks et al. 2013), but younger than the 3084 ± 18 Ma obtained at Fairview (de Ronde et al. 1991). Thus, the ages of the gold mineralisation appear to be spread over a long period of time (i.e., 100 Myr), suggesting that several mineralising episodes of different nature may co-exist, and/or that the dating of the mineralisation is not well constrained.

## 3 Distribution of the gold occurrences

The predictive spatial analysis was carried out by digitisation of the Barberton 1:100,000 metallogenic map (Council for Geoscience, 2000) and all the gold occurrences and their characteristics (i.e., orientation, size, morphology, mining status, name) were imported and processed in a GIS platform (ArcGIS Pro).

Several methods of analysis were performed to investigate the distribution of gold occurrences according to their host stratigraphy, regional structures, density and gold grade. The weight of evidence analysis has shown that stratigraphy was not the major factor controlling the spatial occurrence of gold. The Kernel density map of the occurrences shows that the occurrences are distributed within four main clusters: Barberton, Steynsdorp, Malolotja, and Barbrook areas (Figure 1). The Inverse Distance Weighting interpolation map shows that the deposits have a higher tonnage along the northern flank of the belt. Overall, the angular difference between the trend of occurrences as extracted from the 1:100,000 scale map and the strike of the nearest fault is rather small (55% of the gold occurrences have an angular difference smaller than 20°), suggesting that the BGB gold occurrences may be structurally controlled. This hypothesis has been tested through detailed field structural geological analysis as summarised below.

## 4 Structural control of the hydrothermal and gold mineralisation events

### 4.1 Regional deformation

In the field, we observe three schistosities which were defined according to their mutual overprinting relationships Se (early), Sm (main) and Sl (late). The schistosity Se is defined by aligned small micas and talc sheets, and is steep and E-W to NW-SE striking. It is often observed folded by Fm folds with N-S striking axial planes in the southern BGB and NE-SW-striking ones in the northern BGB. The schistosity Sm is axial planar to Fm folds. Sm is very prominent throughout the entire belt. Petrographic observations reveal that Sm is marked by the alignment of small micas sheets. In a few areas, especially in the south, Sm is commonly folded into Fl folds with steep NW-SE axial planes. The last schistosity Sl is axial planar to Fl fold and is mostly observed in the southern BGB. Sl is defined in microscopy by the alignment of micas (Figure 2a, b and c).

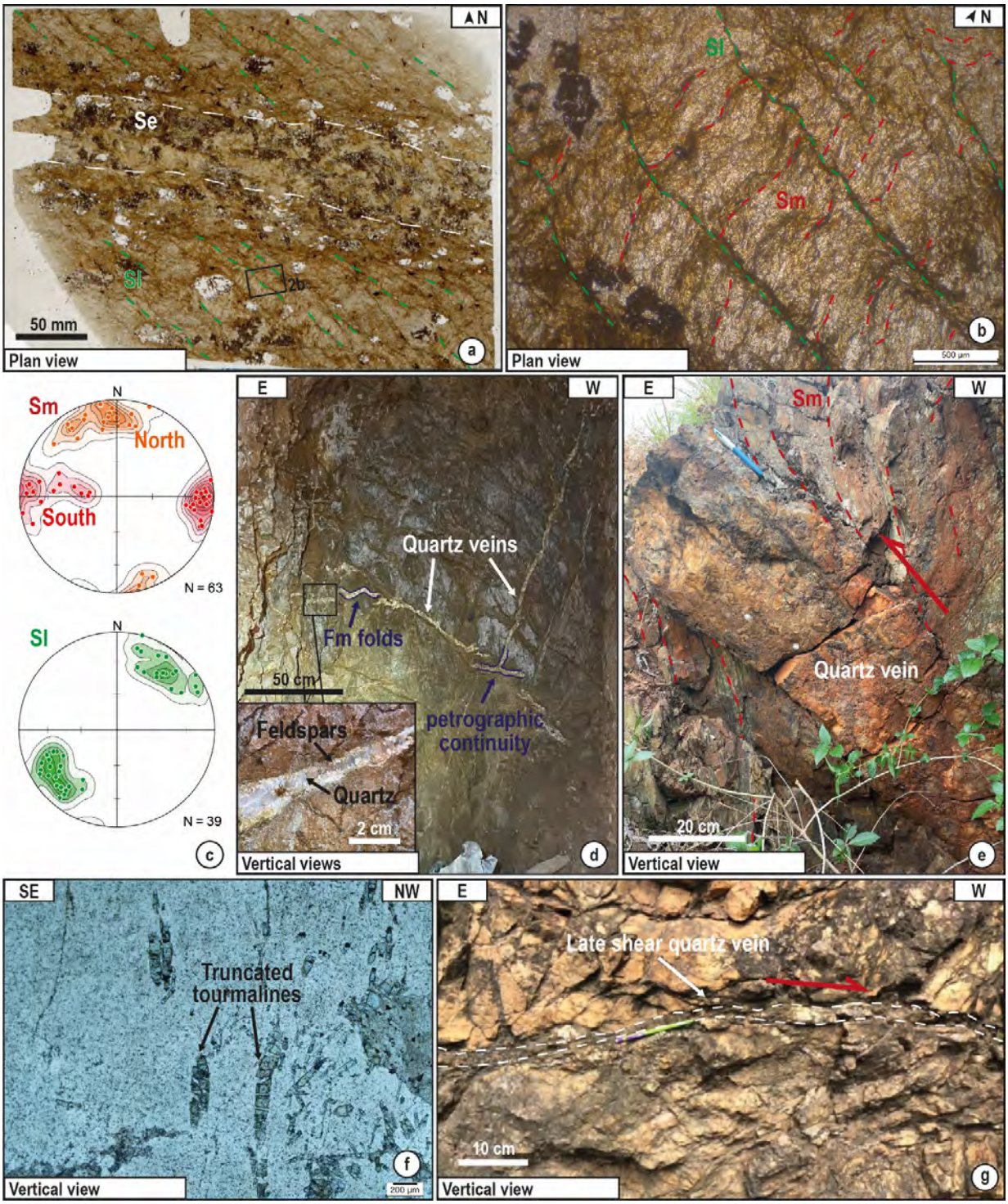


**Figure 2. a** Thin section scan of a sample showing the overprinting relations between Se and Sl. **b** Close up of photo a, with Sm deformed by Sl. **c** Equal-area lower hemisphere projections of Sm and Sl as pole to planes throughout the belt. **d** Field photo of synchronous shallow-dipping folded and steep quartz veins. Inset is a close up view on the quartz-feldspar vein. **e** Photo of a quartz vein located in a shear zone with a reverse motion as seen by the drag folds of the schistosity Sm. The quartz vein is internally brecciated. **f** Photomicrograph of vertical truncated tourmalines in a horizontal quartz-tourmaline vein. **g** Field photo of a late shear horizontal quartz vein.

### 4.2 Hydrothermal vein system

The mineralised system is mainly expressed by shallow-dipping and steep to vertical (Figure 2d and e) mm- to m-thick quartz veins cutting Se, and in places Sm. These two vein sets are in petrographic continuity; hence they are interpreted to form synchronously. Horizontal veins exhibit, in several places, vertical comb quartz or quartz fibres, which can be interpreted as formed by mode I opening as tension gashes resulting from horizontal shortening. In the southern BGB, the quartz veins contain

vertical tourmaline grains, which are truncated by horizontal fractures filled with vein quartz (Figure 2f), also suggesting syn-tectonic mineralisation during horizontal shortening and vertical stretching. These horizontal veins are commonly folded into open to tight buckles, with axial plane parallel to schistosity Sm. Some sub-vertical veins show reverse kinematics particularly in the Steynsdorp and Barberton areas (Figure 2e). This reverse kinematics is consistent with a Dm shortening in thrust or back-thrust (i.e., verging towards the interior of the belt) positions.

The sum of these observations demonstrates that the mineralisation event is syn- to late-Dm. This interpretation is supported by pene-contemporaneous, variably Dm-folded, sub-horizontal tension gashes and sub-vertical veins exhibiting reverse motion. The gold-bearing quartz veins are structurally controlled by the main shortening of the entire belt, which is E-W in the south and NW-SE to N-S in the north.

In several places, crosscutting quartz veins are shear sub-horizontal veins (Figure 2g) or en-echelon quartz veins. This late hydrothermal event seems to have formed by a NE-SW shortening, compatible with Dl. These veins do not appear to be mineralised.

## 5 Mineralogy

The mineralised veins are divided into two types on the basis of contrasting mineralogy. The southern vein system is composed of quartz with a variable amount of tourmaline, feldspar (albite, K-feldspar and plagioclase, Figure 2d and f) and carbonate with alteration halo composed of white mica, albite and tourmaline. Few sulfides are present – mostly pyrite and minor arsenopyrite. The northern vein system is composed of quartz and carbonate veins with a higher amount of sulfides (mostly pyrites). The alteration halo on the edges of the veins is formed by chlorite, micas, and sulfides.

The presence of tourmaline and feldspars in the southern vein system questions the origin of the mineralised fluid, i.e., magmatic-hydrothermal vs orogenic. However, as the potential impact of magmatism on the mineralised event in the southern part of the BGB is not established, this hypothesis remains presently uncertain

## 6 Conclusion

The Barberton Greenstone Belt contains numerous gold occurrences that are heterogeneously distributed throughout the belt. Some areas show higher concentration of gold occurrences, particularly around major structures such as folds and thrust zones. The hydrothermal system is characterised by complex quartz vein networks controlled by two shortening directions. The origin of the NE-SW shortening that formed the late veins is enigmatic. Although the mineralisation seems to be the result of the same structural control, mineralogical differences in the hydrothermal system between the south and the north have been identified and remain to be further explored.


## Acknowledgements

This work benefited greatly from the scientific and financial support of IRP BuCOMO team (https://bucomo.fr/). Chistoph Heubeck, Andrea Els from Barberton Adventure, Astrid Christianson and Teddy Dlamini are acknowledged for their assistance in the field.


## References


Anhaeusser CR (2019) The geology and tectonic evolution of the northwest part of the Barberton Greenstone Belt, South Africa: A review. South African Journal of Geology 122:421–454. https://doi.org/10.25131/sajg.122.0033

Cerda LP, Jones C, Kisters A (2022) The effects of fault-zone architecture, wall-rock competence and fluid pressure variations on hydrothermal veining and gold mineralization along the Sheba Fault, Barberton Greenstone Belt, South Africa. Journal of African Earth Sciences 192:104554. https://doi.org/10.1016/j.jafrearsci.2022.104554

de Ronde CEJ, de Wit MJ (1994) Tectonic history of the Barberton greenstone belt, South Africa: 490 million years of Archean crustal evolution. Tectonics 13:983–1005. https://doi.org/10.1029/94TC00353

de Ronde CEJ, Kamo S, Davis DW, et al (1991) Field, geochemical and U-Pb isotopic constraints from hypabyssal felsic intrusions within the Barberton greenstone belt, South Africa: Implications for tectonics and the timing of gold mineralization. Precambrian Research 49:261–280. https://doi.org/10.1016/0301-9268(91)90037-B

Dirks PHGM, Charlesworth EG, Munyai MR, Wormald R (2013) Stress analysis, post-orogenic extension and 3.01Ga gold mineralisation in the Barberton Greenstone Belt, South Africa. Precambrian Research 226:157–184. https://doi.org/10.1016/j.precamres.2012.12.007

Dziggel A, Poujol M, Otto A, et al (2010) New U–Pb and 40Ar/39Ar ages from the northern margin of the Barberton greenstone belt, South Africa: Implications for the formation of Mesoarchaean gold deposits. Precambrian Research 179:206–220. https://doi.org/10.1016/j.precamres.2010.03.006

Gloyn-Jones J, Kisters A (2019) Ore-shoot formation in the Main Reef Complex of the Fairview Mine—multiphase gold mineralization during regional folding, Barberton Greenstone Belt, South Africa. Miner Deposita 54:1157–1178. https://doi.org/10.1007/s00126-019-00865-9

Jones C, Kisters A (2022) Regional and local controls of hydrothermal fluid flow and gold mineralization in the Sheba and Fairview mines, Barberton Greenstone Belt, South Africa. Ore Geology Reviews 144:104805. https://doi.org/10.1016/j.oregeorev.2022.104805

Lowe DR, Byerly GR (2007) Chapter 5.3 An Overview of the Geology of the Barberton Greenstone Belt and Vicinity: Implications for Early Crustal Development. In: Developments in Precambrian Geology. Elsevier, pp 481–526

Otto A, Dziggel A, Kisters AFM, Meyer FM (2007) The New Consort Gold Mine, Barberton greenstone belt, South Africa: orogenic gold mineralization in a condensed metamorphic profile. Miner Deposita 42:715–735. https://doi.org/10.1007/s00126-007-0135-5

# Tracing gold origin: A neural network approach to trace element geochemistry

**Angel Verbel[1,2], Maria Emilia Schutesky[1], Daniel Gregory[2]**
[1]*Universidade de Brasilia*
[2]*University of Toronto*

**Abstract.** Gold grains have long been used as a vectoring tool for ore deposits, and in recent years, the combination of their geochemistry with conventional machine learning techniques has yielded encouraging results for determining their original ore deposit. Using a personalized neural network, we were able to make better predictions on the origin of individual gold grains while reducing the number of steps required in the classification process. These advances can be used as an exploration tool to constrain the possible origin of gold deposits along with the geological criteria of the target area.

## 1 Introduction

Despite the fact that techniques for integrating artificial intelligence (AI) with data science have existed since the late 1950s (Rosenblatt 1958), their use in geosciences and geochemistry has mostly occurred in the last 20 years (Farnham et al. 2002; Taylor et al. 2010; Ghannadpour et al. 2013; Cone et al. 2020; Liu et al. 2021; Liu and Beaudoin 2021). Given that geosciences applications of AI are still a relatively unexplored area, it opens up opportunities for innovation and the use of AI to comprehend intricate natural processes.

Gold geochemistry is often employed primarily as an exploratory technique to discover ore deposits. In addition to its morphology, which is connected to transportation in the basin, its chemistry is defined by physicochemical processes of formation as well as the geological framework of the deposit (McClenaghan 2005; Chapman et al. 2009; McClenaghan and Cabri 2011; Moles and Chapman 2019). Furthermore, since the 1960s, the introduction of the electron probe micro analyzer (EPMA) has made it possible to determine the chemical composition of natural gold from the diverse range of deposits that it is formed from with high degrees of precision (Rinaldi and Llovet 2015). Antweiler and Campbell (1977) revealed a connection between the temperature at which certain deposits originate and the amounts of Ag, Bi, Pb, and Cu in gold. Later, Morrison et al. (1991) determined the variations in gold fineness from different deposits. Then, Huston et al. (1992) evaluated the variations of trace elements and fineness of VMS deposits in Australia, finding that the content of trace elements in electrum depends on the complexity in the ore fluid. Later, Pochon et al. (2021) established that, given the presence of Ag, Cu, and Hg, it is feasible to distinguish legal from illegal gold that is extracted using Hg in French Guiana. Finally, Liu et al. (2021) and Liu and Beaudoin (2021) identified the chemical signature of gold in each style of deposit, with a rate of successful prediction ranging from 50 up to 97%, depending on the deposit type. They did this by using trace element geochemistry of natural gold grains from a wide variety of deposits around the world in combination with a machine learning algorithm.

## 2 Materials and methods

A total of 674 analyses of gold by EPMA were used to develop the model, these analyses were performed by Liu et al. (2021) and Liu and Beaudoin (2021), as well as 460 LA-ICP-MS for trace element analysis. These data correspond to 5 deposit types in a wide range of geological settings hosted by rocks varying in composition from mafic to sedimentary and ages varying from Archean to Neogene.

### 2.1 Data Processing

Pre-processing of the geochemical data was preformed prior to cluster analysis (Templ et al. 2008). The three datasets were pre-processed by: (1) geochemical feature selection; (2) substitution of censored (below the limit of detections) data; (3) screening missing values; (4) data transformation, to a more symmetric distribution, preserving the modes and removing skewness; and (5) standardization. A parameter was excluded from the database if it could be related through a different parameter (e.g., Fe reported as pct and ppm in this case the analysis with the higher resolution was selected) or >60% of the parameter are censored analysis with the higher resolution will be selected) or >60% of the parameter are ruled out. To process the data the package zCompositions was used in R 4.2.2 (Palarea-Albaladejo and Martín-Fernández 2015). Then the data was replaced and standardized to avoid biasing the model due to an overweight of high concentration elements like Ag. Z-scores were generated for the data set as a standardization procedure, using the following equation where z is the z-score, x is the concentration, μ is the population mean and σ something missing here is the standard deviation of the population (Guilloux et al. 2011):

$$z = \frac{x - \mu}{\sigma}$$

## 2.2 Neural network

The architecture of the neural network consists of a single hidden activation layer of 35 neurons, each of which was activated depending on the Rectified-Linear-Unit (ReLU) activation function to avoid gradient dispersion. The supervised algorithm architecture was completed with the numpy package in Python 3.9.13.

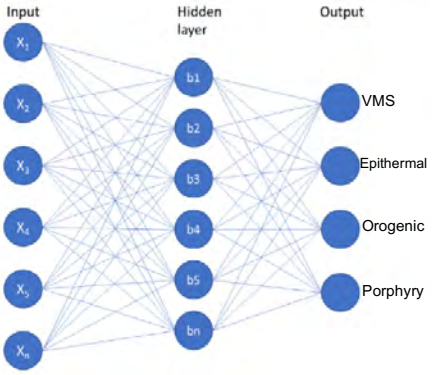


**Figure 1.** Sketch diagram of the architecture of the neural network.

## 3. Results

The first neural network used Au, Ag, Co, Cu, Fe, S, and Hg values in ppm (Figure 2A) as an input layer (normalized raw data); this data was processed with the artificial neural network, generating a total of 495 weights and biases. These results are the heart of the prediction model, since the model is generated under random initial conditions, the data presented provides reproducibility of the results when new data is presented.

Maintaining the same architecture for both models, the results were slightly improved when the LA-ICP-MS data was evaluated in all the deposits that have data with more resolution. For this analysis, the elements used were Ag, Bi, Cd, Cu, Hg, Pb, Pd, S, Sb, and Tl as shown in Figure 2B. In this case Fe was left out given the preliminary results that show that it brought noisy results, decreasing the accuracy for all the ore deposits.

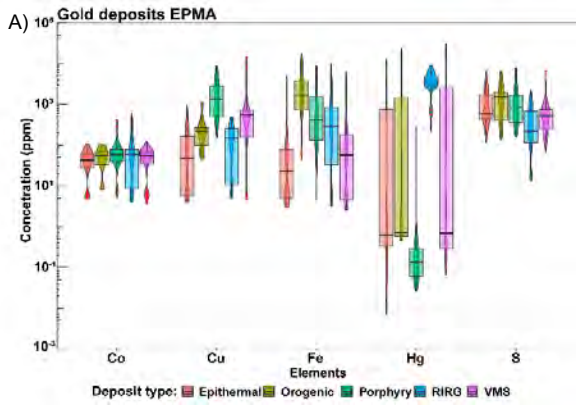


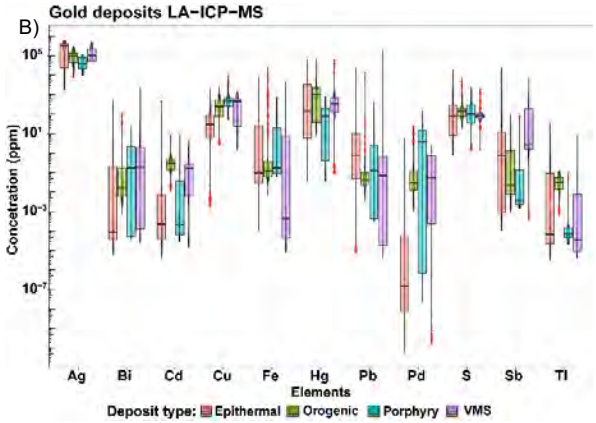


**Figure 2.** Multi-element box (25th & 75th percentile) and whisker (5th & 95th percentile) for selected elements. A) EPMA and B) LA-ICP-MS.

Testing the model with blind data (70 gold analyses randomly selected) for EPMA as well as the LA-ICP-MS model, results in an accuracy of well-classified deposits using the EPMA model of 81% for orogenic deposits, 75% for RIRG deposits, 55% for porphyry deposits, 68% for VMS deposits, and 60% for epithermal deposits (Figure 3A). In contrast, the accuracy of well classified deposits using the LA-ICP-MS model is 85% for orogenic deposits, 62% for porphyry deposits, 72% for VMS deposits, and 64% for epithermal deposits (Figure 3B).

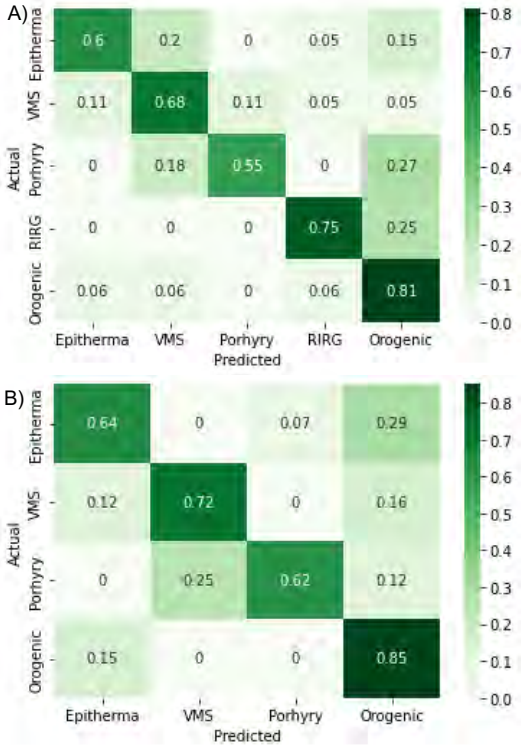


**Figure 3.** Confusion matrix of the results of a neural network algorithm for classification applied on blind data with A) EPMA and B) LA-ICP-MS.

## 4. Discussion

Many attempts have been made to find the relationship between the trace element composition of gold and deposit types (Townley et al. 2003; Chapman et al. 2009; Moles and Chapman 2019; Liu et al. 2021). Generally, the resulting classification tends to be shown as a discrimination diagram (usually ternary diagrams) with fields of large overlaps that do not make a clear classification of the data. In addition, there are ore deposit types that share similar fluid compositions and, therefore, similar trace element content in gold, like orogenic and RIRG deposits (Hart and Goldfarb 2005). For these reasons, the use of a nonlinear machine learning algorithm was selected as an approach to unveil the intricate geochemical signature of gold.

The work of Liu and Beaudoin (2021) and Liu et al. (2021) provided a first inside on the use of machine learning algorithms to understand the chemical signatures of gold as well as the necessary database for a baseline for further applications. In addition to the use of a different machine learning algorithm, our approach used the raw data as a starting point, which simplified the processing of the data, along with a larger blind dataset (i.e., over 3 times larger) than the one used by Liu and Beaudoin (2021), which led to a smaller accuracy compared with the one presented by them but ensured that the result obtained is not affected by a sample bias.

Despite the differences in variability between EPMA and LA-ICP-MS, the results of both neural networks can be taken as similar except for porphyry deposits, which have shown a notable increase in precision. It is believed that this improvement is caused by the addition of new elements, (e.g., Bi, Pb, Pd, Sb) that contribute to the differentiation of these sorts of deposits without affecting them much.

These results could be improved by pre-processing the data with a matrix factorization technique to minimize data dimensionality, but at the expense of increased processing time.

## 5. Conclusions

The use of artificial neural networks to evaluate chemical signatures of natural gold appears to be a powerful technique to unveil this complicated nonlinear problem even with overlaps presented in the trace element concentrations of some deposits.

Chemical zoning in gold could lead to a misclassification of single grains but using the right sample size can ensure the best classification possible for a population of gold grains. The use of this model in gold grains of unknown origin (placer deposits) could be used as an exploration technique to utilize the correct geologic model to find the original source of gold.


## Acknowledgements

This study was financed in part by the Coordenação de Aperfeiçoamento de Pessoal de Nível Superior - Brasil (CAPES) - Finance Code 001 and the Conselho Nacional de Desenvolvimento Científico e Tecnológico (CNPq) by the grant (140810/2021-8).


## References


Antweiler JC, Campbell WL (1977) Application of Gold Compositional Analyses to Mineral Exploration in the United States. In: Developments in Economic Geology. Elsevier, pp 17–29

Chapman RJ, Leake RC, Bond DPG, et al (2009) Chemical and Mineralogical Signatures of Gold Formed in Oxidizing Chloride Hydrothermal Systems and their Significance within Populations of Placer Gold Grains Collected during Reconnaissance. Economic Geology 104:563–585. https://doi.org/10.2113/gsecongeo.104.4.563

Cone KA, Palin RM, Singha K (2020): Unsupervised machine learning with petrological database ApolloBasaltDB reveals complexity in lunar basalt major element oxide and mineral distribution patterns. Icarus 346:113787. https://doi.org/10.1016/j.icarus.2020.113787

Farnham IM, Singh AK, Stetzenbach KJ, Johannesson KH (2002): Treatment of nondetects in multivariate analysis of groundwater geochemistry data. Chemometrics and Intelligent Laboratory Systems 60:265–281. https://doi.org/10.1016/S0169-7439(01)00201-5

Ghannadpour S, Hezarkhani A, Farahbakhsh E (2013): An Investigation of Pb Geochemical Behavior Respect to Those of Fe and Zn Based on kMeans Clustering Method. 291-302 1:

Guilloux J-P, Seney M, Edgar N, Sibille E (2011): Integrated behavioral z-scoring increases the sensitivity and reliability of behavioral phenotyping in mice: Relevance to emotionality and sex. Journal of Neuroscience Methods 197:21–31. https://doi.org/10.1016/j.jneumeth.2011.01.019

Hart CJR, Goldfarb RJ (2005) Distinguishing intrusion-related from orogenic gold systems. pp 125–133

Huston DL, Bottrill RS, Creelman RA, et al (1992) Geologic and geochemical controls on the mineralogy and grain size of gold-bearing phases, eastern Australian volcanic-hosted massive sulfide deposits. Economic Geology 87:542–563. https://doi.org/10.2113/gsecongeo.87.3.542

Liu H, Beaudoin G (2021) Geochemical signatures in native gold derived from Au-bearing ore deposits. Ore Geology Reviews 132:104066. https://doi.org/10.1016/j.oregeorev.2021.104066

Liu H, Beaudoin G, Makvandi S, et al (2021) Multivariate statistical analysis of trace element compositions of native gold from orogenic gold deposits: Implication for mineral exploration. Ore Geology Reviews 131:104061. https://doi.org/10.1016/j.oregeorev.2021.104061

McClenaghan MB (2005) Indicator mineral methods in mineral exploration. GEEA 5:233–245. https://doi.org/10.1144/1467-7873/03-066

McClenaghan MB, Cabri LJ (2011) Review of gold and platinum group element (PGE) indicator minerals methods for surficial sediment sampling. GEEA 11:251–263. https://doi.org/10.1144/1467-7873/10-IM-026

Moles NR, Chapman RJ (2019) Integration of Detrital Gold Microchemistry, Heavy Mineral Distribution, and Sediment Geochemistry to Clarify Regional Metallogeny in Glaciated Terrains: Application in the Caledonides of Southeast Ireland. Economic Geology 114:207–232. https://doi.org/10.5382/econgeo.2019.4628

Morrison GW, Rose WJ, Jaireth S (1991) Geological and geochemical controls on the silver content (fineness) of gold in gold-silver deposits. Ore Geology Reviews 6:333–

364. https://doi.org/10.1016/0169-1368(91)90009-V
Palarea-Albaladejo J, Martín-Fernández JA (2015) zCompositions — R package for multivariate imputation of left-censored data under a compositional approach. Chemometrics and Intelligent Laboratory Systems 143:85–96. https://doi.org/10.1016/j.chemolab.2015.02.019
Pochon A, Desaulty A-M, Bailly L, Lach P (2021) Challenging the traceability of natural gold by combining geochemical methods: French Guiana example. Applied Geochemistry 129:104952. https://doi.org/10.1016/j.apgeochem.2021.104952
Rinaldi R, Llovet X (2015) Electron Probe Microanalysis: A Review of the Past, Present, and Future. Microsc Microanal 21:1053–1069. https://doi.org/10.1017/S1431927615000409
Rosenblatt F (1958) The perceptron: A probabilistic model for information storage and organization in the brain. Psychological Review 65:386–408. https://doi.org/10.1037/h0042519
Taylor GJ, Martel LMV, Karunatillake S, et al (2010) Mapping Mars geochemically. Geology 38:183–186. https://doi.org/10.1130/G30470.1
Templ M, Filzmoser P, Reimann C (2008) Cluster analysis applied to regional geochemical data: Problems and possibilities. Applied Geochemistry 23:2198–2213. https://doi.org/10.1016/j.apgeochem.2008.03.004
Townley BK, Hérail G, Maksaev V, et al (2003) Gold grain morphology and composition as an exploration tool: application to gold exploration in covered areas. GEEA 3:29–38. https://doi.org/10.1144/1467-787302-042

# Early structural architecture controlling komatiite-hosted nickel sulphide and orogenic gold mineralisation at Beta-Hunt Au-Ni mine, Kambalda, WA

**Lauri T. Virnes[1], Nicolas Thébaud[1], Laura Petrella[1], Helen B. Mcfarlane[2], Laure Martin[3], Denis Fourgerouse[4]**
[1]*Centre for Exploration Targeting (CET), University of Western Australia*
[2]*Commonwealth Scientific and Industrial Research Organisation (CSIRO)*
[3]*Centre for Microscopy, Characterisation & Analysis (CMCA), University of western Australia*
[4]*The Institute for Geoscience Research (TIGeR), Curtin University*

**Abstract.** At the Beta-Hunt mine, orogenic gold and komatiite-hosted massive nickel sulphide mineralisation are locally coincident, indicating that crustal architecture could play a role in the localisation of the two mineral systems. A structural framework was derived based on field observations to evaluate how early crustal architecture may have influenced both mineral systems. We propose that SW-dipping $D_0$ growth faults controlled the deposition of komatiite-hosted massive nickel sulphide mineralisation and that these structures were reactivated during SW-NE-directed basin inversion ($D_1$). During the inversion, strain was partitioned into SW-dipping reverse shear planes along lithological contacts and steeply SW-dipping foliation corridors associated with early growth faults. Deformation was assisted by fluid migration causing strong hydrothermal alteration and deposition of gold. During subsequent local $D_2$ extension, the steep foliation corridors became dilated. $D_2$ phase coincided with a major fluid flux, which led to the formation of moderately and steeply NE-dipping hydraulic extension veins and thick sub-vertical breccia bodies following the steep $D_1$ structural corridors. $D_2$ hydrothermal veins represent the main phase of gold deposition. We suggest that at Beta-Hunt, early growth faults related to the formation of nickel sulfide mineralisation were also critical for the localisation of high-grade gold mineralisation.

## 1 Introduction

Understanding deposit scale structural architecture is essential in mid-crustal orogenic gold deposits where fluid flow is highly channelised (Cox 2020). Structural components formed at different times during a deposit's progressive or discrete deformation history control the localisation of fluid channels, enabling the accumulation of economic mineral reserves. At the same time, the presence of fluids changes the mechanical behaviour of rocks during deformation and can influence strain partitioning patterns (Fossen and Cavalcante 2017). Consequently, fluid-assisted deformation is expected to form self-organising systems where fluid flow and localisation of deformation are coupled (Cox 2020). The earliest components of a deposit scale structural architecture can therefore serve as nucleation points for processes that develop into self-enhancing fluid channels, concentrate deformation, and eventually lead to metal accumulation over vast geological time frames spanning multiple mineralising events (Sibson 2020).

This work focuses on the combined komatiite-hosted nickel sulphide and orogenic gold mineralisation of the Beta-Hunt mine in Kambalda, Western Australia, where fluid-enhanced deformation led to the juxtaposition of a structurally controlled orogenic gold mineralisation and a pre-existing komatiite-hosted massive nickel sulphide mineralisation (Neall and Phillips 1987; Stone et al. 2005).

## 2 Geological background

### 2.1 Regional geology

The Norseman-Wiluna greenstone belt is in the central southern part of the Archean Yilgarn Craton, Western Australia, located in the southern part of the Kalgoorlie terrane (Cassidy et al. 2006). The greenstone belt is characterised by a greenstone-greywacke succession containing basalts, komatiites, felsic volcanic and volcanoclastic rocks and clastic sediments (Blewett et al. 2010). The southern Kalgoorlie terrane's stratigraphic sequence chronicles a tectonic history that includes an early failed rifting event of the Yilgarn proto-craton and later basin inversion, with reactivation of crustal-scale fault-shear zones, formation of new regional deformation zones, granitic doming, and rapid uplift. (Miller et al. 2010). A simplified stratigraphic column typical for the research area is shown in Figure 1B.

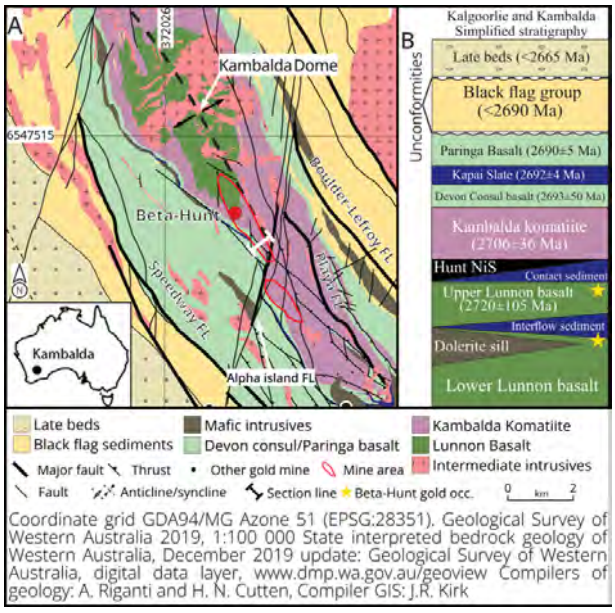

**Figure 1.** Local geology of the Beta-Hunt mine area. A) Geological map of the mine area, modified after GSWA regional map. B) Local stratigraphy modified after Blewett et al. (2010).

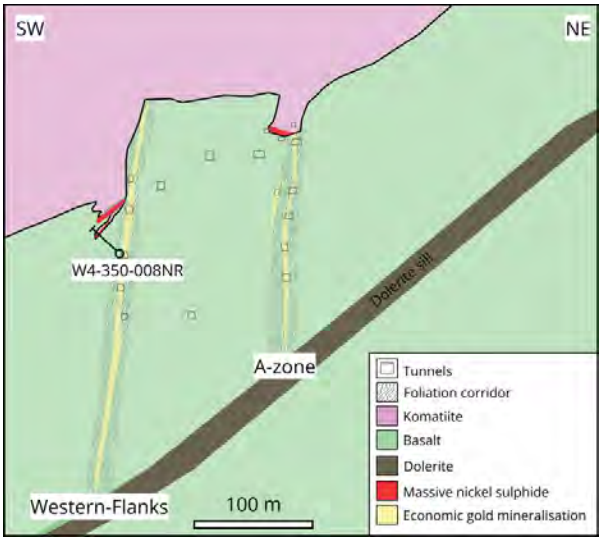


**Figure 2.** General cross-section of the mine looking NW. Section line in Figure 1A.

### 2.2. Local geology

The Beta-Hunt mine is in Western Australia, 55 km SE from the city of Kalgoorlie-Boulder. Karora Resources own the mine and currently produces both gold and nickel ore. The mine is located in the NW part of the Saint-Ives and Kambalda district on the SW limb of the Kambalda anticline, close to the anticline hinge zone (Figure 1A). Consequently, only the lowermost stratigraphic units of the gold district are exposed (Figure 1B). The stratigraphic basement is formed by a thick unit of tholeiitic basalt called the Lunnon Basalt, which is split loosely into two sub-units (Said et al. 2010). A thin discontinuous interflow sediment and a strata sub-parallel dolerite sill mark a transitional interface between the Upper and Lower Lunnon basalts (Figure 1B). The 1 km thick Kambalda Komatiite forms the stratigraphic hanging wall of the deposit (Gresham and Loftus-Hills 1981; Miller et al. 2010). However, only the komatiite's lower contact, associated cherty sedimentary sequence ("the contact sediment") and the nickel sulphide mineralisation lenses are exposed within the mine area.

Nickel sulphide mineralisation occurs as basal, massive sulfides in troughs at the footwall contact as well as disseminated to net-textured, semi-massive sulfides either on top of the massive nickel sulphide bodies or as isolated lenses completely enclosed by komatiite (Gresham and Loftus-Hills 1981).

The gold mineralisation located within the footwall of the Kambalda komatiite is primarily found along steeply SW-dipping, NW-striking structural corridors (the "A-zone" and the "Western Flanks"), where the corridors are primarily marked by zones of strong foliation (Figure 2). Auriferous hydraulic extension veins and breccias form the main portion of the minable gold within and immediately adjacent to the zones of foliation. The gold deposition has been estimated to have occurred at approximately 3-6 km crustal depth at the temperature of 280 – 350 °C and confining pressure of 80 – 180 MPa (Neall and Phillips 1987).

## 3. Methodology

Structural data and observations were collected during detailed underground mapping of the Western Flanks mineralised corridor and the Kambalda komatiite's lower contact. Underground observations were augmented with data from oriented diamond drill cores from the A-zone and Western Flanks gold mineralisation and from the nickel mineralised zone where gold mineralisation is in direct contact with the massive nickel sulphides (drill core W4-350-008NR, Figure 2). Structural orientations presented below are median orientations calculated from the accumulated structural dataset.

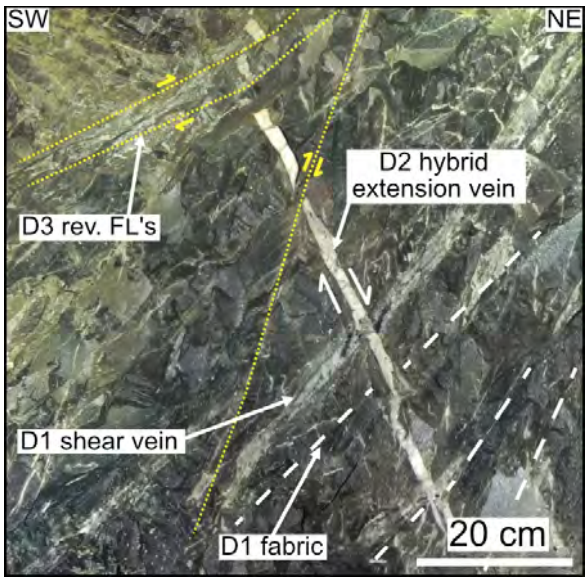


**Figure 3.** Crosscutting relationships between SW-dipping D1 fabric and fabric parallel shear vein, NE-dipping D2 hybrid extension vein, and strongly bleached D3 reverse faults linked to sub-vertical D3 strike-slip faults. At this underground outcrop, the D1 fabric-related pyrite alteration carries 0.5 - 7 g/t Au, and D2 veins carry gold grades between 7 - 19 g/t Au.

## 4. Results: Structural elements

A structural framework for the deposit scale structural architecture of the Beta-Hunt mine was derived from structural observations, analysis and relative timing relationships. Structures related to the four phases are described below:

$D_0$-structures comprise the stratigraphic interfaces formed before and during the regional and district-wide early extension. At Beta-Hunt mine, these boundaries, on average, dip shallowly to moderately to SW (~30/220). Especially

important contacts are the major Kambalda Komatiite-Lunnon Basalt contact and associated massive nickel sulphide troughs, forming the gold mineralisation's hanging wall boundary (Figure 1A and Figure 2). Another important $D_0$ interface, which is not as well constrained as the komatiite contact, is the transition zone between Upper and Lower Lunnon Basalt marked by the interflow sediment and the dolerite sill. These are usually oriented similarly to the komatiite-basalt contact. Finally, steeply SW-dipping, apparent normal faults that offset the komatiite-basalt contact from meters up to a hundred meters are likewise considered as $D_0$ structures.

$D_1$ structures comprise the dominant ductile foliations within the deposit area. Shallow to moderately SW-dipping (~45/230) foliations are most prominently developed along or in the proximity of the primary lithological boundaries, especially along the komatiite-basalt contact and along the dolerite sill (Figure 2). The shallow, anastomosing foliations are associated with asymmetric meso- and microscale deformation fabrics that indicate apparent NE-verging transport. Steeply SW-dipping (~72/226) foliations, highlighted by pervasive biotite-pyrite alteration, define the major corridors of economic mineralisation between the komatiite-basalt contact and the transition between Upper and Lower Lunnon Basalts. Both foliation trends can be associated with foliation parallel, discontinuous quartz-carbonate banding. In addition, a relatively minor set of shallow dipping (~20/252) $D_1$ tension veins crosscut the steep foliations within the mineralised corridors. A sampling of the production headings shows that $D_1$ veins carry low to moderate gold grades (0.3 – 2 g/t Au). Further, the $D_1$ foliations contain very fine-grained free gold where biotite-pyrite alteration is strong (unpublished report, Karora Resources).

$D_2$ structures contain most of the gold associated with the deposit (Figure 3). $D_2$ veins are confined to the steeply dipping and pervasively altered $D_1$ foliation corridors. Veins are usually medium to coarse-grained and composed of quartz-albite-carbonates±sulphide±gold. Two sets of coeval veins are recognised: 1) the most common auriferous veins are millimetre- to decimetre-scale, moderately to steeply NE-dipping (~55/034) hydraulic extension veins, which crosscut the $D_1$ fabrics at a nearly perpendicular angle (Figure 3). The extension veins occur in en-echelon vein sets soft-linked with 2) less numerous but locally dominant, up to 6 meters wide, and very steeply SW-dipping to sub-vertical $D_2$ hydraulic breccia veins. NE-dipping vein sets sometimes branch off or join with the breccia veins. Meanwhile, the breccia veins locally propagate into the wall rocks exploiting the $D_1$ foliation, resulting in much shorter, irregular SW-dipping veins branching from the wider breccia veins.

The most dominant $D_3$ structure is the Alpha Island Fault, which shows an apparent right-lateral movement and displaces the whole deposit by about 500 meters (Figure 1A). Smaller structures include numerous minor strike-slip faults (~70/290 and ~60/330), minor reverse faults (~55/214), and rare sub-vertical tension veins (~70/325) that overprint all previous structural features. The various $D_3$ structures are inferred to be coeval due to similarities in crosscutting relationships and diagnostic pale green sericitisation alteration signatures (Figure 3). The $D_3$ structures are only grade-bearing, where they directly crosscut pre-existing gold-bearing $D_1$-$D_2$ veins and foliations.

## 5. Discussion

### 5.1. Komatiite-hosted nickel sulphide mineralisation

Previous research has recognised the extensive early growth fault network within the Saint-Ives and Kambalda district, highlighting its control on gold mineralisation (e.g., Miller et al. 2010). Here we suggest that this early to syn-magmatic architecture could have been an important control for localising massive nickel sulphide ore bodies. Low-viscosity komatiitic lavas are preferentially channelled along topographic lows, which would develop along fault scarps (Barnes 2006). Such interpretation is further supported when looking at the northern parts of the Kalgoorlie terrane, where a preferential accumulation of nickel mineralisation has been shown to occur where komatiitic lavas cross fault lines (Perring 2015). Recent modelling has further demonstrated that the accumulation of nickel sulfide droplets on the hanging wall of a normal fault is flow-dynamically feasible (Yao and Mungall 2022). The channelisation of komatiitic lavas along deep and narrow channels increases physical contact with substrate rocks leading to thermomechanical erosion, crustal assimilation and sulfur saturation (Staude et al. 2017). At the Beta-Hunt mine, undeformed komatiite and massive nickel sulfide - mineralisation occur in troughs on the hanging wall side of the $D_0$ normal faults, which clearly offset the komatiite footwall basalt contact (Figure 2).

### 5.2. $D_1$ Reverse reactivation of early normal faults

The dominant $D_1$ foliations formed during SW-NE trending sub-horizontal compression. The strain was partitioned along $D_0$ lithological contacts (Sz) and along moderately to steeply dipping structural corridors (S), which bound lava flow channels hosting nickel sulfide mineralisation at the komatiite-basalt contact. We suggest that stratigraphic interfaces were favourably oriented for flexural slip as the development of the Kambalda anticline tilted the rock strata and led to NE-verging transport along the shallow Sz-shear foliations during broadly NE-SW directed shortening (Stone et al. 2005). S-planes, on the other hand, may have essentially recorded coaxial-dominated deformation and formed sub-vertical compressional foliations. Foliations are associated with strong biotite-pyrite-

ankerite alteration, indicating that hydrothermal fluid circulation assisted the ductile deformation.

Fluid-induced reactivation is especially effective during compressional tectonics (Sibson 2020). Reactivation and strain partitioning along pre-existing structure architectural components are favoured as fluid flow becomes highly channelised below ~2 km of crustal depth (Cox 2020). Channelisation occurs as the presence of fluids changes the behaviour of rocks during deformation, enhancing ductile and brittle mechanisms (Fossen 2017). As a region progresses from one deformation phase to another, the coupling of fluid flow and deformation causes pre-existing deformation zones and their damage zones to become preferentially "selected" for reactivation due to their enhanced permeability and mechanical weakness. At the Beta-Hunt mine, this process led to the formation of discrete foliation corridors while the surrounding basaltic host rocks remained relatively undeformed (Figure 2).

### 5.3. Reactivation of $D_1$ fabrics

Analysis of the $D_2$ extension and breccia veins indicates that both are syntectonic fractures that developed into the mesoscopic hydraulic veins observed today during local vertical shortening. Fracturing coincided with a major fluid flux into the system, evident from the decimeter to several meter thicknesses of the veins. During $D_2$, the steeply dipping $D_1$ S-planes became favourable oriented for dilation. Minor deflections of $D_1$ foliations adjacent to $D_2$ breccia veins indicate that these veins are dilated normal faults. $D_2$ veining does not extend significantly into the Kambalda Komatiite or the nickel sulphide mineralised bodies. This is likely because the mechanically weak serpentinised komatiite in the hanging wall was too mechanically weak to brittlely deformed during $D_2$. This may have prevented the fluids from migrating upwards through the ~1 km thick komatiite. Instead, fluid capping led to sustained and relatively stable elevated pressure along the $D_1$ deformation corridors, driving propagation and dilation of the hydraulic veins, lateral fluid advection and gold deposition.

## 6. Conclusion

At the Beta-Hunt mine, structural analysis suggests that early rifting-related growth faults may have contributed to the deposition of massive nickel sulphide ore bodies. These faults were reactivated during $D_1$ compression and developed into gold-mineralised corridors where gold was further enriched in hydraulic veins during local extensional $D_2$ deformation. Natural fluid flow networks tend to form along pre-existing zones of weakness in the middle and lower crust, and the ability of fluids to enhance deformation has caused the repeated reactivation of the structural components of the deposit, resulting in the co-occurrence of gold and nickel sulfide mineralisations.


## Acknowledgements

The study is funded by Australian Research Councils linkage project LP 200200897. Authors would like to give special thanks to Karora Resources and their technical team for their support.


## References


Barnes SJ (2006) Komatiite-Hosted Nickel Sulfide Deposits: Geology, Geochemistry, and Genesis Nickel Deposits of the Yilgarn Craton: Geology, Geochemistry, and Geophysics Applied to Exploration. Society of Economic Geologists, pp 0.

Blewett RS, Czarnota K, Henson PA (2010) Structural-event framework for the eastern Yilgarn Craton, Western Australia, and its implications for orogenic gold. Precambrian Research 183:203-229. doi: 10.1016/j.precamres.2010.04.004.

Cassidy K, Champion DC, Krapez B, Barley ME, Tyler IM (2006) A revised geological framework for the Yilgarn Craton: Western Australia. Western Australia Geological Survey, Record 2006/8:8 p.

Cox SF (2020) Chapter 2: The Dynamics of Permeability Enhancement and Fluid Flow in Overpressured, Fracture-Controlled Hydrothermal Systems In: Rowland JV, Rhys DA (eds) Applied structural geology of ore-forming hydrothermal systems. Society of Economic Geologists, pp 25- 82.

Fossen H, Cavalcante GCG (2017) Shear zones – A review. Earth-Sci Rev 171:434–455. doi: 10.1016/j.earscirev.2017.05.002.

Gresham JJ, Loftus-Hills GD (1981) The geology of the Kambalda nickel field, Western Australia. Economic Geology 76:1373-1416. doi: 10.2113/gsecongeo.76.6.1373.

Miller J, Blewett R, Tunjic J, Connors K (2010) The role of early formed structures on the development of the world class St Ives Goldfield, Yilgarn, WA. Precambrian Res 183:292–315. doi: 10.1016/j.precamres.2010.08.002.

Neall FB, Phillips GN (1987) Fluid-wall rock interaction in an Archean hydrothermal gold deposit; a thermodynamic model for the Hunt Mine, Kambalda. Economic Geology 82:1679-1694. doi: 10.2113/gsecongeo.82.7.1679.

Perring CS (2015) Volcanological and Structural Controls on Mineralization at the Mount Keith and Cliffs Komatiite-Associated Nickel Sulfide Deposits, Agnew-Wiluna Belt, Western Australia—Implications for Ore Genesis and Targeting. Econ Geol 110:1669–1695. doi: 10.2113/econgeo.110.7.1669.

Said N, Kerrich R, Groves D (2010) Geochemical systematics of basalts of the Lower Basalt Unit, 2.7Ga Kambalda Sequence, Yilgarn craton, Australia: Plume impingement at a rifted craton margin. Lithos 115:82-100. doi: 10.1016/j.lithos.2009.11.008.

Sibson RH (2020) Preparation zones for large crustal earthquakes consequent on fault-valve action. Earth, Planets and Space 72. doi: 10.1186/s40623-020-01153-x.

Stone WE, Beresford SW, Archibald NJ (2005) Structural Setting and Shape Analysis of Nickel Sulfide Shoots at the Kambalda Dome, Western Australia: Implications for Deformation and Remobilisation. Econ Geol 100:1441–1455. doi: 10.2113/gsecongeo.100.7.1441.

Yao Z, Mungall JE (2022) Transport and deposition of immiscible sulfide liquid during lateral magma flow. Earth-Sci Rev 227:103964. doi: 10.1016/j.earscirev.2022.103964

# Mineral-specific deportment of gold and other elements in mine tailings from the Witwatersrand goldfields

**Bjorn von der Heyden[1], Steve Chingwaru[1], Margreth Tadie[2]**
*[1] Department of Earth Sciences, Stellenbosch University, Private Bag X1, Matieland, 7602, South Africa*
*[2] Department of Process Engineering, Stellenbosch University, Private Bag X1, Matieland, 7602, South Africa*

**Abstract.** The Witwatersrand Basin is the world's largest gold province hosting over 53 000 tons of native Au predominantly in quartz pebble conglomerates. The Witwatersrand gold tailings dumps are subjected to secondary mining operations which involve traditional extraction techniques (cyanide leaching) that lead to 30-50 % recovery of gold missed by the historical beneficiation. This leaves a projected 1325-1855 tons of refractory gold together with an estimated 30 million tons of sulfide material which reports to the discard stream after secondary mining. The mineralogical deportment of this remaining or refractory gold is not well constrained. Results from the analyses indicate that about 0.71 – 10.21 g/ton of gold is distributed in the heavy mineral concentrates which are predominantly made up of sulfides (35-76%) and oxides (9-20%). Detailed in situ analyses suggest the gold in the concentrate fraction is hosted predominantly in pyrite and arsenian pyrite, Au grades range from 0.1 – 2729 g/ton. Given that the Witwatersrand Goldfield is historically a native gold deposit, identification of 'invisible' gold in detrital pyrites represents a potentially under-exploited resource which explains in part the refractory nature of the 50-70 % Au remaining after secondary mining.

## 1 Introduction

The Witwatersrand Basin represents the world's largest gold mineralization, having produced around 53 000 tons of gold since its discovery in 1884 (Frimmel 2019). Despite having an extensive history of mining the origin of gold mineralisation is still highly debated, with provenance described by metallogenic models. These include the placer model, the modified placer model, and the epigenetic model (Frimmel et al. 1993; Robb and Meyer 1995; Tucker et al. 2016). Recent studies suggest microbial fixation by cyanobacteria on coastal environments, these Au-rich organic mats are reworked mechanically to form the Au-bearing conglomerate placer deposits of the Central Rand Group (Frimmel 2019). The placer- and modified placer models state that the origin of gold within the Witwatersrand Basin was initially concentrated within dense native gold placers then later redistributed and re-precipitated because of several hydrothermal events (Frimmel and Minter 2002). Therefore, gold is suggested to enter the quartz pebble conglomerates (QPC) along with other detrital minerals such as pyrite, uraninite and other oxide phases all these being liberated and eroded from an Archean granite-greenstone hinterland.

Several of these remnants of Archean granite-greenstone exist with notable concentrations of gold mineralization (Pearton and Viljoen 2017). A good example of these vestiges is the Barberton greenstone belt, which hosts countable gold deposits, in which the majority is defined as 'invisible' or 'refractory gold that is incorporated into the sulfide structures of pyrite, arsenopyrite and arsenian pyrite via solid-solution substitution or nanoparticulate inclusions (Anhaeusser 2019; Hofmann et al. 2019). Similarly, invisible gold mineralization (described as very fine ~10 µm) is hosted in the Banded-iron formation Kalgold deposit of the Kraaipan Greenstone, associated with fine-grained sulfides (Harmony Gold 2018; Pearton and Viljoen 2017). This chemical nature of the greenstone belt gold deposits proposes that a considerable percentage of the detrital sulfides within the Witwatersrand QPC should be mineralized in Au. This has been proven to be true by limited data from Witwatersrand detrital pyrite (up to 8 ppm Au and as high as 1400 ppm; (da Costa et al. 2020)).

The traditional Witwatersrand processing methods of standard milling (up to 80% of material less than top-size 75 µm), cyanidation, and carbon-in-pulp have been designed to liberate gold from the ore. These historical liberation methods have efficiencies of ca. 95% (Vaughan 2004), implying 5% of the total gold (i.e., ca. 2650 t Au) is still available for extraction in the historical tailing dumps. Tailing reprocessing units that also make use of cyanidation run at 30-50% efficiency, again implying 50-70% (representing 1325-1855 t Au) is not extracted from the ore. One of the possible explanations is that a significant proportion of the Witwatersrand gold deposits contain 'invisible' or refractory gold, which is inaccessible via cyanidation.

Therefore, the purpose of the study is to conduct mineral-specific gold deportment characterisation to determine the variability and nature of gold in the Witwatersrand tailings.

## 2 Methods

Duplicates of 150 kg of sample material were acquired from four tailings dams storage facilities associated with mining in the Evander, Carletonville, Central Rand and Klerksdorp Goldfields of the Witwatersrand Basin (Fig.1). After homogenisation and representative splitting of these bulk samples, ~1 kg subsamples were further subjected to a series of pre-concentration procedures. The applied techniques were desliming, superpanning and a two-stage heavy liquid separation using tetrabromoethane at 2.95 g/cm$^3$ density and lithium metatungstate at 2.71 g/cm$^3$ density. The resultant

density-defined mineral fractions were a slimes fraction (particle size < 25 µm), a light mineral fraction (< 2.95 g/cm$^3$) and a heavy mineral fraction (> 2.95 g/cm$^3$). Approximately 0.3 g of representative aliquots from each of the density-defined mineral fractions was placed as a monolayer in an epoxy mount, and subsequently diamond polished to a 1 µm finish.

The pre-concentrated samples were subjected to a variety of analytical techniques. Aqua regia digestion and inductively coupled plasma mass spectrometry (ICP-MS) analyses were conducted to determine the bulk trace element concentrations (As, Au, Co, Cu, Hg, Ni, Pb, Sb, Se, Zn & U). This was done on approximately 0.55 g duplicates from each bulk sample, each density fraction and on three blank samples at the Central Analytical Facilities (CAF), Stellenbosch University. Textural descriptions of each epoxy mount were afforded by optical petrography, scanning electron microscopy (Stellenbosch University) and QEMSCAN (University of Cape Town). The QEMSCAN approach was incorporated into the study to determine bulk mineral percentages of the heavy mineral fraction, which in turn was used to validate the assay data derived from acid digestion and for mass balance calculations. Additionally, a false image colour map was generated to assist with the identification of 'visible gold' and potential gold carriers, as well as a visual aid to identify potential grains for subsequent LA ICP-MS analysis.

LA ICP-MS was carried out on 800 grains of oxides (hematite, goethite/limonite, rutile) and sulfides (pyrite, arsenopyrite, galena, sphalerite, chalcopyrite, pentlandite and pyrrhotite) from the heavy minerals fraction mounts using a grid method at CAF, Stellenbosch University with a Resolution 193 nm Excimer laser from Applied spectra, coupled with an Agilent 7700 Q ICP-MS. This was done to obtain concentrations of trace elements (Co, Ni, Cu, Zn, As, Se, Ag, Sb, Te, Au, Hg, Pb and Bi) hosted within each of the mineral phases. Resultant data were processed using LADR from Norris Scientific.

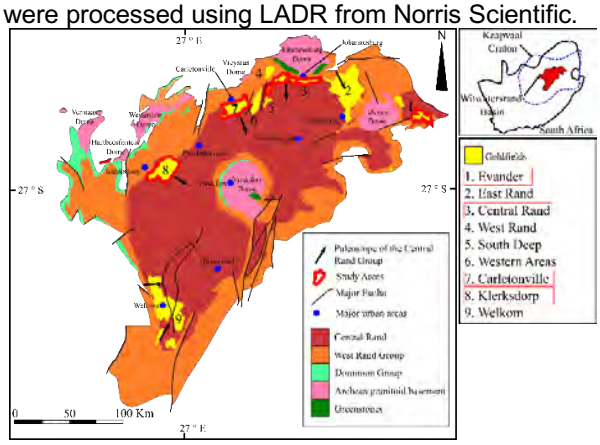


**Figure 1.** A surface geological map of the Witwatersrand basin, displaying the goldfields referred to in the text (from Chingwaru et al. 2023).

## 3 Results and Discussion

### 3.1 Gold deportment according to operational definitions and according to mineralogy

The first step towards identifying the main gold 'carriers' in the Witwatersrand tailings materials was to identify the operationally-defined units which hosted the highest proportions of gold (Fig. 2a). Across all four goldfields evaluated, the heavy mineral fraction consistently hosts the largest relative proportion of gold with aqua regia measured grades of between 0.71 and 10.12 ppm (Fig. 2a). This accounts for 0.89 to 13.23 % for the mass of gold in the samples. The light mineral fraction (d < 2,95 g.cm$^{-3}$; size 15-75 µm) and slimes fraction (< 10 µm) have measured gold concentrations that are an order of magnitude lower, measuring across the four goldfields between 0,05-0,22 ppm and 0,17-0.76 ppm respectively. This preferential partitioning of gold into the heavy mineral fraction may be explained by the presence of nano-particulate native gold grains, or by a chemical association between gold and heavy gangue minerals such as sulfides and oxides (Goodall 2008; Coetzee et al. 2011; Goodall and Butcher 2012).

To elucidate the main mineralogical carriers of gold within the heavy mineral fraction, we utilised the QEMSCAN imagery to identify, locate and quantify the different sulfide minerals present in this fraction. Coupled with optical and SEM microscopy, our results highlight that the mineralogical composition of the heavy mineral fraction comprises 13-44% silicates; 35-76% sulfides; 9-20% oxides; 0.01-0.34% carbonates and phosphates, and no native or 'free' gold observed. Pyrite was the dominant sulfide mineral and textural observations from microscopy (Fig. 2b-d) enabled textural sub-classes of pyrite to be identified (e.g., da Costa et al. 2020). Using the QEMSCAN imagery as a guide, LA ICP-MS was used to quantify the deportment of gold per mineral phase within the heavy mineral fraction. From the pie charts depicted in Figure 2b, it is clear that pyrite and arsenian pyrite host the majority of gold within this fraction. For example, these two minerals account for approximately 65% of gold in the Klerksdorp heavy mineral fraction, 78% of gold in the Carletonville heavy mineral fraction and 85% of gold in the Evander heavy mineral fraction (Fig. 2a). Gold deportment into goethite/limonite, hematite and other sulfide minerals is quantitatively less important (i.e., typically accounting for ~1 – 6% of total gold in the heavy mineral fraction), with the largest concentrations observed in goethite/limonite (0.78 ppm), hematite (0.64 ppm), and pyrrhotite (0.34 ppm) respectively. Based on the textural classification of pyrite grains, we discerned that rounded pyrite grains comprise the highest concentration of gold, recording an average spot concentration value of 21.36 ppm gold and a maximum of 2700 ppm gold. We conform to previous authors' designation of this rounded pyrite class as being detrital in origin, with rounding having occurred during fluvial processing and sedimentation of the Witwatersrand conglomerates (e.g., Agangi et al.

2015; da Costa et al. 2020).

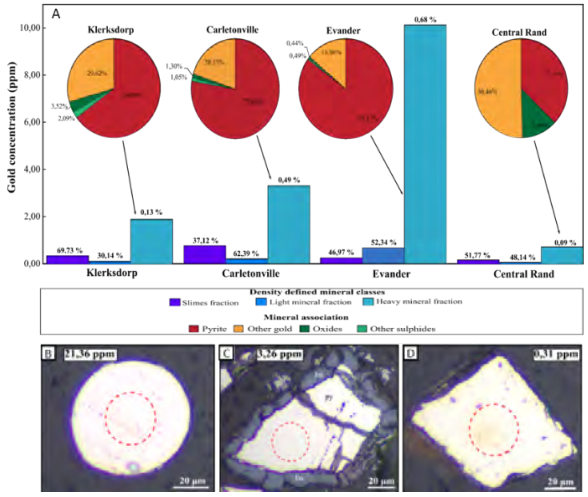


**Figure 2a.** Gold distributions summarised per operational definition and per individual mineral phase. **b-d.** Example spot loci in various pyrite morphological types (**b:** rounded/detrital pyrite, **c:** oxide rim pyrite, and **d:** euhedral pyrite classes respectively). Figures adapted from Chingwaru et al. 2023.

### 3.2 Pyrite chemistry: implications for provenance, economic extraction and the environment

The binary plot of As vs Au is a useful tool for considering the gold endowment of individual pyrite grains in the context of the maximum solubility of gold within the mineral structure (Reich et al. 2005). The upper limit of this stability is given by the gold saturation line (Fig. 3a), above which Au is expected to be present as nanoparticulate inclusions within the confines of the pyrite mineral. Figure 3 plots the chemistry of the pyrite grains investigated in this study, which we believe to represent a cross-section of a variety of pyrite types present in the Witwatersrand sediments (e.g., authigenic pyrite, hydrothermal pyrite formed during modification, detrital pyrite that is not derived from Au deposits, and pyrite derived from possible hinterland Au deposits). Applying the concept of the Clarke value (Fig. 3b), we suggest that the random sampling ensured by our pre-concentration approach and subsequent LA ICP-MS analysis approach should ensure that the bulk of our measurements falls within the low-Au 'normal crustal abundance' main peak of the Clarke distribution. Applying this to our empirical distribution shown on the binary plot (Fig. 3a), we suggest that the low-Au 'normal crustal abundance' field could fall below the line $C_{Au} = 0.0022.C_{As} + 0.2$. The data points for tailings pyrite grains that fall above this line may be representative of pyrite that derives from an Au-enriched source, for example, from possible hinterland orogenic Au deposits. For comparison, we show empirical LA ICP-MS data published for pyrite sampled from orogenic gold deposits in the Barberton greenstone belt, the chemical signatures of which we deem to be representative of a possible granite-greenstone hinterland gold source.

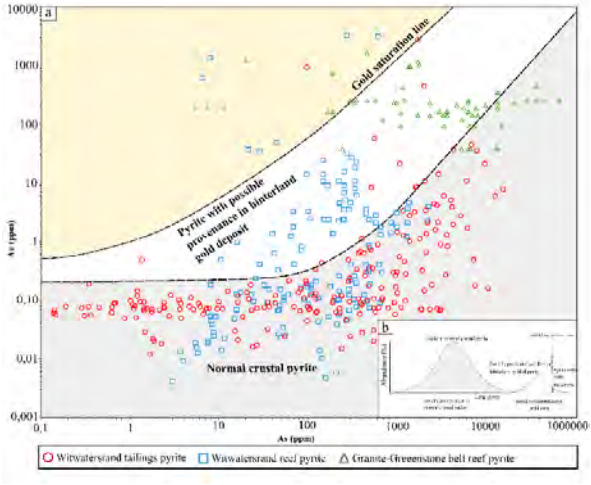


**Figure 3a.** An arsenic/gold scatter plot with concentration points from the Witwatersrand tailings pyrite (this study), Witwatersrand reef pyrite (Large & Maslennikov, 2020; Large et al., 2013; Morishita et al., 2019) and Granite-Greenstone belt auriferous pyrite (Agangi et al., 2014). The gold saturation line by Reich et al. (2005) represents the gold/arsenic limit in which gold occurs as free gold particles in pyrite. Inset diagram (**b**) uses the concept of a bi-modal distribution for metal grades, where Clarke values represent the broad main peak (reflecting normal crustal rocks), whereas the second peak represents the metal distribution specifically in ore deposits and occurrences. Figure from Chingwaru et al. 2023.

The finding that auriferous sulfides are located within the surficial materials of the mine tailings dumps scattered across the Witwatersrand mining precinct has meaningful implications for the secondary mining of this Au resource. Historical mining and processing as well as more recent reprocessing have focussed predominantly on the native gold endowment of the Witwatersrand auriferous conglomerates, thus overlooking the economic opportunity of auriferous pyrite. This 'invisible' gold is known to be inaccessible through direct cyanidation (Coetzee et al. 2011), and may thus be a significant contributor to the 50-70% recovery inefficiencies associated with secondary beneficiation of the Witwatersrand tailings. From an economic standpoint, extraction of auriferous pyrite from these tailings is deemed more favourable due to fine grain sizes and surficial location, respectively negating comminution and the high overheads associated with underground mining.

Environmental benefits would emanate from targeted re-mining of the sulfide fraction of the Witwatersrand tailings dumps. Mass balance calculations from our deportment study highlight that in addition to hosting high gold concentrations, the sulfide fraction hosts on the order of 95% of Zn, Cu, As and Pb; 55-97% of Ni; 64-99% of Co; 77-99% of Se and 84-99% of Sb. Removal of the sulfide component additionally would remove a major contributor to the acid mine drainage pollution

problem in some parts of the Witwatersrand area (e.g. Tutu et al. 2008). The value proposition of such an approach would be further enhanced by the recovery of high-demand heavy metals such as Co, Cu and Ni as by-products, which respectively have average calculated concentrations of 9755 ± 2330 ppm Co, 8771 ± 1817 ppm Cu and 9822 ± 1810 ppm Ni within the sulfide mineral fraction.

## 4 Conclusion

The study suggests that the fraction of gold inaccessible to conventional processing technologies in the Witwatersrand tailings ore material is attributed to a percentage of invisible gold, predominately within the arsenian pyrite and pyrite. Preserved rounded detrital pyrite classes within the tailings dump material exhibit the highest concentration of gold, with a maximum gold concentration similar to auriferous pyrite from existing granite-greenstone belt gold deposits. The residual sulfides in the tailings dump potentially represent a large under-exploited economic resource of up to 420 tons of gold, in which pre-treatment beneficiation can directly improve gold recovery by ~22 % during secondary reprocessing. This will further alleviate the growing ramifications of AMD and effluents with deleterious elements in the Witwatersrand mining region, while potentially recovering additional high-demand by-product metals.

## Acknowledgements

This research was funded by the DST-NRF Centre of Excellence for Integrated Mineral and Energy Resource Analysis (CIMERA) and the Society of Economic Geologists (SEG) Tim Nutt Fund. Thank you to the analytical staff at CAF, Stellenbosch University and QEMSCAN unit, University of Cape Town. We further extend our thanks to the mining houses Harmony Gold limited, DRD Gold Limited and Pan African Resources for sample donations.

## References

Agangi, A., Hofmann, A., Rollion-Bard, C., Marin-Carbonne, J., Cavalazzi, B., Large, R. & Meffre, S. 2015. Gold accumulation in the Archaean Witwatersrand Basin, South Africa-Evidence from concentrically laminated pyrite. Earth-Science Reviews. 140:27–53.

Anhaeusser, C. 2019. The geology and tectonic evolution of the northwest part of the Barberton Greenstone Belt, South Africa: A review. South African Journal of Geology. 122.

Chingwaru, S.J., Von der Heyden, B. and Tadie, M., 2023. An underexploited invisible gold resource in the Archean sulphides of the Witwatersrand tailings dumps. Scientific Reports, 13(1), p.3086.

Coetzee, L.L., Theron, S.J., Martin, G.J., Merwe, J.D. Van Der & Stanek, T.A. 2011. Modern gold deportments and its application to industry. Minerals Engineering. 24(6):565–575.

da Costa, G., Hofmann, A. & Agangi, A. 2020. A revised classification scheme of pyrite in the Witwatersrand Basin and application to placer gold deposits. Earth-Science Reviews. 201.

Frimmel, H.E., Le Roex, A.P., Knight, J. & Minter, W.E.L. 1993. A case study of the postdepositional alteration of the Witwatersrand Basal reef gold placer. Economic Geology.

Frimmel, H.E. & Minter, W.E.L. 2002. Recent Developments Concerning the Geological History and Genesis of the Witwatersrand Gold Deposits, South Africa. In Society of Economic Geologists Integrated Methods for Discovery: Global Exploration in the Twenty-First Century.

Frimmel, H.E. 2019. The Witwatersrand Basin and Its Gold Deposits. In A. Kröner & A. Hofmann (eds.). Cham: Springer International Publishing The Archaean Geology of the Kaapvaal Craton, Southern Africa. 255–275.

Goodall, W.R. 2008. Characterisation of mineralogy and gold deportment for complex tailings deposits using QEMSCAN®. Minerals Engineering. 21(6):518–523.

Goodall, W.R. & Butcher, A.R. 2012. The use of QEMSCAN in practical gold deportment studies. In Vol. 121 Transactions of the Institutions of Mining and Metallurgy, Section C: Mineral Processing and Extractive Metallurgy. 199–204.

Harmony Gold. 2018. Kalgold Greenstone exploration - Harmony Gold Mining. [Online], Available: https://www.harmony.co.za/invest/presentations/2018/send/131-2018/3486-kalgold-greenstone-exploration [2020, November 09]

Hofmann, A., Anhaeusser, C., Dixon, J., Kröner, A., Saha, L., Wilson, A. & Xie, H. 2019. Archaean Granitoid–Greenstone Geology of the Southeastern Part of the Kaapvaal Craton. In Springer The Archaean Geology of the Kaapvaal Craton, Southern Africa. 33–54.

Large, R.R. & Maslennikov, V. V. 2020. Invisible gold paragenesis and geochemistry in pyrite from orogenic and sediment-hosted gold deposits. Minerals. 10(4).

Large, R.R., Meffre, S., Burnett, R., Guy, B., Bull, S., Gilbert, S., Goemann, K. & Danyushevsky, L. 2013. Evidence for an intrabasinal source and multiple concentration processes in the formation of the carbon leader reef, Witwatersrand Supergroup, South Africa. Economic Geology. 108(6):1215–1241.

Morishita, Y., Hammond, N.Q., Momii, K., Konagaya, R., Sano, Y., Takahata, N. & Ueno, H. 2019. Invisible gold in pyrite from epithermal, banded-iron-formation-hosted, and sedimentary gold deposits: Evidence of hydrothermal influence. Minerals. 9(7):447.

Pearton, T. & Viljoen, M. 2017. Gold on the Kaapvaal Craton, outside the Witwatersrand Basin, South Africa. South African Journal of Geology. 120:101–132.

Reich, M., Kesler, S.E., Utsunomiya, S., Palenik, C.S., Chryssoulis, S.L. & Ewing, R.C. 2005. Solubility of gold in arsenian pyrite. Geochimica et Cosmochimica Acta. 69(11):2781–2796.

Robb, L.J. & Meyer, F.M. 1995. The Witwatersrand Basin, South Africa: Geological framework and mineralization processes. Ore Geology Reviews.

Tucker, R.F., Viljoen, R.P. & Viljoen, M.J. 2016. A Review of the Witwatersrand Basin - The World's Greatest Goldfield. Episodes. 39(2):105–133.

Tutu, H., McCarthy, T.S. & Cukrowska, E. 2008. The chemical characteristics of acid mine drainage with particular reference to sources, distribution and remediation: The Witwatersrand Basin, South Africa as a case study. Applied Geochemistry. 23(12):3666–3684.

Vaughan, J.P. 2004. The process mineralogy of gold: The classification of ore types. Jom. 56(7):46–48.

# An integrated approach towards unravelling the gold mineralisation processes around Ardtalnaig, Scotland.

**Shane Webb[1], Taija Torvela[2], Robert Chapman[3], David Selby[4], Robert Gooday[5]**
[1-4]*School of Earth and Environment, University of Leeds, U.K.*
[2]*Durham University, Department of Earth Sciences, Durham University, UK*
[3]*National Museums Scotland, UK*

**Abstract.** In the Caledonides of Britain and Ireland, there are several gold deposits of commercial interest hosted within the Grampian Terrane, which is comprised of Neoproterozoic metasedimentary rocks. One Scottish region that has been the focus of exploration in recent years is the southern margin of Loch Tay, where polymetallic quartz±carbonate veins sporadically outcrop throughout a 100km$^2$ swathe of the Dalradian Supergroup. Genetic aspects of the mineralisation here remain poorly constrained, particularly with regards to the source of the ore-forming fluids. We have used an integrated approach involving petrography, geochronology, sulphur isotope geochemistry and gold microchemistry to rectify this. Rhenium-Osmium (Re-Os) dating of molybdenite from the Tomnadashan Mine, in addition to our paragenetic study, confirms that the initial stage of mineralisation around Loch Tay occurred at ca. 423Ma. The sulphur isotope and gold microchemical data demonstrate that this area, along with the high-grade gold prospect named Lead Trial, likely comprises a magmatic-hydrothermal mineral system in the region. The extent and relation of the Tomnadashan-Lead Trial system to the metasediment-hosted veins throughout the region, which recorded $\delta^{34}S$ values of 5-10‰, remains unknown. It may be possible for other researchers to replicate our integrated approach towards metallogenic studies on other gold deposits.

## 1 Introduction

Around the southern margins of Loch Tay, which is situated in the Perthshire region of Scotland (Figure 1a), there are several gold and base metal deposits. The Tomnadashan and Coire Buidhe mines (Figure 1b) were worked by artisanal methods in the 19th century (Pattrick 1980), whilst the other occurrences of mineralisation were explored by junior exploration companies during the 1980s and 1990s (Corkhill et al. 2010). Neoproterozoic SEDEX mineralisation has been mined for barytes at Foss (Figure 1b) since the 1970s. Green Glen Minerals, a junior exploration company, are currently investigating the auriferous potential of the Lead Trial, which is one of several occurrences of gold mineralisation within the Ardtalnaig Estate (Figure 1c). Despite the extensive history of mineral exploration and extraction around Loch Tay, the genetic aspects of the mineral system are poorly understood. The veins consistently strike NW-SE (120-140°) (Corkhill et al. 2010). This may indicate a contemporaneous mineralisation event throughout the wider region (Figure 1b), with localised paragenetic and mineralogical variations representing subsequent mineralisation events that have affected some localities but not others.

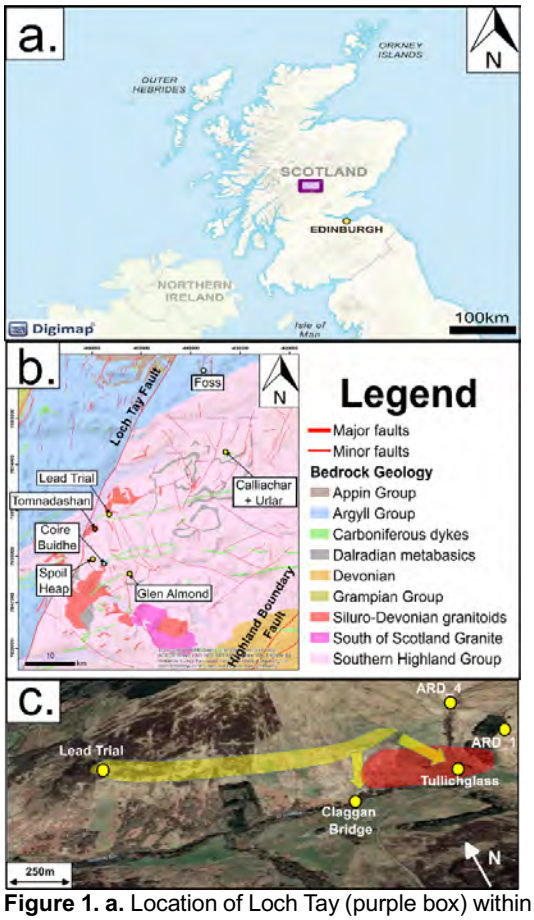


**Figure 1. a.** Location of Loch Tay (purple box) within the northern British Isles. **b.** Geological map of the Study Area, with localities colour coded according to the commercial or historic commodity of interest (yellow = gold, grey = silver, brown = copper, white = barytes). Localities other than Ardtalnaig and Tomnadashan are known as the 'metasediment-hosted veins.' **c.** Sampling localities (yellow) within the Ardtalnaig Estate. The arrows show a detrital contribution of gold from the peak of the hill, whilst the red colouration demonstrates the likely source of gold panned at Claggan Bridge.

The fractures infilled by the veins formed in response to sinistral motion along the Loch Tay Fault during the Scandian phase of the Caledonian Orogeny between 435 and 390Ma (Chew and Strachan 2013). The source of the ore-forming fluids around Loch Tay is unknown. At Calliachar and Urlar (Figure 1b), the fluid inclusion data revealed $CO_2$ contents and salinities typical of 'orogenic' gold deposits (Ixer et al. 1997). However, Tomnadashan has been described as a Cu-Mo porphyry (Pattrick 1984), and the elevated Bi concentrations observed across Figure 1b may be

the result of magmatic mineralisation processes (Corkhill et al. 2010). It can therefore be argued that an intrusion was the source of the ore-forming fluids throughout the region. The issue is complicated further by the ongoing debate regarding the genesis of gold deposits in orogenic belts, with several models involving metamorphic and magmatic fluids being recognised (Mortensen et al. 2022). We have used several analytical techniques to elucidate this problem around Loch Tay. The Re-Os geochronological analyses on molybdenite from Tomnadashan, in addition to a paragenetic study, provide a constraint on the age of the regional mineralising system. We also utilised $\delta^{34}S$ studies on sulphides to assess potential sources of ore-forming fluids, with gold compositional data being used to scrutinise variations within the mineral system around Ardtalnaig (Figure 1c).

## 2 Methodology

A molybdenite sample (TOM_MOLY_SM) was collected from a mineralised quartz stringer at Tomnadashan for Re-Os dating by isotope-dilution negative ion mass spectrometry (ID-NTIMS). This was conducted at Durham University. Whilst paragenetic studies on Tomnadashan do exist (Table 1), these are not supported with petrographic images. To contextualise the Re-Os age for the molybdenite and confirm the paragenesis, we conducted SEM studies on polished blocks of the mineralisation. This work was partially carried out using equipment at a facility operated by National Museums Scotland.

Compositional data was derived from gold particles that were panned from Ardtalnaig (Figure 1c) and Tomnadashan. Particles from each locality were dried and separated into groups of similar sizes. The samples were mounted on polished blocks. An SEM and Electron Microprobe were used to determine the inclusions present and the alloy composition. For the $\delta^{34}S$ studies, sulphides were analysed using an Elementar PYRO cube coupled to an IsoPrime continuous flow mass spectrometer. The samples were weighed into 8 x 5 mm tin cups and combusted at 1150°C.

## 3 The age and paragenetic context of molybdenite at Tomnadashan

TOM_MOLY_SM yielded a Re-Os age of 423±2Ma. At Tomnadashan, a NW-SE trending quartz vein (similar to the other Loch Tay veins) crosscuts the porphyry exposed on the surface (Figure 1b). This vein contains most of the Tomnadashan mineralisation (Naden 2010), which is also disseminated in the granitoid wallrock. The mineralisation postdates emplacement of the porphyry and therefore does not belong to the 'Cu-Mo porphyry' style of mineral deposits. Fluid inclusion data (Naden 2010) still supports a magmatic origin for the ore-forming fluids at Tomnadashan.

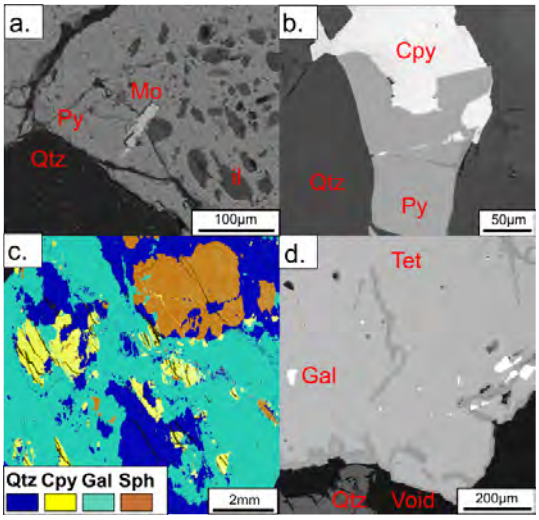


**Figure 3.** SEM images of the mineralisation at Tomnadashan. **a.** Molybdenite inclusion within a large pyrite crystal. **b.** Chalcopyrite overgrowing and crosscutting pyrite. **c.** Phase map demonstrating the co-occurrence of galena, sphalerite and chalcopyrite. **d.** Galena inclusions within tetrahedrite. Figure 3a represents mineralisation disseminated in the granitoid, whilst Figures 3b-d are from the vein. Figures 3a and 3c © National Museums Scotland.

The paragenetic study on Tomnadashan found that molybdenite coprecipitates with pyrite, which is crosscut and overprinted by an event involving chalcopyrite, galena and tetrahedrite precipitation (Figure 3).

| Stage | Description |
|---|---|
| 1 | Pyrite + molybdenite + bismuthinite + tennantite + aikinite + gold. |
| 2 | Chalcopyrite + galena + native bismuth + tetrahedrite. |

**Table 1.** A combination of the paragenetic interpretations that have previously been produced for Tomnadashan (Pattrick 1984; Smith et al. 2003).

Our paragenetic interpretation corresponds with previous work (Table 1). However, the paragenesis we describe here is not comprehensive and there are uncertainties; we need to confirm that the pyrite that is crosscut by the later base metal mineralisation belongs to the same generation as the material coprecipitating with the molybdenite (Figure 3a). There may in fact be several generations of pyrite and chalcopyrite at Tomnadashan. Furthermore, we did not observe all the phases (e.g. gold, tennantite) that were originally described (Table 1). Regardless, our study demonstrates an association between molybdenite and pyrite, with no evidence for multiple generations of molybdenite observed so far. The resulting Re-Os age of ca. 423Ma likely pertains to the initial stage of mineralisation at Tomnadashan. Further Re-Os dating will be

undertaken on the pyrite-hosted molybdenite that is disseminated throughout the granitoid (Figure 3a). This will help us to confirm that all occurrences of molybdenite belong to the same paragenetic stage.

## 4 Sources of ore-forming fluids

The following $\delta^{34}S$ results represent a regional study aimed at establishing the range of $\delta^{34}S$ variation throughout the region.

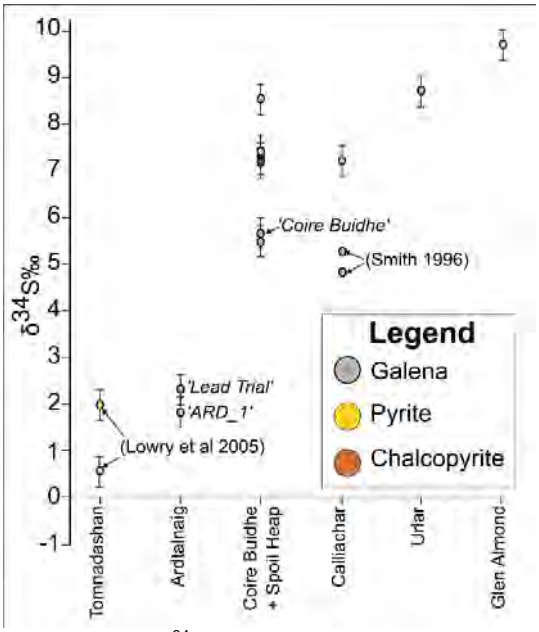


**Figure 4.** The $\delta^{34}S$ values of sulphides at several localities throughout the Loch Tay region. Results from previous studies have been added for context.

Around Ardtalnaig, $\delta^{34}S$ signatures are low relative to the metasediment-hosted veins. Although $\delta^{34}S$ values between different sulphides cannot be directly compared (due to differing isotopic fractionation rates during crystallisation), values <+5‰ typify magmatic sulfur (Ohmoto and Rye 1979). The Tomnadashan pyrite values therefore represent a magmatic source of sulfur too. The metasediment-hosted veins show $\delta^{34}S$ values that are significantly heavier than Tomnadashan and Lead Trial (Figure 4). These results are typical of 'orogenic' gold deposits and may indicate a crustal source of sulfur.

## 5. The microchemical signature of gold around Tomnadashan and Ardtalnaig

The similar microchemical characteristics between Lead Trial and Ardtalnaig (Figure 5) represents a detrital contribution of gold from Lead Trial into the Ardtalnaig Burn (Figure 1c).

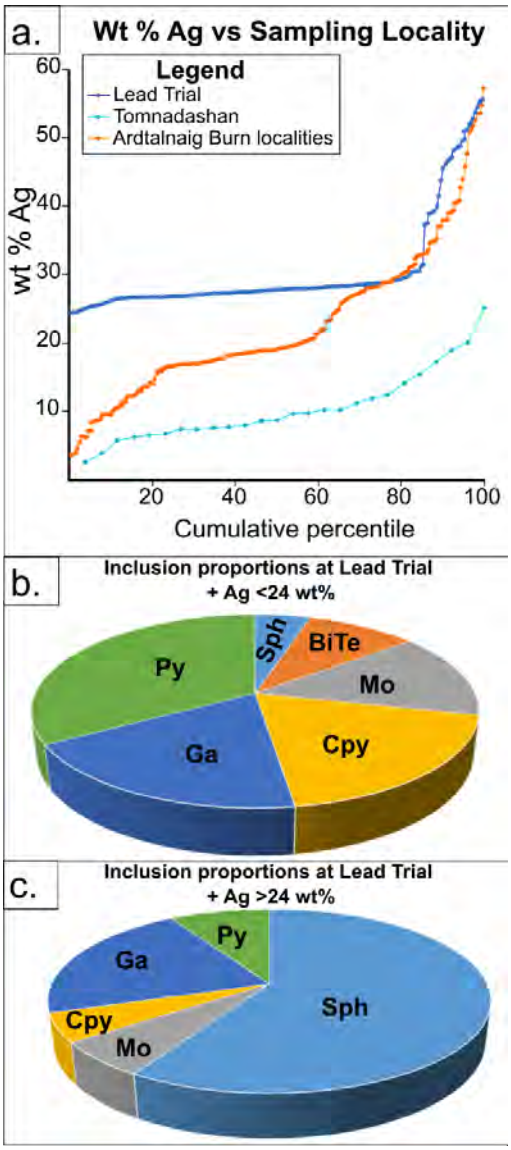


**Figure. 5a.** Wt% Ag in the alloy comprising the gold particles by locality. **b + c.** Pie charts showing inclusion types by proportion.

Gold particles characterised by the higher Ag contents have an inclusion assemblage that is dominated by sphalerite (Figure. 5c; Savastano et al. 2023). Particles from Claggan Bridge and Tullichglass, which are distinguishable by their lower Ag contents (Figure 5a), contain a greater proportion of pyrite inclusions. This phase is rare in the Ag >24 wt% gold particles (Figure 5c), and may indicate the presence of a vertically graded mineralising system at Ardtalnaig, with Lead Trial representing the peak. Further down the hill (Figure 1c), localities such as Tullichglass may demarcate deeper portions of the system, a transition marked by a pyrite + galena assemblage. Gold particles panned from Tomnadashan had much lower Ag contents when compared to the Ardtalnaig localities (Figure 5a). This may represent the deepest known portion of this Ardtalnaig-Tomnadashan system.

## 6. Conclusions

The contemporaneous formation of the veins around Loch Tay means that the age of one deposit (Tomnadashan) is likely to be widely applicable. The paragenetic context of molybdenite here – in the initial stage of mineralisation – indicates that the ca. 423 Ma age of molybdenite likely reflects the upper age of the Loch Tay mineralising system, with the lower age remaining uncertain. Our age of 423±2Ma overlaps with the 425Ma age often quoted for the slab-break off event at the end of the Caledonian Orogeny (Oliver et al. 2008). The $\delta^{34}S$ values from Ardtalnaig and Tomnadashan also support a link between magmatism and mineralisation around Loch Tay. However, the gold microchemical data has revealed that different populations exist within this area, potentially indicating a vertically graded mineral system. Lead Trial represents the peak, with the ore assemblage becoming more pyritic and enriched in Bi and Te with depth. This culminates in the assemblage of porphyry-type minerals preserved at Tomnadashan. Galena from ARD_1 and Lead Trial shows overlapping $\delta^{34}S$ values (Figure 4) - this further supports the notion that mineralisation processes around Ardtalnaig are genetically related and gold compositional variations simply reflect different portions of the same hydrothermal event.

There remains uncertainty regarding the relationship between the metasediment-hosted veins and the Tomnadashan-Ardtalnaig magmatic-hydrothermal system. Isotopically heavy $\delta^{34}S$ values, such as the ones recorded from the metasediment-hosted veins, are typical of 'orogenic' fluids. However, given the contemporaneous nature of mineralisation across the Loch Tay region, these veins are probably not associated with a mineralisation style preceding the formation of the Tomnadashan molybdenite. A more probable scenario involves a magmatic-hydrothermal system originating beneath the Tomnadashan pluton. As ore-forming fluids migrated away from this pluton, they may have mixed with isotopically lighter fluids stored in the metasediments, explaining the elevated $\delta^{34}S$ values observed in the metasediment-hosted veins (Figure 4). However, further research is needed to confirm this hypothesis.

## Acknowledgements

Shane Webb is a PhD student supported by the NERC Panorama Doctoral Training Partnership under grant NE/2445151.

## References

Corkhill C, Ixer R, Mason J, Irving D, Pattrick R (2010) Polymetallic auriferous vein mineralization near Loch Tay, Perthshire, Scotland. Scott J Geol, 46:23-30

Chew D, Strachan R (2013) The Laurentian Caledonides of Scotland and Ireland. Geol Soc Lond Spec Publ, 390:45-91

Ixer R, Pattrick R, Stanley C (1997). Geology, mineralogy and genesis of gold mineralization at Calliachar-Urlar Burn, Scotland. Trans Inst Min Metall Sect B Appl Earth Sci, 106:99-108.

Lowry D, Boyce A, Fallick A, Stephens E, Grassineau N (2005). Terrane and basement discrimination in northern Britain using sulphur isotopes and mineralogy of ore deposits. Geol Soc Lond Spec Publ, 248:133-151.

Mortensen J, Craw D, MacKenzie, D (2022). Concepts and revised models for Phanerozoic orogenic gold deposits. Geol Soc Lon Spec Publ, 516.

Naden J, Gunn A, Shephard T (2010). Fluids and mineralisation in the Scottish Dalradian. Br Geol Surv Intern Rep, OR/09/054.

Ohmoto H, Rye R (1979) Isotopes of sulfur and carbon. In: Barnes H (ed) Geochemistry of Hydrothermal Ore Deposits, 2nd edn. John Wiley and Sons, New York, pp 509-567

Oliver G, Wilde S, Wan Y (2008). Geochronology and geodynamics of Scottish granitoids from the late Neoproterozoic break-up of Rodinia to Palaeozoic collision. J Geol Soc, 165:661-674

Pattrick R (1984). Sulphide mineralogy of the Tomnadashan copper deposit and the Corrie Buie lead veins, south Loch Tayside, Scotland. Mineral Mag, 48:85-91

Savastano L, Chapman R, Torvela T (2023). Metallogeny of gold (from in-situ to placer) in the Loch Tay area of Central Scotland. 17th SGA Bienn Meet.

Smith G, Gunn A, Shepherd T, Coats J, Wiggans G (2003). Gold in the Dalradian terrane: a review of previous work. Br Geol Surv Intern Rep, p. 191.

Smith D (1996) Fractures and mineralisation in the Scottish Dalradian. PhD Thesis, University of Manchester.

# Superimposed orogeny as key to gold hotspot formation at the north Peruvian Gondwana margin

**Daniel Wiemer[1], Steffen G. Hagemann[1], Anthony I.S. Kemp[1], Jon Hronsky[1,2], Laure Martin[1], Trevor Ireland[3], Nicholas Thébaud[1], Carlos Villanes[4]**
*[1]Centre for Exploration Targeting, University of Western Australia, Crawley, WA, Australia*
*[2]Western Mining Services Pty Ltd, Perth, WA, Australia*
*[3]University of Queensland, St. Lucia, QLD, Australia*
*[4]Compañia Minera Poderosa S.A., Lima, Peru*

**Abstract.** The geodynamic processes responsible for the formation of economic gold deposits remain controversial. It is postulated that the generation of gold-rich parental magma plays a crucial role. Two contrasting models prevail: i) selective uptake of gold as an incompatible element during low-degree partial melting of a crustal or upper mantle source, and ii) reactivation of a previously enriched source reservoir. We present bulk-geochemical and zircon U-Pb, Hf and O isotopic data from intrusive rocks that host the north Peruvian Carboniferous Pataz-Parcoy gold vein system to identify potential gold parental magmas and characterize their source. We find that hydrous, metal-enriched mafic rocks were emplaced episodically into the mid crust from ~370 Ma onwards. Zircon Hf isotopic data indicate that these magmas derived from an upper mantle domain that was likely pre-enriched during preceding Ordovician subduction. Sub-mantle $\delta^{18}O$ zircon values imply the presence of remnant subducted oceanic crust, part of which is preserved as an ophiolite, within the upper mantle source. Furthermore, evidence of hydrothermally modified zircon attests to ore-fluid expulsion upon parental magma recharge concomitant with repeated amphibole break-down. The gold vein system formed after final magma emplacement and solidification at ~332 Ma, marking a tectonic switch towards back-arc magmatic activity.

## 1 Introduction and background

The geometry of gold veins hosted within Carboniferous plutonic rocks in the Pataz-Parcoy gold districts of northern Peru is controlled by the inheritance of structures belonging to the Famatinian basement orogen that strikes at oblique angle to the Carboniferous and subsequent Andean orogenic belts (Fig. 1; Wiemer et al., 2021). Major gold deposits are situated in the hanging-wall of the inferred cryptic Famatinian suture between the Gondwana margin and the Paracas micro-terrane (Wiemer et al., 2022). The Famatinian Paracas collision seeded the development of a regional-scale dilational jog as a response to Carboniferous dextral-strike slip along the Rio Marañon Fault (Fig. 1; Wiemer et al., 2021; 2022). The Pataz-Parcoy gold vein system displays characteristics of orogenic gold deposits, although its extent is largely restricted to host rocks ascribed to the Western Plutonic Belt that intruded the Famatinian basement (Fig. 1). The Eastern Plutonic Belt does not host auriferous veins akin to the mesothermal Pataz-Parcoy system and intrusive relationships imply a later relative timing of magmatism. Thus, the timing and geochemical-isotopic signatures of the relatively older Western Plutonic Belt may inform about critical magmatic processes and parental magma and source characteristics responsible for gold deposit formation.

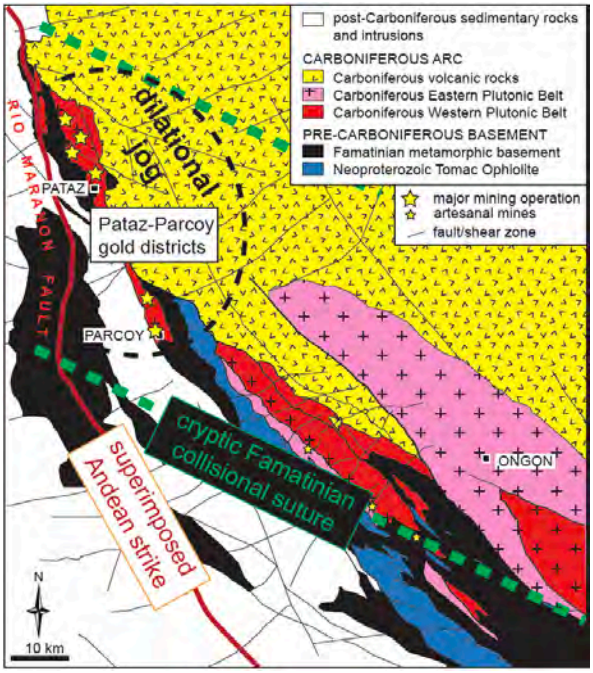


**Figure 1.** Simplified geologic map of the study area, Pataz region, northern Peru (modified after Wiemer et al., 2022).

## 2 Methodology

In combination with petrographic investigations (University of Western Australia, UWA), bulk-rock XRF major oxide and ICP-MS trace element geochemical data were acquired (Bureau Veritas, Canada) from a total of 48 unaltered/fresh samples, including plutonic, sub-volcanic and volcanic rocks from both the Eastern and the Western Plutonic Belt (Fig. 1). Zircon from a total of 14 plutonic rocks from the Eastern and the Western suite and from one metasedimentary rock of the adjacent basement were characterized by CL-SEM imaging (UWA) and selected spots were analyzed by SHRIMP for U-Pb age determination (Australian National University). On the same spots (and/or same zircon domains), LA-ICP-MS trace element and Lu-Hf isotopic data and SIMS O-isotopic data were acquired (UWA).

## 3 Results

### 3.1 Bulk-rock geochemistry

The bulk-rock geochemical data show that the most primitive (~46-58 wt.% $SiO_2$) Pataz rocks, which intruded repeatedly (based on field relationships), are relatively enriched in Au and Cu compared to more evolved igneous components (Fig. 2a and b). The primitive and evolved rocks are separated by a conspicuous silica gap (58-64 wt.% $SiO_2$) that corresponds to a change in the fractionation behaviour, conforming with petrographic observations. The primitive rocks are controlled by initial amphibole accumulation and show no to only weak Eu anomalies, indicating hydrous conditions and suppression of plagioclase crystallization, whereas increasing negative Eu anomalies and decreasing Dy/Yb ratios in the evolved rocks are in accordance with plagioclase and amphibole fractionation (Fig. 2c and d).

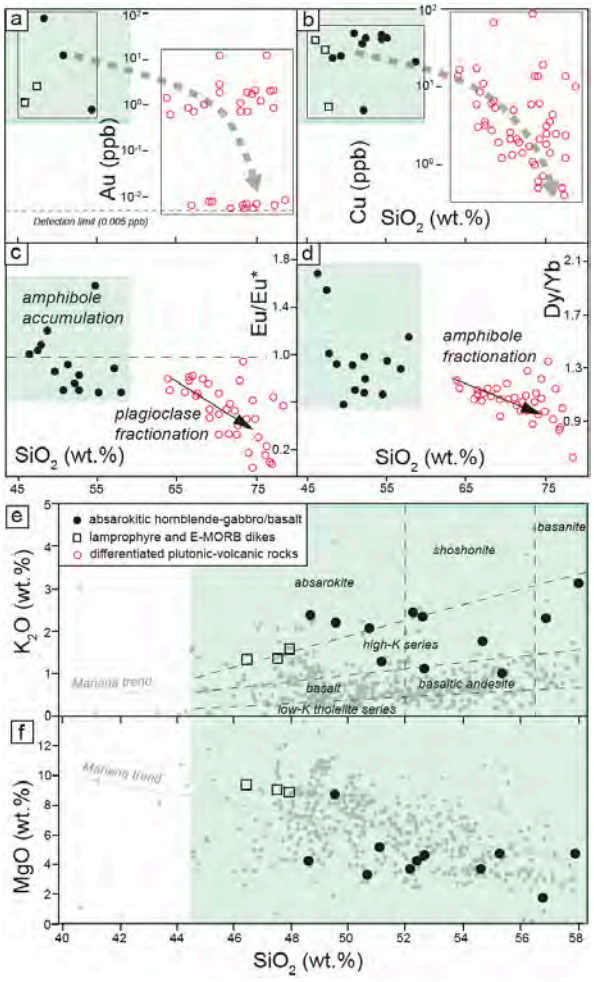


**Figure 2.** Bulk-rock Harker plots using $SiO_2$ as an index of differentiation. **a** Cu. **b** Au. **c** Eu/Eu*. **d** Dy/Yb. **e** $K_2O$. **f** MgO. Mariana arc reference suite downloaded from the GEOROC database (https://georoc.eu/).

The most primitive rocks show elevated $K_2O$ contents at corresponding MgO contents that are in the range of typical arc magmas (Mariana arc reference suite (GEOROC database, https://georoc.eu/) and thus can be classified as absarokites/appinites (Fig. 2e and f). The Pataz absarokitic rocks are also relatively enriched in other incompatible elements, such as Ba, and display a strong affinity to gold parental rocks in the graph of Figure 3 (Loucks and Ballard, 2002). Figure 3 reaffirms the role of hornblende accumulation and suppressed plagioclase crystallization due to hydrous conditions, expressed in the Sr/Y ratio as the denominator in the ordinate of the graph.

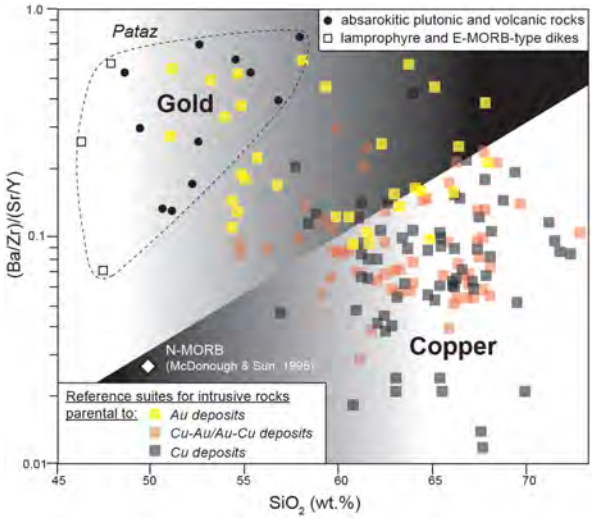


**Figure 3.** Bulk-rock chemical plot distinguishing Au, Au-Cu, and Cu parental intrusive rocks (reference suites after Loucks and Ballard, 2002).

### 3.2 Zircon trace elements, U-Pb geochronology, and Hf-O isotopes

Zircon CL imaging reveals relatively complex internal structures attesting to the presence of multiple truncating domains in all samples. In combination with trace element chemical data magmatic, recrystallized, and hydrothermally modified domains are identified, noting that hydrothermal domains do not occur within zircon from the primitive absarokitic gabbros (Fig. 4a). All analyzed zircons largely fall within the field of the Cu-Au fertile reference suite (Fig. 4b; Lu et al., 2016) and rare earth element (REE) pattern mimic the absence or presence of Eu anomalies of respective bulk-rock samples (Fig. 4c). Magmatic domains yield Ti-temperatures (calculated after Watson and Harrison, 2005) between ca. 650-810°C, indicating that zircon crystallized both from near-solidus melt and from high(er) temperature melt ascribed to repeated recharge episodes. Indeed, due to the re-occurrence of distinct U-Pb age domains throughout all samples, geochronological data are evaluated based on the overall spot age frequency distribution (Fig. 5a). The frequency distribution shows multiple age peaks associated with antecrystic zircon domains. The age peaks are interpreted to reflect episodic recharge

and thermal rejuvenation over a >30-Myr duration for the Western Plutonic suite, whereby troughs in the age distribution match the observation of truncating zircon domains. Outermost oscillatory-zoned magmatic domains (autocrystic) suggest that final magma emplacement of the Western suite occurred between ca. 340-332 Ma (Fig. 5a), followed by a brief episode of apparent magmatic quiescence that correlates with a reported Re-Os molybdenite age for initial gold vein formation (Szappanosné-Vágó et al., 2010) and confirms the required brittle nature (i.e., magma solidification) for fault-fill vein development envisaged by Wiemer et al. (2021).

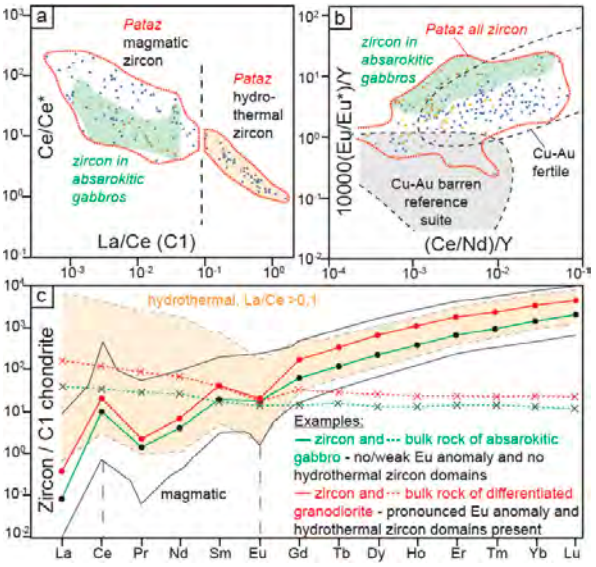


**Figure 4. a** Chemical discrimination of magmatic and hydrothermally modified zircon. **b** Zircon Cu-Au fertility index plot (reference suites after Lu et al., 2016). **c** REE pattern (chondrite values after McDonough and Sun, 1995).

Zircon Hf isotopic compositions of early antecryst domains from the absarokitic gabbros correspond to εHf(t) values of ca. -3 at the onset of magmatic crystallization at ca. 370-360 Ma (Fig. 5b). The εHf(t) of younger antecrystic and autocrystic domains follow near-linear trends for respective samples that can be approximated by their average $^{176}Lu/^{177}Hf$ ratio (~0.0017). The onset of "new" crystallization series in younger sample populations appears to be shifted towards slightly more unradiogenic compositions, i.e., towards εHf(t) of ca. +2 at ca. 340 Ma. On the other hand, either single domains or entire sample populations from the most evolved rock types are characterized by εHf(t) values of ca. -5 to -10 (Fig. 5b). The latter εHf(t) values fall in the range of, and/or approach, those of the adjacent basement metasedimentary rock. The youngest detrital zircon population from the metasedimentary rock yield $^{206}Pb/^{238}U$ spot ages between 494-462 Ma and εHf(t) values between -5.8 and -16.1 (recalculated at 340 Ma using their average zircon $^{176}Lu/^{177}Hf$ ratio of ~0.0008).

Zircon $\delta^{18}O$ values from the Western Plutonic suite largely range between ca. 5.2 and 6.8, generally overlapping the upper limits of the mantle array (Fig. 5c). Zircon from the most evolved rocks (high negative εHf) display elevated $\delta^{18}O$ values of ca. 6.5 to 8, similar to those detected in the basement metasedimentary rocks ($\delta^{18}O$ = 5.6 to 8.3). Samples with younger onset of zircon crystallization indicate the increasing influence of a sub-mantle $\delta^{18}O$ component (Fig. 5c).

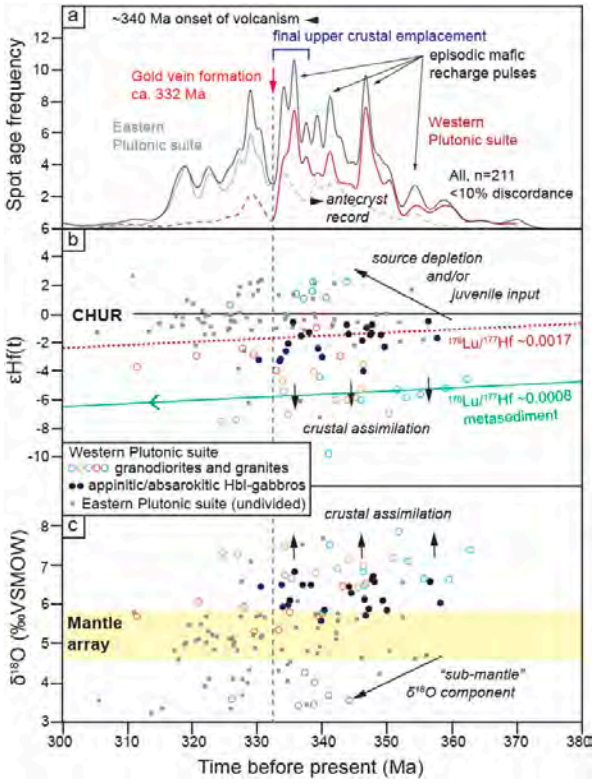


**Figure 5. a** Zircon $^{206}Pb/^{238}U$ spot age frequency Kernel distribution. **b** εHf versus time. **c** $\delta^{18}O$ versus time.

To further test if particularly the isotopic signatures from the absarokitic gabbros are pristine, i.e., characterizing their mantle source, uncontaminated by post-extraction intracrustal assimilation, we introduce the inherited zircon index (IZI; this study). The IZI describes the percentage of inherited (in this case pre-Carboniferous) zircon within a sample population. It is noted that our initial analytical spot selection was conducted irrespective of the internal position of distinct zircon domains, in other words representing a random statistical probe. As shown in Figure 6a and b, the IZI correlates well with the presented Hf and O isotopic data. The samples that contain a high proportion of inherited grains are those that display high negative εHf and high $\delta^{18}O$ values matching the zircon from the basement metasedimentary rock. In contrast, inherited zircons are entirely absent from the absarokitic gabbro samples. Given the overall well-preserved record of zircon domains in combination with Ti-zircon temperatures of up to 810°C we discard the possibility of significant zircon

dissolution. Hence, the overall primitive character of the absarokitic gabbros precludes magma genesis through partial melting of lower crustal rocks, and the absence of inherited zircons supports the fact that no intracrustal assimilation affected the magmas. This suggest that the presented isotopic signatures are pristine and reflect the composition of the mantle source.

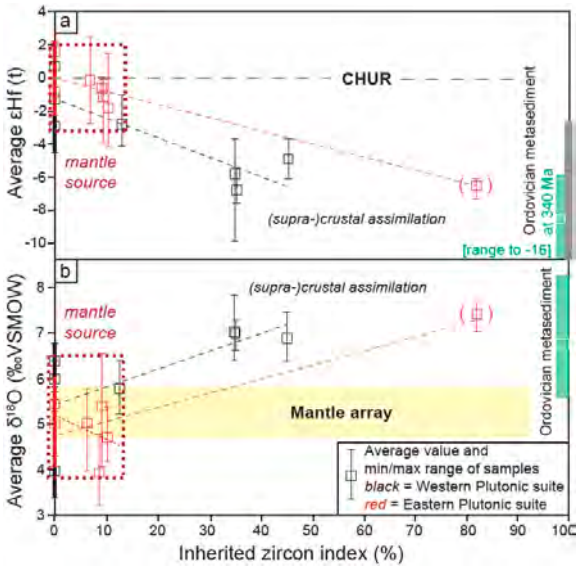


**Figure 6. a** εHf and **b** $\delta^{18}O$ versus the inherited zircon index (IZI; this study).

## 4 Discussion and conclusions

Our data show that most primitive absarokitic gabbros represent the parental magmas for gold in the Pataz region of northern Peru. These magmas intruded episodically since the very onset of Carboniferous subduction-related magmatic activity at ca. 370-360 Ma. Elevated incompatible major and trace element concentrations ($K_2O$, Ba) in combination with enrichment in Au and Cu relative to high MgO and low $SiO_2$ contents suggest that the magmas were generated from a metasomatized, pre-enriched ore fertile upper mantle. This is confirmed by trace element concentrations in zircon. Furthermore, Hf-O zircon isotopic data indicate that only some of the most evolved granitic components in the Pataz magmatic system interacted with adjacent (supra-)crustal components, whereas pristine εHf(t) values (ca. -3) of zircon from the primitive absarokitic gold parental rocks confirm the pre-enriched nature of the mantle source at ca. 370-360 Ma. Mantle pre-enrichment can be ascribed to the preceding Famatinian subduction-collision that has been documented in the area (Wiemer et al., 2022). Indeed, the early onset and repeated intrusion, as well as the overall observed volume of the absarokitic gabbros and equivalent volcanic rocks in the study area, and the inferred genetic link to the more evolved igneous rocks, favour a geodynamic scenario that does not require low-degree partial source melting to selectively uptake gold as an incompatible element. Instead, the preceding Famatinian subduction sufficiently pre-enriched and fertilized the upper mantle. We argue that at the onset of Carboniferous arc formation, heat from subduction related magma production caused the re-melting of fertile portions/regions within the established fossil Famatinian lithospheric mantle, giving rise to the repeated generation of gold-rich absarokitic magma. The episodic nature of recharge remains unclear but may be discussed in the context of energy (heat) transitions upon major bulk melt extraction in the source. Concomitant source depletion (increasing εHf towards +2) was accompanied by increasing consumption of remnant previously subducted oceanic crust (towards sub-mantle $\delta^{18}O$ values, e.g., Cartwright and Valley, 1991). The episodic inferred mid-crustal absarokitic magma replenishment resulted in repeated thermal rejuvenation associated with amphibole break-down that spawned magmatic-hydrothermal transitions, ore-fluid expulsion, hydrothermal zircon modification, and batch extraction of evolved magmas. Magma and fluid discharge from the accumulated mid-crustal reservoir into upper crustal levels occurred between 340-332 Ma.

## Acknowledgements

This research was fully funded by the Compañia Minera Poderosa S.A. (Lima, Perú). The authors thank D. Sologuren Arias and F. Cueva (Compañia Minera Poderosa S.A.) for their continued support.

## References

Cartwright, I., and Valley, J.W. (1991): Low-18O Scourie dike magmas from the Lewisian complex, northwestern Scotland. Geology, v. 19, p. 578-581.

Loucks, R.R., and Ballard, J.R. (2002): Predictive guides to copper and gold mineralization at circum-pacific convergent plate margins. Report 2A: Distinguishing characteristics, petrogenesis and tectonic habitat of copper ore-forming arc magmas, p. 1-105.

Lu, Y.-J., Loucks, R.R., Fiorentini, M., McCuaig, C., Evans, N.J., Yang, Z.-M., Hou, Z.-Q., Kirkland, C.L., Parra-Avila, L.A., and Kobussen, A. (2016): Zircon compositions as pathfinder for porphyry Cu ± Mo ± Au mineral deposits. Society of Economic Geologists. Special Publications Series v. 19, p. 329-347.

McDonough, W.F., and Sun, S.-S. (1995): The composition of the Earth. Chemical Geology, v. 120, p. 223-253.

Szappanosné-Vágó, E., Moritz, R., and Barra, F. (2010): Fluid inclusion investigation and Re-Os dating of the Pataz-Parcoy intrusion-hosted gold deposits, Eastern Cordillera, Peru. EG51, Crustal fluids and gold, p. 260.

Watson, E.B., and Harrison, T.M. (2005): Zircon thermometer reveals minimum melting conditions on earliest Earth. Science, v. 308, p. 841-844.

Wiemer D., Hagemann, S.G., Thébaud, N., and Villanes, C. (2021): Role of basement structural inheritance and strike-slip fault dynamics in the formation of the Pataz gold vein system, Eastern Andean Cordillera, northern Peru. Economic Geology, v. 116, p. 1503-1535.

Wiemer, D., Hagemann, S.G., Hronsky, J., Kemp, A.I.S., Thébaud, N., Ireland, T., and Villanes, C. (2022): Ancient structural inheritance explains gold deposit clustering in northern Peru. Geology, v. 50, p. 1197-1201.

# A lower Cambrian Moroccan Copperbelt? (Tizert copper deposit, Igherm inlier Anti Atlas, Morocco): preliminary results of Cu-Fe-sulfide Re-Os geochronology and stable sulfur isotope data

**Fatiha Askkour[1], Nicolas J. Saintilan[2], Atman Madi[3], Cyril Chelle-Michou[2], Mustapha Souhassou[4], Nourissaid Içame[1], Mehdi Ousbih[1], Jorge E. Spangenberg[5], Lhou maacha[3], Moha Ikenne[1]**
*[1]Laboratory of Applied Geology and Geo-Environment, Ibn Zohr University, Agadir, Morocco.*
*[2]Institute of Geochemistry and Petrology, Department of Earth Sciences, ETH Zurich, Zürich, Switzerland*
*[3]MANAGEM Group, Twin Center, Tour A, BP 5199, Casablanca. Morocco*
*[4]Laboratory of Geo-Bio-Environmental Engineering and Innovation, Research, Ibn Zohr University, Taroudant, Morocco.*
*[5]Institute of Earth Surface Dynamics, University of Lausanne, Building Geopolis, 1015 Lausanne, Switzerland*

**Abstract.** We report new Re-Os data and $\delta^{34}S$ values for bornite and pyrite from the sandstone- and carbonate-hosted Cu deposit at Tizert, Igherm Inlier, Anti-Atlas, Morocco. Bornite and pyrite mineralization is found towards the top of a late Ediacaran siliciclastic and carbonate Basal Series. The latter is part of a continuous Ediacaran sedimentation that filled an incipient intracratonic basin over the eroded topography (including paleohighs) of Paleoproterozoic lithologies of the West African Craton. The Re-Os data provide absolute time stamps of ore formation between ca. 520–514 Ma, at the time of sediment compaction/diagenesis of the Basal Series. Mineralization took place during continuous sedimentation in the Cambrian heralded by deposition of the ca. 542–522 Ma cap rock Lie-de-Vin Series, and before a deepening of the intracratonic basin by the Middle Cambrian. The $\delta^{34}S$ values of pyrite (+22.62 to +24.26 ‰) result from thermochemical sulfate reduction of late Ediacaran seawater sulfate whereas the $\delta^{34}S$ values of bornite (+11.86 to +19.45‰) are compatible with TSR aided by sour gas. Orange-tinted host rocks associated with clots of bornite signal the oxidation of gaseous hydrocarbons and the reduction of seawater sulfate that led to oxidation of iron-bearing phases in the originally greenish host rocks.

## 1 Introduction

Copper (Cu) is one of the 17 critical metals/materials identified by the World Bank as "crosscutting," i.e., it is of paramount importance for the development and implementation on industrial scale of, at least, eight renewable energy and clean storage technologies (WBG 2020). After porphyry Cu deposits, Cu-sulfide deposits in sedimentary rocks (e.g., the Central African Copperbelt; Hitzman et al. 2010) are the main resource of Cu on Earth (Sillitoe, 2012).

In the Anti-Atlas orogenic belt, southwestern Morocco, ca. 200 Cu sulfide deposits and occurrences are hosted by late Ediacaran siliciclastic rocks (Bouchta et al. 1977; Fig. 1) that are part of a transgressive sequence of late Ediacaran and Lower Cambrian siliciclastic and carbonate rocks (Benssaou & Hamoumi 2003). A remarkable pattern of Cu-occurrences around and where the Ediacaran-Cambrian sedimentary sequence flanks pre-Ediacaran basement inliers has been identified (Bouchta et al. 1977; Fig. 1). In light of this pattern identifying a strong control of basement paleotopography on the location of the Cu-deposits, a syn-sedimentary timing of sulfide mineralization was proposed (Pouit 1966; Bouchta et al. 1977; Skacel 1993).

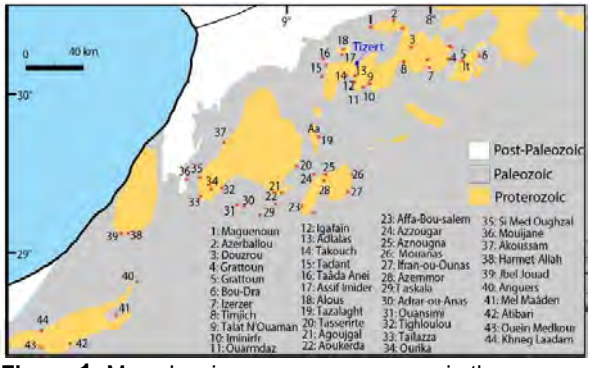

**Figure 1**. Map showing copper occurrence in the Western Anti-Atlas (after Bouchta et al. 1977**)**

The present study focuses on the Tizert deposit, which is the largest known resource in the western Anti-Atlas. The late Ediacaran siliciclastic Basal Series of the Adoudou Formation host stratiform bodies comprising disseminated sulfides and veins (Pouit 1966; Skacel 1993; Oummouch et al. 2017). Here, we present (1) petrographic evidence of the relationship between the host lithologies and Cu-sulfides and pyrite in hand samples, combined with (2) mineral-specific rhenium-osmium (Re-Os) and sulfur ($\delta^{34}S$ – VCDT) isotope geochemistry to constrain the absolute timing of mineralization and identify the source(s) of reduced sulfur for sulfide precipitation, respectively.

## 2 Geological background

The Tizert deposit is located on the edge of the Igherm pre-Ediacaran basement inlier. The latter comprises Paleoproterozoic orthogneiss, migmatites and granites unconformably overlain by limestone, quartzite and ca. 1.75 – 1.65 Ga (Statherian) mafic rocks. The lower Ediacaran (volcani-)clastic rocks of the Tiddiline Formation lie above an erosive contact to this Paleoproterozoic basement (Oummouch et al. 2017, Ikenne et al.

2017). These units are in turn overlain by upper Ediacaran conglomerates, volcaniclastic rocks and glaciogenic deposits of the Ouarzazate Group (591–548 Ma; Walsh et al. 2012; Benziane et al. 2016; Yajioui et al. 2020). The latter is covered by the late Ediacaran Adoudou Formation, including the Basal Series and the Lower Limestone, which are host to the Tizert Cu-sulfide mineralization. The Basal Series starts with a thick Basal Conglomerate (including fluvial sandstone and silt- to sandstone-matrix-supported polymictic conglomerate) followed by the peritidal Basal Limestone, which in turn is overlain by a fining-upward sequence of sandstone and siltstone with distinctive colors, i.e., grey, purple, greenish up stratigraphy. The Basal Series terminates in a silicified stromatolitic dolostone (Tamjout Dolomite) and layered limestone of the Lower Limestone member (Thomas et al. 2002; Maloof et al. 2010; Oummouch et al. 2017). Finally, the Cambrian Lie-de-Vin Series (ca. 542 to ca. 522 ± 2 Ma; Alvaro et al. 2006) marks a significant sea level regression heralding limestone and siltstone deposition, as well as being a regional marker at the Precambrian–Cambrian boundary (Taroudant Group; Oummouch et al. 2017).

## 3 The Tizert Cu deposit

The Tizert Cu-Ag deposit is the largest sediment-hosted copper deposit in the area. Mineralization crops out stained by supergene malachite whereas the hypogene mineralization comprises bornite, chalcocite, covellite, chalcopyrite ad pyrite. Sulfide mineralization is hosted by the Tamjout Dolomite and in the greenish portion of the sandstone-siltstone of the underlying Basal Series (Oummouch et al. 2017; Poot et al. 2020). According to Oummouch et al (2017), the late Ediacaran host rocks accumulated in wide depressions whereas the upper part of the Cambrian sedimentary rocks was deposited across both these paleo-lows and the paleo-reliefs.

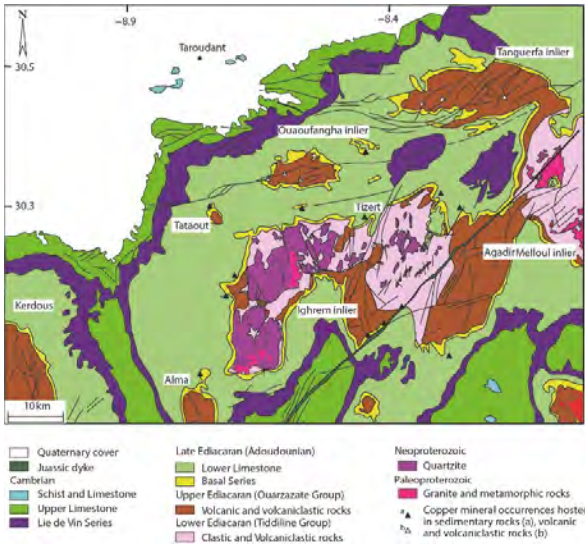


**Figure 2.** Simplified geological map of the Igherm inlier (Modified after Oummouch et al. 2017).

The deposit shows lateral and vertical zonation in sulfide content and sulfide species. Mineralization is found in the upper part of the Basal Series below layered limestone and the cap rock of the Cambrian Lie-de-Vin Series. At the current state of knowledge, without any absolute time stamps on mineralization, it is believed that the mineralization occurred during an advanced stage of sediment compaction and due to the movement of metal-rich fluids originating from evaporite dissolution. A current model proposes that a late diagenetic disseminated mineralization was followed by vein-style mineralization related to compression in the late Carboniferous.

## 4 Working hypotheses and methodology

Stratiform Cu deposits hosted in sedimentary rocks may result from the reduction of oxidized, copper-bearing fluids or cooling of moderate-temperature hydrothermal fluids carrying both Cu and hydrogen sulfide – $H_2S$ (Hitzman et al. 2010; Saintilan et al. 2023). An intracratonic basin, which becomes hydrologically closed, may be an ideal setting for the formation of this type of deposits (Hitzman et al. 2005). During the late Neoproterozoic and early Cambrian eras, the Anti-Atlas was affected by extension and rifting episodes related to the opening of the Iapetus Ocean (Bensaou et al. 2003; Soulaimani et al. 2014). The intracratonic setting of these basins enabled the development of a closed hydrological basin structure, favoring the production of highly saline and oxidized basinal brines at moderate temperatures (see Hitzman et al. 2010).

To test this hypothesis, it is paramount to provide age constraints on the timing of mineralization, the source of metals, and identify the source of $H_2S$. We conduct rhenium-osmium (Re-Os) isotope geochemistry studies (Selby and Creaser, 2001; Hnatyshin et al. 2016) specific to individual monomineralic sulfide mineral separates (Saintilan et al. 2020), i.e., bornite and pyrite here. The purified Re and Os cuts are analyzed by negative thermal ionization mass spectrometry (N-TIMS; Creaser et al. 1991; Völkening et al. 1991). In addition, we use the same mineral separates to constrain the stable sulfur isotope composition ($\delta^{34}S$ – VCDT) of bornite and pyrite using the protocol by Spangenberg et al. (2010).

## 5 Results and preliminary conclusions

Pyrite is found as centimetric clots in the polymictic conglomerate (Fig. 3; TIZ-06). Pyrite-rich zones progressively grade into chalcopyrite-dominated sections. The sulfur isotope composition of the three pyrite samples (TIZ-06a, b, & c) across a 1.5m-long core section is remarkably homogeneous between +22.62 and +24.26 ± 0.30‰ ($n$ = 4). Pyrite has moderate Re and low Os contents (between 10.449 and 44.192 ng $g^{-1}$ Re, and, between 72.5 and 250.8 pg $g^{-1}$ total Os). The $^{187}Re/^{188}Os$ ratios are very high (3,577–21,379) and

positively correlated with highly radiogenic $^{187}Os/^{188}Os$ ratios (31.96–188.96) in the $^{187}Os/^{188}Os$ vs. $^{187}Re/^{188}Os$ space. The Re-Os systematics of five pyrite aliquots from samples TIZ-06a, b and c yield a Model 3 isochron date at 514 ± 2 Ma (mean square weighted deviates – MSWD = 2.3) with an initial $[^{187}Os/^{188}Os]_i$ – $Os_i$ – at 1.19 ± 0.22.

Bornite occurs as bands or dissemination in grey to locally greenish sandstone and siltstone (samples TIZ-02, TIZ-03, TIZ-04, TIZ-05b; Fig. 3) as well as in the form of hydrothermal breccia cemented by coarse-grained calcite with clear signs of hydraulic fracturing of siltstone (TIZ-05a; Fig. 3). The $\delta^{34}S$ values of bornite in samples TIZ-02, TIZ-03, TIZ-04 ranges from +16.46 to +19.45 ± 0.30‰ ($n$ = 6) whereas bornite in samples TIZ-05a & b has the lightest $\delta^{34}S$ values measured in this study (+11.86 to +13.07 ± 0.30‰; $n$ = 4). Bornite has low to moderate Re and low Os contents (between 1.250 and 24.841 ng $g^{-1}$ Re, and, between 21.5 and 344.8 pg $g^{-1}$ total Os). The $^{187}Re/^{188}Os$ ratios are high (47.68–744.21) and positively correlated with high radiogenic $^{187}Os/^{188}Os$ ratios (1.363–7.436) in the $^{187}Os/^{188}Os$ vs. $^{187}Re/^{188}Os$ space. The Re-Os systematics of bornite in samples TIZ-04 and TIZ-05 define a preliminary isochron date at 520 ± 7 Ma (MSWD = 2.4; $n$ = 4) with an $Os_i$ at 1.56 ± 0.02.

Our results suggest that bornite and pyrite mineralization formed at ca. 520–514 Ma at the time of sediment compaction/diagenesis of the Basal Series. This mineralizing process took place during continuous sedimentation in the Cambrian (1) after a signal of sea level regression and deposition of the ca. 542–522 Ma cap rock Lie-de-Vin Series, and (2) before a deepening of the intracratonic basin and deposition of regionally extensive shale by the Middle Cambrian (ca. 509 Ma; Burkhard et al. 2006).

The Ediacaran sulfate isotope record is complicated. The transition from the Proterozoic to the Phanerozoic suggests a dynamic sulfur cycle with $\delta^{34}S$ values of seawater sulfate varying between ca. + 20 and +45 ‰ (Crockford et al. 2019). We interpret that 34S values of pyrite to result from thermochemical sulfate reduction of late Ediacaran seawater sulfate (+22.62 to +24.26 ‰). The lighter 34S values of bornite would be compatible with TSR aided by sour gas (Anderson 2008), i.e., a mixture of TSR-derived H2S from Ediacaran seawater sulfate and very light biogenically-derived $H_2S$ from the sour gas. Petrographic evidence suggests the presence of sour gas pockets in the host sandstone and siltstone. Due to TSR, greenish sandstone-siltstone bearing reduced iron phases was locally turn to orange sandstone-siltstone (associated with bornite clots) where the oxidation of gaseous hydrocarbons and the reduction of seawater sulfate was accompanied by oxidation of iron-bearing phases (Fig. 3; TIZ-04). Ongoing petrographic investigations combined with clumped and stable carbon isotope work on hydrothermal calcite associated with bornite will shed light onto the role and nature of the reducing agent for sulfate. To end with, we interpret the $Os_i$ ratios of the pyrite and bornite isochron regressions (i.e., 1.19 and 1.56, respectively) as being compatible with derivation of Os, and by corollary other metals, from a crustal source. The most likely candidate source rocks lie in the Paleoproterozoic basement including Statherian mafic rocks.

**Figure 3.** Representative mineralized samples from the Tizert deposit utilized in this study. See text for details. All scale bars are 1 cm long.

## Acknowledgments

The authors are indebted to the Moroccan Ministry of Higher Education, Scientific Research and Innovation and the OCP Foundation that funded this work through the APRD research program.

## References

Anderson GM (2008) The mixing hypothesis and the origin of Mississippi Valley-type ore deposits. Economic Geology, 103(8), 1683-1690.

Alvaro JJ, Ezzouhairi H, Vennin E, Ribeiro ML, Clausen S, Charif A, Ayad NA, Moreira ME (2006) The Early-Cambrian Boho volcano of the El Graara massif, Morocco: Petrology, geodynamic setting and coeval sedimentation. J. Afr. Earth Sci. 44, 396–410. doi:10.1016/j.jafrearsci.2005.12.008

Benssaou M, Hamoumi N (2003). Le graben de l'Anti-Atlas occidental (Maroc): Contrôle tectonique de la paléogéographie et des séquences au Cambrien inférieur. Comptes Rendus Geosci. 335, 297

Bouchta R, Boyer F, Routhier P, Saadi M, Salem M (1977) L'aire cuprifère de l'Anti-Atlas (Maroc); permanence et arêtes riches. CR Acad Sci Paris 284:503-506

Burkhard M, Caritg S, Helg U, Robert-Charrue C, Soulaimani A (2006) Tectonics of the anti-atlas of Morocco. Comptes Rendus Geoscience, 338(1-2), 11-24.

Creaser RA, Papanastassiou DA, Wasserburg GJ, (1991) Negative thermal ion mass spectrometry of osmium, rhenium and iridium. Geochim. Cosmochim. Acta 55, 397–401.

Crockford PW, Kunzmann M, Bekker, A, Hayles J, Bao H, Halverson GP, Peng Y, Bui TH, Cox GM, Gibson TM, Wörndle S, Rainbird R, Lepland A, , Swanson-Hysellm NL, Master S, Sreenivas B , Kuznetsov A , Krupenikq V, Wing, B A (2019) Claypool continued: Extending the isotopic record of sedimentary sulfate. Chemical Geology, 513, 200-225.

El Basbas A, Aissa M, Ouguir H, My Lahsen M, Madi A, Zouhair M (2020) Ouansimi copper mineralization (Western Anti-Atlas, Morocco): Paragenetic sequence and circulation of gangue hosted paleofluids 162, 103692

Hitzman M, Kirkham R, Broughton D, Thorson J, Selley D (2005) The sediment-hosted stratiform copper ore

system. In: ECONOMIC GEOLOGY One Hundredth Anniversary Volume.
Hitzman MW, Selley D, Bull S (2010) Formation of sedimentary rockhosted stratiform copper deposits through Earth history. Econ Geol 105:627–639
Hnatyshin D, Kontak DJ, Turner EC, Creaser R A, Morden R, Stern RA (2016) Geochronologic (ReOs) and fluid-chemical constraints on the formation of the Mesoproterozoic-hosted Nanisivik ZnPb deposit, Nunavut, Canada: Evidence for early diagenetic, low-temperature conditions of formation. Ore Geology Reviews, 79, 189-217.
Ikenne M, Söderlund U, Ernst R E, Pin C, Youbi N, Hafid A (2017) A c. 1710 Ma mafic sill emplaced into a quartzite and calcareous series from Ighrem, Anti-Atlas–Morocco: evidence that the Taghdout passive margin sedimentary group is nearly 1 Ga older than previously thought. J of Afr Earth Sc, 127, 62-76.
Maloof AC, Ramezani J, Bowring SA, Fike DA, Porter SM, Mazouad M (2010) Constraints on early Cambrian carbon cycling from the duration of the Nemakit-Daldynian-Tommotian boundary δ13C shift, Morocco. Geology 38, 623–626.
Northey S, Mohr S, Mudd GM, Weng Z, Giurco D (2014a). Modelling future copper ore grade decline based on a detailed assessment of copper resources and mining. Resour. Conservat. Recycl. 83, 190–201.
Oummouch A, Essaifi A, Zayane R, Maddi O, Zouhair M, Maacha L (2017) Geology and Metallogenesis of the Sediment-Hosted Cu-Ag Deposit of Tizert (Igherm Inlier, Anti-Atlas Copperbelt, Morocco). Geofluids, 7508484
Poot J, Verhaert M, Dekoninck A, Oummouch A, El Basbas A, Maacha L, Yans J (2020) Characterization of weathering processes of the giant copper deposit of Tizert (Igherm Inlier, Anti-Atlas, Morocco). Minerals, 10(7), 620.
Pouit G (1966) Paléogéographie et répartition des minéralisations stratiformes de cuivre dans l'Anti-Atlas occidental (Maroc). Chron Rech Min 356:279-289
Saadi M (1968) Les gisements du Cuivre du Maroc principaux résultats de recherches depuis les origines. Mines et Géologie 26 : 7-53
Saintilan NJ, Archer C, Maden C, Samankassou E, Bernasconi SM, Szumigala D, Mahaffey Z, West A, Spangenberg, J E (2023). Metal-rich organic matter and hot continental passive margin: drivers for Devonian copper-cobalt-germanium mineralization in dolomitized reef-bearing carbonate platform. Mineralium Deposita, 58(1), 37-49.
Saintilan NJ, Selby D, Hughes JW, Schlatter D, Kolb J, Boyce A (2020). Mineral separation protocol for accurate and precise rhenium-osmium (Re-Os) geochronology and sulphur isotope composition of individual sulfide species. MethodsX, 7, 100944.
Selby D, Creaser RA (2001) Re-Os geochronology and systematics in molybdenite from the Endako porphyry molybdenum deposit, British Columbia, Canada. Economic Geology, 96(1), 197-204.
Sillitoe HR (2012) Copper provinces. In: Geology and Genesis of Major Copper Deposits and Districts of the World: A Tribute to Richard H. Sillitoe
Skacel J (1993) Gisement cuprifère polygénétique de Tazalagh (Anti-Atlas occidental). Mine, Géologie & Energie 54:127-133
Soulaimani A, Michard A, Ouanaimi H, Baidder L, Raddi Y, Saddiqi O, Rjimati EC (2014) Late Ediacaran-Cambrian structures and their reactivation during the Variscan and Alpine cycles in the Anti-Atlas (Morocco). J. Afr. Earth Sci 98, 94–112.
Spangenberg JE, Lavric JV, Meisser N, Serneels V (2010) Sulfur isotope analysis of cinnabar from Roman wall paintings by elemental analysis/isotope ratio mass spectrometry - tracking the origin of archaeological red pigments and their authenticity. Rapid Commun Mass Spectrom.24:2812–6.
Thomas RJ, Chevallier LP, Gresse PG, Harmer RE, Eglington BM, Armstrong RA, De Beer CH, Martini JEJ, De Kock GS, Macey PH Ingram BA (2002) Precambrian evolution of the Sirwa Window, Anti-Atlas Orogen, Morocco. Precambrian Research, 118, 1–57.
Vernhet E, Youbi N, Chellai EH, Villeneuve, M, El Archi A (2012) The Bou-Azzer glaciation: evidence for an Ediacaran glaciation on the west African craton (anti-atlas, Morocco). Precambrian Research, 196, 106-112.
Völkening J, Walczyk T, Heumann K (1991) Osmium isotopic ratio determination by negative thermal ionization mass spectrometry. Int. J. Spectrometr. Ionic Phys. 105, 147–159.
Walsh GJ, Benziane F, Aleinikoff JN, Harrison RW, Yazidi A, Burton WC, Quick JE, Saadane A (2012) Neoproterozoic tectonic evolution of the jebel Saghro and Bou Azzer—El Graara inliers, eastern and central Anti-Atlas, Morocco. Precambrian Research, 216, 23-62.
Yajioui Z, Karaoui B, Chew D, Breitkreuz, C, Mahmoudi, A (2020) U–Pb zircon geochronology of the Ediacaran volcano-sedimentary succession of the NE Saghro inlier (Anti-Atlas, Morocco): chronostratigraphic correlation on the northwestern margin of Gondwana. Gondwana Research, 87, 263-277.

# Numerical investigation of fluid flow and Cu transport in the Katangan Basin, Central African Copperbelt

**Meissam L. Bahlali[1], Pablo Salinas[1,2], Julia Woitischek[1], Carl Jacquemyn[1], Martin Purkiss[3], Michael C. Daly[3], Matthew D. Jackson[1]**
*[1]Novel Reservoir Modelling and Simulation Group, Department of Earth Science and Engineering, Imperial College London, London, UK*
*[2]Now at OpenGoSim Ltd*
*[3]Department of Earth Sciences, University of Oxford, Oxford, UK*

**Abstract.** Sediment-hosted copper deposits host 23% of the world's copper. The mineral system approach has been applied to characterise the formation of these deposits, sequentially considering source, transport, trap and deposition. Here we focus on basin-scale groundwater flow that transports copper from source to trap. Numerical experiments are conducted to investigate controls on copper transport in the Katangan Basin, Central African Copperbelt. It is shown that density gradients induced by gradients in salinity and temperature play a major role in initiation of convective groundwater flow. The development of these 3D convection cells may explain why mineralisation is often localised, with deposits potentially corresponding to metal-enriched upwelling plumes.

## 1 Introduction

Sediment-hosted copper deposits are of significant commercial interest as they host 23% of the world's known copper deposits. The mineral system approach has been applied to characterise the formation of these deposits, sequentially considering source, transport, trap and deposition. Copper and other metals are widely assumed to be transported by the basin-scale flow of hydrothermal fluids (e.g. Sweeney et al., 1991; El Desouky et al. 2009; Davey et al., 2020).

Source rocks for copper mineralisation in the Katangan Basin, Central African Copperbelt, have been interpreted to be extra-basinal basement or intra-basinal sediments (e.g. Sweeney et al., 1991; El Desouky et al. 2009). The hydrothermal fluids from which the copper deposits formed have been interpreted to be high temperature bittern brines created by advanced evaporation of seawater (Davey et al., 2020). These interpretations suggest significant flow of hydrothermal fluids within and beyond the basin fill sediments. To understand controls on fluid flow requires appropriate fluid-dynamical models that include thermal and salinity controls on fluid density, and capture geological controls on permeability architecture. Previous models of fluid flow in the Katangan Basin used a relatively simple 2D geometry and assumed that saline brines formed by dissolution of halite (Koziy 2007; Koziy et al. 2009).

Here we report 3D numerical experiments to investigate controls on hydrothermal flow and copper transport in the Katangan Basin, using models informed by conceptual geologic understanding of the basin architecture and basin fill sediments at various times during basin evolution.

The aim of the fluid-dynamical modelling is to complement models for mineralisation developed from petrographic, mineralogic, and geochemical studies (e.g. Sweeney et al. 1991, El Desouky et al. 2009) by providing constraints on fluid flow paths within and beyond the basin, along with fluid temperature and salinity. In this context, the current study contributes to understanding of ore-forming processes in the Copperbelt by providing efficient simulations of fluid flow.

## 2 Methodology

The numerical experiments use the open-source Imperial College Finite Element Reservoir Simulator (IC-FERST) code to solve the coupled equations describing fluid flow, heat and solute transport. IC-FERST employs Dynamic Mesh Optimisation (DMO) along with a control-volume-finite element method (CVFE; Jackson et al. 2015, Salinas et al. 2017) to solve the governing equations. DMO allows the resolution of the mesh to vary over time and space to satisfy a user-defined solution precision for selected fields, refining where the solution fields are complex and coarsening elsewhere. Its implementation in IC-FERST has been validated against benchmark solutions (Bahlali et al. 2022, Hamzehloo et al. 2022). The lower computational cost of DMO compared to conventional numerical methods allows for efficient assessment of groundwater flow and metal transport scenarios associated with the mineral system approach, with application here to 3D models of the Katangan Basin at various stages of the basin evolution.

The Zambian Copperbelt is hosted by the Neoproterozoic Katangan basin. Three main litho-stratigraphic architectural elements can be distinguished from bottom to top: (1) a basal red-bed sequence interbedded with mudstones (Lower Roan group); (2) carbonates with salt/evaporite occurrences (Upper Roan group) overlain by (3) reduced shales and carbonates (Nguba, Mwashia and Kundelungu Groups) (Koziy 2007).

A 33km x 34km x 14km geological model (Figure 1) was developed, based on current knowledge of the basin architecture. The geological model corresponds to a sub-basin of the Katangan basin. It is composed of a succession of different hydrological

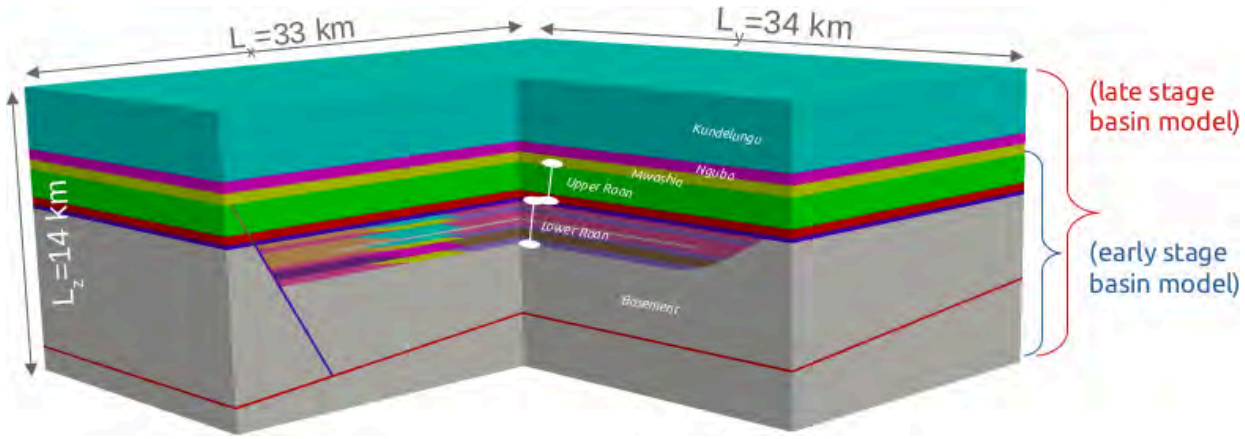


**Figure 1. Schematic of the 3D model for a sub-basin of the Katangan basin, including both early and late stage models.**

units, including basement rocks, the Lower Roan basin-fill deposits, the Upper Roan salt-bearing carbonates, then the overlying Mwashia, Nguba and Kundelungu groups. Two models have been constructed, respectively corresponding to early- (Upper Roan) and late-stages basin evolution (Pre-Lufilian basin-inversion). The early-stage model includes basement, the Lower Roan and Upper Roan subgroups, and corresponds to the time range of salt deposition in the Upper Roan. The late-stage model includes the overlying Mwashia, Nguba and Kundelungu Groups and corresponds to the time range of copper mobilisation and mineralisation. The present work focuses on the early-stage model.

Saline brine is assumed to be formed as a dense residual phase in response to evaporite formation during deposition of the Upper Roan, rather than by dissolution of halite (cf. Koziy et al. 2009). This saline brine is modelled using a source term in the Upper Roan, delivering brine with a total salinity of 30 wt%. The initial brine in the basin has a total salinity of 13 wt%. This is a modelling choice for our base case scenario; more salinity data are available in the literature and can be used to carry out sensitivity studies on the numerical model (El Desouky et al. 2009; Davey et al. 2020). A geothermal gradient of 25°C per km has been imposed.

## 3 Results

A range of numerical experiments have been conducted, varying the permeability of the geological units, the thermal gradient or the salinity in the Upper Roan. Figure 2 shows the effect of the varying the fault permeability on the salt concentration field, considering in this example a very low permeability for the basement (0.000001D). Indeed, in this scenario, away from faults, the basement is not pervasively fractured and the fractures are not connected, so flow is restricted to crystalline matrix with very low porosity and permeability. Note that this is a modelling choice for our base case scenario. In other model runs, higher permeability for the basement can be tested, representing scenarios where the fracturing is more intense. Figure 2(a) shows the scenario with the highest fault permeability (1D) along with the velocity vectors. The velocity vectors show the development of 3D convection cells with highly saline brines percolating downwards through the lower units until reaching the very low permeable basement. The thermally-induced buoyancy originating from the flux of heat into the basin then drives (potentially metal-enriched) upwelling plumes.

Figures 2(b) and 2(c) show the same model but considering lower permeability for the faults (0.01D and 0.001D). The lower the permeability of the faults, the higher the total salt content in the domain. This is explained by the fact that high permeability faults act as conduits for flow. In the early-stage model, the faults cut through the domain from the top boundary; therefore, upwelling brine is channelled through these faults until exiting the domain at the top.

## 4 Conclusions

Density gradients induced by gradients in salinity and temperature play a major role in the initiation of convective groundwater flow. Highly saline, dense brines are created during deposition of salt or by dissolution of salt deposits and form downwards propagating plumes with complex geometry controlled by the interaction of flow instabilities and geologic heterogeneity.

In the presence of permeable faults and fractures in basement rocks, groundwater percolates through and potentially mobilises copper from extra-basinal source rocks. Otherwise, flow is restricted to the permeable basin-fill deposits and potential copper sources are restricted to intra-basinal red-bed deposits and/or intrusive igneous rocks.

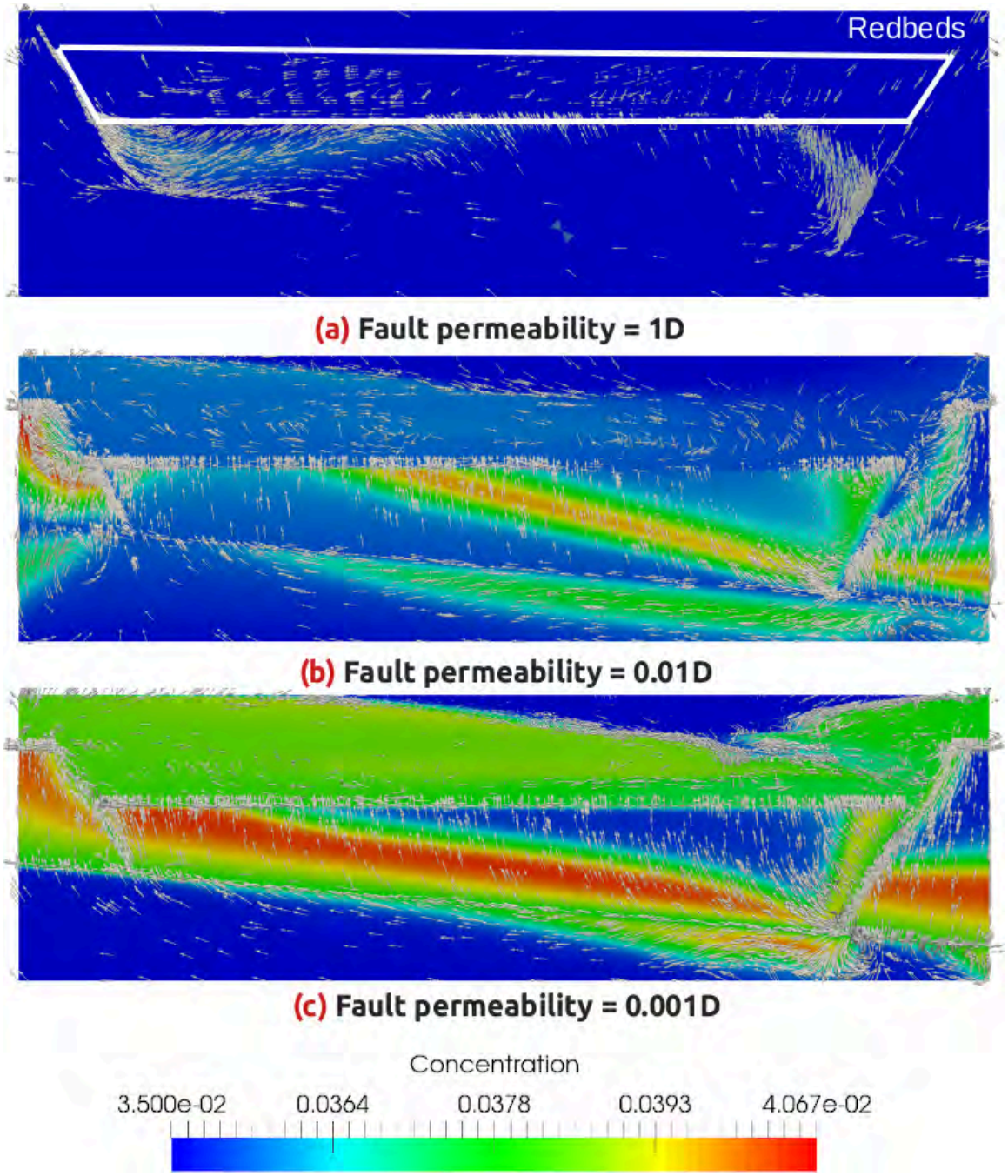


**Figure 2.** Vertical cross-section of the basin, showing salt concentration field for different fault permeability values.

The combination of salinity and temperature gradients drives upwelling plumes of groundwater which can transport copper upwards from deeper intra- or extra-basinal source rocks into organic-rich sedimentary rocks where mineralisation occurs. Development of 3D convection cells may explain why mineralisation is often localised, with deposits potentially corresponding to metal-enriched upwelling plumes.


## Acknowledgements

This work was supported by the UK Natural Environment Research Council (NERC) via the CuBES (Copper Basin Exploration Science) project (grant NE/T003294/1).

## References


Bahlali, M. L., Salinas, P., & Jackson, M. D. (2022). Efficient Numerical Simulation of Density-Driven Flows: Application to the 2-and 3-D Elder Problem. Water Resources Research, 58(8), e2022WR032307.

Davey, J., Roberts, S., Wilkinson, J.J. (2020). Copper- and cobalt-rich, ultrapotassic bittern brines responsible for the formation of the Nkana-Mindola deposits, Zambian Copperbelt. Geology, 49, 341-345.

El Desouky, H.A., Muchez, Ph., Cailteux, J. (2009). Two Cu-Co sulfide stages and contrasting fluid systems in the Katanga Copperbelt, Democratic Republic of Congo. Economic Geology, 36, 315-332.

Jackson, M. D., Percival, J. R., Mostaghimi, P., Tollit, B. S., Pavlidis, D., Pain, C. C., ... & Blunt, M. J. (2015). Reservoir modeling for flow simulation by use of surfaces, adaptive unstructured meshes, and an overlapping-control-volume finite-element method. SPE Reservoir Evaluation & Engineering, 18(02), 115-132.

Hamzehloo, A., Bahlali, M. L., Salinas, P., Jacquemyn, C., Pain, C. C., Butler, A. P., & Jackson, M. D. (2022). Modelling saline intrusion using dynamic mesh optimization with parallel processing. Advances in Water Resources, 164, 104189.

Koziy, L. (2007). Numerical simulation of the ore forming fluid migration in the sediment-hosted stratiform copper deposit, Zambian Copperbelt (Doctoral dissertation, University of Tasmania).

Koziy, L., Bull, S., Large, R., & Selley, D. (2009). Salt as a fluid driver, and basement as a metal source, for stratiform sediment-hosted copper deposits. Geology, 37(12), 1107-1110.

Salinas, P., Pavlidis, D., Xie, Z., Jacquemyn, C., Melnikova, Y., Jackson M. D., & Pain, C. C. (2017). Improving the robustness of the control volume finite element method with application to multiphase porous media flow. International Journal for Numerical Methods in Fluids, 85(4), 235-246.

Sweeney, M. A., Binda, P. L., & Vaughan, D. J. (1991). Genesis of the ores of the Zambian Copperbelt. Ore Geology Reviews, 6(1), 51-76.

# Cobalt-rich manganese nodules in Pliocene marine deposits of the onshore forearc Pisco Basin, Peru

**Ivana C. Carcamo-Valencia[1], Lisard Torró[1], Joaquín A. Proenza[2], Johan S. Ramírez-Briones[1], Luís Ayala[3], Willem Viveen[3], Thomas Aiglsperger[4], Patrice Baby[3,5]**

*[1]Grupo de Investigación en Yacimientos Minerales, Faculty of Sciences and Engineering, Pontifical Catholic University of Peru, Peru*

*[2]Departament de Mineralogia, Petrologia i Geologia Aplicada, Facultat de Ciències de la Terra, Universitat de Barcelona, Spain*

*[3]Grupo de Investigación en Geología Sedimentaria. Faculty of Sciences and Engineering, Pontifical Catholic University of Peru, Peru*

*[4]Dept. Civil Engineering and Natural Resources, Division of Geosciences and Environmental Engineering, Luleå University of Technology, Sweden*

*[5]GET-UMR CNRS/IRD/Univ. Paul Sabatier, Toulouse, France*

**Abstract.** Onshore manganese nodules and vein coatings were recovered from Pliocene sedimentary beds in the Pisco Basin of southern Peru. Identified manganese minerals include todorokite and cryptomelane suggesting a diagenetic origin. However, the chemical composition suggests a mixed hydrogenetic/hydrothermal – diagenetic origin probably due to modification of the geochemical conditions caused by organic matter decay. The onshore exposition of Co-rich (up to 5,080 ppm) Mn nodules in the Pisco Formation suggests a possible novel economic potential to be confirmed by further study.

## 1 Introduction

Ferromanganese nodules commonly occur on sediment-covered abyssal plains at water depths of 3,500-6,500 m, although ocean shallow-water (< 100 m; e.g., the Baltic Sea; Hein et al. 2020) and onshore (Achurra et al. 2009) nodules are known to occur in a few places. Ferromanganese nodules are composed mostly of Fe and Mn oxides that accrete around a hard nucleus on the surface on soft sediments by mainly two mechanisms of formation: hydrogenetic (i.e., direct precipitation from cold, ambient ocean water) and diagenetic (i.e., precipitation occurs from sediment pore fluids; Hein et al. 2020). Hydrogenetic nodules are characteristically composed of vernadite (δ-$MnO_2$) and enriched in Co, Te, Ce and Pt, while diagenetic nodules are typically composed of todorokite and have high Ni, Cu, and Li contents (Hein et al. 2020). A third mechanism for the precipitation of Fe and Mn oxyhydroxides is from hydrothermal fluids in diverse geological settings and temperatures, which may result in the formation of Mn concretions exhibiting a wide range of metal contents (Josso et al. 2017).

Noteworthy, some of the aforementioned elements (Co, Ce, Pt, Li) are referred to as critical raw materials by the European Commission (2020) due to their high economic importance and supply risk. Therefore, Mn nodules come up as promising, significant reservoirs (Hein et al. 2020; Toro et al. 2020).

In Peru, the occurrence of Ni- and Co-rich nodules has been reported in the Pacific abyssal plain (Hein and Koschinsky 2014), but also in the onshore forearc Pisco Basin (region of Ica; 14°22'S, 75°37'W), where on-land Mn nodules were found in diatomites of the Pisco Formation (Bessler 1975). This author described contents of Ni, Co, and Cu up to 1,680, 1,950, and 440 ppm, respectively. We present here a new discovery of Mn nodules hosted by the Pisco Formation located 55 km farther SE, in the Rio Grande Valley near the town of Palpa (14°49'S, 75°23'W; Fig. 1). Chemical and mineralogical characterization of these Mn nodules was carried on to evaluate their genesis and economic potential.

**Figure 1.** Location of Palpa (red star) in the onshore forearc Pisco Basin (gray area) of southern Peru. Modified from Di Celma et al. (2016).

## 2 Geological setting

The Eocene to Pliocene Pisco Basin is located on the Peruvian forearc from 13° to 15° S lat. (León et al. 2008; Di Celma et al. 2016; Viveen and Schlunegger 2018). This basin is divided into two sub-basins, namely the East Pisco and West Pisco basins, which are separated by the actual Coastal Cordillera (Quispe et al. 2018).

The East Pisco basin corresponds to the onshore portion of the basin (Gioncada et al. 2018; Di Celma et al. 2022) and it was a semi-enclosed, shallow embayment (Di Celma et al. 2016).

The Neogene marine Pisco Formation is one of the major lithostratigraphic units exposed in the onshore forearc Pisco Basin (León et al. 2008; Di Celma et al. 2018). It consists of siltstones, sandstone, and diatomites along with volumetrically minor tuffs and dolomites, the latter of which host an extraordinarily diverse vertebrate fossil fauna (Di Celma et al. 2016; Ochoa et al. 2021). The clastic sequence in the Pisco Formation corresponds to a long-term transgression triggered by tectonic changes during the Miocene-Pliocene (Di Celma et al. 2018). The tectonic regime under which the basin formed is still a matter of debate. Some authors have suggested alternating phases of compression and uplift and transtension and subsidence during the Paleogene and Neogene with uplift and compression occurring during the Quaternary due to the arrival of the Nazca Ridge (Clift et al. 2003; Léon et al. 2008; Viveen and Schlunegger 2018; DiCelma et al. 2022). Other authors favor a view in which compression was continuous from the late Oligocene to the Quaternary (Quispe et al. 2018; Ochoa et al. 2021).

The Pisco Formation unconformably overlies the Late Oligocene to Early Miocene marine Chilcatay Formation (Ochoa et al. 2021) and underlies the Quaternary continental Cañete Formation (León et al. 2008).

The Mn nodules in the Rio Grande valley are distributed in a ~10 m thick stratigraphic section within the Pisco Formation considered as Pliocene in age (Ochoa et al. 2021), at 657 m.a.s.l., and approximately 20 m below the conglomerates of the continental Cañete Formation. This section consists of silty clays, siltstones, tuffs, diatomites, sandstones, and conglomerates deposited in a shallow marine environment with volcanic and fluvial influence.

## 3 Methodology

Intraformational Mn nodules and fracture-filling Mn veins have been observed and sampled from two locations (14°49.1'S, 75°23.4'W; 14°48.8'S, 75°23.3'W). The mineralogy was determined by powder XRD using a Bruker D8 Discover diffractometer in Bragg-Brentano θ/2θ geometry of 240 mm radius, at the Centro de Caracterización de Materiales of the Pontifical Catholic University of Peru (CAM−PUCP). Quantitative element screening (analytical package S02) was performed by ALS Scandinavia AB using a combination of $HCl+HNO_3+HF$ digestion, alkali fusion, and applying ICP-SFMS analyses.

## 4 Results

The Mn-Fe oxyhydroxides observed in the Río Grande site show two contrasting morphologies (Fig. 2). The first morphological type corresponds to botryoidal, spherical, discoidal nodules with sizes ranging from a few millimetres (hereinafter referred to as micronodules) to centimetres hosted in silty clays, siltstones, and fine-grained sandstones. The second morphological type occurs filling 0.2 to 0.9-cm wide, NE-oriented, steeply-dipping (74 - 89°) fractures accompanied by fibrous gypsum, and as a coating accreted onto fine-grained rocks.

Three samples of intraformational Mn nodules and two samples of fracture-filling Mn veins were analysed by XRD (Fig. 3). Intraformational Mn nodules yielded similar diffractograms (Fig. 3B) and are composed of different manganese-bearing phases, such as pyrolusite and either hollandite or cryptomelane. In two of these samples, a peak has been identified as possible fenaksite. Fracture-filling Mn veins have the same composition, though one analysis of a Mn coating (Fig. 3A) reveals the presence of todorokite and dolomite. Generally, quartz, plagioclase, and biotite are present in samples of both morphological types.

Table 1 shows part of the elemental inventory of two samples of intraformational Mn nodules. Both yield similar chemical compositions, with 2022-PAL-02 having higher Co contents, at ~0.5 wt%. The contents of other minor and trace elements are below 0.1 wt.%, except for Ti (up to 0.12 wt.%).

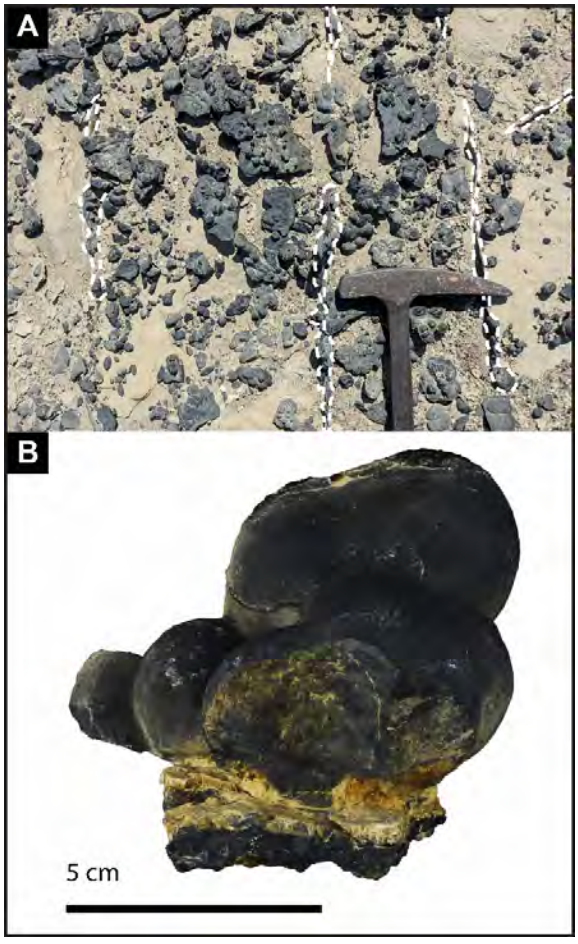

**Figure 2.** A. Outcrop with fracture-filling (white dashed lines) and associate nodules. B. Botryoidal-type, massive Mn intraformational nodule with a smooth, opaque surface. Note that it is associated with gypsum (pale yellow) and a rough bottom Mn-oxides layer.

| | Samples | |
|---|---|---|
| **Element** | **2022_PAL-01** | **2022_PAL-02** |
| MnO *(wt. %)* | 54.2 | 60.7 |
| FeO | 2.85 | 3.09 |
| $SiO_2$ | 25.8 | 18.8 |
| Ni *(ppm)* | 47 | 150 |
| Cu | 260 | 430 |
| Co | 3,500 | 5,080 |
| Zn | 200 | 340 |
| Ti | 1,200 | 1,100 |
| Mn/Fe | 19.0 | 19.6 |

**Table 1.** Contents of selected elements in two Mn nodules.

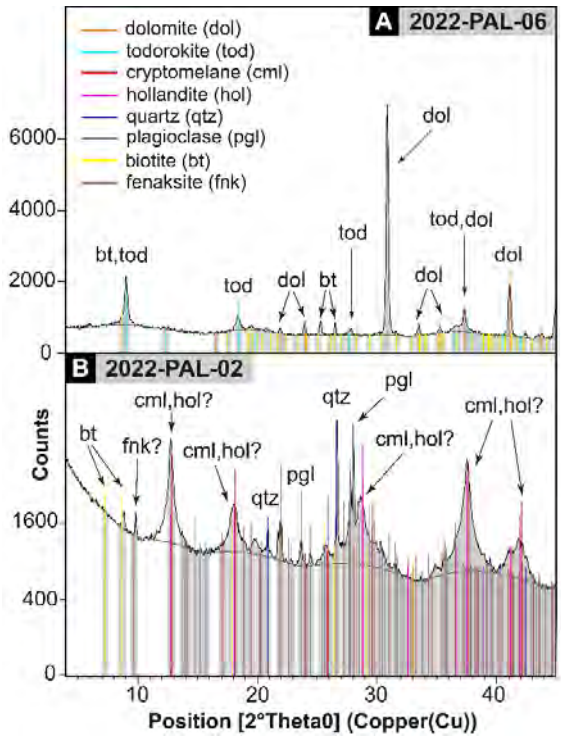


**Figure 3.** Diffractograms of a Mn coating sample (A) and an intraformational Mn nodule sample (B).

## 5 Discussion

In order to constrain the origin of the Mn nodules from the Rio Grande Valley, Mn/Fe ratios were calculated (Table 1). The two analysed samples are characterized by high Mn/Fe ratios (>10), which are typical for Mn nodules formed predominantly by diagenetic processes (Hein et al. 2020). The composition of both samples analysed in this study and other Mn nodules from the Pisco Formation analysed by Bessler (1975) plot in the field of 'mixed origin' in the Fe-Mn-(Co+Ni+Cu)*10 ternary diagram (Fig. 4A) and in the field of 'hydrothermal origin' in the (Ni+Cu)*15-(Fe+Mn)/4-(Zr+Y+Ce)*100 ternary diagram (Fig. 4B). In the Ce/Ce* vs. $Y_N/Ho_{CN}$ diagram (Fig. 5), the sample 2022-PAL-01 plots in the field of 'mixed origin', and the sample 2022-PAL-02 plot in the field of 'hydrogenetic origin'.

The presence of todorokite rather than vernadite in the analyzed Mn coating (Fig. 3A) may indicate a diagenetic origin (Hein et al. 2014). The diffractograms also show cryptomelane, which has been identified in onshore diagenetic nodules from the Chilean Bahía Inglesa Formation (Achurra et al. 2009). Contrasting classifications from mineralogical and geochemical perspectives favour a tentatively mixed hydrogenetic/hydrothermal–diagenetic origin.

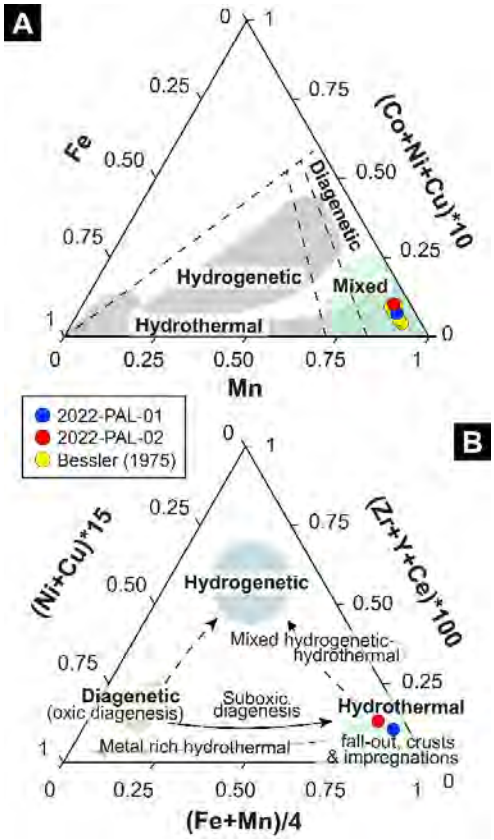


**Figure 4.** A. Ternary Fe - Mn - (Co + Ni + Cu) × 10 plot. Compositional fields are after Bonatti et al. (1972) and Zawadzki et al. (2022). B. Ternary (Ni + Cu) × 15 - (Fe + Mn)/4 - (Zr + Y + Ce) × 100 plot. Compositional fields are after Josso et al. (2017).

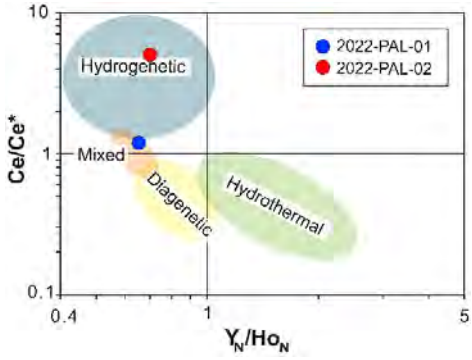


**Figure 5.** Ce/Ce* vs. $(Y/Ho)_{CN}$ plot. $Ce/Ce^*=Ce_{CN}/(0.5*La_{CN}+0.5*Pr_{CN})$, where CN refers to normalization to C1 chondrite using values of Sun and McDonough (1989). Compositional fields are after Bau et al. (2014).

Alternatively, Mn nodules from the Rio Grande Valley could have been formed by a similar process as the one described by Gioncada et al. (2018). In the model proposed by these authors, the decay of organic matter at the bottom of the marginal shallow marine Pisco Basin, coupled to Mn and Fe reduction, could have increased the concentration of these elements in porewater. As a result of the involvement of porewater sulfate acting as an oxidizing agent for organic matter, Fe sulfides may have formed. On the other side, Mn precipitates in renewed oxygenated conditions due to environmental changes linked to climate and/or tectonics. The enrichment in Co shown in our geochemical analysis could be explained by the abundance of diatomites in the Pisco Formation since diatoms use Co to grow (Kellogg et al. 2020).

Our study ushers in the possibility of finding Co-rich Mn nodules formed by non-hydrogenetic processes above the abyssal plains. Coastal shallow marine basins with organic matter-rich environments are prospective for Co-rich ferromanganese oxyhydroxide mineralization.

## 6 Conclusions

The mineralogical and chemical compositions of manganese nodules, veins, and coatings in the upper Pliocene marine Pisco Formation from Rio Grande Valley suggest a dominantly diagenetic origin.

Modification of geochemical conditions due to anaerobic organic matter decay followed by a re-oxygenation event linked to environmental changes could have played a pivotal role in Mn oxyhydroxide precipitation.

The high Co contents (up to 5,080 ppm) and onshore exposition of Mn nodules and veins in the Rio Grande site stand for a novel economic potential to be confirmed by further study.

## Acknowledgements

Pablo Valverde (PUCP) is thanked for assistance during sample preparation and XRD analysis. This research work was economically supported by the FAI-025-2023 project granted by PUCP, and logistically supported by the project 2021 SGR 00239 of the Agència de Gestió d'Ajuts Universitaris i de Recerca de Catalunya.

## References

Achurra LE, Lacassie JP, Le Roux JP, Marquardt C, Belmar M, Ruiz-del-Solar J, Ishman SE (2009) Manganese nodules in the Miocene Bahía Inglesa Formation, north-central Chile: petrography, geochemistry, genesis and palaeoceanographic significance. Sediment Geol 217:128–139

Bau M, Schmidt K, Koschinsky A, Hein JR, Kuhn T, Usui A (2014) Discriminating between different genetic types of marine ferro-manganese crusts and nodules based on rare earth elements and yttrium. Chem Geol 60:1709-1725

Bessler E (1975) Sobre la existencia de los nódulos de manganeso en la Formación Pisco. Boletín SGP 50:10-34

Bonatti E, Kraemer T, Rydell H (1972) Classification and genesis of submarine iron-manganese deposits. Ferromanganese deposits on the ocean floor, pp 149-166

Clift PD, Pecher I, Kukowski N, Hampel A (2003) Tectonic erosion of the Peruvian forearc, Lima basin, by subduction and Nazca ridge collision. Tectonics 22:1023

Di Celma C, Malinverno E, Gariboldi K, Gioncada A, Rustichelli A, Pierantoni PP, Landini W, Bosio G, Tinelli C, Bianucci G (2016) Stratigraphic framework of the late Miocene to Pliocene Pisco Formation at Cerro Colorado (Ica Desert, Peru) J Maps 12:515–529

Di Celma C, Malinverno E, Bosio G, Gariboldi K, Collareta A, Gioncada A, Landini W, Pierantoni P, Bianucci G (2018) Intraformational unconformities as a record of late Miocene eustatic falls of sea level in the Pisco Formation (southern Peru). J Maps 14:607-619

Di Celma C, Pierantoni P, Volatili T, Molli, G, Mazzoli S, Sarti G, Ciattoni S, Bosio G, Malinverno E, Collareta A, Gariboldi K, Gioncada A, Jablonska D, Landini W, Urbina M, Bianucci G (2022) Towards deciphering the Cenozoic evolution of the East Pisco Basin (southern Peru). J Maps 18:1-16

European Commission (2020) Study on the EU's list of Critical Raw Materials (final report). European Commission, Brussels, pp 1–158

Gioncada A, Petrini R, Bosio G, Gariboldi K, Collareta A, Malinverno E, Bonaccorsi E, Di Celma C, Pasero M, Urbina M, Bianucci G (2018) Insights into the diagenetic environment of fossil marine vertebrates of the Pisco Formation (late Miocene, Peru) from mineralogical and Sr-isotope data. J S Am Earth Sci 81:141-152

Hein JR, Koschinsky A (2014) Deep ocean ferromanganese crusts and nodules. In: Holland H, Turekian K (eds) Treatise in Geochemistry, 2nd ed., pp 273-291

Hein JR, Koschinsky A, Kuhn T (2020) Deep-ocean polymetallic nodules as a resource for critical materials. Nat Rev Earth Environ 1:158–169

Josso P, Pelleter E, Pourret O, Fouquet Y, Etoubleau J, Cheron S, Bollinger C (2017) A new discrimination scheme for oceanic ferromanganese deposits using high field strength and rare earth elements. Ore Geol Rev 87:3-15

Kellogg MM, McIlvin MR, Vedamati J, Twining BS, Moffett JW, Marchetti A, Moran DM, Saito MA (2020) Efficient zinc/cobalt inter-replacement in northeast Pacific diatoms and relationship to high surface dissolved Co:Zn ratios. Limnol Oceanogr 65:2557-2582

León WR, Rosell W, Alemán AM, Torres VR, De la Cruz MO (2008) Estratigrafía, sedimentología y evolución tectónica de la cuenca Pisco Oriental. Boletín INGEMMET 27:1-154

Ochoa D, Salas-Gismondi R, DeVries T, Baby P, de Muizon C, Sierra A, Barbosa A, Foster D, Quispe K, Cardich J, Gutiérrez D, Perez A, Valqui J, Urbina M, Carré M (2021) Late Neogene evolution of the Peruvian margin and its ecosystems: a synthesis from the Sacaco record. Int J Earth Sci (Geol Rundsch) 110:995–1025

Quispe K, Baby P, Calderón Y, Hurtado C, Ramírez L (2018) La Cuenca Pisco: nuevo modelo estructural para una cuenca de antearco peruana, evidencias de contexto compresivo, desarrollo de la Cordillera de la Costa, XIX Congreso Peruano de Geología. SGP Lima Peru

Sun SS, McDonough WF (1989) Chemical and isotopic systematics of oceanic basalts: implications for mantle composition and processes. In: Saunders AD, Norry MJ (eds) Magmatism in the Ocean Basins. Geol Soc Spec Publ 42:313-345

Toro N, Jeldres RI, Órdenes JA, Robles P, Navarra A (2020) Manganese nodules in Chile, an alternative for the production of Co and Mn in the future— A review. Minerals 10:674

Viveen W, Schlunegger F (2018) Prolonged extension and subsidence of the Peruvian forearc during the Cenozoic. Tectonophysics 730:48-62

Zawadzki D, Maciąg Ł, Blasco I, González FJ, Wernette B, Marino E, Kozub-Budzyń GA, Piestrzyński A, Wróbel RJ, McCartney K (2022) Geochemistry and mineralogy of ferromanganese crusts from the Western Cocos-Nazca spreading centre, Pacific. Minerals 12:538

# Mineralogy and geochemistry of the Myeonsan Fe-Ti placer deposit, Korea: preliminary results

**Bongsu Chang[1], Jieun Seo[1], Young J. Lee[1], Seon Y. Lee[1], Gilljae Lee[2], Seon -G. Choi[1]**
*[1] Department of Earth and Environmental Sciences, Korea University, Republic of Korea*
*[2] Mineral Resources Research Division, Korea Institute of Geoscience and Mineral Resources, Republic of Korea*

**Abstract.** This study outlines mineralogical and geochemical characteristics of the Myeonsan Fe-Ti ore deposit, which is sedimentary origin located in South Korea. X-ray diffraction with subsequent quantitative phase analysis confirmed hematite, quartz, and rutile as the main constituent minerals, and their contents were 30.9%, 28.4%, and 19.2%, respectively. In addition, < 10% of ilmenite and phyllosilicates, and minor amounts of garnet and wollastonite were identified. Whole-rock chemistry by X-ray fluorescence were consistent with the mineral assemblage data. It is noteworthy that the $TiO_2$ content of > 20% corresponds to a remarkably high grade in sediment-sourced $TiO_2$ ore deposit. From electron microprobe analysis, we figured out the degree of overall oxidation state from hundreds of Fe-Ti mineral composition data. Consequently, it is recognized that Fe-Ti phases in the Myeonsan deposit distributed mainly in hematite, pseudobrookite, and rutile regions on a FeO-$Fe_2O_3$-$TiO_2$ ternary diagram, indicating highly weathered nature of the deposit. In further research, by expanding the target area to entire deposit, we intend to provide practical groundwork for successful mine development.

## 1 Introduction

In 2012, South Korea was ranked as the world's third-largest consumer of the processed product of titanium (e.g., ingot, ferrotitanium, powder etc.). However, there has been no domestic production of commercially viable titanium ores and concentrates to date, which leads to a chronic titanium trade deficit (K-stat 2021). Meanwhile, disruption to the global supply chain caused by recent global events provided an opportunity to reduce the dependence on imports of Critical Minerals including titanium but also to change the policy direction to secure national resource security. It has given the justification that additional costs, time, and efforts are needed to secure resources even if it is beyond economic feasibility.

In South Korea, Fe-Ti placer deposits occurs in the lower part of Paleozoic (Cambrian-Ordovician) basin, Taebaeksan Basin, central-eastern part of the Korean Peninsula (Fig. 1). The deposit is large enough to be ranked in the worldwide distribution of Ti-Zr placer deposits (Hamilton 1995). However, it has been neglected historically because the expected economic efficiency was low due to the inherent characteristic of sedimentary origin, containing considerable amount of quartz and clay minerals. Nevertheless, now is time for accurate and precise research to increase the availability of titanium in the deposit in terms of national resource security.

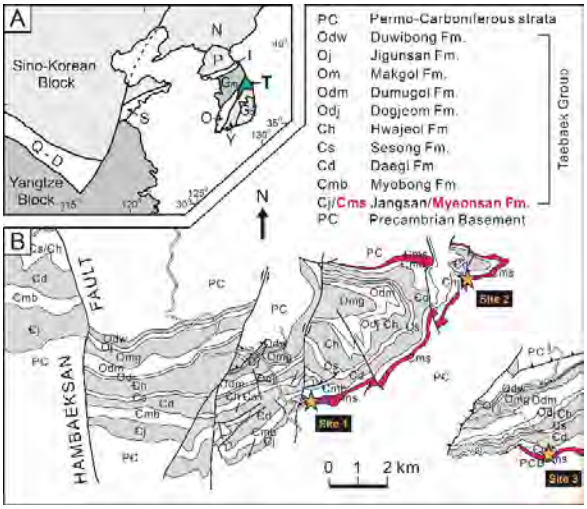


**Figure 1.** (A) Location of the Taebaeksan Basin in the Sino-Korean Block (I, Imjingang Belt; Gb, Gyeongsang Basin; Gm, Gyeonggi Massif; N, Nangnim Massif; O, Okcheon Belt; P, Pyeongnam Basin; Q-D, Qinling-Dabie Belt; S, Sulu Belt; T, Taebaeksan Basin; Y, Yeongnam Massif). (B) Detailed geologic map of the eastern Taebaeksan Basin, showing the distribution of the Myeonsan Formation. Illustration modified from Choi and Chough (2005).

Most previous research on the Taebaeksan Basin, where the orebodies are embedded, were focused on sedimentological and stratigraphical (Kim 1991; Choi and Chough 2005; Chough 2013; Jang and Ryu 2021), paleontological (Choi et al. 2004) as well as tectonic (Chough et al. 2000; Choi 2019) studies targeting carbonate rocks since the basin has the well-preserved continuous sedimentary facies of the lower Paleozoic. Although several studies investigated mineralogy or geochemical properties of the orebodies (Kim 1991; Ryoo and Yoo 2014), there were limitations in spatial extent and analytical methods.

In this study, we report preliminarily mineralogical and geochemical characteristics of the Myeonsan Fe-Ti deposit using quantitative analyses. In addition, Fe-Ti mineral phases, showing diverse degrees of alteration, were also investigated by an electron microprobe analysis. Our findings in this study would be valuable in determining an optimal mining location in future.

## 2 Geology and Depositional environment

The Myeonsan deposit is mainly composed of laminated and cross-bedded sandstones,

mudstones, and thin-bedded conglomerates, and overlies the Precambrian basement unconformably. The thickness of the deposit is approximately 100 m on average. According to sedimentary petrology and sedimentary structures (i.e., interference ripples, trace fossils, mud crack, herringbone stratification, vertical burrows etc.), the orebodies seem to be deposited in tide-dominated shallow marine environments (Kim 1991; Woo et al. 2006).

## 3 Methodology

Powder X-ray diffraction (XRD) profiles were obtained using a Bruker D8 Advance X-ray diffractometer equipped with LynxEye XE-T detector and Cu Kα source. Subsequent quantitative phase analysis was performed using the GUI software Profex (Doebelin and Kleeberg 2015) by the BGMN Rietveld algorithm (Bergmann et al. 1998).

Bulk chemical composition was quantified using Rigaku ZSX Primus II wavelength-dispersive X-ray spectrometer. Quantification was conducted based on a calibration curve method using certified geochemical reference materials.

Mineral compositions of Fe-Ti minerals were determined using a JEOL JXA-iSP100 electron microprobe. Relative proportion of FeO and $Fe_2O_3$ was calculated based on charge balance and stoichiometry (Carmichael 1967).

## 4 Mineral assemblage

Phase identification from XRD profile confirmed constituent minerals in the Fe-Ti ore samples. Hematite, rutile, and ilmenite containing iron and/or titanium were the main component of the placer deposit. In addition, quartz, illite, chlorite, micas (muscovite, biotite), including grossular and wollastonite were identified as gangue minerals.

The relative abundance of each mineral phase was determined by subsequent QPA. Hematite accounted for the largest share at 30.9%, followed by quartz 28.4%, rutile 19.2%, ilmenite 7.8%, illite 5.6%, chlorite 5.4%, micas 2.3%, grossular 0.5%, and wollastonite 0.1%. Since hematite and rutile are weathering products of ilmenite, their high proportion is a general characteristics of Fe-Ti placer deposits. Although the amount of grossular and wollastonite is insignificant (< 1%), furthermore, the identification of these minerals suggests the possibility that the overlying carbonate rocks together with the Myeonsan deposit have thermally metamorphosed or undergone skarnification.

## 5 Whole rock geochemistry

Quantitative analysis using X-ray fluorescence proved that the total $Fe_2O_3$ content was the highest at 33.28%, followed by $SiO_2$ 27.67%, $TiO_2$ 22.46%, $Al_2O_3$ 3.46%, MgO 1.61%, and each of $K_2O$, CaO, MnO, $P_2O_5$, $ZrO_2$ less than 1%. These bulk chemistry data are well consistent with the QPA results with the highest mineral content in the order of hematite ($Fe_2O_3$), quartz ($SiO_2$), and rutile ($TiO_2$).

Although this is a preliminary study with limited samples, we note that the $TiO_2$ content is sufficiently above the typical grade for sedimentary deposit type (< 10% $TiO_2$) and corresponds to a level approaching that of igneous origin (Perks and Mudd 2022).

## 6 Microscopy of Fe-Ti oxide phases

Microscopic investigation by electron microprobe revealed details on Fe-Ti mineral phases in terms of varied weathering states, textures, morphology, and grain size distribution. Fig. 2A shows typical assemblages of constituent minerals in the Myeonsan deposit. Hematite, rutile, pseudobrookite, and their combinations (i.e., exsolution lamellae and its relics) were observed with a size of < ~200 μm, and the edges of the Fe-Ti grains were irregular due to high degree of weathering. In particular, the presence of commonly identifiable single-phase rutile indicates that it corresponds to the final stage of oxidation for primary Ti-rich magnetite (Ondrejka et al. 2015).

Overall, Fe-Ti phases composed of rutile + (Ti-)hematite ± pseudobrookite corresponding to a considerably advanced oxidation stages (e.g., C4–C7 stage, described in Haggerty 1991) were normally observed: (1) rutile + hematite inclusions with irregular patch-form pseudobrookite in a Ti-rich central part of the grain enclosed in hematite (Fig. 2B), (2) hematite partially filling the intergranular space between rutile aggregates, and (3) faint traces of Ti-hematite within rutile at the core of grain with dominant Ti-hematite at the marginal part of the crystal.

In some places, very thin trellis of oxyexsolved ilmenite/magnetite with thick rutile laths, or complete decomposition of primary Ti-rich magnetite to a finely aggregated lamellae of rutile/hematite (Fig. 2C) occurred in the host magnetite. The more advanced oxidation of primary trellis texture yields the

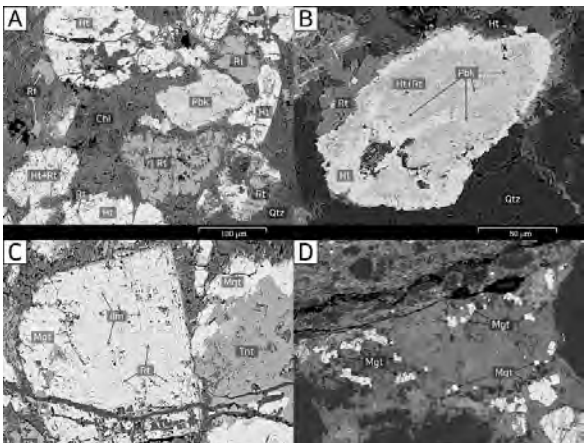


**Figure 2.** Backscattered electron images of selected Fe-Ti oxides including accessory minerals (Rt, rutile; Ilm, ilmenite; Ht, hematite; Mgt, magnetite; Pbk, Pseudobrookite; Tnt, titanite; Qtz, quartz). Details were described in text.

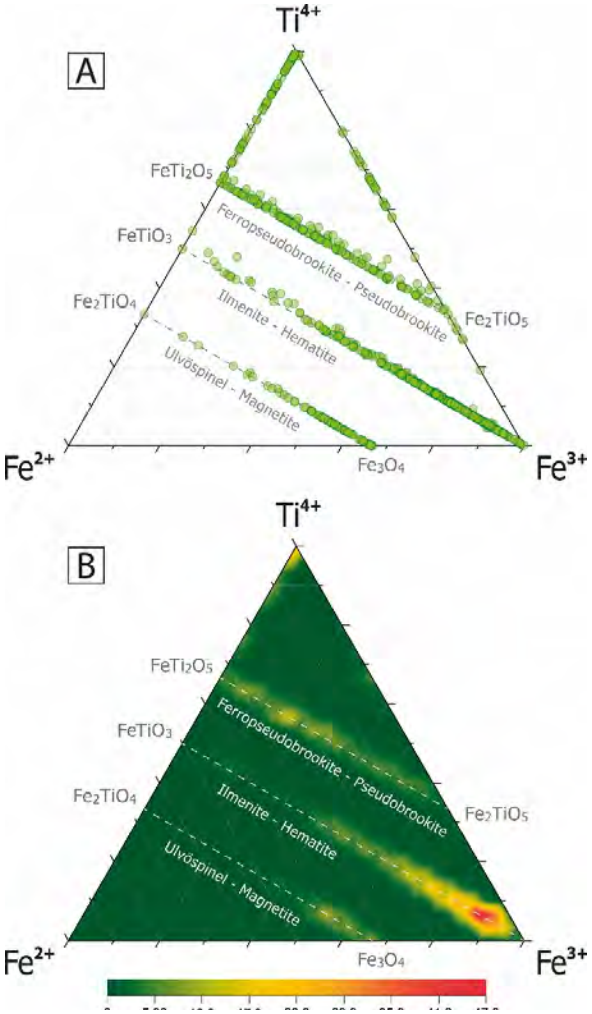


**Figure 3.** Ternary plots of $FeO$-$Fe_2O_3$-$TiO_2$ system, showing the solid solution series pseudobrookite-ferropseudobrookite, hematite-ilmenite, and magnetite-ulvöspinel. (A) Fe-Ti phase distribution based on a total of 720 individual data points from the Myeonsan deposit. Phases were plotted on atomic proportion basis. (B) Probability density plot based on Kernel density estimation.

pseudomorphing of pre-existing ilmenite and magnetite by hematite and rutile. Although rare, arrays of secondary magnetite showing euhedral crystal form were confirmed (Fig. 2D). These are expected to be products of precipitation by hydrothermal fluids, along with the previously identified grossular and wollastonite. As auxiliary minerals, titanite contacted with magnetite, and monazites enclosed in a Fe-Ti oxide crystal (Fig. 2C) were also observed.

To see the overall degree of oxidation state of Fe-Ti oxide phases in the Myeonsan deposit, a total of 720 data from electron microprobe analysis were plotted on a $FeO$-$Fe_2O_3$-$TiO_2$ ternary diagram (Fig. 3A). Note that the distribution of data is rare in the ilmenite and ulvöspinel regions corresponding to the primary phases, whereas it is concentrated in the highly oxidized rutile, pseudobrookite, and hematite regions. These tendencies are more clearly recognizable in a density plot (Fig. 3B).

## 7 Summary and Further research

The Myeonsan deposit is Cambrian placer-type Fe-Ti deposit located in South Korea, mainly composed of heavy mineral phases such as hematite, rutile, and ilmenite with gangue minerals: quartz, illite, chlorite, and micas. A bulk $TiO_2$ content of > 20% corresponds to a level that exceeds the average quality of global sedimentary $TiO_2$ deposit. The overall oxidation state of the Fe-Ti oxide phases in the deposit was classified to a relatively advanced stage beyond C4 stage. The characteristics of these highly weathered Fe-Ti phases increase the rutile content in the deposit, which is an advantage that can offset the disadvantages of sedimentary origin deposit type with high production costs. Rutile is in high demand as the highest-grade natural form of titanium dioxide, but its concentration is intrinsically low compared to ilmenite due to typical mineral assemblages found in ore deposits. To overcome this, an omnidirectional search for additional resources is underway recently, focusing on alternative deposits rich in rutile (e.g., weathered rock types, metamorphic terranes, porphyry systems etc.) (Force 1991; Woodruff et al. 2017; Sovereign Metals 2020). In this context, the revisit of the Myeonsan deposit is expected to contribute to the growth of rutile resources and reserves in terms of the new discovery of rutile-rich sedimentary Fe-Ti placer deposits.

Further research will be focused on identifying the horizontal and vertical distribution of mineral and geochemical characteristics for Fe-Ti mineral phases by expanding the spatial coverage to the entire orebody. Our research data can be a key clue to reveal the spatial evolution process of the basin, which will be the core data for arranging the optimal site to develop Ti producing mine.

## Acknowledgements

Authors thank Dr. Jino Park at Kangwon National University for his kind help during the preparation of geological artwork. This research was supported by grants from the National Research Foundation of Korea funded by the government (grant numbers 2021R1A2C100601111, 2022R1I1A1A01071269).

## References

Bergmann J, Friedel P, Kleeberg R (1998) BGMN—a new fundamental parameters based Rietveld program for laboratory X-ray sources, its use in quantitative analysis and structure investigations. CPD Newsl 20(5):5–8.

Carmichael ISE (1967) The iron-titanium oxides of salic volcanic rocks and their associated ferromagnesian silicates. Contrib Miner Petrol 14:36-64.

Choi DK, Chough SK, Kwon YK, Lee S-B, Woo J, Kang I, Lee HS, Lee SM, Sohn JW, Shinn YJ, Lee D-J (2004) Taebaek Group (Cambrian-Ordovician) in the Seokgaejae section,

Taebaeksan Basin: a refined lower Paleozoic stratigraphy in Korea. Geosci J 8(2):125-151.
Choi DK and Chough SK (2005) The Cambrian-Ordovician stratigraphy of the Taebaeksan Basin, Korea: a review. Geosci J 9(2):187-214.
Choi DK (2019) Evolution of the Taebaeksan Basin, Korea: I, early Paleozoic sedimentation in an epeiric sea and break-up of the Sino-Korean Craton from Gondwana. Isl Arc 28(1):e12275.
Chough SK, Kwon ST, Ree, JH, Choi, DK (2000) Tectonic and sedimentary evolution of the Korean peninsula: a review and new view. Earth-Sci Rev 52(1-3):175-235.
Chough SK (2013) Geology and Sedimentology of the Korean Peninsula. Elsevier, London and Waltham.
Doebelin N, Kleeberg R (2015) Profex: a graphical user interface for the Rietveld refinement program BGMN. J Appl Crystallogr 48(5):1573–1580.
Force ER (1991) Geology of titanium-mineral deposits. Geol Soc Am Special Papers 259. Geol Soc Am.
Haggerty SE (1991) Oxide textures–a mini atlas. In: Donald HL (ed) Oxide Minerals: Petrologic and Magnetic Significance, vol 25, chap 5. Min Soc Am Rev Mineral.
Hamilton NT (1995) Controls on the Global Distribution of Coastal Titanium-Zirconium Placers. Int Geol Rev 37:755-779.
Jang H, Ryu I-C (2021) A review of the stratigraphy of the Lower Paleozoic Joseon Supergroup. J Geol Soc Korea 57(4):495-521.
K-stat (2021) Import and export volume and trade balance of titanium-based goods. Korea International Trade Association. https://stat.kita.net. Accessed 3 March 2023
Kim J-Y (1991) Stratigraphy of the Myeonsan Formation in Samcheoggun, Kangwondo and Ponghwagun, Kyongsangbukdo. J Geol Soc Korea 27(3):225-245.
Ondrejka M, Broska I, Uher P (2015) The late magmatic to subsolidus T-$fO_2$ evolution of the Lower Triassic A-type rhyolites (Silicic Superunit, Western Carpathians, Slovakia): Fe-Ti oxythermometry and petrological implications. Acta Geol Slov 7:51-61.
Perks C, Mudd G (2022) Soft rocks, hard rocks: the world's resources and reserves of Ti and Zr and associated critical minerals. Int Geol Rev 64(7):987-1008.
Ryoo C-R, Yoo J-H (2014) Geological and mineralization of the Myeonsan Formation and its surrounding area in Taebaek Dongjeom area. Proc Korea Soc Eng Geol 37-38.
Sovereign M (2020) Rutile – Overview [Online]. Available: http://sovereignmetals.com.au/projectsrutile/ [Accessed 28 April 2023].
Woo J, Shinn YJ, Kwon YK, Chough SK (2006) The Jangsan and Myeonsan Formations (Early Cambrian) of the Taebaek Group, Mideast Korea: depositional processes and environments. Geosci J 10:35-57.
Woodruff LG, Bedinger GM, Piatak NM (2017) Critical Mineral Resources of the United States–Economic and Environmental Geology and Prospects for Future Supply.

# Depositional environments and metamorphic evolution of the Paleoproterozoic Mn-rich graphitic metasediments

**Augustin Dekoninck[1,2], Thierry De Putter[2], Gilles Ruffet[3], Florias Mees[2], Yves Van Brabant[4], Yishen Zhang[5], Olivier Namur[5], Julie Kapoma[6]**

*[1]Département Géosciences, environnement et société, Laboratoire G-Time, Université Libre de Bruxelles, Belgium.*
*[2]Geodynamics and Mineral Resources unit, Earth Sciences Department, Royal Museum for Central Africa, Belgium.*
*[3]Centre national de la recherche scientifique, UMR 6118, Géosciences Rennes, Université de Rennes 1, France.*
*[4]Geological Survey of Belgium, Belgium.*
*[5]Department of Earth and Environmental Sciences, KU Leuven, Belgium.*
*[6]Geological Survey of Madagascar, Madagascar.*

**Abstract.** The Paleoproterozoic is known to host significant sedimentary manganese accumulations deposited in peri-cratonic areas. Manganese precipitation is systematically associated with C-rich sediments and can lead to economic Mn deposits. However, depositional environments as well as the interrelation between numerous Mn-rich sediments are poorly understood. Here, we investigate the Mn-rich graphitic metasediments of the Ampanihy Mn district (South Madagascar) to characterize paleo-depositional conditions that led to Mn enrichments. The results show that the ore is composed of Mn silicates (spessartine, rhodonite) with locally Mn oxides (jacobsite, pyrophanite). Graphite is ubiquitous, except where Mn oxides occur, but Mn carbonates are absent. The initial sediment was likely a Mn-rich mud/siltstone formed by turbidite flows. Geochemical data additionally show evidence of Mn concentration processes similar to modern ferromanganese nodules. Why these nodules did not transform into Mn carbonates during diagenesis and greenschist grade regional metamorphism remains elusive and is likely related to stoichiometry of Mn and Al that favour spessartine formation. The geochemical composition of these Mn ores is marked by either terrestrial (crustal) or hydrothermal overprint depending on the sampling site location. We therefore argue for a multi-stage model for the formation of (1) C-rich (global), (2) Mn-rich sediments (regional) and (3) hydrothermal enrichment (local).

## 1 Introduction

The Paleoproterozoic era is a key metallogenic period of the Earth's history, recording massive deposition of various commodities (BIF, graphite, manganese) around the world. Although Paleoproterozoic rocks have often undergone metamorphism that obliterated initial sedimentary features, the geochemistry of metal-rich metasediments helps understanding the depositional setting and paleogeographic context of mineral deposits. The Ampanihy area, Madagascar, has many small Mn deposits of Paleoproterozoic age in graphitic metasediments. We investigated several of these Mn-rich metasediments to determine paleogeographic distribution of Mn metallogenic provinces and their connection to pre-Gondwana landscapes.

## 2 Geological setting

The study area is located in Southern Madagascar, to the east of Ampanihy (Fig. 1) where the existence of manganese occurrences was first described in the 40s and 50s (Besairie 1946; Boulanger 1956). Manganese deposits are associated with graphite-bearing paragneiss and share similarities with ores and host-rocks of Africa and India, notably 'gondites' in the Dharwar Craton (Fermor 1909; Besairie 1946). The syngenetic primary ore (protore) is thought to be $Mn^{4+}$-bearing oxide, later altered to Mn silicates (spessartine, rhodonite) and minor carbonates, frequently associated with graphite, during later metamorphism. Secondary supergene ore, again comprised predominantly of oxide phases was formed in later (still undated) chemical weathering episode(s). Occurrences in the Ampanihy district rarely exceed several kilometres in length and a few meters in thickness, however with unknown extension at depth. When compared to other known deposits in the world in the 50s, the Ampanihy district was considered of marginal importance (Boulanger 1956).

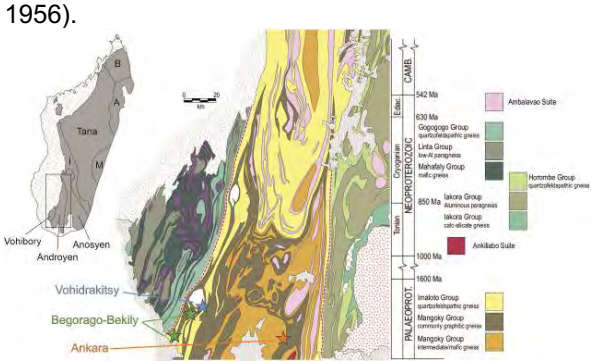


**Figure 1.** Location of the three sub-districts on the geological map of South Madagascar (Boger et al. 2015).

Precambrian Graphite Series in the study area belong to the Paleoproterozoic (1.9-1.7 Ga) Anosyan-Androyan Domain which relates to Indian and Sri Lankan terranes, all of which were sutured with the Great Dharwar Craton, at c. 1.8 Ga (Tucker et al. 2014). More recently, Armistead et al. (2021) challenged this view and suggested that South Madagascar was connected with the Tanzanian Craton rather than the Dharwar. The Anosyan-Androyan Domain experienced two Neoproterozoic metamorphic events, materialized in the study area by two major N-S trending shear zones, linked to an

oblique continental convergence between East and West Gondwana and the accretion with the Neoproterozoic Vohibory Group (Fig. 1). The western Ampanihy shear zone is the oldest (620-600 Ma) and is associated with peak metamorphism (850°C, 7-8 kbar) while the eastern Beraketa shear zone is younger (580-540 Ma) and associated with a lower metamorphic grade (650°C, 4-5 kbar)(de Wit et al. 2001; Tucker et al. 2011, 2014).

## 3 Methods

More than 70 samples were collected from different sub-districts: (1) Ankara, (2) Begorago-Bekily-Ampanihy and (3) Vohidrakitsy (Fig. 1). Of these, 43 samples were mineralized in Mn, either with primary and/or secondary minerals/ore. The samples were studied for their petrography and mineralogy using X-ray diffraction (UNamur), SEM-EDS (UNamur) and EPMA (KULeuven). These samples were further investigated for their whole rock geochemistry at UCLouvain University (including C, N). Raman spectrometry on graphite has been performed at the Royal Belgian Institute of Natural Sciences.

## 4 Results

### 4.1 Mn ore facies

Two main mineralized facies are identified. The more abundant facies is interlayered with barren pink fine- to coarse-grained paragneiss with visible mm-sized orange garnets (typically 1-5 mm)(Fig. 2). The Mn-rich metasediment is a dark grey to black paragneiss in which the colour derives from the presence of impregnative Mn oxides and to a lesser extent, graphite flakes (Fig. 3a). The second facies is a garnet-rich metasediment, sometimes described as “garnetite”.

**Figure 2.** Typical outcrop of the Mn-rich paragneiss facies in the Bekily area.

### 4.2 Mn ore composition

The XRD results show that the Mn ores are predominantly composed of a quartz-spessartine-cryptomelane assemblage. Graphite is ubiquitous in Ankara, Begorago-Bekily and Ampanihy.

Garnet is the major Mn-bearing mineral (Fig. 3) with composition close to the spessartine end member (Fig. 4). However, it displays variable composition in Ca and Fe depending on the sampling site location. Rhodonite is the second most abundant Mn silicate in the protore (Fig. 3a). Its abundance is systematically underestimated as it is frequently altered into secondary Mn oxides in oxidized ore. Mn-rich spinels (jacobsite, franklinite, gahnite) and Mn-rich ilmenite (pyrophanite, ecandrewsite) have been observed in graphite-depleted samples of the Vohidrakitsy sub-district (Fig. 3b).

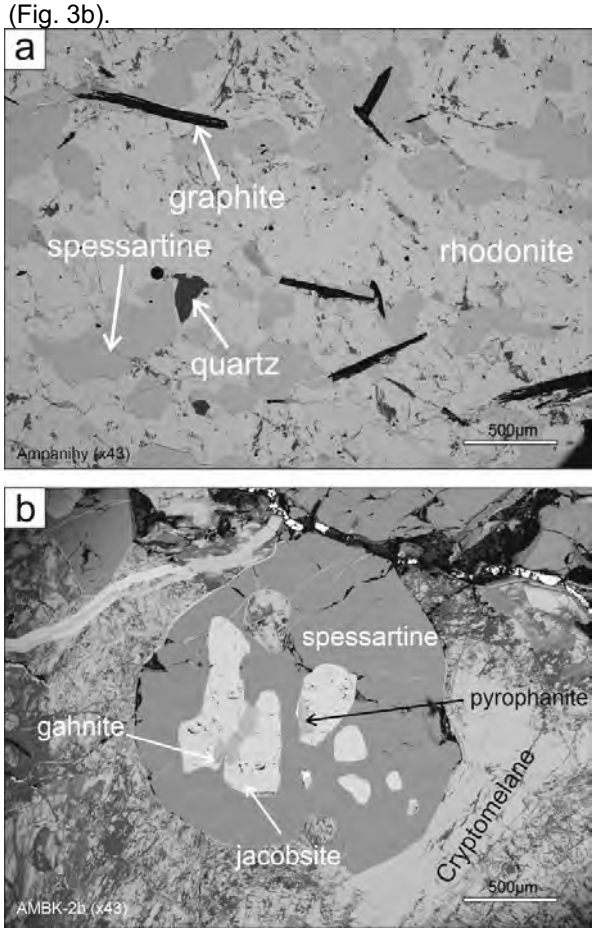


**Figure 3.** SEM view of the Mn ore. a. Rhodonite-rich paragneiss. b. Spessartine containing Mn-rich spinels and ilmenite.

Graphite is a minor phase, which usually occurs as abundant dark grey mm-size flakes. Quartz is ubiquitous in all the samples and shows secondary features such as radial extinction under cross-polarized light and replacement features of graphite flakes. Barite can be a major mineral phase in some samples from the Vohidrakitsy sub-district and occurs in the matrix.

From these results, we divide the primary ore into two spatially independent mineral assemblages: a (1) quartz-spessartine-rhodonite $\pm$ graphite and a (2) quartz-spessartine-rhodonite $\pm$ jacobsite $\pm$ pyrophanite $\pm$ barite. The latter is representative of the Vohidrakitsy sub-district. There

is no indications of Mn carbonate ore in the study area.

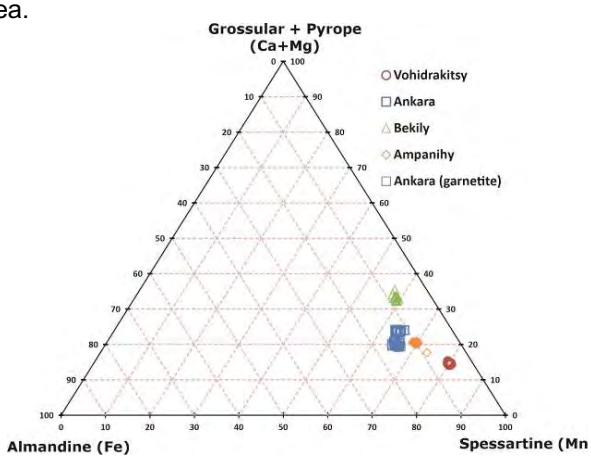


**Figure 4.** Compositional field of Mn-rich garnets from the three sub-districts based on EPMA data.

### 4.3 Whole rock geochemistry

The Ampanihy ore is variously enriched in manganese, from the weakly/moderately protore to the massive Mn oxide crust: $Mn_2O_3$ content ranges from 7.6 to 68.5 wt.%, with an average value of 29.8%. Samples have high silica (up to 82.1 wt.% $SiO_2$) and low to moderate Al (0.7 to 17.3 wt.% $Al_2O_3$).

Trace metal elements display two distinctive geochemical trends: (1) one is enriched in Zn, Sb, As and Ba, and (2) the other is comparatively enriched in Ni, Co and V. Zn-rich samples from the Vohidrakitsy sub-district have low graphite (C < 0.04%).

Rare Earth Elements (REE) patterns, normalized to chondrite C1, are flat, showing a global enrichment higher than 10 (Fig. 5). Only the Ankara sub-district samples show a significant fractionation in the light REE (LREE), providing higher $La_N/Lu_N$ ($1.7 < La_N/Lu_N < 6.0$) ratios than the other sub-districts ($0.5 < La_N/Lu_N < 3.0$) (Fig. 5). The typical Eu anomaly of sedimentary rocks is conspicuous in the whole dataset ($0.3 < Eu_N/Eu_N^* < 0.7$). One remarkable specificity of the Vohidrakitsy REE patterns is the negative Ce anomaly ($0.2 < Ce_N/Ce_N^* < 1.2$) of some samples, whereas the other sub-districts do not display any negative Ce anomaly.

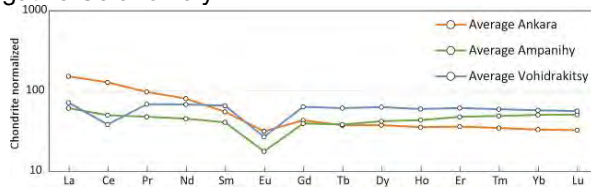


**Figure 5.** Average REE patterns of the three sub-districts of the Ampanihy area compared to chondrite C1 (McDonough and Sun 1995).

### 4.4 Raman spectroscopy on graphite

The results from Raman spectroscopy on graphite flakes show peak metamorphism temperatures between 352-481°C (Fig. 6).

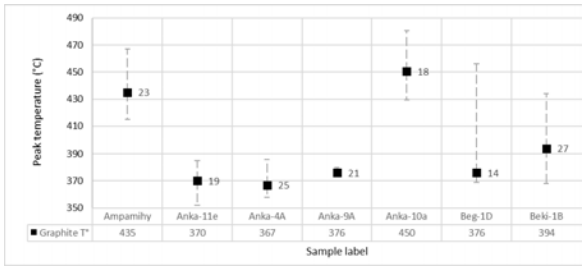


**Figure 6.** Results of the Raman spectroscopy on graphite flakes from the Ampanihy district.

## 5 Discussion

### 5.1 Mn precursor

The metamorphosed Mn deposits of the Ampanihy district belong to type IIA deposits (Dasgupta 1997): the Mn ore is dominated by Mn silicates (spessartine, rhodonite) with minor Mn oxides. Type IIA is usually derived from Mn oxide precursor sediments with various degrees of admixtures of ferruginous oxides/hydroxides, silica and clay minerals (Dasgupta et al. 1990). The abundance of spessartine as the main Mn-carrier in the metasediments requires the existence of a protolith with notable aluminium (i.e., mudstone/siltstone). In the absence of feldspar and complex silicates (i.e., micas) in the ore, Al was likely stoichiometrically equal to Mn in spessartine.

The presence of graphite flakes suggests that the original sediment was rich in organic matter and preserved under conditions in which it was not transformed into carbonates. Accordingly, where graphite is absent, metamorphic Mn oxides occur (Fig. 3d). Turbidite flows can ensure deep deposition and rapid burial of carbon-rich sediments over a wide area. Indeed, the regional abundance of C-rich sediments (locally known as the “Graphite System”) points to large sedimentary basins, possibly along the margins of cratonic landmasses, locally enriched in manganese.

Mn carbonates are regarded as prerequisite ore forming minerals in most sedimentary manganese deposits (Maynard 2014). Their absence in the study area suggests that organic matter was not involved in diagenetic-metamorphic reactions. Mhlanga et al. (2023) recently proposed that primary $Mn^{2+}_{(aq)}$ was likely oxidized to $Mn^{3+}$ rather than $Mn^{4+}$ (as generally proposed) in the Paleoproterozoic Hotazel Formation in South Africa. The major consequence is that $Mn^{3+}$ cannot enter the carbonate lattice, hence the predominance of braunite at Hotazel. This contrasts with models in which carbon plays a significant role in reducing primary ferromanganese nodules into Mn carbonates (Johnson et al. 2016).

### 5.2 Paleodepositional environments

By combining trace elements and REE compositions, we identify three distinct geochemical environments (Fig. 7). These data are in line with the three garnet populations (Fig. 4). The $La_N/Lu_N$ vs (As+Cu+Mo+Pb+V+Zn+Ba)/(Co+Ni) diagram illustrates two end-members. The high La/Lu ratio shows fractionation of LREE, which can be interpreted by a crustal vs mafic source of the sediments (McLennan 1989). The second shows a high metal content which we regard as an hydrothermal input (Nicholson 1992). Therefore, the Mn-rich sediments of the Ampanihy district can be interpreted as a mixing between hydrothermal and continental (crustal) sources. This observation is comparable to some extent with modern Mn polymetallic nodules in the seafloor. We therefore suggest that Mn and associated metals were scavenged from seawater into ferromanganese nodules during the deposition of the sediments.

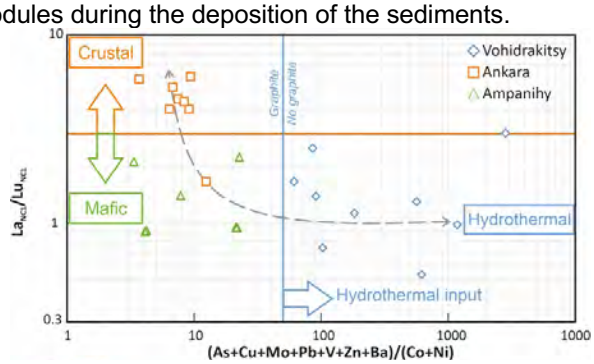


**Figure 7.** Geochemical diagram showing the different depositional environments of the Mn-rich metasediments between crustal and hydrothermal sources.

### 5.3 Mn accumulations in the Paleoproterozoic

Mn deposits of Paleoproterozoic age in Africa (Moanda in Gabon, Kalahari in South Africa, Kisenge in DRC)(Beukes et al. 2016; De Putter et al. 2018) indicate suitable conditions for the deposition of large (sometimes world-class) Mn deposits. Although they have currently no economic potential, the Ampanihy Mn occurrences display strong variations in their geochemical composition, as a result on their source and proximity with hydrothermal centres within the Paleoproterozoic basin. This is a key to reconstruct depositional conditions that led to Mn deposition and associated metals (Ampanihy, Kisenge). Therefore, we propose a multi-scale model: (1) Sedimentation of C-rich sediments occurs at a large scale in peri-cratonic basins, as shown by the wide extension of Graphite Series around cratonic areas, in Africa, Madagascar and India. (2) The deposition of Mn occurs at the district scale, with regional inputs of Mn either deriving from the continent or from hydrothermal vents. Mn ore forms when suitable conditions are met for their precipitation (Maynard 2014). In the Ampanihy area the geochemistry of the Mn-rich metasediments can be comparable to the distribution of trace metals observed in modern ferromanganese nodules. (3) Significant hydrothermal enrichment (in Zn and metalloids) is local and likely occurs after the deposition of the sediments.

## Acknowledgements

We are grateful to the Geological Survey of Madagascar for their help in accessing the field. We thank L. Monin (UCL) for the acquisition of geochemical analyses.

## References

Armistead SE, Collins AS, Schmitt RS, et al (2021) Proterozoic Basin Evolution and Tectonic Geography of Madagascar: Implications for an East Africa Connection During the Paleoproterozoic. Tectonics 40:.

Besairie H (1946) La géologie de Madagascar. Annales géologiques du service des mines 12:32

Beukes NJ, Swindell EPW, Wabo H (2016) Manganese deposits of Africa. Episodes 39:285.

Boger SD, Hirdes W, Ferreira CAM, et al (2015) The 580–520Ma Gondwana suture of Madagascar and its continuation into Antarctica and Africa. Gondwana Research 28:1048–1060.

Boulanger J (1956) Les gîtes manganésifères du sud de Madagascar. Bulletin de la Société française de Minéralogie et de Cristallographie 74:343–344

Dasgupta S (1997) P-T-X relationships during metamorphism of manganese-rich sediments: Current status and future studies. Geological Society, London, Special Publications 119:327–337.

Dasgupta S, Banerjee H, Fukuoka M, et al (1990) Petrogenesis of metemorphosed manganese deposits and the nature of the precursor sediments. Ore Geology Reviews 5:359–384.

De Putter T, Liégeois J-P, Dewaele S, et al (2018) Paleoproterozoic manganese and base metals deposits at Kisenge-Kamata (Katanga, D.R. Congo). Ore Geology Reviews 96:181–200.

de Wit MJ, Bowring SA, Ashwal LD, et al (2001) Age and tectonic evolution of Neoproterozoic ductile shear zones in southwestern Madagascar, with implications for Gondwana studies. Tectonics 20:1–45.

Fermor LL (1909) The manganese-ore of India, Memoirs of the geological survey of India. Government of India

Johnson JE, Webb SM, Ma C, Fischer WW (2016) Manganese mineralogy and diagenesis in the sedimentary rock record. Geochimica et Cosmochimica Acta 173:210–231.

Maynard JB (2014) Manganiferous sediments, rocks, and ores. In: Treatise on Geochemistry. Elsevier, pp 327–349

McDonough WF, Sun S -s. (1995) The composition of the Earth. Chemical Geology 120:223–253.

McLennan SM (1989) Rare earth elements in sedimentary rocks; influence of provenance and sedimentary processes. Reviews in Mineralogy and Geochemistry 21:169–200

Mhlanga XR, Tsikos H, Lee B, et al (2023) The Palaeoproterozoic Hotazel BIF-Mn Formation as an archive of Earth's earliest oxygenation. Earth-Science Reviews 240:104389.

Nicholson K (1992) Contrasting mineralogical-geochemical signatures of manganese oxides; guides to metallogenesis. Economic Geology 87:1253–1264.

Tucker RD, Roig J-Y, Macey PH, et al (2011) A new geological framework for south-central Madagascar, and its relevance to the "out-of-Africa" hypothesis. Precambrian Research 185:109–130.

Tucker RD, Roig J-Y, Moine B, et al (2014) A geological synthesis of the Precambrian shield in Madagascar. Journal of African Earth Sciences 94:9–30.

# Mineralogical variation and paragenesis of the mineralisation and alteration at the Neoproterozoic Rosh Pinah Zn-Pb-Ag deposit, Namibia

**Halleluya Naantu Ekandjo[1], Koen Torremans[2], Murray Hitzman[3], John Güven[4]**
*SFI Research Centre in Applied Geosciences (iCRAG), School of Earth Sciences, University College Dublin, Ireland*

**Abstract.** Significant alteration has affected the rocks at the Rosh Pinah Zn-Pb-Ag deposit. Silicification has previously been identified as the major alteration style that destroyed many of the original textures in the host rocks to the deposit. However, the timing of silicification and the possible presence of other significant alteration events have not been properly constrained, nor have the age and genetic relationships between alteration and mineralisation events. This study combines transmitted and reflected light petrography, scanning electron microscopy, "hot" cathodoluminescence, laser ablation ICP MS and whole rock geochemistry to determine the paragenetic sequence of alteration/mineralisation events at Rosh Pinah. Dominantly replacive pyrite, sphalerite, galena, and minor chalcopyrite, are hosted within weakly metamorphosed altered argillites, siltstones, carbonate rocks and volcanic rocks collectively known at the mine as the Ore Equivalent Horizon. This interval displays variable alteration, with the fine siliciclastic units (argillite and siltstones) affected mainly by silicification and barium enrichment of both detrital and authigenic feldspars and phyllosilicates. Carbonate rocks were affected by multiple dolomitization events.

## 1 Introduction

The Rosh Pinah Zn-Pb-Ag deposit in the Gariep Belt, southern Namibia comprises a significant measured and indicated sulphide resource (19.94 Mt @ 7.38 % Zn, 1.83 % Pb and 27.7 g/t Ag) (Trevali Mining Corporate Presentation 2022). It is located within the arcuate NNW trending Neoproterozoic Gariep Belt in southern Namibia (Fig. 1).

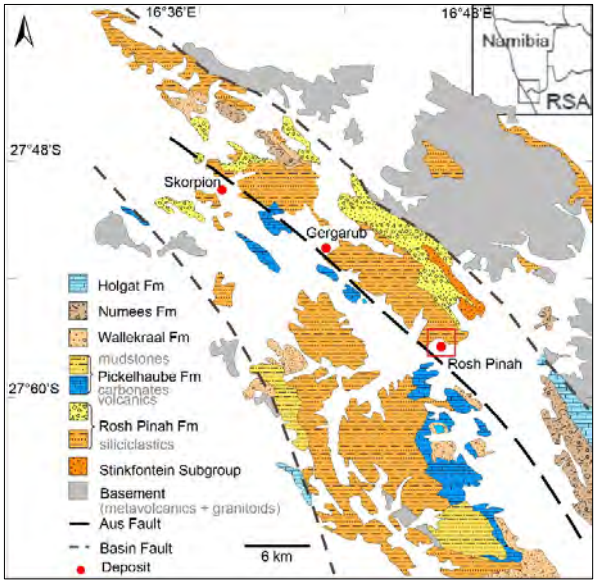


**Figure 1.** A simplified geological map of the Rosh Pinah Graben (modified after Alchin et al. 2005). The economic deposits are represented by red dots. The red box shows the location of the study area. Inset shows location in Southern Africa

The Rosh Pinah deposit occurs within the Rosh Pinah Formation of the Port Nolloth Group, which is comprised of a volcano-sedimentary sequence interpreted to have been deposited in a failed rift (Alchin et al. 2005). The Rosh Pinah Formation has been complexly deformed and experienced greenschist to lower amphibolite facies metamorphism during the Pan African orogeny.

Mineralisation (sphalerite, galena, pyrite with subordinate chalcopyrite) is hosted in the Ore Equivalent Horizon (OEH), a mixed sequence of fine-grained siliciclastic rocks (argillites and siltstones), carbonates, and minor felsic volcanic units. The OEH occurs in between thick, often fining-upward arkose-dominated units.

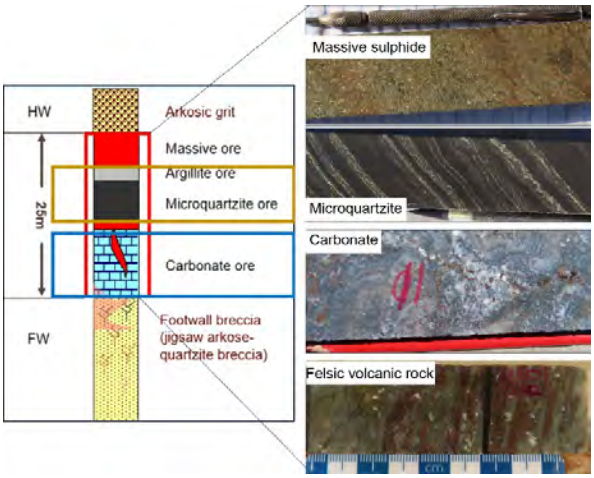


**Figure 2.** Stratigraphic position of the OEH at the Rosh Pinah deposit with corresponding drillcore photographs of individual units (adopted from Mouton unpublished)

Silicification and dolomitisation of the argillite-siltstones and carbonate respectively have been previously identified. However, their timing, the presence of other significant alteration events, and their genetic relationships to mineralisation are poorly understood. This study combines transmitted and reflected light petrography, scanning electron microscopy, hot cathodoluminescence, laser ablation ICP MS and whole rock geochemistry to elucidate types and timing of different alteration and mineralisation phases, and to relate the

alteration/mineralisation to the stratigraphic and structural architecture. It also aims to elucidate the fluid pathways that may have helped localise mineralisation.

## 2 Methodology

Field campaigns aimed at core logging and drill core sampling were carried out between November 2020 and July 2021 and in February 2023. During core logging, details on the lithology, lithofacies, sedimentary features, alteration, and mineralisation were recorded. A total of hundred and one (101) collected core samples of least and intensely altered OEH units were submitted for polished thin section preparation at University College Dublin (UCD) and Vancouver Petrography Laboratory, Canada.

Polished thin sections were examined under transmitted and reflected microscopy in UCD using Nikon LV100NDA/POL microscopes with mechanised stage, and microphotographs were captured using Nikon DS-Ri2 cameras. Further examination was done using a Hitachi TM3030Plus Tabletop scanning electron microscope (SEM) at UCD and a TESCAN TIGER Mira3 field-emission SEM equipped with two oxford X-Max 150mm2 EDS detectors at Trinity College Dublin (TCD). Calibration of the TIGER was done using natural minerals (orthoclase, chromite, diopside, barite, magnetite, kaersutite, apatite, tugtupite, olivine, rutile, rhodonite, quartz). Quantitative analyses were performed at 20kV acceleration voltage. The accelerating voltage for the SEM was 10 kV and the operating voltage for the EDS was 15 kV.

Cathodoluminescence (CL) microscopy was conducted using a HC6-LM cathodoluminescence microscope with an OLYMPUS light microscope attached. The operating conditions for the CL were around 11 kV accelerating voltage and <0.2mA beam current. The CL investigation was conducted at the Natural History Museum, London. Laser ablation inductively coupled plasma mass spectrometry (LA ICP-MS) on the carbonate cements of interest was carried out on a IRIDIA connected to an Agilent 7900 ICP-MS at TCD. Operating conditions included 11Hz repetition time, 300 shoot counts, and 27 seconds ablation time on 25 µm spot size field of view. Data reduction was done using the Iolite software.

To supplement the petrographic observations, sixty-five (65) drill core samples from the argillite and siltstones from the OEH were submitted to ALS Laboratory, Canada for geochemical analysis using ME-MS81d™ (combination of rare earth elements and trace elements by Li Borate Fusion) and ME-ICP06 (four acid digestion and ICP AES for major elements. Additional ME-4ACD81 (four acid digestion and ICP-AES for base metals) will be carried out on the same samples. Sampling for geochemical analyses was designed to include both ore related samples and ore distal samples to test for potential vectors towards mineralisation.

## 3 Results

Reflected light microscopy and SEM has demonstrated a mineralogically simple sulphide suite (sphalerite, galena, pyrite, chalcopyrite, and subordinate pyrrhotite) but their intergrowths and paragenetic sequence is complex (Fig. 3). Mineralisation styles include massive, disseminated, stringers, and sulphides along bedding which have now aligned locally into tectonic cleavage. There is no evidence for mineralization related to syn- or post-orogenic shear zones. The common textures observed from samples studied include framboids, botryoidal, atoll, deformed, disseminated, grain boundary segregations, intergrowths, symplectic (chalcopyrite disease). Most of the mineralisation is interpreted to be replacive with a strong control of sedimentological make-up on sulphide mineralogy and grain size.

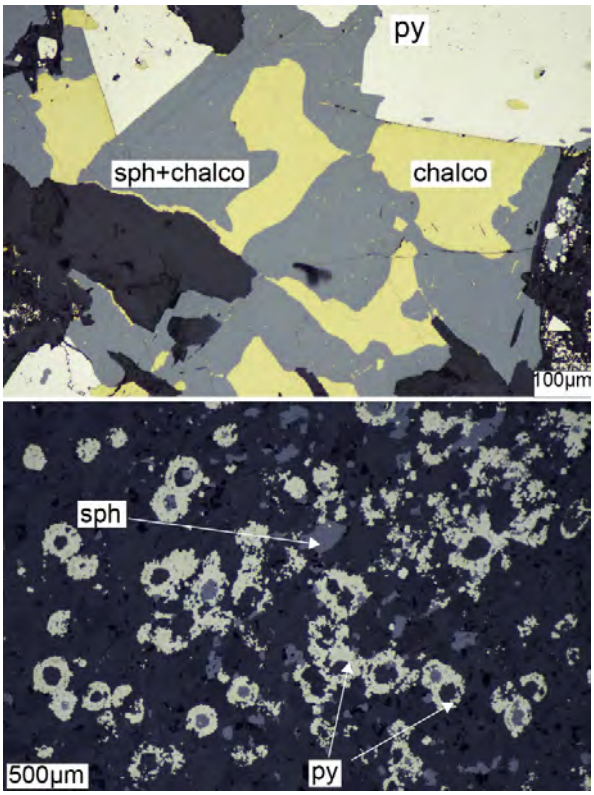


**Figure 3.** Reflected microphotographs of the sulphides at the Rosh Pinah deposit. Top figure shows the simple sulphide mineralogy (pyrite(py) sphalerite (sph) and chalcopyrite (chalco)) replacing earlier cements in host rock. The bottom figure shows atoll textures (sphalerite, pyrite and dolomite).

The local term microquartzite (see Fig. 2) is not a stratigraphic unit, but represents original mudstones and siltstones, with alteration dominated by silicification and Ba-enrichment. As the alteration of the siliciclastic rocks increases, both detrital feldspars and authigenic feldspars are replaced by barium feldspars resulting in the zonation of the

feldspars (Fig. 4). The type and intensity of alteration seem to correlate with original grain size and mineralogy of the sedimentary rocks, with coarse grained units more intensely altered and mineralised, suggesting a permeability control on alteration fluids. Sulphides, mainly sphalerite, galena and pyrite appear to simultaneous with the Ba-alteration of the feldspars (Fig. 4). Locally, enrichment and relative depletion of silica in least-mineralised bands and intensely mineralised band respectively is evident (Fig. 4).

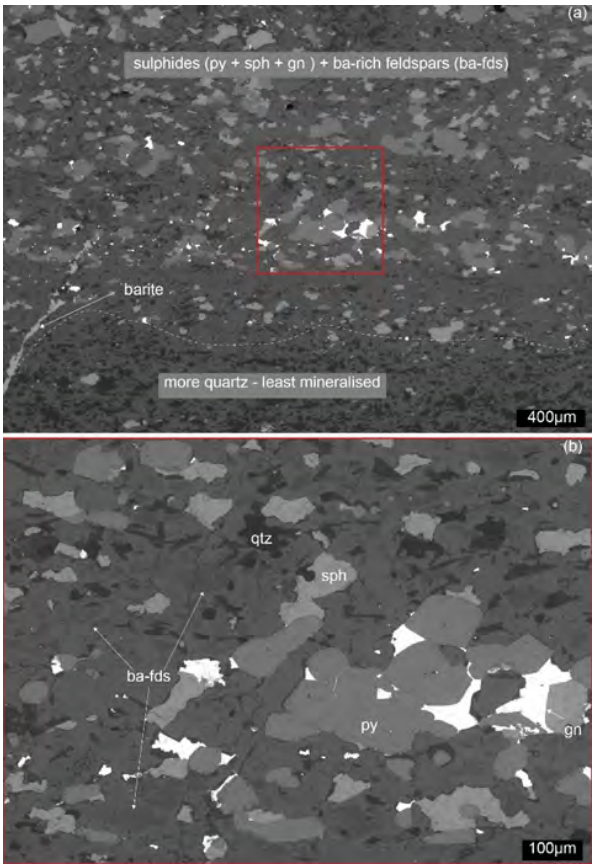


**Figure 4.** SEM Microphotographs of the laminated argillite. (a) shows the different bands with the dotted line demarcated the boundary between two different layers. Note the amount quartz and ba-rich feldspars in each layer. (b) Microphotograph extract from a (red box) showing the ba-enrichment of feldspars and their link with the sulphides.

Many of the carbonates observed at Rosh Pinah deposit are recrystallised and hydrothermally altered (mainly dolomitised). However, our extensive logging coupled with detailed petrography and CL work have demonstrated rare zones where original diagenetic textures in form of fibrous carbonate cements are preserved (Fig. 5). These are currently being examined through LA ICP-MS and C-O and Sr isotopes to determine if an original depositional environment can be constrained.

Several generations of carbonate have been identified, and are labelled as dol 1, dol 2, dol 3, and dol 4 (Fig. 5). Dol 1 represents the fibrous cements attributed to early diagenesis, dol 2 represents white curvilinear cracks associated with the fibrous cements. Dol 3 refers to cements that show dissolution and reprecipitation of dol1 and dol 2, and which is also associated with sulphides. Dol 4 represents white, coarse-grained carbonate associated with sulphides.

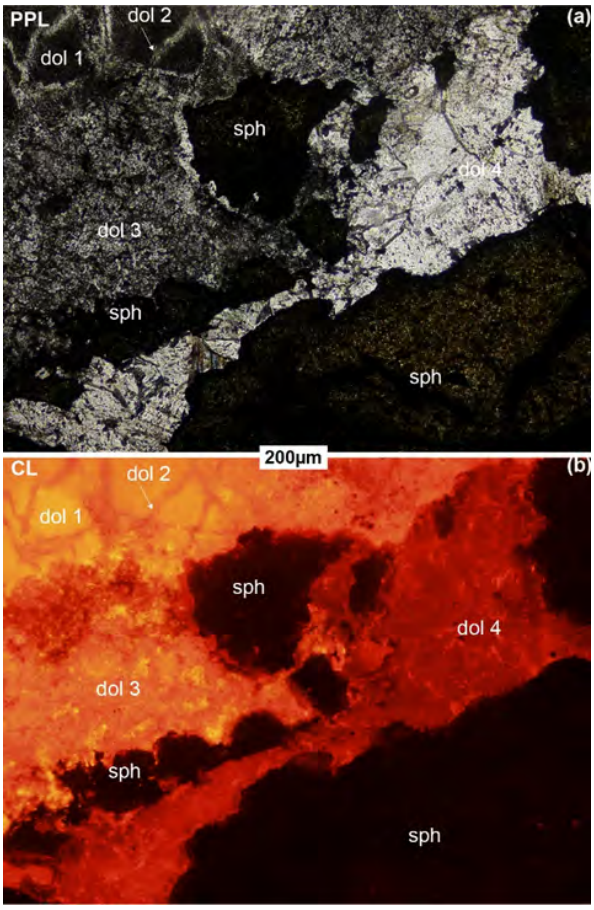


**Figure 5**. Transmitted light (PPL) and CL microphotographs respectively of the rare carbonate cements and other carbonate generation and associated sulphides from the Rosh Pinah OEH. The dark colour associated with dol1 is due to presence of possible organic matter.

## 4 Conclusions

Mineralisation at Rosh Pinah consists of sphalerite, galena, pyrite, and minor chalcopyrite. It is replacing a variable suite of already-consolidated and cemented fine-grained siliciclastics, carbonates and felsic volcanics protoliths. Microquartzite is not a stratigraphic unit but represents original mudstones and siltstones which have now been altered. Silicification is the dominant and most recognized type of alteration, however, barium enrichment of feldspars and phyllosilicates is also prevalent, with the intensity of Ba enrichment alteration increasing towards mineralisation. The majority of the carbonates are recrystallised, however, rare diagenetic textures in form of carbonate cements

are present. It is evident from the carbonate cement that sulphide mineralisation is mainly replacive. The Rosh Pinah story is a complex one, but will surely develop further as all the data is collected and interrogated.

## Acknowledgements

This research has emanated from research supported in part by research grant from Science Foundation Ireland (SFI) under Grant Number 16/RP/3849 and 13/RC2092_P2 and is co-funded by Trevali. Natural History Museum, London is thanked for the use and assistance with their CL facility. Rosh Pinah Mine exploration team and members of iCRAG are thanked for their insightful discussion.

## References

Alchin DJ, Frimmel HE, Jacobs LE (2005) Stratigraphic setting of the metalliferous Rosh Pinah Formation and the Spitzkop and Koivib Suites in the Pan-African Gariep Belt, southwestern Namibia. S Afr J Geol108(1):19-34

Trevali Mining Corporate Presentation (2022) Available at https://trevali.com/site/assets/files/9809/trevali_mining_corporate_presentation_-_june_2022_final.pdf Accessed 13 March 2023

# Litho-structural control of Pb-Ag veins in Jbel Addana district: Case of the Igharassene deposit (Western Anti-Atlas, Morocco)

**Zoubair El ouad[1,2], Mustapha Souhassou[1], Moha Ikenne[2], Hafida ElBilali[3], Brian Cousens[3], Richard Ernst[3]**
*[1]Laboratory of Geo-Bio-Environmental Engineering and Innovation, Research Team: Exploration and Management of Natural and Environmental Resources, Polydisciplinary Faculty of Taroudant, Ibn Zohr University, Taroudant, Morocco.*
*[2]Laboratory of Applied Geology and Geo-Environment, Faculty of Sciences of Agadir, Ibn Zohr University, Agadir, Morocco.*
*[3]Ottawa-Carleton Geoscience Centre, Department of Earth Sciences, Carleton University, Ottawa, Canada,*

**Abstract.** In the Western Anti-Atlas of Morocco, Jbel Addana is an anticline trending NE-SW and located about 30 km south-east of Tagragra d'Akka inlier. It consists of an alternation of quartzites, shales and sandstones represented by the Ktaoua, Rouid-Aïssa and Second Bani Formations of Upper Ordovician age. The Rouid-Aïssa Formation hosts a series of Pb-Ag mineralized sub-parallel veins with vertical dips that form a district subdivided into several deposits. The mineral paragenesis is represented by massive galena with quartz gangue in the quartzitic layers and an iron association with siderite, and goethite in addition to red ochres with malachite in the sandstone levels that are exposed at the surface. The Igharrasene deposit, which occupies the central part of the Addana anticline, is key to understanding the tectonic control of the mineralized veins in this district. Field observations have shown that the mineralized structures correspond to en-echelon veins following two different average directions (N22°E and N114°E), this aspect is expressed by the opening of two sets of en-echelon tension gashes in the same directions mentioned above.

## 1 Introduction

The Pb-Ag district of Jbel Addana is located in the western Anti-Atlas, 35 km southeast of the Precambrian inlier of Tagragra d'Akka. It represents the most external outcrops of the Ordovician belt of Jbel Bani. This district comprises several deposits that developed throughout a 40 km long anticline. The mineralized areas consist of networks of sub-parallel veins with a sub-vertical dip. Mining started in the Middle Ages (Desthieux, 1977) and progressed until 1987. Galena is the main ore exploited with contents around 1280 to 416 g/t Ag and 69.3% Pb (Saadi 1969 ; Desthieux 1977). Since then, all of these deposits have never been studied using modern technologies and thus remain poorly documented. The present study will contribute, on the one hand, to understanding the geodynamic and metallogenic history of the Jbel Addana district, and on the other hand, to the discovery of new reserves that can be exploited.

## 2 Geological setting

Jbel Addana is a NE-SW trending anticline dominated by weakly metamorphosed detrital sedimentary terrains of Upper Ordovician age (Caradoc and Ashgill). These terrains consist of alternating layers of quartzites, shales and sandstones that are attributed to the Ktaoua, Rouid-Aïssa and Second Bani Formations (Figure 1). The Rouid-Aïssa Formation of the Upper Caradoc is represented from the bottom to the top by quartzites superimposed by shales and ends by Addana sandstones, which constitutes the main host of the mineralized bodies.

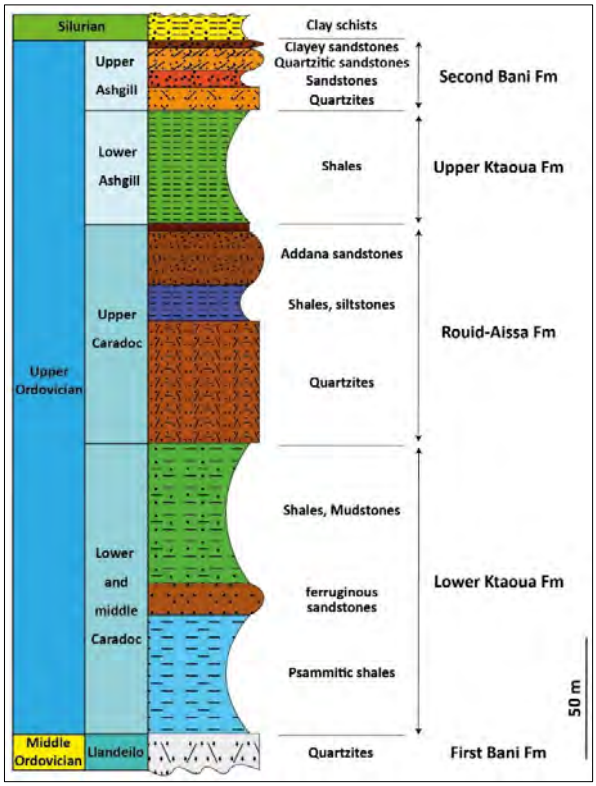


**Figure 4.** Stratigraphic log of the lithological Formations of Jbel Addan (Modified after Desthieux, 1977)

The Igharassene deposit is located at the mid-length of the Jbel Addana anticline and is the only deposit of the district where mineralized quartzites are exposed at the surface. The mineralized bodies correspond to vein-type structures with lead occurrences. Mapping has shown that these structures are developed along two different structural directions (N20°E to N25°E and N114°E to N120°E) (Figure 2)

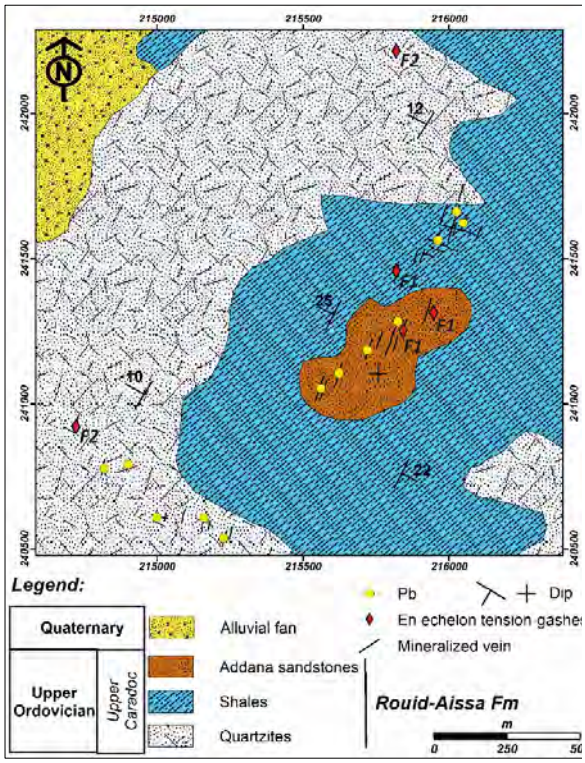


**Figure 5.** Geological map of Igharassene deposit.

## 3 Mineralizations

Based on field observations, macroscopic descriptions of the mineralized structures show that: ***i)*** In the Addana sandstones representing the top of the host Formation, the mineralization is mainly represented by an iron paragenesis with red ochres, goethite and siderite associated with malachite and quartz prisms that show in some cases a centripetal growth (Figure 3 A and B), where galena is not frequent. ***ii)*** Within the quartzites, there is a high enrichment of lead mineralization represented either by macroscopic patches of galena associated with a quartz gangue or by massive textured vein structures (Figure 3 C and D).

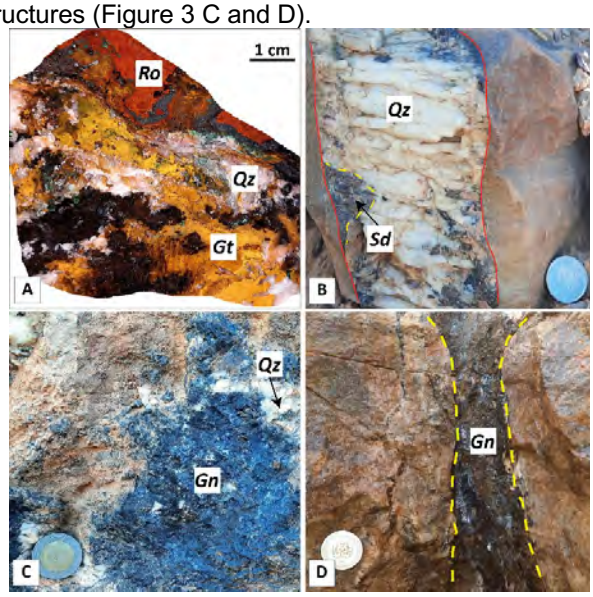


**Figure 6.** Macroscopic aspect of the mineralization of Igharassene deposit. Gn: Galena, Gt: Goethite, Ro: Red ochres, Sd: Siderite.

## 4 Litho-structural control

The Field observations suggest that lithological contrast has a major impact on the development of the mineralized bodies. Thus, the quartzitic and sandstones levels constitute favorable locations to concentrate mineralization, while the shaly levels are characterized by the abundance of weakness planes, which facilitate the release of mineralizing fluids. From a structural point of view, mapping shows that all the mineralized structures of Jbel Addana correspond to en-echelon veins, indicated by the opening of two sets (F1 and F2) of en-echelon tension gashes (Figure 2) in the same directions mentioned above.

The F1 set has an average trend of N22°E and characterizes all deposits that dominate the northeast part of the anticline. This set is controlled by a large sinistral shear zone (Figure 4 A), whereas the F2 set is well represented in all the southwestern deposits with an average trend of N114°E and is controlled by a dextral shear zone (Figure 4 B).

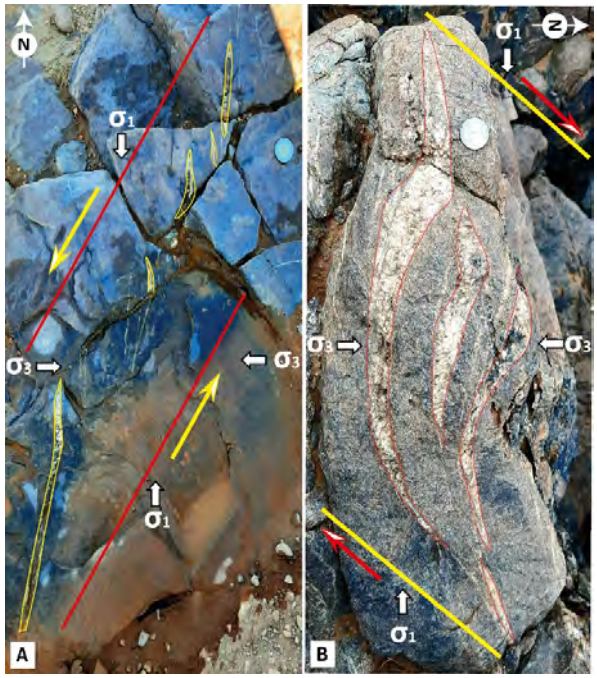


**Figure 7.** Field photographs showing the aspect of en-chelon tension gashes.

## 5 Conclusion

The whole of our field investigations in the Jbel Addana anticline, shows that the igharassen area corresponds to a stress transfer zone. This is indicated by the existence of different direction veins. Inside these veins, the quartz prisms are either orthogonal or oblique to the vein walls. Directional analysis of elongation of these prisms in several locations in the area, suggests a counter-clockwise rotation of the principal stress σ1 between

N25°E and N330°E directions. This rotation of stress has caused the opening of conjugate strike-slip faults, which are occasionally senestial or dextral with directions ranging between N60°E and N310°E.

## Acknowledgements

Our special thanks to the Royal Armed Forces of the Akka region, for having authorised the access to Jbel Addana, and having accompanied us during our field missions.

## References

Desthieux, F (1977) Etude tectonique et métallogénique du Jbel Addana, Ordovicien des plaines du Dra, Maroc présaharien. Notes et Memoires Serv. Géol. Maroc 268:209–236.

Saadi, M (1969) Possibilités minières et hydrogéologiques de la région d'Akka et rôle historique de Tamdoult. Mines et Géologie 30:19–39.

# Germanium-bearing minerals in the Cu-Ag Kupferschiefer deposit in Poland

**Krzysztof Foltyn[1], Władysław Zygo[1], Dariusz Węgrzynek[2], Gabriela A. Kozub-Budzyń[1], Piotr Ducki[3], Jakub Węgrzynowicz[4]**
[1]*Faculty of Geology, Geophysics and Environmental Protection, AGH University of Krakow, Poland*
[2]*Faculty of Physics and Applied Computer Science, AGH University of Krakow, Poland*
[3]PeBeKa *S.A., Lubin, Poland*
[4]*ZG Lubin, KGHM PM S.A., Lubin, Poland*

**Abstract.** Three new occurrences of Ge-bearing minerals have been recently recognized in the Cu-Ag Kupferschiefer deposit in Poland. These are Ge-enriched chalcopyrite from the epigenetic sulphide-calcite veins in the Polkowice-Sieroszowice mine, translucent sphalerite with up to 0.18 wt.% Ge in a sandstone-hosted calcite vein from Lubin mine and massive covellite-galena assemblage at the contact between Zechstein carbonates and Lower Anhydrite in GG1 shaft. Micro-beam X-ray fluorescence distribution maps allowed to recognize two types of germanium distribution in chalcopyrite: oscillatory zoning and a "dendrite-like" organization. Mineralization where argyrodite was found consists of massive covellite with galena, acanthite, jalpaite, sphalerite and pyrite suggesting high sulfidation state of hydrothermal fluids. All reported instances of Ge-enriched mineralization have a common feature. They are all related to local fractures, faults, shear zones or tectonic zones and suggest there might be a direct link between germanium enrichment and structurally-controlled mineralization in the Fore-Sudetic Homocline.

## 1 Introduction

Germanium occurs in minor and trace amounts in various types of mineralization, with economic concentrations in only a handful of them (Bernstein 1985; Höll et al. 2007; Melcher and Buchholz 2014). Germanium minerals tend to be rare, the most common are argyrodite $Ag_8GeS_6$, canfieldite $Ag_8(Sn,Ge)(S,Te)_6$, briartite $Cu_2(Zn,Fe)GeS_4$, reniérite $(Cu,Zn)_{11}(Ge,As)_2Fe_4S_{16}$ and germanite $Cu_{26}Fe_4Ge_4S_{32}$ and have been reported in a limited number of localities (Melcher and Buchholz 2014). Most of the Ge-bearing sulphide ore comes from low temperature zinc deposits, hosted predominantly in carbonate rocks (Bernstein 1985; Höll et al. 2007) where Ge occurs as substitution in the structure of sphalerite and wurtzite.

According to Banaś et al. (2007), copper ores in the Lubin-Sieroszowice Cu-Ag district in SW Poland contain on average 1 ppm of Ge, but locally it can be up to 10 ppm. Despite such low concentrations, Van Nhan (1970) reported a possible occurrence of argyrodite in chalcocite-bornite ore from the Lubin East field, while Harańczyk (1975) described two new germanium minerals in samples from S-372 borehole: morozeviczite $Pb_3Ge_{1-x}S_4$ and polkovicite $(Fe,Pb)_3(Ge,Fe)_{1-x}S_4$. These minerals were found in an epigenetic vein, filling a zone of tectonic cracks within sandstone below Zechstein sediments. However since their discovery they have not been found anywhere else. Foltyn et al. (2022) report high enrichment in germanium (up to 4806 µg/g) coupled with high content of arsenic (up to 1045 µg/g) in chalcopyrite from the carbonate hosted epigenetic sulphide-calcite veins associated with local faults and tectonic zones in the Polkowice-Sieroszowice mine.

The aim of this study is to present three different associations of Ge-bearing minerals in the Cu-Ag Kupferschiefer in Poland and highlight common features to better understand the factors responsible for Ge enrichment in the deposit.

## 2 Geological setting

The Kupferschiefer mineralization in the SW part of the Fore-Sudetic Homocline is a classic example of a sediment-hosted stratiform/stratabound copper deposit (SSC; Figure 1A).

Rift-related tectonism and associated magmatic activity resulted in Lower Rotliegend beds composed of red-coloured clastic sediments and bi-modal volcanics composed of rhyolites, rhyolitic tuffs and trachybasalts. The Upper Rotliegend are terrestrial red beds composed of aeolian sandstones interbedded with deposits of alluvial fans, braided rivers and playas characteristic of fluvial, aeolian and lacustrine sedimentary environments in a land-locked basin and arid climate (Karnkowski 1999; McCann et al. 2006). Marine transgression in the Late Permian, reworked the uppermost part of the Rotliegend forming white sandstones called Weissliegend (Glennie and Buller 1983). The Kupferschiefer is a thin (average 0.3 m thick) layer of black, marine, organic-bearing shale, and represents a change from oxidized to reduced deposition conditions. Oscillatory environmental changes resulted in cyclicity and Zechstein rocks in Poland are subdivided into four evaporitic cycles, referred to as PZ1 (Z1 Werra), PZ2 (Z2 Stassfurt), PZ3 (Z3 Leine), and PZ4 (Z4 and younger formations). In the Lubin-Sieroszowice district, the Kupferschiefer is overlain by the Zechstein Limestone (Ca1) of varying thickness: up to 10 m in the north but it can reach 40-80 m in the southern part. It is followed by the Lower Anhydrite (A1d), the Oldest Halite (Na1), and the Upper Anhydrite (A1g) constituting the first cyclothem series (Tomaszewski 1978). Locally, in the so-called "sandstone elevation" areas, the shale is absent and limestone directly overlies the Weissliegend sandstone.

The Cu-Ag sulphide ores occur at the base of the Zechstein succession (Figure 1B). The main mineralizing process was the migration of low-temperature, oxidizing, metalliferous chloride brines through the anoxic basal sediments of the Zechstein Group (Hitzman et al. 2005).

Epigenetic sulphide veins (with a thickness from a few mm up to 1.5 m, but most commonly few to 20 cm thick) are not very common in the Lubin-Sieroszowice district and most studies focus on stratabound mineralization. Veins are usually steeply dipping (60-90°), have sharp contact with surrounding sandstones or carbonates and usually are related to tectonic zones and fault structures, filling fractures and cracks which intersect the basal Zechstein sequence (Banaś et al. 1998). Crackle breccia and hydraulic breccia (with characteristic jigsaw geometry) suggest that hydraulic fracturing and fault-valve behaviour could be involved in their origin. Proportion of carbonates to sulphides varies and fluctuates between calcite-only and sulphide-dominated antipodes.

Two types of ore veins can be distinguished. The first type is characterized by a copper-rich mineralization consisting of chalcopyrite, bornite, galena and sphalerite (±tennantite), similar to the structurally controlled Cu-As-(Ag) veins from Spessart district in Germany (Schmidt and Friedrich 1998). The second, more unique type, exemplified by a Ni-Co-As±Ba assemblage, is thought to be an analogue of the "Rücken" type mineralization from Mansfeld and Spessart districts (Schmidt and Friedrich 1988).

## 3 Samples and methods

Analyzed samples were collected underground at three locations (Figure 1) and represent three distinct types. The first type consists of a massive chalcopyrite vein in slightly brecciated Zechstein carbonates from the Polkowice-Sieroszowice mine (Figure 2A). The second type comprises 1-3 cm thick calcite veins cutting sandstone with local chalcopyrite disseminations (Figure 2B). Although in the majority of these veins sulphides are absent, one of them contained translucent sphalerite crystals (Figure 2C). The third type represents a unique mineralization found in GG1 shaft. Massive primary covellite and galena (Figure 2D) were found at the contact between Zechstein carbonates (Ca1) and Lower Anhydrite (A1d), approximately 4 m above the copper deposit (Figure 1). Carbonates underlying the mineralization contain a set of steep fractures which might extend down all the way to the base of the unit and form a link to the stratabound Cu-Ag mineralization below.

Optical light microscopy was used for petrographic observations and to select areas for further analyses. In order to assess the content of major elements, microprobe analyses (EPMA) were carried out using a JEOL JXA-8230 SuperProbe at the Laboratory of Critical Elements AGH-KGHM in Kraków. The electron microprobe was operated in the wavelength-dispersive mode at an accelerating voltage of 20kV and a probe current of 20 nA for sulphide minerals and 10 nA for argyrodite. Counting times of 20 s on peak, and of 10 s on both (-) and (+) backgrounds were used for all elements except Ge where 40 s on peak and 20 s on both (-) and (+) backgrounds were used.

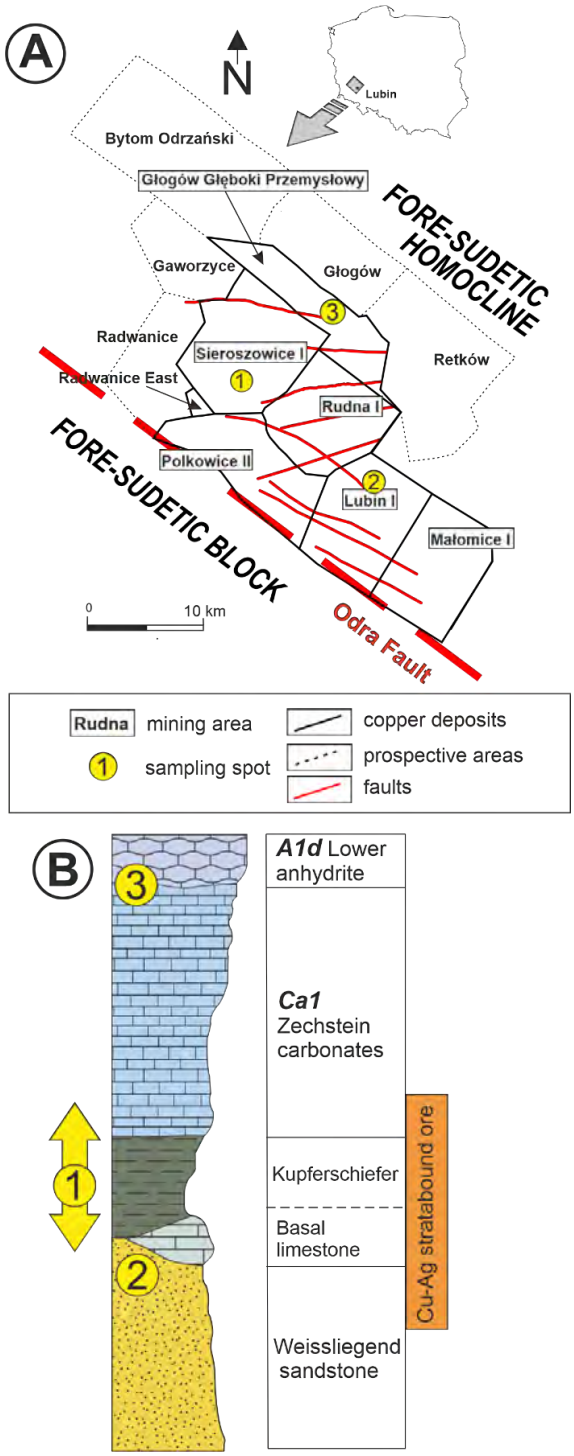


**Figure 1.** Position of sampling spots on a map of the Lubin-Sieroszowice copper district (A) and stratigraphic column (B) (not in scale).

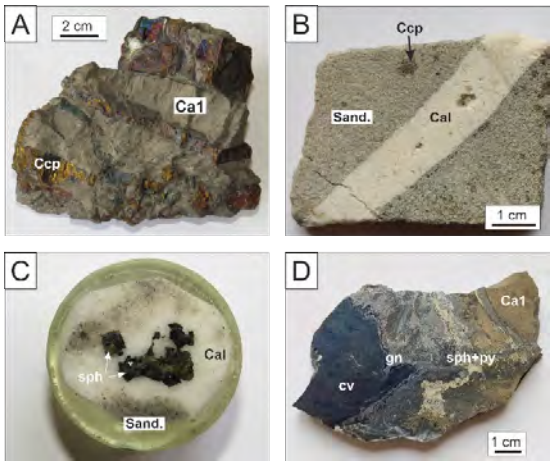


**Figure 2.** Examples of investigated samples: (A) massive chalcopyrite vein in Zechstein carbonates from the Polkowice-Sieroszowice mine; (B) calcite vein cutting sandstone from the Lubin mine; (C) translucent sphalerite in calcite vein from the Lubin mine; (D) massive covellite – galena – sphalerite – pyrite assemblage from the GG1 shaft. Cal – calcite, ccp – chalcopyrite, cv - covellite, gn – galena, py -pyrite, sph – sphalerite.

The following standards and X-ray peaks were used for sulphides: $FeS_2$ (Fe-Kα, S-Kα), chalcopyrite (Cu-Kα), ZnS (Zn-Kα), Ag (Ag-Lα), stibnite (Sb-Lα), CdS (Cd-Lα), GaAs (As-Lα), $Sb_2Se_3$ (Se-Lα), GeS (Ge-Lα) and HgS (Hg-Mα). Data were corrected by the ZAF procedure using dedicated JEOL software.

Micro-beam X-ray fluorescence (micro-XRF) distribution maps were obtained with the M4 TORNADO XRF spectrometer at the Faculty of Physics and Applied Computer Science, AGH University of Science and Technology in Kraków. The spectrometer low-power X-ray tube with a Rh anode was operated at 50 kV and 300-400 μA. The primary X-ray beam was focused to a spot with a diameter of about 20 μm with the use of polycapillary optics. The acquisition of high resolution XRF maps was conducted under 2 mbar vacuum conditions with a step size of 20 μm and 86/90 ms per pixel spectrum collection time for the oscillatory zoning/dendrite-like sample shown in Figure 3. Two silicon drift detectors were used for XRF spectra collection. Micro-XRF mapping produces 2-dimensional maps of element distributions using the energy dispersive XRF spectra collected individually at each pixel of the analysed region. For a given element displayed on a map, pixel intensity is proportional to the mass fraction of the element associated with that pixel, obtained from a "standardless" quantitative analysis of the pixel XRF spectrum. 'Standardless' analysis of the X-ray spectra was carried out using the M4 Tornado's software.

## 4 Results

### 4.1 Germanium-rich chalcopyrite

Germanium-rich chalcopyrite from the Kupferschiefer deposit was investigated with LA-ICP-MS by Foltyn et al. (2022) and concentrations of Ge up to 4806 μg/g were obtained. However, it is important to point out that results were highly variable between spots even on a scale of a single sample, suggesting it is necessary to map the distribution of Ge. Elemental maps obtained with micro-XRF show heterogenous spatial distribution of Ge and allow to distinguish two major types: oscillatory zoning (Figure 3A) and a "dendrite-like" organization (Figure 3B).

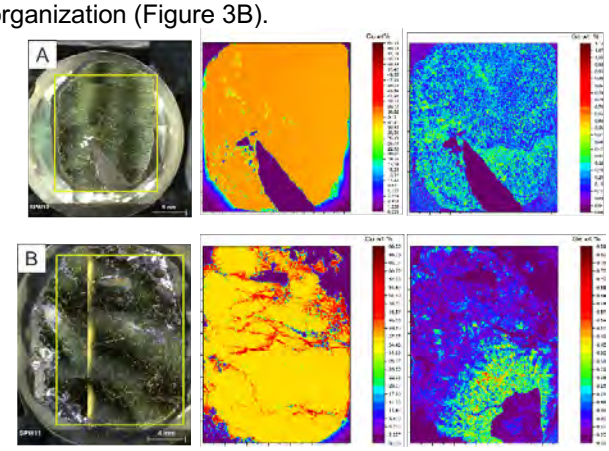


**Figure 3.** Micro-XRF maps of copper (centre) and germanium (right) in massive chalcopyrite from the Polkowice-Sieroszowice mine.

### 4.2 Translucent sphalerite from Lubin

Sphalerite in the stratabound Kupferschiefer ore has a median Ge content of 1.3 μg/g and no values above 10 μg/g are recorded (LA-ICP-MS data); ZnS veinlets cross-cutting chalcopyrite in epigenetic veins show comparable values (Foltyn et al. 2022). Analysed translucent sphalerite from Lubin (Figures 2C and 4A, C and D), although in general similar in composition to the aforementioned sphalerites (very low Fe, Cd in the range of 0.37-0.9 wt.%), is exceptionally enriched in Ge. EMPA measurements reveal values from <0.03 up to 0.18 wt.% Ge (Table 1; mean of 26 spot: 0.1 wt.% Ge).

### 4.3 Argyrodite from Głogów Głęboki

Stratabound Cu-Ag ore in GG1 shaft, dominated by chalcocite (with native silver inclusions) and hosted by sandstone, shale and carbonate units, lies directly below the covellite mineralization at the Ca1-A1d contact. This upper mineralization consists of massive covellite with galena, acanthite, jalpaite, argyrodite (Figure 4B) with disseminated and locally replaced sphalerite and pyrite. Such mineral association is a testimony of higher sulfidation states of hydrothermal fluids, linked to higher sulphur fugacity conditions and/or lower temperatures. This is a reason for a switch from chalcocite-native silver to covellite-jalpaite-acanthite assemblage.

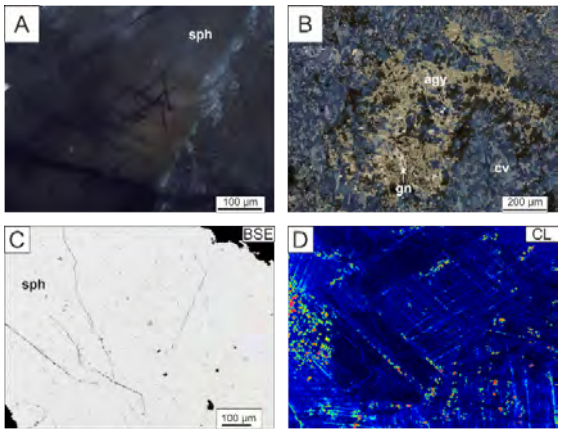


**Figure 4.** (A) Lattice oriented inclusions in translucent sphalerite, reflected light, crossed nicols. (B) Argyrodite intergrowths with galena in massive covellite, reflected light. (C) and (D): respectively BSE and cathodoluminescence picture of translucent sphalerite. Agy – argyrodite, cv – covellite, gn – galena, sph – sphalerite.

Argyrodite contains numerous inclusions/pores and has between 3.9 and 6.47 wt. % Ge with a noticeable admixture of Cu (Table 1). At least two compositional types of sphalerite have been found in this association: one has a typical composition of Kupferschiefer sphalerite (low Fe and 0.5-1% enrichment in Cd) while the second is characterized by a strong enrichment in Cd, Hg and Ge (Table 1).

**Table 1.** Representative WDS analyses of sphalerite and argyrodite.

| | sphalerite | | | | argyrodite | | |
|---|---|---|---|---|---|---|---|
| | *Lubin - s1* | *Lubin -s2* | *GG1-s1* | *GG1-s2* | *GG1-1* | *GG1-2* | *GG1-3* |
| Fe | <0.02 | <0.02 | <0.02 | <0.02 | <0.06 | <0.06 | <0.06 |
| Zn | 67.20 | 67.02 | 62.97 | 62.41 | <0.1 | <0.1 | <0.1 |
| Cu | <0.02 | <0.02 | 0.04 | <0.02 | 4.54 | 2.57 | 3.21 |
| S | 32.89 | 32.90 | 33.12 | 32.56 | 16.79 | 13.80 | 14.17 |
| Ag | <0.02 | <0.02 | - | - | 72.56 | 79.56 | 77.38 |
| Cd | 0.66 | 0.78 | 1.43 | 2.21 | - | - | - |
| Hg | <0.02 | <0.02 | 3.02 | 2.46 | - | - | - |
| Ge | 0.18 | <0.03 | 0.08 | 0.04 | 6.03 | 4.17 | 5.33 |
| Total | 100.93 | 100.69 | 100.66 | 99.67 | 99.92 | 100.11 | 100.08 |

## 5 Conclusions

Presented results are one of the first examples of oscillatory (high and low Ge) zoning in chalcopyrite. Oscillatory zoning is usually associated with minerals displaying high compositional variation such as pyrite-arsenopyrite, tennantite-tetrahedrite or garnets, but it might be more common and occurs in minerals, such as chalcopyrite, which have not been associated with such phenomenon before.

Sphalerite in the Cu-Ag Kupferschiefer in general does not contain significant Ge but in some specific cases, it can be highly enriched in this element (up to. 0.18 wt. %).

All reported instances of germanium-enriched mineralization from the Lubin-Sieroszowice district have a common feature: they are all related to local fractures, faults, shear zones or tectonic zones. This suggest there might be a link between Ge enrichment and overpressured ore-bearing hydrothermal fluids.

## Acknowledgements

This work was supported by statutory funds of the Faculty of Geology, Geophysics and Environmental Protection, AGH University of Science and Technology, Kraków, Poland (No. 16.16.140.315). We would like to thank KGHM PM S.A. for permission to present the results and geologists from the Lubin and Polkowice-Sieroszowice mines for their help and effort with field work and sample collection.

## References

Banaś M, Głuszek A, Jarosz J, Salamon W (1998) Polymetallic veins in the Permian Fore-Sudetic monocline copper deposits. Pr Spec PTMin 10:43-49 (in Polish).

Banaś M, Kijewski P, Salamon W, Pieczonka J, Piestrzyński A (2007) Accessory metals in copper ore. In: Piestrzyński A. (ed) Monograph KGHM PM SA., Lubin, pp 214-228 (in Polish).

Bernstein LR (1985) Germanium geochemistry and mineralogy. Geochim. Cosmochim. Acta. 49:2409-2422. https://doi.org/10.1016/0016-7037(85)90241-8

Foltyn K, Erlandsson VB, Zygo W, Melcher F, Pieczonka J (2022) New perspective on trace element (Re, Ge, Ag) hosts in the Cu-Ag Kupferschiefer deposit, Poland: Insight from a LA-ICP-MS trace element study. Ore Geol. Rev. 143, 104768. https://doi.org/10.1016/j.oregeorev.2022.104768

Glennie KW, Buller AT, (1983) The Permian Weissliegend of NW Europe: the partial deformation of aeolian dune sands caused by the Zechstein transgression. Sediment. Geol. 35:43-81. https://doi.org/10.1016/0037-0738(83)90069-6

Harańczyk C (1975): Morozewiczyt and polkowicyt - typochemical minerals of the Fore-Sudetic Monocline. Rudy i Met. Nieżelazne. 6:288–293 (in Polish).

Höll R, Kling M, Schroll E (2007) Metallogenesis of germanium - A review. Ore Geol. Rev. 30:145-180. https://doi.org/10.1016/j.oregeorev.2005.07.034

Hitzman M, Kirkham R, Broughton D, Thorson J, Selley D (2005) The sediment-hosted stratiform copper ore system. Econ Geol 100th Anniv vol, 609-642.

Karnkowski PW (1999) Origin and evolution of the Polish Rotliegend Basin. Pol. Geol. Inst. Spec. Pap. 3:1-93.

McCann T, Pascal C, Timmerman MJ et al (2006) Post-Variscan (end Carboniferous-Early Permian) basin evolution in western and central Europe. In: Gee DG, Stephenson RA (eds) European Lithosphere Dynamics, Geological Society, London, pp. 355-388. https://doi.org/10.1144/GSL.MEM.2006.032.01.22

Melcher F, Buchholz P (2014) Germanium. Critical Metals Handbook, 177-203

Schmidt FP, Friedrich G (1988) Geologic setting and genesis of Kupferschiefer mineralization in West Germany. In: Friedrich GH, Herzig PM (eds) Base metal sulfide deposits in sedimentary and volcanic environments, Springer, Berlin, Heidelberg, pp. 25-59.

Tomaszewski JB (1978) The geological structure of the Lubin-Sieroszowice region (Lower Silesia). Geol. Sudetica 13: 85-128 (in Polish).

Van Nhan N (1970) New ore minerals of the Lower Silesian Zechstein copper-bearing rocks. Prace Miner. 24:49–60 (in Polish).

# Mineralogy and geochemistry of the Koeris Formation – Evidence of post-depositional base metal mobility within the Aggeneys-Gamsberg ore district, South Africa

**Stefan Höhn[1], Hartwig E. Frimmel[1], Marlene Schneider[1], Nikola Brodtmann[1], Westley Price[2]**
*[1]Bavarian Georesources Centre (BGC), Department of Geodynamics and Geomaterials Research, Institute of Geography and Geology, University of Würzburg, Am Hubland, D-97074 Würzburg, Germany*
*[2]Vedanta Zinc International, Vedanta Resources plc, 1 Penge Road, Aggeneys 8893, South Africa*

**Abstract.** Geochemical investigations on amphibolite of the Koeris Formation in the hanging wall of the world-class Gamsberg Zn deposit show a strong enrichment in Zn and Pb, intuitively interpreted as product of syn-metamorphic interaction between the spatially close sulfidic ore horizon and the amphibolite. Yet, new electron microprobe data reveal that the bulk of the high Zn- and Pb-contents in this amphibolite is hosted by silicates, not sulfides. Rock-forming amphibole has mean Zn and Pb contents of 579 and 377 ppm, respectively, whereas feldspar contains 305 ppm Zn and 220 ppm Pb. Thermodynamic difficulties in forming Zn-rich amphibole and feldspar indicate that at the time when the prograde Klondikean metamorphic event (1040 to 1020 Ma) reached c. 500°C, the Koeris Formation was rich in Zn and Pb but S was either absent or immobilized. This is in agreement with previous studies on the underlying Hotson Formation at Gamsberg, for which a pre-Klondikean weathering-induced mobilization/loss of S without a significant loss in base metals had been suggested.

## 1 Introduction

The Aggeneys-Gamsberg ore district (South Africa) is located about 700 km north of Cape Town (Fig. 1). Deposits in the district, including Gamsberg, have been classified as Broken Hill-type, traditionally interpreted as former sedimentary exhalative (SEDEX) deposits that had become metamorphosed at amphibolite- to granulite-facies conditions (e.g. Sangster 2020). Unusual mineral assemblages, sulfur isotopic characteristics, a pronounced metal zonation across the ore district, and the appearance of various geochemical anomalies in the vicinity of the ore district (e.g. Willner et al. 1990) all seem in contradiction to this genetic model, though. Recent Cu isotope (Höhn et al. 2020) as well as mineral-textural and –chemical studies (Höhn et al. 2021) point, at pre-Klondikean weathering/oxidation of the original sulfidic ore bodies and subsequent (re-) sulfidation during Klondikean (1040 to 1020 Ma) metamorphism.

The meta-volcanosedimentary succession of the Koeris Formation, which unconformably overlies the ore-hosting stratigraphy at Gamsberg, is crucial for the understanding of post-depositional element mobility in and around the deposit. Whereas the meta-volcanosedimentary successions of the Bushmanland Group were deposited before the Okiepian orogeny (1210 to 1180 Ma), structural observations and U-Pb zircon age data indicate deposition of the Koeris Formation between the Okiepian and the Klondikean orogenic events (Cornell et al. 2009; Höhn et al. 2022). Consequently, the Koeris Formation is the only stratigraphic unit in this region that was deposited between these two orogenic events. Geochemical and mineralogical information from the Koeris Formation can thus provide critical information on the extent of weathering and oxidation of an old land surface during a hiatus spanning some 140 Ma and its potential influence on the ore.

## 2 Geological setting

The Koeris Formation is located in the Namaqua Province, which forms the western part of the Mesoproterozoic Namaqua-Natal Metamorphic Belt (Fig. 1). This province comprises several subprovinces that bear characteristics similar to those of accretionary terranes at convergent margins (Colliston et al. 2017). The southern part of the Namaqua Province belongs to the Bushmanland Terrane, which is made up of the Bushmanland Group, the Little Namaqualand Suite, the Aggeneys Suite and the Koeris Formation (Cornell et al. 2009).

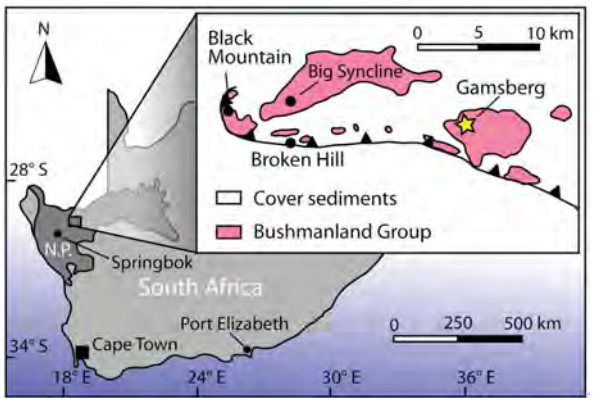


**Figure 1.** Location of the Gamsberg deposit (yellow start) within the Aggeneys-Gamsberg ore district hosted by metamorphic rocks of the Bushmanland Group; N.P.=Namaqua Province (after Stalder and Rozendaal 2004; McClung et al. 2007). Other major deposits indicated by black points

The lower boundary of the meta-volcano-sedimentary Koeris Formation is a widely recognized unconformity to the underlying Hotson Formation of the Bushmanland Group (Fig. 2)

(Rozendaal 1986; Lipson 1990). In most places, the base of the Koeris Formation is identified by the appearance of amphibolite or quartz-feldspar-biotite-muscovite rock, which, in places, is conglomeratic (Praekelt et al. 2006). In the upper parts, the abundance of metavolcanic rocks, meta-arkose and meta-conglomerate make the Koeris Formation distinguishable from the older meta-volcanosedimentary Hotson Formation. At Gamsberg, the uppermost part of the latter consists of various Fe-Mn-rich rocks (C unit), sulfide-rich garnet-apatite ore (B unit) and various garnet-, calcite- and amphibole-rich quarzites (A unit) (Stalder 2004). The apparent top of the Koeris Formation is generally capped by thrust faults and tectonically overlain by older formations of the Bushmanland Group (Praekelt et al. 2006). At various places the Koeris Formation was affected by a late metamorphic, epidote- and chlorite-forming retrograde alteration that mobilized various major and trace elements (Colliston and Schoch 2003; Höhn et al. 2022).

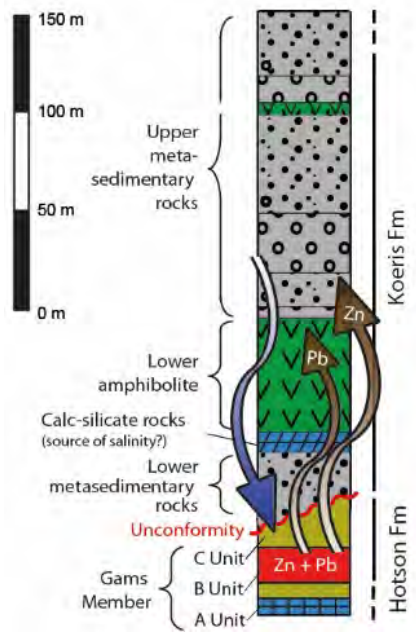


**Figure 2.** Lithological column through the Koeris Formation at Gamsberg (after Praekelt et al. 2006; Rozendaal et al. 2017). Blue and brown arrows mark suggested base metal-poor and base metal-rich fluid flow, respectively, during the Klondikean metamorphism

## 2 Results

A total of 31 whole rock chemical analyses were conducted on 19 drill core segments from various amphibolite layers. Six of those analyses were performed on samples with various degrees of alteration.

### 2.1 Incompatible elements

Compared to N-MORB, all samples of amphibolite of the Koeris Formation at Gamsberg share a common Nb-Ta-trough. Marked positive spikes for Rb and Ba were obtained only for unalterated amphibolite, whereas samples affected by late-metamorphic alteration are barely enriched in these elements (Figs. 3a+b).

### 2.2 Base metals

Amphibolite from the Koeris Formation at Gamsberg shows a strong enrichment in Zn and Pb but not Cu, which is similar to the base metal ratios of the sulfidic Gamsberg deposit in the local footwall of the Koeris Formation. Nevertheless, on the investigated scale of several tens of meters, there is no gradient in base metal contents from the upper Hotson Formation above the Gamsberg deposit into the younger strata of the Koeris Formation. In the latter, the Pb contents are up to 1422 times higher than in N-MORB. However, the amphibolite of the Koeris Formation is basically devoid of sulfides, based on reflected light microscopy and electron microprobe analyses on 154 opaque mineral grains from the altered and unaltered amphibolite. Instead, the amphibolite is rich in oxides, mainly ilmenite, and little titanite. The anomalously high base metal contents are effectively hosted by silicates and oxides (Figs. 4, 5).

Electron microprobe analyses on 38 amphibole grains revealed mean Zn contents of 579 ppm ($\sigma$ = 333). Their Pb contents are slightly lower with a mean value of 377 ppm ($\sigma$ = 264). Feldspar is generally less enriched in base metals with mean Zn and Pb contents of 305 ppm ($\sigma$ = 265) and 220 ppm ($\sigma$ = 183), respectively. Ilmenite is strongly enriched in Pb with a mean of 2010 ppm ($\sigma$ = 2120) compared to Zn with an average of 370 ppm ($\sigma$ = 280).

## 3 Interpretation and discussion

Zn-rich amphiboles are generally rare because at c. 500°C, when most amphiboles start to crystallize, Zn partitions into the fluid rather than amphibole (Ilton and Eugster 1990), and only minor quantities of Zn can be incorporated into the crystal lattice of amphibole. In the case of Gamsberg, the existence of Zn- and Pb-rich amphibole and also feldspar requires, therefore, a strong enrichment of the metamorphic fluid in these elements on the prograde path of the Klondikean metamorphism before reaching c. 500°C.

Another pre-requirement for the crystallization of Zn- and Pb-rich silicates is the absence or immobilization of sulfur. In this regard, Ba can very effectively bind S to form barite. Both amphibolite and metasedimentary rocks of the Koeris Formation are enriched in Ba but barite is generally rare. Furthermore, the fact that the late metamorphic alteration had a major influence on the Ba content of the amphibolite (Fig. 3a) shows that the bulk of Ba in the Koeris Formation is not hosted by highly alteration-resistant barite. However, barite exists

within the Hotson Formation in the footwall of the Koeris Formation predominantly in the lateral extension of the ore horizon but also as disseminated nodules. These spatial relations make it unlikely that barite played a major role in the metamorphic immobilization of S in the Koeris Formation.

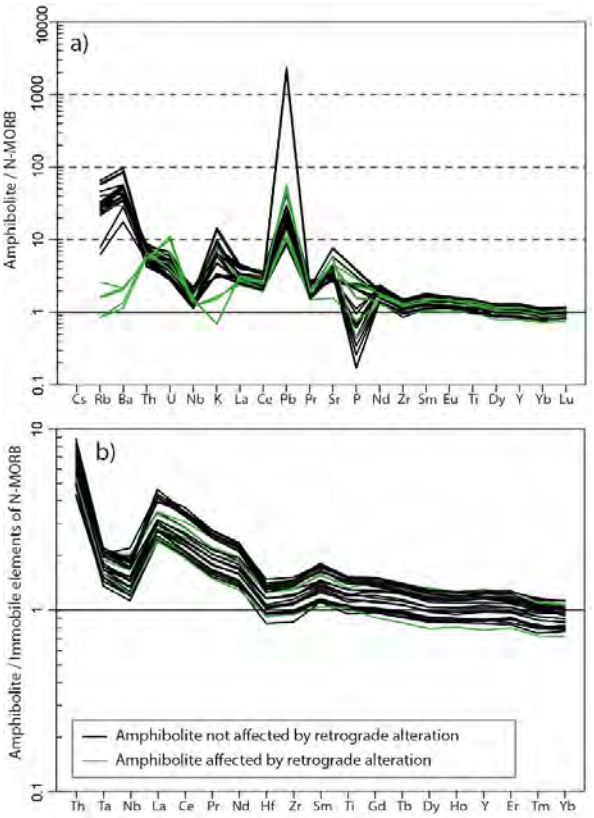


**Figure 3.** Chemical characteristics of the amphibolite of the Koeris Formation at Gamsberg. a) N-MORB-normalized trace-element diagram; b) N-MORB-normalized immobile trace-element diagram; normalization values from Sun and McDonough (1989)

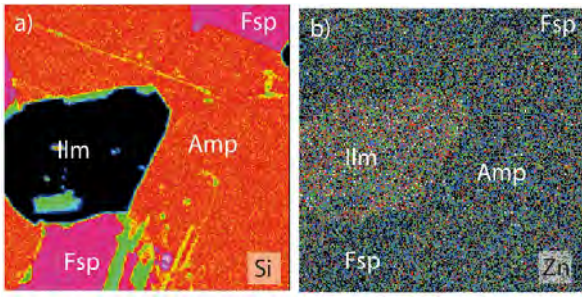


**Figure 4.** Relative element abundance map of a) Si and b) Zn. Fsp = Feldspar, Ilm = Ilmenite, Amp = amphibole

Consequently, the incorporation of Zn and Pb into amphibolite and feldspar of the Koeris Formation is best explained by the early-metamorphic presence of high contents of these elements and a general lack of S at that time. Because of the close spatial association of the Koeris Formation only meters above the ore horizon of the Gamsberg deposit and similar base metal ratios, it is highly likely that the base metal characteristics of the Koeris Formation are the product of an early metamorphic fluid-driven interaction with the ore horizon.

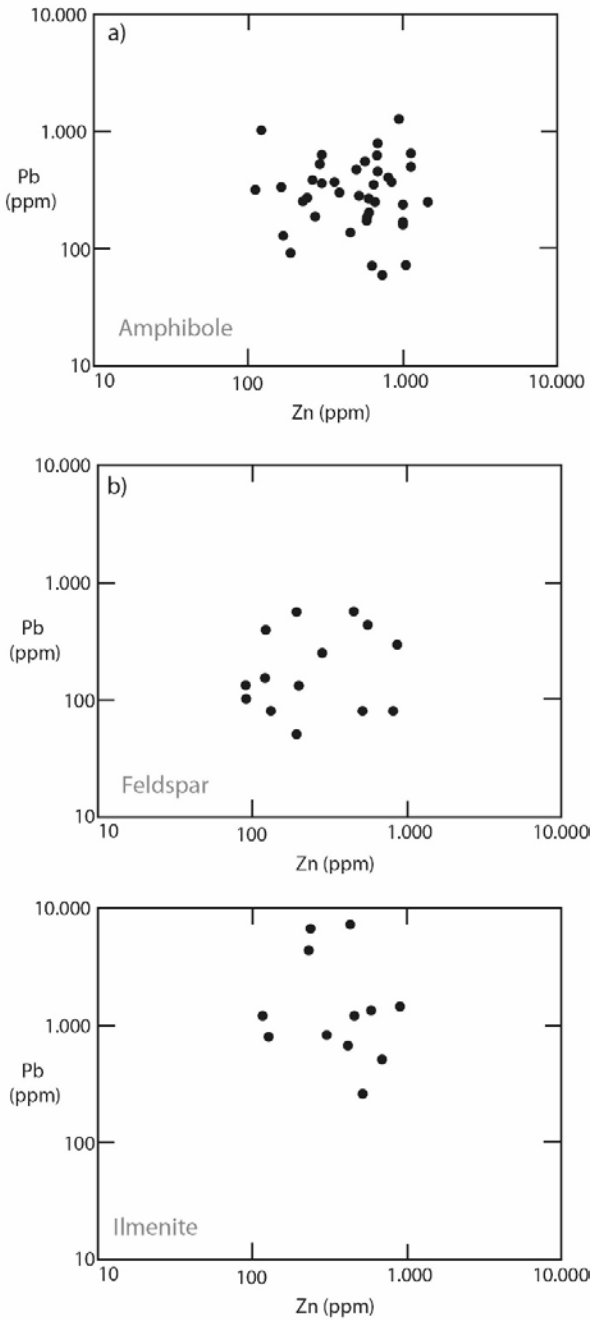


**Figure 5.** Pb/Zn-ratios of a) amphibole, b) feldspar and c) ilmenite of amphibolite from the Koeris Formation at Gamsberg, Aggeneys.

The Hotson Formation is an unlikely source of such fluids because it had already been largely dehydrated by a previous amphibolite-facies metamorphic overprint during the Okiepian orogeny. Common metamorphic fluids do not have a salinity high enough to transport large amounts of base

metals. In the case of the Koeris Formation, the inferred intramontane depositional setting (Höhn et al. 2022) might have provided a suitable setting for deposition also of evaporites. Indirect evidence of this might be found in calc-silicate rocks in the lower parts of the formation (Fig. 2). Thus, saline fluids might have been liberated from the Koeris Formation and infiltrated the medium- to high-grade metamorphic rocks of the Hotson Formation, including the ore horizon (Höhn et al. 2023).

In conclusion, our new data and observations from the Koeris Formation suggest that at Gamsberg, the Hotson Formation was rich in Zn and Pb but lacked S. This supports the notion of a pre-Klondikean loss/mobilization of S form the uppermost part of the Hotson Formation as a result of a weathering-induced oxidation event during the hiatus between the Okiepian and Kondikean orogenic events (Höhn et al. 2020).

## Acknowledgments

We thank Vedanta Resources for granting us access to their facilities and drill core and P. Späthe for the preparation of high-quality (polished) thin sections. The analytical work was funded by the Department of Geodynamics and Geomaterials Research, University of Würzburg.

## References

Colliston WP and Schoch AE (2003) A mid-Proterozoic Volcano-Sedimentary sequence in the Aggeneys Hills Duplex, Namaqua Metamorphic Complex. S Afr J Geol 103:343-360

Colliston WP, Schoch AE, Cole J (2017) The Grenvillian Namaqua fold belt adjacent to the western Kaapvaal Craton: 2. Archaean craton and supercontinent connections. Precambrian Res 300:289-314

Cornell DH, Pettersson Å, Whitehouse MJ, Scherstén A (2009) A new chronostratigraphic paradigm for the age and tectonic history of the Mesoproterozoic Bushmanland ore district, South Africa. Econ Geol 104:385-404

Höhn S, Frimmel HE, Debaille V, Westley P (2020) Pre-Klondikean oxidation prepared the ground for Broken Hill-type mineralization in South Africa. Terra Nova 33:168-173

Höhn S, Frimmel HE, Price W (2021) Syn-metamorphic sulfidation of the Gamsberg zinc deposit, South Africa. Mineral Petrol 115:709-728

Höhn S, Frimmel HE, Price W (2023) Response to: Discussion on “Syn-metamorphic sulfidation of the Gamsberg zinc deposit, South Africa” by Stefan Höhn, Hartwig E. Frimmel, and Westley Price. Mineral Petrol https://doi.org/10.1007/s00710-023-00822-5

Höhn S, Frimmel HE, Will T, Brodtmann N, Price W (2022) The depositional environment of the Koeris Formation in the Aggeneys-Gamsberg ore district, South Africa. S Afr J Geol 125:323-336

Ilton ES, Eugster HP (1990) Partitioning of base metals between silicates, oxides, and a hydrothermal fluid. Part I. Evaluation of data derived from natural and experimental assemblages. In Fluid-Mineral Interactions: A Tribute to H. P. Eugster (eds. RJ Spencer and I-Ming Chou), Spec Publ 2:157-169

Lipson RD (1990) Lithogeochemistry and origin of metasediments hosting the Broken Hill deposit, Aggeneys, South Africa, and implications for ore genesis. Unpublished PhD thesis, University of Cape Town, South Africa. 250pp

McClung CR, Gutzmer J, Beukes NJ, Mezger K, Strauss H, Gertloff E (2007) Geochemistry of bedded barite of the Mesoproterozoic Aggeneys-Gamsberg Broken Hill-Type district, South Africa. Miner Depos 42:537-549

Praekelt HE, Colliston WP, Schoch AE (2006) Lithostratigraphy of the Koeris Formation (Bushmanland Group). South African Committee for Stratigraphy, Council for Geoscience, Lithostratigraphic Series 41. 7pp

Rozendaal A (1986) The Gamsberg zinc deposit, Namaqua District. In: C.R. Anhausser and S. Maske (Editors), Mineral deposits of South Africa. Geological Society of South Africa, Johannesburg, pp 1477-1488

Rozendaal A, Rudnick T-K, Heyn R (2017) Mesoproterozoic base metal sulphide deposits in the Namaqua sector of the Namaqua-Natal Metamorphic Province, South Africa: a review. S Afr J Geol 120:153-186

Sangster DF (2020) Evidence that Broken Hill-type Pb-Zn deposits are metamorphosed SEDEX deposits. Miner Depos 55:1263-1270

Stalder M (2004) Petrology and mineral chemistry of sulphide ores and associated metalliferous rocks of the Gamsberg Zn-Pb deposit, South Africa: Implications for ore genesis and mineral exploration. Unpubl. PhD thesis, University of Stellenbosch

Stalder M, Rozendaal A (2004) Apatite nodules as an indicator of depositional environment and ore genesis for the Mesoproterozoic Broken Hill-type Gamsberg Zn-Pb deposit, Namaqua Province, South Africa. Miner Depos 39:189-203

Sun S-S, McDonough WF (1989) Chemical and isotopic systematics of oceanic basalts: implications for mantle composition and processes. Geological Society London Special Publications 42:313-345

Willner A, Schreyer W, Moore JM (1990) Peraluminous metamorphic rocks from the Namaqualand metamorphic complex (South Africa): Geochemical evidence for an exhalation-related, sedimentary origin in a Mid-Proterozoic rift system. Chem Geol 81:221-240

# LA-ICP-MS trace element geochemistry of chalcopyrite from Tenke Fungurume, Central African Copperbelt

**Qiuping Liu[1], Pascal Mambwe [1,2], Philippe Muchez [1,2]**
*[1.]KU Leuven, Department of Earth and environmental Sciences, Celestijnenlaan 200E, B-3001 Leuven, Belgium*
*[2.] Department of Geology, University of Lubumbashi, B.P.1825, Lubumbashi, Congo*

**Abstract.** Tenke Fungurume is one of the world's premier sediment-hosted copper and cobalt mining districts located in the northwestern part of the Central African Copperbelt. The ore-forming processes for this giant district are subdivided into disseminated, nodule type, a burial (stylolite-related), a pre-folding, a syn-folding, and a post-folding vein I and vein II mineralization stages. This study presents new LA-ICP-MS trace element data on chalcopyrite that shows distinct trace element distributions between the different stages. The stylolite-related veins and nodule type chalcopyrite data are quite consistent, i.e. both are rich in redox sensitive elements (V, Mo, Sb). Both stages are regarded to be of diagenetic origin as proposed for the Kamoto and Luiswishi Cu-Co deposits in the Democratic Republic of Congo. Pre-folding and syn-folding chalcopyrite also share similarities in their trace element distribution, but the former is generally richer for most elements. This could indicate higher precipitation temperature for the pre-folding chalcopyrite, since this latter tends to host more trace elements. The post-folding veins I and II show distinct trace element distributions, which could correspond to different deformation stages. Vein II chalcopyrite is extremely rich in Ge, which could be linked to the post-orogenic fluid forming the Cu-Zn-Pb (Ge, Ag) Kipushi deposit.

## 1 Introduction

The Central African Copperbelt, which straddles the border between the Democratic Republic of Conge (DRC) and Zambia, is well-known for hosting the world's largest and highest grade sedimentary stratiform Cu-Co deposits (Cailteux et al. 2005). The Tenke Fungurume mining district (TFMD) contains large deposits at the northern part of the Congolese Copperbelt, consisting of over 70 separate mineralized blocks, with a total of up to 7.7 million metric tons contained copper reserves, ranking the 3rd largest copper mine in Africa and the 1st cobalt mine in the world (Fay and Barton 2012).

At least two main episodes of mineralization have been recognized by El Desouky et al. (2009) for the Congolese Copperbelt. The first episode of hydrothermal mineralization was responsible for the formation of fine-grained disseminated Cu-Co sulfides, and Cu-Co sulfides in nodules and lenses (type I nodules) (El Desouky et al. 2010; Muchez et al. 2015). The second main mineralization episode was responsible for coarse-grained Cu-Co ores minerals in nodules (type II nodules), veins and as breccia cements (El Desouky et al. 2010). These mineralizing episodes are also recognized at TFMD (Rosenfels and von der Heyden 2022).

Laser ablation inductively coupled plasma mass spectrometry (LA-ICP-MS) has been adopted as a useful tool to differentiate physico-chemical changes in mineralizing fluid and deepen our understanding of ore-forming processes by analyzing trace elements in sulfide minerals such as pyrite (Abraitis et al. 2004) and bornite (Cook et al. 2011). By applying LA-ICP-MS analysis on chalcopyrite, here we report the trace element composition of a set of multistage chalcopyrite from the TFMD. The aim of the study is to determine the physico-chemical fluid characteristics during the protracted period of mineralization, i.e. from diagenesis until late to post-orogenic.

## 2 Geological setting

TFMD is located at the northwestern part of the Katanga Copperbelt (

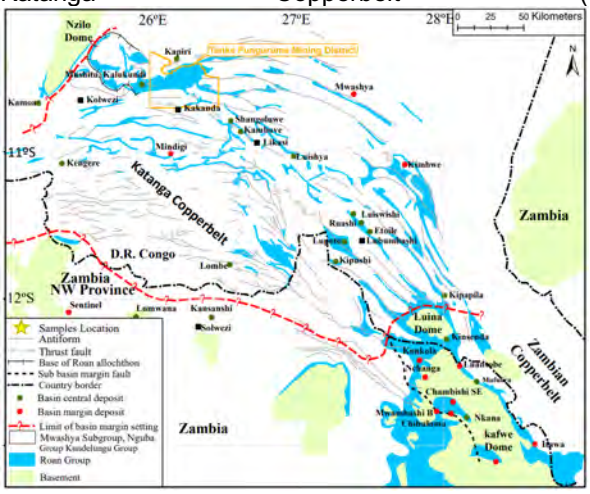


Figure 8). The ore deposits are hosted in the Neoproterozoic Katangan succession which was deposited in an intracratonic sedimentary basin. Sedimentation started well after 880Ma and lasted at least till 570Ma (Armstrong et al. 2005). The ~10km-thick Katanga Supergroup is commonly subdivided into four groups: Roan, Nguba, Kundelungu and Biano groups. The oldest Roan Group consists of clastic sedimentary rocks and carbonates, mainly dolomites and dolomitic shales (Cailteux et al. 2005), which were deposited in a continental rift evolving to

a proto-oceanic rift linked to the breakup of the Rodinia supercontinent (Tembo et al. 1999).

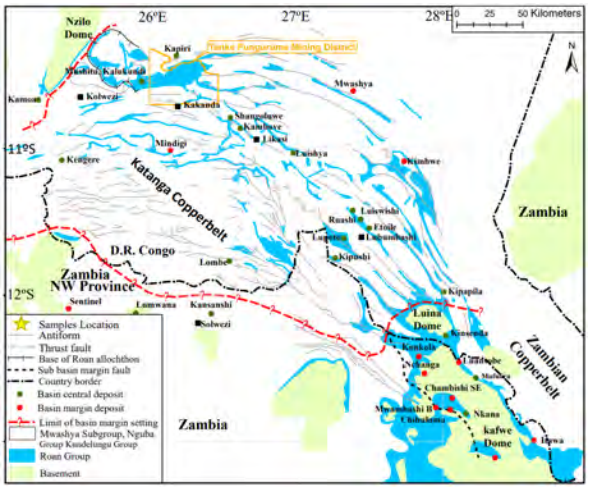


**Figure 8.** Location of TFMD (indicated by the concession boundary) in the KCB (modified after Hitzman et al. 2012 and from Mambwe et al. 2023).

In the DRC, the lowermost Roan is further subdivided into four subgroups, from bottom to the top into the Musonoi, Mines, Fungurume and Mwashya subgroups (Cailteux and De Putter, 2019). The Mines Subgroup is well-known for hosting major Cu-Co mineralization throughout the KCB. It is further subdivided into three formations: the Kamoto, Kinsevere and Kambove formations (Mambwe et al., 2022). The Kamoto Formation hosts the two main orebodies in the Congolese Copperbelt, i.e. the lower and upper orebody.

## 3 Mineralogy

Based on previous macroscopic and microscopic studies (Mambwe et al. 2023) and new incident and transmitted light microscopy of samples from several mineralized blocks in the TFMD, i.e. from Dipeta syncline, Diyenge, Fungurume IV, Kamakonde, Kamalondo, Kyaundji, Kwatebala, Mufufya and Shanika syncline allowed us to decipher the temporal sequence of mineralization stages in relation to the deformation and kinematic processes that affected the rocks. During burial, mineralization formed within nodules, along stylolites, and in jack-type veins (Figure 9a, b). Mineralization along stylolites is mainly irregular, with medium-sized chalcopyrite associated with dolomites (Figure 9a, d). Sulfide-bearing nodules are dominated by chalcopyrite, bornite, carrollite and chalcocite (Figure 9e). Pre-folding veins are characterized by fibrous dolomite growing sub-vertically ((Figure 9c).

Syn-folding veins are recognized by their typical occurrence as arc-shaped saddles in the core of folds. These veins consist of coarse-grained chalcopyrite and dolomite (Figure 9 g, j). At least two generations of post-folding veins are recognized: a very coarse-grained chalcopyrite and dolomite vein cross-cutting the folding (Figure 9 h), and a vein generation cross-cutting the bedding which consists of large chalcopyrite crystals with a smaller amount of carrollite, bornite and chalcocite in association with the gangue minerals quartz and dolomite (Figure 9i, l).

## 4 Methodology

LA-ICP-MS spot analyses were performed with a Teledyne Analyte Excite 193 nm ArF laser connected to an Agilent 8900 Triple Quad ICP-MS, at the Department of Earth and Environmental Sciences, KU Leuven, Belgium. Chalcopyrite was chosen to be ablated with a spot size of 50µm (occasionally 35 µm when the crystal size was too small) with laser fluency set to 4.9 J/cm$^2$, at a 10Hz repetition rate. A 30s pre-ablation background collection was done before the 60s of laser ablation and data acquisition, followed by 30s delay for cell wash-out. The following elements were measured: $^{34}$S, $^{51}$V, $^{52}$Cr, $^{55}$Mn, $^{57}$Fe, $^{59}$Co, $^{60}$Ni, $^{63}$Cu, $^{67}$Zn, $^{71}$Ga, $^{74}$Ge, $^{75}$As, $^{82}$Se, $^{95}$Mo, $^{107}$Ag, $^{111}$Cd, $^{115}$In, $^{118}$Sn, $^{121}$Sb, $^{125}$Te, $^{197}$Au, $^{201}$Hg, $^{205}$Tl, $^{208}$Pb and $^{209}$Bi. Cu was also determined by electron probe microanalysis (EPMA) and was used as internal standard. The USGS pressed powder polysulfide reference material MASS-1 (Wilson et al. 2002) was used as an external standard and NIST 610 and 612 were measured for quality control. Data reduction was performed by the software program Sills according to standard methods (Longerich 1996).

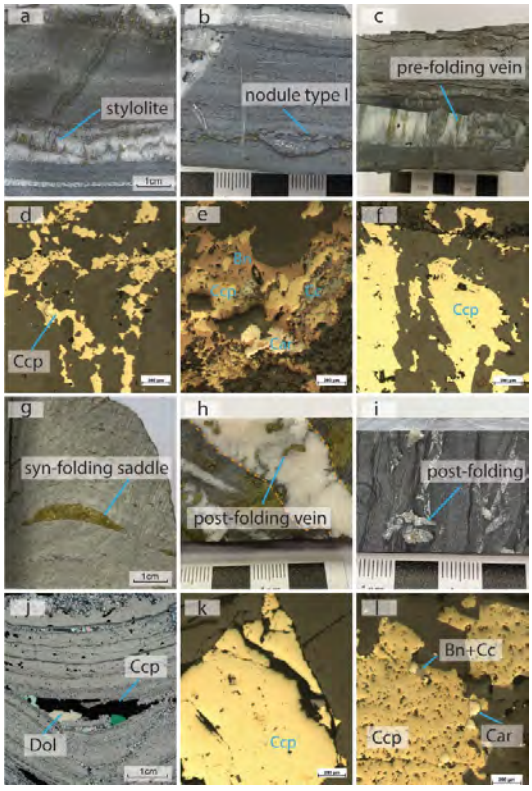


**Figure 9.** Photographs of rock samples (a-c, g-i) from the different mineralization stages recognized at Tenke Fungurume and microphotographs of thin (j) and polished (d,e,f,k,l) sections taken under reflective light: a) chalcopyrite along stylolite, b) chalcopyrite, bornite and carrollite in a nodule, c) chalcopyrite in a pre-folding vein,

d) chalcopyrite present along a stylolite, e) chalcopyrite, bornite, carrollite and chalcocite present in a nodule, f) large chalcopyrite crystals present in a pre-folding vein, g) syn-folding saddle type vein, h). post-folding vein I. i) post-folding vein II. j) syn-folding vein filled with dolomite and chalcopyrite, k) chalcopyrite crystal in post-folding vein I, l) chalcopyrite with small amount of carrollite, bornite and chalcocite from post-folding vein II. Ccp-chalcopyrite, Bn-bornite, Cc-chalcocite, Car-carrollite, Dol-dolomite.

## 5 Results and interpretation

A total of 90 spots were analyzed on chalcopyrite from Tenke Fungurume, the results are plotted in box and whisker diagrams (Figure 10). Representative LA-ICP-MS downhole profiles for nodules, pre-folding and post-folding vein II are shown in Figure 11. Some elements (Cr, Ni, Cd, Te, Au, Hg, Tl) are not shown in the figure since the majority of the results are below detection limit. Trace element concentration of chalcopyrite varies between the different stages. Similar concentration ranges were observed between the horizontal stylolite and the nodules, except for higher Ag, Pb and Bi concentration in the nodules. Pre-folding vein chalcopyrite is characterized by higher content for most elements, i.e. Sn and In are several magnitude higher (Figure 10). The most abundant trace elements are present in the post-folding vein type II chalcopyrite: In (up to 121ppm), Sn (up to 101ppm) and Ge (up to 772ppm). In contrast, the post-folding vein type I is depleted in Ga, Ge, As, Se and In in comparison to vein type II.

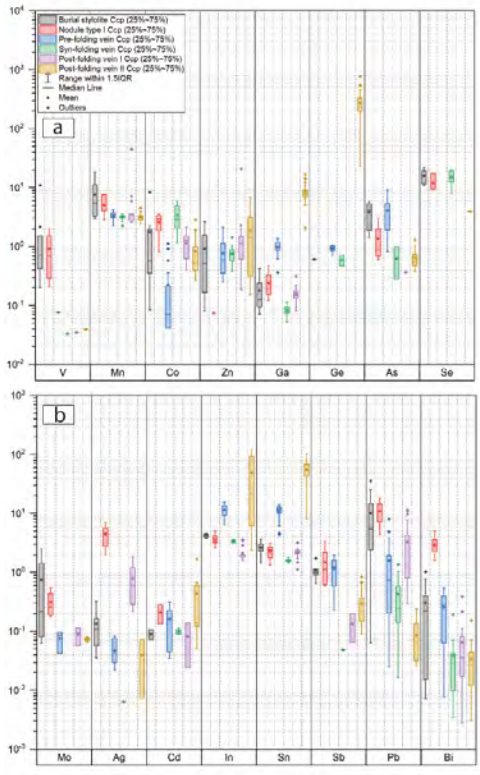


**Figure 10.** Box and whisker plots for the trace element composition of chalcopyrite from different mineralization stages identified in the TFMD.

The trace element concentration from chalcopyrite associated with horizontal stylolites and in the nodules are quite similar for all samples, except for higher Ag, Pb and Bi concentration in the nodules (Figure 10). This higher concentration is not due to micro-inclusions as illustrated by the relatively flat Pb and Bi ablation signature from the time resolved depth profile, compared to the increased signal bump caused by micro-inclusions (Figure 11a). Previous studies have shown the ore minerals in the nodules from Kamoto and Luiswishi (Muchez et al. 2008, 2015; El Desouky et al. 2010) precipitated in relation to a major change in the redox conditions in the host sediments. This is further collaborated by the trace element data. The V, Sb and Mo concentrations in the diagenetic chalcopyrite are several magnitudes higher than in sulfides that formed later in the paragenesis. V, Sb, Mo are redox sensitive elements that are concentrated in minerals at the redox interface (Foltyn et al. 2022).

The pre-folding vein chalcopyrite contains higher trace elements concentrations for most elements than syn-folding chalcopyrite (Figure 10). Since higher temperature chalcopyrite can accommodate more trace elements (George et al. 2016, 2018), we postulate that pre-folding ore-bearing fluids could have had a higher temperature than syn-folding fluid or that at least precipitation of the chalcopyrite occurred at a higher temperature. This interpretation is based on the following arguments: 1) previous research has demonstrated that $Sn^{2+}$ substitutes for $Fe^{2+}$ more at high temperature in chalcopyrite

(Maslennikov et al. 2009), 2) Mo values are expected to be higher at higher chalcopyrite precipitation temperatures (Metz and Trefry 2000; Halbach et al. 2002) and 3) $In^{3+}$ tends to substitute $Fe^{3+}$ at elevated temperature due to the fact that $In^{3+}$ is about 20% larger than $Fe^{3+}$ (Butler and Nesbitt 1999).

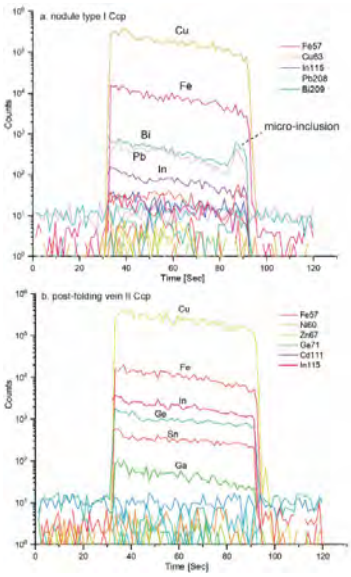


**Figure 11.** Representative time-resolved depth profiles for chalcopyrite.

Chalcopyrite in the post-folding veins shows similar V, Mn, Co, Zn, Mo, Sb and Bi concentrations, but chalcopyrite in vein II is higher in Ga, In and Sn and especially in Ge (Figure 10). High Ge content in chalcopyrite could be due to 1) the occurrence of Ge-bearing submicroscopic phases within chalcopyrite or 2) the presence of Ge as solid solution in chalcopyrite (Reiser et al. 2009). The smooth time-resolved depth profiles (Figure 11) favor the second hypothesis. This significantly higher Ge concentration for the late-stage ore fluid has been also reported in Iberian Pyrite Belt, Portugal (Reiser et al. 2009), Kupferschiefer deposit, Poland (Foltyn et al. 2022) and Kipushi, DRC (Heijlen et al. 2008). For Tenke Fungurume, this higher Ge concentration in chalcopyrite could be related to the post-orogenic mineralization event that led to the formation of the Cu-Zn-Pb (Ge, Ag) Kipushi deposit in the DRC (Heijlen et al. 2008; Kelvin et al. 2022). Distinct trace element distributions between the two post-folding veins indicate different ore-forming fluids, which is linked to different deformation stages.

## 6 Conclusion

Our LA-ICP-MS data show a systematic distribution of the trace element concentrations throughout the different mineralizing stages. The burial stylolite-related and nodule type chalcopyrite data are similar, i.e. both are rich in redox sensitive elements. Both stages are regarded to be of diagenetic origin. Pre-folding and syn-folding chalcopyrite also share similarities in their trace element distribution, but the former one is generally richer in most elements. This could indicate a higher temperature during chalcopyrite precipitation in the pre-folding than in the syn-folding veins. The post-folding veins I and II show distinct trace element distributions, indicating different deformation stages. Vein II chalcopyrite is very rich in Ge, which could be linked to the post-folding fluid forming the Cu-Zn-Pb (Ge, Ag) Kipushi deposit.

## Acknowledgement

We thank dr. Sam Spinks for reviewing this paper. We are grateful to the CSC scholarship (China) for supporting my PhD study at KU Leuven. Alicia Van Ham-Meert is sincerely thanked for helping with the LA-ICPMS analysis. Financial support from the research grant C14/21/056 of the KU Leuven Special Research Fund is acknowledged.

## References

Abraitis PK, Pattrick RAD, Vaughan DJ (2004) Variations in the compositional, textural and electrical properties of natural pyrite: A review. Int. J. Miner. Process 74:41–59.

Armstrong RA, Master S, Robb LJ (2005) Geochronology of the Nchanga Granite, and constraints on the maximum age of the Katanga Supergroup, Zambian Copperbelt. J. Afr. Earth Sci. 42:32–40.

Butler IB, Nesbitt RW (1999) Trace element distributions in the chalcopyrite wall of a black smoker chimney: insights from laser ablation inductively coupled plasma mass spectrometry (LA–ICP–MS). Earth. Planet. Sci. Lett. 167:335–345.

Cailteux, J.L.H., De Putter, T., 2019. The Neoproterozoic Katanga Supergroup (D.R. Congo): State-of-the-art and revisions of the lithostratigraphy, sedimentary basin and geodynamic evolution. 150: 522-531. J. Afr. Earth Sci.

Cailteux JLH, Kampunzu AB, Lerouge C, et al (2005) Genesis of sediment-hosted stratiform copper - Cobalt deposits, central African Copperbelt. J. Afr. Earth Sci. 42:134–158.

Cook NJ, Ciobanu CL, Danyushevsky L v., Gilbert S (2011) Minor and trace elements in bornite and associated Cu-(Fe)-sulfides: A LA-ICP-MS study Bornite mineral chemistry. Geochim. Cosmochim. Acta 75:6473–6496.

El Desouky El Desouky, H., Muchez, Ph., Cailteux J (2009). Two Cu–Co sulfide phases and contrasting fluid systems in the Katanga Copperbelt, Democratic Republic of Congo. Ore Geol. Rev 36: 315-332.

El Desouky HA, Muchez P, Boyce AJ, et al (2010) Genesis of sediment-hosted stratiform copper-cobalt mineralization at Luiswishi and Kamoto, Katanga Copperbelt (Democratic Republic of Congo). Miner. Depos. 45:735–763.

Fay I, Barton MD (2012) Alteration and ore distribution in the Proterozoic Mines Series, Tenke-Fungurume Cu-Co district, Democratic Republic of Congo. Miner. Depos 47:501–519.

Foltyn K, Bertrandsson Erlandsson V, Zygo W, et al (2022) New perspective on trace element (Re, Ge, Ag) hosts in the Cu-Ag Kupferschiefer deposit, Poland: Insight from a LA-ICP-MS trace element study. Ore Geol Rev 143, 104768.

Genna D, Gaboury D (2015) Deciphering the Hydrothermal Evolution of a VMS System by LA-ICP-MS Using Trace Elements in Pyrite: An Example from the Bracemac-McLeod Deposits, Abitibi, Canada, and Implications for

Exploration. Economic Geology 110.8 (2015): 2087-. O 2108.
George LL, Cook NJ, Ciobanu CL (2016) Partitioning of trace elements in co-crystallized sphalerite-galena-chalcopyrite hydrothermal ores. Ore Geol Rev 77:97–116.
George LL, Cook NJ, Crowe BBP, Ciobanu CL (2018) Trace elements in hydrothermal chalcopyrite. Mineral Mag. 82:59–88.
Halbach M, Halbach P, Lüders V (2002) Sulfide-impregnated and pure silica precipitates of hydrothermal origin from the Central Indian Ocean. Chem. Geol. 182:357–375.
Heijlen W, Banks DA, Muchez P, et al. (2008) The Nature of Mineralizing Fluids of the Kipushi Zn-Cu Deposit, Katanga, Democratic Repubic of Congo: Quantitative Fluid Inclusion Analysis using Laser Ablation ICP-MS and Bulk Crush-Leach Methods. Economic Geol. 103:1459-1482.
Keith M, Haase KM, Chivas AR, Klemd R (2022) Phase separation and fluid mixing revealed by trace element signatures in pyrite from porphyry systems. Geochim. Cosmochim Acta 329:185–205.
Longerich, S (1996) Laser Ablation Inductively Coupled Plasma Mass Spectrometric Transient Signal Data Acquisition and Analyte Concentration Calculation. Journal of analytical atomic spectrometry, 11(9), 899-904.
Liu S, Zhang Y, Ai G, et al (2022) LA-ICP-MS trace element geochemistry of sphalerite: Metallogenic constraints on the Qingshuitang Pb–Zn deposit in the Qinhang Ore Belt, South China. Ore Geol Rev 141, 104659.
Metz S, Trefry JH (2000) Chemical and mineralogical influences on concentrations of trace metals in hydrothermal fluids. Geochim. Cosmochim. Acta 64:2267–2279.
Mambwe, P., Shengo, M., Kidyanyama, T, et al. (2022). Geometallurgy of Cobalt Black Ores in the Katanga Copperbelt (Ruashi Cu-Co Deposit): A New Proposal for Enhancing Cobalt Recovery. Minerals 12 (3), 295.
Mambwe P, Swennen R, Cailteux J, Chabu M, Dewaele S, Muchez Ph (2023) Review of the origin of breccias and their resource potential in the Central Africa Copperbelt. Ore Geol. Rev. 156:105389
Maslennikov, V. V., Maslennikova, S. P, et al. (2009). Study of trace element zonation in vent chimneys from the Silurian Yaman-Kasy volcanic-hosted massive sulfide deposit (Southern Urals, Russia) using laser ablation-inductively coupled plasma mass spectrometry (LA-ICPMS). Economic Geology, 104(8), 1111-1141.
Muchez P, André-Mayer AS, El Desouky HA, Reisberg L (2015) Diagenetic origin of the stratiform Cu–Co deposit at Kamoto in the Central African Copperbelt. Miner. Depos. 50:437–447.
Muchez P, Vanderhaeghen P, Desouky H, et al (2008) Anhydrite pseudomorphs and the origin of stratiform Cu - Co ores in the Katangan Copperbelt (Democratic Republic of Congo). Miner. Depos 43:575–589.
Reiser FKM, Guimarães FMG, Pinto ÁMM, et al. (2009) Germanium-rich Chalcopyrite from the Barrigão Remobilised Vein Deposit, Iberian Pyrite Belt, Portugal. Smart Science for Exploration and Mining: Proceedings of the Tenth Biennal SGA Meeting, 2009.
Rosenfels RC, von der Heyden BP (2022) A critical comparison between the Fungurume 8 and 88 Cu-Co deposits, Central African Copperbelt. Ore Geol Rev 140.
Tembo F, Kampunzu AB, Porada H (1999) Tholeiitic magmatism associated with continental rifting in the Lufilian Fold Belt of Zambia. J. Afr. Earth Sci. 28:403–425.
Wilson SA, Ridley WI, Koenig AE (2002) Development of sulfide calibration standards for the laser ablation inductively-coupled plasma mass spectrometry technique. J Anal At Spectrom 17:406–409.

# Geology and geochemistry of the shale-hosted vanadium mineralization at the Van property, Northwest Territories

**Danielle A. McGill[1], Daniel D. Gregory[1], Merilie A. Reynolds[2], Daryll Bien C. Concepcion[1], Stefanie M. Brueckner[3], Chelsey Merrick[1]**
*[1]Department of Earth Sciences, University of Toronto, Canada*
*[2]Northwest Territories Geological Survey, Canada*
*[3]University of Manitoba, Winnipeg, Canada*

**Abstract.** Vanadium (V) is becoming an increasingly important critical element. As such, Canada is increasing exploration efforts to stay ahead of its increasing demand. The Van property, located in the Northwest Territories, is a metalliferous V-rich shale deposit featuring several V-rich showings. Whole rock analyses indicate V concentrations of up to 6390ppm in the mineralized horizon with other enriched elements including Zn, Ni, and Mo. Initial mineralogical analysis indicates V is hosted in different minerals including both sulphides and oxides. Raman spectral analysis of carbonaceous material places the Van property in the low-grade metamorphism temperature range. Through a series of geochemical and mineralogical analyses we hope to determine the depositional setting of the deposit, and the controls of the mineralization. Initial results have proven complex, and it may be likely that more than one process is controlling ore formation in the area.

## 1 Introduction

Vanadium (V) is an increasingly important critical element, in part due to its use in vanadium redox flow batteries, a technology that will support the transition towards a green economy. At present, China, South Africa, and Russia are the leading producers of vanadium (Kelley et al. 2017) with Canada only a very minor producer. However, exploration efforts in the country have been amplified with the aim of staying ahead of the green push and potentially capitalizing on it. The main V deposit types being considered for exploration and development are the sandstone-hosted vanadium (can be with U), vanadiferous titanomagnetite, vanadate and shale-hosted vanadium deposits (Simandl et al. 2022). The focus of this study will be the shale-hosted V. Historically this deposit type has not been exploited as mineralization is generally only a few meters thick and as such has generally not been economic (Kelley et al. 2017). However, with the increasing market value of vanadium, which is projected to increase even further in coming years, this may not always be the case.

The Van property is a V-rich metalliferous shale deposit located in the Mackenzie Mountains on the border of the Northwest Territories and Yukon Territory, Canada, just north of the mining town Tungsten (Figure 1).

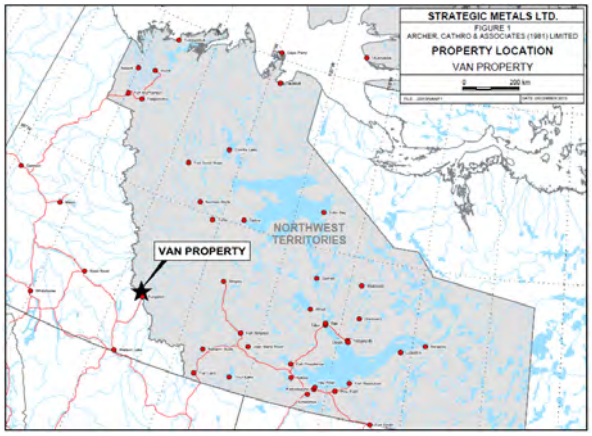


**Figure 1.** Locater map of Van property from 2013 Archer, Cathro & Associates Ltd., Van Property Assessment Report.

Exploration work of Van property began in 1968 and mineral claims covering the area are currently owned by Strategic Metals Ltd. The property contains several showings of shale-hosted V in the lower Ordovician to Devonian Duo Lake Formation of the Road River Group. The dominant structure of the area is a large-scale NW-trending, upright fold, and mirrored stratigraphy can be seen on either side of the valley floor (Figure 2). The genesis of this style of V mineralization is poorly understood and the mineralization at the Van property has not been characterized in detail.

There is a major debate between researchers of this deposit type as to where the V is sourced from. The two main arguments are either the V was sourced from hydrogenous input (Gadd et al. 2019) or through seafloor hydrothermal venting into redox stratified water. If the deposit was formed from hydrogenous input, we would need to understand what occurred in the depositional environment that enriched V to such high levels. If the deposit was formed from a hydrothermal source, we will need to determine the source of the fluids and characterize them. Through a comprehensive evaluation of the deposit's key mechanisms of formation (including but not limited to sedimentation rate, water column anoxia and potential presence of hydrothermal

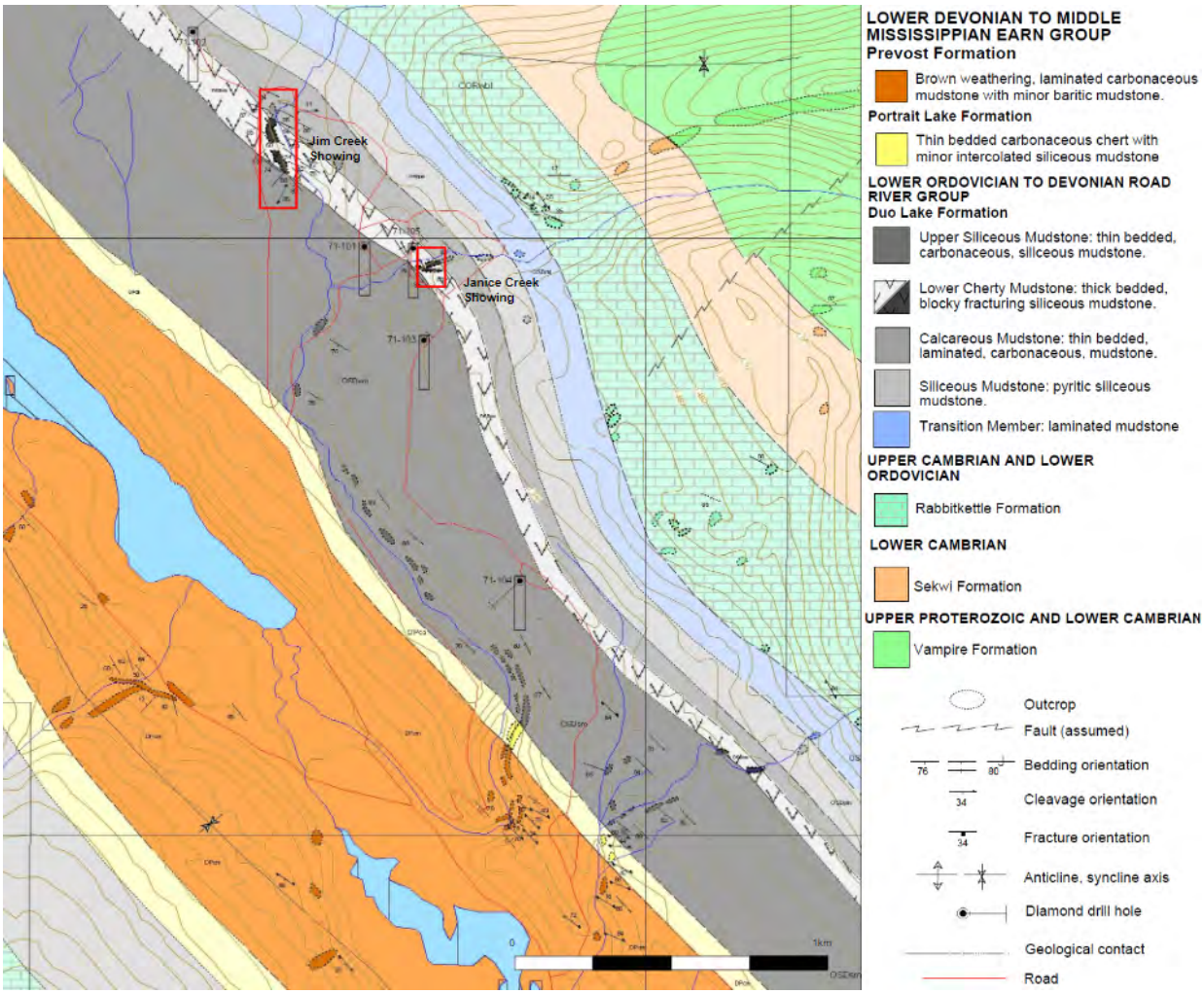


**Figure 2.** Map of the Van property geology from 2013 Archer, Cathro & Associates Ltd. Van Property Assessment Report with additional structural measurements collected in 2022. Primary V showings (Jim and Janice creek) are outlined in red.

fluids) as well as host mineralization, we aim to create a regional geologic model for similar V-rich black shale deposits.

## 2 Methodology

### 2.1 Field work and whole rock geochemistry

In the summer of 2021, 50 samples were collected systematically from the mineralized stratigraphy at the two creek cut showings (Jim and Janice creek; red ellipsoid in Figure 2). A further 28 samples were taken in the summer of 2022 from not only the mineralized horizon but also surrounding lithologies including the older rocks of the Road River Group and the younger rocks of the Earn group. While taking samples, structural measurements were taken and lithologies were described at each outcrop. Upon returning from the field the samples were analyzed with a Bruker portable X-ray fluorescent analyzer (pXRF) which gave preliminary geochemical results. These results were used to determine a subset of samples to be sent off for whole rock geochemical analyses and to be made into thin sections performed by ALS Canada Ltd. and Vancouver Petrographics, respectively.

### 2.2 Scanning electron microscopy

Scanning electron microscopy (SEM) was performed at the University of Toronto with a JEOL 6610LV SEM. Images were taken using a backscattered electron detector and qualitative chemical analyses were performed to identify mineral phases. SEM was used for primary mineralogical characterization as well as to identify V-hosting minerals.

### 2.3 RSCM thermometry

Carbonaceous matter (CM) Raman spectra were obtained at the Royal Ontario Museum using a Horiba Lab RAM ARAMIS Raman spectrometer. The 532nm laser was focused on the sample using a microscope with a 100x objective. The laser power at the surface of the sample was approximately 1mW. The signal was filtered with a D1 filter and dispersed with a 1200 g $mm^{-1}$ grating. The system was calibrated with a silicon wafer before each session. Twenty spectra were recorded per sample over a spectral range of 700 to 2000 $cm^{-1}$. A five-band fitting procedure was performed using Peakfit software. Temperatures were determined using a Raman low-grade CM geothermometer produced by Lahfid et al. (2010).

## 3 Whole rock geochemistry

Fifty samples from the Jim and Janice creek showings as well as surrounding hanging and footwall were sent for whole rock lithogeochemistry utilizing four-acid digestion and full fusion followed by ICP-MS. In the mineralized horizon V concentration ranged from 400ppm to 6390ppm, Zn ranged from 136ppm to 14600ppm. Ni and Mo were also concentrated locally, reaching up to 159 and 77ppm in the mineralized zone, respectively. The mineralized zone is also very organic rich with $C_{org}$ ranging from 5 to 12wt%. Outside of the mineralized horizon, in the younger Prevost formation, barium was enriched with concentrations up to 8.59 wt%.

**Figure 3.** Mineralized zone at Jim creek showing. Vanadium is hosted in a highly folded thick cherty unit interbedded with siliceous mudstone.

## 4 Scanning electron microscopy

Thin sections from different showings and formations were analyzed with the SEM in order to identify mineral phases and any potential spatial differences in the samples. The focus after primary characterization was to identify V-hosting minerals.

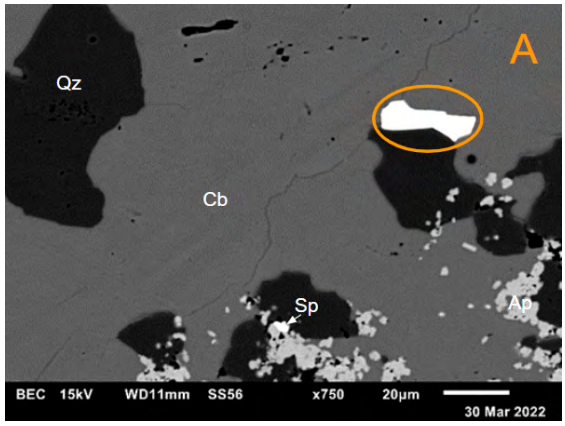


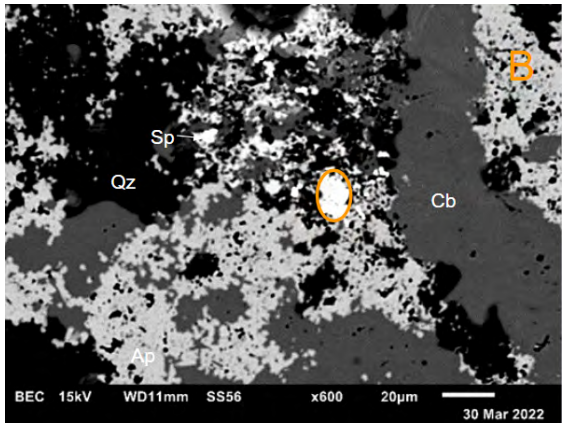


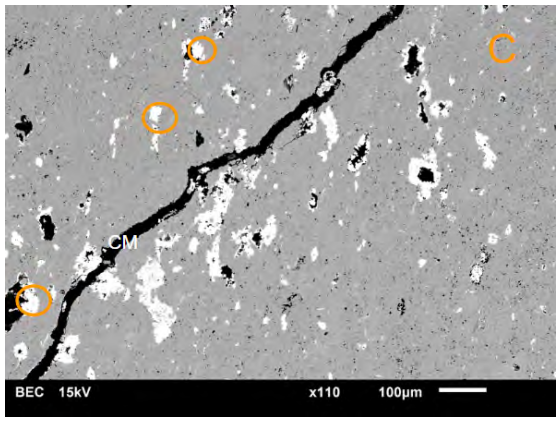


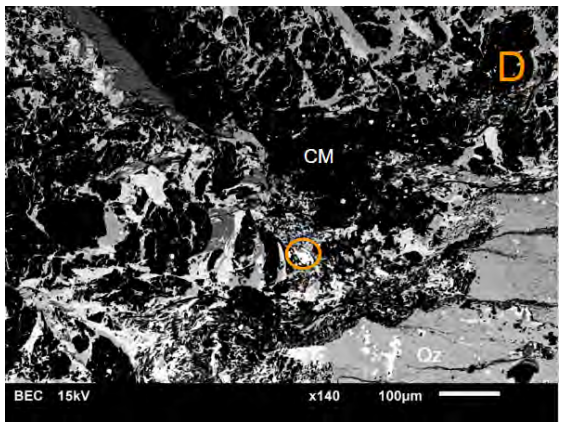

**Figure 4.** SEM backscattered electron images taken of V (orange circles) and host minerals. Qz = quartz, Cb = calcite, CM = carbonaceous matter, Ap = apatite, Sp = sphalerite.

Photos A and B of Figure 4 are from a sample taken from the Janice creek showing. The white minerals circled host the vanadium as a Cu-V sulphide (sulvanite?; Figure 4A), and a Cu-V-As sulphide mineral (colusite?; Figure 4B). Sphalerite is spatially closely associated with these identified V phases. Photo C is from a sample taken from the Jim creek showing. The matrix in this sample is largely quartz with dispersed carbonaceous matter (CM) and CM veinlets. In this case the V is hosted in an iron oxide. Photo D is taken close to the projected mineralized horizon, south of both the Jim and Janice creek showings. The sample features a vein of carbonaceous matter, the margin of which is being analyzed in the photo. The V hosting mineral is also an iron oxide.

## 5 RSCM thermometry

Three samples were selected and analyzed by Raman spectrometer. These include two samples from outside the mineralized horizon in the Prevost formation and older Duo Lake formation horizon (in the hanging and footwall, respectively). The last sample is from the mineralized Jim creek showing. The temperature range of the Van property is low grade at ~310-340°C. Initial analyses indicate a small temperature difference between mineralized and non-mineralized horizons, with the mineralized zone being slightly hotter. If real, this could indicate hot hydrothermal fluids passed through the zone.

**Table 1.** Temperatures between mineralized and non-mineralized horizons.

| Sample | Formation | Temp (°C) |
|---|---|---|
| VAN22-05 | Prevost Fm (hanging wall) | 316 ± 2 |
| VP-67 | Mineralized (Jim creek) | 341 ± 4 |
| VAN22-24 | Duo Lake Fm (footwall) | 310 ± 6 |

## 6 Conclusion

Geochemical and mineralogical analyses have provided a general characterization of the Van property samples. The mineralized horizon features organic-rich shale with elevated V concentrations of up to 6390ppm. V is hosted in different minerals including iron oxides in association with CM veins, and copper sulphides. Initial RSCM thermometry has indicated the Van property to have undergone low grade metamorphism. However, results indicate a potential temperature difference between non-mineralized and mineralized horizons. Additional analysis of other samples from both horizons will confirm whether this difference is real. Further analyses yet to be completed include V-isotope analyses and laser ablation inductively coupled plasma mass spectrometry (LA-ICPMS) of sulphide minerals. Results from these analyses will shed light on the redox controlling processes on ore formation and indicate the composition of metal enriched fluids that may have passed through the area (a potential source for V).

## Acknowledgements

We thank the targeted geoscience initiative program from the Canadian Geologic Survey. We also thank the Natural Sciences and Engineering Research Council of Canada (NSERC) undergraduate summer research award for funding of summer field work and Discovery grant to Dan Gregory for continued funding. We also thank the Northwest Territories Geological Survey and Royal Ontario Museum for their support in this project.

## References

Gadd M.G., et al. (2019) Platinum, Pd, Mo, Au, and Rd deportment in hyper-enriched black shale Ni-Zn-Mo-PGE mineralization, Peel River, Yukon, Canada. Ore Geology Reviews 107: 600-614.https://doi.org/10.1016/j.oregeorev.2019.02.030

Kelley K.D., Scott C.T., Polyak D.E., and Kimball B.E. (2017) Vanadium, chap. U *of* Schulz, K.J., DeYoung, J.H., Jr., Seal, R.R., II, and Bradley, D.C., eds., Critical mineral resources of the United States – Economic and environmental geology and prospects for future supply: U.S Geological Survey Professional Paper 1802: U1-U36. https://doi.org/10.3133/pp1802U

Lahfid A., Beyssac O., Deville E., Negro F., Chopin C. and Goffe B. (2010). Evolution of the Raman spectrum of carbonaceous material in low-grade metasediments of the Glarus Alps (Switzerland). Terra Nova 22:354-60. https://doi.org/10.1111/j.1365-3121.2010.00956.x

Simandl G.J. and Paradis S. (2022) Vanadium as a critical material: economic geology with emphasis on market and the main deposit types. Applied Earth Science 313:218-236. https://doi.org/10.1080/25726838.2022.2102883

# Combined Lithological and Structural Controls on Unconformity Related Uranium Deposits (Eastern Athabasca Basin, Canada)

**Gaétan Milesi[1], Olivier Gerbeaud[2], Thomas Obin[1], Mehdi Serdoun[1], Marc Brouand[2], Sean Bosman[3], Colin Card[3], Amber Doney[4], Anthony Le Beux[2], Julien Mercadier[1]**
*[1]GeoRessouces, CNRS, Université de Lorraine, Labcom CREGU, France*
*[2]ORANO, France*
*[3]Saskatchewan Ministry of Energy and Resources, Saskatchewan Geological Survey, Canada*
*[4]ORANO Canada, Canada*

**Abstract.** The Proterozoic Athabasca Basin (Canada) hosts the highest-grade uranium deposits known. They are unconformity-related uranium deposits, meaning that uranium high grades are localized at the interface between the basin and its underlying crystalline basement. Reactivated fault zones are considered to be a first-order control on the "plumbing system" that triggered the circulation of mineralizing fluids. The geometrical relation between alteration, mineralization and fault/fractured zones is however still unclear in massive uranium deposits (e.g. McArthur River, Cigar Lake) due to massive replacement by clays and massive pitchblende of primary lithological and structural markers. Recent discoveries of small to medium size uranium mineralization in Waterfound and McClean South prospects (eastern Athabasca Basin) allow to transects of mineralized systems with less degree of alteration in the basal part of the Athabasca sandstone and related basement. First results suggest that the clay-replacement halo and the uranium oxides emplacement, is controlled by the combination of a specific structural network and by lithological variations in the basal MFb formation which forms the bottom basin. In such context, mineralizing fluids were strongly channelized along steep/vertical pathways (fracture network) and along sub-horizontal pathways formed by conglomeratic layers, leading to alteration and mineralization zones characteristic of this type of uranium deposits.

## 1 Introduction

Unconformity related uranium (URU) deposits are massive and high-grade orebodies with uranium usually grading over 1% of up to 20% (Cuney, 2009). The Paleo- to Mesoproterozoic Basin Athabasca region (Saskatchewan, Canada) hosts the world's highest grade URU deposits (e.g. McArthur, Cigar Lake). In these deposits, uranium orebodies are characterized by uraninite pods, veins, and semi massive replacements, mainly formed during several episodes of hydrothermal fluid circulation, between 1.6 and 1.0 Ga (Jefferson et al., 2007, Alexandre et al., 2009, Adlakha and Hattori, 2022), although this wide range of ages can be explained by post-crystallization alteration processes that have reopen U-Th-Pb uraninite systems (Martz et al., 2019). Ages obtained on uranium mineralization in the eastern and southwestern border of the Athabasca Basin suggest that these hydrothermal systems associated with the formation of uranium deposits were active at regional scale during the same periods (Kyser et al., 2000, Ledru et al., 2022) but lead to various size of uranium deposits.

These hydrothermal deposits are considered to be formed by circulation of large volume of basin-derived oxidizing brines (e.g. Richard et al., 2016) at the basin/basement interface. Basement graphitic shear zones are well known to have strongly controlled the emplacement of high-grade uranium (Jefferson et al., 2007) and this circulation and related mineralizing processes were triggered after the deposition of the Athabasca Basin by: i) the reactivation of basement-hosted graphitic shear zones initially developed during the Trans-Hudson Orogeny (1.85-1.75 Ga); and ii) the propagation of fracture networks in the basal part of the Athabasca sandstone. Such phenomena led to an intense fluid/rock interaction at the basin/basement interface along complex fault zones and structural networks, forming intense alteration haloes and U pods which characterized URU deposits (Fayek and Kyser, 1997). In this context, structural inheritance and neo-formed fracture networks played a major role controlling the geometry the mineralized ore bodies. The mechanisms of the propagation mode of basement structures within the basal formation of the Athabasca Basin is however still not fully understood, precluding the definition of model of formation and exploration methods for these deposits.

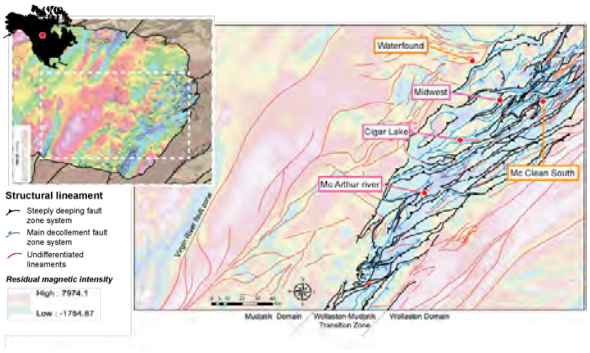


**Figure 1.** Magnetic anomaly maps at the scale of the eastern part of the Athabasca Basin. The main structures are replaced, and the main uranium mines are in purple. Studied Waterfound and McClean South exploration projects are in orange (modified after Ledru et al., 2023).

"Giant" URU deposits are associated with the circulation of a large amount of hydrothermal fluids, resulting in the intense alteration of host-rocks around the deposits (Thomas et al., 2000). Such massive replacement precludes detailed structural and lithological observations, while much more structural information is preserved in peripheral zones of deposits or in prospects where minor intensity of alteration was recognized. Because of the lack of well-preserved material to perform detailed structural and lithological study, the potential role played by lithological variations in the basal part of the basin is usually difficult to decipher in the "giant deposits". Recent discoveries of small to medium size uranium pods both in Waterfound and McClean South prospects (Fig. 1) in the Wollaston Mudjatik Transition Zone, North-East Athabasca Basin (Annesley et al., 2005), allowed to transect mineralized systems with less degree of alteration in the basal part of the Athabasca Basin, in which the basin lithology and fracture systems are still relatively well preserved, and which offer favourable conditions for characterizing the relationships between lithological variations, fracture networks, alteration and uranium mineralization. Based on these observations, we discuss the impact of the structural and lithological properties on the formation of URU deposits.

## 2 Structural and lithological observations

The two prospects were logged in detail (Fig. 2), including structural, lithological and alteration survey, with a specific focus on the basal part of the MFb basin formations (Ramaekers et al., 2007). 6 drill holes in uranium mineralized pods in Waterfound and McClean South prospects were studied: i) 3 uranium mineralized drill cores (WF-67, WF-68 and WF-68-1) for Waterfound, ii) 1 mineralized core (MCS-34) and 2 cores at the vicinity of the mineralization without uranium but intense alteration (MCS-35C and MCS-39C) for McClean South.

The 2 areas are characterized by mineralized zones showing first-order similarities, uranium is mainly localized in basal lithological formations right above the unconformity. The thickness of the basin is different according to the location in the basin: 450 m at Waterfound project and ~200 m for McClean South project (Fig. 2).

For both prospects, the underlying basement is marked by different styles of superposed deformation (Fossen, 2016): ductile deformation (mylonites, Fig.3a), brittle-ductile fault rocks (cohesive cataclasites and breccias, Fig. 3b) and pure brittle deformation (non-cohesive gouges and fault breccias, Fig. 3c). Most of cohesive brittle fault rock intervals are typically developed parallel to the gneiss foliation, suggesting that brittle deformation may have reworked the initial ductile fabric. However, in some cases a neat angular contact is observed between clay-matrix breccia or gouge intervals of 0.1-0.2m in thickness and foliation (Fig. 3c), suggesting that non-cohesive fault rocks were formed during a later tectonic event(s). The results show that the deformation affecting the basal part of the basin is more distributed than in the basement and characterized by successive fractured/faulted zones. Core zones are characterized by gouges (~0.1-0.3 m) and breccias (decametric to pluri-metric) with intense clay alteration associated inside or proximal to fault core (Fig. 2). The faults are mainly subvertical with variable strike orientation, pluri-metric highly fractured damage zones are associated to the basin faults. These damage zones show different degree of alteration (clay/hydrothermal hematite). The fault zones are mainly localized in the first 30 m of the basal part of the basin and have a strong impact on the uranium location (Fig. 2).

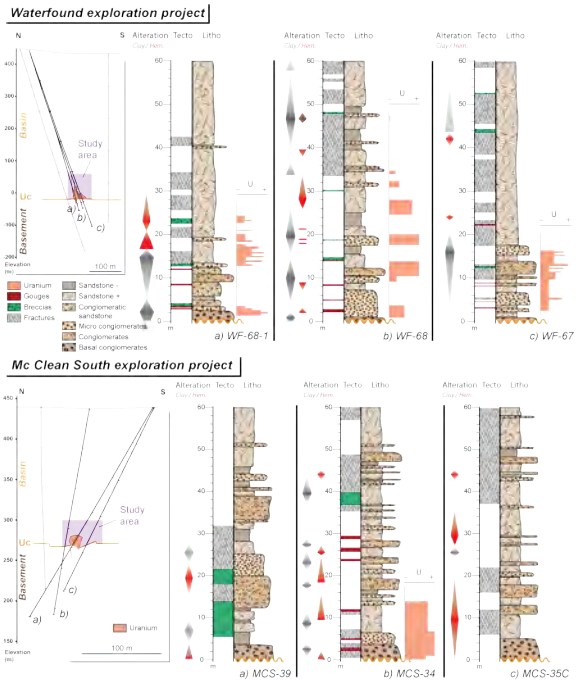


**Figure 2.** Cross section and detailed structural lithological and alteration logging of uranium mineralized fences of Waterfound and Mc Clean South exploration projects.

Important lithological contrasts in the basal MFb formation are observed with numerous conglomeratic sandstones layers interlayered with "gritty" medium- grained sandstone intervals (Fig. 3e). The lithological sequence is characterized by the presence of a common basal conglomerate that can be variable in thickness (Fig. 2). Important lithological vertical and lateral variations are reported for the sedimentary series between conglomeratic and sandstone layers (Fig. 2). The detailed observations showed that some conglomeratic layers are preferentially altered and host preferentially uranium mineralization (Fig. 3e, f, g) compared to sandstone layers. It is important to note that the highest uranium grades and massive clay-replacement (Fig. 3d) are mostly associated with steep fractures and secondary faults. In both

Waterfound and McClean South uranium mineralized pods, uranium mineralization and alteration halo seem to be controlled at first order by steep structures that affect the basal basin formation (fault/fracture system), along with mineralization/alteration "propagating" within conglomeratic sedimentary layers.

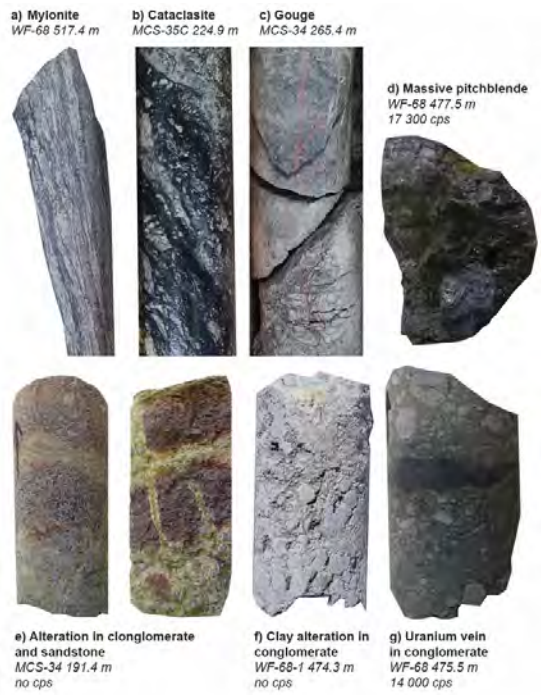


**Figure 3.** Core photos of basement structures (a,b,c) and altered basin lithologies (d,e,f,g) of Waterfound and McClean South exploration projects. See text for details.

## 3 Discussion

The results obtained on Waterfound and McClean South drill cores carried out significant inputs regarding the lithological and structural controls on the development of URU deposits in the Athabasca Basin (Fig. 4). The two case studies are characterized by limited degrees of alteration that favored detailed observations of the structural network and its architecture, and of the initial nature of the basin lithologies and their replacement by alteration. The uranium location appears principally controlled by the presence of fault/fracture zones at the base of the MFb sandstone. Faults and fractures constitute efficient conduits for fluid circulation (Caine et al., 1996; Bense et al., 2013) and can channelized a large volume of fluids as shown by intense clay-replacement in the fault zones of the two projects. The effectiveness of the fault system for the circulation of mineralizing fluids is well demonstrated for the Athabasca Basin (e.g. Cui et al., 2016). At Cigar Lake, the presence of perched uranium mineralization in the upper sedimentary series of Athabasca Basin, far from the unconformity constitutes a good example of this structural control (Bruneton, 1993, Reyx and Ruhlmann, 1993).

The detailed lithological description of the basal MFb sequence showed evidence of a lithological control on clay-alteration and uranium mineralization in basal conglomerates and conglomeratic sandstone located higher in the sedimentary series (WF-68 and WF-68-1 Fig.2). The ability of these conglomeratic lithologies to host preferentially uranium might be a key-parameter for understanding the onset and the geometry of unconformity-type deposits. The ability of the conglomeratic layers to "propagate" fluid flow this may be explained by several reasons: i) "primary" porosity and permeability due to granulometry, detrital grain organization (sorting), matrix properties and ii) mechanical properties of conglomerates compared to the gritty sandstone, variation in the propagation mode of the fracture/fault system (Zhang et al., 1990). These two possible causes can be strongly controlled by the granulometric-clast distribution in the sedimentary column (Taboada et al., 2005; Ballas et al., 2015, Mavko et al., 2020). This lithological control will be highly dependent of the lithological lateral variation, these projects are marked by a poor continuity between the sedimentary layers (except basal conglomerates). The structural framework and fault displacement could play a key role on the continuity of the lithological units which may conditions the lithological control.

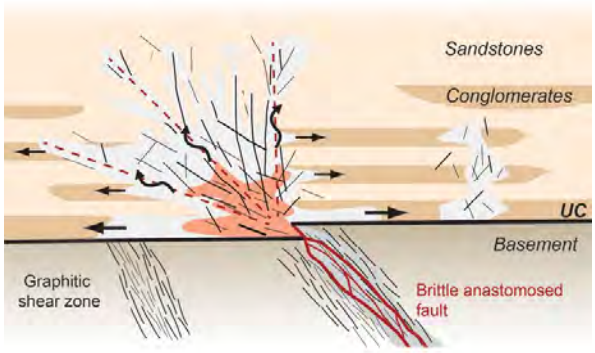


**Figure 4.** Conceptual model of formation of URU deposits of the Athabasca basin showing structural and lithological controls on the formation and geometry of uranium deposit. In orange, uranium mineralization and in grey clay alteration halo associated. The black arrows indicate fluid flow in fault and permeable conglomeratic layers.

This study on Waterfound and McClean South uranium prospects suggests both structural and lithological controls for the formation of the URU mineralization of the Athabasca Basin. These combined controls already shown for other metallogenic context (e.g. Ogata et al., 2014; Rhys et al., 2020) can have a significant impact on the location, the geometry and grade of the unconformity-type deposits. The geometrical relation between mineralization controlled by fractures and conglomeratic layers needs to be further investigated and showed in different prospects of the

Athabasca Basin region, especially for “giant” deposits.

## 4 Conclusion

The detailed structural and lithological observations of uranium-mineralized drill cores from Waterfound and McClean South projects (eastern Athabasca Basin, Canada) allows to study the uranium mineralization system itself and define key parameters and that controlled their formation. Detailed observations on drill cores suggest that the development of the mineralized system, including the clay-replacement halo and the uranium oxides emplacement is controlled by a combination of structural network and lithological features in the basal MFb formation of the Athabasca Basin. The effect of such combined structural and lithological controls on the formation of URU deposits can have significant impact on the geometry, lateral expansion, and uranium grades of the eastern part of the Athabasca Basin Region deposits.

## Acknowledgements

The authors acknowledge ANR funding, grant ANR-21-CHIN-0006 (project Geomin3D), Orano Canada team (M. Anderson; B. Eccles; D. Gerger; C. Khairallah) and ALT company for WellCAD licences. S. Spinks for the abstract review.

## References

Adlakha E & Hattori K (2022) Thermotectonic events recorded by U-Pb geochronology and Zr-in-rutile thermometry of Ti oxides in basement rocks along the P2 fault, eastern Athabasca Basin, Saskatchewan, Canada. GSA Bulletin, 2022, vol. 134, no 3-4, (2022) p. 567-576. https://doi.org/10.1130/B35820.1

Alexandre P, Kyser K, Thomas, D et al. (2009) Geochronology of unconformity-related uranium deposits in the Athabasca Basin, Saskatchewan, Canada and their integration in the evolution of the basin. Mineralium Deposita, 44(1), 41-59. https://doi.org/10.1007/s00126-007-0153-3

Annesley, IR, Madore C, Portella P (2005) Geology and thermotectonic evolution of the western margin of the Trans-Hudson Orogen: evidence from the eastern sub-Athabasca basement, Saskatchewan. Canadian Journal of Earth Sciences, 2005, vol. 42, no 4, p. 573-597. https://doi.org/10.1139/e05-034

Ballas G, Fossen H, Soliva R (2015) Factors controlling permeability of cataclastic deformation bands and faults in porous sandstone reservoirs. Journal of Structural Geology, 76, 1-21. https://doi.org/10.1016/j.jsg.2015.03.013

Bense VF, Gleeson T, Loveless SE et al. (2013) Fault zone hydrogeology. Earth-Science Reviews, 127, 171-192. https://doi.org/10.1016/j.earscirev.2013.09.008

Bruneton P, (1993) Geological environment of the Cigar Lake uranium deposit. Can. J. Earth Sci. 30, 653–673. https://doi.org/10.1139/e93-054

Caine JS, Evans JP, Forster CB (2013) Fault zone architecture and permeability structure. Geology, 24(11), (1996) 1025. https://doi.org/10.1130/0091-7613(1996)024<1025:FZAAPS>2.3.CO;2

Cui T, Yang J, & Samson IM (2012) Tectonic Deformation and Fluid Flow: Implications for the Formation of Unconformity-Related Uranium Deposits. Economic Geology, 107(1), 147-163. https://doi.org/10.2113/econgeo.107.1.147

Cuney M (2009) The extreme diversity of uranium deposits. Mineralium Deposita, 44(1), 3-9. https://doi.org/10.1007/s00126-008-0223-1

Fayek M, & Kyser TK (1997) Characterization of multiple fluid-flow events and rare-earth-element mobility associated with formation of unconformity-type uranium deposits in the Athabasca Basin, Saskatchewan. The Canadian Mineralogist, 35(3), 627-658.

Fossen H, (2016) Structural geology. Cambridge university press.

Jefferson CW, Thomas, DJ, Gandhi, SS et al. (2007) Unconformity-associated uranium deposits of the Athabasca basin, Saskatchewan and Alberta. Bull. Geol. Surv. Canada, 23–67.

Kyser K, Hiatt E, Renac C, et al. (2000) Diagenetic fluids in Paleo-and Meso-Proterozoic sedimentary basins and their implications for long protracted fluid histories. Mineralogical Association of Canada Short Course, 28, 225-262.

Ledru P, Benedictio A, Chi G, et al. (2022) The unconformity-related uranium mineral system of the Athabasca Basin (Canada). Ressources métalliques 2, Decrée, S. ISTE Editions, Londres.

Martz P, Mercadier J, Perret J, et al. (2019) Post-crystallization alteration of natural uraninites: Implications for dating, tracing, and nuclear forensics. Geochimica et Cosmochimica Acta, 249, 138-159. https://doi.org/10.1016/j.gca.2019.01.025

Mavko G, Mukerji T, Dvorkin J (2020) The rock physics handbook. Cambridge university press.

Ogata K, Senger K, Braathen A. et al. (2014) Fracture corridors as seal-bypass systems in siliciclastic reservoir-cap rock successions: Field-based insights from the Jurassic Entrada Formation (SE Utah, USA). Journal of Structural Geology, 66, 162-187. https://doi.org/10.1016/j.jsg.2014.05.005

Ramaekers P, Jefferson CW, Yeo GM, et al. (2007). Revised geological map and stratigraphy of the Athabasca Group, Saskatchewan and Alberta, in Jefferson, C.W., and Delaney, G., eds., EXTECH IV: Geology and Uranium EXploration TECHnology of the Proterozoic Athabasca Basin, Saskatchewan and Alberta: Geological Survey of Canada, Bulletin 588.

Reyx J & Ruhlmann F (1993) Etude metallographique des differentes associations minerales et caracterisation chimique des mineraux uraniferes du gisement de Cigar Lake (Saskatchewan, Canada). Can. J. Earth Sci. 30, 705–719. https://doi.org/10.1139/e93-057

Rhys DA, Lewis PD, Rowland JV (2020) Structural controls on ore localization in epithermal gold-silver deposits: Mineral systems approach. Reviews in Economic Geology, 21 83–145. https://doi.org/10.5382/rev.21.03

Richard A, Cathelineau M, Boiron MC, et al. (2016) Metal-rich fluid inclusions provide new insights into unconformity-related U deposits (Athabasca Basin and Basement, Canada). Mineralium Deposita, 51, 249-270. https://doi.org/10.1007/s00126-015-0601-4

Taboada A, Chang KJ, Radjaï F et al. (2005) Rheology, force transmission, and shear instabilities in frictional granular media form biaxial numerical tests using the contact dynamics method. Journal Geophysical Research 110, B09202. https://doi.org/10.1029/2003JB002955

Thomas DJ, Matthews RB, Sopuck V (2000) Athabasca Basin (Canada) unconformity - type uranium deposits: Exploration model, current mine developments and exploration directions, in Geology and Ore Deposits 2000: The Great Basin and Beyond: Geological Society of Nevada Symposium, Reno, Nevada, May 15-18 2000, Proceedings, v. 1, 103-126.

Zhang J, Wong TF, Davis DM (1990) Micromechanics of pressure-induced grain crushing in porous rocks. J. Geophys. Res. 95, 341e352. https://doi.org/10.1029/JB095iB01p00341

# Solid bitumen in the Central African Copperbelt: implications for understanding the ore-forming processes

**Muchez Philippe[1], Qiuping Liu[1], Mambwe Pascal[1,2], Ralf Littke[3]**
*[1.] KU Leuven, Department of Earth and Environmental Sciences, Celestijnenlaan 200E, B-3001 Leuven, Belgium*
*[2.] Department of Geology, University of Lubumbashi, B.P.1825, Lubumbashi, Congo*
*[3] RWTH Aachen, Institute of Geology and Geochemistry of Petroleum and Coal, Energy and Mineral Resources group, Lochnerstr. 4-20, 52056 Aachen, Germany*

**Abstract.** The Central African Copperbelt is the largest sediment-hosted Cu-Co producing province in the world. The knowledge of the degree of diagenesis or metamorphism the mineralized rocks underwent forms part of an integrated basin analysis approach to understand the ore-forming processes that led to the genesis of these major deposits. The study of solid bitumen reflectance indicates a maximum burial temperature between 200 and 235°C in the Congolese part of the Copperbelt (Tenke Fungurume district and Luiswishi ore deposit) and between 222-250°C in Nkana near the Kafue Dome in Zambia. These temperature ranges are significantly lower than the temperatures of the hydrothermal fluids present during maximum burial and the Pan-African Lufilian orogeny in the Copperbelt. However, solid bitumen indicating high temperatures of 326-366°C have been measured at Tenke Fungurume. The latter temperature range corresponds to the homogenization temperatures measured in fluid inclusions and is interpreted to be due to the pervasive migration of the hydrothermal fluid through the rocks.

## 1 Introduction

The Central African Copperbelt is the largest sediment-hosted Cu-Co producing province in the world (Cailteux et al. 2005). The Cu-Co deposits are situated in the Neoproterozoic to early Cambrian Katanga Supergroup, which was deposited from <880Ma (Armstrong et al. 2005) until <573Ma (Master et al. 2005). The ore-forming processes started during diagenesis and continued after the Pan-African Orogeny (Selley et al. 2005; Dewaele et al. 2006), which occurred between 560 and 500 Ma (Hitzman et al. 2012).

The metamorphic grade of the Katanga Supergroup apparently decreases from upper greenschist facies to effectively unmetamorphosed from the southeast to the northwest in the Lufilian Arc (i.e., from Nkana in northern Zambia to Kamoto in southeastern part of the DR Congo; Cailteux et al. 2005; Eglinger et al. 2013). However, widespread alteration affected the Neoproterozoic rocks and may have obliterated indicators of metamorphic grade.

At Nkana, alteration consists of tremolite, ferroan calcite, talc, muscovite and biotite (Torremans 2016). Quartz and chlorite form pseudomorphs after tremolite. Brems et al. (2009) identified silicification, K-feldspar alteration, albitization, carbonatization and replacement by anhydrite as the main styles of alteration. They also described massive tremolitic shales associated with partly silicified in the lowermost part of the Nkana South Orebody. Fluid inclusion data from both the Nkana and the nearby Musoshi (85 km to the NW) deposits further confirm the importance of K-metasomatism during Cu-Co mineralization followed by Na-metasomatism during basin closure (Richards et al. 1988; Davey et al. 2020). In the northwest of the Lufilian Arc (De Swardt and Drysdall 1964), alteration is characterized by magnesite and dolomite. The grade is assumed to be in the diagenetic realm (Cailteux et al., 2005), but no conclusive evidence has been presented.

A parameter widely used to determine the diagenetic – metamorphic grade or thermal maturity of sedimentary rocks, e.g. in basin analysis and hydrocarbon studies, is the reflectance of vitrinite, an organic maceral (Stach et al. 1982). However, pre-Devonian rocks most often do not contain vitrinite but may have significant amounts of solid bitumen associated with the generation of hydrocarbons (Schoenherr et al. 2007). Solid bitumen has been observed in the Neoproterozoic rocks of the Copperbelt (Heijlen et al. 2008). Several intervals in the Neoproterozoic rocks especially in its lower part (i.e., the Roan Group) are rich in organic matter and suitable for the study of the degree of maturation of the organic matter.

The aim of this study is to determine the thermal maturation degree of the Lower Roan rocks from the mineralized zones at the Nkana and Luiswishi ore deposits and the Tenke Fungurume district, covering a large part of the Lufilian Arc (Fig. 1). The degree of maturation is used to calculate the maximum temperature these rocks reached. We compare these temperatures to metamorphic data from literature and the temperature of the mineralizing fluids present during maximum burial and folding.

## 2 Geological setting

The three ore deposits and associated rocks studied occur in the lower part of the Roan Group. The Nkana deposit is located in the Chambishi-Nkana basin near the northwestern border of the Kafue basement inlier in northern Zambia (Fig. 1). Mineralization occurred along a strike length of almost 14 km from the Nkana South mine site to the Mindola mine site Mindola, with a barren gap of 1.2 km. The Chambishi-Nkana basin is characterized by a geometrically complex structural architecture

which is interpreted to have been generated during a single NE-SW-oriented compressional event linked to the Pan-African Lufilian orogeny (Torremans et al. 2018). This progressive deformation resulted in asymmetric multiscale parasitic fold assemblages, with non-cylindrical NW-SE-oriented periclinal folds at Nkana. The Copperbelt Orebody Member (COM), the primary host of copper around Nkana, consists of variably organic-rich marine shales and siltstones (Selley et al. 2005).

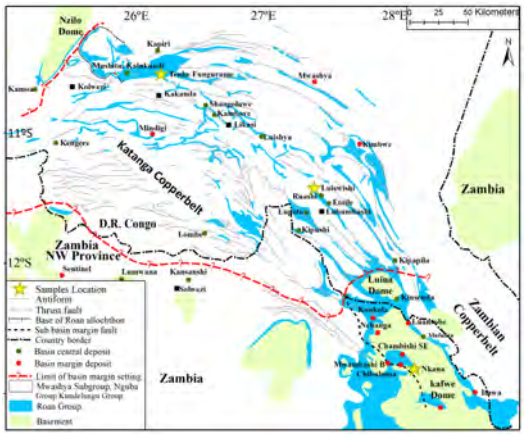


**Figure 1.** Location of the ore deposits studied in the Copperbelt (modified after Hitzman et al. 2012 and Mambwe et al. 2023).

The Luiswishi deposit is in the Katanga province, Democratic Republic of Congo (DRC), approximately 26 km north of Lubumbashi (Fig. 1). Lower and upper Cu-Co-rich orebodies are hosted in the Mines Subgroup, which is broadly correlative with the COM (Cailteux et al. 2005).

The Tenke Fungurume district, in the northwestern part of the Katanga Copperbelt (Fig. 1), is the largest copper-cobalt mining district in the DRC (1600 km$^2$). The Cu-Co mineralization is hosted within the lower (first), upper (second) and third orebodies within the Mines Subgroup, and is mainly present within the large fragments of the breccia (Mambwe et al. 2023). Recently mafic intrusions have been recognized in the Roan. They occur as sills and dikes and can be mapped in the field over a distance of more than a km. Gabbros but also mafic lavas and pyroclastics rocks are well known in the Roan (Kampunzu et al. 2000) and have been dated at 765 ± 5 Ma by U-Pb age dating on zircons. U-Pb age dating of zircons (Key et al. 2001). Zircons in altered volcanic pods in contact with the Nguba glacial deposits show a U-Pb age of 735 Ma (Key et al. 2001).

## 3 Methodology

Drill core samples were collected from mineralized zones at Nkana South and Nkana Central (COM), lower and upper orebodies at Luiswishi, and upper (second) and third orebody at Tenke Fungurume. The total organic content (TOC) of the samples was measured and based on these values, samples were selected for the preparation of polished sections to examine organic matter. Reflected light microscopy indicated that the organic matter present was solid bitumen. The solid bitumen reflectance was measured under reflected light using a Zeiss microphotometric instrument calibrated using a Zeiss yttrium-aluminium-garnet standard (R = 0.889%) and a Zeiss Cubic Zirconia standard (R = 3.125%) at the RWTH Aachen (cf. Schoenherr et al. 2007). The size of the solid bitumen measured ranges between 4 and 15 µm. This size was too small to measure the minimum and maximum reflectance taking into account the anisotropy of the vitrinite particles. Therefore only the random solid bitumen reflectance was measured.

## 4 Results and interpretation

The random solid bitumen reflectance ($BR_r$) measurements show very consistent results for the three deposits studied. At Nkana, solid bitumen reflectance shows a Gaussian distribution and varies between 2.6% and 4.1%, with an average of 3.5% (Table 1). The average $BR_r$ is lower at Luiswishi (2.6%; Table 1), as expected from the general decrease of the metamorphic grade in this direction. At Tenke Fungurume, sample CB22MP46 yielded a mean $BR_r$ of 2.2% (Table 1). Higher reflectance values, between 3.8 and 5.4% with an average $BR_r$ of 4.7% (Table 1) were measured in sample CB22MP49 (Fig. 2). The reflectance values measured at Nkana, Luiswishi and in sample CB22MP46 at Tenke Fungurume are interpreted to reflect the maturation of the solid bitumen during maximum burial. Higher values in sample CB22MP49 reflect higher temperatures which can be caused by hydrothermal fluids, although we cannot exclude the local influence of the mafic intrusion at Tenke Fungurume.

**Table 1.** Solid bitumen reflectance and calculated corresponding vitrinite reflectance of samples from the Nkana (NS12KT17), Luiswishi (LS06HA50) and Tenke Fungurume (CB22MP46, CB22MP49) deposits in the Central African Copperbelt. min.: minimum, max: maximum.

| Sample | Measurement (points) | $BR_r$(%) (min) | $BR_r$(%) (max) | $BR_r$(%) (mean) | $VR_r$(%) (min) | $VR_r$(%) (max) | $VR_r$(%) (mean) |
|---|---|---|---|---|---|---|---|
| CB22MP46 | 152 | 1.49 | 2.84 | 2.10 | 1.66 | 2.93 | 2.24 |
| LS06HA50 | 73 | 2.12 | 3.35 | 2.65 | 2.26 | 3.43 | 2.76 |
| NS12KT17 | 80 | 2.97 | 4.08 | 2.52 | 3.06 | 4.12 | 3.58 |

| | | | | | | | |
|---|---|---|---|---|---|---|---|
| CB22MP49 | 100 | 3.85 | 5.36 | 4.67 | 3.90 | 5.34 | 4.68 |

**Table 2.** Calculated temperatures reached during burial (T burial) or by hydrothermal activity (T hydrothermal) at the Nkana, Luiswishi and Tenke Fungurume deposits based on the calculated vitrinite reflectance data.

| Sample | Measurement (points) | $VR_r$(%) (min) | $VR_r$(%) (max) | $VR_r$(%) (mean) | $T_{min}$(℃) (burial) | $T_{max}$(℃) (burial) | $T_{mean}$(℃) (burial) |
|---|---|---|---|---|---|---|---|
| CB22MP46 | 152 | 1.66 | 2.93 | 2.24 | 176 | 222 | 200 |
| LS06HA50 | 73 | 2.26 | 3.43 | 2.76 | 201 | 234 | 217 |
| NS12KT17 | 80 | 3.06 | 4.12 | 3.58 | 225 | 249 | 238 |
| Sample | Measurement (points) | $VR_r$(%) (min) | $VR_r$(%) (max) | $VR_r$(%) (mean) | $T_{min}$(℃) (hydrothermal) | $T_{max}$(℃) (hydrothermal) | $T_{mean}$(℃) (hydrothermal) |
| CB22MP49 | 100 | 3.90 | 5.34 | 4.68 | 326 | 366 | 350 |

In order to calculate the palaeotemperature from the random solid bitumen reflectance, the $BR_r$ values were converted to random vitrinite reflectance ($VR_r$) based on the equation given by Schoenherr et al. (2007): VRr = ($BR_r$ + 0.2443)/ 1.0495. Barker and Pawlewicz (1994) propose the equation $T_{peak}$ (°C) = (ln($VR_r$) + 1.68)/0.0124 is valid for maximum burial temperatures obtained due to burial of the sedimentary rocks or heating by external sources such as hydrothermal fluids or a proximal intrusion(s). The $T_{peak}$ range at Nkana is from 226 to 250°C (average: 239°C), corresponding to the anchimetamorphic zone (Kisch 1990). This temperature range is lower than the upper greenschist facies based on REY signatures of uranium oxides and the alteration assemblages at Nkana which indicate a temperature greater than 300 and 350°C, respectively (Eglinger et al. 2013). This indicates the hydrothermal mineralizing fluids that moved through the sedimentary basin were at higher temperatures than the host-rock and that these hot fluids did not have an impact on the bitumen reflectance. The calculated maximum burial temperature at Luiswishi is between 201 and 235°C corresponding to the transition of the diagenetic to the anchizone (180-230°C; Kisch 1990; Frey and Robinson 1999). This temperature range is in agreement with the low Y content of uranium oxides dated at ca 530 Ma from Luiswishi and the Kolwezi area which indicate a crystallization temperature below 350°C (Eglinger et al. 2013). The maximum burial temperature of 201-235°C is significantly lower than the minimum temperature of the mineralizing fluid (280-350°C) present during deep burial and orogenesis as deduced from fluid inclusions microthermometry (El Desouky et al. 2009) indicating that the fluid migrated upwards from deeper parts of the basin and likely the basement (Van Wilderode et al. 2015). The maximum burial temperature calculated at Tenke Fungurume is between 200 and 220°C and slightly lower than the temperature at Luiswishi. This is in agreement with the general decrease in the metamorphic to diagenetic grade from the south-east to the north-west in the Copperbelt. Also in these cases the hot mineralizing fluids did not affect the bitumen reflectance in the host rocks.

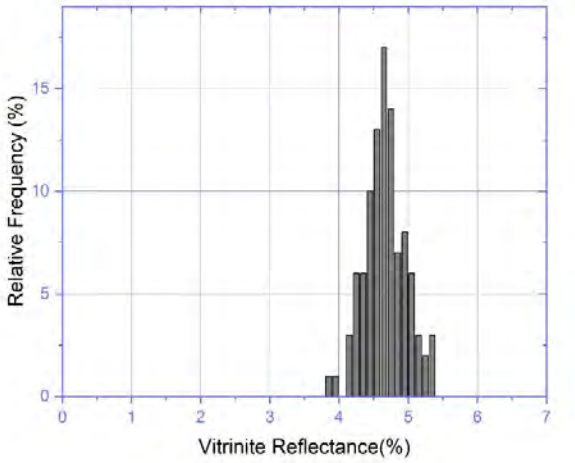


**Figure 2.** Histogram of the solid bitumen reflectance of sample CB22MP49 from Tenke Fungurume in the Congolese Copperbelt.

The temperatures calculated for the solid bitumen in sample CB22MP49 at Tenke Fungurume (326-366°C), corresponds to the homogenization temperatures measured in fluid inclusions in late burial to syn- and late orogenic carbonates and quartz cements associated with massive sulfide mineralization. The observed high thermal maturation is interpreted to be due to the migration of hydrothermal fluids at Tenke Fungurume. The high grade and metal volume of this district could indicate mineralization resulted from a pervasive migration of hot hydrothermal fluids through the rocks at Tenke Fungurume. Basson et al. (2022) recently focused the attention to the particular tectonic position of this district which could form a dilatant zone facilitating the upwards migration of large amounts of hydrothermal fluids and the precipitation of metals at these low-pressure sites.

## 5 Conclusion

The study of solid bitumen reflectance allows us to deduce the maximum temperature that the hosting sediments experienced. Reflectance calculations indicate a maximum burial temperature in the Congolese parts of the Copperbelt of 200-235°C and 222-250°C in Nkana, Zambia. These temperature

ranges are significantly lower than the temperatures of the hydrothermal fluids present during maximum burial and the Pan-African Lufilian orogeny, indicating that these hot fluids did not influence the bitumen reflectance of the host rock. However, solid bitumen indicating high temperatures of 326-366°C, corresponding to that of hydrothermal fluids that have been measured at Tenke Fungurume, is interpreted to be due to the pervasive migration of the hydrothermal fluid through the rocks.

**Acknowledgement**

We thank the reviewer Garth Graham for the constructive comments. The PhDs of Qiuping Liu and Pascal Mambwe are respectively supported by a CSC scholarship (China) and the Marc Vervenne Fund (KU Leuven). Gecamines and Tenke Fungurume Mining are thanked for access to their concessions, the sampling of the boreholes and the permission to publish the results of this research. Thanks to Macherey Donka (RWTH) for the preparation of the polished sections for the study of the organic material. Pascal Mambwe and Philippe Muchez are member of the SIM$^2$ – KU Leuven Institute for Sustainable Metals and Minerals. Financial support from the research grant C14/21/056 of the KU Leuven Special Research Fund is acknowledged.

## References

Armstrong RA, Master S, Robb LJ (2005) Geochronology of the Nchanga Granite, and constraints on the maximum age of the Katanga Supergroup, Zambian Copperbelt. J Afr Earth Sci 42:32-40

Barker CE, Pawlewicz MJ (1994) Calculation of vitrinite reflectance from thermal histories and peak temperatures. A comparison of methods. In: Mukhopadhyay PK, Dow WG (eds.) Vitrinite reflectance as a maturity parameter: applications and limitations. ACS Symposium series, pp 216-229

Basson IJ, McCall M-J, Koegelenberg CK, Jakaitė L (2022) Emplacement and preservation of mineralized écaille within Roan Breccia of the Lufilian Arc, Central African Copperbelt: the Thrust Belt Boudinage model. Mineralium Deposita 58:511-529

Brems D, Muchez Ph, Sikazwe O, Mukumba W (2009) Metallogenesis of the Nkana copper-cobalt South Orebody, Zambia. J Afr Earth Sci 55:185-196

Cailteux JLH, Kampunzu AB, Lerouge C, Kaputo AK, Milesi JP, (2005) Genesis of sediment-hosted stratiform copper-cobalt deposits, central African Copperbelt. J Afri Earth Sci 42:134-158

Davey J, Roberts S, Wilkinson JJ (2020) Copper- and cobalt-rich, ultrapotassic bittern brines responsible for the formation of Nkana-Mindola deposits, Zambian Copperbelt. Geology 49:341-345

De Swardt A, Drysdall A (1964) Precambrian geology and structure in central Northern Rhodesia. Geological Survey of Zambia Memoir, 2:82

Dewaele S, Muchez Ph, Vets J, Fernandez-Alonzo M, Tack L, (2006) Multiphase origin of the stratiform Cu-Co ore deposits in the western part of the Lufilian fold-and-thrust belt, Katanga (Democratic Republic of Congo). J Afr Earth Sci 46:455-469

Eglinger A, André-Mayer A-S, VanderhaegheO, Mercadier J, Cuney M, Decrée S, Feybesse J-L, Milesi J-M (2013) geochemical signatures of uranium oxides in the Lufilian belt: From unconformity-related to syn-metamorphic uranium deposits during the Pan-African orogenic cycle. Ore Geol Rev 54:197-213

Kampunzu AB, Tembo F, Matheis G, Kapenda D, Huntsman-Mapila P (2000) Geochemistry and tectonic setting of mafic igneous units in the Neoproterozoic Katanga basin, central Africa: implications for Rodinia break up. Gondwana Research 3:125-153

Key RM, Liyungu AK, Njamu FM, Somwe V, Banda J, Mosley PN, Armstrong RA (2001) The western arm of the Lufilian Arc in NW Zambia and its potential for copper mineralization. J Afr Earth Sci 33:503-528

El Desouky HA, Muchez P, Cailteux J (2009) Two Cu-Co sulfide phases and contrasting fluid systems in the Katanga Copperbelt, Democratic Republic of Congo. Ore Geol Rev 36:315-332

Frey M, Robinson D (1999) Low-grade metamorphism. Blackwell Science, Oxford.

Heijlen W, Banks D, Muchez Ph, Stensgard BO, Yardley BWD (2008) The nature of mineralizing fluids of the Kipushi Zn-Cu deposit, Katanga, Democratic Republic of Congo: Quantitative fluid inclusion analysis using laser ablation ICP-MS and bulk crush-leach methods. Econ Geol 103:1459-1482

Hitzman MW, Broughton D, Selley D, Woodhead J, Wood D, Bull S, (2012) The Central African Copperbelt: Diverse stratigraphic, structural, and temporal settings the world's largest sedimentary copper district. Society of Economic Geologists Special Publication 16:487-514

Kisch HJ (1990) Calibration of the anchizone: a critical comparison of illite "crystallinity" scales used for definition. J Meta Geol 8:31-46

Mambwe P, Swennen R, Cailteux J, Chabu M, Dewaele S, Muchez Ph (2023) Review of the origin of breccias and their resource potential in the Central Africa Copperbelt. Ore Geol. Rev. 156:105389

Master S, Rainaud C, Armstrong RA, Phillips D, Robb LJ (2005) Provenance ages of the Neoproterozoic Katanga Supergroup (Central African Copperbelt), with implications for basin evolution. J Afr Earth Sci 42:41-60

Richards JP, Krogh TE, Spooner ETC (1988) Fluid inclusion characteristics and U-Pb rutile age of late hydrothermal alteration and veining at the Musoshi stratiform copper deposit, Central African Copper Belt, Zaire. Econ Geology 83:118-139

Selley D, Broughton D, Scott RJ, Hitzman M, Bull SW, Large RR, McGoldrick PJ, Croaker M, Pollington N, Barra F (2005) A new look at the geology of the Zambian Copperbelt. Econ Geol 100:965-1000

Schoenherr J, Littke R, Urai JL, Kukla PA, Rawahi Z, (2007) Polyphase thermal evolution in the Infra-Cambrian Ara Group (South Oman Salt basin) as deduced by maturity of solid reservoir bitumen. Organic Geochemistry 38:1293-1318

Stach E, Mackowsky M-Th, Teichmüller M, Taylor GH, Chandra D, Teichmüller R (1982) Stach's Textbook of Coal Petrology. Gebrüder Borntraeger, Berlin, pp 535

Torremans K (2016) Fracture and seal processes and their effect on the development of transient permeability structures in brittle-ductile environments. PhD Thesis, KU Leuven, Belgium

Torremans K, Muchez Ph, Sintubin M (2018) Non-cylindrical parasitic folding and strain partitioning during the Pan-African Lufilian orogeny in the Chambishi-Nkana basin, Central African Copperbelt. Solid Earth 9:1011-1033

Van Wilderode J, Debruyne D, Torremans K, Elburg MA, Vanhaecke F, Muchez P (2015) Metal sources for the Nkana and Konkola stratiform Cu-Co deposits (Zambian Copperbelt): Insights from Sr and Nd isotope ratios. Ore Geol Rev, 67:127-1

# The Iron Creek Deposit in the Idaho Cobalt Belt: On a Quest for Cobalt Using Co-Registered Datasets Across Scales

**Daniel Schmidt[1], Miranda Lehman[1], Katharina Pfaff[1], Thomas Monecke[1], Albert Hofstra[2], Geoff Phelps[2], Reed Lewis[3], Simon Kocher[1], Zane Jobe[1], Virginia Gillerman[3], Warren Day[2], Mark Caddick[4], Eric Anderson[2], Jacob Harrison[1], Dan Pace[5]**

*[1]Department of Geology and Geological Engineering, Colorado School of Mines, USA*
*[2]U.S. Geological Survey, Denver, USA*
*[3]Idaho Geological Survey, Moscow, USA*
*[4]Department of Geosciences, Virginia Tech, USA*
*[5]Electra Battery Materials, Toronto, CA*

**Abstract.** A thorough understanding of the mineralogy and geochemistry of rocks in the subsurface is key to exploration and assessments for (critical) mineral resources. To achieve this, datasets of various types must be rapidly acquired and interpreted across a range of scales in 3-D. This approach was applied to the strata-bound Iron Creek Co-Cu deposit in the Idaho Cobalt belt. The deposit is hosted in the Apple Creek Formation of the Mesoproterozoic Belt-Purcell basin. At Iron Creek, three discrete Co-rich intervals were identified that are associated with a chlorite-rich alteration halo. X-ray fluorescence, hyperspectral, and magnetic susceptibility data on drill core paired with optical petrography and SEM-based automated mineralogy analysis of thin sections reveal the occurrence of early cobaltiferous pyrite at Iron Creek and magnetite in the Ruby zone. Later main-stage ore minerals include cobaltiferous pyrite with abundant Bi-telluride inclusions and chalcopyrite that are associated with chlorite alteration. Cretaceous syn-metamorphic silicification and quartz veins contain cobaltiferous pyrrhotite and minor galena and sphalerite. Post-metamorphic reequilibration of pyrrhotite resulted in the formation of marcasite/pyrite, and cobaltite-vaesite.

## 1 Introduction

The Iron Creek Co-Cu deposit is located in the south-eastern portion of the Idaho Cobalt belt (ICB), a northwest-trending alignment of cobalt +/- copper deposits and prospects in the Salmon River Mountains of east-central Idaho, USA, that represents a cobalt resource of national importance for the USA (Fig. 1A; Landis and Hofstra 2012). The deposit is hosted within the Mesoproterozoic Apple Creek Formation, a greenschist grade lacustrine succession of argillite-siltite and siliceous units (Ristorcelli and Schlitt 2019). The succession has been divided into five members and the Co-Cu mineralization is contained in the uppermost Banded Siltite member which consists of abundant quartz, muscovite, biotite, and chlorite with minor apatite, plagioclase, and Fe-Mn-oxides. The mineralized rocks contain pyrite, pyrrhotite, chalcopyrite, and magnetite and are generally associated with cross-bedded, quartzite layers (<50 cm). Ore minerals conform to bedding that

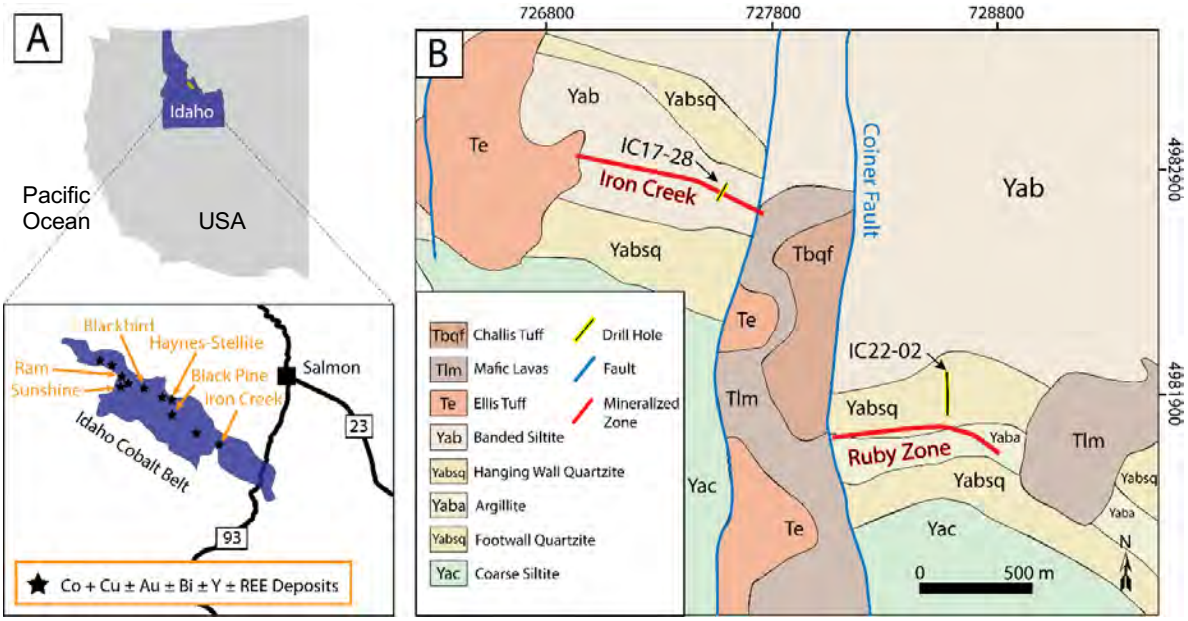


**Figure 1.** A) Idaho Cobalt belt, Idaho, USA, and B) Iron Creek deposit with the Iron Creek and Ruby zone drill collars indicated.

generally strikes north-northwest and dips between 60° and 80° northeast. Cobalt is sequestered mainly in pyrite and Cu is contained mainly in chalcopyrite. The indicated resource for the Iron Creek deposit is 4.5 million tonnes at 0.19% cobalt and 0.73% copper; the inferred resource is 1.2 million tonnes at 0.08% cobalt and 1.34% copper (Perron et al. 2023).

The aim of this study is to better understand the ore and alteration mineralogy, geochemistry, and magnetic susceptibility of rocks in the subsurface, and propose possible ore forming processes for the deposit. Continuous X-ray fluorescence (XRF), short-wave infrared core scanning, and magnetic susceptibility measurements on drill core were evaluated using cluster analysis techniques. Thin sections of representative samples from high-grade ore zones and host rock types were investigated using optical microscopy and scanning electron microscopy-based automated mineralogy, field-emission scanning electron microscopy (FE-SEM) backscatter electron (BSE) imaging, and semi-quantitative energy dispersive spectrometry (EDS). These data were used to advance understanding of the occurrence and geometries of ore bodies and alteration halos, their relation to geologic features and magnetic anomalies, and ore-forming processes.

## 2 Samples

Samples were collected from two drill holes, one from Iron Creek (IC-17-28) and one from the Ruby zone (IC-22-02), that intercept high-grade Cu-Co mineralisation (Fig. 1B). Thirteen additional outcrop samples were collected from representative host rock units in the ICB.

The 293 m long drill hole from Iron Creek intersects the high-grade portions of Co-rich and Cu-Co-rich ore zones. The 374 m long drill hole from the Ruby zone intersects two Co-rich ore zones.

## 3 Methods

Core from both drill holes were analysed using a continuous XRF core-scanner by Minalyze AB with data integrated over 10 cm intervals. To quantify a wide range of elements, drill core was first scanned at 40 kV and 8 mA, for K through Pb, and then scanned at 15 kV and 24 mA with a He flush, to detect lighter elements from Na to Cl. XRF elemental results were then examined and compared to existing multi-element assay data and core logs.

A short-wave infrared (SWIR) push-broom style hyperspectral system (HySpex-SWIR384 camera) was employed to characterize the core using a consistent depth registration. The SWIR wavelength range (960-2500 nm) allows identification of many common alteration minerals. Core scanning and spectral interpretation was performed using Prediktera's Breeze GEO software. Breeze GEO implements the USGS Material Identification and Classification Algorithm to determine mineral classifications and abundances. These scans were used to identify minerals in alteration zones that envelop high-grade ore zones.

Magnetic susceptibility measurements were carried out on core in 10 cm intervals, using a KT-20 magnetic susceptibility meter. The average of three measurements per interval was calculated.

Based on continuous XRF data on core, cluster analysis was used to define six discrete chemofacies and a subsampling strategy was developed to characterize them.

Thin sections and epoxy mounts of subsamples from drill core and field samples were inspected under transmitted and reflected light, FE-SEM BSE and EDS, and SEM-based automated mineralogy using a Hitachi SU5000 platform operated at 20 keV acceleration voltage and a working distance of 10 mm. The Bruker automated mineralogy software package AMICS as well as the TESCAN automated mineralogy software package TIMA were used for data reduction.

## 4 Results and Discussion

X-ray fluorescence results for each drill core were compared to previous multi-element assay analyses (Dan Pace, pers. communication). At Iron Creek, a single main Cu ore body from 63 to 87 m depth was defined, with trends in Cu concentrations in agreement by both methods. Both methods identified three discrete Co-rich intervals (above the 0.18% CoEq cutoff). The first Co-rich interval overlaps with the Cu ore body and the second and third Co-rich intervals lie below the Cu ore body at 116-145 m and at 178-216 m. In the Ruby zone, XRF results were also consistent with assay data identifying two Co-rich intervals between 308 and 313 m (Fig. 2) and 364 and 365 m.

Based on continuous XRF data, Co has a strong positive correlation with As and Se, whereas Cu shows positive correlations with Te, Pb, and Zn. Chromium and Ni concentrations are elevated throughout the drill core and increase toward the Co-rich intervals (>180 ppm Co), where the values are highest (hundreds of ppm). The implied Cr and Ni halo around the Co-rich intervals could represent a useful tool for vectoring toward Co ore.

Short-wave infrared scans revealed a significant increase in the abundance of chlorite-group minerals around mineralised ore zones, whereas muscovite and illite are the predominant phyllosilicates in unmineralised host rocks (Fig. 2).

Magnetic susceptibility data show a significant contrast between host rocks above mineralised zones, below mineralised zones, and in mineralized zones. At Ruby, values outside the ore zones range from 0.85 x $10^{-3}$ to 0.002 x $10^{-3}$ SI, whereas values in the ore zones range from 1.37 x $10^{-3}$ to >2000 x $10^{-3}$ SI (Fig. 2). It is interesting to note that the magnetic susceptibility data acquired on mineralised intercepts are high across more than four meters of core (Fig 2).

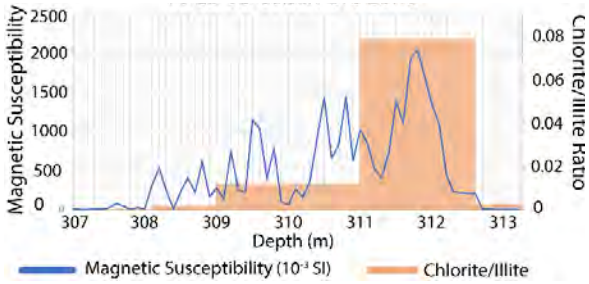


**Figure 2.** IC-22-02 core from the Ruby zone. Magnetic susceptibility data (in units of $10^{-3}$ SI) and chlorite/illite mineral ratios in high-grade cobalt ore between 308 and 313 m.

Petrographic observations of high-grade samples were used to identify a succession of ore and alteration minerals, including five discrete pyrite generations. Early cobaltiferous pyrite (py I) predates the main ore stage and is ubiquitous in samples from Iron Creek (Fig. 3A), whereas early magnetite and lesser pyrite (Fig. 3B) is abundant in samples from the Ruby zone. Early pyrite and magnetite, are associated with abundant biotite. Main stage ore minerals are represented by cobaltiferous pyrite (py II and III) with ubiquitous Bi-telluride inclusions (Figs. 3 C and D), and chalcopyrite with minor cattierite-vaesite accompanying pyrite III. Post ore pyrite (py IV) forms a porous overgrowth on main-stage pyrite II. Main-stage alteration comprises chlorite and muscovite (Fig. 3D). Late-stage, possibly syn-metamorphic silicification and quartz veins host cobaltiferous pyrrhotite with minor galena and sphalerite (Fig. 3E). Subsequent alteration resulted in replacement of Co- and Ni-bearing pyrrhotite by marcasite/pyrite (py V) and cobaltite-vaesite minerals (Fig. 3F). Supergene oxidation and weathering of pyrite led to the formation of jarosite, goethite, hematite and other secondary minerals.

Cobalt-Cu mineralisation is hosted in interlayered siltite, biotite phyllite and quartzite of the banded siltite unit within the Apple Creek Formation. Sediment deposition in the area is bracketed between ~1445 Ma (U-Pb on detrital zircons from the underlying Hoodoo Formation; Link et al. 2007) and ~1409 Ma (U-Pb on detrital zircons from the uppermost part of the banded siltite unit; Aleinikoff et al. 2012). Based on these ages and prior studies by Bookstrom et al. (2016) and Saintilan et al. (2017), we propose that early cobaltiferous pyrite (pyr I) at Iron Creek and early magnetite in the Ruby zone formed before the main ore stage. The epigenetic main-stage ore forming event is linked to emplacement of the ~ 1383-1359 Ma suite of bimodal gabbro-granite intrusions (Big Deer Creek, bordering the north-eastern margin of the ICB, dated at ~1377 ± 4 Ma (U-Pb on xenotime and monazite; Aleinikoff et al. 2012; Slack 2012). Saintilan et al. (2017)'s Re-Os dates on cobaltite from the Blackbird mine, the Haynes-Stellite mine, and the Black Pine mine (Fig. 1A; located to the north-west of Iron Creek in the ICB) led them to propose a model for the multi-stage REE-Y-Co-Cu-Au deposits that involve the discharge of magmatic hydrothermal fluids and convection of evaporitic brines at around 1370 to 1349 Ma.

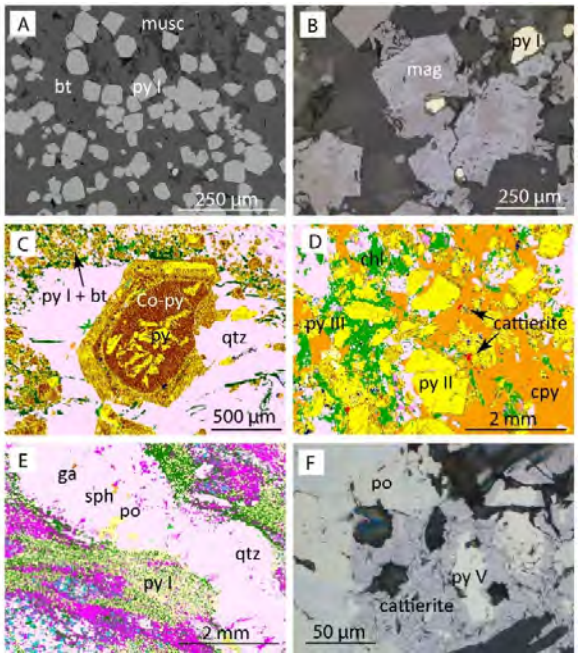


**Figure 3.** A) SEM-BSE image, pyrite I from Iron Creek, B) photomicrograph in reflected light showing early magnetite from the Ruby zone, C-E) automated mineralogy, C) abundant cobaltiferous pyrite I with biotite and later cobaltiferous pyrite II with minor chlorite, D) main-stage ore with abundant cobaltiferous pyrite II and III with chalcopyrite, minor cattierite and chlorite alteration, E) late silicification and quartz veinlet hosting cobaltiferous pyrrhotite, galena and sphalerite, and F) photomicrograph in reflected light showing replacement of pyrrhotite by marcasite/pyrite and cattierite.

Cretaceous metamorphism in the ICB led to a greenschist (Iron Creek) to amphibolite (Blackbird) facies overprint and associated silicification and quartz veining found in the Iron Creek deposit and elsewhere in the ICB (Nash and Hahn 1989, Aleinikoff et al. 2012). Evidence put forward by Saintilan et al. (2017) suggests that Cretaceous deformation and metamorphism during the Cordilleran orogeny remobilised metals in the ICB, which is represented at the Iron Creek deposit by cobaltiferous pyrrhotite, sphalerite, and galena deposited together with quartz in late structures.

Main-stage ore minerals (cobaltiferous pyrite and chalcopyrite) at Iron Creek and the Ruby zone have features that are similar to those in the Mesoproterozoic sediment-hosted Black Butte Co-Cu deposit on the eastern side of the Belt-Purcell basin. Black Butte is thought to have formed from moderate-temperature, reduced basinal brines, which entered pre-mineralised horizons with early-stage pyrite (py I) where main-stage cobaltiferous pyrite and chalcopyrite precipitated (Graham 2011; Pfaff and Graham 2013; Saintilan et al. 2021). Field relationships are consistent with a Mesoproterozoic age of main-stage Cu-Co mineralisation. Saintilan et al. (2021) suggested that Black Butte coincided with

an increased thermal gradient in the eastern portion of the Belt-Purcell basin caused by a tholeiitic dyke swarm around 1455 Ma (Re-Os isochron age).

## 5 Conclusions

Continuous XRF-scanning was used to acquire a complete geochemical dataset that enabled distinction of lithologies, and ore zones based on their chemistry. Short-wave infrared core scanning showed that chlorite-group minerals are abundant around mineralised ore zones, whereas muscovite and illite are predominant in unmineralized host rocks. Magnetic susceptibility data established links between the outcrop and regional scale. Mineralogically and geochemically informed sub-sampling strategies provided a better understanding of the ore and alteration mineralogy.

Three discrete Co-rich ore zones have been identified that are associated with a chlorite-rich alteration halo. Magnetic susceptibility data show a significant contrast between ore zones and host rock. Iron Creek and the Ruby zone differ significantly with early pre-main ore stage cobaltiferous pyrite at Iron Creek and early magnetite at the Ruby zone. Main-stage ore minerals include cobaltiferous pyrite with abundant Bi-telluride inclusions and chalcopyrite. Later silicification and concomitant quartz veining lead to the formation of cobaltiferous pyrrhotite and minor galena and sphalerite. Subsequent fluids caused the breakdown of pyrrhotite and formation of marcasite/pyrite, and cobaltite-vaesite. These insights shed new light on ore forming processes at Iron Creek and will be integrated into the existing body of research on other areas and deposits in the Idaho cobalt belt. Future work will include a more detailed understanding of the significance of the Coiner Fault and genetic relationships between Iron Creek and the Ruby zone.

## Acknowledgements

This study was conducted within the Center to Advance the Science of Exploration to Reclamation in Mining (CASERM), which is an industry-university collaborative research centre between Colorado School of Mines and Virginia Tech under NSF award numbers 1822108 and 1822146. Thanks to Craig Johnson and Karen Kelley for insightful reviews that strengthened this contribution. We thank Kelsey Livingston and Filip Kasprowicz for their invaluable assistance with expedient sample preparation. Any use of trade, firm, or product names is for descriptive purposes only and does not imply endorsement by the U.S. government.

## References

Aleinikoff J et al (2012) Constraints on the Timing of Co-Cu ± Au Mineralization in the Blackbird District, Idaho, Using SHRIMP U-Pb Ages of Monazite and Xenotime Plus Zircon Ages of Related Mesoproterozoic Orthogneisses and Metasedimentary Rocks. Econ Geol 107: 1143-1175

Bookstrom A et al (2016) Geologic history of the Blackbird Co-Cu district in the Lemhi subbasin of the Belt-Purcell Basin. In: Maclean JS, and Sears JW Belt Basin: Window to Mesoproterozoic Earth. Geololgic Society of America, Idaho, pp 185-219 https://doi.org/10.1130/2016.2522(08)

Landis GP, Albert HH (2012) Ore Genesis Constraints on the Idaho Cobalt Belt from Fluid Inclusion Gas, Noble Gas Isotope, and Ion Ratio Analyses. Econ Geol 107: 1189-1205. https://doi.org/10.2113/econgeo.107.6.1189

Graham GE (2011) Geologic and stable isotope investigation of the Sheep Creek Cu-(Co-Ag) deposit with comparison to other sediment-hosted base metal deposits in Mesoproterozoic basins. Dissertation, Colorado School of Mines

Johnson FL et al (1998) Mineral resource appraisal of the Salmon National Forest, Idaho (p. 277). US Geologic Survey Open-File Report 98-478: pp 277 https://doi.org/10.3133/ofr98478

Link PK et al (2007) Detrital zircon populations and provenance of Mesoproterozoic strata of east-central Idaho, U.S.A.: Correlation with Belt Supergroup of southwest Montana. Society for Sed Geology (SEPM) Spec Pub: 101–128.

Nash JT, Hahn GA (1989) Stratabound Co-Cu deposits and mafic volcaniclastic rocks in the Blackbird mining district, Lemhi County, Idaho: Geological Association of Canada Special Paper 36: 339–356

Perron M, Beauvais MR, Kinnan E (2023) NI 43-101 Technical Report and Mineral Resource Estimate for the Iron Creek Cobalt-Copper Property, Lemhi County, Idaho, USA. Prepared for Electra Battery Materials. https://electrabmc.com/wp-content/uploads/2023/03/Iron-Creek-Tech-Report-2023-Final.pdf

Pfaff K, Graham GE (2013) The Black Butte Cu-(Co-Ag) deposit, Montana: A thermodynamic model. GSA Annual Meeting & Exposition, Denver, Colorado, USA

Ristorcelli SJ, Schlitt J (2019) Amended Technical Report and Estimate of Mineral Resources for the Iron Creek Cobalt-Copper Project, Lemhi County, Idaho, USA: NI 43-101 Technical Report prepared for First Cobalt Corp.

Saintilan NJ, Creaser RA, Bookstrom AA (2017) Re-Os systematics and geochemistry of cobaltite (CoAsS) in the Idaho cobalt belt, Belt-Purcell Basin, USA: Evidence for middle Mesoproterozoic sediment-hosted Co-Cu sulfide mineralization with Grenvillian and Cretaceous remobilization, Ore Geology Reviews 86: 509-525. https://doi.org/10.1016/j.oregeorev.2017.02.032.

Saintilan N et al (2021) Synsedimentary to Diagenetic Cu±Co Mineralization in Mesoproterozoic Pyritic Shale Driven by Magmatic-Hydrothermal Activity on the Edge of the Great Falls Tectonic Zone–Black Butte, Helena Embayment, Belt-Purcell Basin, USA: Evidence from Sulfide Re-Os Isotope Geochemistry. Lithosphere 2021: 7866186. https://doi.org/10.2113/2021/7866186

Slack J (2012) Strata-Bound Fe-Co-Cu-Au-Bi-Y-REE Deposits of the Idaho Cobalt Belt: Multistage Hydrothermal Mineralization in a Magmatic-Related Iron Oxide Copper-Gold System. Econ Geol 107: 1089-1113

# The enigmatic nature of normal faults in sediment hosted Zn-Pb deposits

**Christopher Reed[1], Malcolm Wallace[2], Mana Ryuba[2], Nicola Cawood[1], Conor Moynihan[3], Jim McCusker[4], and Sam Spinks[1]**
*[1] Teck Australia Pty Ltd, Australia*
*[2] School of Geography, Earth and Atmospheric Sciences, University of Melbourne*
*[3] Teck Ireland Ltd, Ireland*
*[4] Teck Madencilik, Turkey*

**Abstract.** The common association between sediment-hosted Zn-Pb deposits and normal faults has led to a view that faults are the main conduits for the transport of mineralizing fluids. This is at odds with the petroleum industry where faults commonly act as seals. Here we present two examples of sediment-hosted Zn-Pb deposits where we can demonstrate that the faults were not active during the time of mineralization. Instead, the main fault formed early in the history of the basin and was responsible for the formation of structural and stratigraphic traps. These traps became the focus of later fluids derived from the basin. The presence of hydrocarbons in the deposits suggests that the mineralizing fluids and the hydrocarbons may have shared the same migration pathway. This does not preclude fault rock and fault derived porosity playing a role at a certain scale. However, the general absence of mineralization or related alteration along faults regionally challenges the notion that they are significant conduits. We must therefore take a more holistic view to the generation and migration of fluids responsible for sediment-hosted Zn-Pb deposits and consider a range of basin related processes.

## 1 Introduction

Sedimentary hosted Zn-Pb deposits are often spatially associated with normal faults. This has led to many ore deposit models where the fault is directly related to the formation of the deposit. In many models that fault is considered a conduit that allows deep metal rich fluids to ascend to shallower levels or even to the seafloor (Large et al. 1998). Others suggest a hybrid model where faults act as both regional deep tapping structures but also seals at the trap site (Hayward et al. 2021). These seemingly contradictory hypotheses challenge our understanding of the role of faults in basin fluid flow. They are also at odds with the petroleum industry where faults are typically seen as aquitards or seals to fluid migration (Fulljames et al. 1997; Bretan et al. 2020). Below we consider two mineral deposit examples that challenge the broadly held view of how faults operate as regional conduits for mineralizing fluids.

## 2 Ballinalack

The Ballinalack Deposit is an example of MVT Zn-Pb mineralization in the central Irish Midlands (Stacey et al. 2022). The mineralization is hosted within the Waulsortian Limestone, is diagenetic in origin, and occurs in the hangingwall of a normal fault (the Ballinalack Fault, Figure 1). The deposit occurs in a faulted paleohigh and is capped by an unconformity marked by the Tober Collen Formation. The unconformity constrains the age of the fault to before the emplacement of the mineralization (de Morton et al. 2015). Similarly, the ABL thickens away from the paleohigh suggesting it was present during the deposition on this unit. Further drilling along strike has not identified further zones of mineralization. Given that mineralization is restricted to the paleohigh, we conclude that earlier faulting was important for creating a paleohigh that focused fluids from the adjacent basin into a structural high. The absence of mineralization along the fault suggests that it did not act more broadly as a conduit for ascending fluids.

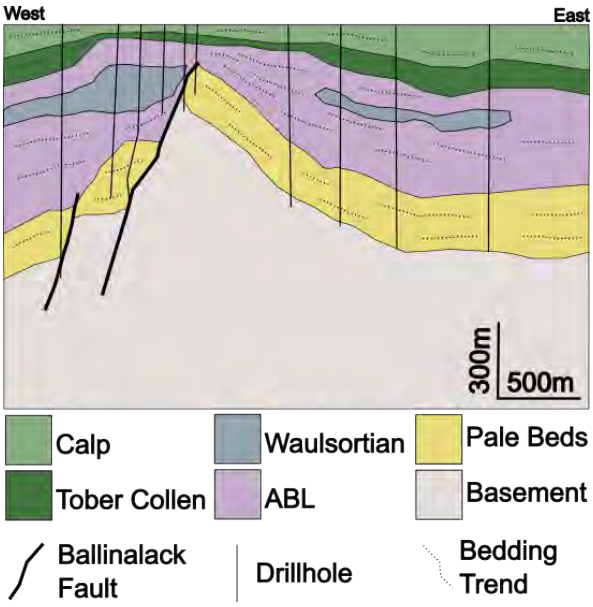


**Figure 1.** EW cross section of the Ballinalack deposit modified from de Morton et al. (2015). The main zone of Zn-Pb mineralization occurs in the Waulsortian Limestone on the hangingwall of the Ballinalack Fault. The ABL Formation thins onto the paleohigh. The Tober Collen Formation sits unconformably on the ABL Formation and constrains the timing of the fault.

## 3 Teena

The Teena deposit in Northern Australia is an example of a sediment-hosted stratiform Zn-Pb deposit (Hayward et al. 2021). It is similar in style to the McArthur River deposit which is located

approximately 10km to the east (Spinks et al. 2021). Both occur in the Paleoproterozoic McArthur Basin.

The Teena mineralization replaces carbonate units within a fine-grained clastic sequence (the Barney Creek Formation) in the hangingwall of a major normal fault (Teena Fault, Figure 2). The major fault system is considered an important structural control for fluid migration (Hayward et al. 2021). Problematically, the Teena fault surface is more akin to a disconformity that overlies an earlier regional deformation event. The basal units of the Barney Creek Formation that host the mineralization, onlap this surface which constrains the age of faulting to before the deposition of the host sequence and the replacement mineralization. Subsequent deformation (during the Isan Orogeny) has further deformed this contact with bedding now near vertical in places. Given the relatively early timing of the faulting, it is difficult to envisage that the Teena fault could have acted as the primary conduit for the ascent of fluids from kilometers depth. Rather a more subtle onlap surface may have been the principal control for trapping basin derived fluids with later deformation obscuring the true nature of the contact.

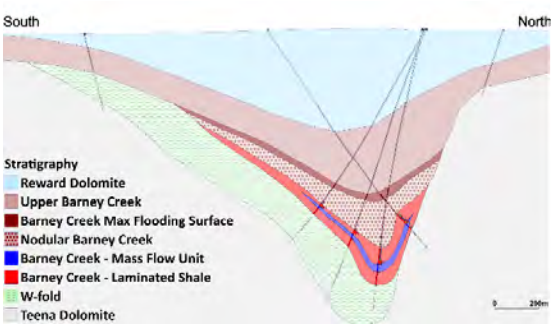


**Figure 2.** NS cross section of the Teena Zn-Pb deposit. The Zn-Pb mineralization occurs in the centre of the Teena Syncline in the Laminated Shale Unit. To the north (right), the basal units of the Barney Creek Formation onlap onto a disconformity (previously interpretated as the Teena Fault). After the main mineralization event, the sequence has been deformed during the Isan Orogeny which has resulted in a tight syncline and obscuring the earlier geometry.

## 3 Discussion

Hydrocarbons migrate in sedimentary basins through a range of processes, principal of which is flow through more permeable stratigraphy to structural and stratigraphic traps (Selley 1998). These traps share many characteristics of those that host Zn-Pb deposits. Many Zn-Pb deposits also preserve evidence of hydrocarbons (Wallace et al. 2002). Hydrocarbons and Zn-rich fluids must therefore at least share the same trap site and by extension the same fluid pathway. A genetic link between the two processes has also been advocated (Sanz-Robinson and Williams-Jones 2019; Stacey et al. 2022).

The observations presented here do not invalidate faults as fluid conduits and controls on the localization of mineralization. Indeed, the importance of fault breccias has been demonstrated at Lisheen, Galmoy and Silvermines (Kyne et al. 2019). Perhaps the more pertinent questions are; how prevalent are these rocks in different mineralized settings, what is the vertical extent for focusing fluids from depth, and how long can they maintain porosity in the burial environment. The answer to these questions is less clear and perhaps more likely these fault zones represent local controls at the trap site rather than the regional fluid flow conduits.

## 4 Conclusion

In summary, we suggest that faulting early in the basin history is responsible for the formation of structural and stratigraphic traps and the faults then act predominately as seals. The trap sites are the focus for burial fluids that migrate to the structural highs through mechanisms more akin to the migration of hydrocarbons in sedimentary basins. The close association between Zn-Pb deposits and faults is therefore a product of early basin development rather than a direct genetic link. To improve discovery rates, we should not assume that faults are the primary control and instead take a more holistic view of basin development that considers the full range of basin processes and the mechanisms of fluid migration.

## Acknowledgements

The authors would like to thank all the Teck Resources team that have contributed to collection and synthesis of the data and ideas presented here.

## References

Bretan PG, Yielding G, Sverdrup E (2020) A knowledge database of hanging-wall traps that are dependent on fault-rock seal. Geological Society, London, Special Publications 496(1):209–222. https://doi.org/10.1144/SP496-2018-157

de Morton SN, Wallace MW, Reed CP, Hewson C, Redmond P, Cross E, Moynihan C (2015) The significance of Tournaisian tectonism in the Dublin basin: Implications for basin evolution and zinc-lead mineralization in the Irish Midlands. Sedimentary Geology 330:32–46. https://doi.org/10.1016/j.sedgeo.2015.09.017

Fulljames JR, Zijerveld LJJ, Franssen RCMW (1997) Fault seal processes: systematic analysis of fault seals over geological and production time scales. In: Norwegian Petroleum Society Special Publications. Elsevier, pp 51–59

Hayward N, Magnall JM, Taylor M, King R, McMillan N, Gleeson SA (2021) The Teena Zn-Pb Deposit (McArthur Basin, Australia). Part I: Syndiagenetic Base Metal Sulfide Mineralization Related to Dynamic Subbasin Evolution. Economic Geology 116(8):1743–1768. https://doi.org/10.5382/econgeo.4846

Kyne R, Torremans K, Güven J, Doyle R, Walsh J (2019) 3-D Modeling of the Lisheen and Silvermines Deposits, County Tipperary, Ireland:Insights into Structural Controls

on the Formation of Irish Zn-Pb Deposits. Economic Geology114(1):93–116. https://doi.org/10.5382/econgeo.2019.4621

Large RR, Bull SW, Cooke DR, McGoldrick PJ (1998) A genetic model for the H.Y.C. Deposit, Australia; based on regional sedimentology, geochemistry, and sulfide-sediment relationships. Economic Geology 93(8):1345–1368. https://doi.org/10.2113/gsecongeo.93.8.1345

Sanz-Robinson J, Williams-Jones AE (2019) Zinc solubility, speciation and deposition: A role for liquid hydrocarbons as ore fluids for Mississippi Valley Type Zn-Pb deposits. Chemical Geology 520:60–68. https://doi.org/10.1016/j.chemgeo.2019.05.002

Selley RC (1998) Elements of petroleum geology, 2nd ed. Academic Press, San Diego

Spinks SC, Pearce MA, Liu W, Kunzmann M, Ryan CG, Moorhead GF, Kirkham R, Blaikie T, Sheldon HA, Schaubs PM, Rickard WDA (2021) Carbonate Replacement as the Principal Ore Formation Process in the Proterozoic McArthur River (HYC) Sediment-Hosted Zn-Pb Deposit, Australia. Economic Geology 116(3):693–718. https://doi.org/10.5382/econgeo.4793

Stacey J, Wallace M, Reed C, Moynihan C, Leonard W, Hood A (2022) A novel chemical model for burial diagenesis and Zn–Pb sulphide precipitation within the Carboniferous Waulsortian Limestone, Ireland. Sedimentary Geology 442:106297. https://doi.org/10.1016/j.sedgeo.2022.106297

Wallace MW, Middleton HA, Johns B, Marshallsea S (2002) Hydrocarbons and Mississippi Valley-type Sulfides in the Devonian Reef Complexes of the eastern Lennard Shelf, Canning Basin, Western Australia. In: The Sedimentary Basins of Western Australia 3. Perth, Western Australia, pp 795–816

# Detrital zircon mineral chemistry and U-Pb geochronology of coastal mineral sands, South Africa: provenance and exploration implications

**Abraham Rozendaal[1], Isabella van Breda[1], René Heyn[1], Carlo Philander[2]**
*[1] Department of Earth Sciences, Stellenbosch University, Stellenbosch, 7602, Western Cape, South Africa.*
*[2] Tronox Mineral Sands Pty Ltd*

**Abstract.** Cenozoic heavy mineral placer deposits along the west and east coast of South Africa have been studied with the aim to determine the relationship between the U-Pb age and mineral chemistry of individual detrital zircons. Provenance characteristics of the geologically complex basement rocks will have an influence on the abundance and quality of zircons supplied to the coastal depocentres and ultimately contribute to the economic viability of heavy mineral concentrations. To this end zircons from two operating mines and a brown- and green-field deposit, were separated and then analysed by LA-ICP-MS.
The results show that zircons wererderived from a magmatic provenance representative of the Mesoproterozoic to the Cambrian periods. Significant quantities of Cretaceous zircons however are limited to the west coast whereas Permian zircons are more prevalent along the east coast. The age-mineral chemistry relationship shows that the Cretaceous zircons are the best quality and Neoproterozoic zircons a heterogeneous population of low quality with respect to deleterious trace elements. Exploration should focus on placers located near ancient and relatively young granitoid intrusives and avoid terranes dominated by Neoproterozoic lithologies in southern Africa.

## 1 Introduction

Heavy mineral placer deposits are important resources of zircon and titanium oxides used in the paint, ceramics and specialized metals industry. These deposits are the focus of global exploration. The extensive coastline of South Africa, hosts amongst the largest placer deposits in the world (>1 billion tons at >5% Total Heavy Minerals (THM). Producing operations include Namakwa Sands and Tormin on the west coast as well as Fairbreeze and Richards Bay on the east coast (Fig. 1). The coastline offers significant brownfields and greenfields exploration potential.

The heavy mineral suite of the Namakwa Sands mine is the best studied with respect to mineralogy, mineral chemistry, zircon geochronology and genesis (Philander and Rozendaal 2015). The results indicate the relationship between zircon age (provenance) and the economically important, trace element chemistry (quality). The aim of this study is to confirm and quantify this relationship regionally by expanding the present database of Namakwa Sands and surroundings as well as to extend it towards the north along the west coast (Groen River). The Fairbreeze mine will be included to demonstrate the east-west coastal relationship.

**Figure 1**. Map of southern Africa showing the distribution of operating heavy mineral sand mines (red dots) and prospects (black dots). Map modified after Rozendaal et al. 2017.

## 2 Methodology

A total of 12 composite sand samples from four localities have been selected and include Groen River, Namakwa Sands and its satellite deposit Hartebeeste Kom as well as Fairbreeze (Fig. 1). These composites are representative of the most significant mineralized units in the coastal stratigraphy and derived from extensive, grid based exploratory auger and reverse circulation percussion drilling. The final saleable zircon concentrate produced at the Namakwa sands mine, was also included in the population.

Following drilling, the heavy mineral fraction (THM) was separated from every 1m sample by bromoform (ρ 2.9 g/cm$^3$). A composite was made of the THM based on geo-unit categorization and selective splitting to ensure representivity. The THM fraction was magnetically separated, zircons were hand-picked from the non-magnetic fraction, and zircons were mounted and prepared for scanning electron microscopy (SEM) imaging. Cathodoluminescence (CL) images were captured with a Zeiss MERLIN Field Emission Scanning Electron Microscope (FE-SEM) of the Electron Microbeam Unit, Central Analytical Facility (CAF), Stellenbosch University (SU).

To define the relationship between U-Pb age and trace element composition of the single zircon grains, two analytical spots were required. Spot position was guided by CL images and were placed in the same growth zone, core and/or rim to ensure a high degree of comparability (Fig. 2).

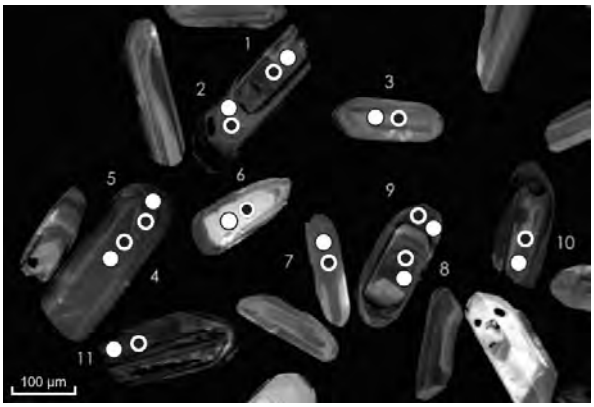


**Figure 2**. CL image showing spot selection for trace element mineral chemistry (white spots) and U-Pb geochronology (black spots) analyses.

Zircon U-Pb isotopic data was collected at the CAF, Stellenbosch University (SU) and at the EarthLab of the School of Geosciences, University of the Witwatersrand (UW), respectively. An Applied Spectra RESOlution 193 nm ArF excimer laser ablation system (SE-155) was employed at both facilities, coupled to a Thermo Scientific Element 2 (SU) or Element XR (UW) magnetic sector field inductively coupled plasma mass spectrometer. All zircon LA-ICP-MS trace element measurements were collected and processed at CAF, SU using a RESOlution 193 nm Excimer laser from Applied Spectra, connected to an Agilent 8800 QQQ ICP-MS.

## 3 Geological setting

All the heavy mineral deposits along the South African coast are hosted by a Cenozoic sequence of marine and aeolian siliciclastic sediments (Roberts et al. 2006). The regionally developed heavy mineral concentrations are the result of major marine transgression (producing wave-cut terraces), regression and progradation episodes along a post-Gondwana African passive margin. Extensive terrigenous reworking of the marine sediments produced mature aeolian sands and concentrated the heavy minerals. These unconsolidated sediments occur along the entire South African coastline. Within this depositional scenario the most significant heavy mineral concentrations occur near present-day or ancient fluvial systems which supplied heavy minerals from the hinterland.

Along the South African west coast the Cenozoic stratigraphic sequence is referred to as the West Coast Group and the Maputaland Group along the South African east coast (Figs. 1 and 3).

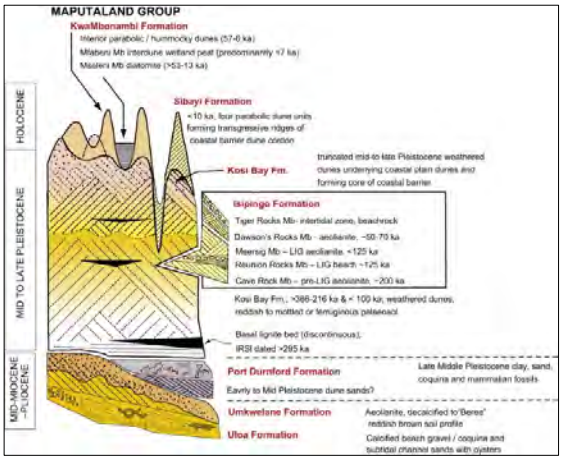


**Figure 3**. Lithostratigraphic composite section of the Maputalang Group along the South African east coast. The Fairbreeze deposit is hosted by the mineralized red aeolian sands of the Umkwelane and Khosi Bay Formations (after Botha 2018).

### 3.1 Basement characteristics

Lithologies forming the basement and main provenance of the Cenozoic Groups are diverse. Geographically the Paleo- to largely Mesoproterozoic Namaqua-Natal Metamorphic Province (NNMP) has the widest distribution, stretching from the west to the east coast. It has been subdivided into several subprovinces and tectonostratigraphic terranes based on regionally developed structural discontinuities, and metamorphic and lithological differences (Fig. 4; Cornell et al. 2006).

The overlying Neoproterozoic volcano-sedimentary lithologies of the orogenic Gariep and Saldania Belts are only developed along the west and south coast and the latter has been syn- to-post-tectonically intruded by Cambrian granitoids. Distribution of the Cambrian Nama and Vanrhynsdorp Groups are also restricted to the west coast (Gresse et al. 2006). Sediments of the Palaeozoic Cape Super Group and Palaeozoic-Mesozoic Karoo Supergroup cover most of the inland area. The youngest basement rocks are rift related Early- to Late-Cretaceous granitoid dyke and plug-like intrusive rocks confined to the west coast.

## 4 Results

Zircons selected for analyses are diverse with respect to morphology, colour, and size. Colourless zircons are the most abundant, with minor coloured grains. Metamict zircons are restricted to the west coast and were not suited for analysis. Some east coast zircons have inclusions and are well rounded compared to the west coast. Sedimentologically, this indicates a higher maturity.

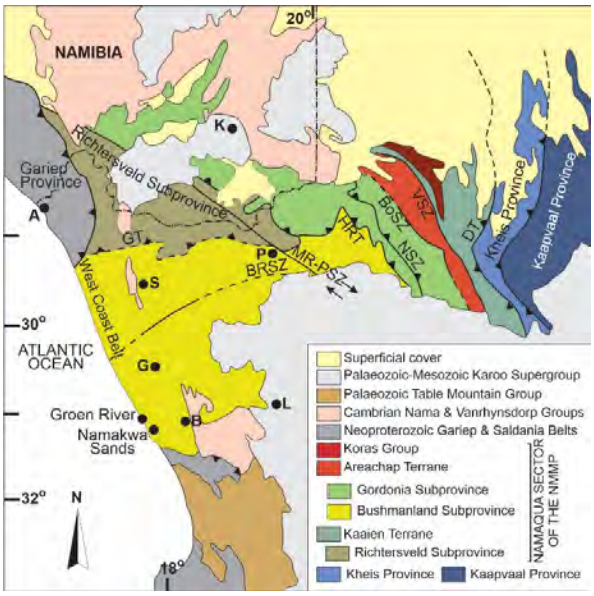


**Figure 4.** Basement rocks and main provenance of the Cenozoic sediments along the west coast. (Adapted from Macey et al 2014).

### 4.1 Zircon geochemistry

The most abundant trace elements hosted by the zircon population are Hf, Fe, Y, P, ∑REE, Al, K and U with lesser concentrations of Th, Sc, Ti, Pb, Mo and Nb. Most of these elements show similar median values throughout the dataset, Fairbreeze however recorded a lower Ti and slightly elevated Sc content. Individual Th/U ratios indicate that most of the zircons are of magmatic origin. The best discriminatory elements were U, Th and Pb (Fig.6)

### 4.2 Zircon geochronology

The range of ages displayed by the individual stratigraphic units was very similar and allowed the data to be presented as a single composite per locality. Along the west coast four age groups dominate and consist of: Early Cretaceous (~141 - 133Ma), Neoproterozoic (~631 to 551Ma), Cambrian (~550-460 Ma) and Mesoproterozoic (1168-1011Ma; Fig. 5a, b). The Fairbreeze deposit also displays four well defined age groups consisting of Permian (~366-263Ma), Neoproterozoic (~713 to 549Ma), Cambrian (~537-472Ma), and Mesoproterozoic (~1288-1011Ma; Fig. 5c). Quantitatively the combined Neoprotezoic-Cambrian zircon population dominates for the west coast but this is less distinct for the east coast. Early Cretaceous zircons are absent along the latter whereas Permian zircons are rare on the west coast. This distribution is provenance controlled.

### 4.3 Relationship between zircon U-Pb age and chemistry

The trace elements selected to demonstrate the age –chemistry relationship include U+Th and Pb whereas the P and Ti relationships are less well defined.

P and Ti,

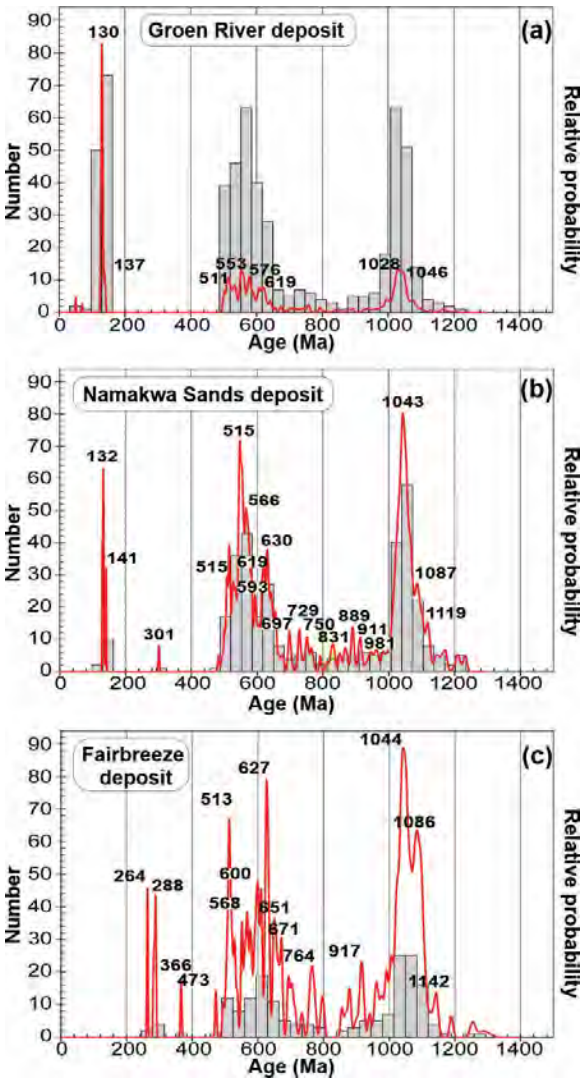


**Figure 5**. Age distribution of detrital zircons from a) Groen River, b) Namakwa Sands (both west coast), and c) Fairbreeze (east coast) deposits. Relative probability curves shown in red.

These substitution elements in zircon (U, Th, P and Ti) are considered contaminants and their concentration is an indication of the commercial quality zircon. . The (U+Th) vs Pb plot shows a positive linear relationship for the major age groups which are separated by differences in the (U+Th)/Pb ratio (Fig 6a,b). Along the west coast the Cretaceous population shows a ratio of 100 which is the highest and indicates an increase in (U+Th)/Pb ratio with decrease in age. The Mesoproterozoic grains do not contain more U+Th than the Neoproterozoic and Cambrian groups but the wide scattering of Neoproterozoic grains indicate a heterogeneous population. The U+Th content of Cretaceous zircons is the lowest of all age groups. Most (~80%) zircons contain less than 500ppm U+Th but is exceeded mainly by the Mesoproterozoic and Neoproterozoic

groups. The Fairview population displays similar trends (Fig. 6c). Permian grains however are U+Th enriched but the entire population is depleted compared to the west coast.

Iron content of zircons decrease with relative age. Heterogeneity of Neoproterozoic population is also confirmed by the iron content. Both P and Ti show a poor correlation with age.

## 5 Conclusions

Effectively all zircons have a magmatic provenance. The various age groups can be separated on their U+Th/Pb ratio. The youngest zircons have the highest ratio compared to the oldest and this distinction could be a function of secondary Pb generation by radioactive decay.

Cretaceous zircons have low concentrations of contaminant trace elements such as U, Th, Pb, Ti, and P and are of the best commercial quality . These are sourced from proximal granitoids with distribution limited to the west coast.

Neoproterozoic zircons are heterogeneous in composition and indicate a highly diverse provenance difficult to identify. The Mesoproterozoic and Cambrian zircons are relatively homogeneous and provenance is related to granitoids of the NNMP and granites of the Cape Granite suite along the west coast and their equivalents along the east coast. Reworked zircons from the above periods and Permian are sourced from the younger overlying sedimentary rocks.

From a zircon abundance and quality perspective, exploration should locally and probably globally focus on coastal areas with proximal, exposed granitoid terranes from the Mesoproterozoic, Cambrian and Cretaceous periods. The heterogeneity of Neoproterozoic zircons would make tarranes dominated by lithologies from that period, a less attractive target.

## 6 Acknowledgements

The research project was financed and logistically supported by Tronox Mineral Sands Pty Ltd. Their contributions are much appreciated.

## 7 References

Botha G (2018) Lithostratigraphy of the late Cenozoic Maputaland Group. South Afr J Geol 121(1):95-108

Cornell D, Thomas R, Moen H, Reid D, Moore J, Gibson R (2006) The Namaqua-Natal Province. In: Johnson M, Anhaeusser C, Thomas R (eds) The Geology of South Africa. Geological Society of South Africa, Johannesburg, pp 325-379.

Gresse PG, Von Veh MW, Frimmel HE (2006) Namibian (Neoproterozoic) to Early Cambrian successions. In: Johnson M, Anhaeusser C, Thomas R (eds) The Geology of South Africa. Geological Society of South Africa, Johannesburg, pp 395-420

Macey PH, Minnaar H, Miller, JA, Lambert C, Groenewald C, Diener J, Le Roux P, Frei D (2014) Precambrian geology of the region south of Warmbad from Haib to Vellorsdrif, Southern Namibia. Council for Geoscience, South Africa 1-3

Philander C, Rozendaal A (2015) Detrital zircon geochemistry and U–Pb geochronology as an indicator of provenance of the Namakwa Sands heavy mineral deposit, West coast of South Africa. Sediment Geol. 328:1-16

Roberts DL, Botha GA, Maud RR, Pether J (2006) Coastal Cenozoic deposits. In: Johnson MR, Anhaeusser CR, Thomas RJ (eds) The Geology of South Africa. Geological Society of South Africa, Johannesburg, pp 605-628

Rozendaal A, Philander C, Heyn R (2017) The coastal heavy mineral sand deposits of Africa. South Afr J Geol 120(1):133-152

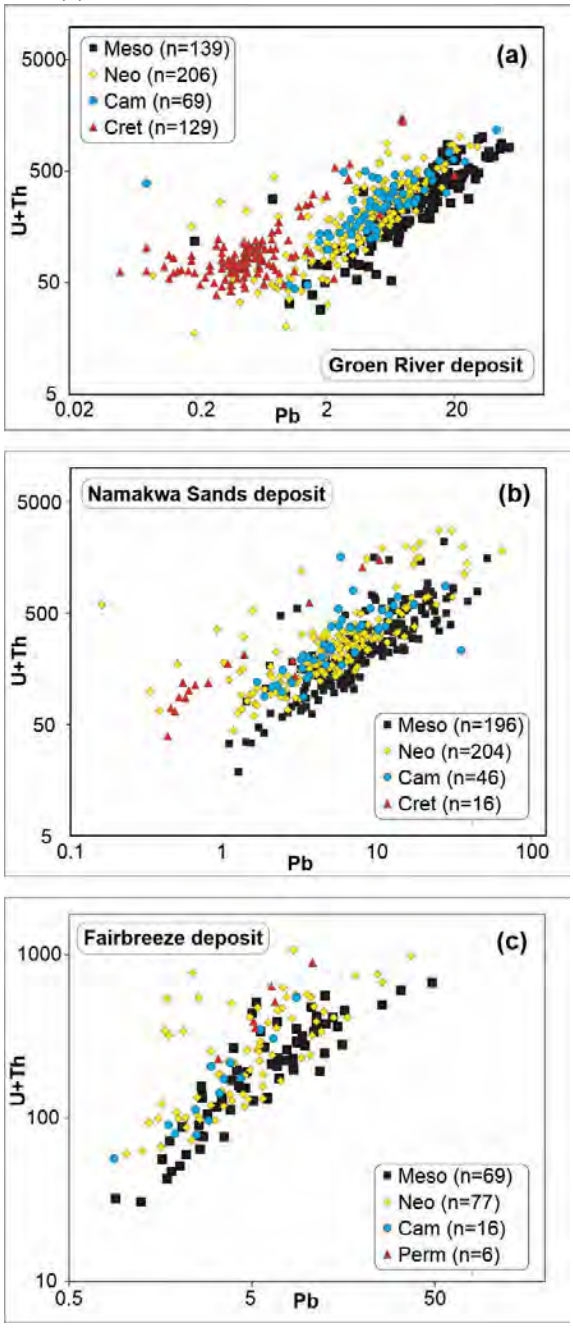


**Figure 6**. Binary diagrams showing the relationship between zircon age and U+Th vs Pb for the deposits studied.

# Co-evolution of pyrite $\delta^{66}Zn$ and sphalerite-pyrite-galena modal proportions in the ca. 1,828 Ma Mississippi Valley-type Zn-Pb Black Angel deposit, Greenland: insights into the chemical potential of sedimentary carbonates for Zn mineralization

**Nicolas J. Saintilan[1], Corey Archer[1], Kristoffer Szilas[2], and Diogo Rosa[3]**
*[1]Institute of Geochemistry and Petrology, Department of Earth Sciences, ETH Zürich, Zürich, Switzerland*
*[2]Department of Geosciences and Natural Resource Management, University of Copenhagen, Copenhagen, Denmark*
*[3]Department of Mapping and Mineral Resources, Geological Survey of Denmark and Greenland (GEUS), Copenhagen, Denmark*

**Abstract.** The Black Angel deposit formed 1828 ± 17 million years ago (pyrite Re-Os model age) in a foreland basin setting to the advancing Rinkian and Nagssugtoqidian orogens. Mineralizing processes were active at the time of building of the Rinkian foreland fold-and-thrust system. A source of Os, and by corollary other metals, in the Archean Rae Craton is identified in sphalerite-pyrite ± galena samples. A co-evolution of $\delta^{66}Zn_{pyrite}$ with sulfide modal proportions is evident. The narrow and uniform $\delta^{66}Zn_{pyrite}$ composition of sphalerite-pyrite ± galena samples (+0.30 to +0.33‰), which overlaps with $\delta^{66}Zn$ of the upper continental crust (+0.35 ± 0.05 ‰), may be compatible with Zn saturation caused by dissolution/assimilation of carbonate which would result in near-quantitative sphalerite precipitation. Conversely, $\delta^{66}Zn_{pyrite}$ in the massive pyrite body and in pyrite-galena ± sphalerite samples (+0.14 to +0.21‰) associated with more pelitic carbonate is compatible with disequilibrium conditions and rapid precipitation without sufficient carbonate dissolution/replacement to reach near-neutral pH for sphalerite precipitation. We further assume that the difference of metal endowment between Zn-Pb carbonate-hosted and Pb-Zn sandstone-hosted MVT deposits could be related to dissolution of Zn-bearing, clean, sedimentary carbonate rocks that control sphalerite saturation and precipitation.

## 1 Introduction and rationale of the study

The Black Angel deposit on the West coast of Greenland (Fig. 1a) is a remarkable Mississippi Valley-type (MVT) zinc-lead (Zn-Pb) deposit hosted by Paleoproterozoic carbonate rocks of the Mârmorilik Formation (maximum depositional age at ca. 1,915 million years ago – Ma; Guarnieri and Baker 2022; Rosa et al. 2022). Black Angel has an established link with high salinity basinal brines responsible for abundant anhydrite deposition in the Mârmorilik Formation (Rosa et al. 2022). Given the well-established model for MVT deposits, a timing of ore deposition during basin inversion and compressive tectonics is envisaged. In addition, this model suggests that weakly acidic, chloride-bearing, basinal brines leach metals from basement rocks for epigenetic Zn, Pb, and Fe-sulfide mineralization (Leach et al. 2005). This paper provides pyrite-specific rhenium-osmium (Re-Os) radiogenic isotope geochemistry data to constrain the absolute timing of mineralization. In addition, we document sulfide modal proportions and present preliminary results of transition metal Zn stable isotope geochemistry in pyrite to provide insights into depositional processes of hydrothermal mineralization.

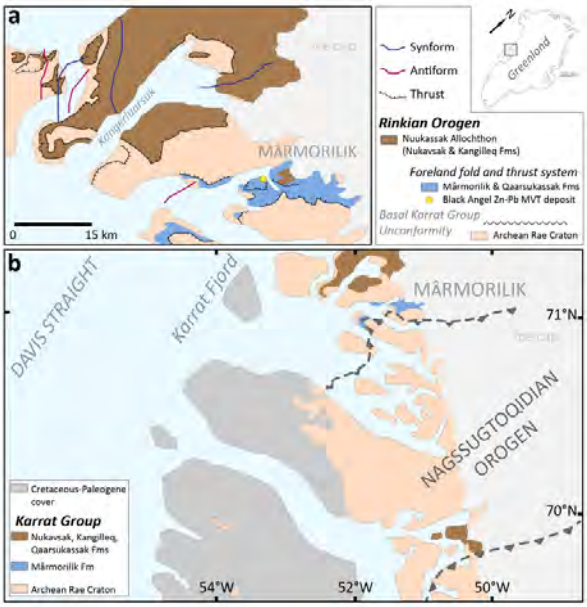


**Figure 1**. **a**. Geological map of the Mârmorilik area. **b**. Regional geological map showing the position of the Mârmorilik area (modified after Rosa et al. 2022; Guarnieri et al. 2022). See text for details.

## 2 Geodynamics and existing geochronology

The Mârmorilik Formation comprises a sulfate-rich, evaporative, stromatolite-bearing carbonate sequence deposited in platformal setting that extended, prior to deformation, over 85 km towards the present-day southwest of the Karrat Fjord (Fig. 1b; Guarnieri and Baker 2022). This formation is part of the Karrat Group that was originally deposited in an intra-cratonic sag basin after ca. 2,000 Ma with basal siliciclastic rocks of the Qaarsukassak Formation and the Mârmorilik Formation overlying Archean gneiss of the Rae Craton (Fig. 1; Guarnieri and Baker 2022; Guarnieri et al. 2022). Deposition of the Mârmorilik Formation took place in rift setting

where platformal, stromatolitic, carbonate rocks were deposited in sub-basins, between horsts of Archean Rae Craton gneisses, and above blocks faulted along listric faults (Guarnieri and Baker 2022). These listric faults accommodated NW-SE extension followed by the progressive drowning of the carbonate platform heralding deposition of syn-rift siliciclastic turbidites of the Nûkavsak Formation intercalated with mafic (meta-)volcanic rocks of the Kangilleq Formation (Guarnieri and Baker 2022; Guarnieri et al. 2022). This lithostratigraphic sequence and structural features are compatible with deposition of the Karrat Group rocks in the foreland of the Rinkian Orogeny (part of the Trans-Hudson Orogeny; St-Onge et al. 2019; Rosa et al. 2022). Rinkian peak metamorphism took place at ca. 1,830–1,826 Ma and was followed by thrusting and folding of Archaean gneisses and Paleoproterozoic supracrustal rocks (including the Mârmorilik Formation; Kirkland et al. 2017; Guarnieri et al. 2022). The southernmost part of the Karrat fjord, where the Black Angel deposit lies, was subsequently affected by deformation related to the Nagssugtoqidian Orogeny (i.e., collision between the Rae and North Atlantic Cratons; Grocott and McCaffrey 2017). Indeed, following peak Nagssugtoqidian metamorphism at ca. 1,850 Ma (Kalsbeek et al. 1987), N-S shortening and folding took place at ca. 1,825 Ma in the Black Angel area. These orogenic time stamps were interpreted as placing tentative age estimates for mineralization at Black Angel between ca. 1,860 and 1,830 Ma (Rosa et al. 2022).

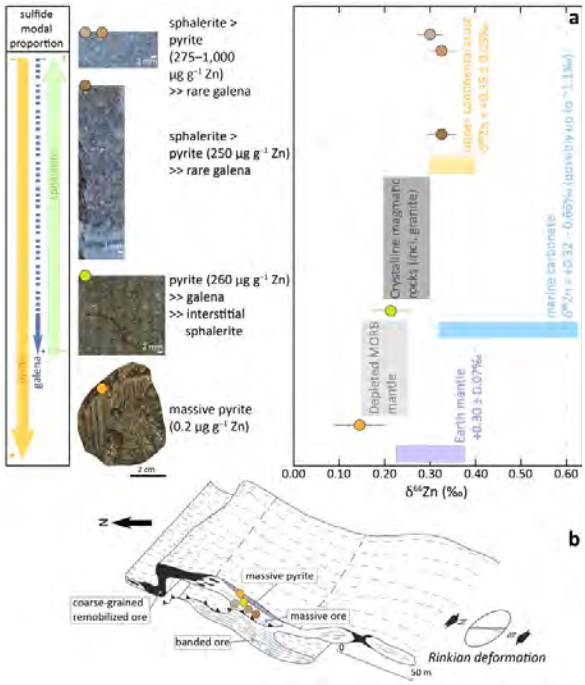


**Figure 2**. **a**. Macrophotographs of the samples utilized in the present study. The sulfide mineralogy and $\delta^{66}$Zn composition of pyrite in each sample is shown. $\delta^{66}$Zn values for the "depleted MORB mantle", for crystalline magmatic rocks, and for marine carbonates are after Pichat et al. (2003), Isson et al. (2018), and Baumgartner et al. (2021 and references therein). **b**. Schematic representation of the Angel orebody (from Rosa et al. 2022) and location of the ore and pyrite samples analyzed in this study.

## 3 Samples and methods

Five sulfide-mineralized samples (massive pyrite: MAR-1; pyrite-galena ± sphalerite: MAR 2085; sphalerite-pyrite ± galena: MAR 12774-U, MAR 12774-L, MAR 12578; Fig. 2) were collected from the archive at the Geological Survey of Greenland and Denmark (GEUS). Samples were cut and cleaned using silicon carbide sandpaper to remove any metal contamination introduced by sawing. Mineral separates of pyrite were produced following the protocol of Saintilan et al. (2020a). Traces of sphalerite in pyrite mineral separates were removed by hand-picking. For each analysis, between 385 and 530 mg of pyrite separate was transferred into a thick-walled borosilicate Carius tube (Shirey and Walker 1995). Each sulfide aliquot was dissolved in inverse Aqua Regia with a known amount of "$^{185}$Re+$^{190}$Os spike" solution at 220ºC for 24 h (Laboratory of Rhenium-Osmium Isotope Geochemistry and Geochronology, Institute of Geochemistry and Petrology, ETH Zürich). The laboratory protocol used in the present work is described in Selby and Creaser (2001) and Hnatyshin et al. (2016). The Re and Os isotopic compositions were determined by negative thermal ionization mass spectrometry using a Thermo Scientific Triton mass spectrometer (Creaser et al. 1991; Völkening et al. 1991). Preliminary analysis of MAR-1 (massive pyrite sample) signaled an Os budget dominated by radiogenic $^{187}$Os* and lacking common Os. Therefore, a new analysis was performed by using the same protocol as above but with a known amount of "$^{185}$Re+$^{188}$Os+$^{190}$Os spike" solution. Individual model age *t* for this pyrite aliquot is calculated as follows:

$$t = (1/\lambda) \bullet \ln(^{187}Os^*/^{187}Re + 1)$$

Zinc stable isotope geochemistry (protocol by Archer and Vance, 2004) utilized sub-aliquots of the pyrite mineral separates of MAR-1, MAR-2085, MAR 12774-U, MAR 12774-L, and MAR 12578. Isotopic analyses were performed using a Thermo-Finnigan NeptunePlus at ETH Zürich. Zinc was introduced into the mass spectrometer in 0.3 M nitric acid via a nebulizer attached to an Aridus system. Mass discrimination was corrected using the double spike technique. All Zn isotopic compositions are given in standard notation as follows relative to the JMC Lyon Zn standard:

$$\delta^{66}Zn_{pyrite} = 1000\left[\frac{\left(^{66}Zn/^{64}Zn\right)pyrite}{\left(^{66}Zn/^{64}Zn\right)Lyon\ JMC} - 1\right]$$

Long-term reproducibility of isotopic analyses was assessed over the course of this and parallel studies through repeated measurements of the AA-ETH standard calibrated against the JMC Lyon standard as well as a secondary standard for Zn (IRMM-

3702). These calibrated standards give $\delta^{66}Zn_{LyonsJMC}$ = +0.30 ± 0.06‰.

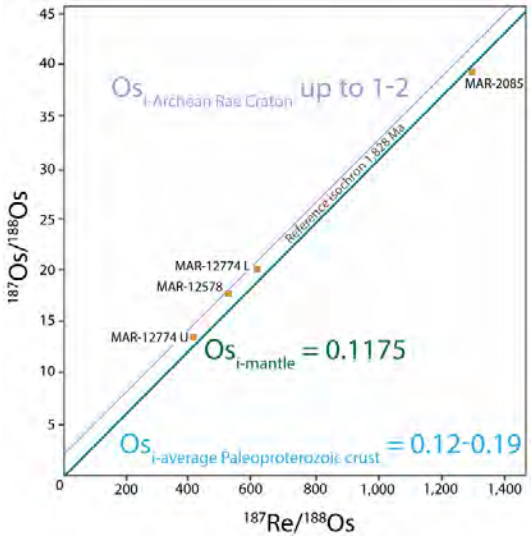


**Figure 3**. Data points for pyrite in samples MAR-2085, MAR-12774 U, MAR-12774 L, and MAR-12578 in the $^{187}Os/^{188}Os$ vs. $^{187}Re/^{188}Os$ space. Reference isochrons at 1,828 Ma (model Re-Os age of pyrite in MAR-1) at variable $^{187}Os/^{188}Os$ initial isotopic ratios ($Os_i$) of the mantle and the continental crust in the Paleoproterozoic, and the Archean Rae Craton in the basement are shown.

## 4 Results

Pyrite in sample MAR-1 has low Re (834 ± 5 pg $g^{-1}$) and very low radiogenic $^{187}Os^*$ (16.21 ± 0.05 pg $g^{-1}$) contents. Its $^{187}Re$-$^{187}Os$ model age is 1,828 ± 17 Ma (2 = 0.9% total uncertainty). Pyrite in the four pyrite-galena ± sphalerite and sphalerite-pyrite ± galena- samples have low to moderate Re, and very low Os contents (0.274 to 4.067 ng $g^{-1}$ Re; 6.22 to 123.44 pg $g^{-1}$ Os). The $^{187}Re/^{188}Os$ ratios are very high (412–1,296) and positively correlated with highly radiogenic $^{187}Os/^{188}Os$ ratios (13.48–39.32) in the $^{187}Os/^{188}Os$ vs. $^{187}Re/^{188}Os$ space (Fig. 3). All data points plot along 1,828-Ma-reference isochrons with initial Os isotope compositions ($Os_i$) modelled for 1) upper depleted mantle in the Paleoproterozoic (0.1175; calculated after Meisel et al. 1996), 2) upper continental crust at ca. 2,000–1,800 Ma (0.12–0.19; estimates after Chen et al. 2016), and 3) Archean Rae Craton basement to the Black Angel deposit (estimate based on the range of $Os_i$ for the neighbouring North Atlantic Craton by the Neoarchean, Saintilan et al. 2020b; Fig. 3).

The $\delta^{66}Zn_{pyrite}$ values range from +0.14 ± 0.06 to +0.33 ± 0.04‰ (Table 1; Fig. 2). Values from the Zn-Pb-poor samples (MAR-1 & MAR-2085) overlap with the range of $\delta^{66}Zn$ compositions for depleted MORB mantle and crystalline magmatic rocks. In contrast, the $\delta^{66}Zn_{pyrite}$ values in the sphalerite-pyrite ± galena samples overlap with the range of $\delta^{66}Zn$ compositions for the upper continental crust and for marine carbonates (Fig. 2a; cf. Pichat et al. 2003; Isson et al. 2018; Baumgartner et al. 2021).

**Table 1**. Zn isotope data for pyrite from Black Angel, Greenland.

| Sample ID | $\delta^{66}Zn$ (‰) |
|---|---|
| MAR-12774 U | +0.30 ± 0.03 |
| MAR-12774 L | +0.33 ± 0.04 |
| MAR-12578 | +0.33 ± 0.04 |
| MAR-2085 | +0.21 ± 0.05 |
| MAR-1 | +0.14 ± 0.06 |

## 5 Conclusions

The pyrite Re-Os model age of 1,828 ± 17 Ma overlaps with the timing of Rinkian peak metamorphism at ca. 1,830–1,826 Ma in the core of orogen, heralding subsequent thrusting and folding of Archean gneisses together with the Paleoproterozoic supracrustal rocks (i.e., Rinkian foreland fold-and-thrust system; cf. Guarnieri et al. 2022). This age also corresponds to incipient inversion of block-bounding listric faults in the Karrat foreland basin after Rinkian peak metamorphism (1,830–1,800 Ma; Guarnieri and Baker 2022). According to the model for MVT deposits (Leach et al. 2005), such a tectonic configuration is prone to having those extensional (here described as listric) faults acting as conduits for metal-bearing, basinal brines that interacted with basement rocks and pre- to syn-rift supracrustal rocks. The position of the four preliminary Re-Os data points for all sphalerite-pyrite ± galena, and, pyrite-galena ± sphalerite samples along 1,828-Ma-reference lines (Fig. 3) suggest that (1) Zn-Pb and pyrite-dominated mineralization is coeval within error, (2) the Archean basement of the Rae Craton stands as the most likely and dominant source of Os, and by corollary other metals, for Zn-Pb-sulfide mineralization.

A co-evolution of $\delta^{66}Zn_{pyrite}$ and sphalerite-pyrite-galena modal proportions is suggested by $\delta^{66}Zn_{pyrite}$ in pyrite-only and pyrite-galena ± sphalerite samples at +0.14 to +0.21‰ (MAR-1 & MAR-2085) vs. higher $\delta^{66}Zn_{pyrite}$ in sphalerite-pyrite ± galena samples (+0.30 to +0.33‰; MAR-12774 U & L and MAR-12578; Fig. 2). The narrow range of $\delta^{66}Zn_{pyrite}$ values in these three samples is typical of the upper continental crust (median = +0.35 ± 0.05 ‰). Such a rather uniform Zn isotope composition may be compatible with Zn saturation in the system resulting in near-quantitative sphalerite precipitation during ore formation (Baumgartner et al. 2021). In fact, we hypothesize that during MVT Zn-Pb-sulfide mineralization in the Mârmorilik carbonate rocks, transient high $P_{CO_2}$ conditions of hydrothermal solutions may be achieved due to carbonate dissolution/replacement. Such conditions would favor ZnS precipitation with $\delta^{66}Zn_{ZnS}$ unfractionated with respect to the Zn isotopic composition of the parent, acidic, hydrothermal fluid (Fujii et al. 2011; Baumgartner et al. 2021) leaching metals from the upper continental crust. We conceptualize and will test the hypothesis that the Zn contents (~40–90 μg $g^{-1}$ Zn) of clean sedimentary carbonates may be one pre-requisite to trigger excess Zn in the fluids and

subsequent batch precipitation of ZnS in the presence of reduced sulfur when the chemical potential of carbonates buffers a near-neutral pH (pH ≈ 6–7) in carbonate-hosted MVT deposit.

In contrast, we propose that the massive pyrite body in the Black Angel MVT deposit likely results from insufficient pH buffering to trigger voluminous ZnS saturation, i.e., pH remaining at ca. 3–4 (see Spinks et al. 2021, their Fig. 15 of thermodynamic modeling). Our $\delta^{66}Zn_{pyrite}$ values (+0.14 to +0.21‰) for the pyrite-only and pyrite-galena ± sphalerite samples, which are much lighter than the typical $\delta^{66}Zn$ values for the upper continental crust, are compatible with rapid precipitation, under disequilibrium conditions (Wilkinson et al. 2005) without sufficient and/or efficient carbonate dissolution/replacement.

Our preliminary findings in the Black Angel MVT deposit pave the way to test whether the chemical potential of carbonate bereft of detrital components is key in moving paragenesis from pyrite-only and pyrite-galena ± sphalerite to sphalerite-pyrite ± galena with efficient host carbonate dissolution/replacement. The latter may lead to Zn saturation by strong pH buffering and incorporation of carbonate-derived Zn.

## Acknowledgements

The authors are indebted to GEUS for access to legacy samples from the now closed Black Angel mine.

## References

Archer C, Vance, D (2004) Mass discrimination correction in multiple-collector plasma source mass spectrometry: an example using Cu and Zn isotopes. J Anal At Spectrom, 19:656-665.

Baumgartner RJ, Kunzmann M, Spinks S, Bian X, John SG, Blaikie TN, Hu S (2021) Zinc isotope composition of the Proterozoic clastic-dominated McArthur River Zn-Pb-Ag deposit, northern Australia. Ore Geol Rev 139:104545.

Chen K, Walker RJ, Rudnick RL, Gao S, Gaschnig RM, Puchtel IS, Tang M, Hu ZC (2016) Platinum-group element abundances and Re–Os isotopic systematics of the upper continental crust through time: Evidence from glacial diamictites. Geochim Cosmochim Acta 191:1-16.

Creaser RA, Papanastassiou DA, Wasserburg GJ (1991) Negative thermal ion mass spectrometry of osmium, rhenium and iridium. Geochim Cosmochim Acta, 55:397–401.

Fujii T, Moynier F, PonsML, Albarède F (2011) The origin of Zn isotope fractionation in sulfides. Geochim Cosmochim Acta, 55:397–401.

Grocott J, McCaffrey K (2017) Basin evolution and destruction in an Early Proterozoic continental margin: the Rinkian fold–thrust belt of central West Greenland. J Geol Soc 174(3):453–467

Guarnieri P, Baker, N (2022) Tectonic inversion of listric normal faults in the foreland of the Rinkian orogen (Maarmorilik, central West Greenland). J Struct Geol 159:104598.

Guarnieri P, Baker N, Rosa D, Sørensen EV (2022) Geological map of Greenland 1:100 000, Pannertooq 72 V.2 Syd. Geological Survey of Denmark and Greenland, Copenhagen

Hnatyshin D, Kontak DJ, Turner EC, Creaser RA, Morden R, Stern RA (2016) Geochronologic (Re-Os) and fluid-chemical constraints on the formation of the Mesoproterozoic-hosted Nanisivik Zn-Pb deposit, Nunavut, Canada: Evidence for early diagenetic, low-temperature conditions of formation. Ore Geol. Rev., 79:189-217.

Isson TT, Love GD, Dupont CL et al. (2018) Tracking the rise of eukaryotes to ecological dominance with zinc isotopes. Geobiology 16:541-552.

Kalsbeek F, Pidgeon RT, Taylor PN (1987) Nagssugtoqidian mobile belt of West Greenland: a cryptic 1850 Ma suture between two Archaean continents–chemical and isotopic evidence. Earth Planet Sci Lett 85:365–385

Kirkland CL, Hollis J, Danišík M, Petersen J, Evans NJ, McDonald BJ (2017) Apatite and titanite from the Karrat Group, Greenland; implications for charting the thermal evolution of crust from the U-Pb geochronology of common Pb bearing phases. Precambr Res 300:107–120

Leach DL, Sangster DF, Kelley KD, Large RR, Garven G, Allen CR, Gutzmer J, Walters S (2005) Sediment-hosted lead–zinc depos- its: a global perspective. In: Hedenquist JW, Thompson JFH, Goldfarb RJ, Richards JP (eds) Econ Geol 100th Anniversary Volume, pp 561–607

Meisel T, Walker RJ, Morgan JW (1996) The osmium isotopic composition of the Earth's primitive upper mantle. Nature 383: 517-520.

Pichat S, Douchet C, Albarède F (2003) Zinc isotope variations in deep-sea carbonates from the eastern equatorial Pacific over the last 175 ka. Earth Planet Sci Lett 210:167–178.

Rosa D, Leach D, Guarnieri P, Bekker A (2022) The Black Angel deposit, Greenland: a Paleoproterozoic evaporite-related Mississippi Valley-type Zn-Pb deposit. Miner

Saintilan NJ, Selby D, Hughes JW, Schlatter D, Kolb J, Boyce A (2020a) Mineral separation protocol for accurate and precise rhenium-osmium (Re-Os) geochronology and sulfur isotope composition of individual sulfide species. MethodsX, 7:100944.

Saintilan NJ, Selby D, Hughes JW, Schlatter DM, Kolb J, Boyce A (2020b) Source of gold in Neoarchean orogenic-type deposits in the North Atlantic Craton, Greenland: Insights for a proto-source of gold in sub-seafloor hydrothermal arsenopyrite in the Mesoarchean. Precambr Res 343: 105717.

Selby D, Creaser RA (2001) Re-Os geochronology and systematics in molybdenite from the Endako porphyry molybdenum deposit, British Columbia, Canada. Econ. Geol., 96:197-204.

Shirey SB, Walker RJ (1995) Carius tube digestion for low-blank rhenium-osmium analysis. Anal. Chem., 67:2136–2141.

Spinks SC, Pearce PA, Liu W, Kunzmann M, Ryan CG, Moorhead GF, Kirkham R, Blaikie T, Sheldon HA, Schaubs PM, Rickard WDA (2021) Carbonate replacement as the principal ore formation process in the Proterozoic McArthur River (HYC) sediment-hosted Zn-Pb deposit, Australia. Econ Geol 116:693-718.

St-Onge MR, van Gool JAM, Garde AA, Scott DJ (2009) Correlation of Archaean and Paleoproterozoic units between northeastern Canada and western Greenland: constraining the pre-collisional upper plate accretionary history of the Trans-Hudson orogeny. In: Cawood PA and Kroner A (Eds) Earth Accretionary Systems in Space and Time. The Geological Society, London, Special Publications, 318: 193–235.

Völkening J, Walczyk T, Heumann K (1991) Osmium isotopic ratio determination by negative thermal ionization mass spectrometry. Inter. J Spectro. Ionic Phys., 105:147–159

Wilkinson JJ, Weiss DJ, Mason TFD, Coles BJ (2005) Zinc isotope variation in hydrothermal systems: Preliminary evidence from the Irish midlands ore field. Econ Geol 100:583–590.

# Metallogenic models of sediment-hosted hydrothermal Zn-Pb deposits related to different tectonic settings

**Marta Sośnicka**[1]
[1]*GFZ German Research Centre for Geosciences, Telegrafenberg, D-14473 Potsdam*

**Abstract.** Sediment-hosted deposits are invaluable sources of Zn-Pb and potential repositories of critical metals such as Ge, Ga, In, Cd or Ag. This group of deposits is highly diverse and include various hydrothermal stratiform, stratabound and vein-type ore deposits, which often face genetic classification dilemma. Among genetic aspects the tectonic control and host lithology appear to play a principal role in the distribution of these deposits in sedimentary settings worldwide. This contribution focuses primarily on a brief review of selected genetic concepts with an emphasis on new developments in understanding the selected aspects of the Zn-Pb ore-forming systems, which were active under extensional and compressional tectonic regimes.

## 1 Introduction

Sediment-hosted Zn-Pb deposits account for the world's highest ore grades and largest resources among other Zn-Pb-producing ore deposit types (Leach et al. 2005). The concerns about the continuity of future Zn-Pb supply intensify due to progressive ore grade decline, refractory character of ores, lack of major large tonnage ore deposit discoveries for over two decades, resulting in falling resource, and prognoses of ever-increasing global demand for Zn- Pb. The latter, is predicted to exceed the currently available resources in 2050-2100 (Mudd et al. 2017).

The economic value of sediment-hosted base metal deposits is expected to increase over time also due to abundance of valuable critical or "high-tech" metal substitutions, such as In, Cd, Ge, Ga or Ag, typical for sphalerite-rich ores (Cook et al. 2009). While the latter are by-product metals that are nowadays more extensively used in developing green and strategic technologies (Jowitt and McNulty 2021), Zn and Pb have long played significant role in numerous technological industries and have a long history of mining.

The "high-tech" by-product commodities occur at economic to sub-economic concentrations and can be recovered with economic benefit upon development of more efficient ore processing technologies. The progressive and feasible improvement of modern technologies that support the sustainable industry sector will strongly depend on the continuity of the supply of these metals. Further ore deposit discoveries are a prerequisite to achieve the metal supply security in the future (Hoggard et al. 2020). For successful and cost-effective exploration development and advancement of genetic models of sediment-hosted Zn-Pb mineral systems of high economic potential at shallow as well as deeper crustal levels (Sośnicka and Lüders 2019) are vital. An in-depth understanding of the interplay of tectonic settings and processes that lead to ore deposition is a key factor in facilitating exploration efforts that may increase the chances of an uninterrupted supply of important raw materials.

Except the well-known world-class Zn-Pb ore deposits and districts, typically in siliciclastic rocks (SEDEX) or platform carbonates (MVT) (Ridley 2013), there are also numerous hydrothermal deposits of unclear origin or which do not fit into the early defined, classic genetic models (Sangster 1996; Warren 2016). Such metal deposits include various hydrothermal massive, stratabound and vein-type deposits in sedimentary settings (Haest and Muchez 2010). It cannot be ruled out that these deposits will gain significant economic importance in the upcoming future due to foreseen increased base metal demand. The root of the ambiguity in the current classification schemes and genetic models of the sediment-hosted Zn-Pb deposits lies primarily in application of differing criteria, such as differences in the ore deposition site, timing of the ore formation relative to the host rock deposition or varying ore genetic aspects (Leach et al. 2005; Wilkinson 2014). This results in an ongoing controversy as a common consensus has not been reached up to date.

Crustal tectonic events are relevant to the origin of numerous sediment-hosted ore deposits. Therefore, this contribution focusses most of all on new advancements in understanding the selected aspects of ore-forming processes and their relation to tectonic settings, as these features significantly shaped genetic models of hydrothermal Zn-Pb deposits in sedimentary settings.

## 2 Tectonic settings of Zn-Pb ore formation

The majority of Zn-Pb ore deposits in sedimentary settings are hosted by rift or passive-margin rock sequences. During structural evolution of the basin these sequences are subjected to substantial thermal and chemical alteration by fluids of different origin. Tectonic activity as well as halokinesis at different stages of basin evolution facilitate fluid migration to potential ore deposition sites. The well-known tectonic settings of Zn-Pb ore deposition include continental rifts and shelves, collisional orogenic forelands, back-arc basins and continental sag basins (Leach et al. 2010). Primarily, both extensional (Muchez et al. 2005) and compressional tectonic regimes (Leach et al. 2005) are favourable for Zn-Pb ore deposition.

### 2.1 Extensional regime

The onset of extensional regime initiates development of continental rifting and leads to progressive crustal thinning and propagation of normal faults in the subsiding basin. With time this leads to an emergence of passive margins on the rifted continental edges. Such settings favour sedimentation of slope facies, such as various siliciclastic rocks and carbonates, as well as platform carbonates typical of continental shelf facies. These rock lithologies are the most common Zn-Pb ore deposition sites/hosts. During crustal extension, normal faults that entrain migrating fluids as far into the crystalline basement, largely control the development of Zn-Pb-bearing hydrothermal systems. The Zn-Pb enrichment of the descending fluids is primarily attributed to extensive interactions with rock sequences and crystalline basement (Muchez et al. 2005). The vertical structural framework coupled with increased heat-flow play an important role in transfer of fluids between metal source regions and the ore deposition sites.

Based on fluid inclusion data, the Zn-Pb-bearing fluids in extensional settings, have been constrained to basinal brines of temperatures and salinities with the most common ranges between 100–200°C and 13–28 wt% NaCl equiv., respectively (Wilkinson 2014). These fluids primarily originated from seawater evaporation, chemically evolved to different degrees, and/or resided in different metal source regions for various periods of time (Muchez et al. 2005). Ore precipitation mechanisms vary between deposits and largely depend on the number of fluid types involved, their salinity and chemical compositions, availability of ligands, metals and/or reductants and physico-chemical conditions at the ore deposition site.

The formation of numerous types of sediment-hosted Zn-Pb deposits in Europe (e.g. SEDEX Rammelsberg or Meggen, Germany) as well as MVT deposits of the Lennard Shelf in Australia, has been ascribed to extensional tectonic regime, e.g., in back-arc basin and continental rift environments (Leach et al. 2001, 2010; Muchez et al. 2005). Another example are major deposits of the Irish-type, which formed during extensional rifting events in the Lower Carboniferous (Wilkinson 2014).

### 2.2 Compressional regime

The Zn-Pb ore deposits which formed under compressional regime are often tied to multistage ore genesis and/or result from re-working of pre-existing ore deposits which formed during extension events. Of sediment-hosted Zn-Pb deposits the majority of those classified into the MVT-style group is associated with main Phanerozoic compressional events leading to assimilation of continents and/or microplates (Leach et al. 2005, 2010). Yet, due to conflicting geologic, isotopic, and age evidence, this viewpoint has been for long the subject of heated debate (Bradley et al. 2004; Kesler et al. 2004). The orogenic collision of arc crust with passive margins has been recognized as a driver of lateral migration of metalliferous basinal brine to ore deposition sites on a passive margin, which tend to be subsequently covered by foreland basin sediments (Leach et al. 2010). Other important tectonic settings related to compressional regime include inversion orogens as well as fold-and-thrust belts (Leach et al. 2005).
Intensified mobility of evaporites in salt domes and/or beds during compressional stages, in the intracontinental evaporite basins, facilitate focussing of the fluid flow to ore traps as well as constitute an alternative source of halogens and sulphur. Therefore, the salinity of ore-forming fluids in compressional settings can result from seawater evaporation and/or it can be acquired by significant dissolution of evaporites (e.g. Sośnicka et al. 2023). Furthermore, there is a distinct group of Zn-Pb ore deposits, also considered as MVT sub-group, associated with salt diapirs, especially the sulphate-rich caprocks (Kyle and Posey 1991). Such deposits, e.g., in Tunisia, formed by orogenic-driven ascent of metalliferous fluids along diapir peripheries and adjacent faults, towards petroleum-bearing sequences and diapiric caprocks (Rddad et al. 2019, Jemmali et al. 2022). In the fold-and-thrust belts, salt tectonics is also crucial for the formation of Zn-Pb ore deposits beneath the salt-lubricated detachment planes, e.g. in Gays River or Jubilee deposits, Canada (Warren 2016).

Basin inversion coupled with wrench tectonics triggers re-activation of pre-existing structural framework and is manifested by the formation of thrust zones, horst and graben topography as well as flower and pop-up structures at the flanks of the basin (e.g. Kockel 2003). Such complex structural re-configuration facilitates renewed fluid migration and ore formation. The inversion-driven fluid flow has been proposed, e.g., for shale-hosted Century deposit, Australia (Broadbent et al. 1998). Recently, Zechstein Ca2 carbonate-hosted, deep-seated Zn-Pb ores in the inverted Lower Saxony Basin (North German Basin) have been ascribed to MVT-style (Sośnicka and Lüders 2019). In the Permian rock record, such mineralization has not been known so far (Leach et al. 2005). The case of Zechstein-hosted Zn-Pb ores amplifies the importance of interactions between hydrothermal systems and hydrocarbon reservoirs in ore genesis (Sośnicka and Lüders 2019, 2020). Compositions and isotopic signatures of fluid inclusions from these deposits provide direct and undoubtful evidence of thermochemical sulphate reduction (TSR) in gas pools, namely the reaction of coal-derived, reservoir dry gas ($CH_4$-dominated) with sulphate, that led to generation of $H_2S$-rich sour gas, consumed for Zn-Pb sulphide deposition (Sośnicka and Lüders 2019, 2020, 2021; Sośnicka et al. 2023).

## 3 Conclusions and outlook

The great diversity of sediment-hosted Zn-Pb deposits, as presented here, makes it difficult to

define a fully integrated genetic classification scheme. The current generalized scheme is unquestionably successfully applied in exploration, however a different, more specific take on genetic models may be required at particular ore deposition sites. Scientific challenges ahead pertain to constraining sulphur sources, identifying fluid migration pathways, providing sufficient evidence for proposed precipitation mechanisms, improving and/or developing new age dating techniques and better characterisation of ore-forming fluids in many more Zn-Pb hydrothermal systems worldwide.

## References


Bradley DC, Leach DL, Symons D, et al (2004) Reply to Discussion on “Tectonic controls of Mississippi Valley-type lead–zinc mineralization in orogenic forelands” by S.E. Kesler, J.T. Christensen, R.D. Hagni, W. Heijlen, J.R. Kyle, K.C. Misra, P. Muchez, and R. van der Voo, Mineralium Deposita. Miner Deposita 39:515–519. https://doi.org/10.1007/s00126-004-0420-5

Broadbent GC, Myers RE, Wright JV (1998) Geology and origin of shale-hosted Zn-Pb-Ag mineralization at the Century Deposit, Northwest Queensland, Australia. Economic Geology 93:1264–1294. https://doi.org/10.2113/gsecongeo.93.8.1264

Cook NJ, Ciobanu CL, Pring A, et al (2009) Trace and minor elements in sphalerite: A LA-ICPMS study. Geochim Cosmochim Ac 73:4761–4791. https://doi.org/10.1016/j.gca.2009.05.045

de Graaf S, Lüders V, Banks DA, et al (2020) Fluid evolution and ore deposition in the Harz Mountains revisited: isotope and crush-leach analyses of fluid inclusions. Miner Deposita 55:47–62. https://doi.org/10.1007/s00126-019-00880-w

Haest M, Muchez P (2010) Stratiform and vein-type deposits in the Pan-African Orogen in Central and Southern Africa: evidence for multiphase mineralisation. Geologica Belgica

Hoggard MJ, Czarnota K, Richards FD, et al (2020) Global distribution of sediment-hosted metals controlled by craton edge stability. Nat Geosci 13:504–510. https://doi.org/10.1038/s41561-020-0593-2

Jemmali N, Rddad L, Sośnicka M, et al (2022) Genesis of Zn-Pb-(Ba-Sr) mineralization in the peridiapiric cover of Jebel El Akhouat, Ech Chehid salt dome, Northern Tunisia. Miner Petrol 116:71–91. https://doi.org/10.1007/s00710-021-00767-7

Jowitt SM, McNulty BA (2021) Battery and Energy Metals: Future Drivers of the Minerals Industry? SEG Discovery 11–18. https://doi.org/10.5382/2021-127.fea-01

Kesler SE, Chesley JT, Christensen JN, et al (2004) Discussion of “Tectonic controls of Mississippi Valley-type lead-zinc mineralization in orogenic forelands” by D.C. Bradley and D.L. Leach. Mineralium Deposita 39:512–514. https://doi.org/10.1007/s00126-004-0422-3

Kockel F (2003) Inversion structures in Central Europe - Expressions and reasons, an open discussion. Netherlands Journal of Geosciences 82:351–366. https://doi.org/10.1017/S0016774600020187

Kyle JR, Posey HH (1991) Chapter 5 Halokinesis, Cap Rock Development, and Salt Dome Mineral Resources. In: Melvin JL (ed) Developments in Sedimentology. Elsevier, pp 413–474

Leach D, Bradley DC, Huston D, et al (2010) Sediment-Hosted Lead-Zinc Deposits in Earth History. Economic Geology 105:593–625. https://doi.org/10.2113/gsecongeo.105.3.593

Leach DL, Bradley D, Lewchuk MT, et al (2001) Mississippi Valley-type lead–zinc deposits through geological time: implications from recent age-dating research. Mineralium Deposita 36:711–740. https://doi.org/10.1007/s001260100208

Leach DL, Sangster DF, Kelley KD, et al (2005) Sediment-Hosted Lead-Zinc Deposits: A Global Perspective. In: Hedenquist JW, Thompson JFH, Goldfarb RJ, Richards JP (eds) 100th Anniversary Volume. Society of Economic Geologists, p 561−608

Möller P, Lüders V (eds) (1993) Formation of hydrothermal vein deposits. A case study of the Pb-Zn, barite and fluorite deposits of the Harz Mountains. Gebrüder Borntraeger, Berlin - Stuttgart

Muchez P, Heijlen W, Banks D, et al (2005) 7: Extensional tectonics and the timing and formation of basin-hosted deposits in Europe. Ore Geology Reviews 27:241–267. https://doi.org/10.1016/j.oregeorev.2005.07.013

Mudd GM, Jowitt SM, Werner TT (2017) The world’s lead-zinc mineral resources: Scarcity, data, issues and opportunities. Ore Geology Reviews 80:1160–1190. https://doi.org/10.1016/j.oregeorev.2016.08.010

Rddad L, Jemmali N, Sośnicka M, Cousens B (2019) The Genesis of the Salt Diapir-Related Mississippi Valley-Type Ba-Pb-(± Zn) Ore of the Slata District, Tunisia: The Role of Halokinesis, Hydrocarbon Migration, and Alpine Orogenesis. Economic Geology 114:1599–1620. https://doi.org/10.5382/econgeo.4687

Ridley J (2013) Ore Deposit Geology, 1st edition. Cambridge University Press, Cambridge: New York

Sangster DF (ed) (1996) Carbonate-Hosted Lead-Zinc Deposits. Society of Economic Geologists, Littleton, Co

Sośnicka M, Lüders V (2019) Super-deep, TSR-controlled Phanerozoic MVT type Zn-Pb deposits hosted by Zechstein-2 gas reservoir carbonate (Ca2), Lower Saxony Basin, Germany. Chem Geol 508:62–77. https://doi.org/10.1016/j.chemgeo.2018.04.025

Sośnicka M, Lüders V (2020) Fluid inclusion evidence for low-temperature thermochemical sulfate reduction (TSR) of dry coal gas in Upper Permian carbonate reservoirs (Zechstein, Ca2) in the North German Basin. Chem Geol 534:119453. https://doi.org/10.1016/j.chemgeo.2019.119453

Sośnicka M, Lüders V (2021) Phase transitions in natural C-O-H-N-S fluid inclusions - implications for gas mixtures and the behavior of solid $H_2S$ at low temperatures. Nat Commun 12:6975. https://doi.org/10.1038/s41467-021-27269-6

Sośnicka M, Lüders V, Duschl F, et al (2023) Metal budget and origin of aqueous brines depositing deep-seated Zn-Pb mineralization linked to hydrocarbon reservoirs, North German Basin. Mineralium Deposita. https://doi.org/10.1007/s00126-023-01173-z

Warren JK (2016) Evaporites. Springer International Publishing, Cham

Wilkinson JJ (2014) Sediment-Hosted Zinc–Lead Mineralization: Processes and Perspectives. In: Holland HD, Turekian KK (eds) Treatise on Geochemistry (Second Edition). Elsevier, Oxford, pp 219–249

# Contrasted sources of metals between small and giant sediment-hosted Pb-Zn deposits in the San Vicente district, Peru

**Cyril Chelle-Michou[1], Lena Bastian[1], Candice Filoche[1], Jörn-Frederik Wotzlaw[1], Dawid Szymanowski[1], Lorenzo Tavazzani[1], Lluis Fontboté[2]**
*[1]Department of Earth Sciences, ETH Zurich, Switzerland*
*[2]Department of Earth Sciences, University of Geneva, Switzerland*

**Abstract.** The source of metals (Zn-Pb) in carbonate-hosted, Mississippi Valley-type deposits can be traced through Pb isotopic fingerprinting of ore minerals (sulphides). In this work we revisit the Pb isotopic systematic of the giant Zn-Pb deposit of San Vicente Peru, in light of an updated methodological and conceptual framework. Our new, high-precision (ID-TIMS) Pb isotopic dataset allows a distinction between different mineralization localities and stages in the San Vicente district. The largest deposit, San Vicente, displays a much wider range of radiogenic Pb compositions ($^{206}Pb/^{204}Pb$ = 18.8-19.3) than smaller mineralized occurrences, which form two clusters at less radiogenic Pb values ($^{206}Pb/^{204}Pb$ = 18.8-18.9 and ~18.6). While a more expansive study of potential regional source rocks is required to trace metal transport in the district, this dataset already confirms the growing body of evidence for a more diverse source of metals in giants than in small MVT deposits.

## 1 Introduction

Mississippi Valley type (MVT) Pb-Zn deposits usually (but not exclusively) develop in permeable units within continental platform carbonate sequences with geometries resembling those of hydrocarbon traps (Kesler et al. 1994). Fluid inclusion studies have recognized that the metalliferous fluids are seawater-derived brines akin to oil field brines with salinities of 10-30 wt.% NaCl equivalent and homogenisation temperatures ranging from 70 to 170 °C (Basuki and Spooner 2002; Leach et al. 2005). The metal content in such fluids is strongly negatively correlated with the abundance of reduced sulphur and can reach up to several thousands of parts per million in some cases (Hanor 1994; Wilkinson et al. 2009; Appold and Wenz, 2011). Sulphide precipitation is thought to result either from the mixing of the metal-bearing brine with a reduced sulphur-bearing fluid, or from the in-situ reduction of the sulphate-bearing metalliferous fluid (e.g., by hydrocarbons or organic matter; Kesler et al. 1994; Anderson 1975, 2008)

Highly radiogenic Pb isotopic compositions suggest that the metals are leached from basement rocks and their weathered or detrital product at the base of the basin (Goldhaber et al. 1995). Chemical considerations further highlight that continental (volcano-)sedimentary rocks would act as an ideal metal source due to their common oxidizing character and high permeability.

However, recent high-precision Pb isotopic studies have challenged this view and suggest that hydrocarbon source rocks (black shales) may act as significant contributors of metals in some MVT deposits (Saintilan et al. 2019, Milot et al 2021). This is corroborated by experimental work showing that crude oil can dissolve significant amounts of base metals (e.g., Migdisov et al. 2017).

Here we reassess the Pb isotope systematics of the San Vicente MVT district, Peru, to further explore the source(s) of metals in MVT deposits. Specifically, we focus of the giant San Vicente deposit (ca. 31.5 Mt at 9.0 wt% Zn and 0.7 wt% Pb) and the satellite occurrences of Chilpes and Huacrash.

## 2 Geological setting

San Vicente is the southernmost district of a 700 km long MVT belt extending from northern to central Peru along the eastern Cordillera of the Andes (Fig. 1). Along this belt, the Pb-Zn mineralization occurred in the Pucará Group, a wide Upper Triassic to Lower Jurassic carbonate platform (Rosas et al. 2007).

In addition to the major San Vicente deposit that has been mined since 1970, the San Vicente district contains a dozen small Pb-Zn deposits and occurrences (including Chilpes and Huacrash; Fig. 1), some of which have been previously mined out or partially explored. The ore bodies mostly occur in dolomitic units as bedding-parallel lens-shaped bodies up to several hundred-meters long and several meters thick and as crosscutting breccia bodies. Both styles show structural control (Fontboté and Gorzawski 1990; Torró et al. 2023).

Petrographic observations and geochemical data suggest that San Vicente is the result of two mineralization steps (Fig. 2; Torró et al. 2023). The first step largely dominates in volume and is characterized by abundant (generally dark) sphalerite and galena synchronous with replacement dolomite and showing a characteristic zebra or breccia texture. The second step is volumetrically minor at San Vicente, where it occurs mainly in steep veins cross cutting the previously formed ore bodies but dominates the record at Chilpes and Huacrash; this step is characterized by light-coloured sphalerite (orange, yellow, white) rich in Ge and Ga, galena and white sparry dolomite. Minor pyrite/marcasite is present across the entire paragenesis (Fig. 2). The paragenesis of the other occurrences is yet to be studied.

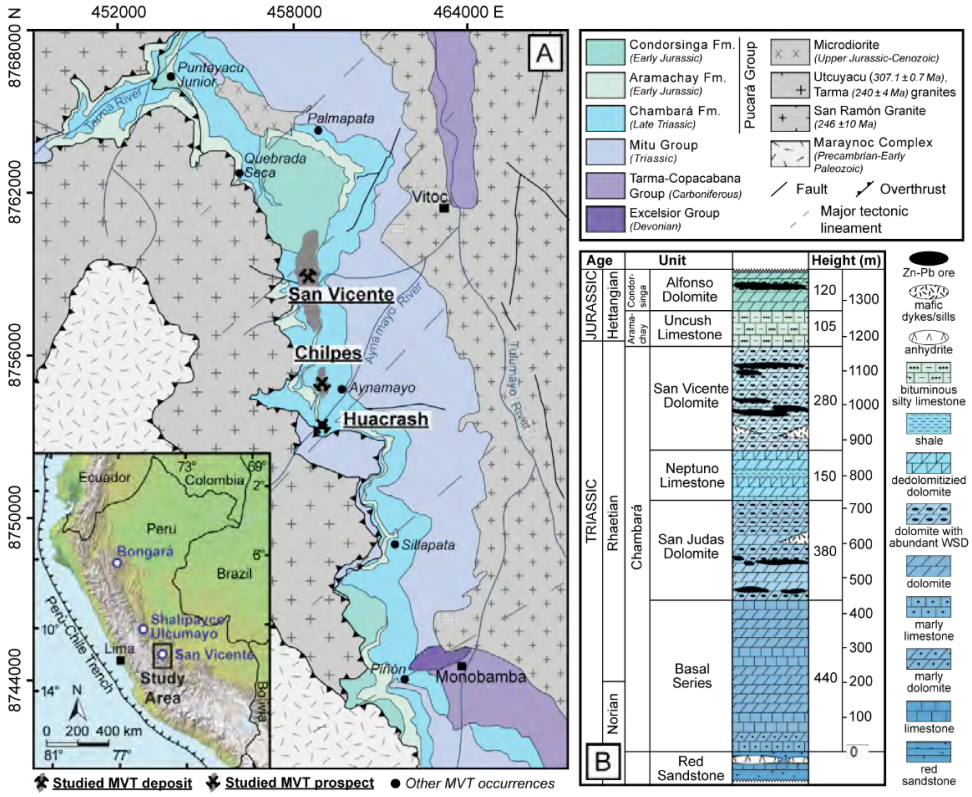


**Figure 1.** Location and geological map and stratigraphy of the San Vicente district showing the location of the studied deposits (UTM coordinates). Modified from Spangenberg et al. 1999 and Torró et al. 2023.

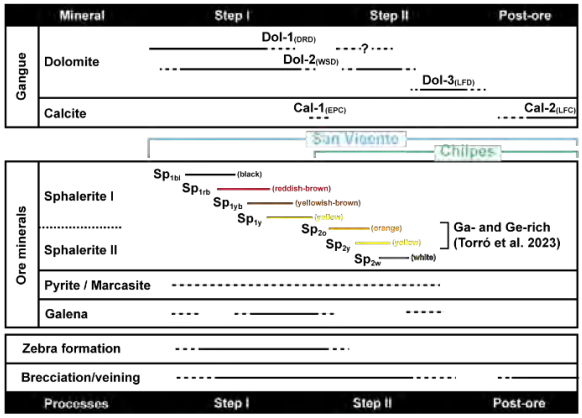


**Figure 2.** Paragenetic sequence of the San Vicente district showing relative timing of gangue and ore mineral generations based on the studied samples, Spangenberg et al. (1999) and Torró et al. (2023).

## 3 Methods

Separates of galena (n = 45), sphalerite (n = 26), pyrite (n = 4) and marcasite (recrystallized to pyrite; n = 5) covering the two mineralization steps and the entire spatial extent of the San Vicente deposit, Chilpes and Huacrash were extracted from hand samples. The Pb isotope compositions of the sulphides were measured at high precision and accuracy by isotope dilution thermal ionisation mass spectrometry (ID-TIMS) with an in-house $^{202}Pb$-$^{205}Pb$ tracer solution calibrated against NIST SRM981 and SRM982 at the Department of Earth Science of ETH Zurich.

To identify the potential source(s) of Pb in the San Vicente district (in addition to the isotope data for new mineral separates of ore samples presented here), a series of pre-Jurassic intrusive, metamorphic and siliciclastic rocks from around the district are being prepared for leachate-residue paired Pb isotopic analyses following the protocol of Chiaradia and Fontboté (2003). This allows to simulate the incongruent leaching of the labile Pb fraction by a hydrothermal fluid. This labile Pb usually has a Pb isotopic composition distinct from that of the bulk rock (Chiaradia and Fontboté 2003; Saintilan et al. 2019). Furthermore, in order to test the possible contribution of hydrocarbons to the Pb budget of the district, the Pb isotopic composition of the organic solvent-extractable organic matter will be measured from organic-rich limestone and shale units of the local Pucará Group (Uncush and Neptuno Limestone), together with that of bitumen sampled in underground fault gouge (see detailed method in Saintilan et al. 2019).

## 4 Results

Our new high-precision sulphide Pb isotope dataset on the San Vicente district is shown on Figure 3. The data cluster in three groups. The most radiogenic group ($^{206}Pb/^{204}Pb$ = 19.0-19.3) is representative of sulphides (sphalerite, galena, pyrite and marcasite) from the first (and main) mineralization step at San Vicente. The least radiogenic group ($^{206}Pb/^{204}Pb$ ~ 18.6) corresponds mainly to galena grains from Chilpes and Huacrash. The intermediate group

($^{206}Pb/^{204}Pb$ = 18.8-18.9) features orange sphalerite from all three deposits studied here as well as pyrite from Chilpes.

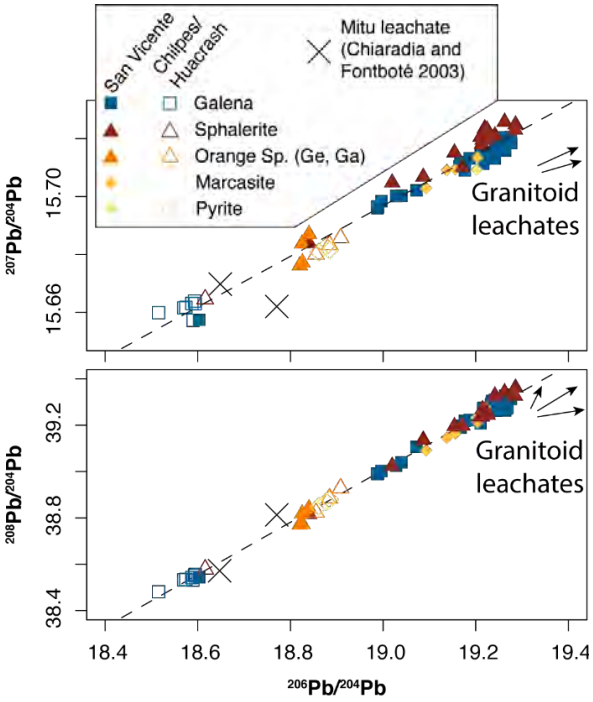


**Figure 3.** $^{206}Pb/^{204}Pb$ vs $^{207}Pb/^{204}Pb$ and $^{206}Pb/^{204}Pb$ vs $^{208}Pb/^{204}Pb$ plots showing the high-precision isotopic composition of different sulphides from the San Vicente district. Leachates from the Mitu red-beds and regional granitoids from Chiaradia and Fontboté (2003) are shown for indication.

## 5 Discussion

### 5.1 Tracking the evolution of a district-scale hydrothermal system

These new data highlights that the Pb isotopic composition of the giant San Vicente deposit is distinctly more radiogenic than that of the two studied smaller deposits (located only a few kilometres south of San Vicente; Fig. 1). Interestingly, the Pb- isotope data confirm that the second mineralization step at San Vicente, characterized by the orange-sphalerite in cross cutting veins, is closely related to the formation of Chilpes and Huacrash, probably corresponding to a common district-scale fluid flow event. These relationships suggest that the two mineralization steps tapped different Pb reservoirs. This implies that the hydrological system established during the main step mineralization at San Vicente was markedly disturbed and reorganised itself to form the district-scale second step mineralization.

It is noteworthy that the orange sphalerite and the galena from the second-step mineralization show different Pb isotopic composition (Fig. 3). It suggests that the second mineralization step may in fact correspond to two sub-steps tapping distinct source rocks.

### 5.2 Source(s) of metals

The analysed sulphides define a line with a slope of 0.08598 ± 0.00324 (95% confidence) in the $^{206}Pb/^{204}Pb$ vs $^{207}Pb/^{204}Pb$ space (dashed line, Fig. 3). We obtain an identical slope (within uncertainty) by sub-selecting data from the first or second step sulphides, respectively. Assuming a mineralization age of 85 ± 15 Ma, we calculated Pb source model ages of 1.28 ± 0.07 Ga. The absence of extensive volume of rocks of this age in the Andean basement of central Peru (e.g., Mišković et al. 2009) suggests that the slope defined by sulphides of the San Vicente district define a mixing line rather than a paleoisochron.

The similar slope of the mixing line between the first and second step mineralization events suggests that metals of both mineralization steps come from two main sources that have mixed in different proportions. While high-precision Pb isotopic data of leachates from potential regional source rocks are being acquired, lower precision data from Chiaradia and Fontboté (2003) on leachates from these rocks already provide some useful insights. Indeed, the Pb isotopic composition of leachates from the Mitu group (a regionally extensive Triassic volcanoclastic and red-bed continental unit) plot very close to the least radiogenic sulphide group (mostly galena) from Chilpes an Huacrash (Fig. 3). This suggests that the Mitu Group may correspond to the low radiogenic source of metals across the district. The oxidized and permeable nature of this unit makes it an ideal source rock for metals. However, while leachates from intrusive rocks (granite, granodiorite) tend to be distinctly more radiogenic ($^{206}Pb/^{204}Pb$ > 20 but plotting below the dashed sulphide line in Fig. 3; Chiaradia and Fontboté 2003), available data do not allow determining the nature of the radiogenic component with confidence. Further the potential of hydrocarbon source rocks in sourcing an important fraction of metals (as it has been suggested for the Laisvall MVT deposit, Sweden; Saintilan et al. 2019) has yet to be tested.

## 6 Preliminary conclusions

Our new high-precision Pb isotope dataset from the San Vicente district highlights that:

- Pb is significantly more radiogenic in the giant San Vicente deposit than in the small deposits and occurrences of the same district;
- Metals in the district have possibly been sourced from the regionally extensive red beds of the Mitu group and from another unspecified more radiogenic source (possibly pre-Jurassic granitoids);
- The giant San Vicente deposit is associated with a more diverse metal source than the small deposits, which might be a trait specific to giant MVT deposits (e.g., Saintilan et al. 2019). This

is consistent with the proportionally large volumes of rocks that need to be leached to source giant deposits containing several million tons of Pb + Zn.

Ongoing high-precision Pb isotope analyses on potential source rocks (including granitoid, gneisses, siliciclastic sediments, and hydrocarbon source rocks) will help clarifying and quantifying the various origins of metals in the San Vicente district.

## Acknowledgements

We thank the San Vicente geology staff for assistance during sampling, and Maria Paula Castellanos for support during lab work.

## References

Anderson GM (1975) Precipitation of Mississippi Valley-type ores. Econ Geol 70:937–942. https://doi.org/10.2113/gsecongeo.70.5.937

Anderson GM (2008) The mixing hypothesis and the origin of Mississippi Valley-type ore deposits. Economic Geology 103:1683–1690. https://doi.org/10.2113/gsecongeo.103.8.1683

Appold MS, Wenz Z (2011) Composition of ore fluid inclusions from the Viburnum Trend, Southeast Missouri district, United States: Implications for transport and precipitation mechanisms. Economic Geology 106:55–78. https://doi.org/10.2113/econgeo.106.1.55

Basuki NI, Spooner ETC (2002) A Review of Fluid Inclusion Temperatures and Salinities in Mississippi Valley-type Zn-Pb Deposits: Identifying Thresholds for Metal Transport. Explor Min Geol 11:1–17. https://doi.org/10.2113/11.1-4.1

Chiaradia M, Fontboté L (2003) Separate lead isotope analyses of leachate and residue rock fractions: implications for metal source tracing in ore deposit studies. Mineralium Deposita. https://doi.org/10.1007/s00126-002-0301-8

Fontboté L, Gorzawski H (1990) Genesis of the mississippi valley-type Zn-Pb deposit of San Vicente, central Peru; geologic and isotopic (Sr, O, C, S, Pb) evidence. Econ Geol 85:1402–1437. https://doi.org/10.2113/gsecongeo.85.7.1402

Goldhaber MB, Church SE, Doe BR, et al (1995) Lead and sulfur isotope investigation of Paleozoic sedimentary rocks from the southern Midcontinent of the United States; implications for paleohydrology and ore genesis of the Southeast Missouri lead belts. Economic Geology 90:1875–1910. https://doi.org/10.2113/gsecongeo.90.7.1875

Hanor JS (1994) Origin of saline fluids in sedimentary basins. Geological Soc Lond Special Publ 78:151–174. https://doi.org/10.1144/gsl.sp.1994.078.01.13

Kesler SE, Jones HD, Furman FC, et al (1994) Role of crude oil in the genesis of Mississippi Valley-type deposits: Evidence from the Cincinnati arch. Geology 22:609–612. https://doi.org/10.1130/0091-7613(1994)022<0609:rocoit>2.3.co;2

Leach DL, Sangster DF, Kelley KD, et al (2005) Sediment-Hosted Lead-Zinc Deposits: A Global Perspective. In: Hedenquist JW, Thompson JFH, Goldfarb RJ, Richards JP (eds) Economic Geology 100th Anniversary Volume. Soc Econ Geol, Littleton, pp. 561–607. https://doi.org/10.5382/AV100.18

Migdisov AA, Guo X, Williams-Jones AE, et al (2017) Hydrocarbons as ore fluids. Geochemical Perspectives Letters 47–52. https://doi.org/10.7185/geochemlet.1745

Milot J, Blichert-Toft J, Sanz MA, et al (2021) The significance of galena Pb model ages and the formation of large Pb-Zn sedimentary deposits. Chem Geol 583:120444. https://doi.org/10.1016/j.chemgeo.2021.120444

Mišković A, Spikings RA, Chew DM, et al (2009) Tectonomagmatic evolution of Western Amazonia: geochemical characterization and zircon U-Pb geochronologic constraints from the Peruvian Eastern Cordilleran granitoids. Geological Society of America Bulletin 121:1298–1324. https://doi.org/10.1130/b26488.1

Rosas S, Fontboté L, Tankard A (2007) Tectonic evolution and paleogeography of the Mesozoic Pucará Basin, central Peru. Journal of South American Earth Sciences 24:1–24. https://doi.org/10.1016/j.jsames.2007.03.002

Saintilan NJ, Spangenberg JE, Chiaradia M, et al (2019) Petroleum as source and carrier of metals in epigenetic sediment-hosted mineralization. Sci Rep-uk 9:8283. https://doi.org/10.1038/s41598-019-44770-7

Spangenberg JE, Fontbote L, Macko SA (1999) An evaluation of the inorganic and organic geochemistry of the San Vicente mississippi valley-type zinc-lead district, central Peru; implications for ore fluid composition, mixing processes, and sulfate reduction. Econ Geol 94:1067–1092. https://doi.org/10.2113/gsecongeo.94.7.1067

Torró L, Millán-Nuñez AJ, Benites D, et al (2023) Germanium- and gallium-rich sphalerite in Mississippi Valley–type deposits: the San Vicente district and the Shalipayco deposit, Peru. Mineral Deposita 1–28. https://doi.org/10.1007/s00126-023-01160-4

Wilkinson JJ, Stoffell B, Wilkinson CC, et al (2009) Anomalously Metal-Rich Fluids Form Hydrothermal Ore Deposits. Science 323:764–767. https://doi.org/10.1126/science.1164436

# Trace elements variation in gangue carbonates reveal redox and temperature shifts in Mississippi Valley-type, Zn-Pb deposits

**Lorenzo Tavazzani[1], Lluis Fontboté[2], Cyril Chelle-Michou[1]**
*[1]ETH Zürich, Department of Earth Sciences, Zürich, Switzerland*
*[2] University of Geneva, Department of Earth Sciences, Geneva, Switzerland*

**Abstract.** Variation of trace element contents in gangue carbonate can track changes in fluid chemistry of MVT style Zn-Pb mineralization events. In this work, we analyzed gangue carbonates in syn- to post-ore carbonate generations in the MVT district of San Vicente, Peru by LA-ICP-MS. Covariation of Fe and Mn is interpreted through the lens of thermochemical modelling and indicates a shift from reducing to oxidizing conditions between syn- and post-ore carbonate generations. Moreover, we show that uptake of Fe in carbonates is strongly controlled by temperature of hydrothermal fluids, providing a qualitative mean to assess thermal gradients across MVT provinces and mineralization stages. Ultimately, we provide a framework to interpret compositional data of carbonates in MVT systems, which can shed light on the mechanisms of ore generation and dispersion in basinal-scale hydrothermal systems.

## 1 Introduction

A large fraction of the world's Zn resources are hosted in MVT deposits, chiefly stratabound carbonate-hosted Zn-Pb sulfide mineralization associated with the circulation of metalliferous, warm basinal brines (75-200 °C) and dolomitization events (Leach et al. 2005). These deposits are typically part of basin-scale hydrothermal systems that concentrate metals to economic grade at sites where oxidized metalliferous brines encounter reduced $H_2S$ and/or hydrocarbon-bearing traps (Szmihelsky et al. 2020). Favourable conditions for metal precipitation also change over time, as host rock and basinal fluids progressively react with incoming, oxidized metalliferous brines, altering the compositional and physical state of hydrothermal systems.

In MVT deposits, the crystallization of gangue carbonates can precede, accompany, and postdate sulfide precipitation. Therefore, tracking changes in distribution of temperature and redox-controlled elements across carbonate generations has the potential to identify changes in fluid physiochemical conditions that promote sulfide deposition, and also cease the mineralization events. In this study, we highlight the potential of carbonate minor- and trace-element geochemistry to track the onset and termination of Zn-Pb mineralization through an extensive laser ablation-inductively couple-mass spectrometry (LA-ICP-MS) study of gangue carbonate generations from the world-class MVT district of San Vicente, Peru.

## 2 Geologic setting

### 2.1 San Vicente district

A series of MVT Zn-Pb districts and deposits stretches ~700 km along the N-S oriented sub-Andean thrust and fold belt in central and northern Peru (Fig. 1). Along this belt, Zn-Pb mineralization is hosted in the Pucará Group, a wide Upper Triassic to Lower Jurassic carbonate platform deposited on the western margin of the Amazonian craton (Rosas et al. 2007). Three Zn-Pb districts are known along this belt, Bongará, Shalipayco-Ulcumayo, and San Vicente (Fig. 1). San Vicente is the southernmost of these and includes the large, currently exploited San Vicente deposit (31.5 Mt of accumulated production and reserve at 9.0 wt% Zn and 0.7 wt% Pb; SIMSA written communication) as well as numerous Zn-Pb occurrences, including the Chilpes deposit (~0.5 Mt at 5.0 wt% Zn and 1.3 wt% Pb).

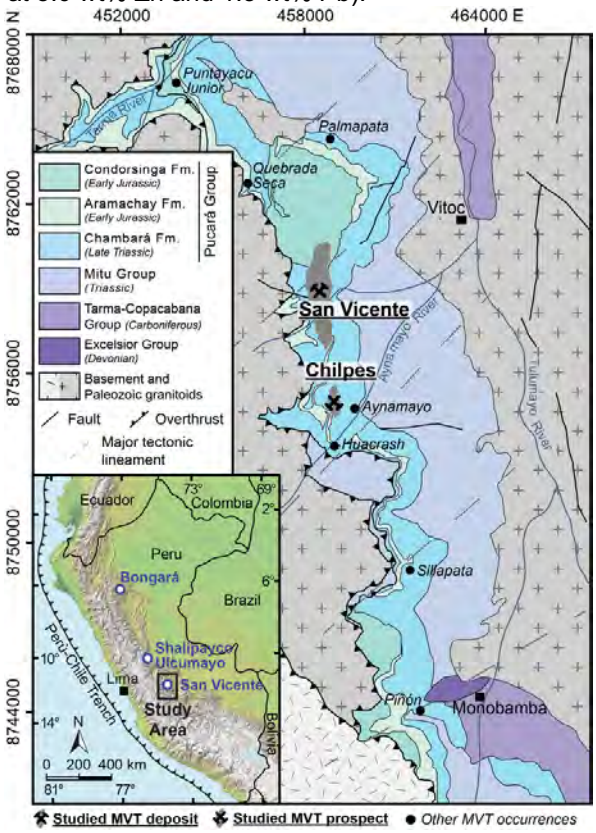


**Figure 1.** Geological map of the San Vicente district (from Torró et al., 2023). Inset shows location of San Vicente and main Zn-Pb districts of the Peruvian MVT belt.

In this district, the Zn-Pb ore is hosted in the San Judas, San Vicente and Alfonso dolomite units of the Pucará Group and occurs mostly as bedding-parallel, lens-shaped bodies (mantos) up to hundreds of meters long and several meters thick and cross-cutting bodies (Fontboté and Gorzawski 1990), both types are interpreted to have been formed along NW-SE directed fractures (Torró et al. 2023).

The main ore minerals are sphalerite and galena showing sulphur isotopic signatures typical of thermochemically reduced marine sulfate. Sphalerite petrography and trace element geochemistry indicate two distinct mineralization steps in the San Vicente deposit, with the second one, volumetrically minor, characterized by Ga- and Ge-rich sphalerite mainly in cross-cutting, steep veins. The Chilpes mineralization was produced during a single episode, likely related to the second San Vicente mineralization step (Torró et al. 2023). In both deposits, sulfides are spatially associated with syn- to post-ore hydrothermal carbonates.

### 2.1 Carbonate petrography

Four main generations of hydrothermal carbonates

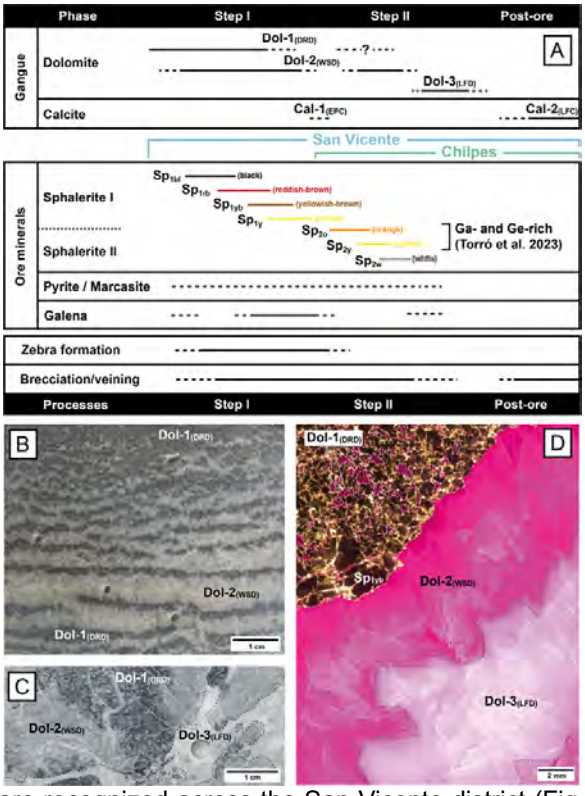


are recognized across the San Vicente district (Fig. 2).

**Figure 2.** (A) Paragenetic sequence of the San Vicente district based on the studied samples, Spangenberg et al. (1999), and Torró et al. (2023). Dashed lines represent lesser abundance; Sp=sphalerite. Mesoscopic features of (B) zebra textures and (C) post-ore dolomite (LFD) crosscutting syn-ore generations. (D) Textural relationships between dolomite generations are highlighted by CL.

Optically dark, fine- to medium-grained, inclusion-rich, replacive dolomite (DRD) and coarse-grained, white sparry dolomite (WSD) represent the syn-ore carbonates in both the San Vicente and Chilpes deposits (Fig. 2). The DRD generation contains disseminated organic matter and is dull red to non-luminescent under cathodoluminescence (CL; Fig. 2D). In mineralized samples, DRD is commonly intergrown with and overgrown by sulfides (Fig. 2D). The WSD generation consists of coarsely crystalline saddle dolomite virtually free of inclusions and shows heterogeneously bright red to pink CL (Fig. 2D). This generation commonly grows syntaxially on replacive dolomite (DRD) and sulfide domains (Fig. 2D). Alternating bands of these two dolomites produce distinctive rhythmic structures ("zebra" texture; Fig. 2B) that are characteristic of the Peruvian and many MVT deposits worldwide (Fontboté and Gorzawski 1990). Remaining central spaces in WSD domains of zebra structures are commonly filled by a xenomorphic dolomite (LFD) that displays a characteristic bright-white CL response (Fig. 2D). This dolomite generation, which post-dates the ore deposition is also found as a cement in non-mineralized dissolution-hydraulic breccias (Fig. 2C). These three, syn- to post-ore hydrothermal dolomite generations are locally crosscut by thin calcite veins (LFC) that under CL appear dull to bright yellow. Calcite is also found as open-space filling in the same textural position as xenomorphic dolomite and pseudomorphically replacing sulphate in fine grade dolomite layers (EPC).

## 3 Methods

### 3.1 LA-ICP-MS

Dolomite and calcite trace element analyses were performed on the epoxy-embedded rock chips by LA-ICP-MS at the ERDW department of ETH Zurich (Switzerland) using an ASI RESOlution S-155 excimer (ArF, 193 nm) laser ablation system coupled to a Thermo Element XR sector-field ICP-MS. Distinct carbonate phases were identified prior to analyses through CL microscopy. Additional CL imaging after acquisition ensured removal of misplaced or defective (e.g., fractures, voids, etc…) analytical spots during data reduction.

For trace element analyses, NIST SRM612 was used a primary reference material and USGS GSD-1G glass was analyzed during each session as a validation reference material to check accuracy and reproducibility. A 43 µm spot size and 4.0 Hz repetition rate with a laser energy density on sample surface of ca. 2 J/cm$^2$ were used for ablation of unknowns and reference materials.

The ablation aerosol was mixed in the fast washout S-155 ablation cell (Laurin Technic) with carrier gas consisting of helium (ca. 0.5 L min$^{-1}$) and make-up gas consisting of argon (ca. 1 L min$^{-1}$) and

nitrogen (2 mL $min^{-1}$). The ablated aerosol was then homogenized by flushing through a squid device before introduction into the plasma torch.

The raw intensities were processed offline with Iolite v. 4.5. software (Paton et al. 2011). CaO contents of 30.41 wt% and 56.03 wt% were used as internal standard for relative sensitivity correction of dolomite and calcite materials respectively. A further matrix correction factor was applied to mass $^{57}Fe$ (up to 50%) based on offset between average contents obtained on calcite reference material WC-1 and reported values (Roberts et al. 2017).

### 3.2 Eh-pH (Pourbaix) diagrams

To evaluate the effect of temperature, oxygen fugacity (Eh) and acidity (pH) on trace metals (Mn, Fe) solubility in basinal fluids, we calculated predominance boundaries and solubility contours for part of the Fe-Mn-O-H system. Boundaries are calculated after equations of Pourbaix (1963) and using the FactSage thermochemical software and database (Bale et al. 2009) for molar concentrations of $Fe^{2+}$ and $Mn^{2+}$ of $10^{-10}$, $10^{-8}$, $10^{-6}$ and $10^{-4}$ at a range of Eh (-0.5 to 1.0 V), pH (4.5 to 8.5 pH) and temperature (50-150°C), conditions characteristic of fluid flow in sedimentary basins. In addition, we calculated the sulfate-sulfide and carbonate-carbonic acid ($HCO^{3-}$) boundaries at same Eh, pH ranges and temperature intervals.

## 4 Results

Ore metal (Zn, Pb) contents vary by a few orders of magnitude between syn- and post-ore carbonates (100 to 1 ppm for Zn and 10 to 0.01 ppm for Pb; Fig. 3A, B; Spangenberg et al., 1999). Trace metals (Fe, Mn) also vary systematically across carbonate generations. Syn-ore dolomite (DRD, WSD) display a wide range of Fe (100-5000 ppm) and Mn (500-2500 ppm) contents (Fig. 3C). In this compositional space, San Vicente and Chilpes syn-ore dolomite display oblique covariation trends with a notable, systematic offset toward higher Fe contents for samples from the Chilpes deposit (Fig. 3C). Xenomorphic, void-filling dolomite (LFD) is depleted in Fe (< 500 ppm) and highly variable in Mn (500-2500 ppm), with compositions distributed along a vertical trend (Fig. 3C). Conversely, vein-forming and open-space filling calcite (LFC) show low Mn (< 500 ppm) and very little Fe (< 20 ppm) (Fig. 3C).

Pourbaix diagrams showcase decoupled solubility of $Fe^{2+}$ and $Mn^{2+}$ in low temperature hydrothermal fluids, with both elements soluble at Eh-pH conditions buffered by host-rock Pucará carbonates (R; Fig. 4) and only $Mn^{2+}$ in solution at conditions dominated by incoming oxidizing fluids (F; Fig. 4). These plots also display the significant effect of fluid temperature on the solubility of $Fe^{2+}$ at rock-buffered conditions (Fig. 4). At lower temperature the solubility field of $Fe^{2+}$ expands towards higher molar concentrations. Assuming a fluid which Eh-pH conditions are buffered by a carbonate host-rock rich in organic matter (and with sulphates present), the molar concentration increases from ~$10^{-9}$ to ~$10^{-6}$ if the temperature decreases from 150 °C to 50 °C.

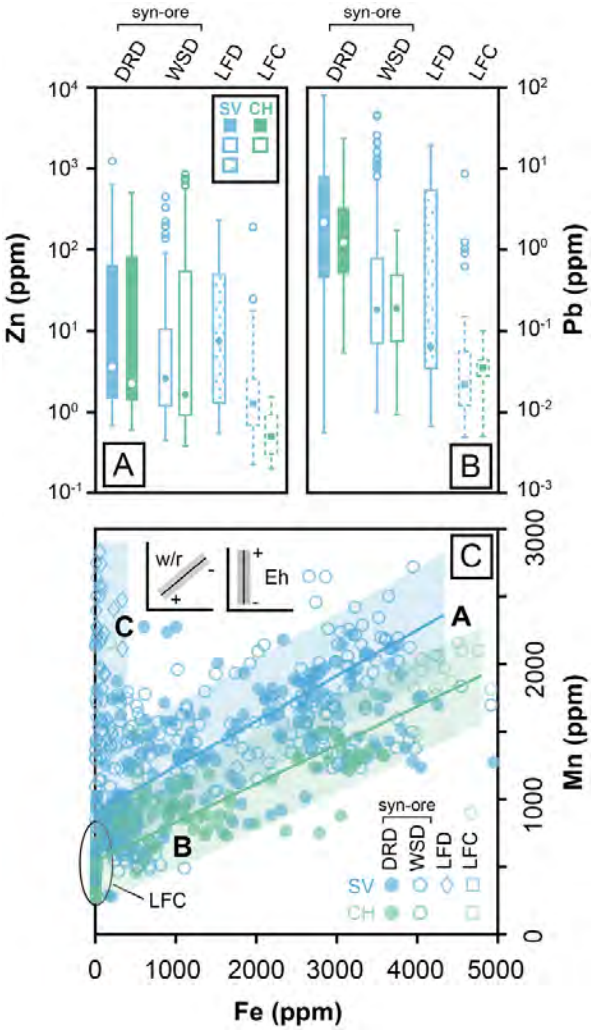


**Figure 3.** (A-B) Zn and Pb contents in the four main generations of carbonates from the Chilpes and San Vicente deposits. (C) Mn and Fe content variations in the four main carbonate generations.

## 5 Discussion

### 5.1 Tracking hydrothermal fluids evolution

The onset and termination of mineralization episodes in MVT deposits are tied to changes in physicochemical conditions ($fO_2$, pH, T) of metal-bearing brines mainly caused by interaction with other fluids and host rock (Szmihelsky et al. 2020). In hydrothermal carbonates of the San Vicente district, redox-state controlled elements Fe and Mn define two distinct compositional trends (Fig. 3C), one for syn-ore (DRD and WSD) and one for post-ore dolomite (LFD). The syn-ore dolomite covariation trend (A-B; Fig. 3B) can be interpreted as the result of carbonate precipitation from a slightly acidic, metal rich, oxidizing fluid (Spangenberg et al., 1999) largely buffered by hydrocarbons and $H_2S$ hosted in the carbonates of the Pucará Group (Fig.

4). Concentrations of $Mn^{2+}$ and $Fe^{2+}$ (as well as Pb and Zn, Fig. 3A, B) in solution progressively decrease upon sulfides and carbonate precipitation, until the fluid becomes depleted in both elements (B; Fig. 3C). After a time, due to interaction with incoming oxidizing fluid, the Pucará Group carbonates would have lost their $\mathit{f}O_2$ buffering capacity through $H_2S$ consumption (sulfide precipitation) and hydrocarbon oxidation. Under this newly established, fluid-dominate and oxidized conditions only $Mn^{2+}$ could be transported and incorporated into precipitating carbonates (Fig. 4) generating the low Fe and variable Mn trend (B-C; Fig. 3C) of post-ore stage dolomite (LFD).

Overall, trace element distribution in gangue carbonates of San Vicente preserve a history of fluid evolution consistent with ore precipitation initiated at reduced conditions, followed by a shift to oxidizing conditions that spelled the end of the mineralization.

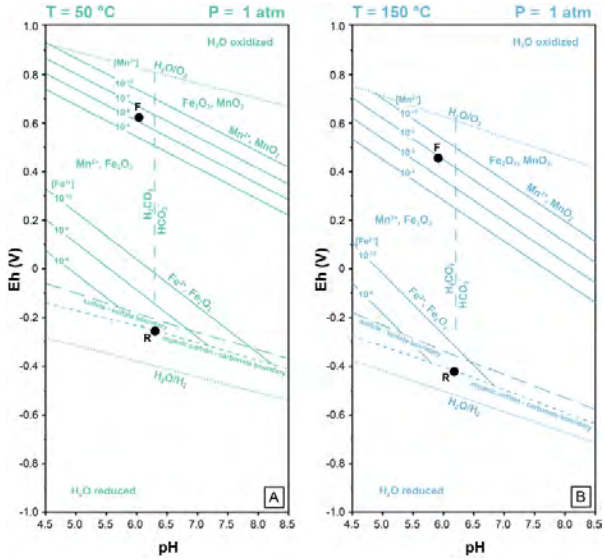


**Figure 4.** Eh-pH diagram for part of the system Fe-Mn-O-H, parameters for boundary calculations are reported in text. The dark circles F and R are idealized representation of the Eh-pH location of rock (R) and metalliferous fluid (F) during the interaction of incoming acidic and oxidizing fluid with host dolomite of the Pucará Group.

### 5.2 Contrasting fluid temperatures across a MVT district

Sphalerite thermometry suggests different mineralizing fluid temperatures between the San Vicente and Chilpes deposits (Torró et al. 2023), with Chilpes stage II sphalerite displaying systematically lower crystallization temperatures (~50 °C colder). The higher Fe values (at equivalent Mn contents; Fig. 3C) measured in carbonates from Chilpes also point to a thermal difference between the two deposits (and mineralization stages; Fig.2). Specifically, Pourbaix diagrams highlight the strong temperature effect on $Fe^{2+}$ solubility at rock-buffered conditions (Fig. 4), with increasing content of iron in solution at lower temperatures. We propose that relative differences in Fe content in syn-ore gangue carbonates can provide a first, qualitative assessment of the direction of thermal gradients across deposits and between mineralization stages.

## 6 Conclusion

In this contribution we demonstrate how trace elements distribution in syn- to post-ore gangue carbonates can showcase the temporal and spatial heterogeneities of hydrothermal fluid conditions ($\mathit{f}O_2$, pH, T) in MVT districts:

(1) Covariation of Fe and Mn can track shifts in the $fO_2$ state of hydrothermal systems from conditions favourable to sulphide deposition (i.e. rock-buffered, reduced) to barren (i.e fluid-dominated, oxidized).

(2) Relative differences in Fe intake between successive mineralization stages and mineralized locations provides a qualitative assessment of lateral and/or temporal gradients in fluid temperature at the time of sulphide deposition.

## Acknowledgements

The authors thank L. Bastian and N. Looser for assistance with sample preparation and CL imaging and the San Vicente (SIMSA) geology staff for assistance in the sampling.

## References

Bale CW, Bélisle E, Chartrand P, et al (2009) FactSage thermochemical software and databases — recent developments. Calphad 33:295–311.

Fontboté L, Gorzawski H (1990) Genesis of the Mississippi Valley-type Zn-Pb deposit of San Vicente, central Peru; geologic and isotopic (Sr, O, C, S, Pb) evidence. Economic Geology 85:1402–1437.

Leach DL, Sangster DF, Kelley KD, et al (2005) Sediment-Hosted Lead-Zinc DepositsA Global Perspective. In: One Hundredth Anniversary Volume. Society of Economic Geologists

Paton C, Hellstrom J, Paul B, et al (2011) Iolite: Freeware for the visualisation and processing of mass spectrometric data. J Anal At Spectrom 26:2508.

Pourbaix M, Burbank J (1964) Atlas D-Equilibres Electrochimiques. Journal of The Electrochemical Society 111: 14C.

Roberts NMW, Rasbury ET, Parrish RR, et al (2017) A calcite reference material for LA-ICP-MS U-Pb geochronology. Geochem Geophys Geosyst 18:2807–2814.

Rosas S, Fontboté L, Tankard A (2007) Tectonic evolution and paleogeography of the Mesozoic Pucará Basin, central Peru. Journal of South American Earth Sciences 24:1–24.

Spangenberg JE, Fontbote L, Macko SA (1999) An evaluation of the inorganic and organic geochemistry of the San Vicente Mississippi valley-type zinc-lead district, central Peru; implications for ore fluid composition, mixing processes, and sulfate reduction. Economic Geology 94:1067–1092.

Szmihelsky M, Steele-MacInnis M, Bain WM, et al (2021) Mixing of brine with oil triggered sphalerite deposition at Pine Point, Northwest Territories, Canada. Geology 49:488–492.

Torró L, Millán-Nuñez AJ, Benites D, et al (2023) Germanium- and gallium-rich sphalerite in Mississippi Valley–type deposits: the San Vicente district and the Shalipayco deposit, Peru. Miner Deposita.

# Multiple mineralization and fluid flow phases in the Central African Copperbelt – Implications for the age dating of the ore-forming processes

**Jessica Torres[1], Philippe Muchez[1]**
*[1]KU Leuven, Department of Earth and Environmental Sciences, Leuven, Belgium*

**Abstract.** Cobalt (Co) and copper (Cu) are both strategic elements of crucial importance for the European and world economies. This project focuses on the sediment-hosted Cu and Co deposits in the Katanga Copperbelt, DRC, where two main hypogene mineralization stages have been proposed: the first occurred during diagenesis and the second during maximum burial and orogenesis of the sedimentary strata. Detailed cathodoluminescence petrography was performed on dolomites from nodules and veins to assess and distinguish the different cementation and recrystallization phases for each main stage, and microthermometric analyses were conducted on dolomite and quartz to evaluate the evolution of the fluids present during the mineralization, recrystallization, and fluid flow events. Nearly all dolomite crystals analyzed show intense recrystallization features reflecting multiple phases, and at least two generations of authigenic quartz and sulfides were observed. The fluid inclusion results also present evidence of the pervasive influence of late high temperature and high salinity fluids in the first stage of nodules and lenses hosting ore minerals.

## 1 Introduction

The Central African Copperbelt is one of the world's largest sediment-hosted Cu-Co provinces, containing 200 Mt of Cu and 8 Mt of Co distributed in dozens of deposits (Hitzman et al. 2012). While numerous models have been proposed for the genesis of the mineralization, – from magmatic to syn-sedimentary, to diagenetic and orogenic, or with a multi-phase origin – the recently mostly accepted one involves the presence of at least two main stages of ore formation (Cailteux et al. 2005; Selley et al. 2005; Dewaele et al. 2006). Each of these two stages has a distinct signature of fluid salinity and temperature, the first one associated with diagenesis of the sediments and the second taking place subsequently during deep burial and orogenesis.

The fluid related to the diagenetic hydrothermal mineralization stage has intermediate salinity between 5 and 12 weight percent NaCl equivalent (wt% NaCl eq.) and temperature between 115°C and 220°C (Dewaele et al. 2006; El Desouky et al. 2009). This fluid is interpreted as a residual brine generated during the deposition of the basin-wide salt sheets during the early Neoproterozoic (~800 Ma; Selley et al. 2018). The range in salinity and temperature of the second fluid, responsible for the mineralization stage near maximum burial and deformation conditions, is between 35 and 42 wt% NaCl eq. and 290°C and 380°C, respectively (El Desouky et al. 2009; Sośnicka et al. 2019). The high salinity of this fluid can be explained by an evaporated fluid that dissolved salts (NaCl) at high temperature or by the mixing of residual and halite dissolution-related brines, based on the Na-Cl-Br systematics (Selley et al. 2018).

Additionally, a third fluid with a minimum temperature of 90°C and salinity of 0.5-4.0 wt% NaCl eq. has also been recognized (Cailteux et al. 2018). This meteoric fluid could have mixed with the saline fluid at depth and may have caused the further dissolution of the residual evaporites and the multiphase origin of the brecciation observed in the Copperbelt (Cailteux et al. 2018). This superposition of fluid flow phases is of major importance in the age dating of the ambient processes. However, even though the Re-Os and U-Pb isotopic systems have been successfully applied to date mineralizing processes in the Copperbelt, a common problem is the wide and sometimes even geologically unrealistic ages obtained (Decrée et al. 2014; Muchez et al. 2015). These inconsistencies can be explained by a mixing of different mineral generations during mineral extraction for isotopic analysis, the remobilization and recrystallization of the ore and gangue phases that variably reset the isotope systematics, and (partly) also by the isotopic resetting of the ages due to diffusion and loss of isotopes (Chaudhari et al. 2022). Nonetheless, many of the geochronology studies were not supported by careful petrography and geochemical mapping to identify variations in geochemistry within and between the minerals analyzed. Such analyses could allow the identification of different generations and recrystallization episodes that may be crucial to understand the ore-forming processes and the apparent age inconsistencies, which is the aim of this study.

## 2 Methodology

Sixteen samples from the Kamoto, Kambove West, and Luiswishi deposits were selected for this study, which encompass the West, Center, and East of the Lufilian Orogen, respectively (Fig. 1). Mineralized nodules and veins, which record hydrothermal events, were described petrographically and studied by cathodoluminescence to identify the different cementation and recrystallization episodes. Ten of the samples represent recrystallized nodules of diagenetic (type I) mineralization, three of which were compiled from El Desouky (2009) – one duplicated in this study – and three were compiled from Dewaele et al. 2006; one sample represents the maximum burial/orogenic (type II) nodule; one is a deformed nodule; and four samples contain

dolomite(-quartz) veins – three samples of the diagenetic stage also include veins cross-cutting the nodules, which totalize seven samples with veins. The carbonates occur mostly as saddle dolomite or sparry dolomite cements associated with the Cu and/or Co ores and authigenic quartz.

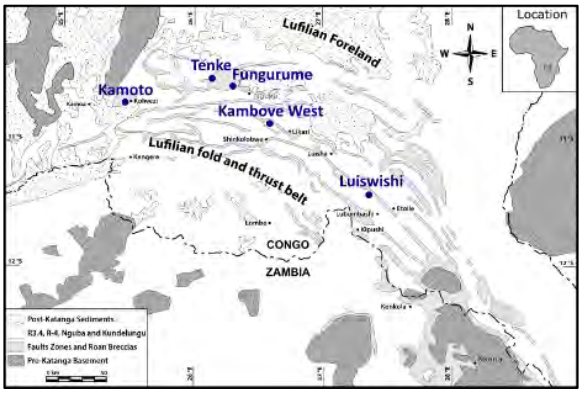


**Figure 1.** Location map of the Cu and Co deposits studied (in blue) and their position in the Lufilian Orogen.

For microthermometry, wafers of approximately 200 µm were prepared for each sample at the Department of Earth and Environmental Sciences, KU Leuven. Two microscopes were used for the petrographic and microthermometric studies, i.e. Olympus BX41 and BX51, the latter with a mounted LINKAM MDS heating and cooling stage. Primary inclusions were identified according to the criteria described by Shepherd et al. (1985), Goldstein and Reynolds (1994), and Goldstein (2003). Two (L+V), three (L+S+V), and more phases (L+S1+Sx+V) aqueous primary inclusions are present in both dolomite and quartz. Temperature of halite dissolution ($Ts_H$), temperature of homogenization (Th), temperature of first melting (Tfm), and the final melting of ice ($Tm_{ice}$) or hydrohalite ($Tm_{HH}$) were measured in appropriate fluid inclusion assemblages. A large number of primary fluid inclusions decrepitated at temperatures after the dissolution of halite but before the temperature of homogenization, precluding the measurement of Th. Salinities are reported as weight percent NaCl equivalent (wt% NaCl eq.). For the three-phase fluid inclusions containing halite, the salinity was calculated based on the equations of Sterner et al. (1988). For bi-phase inclusions containing liquid and vapor and where ice was the last phase to melt, the salinity was calculated based on the equation of Bodnar (1993). For bi-phase inclusions where hydrohalite was the last phase to melt, the salinity was calculated based on the equation of Steele-Macinnis et al. (2011), considering the molar fraction of NaCl = 1.

## 3 Petrography of the mineralization stages and veins

### 3.1 Nodule type I mineralization

In type I mineralization stage samples, the nodules, lenses, and layers consist primarily of dolomite, authigenic quartz, and Cu, Co, and Fe sulfides. These minerals appear as fine-grained crystals, where the dolomite was replaced by authigenic quartz and sulfides. These nodules, of approximately 0.6 cm maximum width, are pseudomorphs after anhydrite and gypsum (Muchez et al. 2008), with lenticular to oval shapes parallel to the stratification. Framboidal pyrite is common, and the main hypogene sulfide minerals include chalcopyrite, carrollite, bornite, and chalcocite. These minerals also occur disseminated in the matrix of nodule-hosting rocks, composed of organic-rich dolomitic shale or clayey dolomite.

All type I samples in this study are recrystallized and show distinct luminescence colors and intensities, as observed with cathodoluminescence petrography (Fig. 2). However, they still often preserve the primary dolomite generation, recognized by a dark pink luminescence. Dolomite crystals are sometimes coarse-grained and are not only replaced by but also replace the authigenic quartz and the sulfides. Therefore, the authigenic quartz was observed as at least two generations. The first precipitated before the dolomite and was replaced by it, and the second, more pervasive throughout the samples, precipitated later and replaced all dolomite generations, as observed in Figure 2.

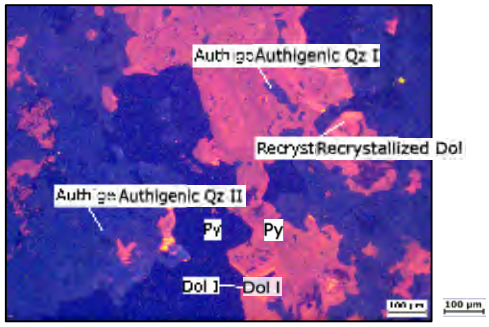


**Figure 2.** Example of type I nodule from the Kamoto deposit. The cathodoluminescence image shows primary (Dol I) and recrystallized dolomite and stages I and II of authigenic quartz; Py: pyrite.

### 3.2 Nodule type II mineralization

The second mineralization stage comprises nodules and lenses reaching up to 1.5 cm, in which the authigenic quartz and the sulfides were replaced by dolomite crystals. They are not necessarily parallel to the stratification and have varying shapes, with coarser grain size and free-growing crystals (Fig. 3). The main hypogene mineralization consists of chalcopyrite, carrollite, bornite, and chalcocite, also disseminated in the matrix, which can have varying contents of organic matter.

Although some recrystallization was also observed in this coarser-grained dolomite, it occurs to a much less extent when compared to type I

nodules, and new cements occur at the rims of the crystals (Fig. 3).

### 3.3 Veins and deformed nodules

The veins are composed of very coarse-grained dolomites and sulfides (Fig. 4) but can also consist of almost pure quartz. They often crosscut both types I and II nodules and lenses. Associated sulfides include chalcopyrite, carrollite, chalcocite, and digenite. As within the nodules, the dolomite replaces and is replaced by authigenic quartz, and shows different recrystallization phases (Fig. 4).

Deformed nodules and lenses were observed in one sample and have the same features as the recrystallized type I nodules. However, they present a wavy pattern following the folding of the host rock.

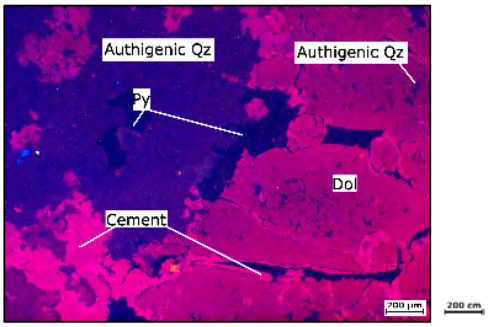


**Figure 3.** Example of type II nodule from the Luiswishi deposit. The cathodoluminescence image shows a first dolomite generation which is overgrown by dolomite cement; Py: pyrite.

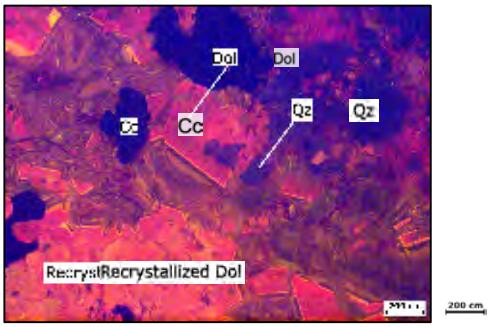


**Figure 4.** Example of vein from the Kambove West deposit. The cathodoluminescence image shows primary (Dol) and multiple recrystallization phases of dolomite; Cc: chalcocite.

## 4 Microthermometry

The fluid inclusions occur mainly in distinct assemblages or isolated, and were classified according to the number of phases present: a) type i, liquid and vapor; b) type ii, liquid, vapor, and solid halite; and c) type iii, with liquid, vapor, solid halite, anhydrite, and other unknown solids. The inclusions occurring in distinct assemblages are interpreted to have primary origin regarding the phase (primary, recrystallized, or cement) in which they appear.

Two main groups can be observed in the diagrams of Figures 5 and 6. The first group represents fluid inclusions in the first quartz generation from type I nodules, with salinity ranging from 6 to 21 wt% NaCl eq. Six inclusions measured in dolomite also belong to this group but with lower salinity values starting from 2 wt% NaCl eq. The second group involves all the stages, including the veins and deformed nodules. In this group, fluid inclusions from the second quartz generation in type I nodules and authigenic quartz from type II nodules and veins have a wide range of salinities (29 to 45 wt% NaCl eq.). Inclusions in dolomite have very similar salinities (26 and 46 wt% NaCl eq.).

Figure 6 shows the relationship between Th and the calculated salinity. Type I nodules occur in two groups, the first with fluid inclusions in authigenic quartz I with salinities of 4-21 wt% NaCl eq. and Th of 80-220°C, and the second with authigenic quartz II and recrystallized dolomite from with salinities of 34-46 wt% NaCl eq., and Th of 280-400°C. Type II nodules appear with a narrower range, but also with high salinity (~35 wt% NaCl eq.) and high Th (~300-315°C). Most of the veins occur in the transition between the two groups previously discussed, with ~26 wt% NaCl eq. and Th from 235 to 365°C. Nonetheless, some inclusions contain higher salinity fluids (average of 38 wt% NaCl eq.; Fig. 5).

**Table 1.** Summary of the microthermometric analysis of primary fluid inclusions in dolomite and quartz for Cu-Co deposits in the Katanga Copperbelt, including the microthermometric data for quartz in type I nodules from Dewaele et al. (2006) and El Desouky (2009).

| Stage | Fl Type | Host | Th | | | | Salinity | | | |
|---|---|---|---|---|---|---|---|---|---|---|
| | | | Avg | Min | Max | n | Avg | Min | Max | n |
| Deformed nodules | ii | Qz | - | - | - | - | 32 | 29 | 34 | 17 |
| | iii | Qz | 266 | 266 | 266 | 1 | 32 | 29 | 34 | 10 |
| Nodule Type I | i | Dol | 201 | 190 | 209 | 3 | 6 | 2 | 13 | 7 |
| | | Qz | 169 | 80 | 341 | 91 | 15 | 6 | 30 | 52 |
| | ii | Dol | 321 | 280 | 362 | 11 | 38 | 30 | 46 | 46 |
| | | Qz | 345 | 300 | 398 | 26 | 41 | 30 | 46 | 55 |
| | iii | Dol | - | - | - | - | 31 | 30 | 31 | 5 |
| | | Qz | - | - | - | - | 37 | 35 | 42 | 14 |
| Nodule Type II | ii | Dol | 306 | 298 | 313 | 8 | 36 | 34 | 40 | 17 |
| Vein | i | Dol | 323 | 235 | 369 | 13 | 27 | 26 | 27 | 12 |
| | ii | Dol | 332 | 322 | 348 | 3 | 38 | 28 | 44 | 56 |
| | | Qz | - | - | - | - | 35 | 35 | 35 | 1 |
| | iii | Dol | - | - | - | - | 31 | 28 | 38 | 7 |

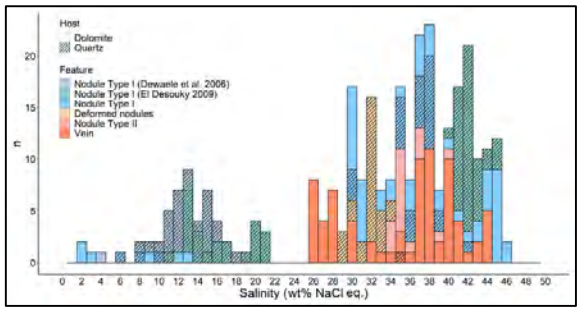


**Figure 5.** Calculated salinity for the five mineralization stages defined in this study. See text for their description.

## 5 Discussion and conclusion

The detailed cathodoluminescence petrography on dolomite crystals in samples from different deposits and generations shows extensive recrystallization events which took place in the Katanga basin. Even though there is no direct correlation between the recrystallization and the microthermometry results,

fluid inclusion analyses confirm the influence of high Th and high salinity fluids on type I nodules and lenses.

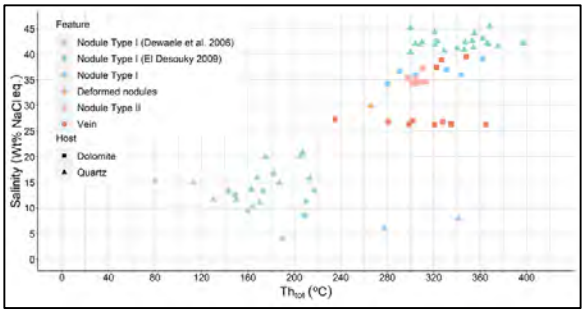


**Figure 6.** Th *versus* calculated salinity for the five mineralization stages defined in this study.

In Figure 5, the first assemblage of fluid inclusions observed for type I nodules and lenses represents the original diagenetic conditions, consistent with the results of Dewaele et al. (2006) and El Desouky et al. (2009). The second assemblage reveals the recrystallization and later dolomite and quartz cementation in the type I nodules, the dolomites and quartz in the type II nodules, and in the veins, which contain high Th and high salinity fluids associated with maximum burial and orogenic deformation.

These results, which point to a pervasive recrystallization and multiple cementation phases in the Katanga Copperbelt, will further help the interpretation of the current wide range and sometimes unrealistic ages obtained to date the ore-forming processes in the region.

## Acknowledgments

We thank Mr. Herman Nijs for the preparation of the thick sections and wafers, and Garth Graham for the constructive review and helpful comments. Both authors are members of the SIM² - KU Leuven Institute for Sustainable Metals and Materials. Financial support from the research grant C14/21/056 of the KU Leuven Special Research Fund is acknowledged.

## References

Bodnar RJ (1993) Revised equation and table for determining the freezing point depression of H2O-NaCl solutions. Geochimica et Cosmochimica Acta 57:683-684

Cailteux JLH, Kampunzu AB, Lerouge C, Kaputo AK, Milesi JP (2005) Genesis of sediment-hosted stratiform copper–cobalt deposits, central African Copperbelt. J Afr Earth Sci 42:134-158

Cailteux JLH, Muchez P, De Cuyper J, Dewaele S, De Putter T (2018) Origin of the megabreccias in the Katanga Copperbelt (D.R.Congo). J Afr Earth Sci 140:76-93

Chaudhari A, Brugger J, Ram R, Chowdhury P, Etschmann B, Guagliardo P, Xia F, Pring A, Gervinskas G, Liu A, Frierdich A (2022) Synchronous solid-state diffusion, dissolution-reprecipitation, and recrystallization leading to isotopic resetting: insights from chalcopyrite replacement by copper sulfides. Geochimica et Cosmochimica Acta 331:48-68

Decrée S, Deloule É, De Putter T, Dewaele S, Mees F, Baele J-M, Marignac C (2014) Dating of U-rich heterogenite: New insights into U deposit genesis and U cycling in the Katanga Copperbelt. Precambrian Research 241:17-28.

Dewaele S, Muchez P, Vets J, Fernandez-Alonzo M, Tack L (2006) Multiphase origin of the Cu–Co ore deposits in the western part of the Lufilian fold-and-thrust belt, Katanga (Democratic Republic of Congo). J Afr Earth Sci 46:455-469

El Desouky HA (2009) Metallogenesis of stratiform copper deposits in the Lufilian orogen, Democratic Republic Congo. Ph.D. Thesis, KU Leuven, Faculteit Wetenschappen, pp 210

El Desouky HA, Muchez P, Cailteux J (2009) Two Cu–Co sulfide phases and contrasting fluid systems in the Katanga Copperbelt, Democratic Republic of Congo. Ore Geol Rev 36:315-332

Goldstein R (2003) Petrographic analysis of fluid inclusions. In: Samson I, Anderson A, Marshall D (eds) Fluid Inclusions: Analysis and Interpretation. Mineralogical Association of Canada, pp 9-53

Goldstein RH, Reynolds TJ (1994) Systematics of Fluid Inclusions in Diagenetic Minerals. SEPM Soc Sed Geol 31

Hitzman M, Broughton DW, Selley D, Woodhead J, Wood DL, Bull SW (2012) The Central African Copperbelt: diverse stratigraphic, structural, and temporal settings in the world's largest sedimentary copper district. Society of Economic Geologists Special Publications Series 16:487-514

Muchez P, Vanderhaeghen P, El Desouky H, Schneider J, Boyce A, Dewaele S, Cailteux J (2008) Anhydrite pseudomorphs and the origin of stratiform Cu–Co ores in the Katangan Copperbelt (Democratic Republic of Congo). Mineralium Deposita 43:575-589

Muchez P, André-Mayer A-S, El Desouky HA, Reisberg L (2015) Diagenetic origin of the stratiform Cu–Co deposit at Kamoto in the Central African Copperbelt. Mineralium Deposita 50:437-447

Selley D, Broughton D, Scott R, Hitzman M, Bull S, Large R, McGoldrick P, Croaker M, Pollington N, Barra F (2005) A New Look at the Geology of the Zambian Copperbelt. In: Hedenquist JW, Thompson JFH, Goldfarb RJ, Richards JP (eds), Economic Geology One Hundredth Anniversary Volume. Society of Economic Geologists, Littleton, pp 965-1000.

Selley D, Scott R, Emsbo P, Koziy L, Hitzman MW, Bull SW, Duffett M, Sebagenzi S, Halpin J, Broughton DW (2018) Structural Configuration of the Central African Copperbelt: Roles of Evaporites in Structural Evolution, Basin Hydrology, and Ore Location. In: Arribas AM, Mauk JL (eds) Metals, Minerals, and Society. Society of Economic Geologists, Littleton, pp 115-156

Shepherd TJ, Rankin AH, Alderton DHM (1985) A Practical Guide to Fluid Inclusion Studies. Glasgow and London (Blackie) 239

Sośnicka M, Gigler GM, Kinnaird JA, Przybyłowicz WJ, Chimvinga J, Master S, Plessen B (2019) Mineralizing fluids of the supergene-enriched Mashitu South Cu-Co deposit, Katanga Copperbelt, DRC. Ore Geol Rev 109:201-228

Steele-MacInnis M, Bodnar RJ, Naden J (2011) Numerical model to determine the composition of $H_2O$–NaCl–$CaCl_2$ fluid inclusions based on microthermometric and microanalytical data. Geochimica et Cosmochimica Acta 75:21-40

Sterner SM, Hall DL, Bodnar RJ (1988) Synthetic fluid inclusions. V. Solubility relations in the system NaCl-KCl-$H_2O$ under vapor-saturated conditions. Geochimica et Cosmochimica Acta 52:989-1005

# Mineralogical mapping of potential source, aquifer and trap rocks from the Central African Copperbelt

**Veronica G. Trevisan[1], Jamie J. Wilkinson[1,2], Martin Purkiss[3], Mike Daly[3]**
*[1]London Centre for Ore Deposits and Exploration (LODE), Research Department, Natural History Museum, London, UK*
*[2]Department of Earth Science and Engineering, Imperial College London, UK*
*[3]Department of Earth Sciences, University of Oxford, UK*

**Abstract.** The Central African Copperbelt (CACB) is the world's largest repository of sediment-hosted copper and cobalt, which are critical for electricity transmission and the production of batteries needed to help decarbonise society. Key knowledge gaps regarding this mineral system include the scale and nature of alteration mineral assemblage zoning and mineral major and trace element chemistry patterns. A detailed characterization of these gaps can help guide exploration for technology metals across different sedimentary basins. Here, we present TESCAN TIMA® automated mineral mapping results on (meta)sedimentary rocks from contrasting geological domains in the CACB. Our initial findings confirm the higher metamorphic grade and metamorphic textures in rocks from the Domes region, Kansanshi mine and in the Muva Group from the Fishtie deposit. Initial results also suggest a dominantly Mg-rich (±Na, ±Ca) alteration in the Domes region and Kansanshi mine, whereas in the Classical Zambian Copperbelt (ZCB) a dominant K-rich (± Ca, ±Mg, ±Na) alteration is recognized. At Fishtie, alteration is principally characterized by Fe-Mg metasomatism. Future work will include whole-rock geochemistry, mineral chemistry of key alteration and accessory mineral phases, and data interrogation through multivariate statistical techniques.

## 1 Introduction

The criticality of Cu, Co (±V) in battery technology and electricity transmission has established them as key components of the carbon-free energy transition. A major proportion of these elements are sourced from sedimentary basin-hosted deposits, formed from large-scale fluid flow systems (Hitzman et al. 2010). Recent work has shown that diverse basin architectures and processes were responsible for their genesis (McGowan et al. 2003; Selley et al. 2005; Muchez et al. 2010; Sillitoe et al. 2010) yet we still do not understand why so few basins become highly endowed with metals.

The primary aim of the UKRI/NERC CuBES (Copper Basin Exploration Science: a mineral and petroleum systems approach) project is to address the fundamental geodynamic and geological context for the development of exceptionally endowed Cu-Co(-V) basins, such as the Katangan in the CACB, and how they are best identified (Fig. 1).

As part of the CuBES project, the main aims of this postdoctoral research in the Katangan basin (CACB) are fourfold: 1) to establish the mineralogical residence of metals and trace elements of interest in potential source rocks (WP2); 2) to characterise hydrothermal alteration from the edge of mineralised zones out to background sites (WP2); 3) to understand hydrothermal extraction of metals from oxidised continental red beds (WP3); 4) to develop new geochemical tools to identify fertile basins or sub-basins and to target within mineral systems (WP4).

The general approach involves sampling of drillholes and outcrops along-strike within the main ore horizons and up stratigraphy in near-deposit settings and on a wider basin-scale, petrography of thin sections and polished blocks, whole rock analyses, mineral chemistry of alteration and accessory phases, and data interrogation using multivariate statistical techniques.

Here, we report a mineralogical characterization of (meta)sedimentary rocks from contrasting geological domains in the CACB using the TESCAN Integrated Mineral Analyzer (TIMA)® automated SEM system located in the Imaging and Analysis Centre (IAC) at the Natural History Museum.

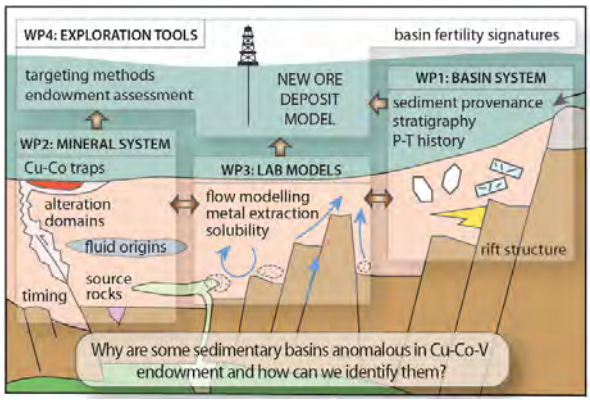


**Figure 1.** Cartoon illustrating CuBES research project structure.

## 2 The Central African Copperbelt

The CACB, including the Zambian Copperbelt (ZCB), Congolese Copperbelt (CCB), and deposits in the Northwest Province of Zambia, is the world's premier sediment-hosted Cu province (Hitzman et al. 2012; Selley et al. 2018) (Fig. 2). Deposits are hosted in Neoproterozoic (meta)sedimentary rocks, including abundant evaporite deposits, of the Katangan Supergroup deposited in a series of intra-continental rift basins with (Hitzman et al. 2012).

The Katangan basin initiated at ~840 Ma (Selley et al. 2018) and early rift-stage basal clastic sediments were deposited, followed by mixed clastic-carbonate and evaporitic carbonates. These are followed by a second stage of clastic and mafic rocks related to renewed rifting. Widespread glacial

and postglacial deposits cover this lower part of the basinal sequence and mark an uppermost limit to the distribution of major copper deposits. Subsequent deposition of relatively monotonous, non-evaporitic basin fill of clastic and carbonate successions preceded basin inversion during the Pan-African (~590–500 Ma) in the Lufilian orogeny (Hitzman et al. 2012).

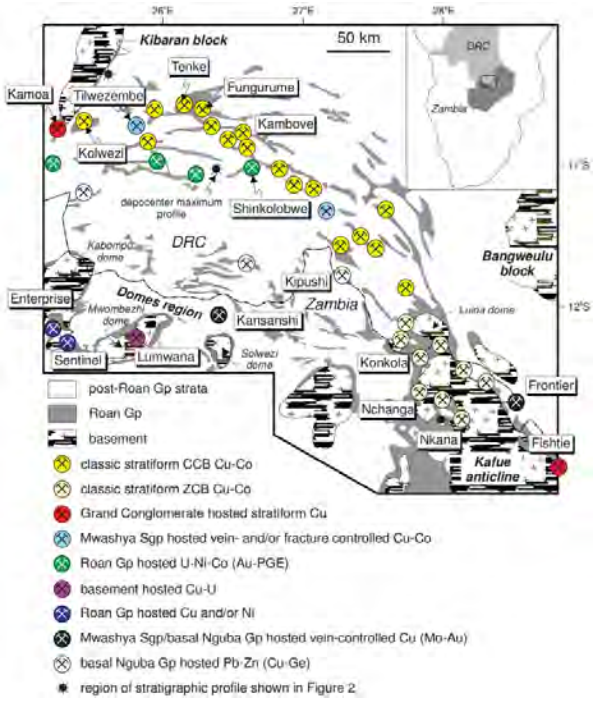


**Figure 2.** Basic geologic map of the Central African Copperbelt, showing the distribution of various ore types. Abbreviations: CCB = Congolese Copperbelt, DRC = Democratic Republic of Congo, Gp = Group, PGE = platinum group element, Sgp = Subgroup, ZCB = Zambian Copperbelt. Inset shows map location in Africa (Selley et al. 2018).

The CACB contains copper deposits at several stratigraphic levels. These deposits display differing styles and textures of mineralization and alteration types. Deposits may contain either or both disseminated, generally fine-grained sulphides and vein-hosted, generally coarse-grained sulphides. Nevertheless, there are shared characteristics among most deposits. Deposits are hosted at stratigraphic or structural redox boundaries. Ore sulphide zonation within deposits occurs on multiple scales, with complexity of zoning broadly related to the complexity of the host-rock sequence. Macrostructural controls on deposit position suggest that extensional faults were important in controlling fluid flow, either directly or indirectly through influence on sedimentary and probably diagenetic facies variation. The stratigraphic section within which the deposits are located was affected by regional potassic, magnesian, silicic, and/or sodic alteration controlled partly by lithology and indicative of the passage of brines (Hitzman et al. 2012). Particularly for the classical ZCB, highly potassic residual brines (i.e., formed during advanced evaporation of seawater), anomalously enriched in Cu, Co, Pb and Zn, were responsible for ore formation (Davey et al. 2021).

## 3 Initial results: TESCAN TIMA® automated mineral mapping

### 3.1 Domes region

Samples from the Domes region include a schist from the basement in the Solwezi Dome, meta-siltstones from the Nguba Group in the Luswishi Dome area, and a meta-sandstone from the Lower Roan Group in the Konkola Dome. Although the metamorphic fabric is still preserved, the primary meta-sedimentary mineralogy has been variably affected and modified by interaction with hydrothermal fluids.

Consistently identified major phases in the Solwezi schist samples include biotite, plagioclase, quartz and muscovite, whereas accessory phases consist of apatite, rutile and zircon. Local chalcocite and bornite have also been observed (Fig. 3a).

The Konkola meta-sandstone consists of quartz, muscovite and biotite. Local clinochlore, amphibole, K-feldspar and zircon have been mapped.

The Nguba meta-siltstones in the Luswishi Dome area comprise albite, quartz, dolomite and ankerite. In one sample, coarse porphyroblasts (scapolite?) have been replaced by albite and chlorite. Ore minerals are represented by pyrite, chalcopyrite and, to a lesser extent, pyrrhotite. Accessory phases include rutile, monazite and apatite.

### 3.2 Kansanshi Cu-Au mine

The lower stratigraphy at Kansanshi is represented by numerous (meta-) sandstones from the Lower Roan Group (Fig. 3b) and a talc-quartz-kyanite-biotite schist, possibly allochthonous Lower Roan Group. In addition to the common phases, such as quartz, muscovite, biotite and feldspar, some of these meta-sandstones also contain anhydrite, amphibole, Mg-rich phosphate, carbonate (calcite and/or dolomite), clinozoisite and chlorite. Accessory phases include rutile, monazite, zircon and apatite. Higher in the stratigraphy, a sample of carbonate and a carbonaceous metapelite consist essentially of dolomite (>50 wt.%) and minor calcite, quartz, biotite and muscovite. These have been interpreted to form part of a Lufilian thrust sheet emplaced over Lower Roan basal clastics.

The Nguba Group is here represented by a deformed shale consisting of quartz, plagioclase, ankerite, muscovite, chlorite, biotite and minor pyrrhotite. Apatite and rutile are the accessory phases.

The top section of the stratigraphy is represented by two samples also correlated with the Lufilian thrust sheet: (i) a meta-sandstone with calcite, quartz, plagioclase, muscovite and minor pyrrhotite. Accessory phases include apatite and rutile; and (ii)

a mineralised shale with quartz, plagioclase, muscovite and biotite. Pyrrhotite is the only sulphide phase, and rutile and apatite are the accessories.

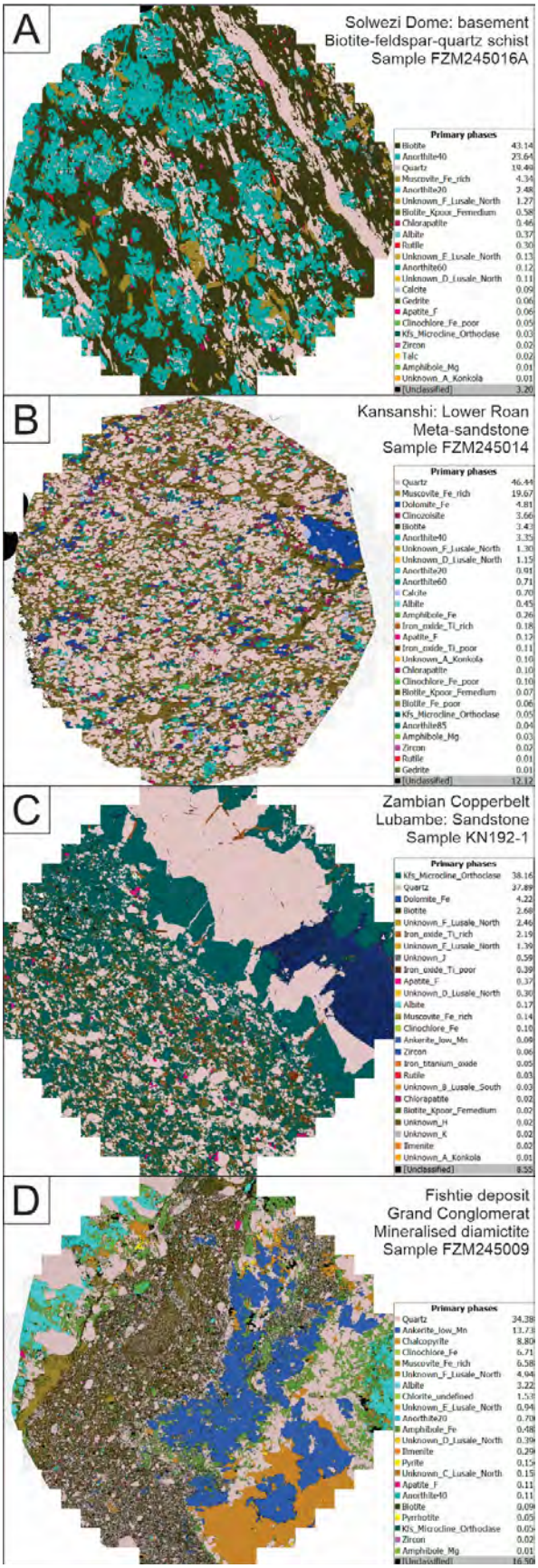


**Figure 3.** TESCAN TIMA® automated SEM mineral map of metasedimentary rocks from the (a) Domes region, (b) Kansanshi Cu-Au mine, (c) Zambian Copperbelt, and (d) Fishtie Cu deposit.

### 3.3 Classical Zambian Copperbelt

Samples from the Fitwaola open pit mine consist of a banded siliceous rock with quartz and talc, and a banded clastic rock with plagioclase, quartz, biotite, iron oxide and K-feldspar. Apatite and rutile are the accessory phases. Both samples are interpreted to form part of the Lower Roan Group.

The Kinsenda copper mine, located on the southern edge of the Luina Dome (Democratic Republic of Congo), is here represented by two samples of mineralised conglomerate of the Lower Roan Group. The clasts are of quartz, whereas the matrix consists of muscovite, chalcocite, yarrowite ($Cu_9S_8$) and minor bornite.

At Lubambe, the Lower Roan Group is represented by sandstone and conglomerate samples. Major phases in both rock types include K-feldspar, quartz, carbonate (calcite and/or dolomite), biotite, muscovite and iron oxide. Apatite, rutile and zircon are the accessory phases (Fig. 3c). The Upper Roan sequence includes silty and muddy carbonates alternating with breccias and shale. The breccias consist of albite, quartz, dolomite, clinochlore, biotite, K-feldspar, amphibole and iron oxide with accessory apatite, rutile and zircon. The Mwashia Subgroup is illustrated by a mudstone with an undefined phase, possibly representing a mixture of different minerals, dolomite, biotite, quartz, albite, muscovite, iron oxide and amphibole. Finally, the Nbuba Group is characterized by a diamictite (possibly correlated with the Grand Conglomerat) with quartz, dolomite, an undefined phase, also possibly representing a mixture of different minerals, biotite, muscovite, K-feldspar, pyrite, ankerite and amphibole. Both the Mwashia and Nguba rocks have apatite and rutile as accessory minerals.

### 3.4 Fishtie Cu deposit

Samples from the Fishtie deposit include rock types from the Muva Group, Mwashia Subgroup, Nguba Group and Kudelungu Group. The Muva meta-sandstones exhibit metamorphic fabric represented by schistosity (shear bands?) and recrystallization. Consistently identified major phases include muscovite, quartz, clinochlore, amphibole and biotite, with accessory rutile, apatite, zircon and ilmenite.

The main rock types of the Mwashia Subgroup include (pebbly-) sandstones, conglomerates and quartzites. These consist of quartz, K-feldspar, dolomite, muscovite, ankerite and amphibole. Accessories include apatite, zircon, rutile, iron oxide and ilmenite.

The Nguba Group is illustrated by barren and mineralised diamictites (Grand Conglomerat), and shale. The first consists of quartz, muscovite, K-

feldspar, barite, biotite, amphibole and a few very fine-grained undefined phases, possibly representing a mixture of different minerals. The second includes quartz, clinochlore, biotite, muscovite, amphibole, bornite, chalcopyrite and wittichenite ($Cu_3BiS_3$) (Fig. 3d). Rutile and apatite represent the accessories. The shale is essentially characterized by very fine-grained undefined phases, plus quartz, albite, muscovite, amphibole, ankerite and chlorite, with accessory ilmenite, apatite and clinozoisite.

Kundelungu Group samples include a shale and a sandstone. The first consists of albite, quartz, some undefined phases (mineral mixtures), muscovite, ankerite, chlorite, amphibole, minor pyrrhotite and chalcopyrite, as well as ilmenite, apatite and clinozoisite as accessories. The second comprises quartz, albite, undefined phases, muscovite, clinochlore and iron oxide. Accessory phases are represented by apatite, rutile and zircon.

## 4 Initial observations and future work

Preliminary results using the TESCAN TIMA® automated SEM system for mineral mapping and texture investigation of samples with a wide spatial and stratigraphic distribution in the CACB confirm the higher metamorphic grade and metamorphic textures in rocks from the Domes region, Kansanshi mine and the Muva Group from the Fishtie deposit. Although complex and protracted, initial results also suggest a dominantly Mg-rich (±Na, ±Ca) alteration in the Domes region and Kansanshi mine, whereas in the Classical ZCB a dominant K-rich (± Ca, ±Mg, ±Na) alteration is recognized. At Fishtie, a Fe-Mg metasomatism predominates. It is clear that the alteration-mineralisation characteristics in the different regions are sufficiently different to be considered separate mineral systems from a hydrothermal processes perspective.

Future work will include conventional multielement whole-rock geochemistry, mineral chemistry in potential key alteration and accessory mineral phases using analytical SEM, microprobe and LA-ICP-MS, and data interrogation through supervised and un-supervised multivariate statistical techniques.

## Acknowledgements

This work was supported by the highlight topic grant “CuBES” awarded by the Natural Environment Research Council, UK (NE/T002921/1). The NHM IAC team are thanked for their assistance with samples preparation (Callum Hatch and Godwin Fernandes) and TESCAN TIMA® imaging and data processing (Cindy Broderick and Will Brownscombe). We also thank First Quantum Minerals, in particular Tom Wesby, Rob Sievwright, Munshya Zimba, Leman Mpokosa and the Zambian team, for providing samples for this study and helpful discussions.

## References

Davey J, Roberts S, Wilkinson J (2021) Copper- and cobalt-rich, ultrapotassic bittern brines responsible for the formation of the Nkana-Mindola deposits, Zambian Copperbelt. Geology 49: 341-345

Hitzman MW, Selley D, Bull S (2010) Formation of sedimentary rock-hosted stratiform copper deposits through Earth History. Economic Geology 105: 627-639

Hitzman MW, Broughton D, Selley D, Woodhead J, Wood D, Bull S (2012) The Central African Copperbelt: Diverse stratigraphic, structural, and temporal settings in the world’s largest sedimentary Ccpper district. SEG Special Publication 16: 487-514

McGowan RR, Roberts S, Foster RP, Boyce AJ, Coller D (2003) Origin of the copper-cobalt deposits of the Zambian Copperbelt: An epigenetic view from Nchanga. Geology 31 (6): 497-500

Muchez Ph, Brems D, Clara E, De Cleyn A, Lammens L, Boyce A, De Muynck D, Mukumba W, Sikazwe O (2010) Evolution of Cu–Co mineralizing fluids at Nkana Mine, Central African Copperbelt, Zambia. Journal of African Earth Sciences 58: 457-474

Selley D, Broughton D, Scott R, Hitzman M, Bull S, Large R, McGoldrick P, Croaker M, Pollington N, Barra F (2005) A New Look at the Geology of the Zambian Copperbelt. SEC 100th Anniversary Volume 965-1000

Selley D, Scott R, Emsbo P, Koziy L, Hitzman MW, Bull SW, Duffett M, Sebagenzi S, Halpin J, Broughton D (2018) Structural Configuration of the Central African Copperbelt: Roles of Evaporites in Structural Evolution, Basin Hydrology, and Ore Location. SEG Special Publication 21: 115-156

Sillitoe RH, Perello J, Garcia A (2010) Sulfide-bearing veinlets throughout the dtratiform mineralization of the Central African Copperbelt: Temporal and genetic Implications. Economic Geology 105 (8): 1361-1368

# District scale basin development interpretations utilizing stratigraphic correlation – Structural target generation for Kipushi style Zn-Cu-Pb deposits in Southern Congolese Copperbelt

**Helen C. Twigg[1], Murray W. Hitzman[1]**
*[1] iCRAG, School of Earth Sciences, University College Dublin, Belfield, Dublin, Ireland*

**Abstract.** District scale basin modelling is used as a tool to explore the controlling factors of Zn-Cu-Pb massive sulphide and vein-fracture hosted Cu mineralisation in the Southern Congolese Copperbelt – an underexplored region of the Central African Copperbelt. This study uses district scale mapping and cross section interpretations to investigate basin architecture between the Southern and Central Congolese Copperbelt where ore deposit types transition from Cu-Co stratiform ore bodies to carbonate hosted Zn-Pb-Cu massive sulphide bodies. The study area was historically poorly mapped due to a thick weathering profile, low topographic relief and limited economic interest. A new lithostratigraphic map and district scale cross sections were created by integrating high resolution airborne magnetic surveys, soil geochemical data and drillholes that provided baseline data around the Kipushi anticlinal structure. The Neoproterozoic Katangan stratigraphy which hosts the mineral deposits dramatically thickens to the SW from the Kipushi mine suggesting that a basement high separated the central and southern portions of the Congolese Copperbelt into sub-basins. The interpreted basement high coincides with the loss of the Mines Subgroup, a change in structural deformation style, and ore deposit type.

## 1 Introduction

The Central African Copperbelt (CACB) located in southern Democratic Republic of Congo (DRC) and northwestern Zambia contains 48% of the world's cobalt reserves and significant resources of copper, zinc, nickel, and gold (USGS 2023) hosted within the Neoproterozoic-Cambrian Katangan siliciclastic and carbonate basin. The Katanga Supergroup carbonate and siliciclastic metasedimentary rocks were deposited in an epicontinental basin formed during the break-up of Rhodinia. Multiphase hypogene mineralization in the Katangan basin occurred over a time frame of >300 million years linked to basin rift and inversion events and, salt evacuation and dissolution. Within the Congolese Copperbelt (CCB) polymetallic deposits are distributed in distinct belts of Cu-Co, U-Ni-Co, and Zn-Pb-Cu-Ge ores (Figure 1) distributed from the northern basin margin southwards towards the basin centre (Selley et al. 2018 and references therein).

The Katangan Supergroup is subdivided into three groups by two basin-wide glaciogenic diamictite units. The Mwale Formation linked to the Sturtian glaciation separates the basal Roan Group, from the overlying Nguba Group. The Kyandamu Formation associated with the younger Marinoan glaciation is located at the base of the Kundelungu Group (Table 1). The Roan Group displays distinct stratigraphic sequences in Zambia and the DRC reflecting different depositional environments during initial extension after 880Ma. The Zambian Roan Group is composed of the siliciclastic basal Mindola Subgroup, the mixed carbonate and siliciclastic Kitwe Subgroup, and the upper carbonate dominated Kirilamombwe Subgroup. The Congolese Roan Group is dominated by carbonate and former evaporite units in the Mines and Fungerume subgroups. The lowermost Musoni Subgroup (formerly the R.A.T.) representing synrift sediments are not fully exposed due to decoupling of the stratigraphy along the 'R.A.T. Breche' zones of megabreccia interpreted as residuum after evaporites (Jackson et al. 2003). This breccia contains mega clasts of the Musoni, Mines and Fungerume subgroups (Table 1) interpreted as blocks of intrasalt units. Mines Subgroup blocks host the 'classical' DRC stratiform Cu-Co deposits in megabreccia zones which have been interpreted as salt diapirs, salt walls, thrust decollements and tectonic breccias. These zones are located conformably below the Roan Group Kansuki Formation but locally cross-cut stratigraphy. The overlying Mwashya Subgroup records a second extensional event dated to 765-735 Ma. Katangan stratigraphy from the Mwashya Subgroup upwards are broadly correlative across the Congolese and Zambian Copperbelt.

The CACB is well explored in the near surface for 'classical' stratiform Cu-Co deposits hosted in the Mines Subgroup in the CCB and the Kitwe Formation of the Zambian Copperbelt (ZCB). Exploration for vein and fracture hosted Cu and carbonate replacement Zn-Cu-Pb deposits is immature and exploration models for these types of deposits in the CACB are poorly developed. The structural control, basin development history and fluid flow pathways are poorly understood especially in the decoupled Congolese Copperbelt. Three occurrences of Zn-Cu-Pb mineralisation are known in the Southern CCB, Kipushi, Lombe and Kenegere (Kampunzu et al. 2009; Haest and Muchez 2011). All form pipe like orebodies in secondary faults splaying from or adjacent to major structures (Batumike et al. 2007). Mineralisation affected platform carbonates of the Kaponda, Kakontwe and Kipushi formations which are locally rich in organic matter primarily adjacent to high angle structures. The wider geology around these deposits is poorly mapped and little understood.

This study provides a method to map and interpret lithology, stratigraphy and structures in an area with limited outcrop. Basin architecture is investigated by tracking facies changes within depocentres and relating them to the structures that controlled deposition and could have provided fluid pathways for epigenetic mineralisation.

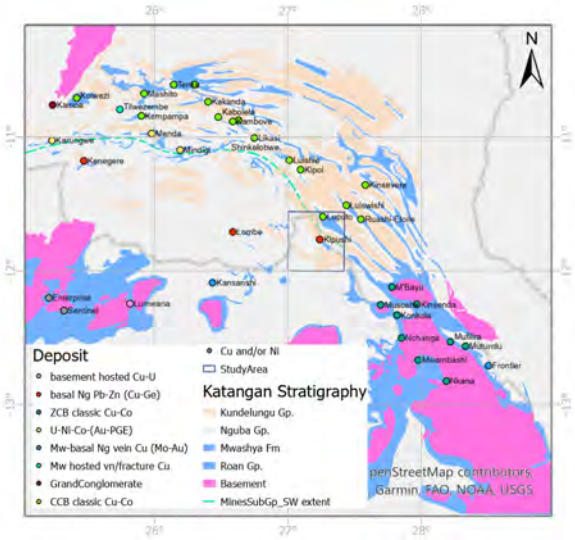


**Figure 1.** Central African Copperbelt and deposit type locations within the study area. Modified after Torremans et al. 2018; Selley et al. 2018.

## 2 Methodology

### 2.1 Geological Mapping

Areas with outcrops or containing drill holes were utilized to relate known geological lithologies with soil geochemical results using major element and trace element ratios. Soil multi-element geochemistry results were interpreted manually using ioGAS™ software and element mobility in weathering profiles were checked in drillholes to assist mapping interpretation. In addition, stratigraphic contacts, unconformities and structures were mapped from airborne magnetic survey data. Surface bedding intersections were sourced from multiple generations of mapping, 1950-60's era mapping by RST (Zambia), Gécamines (D.R.C.) and recent exploration company mapping data. Additional bedding and structural orientations were taken or calculated from drillhole data.

### 2.2 Cross Section Creation

The supra-salt stratigraphy from the Kansuki Formation to the Gombella Subgroup (Table 1) was composited or split into unconformity bound packages which were of an appropriate thickness for district scale modelling. Cross section locations were picked to cover drillhole fences or mapping traverses which resulted in irregular spacing of 5–7km apart. Cross sections were created in Move™ software oriented perpendicular to strike between NE-SW to NNE-SSW. Interpretations were created using the surface map, drillhole data, and surface and down hole bedding orientations.

Data limitations include: limited or no outcrop of upper Roan and lower Nguba groups SW of the Kipushi anticline; little orientation data for the western part of the study area; poor soil geochemical data in the NW region; and limited access to historical holes and incomplete records of historical holes. Geological interpretations were verified using the sequential restoration technique suitable for salt structures (Rowan 1993).

| Age (Ma) | | | Group | Subgroup | Formation | Lithology | Thickness (m) | Modeling Units |
|---|---|---|---|---|---|---|---|---|
| | Early Paleozoic | | Blanco | | | | | |
| 530 | Neoproterozoic | Ediacaran | Kundelungu | Ngule Ku 3 | Sampwe | No drillhole or ourcrop information | | |
| | | | | | Kiubo | | | |
| | | | | | Mongwe | | | |
| | | | | | Lubudi | | | |
| | | | | Gombella Ku 2 | Kanianga | alternating massive mudstone-sandstone beds followed by turbidite deposits | 570 | Lower Kundelungu |
| | | | | | Lusele | dolomicrite, argillacous at top | 15 | |
| 635 | | | | Ku 1 | Kyandamu | diamictite with basal finely laminated mudstone | 70 | |
| 660 | | Cryogenian | Nguba | Bunkeya Ng3 | Upper Monwezi | Lower Monwezi facies + interbedded mudstone-siltstone, sandstone, $T_{BD}$, $T_{CDE}$ and $T_{ABCDE}$ turbidite deposits. Occassional diagenetic evaporite growths | 125-610 | Upper Monwezi |
| | | | | | Lower Monwezi | laminated mudstone and siltstones, occassional sand beds | 190-266 | Lower Monwezi |
| | | | | | Upper Katete | dolostone, carbonacous dolostone and shales, alternating dolostone and mudstone | 355-750 | Upper Katete |
| | | | | | | | | Mid Katete |
| | | | | | Lower Kaktete (Serie Recurrente) | thickly and thinly interbedded or interlaminated Mg enriched mudstone and evaporative dolostone. Laminated Mg rich dolostone | 130-425 | Lower Katete |
| | | | | Muombe Ng2 | Kipushi | laminated dolostone | 25 | Muombe |
| | | | | | Kakontwe | microbial laminated dolostone | 520-625 | |
| | | | | | | carbonaceous dolostone | | |
| | | | | | | dolomicrite? | | |
| 680 | | | | | Kaponda | tiger striped laminated dolostone - only intersected as rudstone clasts | 210 | |
| 715 | | | | Ng1 | Mwale | debrite interbedded with turbites | 90-725 | Mwale |
| | | Tonian | Roan | Mwashya R4 | Kazandi | siltstone-mudstone thin $T_{DE}$ turbidites, with | 80-190 | Mwashya & Kansuki |
| | | | | | Kafubu | carbonaceous shales | 45 | |
| 735 | | | | | Kamoya | dolomitic siltstone, sandstone conglomerate and chert | 120 | |
| 765 | | | | Fungerume R3 | Kansuki | laminated mudstone-siltstone with nodules, Mg-dolostone after evaporite | 95-190 | |
| | | | | | Br | heterogeneous megabreccia | n/a | Roan Breccia |
| | | | | | Mofya | interbedded hematitc mudstone and dolomite with evaporitic textures | n/a blocks in breccia | |
| | | | | | Br | heterogeneous megabreccia | n/a | |
| | | | | | Tenke | No exposure in study area due to the decoupling of the pre-salt lower and mid Roan section of the Katangan stratigraphy | | |
| | | | | | Dipeta | | | |
| | | | | | Br | | | |
| | | | | | R.G.S. | | | |
| | | | | Mines R2 | Kambove | | | |
| | | | | | Dol. Shales | | | |
| | | | | | Kamoto | | | |
| | | | | Musoni R1 | Br | | | |
| | | | | | R.A.T. | | | |
| <883 | | | | Syn rift? | | | | |
| | | | Basement | | | No exposure in study area | | |

**Table 1.** Greater Kalindi area stratigraphic descriptions based on the Congolese Copperbelt stratigraphy (Cailteux et al. 2005, Cailteux and De Putter 2019; Batumike et al. 2007)

## 3 Results

Unconformities identified from the new interpretation of surface geology indicate that accommodation development increased west and SW of Kipushi during deposition of the middle and upper Katete Formation and lower Monwezi Formation (Figure 2). A low-angle unconformity is interpreted at the base of the Kyandamu Formation where the Upper Monwezi top laps the glaciogenic diamictite at the base of the Kundelungu Supergroup.

The modelled supra-salt stratigraphy increases in thickness from 2,200m at Kipushi, to 5,000m plus in the centre of the study area. The thickness of the Mwashya Subgroup appears slightly thicker on the SW limb (Table 2), but data resolution is poor for this unit and based entirely on historical mapping. The Mwale Formation is 4.9 times thicker to the SW of the Kipushi anticline compared to its thickness at the Kipushi deposit. The Kakontwe Formation is 1.3

times thicker in the SW limb. These relationships indicate that accommodation space during late Roan to early Nguba group time was filled by Mwale Formation glaciogenic diamictite deposits. The Katete Formation is 4.3 times as thick in the SW limb compared to Kipushi. The lowermost unit, the 'Série Recurrent' appears conformable with the underlying Kakontwe Formation. Units within the Middle and Upper Katete onlap onto the Série Recurrent. The Monwezi Formation is 3.8 times thicker in the SW limb than at Kipushi. The lower Monwezi onlaps onto the Katete Formation below. The Upper Monwezi top laps onto a low-angle unconformity at the base of the Kyandamu Formation and thus forms the base of the Kundelungu Group. In contrast to the Nguba Group, stratigraphic units within the lower Kundelungu Group exhibit a consistent thickness across the study area.

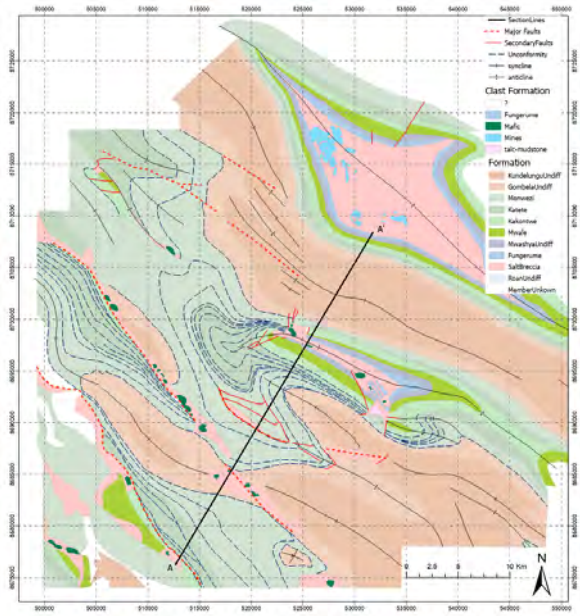


**Figure 2.** Stratigraphic map of study area derived from integrated geophysical and geochemical surveys.

| Stratigraphic Unit | Thickness | |
|---|---|---|
| | SW limb (m) | NE limb (m) |
| Lower Kundelungu | 600 | 575 |
| Upper Monwezi Fm. | 600 | 280 |
| Lower Monwezi Fm. | 460 | |
| Upper Katete Fm. | 460 | |
| Mid Katete Fm. | 480 | 200 |
| Lower Katete Fm. | 370 | |
| Kakontwe Fm. | 830 | 640 |
| Mwale Fm. | 730 | 150 |
| Mwashya Sub Gp. | 275 | 200 |
| Total | 4345 | 2045 |

**Table 2.** Stratigraphic thickness changes across the Kipushi anticline.

Blocks within the Roan Breche, interpreted as residuum after salt (Jackson et al. 2003; Hitzman et al. 2012; Selley et al. 2018), consist of megaclasts of Fungerume Group carbonate and siliciclastic rocks and Mwashya Subgroup aged mafic intrusions. No blocks of the Mines Subgroup were observed in this or previous studies (Intiomale, 1982).

## 4 Discussion and conclusions

The Kipushi mine is located adjacent to a sudden stratigraphic thickness change which is interpreted to have resulted from down drop along a major structure. Thick Mwale Formation deposits in the SW of the Kipushi deposit suggest that the glacial diamictites, interpreted as debrite deposits, were channelled into, and filled the deeper parts of the local depocentre. The overlying Kakontwe Formation is 30% thicker to the SW of the Kipushi structure which indicates a continued but less significant creation of accommodation space. The sudden increase in thickness of the Katete and Monwezi formations SW of Kipushi could be interpreted as reactivation of the same Kipushi structure. However, the geometry of the newly mapped unconformities, forming a series of compound and rapidly tapering sequences which onlap the lower Katete Formation adjacent to the Kipushi structure that contains a megabreccia with Roan Group clasts, suggests that accommodation centres (minibasins) were created by salt withdrawal feeding salt diapirs.

There is a significant change in composition of the megabreccia clasts from the Luputo megabreccia cored anticline to the northeast of Kipushi (Figure 2) and the Kipushi megabreccia cored anticline. Mines Subgroup rocks have not been observed at Kipushi although probable Mwashya Subgroup age mafic intrusive and Fungerume Subgroup clasts are present. The relationship indicates a fundamental change in the mid- to lower Roan Group stratigraphy between the two anticlines. The Mines Subgroup may not have been deposited at Kipushi or, if present, these units were not entrained in salt perhaps due to an insufficient thickness of salt to allow diapirism. The observed relationships suggest a significant basin boundary between Kipushi and Luputo.

Periodic linking between suprasalt structures affecting Nguba and Kundelungu group strata and the interpreted basement structure would allow the upward migration of hot and saline migrating fluid described at the Kipush Cu-Zn-Pb mine (Heijlen et al. 2008). The cryptic basement structures would also influence the formation of salt diapirs and associated hydrocarbon and sour gas traps which can in turn form reduced trap sites for metals.

## Acknowledgements

This publication is the result of research supported in part by a research grant from Science Foundation Ireland (SFI) under grant number 13/RC/2092 and 16/SP/4319, and is co-funded under the European

Regional Development Fund and by iCRAG industry partners Rio Tinto Exploration and First Quantum Mining. Special thanks to Ghislain Kabunda and Munshya Zimba at FQM, and Sandy Walker, Grainne Byrne and Shebo Lubasi at RTX for logistical support and stimulating discussions. We are grateful to Petroleum Experts for providing academic licences for the Move suite.

## References

Batumike MJ, Cailteux JLH, Kampunzu AB (2007) Lithostratigraphy, basin development, base metal deposits, and regional correlations of the Neoproterozoic Nguba and Kundelungu rock successions, central African Copperbelt. Gondwana Research 11:432-447.

Cailteux JLH, Kampunzu AB, Lerouge C, Kaputo AK, Milesi, JP (2005) Genesis of sediment-hosted stratiform copper-cobalt deposits, Central African Copperbelt. Journal of African Earth Sciences 43:134-158.

Cailteux JLH, and De Putter T (2019) The Neoproterozoic Katanga Supergroup (D.R. Congo): State-of-the-art and revisions of the lithostratigraphy, sedimentary basin and geodynamic evolution. Journal of African Earth Sciences 150:522-531.

Haest M and Muchez P (2011) Stratiform and vein-type deposits in the Pan-African orogen in Central and Southern Africa: Evidence for multiphase mineralisation. Geologica Belgica 14:23-44.

Heijlen W, Banks DA, Muchez P, Stensgard BM, Yardly BWD (2008) The nature of mineralising fluids of the Kipushi Zn-Cu deposit, Katanga Democratic Republic of Congo: quantitative fluid inclusion analysis using laser ablation ICP-MS and bulk crush leach methods. Economic Geology 103:1459-1482.

Hitzman MW, Broughton D, Selley D, Woodhead J, Wood D, and Bull S (2012) The Central African Copperbelt: diverse stratigraphic, structural, and temporal settings in the World's largest sedimentary copper district. In: Hedenquist JW, Harris M, and Camus F (ed) Geology and Genesis of Major Copper Deposits and Districts of the World: A Tribute to Richard H. Sillitoe: SEG Special Publication 16 pp 487-514.

Intiomale MM (1982) Le gisement Zn-Pb-Cu-de Kipushi (Shaba-Zaire) etude geologique et metallogenique. Dissertation, Universite Catholique de Louvain.

Jackson MPA, Warin ON, Woad GM, and Hudec MR (2003) Neoproterozoic allochthonous salt tectonics during the Lufilian orogeny in the Katangan Copperbelt, central Africa. Geological Society of America Bulletin 115:314-330.

Kampunzu AB, Cailteux JLH, Kamona AF, Intiomale MM, Melcher F (2009) Sediment-hosted Zn-Pb-Cu deposits in the Central African Copperbelt, Ore Geology Reviews, 35:263-297.

Rowan MG (1993) A systematic technique for sequential restoration of salt structures. Tectonophysics 228:331-348.

Selley D, Scott R, Emsbo P, et al (2018) Structural configuration of the Central African Copperbelt: Roles of evaporites in structural evolution, basin hydrology, and ore location. In: Metals, Minerals, and Society, Arribas AM and Mauk JL (eds), Society of Economic Geologists Special Publication 21 pp 115-156.

Torremans K, Muchez P, and Sintubin M (2018) Non-cyclindrical parasitic folding and strain partitioning during Pan-Lufilian orogeny in the Chambishi-Nkana Basin, Central African Copperbelt. Solid Earth 9:1011-1033.

U.S. Geological Survey (2023) Mineral commodity summaries 2023. U.S. Geological Survey, 210 p., https://doi.org/10.3133/mcs2023.

# An experimental study of metal extraction from red-bed sandstones as potential source rocks for sediment-hosted copper deposits

**Julia Woitischek[1], Jamie J. Wilkinson[1,2], Emma Humphreys-Williams[2], Matthew D. Jackson[1]**
*[1] Department of Earth Sciences and Engineering, Imperial College London, London, U.K.*
*[2] Department of Earth Sciences, Natural History Museum, London, U.K.*

**Abstract.** Understanding the extraction, transport and deposition of metals to form ore bodies in sedimentary basins is important because basin-hosted copper deposits host more than 23 % of the world's discovered copper as well as other metals such as vanadium and cobalt. These critical metals are key for the ongoing energy transition. Red bed sandstones have been identified as potential metal sources for sedimentary basin-hosted copper deposits because they are typically found in copper-bearing basins and their iron oxide coatings can adsorb metals. Thus, dissolution of these coatings could lead to the formation of an ore fluid. However, previous experiments to understand the extraction and mobility of copper and other trace metals in sedimentary basins have not considered flow effects, elevated temperatures, or natural brine compositions. Here, we report new experiments to quantify the release of metals from red bed sandstones in contact with: (i) aqua regia; and (ii) a variety of natural brines over a range of temperatures.

## 1 Introduction

Sediment-hosted ore deposits are economically important because they contain 23% of the world's discovered copper and 12% of its silver (Brown 2007, Figure 1).

**Figure 1.** Global distribution of major sediment hosted copper deposits.

Sediment-hosted copper deposits form when metals are extracted by brines from a source rock and transported to a deposit site where they precipitate. The carrier brines are interpreted to be saline brines formed either by the dissolution of evaporites by descending oxygen-rich meteoric water (Brown 2005; Cao and Hu 2021), or during the precipitation of evaporites such as halite and/or gypsum and/or potash salts from seawater (Carpenter et al. 1974, Wilkinson et al. 2005, 2009, Hitzman et al. 2010). As there are secular variations in the seawater chemistry through Earth history, two types of seawater can be involved: (i) calcite ($CaCl_2$) type or (ii) magnesium ($MgSO_4$) type (Lowenstein 2001, Lowenstein and Timofeeff 2008).

Among possible source rocks are red bed sandstones because they are typically found in copper-bearing basins and metals can be adsorbed on their iron oxide coatings (Figure 2). Hence, dissolution of these coatings could lead to the formation of an ore forming fluid (Hitzman et al. 2010, Parnell et al. 2021) but the efficiency of metal extraction by saline brines of different compositions has not yet been tested experimentally.

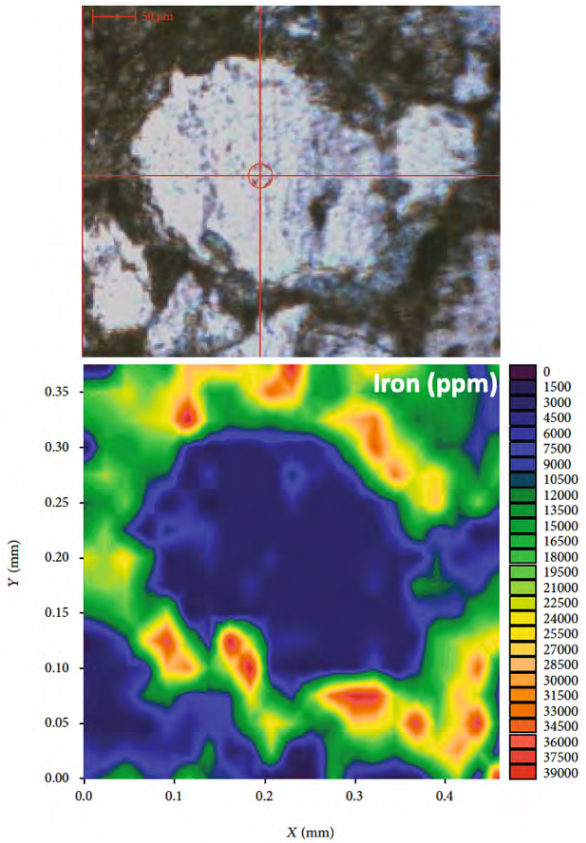


**Figure 2.** LA- ICP-MS maps for iron in grain coatings of red bed sandstones (Parnell et al. 2021). Very high Fe levels are indicated by the red colour and can reach up to 39000 ppm.

In the present study, we performed acid and brine leaching experiment on 51 red bed sandstone samples from a range of different ore-bearing basins. We show that the trace metal concentrations leached from different red bed sandstones varies significantly as well as their availability to exchange

protons. The overall aim is to identify possible source rocks and deepen our understanding in natural metal extraction processes during ore fluid formation.

Few previous studies have attempted to quantify the release of trace metals from red bed sandstones. Parnell et al. (2021) used an acid mixture of HCl and $HNO_3$ (aqua regia) to dissolve iron oxide coatings from red bed sandstones and measure the metals released. They observed a positive correlation between iron and vanadium, selenium, uranium, and lead whereas there is no correlation between iron and copper. They argued that the mass of metal released per unit mass of sandstone was sufficiently high that leaching could produce ore-forming fluids. However, they did not test the efficiency of natural brines in leaching metals.

Purser et al. (2014) studied the impact of $CO_2$ on iron release in red bed sandstones (bleaching) in contact with synthetic brine or diluted surface water. They found that $CO_2$ does not cause any iron release in red bed sandstones.

Rose and Bianchi-Mosquera (1993) conducted experiments to study the adsorption of metals on iron oxides. Their results showed that under oxidising conditions, Cu adsorbs strongly on Fe oxides compared to its behaviour under reduced conditions where it forms strong chloride complexes in solution. These previous studies are insightful, but do not explore the effect of elevated temperature or natural brines on metal leaching from red-bed sandstones.

Here we present a new experimental set-up to study copper and other trace metal mobilisation and transport in red bed sandstones that includes: (i) acid leaching experiments (after Parnell et al. 2021) to identify total leachable metal content, and (ii) brine leaching experiments that attempt to replicate conditions in natural systems.

## 2 Methodology

### 2.1 Aqua regia leaching experiments at 90 °C

For the acid leaching experiments, 4 ml of aqua regia ($3HCl:1HNO_3$) was added to 150 mg of disaggregated sandstone in the grain size fraction of 500 to 250 micrometre. Then the mixture was placed on a hotplate at 90 ºC until the grains were bleached (Figure 3). We assumed that bleaching corresponds to metal liberation from the iron-oxide coatings into the liquid. The leached solutions was separated from the residual solid and analysed for their elemental concentrations by ICP-MS/AES.

**Figure 3.** Typical sandstone samples after (above) and before (below) leaching with aqua regia.

### 2.1 Brine leaching experiments at 50 and 200 °C

For the brine leaching experiments we used modern formation water and evaporated magnesium and calcite seawater at 2 different evaporation degrees, at the onset of: (i) halite precipitation and (ii) sylvite precipitation. In the experiments, disaggregated sandstones and brines were mixed in a liquid-to-rock ratio of 2:1 and placed on a shaker at 50 or 200 °C. The pH value of selected experiments were monitored on a weekly basis over the ca. 3 months duration of the experiments.

## 3 Preliminary results

Leaching under aqua regia revealed a significant variability of trace element concentration from the red bed sandstones, with ore-bearing basins displaying higher trace metal concentrations. We found the highest concentrations of copper and

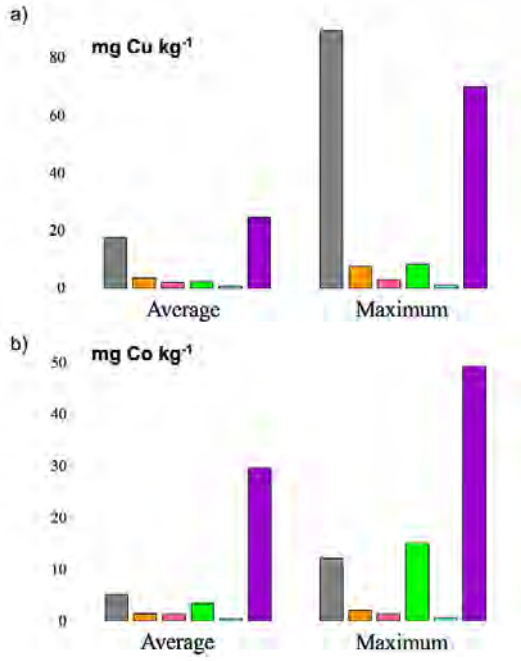


cobalt in samples from the Neuquén Basin (Argentina) and Katanga Basin (Zambia) (Figure 4).

**Figure 4.** Histogram showing the total leachable amount of (a) copper and (b) cobalt per kg rock of the Neuquén basin (grey) and Katanga Basin (purple) compared against samples from the Black Mesa Basin (orange), Altiplano

Basin (pink), Munster Basin (green) and Vale of Eden (blue).

Furthermore, acid leaching produces a positive correlation between iron in the leach solution and some trace metals including vanadium, chromium, nickel, and titanium, suggesting these metals are also incorporated in oxide grain coatings (Figure 5a). In figure 5b, copper shows a weaker positive correlation with iron compared to vanadium. This might indicate that copper might be incorporated in other silicates as well.

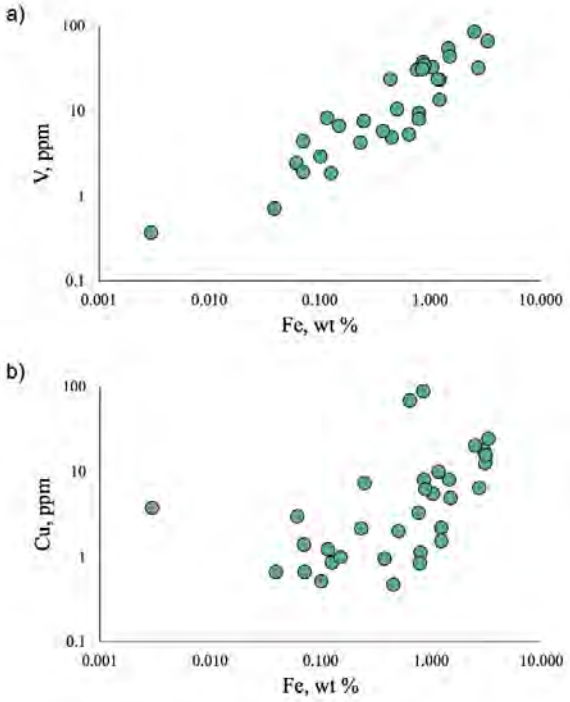


**Figure 5.** Plots showing the total leachable iron against (a) leachable vanadium and (b) leachable copper in aqua regia leaching experiments on red bed sandstones.

Results from the brine leaching experiments show that sandstones have a highly variable ability to exchange protons and therefore buffer pH; some experiments show little pH change whereas others show a decrease to pH 3 over several months (Figure 6). Experiments are ongoing to understand the proton exchange mechanism(s) and the potential impact of natural low pH on metal extraction.

**Figure 6.** Typical pH evolution over time of the sandstone samples tested in 5 different brines: magnesium seawater at the onset of halite (yellow), magnesium seawater at the onset of sylvite (blue), calcite seawater at the onset of halite (orange), calcite seawater at the onset of sylvite (purple), formation water (black)

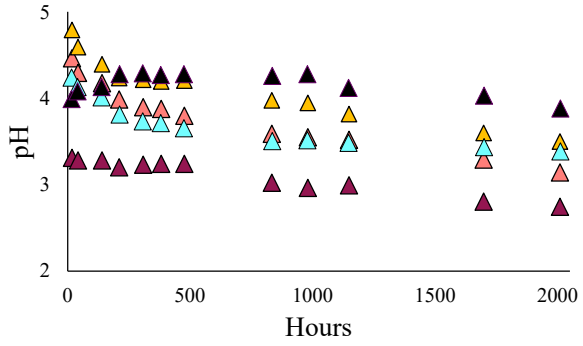


## Acknowledgements

This work was supported by the UK Natural Environment Research Council (NERC) via the CuBES (Copper Basin Exploration Science) project (grant NE/T003294/1).

## References

Brown AC (2005) Refinements for footwall red-bed diagenesis in the sediment-hosted stratiform copper deposits model. Econ Geol 100:765-771.

Brown AC (2007) World-class sediment-hosted stratiform copper deposits: Characteristics, genetic concepts and metallotects. Aust J Earth Sci 44:317-328.

Cao Y, Xu H (2021) A Rapid Cu Enrichment Mechanism for Cu-Bearing Brine in Kuqa Basin, Xianjiang, China: Controlled by Crystallized Sequence of Saline Minerals. Geofluids 5550271.

Carpenter AB, Trout ML, Picket EE (1974) Preliminary Report on the Origin and Chemical evolution of Lead- and Zinc-Rich Oil Field Brines in Central Mississippi. Econ Geol 69:1191-1206.

Hitzman MW, Selley D, Bull S (2010) Formation of Sedimentary Rock-Hosted Copper Deposits through Earth History. Econ Geol 105: 627-639.

Lowenstein TK, Timofeeff MN, Brennan ST, Hardie LA, Demicco RV (2001) Oscillations in Phanerozoic Seawater Chemistry: Evidence from Fluid Inclusions. Science 294: 5544.

Lowenstein TK, Timofeeff MN (2008) Secular variations in seawater chemistry as a control on the chemistry of basinal brines: test of the hypothesis. Geofluids 8:77-92.

Parnell J, Wang X, Raab A, Feldmann J, Brolly C, Michie R, Amstrong J (2021) Metal Flux from Dissolution of Iron Oxide Grain Coatings in Sandstones. Geofluids:5513490.

Purser G, Rochelle CA, Rushton J, Pearce JM, Wagner D (2014). An experimental and analogue study from iron release from red sandstones. Energy Procedia 63:3268-3274.

Rose AW, Bianchi-Mosquera GC (1993) Adsorption of Cu, Pb, Zn, Co, Ni and Ag on Goethite and Hematite: A Control on Metal Mobilization from Red Beds into Stratiform Copper Deposits. Econ Geol 88:1226-1236.

Wilkinson JJ, Everett CE, Boyce AJ, Gleeson SA, Rye DM (2005) Intracratonic crustal seawater circulation and the genesis of the subseafloor zinc-lead mineralization in the Irish orefield. Geology 33: 805-808.

Wilkinson JJ, Stoffell B, Wilkinson CC, Jeffries TE, Appold MS (2009) Anomalously metal-rich fluids form hydrothermal ore deposits. Science 323:764-767.

# Regolith-hosted rare earth genesis under humid climates in the Coastal Cordillera of the Central Andes

**Nicolás Bustos[1,2], Carlos Marquardt[1,2], Tomás Roquer[1,2], Paulina Vergara[1,2]**
[1] *Departamento de Ingeniería Estructural y Geotécnica, Pontificia Universidad Católica de Chile, Santiago, Chile*
[2] *Departamento de Ingeniería de Minería, Pontificia Universidad Católica de Chile, Santiago, Chile*

**Abstract.** Regolith-hosted rare earth element deposits (RH-REE) have been recently found in Chile, nonetheless their ore formation controls, which include temperate to arid climate, intrusive rocks with weatherable REE minerals, and gentle slopes or pediplains, among others, differ from the most common deposits in Asia. This work addresses mineralization and exploration methods for RH-REE deposits across the Chilean Coastal Range. The studied prospect is associated with late Carboniferous I-type tonalitic intrusions. Mineralogical analysis (TIMA-X) indicates that allanite and monazite are the main REE-bearing minerals in the host rock. The regolith in the study area is up to 60 m deep and contains an exchangeable-REE concentration up to 2000 ppm, as determined by portable X-ray fluorescence (pXRF) and ICP-MS. We were able to recognize that REE-adsorption takes place both in preserved and partially eroded regoliths. Progressive weathering of these regoliths causes the pedolith/saprolith limit to be dynamic and accumulate REE due to the breakdown of allanite and monazite. Our data shows that the search for pediplains on suitable lithologies, mapping of regolith profiles, and their analysis via pXRF by quantifying yttrium, appears to be a suitable strategy for early exploration of RH-REE deposits in the Chilean Coastal Range.

## 1 Introduction

The rare earth elements (REE) correspond to the 15 elements of the lanthanides, plus Sc and Y (due to geochemical similarities). These elements have high geochemical affinity among each other and are divided, according to their atomic number and their different physiochemical and geochemical properties, into light (LREE: La–Eu) and heavy rare earth elements (HREE: Gd–Lu) (Sanematsu and Watanabe 2016).

In RH-REE deposits, REE are transported by meteoric fluids during weathering and adsorbed by neoformed clay minerals (Foley and Ayuso 2015), such as kaolinite, halloysite, and illite, under appropriate climatic and topographic conditions. Later preservation of these REE-rich regolith horizons from erosion depends on underground water flow and erosion controls. These ore formation constraints can be met in various areas of the planet that are underexplored for RH-REE.

RH-REE deposits occur within the Chilean Coastal Range (https://www.aclara-re.com/) since they meet suitable geological and climatic criteria (Sanematsu and Watanabe 2016; Li et al. 2017). These include granitic I-type lithologies with weatherable REE-minerals, deep regoliths (locally up to 60 m), low-slope paleosurfaces, and a temperate climate that would allow the occurrence of supergene pedogenetic processes during which the enrichment of exchangeable REE could take place. The key element that varies between well-known Asian deposits and the ones found in the Coastal Cordillera is the climate setting; this directly affects pediment preservation and formation.

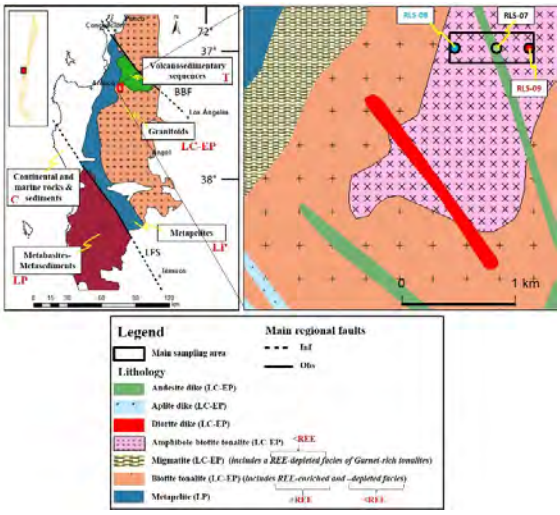


**Figure 1.** Regional and local geological maps. BBF: Biobío Fault System. LFS: Lanalhue Fault System. C: Cenozoic. T: Triassic. LC-EP: late Carboniferous to early Permian. LP: late Paleozoic. Regional case adapted and simplified from Alarcón and Álvarez (2019) and Glodny et al. (2008).

## 2 Methodology

### 2.1 Sampling information

A specific work area was determined to search and map outcrops of fresh rocks and regoliths which are favorable to the formation of RH-REE, namely amphibole-biotite tonalite and biotite tonalite (see Figure 1). In the work area, a more focused sampling area was selected after searching for a geomorphically suitable spot in terms of deep regolith formation and low slope pediplains or potential pediments.

### 2.2 Geochemical, petrographic, and geomorphic characterizations

The samples analyzed with ICP-MS include regolith samples obtained from 32 drillholes (total of 319 sub-samples when considering meter-by-meter compositing), as well as one rock sample obtained on the surface. The drillhole samples were analyzed

to quantify the exchangeable-REE fraction (ICP-MS_DD) and the surface samples were analyzed for total rock (ICP-MS_T).

The samples analyzed for geochemistry were checked with QA/QC by the mining firm. The samples' desorption was carried out in two stages (hence, DD: "double desorption") to replicate the recovery obtained by the industrial-scaled metallurgical process, whilst stabilizing the pH at 4 throughout the process by adding drops of $H_2SO_4$ (sulfuric acid) and $NH_4OH$ (ammonium hydroxide). These two sequential desorptions utilized $(NH_4)_2SO_4$ (ammonium sulfate) at 0.4 M and distilled water as leaching agents to release the exchangeable ions into the solution for later ICP-MS analysis.

The pXRF analysis of the samples was carried out with a Niton® XL3t GOLDD+ instrument, which was used to perform a total rock analysis focusing on trace elements (pXRF_T). The analysis and sample manipulation were based on established methods, and the samples fulfilled standards that maximize the precision of the analyses: moisture content, granulometry, container, thickness of sample, and analysis time.

Petrographic analyses were conducted with the automatic mineralogy instrument TIMA-X (TESCAN Integrated Mineral Analyzer), to characterize the mineralogy of each lithology. The instrument is equipped with four EDS EDAX Element 30 detectors and the analyses were carried out with an 8.0 µm resolution and 1000 counts per pixel. This technology cannot correctly identify minerals with concentrations <0.1%.

In terms of remote geomorphology, we propose an adaptation of Bowles and Cowgill's (2012) methodology to identify marine terraces. Using this methodology, it was sought to generate, starting from slope and roughness maps, a map known as a Surface Classification Model (SCM). Besides the experience provided by the cited article, information from swath profiles and satellite maps was used to identify geomorphic targets with high pediment quality (see Figure 2).

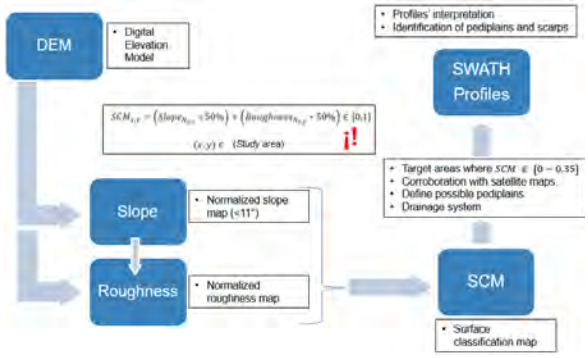


**Figure 2.** Morphometric methodology and sequential steps towards identification of targets where RH-REE deposits could be preserved.

## 3 Geological framework

Within the study area, a Paleozoic metamorphic unit of metapelite presents a contact aureole characterized by migmatite outcroppings due to late Carboniferous–early Permian granitic intrusions (Alarcón and Álvarez 2019). The granitic units are composed mainly of biotite tonalite and amphibole-biotite tonalite (Figure 1). They have been described under mineralogical and geochemical criteria as I-type (Hervé et al. 1988; Creixell 2001), and are, thus, a potential source for RH-REE mineralization.

These tonalitic intrusions have a higher potential to form RH-REE deposits because: (1) geochemical, mineralogical, and petrographic analyses of fresh rock samples have proven the existence of elevated REE concentrations; and (2) they correspond to the preferential lithology (granitoids) reported by several authors in terms of regolith formation and REE-adsorption processes (e.g., Sanematsu and Watanabe 2016; Li et al. 2017; Li et al. 2019).

The local tonalites formed from calc-alkaline magmas generated in an active continental margin (Creixell 2001). The tonalites crystalized at a lower temperature (~600 °C), compared to other granitic non-marginal facies of the larger pluton (up to 700 °C), due to an additional H2O contribution from the dehydration of the host rock (Creixell 2001). The tonalites have metaluminous composition (A/CNK = 0.77–0.98), whereas existent garnet-rich marginal facies have peraluminous composition (A/CNK = 1.01). Granite discrimination diagrams classify the tonalites as low-K and sub-alkaline (Creixell 2001).

## 4 Geomorphic framework

The study area has currently a temperate climate with a mean annual temperature of 12.9 °C and mean annual precipitation of 715.6 mm (Dirección Meteorológica de Chile 2020). These conditions are thought to have been rather stable during the Quaternary. The field observations showed that regoliths that were developed upon local intrusive rocks could reach thicknesses of up to 60 m.

Two families of soil profiles are described within the study area. On one hand, there is the case of highly preserved regoliths (Figure 3A), where exchangeable-REE mineralization occurs exactly along the contact between the pedolith and saprolith. On the other hand, some regoliths show evidence of higher local erosion rates (Figure 3B), as the original pedolith was partly removed; here, the upper layers correspond to a thinner newly formed pedolith with an important re-concentration of exchangeable REE. Evidence of these higher local erosion rates is, chiefly, the lack of depletion zones of mobile elements at the top of the regolith profile.

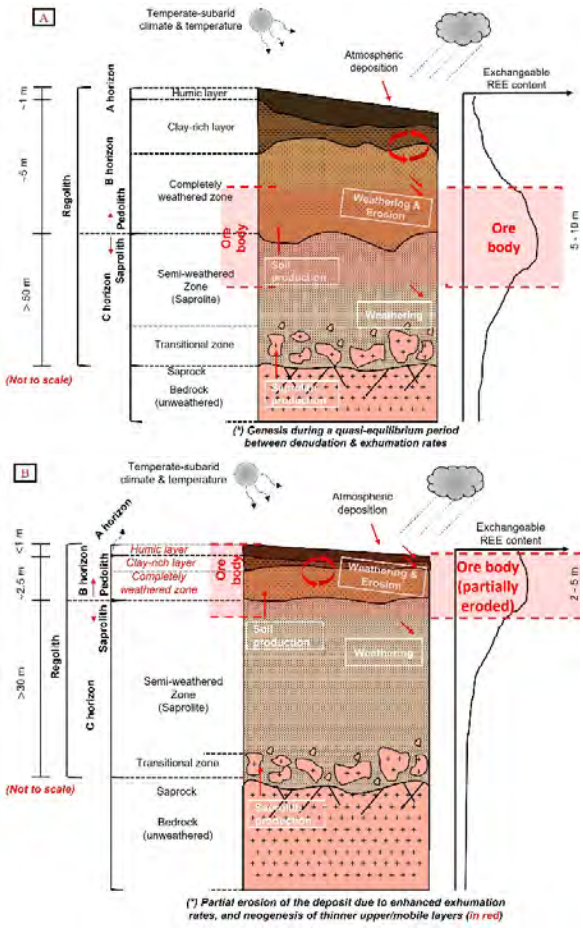


**Figure 3.** **a** Preserved regolith profiles. **b** Partially eroded regolith profiles.

## 5 Geochemical results from drillholes

Based on the TIMA-X analyses, two main REE-bearing minerals (both LREE-dominant) were identified: allanite, $Ca,(Ce,La)(Al_2Fe^{2+})[Si_2O_7][SiO_4]O(OH)$, and monazite, $(Ce,Nd,La)(PO_4)$. Two other REE-bearing minerals were also detected, although at much lower concentrations: parisite (LREE-dominant) and xenotime (HREE+Y-dominant).

The obtained data (Figures 4,5) show the variation of major elements across the soil profile and their relationship to yttrium concentration, which encompass the accumulation zone of exchangeable REE, and with mobile elements (Ca, K, Sr). Furthermore, the REE-dominance and concentration of the ore body of each drillhole is showed.

The evolution of several geochemical ratios across preserved and partially eroded regoliths is presented in Figure 5. It is shown that LREE predominate in shallow horizons of the regolith; this can be proven be checking the evolution of $(La/Yb)_N$ and how this ratio progressively decreases towards deeper zones (6–2).

In partially eroded regoliths, this behaviour is very similar, although it begins with lower values, due to local erosion. Finally, among preserved regoliths, the cerium anomaly (Ce/Ce*) has a rising trend with increasing depth but remains as a negative anomaly (i.e., Ce/Ce* < 1) down to a depth of 10 m.

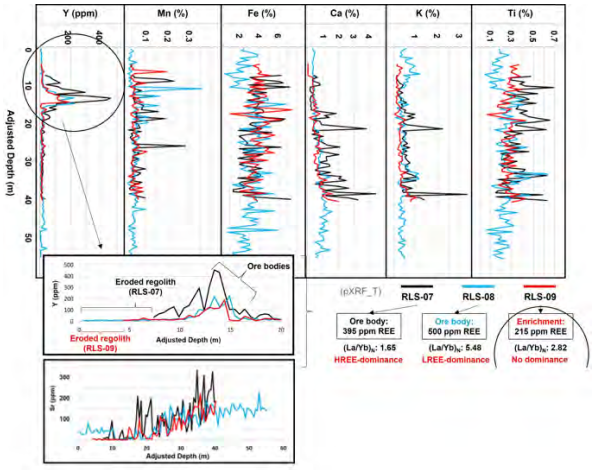


**Figure 4.** Concentrations of major elements and yttrium across the regolith profiles of three drillholes obtained by portable X-ray fluorescence (pXRF) analysis. pXRF_T: pXRF (total fraction).

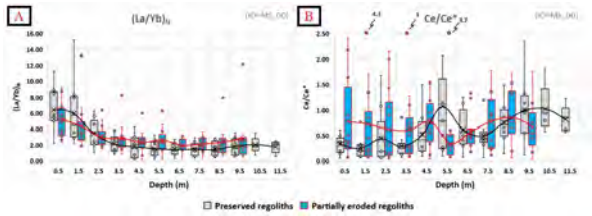


**Figure 5.** Variation of geochemical ratios across the regolith profile. ICP-MS_DD: ICP-MS (exchangeable fraction). **a** Normalized Lanthanum-Ytterbium ratio. **b** Cerium anomaly.

## 6 Analytic conciliation: approximation for an RH-REE-deposit model

The morphometric analysis of the study area is indeed placed upon a preferential zone with SCM values <0.35. This can be seen more detailed in Figure 6.

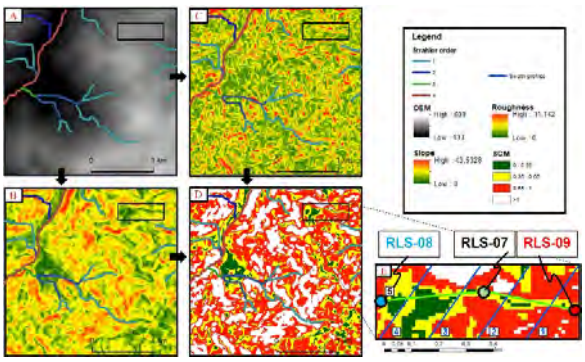


**Figure 6.** Results of the morphometric analysis. **a** DEM (12.5-m resolution). **b** Slope map. **c** Roughness map. **d** Normalized SCM map. **e** SCM map magnification. The maps also include the drainage system (Strahler method).

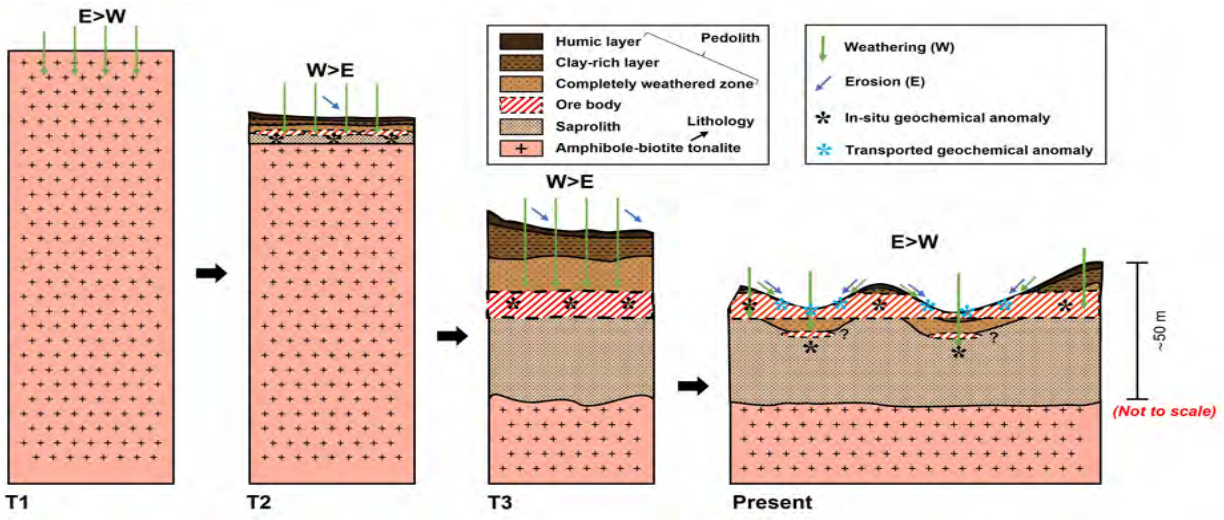


**Figure 7.** Scheme of the geomorphic evolution proposed for RH-REE deposits in the region. T1: Pediment formation. T2: Start of chemical and physical weathering processes; REE transportation takes place, and the enriched fluids permit a first adsorption and previous secondary clay mineral formation. T3: genesis of the RH-REE deposit due to adsorption; at this point, the erosion rates increase. Present: erosion of the local morphology due to the development of drainage systems; deposit's partial/local erosion.

The differences between preserved and partially eroded regoliths demand a process able to account for both chemical and physical differences in these profiles. We suggest that preserved regoliths - and the REE mineralization associated with them - represent an early pedogenetic process that was fully preserved from erosion. Partially eroded regoliths, on the other hand, underwent a second pedogenetic stage that was able to re-fractionate the REE, or even that some elements are preferentially adsorbed under specific environments, such as pH, temperature, or exchange capacity of secondary clays. Thus, the large increase of REE ratios within exposed mineralized horizons of partially eroded regoliths could be explained by shallow and younger enrichment processes. These processes were likely lateral leaching events that affect REE-rich minerals that are more susceptible to chemical weathering under shallow conditions.

## 7 Conclusions

We were able to detect, describe, and discuss the essential geological processes that led to the formation of RH-REE deposits where both hypogene and supergene processes are involved. The final ore control processes require regolith formation and evolution: (1) exhumation and pediment formation, (2) development of deep weathering profiles (i.e., REE-remobilization: REE-precipitation into secondary minerals and REE-adsorption onto clay minerals), and (3) preservation of the mineralized bodies. For the time being, the reconciliation of geomorphic and petrographic information, that is, the search for pediplains and favorable regoliths developed on adequate lithologies, appears to be a suitable method for addressing the problem of exploring for RH-REE deposits in Coastal Cordillera.

## Acknowledgements

We would like to thank the entire geological team of the mining firm Aclara for their support, and for giving us access to their geological data.

## References

Alarcón, A., Álvarez, F., 2019. Caracterización óptica y composicional del concentrado de minerales de uranio, torio y tierras raras en las pegmatitas de poñen y Parque Coyanmahuida. Universidad de Concepción, Concepción, Chile (undergraduate thesis).

Bowles, C., Cowgill, E., 2012. Discovering marine terraces using airborne LiDAR along the Mendocino-Sonoma coast, northern California. Geosphere 8 (2), 386–402.

Creixell, C., 2001. Petrología y Geotermobarometría de las Rocas Intrusivas de la Cordillera de la Costa entre los 36°30' y 38°00' S. Universidad de Concepción, Concepción, Chile (undergraduate thesis).

Foley, N., Ayuso, R., 2015. REE enrichment in granite-derived regolith deposits of the Southeastern United. In: Geological Survey, 131-138. States: Prospective Source Rocks and Accumulation Processes.

Glodny, J., Echtler, H., Collao, S., Ardiles, M., Burón, P., Figueroa, O., 2008. Differential late Paleozoic active margin evolution in South-Central Chile (37°S–40°S) – the Lanalhue Fault Zone. J. S. Am. Earth Sci. 26, 397–411.

Hervé, F., Munizaga, F., Parada, M., Brook, M., Pankhurst, R., Snelling, N., Drake, R., 1988. Granitoids of the Coast Range of Central Chile: geochronology and geologic setting. J. S. Am. Earth Sci. 1 (2), 185–194.

Li, M., Zhou, M., Zhao, W., 2017. Nature of parent rocks, mineralization styles and ore genesis of regolith-hosted REE deposits in South China: an integrated genetic model. J. Asian Earth Sci. 148, 65–95.

Li, M., Zhou, M., Williams-Jones, A., 2019. The genesis of regolith-hosted heavy rare earth element deposits: insights from the world-class Zudong Deposit in Jiangxi Province, South China. Econ. Geol. 114, 541–568.

Sanematsu, K., Watanabe, Y., 2016. Characteristics and genesis of ion adsorption-type rare Earth element deposits. Rev. Econ. Geol. 18, 55–79.

# Mn-Ni-Co oxy-hydroxides from Ni-Co laterites of Moa-Bay mining district, eastern Cuba

**Diego Domínguez-Carretero[1], Cristina Villanova-de-Benavent[1], Cristina Domènech[1], Joaquín A. Proenza[1]**
*[1]Departament de Mineralogia, Petrologia i Geologia Aplicada, Facultat de Ciències de la Terra, Universitat de Barcelona (UB), Spain*

**Abstract.** Ni and Co have been listed as critical energy metals for a sustainable economic development by several government agencies. Ni-Co laterite deposits are among the first resources of both metals in the world. The correct identification of Ni- and Co-bearing mineral phases is essential to increase the efficiency of extraction of both metals in these deposits. Mn-Ni-Co oxy-hydroxides are key mineral phases because they contain important Ni and Co concentrations. In this study, we have investigated the chemical differences among Mn-Ni-Co oxy-hydroxides formed in the saprolitic and limonitic horizons from lateritic deposits of the Moa Bay lateritic mining district (eastern Cuba). Mn-Ni-Co oxyhydroxides formed in the saprolitic horizons are classified as Ni-asbolane and lack Al and Co. They would have formed at slightly alkaline conditions (pH < 8). Conversely, the ones formed in the limonitic horizon are more enriched in Ni, Co and Al, and poor in Mg, being catalogued as lithiophorite and lithiophorite-asbolane intermediates, and would have formed at more acidic (pH ~ 6) and oxidizing conditions. Finally, several hundreds of ppm of Sc have been measured in Mn-Ni-Co oxyhydroxides from the limonitic horizon, therefore making these minerals interesting targets for the potential extraction of this critical metal as a by-product.

## 1 Introduction

Ni-Co laterite deposits, formed by the chemical and mechanical weathering of ultramafic rocks, account for 60% of Ni and 37% of Co worldwide resources (Newsome et al., 2019; USGS, 2021). Both metals have been classified by several government agencies (e.g., Australia's National Science Agency, Department of Natural Resources Canada, United States Geological Survey) as critical due to their numerous applications in the steel and electric battery industries. Nowadays, Cuban laterites contain up to 6% of Ni and 7% of Co worldwide reserves (USGS, 2021).

The ore mineralogy in Ni-Co laterites is complex and very heterogeneous. There are still knowledge gaps regarding which mineral phases contain Ni and/or Co, thus making the metallurgical processes inefficient (Elias, 2002; Hernández et al., 2007; Marsh et al., 2013).

In this study, we focus on a detailed characterization of Mn-Ni-Co oxy-hydroxides, a chemically heterogeneous group of ore minerals with highly variable Ni and Co contents. Hence, we have analyzed different samples from the saprolitic and the limonitic horizons of the world-class oxide-type lateritic mining district of Moa Bay (eastern Cuba). These new data allow the chemical distinction between Mn-Co-Ni oxy-hydroxides formed in the saprolitic and limonitic horizons, and ultimately to better understand their formation processes.

## 2 Geological Setting

Eastern Cuba contains the largest exposure of ophiolitic rocks across the Cuban ophiolitic belt, grouped into the so-called Mayarí-Baracoa Ophiolite Belt (MBOB). The MBOB is Cretaceous in age (90-136 Ma; Iturralde-Vinent et al. 2016; Rojas-Agramonte et al. 2016; Proenza et al. 2018) and it is divided into the Mayarí-Cristal (western part) and the Moa-Baracoa (eastern part) massifs. The Mayarí-Cristal massif is mainly formed by a 5 km thick, highly serpentinized harzburgite tectonite, crosscut by several generations of websterite and gabbro dykes of Island Arc Tholeiite (IAT) affinity (Marchesi et al. 2006, 2007). The ultramafic rocks overthrust a crustal unit consisting of gabbros, microgabbros and abundant diabase dikes (Proenza et al. 1999; Marchesi et al. 2006, 2007). The Moa-Baracoa massif, on the other hand, is composed by a 2.2 km thick mantle-tectonite harzburgite with subordinate dunite and a very well-preserved Moho Transition Zone (MTZ). Layered and isotropic gabbros and pillow basalts with a back-arc geochemical affinity are tectonically overlain by the mantle sequence (Proenza et al. 2006, 2018; Marchesi et al. 2006, 2007).

Eastern Cuba contains one of the largest Ni-Co laterite mining provinces in the world, of about 100 $km^2$ (Lewis et al., 2006), which includes important mining districts such as Moa Bay (hosted within the Moa-Baracoa massif; Fig.1), Pinares de Mayarí or Nicaro. The laterization of the Moa Bay serpentinites started in the Miocene and continued until the present-day (Lewis et al., 2006 and references therein).

The Mn-Ni-Co oxy-hydroxides studied in this work were obtained from the oxide-type deposits of Yagrumaje Norte and Punta Gorda, with thick limonitic horizons, and from the hydrous Mg-silicate type deposit of Yamanigüey, with a large saprolitic horizon, all belonging to the Moa Bay district.

## 3. Analytical methods

Polished thin-sections from laterite samples of the studied deposits were analyzed, in a first stage, under a conventional petrographic polarized light microscope at the Universitat de Barcelona (UB) and later, by scanning electron microscopy using a JEOL JSM-7100 field-emission SEM at 20 kV and 5 nA at

the Centres Científics i Tecnològics of the same university (CCiT-UB).

Quantitative electron microprobe analyses (EMPA) on Mn-Ni-Co oxy-hydroxides were also conducted at the CCiT-UB, in a JEOL JXA-8230 equipped with five wavelength-dispersive spectrometers (WDS) operating at 15 kV and 15 nA, with a 1-2 µm beam diameter and 10-30 s (3 minutes in the case of Sc) counting time per element. Wollastonite (Si), corundum (Al), orthoclase (K), hematite (Fe), periclase (Mg), rhodonite (Mn), NiO (Ni), metallic Co (Co), rutile (Ti), Cr2O3 (Cr), metallic Sc (Sc) were used as standards.

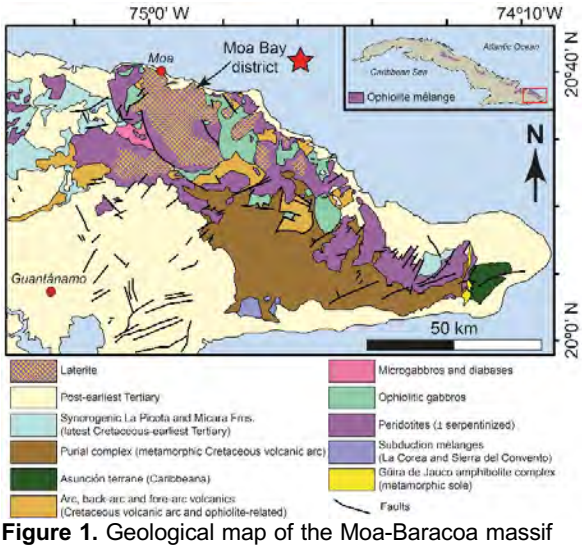


**Figure 1.** Geological map of the Moa-Baracoa massif (Eastern Cuba) with the location of the Moa Bay Ni-Co laterite mining district.

## 4. Mineral petrography and chemistry

The studied Mn-Ni-Co oxy-hydroxides from the limonitic and saprolitic horizons differ regarding their textures and chemical composition.

### 4.1 Limonitic horizon

Samples from the limonitic horizons of Punta Gorda and Yagrumaje Norte deposits consist mainly of goethite with minor amounts of gibbsite, hematite, maghemite, Cr-spinel and Mn-Ni-Co oxy-hydroxides. Mn-Ni-Co oxy-hydroxides are found either replacing goethite or as colloform aggregate individual grains (Fig. 2a) with significant variations in Mn, Co, Ni (Fig. 3), Fe and Al contents. The chemical composition of Mn-Ni-Co oxy-hydroxides shows high variations in MnO (21.5-69.7 wt.%; median value of 36.9 wt.%), FeO (0.45-27.7 wt.%; median value of 3.60 wt.%), NiO (0.8-19.8 wt.%; median value of 10.6 wt.%), $Al_2O_3$ (1.25-19.7 wt.%; median value of 6.10 wt.%) and CoO (0.75-10.2 wt.%; median value of 6.41 wt.%). The analyzed grains have low concentrations of $K_2O$ (median values of 1.79 wt.%), MgO (median value of 0.49 wt.%) and $SiO_2$ (median value of 0.42 wt.%). The analyzed Mn-Ni-Co oxy-hydroxides from Punta Gorda yield up to 204 ppm Sc.

### 4.2 Saprolitic horizon

The studied samples from the saprolitic horizon of Yamanigüey deposit are mainly composed by serpentine, Ni-rich secondary serpentine, with minor magnetite, Cr-spinel, garnierite and Mn-Ni-Co oxy-hydroxides. The studied Mn-Ni-Co oxy-hydroxides are found as fibrous crystals replacing garnierite in veins crosscutting secondary serpentine (Fig. 2b). Regarding their chemical composition, the analyzed grains have high concentrations of MnO (34.6-56.6 wt.%; median value of 52.2 wt.%), moderate concentrations of MgO (6.5-13.2 wt.%; median value of 7.58 wt.%), NiO (4.68-7.46 wt.%; median value of 5.95 wt.%), $SiO_2$ (2.49-21.2 wt.%; median value of 5.04 wt.%), FeO (1.35-4.71 wt.%; median value of 1.68 wt.%), and very low concentrations of CoO (up to 0.27 wt.%) and $Al_2O_3$ (up to 0.02 wt.%).

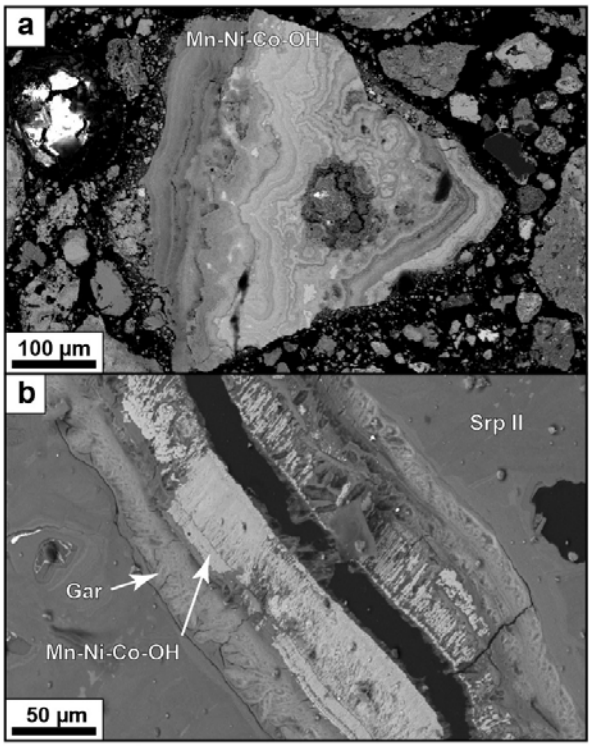


**Figure 2.** a) Mn-Ni-Co oxy-hydroxides from the limonitic horizon of the Punta Gorda deposit with colloform texture. b) Fibrous Mn-Ni-Co oxy-hydroxides from the saprolitic horizon of the Yamanigüey deposit in a garnierite vein crosscutting Ni-rich secondary serpentine. Abbreviations: Mn-Ni-Co-OH: Mn-Ni-Co oxy-hydroxide; Gar: Garnierite; Srp II: Ni-rich secondary serpentine.

## 5. Final remarks

The studied Mn-Ni-Co oxy-hydroxides have a distinctive composition in the limonitic and in the saprolitic horizon. Mn-Ni-Co oxy-hydroxides from the

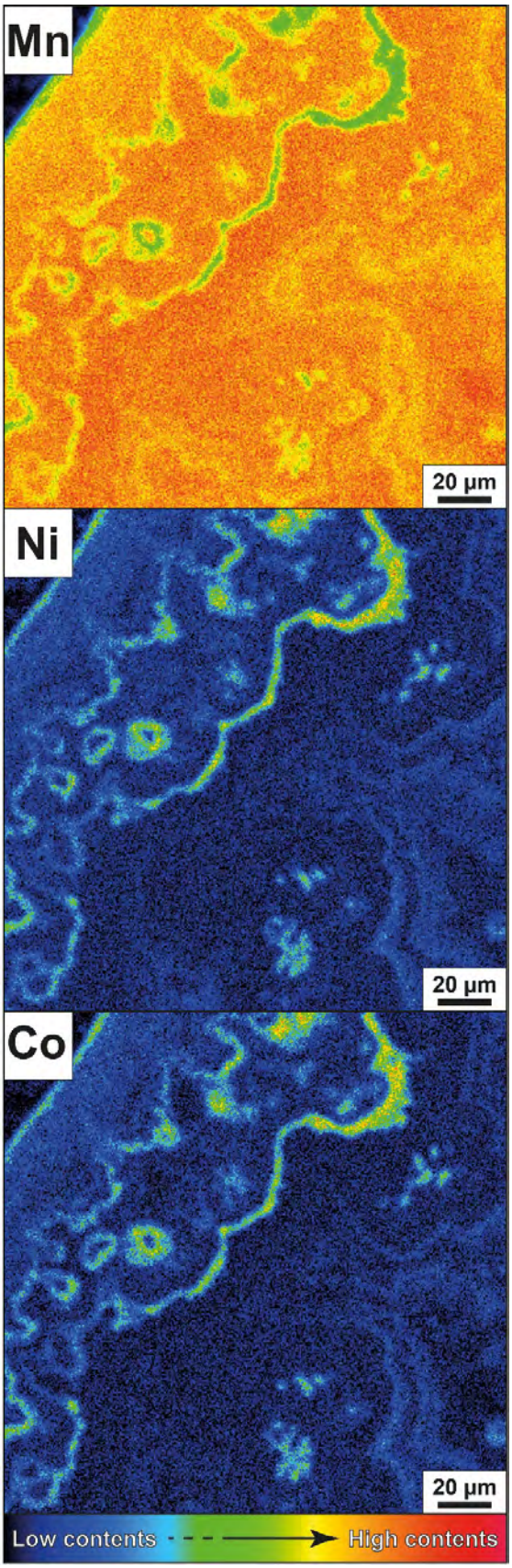


**Figure 3.** EMPA elemental maps for Mn, Ni and Co from a colloform Mn-Ni-Co oxy-hydroxide from the limonitic horizon of the Punta Gorda deposit.

saprolitic horizon have high Mg and Mn contents, and have almost no Al nor Co, and are clearly classified as Ni-asbolanes (Fig. 4). However, Mn-Ni-Co oxy-hydroxides from the limonitic horizon have very low Si and Mg contents and higher Al and Co, and they are classified as lithiophorite-asbolane intermediates or as lithophorite (Fig. 4). Consequently, as Co in laterite deposits is still exploited as a by-product, in terms of metal extraction, lithiophorite and lithiophorite-asbolane intermediates from the limonitic horizon (enriched in Ni and Co) represent a more attractive target than the Ni-asbolane from the saprolitic horizon (enriched exclusively in Ni).

Ni-asbolane in the saprolitic horizon is replacing garnierite, whose formation is associated with aqueous, alkaline (pH > 8), Ni-rich solutions (Villanova-de-Benavent et al., 2014). Consequently, Ni-asbolane formation might take place at slightly more acidic conditions, in which garnierite solubility increases.

Lithiophorite and lithiophorite-asbolane intermediates, very abundant in the limonitic horizon (Fig. 4), present either as a newly formed mineral aggregate or replacing previous Fe-oxy-hydroxides, would form under acidic (pH ~ 6) and oxidizing (Eh > 0V) conditions (Llorca, 1993).

Scandium is another critical metal that can be extracted from Ni-Co laterites as a by-product (Wang et al., 2011). Scandium content in laterites is highly correlated with their $Fe_2O_3$ content (Audet, 2008; Aiglsperger et al., 2016), as Sc may substitute $Fe^{3+}$ in the goethite crystal structure (Levard et al., 2018). However, our preliminary results show how Mn-Ni-Co oxy-hydroxides, specifically lithiophorite and lithiophorite-asbolane intermediates enriched in Al, can contain several hundreds of ppm of Sc, making Mn-Ni-Co oxy-hydroxides a target mineral not only for Ni and Co, but also for Sc.

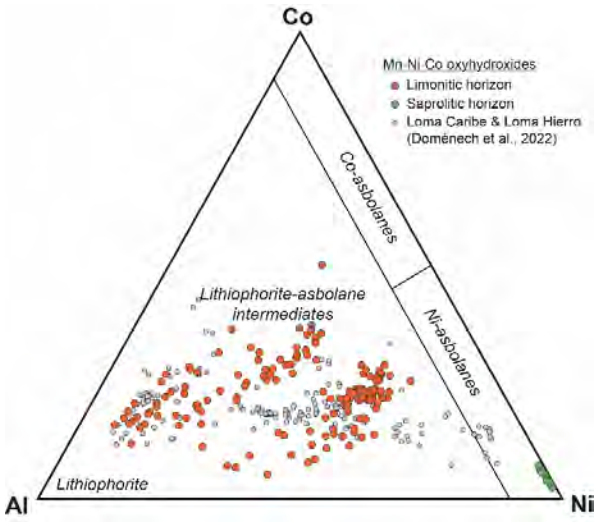


**Figure 4.** Ternary plot representing Mn, Ni and Co in cation proportions on the basis of 100 oxygens obtained from EMPA analyses on Mn-Ni-Co oxy-hydroxides.

In conclusion, our results show how the precipitation of Mn-Ni-Co oxy-hydroxides is controlled by the Eh-pH variations along the lateritic profile as proposed by Llorca (1993). During early stages of weathering, in the saprolitic zone, at slightly alkaline conditions, Ni-rich asbolane precipitates and replaces silicates, such as serpentine or garnierite. However, during more advanced stages of weathering, in the limonitic zone, when the conditions are oxidizing and slightly acidic, Ni-rich asbolane is not stable any longer, and asbolane-lithiphorite intermediates and lithiphorite precipitate.

## Acknowledgements

This research was financially supported by Grant PID 2019-105625RB-C21 funded by MCIN/AEI/10.13039/501100011033 and by Grant 2021 SGR 00239 funded by Gestió d'Ajuts Universitaris i de Recerca de Catalunya. Additional funding was provided by a "Ayudas predoctorales 2020" number PRE 2020-092140 PhD grant to DD-C by the Spanish Ministry of Science and Innovation.

## References

Aiglsperger, T., Proenza, J.A., Lewis, J.F., Labrador, M., Svotjka, M., Rojas-Purón, A., Longo, F., Durisova, J. (2016). Critical metals (REE, Sc, PGE) in Ni laterites from Cuba and the Dominican Republic. Ore Geology Reviews 2016 73, 127-147.

Audet, M.A. (2008). Le massif du Koniambo, Nouvelle-Calédonie Formation et obduction d'un complexe ophiolitique du type SSZ. Enrichissement en nickel, cobalt et scandium dans les profils résiduels (PhD thesis (in French), 327 pp.).

Domènech
, C., Villanova-de-Benavent, C., Proenza, J.A., Tauler, E., Lara, L., Galí, S., Soler, J.M., Campeny, M., Ibañez-Insa, J. (2022). Co–Mn Mineralisations in the Ni Laterite Deposits of Loma Caribe (Dominican Republic) and Loma de Hierro (Venezuela). Minerals 12, 927.

Elias, M. (2002). Nickel laterite deposits – geological overview, resources and exploitation. Centre for Ore Deposit Research, University of Tasmania, Special Publication, 4, 205-220.

Hernández, C. M., Banza, A., Gock, E. (2007). Recovery of metals from Cuban nickel tailings by leaching with organic acids followed by precipitation and magnetic separation. Journal of Hazardous Materials, 139, 25–30.

Iturralde-Vinent, M.A., Garcia-Casco, A., Rojas-Agramonte, Y., Proenza, J.A., Murphy, J.B., Stern, R.J. (2016). The geology of Cuba: A brief overview and synthesis. GSA Today 26, 4-10.

Levard, C., Borschneck, D., Grauby, O., Rose, J., Ambrosi, J.P. (2018). Goethite, a tailor-made host for the critical metal scandium:The $Fe_xSc_{(1-x)}OOH$ solid solution. Geochemical Perspectives Letters 9, 16-20.

Lewis, J.F., Draper, G., Proenza, J.A., Espaillat, J., Jimenez. J. (2006). Ophiolite- Related Ultramafic Rocks (Serpentinites) in the Caribbean Region: A Review of their occurrence, Composition, Origin, Emplacement and Nickel Laterite Soils. Geologica Acta 4, 237-263.

Llorca, S.M. (1993). Metallogeny of supergene cobalt mineralization, New Caledonia. Australian Journal of Earth Sciences, 40, 377-385.

Marchesi, C., Garrido, C.J., Godard, M., Proenza, J.A., Gervilla, F., Blanco-Moreno, J. (2006). Petrogenesis of highly depleted peridotites and gabbroic rocks from the Mayarí-Baracoa Ophiolitic Belt (eastern Cuba). Contributions to Mineralogy and Petrology 151(6),717.

Marchesi, C., Garrido, C.J., Bosch, D., Proenza, J.A., Gervilla, F., Monié, P., Rodriguez-Vega, A. (2007). Geochemistry of Cretaceous magmatism in eastern Cuba: recycling of North American continental sediments and implications for subduction polarity in the Greater Antilles Paleo-arc. Journal of Petrology 48, 1813–1840.

Marsh, E., Anderson, E., Gray, F. (2013). Nickel-cobalt laterites—A deposit model, chapter H of Mineral deposit models for resource assessment: U.S. Geological Survey Scientific Investigations Report 2010–5070–H, 38 p.

Newsome, L., Arguedas, A.F.S., Coker, V., Boothman, C., Lloyd, J. (2019). Manganese and cobalt redox cycling in laterites; Biogeochemical and bioprocessing implications. Chemical Geology, 531, 119330.

Proenza, J.A., Díaz-Martínez, R., Iriondo, A., Marchesi, C., Melgarejo, J.C., Gervilla, F., Garrido, C.J., Rodríguez-Vega, A., Lozano-Santacruz, R., Blanco-Moreno, J.A. (2006). Primitive island-arc Cretaceous volcanic rocks in eastern Cuba: the Téneme Formation. Geologica Acta 4, 103-121.

Proenza, J.A., Gervilla, F., Melgarejo, J.C., Bodinier, J.L. (1999). Al- and Cr-rich chromitites from the Mayarí-Baracoa ophiolitic belt (eastern Cuba); consequence of interaction between volatilerich melts and peridotites in suprasubduction mantle. Economic Geology 94, 547-566.

Proenza, J.A., González-Jiménez, J.M., Garcia-Casco, A., Belousova, E., Griffin, W.L., Talavera, C., Rojas-Agramonte, Y., Aiglsperger, T., Navarro-Ciurana, D., Pujol-Solà, N., Gervilla, F., O'Reilly, S.Y., Jacob, D.E. (2018). Cold plumes trigger contamination of oceanic mantle wedges with continental crust-derived sediments: Evidence from chromitite zircon grains of eastern Cuban ophiolites. Geoscience Frontiers 9(6), 1921–1936.

Rojas-Agramonte, Y., Garcia-Casco, A., Kemp, A., Kröner, A., Proenza, J.A., Lázaro, C., Liu, D. (2016). Recycling and transport of continental material through the mantle wedge above subduction zones: A Caribbean example. Earth and Planetary Science Letters 436, 93–107.

Villanova-de-Benavent, C., Proenza, J.A., Galí, S., García-Casco, A., Tauler, E., Lewis, J.F., Longo, F. (2014). Garnierites and garnierites: textures, mineralogy and geochemistry of garnierites in the Falcondo Ni-laterite deposit, Dominican Republic. Ore Geology Reviews 58, 91–109.

Wang, W., Pranolo, Y., Cheng, C.Y. (2011). Metallurgical processes for scandium recovery from various resources: a review. Hydrometallurgy 108, 100–108

USGS (2021). Mineral Commodity Summaries 2021: US Geological Survey; US Geological Survey: Reston, VA, USA; 200p.

# Clay-hosted REE mineralisation under the microscope

**Michael Gazley[1,2], Manuel Knorsch[3], Kat Lilly[1], Muhammet Kartal[3], Eliza Trunfull[3], Agnieszka Piechocka[3]**
*[1]RSC, 225 Thorndon Quay, Wellington, New Zealand*
*[2]School of Geography, Environment and Earth Science, Victoria University of Wellington, New Zealand*
*[3]RSC, 15 Rheola St, West Perth, Australia*

**Abstract.** Rare earth elements (REEs) are in high demand due to their application in renewable technologies and electromobility. Particular exploration focus is on clay-hosted REE deposits, which typically have a higher proportion of heavy REEs (e.g. terbium and dysprosium) relative to light REEs, which enhance high-temperature properties of permanent magnets. Academic studies have focussed on clay-hosted REE deposits in China, and little is known about the mineralogy and viability of clay-hosted REE projects in Australia. In this study, we: 1) examine the deportment of REEs within clay horizons along with the degree of weathering, 2) contrast relict primary REE minerals with secondary REE minerals formed in the weathering horizon, and 3) quantify the clay mineralogy of various Australian clay-hosted REE projects. The outcomes of this microcharacterisation study illustrate the unique mineralogy of REE clay deposits and indicate the extent to which REEs may be recoverable from the clay horizons.

## 1 Introduction

Clay-hosted REE deposits, also termed regolith-hosted REE deposits, are mined in the Jiangxi, Guangdong, Fujian, Hunan, Guangxi and Yunnan provinces in South China, and in Malaysia. The deposits are typically formed on ridges during weathering of REE-bearing Cretaceous-to-Jurassic volcanic and granitic rocks. The REE content of the clay horizon may increase up to five times relative to the underlying source rock (Bao and Zhao 2008; Foley and Ayuso 2015). Rare earth elements are released from the underlying magmatic rocks from primary REE host minerals such as allanite, apatite, monazite, titanite, bastnaesite, synchysite, fluorite, or xenotime (Li et al. 2017). During the breakdown of primary host minerals, the REEs may be adsorbed onto the surface of clay minerals such as kaolinite, halloysite, illite, smectite, or vermiculite to form ionic clay-hosted mineralisation (Mukai et al. 2020). In this style of deposit the REEs can be extracted via ionic solutions that preferentially scavenge the REEs but do not dissolve the clay minerals.

The proportion of REEs adsorbed to clay minerals compared to those trapped within acid-resistant, REE-bearing, minerals (e.g. monazite) is a critical factor in determining the economic viability of a REE clay project. Various microcharacterisation studies have been published on prominent clay hosted deposits in China and Madagascar (e.g. Borst et al. 2020); however, little is known about the plethora of clay-hosted REE deposits in Australia.

Current price fluctuations, focus on critical minerals, risk of disrupted supply chains, and governmental support have recently triggered intense exploration efforts for clay-hosted REE mineralisation in Australia, with >50 projects being pursued by junior exploration companies. The information provided in company reports typically relates to the distribution of REEs within the clay horizon from aircore drilling results. However, little is known about the REE mineralogy, which is crucial in identifying the economic potential of clay-hosted REE deposits.

This talk will focus on scanning electron microscopy (SEM) and whole-rock geochemistry results of clay and bedrock from multiple Australian REE clay projects, which assists in identifying their individual mineralogical signatures and secondary/primary REE minerals.

## 2 Methods

### 2.1 SEM analysis

A thin layer of clay material was smeared onto carbon tape and outgassed for 48 hours in the vacuum chamber of a Quorum Q 150TE plus carbon coater prior to carbon coating. Rock-chip and selected clay samples were either mounted in 30 mm epoxy rounds or prepared as thin sections and analysed using a Zeiss Axiolab 5 petrographic microscope.

Analyses via SEM were performed using a Hitachi SU3900 with two Bruker XFlash 6160 energy-dispersive spectroscopy (EDS) detectors. Backscatter electron (BSE) and secondary electron (SE) images are collected of smear samples using a low acceleration voltage (5–10 keV) and a short working distance (~6 mm).

### 2.2 Geochemical analysis

The geochemical analysis technique utilised in clay-hosted REE projects is dependent on the individual exploration company and commercial laboratory. Samples typically are from air core, reverse circulation, or sonic drilling. Most available datasets are 4-acid digest multi-element suite, which includes the total REE suite. However this technique may not dissolve acid-resistate REE-bearing phosphate minerals and therefore does not reliably indicate the samples total REE content. In contrast, borate Fusion techniques are also applied as a standard method for analysing the REE content of a sample and includes REE within acid resistate minerals.

For selected projects, early metallurgical test work is presented using ionic solutions (e.g. ammonium sulphate at pH 4), which can be compared to 4-acid or flux-fusion data.

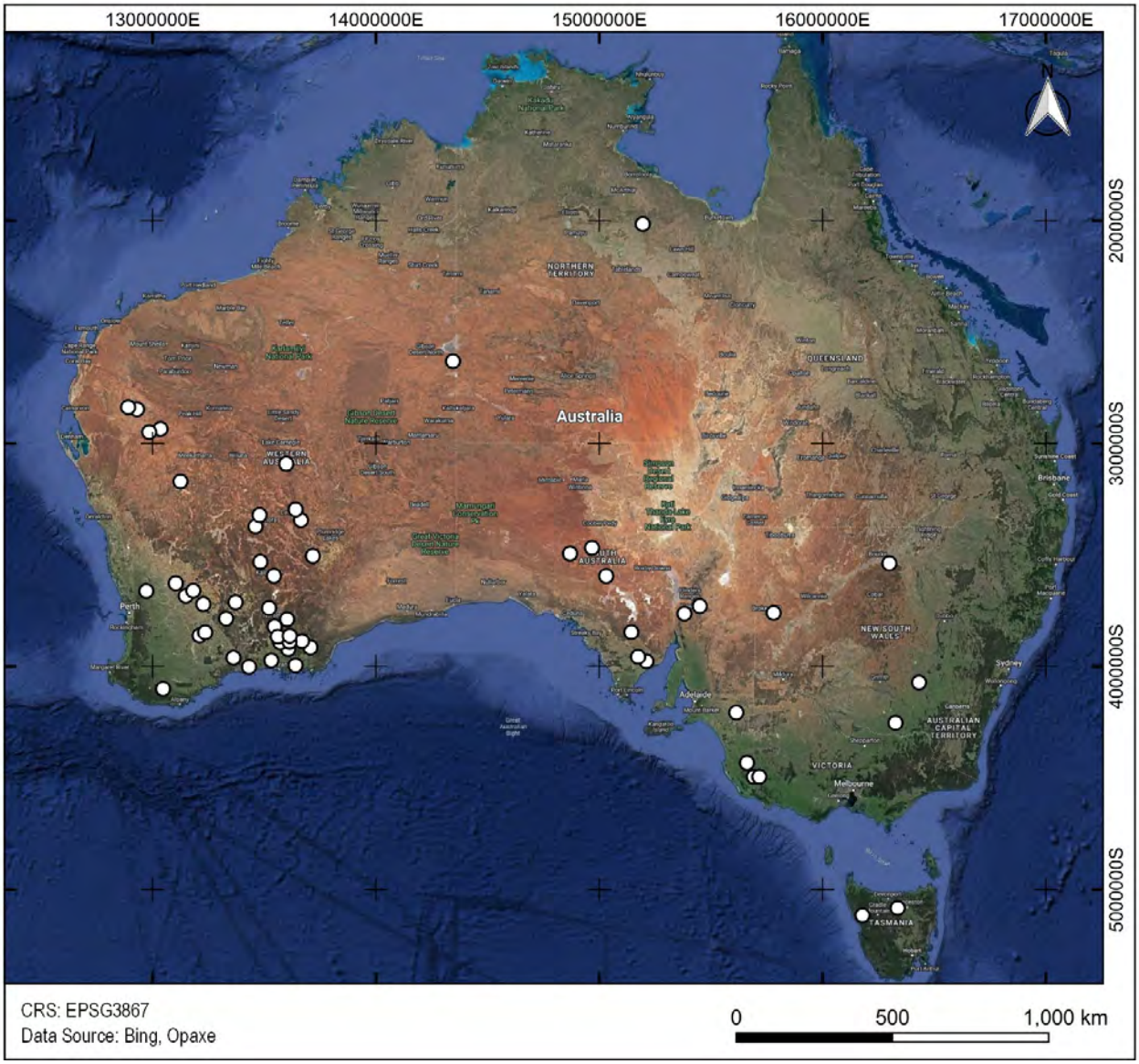


**Figure 1:** Overview of >50 active rare earth clay projects in Australia, including but not limited to ABx Group, Ardea Resources, Asra Minerals, Auric Mining, Auroch Minerals, Ausmon Resources, Australian Rare Earths, Castillo Copper, ChemX Materials, Desert Metals, Dundas Minerals, Emetals, EMU NL, Forrestania Resources, Godolphin Resources, Golden Mile Resources, Heavy Rare Earths, Horizon Minerals, Indiana Resources, Investigator Resources, iTech Minerals, Kingfisher Mining, Krakatoa Resources, Krakatoa Resources, Lanthanein Resources, Latin Resources, Magnetic Resources, Mamba Exploration, Marmota, Marquee Resources, Meeka Metals, Miramar Resources, Mount Ridley Mines, Moho Resources, Mt Monger Resources, Narryer Metals, Norwest Minerals, OD6, Petratherm, Pursuit Minerals, Resource Base, Sky Metals, Summit Minerals, Tambourah Metals, Taruga Minerals, Terrain Minerals, Traka Resources, Transition Minerals, Venus Metals, Venture Minerals, Victory Goldfield, Voltaic Strategic Resources, West Cobar Metals, and White Cliff Minerals.

## 3 Results and Discussion

### 3.1 Overview

A review of exploration activity identified 56 clay-hosted REE projects (Figure 1). Data compiled focused on Australian Stock Exchange (ASX) listed exploration companies and the actual number of projects is expected to be larger. The majority of REE projects (39) are within Western Australia, located in areas with granitic bedrock in the Albany-Fraser Orogen and central Yilgarn Craton. Another cluster is within the Delamerian Orogen and Gawler Craton within South Australia. Almost all clay-hosted REE discoveries in Australia were made within the last three years and information on mineralogy is scarce.

### 3.2 Primary REE Minerals

Primary REE minerals identified in the SEM study of various REE clay projects include allanite, apatite, Ca-REE fluorocarbonates, fluorite, monazite, titanite, and zircon. These primary magmatic minerals were identified within granitic source rocks that have been partially weathered. Allanite is the dominant primary REE mineral in granitic source

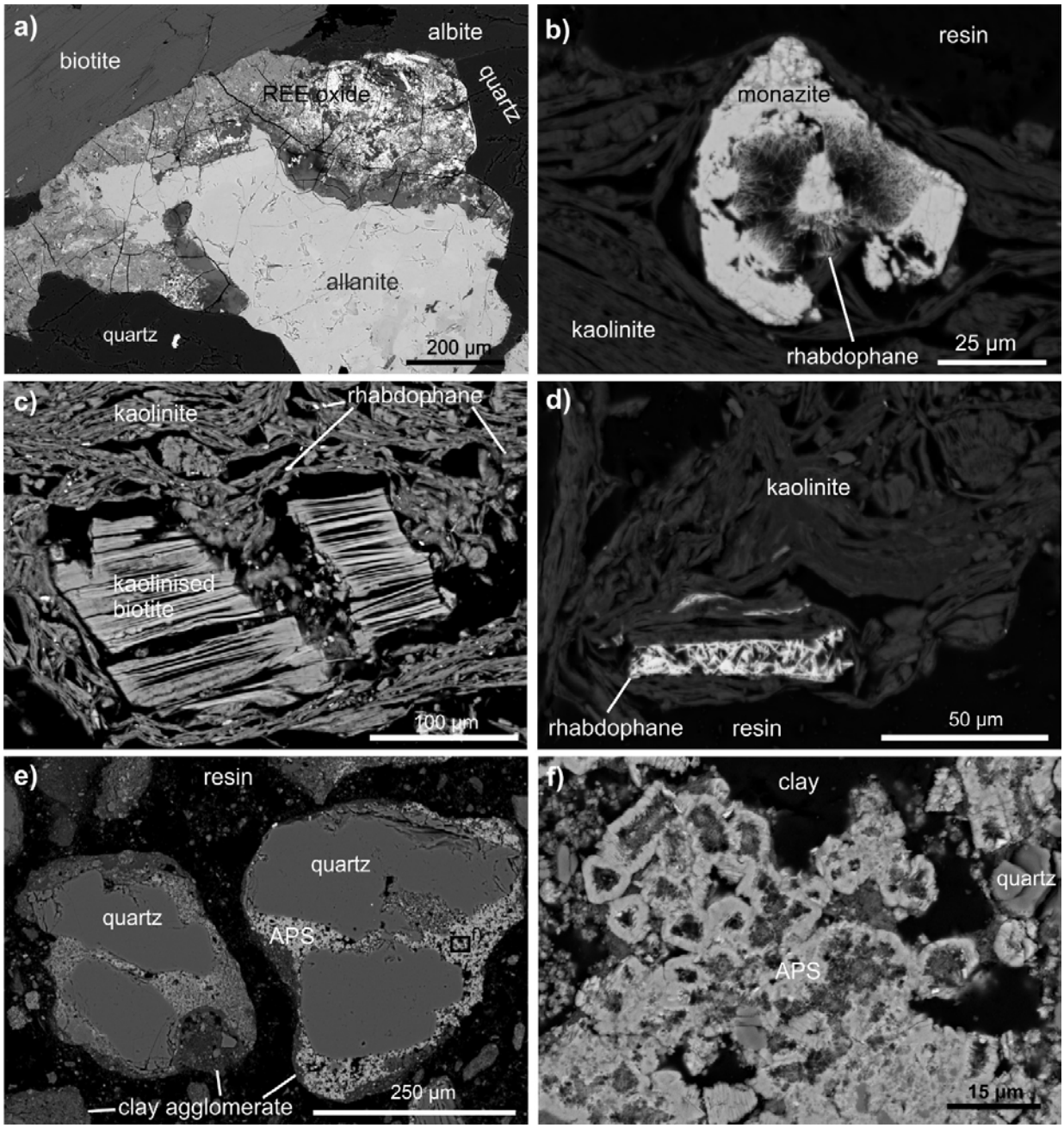


**Figure 2:** Primary and secondary REE mineralogy in selected Australian REE clay deposits. a) Breakdown of allanite to various Fe and REE oxides in monzogranite; b) Relict monazite in the clay horizon with overgrowth of acicular rhabdophane; c) kaolinite with exfoliated biotite. Note the minute rhabdophane aggregates within kaolinite; d) fibrous rhabdophane growing within kaolinite sheets; e–f) REE-Ba-Ca-bearing Aluminium Phosphate Sulphate minerals (APS) growing in atoll texture around dissolved quartz grains.

rock at one project, and is partially weathered to a complex assemblage Fe/REE (oxyhydr)oxides (Figure 2a). Notably, allanite is the least stable mineral during weathering in the sample in Figure 2a and readily releases REEs during weathering to the clay horizon.

The loss on ignition (LOI) at 1100 °C is typically >8.75 wt.% in fully weathered kaolinite-halloysite horizons (Du Plessis et al. 2021) and can be used as a proxy for the degree of weathering. Clay samples with LOI ≈ 4–5 wt.% contain abundant relict quartz and primary REE minerals both as liberated minerals or inclusions within quartz. In some instances, primary, granular, monazite with rounded corners (e.g. Schulz 2021) remains intact, suggesting that (some) REEs have not been mobilised during weathering and are locked within primary magmatic minerals such as monazite.

### 3.3 Secondary REE Minerals

In other instances, monazite is partially dissolved and secondary acicular REE phosphates are observed nucleating on monazite (Figure 2b). The secondary phase is likely rhabdophane [$REE(PO_4) \cdot$

$nH_2O$] which precipitates during the breakdown of monazite.

Rhabdophane is abundant in the clay horizon of multiple REE clay projects and hosts a portion of the REE content, which is not adsorbed onto the surface on clay minerals. Rhabdophane also grows in needle-like aggregates within kaolinite layers at various size fractions (Figure 2c–d). In contrast to the replacement texture observed in Figure 2b, this textural variety of rhabdophane is not directly related to the breakdown of monazite.

Some exotic REE minerals are also present in clay hosted REE mineralisation. One studied project contains abundant REE-Ba-Ca-bearing Aluminium Phosphate Sulphate minerals of variable composition that are likely attributed to the plumbogummite subgroup of the alunite supergroup, that includes florencite [$REEAl_3(PO_4)_2(OH)_6$], crandallite [$CaAl_3(PO_4)(PO_3OH)(OH)_6$], or gorceixite [$BaAl_3(PO_4)(PO_3OH)(OH)_6$]. These phosphate minerals crystallise in atoll like textures enveloping weathered quartz grains (Figure 2e–f).

## 4 Conclusion

Rare earth clay projects in Australia are abundant within Archean Cratons within Western Australia and South Australia. Most projects are in their infancy, and it is yet to be determined which prospects host economic, extractable quantities of REEs. Microcharacterisation of REE projects is crucial to identifying primary and secondary REE minerals, which may not be recovered using ionic solutions, as well as clay mineralogy, the degree of weathering and the presence of deleterious minerals. Each prospect analysed in this study is unique in terms of the above-mentioned parameters and therefore may require unique processing techniques for REE extraction.


## Acknowledgements

The authors are thankful to several Australian exploration companies for allowing us to present their SEM data in this study.


## References


Bao Z, and Zhao Z (2008) Geochemistry of mineralization with exchangeable REY in the weathering crusts of granitic rocks in South China. Ore Geol Rev, 33:519–535. https://doi.org/10.1016/j.oregeorev.2007.03.005

Borst AM, Smith MP, Finch AA, Estrade G, Villanova-de-Benavent C, Nason P, Marquis E, Horsburgh NJ, Goodenough KM, Xu C, Kynický J, and Geraki K (2020) Adsorption of rare earth elements in regolith-hosted clay deposits. Nat Comm, 11:4386. https://doi.org/10.1038/s41467-020-17801-5

Du Plessis PI, Gazley MF, Tay SL, Trunfull EF, Knorsch M, Branch T, and Fourie LF (2021) Quantification of Kaolinite and Halloysite Using Machine Learning from FTIR, XRF, and Brightness Data. Minerals, 11:1350. https://doi.org/10.3390/min11121350

Foley N, and Ayuso R (2015) REE enrichment in granite-derived regolith deposits of the Southeastern United States: Prospective source rocks and accumulation processes. British Columbia Geol Survey Paper 3:131-138.

Li YHM, Zhao WW, and Zhou M-F (2017) Nature of parent rocks, mineralization styles and ore genesis of regolith-hosted REE deposits in South China: an integrated genetic model. J Asian Earth Sci, 148:65–95. https://doi.org/10.1016/j.jseaes.2017.08.004

Mukai H, Kon Y, Sanematsu K, Takahashi Y, and Ito M (2020) Microscopic analyses of weathered granite in ion-adsorption rare earth deposit of Jianxi Province, China. Sci Rep, 10:20194. https://doi.org/10.1038/s41598-020-76981-8

Schulz B (2021) Monazite Microstructures and Their Interpretation in Petrochronology. Front Earth Sci, 9:668566. https://doi.org/10.3389/feart.2021.668566

# Zinc incorporation into carbonate minerals from the Selac area, Kosovo

**Konrad Kluza[1], Jaroslav Pršek[1], Sławomir Mederski[1], Zdeněk Dolníček[2], Jiří Sejkora[2]**
*[1] AGH University of Science and Technology, Kraków, Poland*
*[2] Department of Mineralogy and Petrology, National Museum, Prague, Czech Republic*

**Abstract.** Chemical composition of carbonate minerals from the Selac area in Kosovo was studied. Samples from three sampling areas were analysed by using transmitted-light microscopy and electron microprobe. The main hydrothermal vein mineral is dolomite, which is characterized by enrichments in ZnO (up to 7.2 wt.%) and FeO (up to 12.78 wt.%). Another carbonate minerals found in veins: calcite, magnesite, and siderite are also characterized by zinc incorporation. Two substitutional trends are observed in the Selac dolomites: Fe+Mn enrichment as well as Zn enrichment both substituting Mg.

## 1 Introduction

Zinc in the nature forms a variety of its own minerals included sulfides, sulfates, oxides, carbonates, phosphates, and silicates, but can also substitute into other minerals (Barak and Helmke 1993). Historically, zinc was mined from non-sulfide deposits (where smithsonite and hemimorphite are the main ore minerals), but over time and the development of processing methods, sulfide deposits rich in sphalerite have become the main source of zinc on the market. However, in recent years there has been a trend in the market to return to exploration and exploitation of non-sulfide zinc deposits, which, moreover, results in the presence of new research on this type of deposits, as well as the processes responsible for their formation (Boni and Mondillo 2015). Hitzman et al. (2003) distinguish two major subtypes of non-sulfide zinc deposits: supergene (related to oxidation of sulfide–type deposits) and hypogene (associated with silicates and zinc oxides).

Carbonates are minerals widely spread in nature and common in different environments (sedimentary basins and hydrothermal environment). One of the well-known member is dolomite $CaMg(CO_3)_2$, which can be primary in various environments (including hydrothermal), but can also be formed by dolomitization of pre-existing carbonate rocks. During dolomitization secondary porosity is generated, one of the key factors for origin of MVT and carbonate-replacement Zn-Pb deposits. In addition, it has a major impact on younger processes linked to later supergene processes responsible for the formation of non-sulfide deposits (Boni et al. 2011). Dolomite could easily incorporate various elements as Mn, Fe, and Zn.

The phenomenon of dedolomitization described by Fairbridge (1978) provides the recrystallization of dolomite to calcite as a result of weathering. Boni et al. (2011) describes the phenomenon of 'zincization' as the incorporation of Zn in dolomite, followed by the formation of smithsonite, in the context of supergene non-sulfide deposits.

## 2 Geology

The Selac area is located in the northern part of Kosovo, near the famous Pb-Zn-Ag Stan Terg deposit. That area is a part of the Trepça Mineral Belt, which is main metallogenic belt in Kosovo and belongs to bigger suture zone named Vardar Zone (Fig. 1). Mineralization and alterations in that area have hydrothermal origin and are related to Oligocene-Miocene volcanic activity (Strmić Palinkaš et al. 2013).

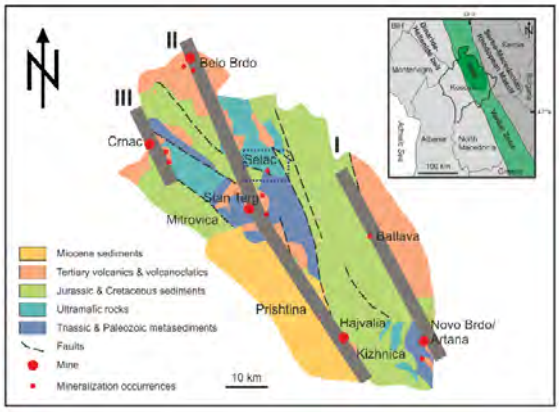


**Figure 1.** Geological map of Trepça Mineral Belt, Kosovo (modified after Strmić Palinkaš et al. 2013; Mederski et al. 2021) with marked study area. I – Batlava – Artana zone, II – Belo Brdo - Stan Terg -Hajvalia zone, III – Crnac zone.

Lithologies in the Selac area are represented mainly by Jurassic ultrabasic rocks and serpentinites which occurs together with ophiolite and mélange with small amount of Paleozoic crystalline basement (formed by schist and phyllites) with intensive Tertiary unit represented by volcanics, sub-volcanic intrusive and pyroclastic rocks (Mederski et al. 2021). On the border between serpentinites and volcanic rocks, as well as in tectonic zones hydrothermally altered rocks - listvenites occur. Listvenites often host hydrothermal mineralization (Mederski et al. 2021).

Mineralogy of the studied listvenites and hydrothermal veins consists of carbonates (dolomite, magnesite), quartz, chalcedony, and fuchsite. Ore mineralization is represented by galena, sphalerite, nickeline, maucherite, gersdorffite, rammelsbergite, polydymite, marcasite, pyrite, millerite, and chromite (Mederski et al. 2021).

| Dolomite N = 316 | | Oxide in wt. % | | | | | | | | | | | |
|---|---|---|---|---|---|---|---|---|---|---|---|---|---|
| | | MgO | $P_2O_5$ | CaO | MnO | PbO | FeO | ZnO | CoO | NiO | CuO | $Al_2O_3$ | BaO |
| **SL_I** N = 29 | *Minimum* | 15.82 | 0.04 | 27.32 | 0.06 | b.d.l. | 1.03 | b.d.l. | b.d.l. | 0.08 | b.d.l. | 0.03 | b.d.l. |
| | *Maximum* | 22.64 | 0.18 | 30.25 | 0.36 | b.d.l. | 9.92 | b.d.l. | b.d.l. | 0.21 | b.d.l. | 0.30 | b.d.l. |
| | *Median* | 20.27 | 0.11 | 29.22 | 0.17 | b.d.l. | 3.99 | b.d.l. | b.d.l. | 0.14 | b.d.l. | 0.05 | b.d.l. |
| **SL_II** N = 254 | *Minimum* | 11.84 | 0.01 | 16.10 | 0.05 | 0.13 | 0.09 | 0.14 | 0.06 | 0.07 | b.d.l. | 0.03 | b.d.l. |
| | *Maximum* | 23.40 | 0.63 | 31.80 | 1.00 | 1.16 | 11.12 | 7.20 | 0.13 | 12.92 | b.d.l. | 1.88 | b.d.l. |
| | *Median* | 17.82 | 0.08 | 28.26 | 0.20 | 0.26 | 5.41 | 1.28 | 0.08 | 0.12 | b.d.l. | 0.06 | b.d.l. |
| **SL_III** N = 33 | *Minimum* | 9.66 | 0.01 | 21.19 | 0.08 | 0.19 | 0.10 | 0.20 | 0.01 | 0.12 | 0.01 | 0.03 | 0.01 |
| | *Maximum* | 19.16 | 0.16 | 29.20 | 0.68 | 12.43 | 12.78 | 7.16 | 0.05 | 0.45 | 0.09 | 0.50 | 0.09 |
| | *Median* | 15.05 | 0.08 | 28.32 | 0.23 | 0.39 | 4.49 | 1.10 | 0.02 | 0.21 | 0.04 | 0.15 | 0.03 |
| **Calcite** N = 9 | *Minimum* | 0.23 | 0.03 | 37.08 | 0.05 | 0.31 | 0.16 | 0.19 | 0.01 | 0.09 | b.d.l. | 0.04 | 0.03 |
| | *Maximum* | 7.28 | 0.44 | 57.56 | 0.48 | 7.63 | 6.61 | 3.10 | 0.01 | 0.09 | b.d.l. | 0.07 | 0.25 |
| | *Median* | 0.52 | 0.04 | 51.60 | 0.09 | 2.25 | 0.39 | 1.07 | 0.01 | 0.09 | b.d.l. | 0.06 | 0.03 |
| **Magnesite** N = 15 | *Minimum* | 15.93 | 0.03 | 0.03 | 0.05 | 0.19 | 3.57 | 1.44 | 0.10 | 0.08 | b.d.l. | 0.03 | b.d.l. |
| | *Maximum* | 47.67 | 0.05 | 10.07 | 0.43 | 0.19 | 23.30 | 14.61 | 0.10 | 1.74 | b.d.l. | 0.07 | b.d.l. |
| | *Median* | 33.88 | 0.04 | 0.22 | 0.23 | 0.19 | 13.40 | 6.36 | 0.10 | 0.13 | b.d.l. | 0.05 | b.d.l. |
| **Siderite** N = 2 | *Minimum* | 14.62 | 0.00 | 0.42 | 0.49 | b.d.l. | 28.59 | 1.65 | 0.08 | 0.52 | b.d.l. | b.d.l. | b.d.l. |
| | *Maximum* | 14.74 | 0.00 | 0.70 | 0.93 | b.d.l. | 36.99 | 11.55 | 0.08 | 0.95 | b.d.l. | b.d.l. | b.d.l. |
| | *Median* | 14.68 | 0.00 | 0.56 | 0.71 | b.d.l. | 32.79 | 6.60 | 0.08 | 0.74 | b.d.l. | b.d.l. | b.d.l. |

**Table 1.** Chemical composition of carbonates from Selac area; b.d.l. = below detection limit.

## 3 Methods

### 3.1 Investigated material

Representative samples of dolomite vein were collected from the outcrops surrounding the village Selac in Kosovo. Samples comes from massive dolomite veins and with macroscopically visible nickel arsenide crystals. Sample area has 1.5 km width (Fig. 2), where three outcrops in the same tectonic zone were investigated. Sample location Sl_I is the most easterly. Rock samples are strongly carbonated and silicified with a lot of carbonates or silica veins; breccia also occurs. Sample location SL_II is the most westerly sample point. Rock samples are collected from coarse-crystalline carbonate vein. Dolomite veins with visible zonality was found. Sample location Sl_III is located near the Selac village. Samples are strongly silicified with visible carbonate vein and Ni mineralization; breccia is also found.

**Figure 2.** Map of the Selac area with marked sample spots.

### 3.2 Analytical techniques

Preliminary petrographic investigation of carbonates from the Selac area was conducted in transmitted-light microscopy. Chemical analyses of representative ore samples were determined by a Cameca SX100 electron microprobe (EPMA) at the Department of Mineralogy and Petrology, National Museum in Prague. Operating conditions were an accelerating voltage of 15 kV, a beam current 5, 8, 10 nA, peak time of 20 sec, and a background time of 10 sec. Natural and synthetic standards were used. The natural standards were: diopside, wollastonite, rhodonite, celestite, wulfenite, haematite, barite, fluoroapatite, chalcopyrite, sanidine, whereas the synthetic standards were ZnO, Co. Spectral lines MgKα, PKα, SiKα, CaKα, MnKα, SKα, SrLβ, PbMα, FeKα, ZnKα, CoKα, NiKα, CuKα, AlKα, BaLα were used for analyses.

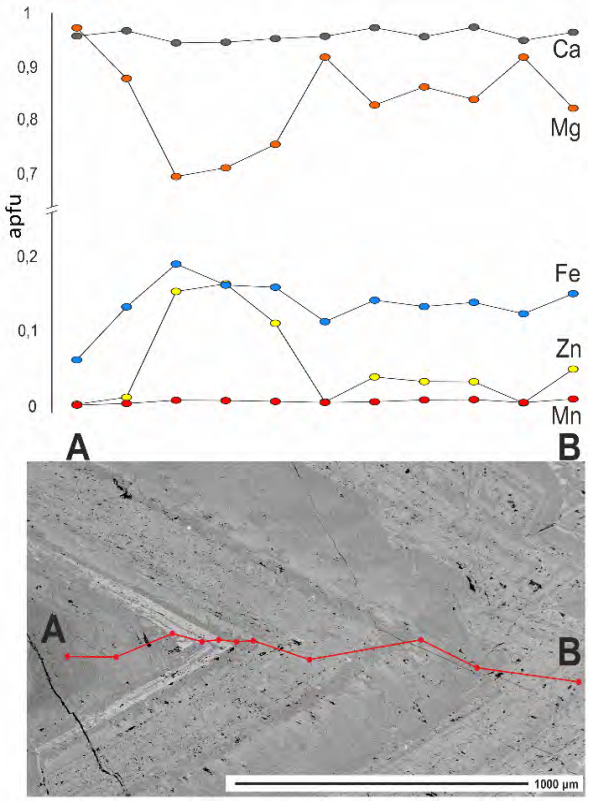


**Figure 3.** Oscillatory zoned dolomite crystal from Selac. Brighter zones are enriched in Fe and Zn, and depleted in Mg.

## 4 Results

### 4.1 Dolomite

Dolomite occurs mostly in crystal forms with a wide range of crystal size (from few μm up to few mm). They are showing a specific crystal structure – enormous amount of chipping visible in transmitted-light microscopy which are arranged perpendicular to the crystallization directions of the crystals. Moreover, they create zones which are better visible by using SEM. Zonation in that area are caused by varying metal content – Mg, Fe, Mn, Zn. Two zone types in dolomite are recognized. Firstly, oscillatory Fe-Mn rich zones without or with low amount of Zn and secondly, irregular zones with high Fe and Zn content (Fig.3, Fig.4).

Generally, dolomite from the Selac is characterized by relatively constant CaO content and enrichments in Fe, Mn, Zn, Pb and Ni on magnesium position.

Dolomite from Sl_I is characterized by MgO content between the 15.8 to 22.6 wt.%, while average content of CaO is equal to 29.2 wt.%. It is worth to notice that enrichment in FeO is up to 9.9 wt.%. Additionally, there is no enrichment in ZnO observed here (Tab.1).

Dolomite from Sl_II and Sl_III shows some similarities. Content of MgO in Sl_II varies from 11.8 to 23.4 wt.% and in SL_III between 9.7 and 19.2 wt.%. Average content of CaO is similar: 28.2 wt.% in Sl_II and 27.7 wt.% in Sl_III. Dolomites from these areas show the presence of Fe and Zn. Median of FeO content is 5.41 wt.% in Sl_II and 4.5 wt.% in Sl_III, whereas median of ZnO content is 1.3 wt.% in Sl_II and 1.1 wt.% in Sl_III. Additionally, some dolomite zones from the Sl_III are characterized by the unusual PbO enrichment in maximum up to 12.4 wt.%, (with median equals 0.4 wt.%), while some dolomite zones from the Sl_II show NiO enrichment (up to 12.9 wt.%, and median equals 0.1 wt.%) (Tab.1).

### 4.2 Other carbonates

Other minor carbonates are represented mostly by calcite, zoned and brecciated magnesite, and rarely siderite. Calcite mostly forms the small veinlets and sometimes overgrow dolomite crystals. Magnesite and siderite build host rock (serpentinite) and they occur in massive form or as a relict in quartz/dolomite veinlets (Fig.4).

Composition of calcite shows enrichment of MgO (up to 7.3 wt.%), PbO (up to 7.6 wt.%), FeO (up to 6.6 wt.%) and ZnO (up to 3.1 wt.%) (Tab.1). Magnesite is characterized by wide range of MgO (15.9-47.7 wt.%) and FeO (3.6-23.3 wt.%), there are also visible enrichment in ZnO up to 14.6 wt.% and rarely increased amount of CaO (up to 10.1 wt.%) (Tab.1). Siderite is characterized by FeO content between 28.6 wt.% and 37.0 wt.% and MgO content which median is equal 14.68 wt.%. In siderite is visible increased content of ZnO, which median is 6.6 wt.%. (Tab.1).

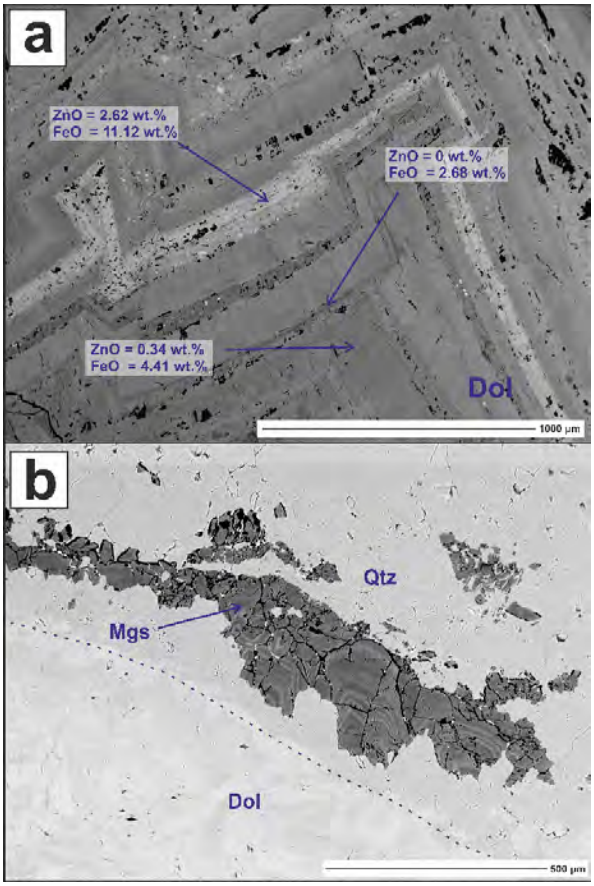


**Figure 4.** BSE images, **a -** dolomite crystal with oscillatory zones; **b** - Magnesite relict in quartz-dolomite vein.

## 5 Discussion

Observation of the textures, as well as the chemical composition of the carbonates from the Selac dolomite vein indicates the multi-stage formation of these veins. Breccias, overgrown textures and zonations (oscillatory and irregular), suggest variable crystallization conditions. In addition, two major substitutional trends are observed that reflect the processes responsible for vein formation in Selac (Fig.5).

Firstly, primary - oscillatory zonation in dolomite crystals can be a result of $(Fe^{2+} + Mn^{2+}) \leftrightarrow Mg^{2+}$ substitution (which is observed mainly in Sl_I) may have the hydrothermal origin, what is common in Kosovo and TMB, where the occurrence of Mn in carbonate minerals is typical in many hydrothermal localities (Mederski et al. 2021)

Secondly, irregular zonation characterized by perpendicular to crystal borders chipping, may be as a result of $Zn^{2+} \leftrightarrow Mg^{2+}$, what has been so far described by Boni et al. (2011) as a dedolomitization phenomenon in dolomite mineral. Together with supergene alteration of Zn-Pb sulfide ores it results in formation of nonsulfide deposits.

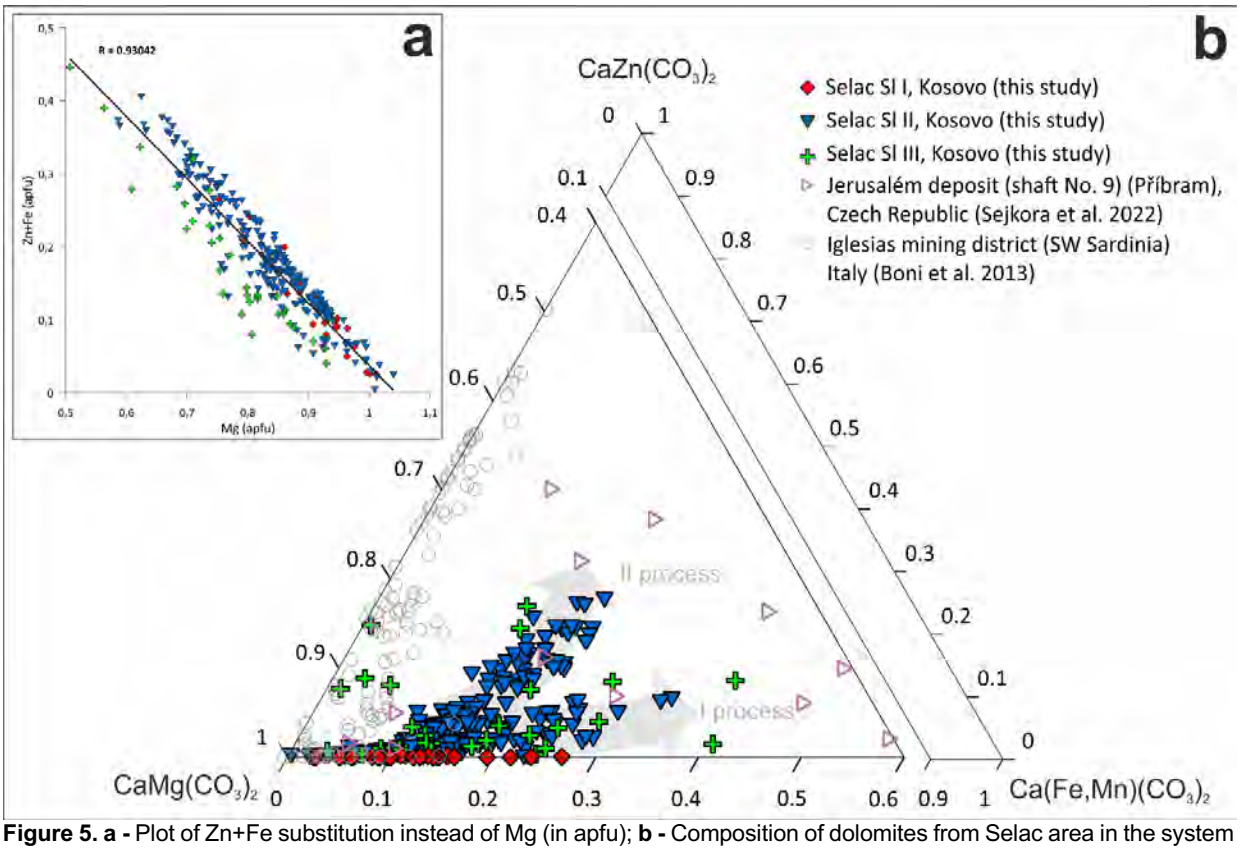


**Figure 5. a -** Plot of Zn+Fe substitution instead of Mg (in apfu); **b -** Composition of dolomites from Selac area in the system $CaMg(CO_3)_2$ – $Ca(Fe,Mn)(CO_3)_2$ – $CaZn(CO_3)_2$, with comparison of data from Boni et al. 2013 and Sejkora et al. 2022.

On the other hand, Sejkora et al. (2022) described Zn-enriched dolomites of hydrothermal origin from the Jerusalém deposit from the Příbram uranium and base-metal district (Czech Republic). Zn rich dolomites from this locality are also rich in Mn and Fe and occur in paragenesis with quartz, siderite, willemite, Cu arsenides, or Cu-Ag sulfides. The formation temperatures of this paragenesis, depending on the thermometer used, range from 70 to 136 °C (Sejkora et al. 2022).

A similar situation is found at Selac, where Zn-rich dolomite occurs in paragenesis with arsenide (Ni) association and is suspected to be of hydrothermal origin. Probably, the presence of Zn in dolomites from Selac is due to low sulfur activity in hydrothermal fluids. This fact is mentioned by Mederski et al. (2021), who referred to the above conditions for the formation of arsenide Ni association, as well as gersdorffite with a high As/S ratio. Confirmation of the potential low temperatures of this unique association in Selac requires further fluid inclusion studies.

## Acknowledgements

We would like to thank the many AGH students for their help in the fieldworks. Special thanks for their significant contribution to the fieldwork goes to Burim Asllani, Astrit Shala, and Maciej Jeż.

## References

Barak P, Helmke PA (1993) The Chemistry of Zinc. Part of the Developments in Plant and Soil Sciences book series (DPSS 55)

Boni M, Mondillo N (2015) The “Calamines” and the “Others”: The great family of supergene nonsulfide zinc ores. Ore Geol Rev 67:208-233

Boni M, Mondillo N, Balassone G, Joachimski M, Colella A (2013) Zincian dolomite related to supergene alteration in the Iglesias mining district (SW Sardinia). Int J Earth Sci 102:61-71

Boni M, Mondillo N, Balassone G, (2011) Zincian dolomite: A peculiar dedolomitization case? Geology 39/2:183-186

Fairbridge, RW (1978) Dedolomitization. The encyclopedia of sedimentology. 233–235

Hitzman MW, Reynolds NA, Sangster DF, Allen CR, Carman CE (2003) Classification, Genesis and Exploration Guides for Nonsulfide Zinc Deposits. Econ Geol 98: 685-714

Hyseni S, Durmishaj B, Fetahaj B, Shala F, Berisha A, Large D (2010) Trepça Ore Belt and Stan Terg mine – Geological overview and interpretation, Kosovo (SE Europe). Geologija 53/1:87-92

Mederski S, Wojsław M, Pršek J, Majzlan J, Kiefer S, Asllani B (2021) A geochemical study of gersdorffite from the Trepça Mineral Belt, Vardar Zone, Kosovo. J Geosci 66:97-115

Sejkora J, Dolníček Z, Škácha P, Ulmanová J, Vrtiška L (2022) Unusual mineralization with willemite from the area of the central part of the Příbram uranium and base-metal district (Czech Republic). Bull Mineral Petrolog 20/2:224-242

Strmić Palinkaš S, Palinkaš LA, Renac Ch, Spangenberg JE, Lüders V, Molnar F, Maliqi G (2013) Metallogenic Model of the Trepça Pb-Zn-Ag Skarn Deposit, Kosovo: Evidence from Fluid Inclusions, Rare Earth Elements, and Stable Isotope Data. Econ Geol 108:135-162

# Germanium mineralization in subbituminous coal from the Sokolov Basin, Czech Republic: The origin and volatility of Ge

**Kříbek B[1], Rohovec J[2], Bičáková O[3], Tuhý M[1,4], Sýkorová I[3], Straka P[3] Pticen F[1], Vymazalová A[1] Poňavič M[1]**
*[1]Czech Geological Survey, Geologická 6, 152 00 Prague 5, Czech Republic*
*[2]Institute of Geology, Academy of Sciences of the Czech Republic, Rozvojová 269, 165 00 Prague 6, Czech Republic*
*[3]Institute of Rock Structure and Mechanics, Czech Academy of Sciences, V Holešovičkách 41, 182 09 Prague 8, Czech Republic*
*[4]Institute of Geochemistry, Mineralogy and Mineral Resources, Faculty of Science, Charles University, Albertov 6, 128 00 Prague 2, Czech Republic*

**Abstract.** Miocene subbituminous coal (ortho-lignite) from the Sokolov coal basin (Ohře Graben, Czech Republic) contains up to 400 ppm Ge. However, the regional distribution of Ge in the studied Antonín and Josef coal seams is highly variable. The highest Ge concentrations are confined to the interface between the coal seams and the crystalline basement. Germanium in coal is bound mostly to pyritized coal macerals. The origin of Ge mineralization is explained by the infiltration of Ge-bearing solutions during the weathering of crystalline rocks and/or hydrothermal activity along the border faults of the coal basin. In calcination or gasification of coal, Ge was released in a vapour phase at temperatures of 780 to 810 °C. Very high Ge concentrations (up to 8,380 ppm) were found in fly ash.

## 1 Introduction

The continental Ohře (Eger) Graben (Czech Republic) hosts the Most, Sokolov and Cheb basins, filled with thick Paleogene to Pliocene siliciclastic sediments and coal seams (Rojík et al., 2014; Fig. 1a). In the Sokolov basin (Fig. 1b), the Antonín and Anežka coal seams are developed in Miocene sedimentary units, and the underlying Josef Seam in Oligocene sediments. All seams are relatively high in sulphur and arsenic. The main objective of this study was to study the areal distribution and binding of Ge in the Antonín and Josef seams and to assess the volatility of Ge during coal calcination or gasification as a prerequisite for the possibility of industrial germanium production.

## 2 Materials and Methods

To evaluate the distribution of Ge in the Antonín and Josef seams, 26 samples were collected from the individual technological position of the seams. Samples were dried, crushed and calcined to temperature of 200, 500, 700 900 and 1100 °C in the laboratory furnace. The thermodesorption (TD) analysis of the coal sample was performed using the setup introduced by Tuhý et al. (2021). It consists of a combustion unit (Clasic CZ, Czech Republic) connected at the outlet to an ICP-OES plasma torch (Iris Intrepid II XSP ICP-OES; Thermo-Scientific, USA; Fig. 2). The device operates under a continuous argon flow. The samples were heated from 25 °C to 900 °C with a linear gradient of 50 °C per minute. The elements of interest (As, Ge, Hg and S) were continuously and simultaneously detected (at analytical lines of 189.0 nm, 206.8 nm, 184.9 nm and 182.0 nm, respectively). The gasification of a constant weight coal sample was performed in the gasification unit (Fig. 3). The coal sample was heated to the temperature of 900 °C.

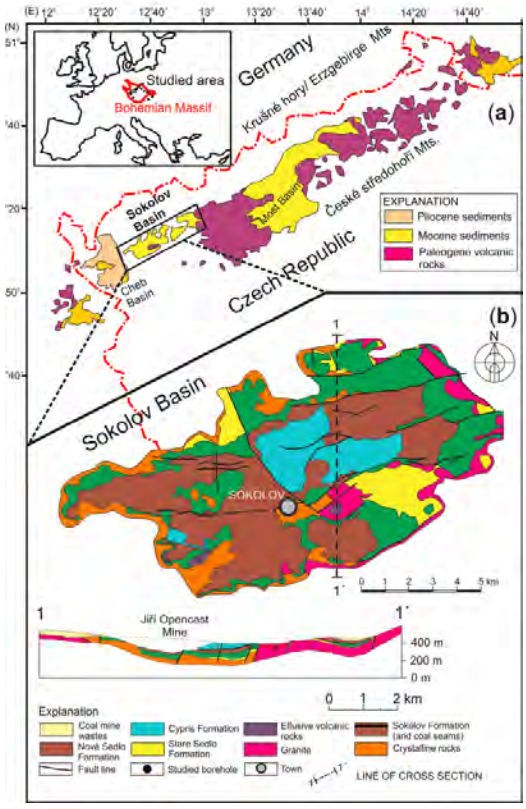


**Figure 1.** A geological sketch map of the Ohře Graben (**a**); modified after Matys Grygar and Mach (2013), and detailed map of the Sokolov Basin (**b**) (after Rojík et al. 2014).

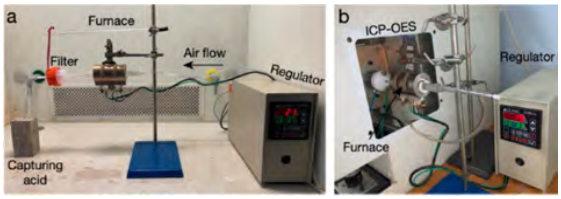

**Figure 2.** Thermodesorption of Ge, As, Hg and S was performed using coal combustion in a glass reactor (**a**). The coal sample was heated to a temperature of 1200 °C and the concentrations of elements in a gas phase were continuously monitored by an emission spectrometer with inductively coupled plasma (**b**).

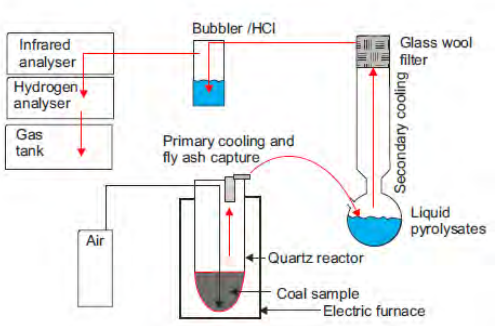


**Figure 3.** A simplified scheme of the laboratory pyrolysis unit. Unit drivers were omitted.

## 3 Results and Discussion

### 2.1 Germanium mineralization in coal

The concentrations of Ge and other selected elements in the Antonín and Josef coal seams are given in Table 1. Low Ge concentrations were found in coal of the central part of the basin, while high Ge contents (up to 380 ppm) were found only in its peripheral part, along the contact with the underlying Krušné hory Crystalline rocks (Fig. 4).

**Table 1.** Concentrations of Ge and other selected elements in the marginal and central part of the Antonín and Josef coal seems (Sokolov Basin, Czech Republic). Concentrations of $C_{org}$ and $S_{tot}$ are given in wt.%, those of Cu, Ge, As and Mo in ppm, those of Hg in ppb. n= 26.

| | Cu | Ge | As | Mo | Hg | $C_{org}$ | $S_{tot}$ |
|---|---|---|---|---|---|---|---|
| Antonín and Josef seams, peripheral part of the Sokolov basin, contact with the crystalline basement | | | | | | | |
| Max. | 7 | 411 | 411 | 12.3 | 200 | 43.2 | 6.8 |
| Average | 9 | 396 | 398 | 11.3 | 120 | 46.6 | 5.9 |
| Min. | 11 | 350 | 390 | 10.3 | 80 | 378 | 4.5 |
| Antonín and Josef seams, central part of the Sokolov basin | | | | | | | |
| Max. | 190 | 13.7 | 318 | 9.82 | 12 | 61.1 | 7.4 |
| Average | 81 | 5.52 | 164 | 7.69 | 8 | 54.9 | 5.1 |
| Min. | 25 | 1.11 | 37 | 3.55 | 10 | 51.4 | 1.7 |

The high contents of Ge in the marginal part of the seams can be explained by its introduction during weathering of the mineralized crystalline basement and/or hydrothermal activity along the marginal faults. The same mechanism has been reported by Dai et al. (2014) in the study of Ge mineralization of the Lincang deposit in the Yunnan region, NW China. Dai et al. consider the mineralization to be epigenetic.

Germanium-rich coal consists mainly of macerals of the huminite group (55 – 63 vol.%). It is dominated by completely gelled ulminite (24 – 27 vol.%), followed by textinite (remnants of cell structures) and attrinite. Macerals of the liptinite and fusinite groups are less common and do not contain Ge. The inorganic components are dominated by clay minerals, pyrite and quartz (Havelcová et al., 2015). Germanium is dispersed in the mass of fully gelled ulminite but is particularly concentrated in strongly pyritized textinite. This is confirmed by the good correlation between the distributions of Ge and S (Fig. 5).

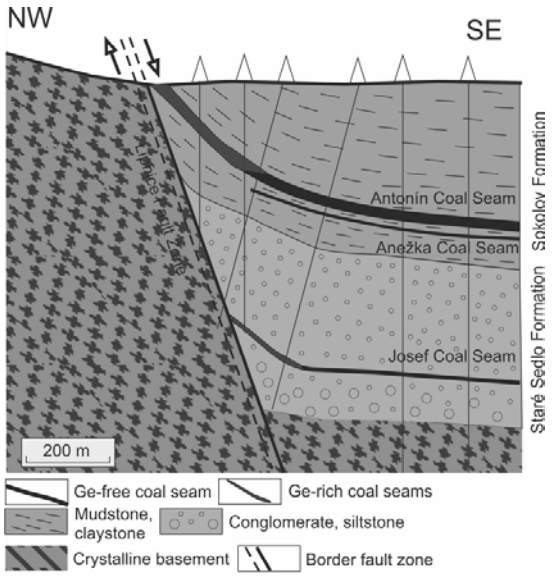


**Figure 4.** Geological position of high Ge contents in the Antonín and Josef seams in the Sokolov Basin. Elevated Ge contents are bound only to seams that closely adjoin the tectonically strongly affected rocks of the underlying crystalline unit. Germanium concentrations in the seams in the central part of the basin are very low (Table 1). Not to scale.

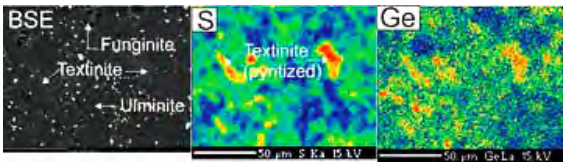


**Figure 5.** The distribution of S and Ge in coal of the Antonín Seam. Germanium is dispersed in ulminite but the highest Ge contents are bound to pyritized fragments of porous textinite.

### 3.2 Calcination of coal

During the calcination of coal samples with high Ge contents in a laboratory oven, the concentrations of Ge and other “volatile” elements were found to generally increase at lower temperatures and then

gradually decrease, due to their volatilization. The concentrations of Ge in coal ash, for example, gradually increase up to the temperature of 700 °C but rapidly decrease at higher temperatures (Fig. 6). At the calcination temperature of 700 °C, the concentration of Ge was found to increase from 420 ppm (in the original coal) to 1180 ppm in the calcinated coal residuum.

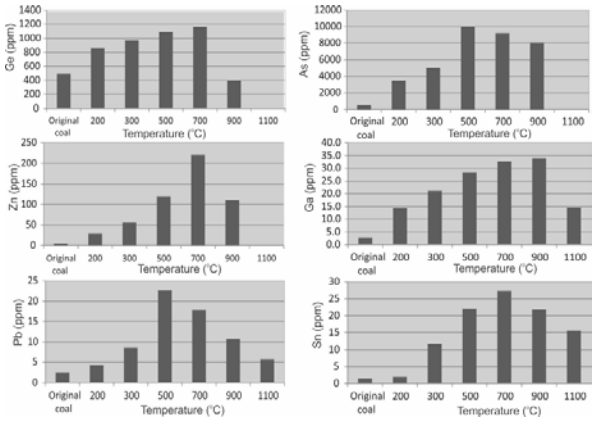


**Figure 6.** Concentrations of Ge and other volatile elements in calcinated coal residuum at temperatures in the range of 200 to 1100 °C. The Antonín Coal seam, sample HU 28/2022.

The highest concentrations of Ge (0.8 to 1.2 wt.%) were found in irregular clusters of hematite, whose morphology resembles pyritized particles of organic macerals, especially textinite (Fig. 7a, Fig. 8). In contrast, globular formations of hematite whose morphology resembles early diagenetic framboidal pyrite (Fig. 7b) are Ge-free. This suggests that the formation of Ge-rich coal is not linked to the early diagenetic stage of organic matter development, when framboidal pyrite is usually formed, but to the late diagenetic or epigenetic stages of seam evolution, and is associated with pyritization of porous organic remains.

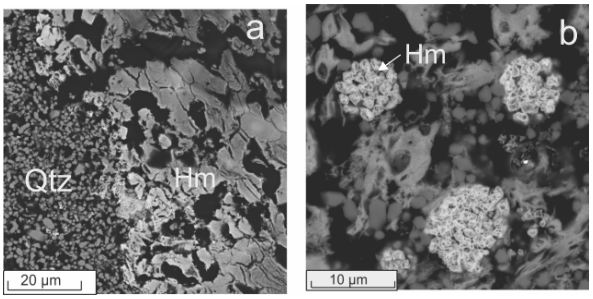


**Figure 7.** Two morphological types of hematite in coal after calcination at 700 °C. **a**: Porous hematite aggregates (Hm) are interpreted as an oxidation product of the pyritized coal fragment. This type of hematite aggregates shows Ge contents of max. 1.2 wt.%. **b**: Globular form of hematite aggregates, probably representing an oxidative product of pyrite framboids. Germanium was not detected in this morphological type of hematite. Qtz: authigenic quartz grains.

**Figure 8.** Distributrion of Fe (b) and Ge (c) in porous hematite cluster in the calcination residuum whose

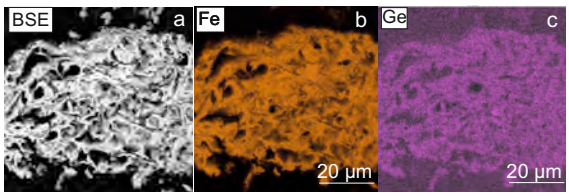


morphology resembles pyritized particles of organic macerals. Back scattered electrons (BSU).

### 3.3 Continuous monitoring of the Ge, S, Hg and As thermodesorption

Simultaneous volatilization of S, Hg and As occurred initially at temperatures around 350 °C, suggesting their similar speciation most probably in sulphides/sulphosalts. Maximum As release was observed at around 600 °C, followed by a sharp decrease. Germanium started to mobilize at temperatures of >700 °C and showed a single discrete peak at 800 °C (Fig. 9). This corresponds to the results of coal calcination in a laboratory furnace (Fig. 6).

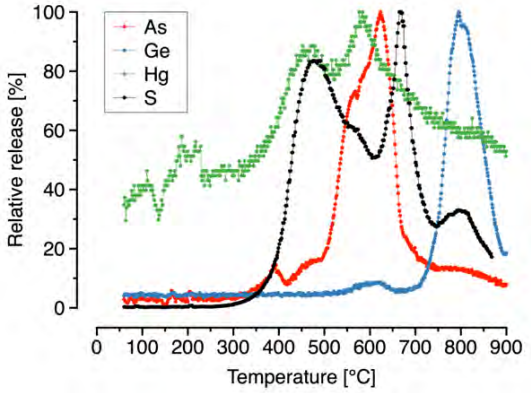


**Figure 9.** Relative release of elements from a coal sample (G21) as a function of temperature obtained by a combustion-simulating setup with a continuous temperature increase and online ICP-OES detection. For a better comparison of the individual curves, data were normalized to the maximum peak.

### 3.4 Gasification of coal at the temperature of 900 °C.

The previous experiments revealed that the thermodesorption of Ge occurs at temperature around 800 °C. In order to achieve complete gasification of Ge, coal samples were gasified at a quartz reactor, at the temperature of 900 °C. Due to exothermic character of the coal gasification, the temperature inside the sample increased and fluctuated between 910 and 950 °C and was monitored by a thermocouple in the coal sample. The simplified scheme of the gasification apparatus is shown in Figure 3. Experiment was carried out in duplicate.

The concentration of Ge and other elements were recorded in an original coal sample, in a solid coal residue after thermal treatment, in a primary cooling unit where flay ash was collected, in liquid

pyrolysate, glass wool filters and in bubbler filled with 0.5 M HCl (Fig.3).

Compared to original coal (average concentration of Ge: 134 ppm; Table 2), the concentration of Ge in the coal residue in the reactor was below the detection limit of the analytical method used (XRF) (Table 2).

The highest concentrations of Ge were recorded in fly ash (average Ge concentration: 8,380 ppm) and in filters (3,072 ppm). The results of the powder X-ray diffraction showed that the fly ash consists of a large amount of amorphous aluminosilicates, quartz and small amount of anatase ($TiO_2$). Of the Ge compounds, $GeO_2$ (trigonal variety) and GeS (orthorhombic variety) were identified. This indicates that Ge in fly ash is bound to solid particles. However, it cannot be ruled out that a part of Ge is binded by sorption to other components of the system, especially to amorphous aluminosilicates or to hematite.

The Ge concentrations in a liquid gasification product were very low and ranged between 64.2 in liquid pyrolysate and 2.99 ppm in a bubbler filled with 0.5 M HCl (Table 2).

**Table 2.** Average concentrations of Ge, As and Hg during gasification of brown coal samples at a temperature of 900 °C ($n$ = 2).

| Substrate | Ge | As | Hg |
|---|---|---|---|
| Coal sample before gasification | 134 | 870 | <LOD |
| Coal sample after gasification (coal solid residuum) | <LOD | 1042 | <LOD |
| Fly ash | 8,380 | 10,522 | 2,200 |
| Liquid pyrolysate | 64.2 | 30.5 | 0.735 |
| Glass wool filter | 3,072 | 3,595 | 614 |
| Bubbler / 0.5 M HCl | 2.99 | 3.11 | 1.23 |

## 4 Conclusions

Germanium mineralization in the Sokolov Basin is restricted to the contact of the coal seams with the crystalline basement. In the central part of the basin, Ge concentrations are very low. This suggests that the source of Ge can be seen either in low-temperature weathering of crystalline rocks or in a hydrothermal activity associated with movements along border faults of the sedimentary basin. Germanium in coal is dispersed in gelified coal organic matter. However, the highest Ge concentration was recorded in pyritized fragments of porous coal macerals. On the other hand, Ge was not recorded in framboidal pyrite, which was formed during the early diagenesis of coal seams. This confirms that the Ge ore mineralization is confined to the late diagenetic or epigenetic stages of the development of coal seams.

During the calcination of coal, Ge concentrations in the ash gradually increase up to a temperature of 700 °C. At this temperature, Ge in the calcinated coal residuum is mainly bound to hematite, which is formed during pyrite oxidation. The concentrations of Ge in hematite reach max. 1.2 wt.%. At higher temperatures, Ge concentrations sharply decrease.

Continuous monitoring of the thermodesorption confirmed that Ge is volatilized at ~800 °C. In contrast, a significant part of potentially harmful elements (S, As and Hg) are released at lower temperatures. The observed differences in the volatility of Ge S, As and Hg allow us to consider the separation of Ge and more volatile elements at different gasification temperatures.

During the laboratory gasification of coal in a quartz reactor at a temperature of 900 °C, the highest concentrations of Ge were found to be bound to fly ash or to glass wool filters. In the fly ash, Ge was present in the form of $GeO_2$ and GeS. The presence of GeS indicates a reaction between $Ge_{(vapour)}$ and $S_{(vapour)}$ during the gasification. The amount of Ge in the liquid gasification product was very low. This indicates that the fly ash captured on dry or water filters at high temperatures of coal gasification or combustion and subsequent Ge extraction with acids (HCl, $H_2SO_4$) or organic extractants can be an effective method of industrial Ge recovery.

## Acknowledgements

The authors are grateful to Project No. SS02030023 “Rock Environment and Natural Resources (RENS)” of the Technology Agency of the Czech Republic for funding. Research at the Institute of Geology of the Czech Academy of Sciences was co-financed by institutional support RVO 67985831.

## References

Dai S, Wang P, Colin R.W, Tang Y. Song X, Jiahuna J, Hower JC, Li T, Seredin V, Wagner NJ, Yaofa J, Wang X, Liu J (2014) Elemental and mineralogical anomalies in the coal-hosted Ge ore deposit of Lincang, Yunnan, southwestern China: Key role of $N_2$–$CO_2$-mixed hydrothermal solutions. Int J Coal Geol 152:19–46.

Havelcová M, Sýkorová I, Mach K, Trejtnarová H, Blažek J (2015) Petrology and organic geochemistry of the lower Miocene lacustrine sediments (Most Basin, Eger Graben, Czech Republic). Int J Coal Geol 139:26–39.

Matys Grygar T, Mach K (2012) Regional chemostratigraphic key horizons in the macrofossil-barren siliciclastic lower Miocene lacustrine sediments (Most Basin, Eger Graben, Czech Republic). Bulletin of Geosciences 88:557–571.

Rojík P, Dašková J, Kvaček Z, Pešek J, Sýkorová I, Teodoridis V (2014) The Sokolov Basin. *In*: Pešek J (ed.) *Tertiary Basins and Lignite Deposits of the Czech Republic*. Czech Geol Survey, Prague, pp 90–142.

Tuhý M, Ettler V, Rohovec J, Matoušková Š, Mihaljevič M, Kříbek B, Mapani B (2021) Metal(loid)s remobilization and mineralogical transformations in smelter-polluted savanna soils under simulated wildfire conditions. J Environmental Management 293:112899.

# Weathering processes associated to the formation of supergene Cu-As-Pb-Zn minerals at the Cap Garonne mine (France, Provence)

**Julien Poot[1], Johan Yans[1], Gaëtan Rochez[1], Pierre Buelens[2], Augustin Dekoninck[2]**
*[1]University of Namur, Department of Geology, Institute of Life-Earth-Environment, Namur, Belgium*
*[2]Université Libre de Bruxelles, Laboratoire G-Time, Département Géosciences, Environnement et Société, Brussels, Belgium*

**Abstract.** The Cap Garonne mine hosts more than 150 minerals (16 of them are type-locality) with a large part related to supergene processes. Primary mineralization mostly consists of tennantite [$(Cu,Zn,Ag,Fe)_{12}As_4S_{13}$] and galena [PbS] in a few-meters thick Permo-Triassic (P-Tr) fluviatile conglomerate. The secondary mineralization is very diverse and mainly consists in a succession of covellite [CuS], olivenite [$Cu_2(AsO_4)(OH)$], brochantite [$Cu_4(SO_4)(OH)_6$] and anglesite [$PbSO_4$] , cerussite [$PbCO_3$], malachite [$Cu_2(CO_3)(OH)_2$], and azurite [$Cu_3(CO_3)_2(OH)_2$]. The acidic fluids generated by the oxidation of primary sulfides led to the formation of secondary sulfides and some arsenates. The further neutralization processes, mostly by the calcite contained in the cement of the host conglomerate, allowed the precipitation of arsenates, sulfates and carbonates.

## 1 Introduction

The Cap Garonne old mine is located SW of the Maures Massif and S of the Permian Depression in the Toulon-Cuers Basin. The Cu-Pb-As-Zn mineralization contains a rich mineralogical assemblage of more than 150 species including 16 type-locality (Favreau et al. 2014 and personal comm. of the AAMCG). Most of them are micromineralization (e.g. galeaclolusite [$Al_6(AsO_4)_3(OH)_9(H_2O)_4]\cdot 8H_2O$]) (Grey et al. 2021). The primary mineralization is mostly represented by tennantite and galena, with some occurrences of chalcopyrite, rarely sphalerite and pyrite (Chiappero 1993; Guillemin 1952). Secondary sulfides are limited to chalcocite, digenite and covellite. Secondary minerals cover a wide range among sulfates, carbonates and arsenates. The mining site is separated in two blocks by an E-W vertical fault (Figure 1A) with the southern mine hosting Cu-As mineralization (Figure 1B), while the northern mine mainly consists in Cu-As-Pb(-Zn) mineralization (Figure 1C). The first written records of the Cap Garonne mines date back to the 17th century, although the first mining license was not granted until the mid-19th century. The mines were never continuously exploited and were closed in 1917 after about 30 years of exploitation, mainly due to the fluctuation of copper price and other new deposit types with better grades. During this period, 30,000 tons of Cu ore (5 wt. %) and 500 tons of Pb ore (7-16 wt. %) were produced (Favreau et al. 2014).

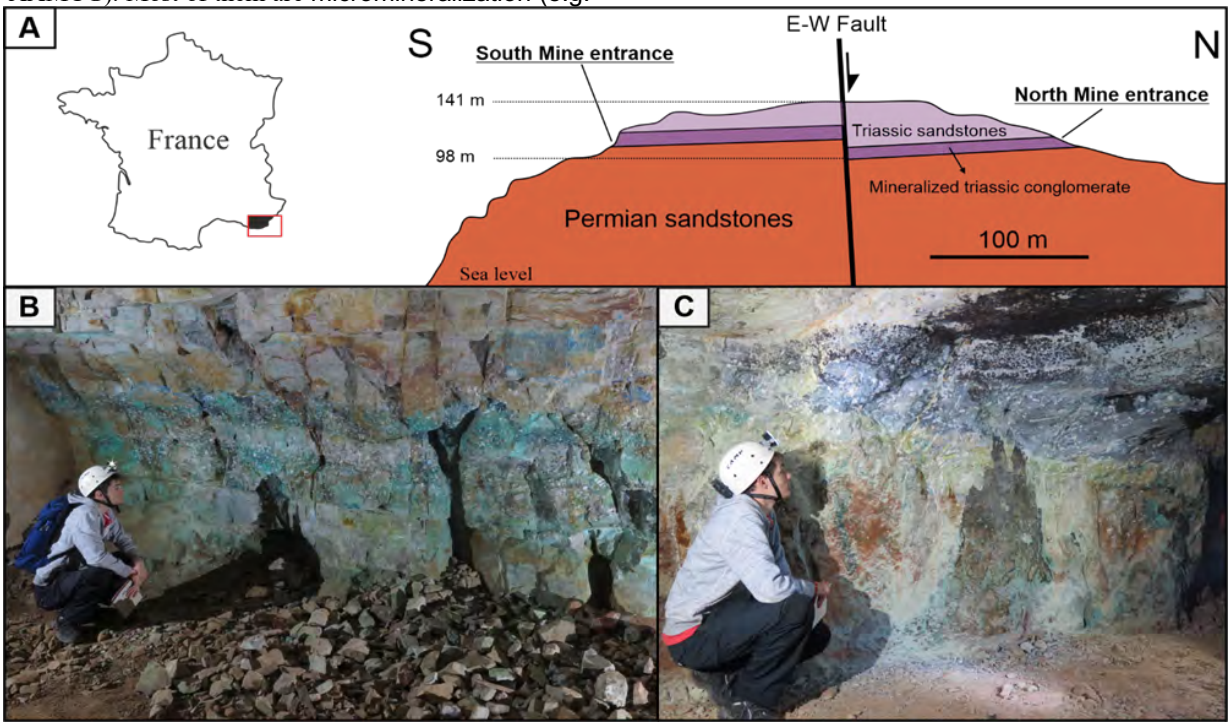


**Figure 1.** (A) Location and geological section of the Cap Garonne mine (modified from Guillemin 1952; Favreau et al. 2014). (B) Southern mine. (C) Northern mine.

## 2 Methodology

Most samples were collected from both sides of the Cap Garonne old mine. Permian and Triassic host rocks mostly come from the Colle Noire Massif. The analyses used to study these samples include X-ray diffraction (XRD), whole rock (46 samples) geochemistry (major, minor and trace elements), scanning electron microscopy (SEM), transmission and reflection light microscopy.

## 3 Results

### 3.1 Host (fresh) rocks

P-Tr transition rocks consist of sandstones, siltstones and several lenses of conglomerate with (pluri)centimetric quartz pebbles. The fresh Early Triassic conglomerate (Port-Issol Fm.) locally hosts the Cap Garonne mineralization and shows a carbonate cement. The overlying reddish Permian sandstone and the entire sandy Triassic sequence have a decreasing carbonate content compared to the P-Tr conglomerate. Carbonates, mostly calcite, also occur as veins and cm-size geodes in Permian rocks. Major mineral phases observed in these host rocks are quartz, muscovite, calcite, feldspars and barite.

### 3.2 Southern mine

The southern mine exposes Cu-As mineralization with tennantite as the most abundant primary sulfide, mostly in the conglomerate and generally associated with malachite and azurite (Figure 2A). Secondary mineralization is observed as incrustation and stratabound fill in (micro)fractures (Figure 2B) or within the intergranular volume of the rock.

Secondary copper sulfides phases are digenite [$Cu_9S_5$], chalcocite [$Cu_2S$], covellite, djurleite [$Cu_{31}S_{16}$], generally surrounding tennantite. Other minerals such as mansfieldite [$AlAsO_4.2H_2O$] antlerite [$Cu_3(SO_4)(OH)_4$] brochantite, pharmacoalumite [$KAl_4(AsO4)_3(OH)_4.6.5H_2O$], (arseno)gorceixite [$BaAl_3(AsO_4,PO_4)_2(OH)_5.H_2O$], camerolaïte [$Cu_4Al_2(HSbO_4,SO_4)(CO_3)(OH)_{10}.2H_2O$] and barite are also observed. Olivenite can be observed in tennantite, with small concretions of cornwallite or cornubite (polymorphs of [$Cu_5(AsO_4)_2(OH)_4$]) or even associated with malachite and azurite veins (Figure 2B). Pluri-centimetric clay levels can also be observed in the galleries and often contain azurite veins and pebbles.

### 3.3 Northern mine

The north mine includes both Pb-Zn and Cu-As mineralization (Figure 3). The layout of the mineralization is the same as to the southern mine. Galena and sphalerite also are primary sulfides in addition to tennantite. Rare Co- and Ni-bearing sulfides can also be observed such as gersdorffite or Ni-rich cobaltite [(Ni,Co)AsS].Secondary mineralization is also directly associated with primary sulfides and is made of anglesite, mimetite [$Pb_5(AsO_4)_3Cl$] and other Cu-As minerals observed also in the southern mine. Most Pb-Cu arsenates (Figure 3) are recognized as thin crusts close to the Pb zone. Rare erythrite [$Co_3(AsO_4)_2.8H_2O$] is identified in Co-bearing pocket, as micromineralization. Iron oxides are observed as crusts or veins filling generally intersecting the Cu-As-Pb-Zn mineralization.

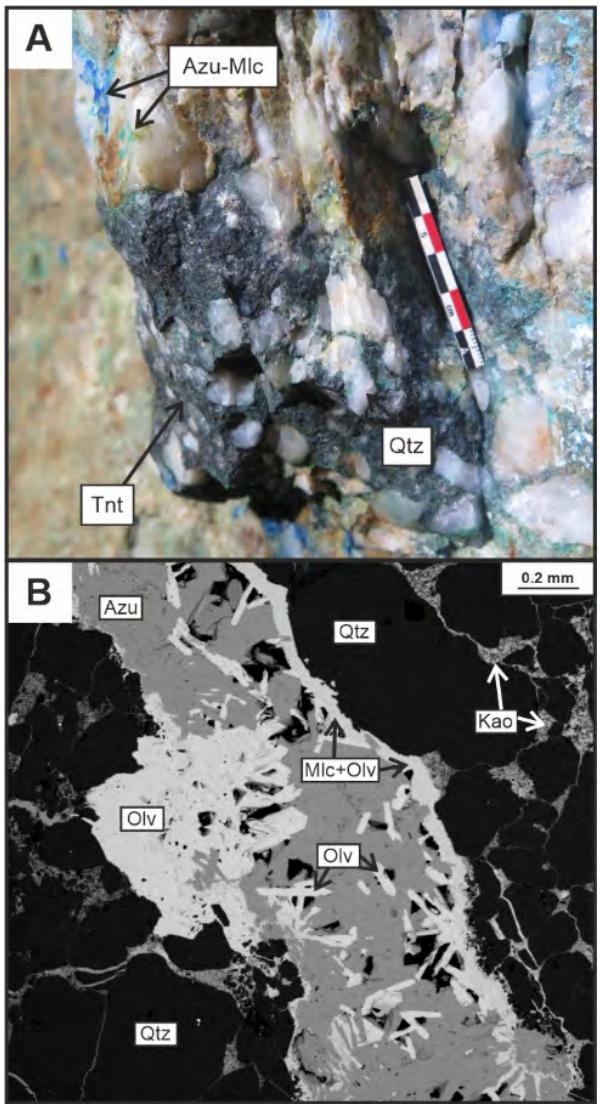


**Figure 2.** (A) Tennantite (Tnt) and azurite-malachite (Azu-Mlc) mineralization in P-Tr conglomerate, southern mine. (B) SEM microphotographs of mineralized vein of azurite, olivenite (Olv) and malachite, with small veins fill of kaolinite (Kao).

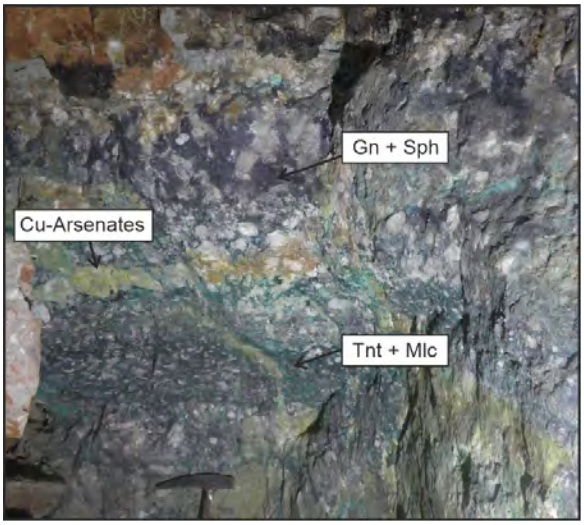


**Figure 3.** Association of Cu-As and Pb-Zn mineralization in north mine (Gn = Galena, Sph = Sphalerite).

## 4 Weathering processes

### 4.1 Paragenesis

The paragenetic sequence for the Cu-As zone is sulfides I → sulfides II → arsenates (Cu-depleted) → Cu-arsenates → sulfates → carbonates. The oxidation of tennantite with $O_2$-rich meteoric water allows the formation of secondary Cu-sulfides surrounding the primary sulfide. Cu-depleted arsenates such as mansfieldite, arsenogorceixite or pharmacoalumite are formed after sulfides II and prior to Cu-arsenates filling, such as olivenite (Figure 4). This suggests that early arsenates incorporate cations from the host rocks (K, Ba, Al, Fe), instead of Cu, at this point crystallized as secondary sulfides. Olivenite precipitation occurs under less acidic and more oxidizing conditions, which involves a neutralization of acidic fluids with in-situ phyllosilicates. With tennantite still being oxidized, olivenite formation leads to an excess of $Cu^{2+}$ in solution and allows local precipitation of secondary Cu arsenates, such as cornubite or cornwallite located between tennantite and olivenite. Accumulation of sulfate potentially leads to the precipitation of brochantite or antlerite after the first neutralization episode. Finally, dissolution of the carbonated cement in the fluids completely neutralizes the system, and precipitates malachite and azurite in the mineralized levels as a result.

Regarding the Pb-Zn zone, the paragenetic sequence is quite similar but quite simpler. Galena oxidizes into an anglesite matrix which is stable under a wide range of pH and Eh. This prevents further oxidation of galena and sphalerite. The neutralization by carbonate also allows the formation of cerussite. However, as few Zn supergene mineralisation (e.g. adamite [$Zn_2AsO_4(OH)$]) is observed, it is suggested that Zn is located as substitution in Cu secondary minerals.

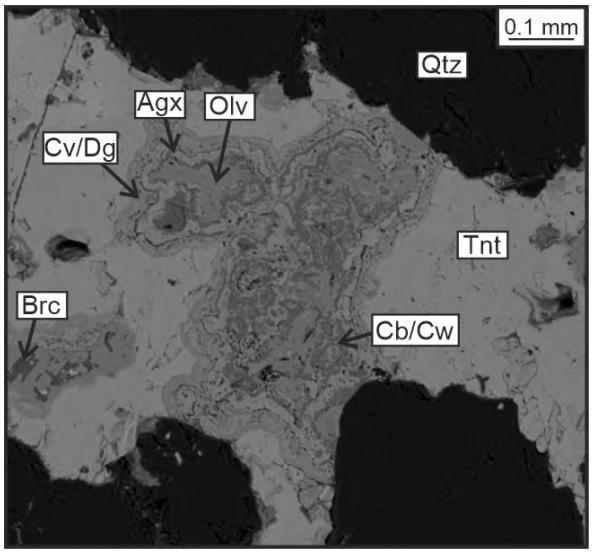


**Figure 4.** SEM microphotographs with tennantite and associated weathering phases (Cb/Cw = cornubite, cornwallite, Agx = arsenogorceixite, Cv/Dg = covellite, digenite).

### 4.2 Supergene model

At Cap Garonne the Permo-Triassic transition starts with maximum 8m-thick conglomerate intersected by several clay lenses (Durand 2008). Then hydrothermal activity with S-enriched mesothermal fluids allows the formation of two separate levels: the lower level with mostly tennantite while the upper level contains galena with some sphalerite and tennantite. These sulfides could possibly be related to the Permian volcanic activity of the Colle Noire Massif (Vuillet 1995).

Once the protore formed, weathering processes can start with the percolation of meteoric fluids through fractures and porosity. Those fluids lead to oxidation of sulfides and release acidic fluids rich in various metals. This process may be exacerbated by the longer residence time of meteoric fluids due to the presence of clay levels. Secondary minerals then precipitate according to the sequence mentioned in section 4.1, with various patterns in the northern or southern mine. The structural offset between the northern and southern mines (Figure 1), combined with the absence of any Pb-Zn mineralization in the southern mine suggets an initial erosion of the Pb-Zn level south of the E-W fault.

The precise age of the secondary mineralization is difficult to estimate but probably belongs to the major periods of weathering in the area, during early Cretaceous, Eocene and late Oligocene (Hautmann and Lippolt 2000, Dekoninck et al. 2019). However, the deposit is located a few meters below the surface and then ongoing weathering is observed and lead to some new (micro)mineralization.

## 5 Conclusion

At Cap Garonne the polymetallic character of the protore is at the origin of a very diversified secondary mineralization. Southern mine is characterized by a

Cu-As mineralization while the northern mine also shows Pb-Zn minerals. The mineralization sequences are quite similar in both parts of the mine and show a pattern as follows: (i) sulfides I, (ii) sulfides II, (iii) arsenates, sulfates and sulfo-arsenates, (iv) carbonates. Neutralization process mainly comes from carbonates from the cement of the P-Tr conglomerate. Secondary mineralization occurs in the vicinity of the primary sulfides which supports a very low mobility of the metals and thus reduces the potential environmental issues.

## Acknowledgements

We thank the AAMCG (Association des Amis de la Mine du Cap Garonne) for access to the mine and sampling.

## References

Chiappero P-J (1993) Les arséniates de cuivre naturels : Systèmatique et approche des conditions de genèse par les synthèses. Applications au gisement plumbocuprifère de Cap Garonne (Var, France). Thèse de doctorat, Université d'Orléans.

Dekoninck A, Monié P, Blockmans S, et al (2019) Genesis and 40Ar/39Ar dating of K-Mn oxides from the Stavelot Massif (Ardenne, Belgium): Insights into Oligocene to Pliocene weathering periods in Western Europe. Ore Geol Rev 115:103191

Durand M (2008) Permian to Triassic continental successions in southern Provence (France): An overview. Boll della Soc Geol Ital 127:697–716.

Favreau G, Galéa-Clolus V, Brun P, Cotte J-P, Bono H, Merlin T, Monniot P (2014) Cap Garonne. Association Française de Microminéralogie, France.

Grey IE, Favreau G, Mills SJ, et al (2021) Galeaclolusite, $[Al_6(AsO_4)_3(OH)_9(H_2O)_4]\cdot 8H_2O$, a new bulachite-related mineral from Cap Garonne, France . Mineral Mag 85:142–148.

Guillemin C (1952) Etude minéralogique et métallogénique du gîte plumbocuprifère du Cap Garonne (Var). Bull la Société française Minéralogie Cristallogr 75:70–160.

Hautmann S, Lippolt HJ (2000) $^{40}Ar/^{39}Ar$ dating of central European K-Mn oxides - a chronological framework of supergene alteration processes during the Neogene. Chem Geol 170:37–80.

Vuillet J (1995) Etude géologique du Massif de la Colle Noire, à l'Est de Toulon. Université des sciences de Marseille, Marseille.

# A hydrous Mg silicate Ni deposit within the oxide type Moa Bay laterite mining district, eastern Cuba

**Cristina Villanova-de-Benavent[1], Esperança Tauler[1], Diego Domínguez-Carretero[1], Cristina Domènech[1], Salvador Galí[1], Joaquín A. Proenza[1]**

*[1]Departament de Mineralogia, Petrologia i Geologia Aplicada, Facultat de Ciències de la Terra, Universitat de Barcelona (UB), Spain*

**Abstract.** Moa Bay is a world-class Ni laterite mining district with reserve estimates of 53.4 Mt at 1.16 % grade Ni. The vast majority of the deposits belong to the oxide type, and are mined for their Ni-bearing Fe-oxyhydroxides in the oxide zone. One exception is Yamanigüey which can be classified as a hydrous Mg silicate Ni-laterite deposit. The study of a weathering profile of this deposit reveals that it is characterised by a thick saprolite horizon containing secondary Ni-bearing serpentines with 0.6 to 4.8 wt.% NiO, crosscut by garnierite veins. Garnierites from Yamanigüey consist of mixtures between serpentine- and talc-like particles, with 10.9-32.5 wt.% NiO, and Ni being concentrated in the talc-dominant garnierites. The garnierite veins display oscillatory compositional zoning, with lower Mg contents towards the centre of the vein, which may suggest that the precipitation of garnierites is multi-episodic.

## 1 Introduction

Ni-Co laterite deposits are regoliths formed after chemical and mechanical weathering of ultramafic rocks under tropical and subtropical climates (e.g. Elias 2002). Recently, Ni-laterites surpassed sulphide ores as the main source of Ni, and currently account for 60% of Ni worldwide resources (USGS 2021). The Caribbean area is a major host of Ni-laterite occurrences, and only Cuba represents up to 6% Ni of the worldwide reserves (USGS, 2021). In particular, Eastern Cuba hosts one of the largest Ni-laterite provinces in the world, and includes Moa Bay, Pinares de Mayarí and Nicaro (Lewis et al. 2006 an references therein). Most of the Ni-laterite deposits at the Moa Bay mining district belong to the oxide type (see Brand et al. 1998), but a few present features typical of the hydrous Mg silicate type, one of them being the Yamanigüey deposit (Figure 1). Reserve estimates at Moa Bay are at least 53.4 Mt at 1.16 % Ni, while provable and proven reserves at Yamanigüey are 0.9 Mt at 1.33 % Ni (CSA Global Report Nº R117 2019).

Laterite deposits in Eastern Cuba were first mined in the early 1940s. Since then, different companies, including the Cuban government's state mining company, exploited other concessions around the city of Moa. Nowadays, operations are led by Moa JV (a 50:50 partnership between Sherritt and General Nickel Company S.A. of Cuba). Despite mining activities are focused on the oxide zone, there has been exploration in the saprolite zone since the early 1980s (CSA Global Report Nº R117 2019).

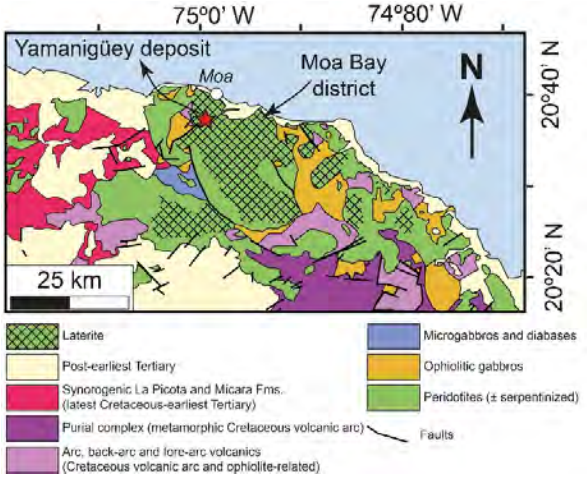


The aim of this work is to study the geochemistry, mineralogy, and the Ni distribution across the Ni-bearing phases along a Ni-laterite profile of the hydrous Mg silicate type Yamanigüey deposit.

**Figure 1.** Geological map of the Moa Bay Ni-Co laterite mining district within the Moa-Baracoa massif (Eastern Cuba). The red star marks the location of the Yamanigüey deposit.

## 2 Geological Setting

The Moa Bay Ni-laterites formed after exposure and weathering of the ultramafic rocks of the Cretaceous Mayarí-Baracoa Ophiolite Belt (MBOB; Lewis et al. 2006; Iturralde-Vinent et al. 2016; Proenza et al. 2018) in Eastern Cuba. This ophiolite belt can be divided into two massifs: i) Mayarí Cristal (to the West), and ii) Moa-Baracoa (to the East), neither of them showing a complete ophiolitic sequence (Proenza et al. 1999). The Moa-Baracoa massif is 2.2 km thick, and consists of partly serpentinised harzburgite tectonites with minor dunite. Plagioclase-bearing dunites, wehrlites, lherzolites and pyroxenites have also been described (Marchesi et al., 2006). Interestingly, the Moho transition zone (MTZ) is clearly preserved. The top of the sequence is composed of layered and isotropic gabbros, pillow basalts with a back-arc affinity, chert and limestone; but it is tectonically over-thrusted by the mantle sequence (Proenza et al. 1999, 2006, 2018; Marchesi et al. 2006, 2007).

Laterisation of the Moa Bay serpentinites began in the Miocene and is still ongoing (Lewis et al. 2006 and references therein). Ni-laterite deposits in the

Moa Bay district include Moa Oriental, Moa Occidental, Punta Gorda, Yagrumaje, Camarioca Norte, Camarioca Sur, La Delta, Cantarrana, Santa Teresita, Zona A, Zona Central, Playa la Vaca, Zona Septentrional and Yamanigüey (Lavaut 1998; CSA Global Report Nº R117 2019).

Yamanigüey is part of the Moa Occidental deposit, and is located near the city of Moa (Holguín province), in Eastern Cuba (Figure 1) (Marrero-Leyva et al., 2006). It extends over 1.2 $km^2$, and is located at 200 masl forming a stepped plateau with altitudes decreasing towards the northeast.

## 3. Analytical methods

Twenty samples were collected every 50 cm along one 10 m-long profile from Yamanigüey. Whole rock analyses were carried out at Actlabs Laboratories (Ontario, Canada) with the analytical packages "4C-Laterites" (fusion X-ray fluorescence-XRF) and "4-Lithores" (fusion inductively coupled plasma emission mass spectrometry-ICPMS).

X-ray diffraction analyses were performed on a fraction of the samples ground with agate mortar and pestle, in a PANalytical X'Pert PRO MPD Alpha1 powder diffractometer in Bragg-Brentano h/2h geometry of 240 mm of radius, nickel filtered Cu Ka radiation (k = 1.5418 Å), with 45 kV–40 mA and a sample spinning time of 2 revolutions per second. A variable divergence slit kept an area illuminated constant (10 mm), a mask was used to limit the length of the beam to 12 mm, and axial divergence Soller slits of 0.04 radians were used. The samples were scanned from 4 to 80° 2θ with a step size of 0.017° and measuring time of 50 seconds per step, using an X'Celerator detector (active length = 2.122°).

Polished thin sections were prepared and examined under a petrographic polarised light microscope at the Universitat de Barcelona, and using an Environmental Scanning Electron Microscope (SEM) Quanta 200 FEI, XTE 325/D8395 equipped with an INCA Energy 250 Energy Dispersive Spectrometry (EDS) microanalysis system at 20 kV and 5 nA. Finally, quantitative electron microprobe analyses (EMPA) on Ni-bearing minerals were obtained in a JEOL JXA-8230 equipped with five Wavelength Dispersive Spectrometers (WDS), at 15 kV and 15 nA, with a 1-2 µm beam diameter and 10-30 s counting time per element. The standards used were: wollastonite (Si), corundum (Al), orthoclase (K), hematite (Fe), periclase (Mg), rhodonite (Mn), NiO (Ni), metallic Co (Co), rutile (Ti), $Cr_2O_3$ (Cr). XRD, SEM and EMPA analyses were carried out at the Centres Científics i Tecnològics of the Universitat de Barcelona (CCiT-UB).

## 4. Results and discussion

### 4.1. Whole rock geochemistry

The sampled profile consists of, from the bottom to the top: i) a serpentinised bedrock (8.5-10.0 m), ii) a saprolite zone (3.0-8.5 m), and iii) an oxide zone (0-3.0 m).

The bedrock is a dark green, heavily fractured, massive peridotite with a moderate degree of serpentinisation. It contains 36-39 wt.% $SiO_2$, 37-38 wt.% MgO, 7-8 wt.% $Fe_2O_3$, <2 wt.% $Al_2O_3$, <1 wt.% MnO, <0.3 wt.% NiO, and 95-110 ppm Co.

The saprolite is a darker green, cohesive rock towards the bedrock that evolves to a dull green softer material towards the top of the horizon. It is crosscut by numerous small silica and garnierite veinlets. Its whole rock composition is 35-42 wt.% $SiO_2$, 30-38 wt.% MgO, 8-13 wt.% $Fe_2O_3$, <10 wt.% $Al_2O_3$, <1 wt.% MnO, 0.3-3.6 wt.% NiO, and 60-110 ppm Co.

The oxide zone consists of brownish yellow loose material made up of Fe oxyhydroxides with small Mn oxyhydroxide and silica veinlets. This horizon is characterised by remarkable Ni (0.7-2.1 wt.% NiO), and Co contents (up to 0.6 wt.% CoO), and also 36-71 wt.% $Fe_2O_3$, 6-38 wt.% $Al_2O_3$, <3 wt.% MnO, 1-5 wt.% $SiO_2$, and <2 wt.% MgO.

### 4.2. Mineralogy and petrography of the laterite profile

The bedrock is composed of olivine and minor orthopyroxene, both replaced and/or surrounded by serpentine, with lesser amounts of subhedral Cr-spinel and magnetite. Serpentine yields less than 0.5 wt.% NiO.

The saprolite horizon mainly consists of primary serpentine (Ni-poor, hereafter "serpentine I"), secondary serpentine (Ni-rich, hereafter "serpentine II"), with smaller amounts of magnetite, Cr-spinel, garnierite and Mn-Ni-Co oxyhydroxides. Serpentine is the main constituent, and only a few isolated, rounded relicts of olivine and pyroxene may be found within the serpentine matrix. Serpentine occurs as veins crosscutting the primary bedrock mineralogy (the typical mesh texture in serpentinised ultramafic rocks), and as pseudomorphs of olivine and pyroxene (Figure 2).

It must be noted that serpentine II predominates over serpentine I in the saprolite horizon. The average structural formula of serpentine I from Yamanigüey is $Mg_{2.60}Fe_{0.28}Ni_{0.01}Al_{0.03}Si_{2.02}O_5(OH)_4$, with Ni contents below 0.45 wt.% NiO, and between 3.55 and 12.30 wt.% FeO. In contrast, the average structural formula of serpentine II is $Mg_{2.30}Fe_{0.47}Ni_{0.08}Al_{0.04}Si_{2.03}O_5(OH)_4$, and Ni ranging from 0.56 to 4.81 wt.% NiO and Fe from 5.26 to 28.58 wt.% $Fe_2O_3$. As stated by Golightly & Arancibia (1979), Pelletier (1996) and in Villanova-de-Benavent et al. (2017), serpentine II is enriched in Ni and Fe with respect to serpentine I, however, serpentine II from Yamanigüey contains more Fe than the secondary serpentines reported in these works. Besides, serpentine II is less stoichiometric than serpentine I, which has been linked to vacancies in the octahedral layer, possibly due to the

substitution of Mg by $Fe^{3+}$ (Golightly & Arancibia, 1979; Villanova-de-Benavent et al. 2017). In addition, long and thin magnetite aggregates

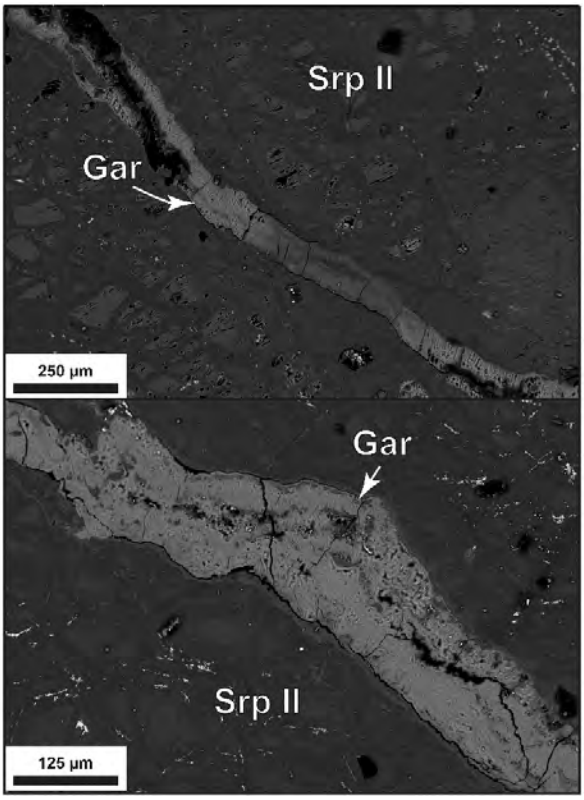


frequently occur along some of the serpentine veinlets (remnants of the primary serpentine mesh of the bedrock). There are also rounded subhedral, partially altered, Cr-spinel grains.

**Figure 2.** Backscattered electron (BSE) images of serpentine II (Srp II) veinlets and pseudomorphs after olivine and pyroxene, crosscut by garnierite (Gar) veins.

The most notable feature in this horizon is the presence of micrometre-thick garnierite veins that crosscut the serpentine matrix (Figure 2). These garnierites yield 39.56-52.53 wt.% $SiO_2$, 10.92-32.49 wt.% NiO and 0.52-11.0 wt.% $Fe_2O_3$. They can be classified as mixtures of serpentine and talc-like (a.k.a. *kerolite-pimelite*) garnierites (Figure 3). As observed in Falcondo, the talc-dominated garnierites contain the highest Ni (Figure 3, Villanova-de-Benavent et al. 2016). These veinlets display an oscillatory compositional zoning, with higher Ni contents towards the edges of the vein, and higher Mg contents towards the centre of the vein (Figure 4). This suggests that the precipitation of garnierites is multi-episodic (as in Falcondo, see Villanova-de-Benavent et al. 2014) and that the composition of the percolating aqueous solutions may vary in short periods of time.

The Mn-Ni-Co oxy-hydroxides of the saprolite horizon occur as fibrous crystals overgrowing garnierite (Domínguez-Carretero et al. 2023).

The oxide zone is mostly composed of goethite with minor hematite, gibbsite, Cr-spinel, maghemite, and Mn-Co-Ni oxyhydroxides. Dominant goethite forms fine-grained aggregates with very little to no cohesion and remarkable porosity. It may occur as botryoidal aggregates or as pseudomorphs of the primary bedrock minerals (e.g., olivine). The mineral chemistry of goethite reveals NiO contents up to 0.81 wt.%. Subhedral Cr-spinel relicts, and small

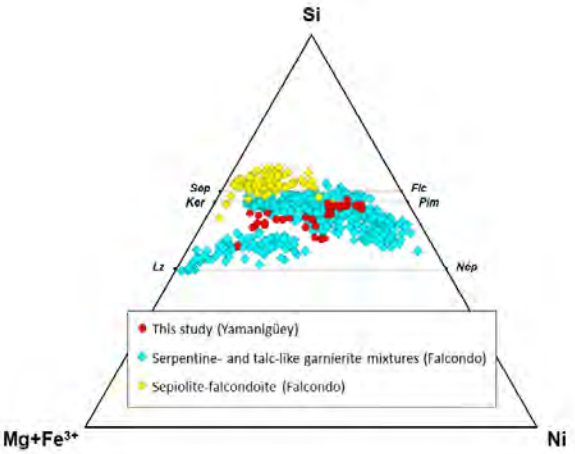


maghemite and hematite grains are found within the goethite matrix. Mn-Ni-Co oxyhydroxides in the oxide zone occur mainly as colloform aggregate grains (Domínguez-Carretero et al. 2023).

**Figure 3.** Ternary plot representing Mg, Ni and Si in garnierites from Yamanigüey obtained by EMPA (cation proportions calculated on the basis of 100 oxygens). Data from the Falcondo mining district (Villanova-de-Benavent et al. 2014) is shown for comparison.

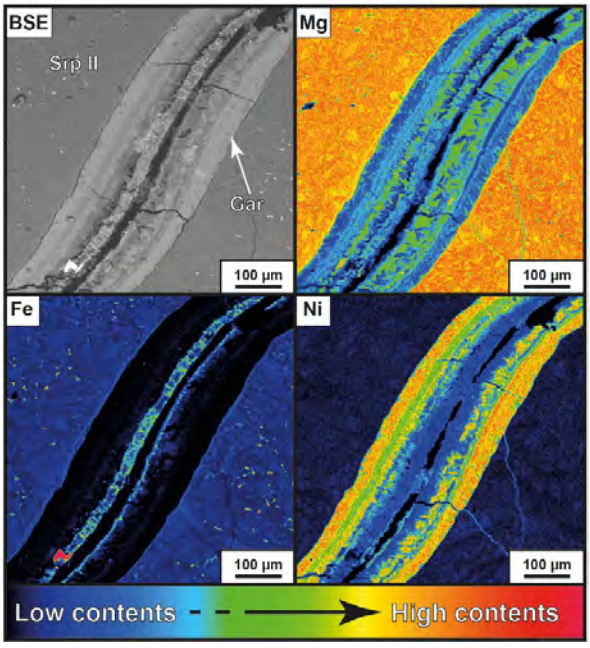


**Figure 4.** Garnierite (Gar) vein crosscutting serpentine II (Srp II) in a sample from the saprolite horizon of the Yamanigüey deposit, Moa Bay (clock-wise from the upper left): BSE image; and Mg, Ni and Fe X-ray element maps, obtained with EMPA.

## 5. Final remarks

The studied Ni-laterite profile from Yamanigüey is similar to the hydrous Mg silicate type profiles that have been described in the Falcondo mining district (Dominican Republic, e.g. Villanova-de-Benavent et al. 2017; Tauler et al. 2017) and the ones in New Caledonia (e.g. Wells et al. 2009), in terms of thickness of the saprolite horizon, element distribution along the profile, mineralogy and chemical composition of Ni ores. In fact, it is more similar to those than to the majority of Ni-laterite deposits at Moa Bay, only a few kilometres away. For this reason, more data on the Yamanigüey deposit is necessary in order to shed light on the factors leading to the formation of Ni-Fe-oxyhydroxide- versus Ni-silicate-dominated profiles in the Moa Bay mining district.

## Acknowledgements

This research was financially supported by Grant PID 2019-105625RB-C21 funded by MCIN/AEI/10.13039/501100011033 and by Grant 2021 SGR 00239 funded by Gestió d'Ajuts Universitaris i de Recerca de Catalunya. Additional funding was provided by a "Ayudas predoctorales 2020" number PRE 2020-092140 PhD grant to DD-C by the Spanish Ministry of Science and Innovation.

## References

Brand NW, Butt CRM, Elias M (1998) Nickel laterites: classification and features. AGSO J Australian Geol Geoph 17:81–88.

CSA Global Report Nº R117 (2019). Technical Report "Moa Nickel Project, Cuba", NI 43-101. Available at: www.csaglobal.com (Accessed 11.03.2023).

Domínguez-Carretero, D.; Villanova-de-Benavent, C.; Domènech, C.; Proenza, J.A. (2023). Mn-Ni-Co oxy-hydroxides from Ni-Co laterites of Moa-Bay mining district, eastern Cuba. This volume.

Elias, M. (2002). Nickel laterite deposits – geological overview, resources and exploitation. Centre for Ore Deposit Research, University of Tasmania, Special Publication, 4, 205-220.

Golightly, J.P., Arancibia, O.N. (1979). The chemical composition and infrared spectrum of nickel- and iron-substituted serpentine form a nickeliferous laterite profile, Soroako, Indonesia. Canadian Mineralogist 17, 719–728.

Iturralde-Vinent, M.A., García-Casco, A., Rojas-Agramonte, Y., Proenza, J.A., Murphy, J.B., Stern, R.J. (2016). The geology of Cuba: A brief overview and synthesis. GSA Today 26, 4-10.

Lavaut, W. (1998). Tendencias geológicas del intemperismo de las rocas ultramáficas en Cuba oriental. Revista Minera de Geología 15, 9-16.

Lewis, J.F., Draper, G., Proenza, J.A., Espaillat, J., Jimenez. J. (2006). Ophiolite- Related Ultramafic Rocks (Serpentinites) in the Caribbean Region: A Review of their occurrence, Composition, Origin, Emplacement and Nickel Laterite Soils. Geologica Acta 4, 237-263.

Marchesi, C., Garrido, C.J., Godard, M., Proenza, J.A., Gervilla, F., Blanco-Moreno, J. (2006). Petrogenesis of highly depleted peridotites and gabbroic rocks from the Mayarí-Baracoa Ophiolitic Belt (eastern Cuba). Contributions to Mineralogy and Petrology 151(6),717.

Marchesi, C., Garrido, C.J., Bosch, D., Proenza, J.A., Gervilla, F., Monié, P., Rodriguez-Vega, A. (2007). Geochemistry of Cretaceous magmatism in eastern Cuba: recycling of North American continental sediments and implications for subduction polarity in the Greater Antilles Paleo-arc. Journal of Petrology 48, 1813–1840.

Marrero-Leyva, N. (2006). Caracterización Mineralógica del Perfil Saprolítico del Depósito de Lateritas Niquelíferas Yamanigüey. Diploma de Estudios Avanzados, Universidad de Barcelona, 56 pp.

Pelletier, B (1996). Serpentines in nickel silicate ore from New Caledonia. Australasian Institute of Mining and Metallurgy Publication Series – Nickel Conference, Kalgoorlie (Western Australia) 6/96:197–205.

Proenza, J.A., Díaz-Martínez, R., Iriondo, A., Marchesi, C., Melgarejo, J.C., Gervilla, F., Garrido, C.J., Rodríguez-Vega, A., Lozano-Santacruz, R., Blanco-Moreno, J.A. (2006). Primitive island-arc Cretaceous volcanic rocks in eastern Cuba: the Téneme Formation. Geologica Acta 4, 103-121.

Proenza, J.A., Gervilla, F., Melgarejo, J.C., Bodinier, J.L. (1999). Al- and Cr-rich chromitites from the Mayarí-Baracoa ophiolitic belt (eastern Cuba); consequence of interaction between volatile rich melts and peridotites in suprasubduction mantle. Economic Geology 94, 547-566.

Proenza, J.A., González-Jiménez, J.M., Garcia-Casco, A., Belousova, E., Griffin, W.L., Talavera, C., Rojas-Agramonte, Y., Aiglsperger, T., Navarro-Ciurana, D., Pujol-Solà, N., Gervilla, F., O'Reilly, S.Y., Jacob, D.E. (2018). Cold plumes trigger contamination of oceanic mantle wedges with continental crust-derived sediments: Evidence from chromitite zircon grains of eastern Cuban ophiolites. Geoscience Frontiers 9(6), 1921–1936.

Rojas-Agramonte, Y., Garcia-Casco, A., Kemp, A., Kröner, A., Proenza, J.A., Lázaro, C., Liu, D. (2016). Recycling and transport of continental material through the mantle wedge above subduction zones: A Caribbean example. Earth and Planetary Science Letters 436, 93–107.

Tauler, E., Lewis, J.F., Villanova-de-Benavent, C., Aiglsperger, T., Proenza, J.A., Domènech, C., Gallardo, T., Longo, F., Galí, S. (2017). Discovery of Ni-smectite rich saprolite at Loma Ortega, Falcondo mining district (Dominican Republic): geochemistry and mineralogy of an unusual case of 'hybrid hydrous Mg silicate-clay silicate' type Ni-laterite. Mineralium Deposita 52, 1011-1030.

USGS (2021). Mineral Commodity Summaries 2021: US Geological Survey; US Geological Survey: Reston, VA, USA; 200p.

Villanova-de-Benavent, C., Proenza, J.A., Galí, S., García-Casco, A., Tauler, E., Lewis, J.F., Longo, F. (2014). Garnierites and garnierites: textures, mineralogy and geochemistry of garnierites in the Falcondo Ni-laterite deposit, Dominican Republic. Ore Geology Reviews 58, 91–109.

Villanova-de-Benavent, C., Nieto, F., Viti, C., Proenza, J.A., Galí, S., Roqué-Rosell, J. (2016). Ni-phyllosilicates (garnierites) from the Falcondo Ni-laterite deposit (Dominican Republic): Mineralogy, nanotextures, and formation mechanisms by HRTEM and AEM. American Mineralogist 101, 1460-1473.

Villanova-de-Benavent, C., Domènech, C., Tauler, E., Galí, S., Tassara, S., Proenza, J.A. (2017). Fe–Ni-bearing serpentines from the saprolite horizon of Caribbean Ni-laterite deposits: new insights from thermodynamic calculations. Mineralium Deposita 52, 979–992.

Wells, M.A., Ramanaidou, E.R., Verrall, M., and Tessarolo, C. (2009). Mineralogy and crystal chemistry of "garnierites" in the Goro lateritic nickel deposit, New Caledonia. European Journal of Mineralogy, 21, 467–483.

# 17th Biennial SGA Meeting

ETH Zurich, Switzerland

August 28 – September 1